| Contractor Document Information | | | |
|---|---|---|---|
| **Contractor Name** | MetOceanWorks | | |
| **Contractor Doc No** | SSE_C00002_R03_Metocean_Data_Overview | **Contractor Doc Rev** | 03 |
| **Document Title** | Metocean Data Overview, Arklow Bank Offshore Wind Farm | | |

| **Document Number:** |
|---|
| **LF100034-ENG-MO-REP-0003 - Metocean Modelling Report** |

| Revision Information | | | | | |
|---|---|---|---|---|---|
| **Rev** | **Document Issue Status** | **Date** | **Originator** | **Checker** | **Approver** |
| 03 | Final approved by client | 23.09.2021 | | | |
| 02 | Updated to include latest measurements for validation. | 13.08.2021 | | | |
| 01 | Draft | 13.04.2021 | | | |
| | | | | | |

| Acceptance of Contractor Document | | | |
|---|---|---|---|
| **Code** | **Description of Code** | **SSE Designated Signatory** | **Date** |
| 1 | Accepted | Jacob Royle<br>Andrew Berkeley | 23.09.2021 |
| 2 | Accepted with Comments | | |
| 3 | Rejected | | |
| 4 | For Information Only | | |

MetOceanWorks

# Metocean Data Overview

# Arklow Bank Offshore Wind Farm

23 September 2021

MetOceanWorks Reference:

SSE_C00002_R03_Metocean_Data_Overview

Commercial in Confidence

Andrew Watson MSc CSci CMarSci MIMarEST

Senior Metocean Consultant & Director

andrew.watson@metoceanworks.com

Contact +44 (0)7763 896635

MetOceanWorks Ltd is Registered in England and Wales, Company Number 8078702

| Revision | Description | Prepared | Reviewed | Date |
|---|---|---|---|---|
| 03 | Final | Andrew Watson | | 23 September 2021 |
| 02 | Draft | Dave Quantrell<br>Andrew Watson | Andrew Watson | 13 August 2021 |
| 01 | Draft | Dave Quantrell<br>Andrew Watson<br>Jamie Hernon | Andrew Watson | 13 April 2021 |

## Disclaimer

MetOceanWorks has prepared this report for the sole use of the client and for the intended purposes as stated in the agreement between MetOceanWorks and the client under which this report was completed. MetOceanWorks has exercised due and customary care in preparing this report but has not, save as specifically stated, independently verified information provided by others. No other warranty, express or implied, is made in relation to the contents of this report. The use of this report, or reliance on its content, by unauthorised third parties without written permission from MetOceanWorks shall be at their own risk, and MetOceanWorks accepts no duty of care to such third parties. Any recommendations, opinions or findings stated in this report are based on facts and circumstances as they existed at the time the report was prepared. Any changes in such facts and circumstances may adversely affect the recommendations, opinions or findings contained in this report.

# Table of contents

1 Definitions ..... 15
1.1 Units and Conventions ..... 15
1.2 Glossary of commonly used metocean terms ..... 15
2 Introduction ..... 17
2.1 Background ..... 17
2.2 Report Structure ..... 18
3 Bathymetry and Coastline ..... 19
3.1 Bathymetry ..... 19
3.2 Bathymetry Datum Conversion ..... 21
3.3 Coastline ..... 22
4 Winds ..... 23
4.1 Introduction ..... 23
4.2 Modelled Wind Data ..... 23
4.3 Measured Wind Data ..... 24
4.4 Model Validation ..... 25
5 Hydrodynamics ..... 34
5.1 Measured Hydrodynamic Data ..... 34
5.1.1 Measured Current Profiles ..... 35
5.2 Modelling Software ..... 35
5.3 Model Boundary Conditions and Spatial Extent ..... 35
5.4 Model Sensitivity Testing ..... 38
5.4.1 Mesh Resolution ..... 38
5.4.2 Bed Resistance ..... 44
5.5 Final Model Parameter Settings ..... 44
5.6 Hindcast Uniformity ..... 44
5.7 Model Validation ..... 45
6 Waves ..... 67
6.1 Measured Wave Data ..... 67
6.2 Modelling Software ..... 68
6.3 Model Boundary Conditions ..... 69

6.4 Model Sensitivity Testing ..... 70
6.4.1 Grid Resolution ..... 70
6.4.2 Directional Discretisation ..... 75
6.5 Final Model Parameter Settings ..... 80
6.6 Hindcast Uniformity ..... 80
6.7 Model Validation ..... 80
6.8 Wave Breaking ..... 93
7 Spatial Maps ..... 94
7.1 Introduction ..... 94
7.2 Waves ..... 94
7.2.1 Operational Statistics ..... 94
7.2.2 Extreme Criteria ..... 98
7.3 Currents and Water Levels ..... 106
8 Climate Change ..... 110
8.1 Winds ..... 110
8.1.1 Mean wind speeds ..... 111
8.1.2 Extreme winds ..... 113
8.2 Waves ..... 114
8.3 Mean Sea Level ..... 115
8.4 Surge and Extreme Total Water Levels ..... 119
9 References ..... 122
Appendix A. Bathymetry Merging ..... 125
Appendix B. Wind Field Validation and Calibration ..... 131
B.1 Introduction ..... 131
B.2 Modelled Data ..... 131
B.3 Measured Data ..... 132
B.4 Model Validation ..... 134
B.4.1 Methodology ..... 134
B.4.2 Arklow Met Mast (Original and Synthesised) ..... 135
B.4.2.1 Overview ..... 135
B.4.2.2 Quality Control ..... 136
B.4.2.3 Wind Speed Validation: Original Dataset ..... 140

B.4.2.4 Wind Speed Validation: Synthesised Dataset ..... 145
B.4.2.5 Wind Direction Validation ..... 147
B.4.3 Arklow LiDAR ..... 149
B.4.3.1 Overview ..... 149
B.4.3.2 Quality Control ..... 149
B.4.3.3 Model Validation ..... 149
B.4.4 M2 and M5 Buoys ..... 154
B.4.4.1 Overview ..... 154
B.4.4.2 Quality Control ..... 154
B.4.4.3 Model Validation ..... 157
B.4.5 Splaugh and Coningbeg ..... 162
B.4.5.1 Overview ..... 162
B.4.5.2 Quality Control ..... 162
B.4.5.3 Model Validation ..... 164
B.5 Vortex 10m Calibration ..... 169
B.5.1 Overview ..... 169
B.5.2 Methodology ..... 169
B.5.3 Results ..... 174
B.6 ERA5 10m Calibration ..... 180
**Appendix C. Wave Model Validation ..... 183**
C.1 Introduction ..... 183
C.2 Modelled Data ..... 184
C.3 Measured Data ..... 185
C.3.1 Overview ..... 185
C.3.2 AWACs A, B1, C, D1 and E ..... 187
C.3.2.1 Overview ..... 187
C.3.2.2 Measurement Considerations ..... 188
C.3.2.3 Data Review and Quality Control ..... 192
C.3.3 M2 and M5 Buoys ..... 193
C.3.3.1 Overview ..... 193
C.3.3.2 Data Review and Quality Control ..... 193
C.3.4 Splaugh ..... 195
C.3.4.1 Overview ..... 195

C.3.4.2 Data Review and Quality Control ..... 196
C.4 Parameter Derivation ..... 198
C.4.1 Introduction ..... 198
C.4.2 Omni-directional Parameters from Spectral Moments (Hm0, Tm01, Tm02) ..... 199
C.4.2.1 Example Spectrum ..... 199
C.4.2.2 AWAC Measurements ..... 201
C.4.2.3 AWAC Validation Plots ..... 202
C.4.2.4 M2, M5 and Splaugh Validation Plots ..... 203
C.4.3 Peak Period (Tp) ..... 203
C.4.4 Mean Wave Direction (Mdir) ..... 204
C.5 Wave Parameter Validation ..... 205
C.5.1 Introduction ..... 205
C.5.2 AWAC A ..... 206
C.5.3 AWAC B1 ..... 210
C.5.4 AWAC C ..... 214
C.5.5 AWAC D1 ..... 218
C.5.6 AWAC E ..... 222
C.5.7 M2, M5 and Splaugh ..... 227
C.6 Directional Sector Validation ..... 229
C.6.1 Introduction ..... 229
C.6.2 45° Sectors ..... 229
C.6.2.1 Sector Specification ..... 229
C.6.2.2 Overview ..... 230
C.6.2.3 AWAC A ..... 231
C.6.2.4 AWAC B1 ..... 238
C.6.2.5 AWAC C ..... 245
C.6.2.6 AWAC D1 ..... 252
C.6.2.7 AWAC E ..... 259
C.6.3 Custom Sectors ..... 266
C.6.3.1 Sector Specification ..... 266
C.6.3.2 Overview ..... 267
C.6.3.3 AWAC A ..... 267
C.6.3.4 AWAC B1 ..... 271
C.6.3.5 AWAC C ..... 275

C.6.3.6 AWAC D1 ..... 279
C.6.3.7 AWAC E ..... 283
C.7 Spectral Validation ..... 287
C.7.1 Introduction ..... 287
C.7.2 AWAC A ..... 288
C.7.2.1 Omni-Directional ..... 288
C.7.2.2 45° Sectors ..... 289
C.7.2.3 Custom Sectors ..... 294
C.7.3 AWAC B1 ..... 297
C.7.3.1 Omni-Directional ..... 297
C.7.3.2 45° Sectors ..... 298
C.7.3.3 Custom Sectors ..... 303
C.7.4 AWAC C ..... 306
C.7.4.1 Omni-Directional ..... 306
C.7.4.2 45° Sectors ..... 307
C.7.4.3 Custom Sectors ..... 312
C.7.5 AWAC D1 ..... 315
C.7.5.1 Omni-Directional ..... 315
C.7.5.2 45° Sectors ..... 316
C.7.5.3 Custom Sectors ..... 321
C.7.6 AWAC E ..... 324
C.7.6.1 Omni-Directional ..... 324
C.7.6.2 45° Sectors ..... 325
C.7.6.3 Custom Sectors ..... 330
C.8 Selected Events ..... 333
C.8.1 Introduction ..... 333
C.8.2 AWAC A ..... 334
C.8.3 AWAC B1 ..... 344
C.8.4 AWAC C ..... 354
C.8.5 AWAC D1 ..... 364
C.8.6 AWAC E ..... 374
C.9 Event Peak Comparison ..... 384

**Appendix D. Peak Periods at AWAC E ..... 391**

D.1 Introduction ..... 391
D.2 Peak Periods from Other Instruments ..... 393
D.3 Instrument Setup ..... 394
D.4 Spatial Variability ..... 396
D.5 Wave Parameters ..... 397
D.6 Wave Spectra ..... 401
D.7 Peak Symmetry ..... 406
D.8 Spectral Energy by Frequency Band ..... 408
D.9 Summary ..... 409

**Appendix E. JONSWAP Fitting ..... 410**

E.1 Introduction ..... 410
E.2 Partitioning ..... 410
E.2.1 Wave System Identification ..... 411
E.2.2 Wave System Classification ..... 414
E.2.3 Combining Systems ..... 417
E.2.4 Additional Considerations ..... 418
E.3 Fitting of Spectral Shapes ..... 418
E.3.1 JONSWAP Spectral Shape ..... 418
E.3.2 Cos2n Directional Distribution ..... 419

**Appendix F. Wind and Wave Averaging Periods ..... 420**

F.1 Overview ..... 420
F.2 Diagnostic Plots ..... 422
F.3 Wind Hindcast ..... 423
F.4 Wave Hindcast ..... 426

**Appendix G. Extreme Value Maps Methodology ..... 428**

G.1 Introduction ..... 428
G.2 General Approach, Single Location ..... 428
G.3 Automated Fit Assessment ..... 429
G.3.1 Storm Peaks ..... 429
G.3.2 Distribution Fitting ..... 430
G.3.3 Fit Assessment ..... 430
G.3.4 Extreme Value Selection ..... 432
G.3.5 Parameter Settings ..... 433

G.3.6 Largest Storm Peak ..... 434
G.4 Hmax and Cmax ..... 437
G.4.1 Methodology, Single Location ..... 437
G.4.2 Automated Fitting ..... 438
G.4.3 Short term wave height distributions ..... 438
G.4.4 Short term crest height distribution ..... 443
G.5 Below MSL extreme values ..... 444
G.5.1 Hm0 ..... 444
G.5.2 Hmax and Cmax ..... 445
Appendix H. Measured Current Profiles ..... 446
H.1 Introduction ..... 446
H.2 Data Overview ..... 447
H.3 Percentiles by Height Level ..... 451
H.4 Individual Profile Shapes ..... 455
H.5 Normalised Profiles ..... 459
H.6 Selected Profile Shapes: Highest Current Speeds ..... 468
Appendix I. Effects of Bedform Evolution ..... 472
I.1 Introduction ..... 472
I.2 Parameter Maps ..... 472
I.3 Difference Maps ..... 481
I.4 Selected Location Comparisons ..... 490
I.4.1 Comparison Plots, R1 ..... 493
I.4.2 Comparison Plots, R6 ..... 496
I.4.3 Comparison Plots, R9 ..... 499

# List of Figures

Figure 2.1: Arklow Bank Wind Farm lease area and geographic context. ..... 17
Figure 3.1: Coverage of Oceanwise data, and DTM tiles procured shown in green. ..... 20
Figure 3.2. Available bathymetry surveys from SeaDataNet (left panel), and merged SeaDataNet bathymetry surveys and SPL 2019 bathymetry overlain (right panel). ..... 21
Figure 3.3: Comparisons between FES2014 and VORF derived datums. ..... 22
Figure 4.1: Coverage of Vortex wind hindcast dataset supplied by SPL. ..... 23
Figure 4.2: Wind measurement locations. ..... 25
Figure 4.3: Calibrated Vortex Model vs. Measured, Arklow Met Mast at 10 m. ..... 26
Figure 4.4: Calibrated ERA5 Model vs. Measured, Arklow Met Mast at 10 m. ..... 27
Figure 4.5: Calibrated Vortex Model vs. Measured, Arklow LiDAR at 10 m. ..... 28
Figure 4.6: Calibrated ERA5 Model vs. Measured, Arklow LiDAR at 10 m. ..... 29
Figure 4.7: Calibrated Vortex Model vs. Measured, M2 at 10 m. ..... 30
Figure 4.8: Calibrated ERA5 Model vs. Measured, M2 at 10 m. ..... 31
Figure 4.9: Calibrated Vortex Model vs. Measured, M5 at 10 m. ..... 32
Figure 4.10: Calibrated ERA5 Model vs. Measured, M5 at 10 m. ..... 33
Figure 5.1: Measured datasets used for hydrodynamic model validation. ..... 35
Figure 5.2 Regional European MIKE21 flexible model mesh. Bathymetry in m MSL. ..... 36
Figure 5.3 Zoom in of Irish east coast region of MIKE21 flexible model mesh. Bathymetry in mMSL. ..... 37
Figure 5.4. Hydrodynamic mesh with 150 m resolution within the wind farm lease area and surrounds. ..... 38
Figure 5.5. Hydrodynamic mesh with 75 m resolution within the wind farm lease area and surrounds. ..... 39
Figure 5.6. Hydrodynamic mesh with 37.5 m resolution within the wind farm lease area and surrounds. ..... 39
Figure 5.7. Results of model runs with differing mesh resolutions, at AWAC A. Top row = water level, middle row = current speed, bottom row = current direction. Left column 150 m vs. 75 m. Middle column 37.5 m vs. 150 m. Right column = 75 m vs. 37.5 m. ..... 40
Figure 5.8. Results of model runs with differing mesh resolutions, at Centre of Bank. Top row = water level, middle row = current speed, bottom row = current direction. Left column 150 m vs. 75 m. Middle column 37.5 m vs. 150 m. Right column = 75 m vs. 37.5 m. ..... 41
Figure 5.9. Results of model runs with differing mesh resolutions, at AWAC E. Top row = water level, middle row = current speed, bottom row = current direction. Left column 150 m vs. 75 m. Middle column 37.5 m vs. 150 m. Right column = 75 m vs. 37.5 m. ..... 42
Figure 5.10. Results of model runs with differing mesh resolutions, at the Cable Route. Top row = water level, middle row = current speed, bottom row = current direction. Left column 150 m vs. 75 m. Middle column 37.5 m vs. 150 m. Right column = 75 m vs. 37.5 m. ..... 43
Figure 5.11. Positions of AWAC E for three deployments compared to the closest model gid points. ..... 46
Figure 5.12: Comparison of measured and modelled water levels at Howth. ..... 47
Figure 5.13: Comparison of measured and modelled water levels at Dublin Port. ..... 47
Figure 5.14: Comparison of measured and modelled water levels at Arklow Harbour (European model). ..... 48
Figure 5.15: Comparison of measured and modelled water levels at Rosslare. ..... 48
Figure 5.16: Comparison of measured and modelled water levels at Dunmore East. ..... 49
Figure 5.17: Comparison of measured and modelled water levels at Ballycotton. ..... 49
Figure 5.18: Comparison of measured and modelled water levels at Arklow Harbour (local model). ..... 50
Figure 5.19: Comparison of measured and modelled water levels at AWAC A (all deployments). ..... 50
Figure 5.20: Comparison of measured and modelled water levels at AWAC B1 (deployment 2). ..... 51

Figure 5.21: Comparison of measured and modelled water levels at AWAC B1 (deployment 3). ..... 51
Figure 5.22: Comparison of measured and modelled water levels at AWAC B1 (all deployments). ..... 52
Figure 5.23: Comparison of measured and modelled water levels at AWAC C (all deployments). ..... 52
Figure 5.24: Comparison of measured and modelled water levels at AWAC D1 (all deployments). ..... 53
Figure 5.25: Comparison of measured and modelled water levels at AWAC E (all deployments). ..... 53
Figure 5.26: Comparison of measured and modelled depth-average currents at AWAC A (all deployments). .. 54
Figure 5.27: Comparison of measured and modelled depth-average currents at AWAC B1 (all deployments). 54
Figure 5.28: Comparison of measured and modelled depth-average currents at AWAC C (all deployments). .. 55
Figure 5.29: Comparison of measured and modelled depth-average currents at AWAC D1 (all deployments). 55
Figure 5.30: Comparison of measured and modelled depth-average currents at AWAC E (all deployments).... 56
Figure 5.31: Time-series comparison of modelled and measured depth-average currents during spring tides at AWAC A. ..... 57
Figure 5.32: Time-series comparison of modelled and measured depth-average currents during neap tides at AWAC A. ..... 58
Figure 5.33: Time-series comparison of modelled and measured depth-average currents during spring tides at AWAC B1. ..... 59
Figure 5.34: Time-series comparison of modelled and measured depth-average currents during neap tides at AWAC B1. ..... 60
Figure 5.35: Time-series comparison of modelled and measured depth-average currents during spring tides at AWAC C. ..... 61
Figure 5.36: Time-series comparison of modelled and measured depth-average currents during neap tides at AWAC C. ..... 62
Figure 5.37: Time-series comparison of modelled and measured depth-average currents during spring tides at AWAC D1. ..... 63
Figure 5.38: Time-series comparison of modelled and measured depth-average currents during neap tides at AWAC D1. ..... 64
Figure 5.39: Time-series comparison of modelled and measured depth-average currents during spring tides at AWAC E. ..... 65
Figure 5.40: Time-series comparison of modelled and measured depth-average currents during neap tides at AWAC E. ..... 66
Figure 6.1: Locations of the wave measurement devices. ..... 68
Figure 6.2: Wave model domains. ..... 69
Figure 6.3. Results of model runs with differing spatial resolutions, at AWAC A. Top row = significant wave height, middle row = mean zero-crossing wave period, bottom row = mean wave direction. Left column 220 m resolution vs. 110 m resolution. Middle column 55 m resolution vs. 220 m resolution. Right column = 110 m resolution vs. 55 m resolution. ..... 71
Figure 6.4. Results of model runs with differing spatial resolutions, at Centre of Bank. Top row = significant wave height, middle row = mean zero-crossing wave period, bottom row = mean wave direction. Left column 220 m resolution vs. 110 m resolution. Middle column 55 m resolution vs. 220 m resolution. Right column = 110 m resolution vs. 55 m resolution. ..... 72
Figure 6.5. Results of model runs with differing spatial resolutions, at AWAC E. Top row = significant wave height, middle row = mean zero-crossing wave period, bottom row = mean wave direction. Left column 220 m resolution vs. 110 m resolution. Middle column 55 m resolution vs. 220 m resolution. Right column = 110 m resolution vs. 55 m resolution. ..... 73

Figure 6.6. Results of model runs with differing spatial resolutions, at the Cable Route. Top row = significant wave height, middle row = mean zero-crossing wave period, bottom row = mean wave direction. Left column 220 m resolution vs. 110 m resolution. Middle column 55 m resolution vs. 220 m resolution. Right column = 110 m resolution vs. 55 m resolution. ..... 74
Figure 6.7. Results of model runs with differing numbers of directional bins, at AWAC A. Top row = significant wave height, middle row = mean zero-crossing wave period, bottom row = mean wave direction. Left column 24 directional bins vs. 36 directional bins. Middle column 48 directional bins vs. 24 directional bins. Right column = 36 directional bins vs. 48 directional bins. ..... 76
Figure 6.8. Results of model runs with differing numbers of directional bins, at Centre of Bank. Top row = significant wave height, middle row = mean zero-crossing wave period, bottom row = mean wave direction. Left column 24 directional bins vs. 36 directional bins. Middle column 48 directional bins vs. 24 directional bins. Right column = 36 directional bins vs. 48 directional bins. ..... 77
Figure 6.9. Results of model runs with differing numbers of directional bins, at AWAC E. Top row = significant wave height, middle row = mean zero-crossing wave period, bottom row = mean wave direction. Left column 24 directional bins vs. 36 directional bins. Middle column 48 directional bins vs. 24 directional bins. Right column = 36 directional bins vs. 48 directional bins. ..... 78
Figure 6.10. Results of model runs with differing numbers of directional bins, at the Cable Route. Top row = significant wave height, middle row = mean zero-crossing wave period, bottom row = mean wave direction. Left column 24 directional bins vs. 36 directional bins. Middle column 48 directional bins vs. 24 directional bins. Right column = 36 directional bins vs. 48 directional bins. ..... 79
Figure 6.11. M2, Hm0 validation. ..... 82
Figure 6.12. M5, Hm0 validation. ..... 82
Figure 6.13. AWAC A, Hm0 validation, all data. ..... 83
Figure 6.14. AWAC A, Mdir validation, all data. ..... 83
Figure 6.15. AWAC A, Tm02 validation, timestamps with Hm0 > 0.5 m, all data. ..... 84
Figure 6.16. AWAC A, Tp validation, timestamps with Hm0 > 0.5 m, all data. ..... 84
Figure 6.17. AWAC B1, Hm0 validation, all data. ..... 85
Figure 6.18. AWAC B1, Mdir validation, all data. ..... 85
Figure 6.19. AWAC B1, Tm02 validation, timestamps with Hm0 > 0.5 m, all data. ..... 86
Figure 6.20. AWAC B1, Tp validation, timestamps with Hm0 > 0.5 m, all data. ..... 86
Figure 6.21. AWAC C, Hm0 validation, all data. ..... 87
Figure 6.22. AWAC C, Mdir validation, all data. ..... 87
Figure 6.23. AWAC C, Tm02 validation, timestamps with Hm0 > 0.5 m, all data. ..... 88
Figure 6.24. AWAC C, Tp validation, timestamps with Hm0 > 0.5 m, all data. ..... 88
Figure 6.25. AWAC D1, Hm0 validation, all data. ..... 89
Figure 6.26. AWAC D1, Mdir validation, all data. ..... 89
Figure 6.27. AWAC D1, Tm02 validation, timestamps with Hm0 > 0.5 m, all data. ..... 90
Figure 6.28. AWAC D1, Tp validation, timestamps with Hm0 > 0.5 m, all data. ..... 90
Figure 6.29. AWAC E, Hm0 validation, all data. ..... 91
Figure 6.30. AWAC E, Mdir validation, all data. ..... 91
Figure 6.31. AWAC E, Tm02 validation, timestamps with Hm0 > 0.5 m, all data. ..... 92
Figure 6.32. AWAC E, Tp validation, timestamps with Hm0 > 0.5 m, all data. ..... 92
Figure 6.33. Satellite image of the mid-section of Arklow Bank (from ESA and Sentinel 2, May 2020). ..... 93
Figure 7.1: Mean Hm0 (left), 2nd power mean Hm0 (centre) and 5th power mean Hm0 (right). ..... 95
Figure 7.2: Percentiles of Hm0: 50th percentile (left), 90th percentile (centre) and 95th percentile (right). ..... 96



Figure 7.3: Percentiles and maxima of Hm0: 99th percentile (left), 99.9th percentile (centre) and maximum (right). ..... 97
Figure 7.4: Difference between highest and second highest Hm0 peak across the region. ..... 99
Figure 7.5: Extreme values of Hm0: 1-year (left), 50-year (centre) and 100-year (right). ..... 100
Figure 7.6: Extreme values of Hmax: 1-year (left), 50-year (centre) and 100-year (right). ..... 101
Figure 7.7: Extreme values of Cmax above still water level: 1-year (left), 50-year (centre) and 100-year (right). ..... 102
Figure 7.8: Extreme values of Hm0, water levels below MSL only: 1-year (left), 50-year (centre) and 100-year (right). ..... 103
Figure 7.9: Extreme values of Hmax, water levels below MSL only: 1-year (left), 50-year (centre) and 100-year (right). ..... 104
Figure 7.10: Extreme values of Cmax above still water level, water levels below MSL only: 1-year (left), 50-year (centre) and 100-year (right). ..... 105
Figure 7.11: Minimum water level (tide + surge) (left), maximum water level (tide + surge) (centre) and mean depth-averaged current speed (right). ..... 107
Figure 7.12: Percentiles of depth-averaged current speed: 50$^{th}$ percentile (left), 90$^{th}$ percentile (centre) and 95$^{th}$ percentile (right). ..... 108
Figure 7.13: Percentiles and maxima of depth-averaged current speed: 99$^{th}$ percentile (left), 99.9$^{th}$ percentile (centre) and maximum (right). ..... 109
Figure 8.1: Averaged changes in the mean of the daily averaged 10 m wind speeds. Adapted from [6]. ..... 111
Figure 8.2: Global projections for changes in winter mean near surface wind speed over the UK for 1900-2100 with respect to 1981-2000. ..... 112
Figure 8.3: Expected percent change in the average over period 2081–2100 relative to 2000–2019. ..... 114
Figure 8.4: Absolute change (m) in mean significant wave height (top) and mean annual maximum significant wave height (below). Global model (left) and regional (right). ..... 115
Figure 8.5: Global mean sea level rise from 2006 to 2100 as determined by multi-model simulations. ..... 116
Figure 8.6: The effect of GIA on sea level. ..... 117
Figure 8.7: Time series of time-mean sea level change around the UK. ..... 118
Figure 8.8: Projected 21st century trend in skew surge extremes from two different climate models. ..... 119
Figure 8.9: Spatial pattern of the illustrative high-end projection of 21st century trend in one-year return level of skew surge (left) and 200-year return level of skew surge (right). This does not include any time-mean sea level change. ..... 120
Figure 8.10: Future extreme still water levels at Holyhead, Wales, relative to the 2017 zero-level of Ordnance Datum Newlyn. ..... 121

# List of Tables

Table 4.1: Measured datasets used for wind model validation. ..... 24
Table 5.1: Measured datasets used for hydrodynamic model validation. ..... 34
Table 5.2: Final model parameter settings. ..... 44
Table 6.1: Measured datasets used for wave model validation. ..... 67
Table 8.1: Projected change in tropical cyclone activity over the North Atlantic. ..... 113
Table 8.2: Projections of sea level change offshore of Capel Carmel, Wales, for various scenarios and probability levels. ..... 119

# 1 Definitions

## 1.1 Units and Conventions

The following list describes the units and conventions used in this report. Unless stated otherwise, units have been expressed using the SI convention.

- Wind direction is expressed in compass points or degrees, relative to true North [°T], and describes the direction **from** which the winds are blowing.
- Wind speeds are expressed in metres per second [m/s].
- Wave direction is expressed in compass points or degrees, relative to true North [°T], and describes the direction **from** which the waves are propagating.
- Wave heights are expressed in metres [m].
- Wave periods are expressed in seconds [s].
- Current direction is expressed in compass points or degrees, relative to true North [°T], and describes the direction **towards** which the currents are flowing.
- Current speeds are expressed in metres per second [m/s].
- Water levels are expressed in metres [m].
- Positions are quoted relative to WGS 84 except where stated.
- All times are quoted in Coordinated Universal Time [UTC].

## 1.2 Glossary of commonly used metocean terms

The following list describes common metocean terms used throughout this report.

| Winds | Description |
|---|---|
| ASL | Above sea level. Refers to the height of wind measurements from floating buoys above sea level. |
| AMSL | Above mean sea level. Refers to the height of wind measurements from fixed structures, such as met masts, above mean sea level. |
| Wind speed | Magnitude of local wind flow. Wind speed alone is meaningless without reference to the sampling duration and height asl. Wind speed is usually taken as the hourly mean wind speed at 10m asl. |
| $U_{3\text{-hr}}$ | Mean wind speed averaged over a 3-hour period. |
| $U_{1\text{-hr}}$ | Mean wind speed averaged over a 3-hour period. |
| $U_{10}$10-min | The highest value taken from a rolling 10-minute average wind speed throughout 1 hour. |
| **Waves** | **Description** |
| Cmax | The maximum individual wave crest elevation occurring within a defined period. |
| Cmp | The most probable maximum individual wave crest elevation occurring within a storm. |
| Hmax | The maximum individual wave height occurring within a defined period. |
| Hmp | The most probable maximum individual wave height occurring within a storm. |
| Hm0 | Significant wave height. Approximately the average height of the highest one third of the waves in a defined period, estimated from the wave spectrum as $4\sqrt{m_0}$ . |
| $m_0$, $m_1$, $m_2$ | The zeroth, first and second moments of the wave spectrum respectively. |

| | |
|---|---|
| Mdir | Mean wave direction, estimated from the wave spectrum. |
| Significant steepness | A measure of the steepness of the sea state, though with no precise physical meaning. Calculated from the wave spectrum as $2\pi H_{m0} / gT_{m02}{}^2$ where $g$ denotes the acceleration of gravity. |
| Tass | The period associated with Hmax. |
| Tm01 | The mean wave period, estimated from the wave spectrum as $m_0/m_1$. |
| Tm02 | The mean zero-crossing wave period. Estimated from the wave spectrum as $\sqrt{m_0/m_2}$. |
| Tp | The spectral peak period. The period at which most energy is present in the wave spectrum. |
| Wave crest elevation | The vertical distance between the still water level and the maximum elevation of an individual wave. |
| Wave height | The vertical distance between the minimum and maximum elevations of an individual wave. |
| **Levels** | **Description** |
| ETWL | Extreme Total Water Level. |
| LAT | Lowest Astronomical Tide. Minimum level of sea surface due to tidal forcing alone. |
| HAT | Highest Astronomical Tide. Maximum level of sea surface due to tidal forcing alone. |
| MHW | Mean High Water. Mean of all high water levels. |
| MHWN | Mean High Water Neap. Mean high water level during neap phase of tidal cycle. |
| MHWS | Mean High Water Spring. Mean high water level during spring phase of tidal cycle. |
| MLW | Mean Low Water. Mean of all low water levels. |
| MLWN | Mean Low Water Neap. Mean low water level during neap phase of tidal cycle. |
| MLWS | Mean Low Water Spring. Mean low water level during spring phase of tidal cycle. |
| MSL | Mean Sea Level. Mean sea surface elevation over a prolonged period of time. |
| Residual level | Difference between the tidal level estimated by harmonic analysis/prediction and the actual level. Includes any errors due to failure to adequately resolve the tidal signal. Includes meteorologically induced storm surge. |
| Still water level | Instantaneous water level in the absence of waves, but including water level variations due to tide and meteorologically induced forcing. |
| Tidal level | Still water level relative to a defined datum due to astronomical forcing. Tidal elevations exclude all meteorologically induced forcing. |
| **Currents** | **Description** |
| Current speed | Magnitude of local current flow. |
| Tidal current | Current driven by astronomical forcing. |
| Total current | Combination of tidal and residual current. |
| Surge current | Current driven by processes excluding astronomical forcing and wave induced motions. |

# 2 Introduction

## 2.1 Background

Sure Partners Limited (SPL) is developing the Arklow Bank Wind Farm (ABWF) located in the Irish Sea. ABWF is situated on a long narrow sandbank approximately 10 km off the Wicklow Coast, near the town of Arklow (see Figure 2.1). The site area is approximately 27 km x 2.5 km and water depths within the lease area range from approximately 2 m to more than 40 m below LAT.

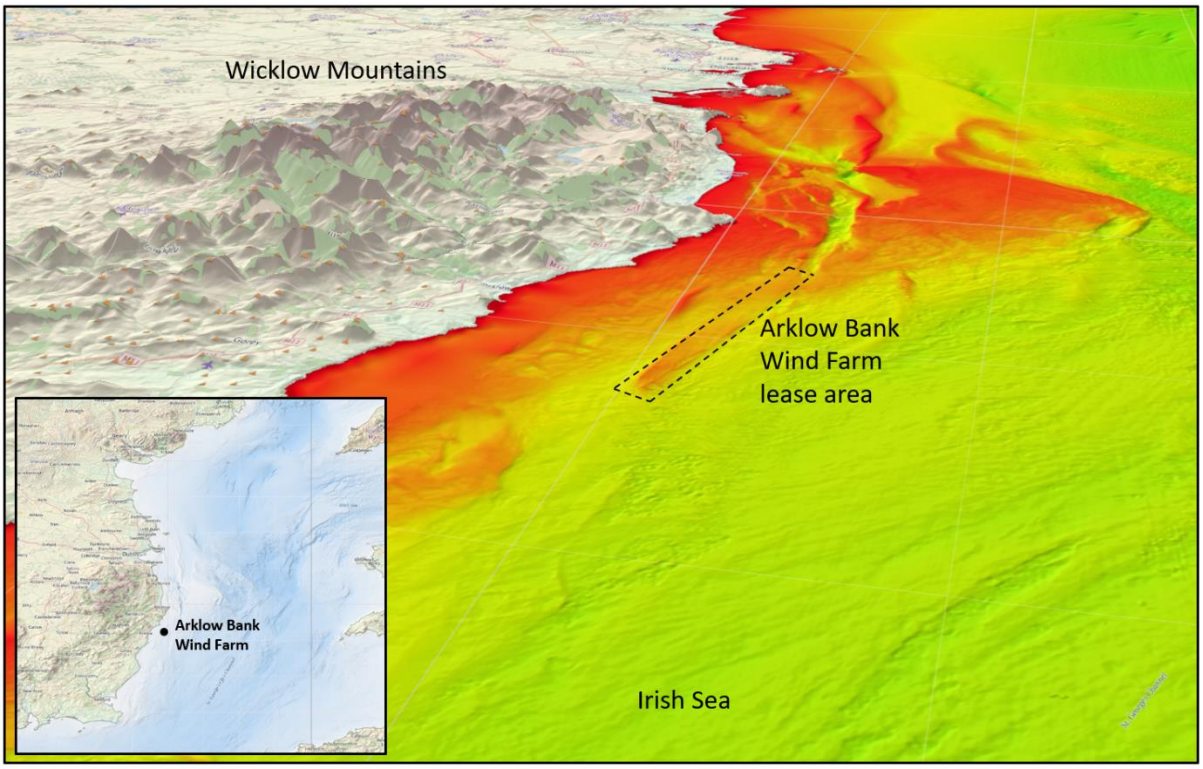



Figure 2.1: Arklow Bank Wind Farm lease area and geographic context.

Sure Partners Limited requires full metocean modelling for ABWF, including wave and hydrodynamic modelling at a suitable resolution over a relevant time period, and have contracted MetOceanWorks to perform these tasks. Data output from these models will ultimately be used to conduct a suite of analyses resulting in an appropriate level of information to inform a Site Conditions Assessment (SCA) module (as defined in IEC 61400-22) as well as providing input to weather window and cycle analyses.

## 2.2 Report Structure

This Metocean Data Overview document describes the various data sources and models used throughout the study.

Modelling details are discussed in Sections 3 to 5, initially introducing common model inputs (Section 3) before moving onto the models themselves. By way of introduction to the overall approach:

- **Wind** data used to derive criteria originate from the ECMWF ERA5 and VORTEX downscaled ERA5 model. See Section 4 for details.
- **Hydrodynamics** are modelled using the MIKE21FM 2D flexible mesh modelling package, a comprehensive modelling system for two-dimensional water modelling developed at the Danish Hydraulic Institute (DHI). Modelled currents and water levels have been validated against measurements from several locations within the wind farm zone, with additional long-term regional measurements used for validating water levels. See Section 5 for details.
- **Waves** are modelled with a bespoke SWAN (Simulating Waves Nearshore) model with high resolution regional nests, to produce a 39-year wave hindcast between 1982 and 2020 inclusive. The model has been extensively validated against measured datasets in the region. See Section 5 for details.

Thereafter, Section 7 presents map plots to illustrate the spatial variability of metocean parameters across the lease area and surrounds, whilst Section 8 provides a summary of possible changes to metocean conditions at the site driven by climate change. The document concludes with a list of the references used throughout (Section 9) and various appendices providing more detail on a number of topics outlined in preceding sections.

The first revision of this report (SSE_C00002_R01_Metocean_Data_Overview) was written following the retrieval of measured data from the first of three deployments. It has subsequently been updated (SSE_C00002_R02_Metocean_Data_Overview) to make use of the full duration of observations. However, these updates only pertain to the model validations presented in Section 5, Section 6 and Appendix C.

# 3 Bathymetry and Coastline

## 3.1 Bathymetry

A representative bathymetry dataset was required as input to the wave and hydrodynamic models. This was achieved by merging four different datasets which originated from:

- European Marine Observation and Data Network (EMODnet)
- Oceanwise
- SeaDataNet
- SPL-supplied survey data from 2019

Far-field bathymetry data for the models were sourced from the EMODnet Bathymetry Data Portal[1]. EMODnet provides a service for viewing and downloading a harmonised Digital Terrain Model (DTM) for the European sea regions that is generated by an ever-increasing number of bathymetric survey data sets provided by national hydrographic institutions, research bodies and academia. As of 2018, these data are available at a resolution of approximately 130 m.

These data were then merged with Oceanwise raster charts which have a resolution of 1 arc-second (or approximately 25 m, depending on latitude), whereby physical features such as trenches, ridges, sand banks and sand waves are well represented. Figure 3.1 shows the available coverage of Oceanwise data with the tiles procured highlighted in green.

To provide the highest possible resolution input data for the Western Irish Sea, surrounding Arklow Bank, individual survey datasets were procured from SeaDataNet. Available survey datasets in the region of the project are shown in the left panel of Figure 3.2 (note different colour-scales to emphasise boundaries between different surveys) and have various resolutions between approximately 4 m and 11 m. Overlapping or duplicated datasets were removed, leaving 22 individual survey datasets which were merged, and any small gaps were filled using interpolation. The final merged and interpolated dataset is shown in the right panel of Figure 3.2.

The SPL-supplied survey data from 2019 are also highlighted in this figure, using a different colour scale. These data have a spatial resolution of 1 m and cover the entire wind farm lease area.

A critical aspect of the bathymetry development for the numerical modelling purposes was to ensure no vertical discontinuities at the boundaries between the SeaDataNet and 2019 survey data. Therefore, the two datasets were merged using a tapering method to avoid sudden vertical shifts at dataset edges. Full details of this tapering process are provided in Appendix A.

[1] http://www.emodnet-bathymetry.eu

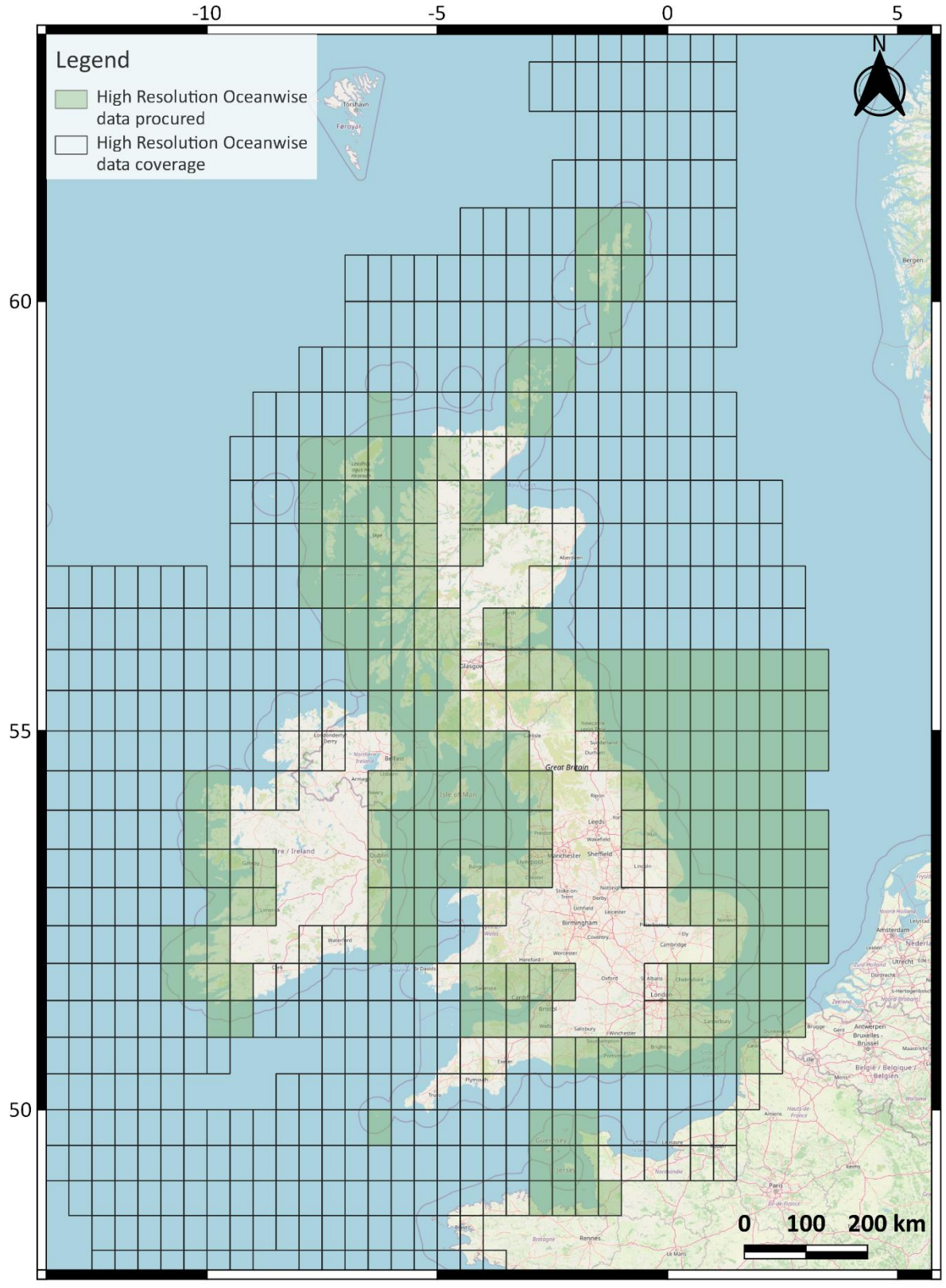



Figure 3.1: Coverage of Oceanwise data, and DTM tiles procured shown in green.

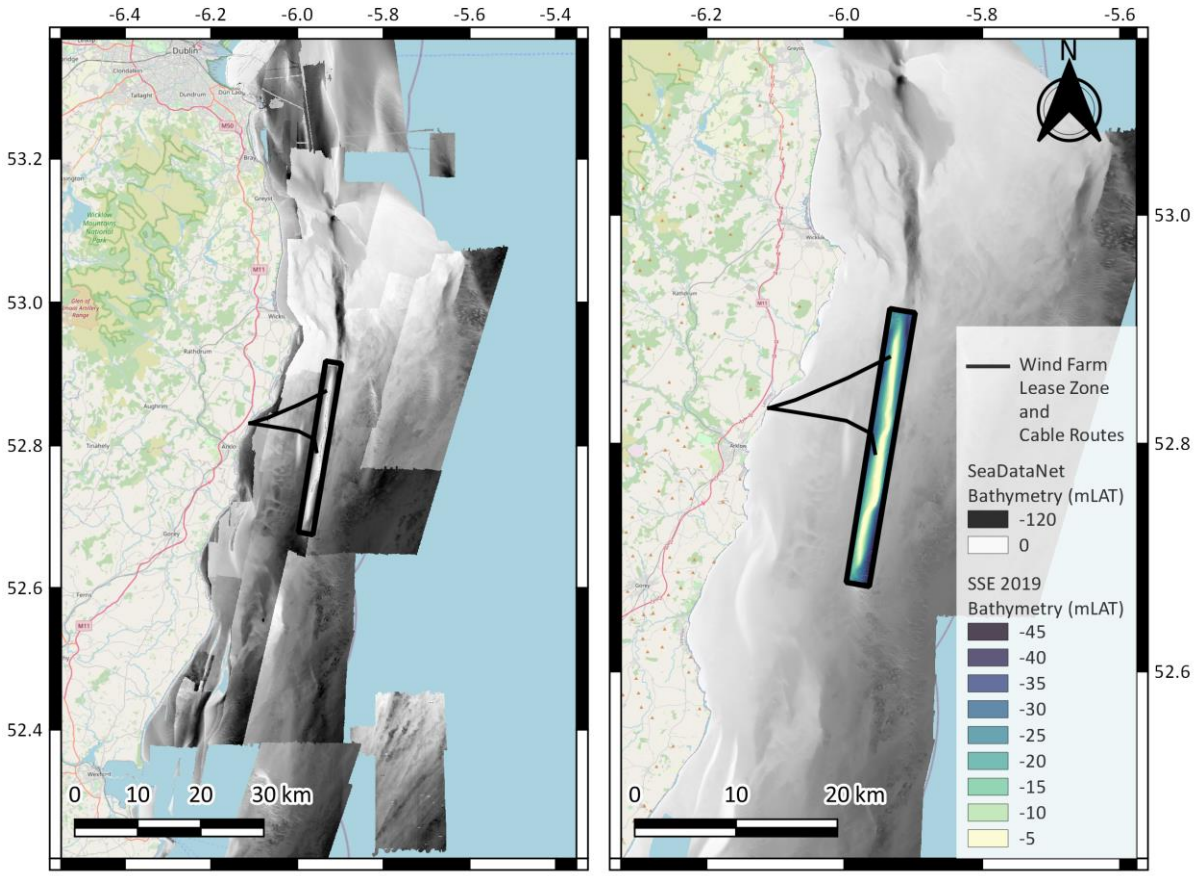



Figure 3.2. Available bathymetry surveys from SeaDataNet (left panel), and merged SeaDataNet bathymetry surveys and SPL 2019 bathymetry overlain (right panel).

## 3.2 Bathymetry Datum Conversion

The bathymetry data were converted from LAT to MSL datum prior to use as required by both the SWAN and MIKE21 modelling software. These datum differences were calculated from the Finite Element Solution FES2014 dataset, a 35-constituent, global tidal database available from AVISO[2]. We acknowledge that Vertical Offshore Reference Frames (VORF) data were made available for use on this project. These data are the result of an ongoing collaboration between University College London and the United Kingdom Hydrographic Office[3]. They provide a set of high-resolution surfaces which together define the vertical datum for hydrographic surveying and charting in the United Kingdom and Ireland with a stated accuracy is 0.1 m. Comparisons between FES2014 and VORF derived datum differences are shown in Figure 3.3 and demonstrate differences between the two that are within the stated accuracy of the VORF product. This image also highlights the limited coverage of the VORF data provided and hence why the FES2014 data were preferentially used. However, the reader should note that VORF will be used for all reporting where the provision of LAT to MSL datums are required.

[2] https://www.aviso.altimetry.fr/en/data/products/auxiliary-products/global-tide-fes.html
[3] https://www.ucl.ac.uk/civil-environmental-geomatic-engineering/research/groups-centres-and-sections/vertical-offshore-reference-frames-vorf

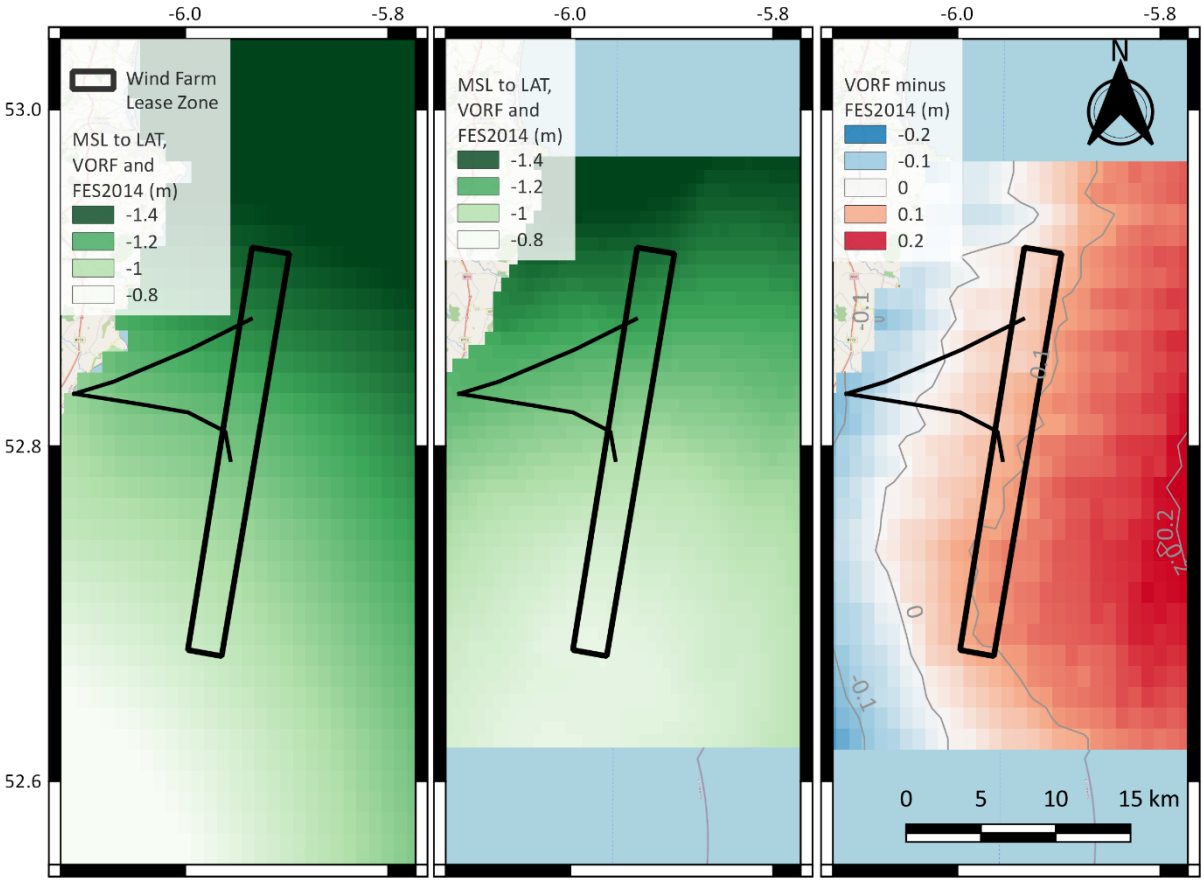



Figure 3.3: Comparisons between FES2014 and VORF derived datums.

## 3.3 Coastline

The coastlines of England, Scotland and Wales were discretised using the Boundary-Line™ mean high water mark vector product, from the Ordnance Survey, which describes the position of Mean High-Water Springs. For continental Europe, the island of Ireland, and the Isle of Man, the coastline layer from OpenStreetMap was used. These data were used in conjunction with satellite imagery to provide the most accurate and appropriate coastline description for the models. Furthermore, they were found to have a better representation of coastal features than data available from the Ordnance Survey Ireland.

# 4 Winds

## 4.1 Introduction

ABWF is close to the Irish coastline and the nearby Wicklow mountains resulting in complexity to the local wind regime. An accurate description of the local wind fields is important to this study, both in terms of the vertical wind profile experienced by prospective wind turbines and their structures, and in terms of the surface winds that affect local wave growth. Therefore, the wind fields have been carefully considered such that the combined effects of wind and waves can be described accurately and coherently.

## 4.2 Modelled Wind Data

A bespoke down-scaled wind field dataset of the Irish Sea, with an approximate resolution of 3km, was supplied by Sure Partners Limited. This was sourced from Vortex Factoria de Càlculs SL (Vortex), and was derived as a downscaled implementation of the European Centre for Medium-Range Weather Forecasts (ECMWF) ReAnalysis 5 (ERA5).

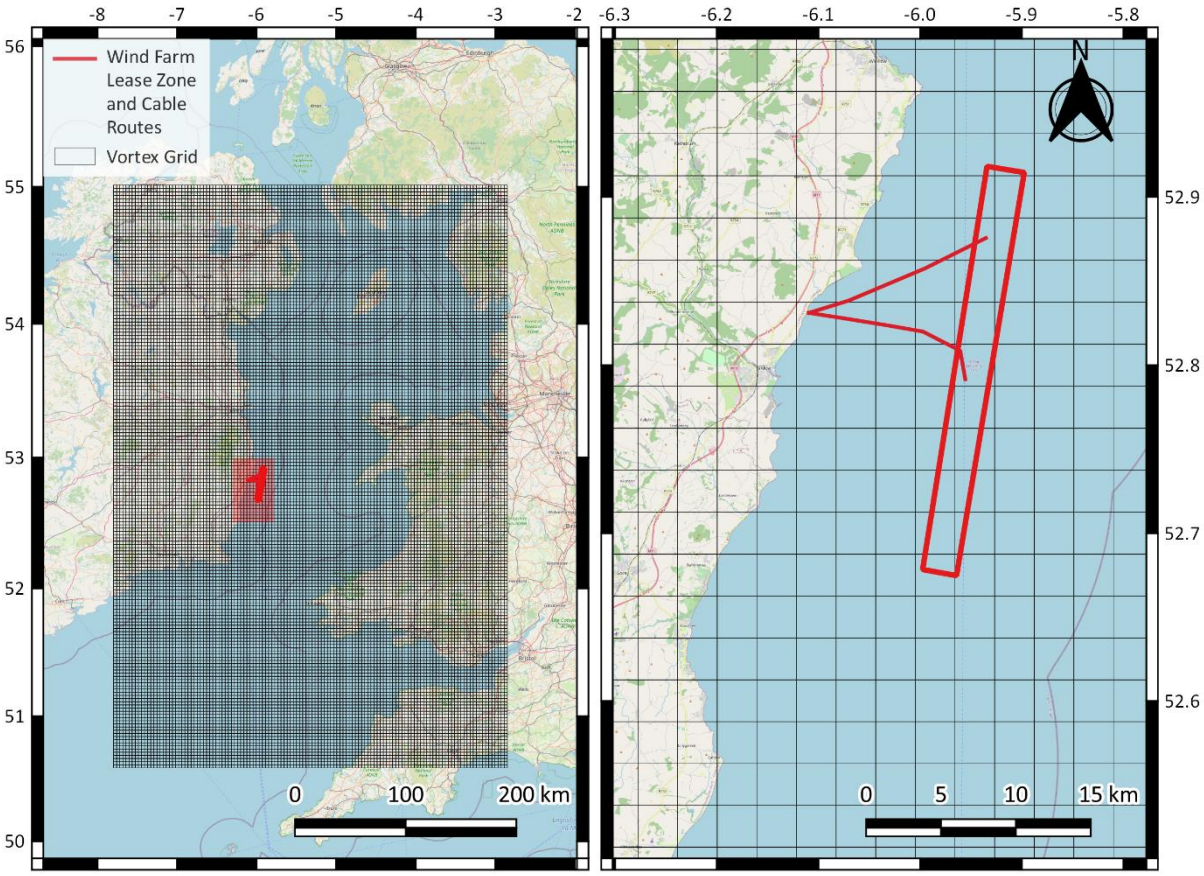



Figure 4.1: Coverage of Vortex wind hindcast dataset supplied by SPL.

Additionally, gridded modelled ECMWF ERA5 data were used to drive regional scale models directly. ERA5 is the fifth and latest major global reanalysis produced by ECMWF and data are available on a regular latitude-

longitude grid at 0.25-degree (approximately 28 km) resolution via the Copernicus Climate Change Service (C3S) Climate Data Store.

Data from both models were acquired at hourly intervals between January 1982 and February 2021 at 10m as well as higher elevations. Here, we focus on data at 10m which were used to drive the wave and hydrodynamic models.

An averaging period of 3-hours should be associated with modelled wind speeds. Please see Appendix F for more details.

## 4.3 Measured Wind Data

A number of measured datasets relevant to Arklow were provided by Sure Partners Limited for validation of the wind models. These were supplemented with buoy data acquired from the Irish Marine Institute and the Commissioners of Irish Lights. Details are given in Table 4.1 and Figure 4.2.

Table 4.1: Measured datasets used for wind model validation.

| Dataset | Location | Time Period | Height Range |
|---|---|---|---|
| **Arklow Met Mast** | 52.8855 °N, 5.9234 °W | 21-Feb-2001 to 26-Aug-2019 | 15.0 to 42.5 mAMSL |
| **Arklow LiDAR** | 52.8855 °N, 5.9234 °W | 07-Nov-2019 to 05-Nov-2020 | 21.3 to 299.3 mAMSL |
| **M2** | 53.4836 °N, 5.4302 °W | 26-Oct-2010 to 27-Apr-2020 | 3.5 mASL |
| **M5** | 51.6904 °N, 6.7043 °W | 21-Feb-2012 to 27-Apr-2020 | 3.5 mASL |
| **Splaugh** | 52.2394 °N, 6.2788 °W | 01-Apr-2016 to 01-Jan-2018 | 5.0 mASL |
| **Coningbeg** | 52.0539 °N, 6.6411 °W | 08-Apr-2016 to 01-Jan-2018 | 8.0 mASL |

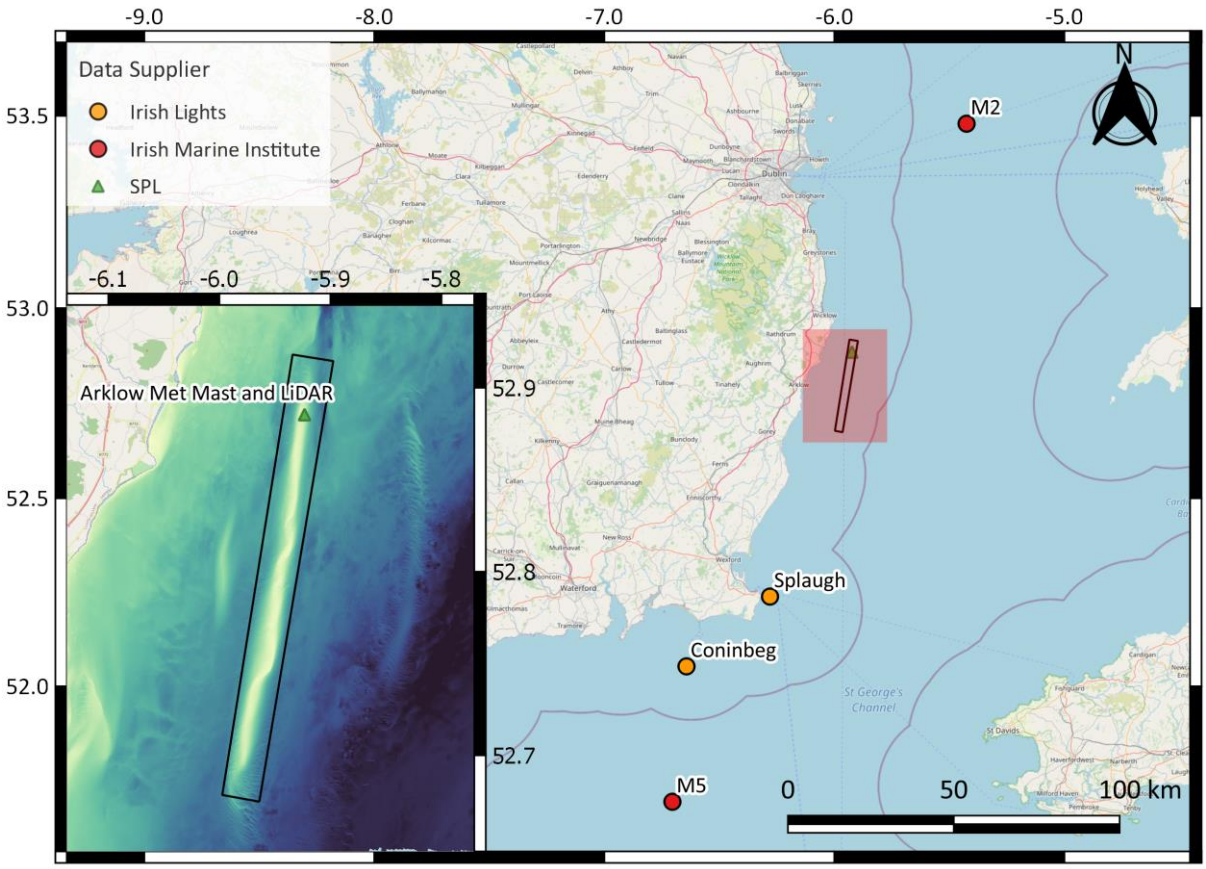



Figure 4.2: Wind measurement locations.

## 4.4 Model Validation

Prior to use both the Vortex downscaled and the raw ERA5 data were subjected to calibration. Here we provide validation plots of the calibrated modelled 10 m wind speeds at Arklow, M2, and M5. More details can be found in in Appendix B.

Following MetOceanWorks' adjustment, the modelled values are in good overall agreement with the measured data, as seen in Figure 4.3 through to Figure 4.10 and are deemed of a high quality, suitable as inputs to the wave and hydrodynamic models. Furthermore, there is little difference in terms of performance between the calibrated ERA5 and Vortex data.

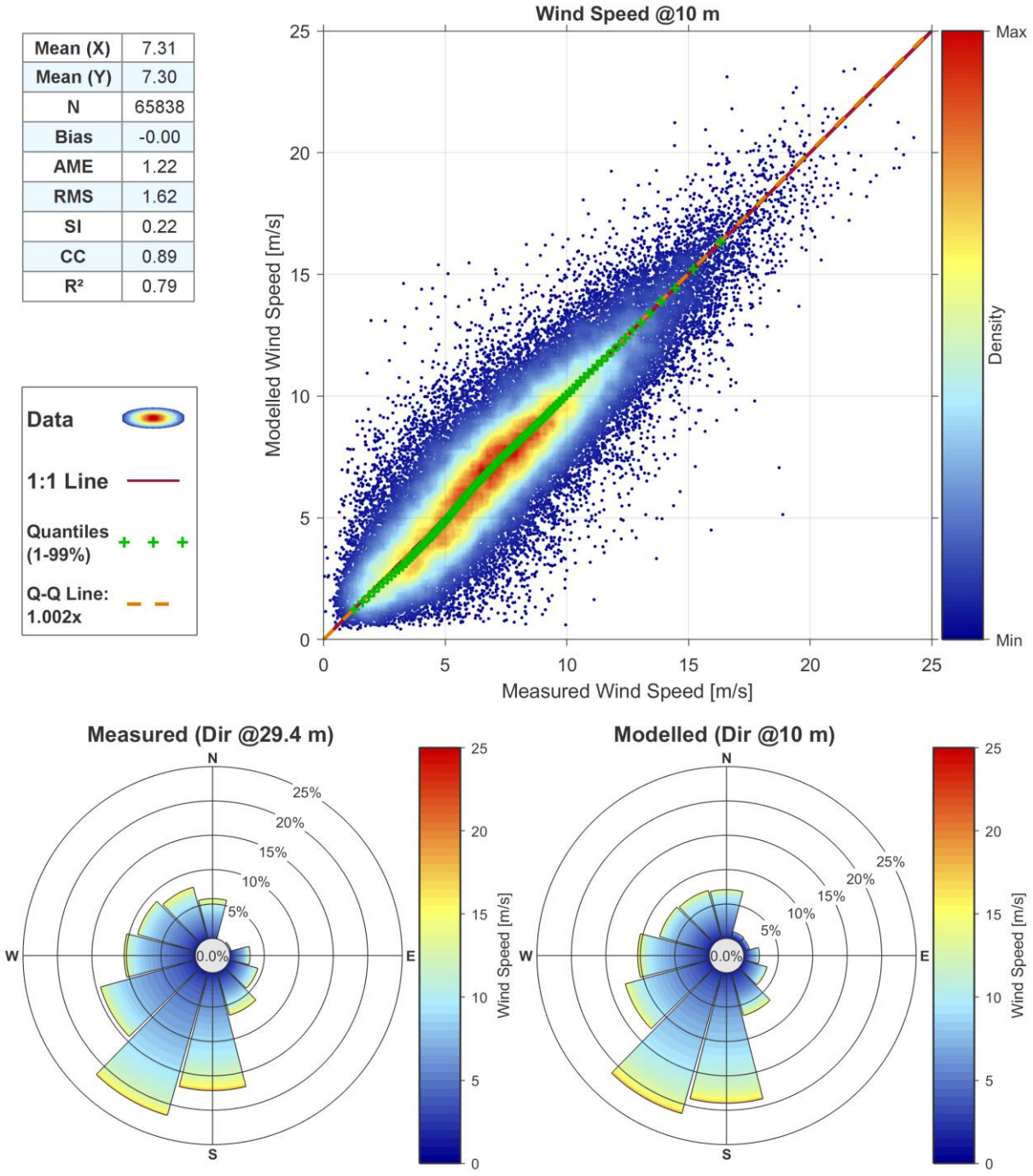



Figure 4.3: Calibrated Vortex Model vs. Measured, Arklow Met Mast at 10 m.

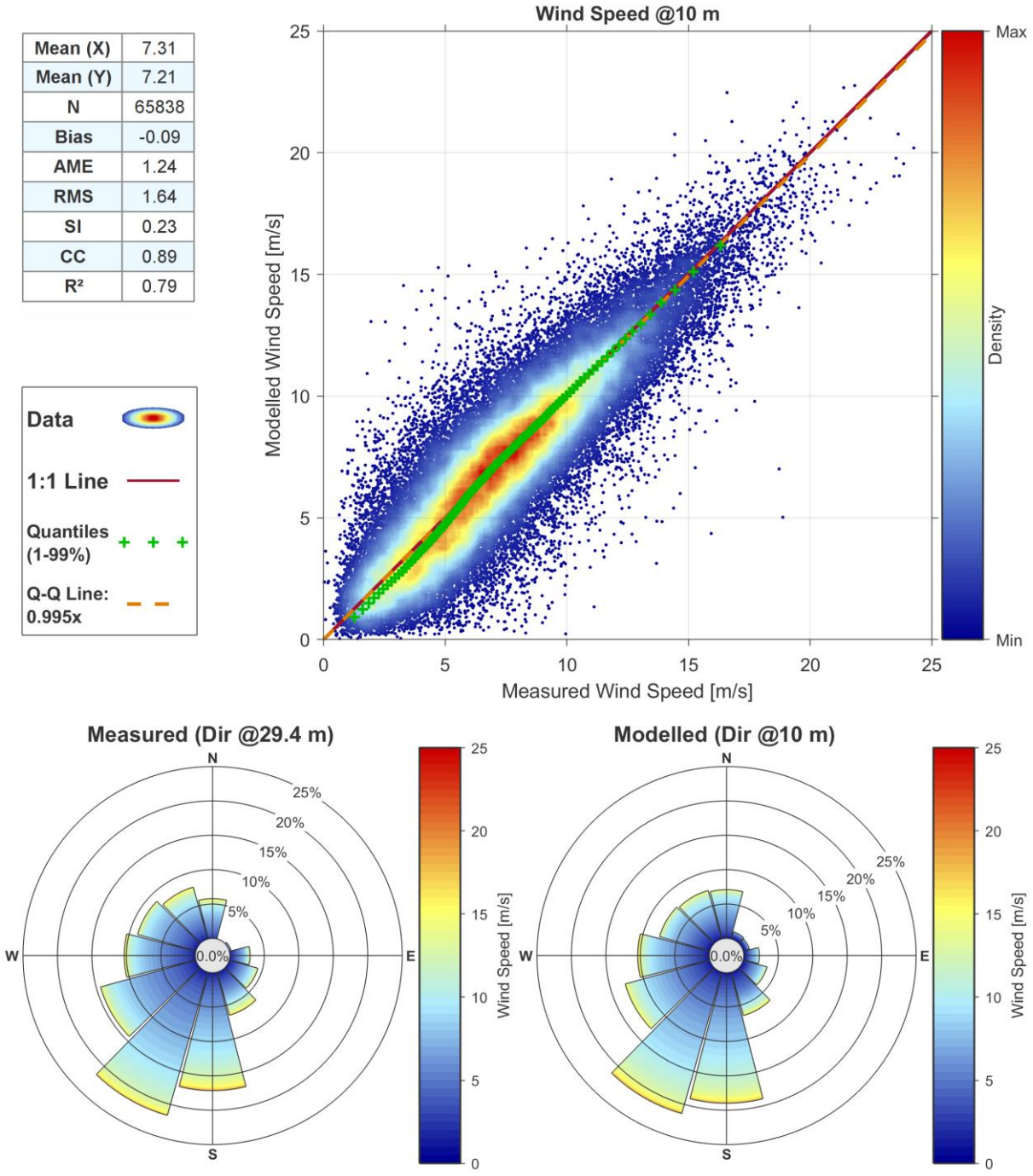



Figure 4.4: Calibrated ERA5 Model vs. Measured, Arklow Met Mast at 10 m.

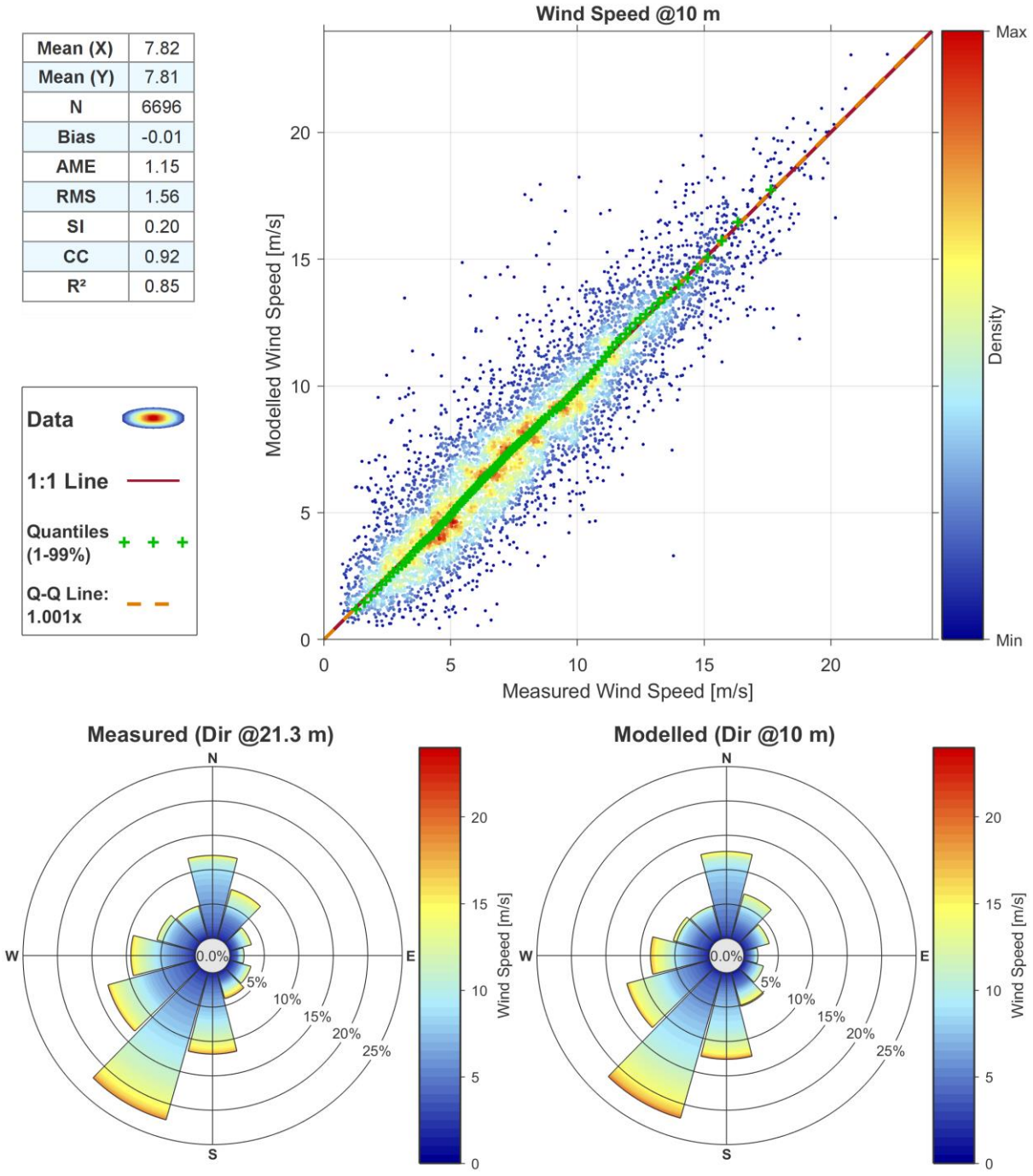



Figure 4.5: Calibrated Vortex Model vs. Measured, Arklow LiDAR at 10 m.

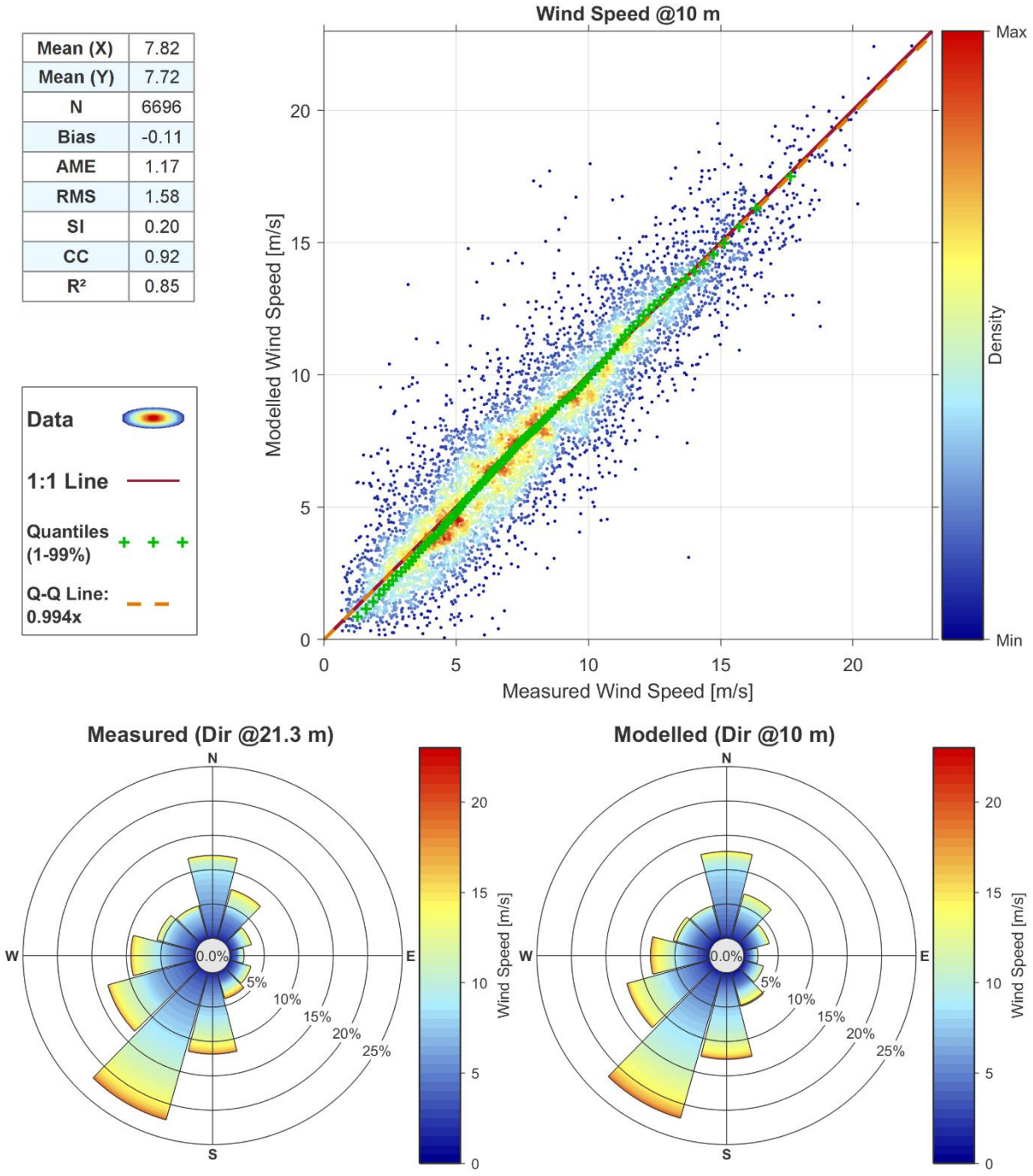



Figure 4.6: Calibrated ERA5 Model vs. Measured, Arklow LiDAR at 10 m.

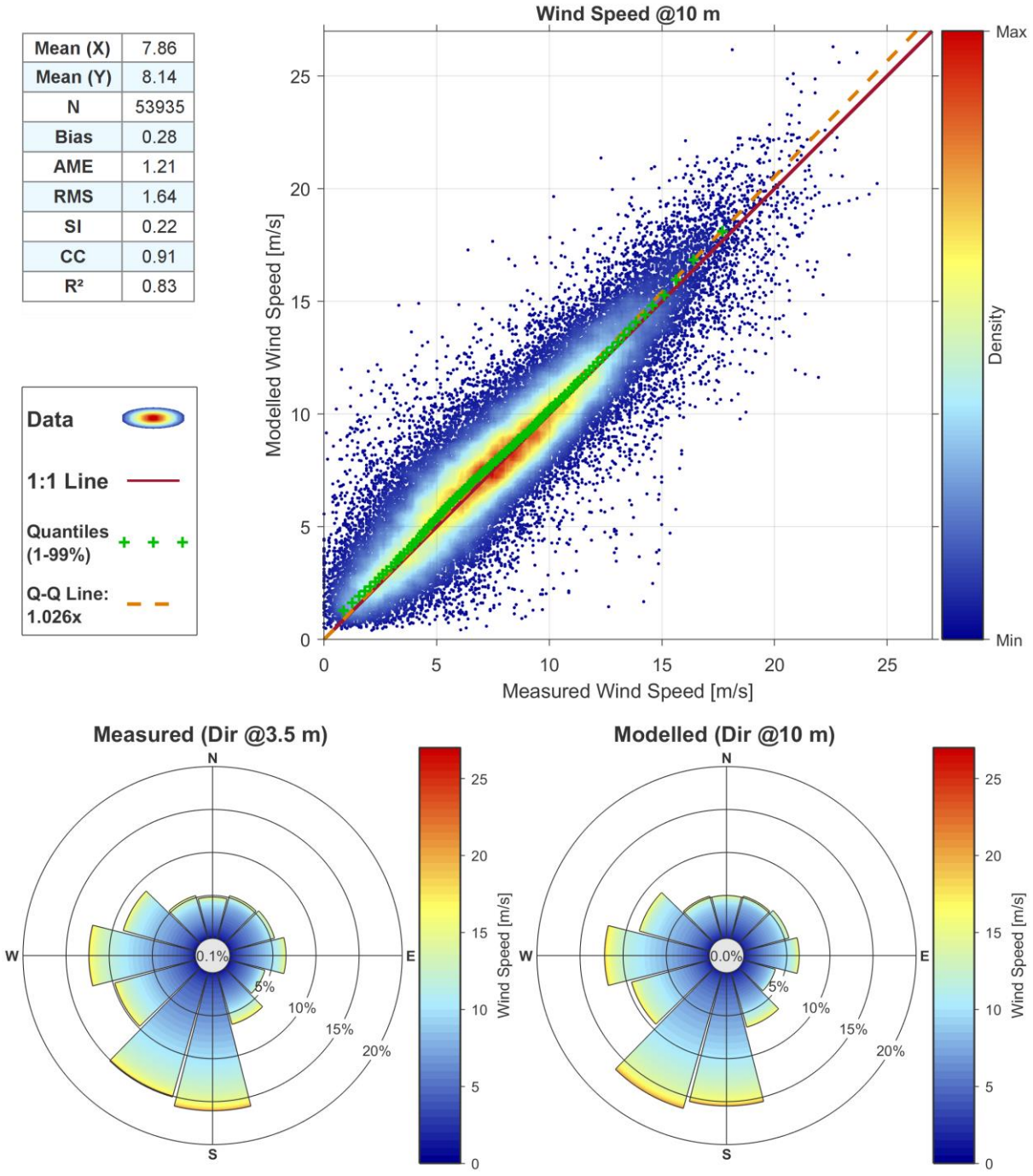



Figure 4.7: Calibrated Vortex Model vs. Measured, M2 at 10 m.

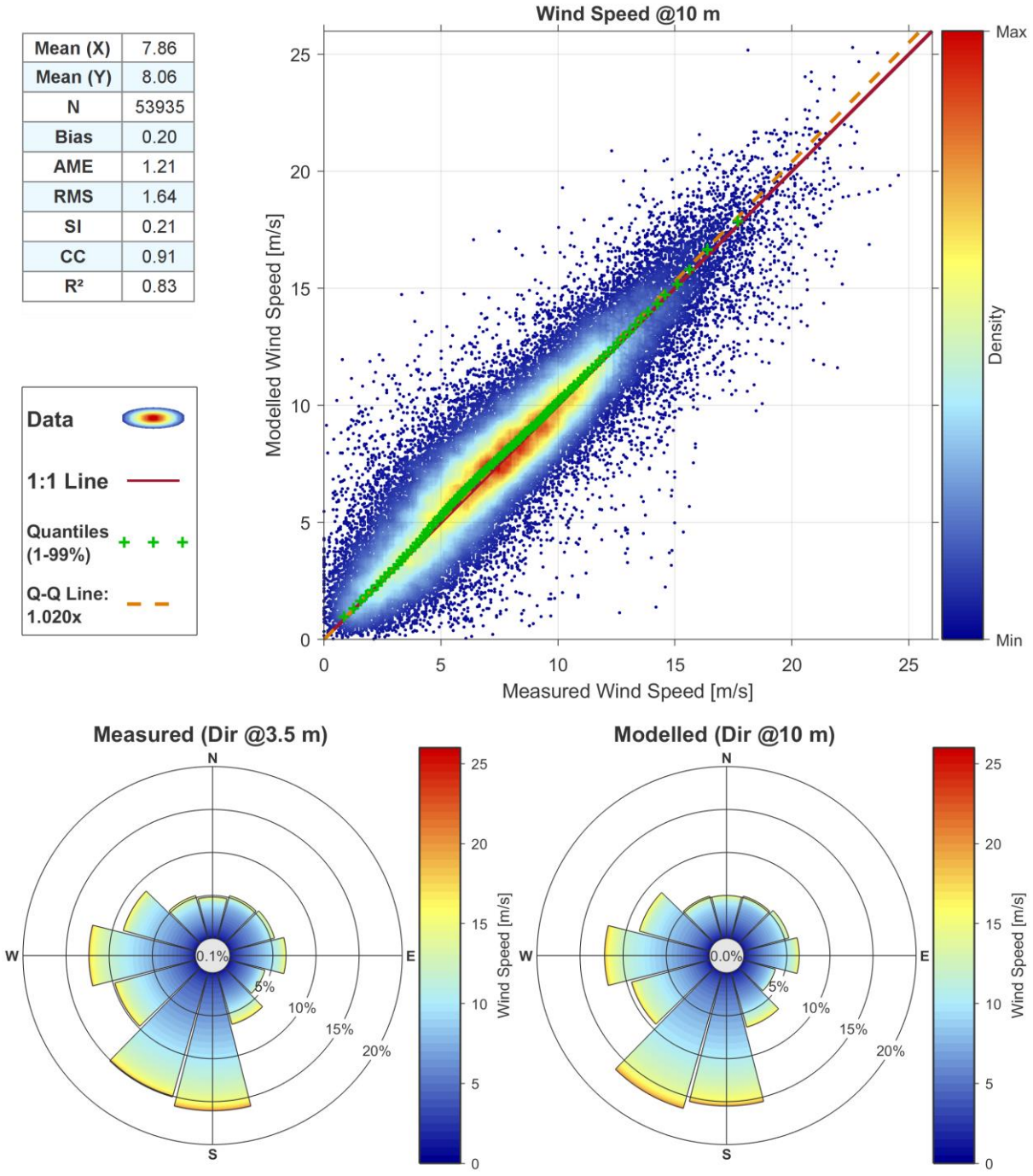



Figure 4.8: Calibrated ERA5 Model vs. Measured, M2 at 10 m.

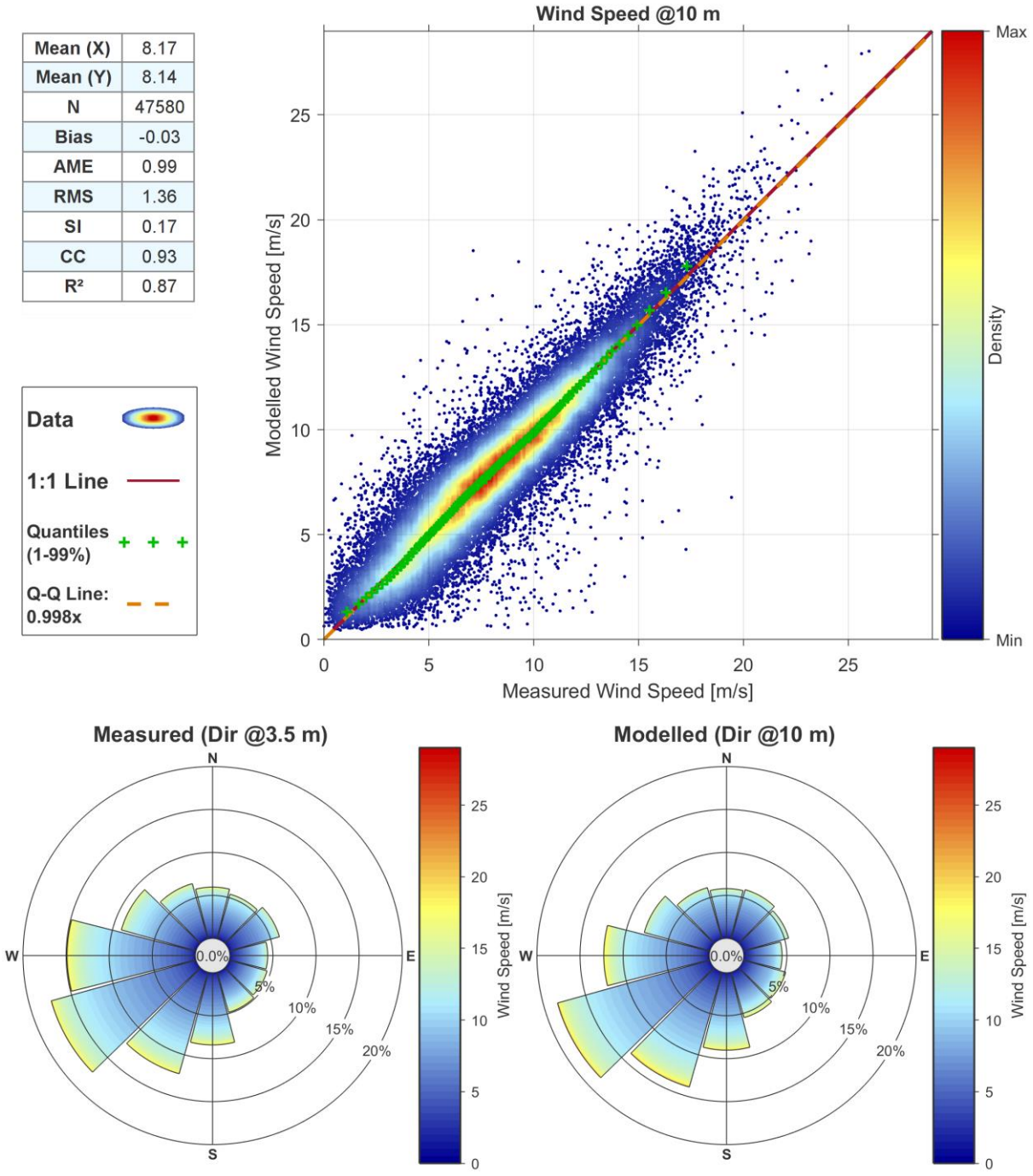



Figure 4.9: Calibrated Vortex Model vs. Measured, M5 at 10 m.

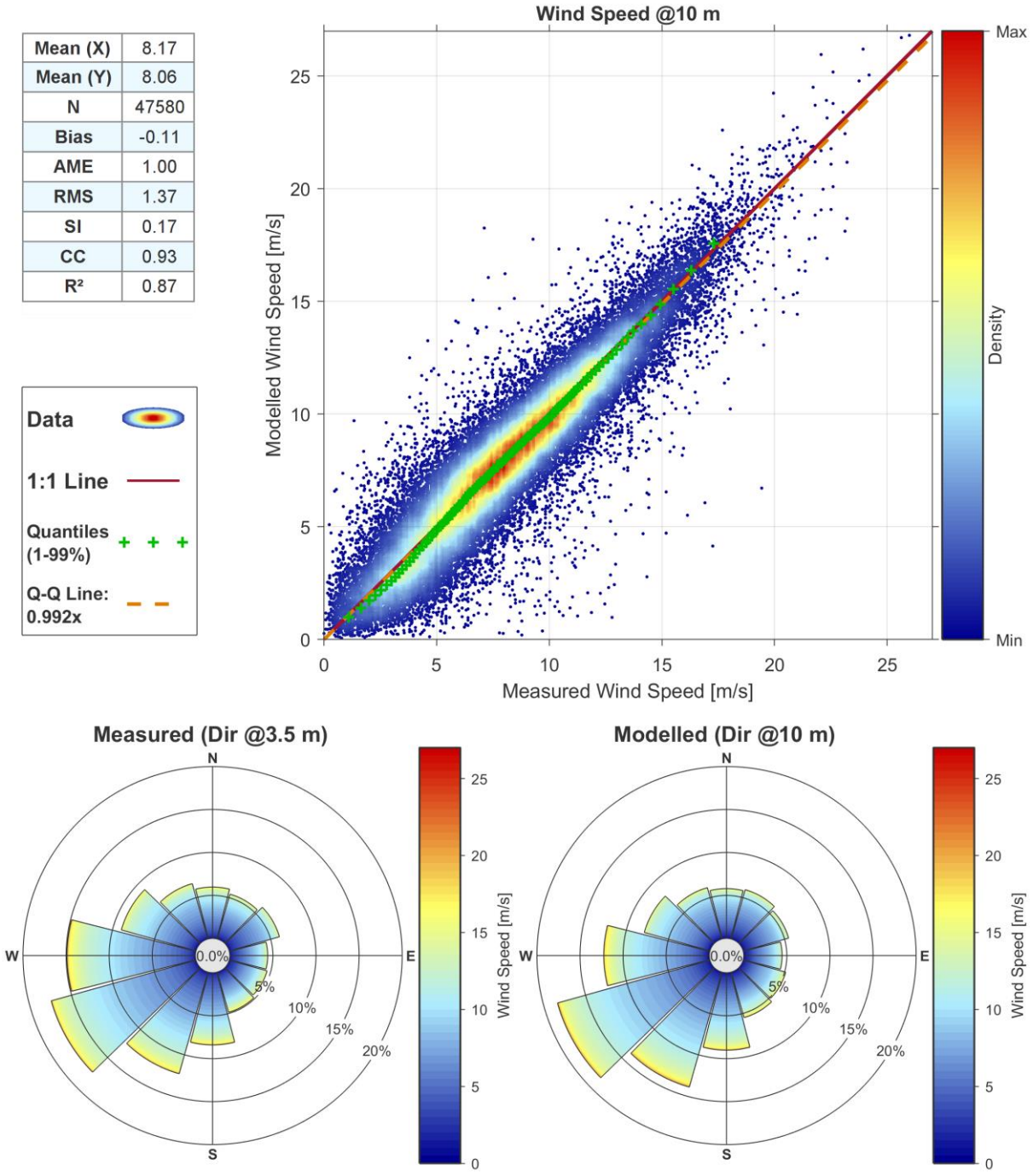



Figure 4.10: Calibrated ERA5 Model vs. Measured, M5 at 10 m.

# 5 Hydrodynamics

Current and water level parameters were produced from a high-resolution local, flexible mesh hydrodynamic model. Boundary conditions to this model originated from a project-specific version of the MetOceanWorks' European Hindcast Model, which has been validated against several datasets to ensure accurate propagation of the tidal wave from open water into the Irish Sea. The local model was subjected to sensitivity testing and validation, before depth-averaged currents and water-levels were output at 20-minute intervals for the 39-year period between January 1982 and February 2021.

Model parameters should be considered as representative of 10-minute averages.

## 5.1 Measured Hydrodynamic Data

To support calibration and validation of the hydrodynamic model, measured data were acquired from the Irish Marine Institute, the Office of Public Works as well as those provided by Sure Partners Limited. An overview of the measured datasets can be found in Table 5.1 and Figure 5.1.

Table 5.1: Measured datasets used for hydrodynamic model validation.

| Dataset | Location | Time Period | Water Depth [mMSL] | Currents | Water Levels |
|---|---|---|---|---|---|
| **AWAC A** | 52.9087 °N, 5.9167 °W | 6-Nov-2019 to 7-Mar-2021 | 27.4† | ✓ | ✓ |
| **AWAC B1** | 52.8496 °N, 5.9466 °W | 2-Aug-2020 to 7-Mar-2021 | 30.2 | ✓ | ✓ |
| **AWAC C** | 52.8218 °N, 6.0206 °W | 24-Nov-2019 to 19-May-2020 | 26.3 | ✓ | ✓ |
| **AWAC D1** | 52.8218 °N, 6.0206 °W | 1-Aug-2020 to 7-Mar-2021 | 30.5 | ✓ | ✓ |
| **AWAC E** | 52.6906 °N, 5.9940 °W | 24-Nov-2019 to 8-Mar-2021 | 39.6.7 | ✓ | ✓ |
| **Howth Harbour** | 53.3915 °N, 6.0683 °W | 13-Feb-2007 to 26-Nov-2019 | Coastal* | x | ✓ |
| **Dublin Port** | 53.3457 °N, 6.2217 °W | 6-Nov-2009 to 1-Jan-2019 | Coastal* | x | ✓ |
| **Arklow Harbour** | 52.7920 °N, 6.1452 °W | 26-Aug-2003 to 1-Jan-2020 | Coastal* | x | ✓ |
| **Rosslare Harbour** | 52.2546 °N, 6.6648 °W | 4-Dec-2018 to 3-Jul-2020 | Coastal* | x | ✓ |
| **Dunmore East Harbour** | 52.1477 °N, 6.9919 °W | 23-Apr-2012 to 3-Jul-2020 | Coastal* | x | ✓ |
| **Ballycotton Harbour** | 51.8278 °N, 8.0007 °W | 7-Oct-2010 to 3-Jul-2020 | Coastal* | x | ✓ |

* Throughout, the term "*Coastal*" is used to denote an instrument mounted to a harbour wall.

† No valid data was recorded was at AWAC A during Deployment 2 after 5th August 2020.

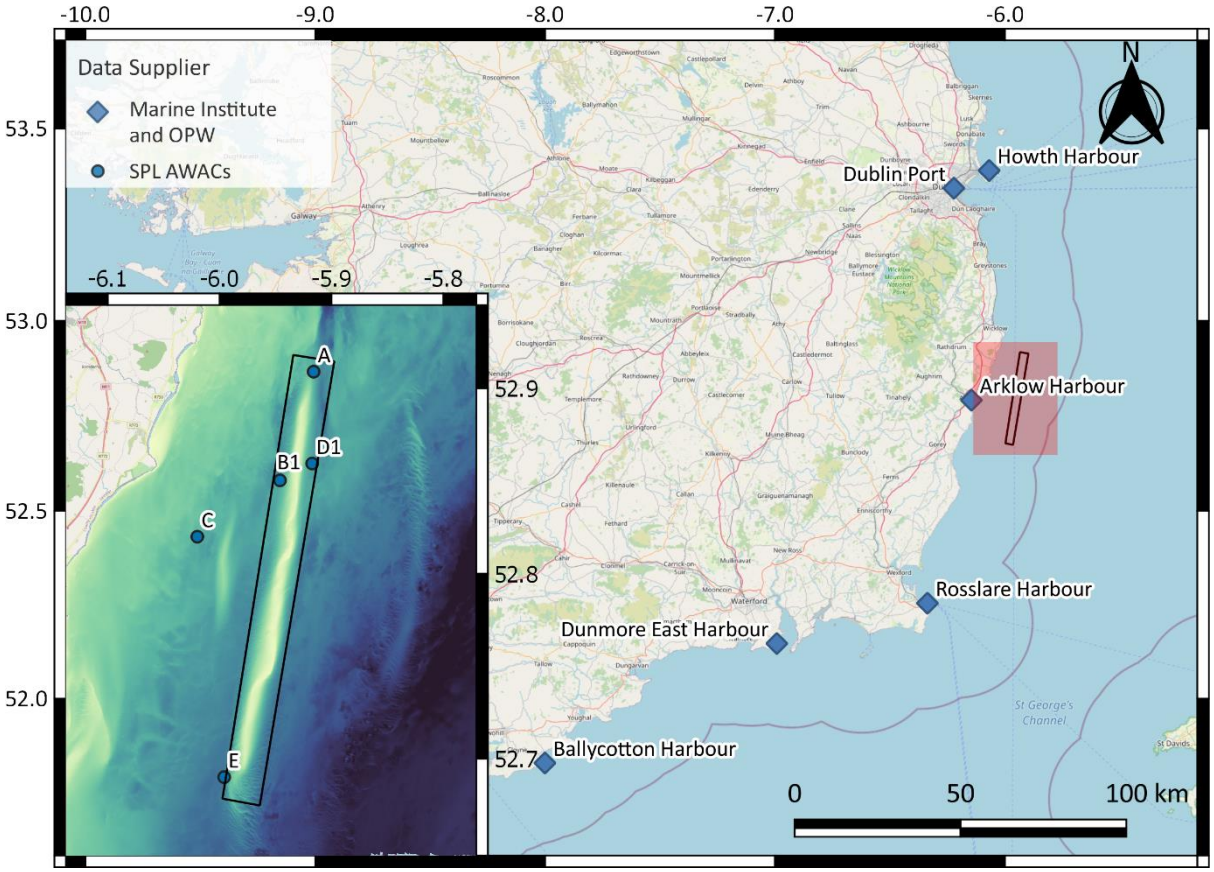



Figure 5.1: Measured datasets used for hydrodynamic model validation.

### 5.1.1 Measured Current Profiles

The vertical profiles of measured currents are reviewed in Appendix H and are fitted to the theoretical power law to obtain a recommended exponent, α, for the translation of currents between different depths. For higher current speeds, an exponent of 1/7 is recommended within the lease zone whilst an exponent of 1/9 may be more appropriate along the cable corridor.

## 5.2 Modelling Software

The hydrodynamic model has been developed using the MIKE21FM 2D flexible mesh modelling package, a comprehensive modelling system for two-dimensional water modelling developed at the Danish Hydraulic Institute (DHI).

## 5.3 Model Boundary Conditions and Spatial Extent

Tidal boundary conditions to the European model originate from the Finite Element Solution FES2014 dataset. This 35-constituent, global data-set has been produced using numerical modelling which assimilates satellite observations of water level and has, in our opinion, the best skill of any publicly-available global tide model. The dataset includes tide elevations (amplitude and phase) and tide currents on a 0.0625-degree

(approximately 7 km) grid. The model was driven using water levels varying along three open boundaries, as shown in Figure 5.2.

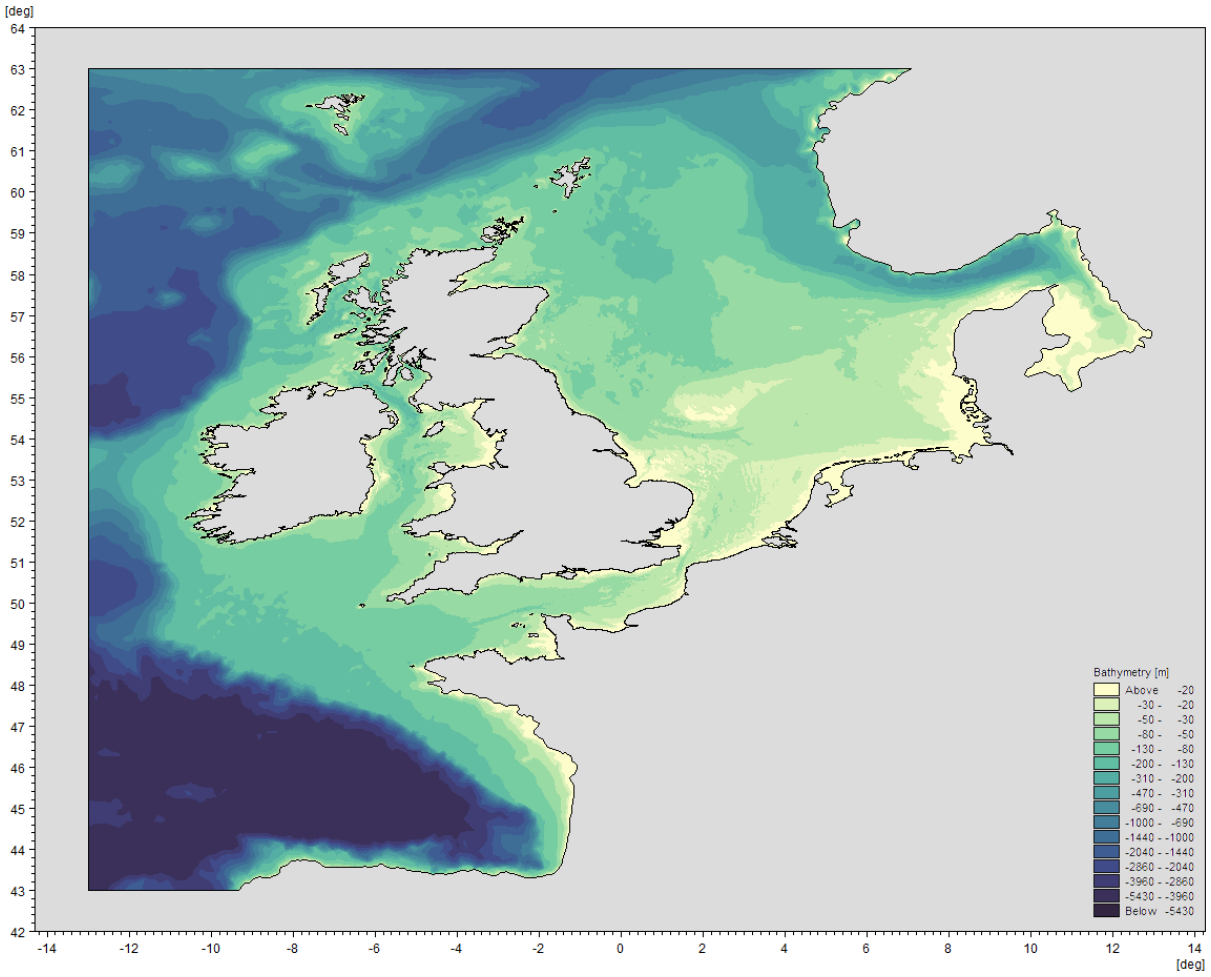



Figure 5.2 Regional European MIKE21 flexible model mesh. Bathymetry in m MSL.

The local hydrodynamic model shown in the right-hand panel of Figure 5.3 was driven at its external boundaries by velocities (north and south) and water levels (east) from the European-scale model. The velocity boundaries were selected to reflect the principal axis of current flow, aligned with the coast i.e. flow will predominantly be perpendicular to these boundaries. Due to model constraints, water-levels and velocities cannot be specified on the same boundary, as a result water-levels were applied along the eastern edge.

The model had a spatial resolution of 75 m within the wind park lease boundary including a 2 km buffer surrounding it. Beyond this buffer, the model had a resolution of approximately 150 m in depths shallower than 40 m and a resolution of 225 m further offshore.

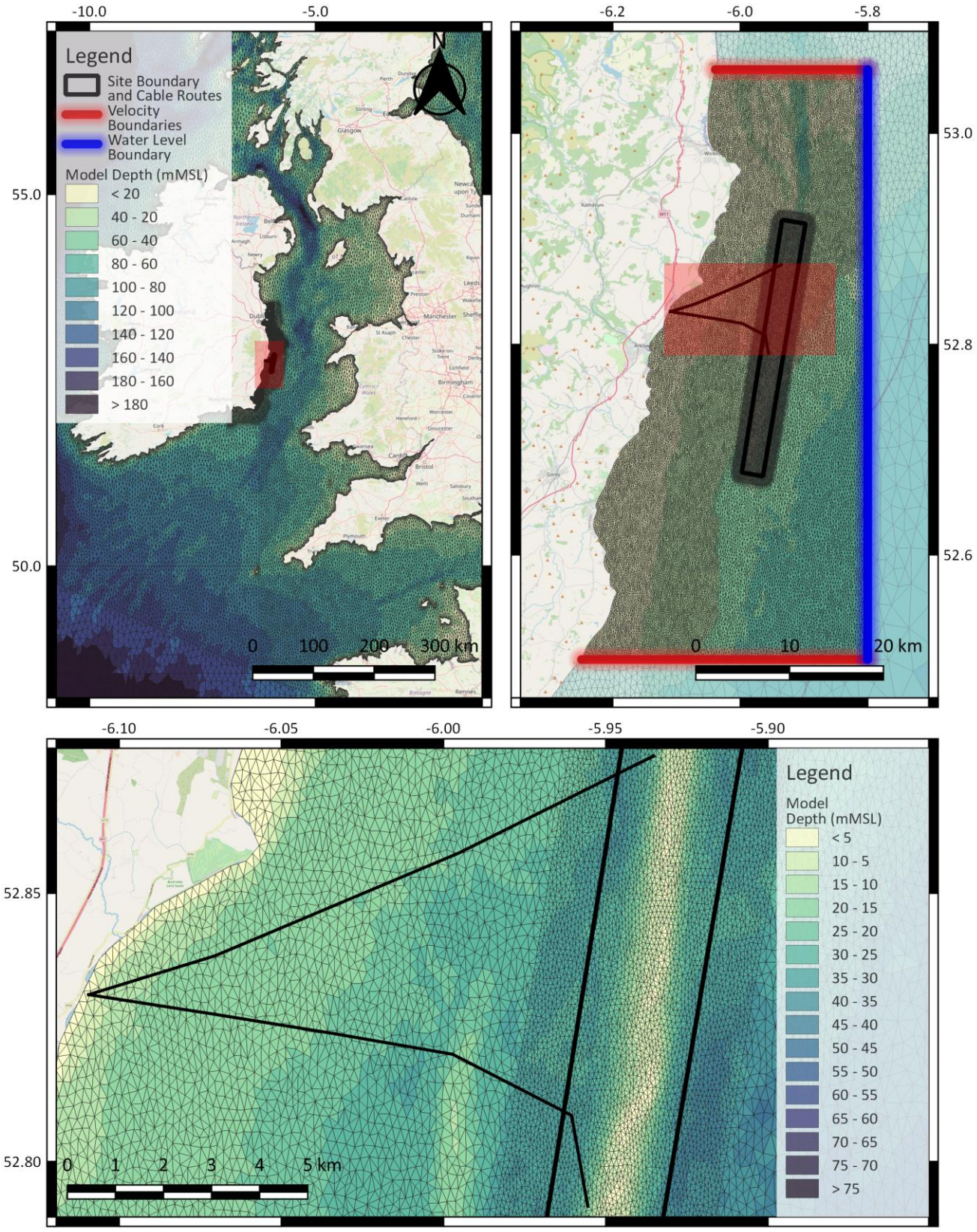



Figure 5.3 Zoom in of Irish east coast region of MIKE21 flexible model mesh. Bathymetry in mMSL.

Atmospheric forcing for the hydrodynamic model originated from the ECMWF ERA5 dataset and was applied to ensure that atmospheric surge effects were properly represented in the model. This comprised of MetOceanWorks adjusted wind speeds, unadjusted wind directions, and unadjusted pressure fields. It was necessary to drive the large-scale model with ERA5 data, given that it covered a much larger domain than the Vortex wind fields. Using different atmospherics at the local level would have risked introducing numerical instability to the model, therefore ERA5 data was used at this level also. Given the similarity between the two atmospheric datasets, as demonstrated in Section 4.4, any difference would likely have a marginal impact over the small length scales of the local model. Furthermore, the site is tidally dominated which further reduces the overall contribution of wind input at the site.

## 5.4 Model Sensitivity Testing

The model was subjected to a series of sensitivity tests to determine the effects of tuning various input parameters.

### 5.4.1 Mesh Resolution

To ensure that an appropriate mesh density was selected for the final hydrodynamic model, a series of tests were carried out to demonstrate convergence of results. Models with varying mesh resolutions within the wind farm zone were deployed, and the effects of varying mesh resolution were analysed at four locations. Mesh resolutions of 150, 75 and 37.5 m were used in these tests (see Figure 5.4 to Figure 5.6. Hydrodynamic mesh with 37.5 m resolution within the wind farm lease area and surrounds., which also show the analysis locations), with comparisons given in Figure 5.7 to Figure 5.10.

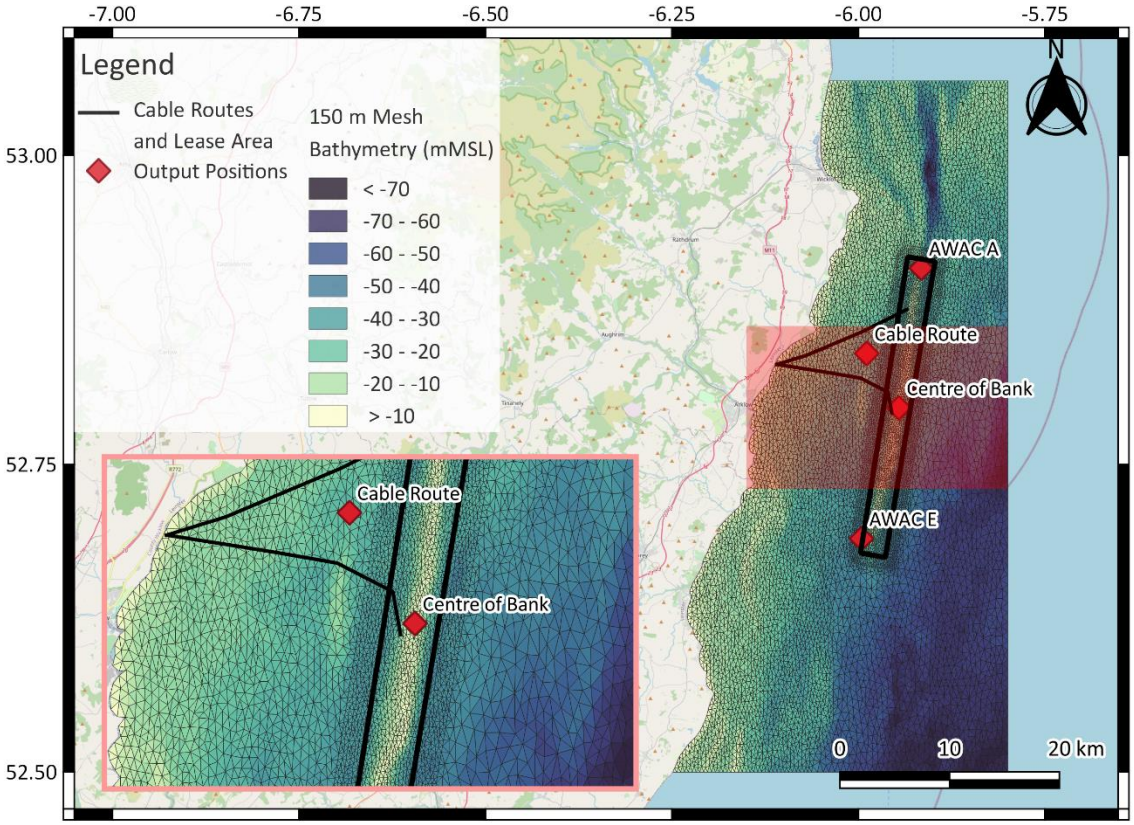



Figure 5.4. Hydrodynamic mesh with 150 m resolution within the wind farm lease area and surrounds.

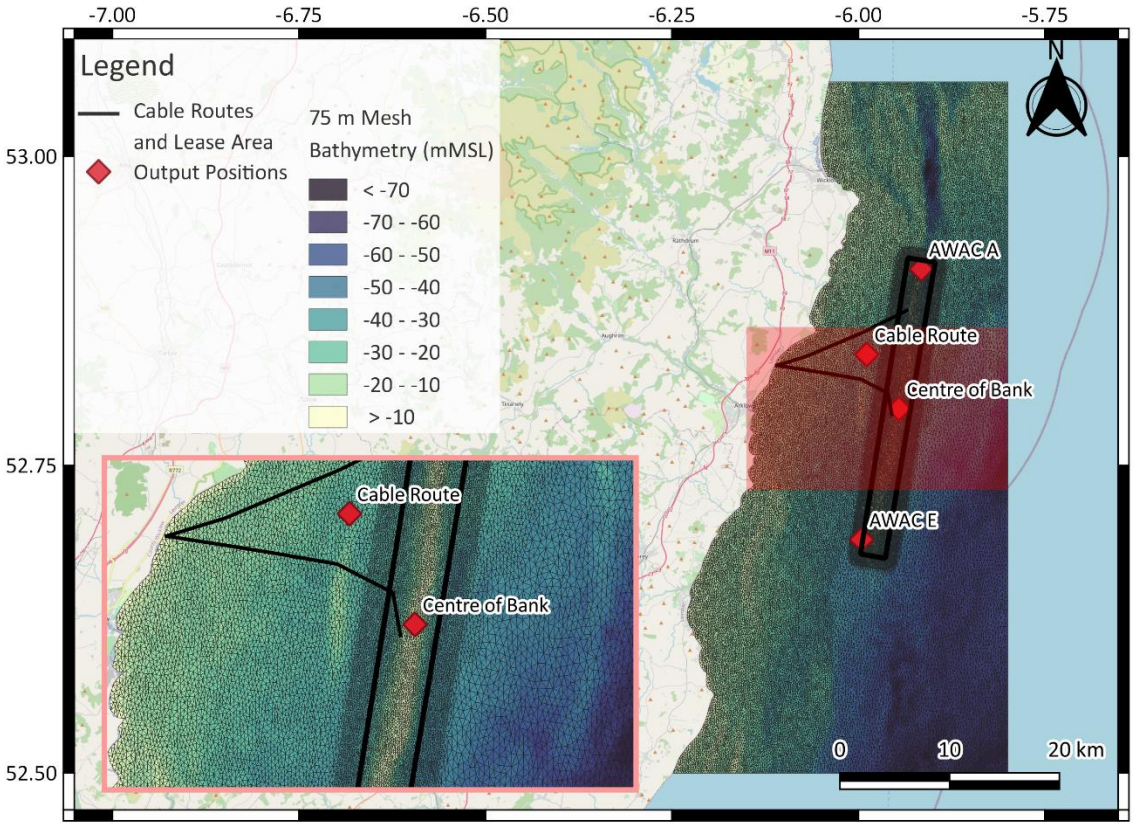



Figure 5.5. Hydrodynamic mesh with 75 m resolution within the wind farm lease area and surrounds.

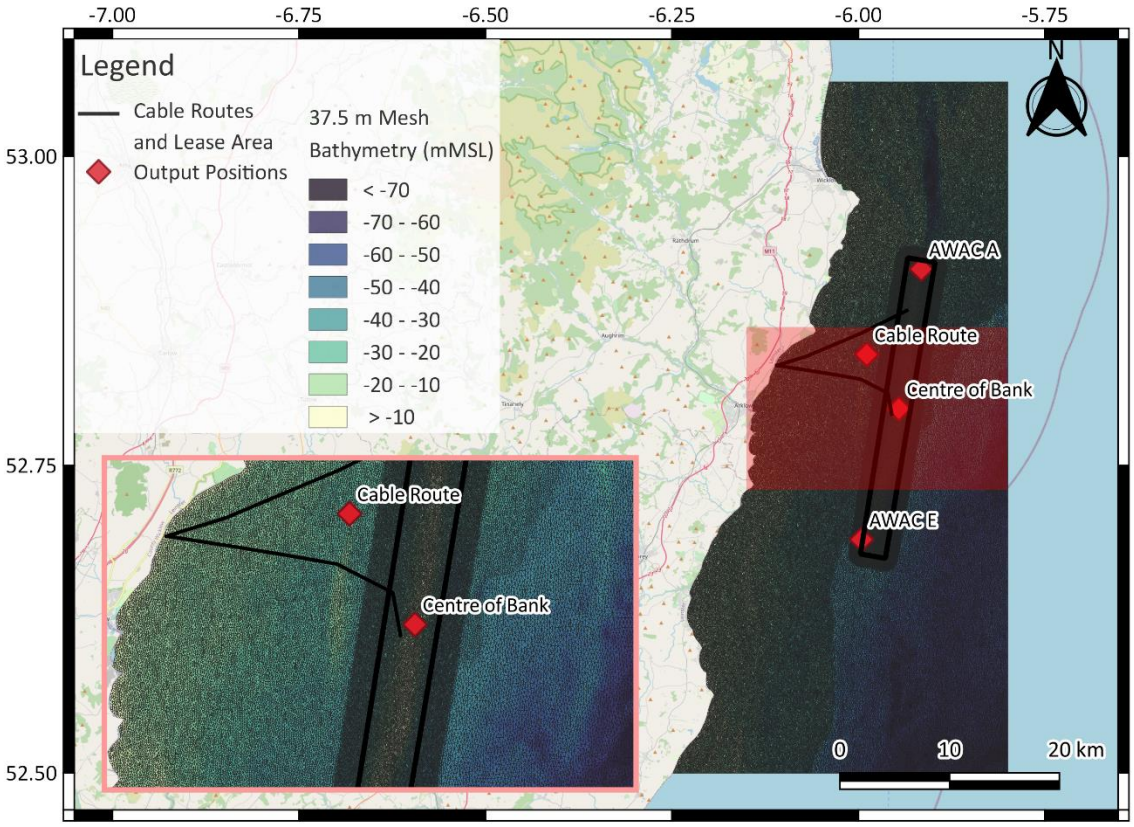



Figure 5.6. Hydrodynamic mesh with 37.5 m resolution within the wind farm lease area and surrounds.

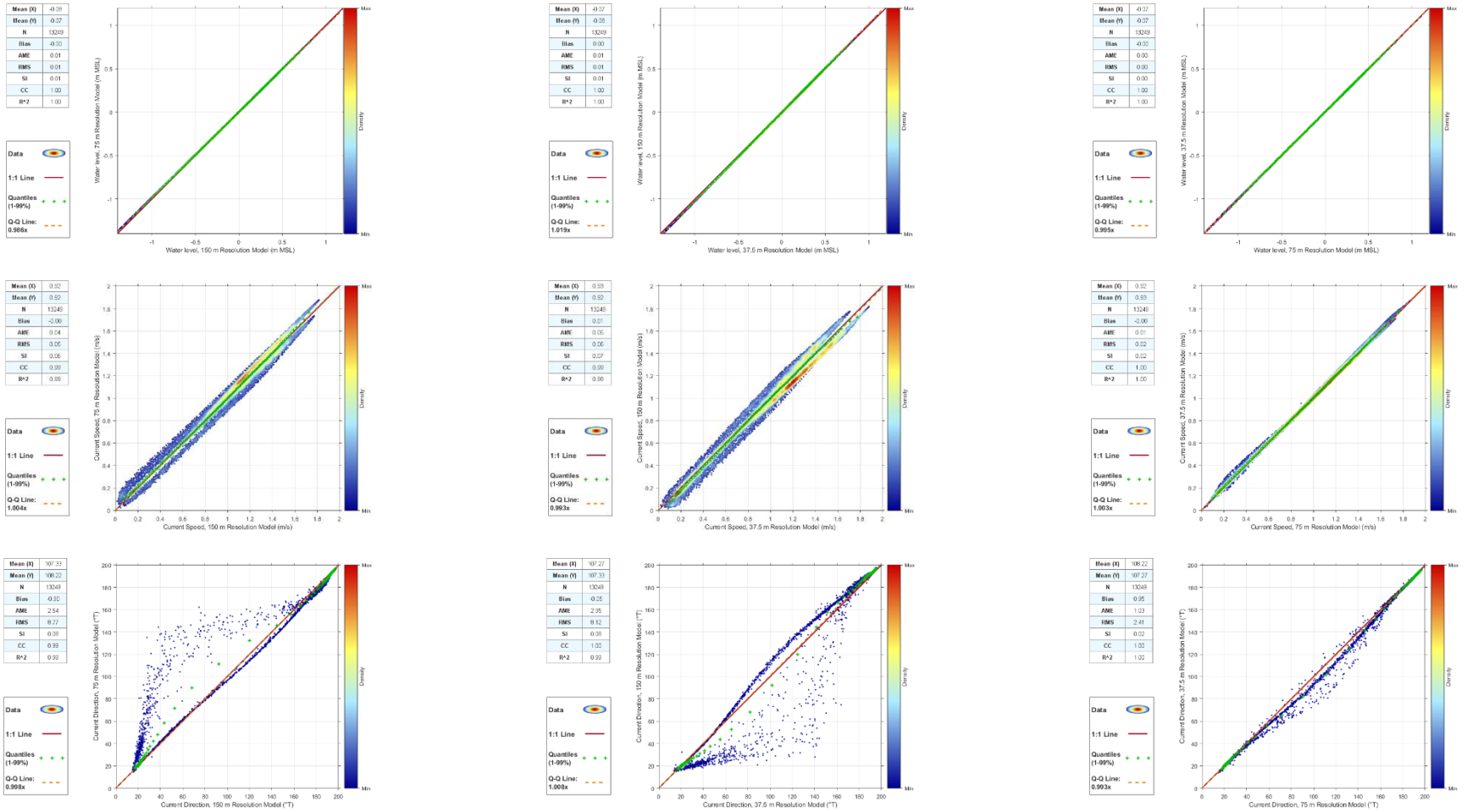



Figure 5.7. Results of model runs with differing mesh resolutions, at AWAC A. Top row = water level, middle row = current speed, bottom row = current direction. Left column 150 m vs. 75 m. Middle column 37.5 m vs. 150 m. Right column = 75 m vs. 37.5 m.

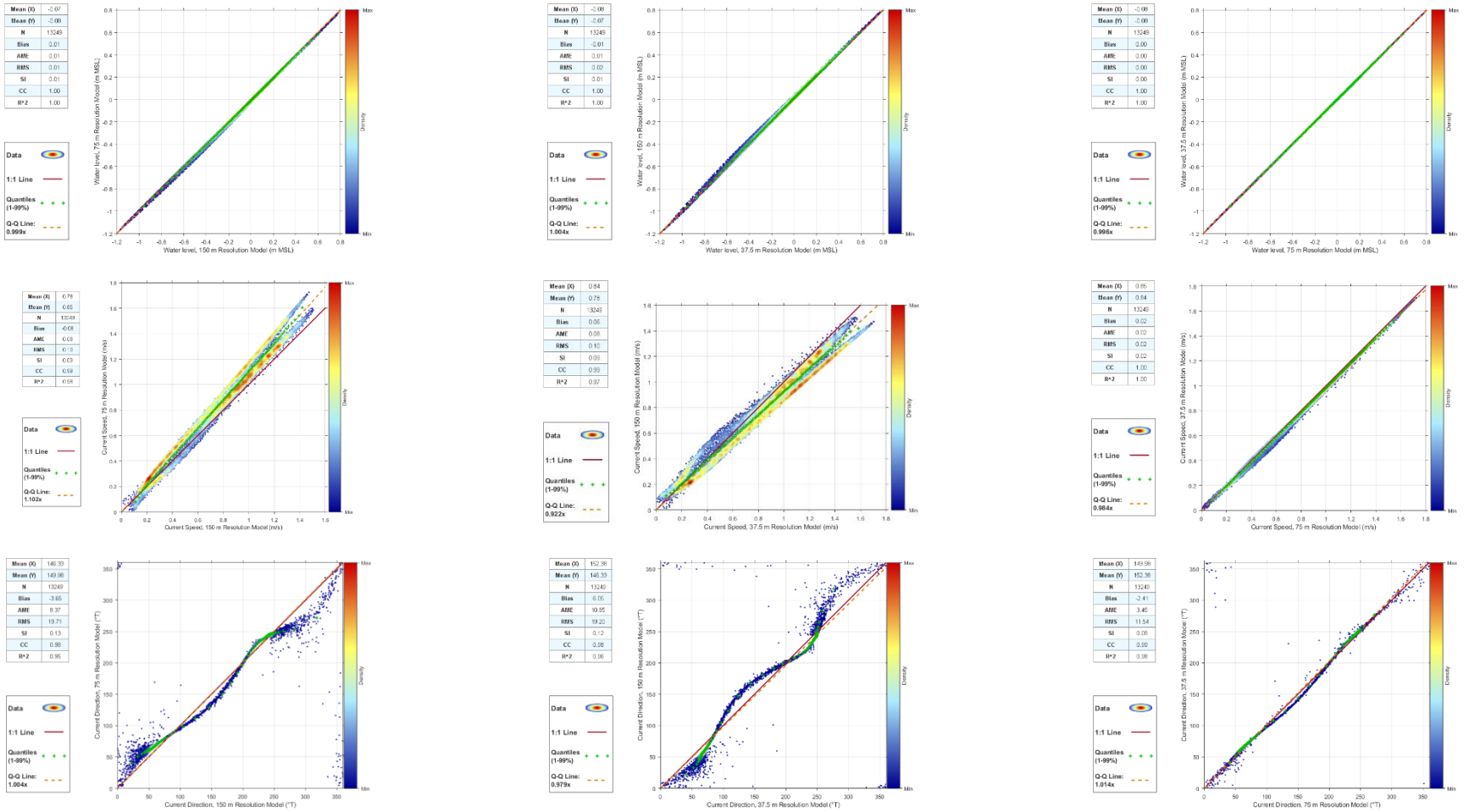



Figure 5.8. Results of model runs with differing mesh resolutions, at Centre of Bank. Top row = water level, middle row = current speed, bottom row = current direction. Left column 150 m vs. 75 m. Middle column 37.5 m vs. 150 m. Right column = 75 m vs. 37.5 m.

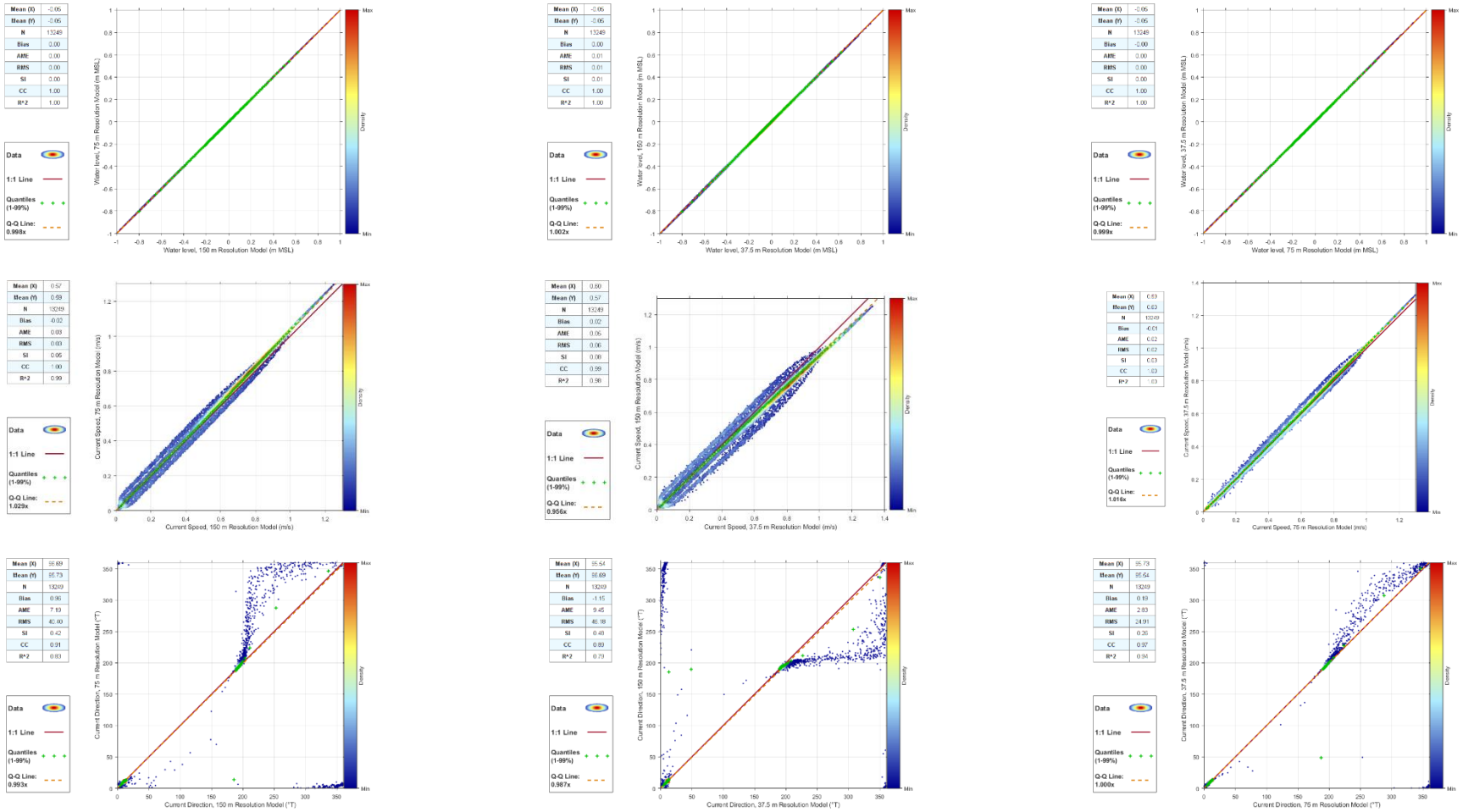


Figure 5.9. Results of model runs with differing mesh resolutions, at AWAC E. Top row = water level, middle row = current speed, bottom row = current direction. Left column 150 m vs. 75 m. Middle column 37.5 m vs. 150 m. Right column = 75 m vs. 37.5 m.

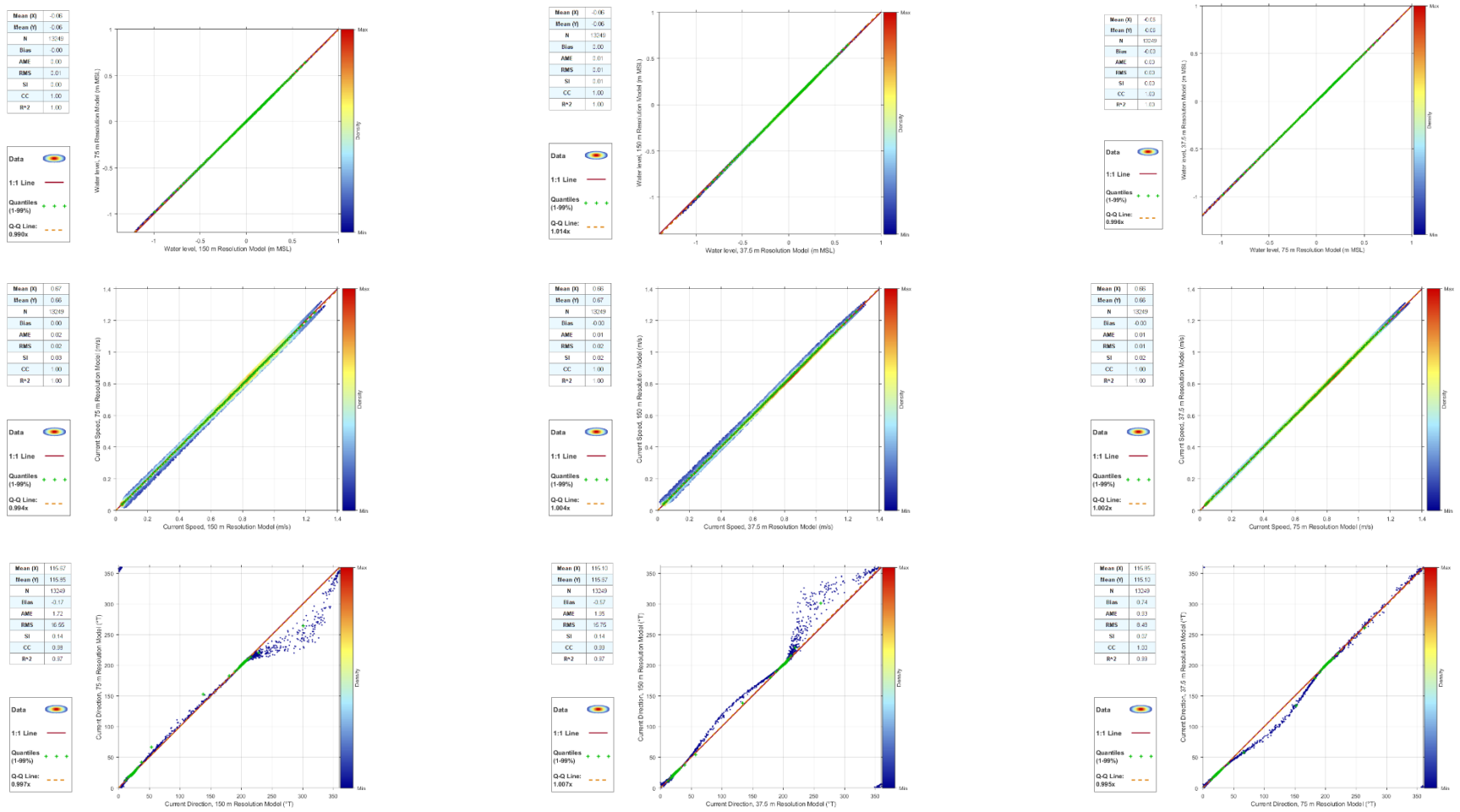



Figure 5.10. Results of model runs with differing mesh resolutions, at the Cable Route. Top row = water level, middle row = current speed, bottom row = current direction. Left column 150 m vs. 75 m. Middle column 37.5 m vs. 150 m. Right column = 75 m vs. 37.5 m.

In these tests, we can consider the highest resolution model to be the 'standard' against which the other resolutions can be judged, on the basis that we assume that the highest resolution model should produce the more accurate results.

Figure 5.7 to Figure 5.10 show that the impacts of mesh resolution on current speed and direction can be large at certain locations, particularly when considering current directions at certain states of the tide (flood or ebb). In general, water levels (top row of each figure) are unaffected by changes in mesh resolution.

As expected, the largest differences are observed when comparing the highest and lowest resolution models (middle columns of each figure).

The right-hand columns of each figure show that there is limited difference between a model with resolution of 75 m or 37.5 m, suggesting that there is little additional 'accuracy' to be achieved in increasing the resolution above 75 m. Therefore, a final mesh resolution of 75 m was selected, it being the highest resolution that could be achieved with an acceptable runtime.

Using 75 m resolution in the wind farm zone, the entire model consisted of approximately 227,500 triangular tessellations.

### 5.4.2 Bed Resistance

Various uniform and spatially-varying bed roughness values were tested as part of model calibration. A spatially-varying bed roughness was eventually chosen for the final production hindcast run, which provided the best overall representation of water levels and currents at each validation site.

## 5.5 Final Model Parameter Settings

The following model settings were used for the hindcast:

Table 5.2: Final model parameter settings.

| Parameter | Setting |
|---|---|
| Minimum and maximum time step | 0.1 and 120 seconds |
| Wind friction | 0.001255 at 7m/s and 0.002425 at 25m/s |
| Critical CFL number | 1 |
| Drying, flooding and wetting depth | 0.01 m, 0.05 m, 0.1 m |
| Horizontal eddy viscosity formulation | Smagorinsky, constant = 0.28 |
| Minimum and maximum eddy viscosity | 0.0000018, 100,000 $m^2$/second |
| Bed resistance | Variable Manning's M |

## 5.6 Hindcast Uniformity

In terms of input model boundary conditions, the model is expected to yield results of a uniform quality (i.e. equivalent to the level of validation detailed in the following Section 5.7) throughout the hindcast period.

However, Arklow Bank is subject to short term movement and so bedform evolution will undoubtedly have localised effects on the uniformity of the hydrodynamic regime over the lifetime of the windfarm. Analysis of

the bathymetry surveys from 2016 and 2019 show that in some locations, the position of crest of the bank has made a net shift of up to 350 m east or west over the three-year period. This dynamic behaviour is an important aspect of the site, with keen consideration required to ensure that its potential impact is fully appreciated. With this in mind, a review of the sensitivity of modelled current speeds to changes in bathymetry is presented in Appendix I. For this review, the hydrodynamic model was run for the two-year period from 2016 to 2017 using bathymetry from three different surveys carried out in 2000, 2016 and 2019. The results presented describe the sensitivity of the hindcast to geomorphological change and contextualise the envelope of uncertainty associated with current parameters arising from bedform migration.

## 5.7 Model Validation

The model was initially tuned using tidal forcing only such that modelled and measured tidal water levels agreed well. Atmospheric forcing was then introduced and the model was further calibrated against the measured current datasets until it demonstrated good skill.

Water levels from the European-scale hydrodynamic model are compared against long term measurements (2000-2019) at Howth, Dublin Port, Arklow, Rosslare, Dunmore East and Ballycotton in Figure 5.12 to Figure 5.17. With low mean errors, correlation coefficients close to unity and low scatter indices, these comparisons demonstrate excellent model skill for the large-scale model.

Water-level comparisons from the local model are presented again for Arklow Harbour and then for AWACs A, B1, C, D1 and E in Figure 5.18 to Figure 5.25. Figures for the AWACs show higher scatter indices which is likely the result of reduced accuracy achieved by a bed-mounted instrument on a mobile substrate compared to a fixed coastal tide gauge. In particular, the data report accompanying the AWAC measurements [1] notes that:

> *AWACs installed during Deployments 2 and 3 at Locations B1, D1 and E suffered from seabed frame movement. This intermittently affected the turbidity, current and wave data return for these locations. Additionally, the internal compass failed to update during the frame movement.*

Although the report goes on to detail a number of correction steps, a degradation in accuracy is still apparent, particularly between deployments at AWAC B1. Figure 5.20 presents a validation plot for deployment 2 which demonstrates excellent model skill, with a scatter index of 0.06 and an average mean error of 5 cm. For deployment 3 (Figure 5.21), the scatter index and average mean error more than doubles which is undoubtedly the result of instrument movement. This has the net effect of deteriorating the validation plot across all deployments presented in Figure 5.22.

Current speed validations for the local model are presented in Figure 5.26 to Figure 5.30. During the validation process, sensitivity testing revealed that 'micro-siting' of the output positions within a few grid cells of the measurement locations gave rise to differences in results. This is unsurprising given the dynamic behaviour of the Bank morphology discussed in the previous section as well as the difference in instrument position between deployments (see for example Figure 5.11). Such differences were particularly apparent at AWAC E where horizontal gradients in current speed occur due to sheltering from the bank on the ebbing tide, and local flow accelerations (possibly due to local bathymetric features such as sandwaves) on the flooding tide.

As a result, for each of the current speed validations, we have selected the best validation that is within at most a few grid cells of the average instrument position across all deployments. These regressions of modelled and measured depth-average current speeds for AWACs A, B1, C, D1 and E demonstrate good overall performance with marginally reduced skill at AWAC E.

Time-series comparisons of modelled and measured hydrodynamics during spring and neap tidal conditions are presented at each of the AWAC locations in Figure 5.31 to Figure 5.40. Figure 5.39 reveals that it is a small over-prediction on the ebbing tide which reduces the model skill at AWAC E. This can likely be attributed to morphological changes between the last bathymetry survey in 2019 and when the hydrodynamic measurements were actually taken in 2020. The small direction offset between modelled and measured currents of approximately 5 degrees seen at AWAC A in Figure 5.31 are also likely due to morphological changes combined with a small amount of uncertainty around the exact instrument position.

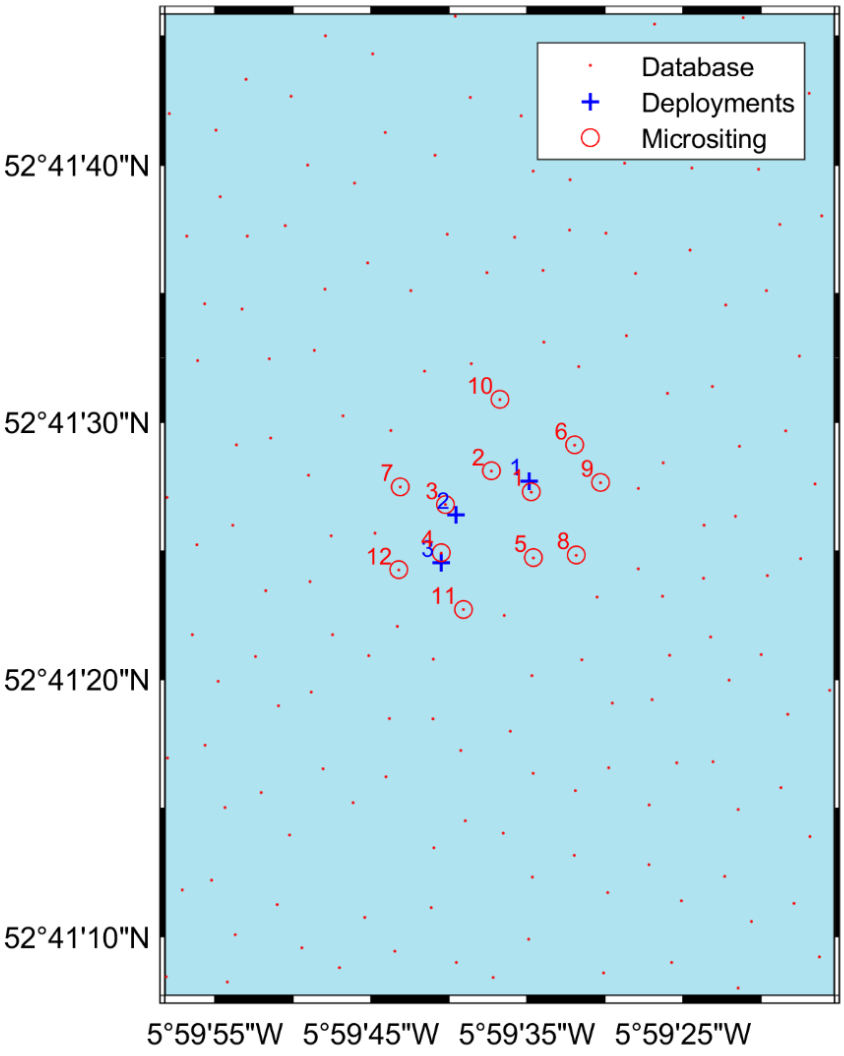



Figure 5.11. Positions of AWAC E for three deployments compared to the closest model gid points.

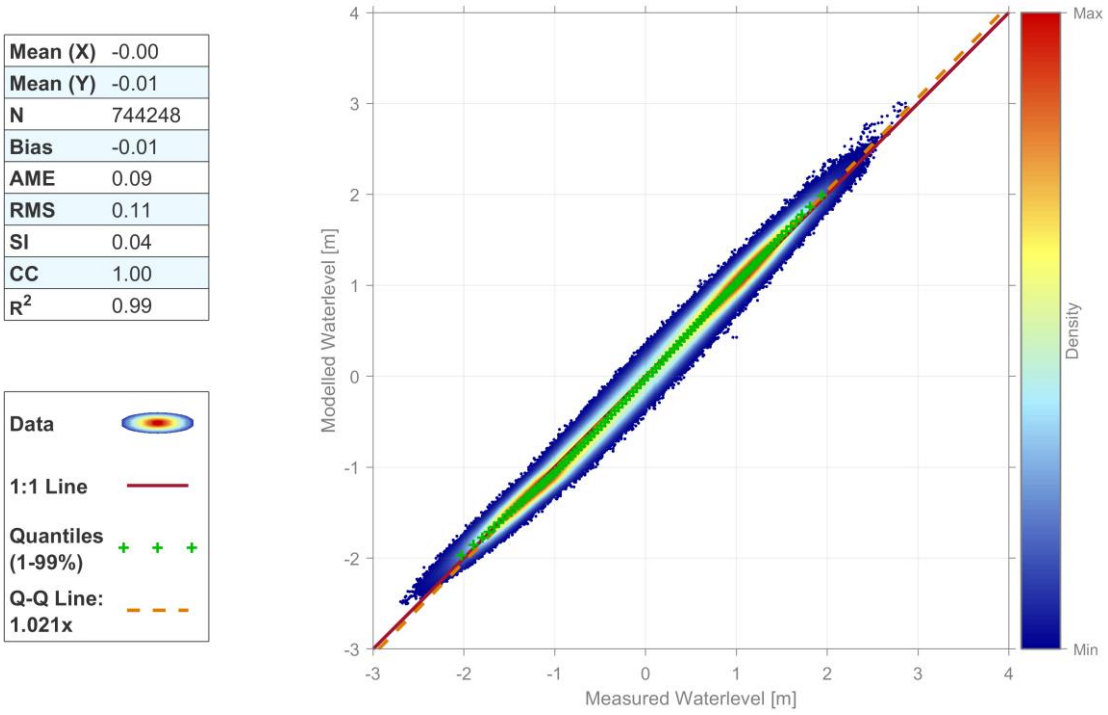



Figure 5.12: Comparison of measured and modelled water levels at Howth.

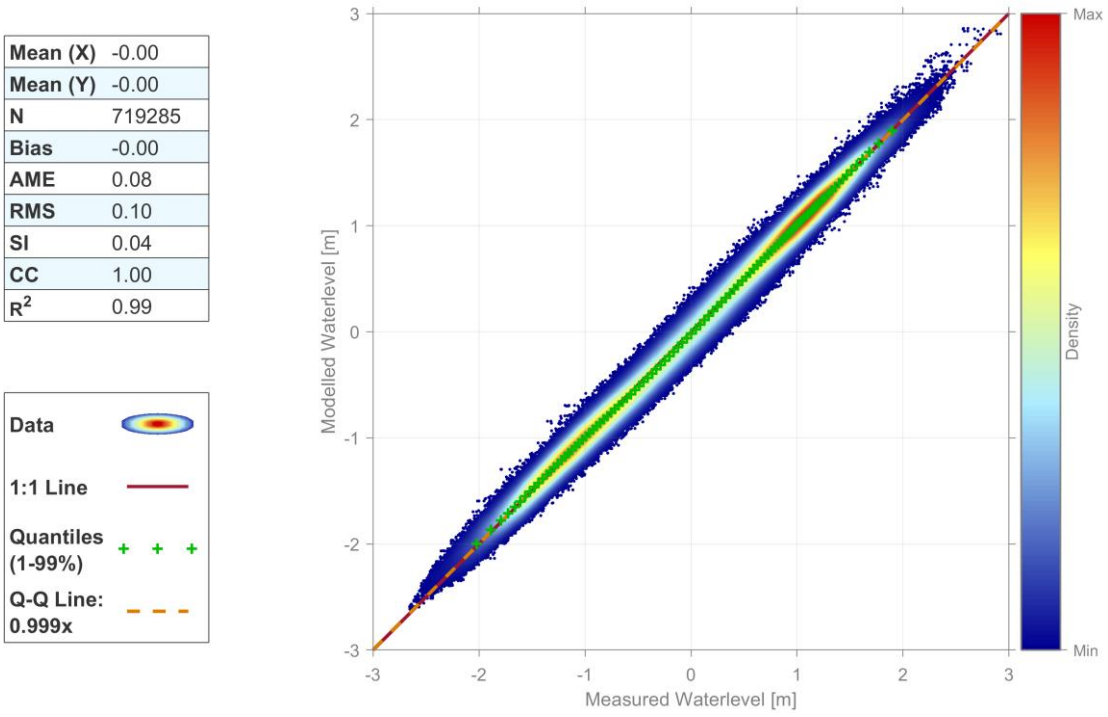



Figure 5.13: Comparison of measured and modelled water levels at Dublin Port.

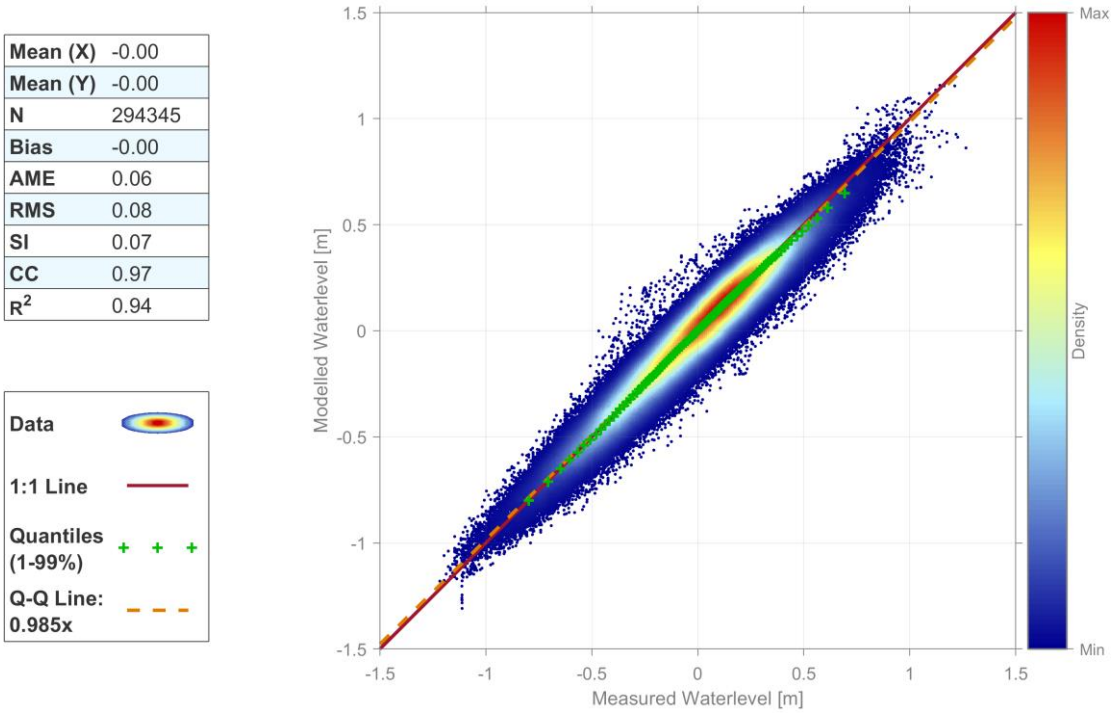



Figure 5.14: Comparison of measured and modelled water levels at Arklow Harbour (European model).

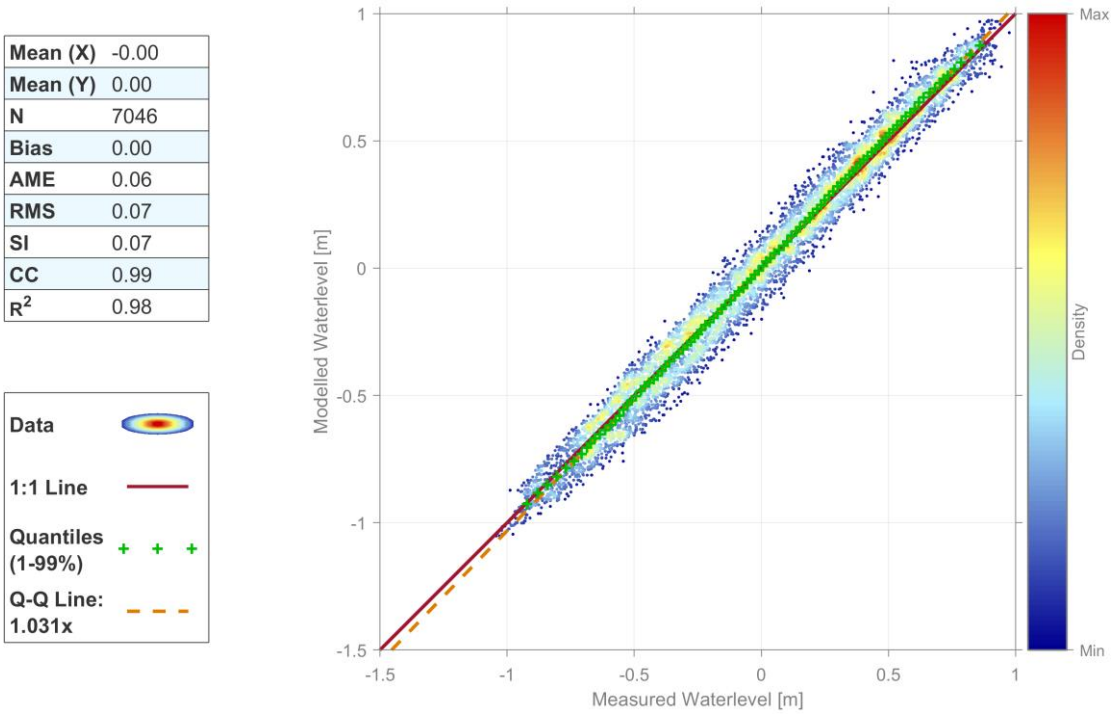



Figure 5.15: Comparison of measured and modelled water levels at Rosslare.

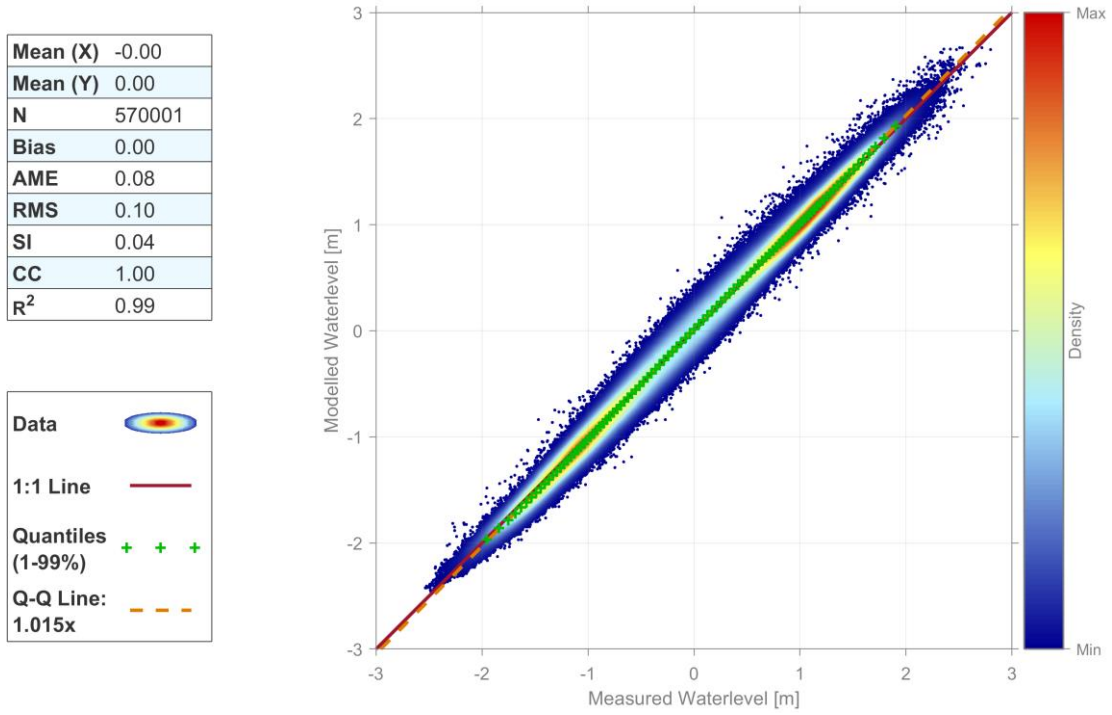



Figure 5.16: Comparison of measured and modelled water levels at Dunmore East.

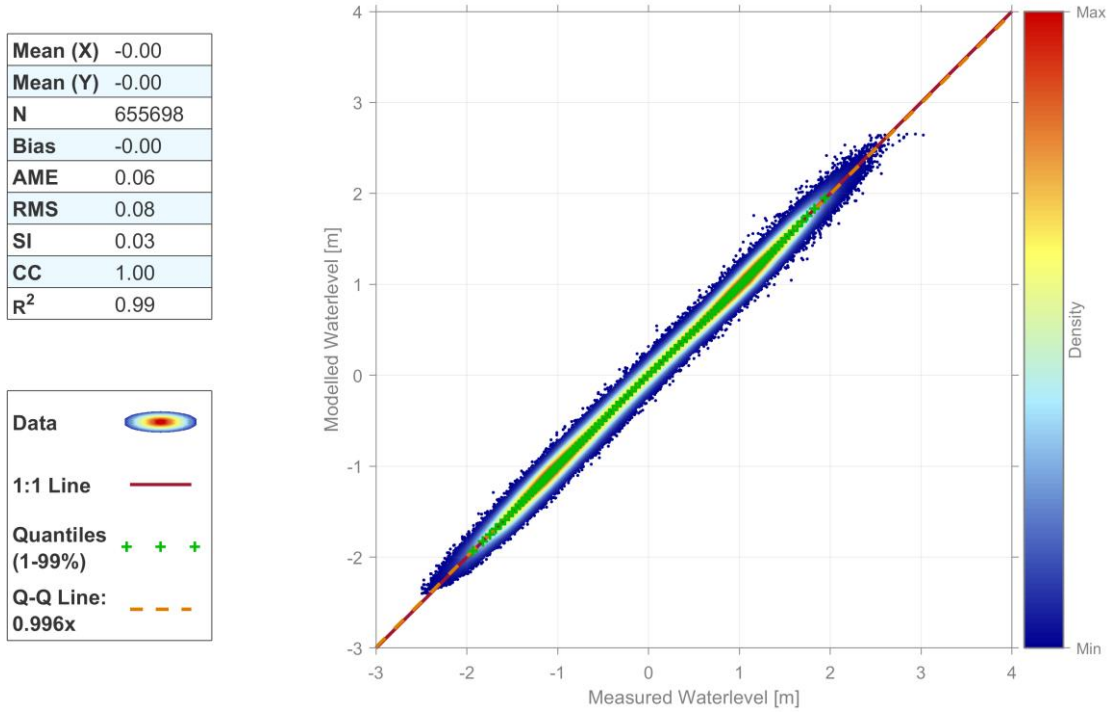



Figure 5.17: Comparison of measured and modelled water levels at Ballycotton.

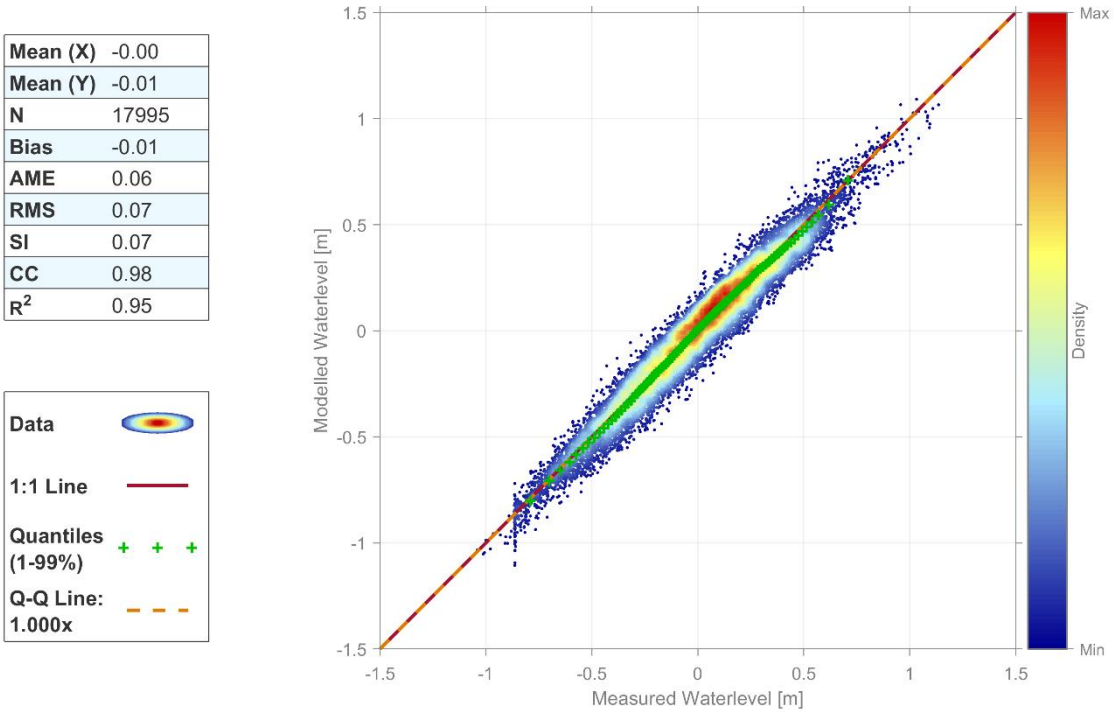



Figure 5.18: Comparison of measured and modelled water levels at Arklow Harbour (local model).

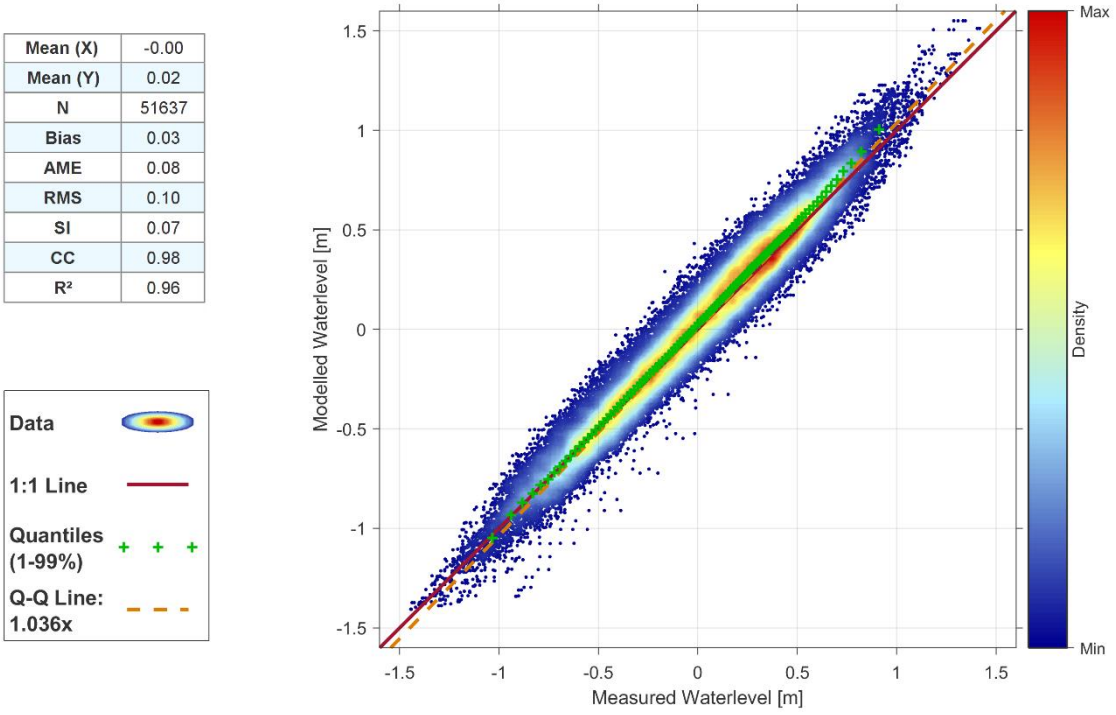



Figure 5.19: Comparison of measured and modelled water levels at AWAC A (all deployments).

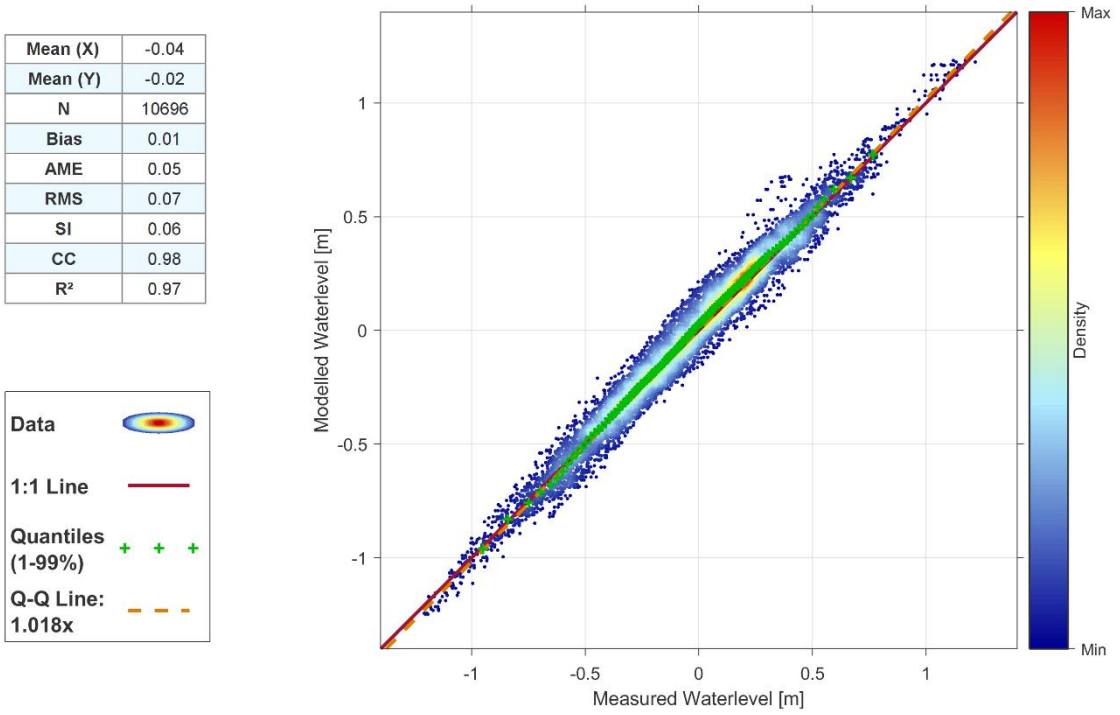



Figure 5.20: Comparison of measured and modelled water levels at AWAC B1 (deployment 2).

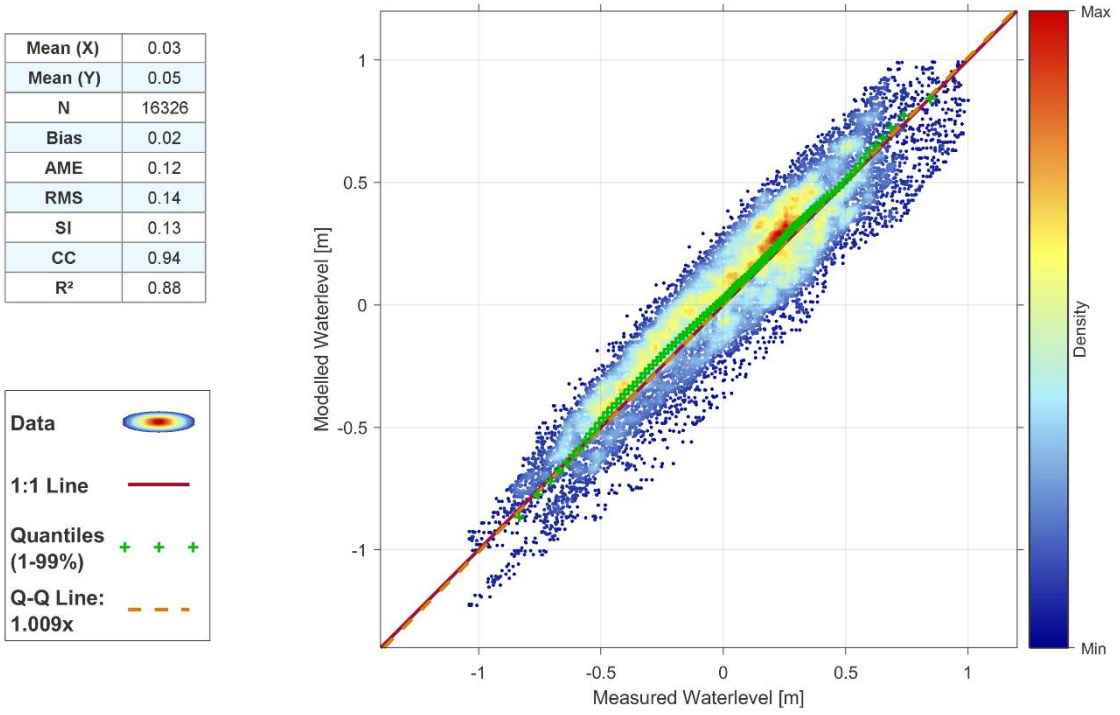



Figure 5.21: Comparison of measured and modelled water levels at AWAC B1 (deployment 3).

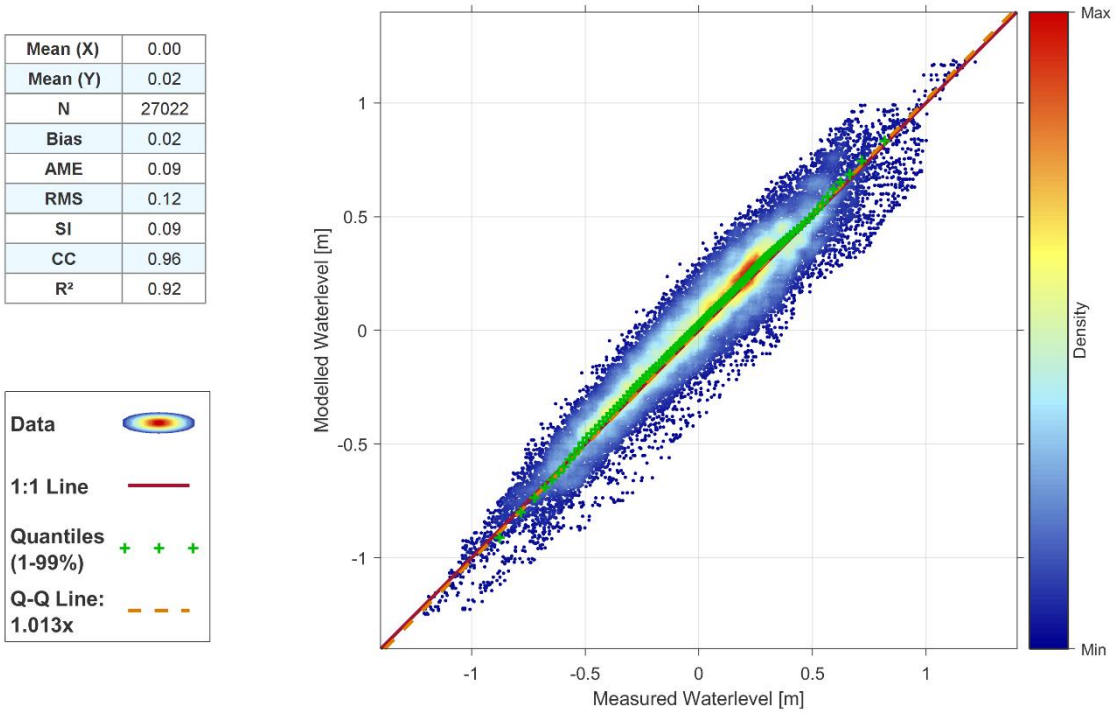



Figure 5.22: Comparison of measured and modelled water levels at AWAC B1 (all deployments).

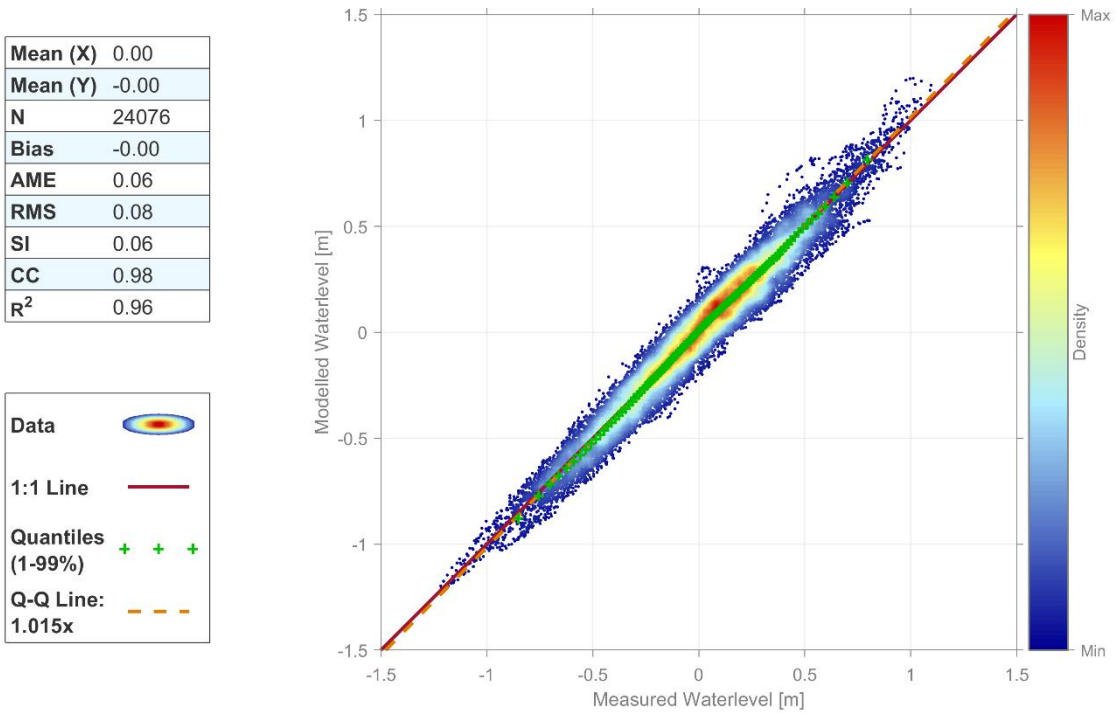



Figure 5.23: Comparison of measured and modelled water levels at AWAC C (all deployments).

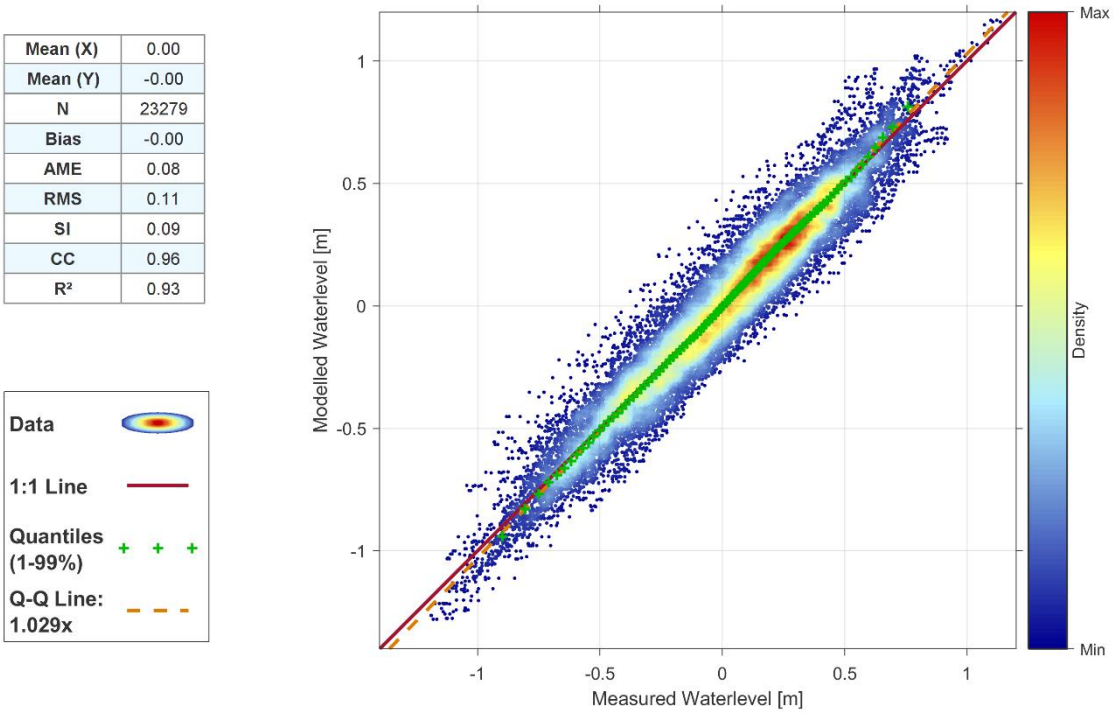



Figure 5.24: Comparison of measured and modelled water levels at AWAC D1 (all deployments).

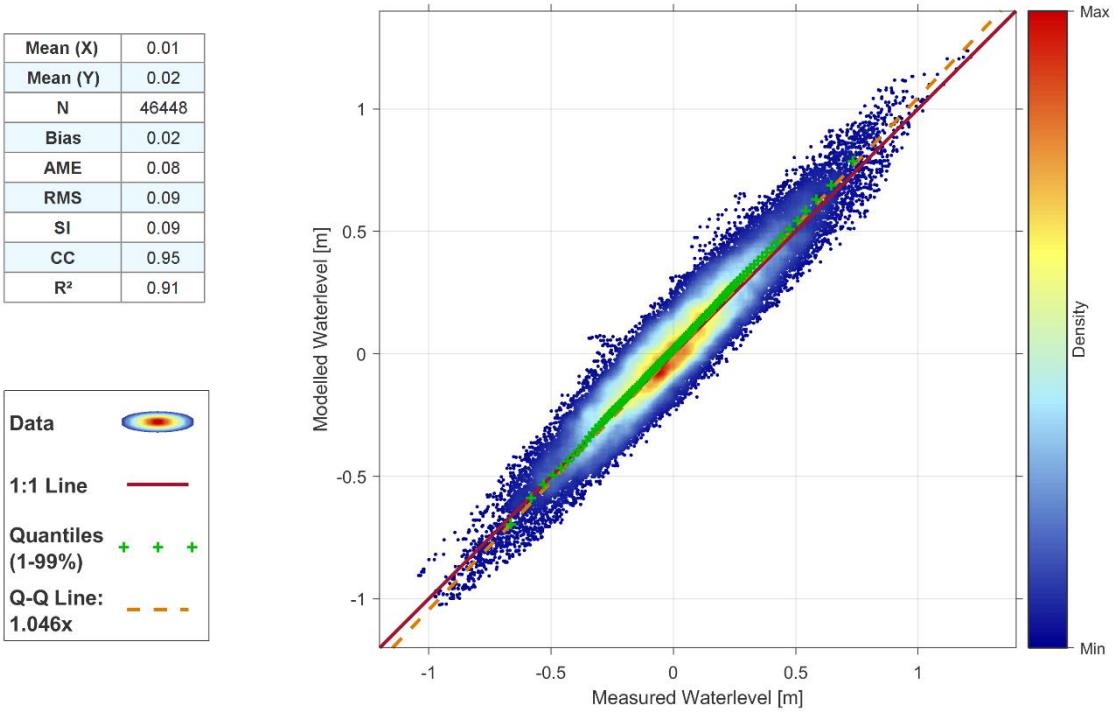



Figure 5.25: Comparison of measured and modelled water levels at AWAC E (all deployments).

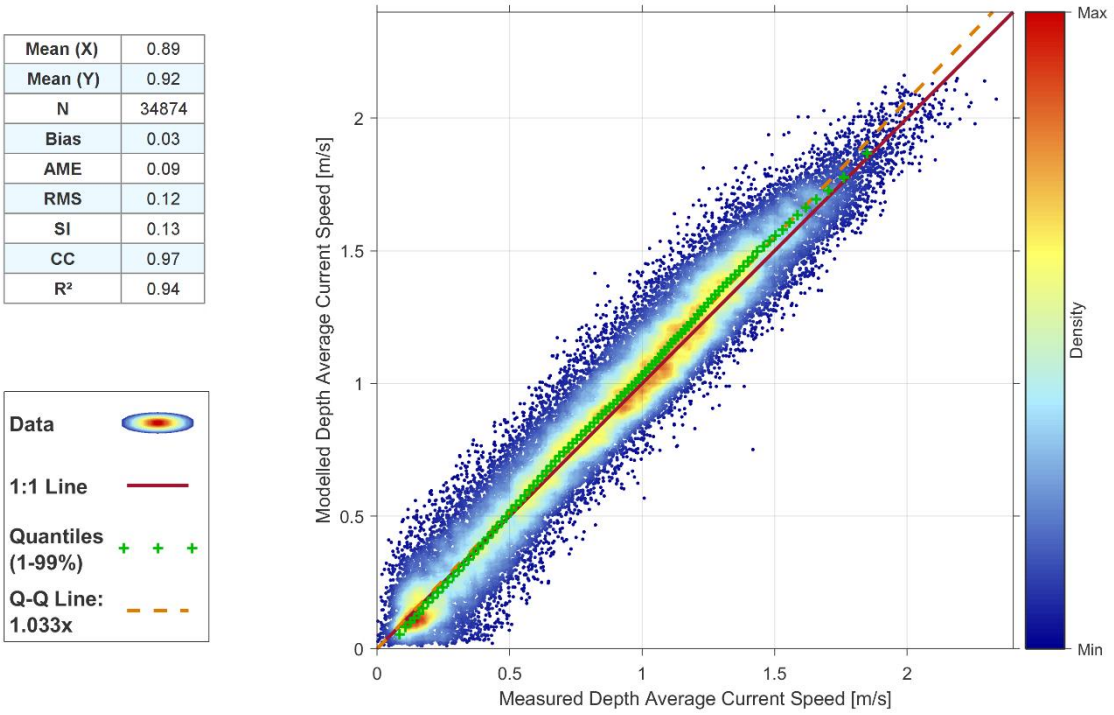



Figure 5.26: Comparison of measured and modelled depth-average currents at AWAC A (all deployments).

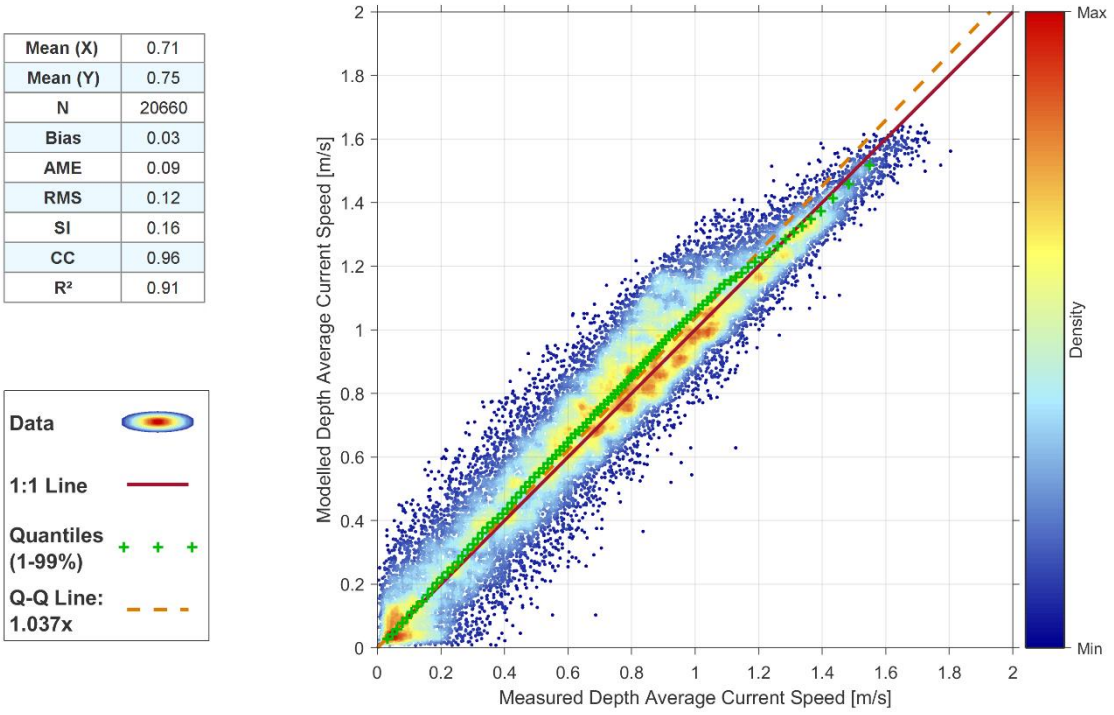



Figure 5.27: Comparison of measured and modelled depth-average currents at AWAC B1 (all deployments).

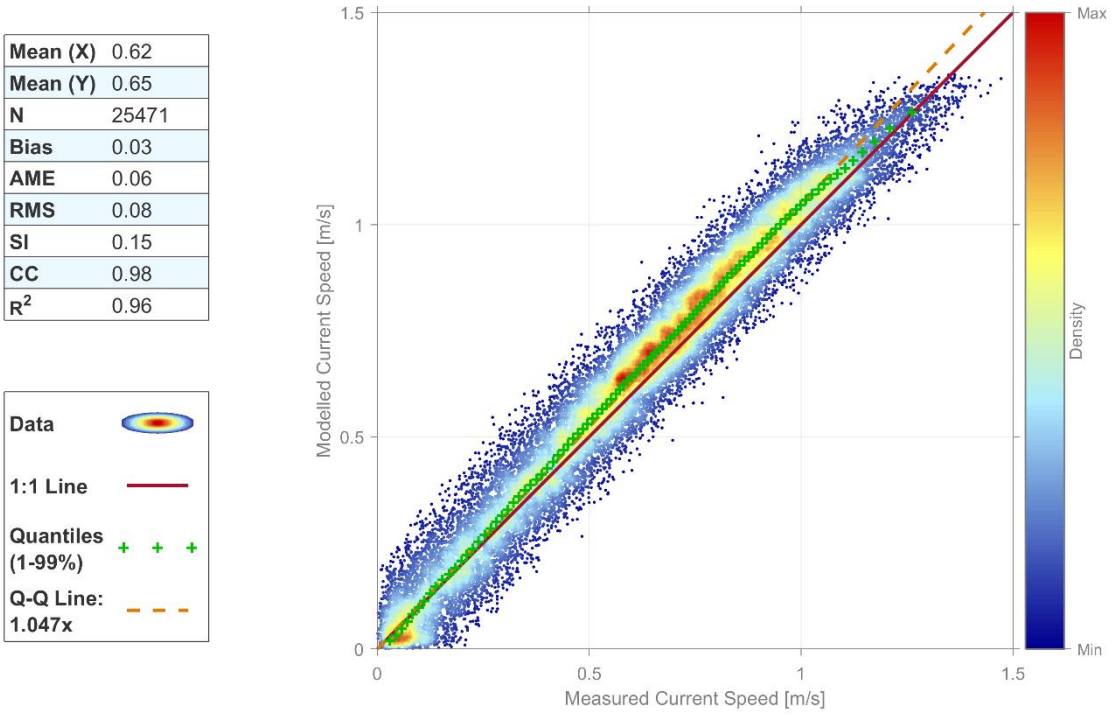



Figure 5.28: Comparison of measured and modelled depth-average currents at AWAC C (all deployments).

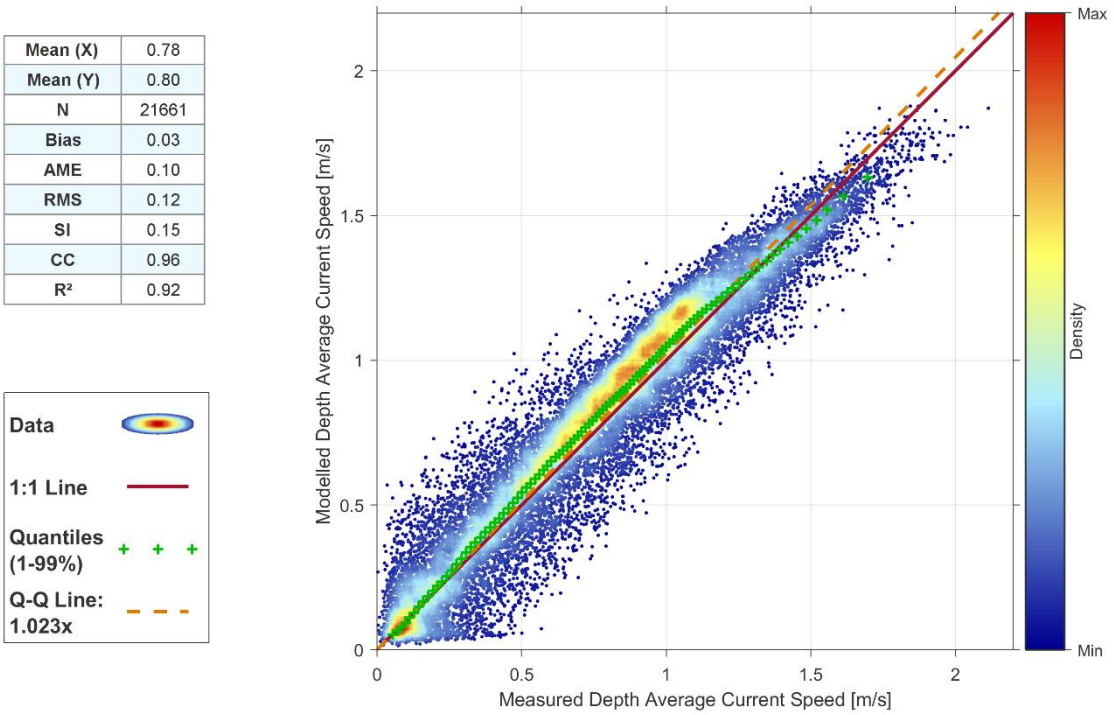



Figure 5.29: Comparison of measured and modelled depth-average currents at AWAC D1 (all deployments).

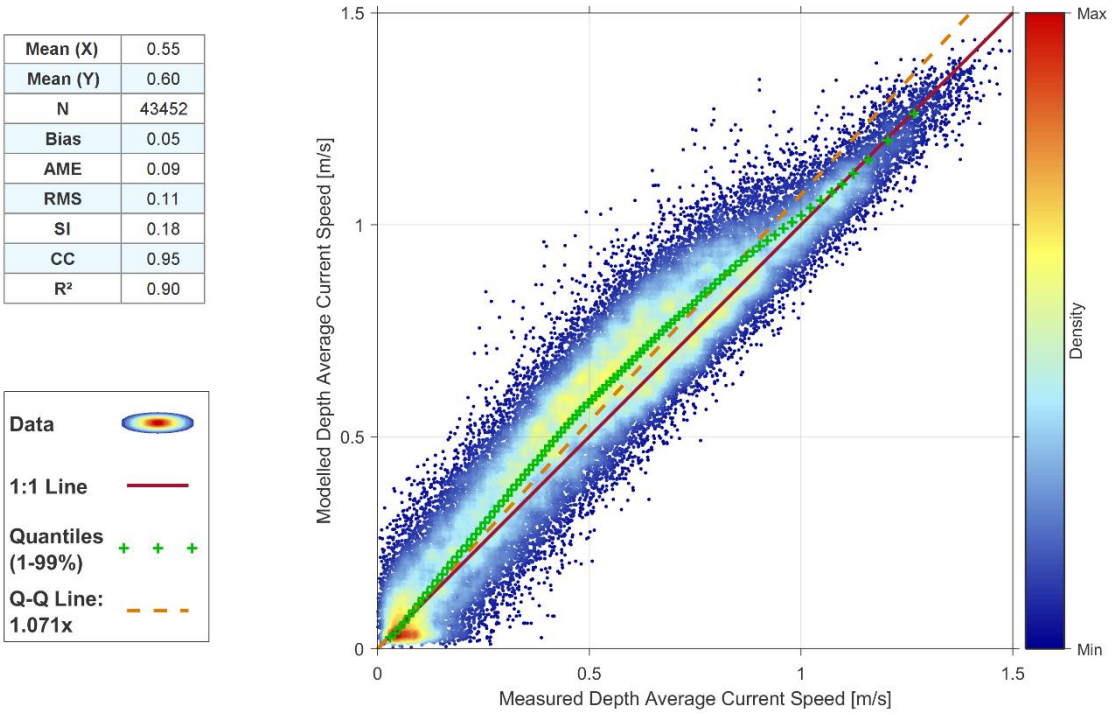



Figure 5.30: Comparison of measured and modelled depth-average currents at AWAC E (all deployments).

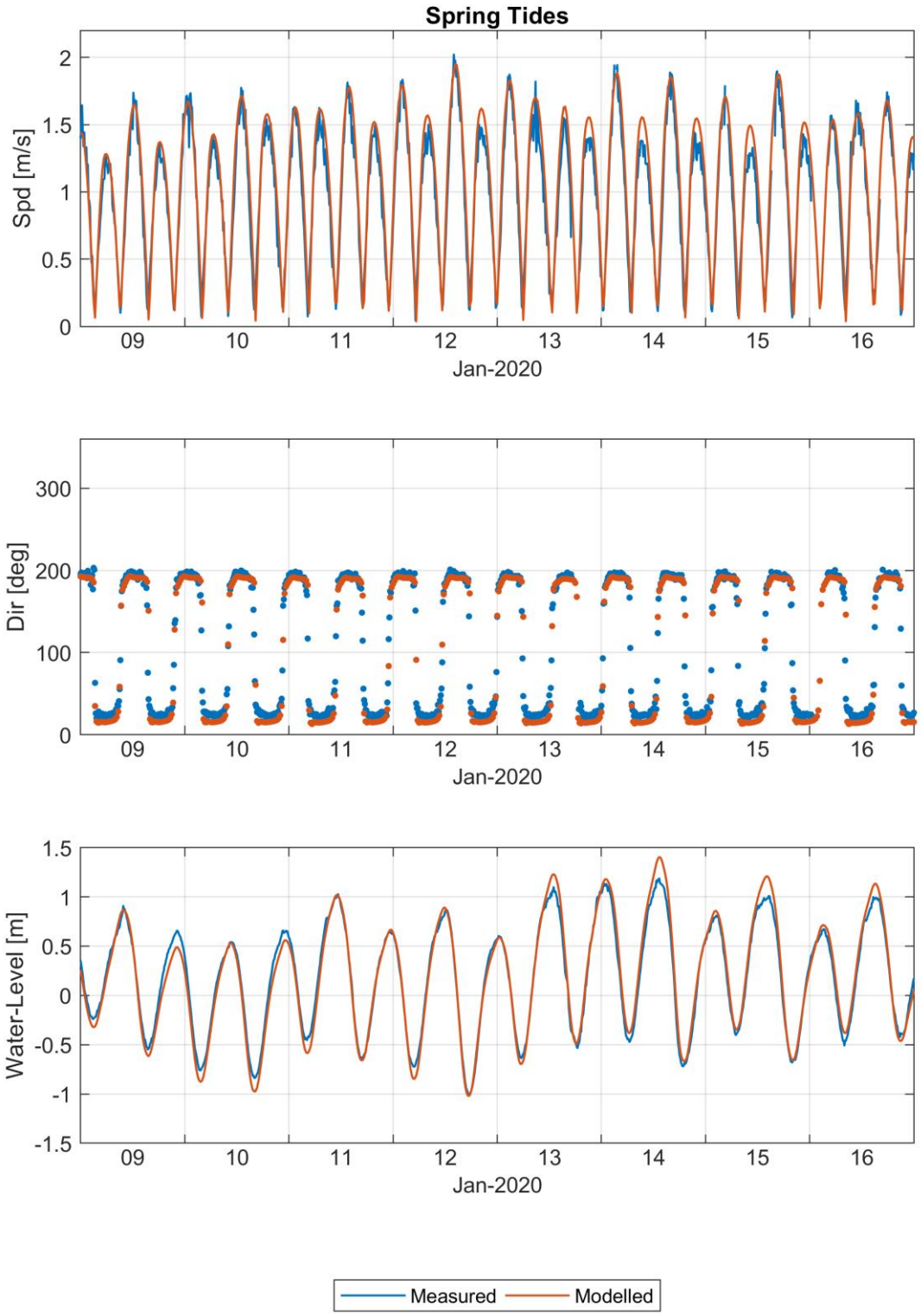



Figure 5.31: Time-series comparison of modelled and measured depth-average currents during spring tides at AWAC A.

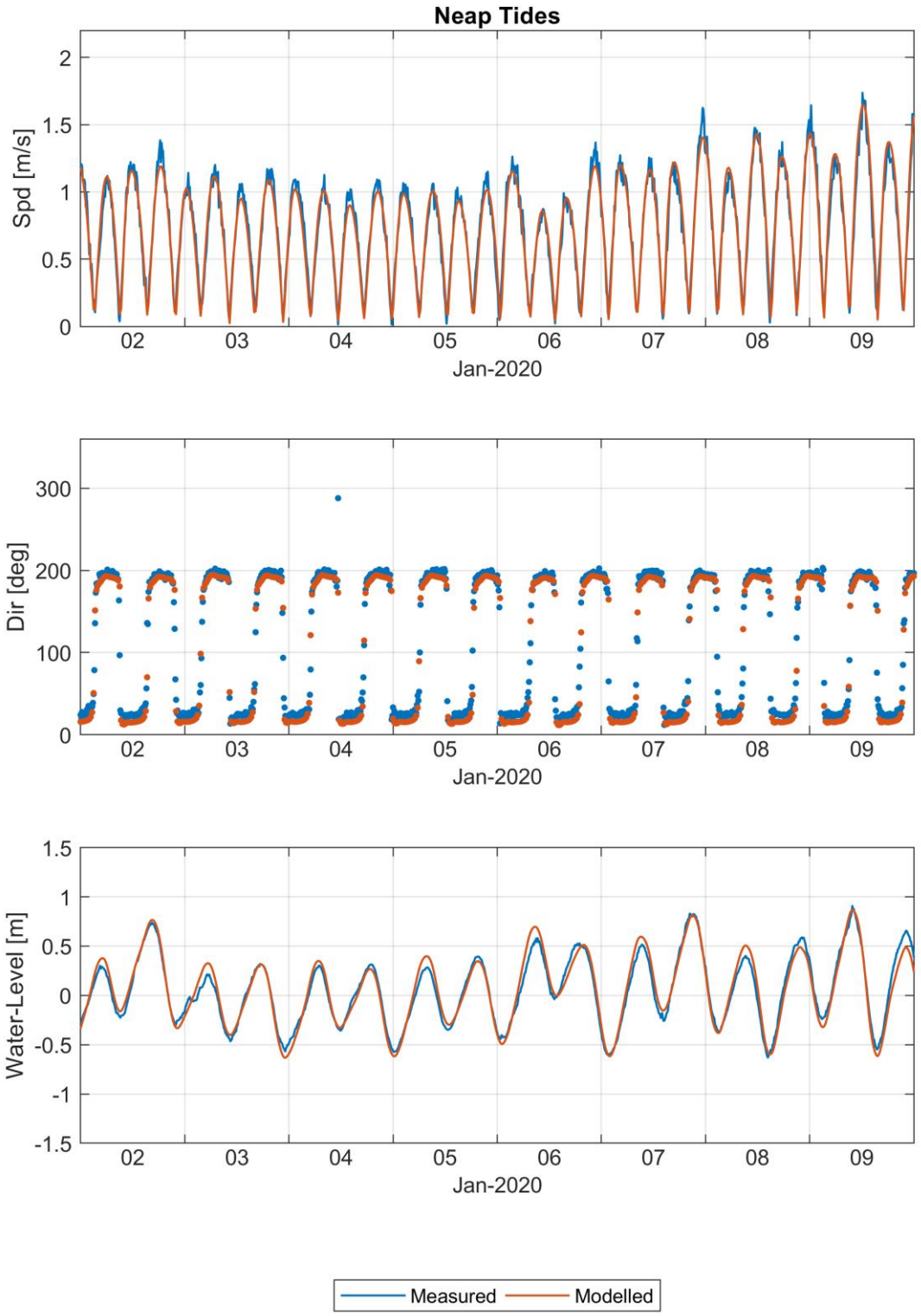



Figure 5.32: Time-series comparison of modelled and measured depth-average currents during neap tides at AWAC A.

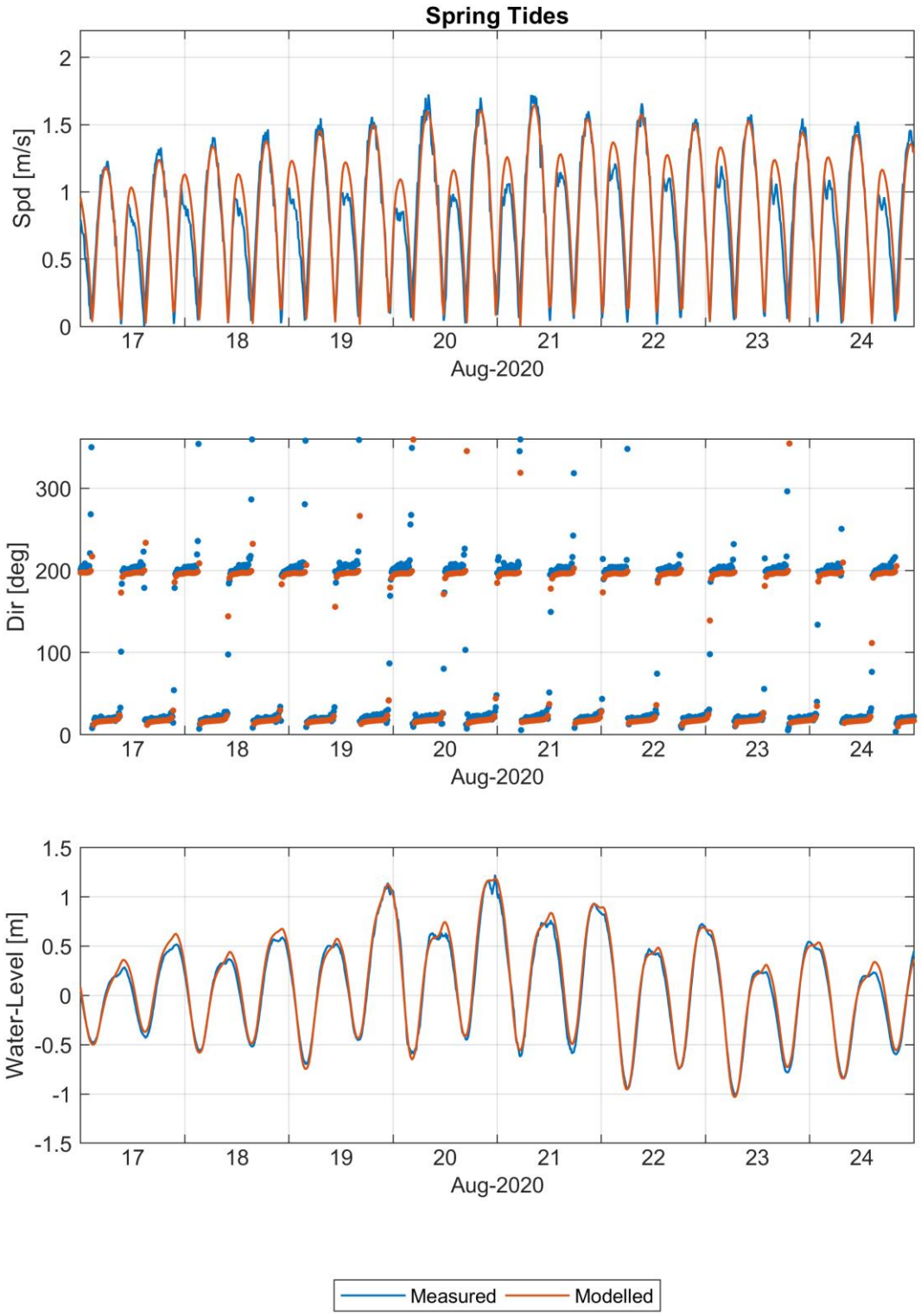



Figure 5.33: Time-series comparison of modelled and measured depth-average currents during spring tides at AWAC B1.

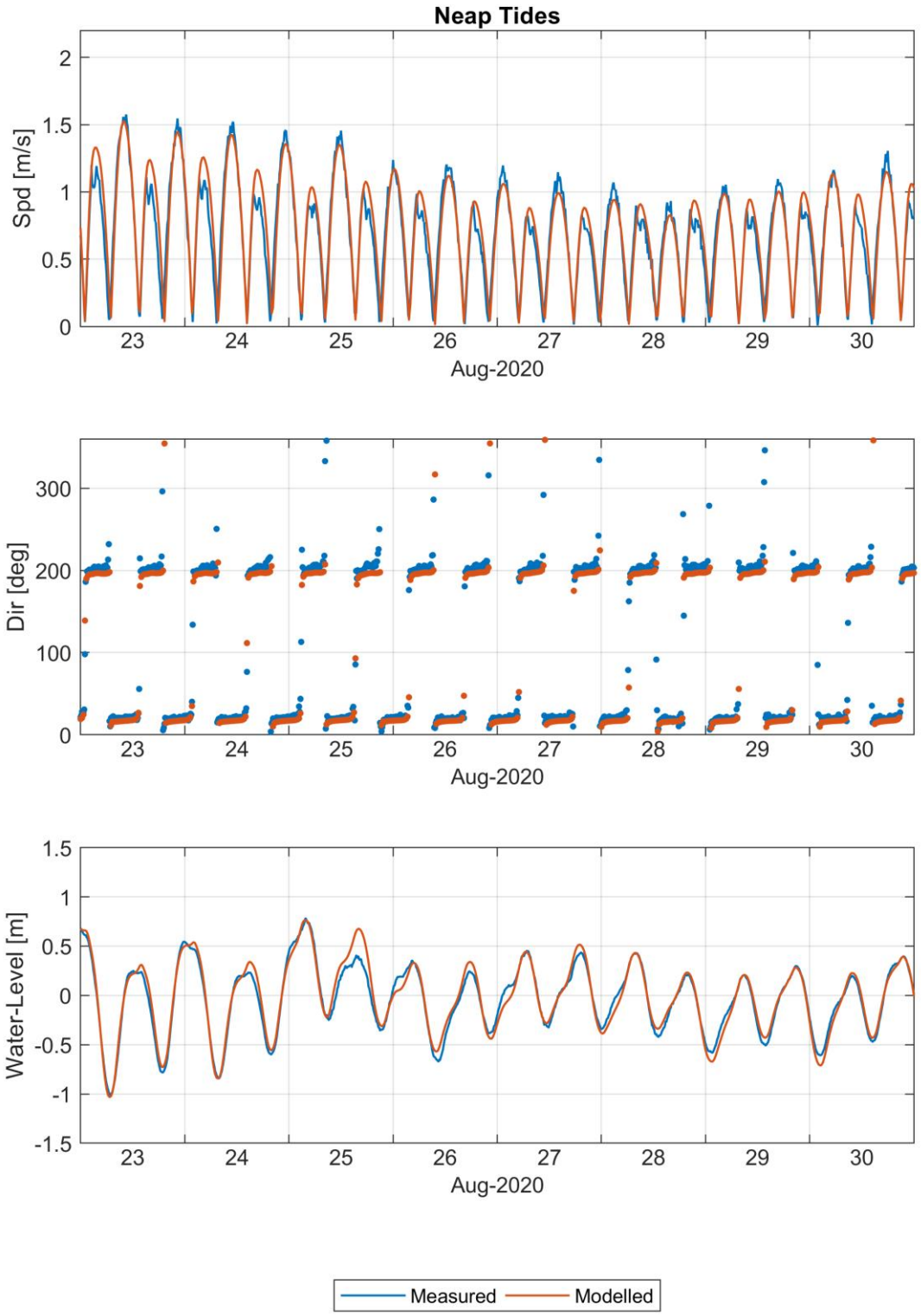



Figure 5.34: Time-series comparison of modelled and measured depth-average currents during neap tides at AWAC B1.

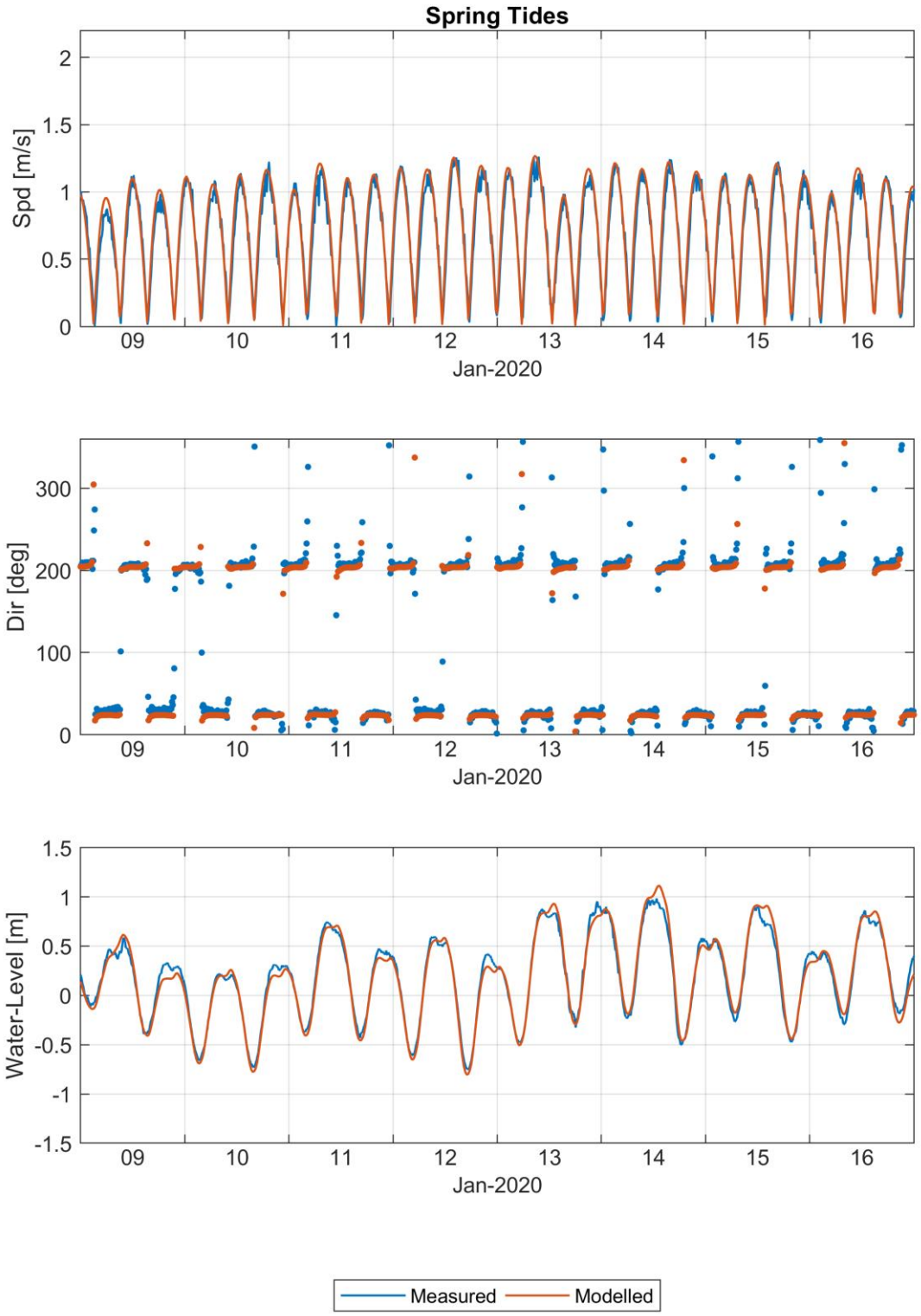



Figure 5.35: Time-series comparison of modelled and measured depth-average currents during spring tides at AWAC C.

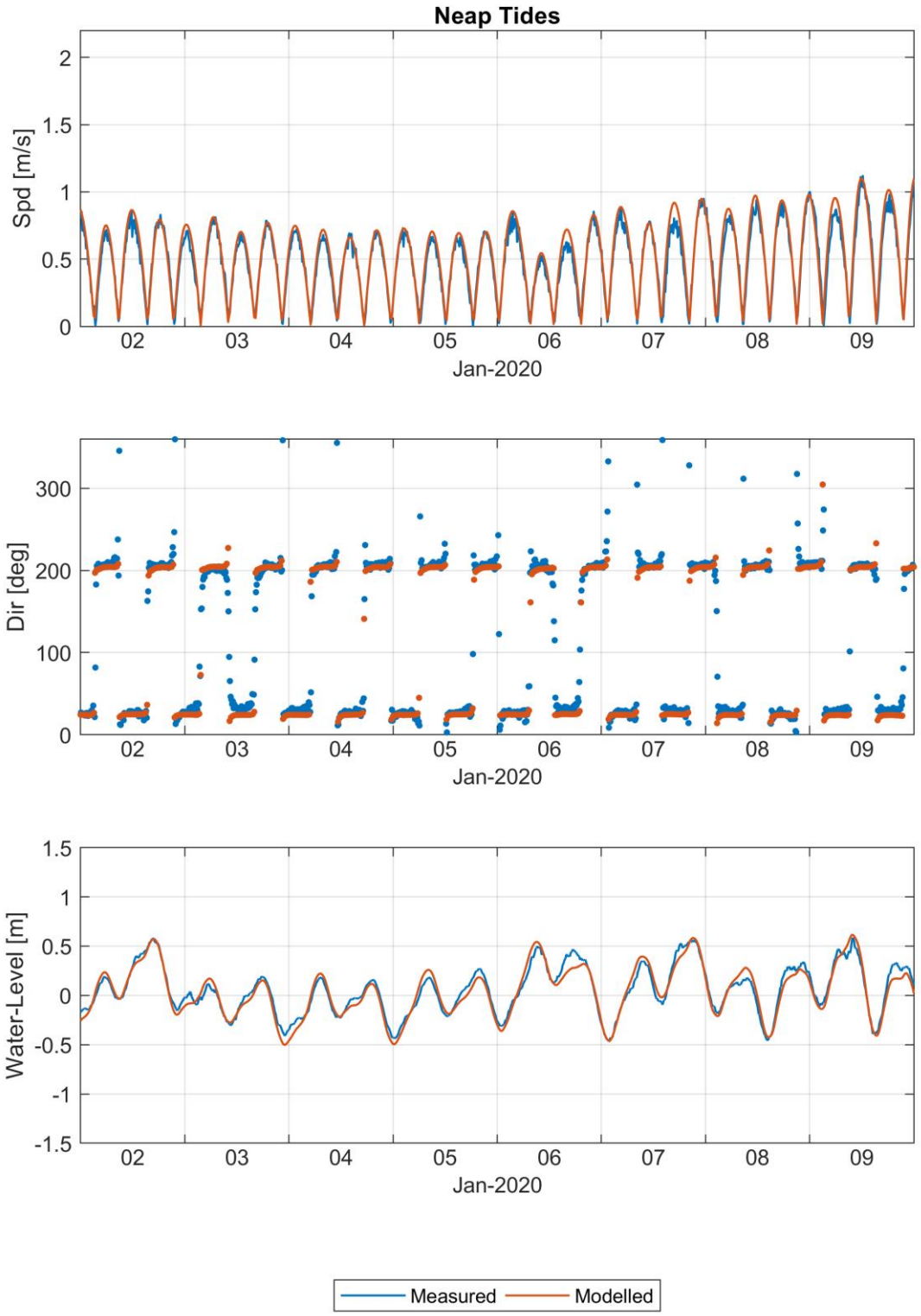



Figure 5.36: Time-series comparison of modelled and measured depth-average currents during neap tides at AWAC C.

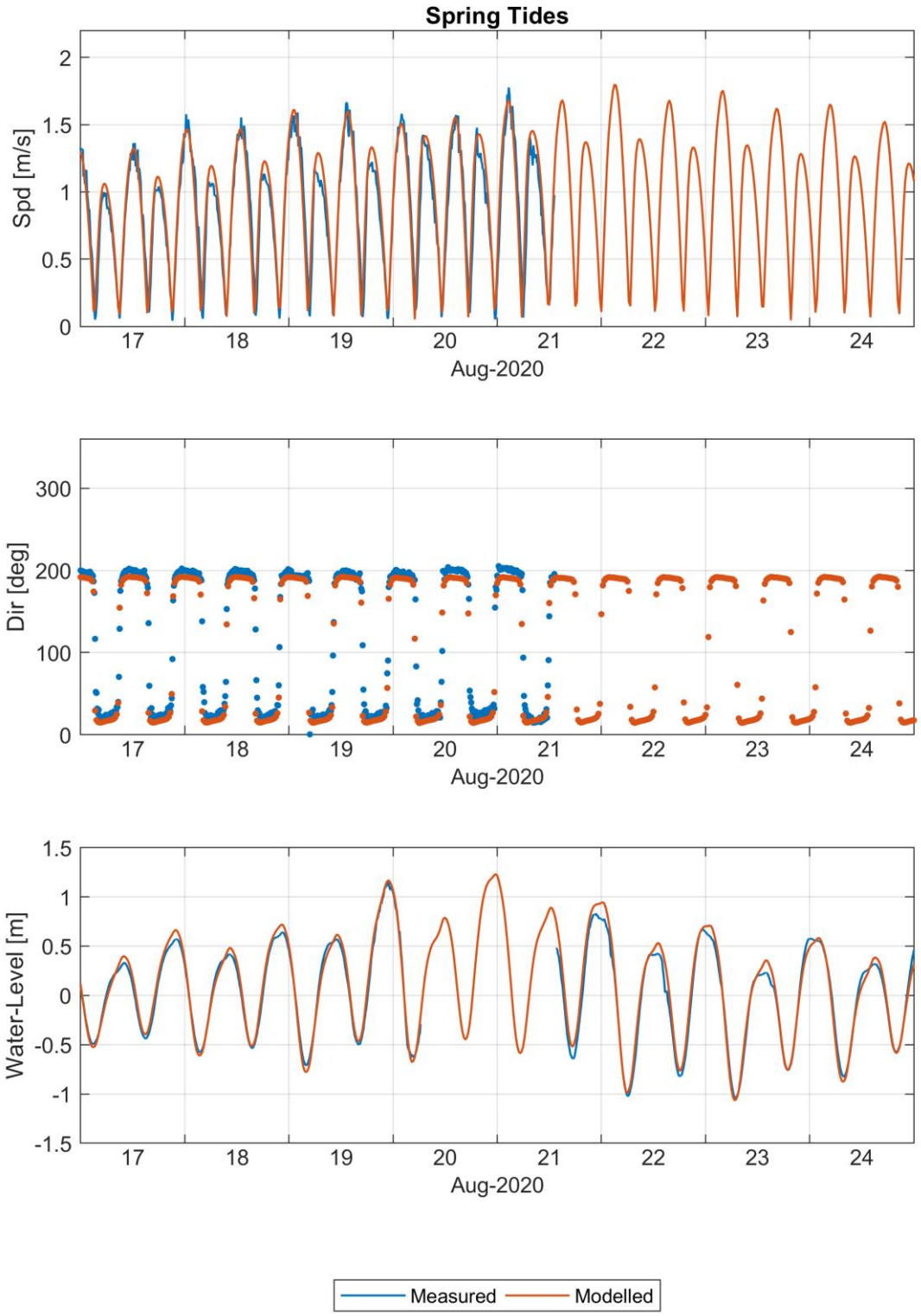



Figure 5.37: Time-series comparison of modelled and measured depth-average currents during spring tides at AWAC D1.

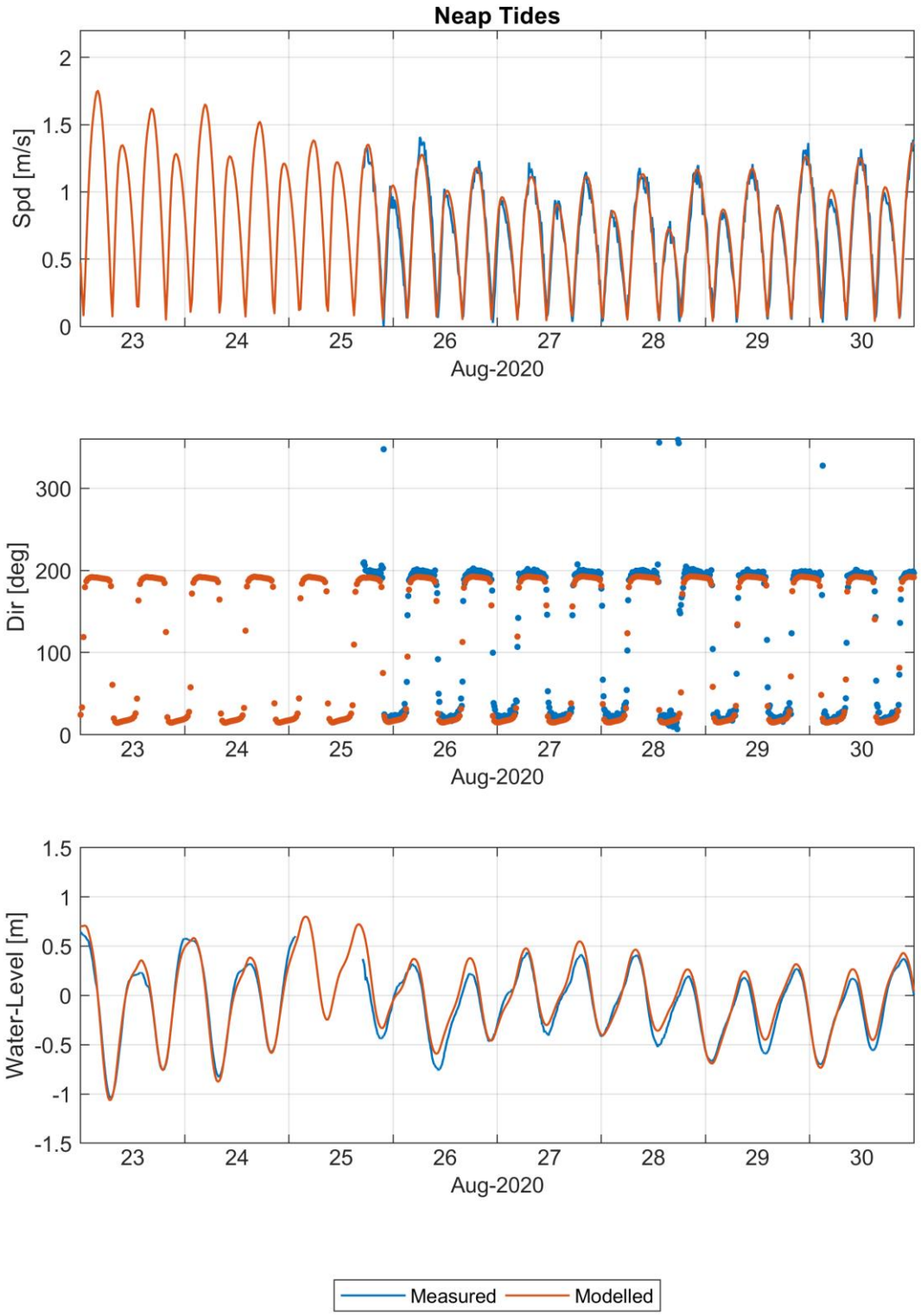



Figure 5.38: Time-series comparison of modelled and measured depth-average currents during neap tides at AWAC D1.

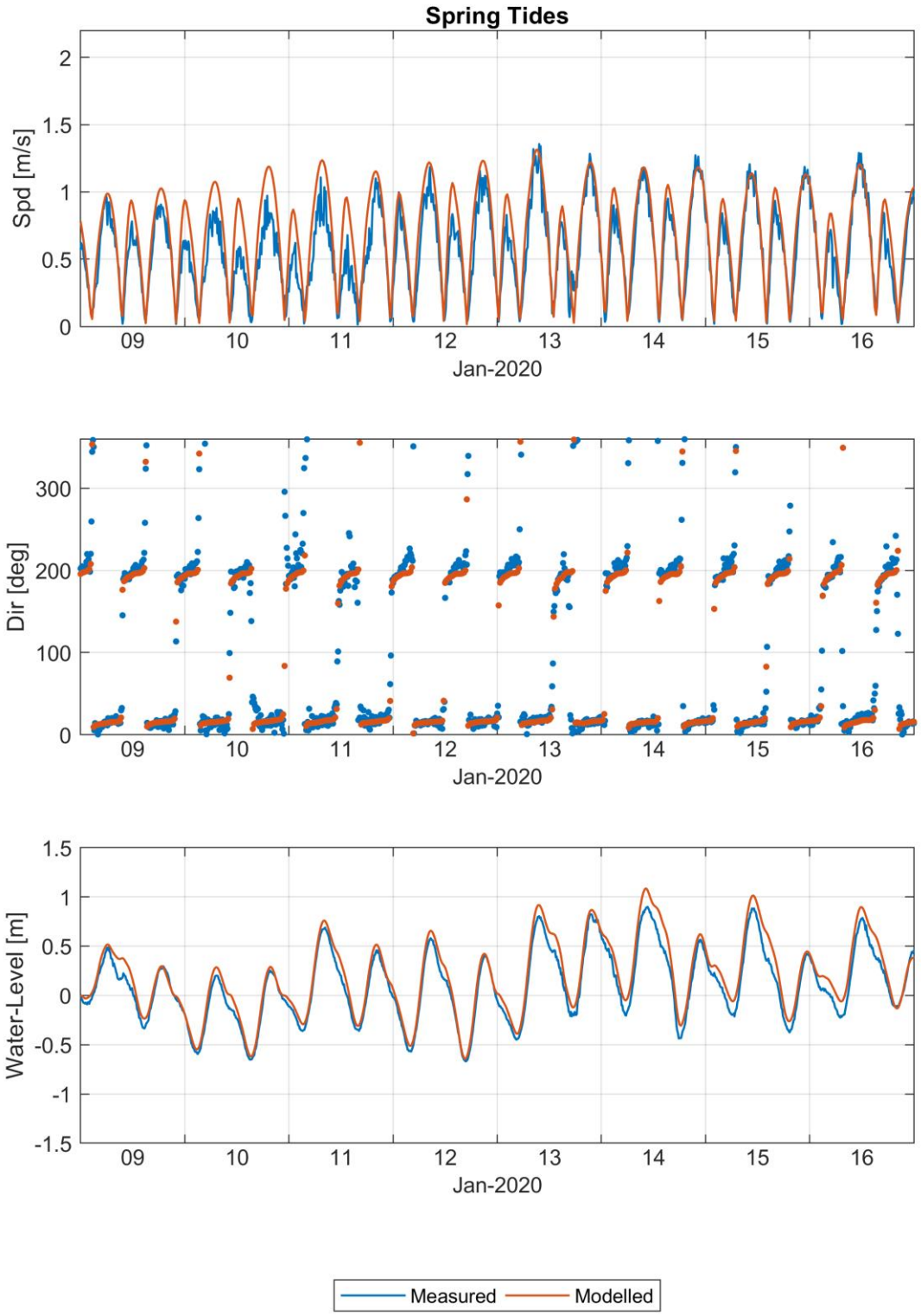



Figure 5.39: Time-series comparison of modelled and measured depth-average currents during spring tides at AWAC E.

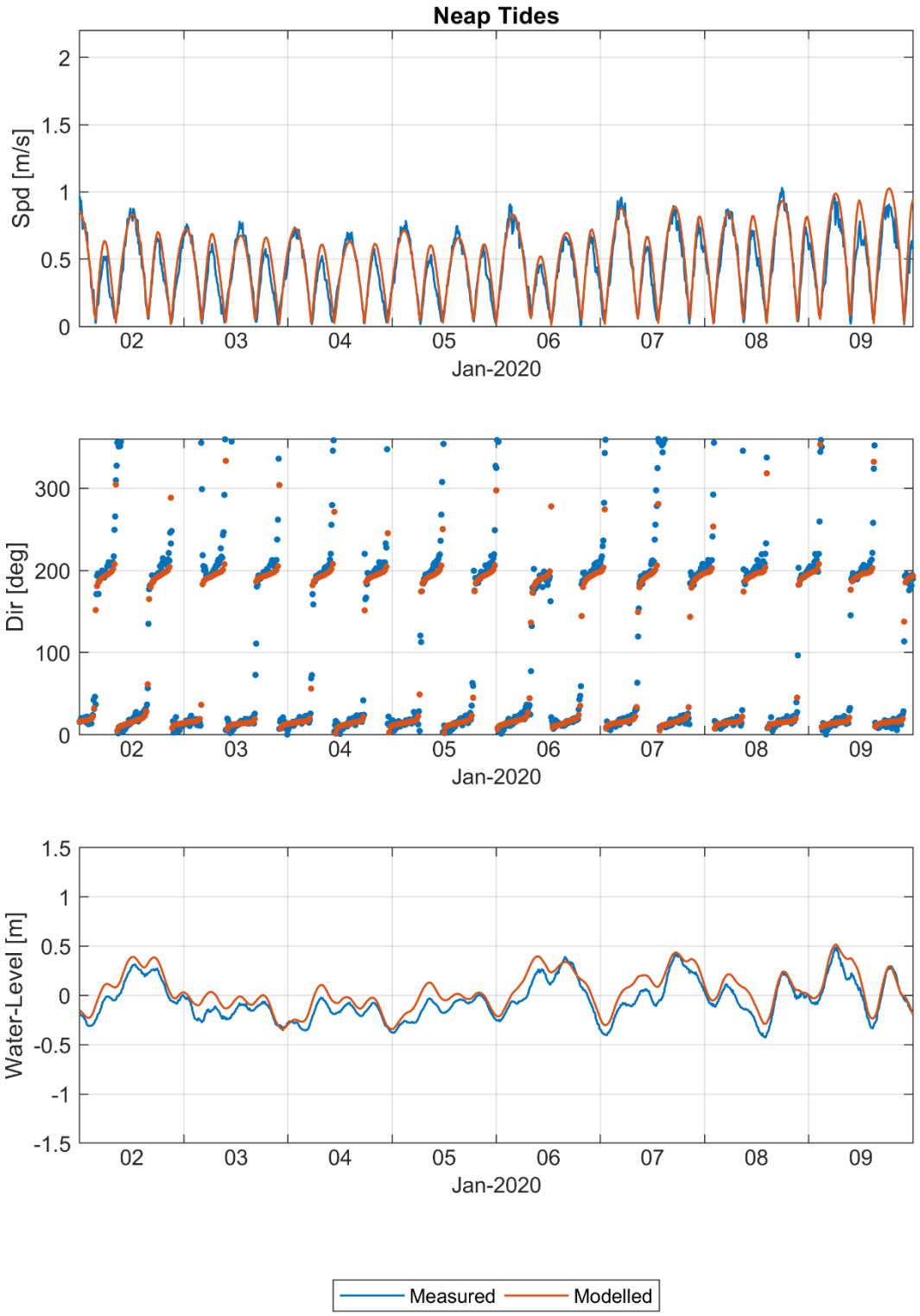



Figure 5.40: Time-series comparison of modelled and measured depth-average currents during neap tides at AWAC E.

# 6 Waves

Wave data were produced using a large-scale Irish Sea SWAN model with higher resolution nested models, culminating in a final model local to Arklow Bank. The models were subjected to sensitivity testing and validation, before time-series data were output at hourly intervals for the period January 1982 to March 2021.

Model parameters should be considered as representative of a 3-hour sea-state. Please see Appendix F for more details.

## 6.1 Measured Wave Data

To support calibration and validation of the wave model, measured data were provided by Sure Partners Limited which were collected over three deployments. These were supplemented with data acquired from the Irish Marine Institute and the Commissioners of Irish Lights. Details of these datasets are provided in Table 6.1 below and illustrated in Figure 6.1 overleaf.

Table 6.1: Measured datasets used for wave model validation.

| Dataset | Deployment | Location | Time Period | Water Depth [m MSL] |
|---|---|---|---|---|
| **AWAC A** | 1 | 52.9096 °N, 5.9157 °W | 6-Nov-2019 to 18-May-2020 | 27.4 |
| | 2 | 52.9079 °N, 5.9172 °W | 1-Aug-2020 to 16-Oct-2020* | |
| | 3 | 52.9085 °N, 5.9172 °W | 5-Nov-2020 to 7-Mar-2021 | |
| **AWAC B1** | 2 | 52.8504 °N, 5.9461 °W | 2-Aug-2020 to 15-Oct-2020 | 30.2 |
| | 3 | 52.8487 °N, 5.9471 °W | 7-Nov-2020 to 7-Mar-2021 | |
| **AWAC C** | 1 | 52.8218 °N, 6.0206 °W | 24-Nov-2019 to 19-May-2020 | 26.3 |
| **AWAC D1** | 2 | 52.8595 °N, 6.9173 °W | 1-Aug-2020 to 16-Oct-2020 | 30.5 |
| | 3 | 52.8583 °N, 6.9169 °W | 7-Nov-2020 to 7-Mar-2021 | |
| **AWAC E** | 1 | 52.6910 °N, 5.9930 °W | 24-Nov-2019 to 19-May-2020 | 39.6 |
| | 2 | 52.6907 °N, 5.9943 °W | 2-Aug-2020 to 15-Oct-2020 | |
| | 3 | 52.6902 °N, 5.9946 °W | 22-Nov-2020 to 8-Mar-2021 | |
| **M2** | - | 53.4836 °N, 5.4302 °W | 3-May-2001 to 27-Apr-2020 | 89.4 |
| **M5** | - | 51.6904 °N, 6.7043 °W | 18-Oct-2004 to 27-Apr-2020 | 72.3 |

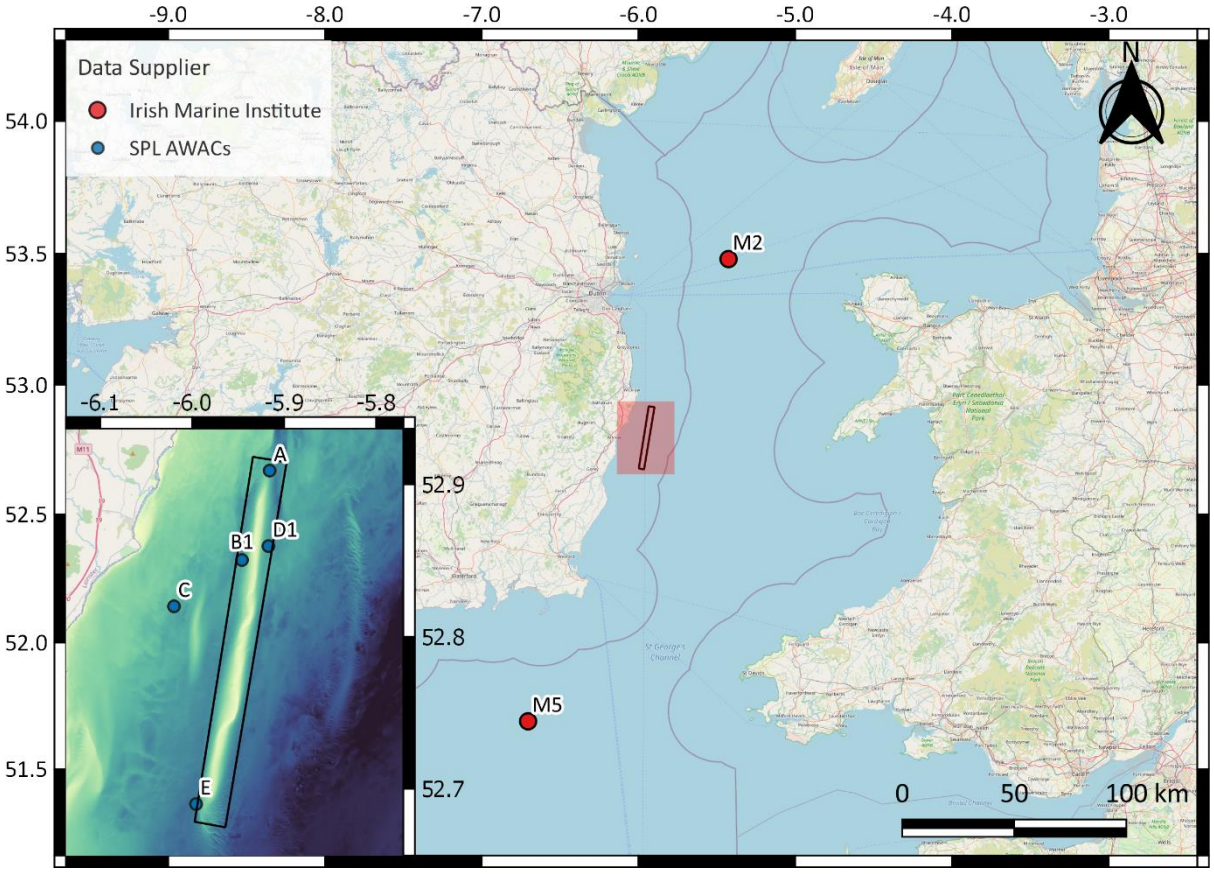



Figure 6.1: Locations of the wave measurement devices.

## 6.2 Modelling Software

A bespoke SWAN wave model was deployed, with high resolution regional nests, to produce a 39-year wave hindcast between January 1982 and February 2021. SWAN is a third-generation wave model, developed at Delft University of Technology, which computes random, short-crested wind-generated waves in coastal regions and inland waters. SWAN accounts for the following physics:

- Wave propagation in time and space, shoaling, refraction due to current and depth, frequency shifting due to currents and non-stationary depth.
- Wave generation by wind.
- Three- and four-wave interactions.
- Whitecapping, bottom friction and depth-induced breaking.
- Wave-induced set-up.
- Transmission through and reflection (specular and diffuse) against obstacles.
- Diffraction.

The large-scale model used a spatial resolution of 5.5 km whilst the highest resolution nested model had a horizontal resolution of approximately 110 m. The wave model extents and resolutions are shown in Figure 6.2 below.

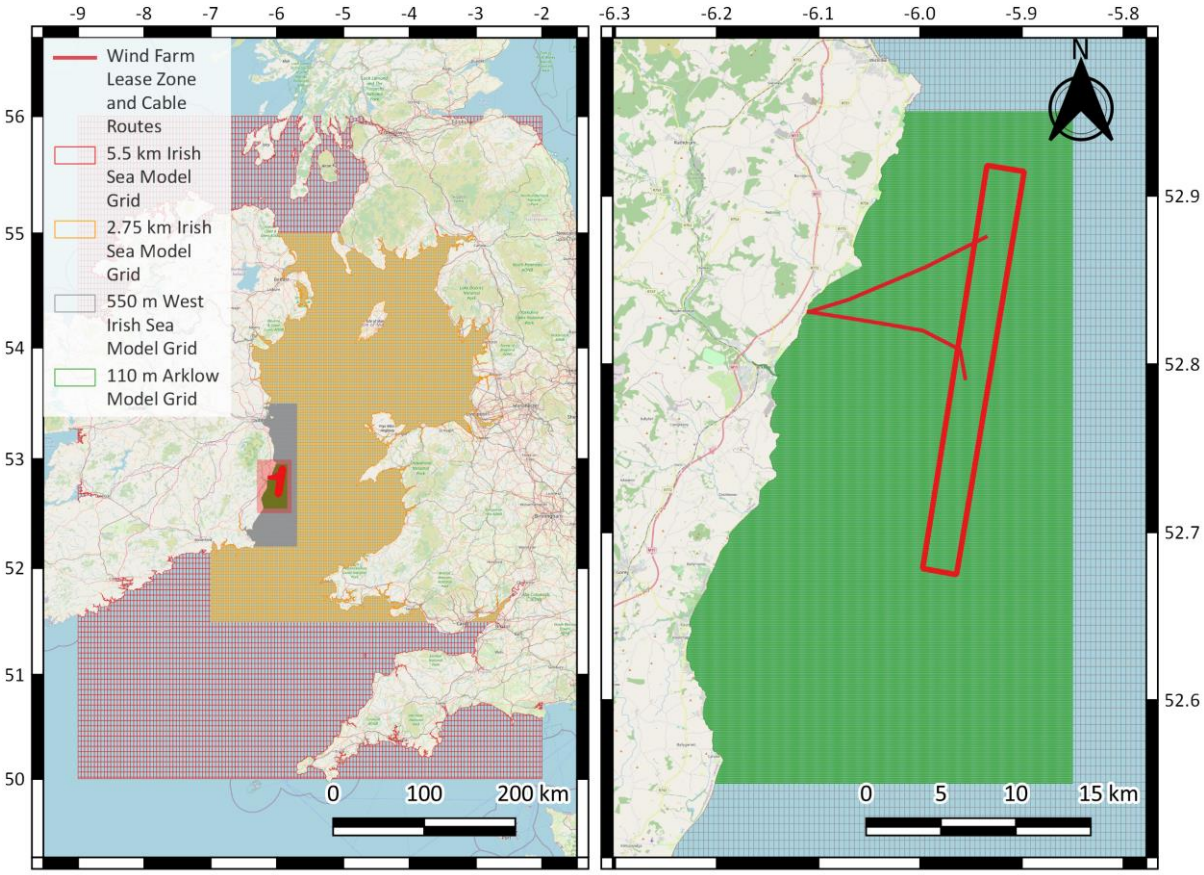



Figure 6.2: Wave model domains.

## 6.3 Model Boundary Conditions

Spectral wave boundary conditions to the large domain 5.5 km model originated from ECMWF ReAnalysis 5 (ERA5). ERA5 incorporates a model with three fully coupled components for the atmosphere, land surface, and ocean waves. The wave model is based on the Wave Analysis Model (WAM) approach (Komen et al, 1994 [2]). The horizontal resolution of the output wave data is 0.5 degree (approximately 56 km) and wave spectra are discretised using 24 directions and 30 frequencies from 0.0345 to 0.5473 Hz. Data are available every hour between 1950 and present. MetOceanWorks adjusted ERA5 wind fields were applied to the large-scale Irish Sea 5.5 km model and spectral outputs from this model provided boundaries to the higher resolution nested models which were driven using MetOceanWorks adjusted Vortex down-scaled wind fields. Modelled hydrodynamics (see Section 5) were included in the high-resolution nested wave model with a one-way coupling such that the hydrodynamics modified the waves but not the other way around.

## 6.4 Model Sensitivity Testing

### 6.4.1 Grid Resolution

To ensure that an appropriate model grid resolution was selected for the final wave model, a series of tests were carried out to demonstrate convergence of results. Models with varying spatial resolutions were deployed, and the effects of varying grid resolution were analysed at four locations shown in Figure 5.4. 220, 110 and 55 m spatial resolutions were used in these tests. The comparisons are shown in Figure 6.3 to Figure 6.6.

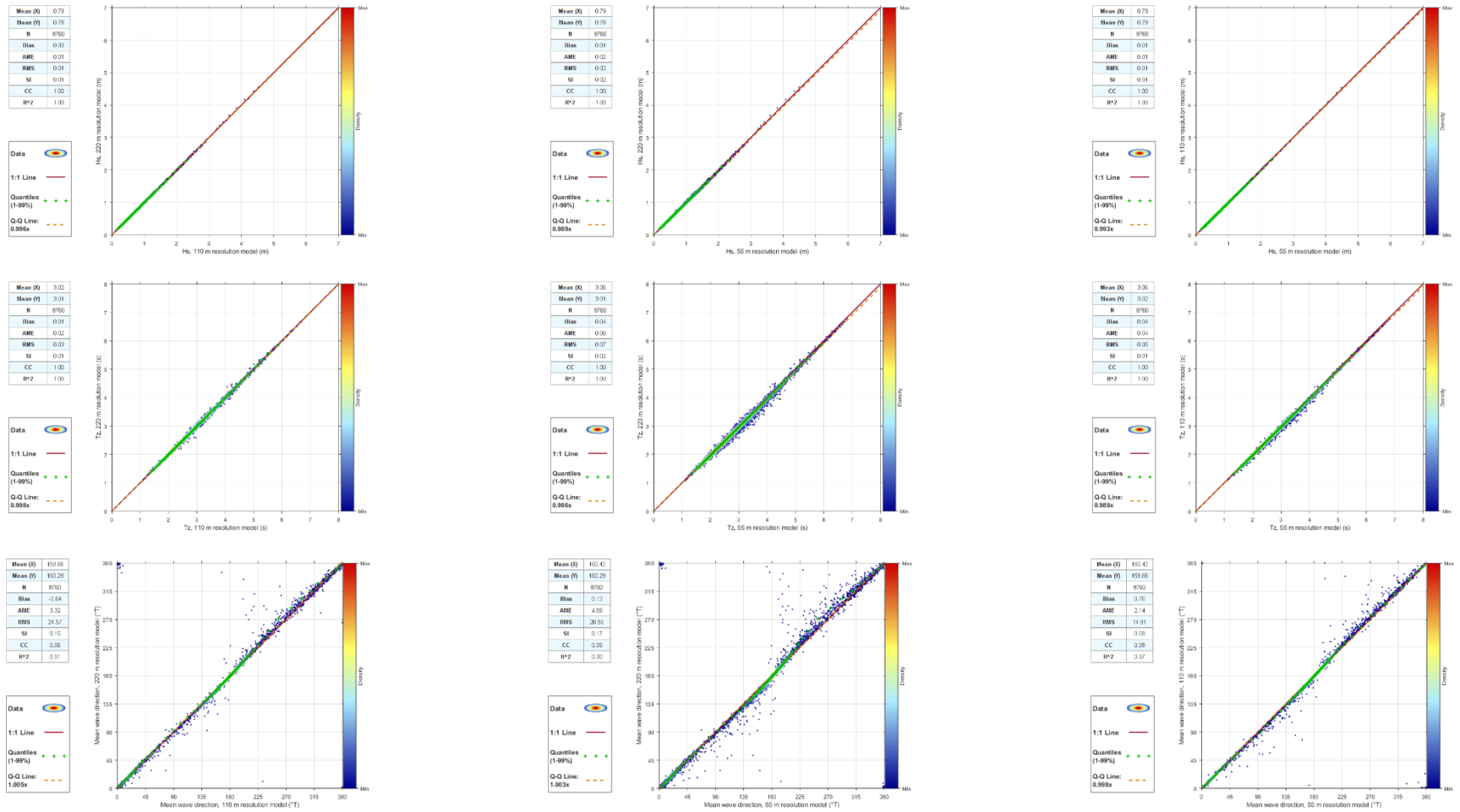



Figure 6.3. Results of model runs with differing spatial resolutions, at AWAC A. Top row = significant wave height, middle row = mean zero-crossing wave period, bottom row = mean wave direction. Left column 220 m resolution vs. 110 m resolution. Middle column 55 m resolution vs. 220 m resolution. Right column = 110 m resolution vs. 55 m resolution.

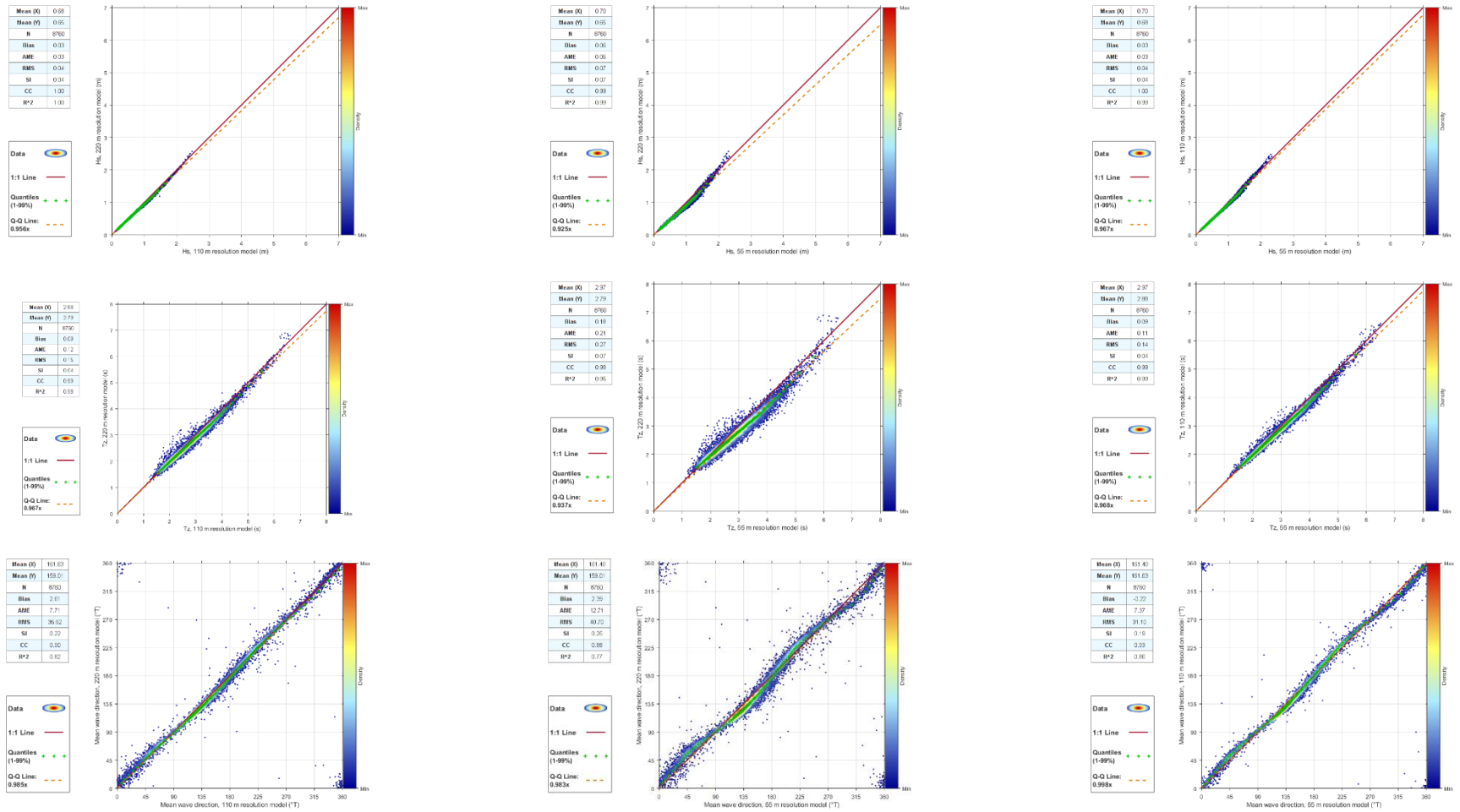



Figure 6.4. Results of model runs with differing spatial resolutions, at Centre of Bank. Top row = significant wave height, middle row = mean zero-crossing wave period, bottom row = mean wave direction. Left column 220 m resolution vs. 110 m resolution. Middle column 55 m resolution vs. 220 m resolution. Right column = 110 m resolution vs. 55 m resolution.

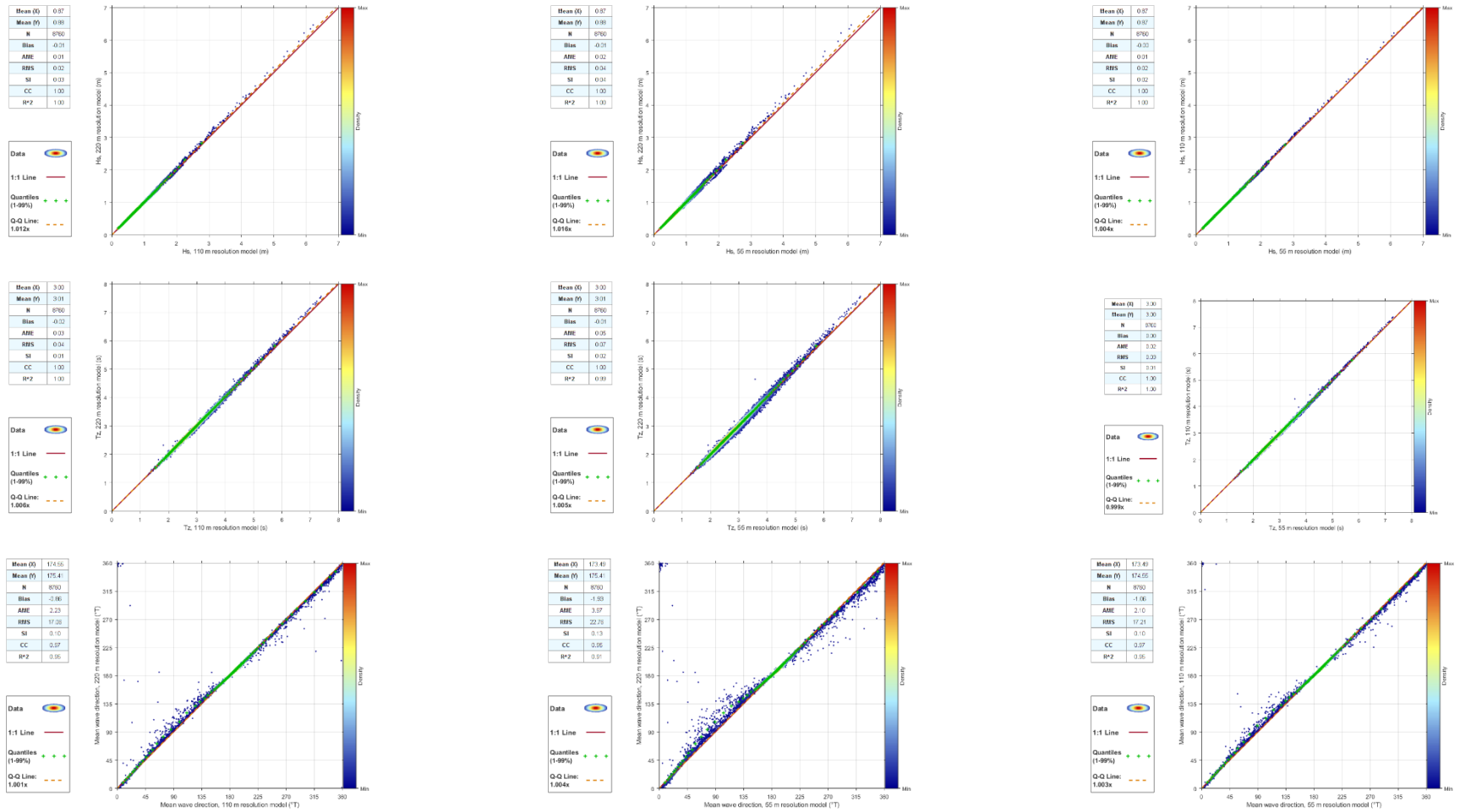


Figure 6.5. Results of model runs with differing spatial resolutions, at AWAC E. Top row = significant wave height, middle row = mean zero-crossing wave period, bottom row = mean wave direction. Left column 220 m resolution vs. 110 m resolution. Middle column 55 m resolution vs. 220 m resolution. Right column = 110 m resolution vs. 55 m resolution.

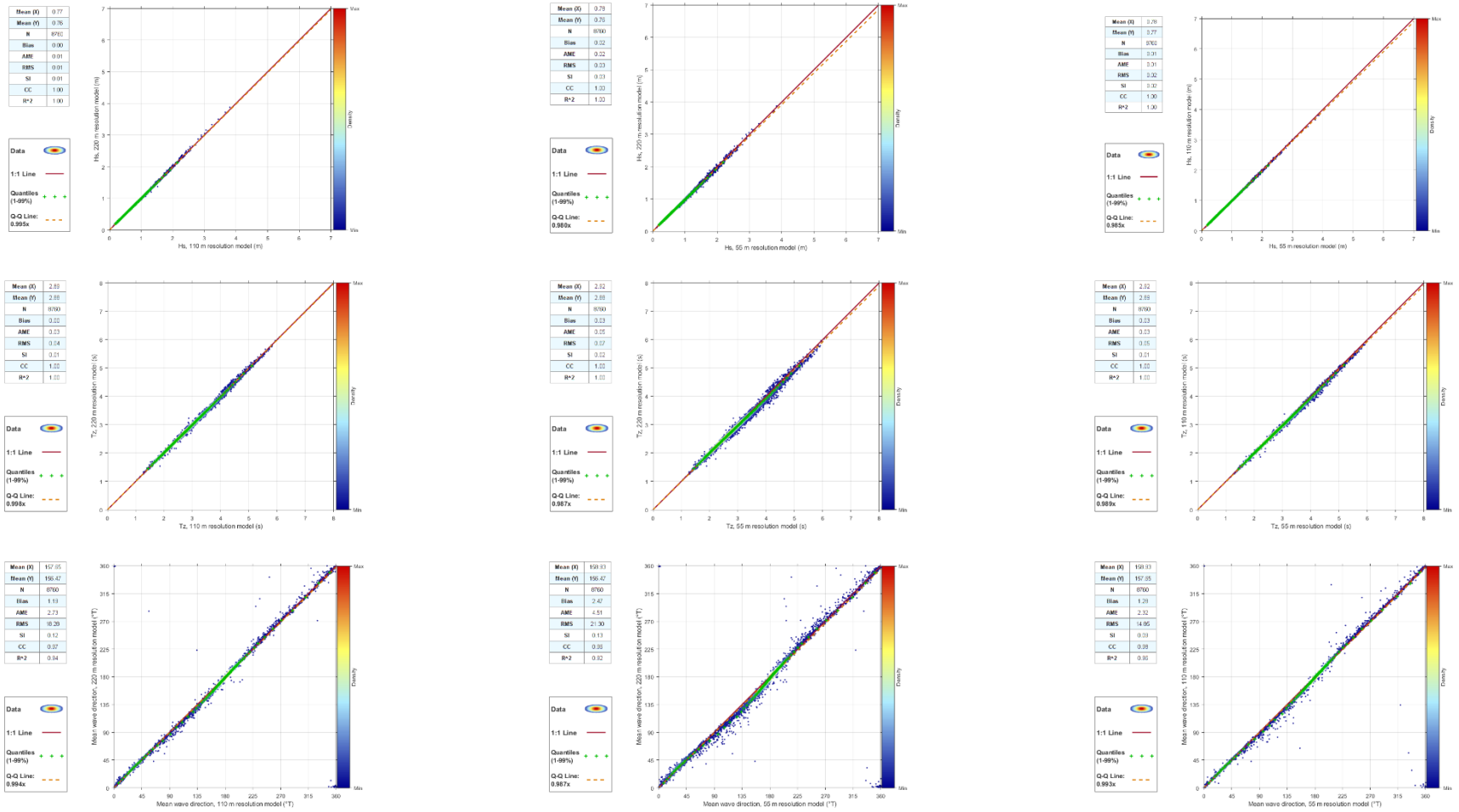


Figure 6.6. Results of model runs with differing spatial resolutions, at the Cable Route. Top row = significant wave height, middle row = mean zero-crossing wave period, bottom row = mean wave direction. Left column 220 m resolution vs. 110 m resolution. Middle column 55 m resolution vs. 220 m resolution. Right column = 110 m resolution vs. 55 m resolution.



In these tests, we can consider the highest spatial resolution model to be the 'standard' against which the other resolutions can be judged, on the basis that we assume that the highest spatial resolution model should produce the more accurate results.

Figure 6.3 to Figure 6.6 show that there can be some small impacts of spatial resolution on wave period and direction at certain locations, particularly at the centre of bank location, where the water depths are shallowest. In general, wave heights (top row of each figure) are unaffected by changes in spatial resolution.

As expected, the largest differences are observed when comparing the highest and lowest spatial resolution models (middle columns of each figure).

The right-hand columns of each figure show that there is limited difference between a model with 110 m or 55 m spatial resolution, suggesting that there is little additional 'accuracy' to be achieved in increasing resolution above 110 m. Therefore, a final spatial resolution of 110 m was selected, it being the highest resolution that could be achieved with a practicable runtime.

### 6.4.2 Directional Discretisation

Similar tests were also carried out with varying numbers of directional bins to discretise spectra within the model; 24, 36 and 48 directional bins were tested with results presented in Figure 5.7 to Figure 5.10.

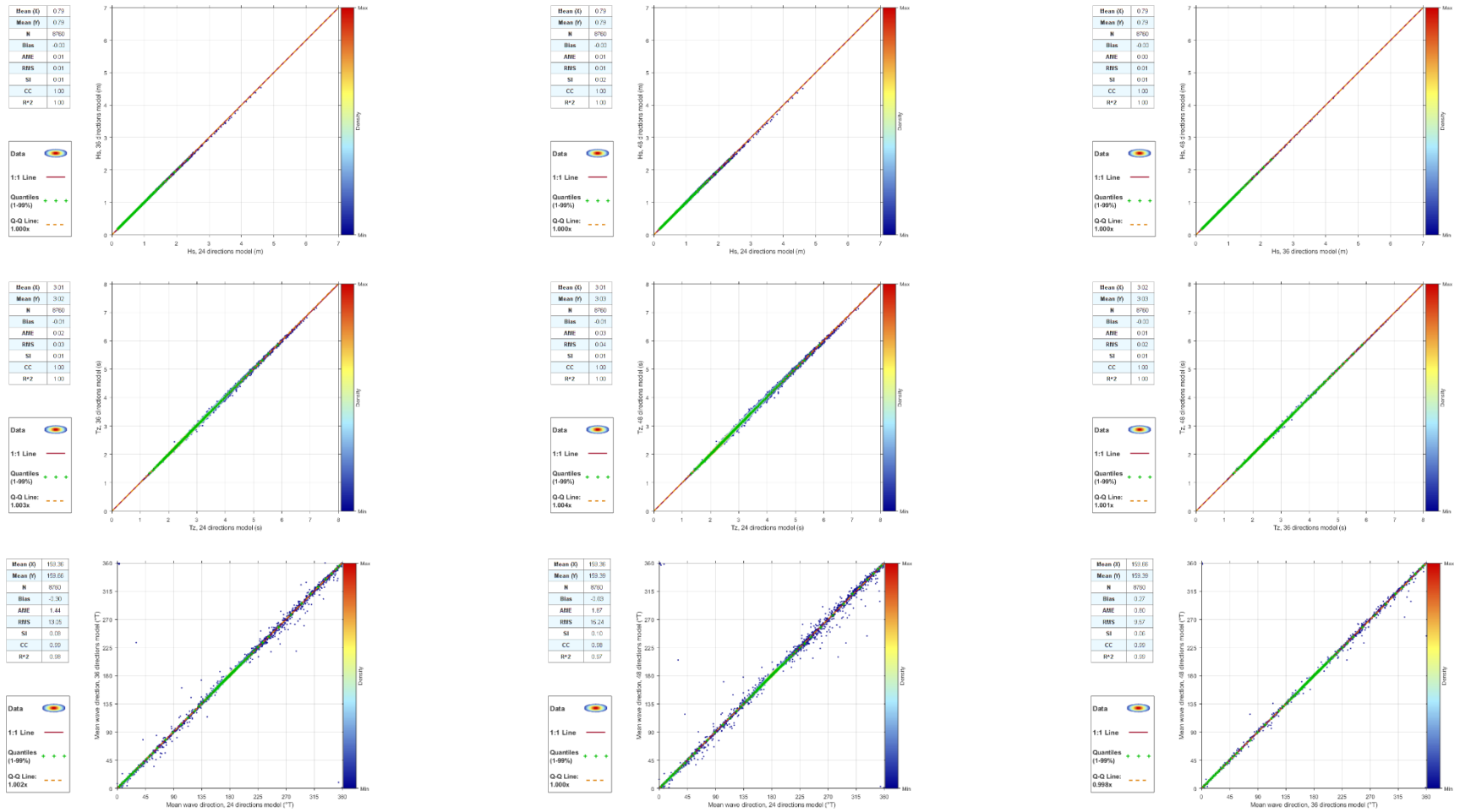


Figure 6.7. Results of model runs with differing numbers of directional bins, at AWAC A. Top row = significant wave height, middle row = mean zero-crossing wave period, bottom row = mean wave direction. Left column 24 directional bins vs. 36 directional bins. Middle column 48 directional bins vs. 24 directional bins. Right column = 36 directional bins vs. 48 directional bins.

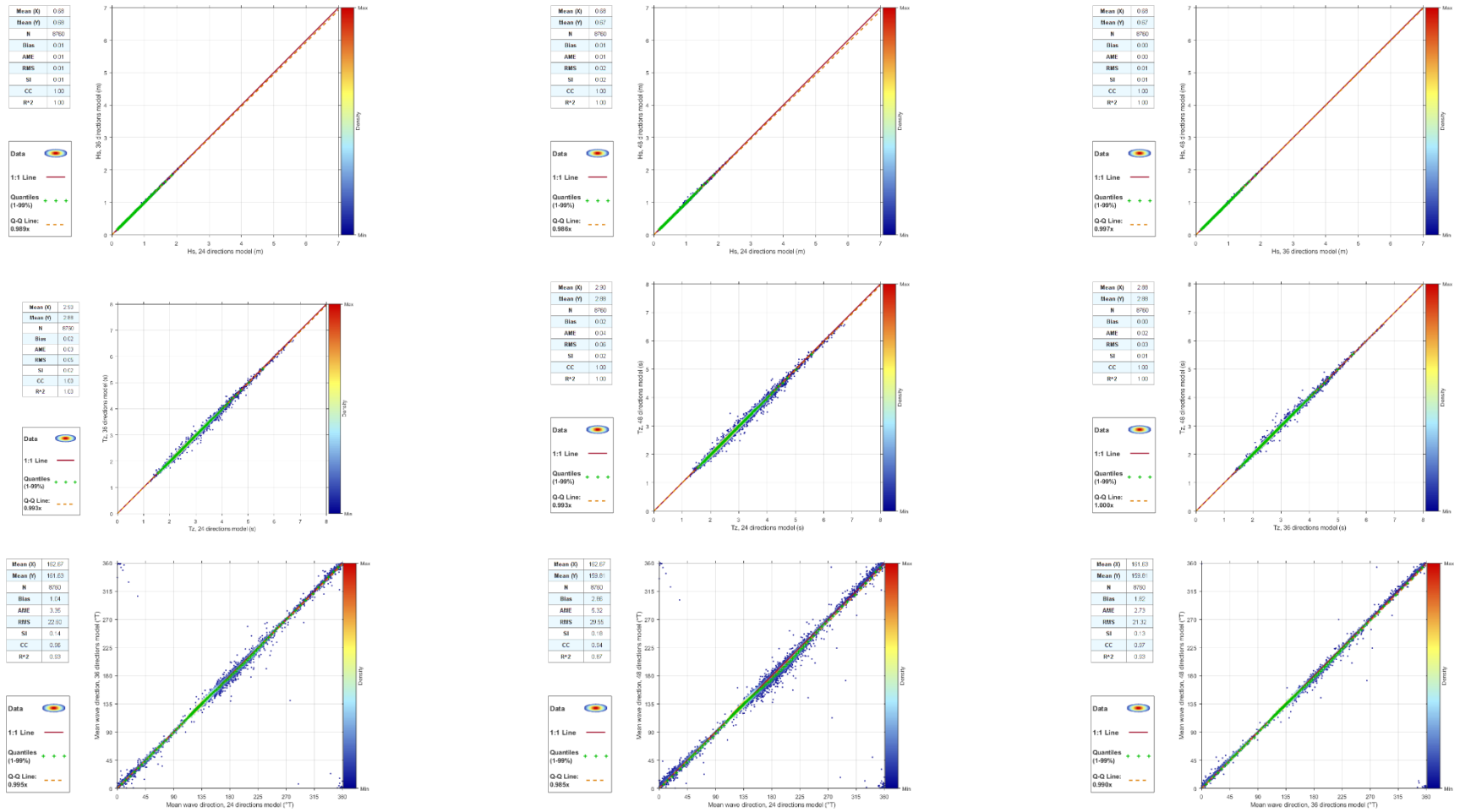


Figure 6.8. Results of model runs with differing numbers of directional bins, at Centre of Bank. Top row = significant wave height, middle row = mean zero-crossing wave period, bottom row = mean wave direction. Left column 24 directional bins vs. 36 directional bins. Middle column 48 directional bins vs. 24 directional bins. Right column = 36 directional bins vs. 48 directional bins.

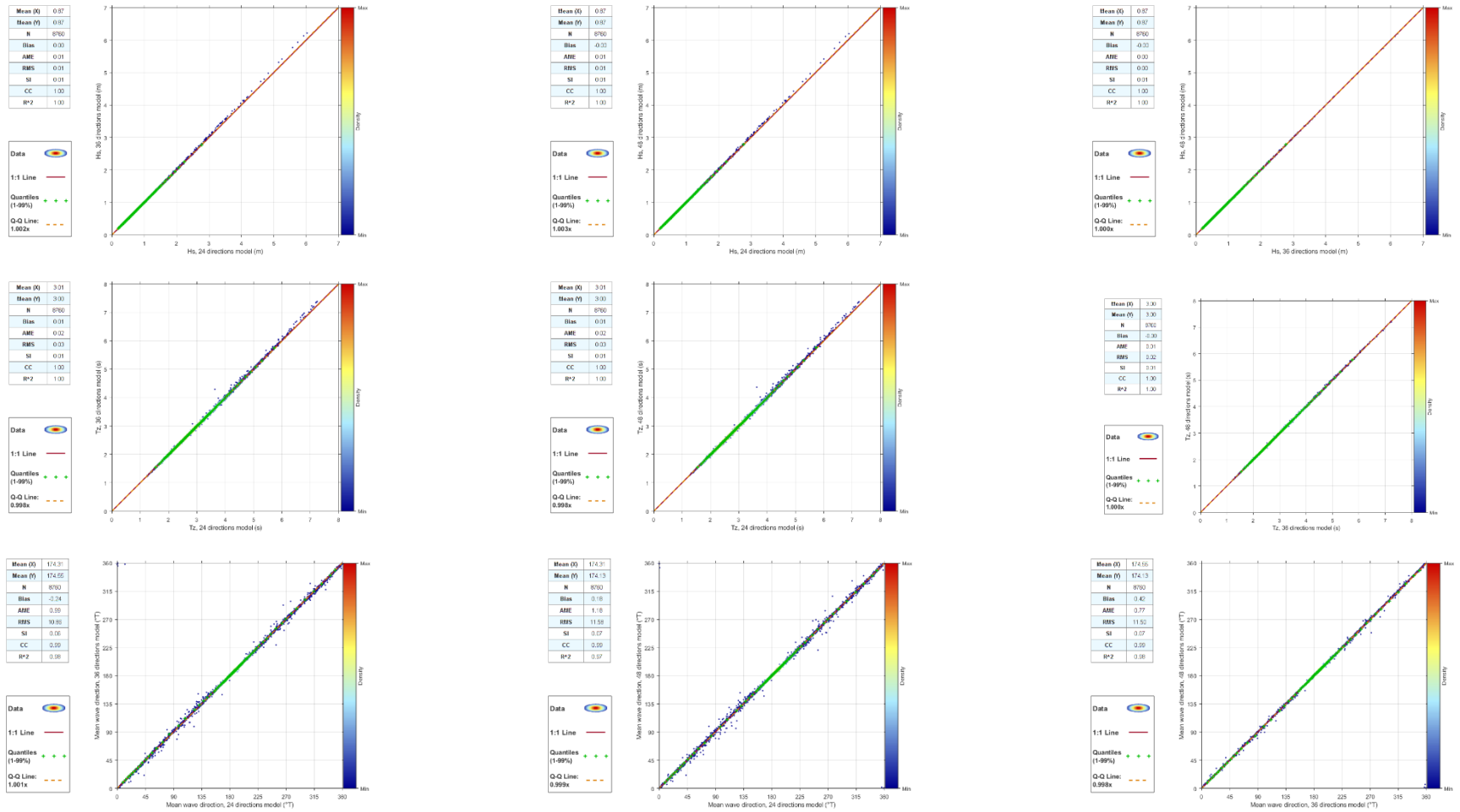



Figure 6.9. Results of model runs with differing numbers of directional bins, at AWAC E. Top row = significant wave height, middle row = mean zero-crossing wave period, bottom row = mean wave direction. Left column 24 directional bins vs. 36 directional bins. Middle column 48 directional bins vs. 24 directional bins. Right column = 36 directional bins vs. 48 directional bins.

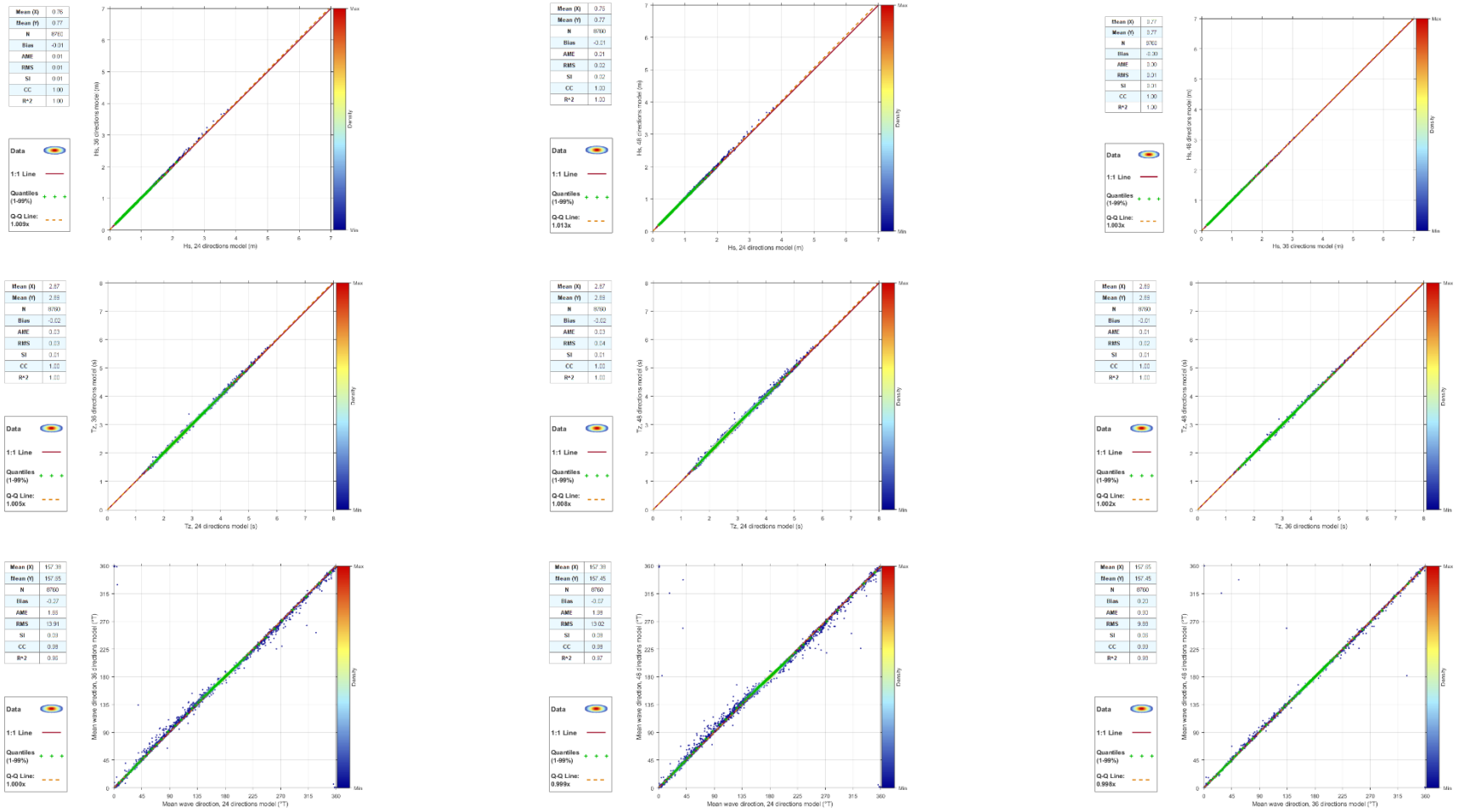


Figure 6.10. Results of model runs with differing numbers of directional bins, at the Cable Route. Top row = significant wave height, middle row = mean zero-crossing wave period, bottom row = mean wave direction. Left column 24 directional bins vs. 36 directional bins. Middle column 48 directional bins vs. 24 directional bins. Right column = 36 directional bins vs. 48 directional bins.

In these tests, we can consider the highest resolution directional discretisation model to be the 'standard' against which the other directional resolutions can be judged, on the basis that we assume that the highest resolution model should produce the more accurate results.

Figure 5.7 to Figure 5.10 show that there can be some small impacts of directional discretisation on wave period and direction at certain locations, particularly at the centre of bank location, where the water depths are shallowest. In general, wave heights (top row of each figure) are unaffected by changes in directional discretisation.

As expected, the largest differences are observed when comparing the highest and lowest directional resolution models (middle columns of each figure).

The right-hand columns of each figure show that there is limited difference between a model with directional resolution of 36 bins or 48 bins, suggesting that there is little additional 'accuracy' to be achieved in increasing the resolution above 36 bins. Therefore, a final directional discretisation of 36 bins was selected, it being the highest directional resolution that could be achieved with a practicable runtime.

## 6.5 Final Model Parameter Settings

The model was run in non-stationary mode to allow proper wave growth within the model domain and data were output from the model every 1 hour. Within the model, wave spectra were discretised using 36 directions and 36 frequencies from 0.0345 to 0.9695Hz. The physics schemes and parameterisations used in this model have been refined by MetOceanWorks over many years, running thousands of scenarios. For the production run, we used SWAN cycle III version 40.91ABC and employed the expression by Komen for white capping and for wind. Triads were included and quadruplet interactions were estimated using the Discrete Interaction Approximation (DIA) by Hasselmann. The JONSWAP (Joint North Sea Wave Project) bottom friction formulation was used and depth-limited wave breaking was modelled according to the bore-model of Battjes and Janssen. Diffraction was switched on within the model. Please see "Swan cycle III version 40.91 ABC - Scientific and Technical Documentation" [3] for further details.

## 6.6 Hindcast Uniformity

In terms of model boundary conditions, the model is expected to yield results of a uniform quality (i.e. equivalent to the level of validation detailed in Section 6.7) throughout the hindcast period.

However, the reader is again reminded that Arklow Bank is subject to short term movement and so bedform evolution has localised effects on the wave regime. The review of sensitivity to changes in bathymetry which is presented in Appendix I also considers the effects on wave heights.

## 6.7 Model Validation

The wave model has been extensively validated against the measured wave data detailed in Table 6.1 (see also Appendix C), with pertinent results presented in the following pages. Validations for the M2 and M5 buoys (Figure 6.11 and Figure 6.12) take model data from the 2.75 km Irish Sea model, whilst those for the three AWACs (Figure 6.13 through Figure 6.32) use data from the 110 m Arklow model. These assessments demonstrate good model skill in terms of wave height, direction and period under both ambient and storm conditions. Scatter plots with overlaid Quantile-Quantiles are presented and generally yield high correlation



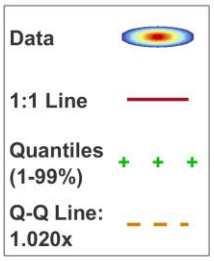
coefficients, relatively low scatter indices and slopes close to unity. The comparisons suggest some conservatism in modelled wave heights at the southern end of Arklow Bank which reduces towards the north.

Note that 'micro-siting' of the model output positions within a few grid cells of the measurement locations was explored, as with the hydrodynamic model (see Section 5.7). As a result, for each of the wave validations, we have selected the best validation that is within at most a few grid cells of the average instrument position across all deployments.

More detailed validation information can be found in Appendix C, including spectral comparisons and review of the suitability of JONSWAP to provide a simplified representation of the modelled spectra.

Behaviour of Tp for higher wave periods at AWAC E is explored in more detail in Appendix D.

| | |
|---|---|
| Mean (X) | 1.20 |
| Mean (Y) | 1.22 |
| N | 119977 |
| Bias | 0.02 |
| AME | 0.19 |
| RMS | 0.26 |
| SI | 0.22 |
| CC | 0.94 |
| $R^2$ | 0.88 |



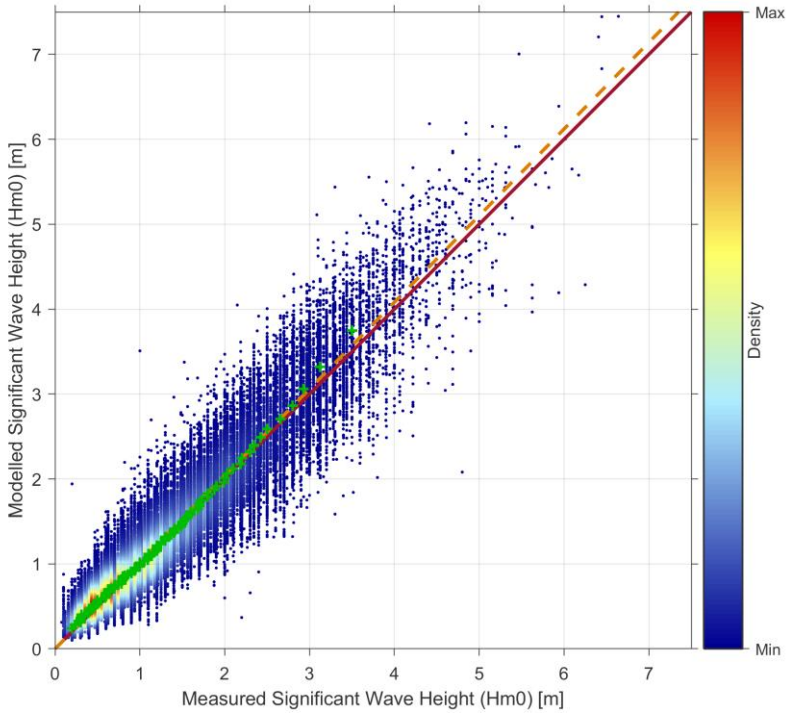
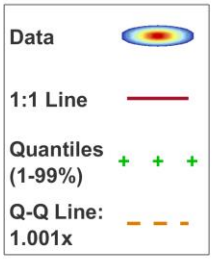




Figure 6.11. M2, Hm0 validation.

| | |
|---|---|
| Mean (X) | 1.86 |
| Mean (Y) | 1.89 |
| N | 93559 |
| Bias | 0.03 |
| AME | 0.19 |
| RMS | 0.26 |
| SI | 0.14 |
| CC | 0.97 |
| $R^2$ | 0.94 |



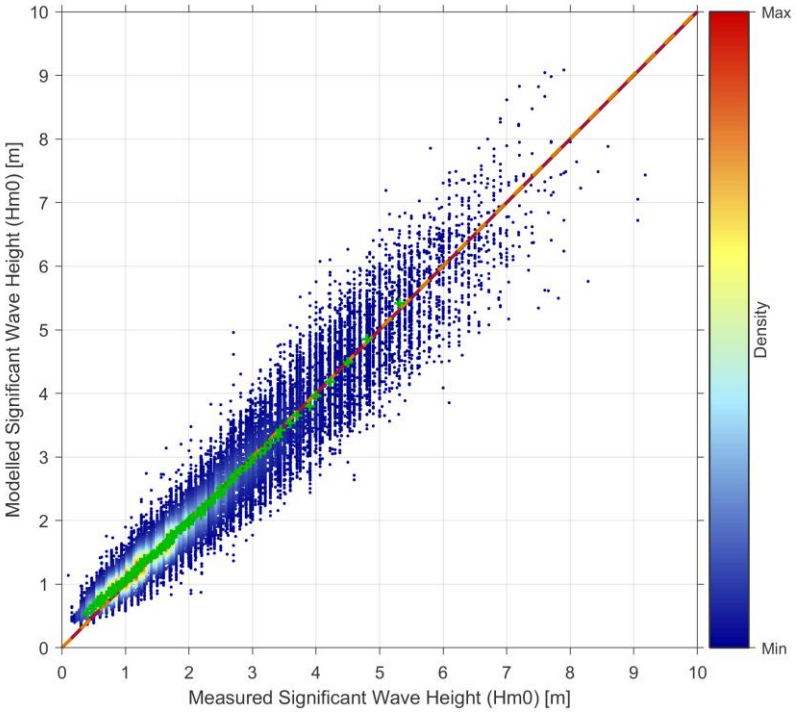




Figure 6.12. M5, Hm0 validation.

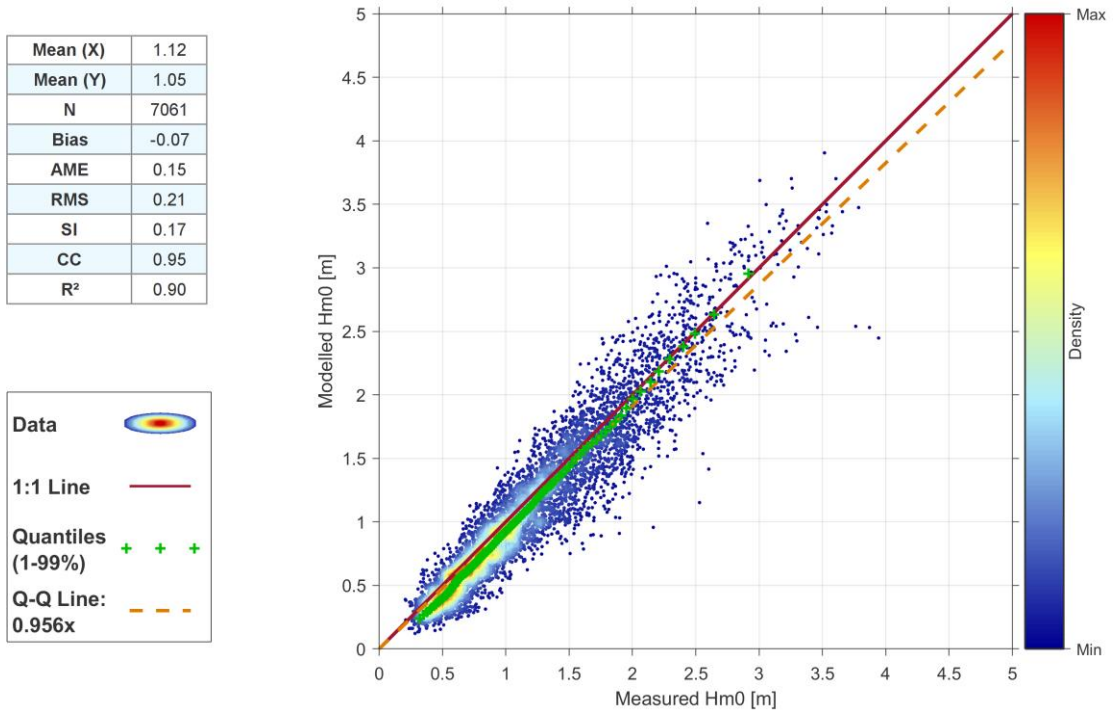



Figure 6.13. AWAC A, Hm0 validation, all data.

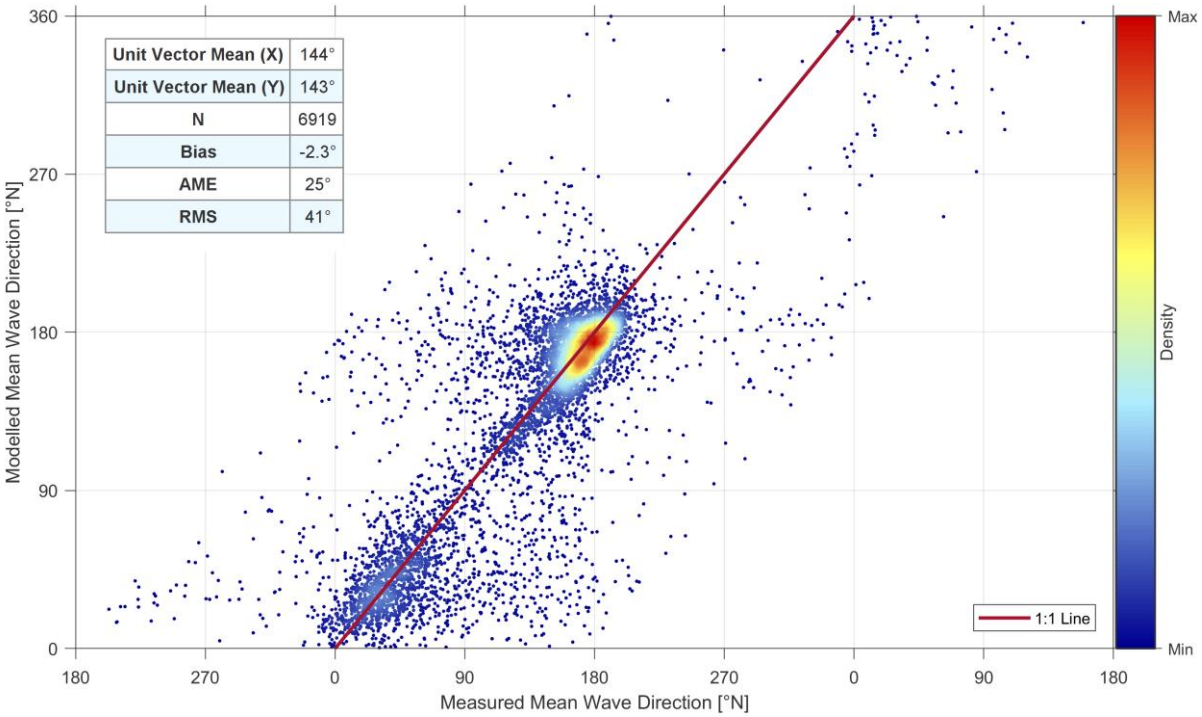



Figure 6.14. AWAC A, Mdir validation, all data.

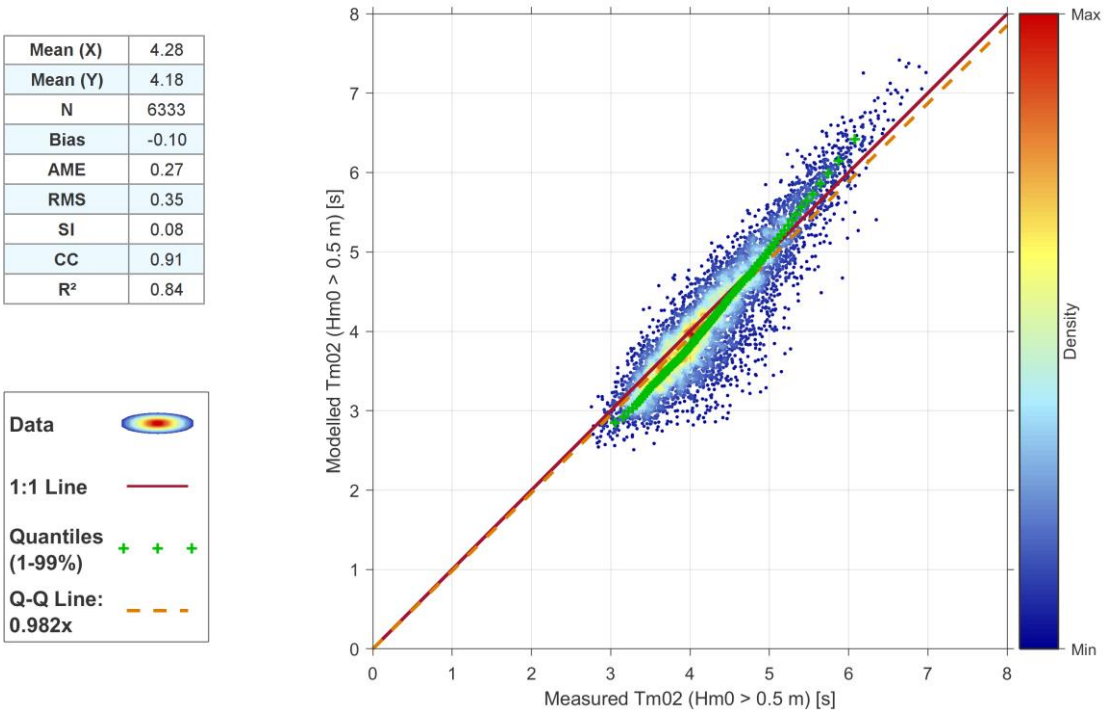



Figure 6.15. AWAC A, Tm02 validation, timestamps with Hm0 > 0.5 m, all data.

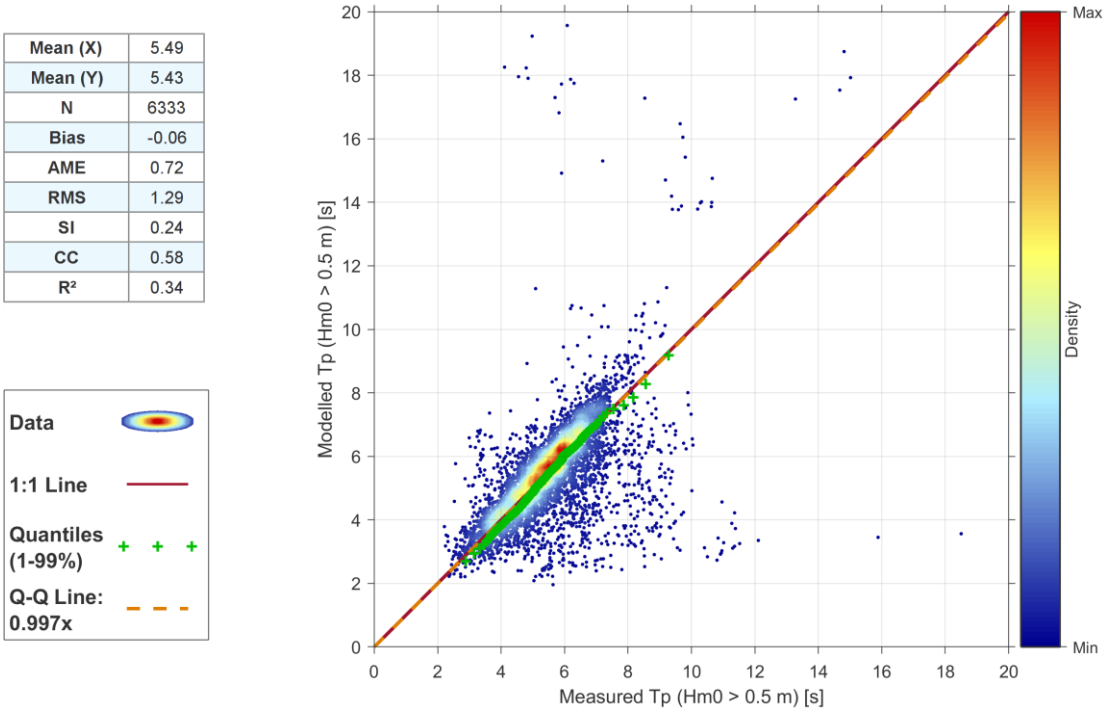



Figure 6.16. AWAC A, Tp validation, timestamps with Hm0 > 0.5 m, all data.

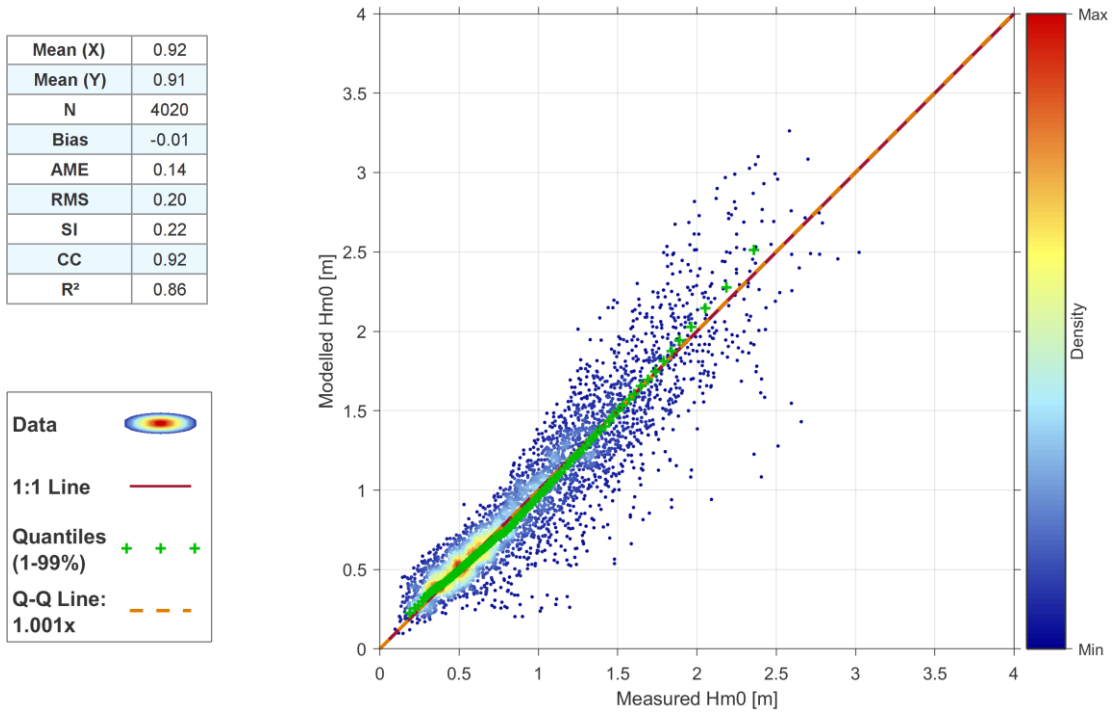



Figure 6.17. AWAC B1, Hm0 validation, all data.

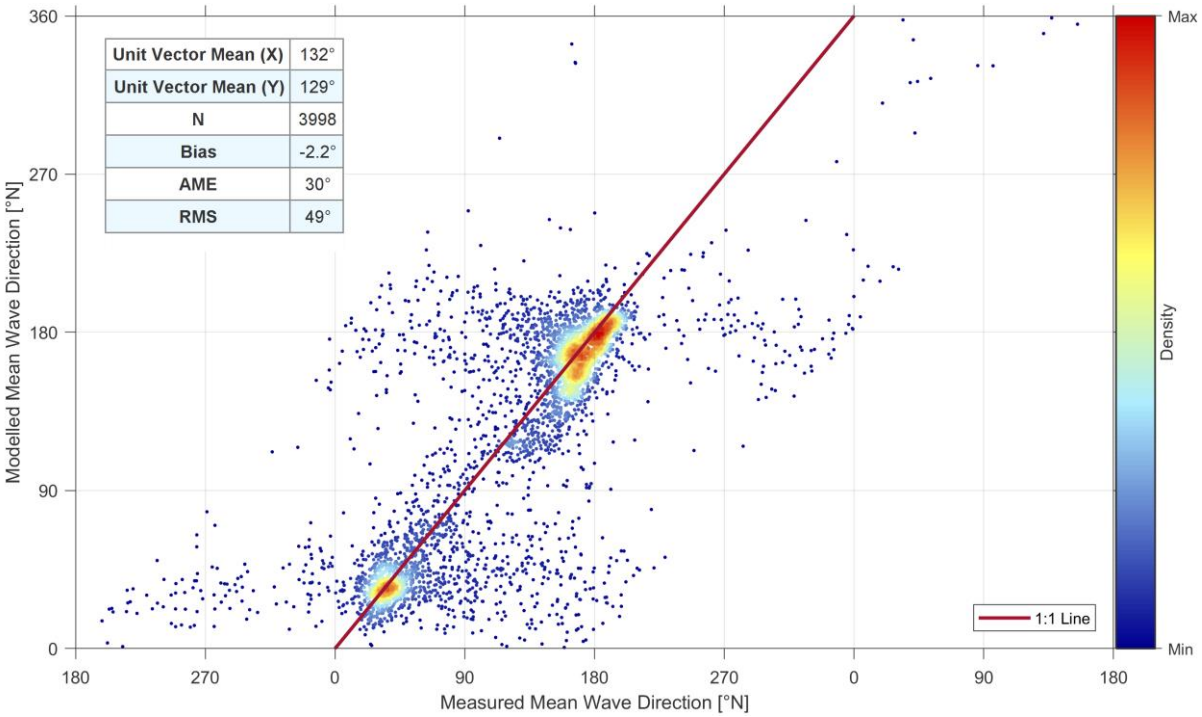



Figure 6.18. AWAC B1, Mdir validation, all data.

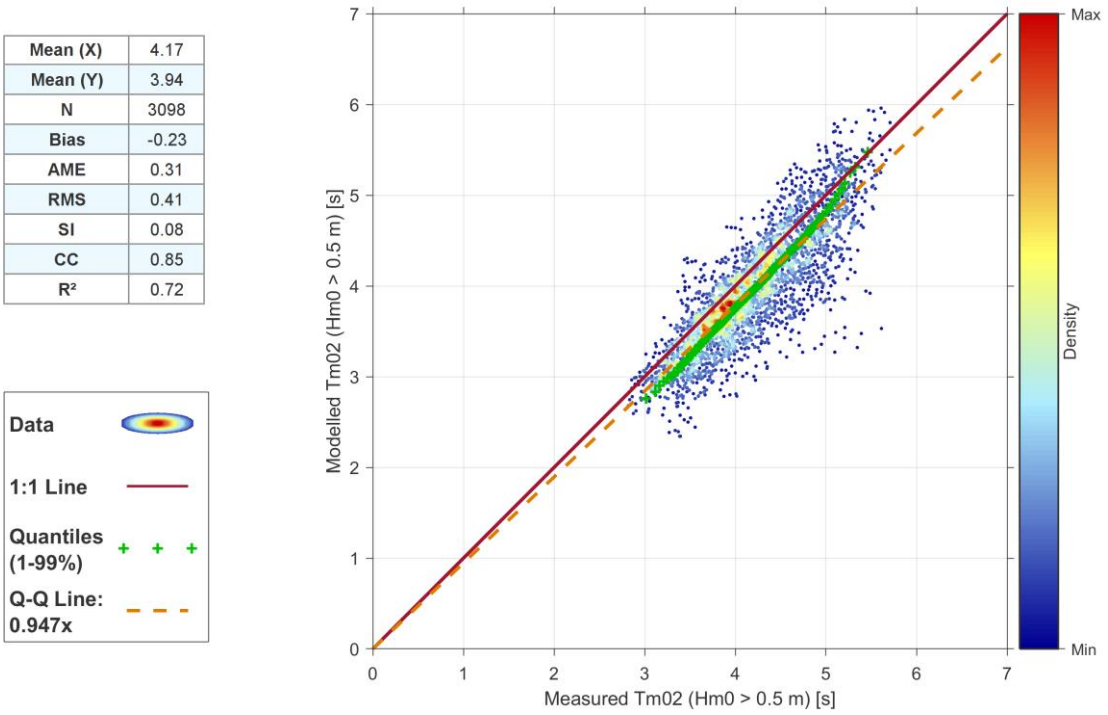



Figure 6.19. AWAC B1, Tm02 validation, timestamps with Hm0 > 0.5 m, all data.

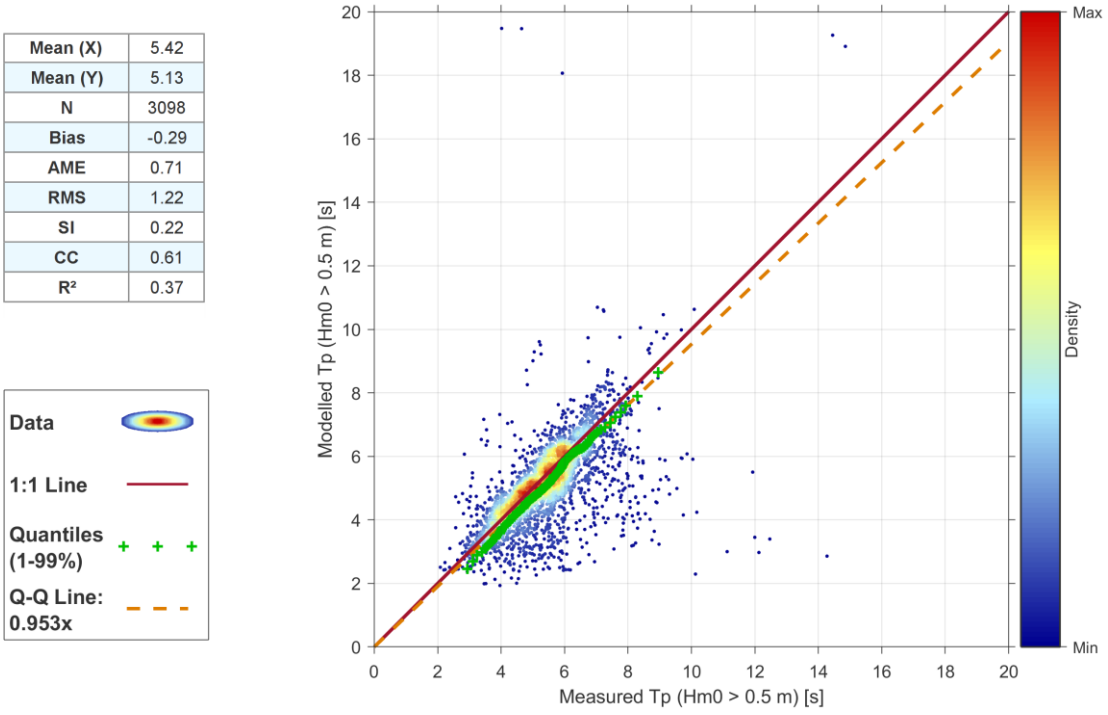



Figure 6.20. AWAC B1, Tp validation, timestamps with Hm0 > 0.5 m, all data.

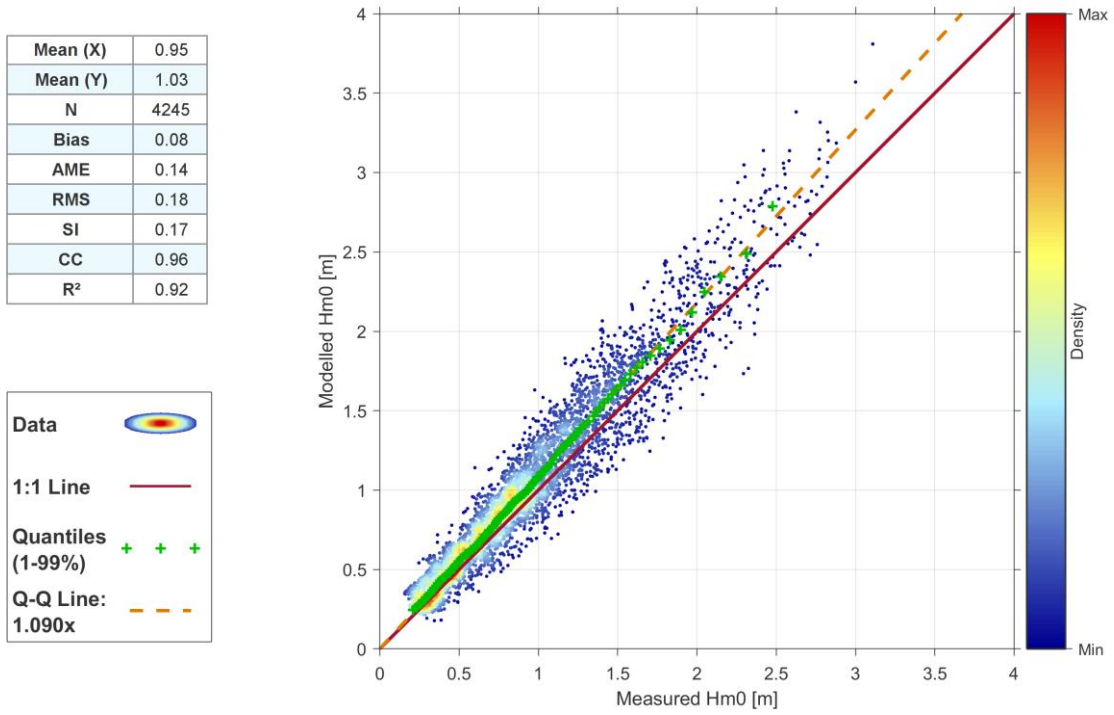



Figure 6.21. AWAC C, Hm0 validation, all data.

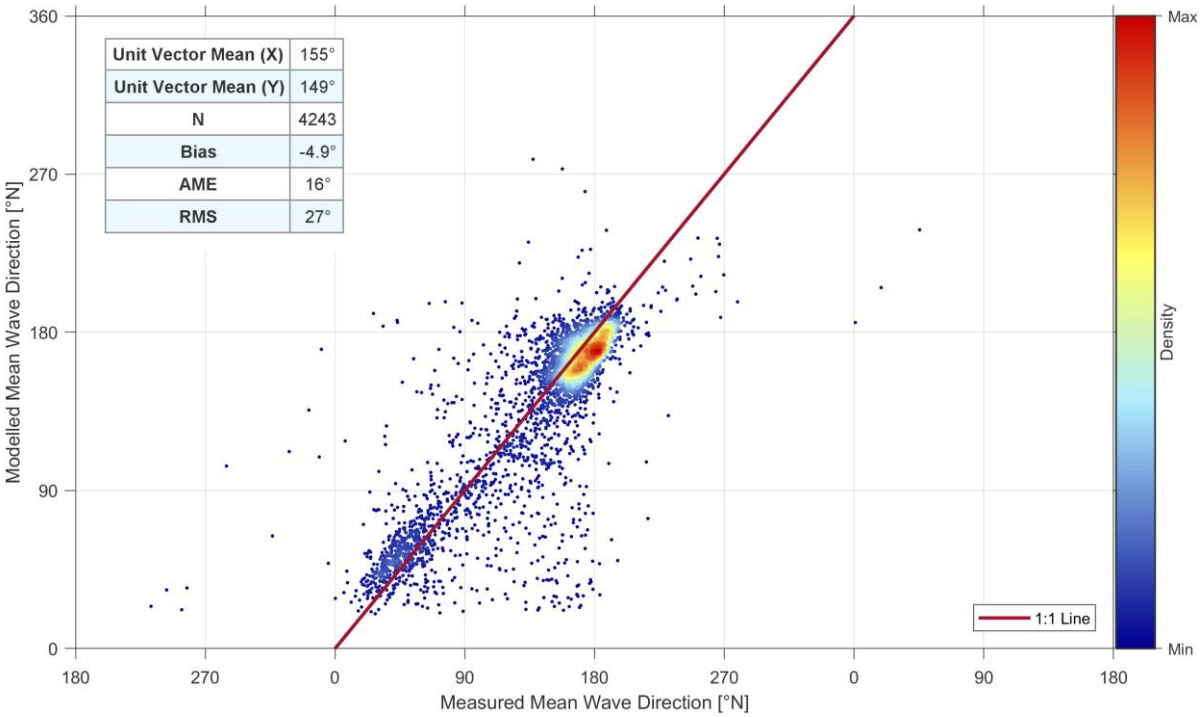



Figure 6.22. AWAC C, Mdir validation, all data.

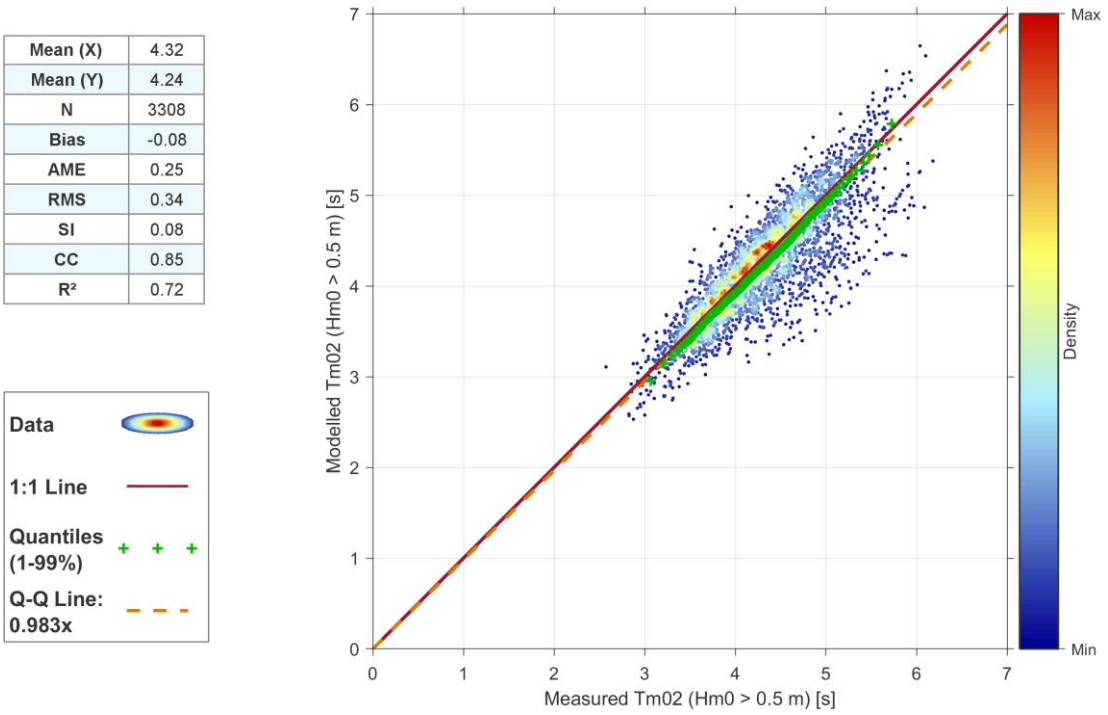



Figure 6.23. AWAC C, Tm02 validation, timestamps with Hm0 > 0.5 m, all data.

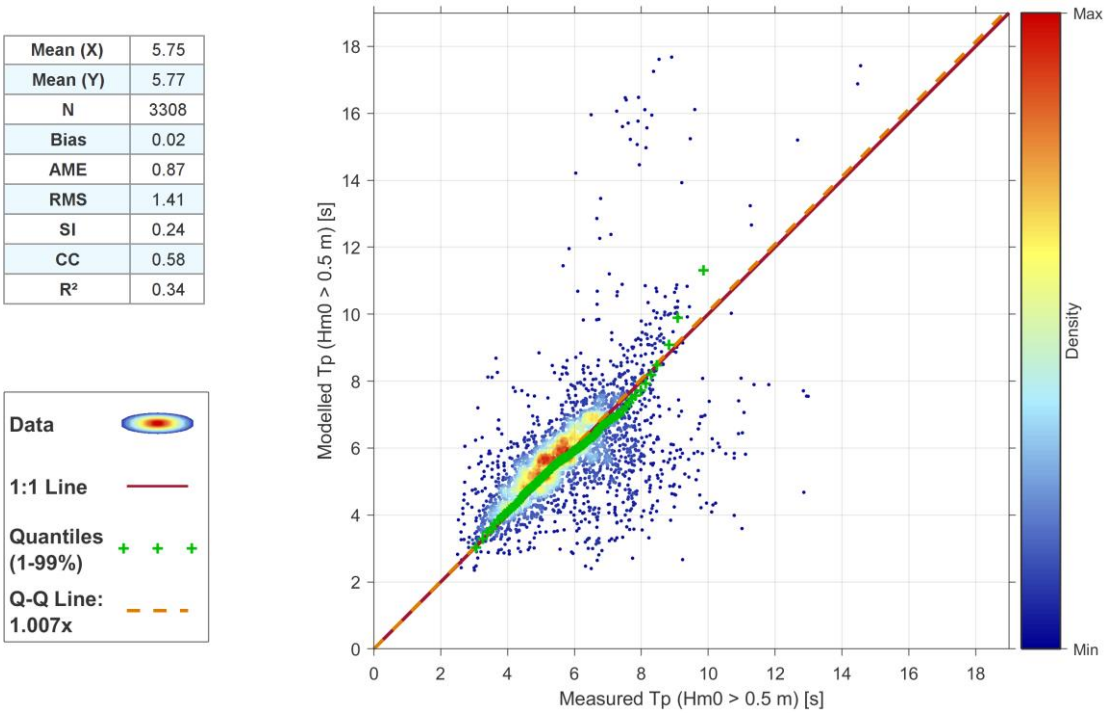



Figure 6.24. AWAC C, Tp validation, timestamps with Hm0 > 0.5 m, all data.

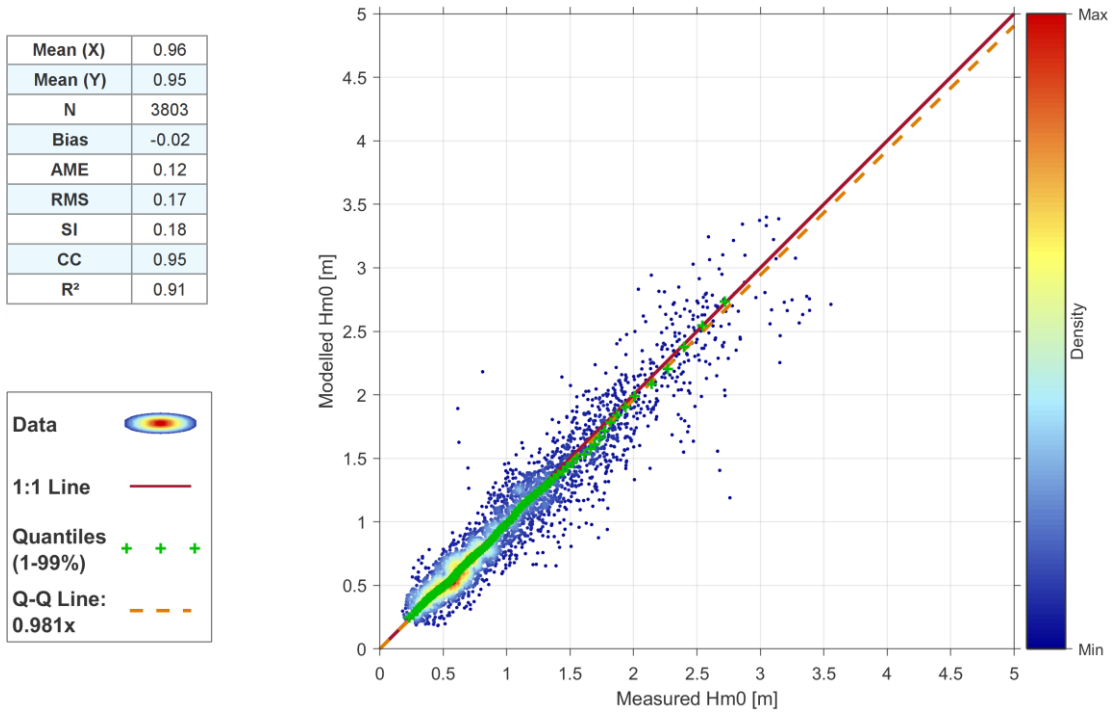



Figure 6.25. AWAC D1, Hm0 validation, all data.

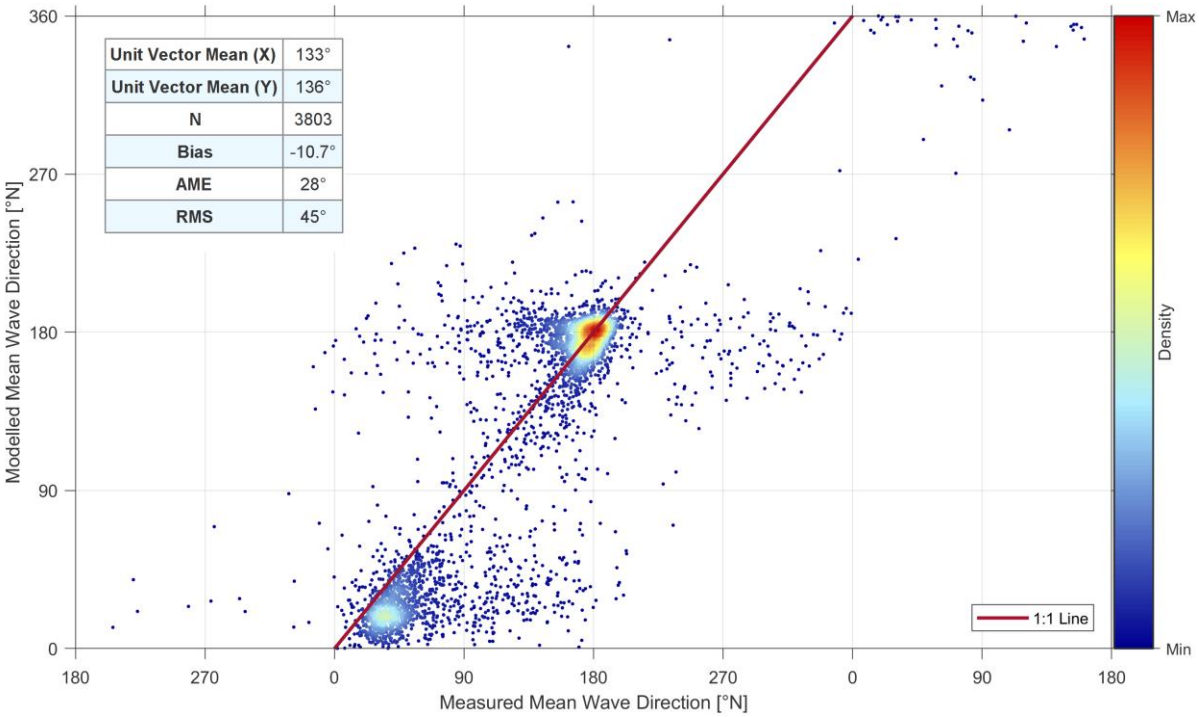



Figure 6.26. AWAC D1, Mdir validation, all data.

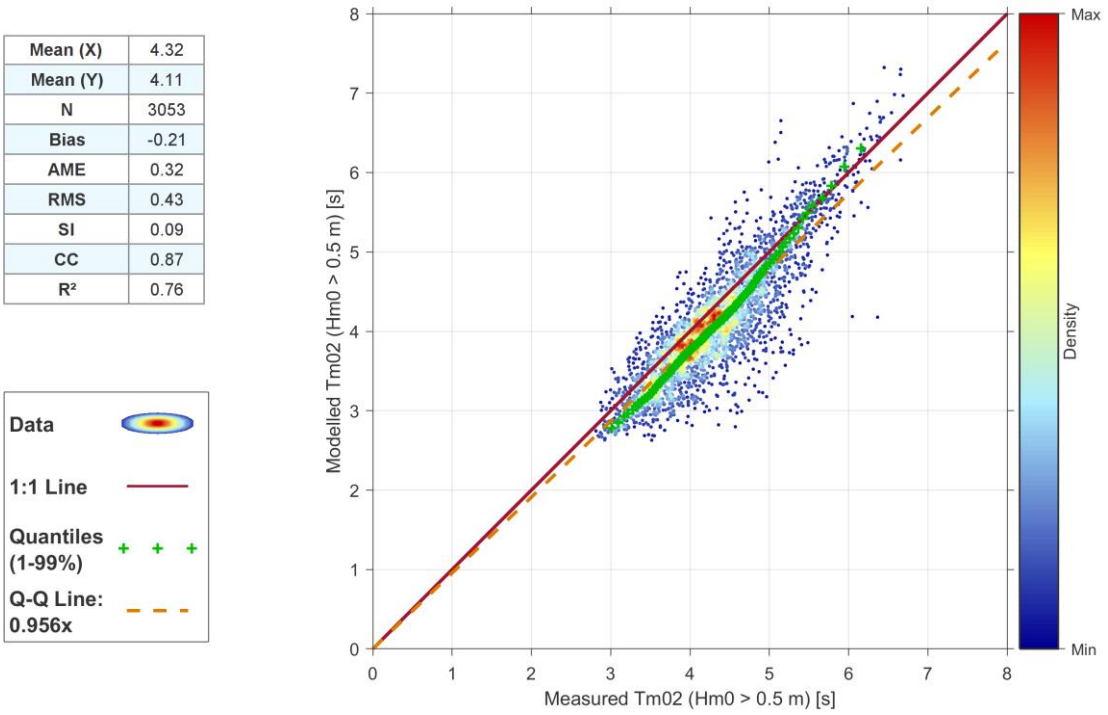



Figure 6.27. AWAC D1, Tm02 validation, timestamps with Hm0 > 0.5 m, all data.

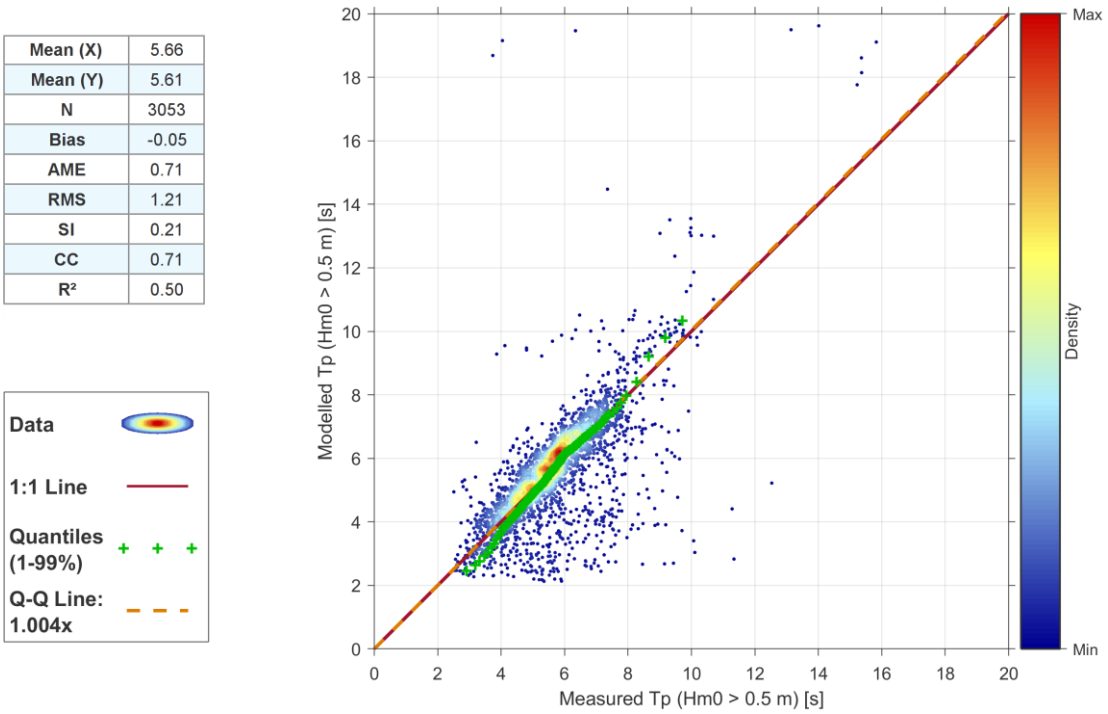



Figure 6.28. AWAC D1, Tp validation, timestamps with Hm0 > 0.5 m, all data.

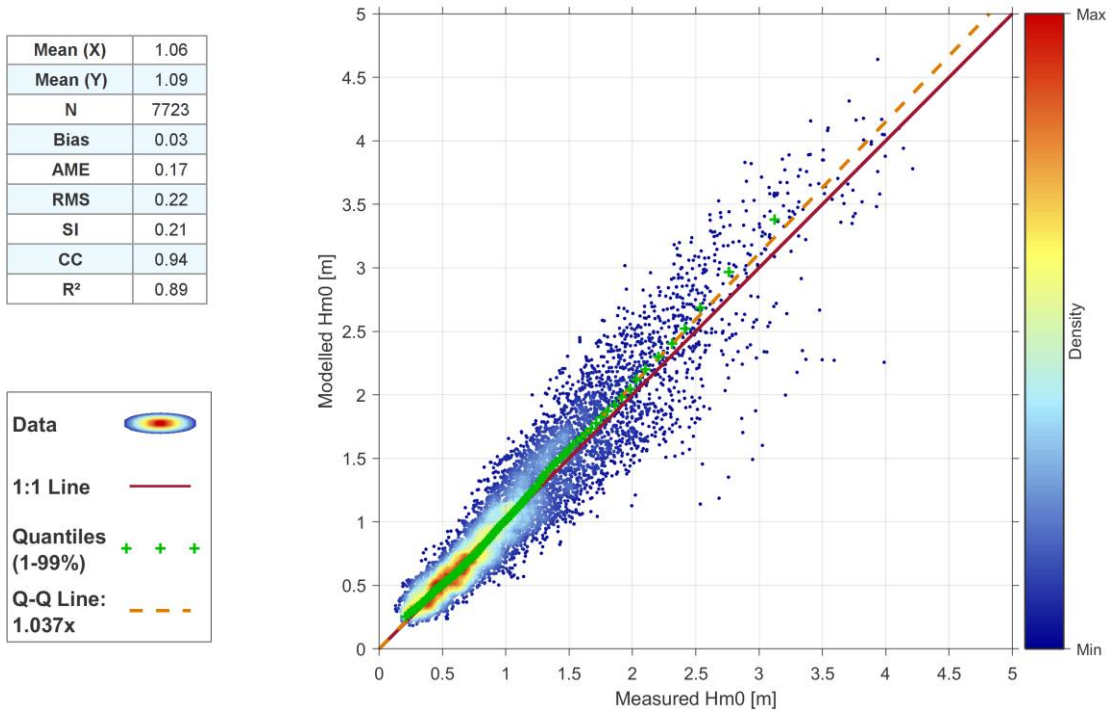



Figure 6.29. AWAC E, Hm0 validation, all data.

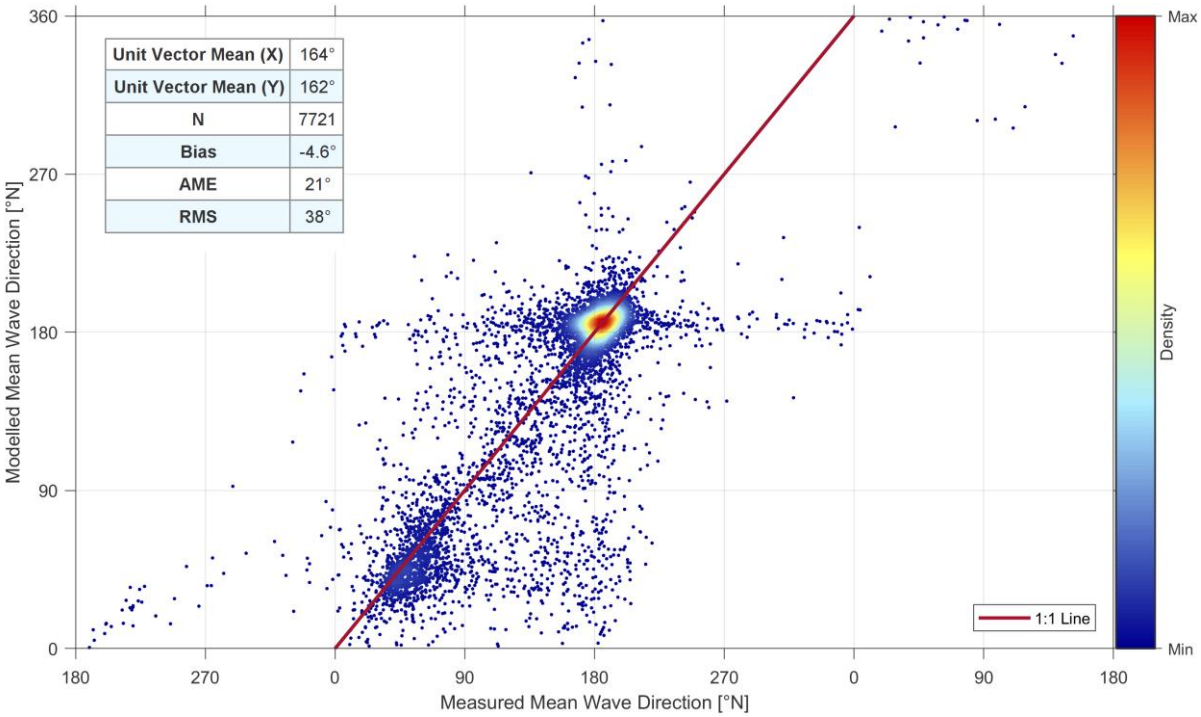



Figure 6.30. AWAC E, Mdir validation, all data.

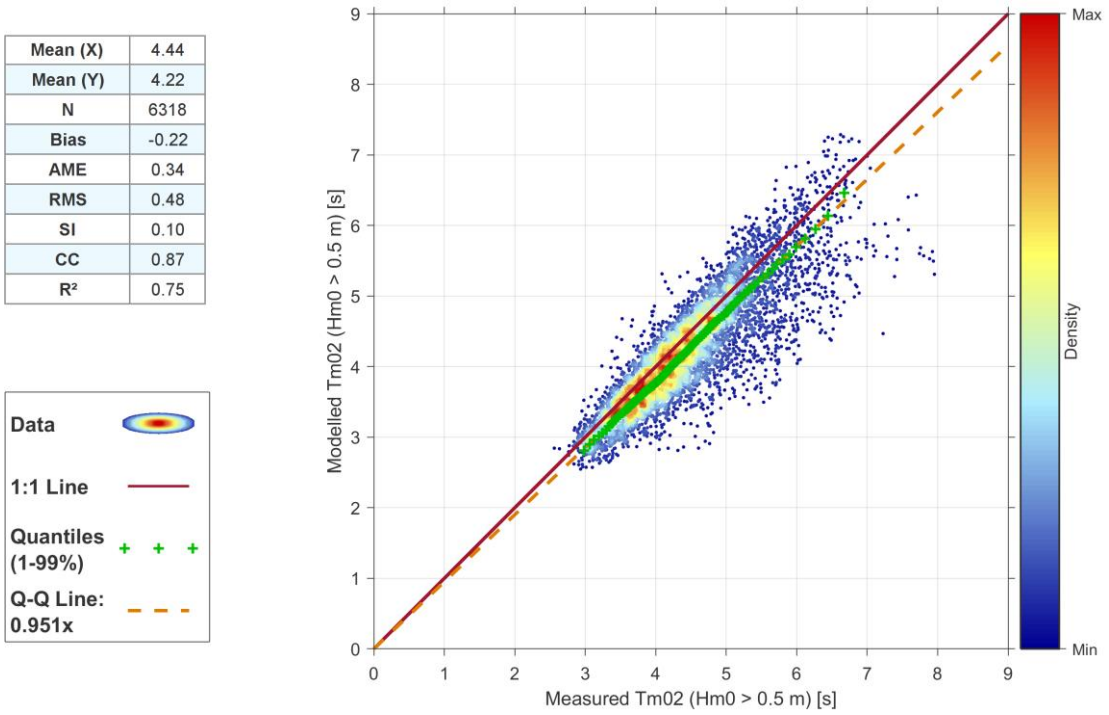



Figure 6.31. AWAC E, Tm02 validation, timestamps with Hm0 > 0.5 m, all data.

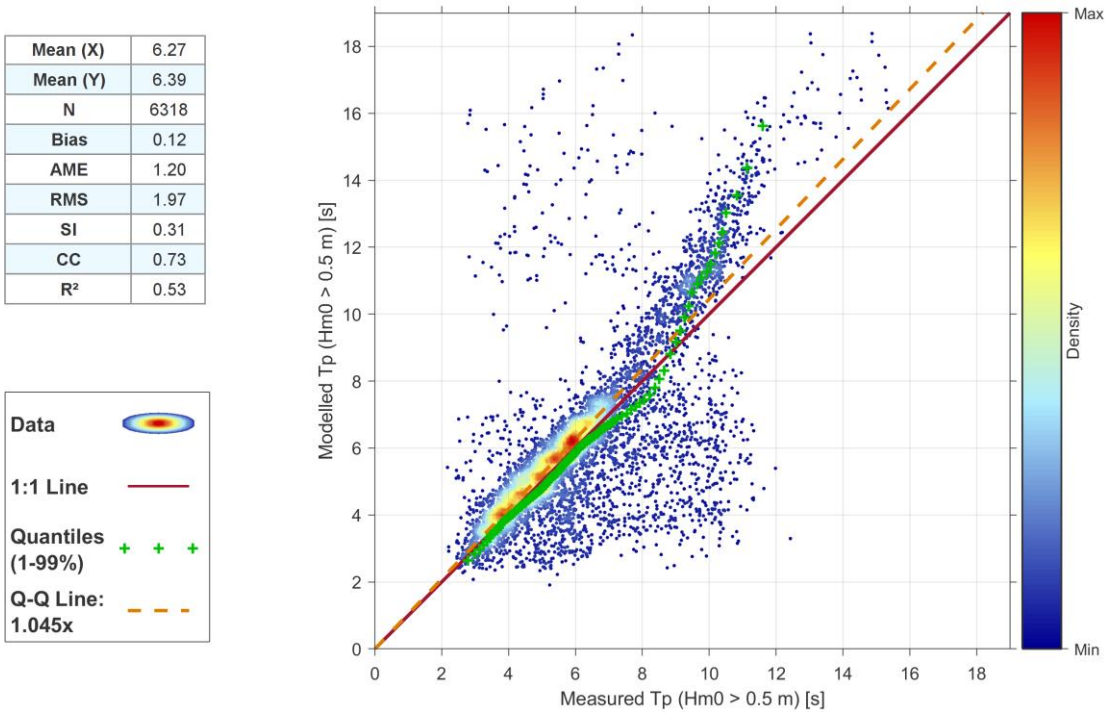



Figure 6.32. AWAC E, Tp validation, timestamps with Hm0 > 0.5 m, all data.

## 6.8 Wave Breaking

As waves move from deeper to shallower water, they start to "feel" the effect of the seabed when the water depth becomes less than about half the wavelength. As this happens, the wave propagation velocity reduces. For the propagation velocity to decrease whilst maintaining the same period between successive wave crests, the waves must steepen. Once the waves become too steep, they will break, either as surging, plunging, or spilling breakers (depending upon the incident wave steepness and/or the local seabed slope). Typically, depth-induced breaking occurs when individual wave heights exceed 0.78 times the water depth. With water depths of 51 to 2 m MSL within the lease area, depth-induced wave breaking is expected to occur regularly in the shallower parts of the site.

Figure 6.33 shows wave crests, white-capping, wave refraction onto the crest of the bank and extensive areas with wave breaking in the shallow water.

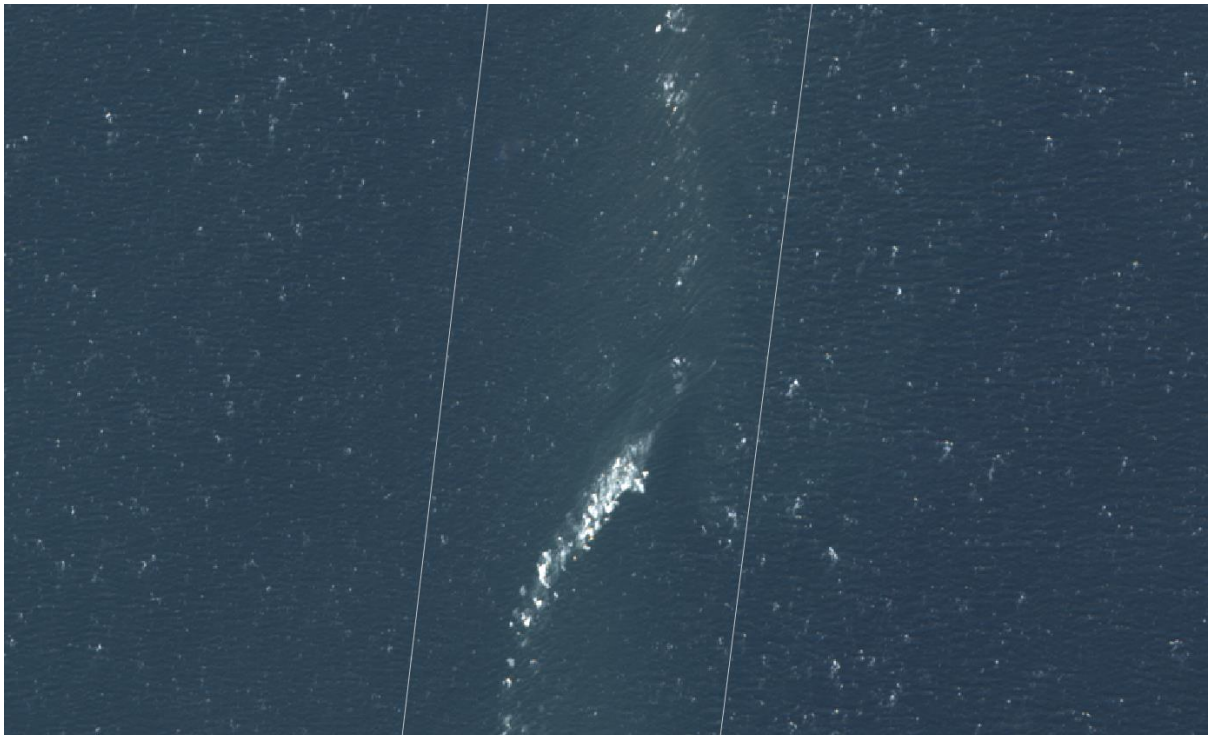


Figure 6.33. Satellite image of the mid-section of Arklow Bank (from ESA and Sentinel 2, May 2020).

Plunging breakers can induce significant slap and slam loading on offshore structures. Our initial, high-level assessment reveals that there are significant regions across the lease area which have water depths small enough to induce wave breaking, in conjunction with slopes steep enough to give rise to plunging breakers.

# 7 Spatial Maps

## 7.1 Introduction

In this Section, map plots are provided to illustrate the spatial variability of metocean parameters across the lease area and surrounds. Maps of wave parameters are included in Section 7.2, followed by current speeds and water levels in Section 7.3. The full duration of the hindcast period is used throughout.

## 7.2 Waves

### 7.2.1 Operational Statistics

In Figure 7.1 through Figure 7.3 the following statistics are shown for significant wave height:

- Time-averaged **mean** significant wave height.
- Time-averaged power means of significant wave height **$\langle H_{m0} \rangle_{(2)}$ and $\langle H_{m0} \rangle_{(5)}$** whereby:

$$\langle H_{mo} \rangle_{(m)} = \left[ \frac{1}{N} \sum_{n=1}^{N} \left( H_{m0,n} \right)^{m} \right]^{1/m}$$

  With $H_{m0,n}$ being the total significant wave height at time step $n$, $m$ a coefficient (2 or 5), and the sum taken over all $N$ steps of the dataset.
- **50$^{th}$, 90$^{th}$, 95$^{th}$, 99$^{th}$ and 99.9$^{th}$ percentiles** of significant wave height.
- **Maximum** significant wave height.

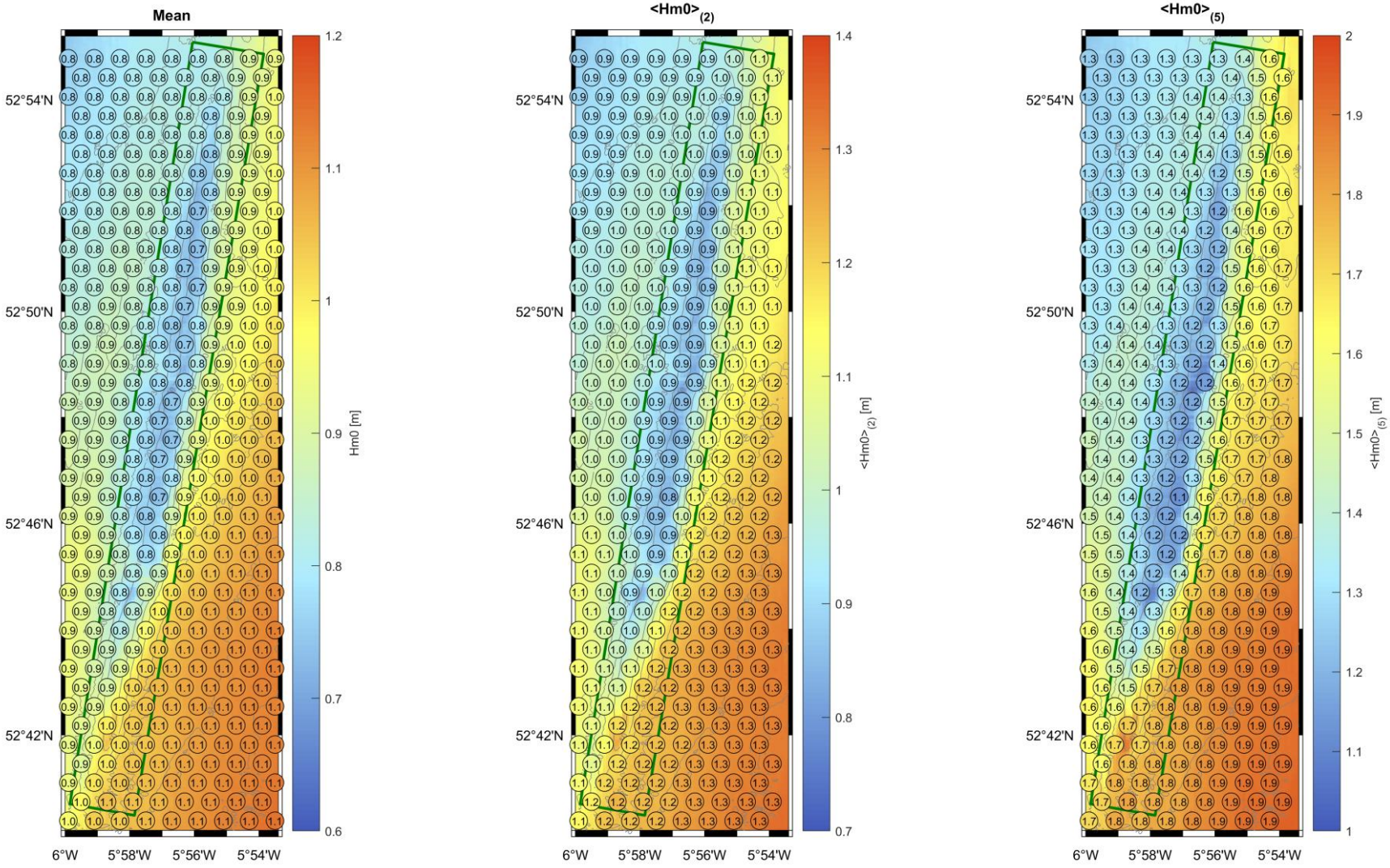



Figure 7.1: Mean Hm0 (left), 2nd power mean Hm0 (centre) and 5th power mean Hm0 (right).

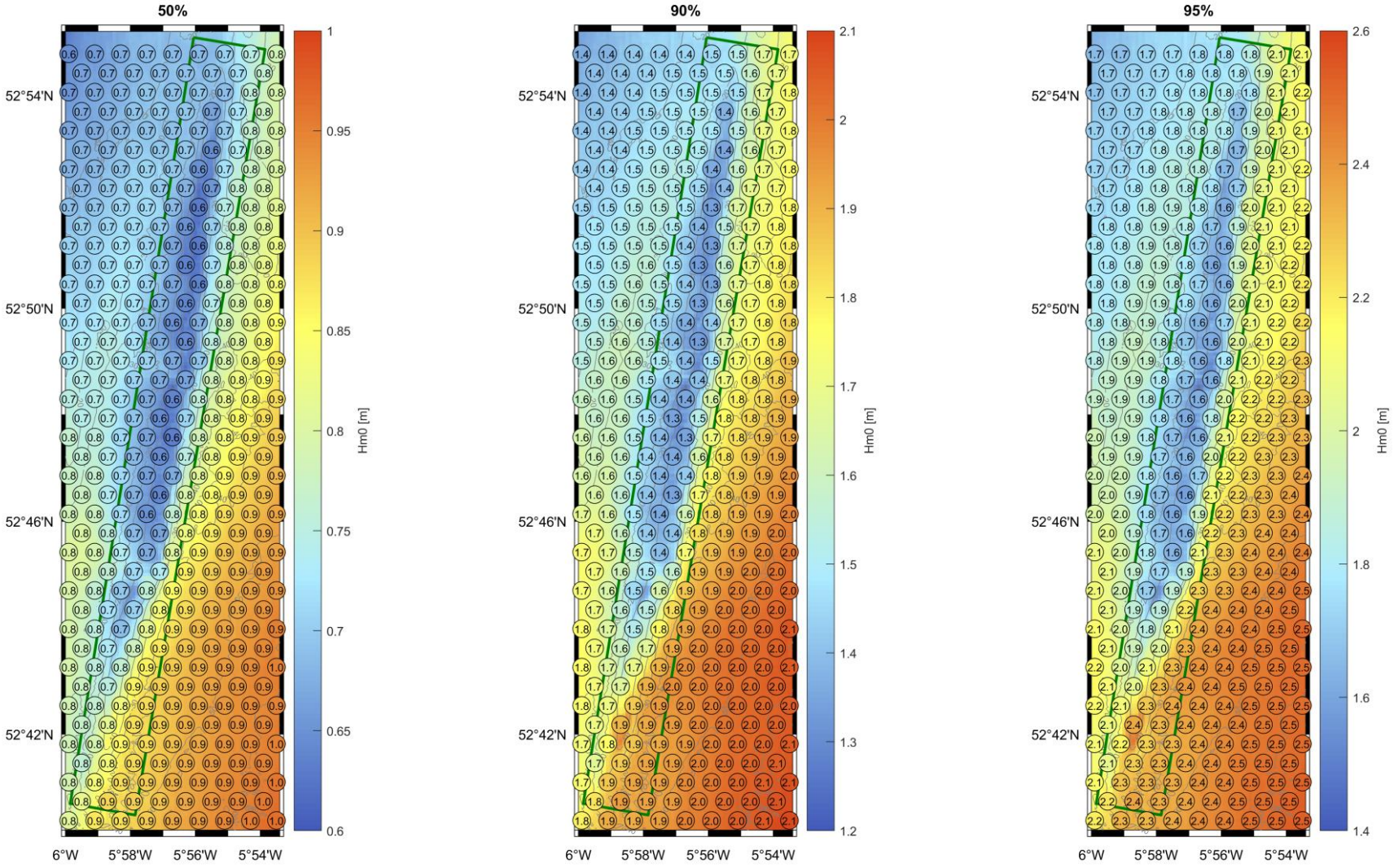



Figure 7.2: Percentiles of Hm0: 50th percentile (left), 90th percentile (centre) and 95th percentile (right).

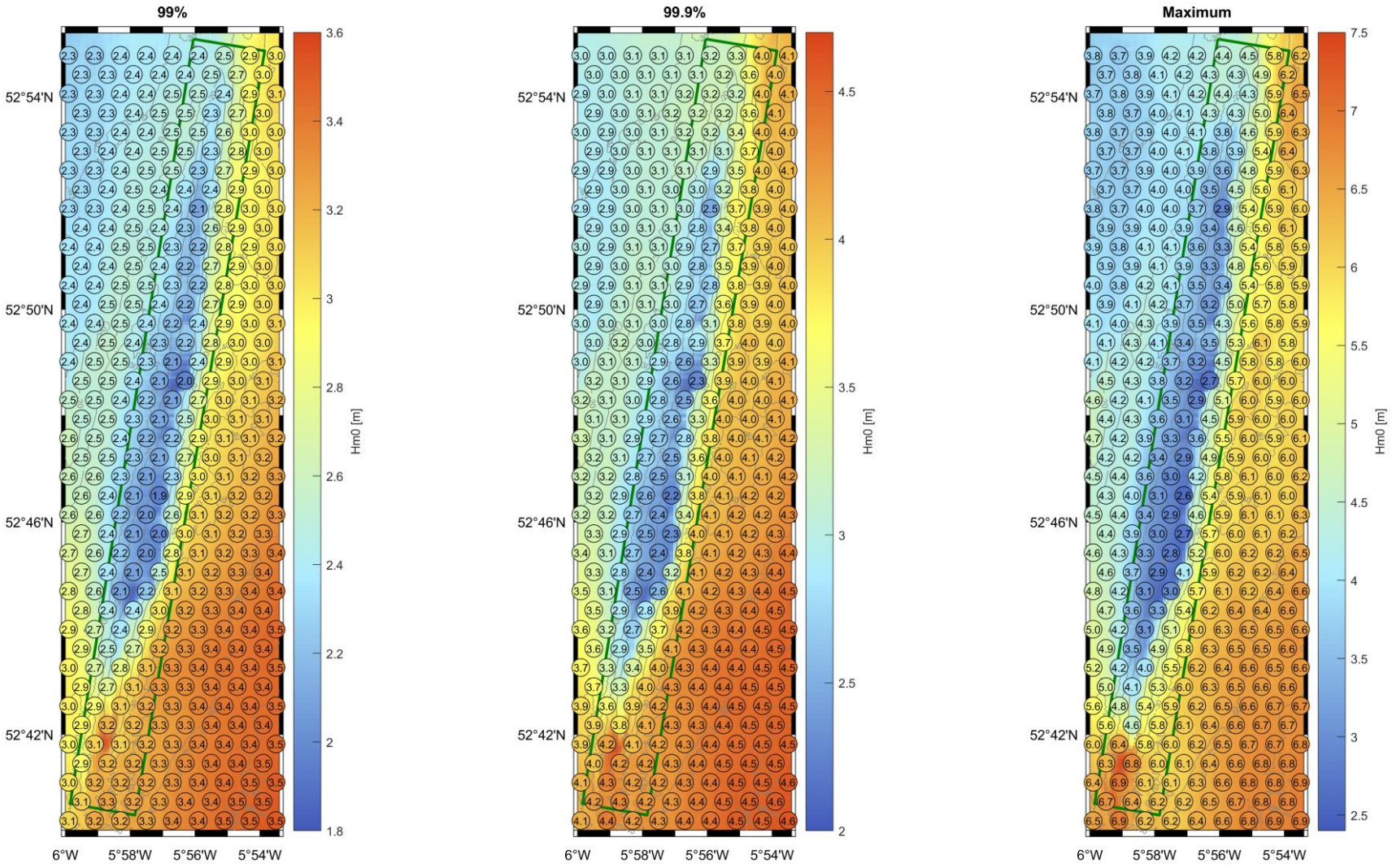



Figure 7.3: Percentiles and maxima of Hm0: 99th percentile (left), 99.9th percentile (centre) and maximum (right).

### 7.2.2 Extreme Criteria

Maps showing extreme values associated with 1-, 50- and 100-year return periods are shown in Figure 7.5 through Figure 7.10, for the following parameters:

- **Significant wave height** (Figure 7.5)
- **Maximum individual wave height** (Figure 7.6)
- **Maximum individual crest height above still water level** (Figure 7.7)
- **Significant wave height for sea states with water level below MSL** (Figure 7.8)
- **Maximum individual wave height for sea states with water level below MSL** (Figure 7.9)
- **Maximum individual crest height above still water level for sea states with water level below MSL** (Figure 7.10)

Details of the methodology used to create these maps can be found in Appendix G. As outlined in more detail therein, note that the maps are intended to provide a general overview of behaviour in the region of interest, rather than detailed design criteria. In particular, the need to generate extreme values at over 18,000 grid points means that results for individual locations are not subject to the same level of scrutiny as would generally be necessary in determining location-specific design criteria.

Prior to the extreme value maps themselves, it is perhaps also worth highlighting one of the key features of the largest wave heights determined by the wave model. Figure 7.4 shows the difference between the highest and the second highest Hm0 storm peaks across the region of interest. To the very south, and to a lesser extent the far east, these differences are substantial. For most of the rest of the lease area, they are minimal. As a result, to the very south, and to a lesser extent the far east, extreme values are far more heavily influenced by a single event than other regions. More details, including example extreme value fits, can be found in Section G.3.6 of Appendix G.

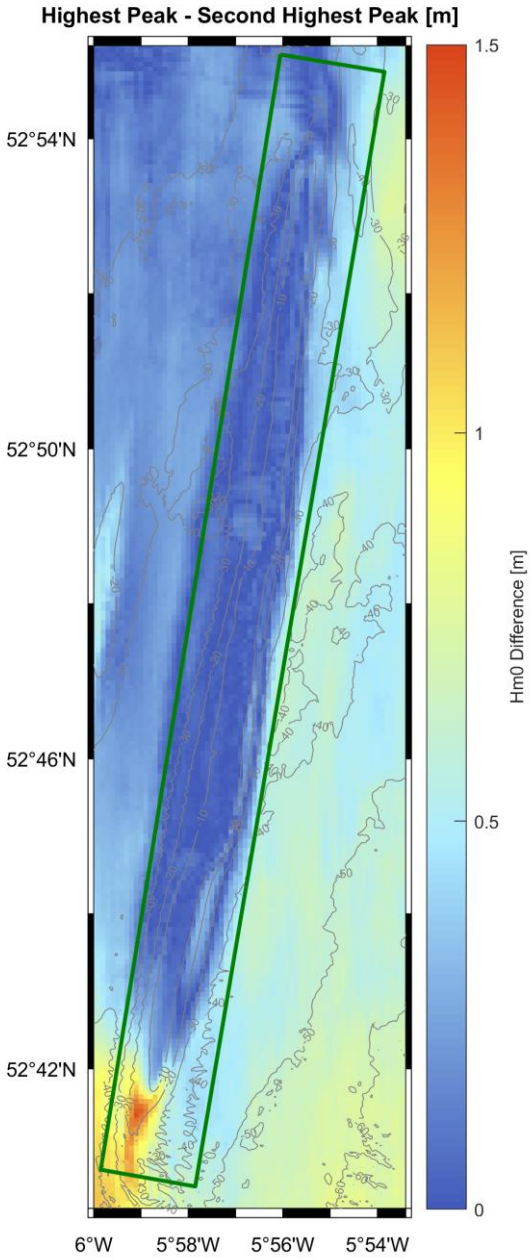



Figure 7.4: Difference between highest and second highest Hm0 peak across the region.

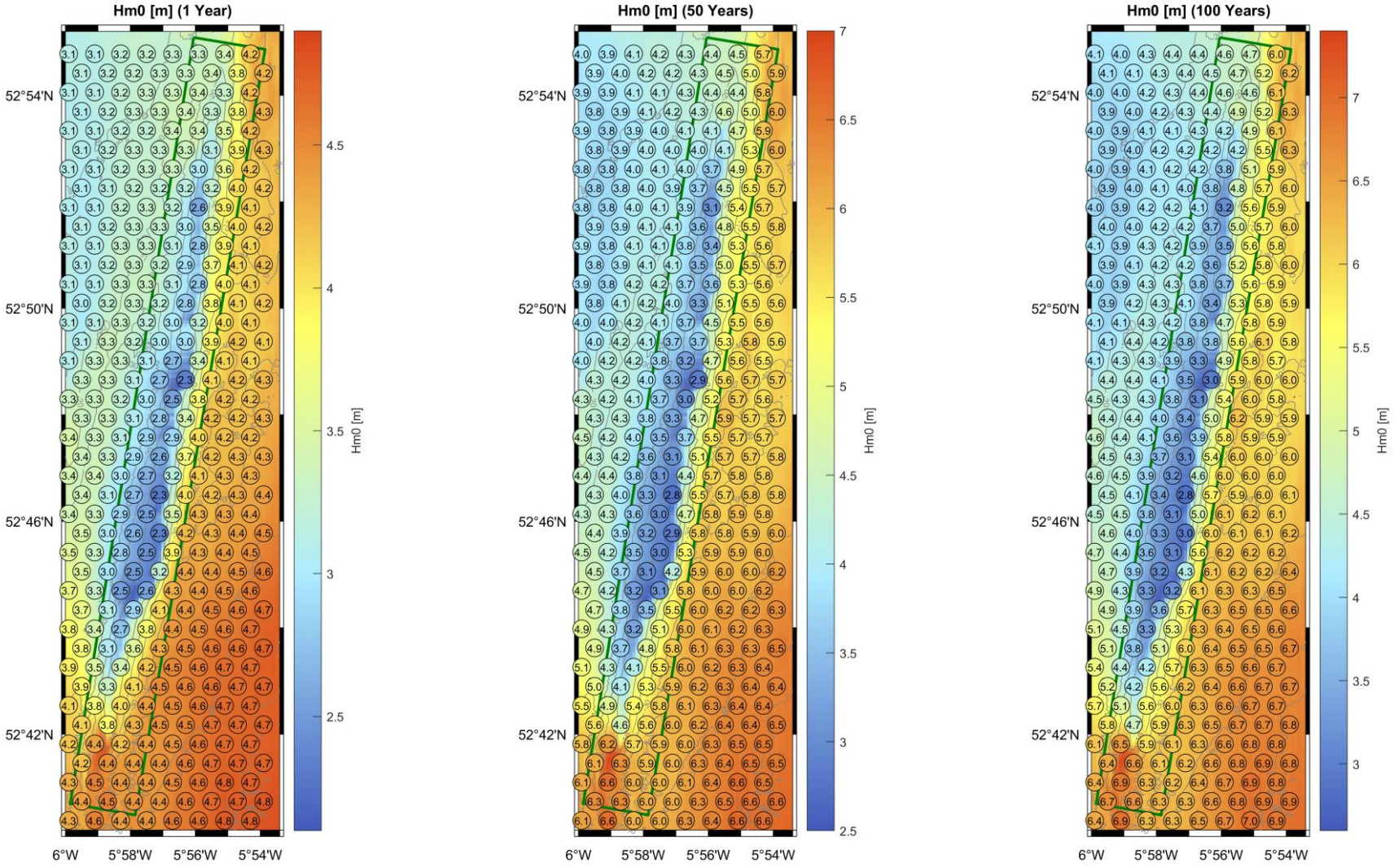



Figure 7.5: Extreme values of Hm0: 1-year (left), 50-year (centre) and 100-year (right).

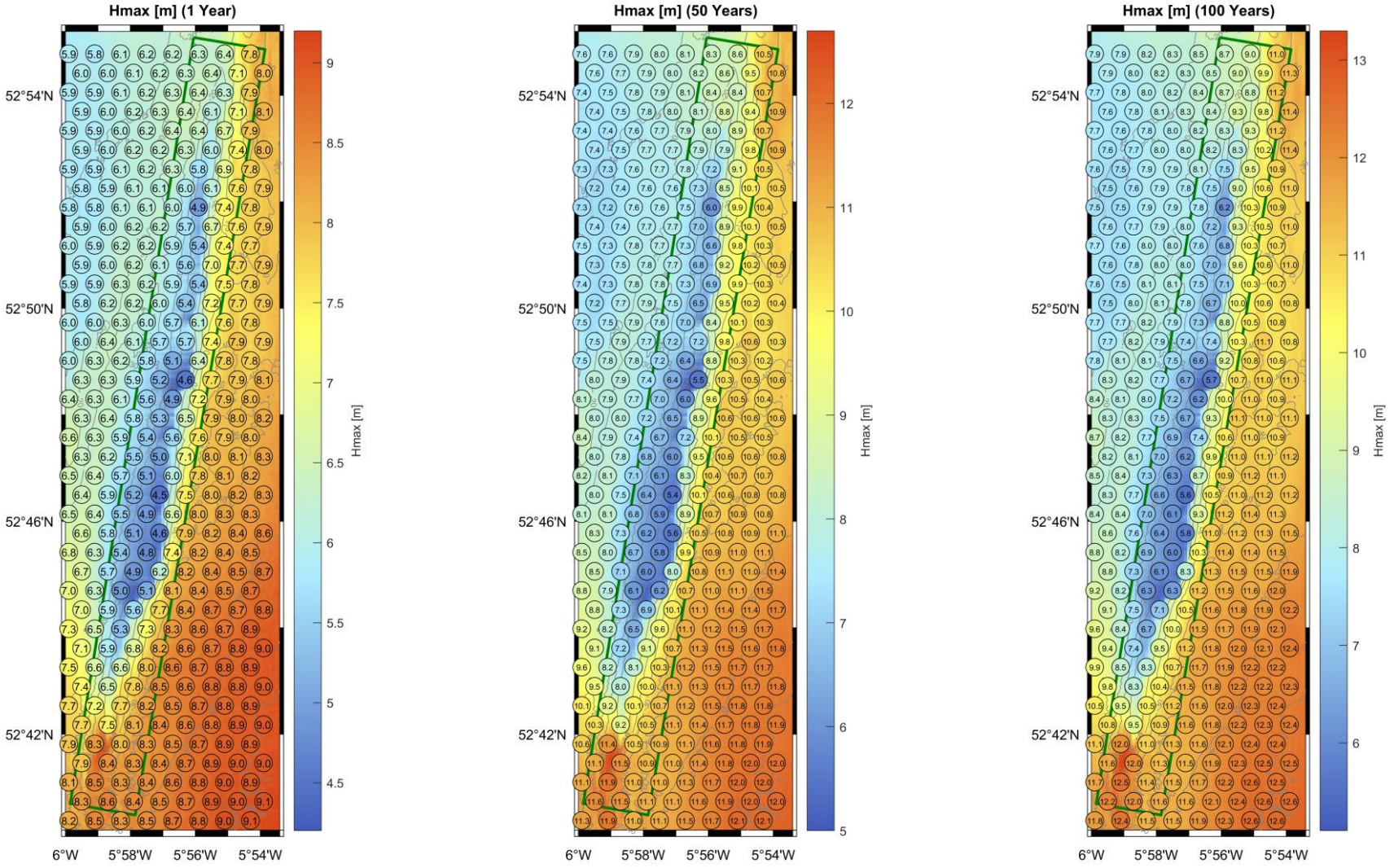



Figure 7.6: Extreme values of Hmax: 1-year (left), 50-year (centre) and 100-year (right).

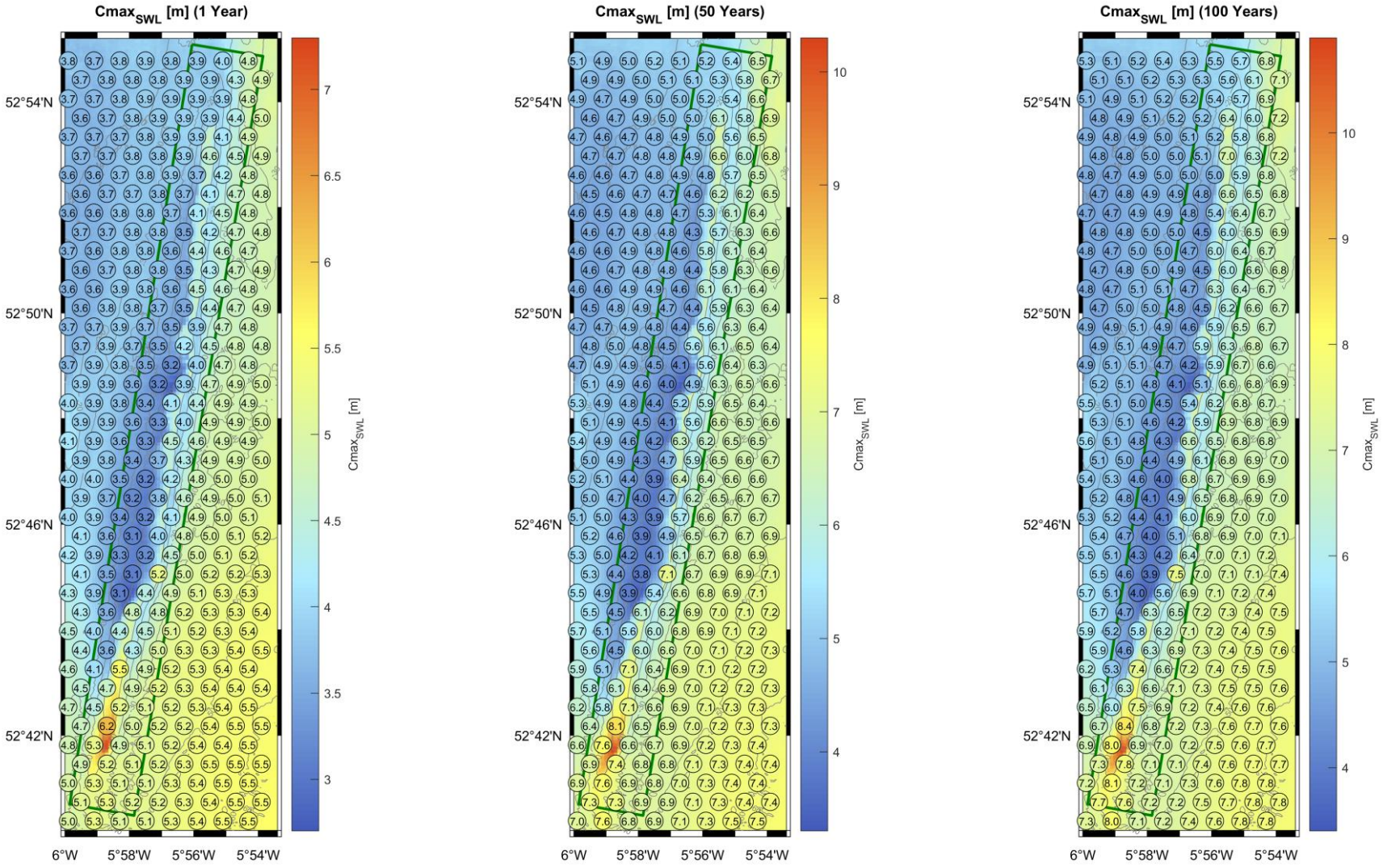



Figure 7.7: Extreme values of Cmax above still water level: 1-year (left), 50-year (centre) and 100-year (right).

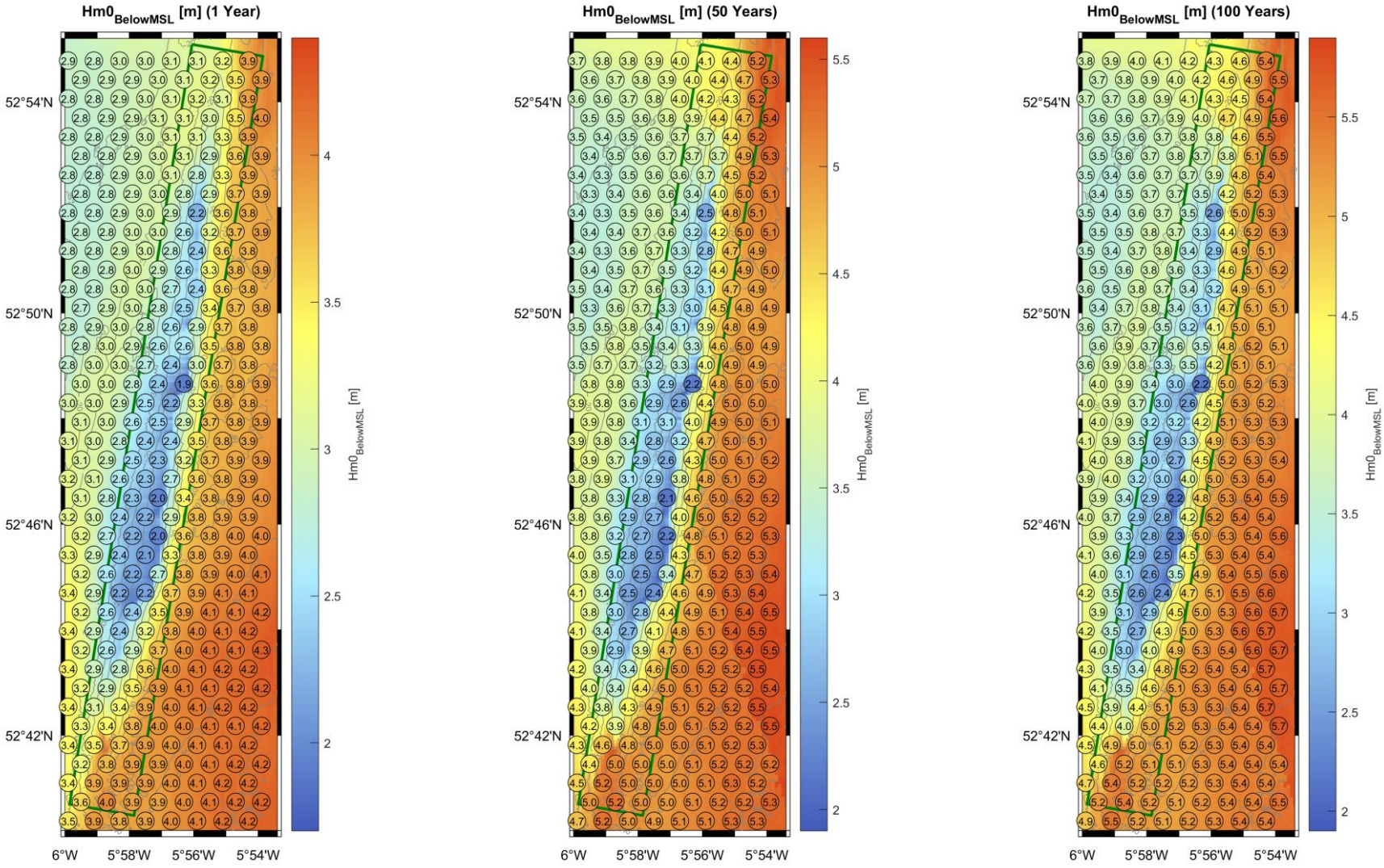



Figure 7.8: Extreme values of Hm0, water levels below MSL only: 1-year (left), 50-year (centre) and 100-year (right).

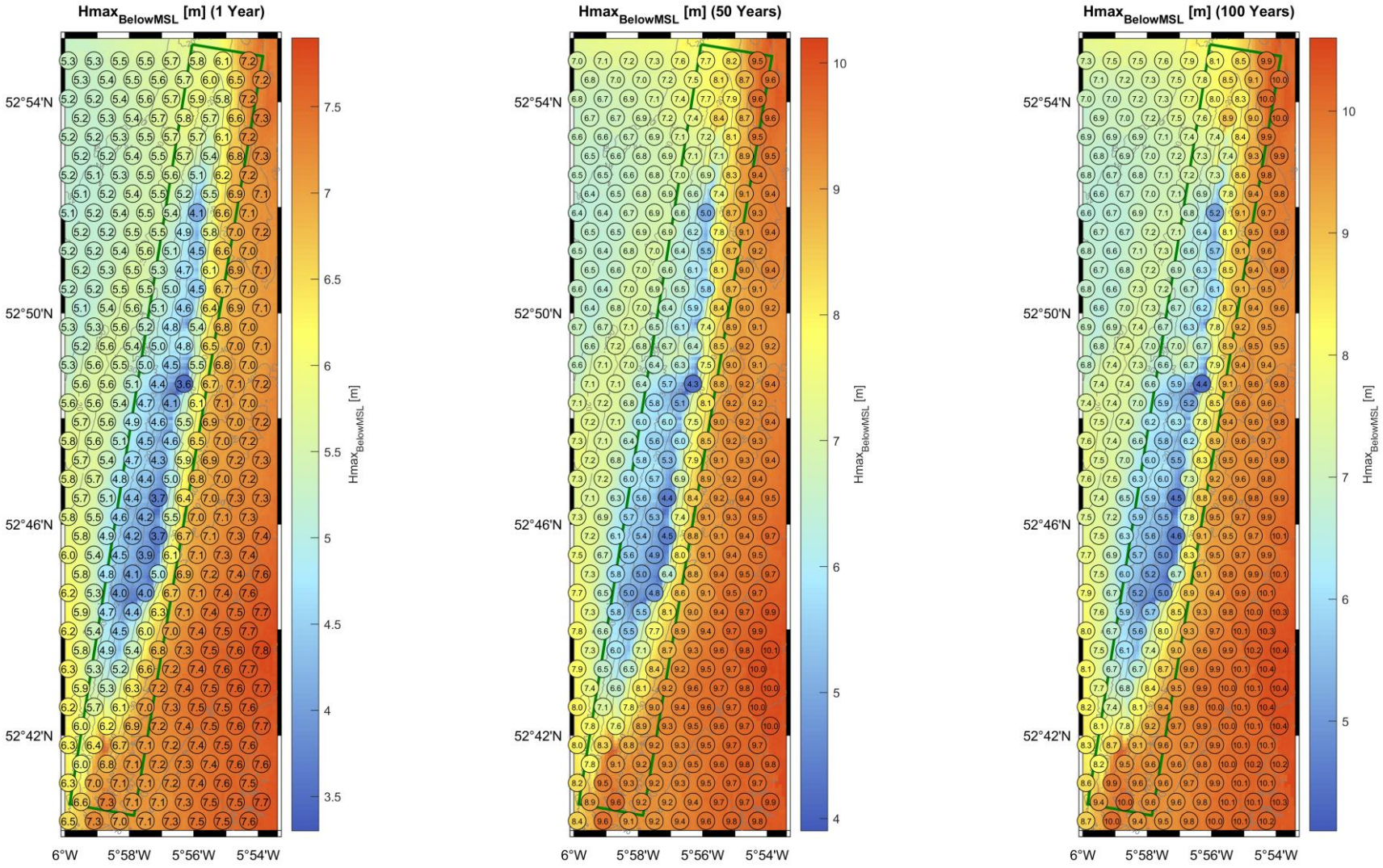



Figure 7.9: Extreme values of Hmax, water levels below MSL only: 1-year (left), 50-year (centre) and 100-year (right).

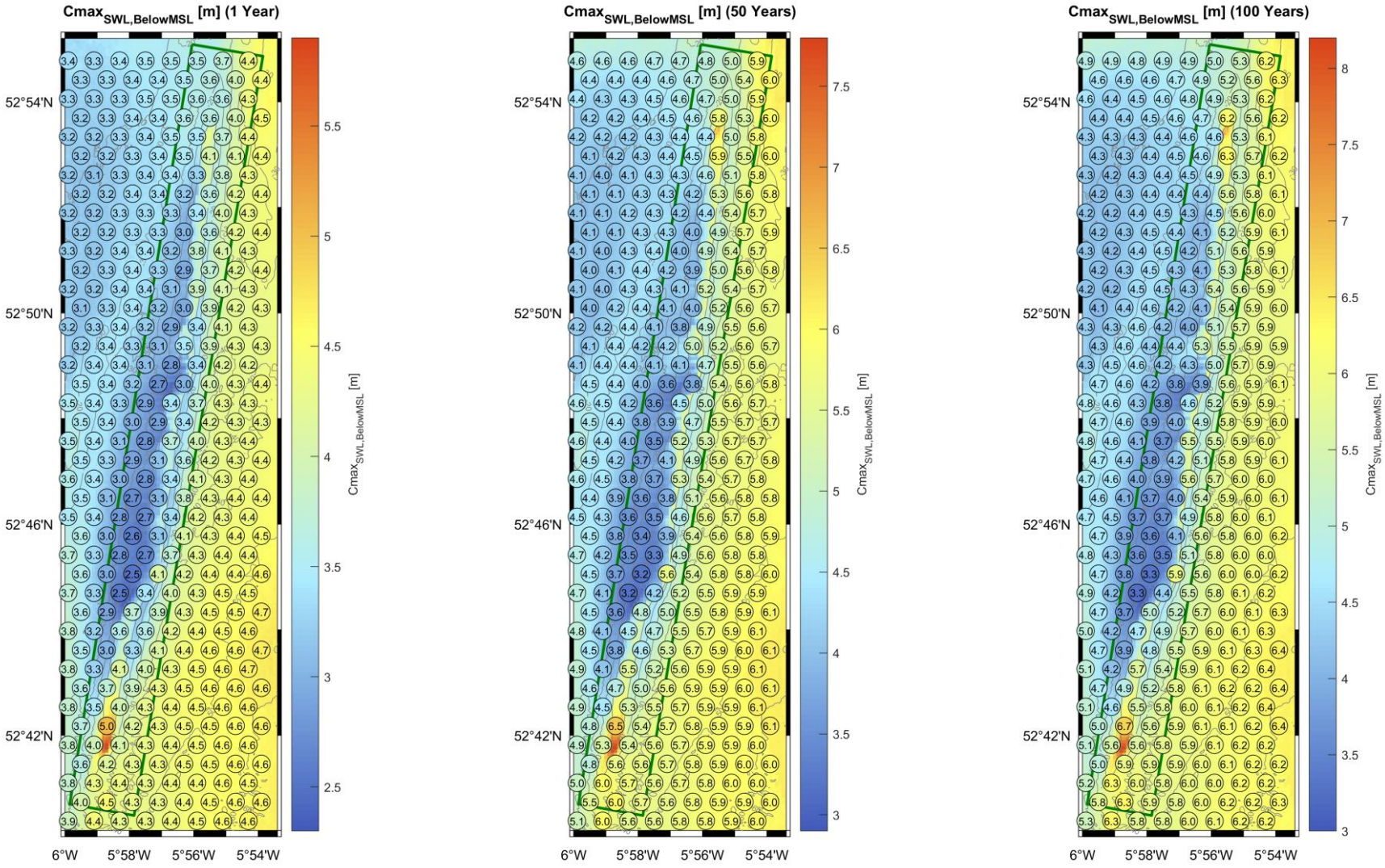



Figure 7.10: Extreme values of Cmax above still water level, water levels below MSL only: 1-year (left), 50-year (centre) and 100-year (right).

## 7.3 Currents and Water Levels

In Figure 7.11 through Figure 7.13 the following statistics are shown for water levels and current speeds:

- **Maximum and minimum water levels** (combined tide and surge).
- **50$^{th}$, 90$^{th}$, 95$^{th}$, 99$^{th}$ and 99.9$^{th}$ percentiles** of depth-averaged current speed.
- **Maximum** of depth-averaged current speed.

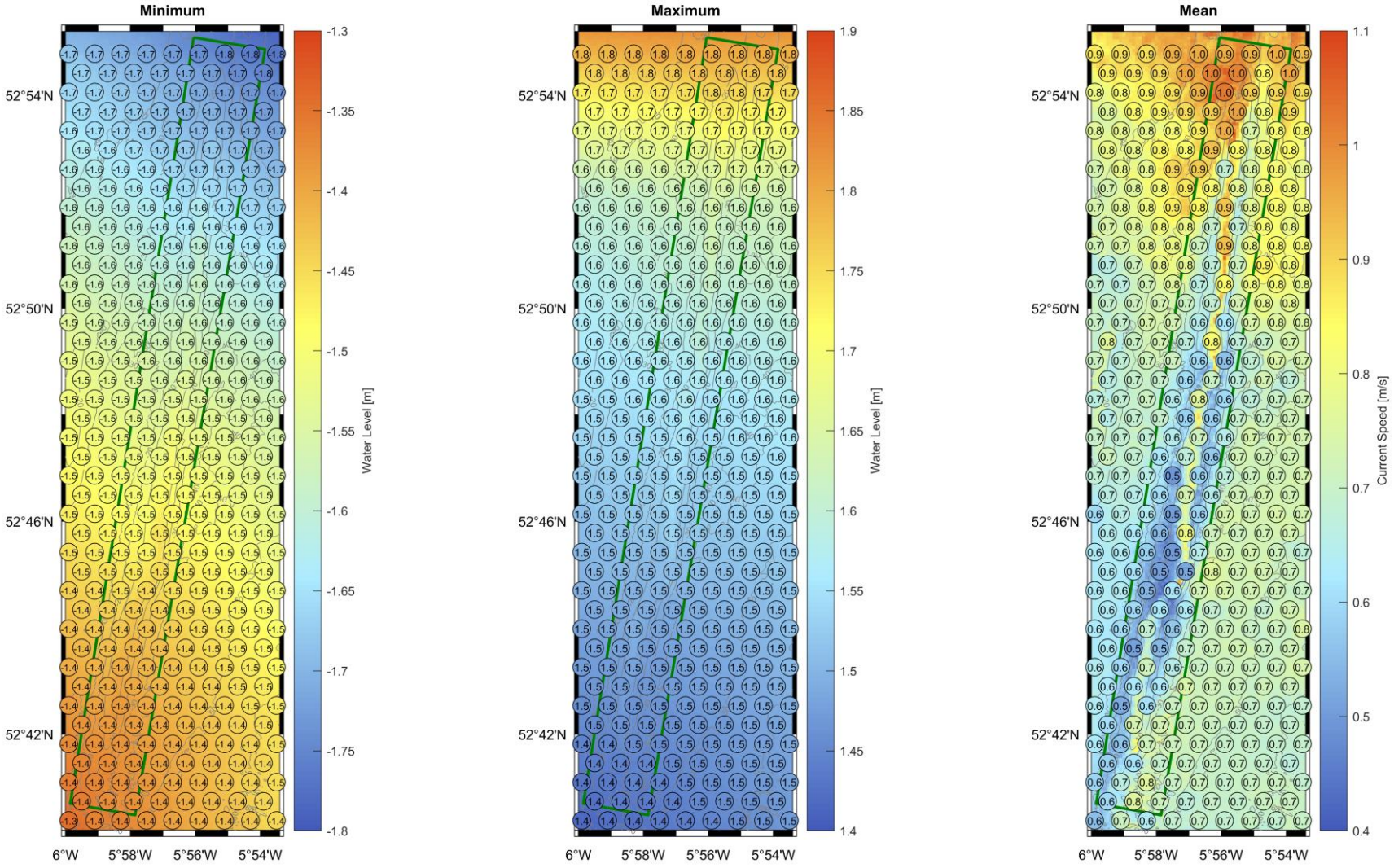



Figure 7.11: Minimum water level (tide + surge) (left), maximum water level (tide + surge) (centre) and mean depth-averaged current speed (right).

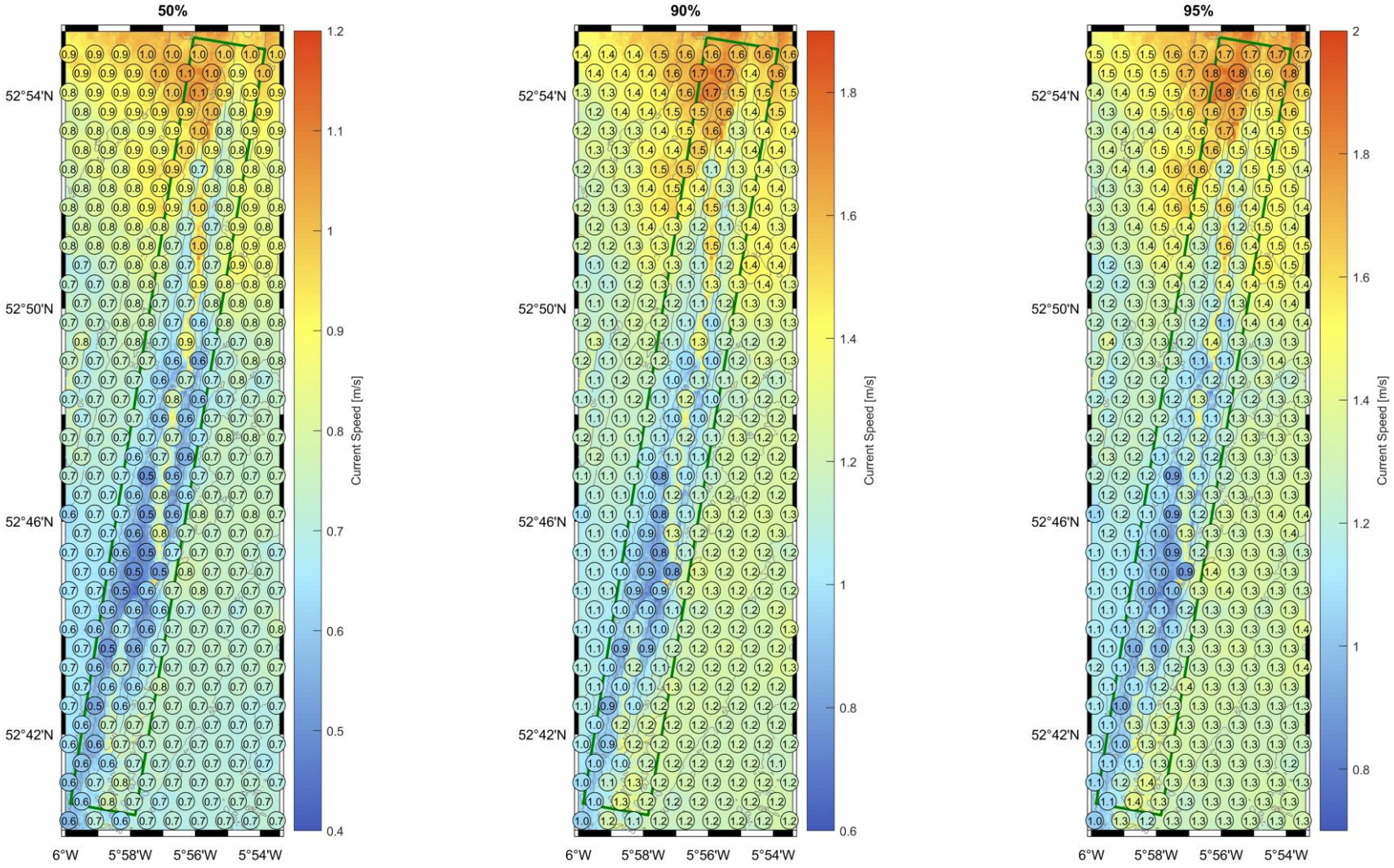



Figure 7.12: Percentiles of depth-averaged current speed: 50th percentile (left), 90th percentile (centre) and 95th percentile (right).

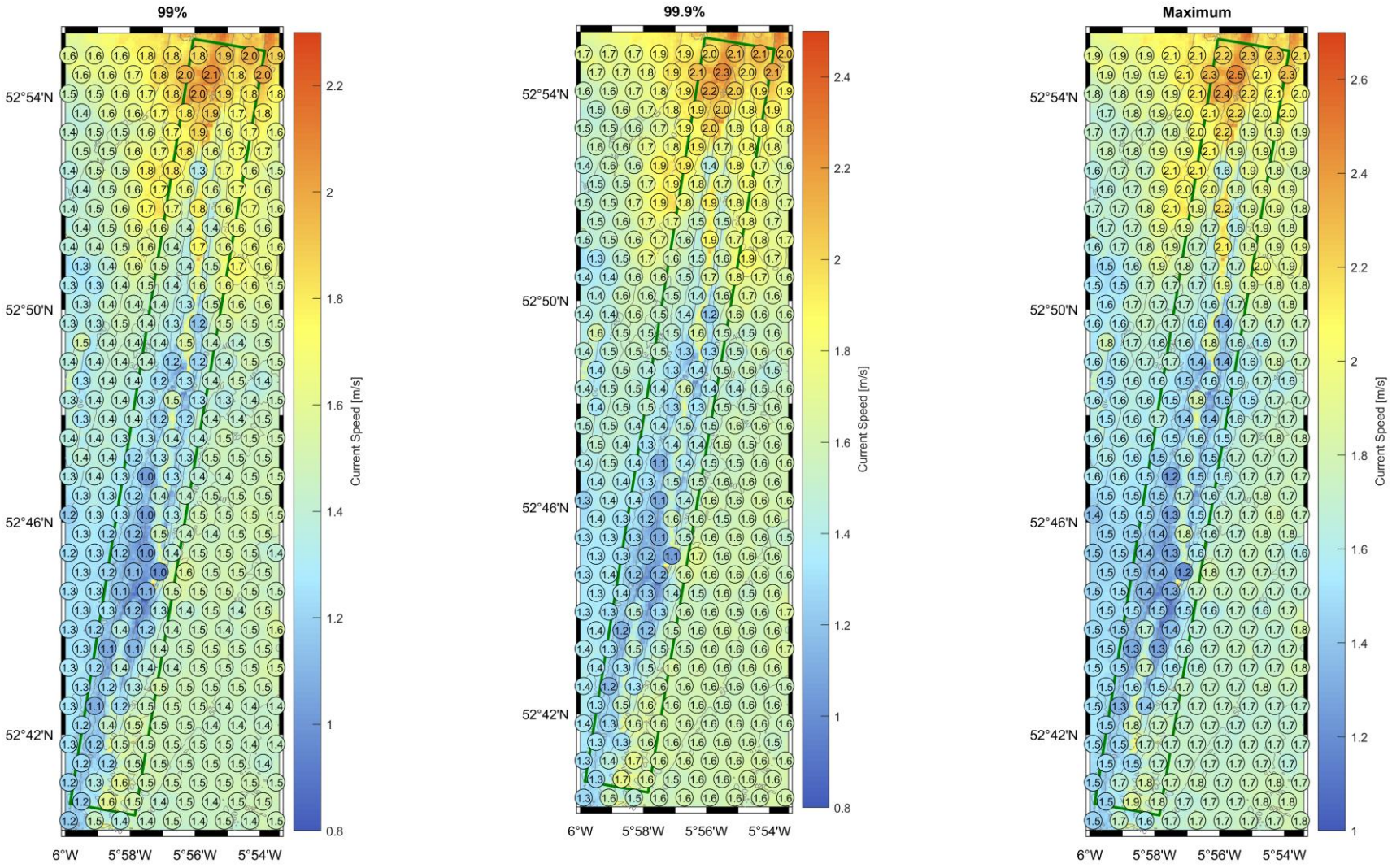



Figure 7.13: Percentiles and maxima of depth-averaged current speed: 99th percentile (left), 99.9th percentile (centre) and maximum (right).

# 8 Climate Change

Here we examine the possible changes to the metocean climate at the site because of climate change. Specifically, we look at the following parameters:

- Winds
- Waves
- Mean Sea Level, and
- Surges and Extreme Total Water Levels.

SSE uses the projections from UKCP18 [4] for its considerations of climate change for the project (ref. email Andrew Berkeley 1 October 2020). Therefore, herein we use UKCP18 as a primary data source for our analysis of the impacts of climate change at the site. Noting that UKCP18 is a UK-focussed publication (although some aspects include the entire British Isles), we supplement the projections with information from the Intergovernmental Panel on Climate Change (IPCC) Fifth Assessment Report [5], where appropriate.

UKCP18 has been based upon a set of global climate model projections, comprising simulations from both the latest Met Office Hadley Centre climate model and global climate models from around the world, including from the IPCC Fifth Assessment Report, and a set of regional climate model projections on a finer scale (12 km) for the UK and Europe. Further details about the science informing UKCP18 can be found within the UKCP18 Overview Report.

The UKCP18 and IPCC Fifth Assessment Report projections use Representative Concentration Pathways (RCPs) to describe four different 21$^{st}$ century scenarios of Greenhouse gas emissions and atmospheric concentrations, air pollutant emissions and land use. The RCPs include a stringent mitigation scenario (RCP2.6), two intermediate scenarios (RCP4.5 and RCP6.0) and one scenario with very high greenhouse gas emissions (RCP8.5). Scenarios without additional efforts to constrain emissions ('baseline scenarios') lead to pathways ranging between RCP6.0 and RCP8.5. RCP2.6 is representative of a scenario that aims to keep global warming less than 2°C above pre-industrial temperatures.

Climate change projections, and therefore, the response of metocean parameters to changes in the climate, are associated with considerable uncertainty, and so the details provided herein should be treated with appropriate caution if they are to be applied to engineering design. Users of this information are advised to consult the relevant literature to supplement their understanding of any uncertainties if important decisions are to be made based upon this assessment.

## 8.1 Winds

Direct investigation of past changes in wind climatology has been hampered by the sparseness of long-term, high-quality wind measurements from terrestrial anemometers, arising from the influence of changes in instrumentation, station location, and surrounding land use.

Early marine observations of wind speed were based on ship speed through the water, sails carried, or on visual estimates of sea state converted to wind speed using the Beaufort scale. Anemometer measurements were introduced starting in the 1950s, with mean anemometer height increasing over time. Surface winds have been measured from space using various microwave-range instruments since the late 1970s.

The lack of a single source of longer-term reliable measurements of winds, along with the high level of variability at different temporal scales, has meant that separating long-term climate trends in wind speed from

background variability is difficult. This inhibits robust calibration and validation of climate models against suitable observations. Therefore, climate projections for wind tend to focus on qualitative predictions of changes in the track of regional weather systems, and on predictions of the intensity and frequency of extreme weather events.

### 8.1.1 Mean wind speeds

Figure 8.1 shows averaged changes from a 19-member ensemble of Global Climate Models from the IPCC's Fourth Assessment Report (CMIP3) in the mean of the daily averaged 10 m wind speeds (top) and 99$^{th}$ percentile of the daily averaged 10 m wind speeds (bottom) for the period 2081-2100 relative to 1981-2000 (% change) for December to February (left) and June to August (right) plotted only where more than 66% of the models agree on the sign of the change. Black stippling indicates areas where more than 90% of the models agree on the sign of the change. Red stippling indicates areas where more than 66% of models agree on a small change between ±2%.

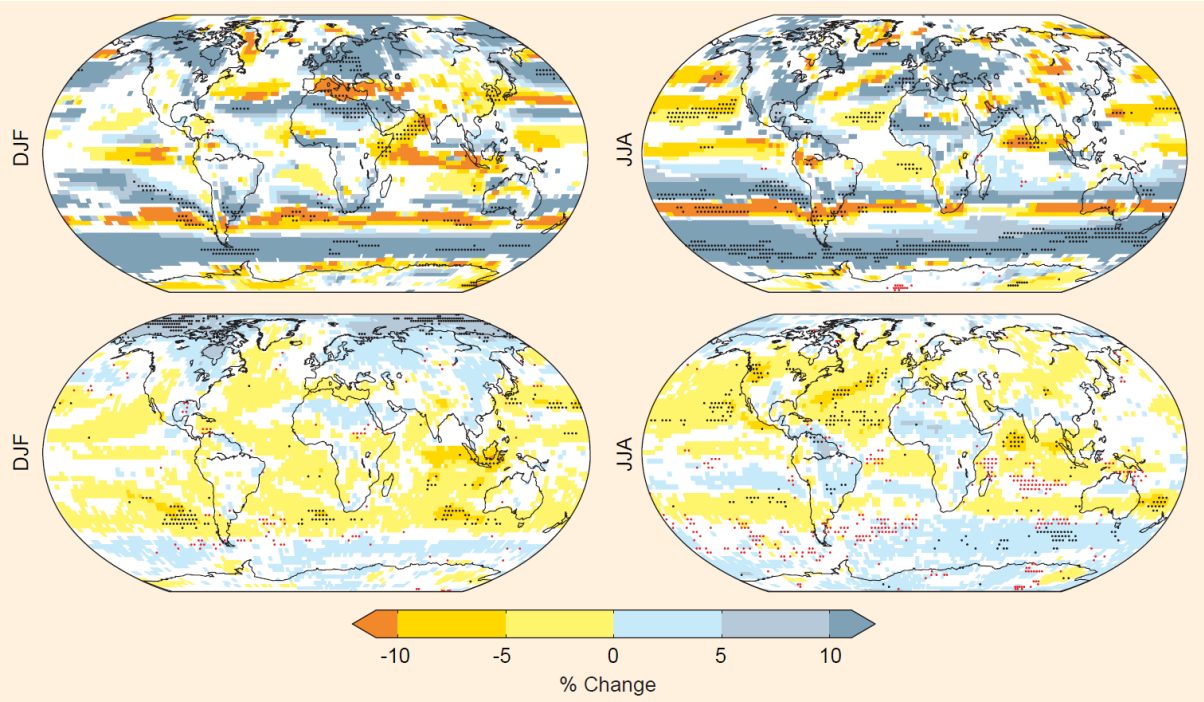



Figure 8.1: Averaged changes in the mean of the daily averaged 10 m wind speeds. Adapted from [6].

The images suggest an increase in mean and 99$^{th}$ percentile wind speeds over Europe, except for the 99$^{th}$ percentile of the summer wind speeds, which show a slight decrease.

Despite the detail provided in Figure 8.1, the relatively few studies of projected winds, combined with shortcomings in the simulation of extreme winds and the different models, regions, and methods used to develop projections of this quantity, means that the IPCC ascribes low confidence in the projections of changes in winds discussed above.

UKCP18 provides a summary of future mean wind speeds over the UK based on projections from a set of 28 models of future climates at 60 km grid resolution, showing how the 21$^{st}$ Century climate may evolve under the highest emission scenario, RCP8.5. It incorporates 15 Perturbed Physics Ensemble members (PPE-15) of the Met Office Hadley Centre model, HadGEM3-GC3.05, and 13 other climate models selected from the

climate models that informed the Intergovernmental Panel on Climate Change's 5th Assessment Report (CMIP5).

The projections over the UK show:

- an increase in near surface wind speeds over the UK for the second half of the 21st century for the winter season when more significant impacts of wind are experienced (see Figure 8.2). This is accompanied by an increase in frequency of winter storms over the UK. However, the increase in wind speeds is modest compared to interannual variability for the PPE-15.
- no trend in the wind speed over the UK for the mean of the CMIP5.

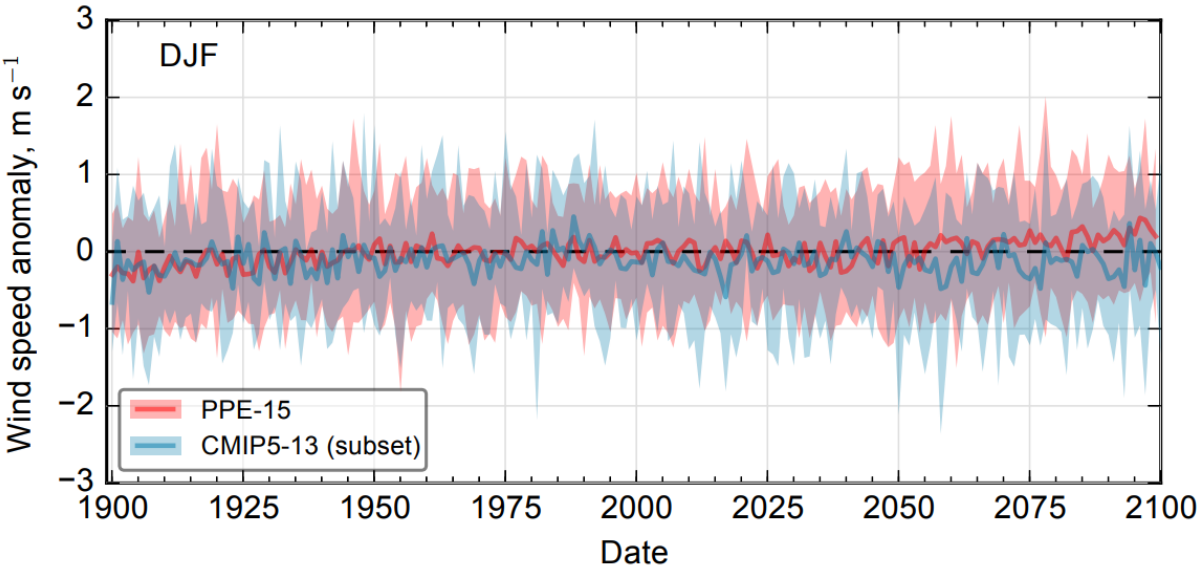



Figure 8.2: Global projections for changes in winter mean near surface wind speed over the UK for 1900-2100 with respect to 1981-2000.

In Figure 8.2, the red line is the mean of the PPE-15 and blue line is the mean of the CMIP5. The red and blue shading represents the range of values from PPE-15 and CMIP5, respectively. Whilst these are UK-specific projections, given that the island of Ireland is affected by largely similar weather systems, it can reasonably be assumed that these projections would be valid (within the level of inter-annual variability) for the site.

### 8.1.2 Extreme winds

Table 8.1 shows a summary of studies exploring near-term projections of tropical cyclone (TC) activity over the North Atlantic. Remnants of these systems can propagate to the study site, producing extreme wind events.

Table 8.1: Projected change in tropical cyclone activity over the North Atlantic.

| Projected Change | Notes | Reference |
|---|---|---|
| Linear trend in TC frequency 2001–2050: Ensemble-mean non-significant decrease in TC frequency (–5%). Ensemble range of –50% to +30%. | Statistical downscaling of CMIP3 models under A1B scenario. | [7] |
| TC frequency averaged 2016–2035 minus 1986–2005: Ensemble-mean non-significant increase for RCP2.6 (4%), non-significant decrease for RCP4.5 (–2%) and RCP8.5 (–1%). Ensemble range of –30% to 27% across all scenarios/models. | Statistical downscaling of CMIP5 RCP2.6, RCP4.5 and RCP8.5 | [7] |
| Power Dissipation Index averaged 2016–2035 minus 1986–2005: Ensemble mean significant increase for RCP2.6 (23%) and RCP8.5 (17%), non-significant increase for RCP4.5 (10%). Ensemble range of –43% to 78% across all scenarios/models. | Statistical downscaling of CMIP5 RCP2.6, RCP4.5 and RCP4.5 | [8] |
| Difference 2016–2035 minus 1986–2005 averages: Significant decrease (–20%) to overall TC and hurricane frequency. Significant increase (+45%) in number of Category 4–5 TCs. Significant increase in precipitation of hurricanes (11%) and tropical storms (18%). | Double dynamical refinement of CMIP5 RCP4.5 multi-model ensemble projections. | [9] |

In general, the studies in Table 8.1 suggest a decrease in the frequency of tropical cyclones over the North Atlantic, but an increase in their magnitude.

Figure 8.3 shows the expected percent change in the average of four tropical cyclone metrics based on expert judgement after subjective normalisation of the model projections. The modelling is based on a scenario with a more integrated world, with a balanced emphasis on all energy sources. The four metrics are: percent change in (I) the total annual frequency of tropical storms, (II) the annual frequency of Category 4 and 5 storms, (III) the mean Lifetime Maximum Intensity (LMI; the maximum intensity achieved during a storm's lifetime) and (IV) the precipitation rate within 200 km of the storm centre at the time of LMI. For each metric plotted, the solid blue line is the best guess of the expected percent change, and the coloured bar provides the 67% (likely) confidence interval for this value (note that this interval ranges across –100% to +200% for the annual frequency of Category 4 and 5 storms in the North Atlantic). Where a metric is not plotted, there are insufficient data (denoted 'insf. d.') available to complete an assessment. A randomly drawn (and coloured) selection of historical storm tracks is underlain to identify regions of tropical cyclone activity.

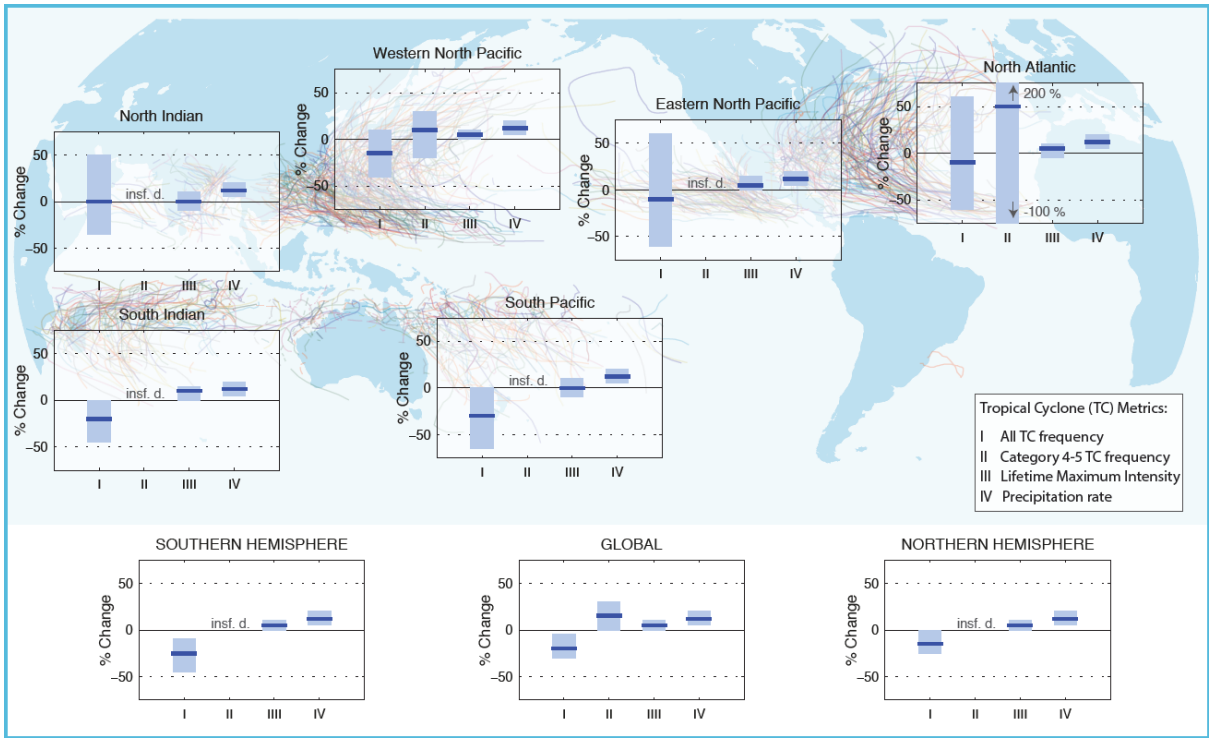



Figure 8.3: Expected percent change in the average over period 2081–2100 relative to 2000–2019.

For the North Atlantic, Figure 8.3 corroborates the findings in Table 8.1: A slight decrease in the frequency of tropical cyclones, but an increase in the frequency of more intense storms (albeit with a large variance in the model outcomes), and an increase in the maximum magnitude (LMI) of storms. In some models, storm activity over Western Europe increases by 50% [10] or by an amount comparable to the natural variability [11], [12].

Regional increases in winter wind storm risk over Europe due to changes in storm tracks are also supported by a number of regional studies (e.g., [11], [13], [14], [15], [16], [17], [18], [19], [20]). These studies also provide a general picture of an increasing trend in extreme winds over northern Europe despite a range of different downscaling models used, the different global climate models in which the downscaling is undertaken, and different metrics used to quantify extreme winds.

However, global climate models at their current resolution are unable to resolve small-scale phenomena such as tropical cyclones, tornadoes, and mesoscale convective complexes that are associated with particularly severe winds. There is thus low confidence in projections of changes in such small-scale systems because of limited studies, uncertainties in the historical tropical cyclone records, incomplete understanding of the physical mechanisms linking tropical cyclone metrics to climate change, inability of climate models to resolve these phenomena, and possible competing factors affecting future changes.

## 8.2 Waves

UKCP18 provides projections of changes in wave climate based on an ensemble of seven CMIP5-based global wave models, and a high-resolution regional model based on a single CMIP5 member under RCP4.5 and RCP8.5. The modelling also includes Irish waters. These models are used to explore potential changes in mean and mean annual maximum significant wave height (SWH). Figure 8.4 shows the projected changes under RCP8.5 for the end of this century. Grey masking indicates where natural variability (according to the Kruskal-Wallis test), or signal-to-noise ratio, is below 75%.

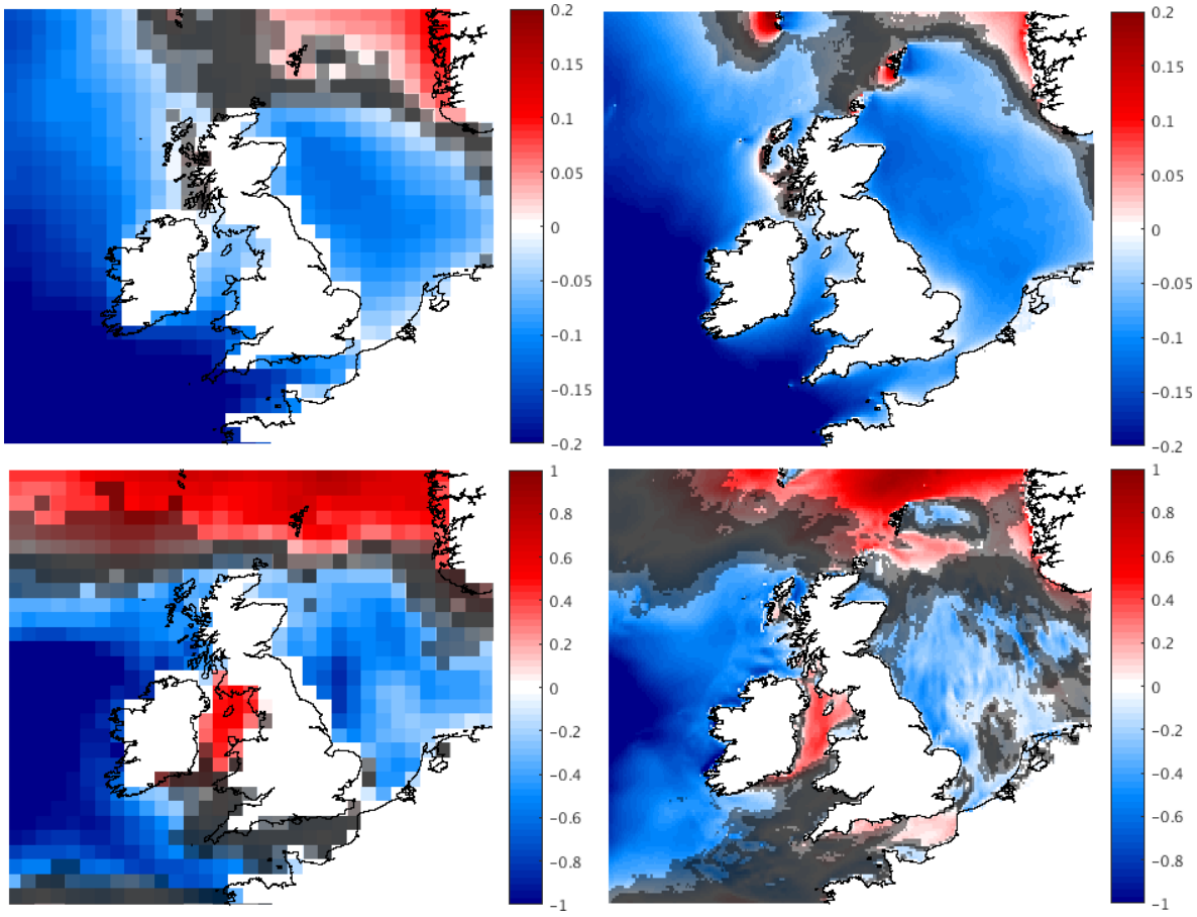



Figure 8.4: Absolute change (m) in mean significant wave height (top) and mean annual maximum significant wave height (below). Global model (left) and regional (right).

Importantly, Figure 8.4 shows that the global and regional wave model results are consistent in their overall direction and magnitude of change, adding to confidence in the projections. In general, the models predict a reduction in mean significant wave height of around 0.07 m, and an increase in the mean annual maximum significant wave height of around 0.25 m, in the vicinity of the project site under RCP8.5, by the end of this century. This is consistent with the predictions of increases in magnitude of extreme wind events in the vicinity of the study site, as discussed in Section 8.1.

Stronger reductions in the mean significant wave height were observed for mid-21st century than end-21st century, which suggests that both low-frequency internal variability and climate change may be playing a role in shaping the simulated wave response.

Given the inherent uncertainty in projections of storm track changes and the limited sample size available, the wave projections presented here should be viewed as indicative of the potential changes with low confidence.

## 8.3 Mean Sea Level

Global mean sea level (GMSL) rise is caused by thermal expansion of seawater, and by the input of water to the ocean from the loss of land-based ice and water. Regional sea level and spatial changes can occur due to changes in land-based ice and water storage and the resulting impact on Earth's gravitational field, and other

effects. Local changes in seawater density and ocean circulation also give rise to spatial differences. The continuing geological response to the last deglaciation also brings about a spatial pattern of regional sea level change across the UK and North Sea that is affected by vertical land motion.

The Intergovernmental Panel on Climate Change (IPCC) Fifth Annual Report (AR5) in 2013 states that under all RCP scenarios, the rate of global mean sea level rise (Figure 8.5) will very likely exceed the observed rate of 2.0 [1.7–2.3] mm/year during 1971–2010, with the rate of rise for RCP8.5 during 2081–2100 of 8 to 16 mm/year (medium confidence).

Figure 8.5 shows global mean sea level rise from 2006 to 2100. All changes are relative to 1986–2005. Time series of projections and a measure of uncertainty (shading) are shown for scenarios RCP2.6 (blue) and RCP8.5 (red). The mean and associated uncertainties averaged over 2081–2100 are given for all RCP scenarios as coloured vertical bars at the right-hand side of the image.

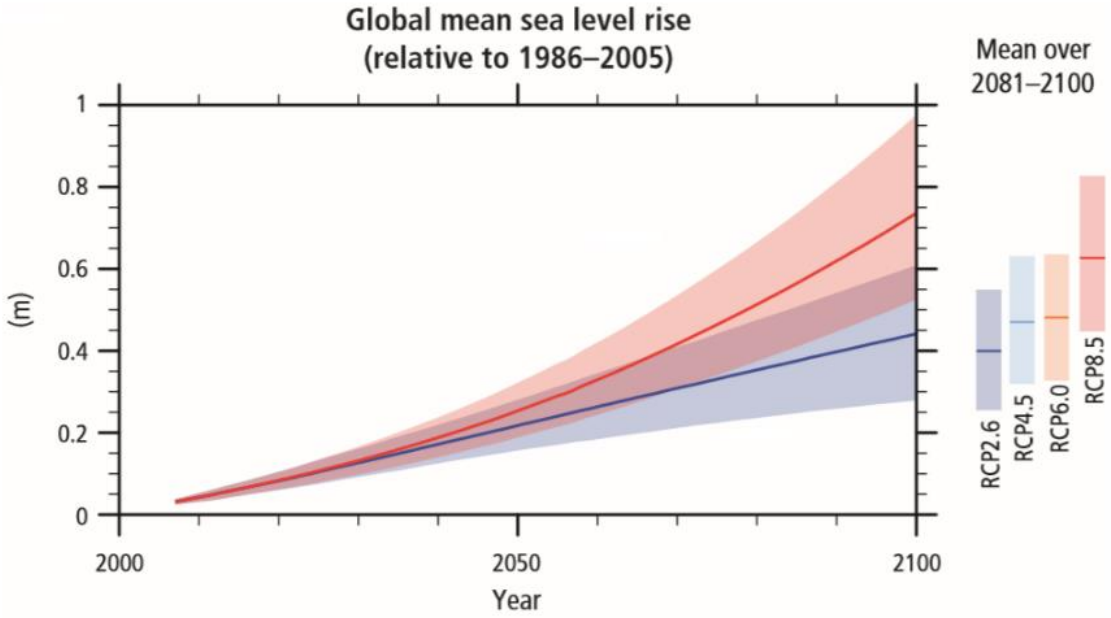



Figure 8.5: Global mean sea level rise from 2006 to 2100 as determined by multi-model simulations.

In the UK and Ireland, the UKCP18 report states that 21st century projections of time-mean sea level change vary substantially by climate change scenario and geographic location.

The UKCP18 projections include the continuing geological response to the last deglaciation - referred to as glacial isostatic adjustment (GIA) - which gives rise to a spatial pattern of sea level change across the UK and Ireland with peak magnitudes of approximately +/- 1 mm per year. This pattern is characterised by sea level fall centred on Western Scotland. The effect is shown in Figure 8.6. The project site is in an area of minimal change due to GIA (*circa* 0.3 mm/year sea level fall).

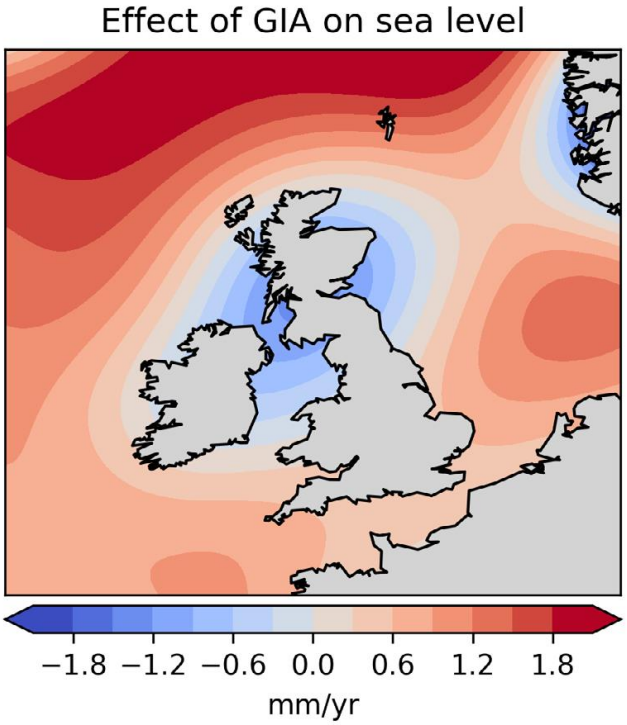



Figure 8.6: The effect of GIA on sea level.

The UKCP18 21st century time-mean sea level projections build upon the materials and methods described in the IPCC AR5. All RCP scenarios show substantial sea level rise over the 21st century. There are substantial variations in coastal sea level projections around the UK and Ireland associated with both the RCP climate change scenario and geographic location. Typically, the south of the British Isles will experience a greater projected sea level rise, with values similar to the global mean projections. In the north of the British Isles, sea level rise projections are substantially lower than the global mean, and minimum values are centred on South West Scotland. This pattern is shown in Figure 8.7. On these graphs, the solid line and shaded regions represent the central estimate and ranges for each RCP scenario as indicated in the legend. The dashed lines indicate the overall range across RCP scenarios. In the maps, the spatial pattern of change at 2100 and associated with the central estimate of each RCP scenario is shown. All projections are presented relative to a baseline period of 1981-2000.

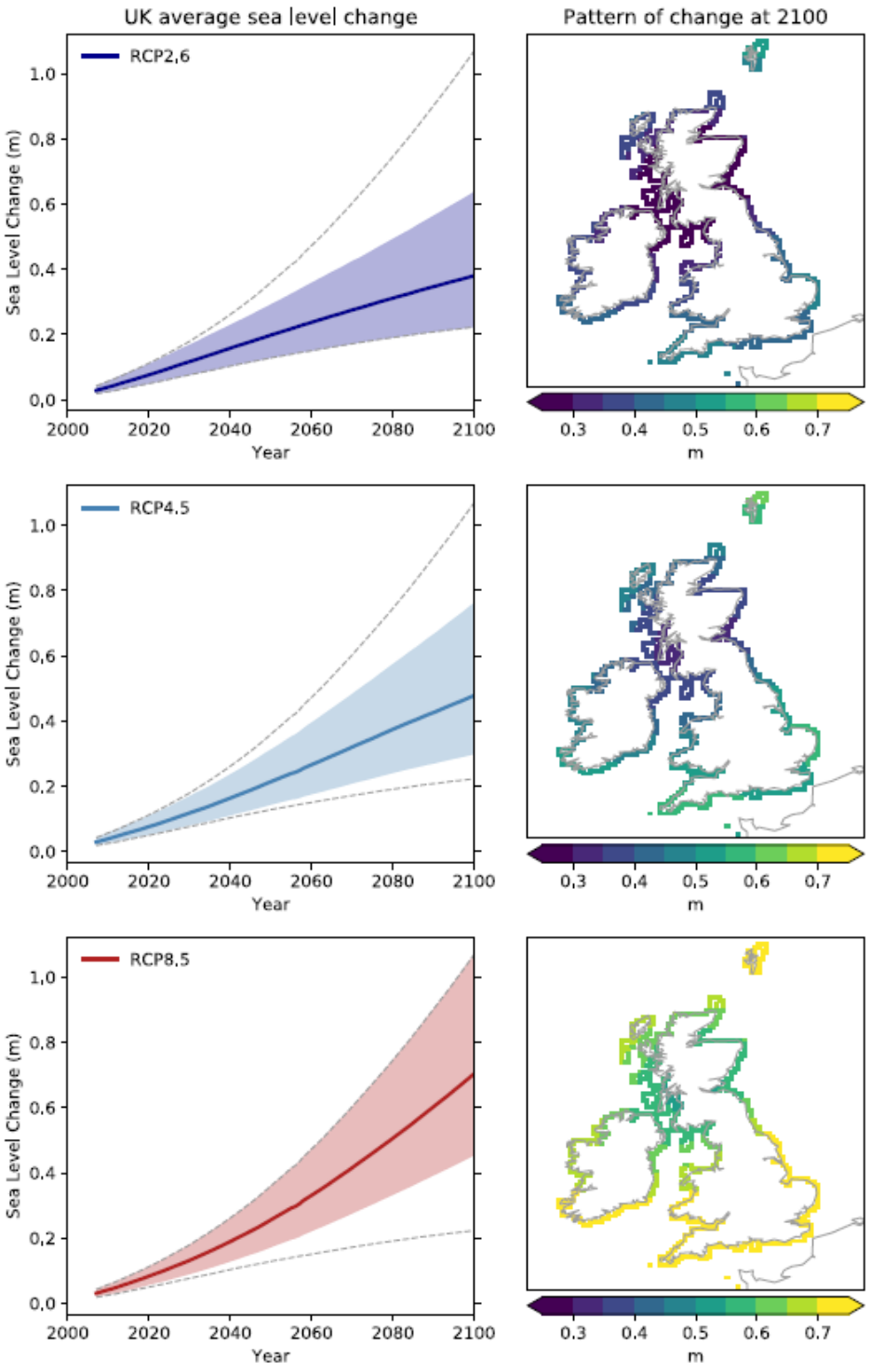



Figure 8.7: Time series of time-mean sea level change around the UK.

Table 8.2 shows the range of projections offshore of Capel Carmel, Wales, which is the closest UKCP sea level projection site to the project, for a baseline period of 1981 to 2000. We recommend using the P50 values from RCP 8.5.

Table 8.2: Projections of sea level change offshore of Capel Carmel, Wales, for various scenarios and probability levels.

| Year | RCP 2.6 | | | RCP 4.5 | | | RCP 8.5 | | |
|---|---|---|---|---|---|---|---|---|---|
| | P5 | P50 | P95 | P5 | P50 | P95 | P5 | P50 | P95 |
| **2020** | 0.04 | 0.07 | 0.10 | 0.05 | 0.07 | 0.10 | 0.05 | 0.08 | 0.11 |
| **2030** | 0.07 | 0.11 | 0.16 | 0.07 | 0.11 | 0.16 | 0.08 | 0.12 | 0.17 |
| **2040** | 0.09 | 0.15 | 0.22 | 0.10 | 0.15 | 0.23 | 0.12 | 0.18 | 0.25 |
| **2050** | 0.12 | 0.19 | 0.28 | 0.13 | 0.20 | 0.30 | 0.16 | 0.24 | 0.35 |
| **2060** | 0.14 | 0.22 | 0.35 | 0.16 | 0.25 | 0.38 | 0.21 | 0.32 | 0.46 |
| **2070** | 0.16 | 0.26 | 0.41 | 0.19 | 0.30 | 0.47 | 0.26 | 0.40 | 0.59 |
| **2080** | 0.17 | 0.29 | 0.48 | 0.22 | 0.36 | 0.56 | 0.32 | 0.49 | 0.73 |
| **2090** | 0.19 | 0.33 | 0.55 | 0.25 | 0.41 | 0.65 | 0.37 | 0.58 | 0.88 |

## 8.4 Surge and Extreme Total Water Levels

UKCP18 projections of change in coastal extreme total water levels are dominated by time-mean sea level increase. There is, however, a potential for an additional contribution due to changes in atmospheric storminess over the 21st century.

UKCP18 presents results from an ensemble of regionally-downscaled climate model simulations under RCP8.5 that samples a range of storminess change. Figure 8.8 shows the projected 21st century trend in skew surge extremes from the HadGEM2-ES-RCA4 model (left) and the MPI-ESM-LR-RCA4 model (right) simulations, shown using the same colour scale in both plots. The metric of change is the 21st century trend in the one-year return level of skew surge, which for these simulations, also applies to all other return periods.

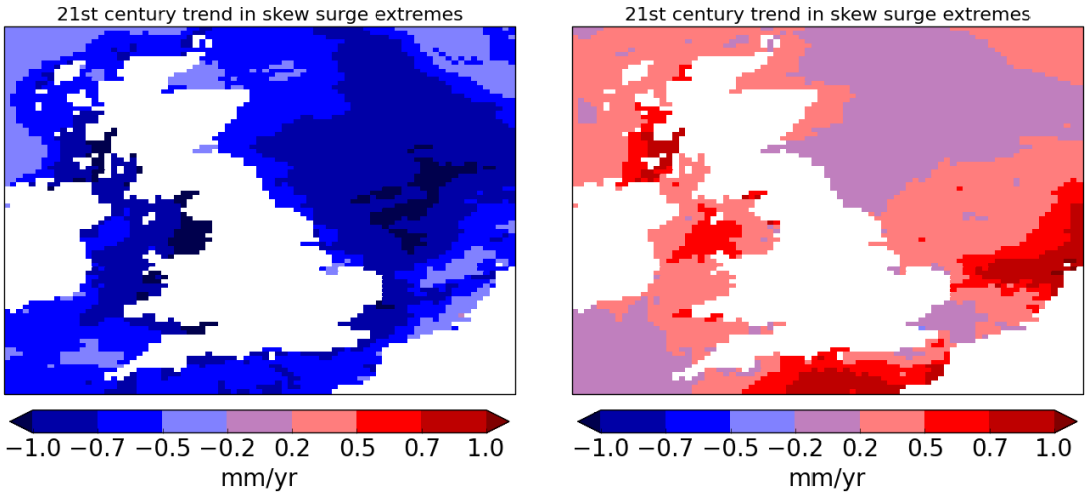



Figure 8.8: Projected 21st century trend in skew surge extremes from two different climate models.

The results shown (uniformly negative in HadGEM2-ES-RCA4 and almost uniformly positive in MPI-ESM-LR-RCA4) suggest that these trends are the result of large-scale atmospheric storminess change over the 21st

century in the driving models, and the contrast between the two results underscores the uncertainty in model projections of atmospheric storminess. For comparison, the current observed rate of global mean sea level increase is around 3.2 mm per year and typical projected rates averaged over the 21st century are around twice the current observed rate. Thus, we see that even the largest projected fluctuations due to changes in storminess in the RCA4-downscaled simulations are smaller by about an order of magnitude than typical projected changes in mean sea level.

Considering the disagreement between these simulations, UKCP18 concludes that a trend of zero is the best estimate based on the RCA4-downscaled simulations; in this case all of the change in the water level extremes during the 21st century would come from the change in the mean sea level (plus other sources such as the change in surface waves and other secondary contributions), and none of the change would come from changes in atmospheric storminess.

UKCP18 also presents an illustrative "high-end" projection based on the global model simulation under RCP8.5 likely to give the largest change in skew surge at some locations around north western Europe. This is included as a tool for sensitivity testing and contingency planning where a higher level of protection is needed and is an illustrative simulation only. Spatial patterns of the 21st century trend in 1 and 200-year return level of skew surge from this simulation are shown in Figure 8.9.

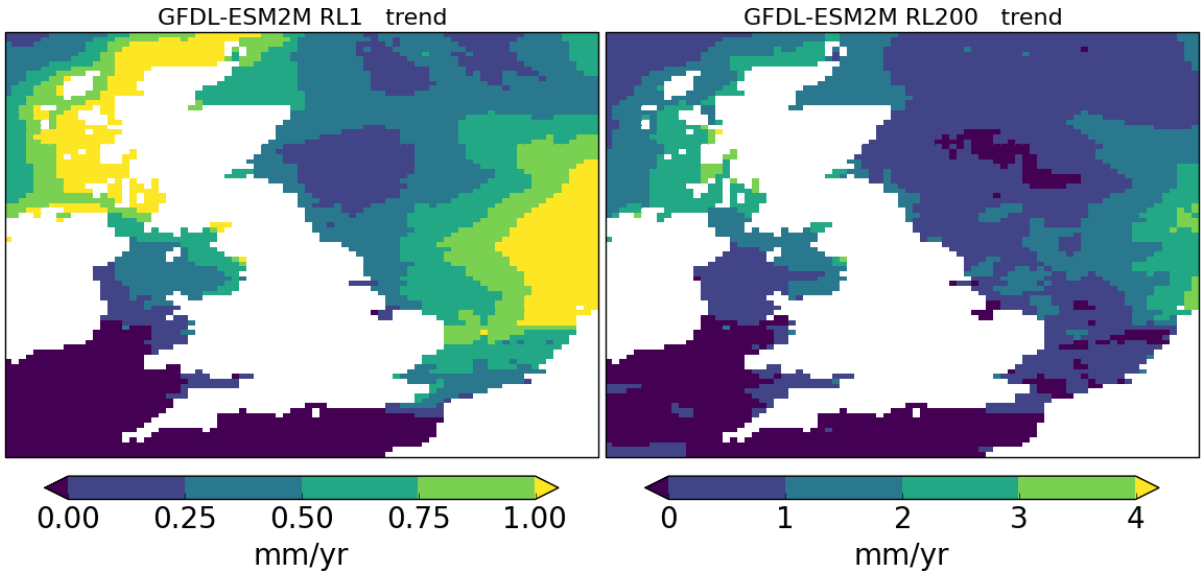



Figure 8.9: Spatial pattern of the illustrative high-end projection of 21st century trend in one-year return level of skew surge (left) and 200-year return level of skew surge (right). This does not include any time-mean sea level change.

Under this projection, 0.33 and 0.91 mm/year increases in the 1 and 200-year return levels of atmospheric storminess contribution to skew surge at Holyhead, Wales are predicted. However, mean sea level change is still expected to be the dominant source of increase and uncertainty in extreme still water levels.

UKCP18 also provides future extreme total still water levels at selected UK tide gauge locations for the period 2010-2100. Figure 8.10 shows projections of extreme total water levels at Holyhead, Wales, for the year 2060, for RCP 2.6, 4.5 and 8.5.

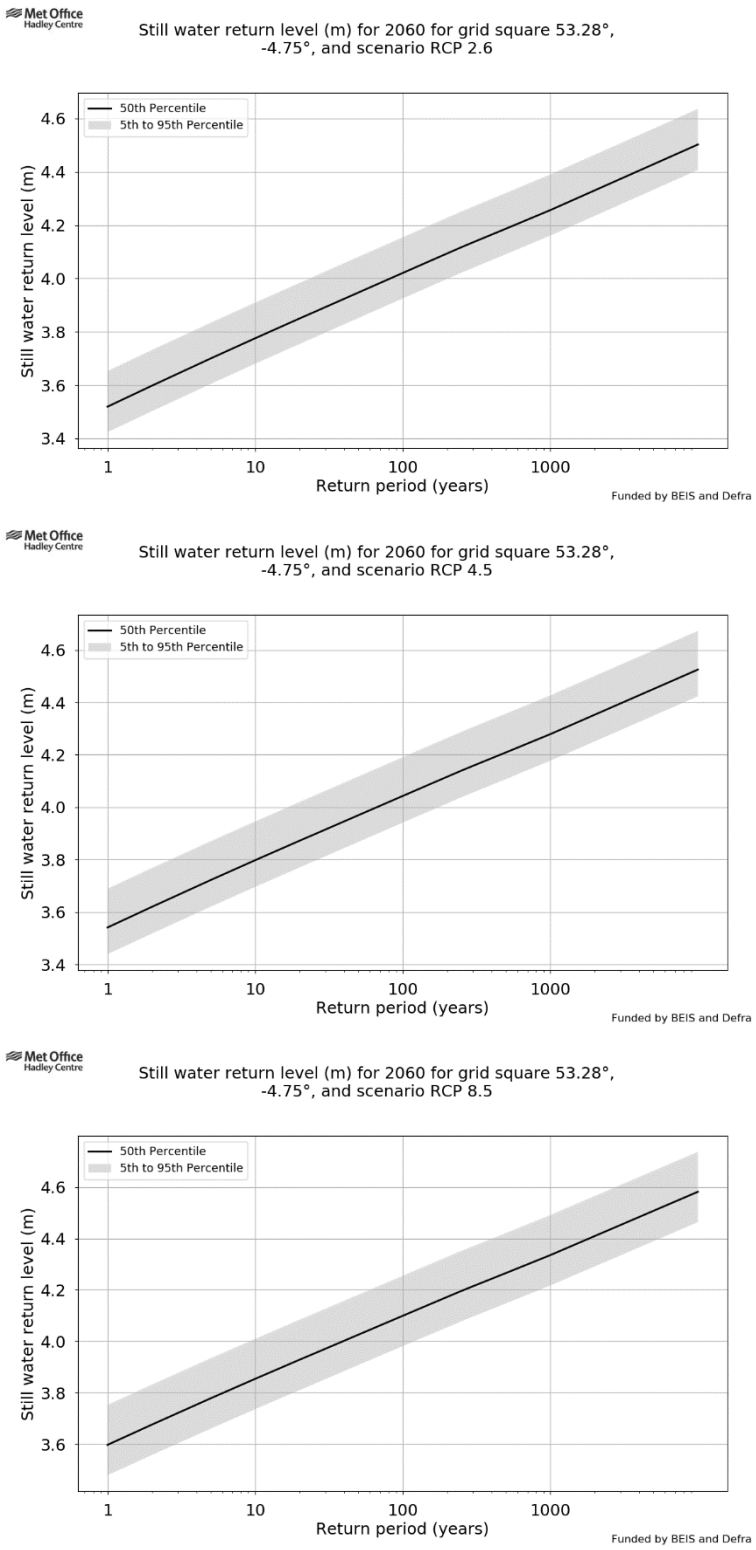



Figure 8.10: Future extreme still water levels at Holyhead, Wales, relative to the 2017 zero-level of Ordnance Datum Newlyn.

The projections of extreme total water levels do not vary greatly between different RCPs, lending further weight to the previous assertion that mean sea level change is expected to be the dominant source of increase in total water levels.

# 9 References

[1] Fugro GB Marine, “Final Data Report, Arklow Offshore Wind Farm Metocean Survey, Ref: 181399-R-03(01), Draft,” 21 April 2021.

[2] G. J. Komen, L. Cavaleri, M. Donelan, K. Hasselmann, S. Hasselmann and P. A. E. M. Janssen, Dynamics and Modelling of Ocean Waves, Cambridge, UK: Cambridge University Press, 1994.

[3] SWAN team, Delft University of Technology, “Swan cycle III version 40.91 ABC - Scientific and Technical Documentation,” 2013.

[4] UKCP18, “UK Climate Projections (UKCP) - Met Office,” Met Office, [Online]. Available: https://www.metoffice.gov.uk/research/approach/collaboration/ukcp/index. [Accessed October 2019].

[5] T. Stocker, D. Qin, G.-K. Plattner, M. Tignor, S. Allen, J. Boschung, A. Nauels, Y. Xia, V. Bex and P. Midgley, “Climate Change 2013: The Physical Science Basis. Contribution of Working Group I to the Fifth Assessment Report of the Intergovernmental Panel on Climate Change,” Intergovernmental Panel on Climate Change, Cambridge, United Kingdom and New York, NY, USA, 2013.

[6] K. McInnes, T. Erwin and J. Bathols, “Global Climate Model projected changes in 10 m wind speed and direction due to anthropogenic climate change,” *Atmospheric Science Letters,* 2011.

[7] G. Villarini and G. A. Vecchi, “Twenty-first-century projections of North Atlantic tropical storms from CMIP5 models,” *Nature Clim. Change,* no. 2, pp. 604-607, 2012.

[8] G. Villarini and G. A. Vecchi, “Projected increases in North Atlantic tropical cyclone intensity from CMIP5 models,” *J. Clim.,* no. 26, pp. 3231-3240, 2013.

[9] T. R. Knutson and e. al., “Dynamical downscaling projections of 21st century Atlantic hurricane activity: CMIP3 and CMIP5 model-based scenarios,” *J. Clim.,* no. 26, pp. 6591-6617, 2013.

[10] R. E. McDonald, “Understanding the impact of climate change on Northern Hemisphere extra-tropical cyclones,” *Clim. Dyn.,* no. 37, pp. 1399-1425, 2011.

[11] J. G. Pinto, U. Ulbrich, G. C. Leckebusch, T. Spangehl, M. Reyers and S. Zacharias, “Changes in storm track and cyclone activity in three SRES ensemble experiments with the ECHAM5/MPI-OM1 GCM,” *Clim. Dyn.,* no. 29, pp. 195-210, 2007.

[12] T. Woollings, J. Gregory, J. Pinto, M. Reyers and D. Brayshaw, “Response of the North Atlantic storm track to climate change shaped by ocean-atmosphere coupling,” *Nature Geosci.,* no. 5, pp. 313-317, 2012.

[13] J. B. Debernard and L. P. Røed, “Future wind, wave and storm surge climate in the Northern Seas: A revisit,” *Tellus A,* no. 60, pp. 427-438, 2008.

[14] G. C. Leckebusch, U. Ulbrich, L. Froehlich and J. G. Pinto, "Property loss potentials for European midlatitude storms in a changing climate," *Geophys. Res. Lett.,* no. 34, 2008.

[15] A. Sterl, H. v. d. Brink, H. d. Vries, R. Haarsma and E. v. Meijgaard, "An ensemble study of extreme North Sea storm surges in a changing climate," *Ocean Sci. Discuss.,* no. 6, pp. 1031-1059, 2009.

[16] M. G. Donat, G. C. Leckebusch, S. Wild and U. Ulbrich, "Future changes in European winter storm losses and extreme wind speeds inferred from GCM and RCM multi-model simulations," *Nat. Hazards Earth Syst.,* no. 11, pp. 1351-1370, 2011.

[17] M. Beniston, D. Stephenson, O. Christensen, C. Ferro, C. Frei, S. Goyette, K. Halsnaes, T. Holt, K. Jylha, B. Koffi, J. Palutikof, R. Schoell, T. Semmler and K. Woth, "Future extreme events in European climate: an exploration of regional climate model projections," *Climatic Change,* no. 81, pp. 71-95, 2007.

[18] B. Rockel and K. Woth, "Extremes of near-surface wind speed over Europe and their future changes as estimated from an ensemble of RCM simulations," *Climatic Change,* no. 81(S1), pp. 267-280, 2007.

[19] J. Haugen and T. Iversen, "Response in extremes of daily precipitation and wind from a downscaled multi-model ensemble of anthropogenic global climate change scenarios," *Tellus Series A – Dynamic Meteorology and Oceanography,* vol. 60, no. 3, pp. 411-426, 2008.

[20] M. Rauthe, M. Kunz and C. Kottmeier, "Changes in wind gust extremes over Central Europe derived from a small ensemble of high resolution regional climate models," *Meteorologische Zeitschrift,* no. 19(3), pp. 299-312, 2010.

[21] SSE Renewables, Technical Analysis Team, *Wind Analysis Report, Arklow Bank Wind Farm, ROI Offshore Rev01,* 2020.

[22] DNVGL, "DNVGL-RP-C205. Recommended Practice – Environmental conditions and environmental loads.," DNVGL, December 2019.

[23] S. Emeis, Wind Energy Meteorology, 2nd ed., 2018.

[24] ISO, "ISO 19901-1:2015 Petroleum and natural gas industries – Specific requirements for offshore structures – Part 1: Metocean design and operating considerations. Second Edition.," ISO, 2015.

[25] Nortek AS, "The Comprehensive Manual for ADCP's; AWAC, Aquadopp, Aquadopp deepwater, Aquadopp Profiler, Aquadopp Profiler Z-cell, 2D Horizontal Profiler," 2018.

[26] T. Dabrowski, G. Westbrook, K. Lyons, G. Nolan, M. Gillooly, M. Roper and K. Adlum, "The Irish National Data Buoy Network deployed offshore for monitoring weather and ocean properties," in *The Irish Meteorological Society Symposium*, National University of Ireland, Galway, 2014.

[27] SWAN team, Delft University of Technology, "Swan cycle III version 40.91 ABC - User Manual," 2013.

[28] J. L. Hanson and O. M. Phillips, "Automated Analysis of Ocean Surface Directional Wave Spectra," *J. Atmos. Oceanic. Technol.,* vol. 18, pp. 277-293, 2001.

[29] International Electrotechnical Commission, "IEC-61400-3: Wind Turbines – Part 3: Design Requirements



for Offshore Wind Turbines. Edition 1.0.," 2009-02.

[30] P. S. Tromans and L. Vanderschuren, "Response based design conditions in the North Sea: application of a new method," *Proc. 27th Offshore Technology Conference, OTC 7683,* 1995.

[31] G. Forristall, "On the statistical distribution of wave heights in a storm," *J. Geophys. Res. ,* no. 83, pp. 2353- 2358, 1978.

[32] Y. Wu, D. Randell, M. Christou, K. Ewans and P. Jonathan, "On the distribution of wave height in shallow water," *Coastal Engineering,* vol. 111, pp. 39-49, 2016.

# Appendix A. Bathymetry Merging

In order to create model bathymetry representative of 2019, SeaDataNet bathymetry for the wider region and 2019 survey bathymetry (see Section 3.1) were merged. The two datasets are shown in Figure A.1.

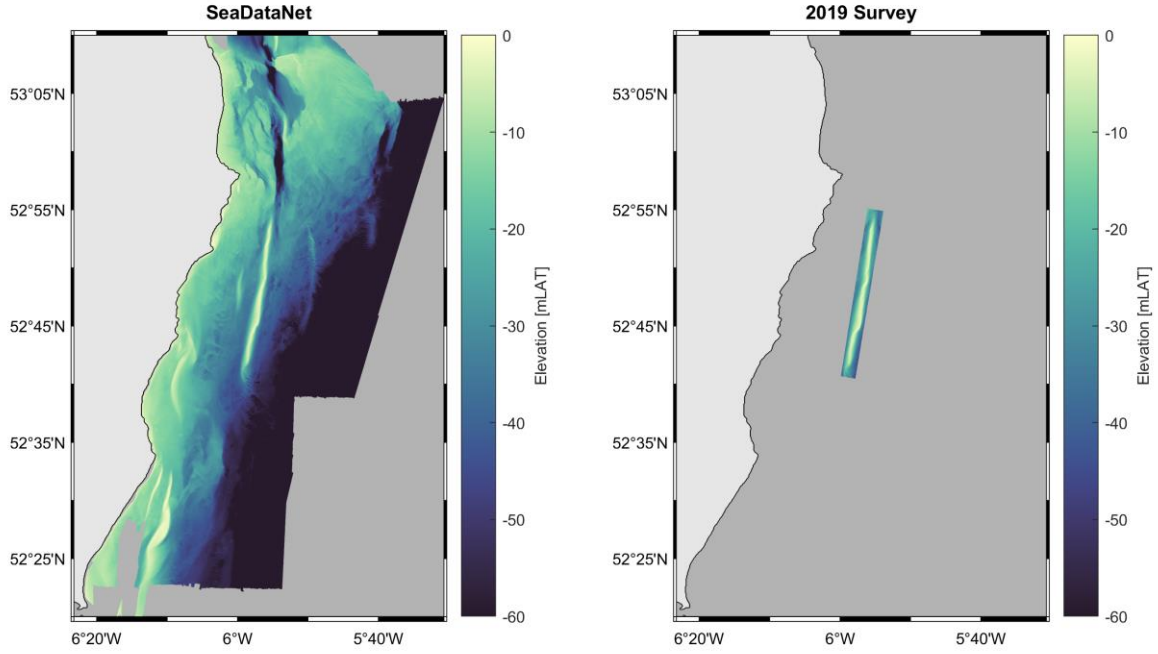



Figure A.1. SeaDataNet and 2019 bathymetry data.

To ensure the merging step did not artificially introduce any sudden jumps at the boundary between the two datasets, a tapering method was employed as follows:

**STEP 1: Calculate elevations on a common grid**

Calculations are performed on a regular horizontal grid of approximately 30 m, less than half the resolution of finest model grid cell. The SeaDataNet bathymetry and 2019 survey bathymetry were transformed to this grid by taking mean values across each grid cell.

**STEP 2: Define the merging region**

The region over which the bathymetry will be merged is defined in two parts:

a) An *inner* region, in which the re-gridded 2019 survey data (from STEP 1) is used unchanged.
b) A distance outside this region across which tapering takes place.

For this merge, the inner region is taken to be the full set of re-gridded 2019 survey data, and the taper is applied within 250 m of this region, as shown in Figure A.2.

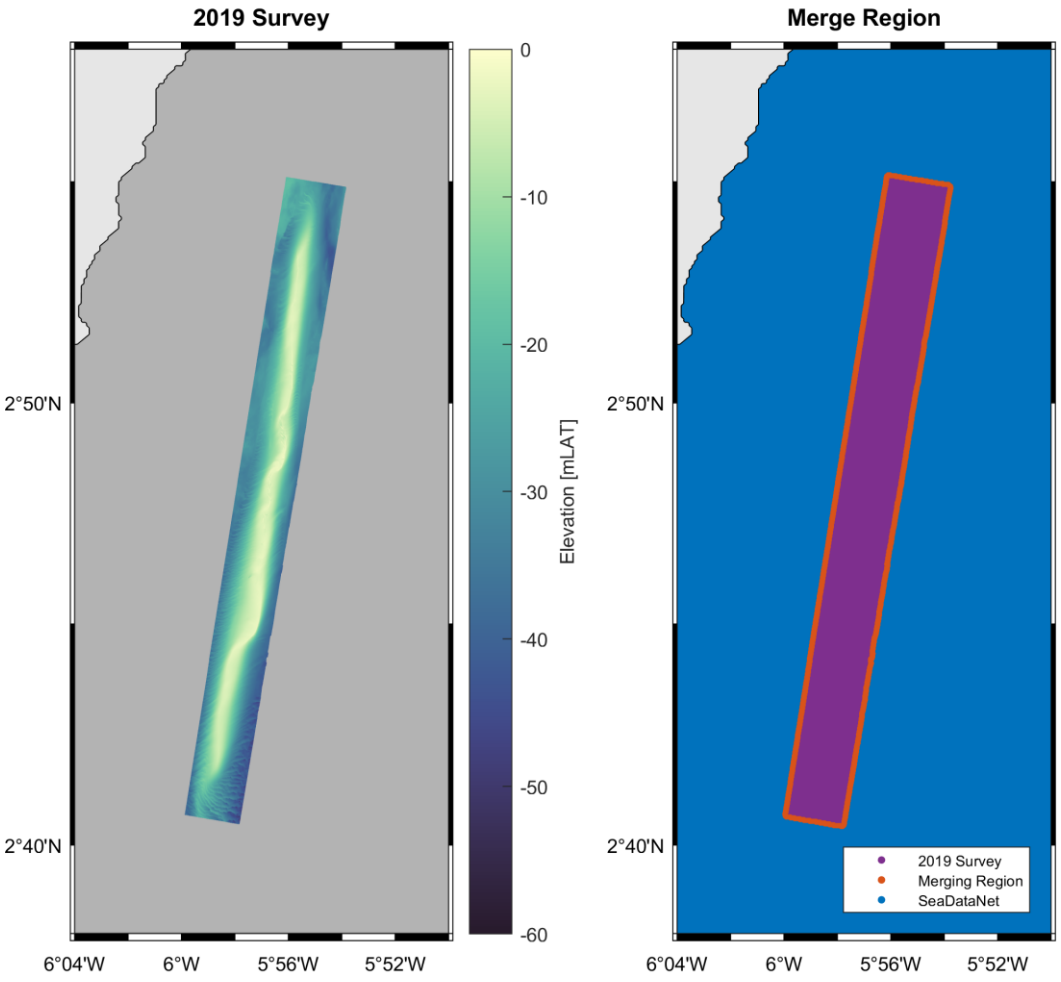



Figure A.2. Merging region.

**STEP 3: Apply the taper**

For each point within the merging region:

1. Find the closest point within the *inner* region, and its distance from the point being considered. This distance is denoted hereafter $d_{in}$.

2. Normalise this value so that it is zero on the boundary of the inner region, increasing linearly to one 250 m away. If we denote this normalised value $n_{in}$ then:

$$n_{in} = \frac{d_{in}}{250}$$

   Note that since we are only considering locations within 250m of the inner zone, this does not increase above 1.

3. Apply a cosine taper to this value such that it *smoothly* changes from *one* at the boundary of the inner region to *zero* 250 m away. If we denote this as $c_{in}$ then:

$$c_{in} = 0.5 \cdot \cos(n_{in}\pi) + 0.5$$

4. At the closest point found within the *inner* region found above, calculate the difference between the 2019 bathymetry and the SeaDataNet bathymetry, i.e.:

$$\delta_{in} = z_{2019} - z_{SeaDataNet}$$

This is the value we would *add* to SeaDataNet bathymetry that is exactly *on* the inner boundary.

5. Combine this "inner boundary offset" with the smooth distance from the inner boundary and the SeaDataNet to give a final adjusted elevation of:

$$z_{adjusted} = z_{SeaDataNet} + \delta_{in} \cdot c_{in}$$

For illustrative purposes, the values of a number of these parameters are shown for a small section of the southern end of the merge region in Figure A.3 below.

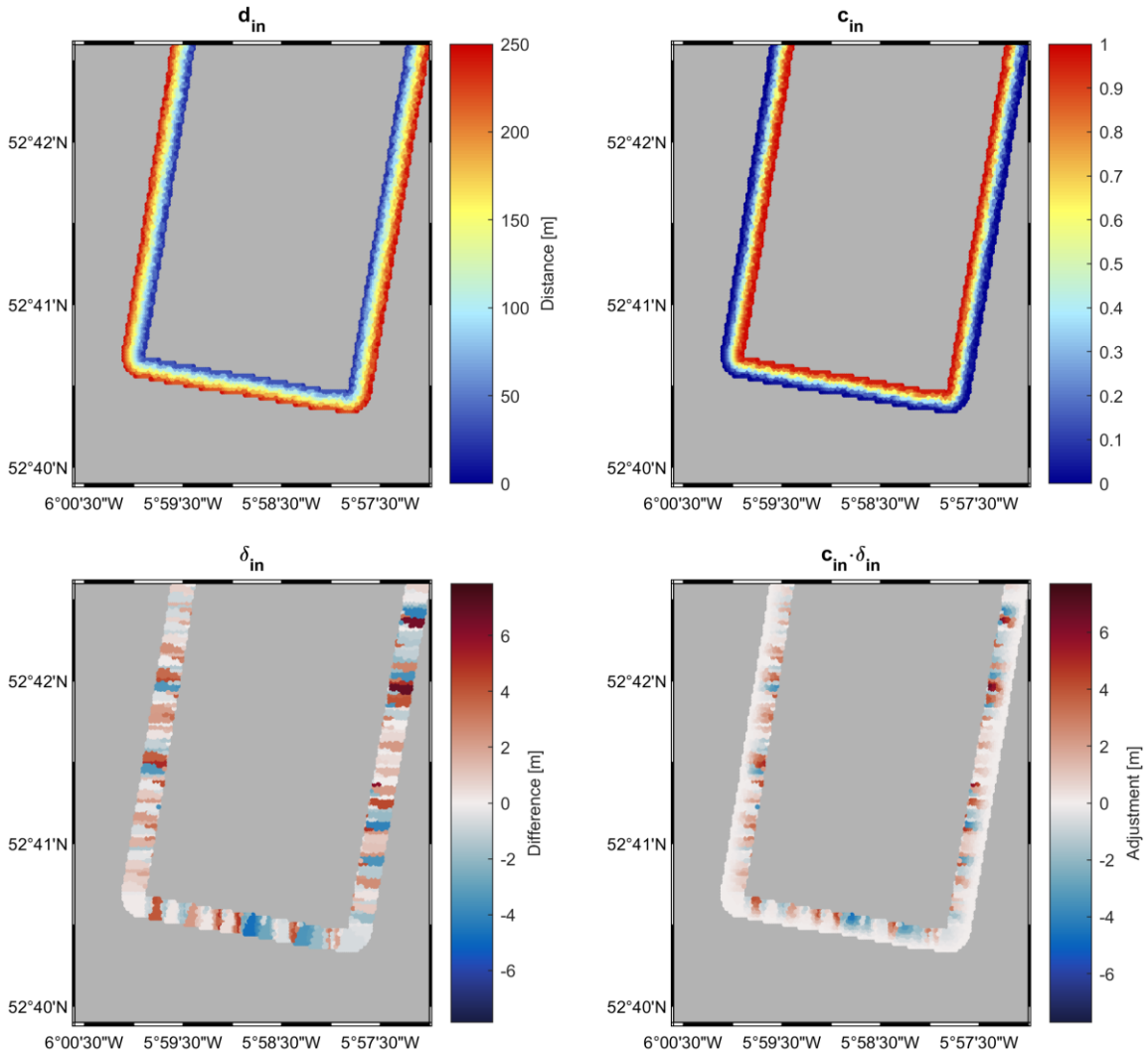



Figure A.3. Taper parameters, southern end of merge region.

**STEP 4: Review diagnostic plots**

A number of diagnostic plots are subsequently reviewed to ensure no unwanted artifacts are introduced into the resulting bathymetry. A selection of these are shown in Figure A.4 through Figure A.8.

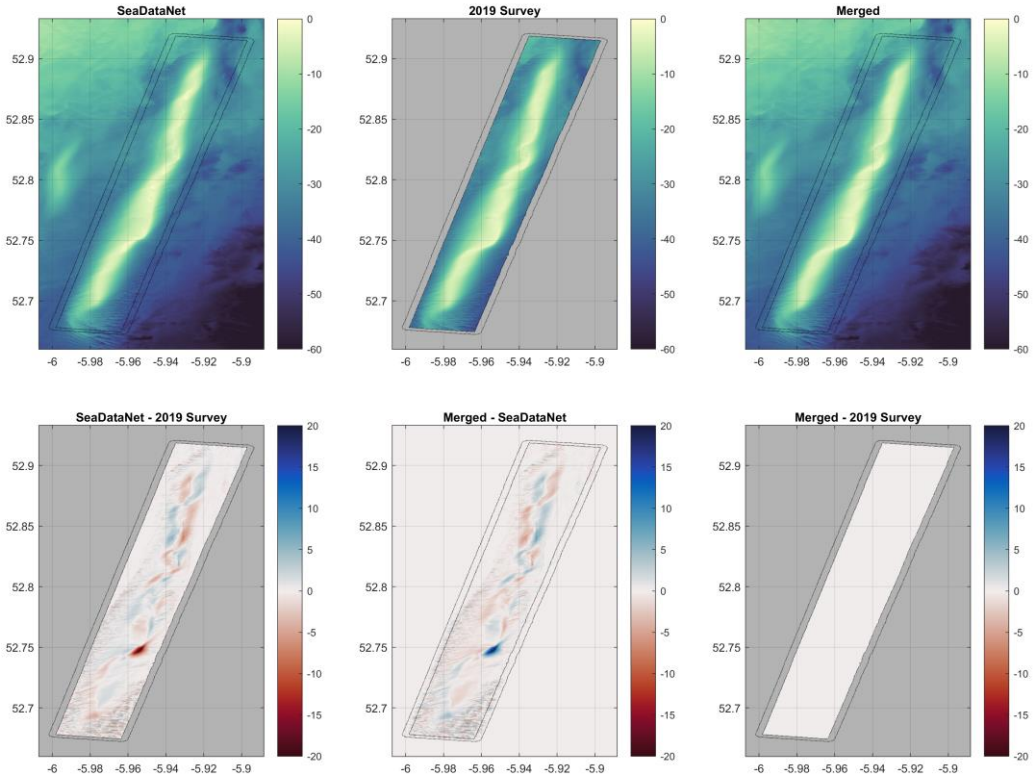



Figure A.4. Bathymetry merge 2019 to SeaDataNet – diagnostic plot – overview.

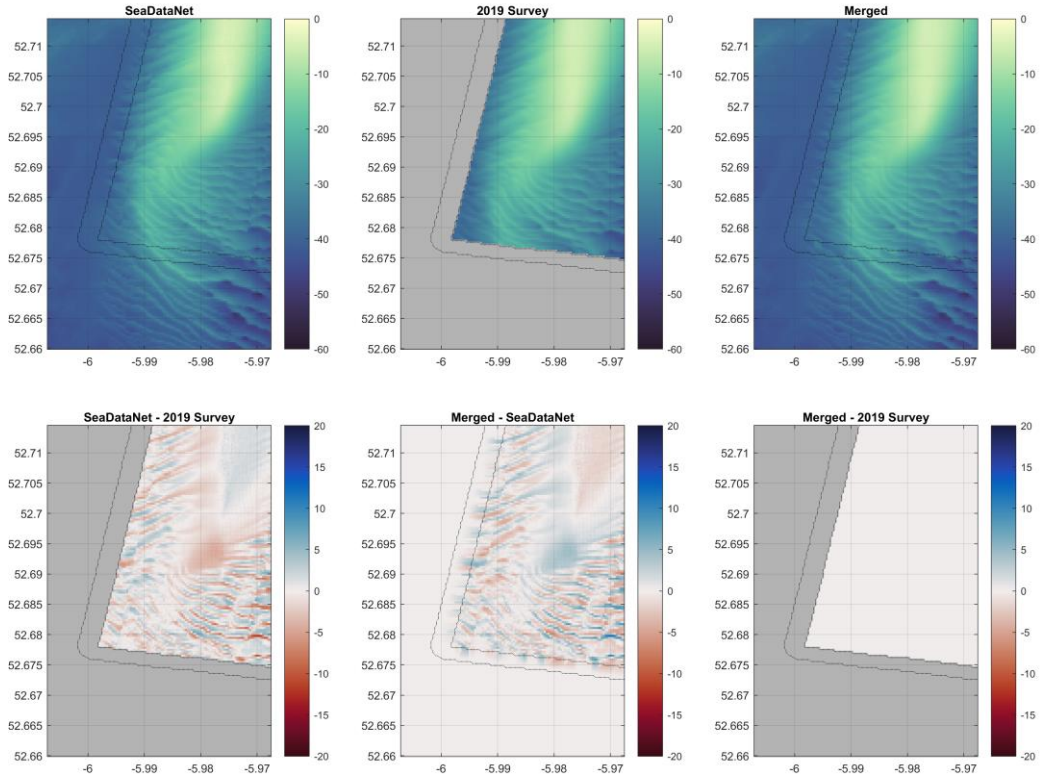



Figure A.5. Bathymetry merge 2019 to SeaDataNet – diagnostic plot – southwest corner.

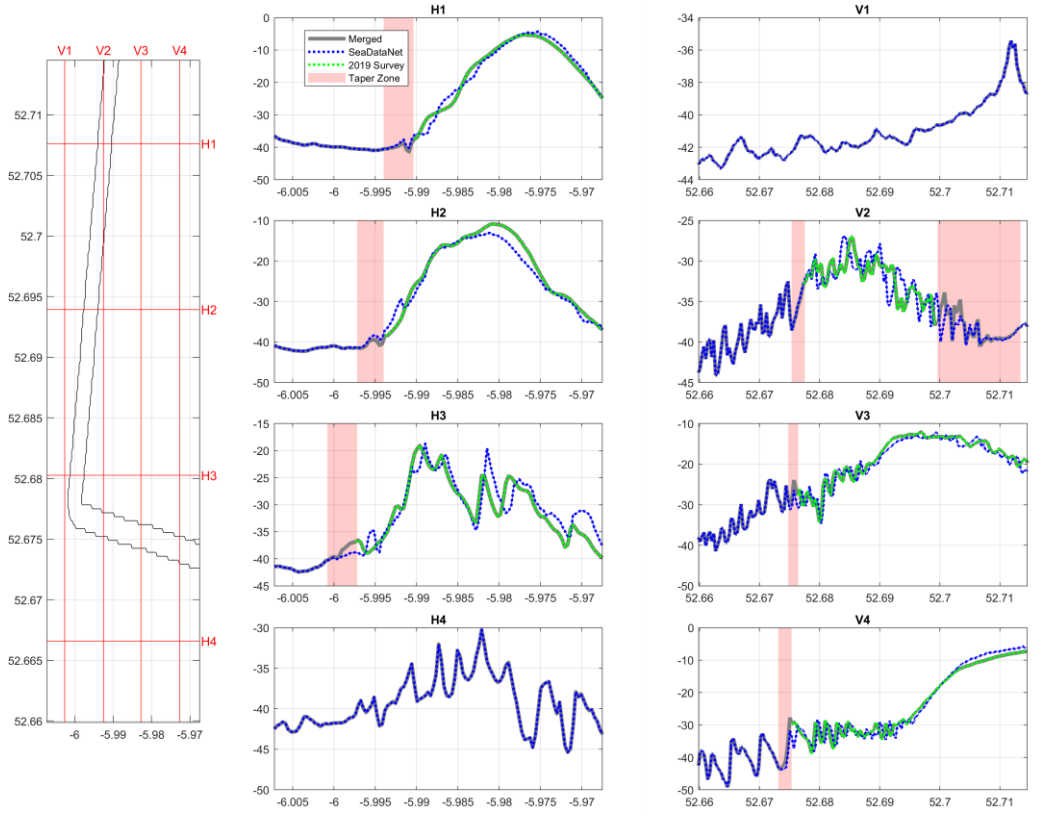



Figure A.6. Bathymetry merge 2019 to SeaDataNet – transect diagnostic plot – southwest corner.

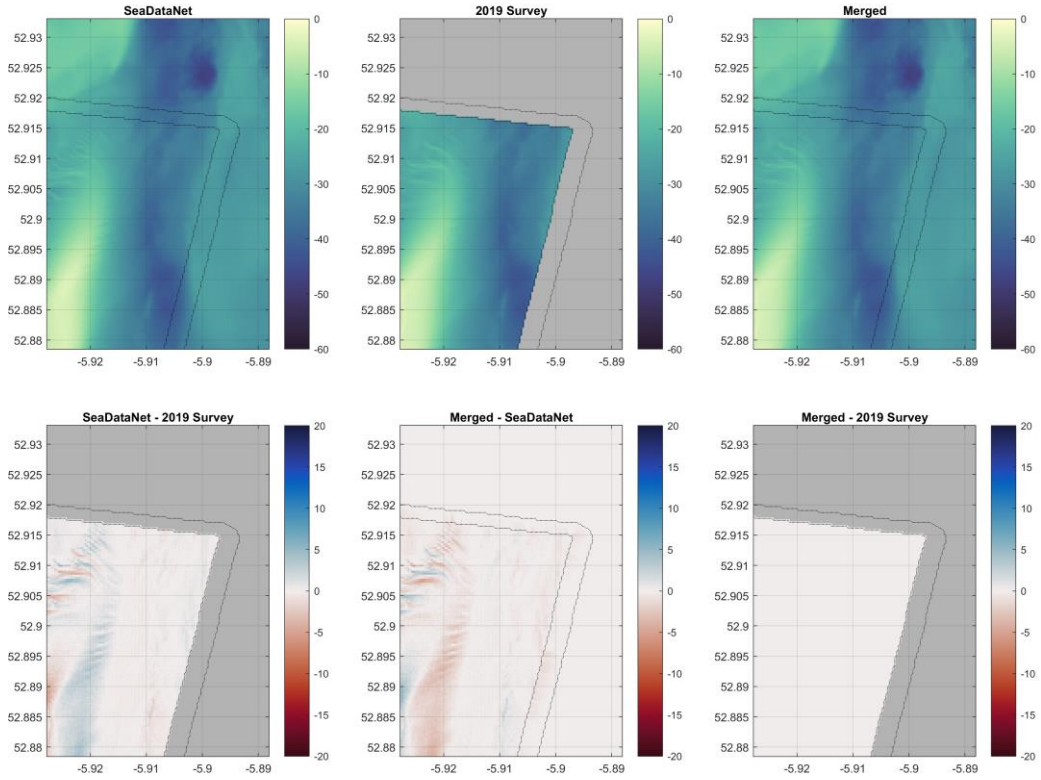



Figure A.7. Bathymetry merge 2019 to SeaDataNet – diagnostic plot – northeast corner.

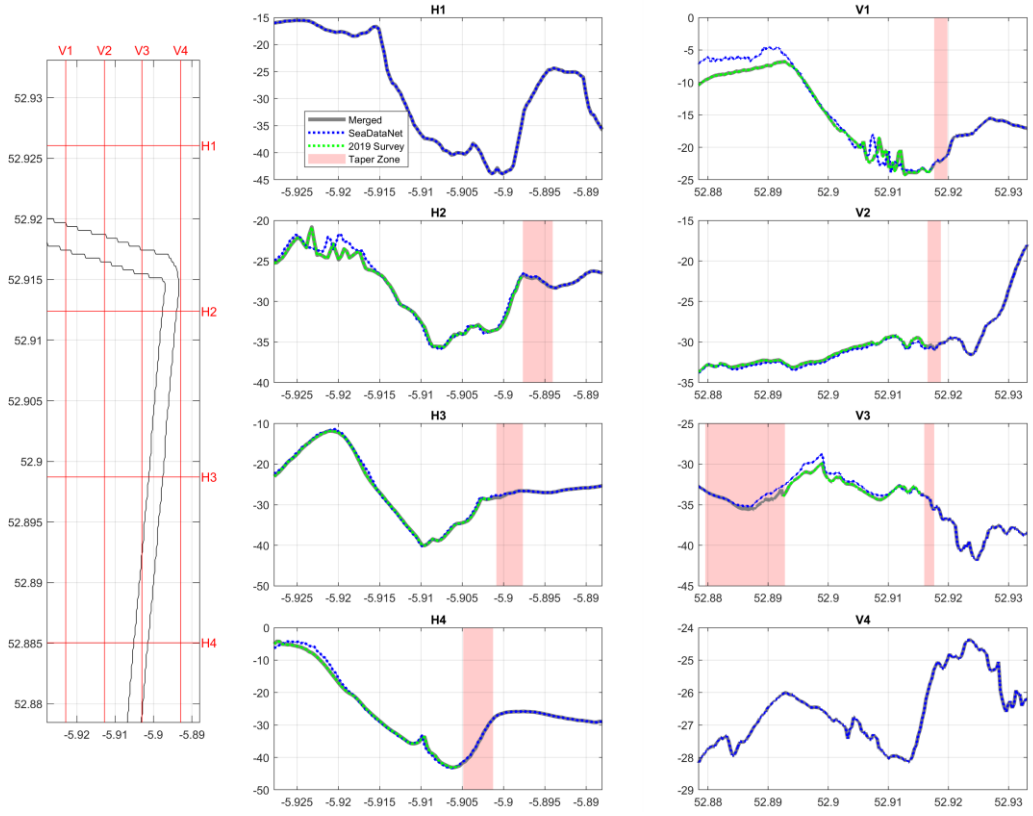



Figure A.8. Bathymetry merge 2019 to SeaDataNet – transect diagnostic plot – northeast corner.

# Appendix B. Wind Field Validation and Calibration

## B.1 Introduction

In Section 4, modelled and measured wind datasets used in this project were introduced, and a number of validation details included, showing the suitability of the modelled data for use in driving metocean models. Prior to carrying out these validations, a number of preliminary steps are needed, to:

- Review the quality of the measured datasets, and apply any quality control (QC) deemed appropriate.
- Adjust wind speeds to compensate for differences between measurement heights, and representative model heights.
- Make any adjustments necessary to compensate for differences in averaging periods between the model and measurements.

These are the subject of Sections B.2 and B.4 of this Appendix respectively. As noted in Section 4, a calibration is then applied to the wind fields at 10 m, and this is described in Section B.5 and Section B.6.

## B.2 Modelled Data

A bespoke 3 km resolution down-scaled wind field dataset of the Irish Sea was supplied by Sure Partners. This was sourced from Vortex Factoria de Càlculs SL (Vortex), and was derived as a downscaled implementation of the European Centre for Medium-Range Weather Forecasts (ECMWF) ReAnalysis 5 (ERA5).

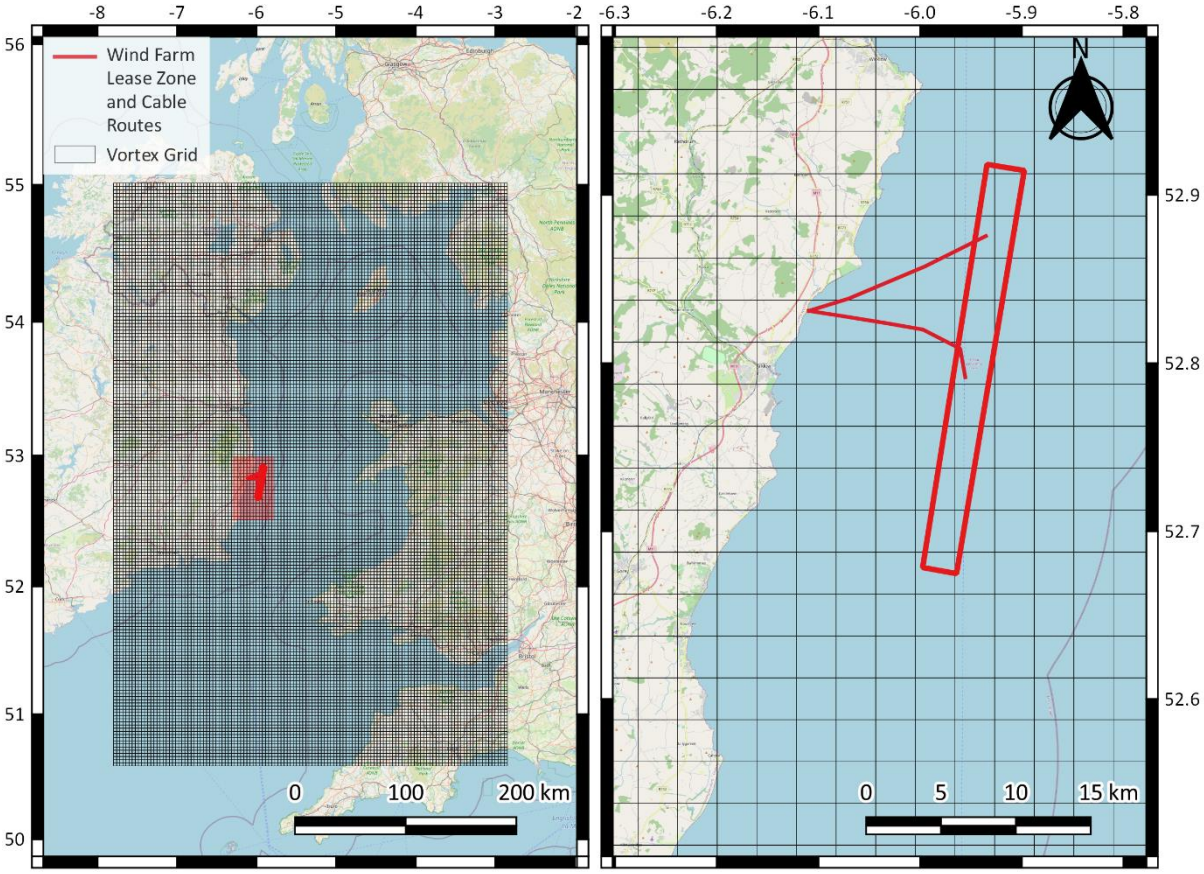



Figure B.1: Coverage of Vortex wind hindcast dataset supplied by SPL.

Additionally, gridded modelled ECMWF ERA5 data covering the wider European area were obtained to drive regional scale models. ERA5 is the fifth and latest major global reanalysis produced by ECMWF and atmospheric data are available on a regular latitude-longitude grid at 0.25-degree x 0.25-degree resolution.

Data from both models were acquired at hourly intervals between 1982 and 2020 at 10m and 100m. Additional elevations were available for the Vortex modelled dataset. In this Appendix, we largely focus on the Vortex downscaled winds. These data are used to illustrate the necessary steps for model validation and subsequent model calibration. A short description of the calibration process for the ERA5 wind fields *is* described in Section B.6. However, much of this information is proprietary in nature and so details are relatively brief.

## B.3 Measured Data

The Vortex modelled data described in the previous Section were compared to the measured datasets shown in Table B.1. Please note that for the sake of clarity, two datasets are considered separately for the Arklow met mast:

- **Arklow Met Mast (Original)** is used to describe the set of measurements from the five individual anemometers and two wind vanes on the Arklow met mast.
- **Arklow Met Mast (Synthesised)** is used to describe a single set of speeds at an elevation of 42.5 m synthesised by SSE from the highest two anemometers on the met mast, combined with a single set of directions derived by SSE from the two wind vanes.

The locations of these datasets are shown in Figure B.2.

Table B.1: Measured datasets.

| Dataset | Location | Wind Speed Heights | Time Period | Averaging Period |
|---|---|---|---|---|
| **Arklow Met Mast (Original)** | 52.8855 °N 5.9234 °W | 15.0, 22.3, 29.6, 39.5, 42.5 mAMSL* | 21-Feb-2001 to 26-Aug-2019 | 10 min |
| **Arklow Met Mast (Synthesised)** | 52.8855 °N 5.9234 °W | 42.5 mAMSL* | 21-Feb-2001 to 05-Jun-2016 | 10 min |
| **Arklow LiDAR** | 52.8855 °N 5.9234 °W | 21.3, 42.3, 49.3, 74.3, 99.3, 129.3, 159.3, 184.3, 219.3, 299.3 mAMSL | 07-Nov-2019 to 05-Nov-2020 | 10 min |
| **M2** | 53.4836 °N 5.4302 °W | 3.5 mASL | 26-Oct-2010 to 27-Apr-2020 † | 10 min reported hourly |
| **M5** | 51.6904 °N 6.7043 °W | 3.5 mASL | 21-Feb-2012 to 27-Apr-2020 † | 10 min reported hourly |
| **Splaugh** | 52.2394 °N 6.2788 °W | 5.0 mASL | 01-Apr-2016 to 01-Jan-2018 | 10 min |
| **Coningbeg** | 52.0539 °N 6.6411 °W | 8.0 mASL | 08-Apr-2016 to 01-Jan-2018 | 10 min |

* Heights stated for the two Arklow Met Masts are those used throughout the analyses which follow. As described in the Wind Analysis Report [21] supplied by SSE, true heights have been determined to be 0.35 m higher, however it has been agreed to keep those given to avoid confusion.

† Both M2 and M5 begin much earlier, in May 2001 and October 2004 respectively. However, as discussed in Section B.4.4, earlier data appears to be of lower quality, and thus only the time periods given above are used for model validation.

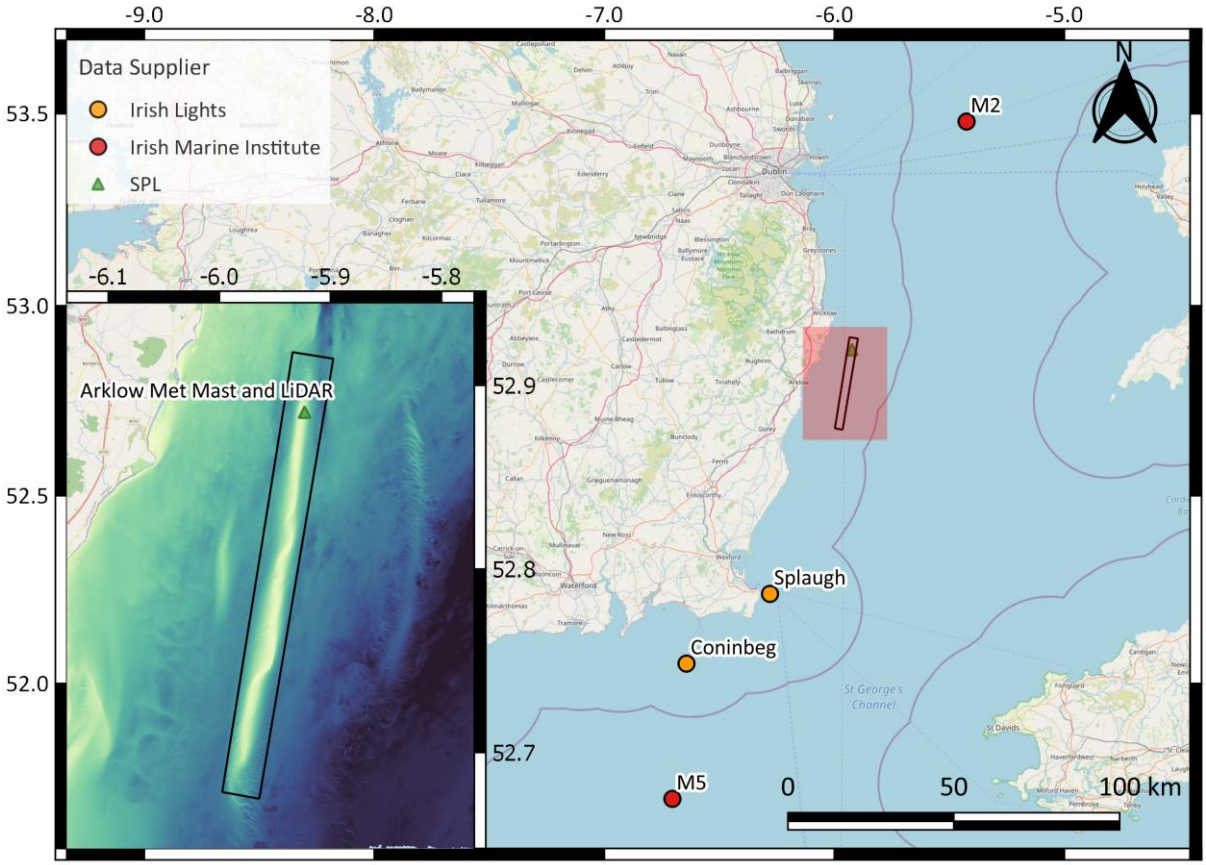



Figure B.2. Measured datasets.

## B.4 Model Validation

### B.4.1 Methodology

In this Section, numerous validation plots comparing modelled to measured data are included. Throughout, modelled data is taken from the nearest modelled node to the measurement location. Prior to carrying out such comparisons, a number of adjustments need to be made to the datasets to compensate for differences between elevation levels and averaging periods. For all datasets, these are as follows:

**Averaging Period**

The stated averaging period of the modelled data is approximately hourly. Thus, prior to comparison and where possible, *measured* data are averaged every hour to form a 1-hour mean wind speed dataset. A minimum of 60% of the data expected per hour, based on the mode timestep of the measurements, is required for an average to be calculated, otherwise data for the hour is considered "missing" and not included in comparisons.

**Elevation**

*Modelled* wind speeds are determined at each *measured* elevation for each timestep independently as follows:

a) If a modelled level matches the measured elevation, wind speeds from this model level are used unadjusted.
b) Otherwise, two modelled levels, $z_1$ and $z_2$ are selected as:
   - The modelled levels above and below the measured elevation *if* said elevation is within the range of two model levels.
   - The closest two modelled levels *if* the measured elevation is above or below *all* modelled wind speed levels.
c) A power law exponent, $\alpha$, is determined from the wind speeds at these levels by solving the equation:

$$U_{model}(z_2) = U_{model}(z_1)\left(\frac{z_2}{z_1}\right)^{\alpha}$$

   for $\alpha$, where $U_{model}(z)$ is modelled wind speed at elevation $z$.
d) The modelled wind speed at *measurement* height $z_{measured}$ is then calculated according to:

$$U_{model}(z_{measured}) = U_{model}(z_1)\left(\frac{z_{measured}}{z_1}\right)^{\alpha}$$

As noted above, this calculation is carried out independently for each timestep, and in particular $\alpha$ will vary throughout the time series. After the two adjustments described above, all validation comparisons are for one-hour mean wind speeds at *measured* elevations. M2 and M5 are exceptions to this, since there is insufficient data to calculate hourly means, and the original ten-minute averages reported hourly are used.



## B.4.2 Arklow Met Mast (Original and Synthesised)

### B.4.2.1 Overview

The Arklow Met Mast was installed in January 2001, and decommissioned in October 2019, to be replaced by a LiDAR (see Section B.4.3) at the same location, at the northern end of the Arklow Bank. Though there exist significant periods where no data were recorded, some 16 years of wind speeds and directions are available, with wind speeds spanning elevations between 15 and 42.5 mMSL. Full details of the met mast, and the recorded data can be found in the SSE met mast and LiDAR Wind Analysis Report [21], but by way of summary:

- The met mast has five anemometers, with heights documented as 42.5, 39.5, 29.6, 22.3 and 15 m above mean sea level (AMSL). Measurements of platform height taken during the LiDAR installation show that these are all approximately 0.35 m lower than actual heights, however after discussion with SSE, it has been agreed that to avoid confusion the aforementioned elevations will be used throughout this analysis (i.e. they are *not* corrected by adding 0.35 m).
- The lower four anemometers are all at an orientation of 237 °N, with the highest above the mast.
- The met mast has two wind vanes, with documented heights of 29.4 and 39.3 m. Again, these are approximately 0.35 m lower than actual heights, but again, throughout this analysis no correction is applied and these originally documented heights are used.
- Both anemometers are at an orientation of 147 °N.
- The booms on which all anemometers except the highest are installed are, according to [21], "*significantly off from complying to current IEC standards*". The highest anemometer "*may be within guidelines though this is not clear as dimensions of the full structure are not available*".

Though there are certainly limitations to the measurement setup here, there is still a large volume of data which may prove invaluable for model validation, even if some caution is necessary for some directional sectors.

In order to address some of these limitations, rather than directly using the measurements from individual sensors described above, the SSE Wind Analysis Report [21] derives a "synthesised" dataset for the analyses included therein. Once again, full details can be found in [21] but by way of overview:

- A single set of wind speeds at 42.5 mAMSL are derived by starting with measurements from the highest anemometer, but infilling where necessary and possible with data synthesised from measurements taken by anemometer at 39.5 mAMSL. (See Section 3.4.2 of [21] for more details)
- A single set of wind directions are derived in a similar manner, prioritising the wind vane at 39.3 mAMSL, and discarding data where the directions from the two wind vanes differ by more than might reasonably be expected. (See Section 3.3.3 of [21] more details)

This results in approximately 13 years of data, being shorter than the approx. 16 years of original data since from June 2016 through to August 2019, only one anemometer – that at 29.6 mAMSL – was still working, and was not used in the synthesising process since there were no other anemometers against which to corroborate its accuracy.

Although this synthesised dataset is expected to be of higher quality than the measurements from individual levels, using it alone for model validation would lead to ignoring all data from the 15, 22.3 and 29.6 mAMSL levels. Thus instead, validation is carried out against two datasets, one denoted Arklow Met Mast (Original), which uses measurements from each level independently, and one denoted Arklow Met Mast (Synthesised) which uses the combined dataset.



### B.4.2.2 Quality Control

As described in the SSE Wind Analysis Report [21] for the Arklow Met Mast and LiDAR, a number of steps were taken in order to review the data, and flag faulty values as necessary. The data file supplied to MetOceanWorks specifies that values *are* included for the following flags:

> <Unflagged data>, PotVaneIssuesManual, PotVaneIssuesRules, Synthesized, WS1_Finial_E_Shade, WS1_Finial_N_Shade, WS2_TowerShadeFinial, WS2_TowerShadeNoFinial, WS3_TowerShade, WS4_TowerShade, WS5_TowerShade

but omitted for data flagged by:

> Dir2Issue, Invalid, PotentialWS1Issue, VaneFault, WS1failure

For the validations which follow, we begin with the assumption that invalid data *has* been removed (although it is also reviewed – see below), with the exception of the effects of shading caused by the mast or lightning finials on top of the mast. Based on information included in [21], these effects are applied as follows:

- For the anemometer at the highest level (42.5 m) of the Arklow Met Mast (*Original*) dataset, wind speeds corresponding to directions in the shade of the two lightning finials, i.e. the ranges 2 to 18 and 52 to 68 °N, are considered invalid and removed prior to validation.
- Wind speeds from this anemometer also form the basis for the 42.5 m level of the Arklow Met Mast (*Synthesised*) dataset. However, winds arriving from the shaded sector between 2 and 18 °N are synthesised from the lower anemometer at 39.5 m. Thus, for the highest level of the synthesised dataset, only wind speeds corresponding to the directions 52 to 68 °N, are considered invalid and removed prior to validation.
- For lower levels of the Arklow Met Mast (Original) dataset, wind anemometers are affected by the mast itself, with the largest impact at the lowest level, where directions between 7 and 67 °N should be treated as suspect. It is unclear as to how this range changes with height, and as such, wind speeds corresponding to this directional range are considered suspect at all levels affected by the mast, *except* that at 39.5 m. Since data from this level are used between 2 and 18 °N in the synthesised dataset, they are assumed to be valid in this range, and as such data are considered invalid only between 18 and 67 °N.
- Wind vanes are also affected by the mast, over the range 315 to 20 °N. These are *not* removed from the analysis, but instead:
    - This range is highlighted on directional validation plots as being affected by the mast.
    - Where wind speeds are compared by direction, the values are used as is. This may lead to some misclassification of wind speeds by directional bin, however this seems preferable to simply omitting the data.

Note that for both the Original and Synthesised datasets, the *combined* directional signal (i.e. that of the Synthesised dataset rather than from individual vanes) was used to determine timestamps affected by shading.

After values were removed due to shading effects, the data were manually reviewed as both time-series and scatter plots. No algorithmic filtering was applied; however, a number of criteria were considered during manual review. To some extent, a complete list of these criteria is impossible – there are a huge number of behaviours which, if sighted, would be considered suspicious (negative speeds, very large speeds, constant derivatives, repeated patterns, etc.) – however amongst the most relevant are:

- Repeated values (including repeated zeros)
- Spikes
- Step changes
- Unexpected long-term trends
- Unexpectedly large differences between sensors at neighbouring levels

Aside from five isolated timesteps, where values at, or close to zero are shown for instruments which are not expected to be recording[4] no additional data were removed as a result of this review. A number of short periods of repeated directional values were checked and found to all correspond to periods of very low wind speeds.

Scatter plots do highlight significant directional differences when comparing measurements at neighbouring levels, in particular between the two lowest and two highest levels of the met mast. For example, Figure B.3 compares higher wind speeds at these levels, whilst Figure B.4 shows wind speed ratios at these levels by direction.

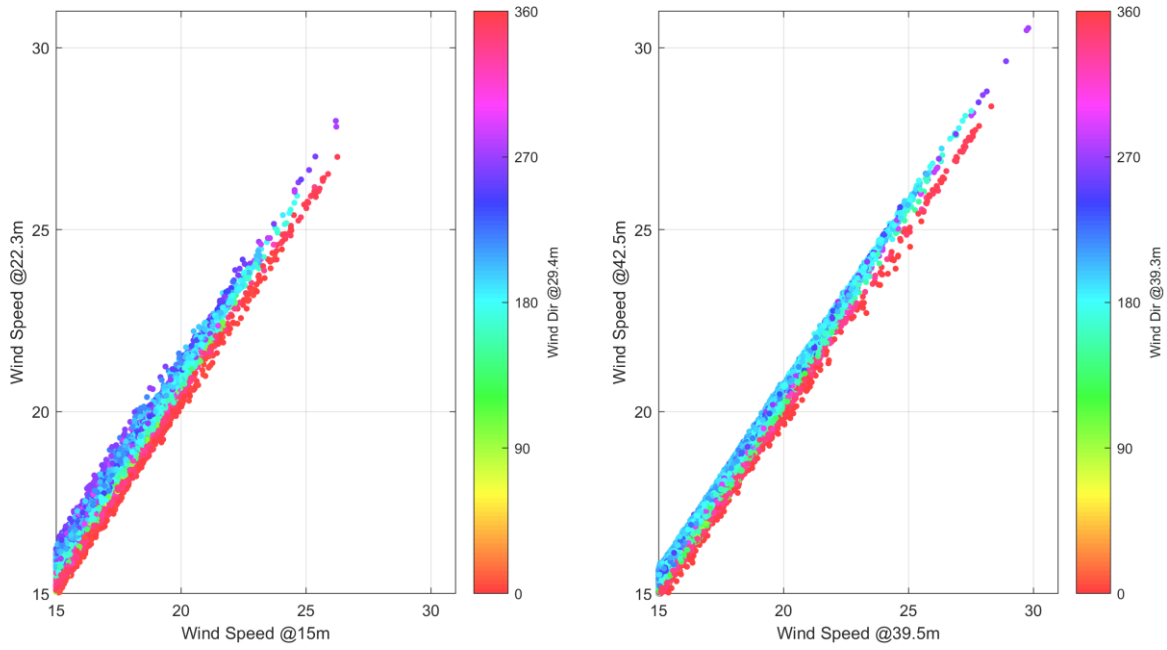



Figure B.3. Directional behaviour, Arklow Met Mast (Original).

[4] The cause is unknown, though may perhaps reflect some form of restart of logging, since all immediately follow a record with no data for *any* instrument, including for temperature and pressure. Timestamps are 2011-03-17 17:10, 2011-03-18 17:40, 2011-03-28 12:30, 2018-04-10 23:10 and 2018-05-18 11:40.

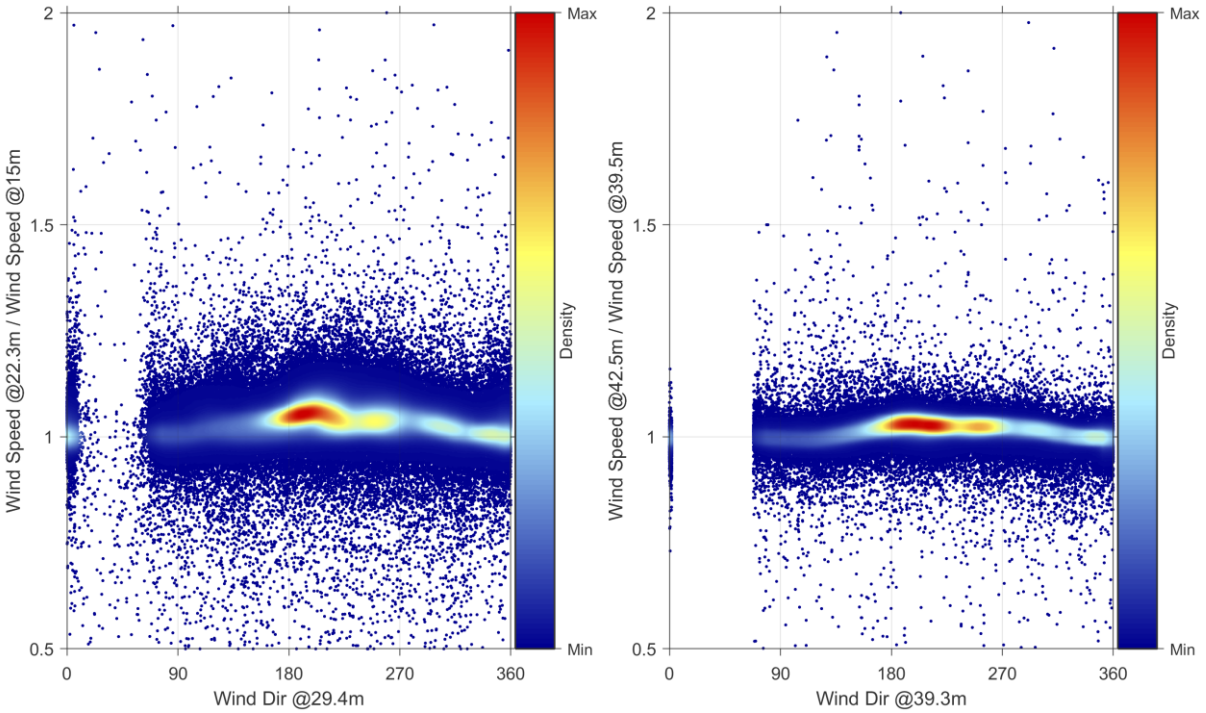



Figure B.4: Directional speed ratios, Arklow Met Mast (Original).

Such differences cannot be seen in the LiDAR data (see Figure B.5 and Figure B.6), although there is only a single year of data when compared to the sixteen years from the met mast. Indeed, as shown in Figure B.7, a very large proportion of the highest wind speeds from the north occur on a *single day,* February 27th 2001.

Given the proximity of this northern direction to the sheltered regions of the anemometers, it is certainly possible that the differences seen are caused by the mast itself, rather being a natural effect. At the same time, there is perhaps not enough evidence to simply reject the northern data because of these differences. For the present purposes then, we treat the above data as being valid whilst noting that:

- The uncertainty with regard to these data should be borne in mind when reviewing any validation plots for the Arklow met mast.
- The bulk calibration of the model data is based not only on data from all directions at the met mast, but also on comparisons at a number of other locations. As such, the effect of any errors here – which Figure B.3 suggests are generally less than 1 m/s – will be greatly reduced in any final calibration.

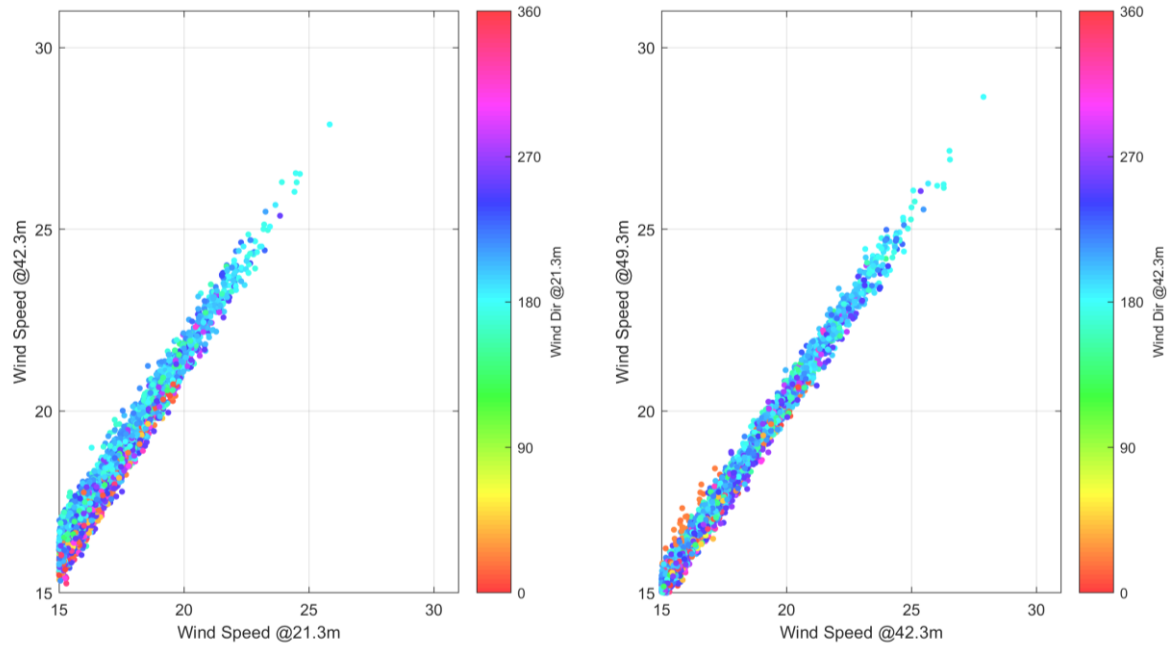



Figure B.5. Directional behaviour, Arklow LiDAR.

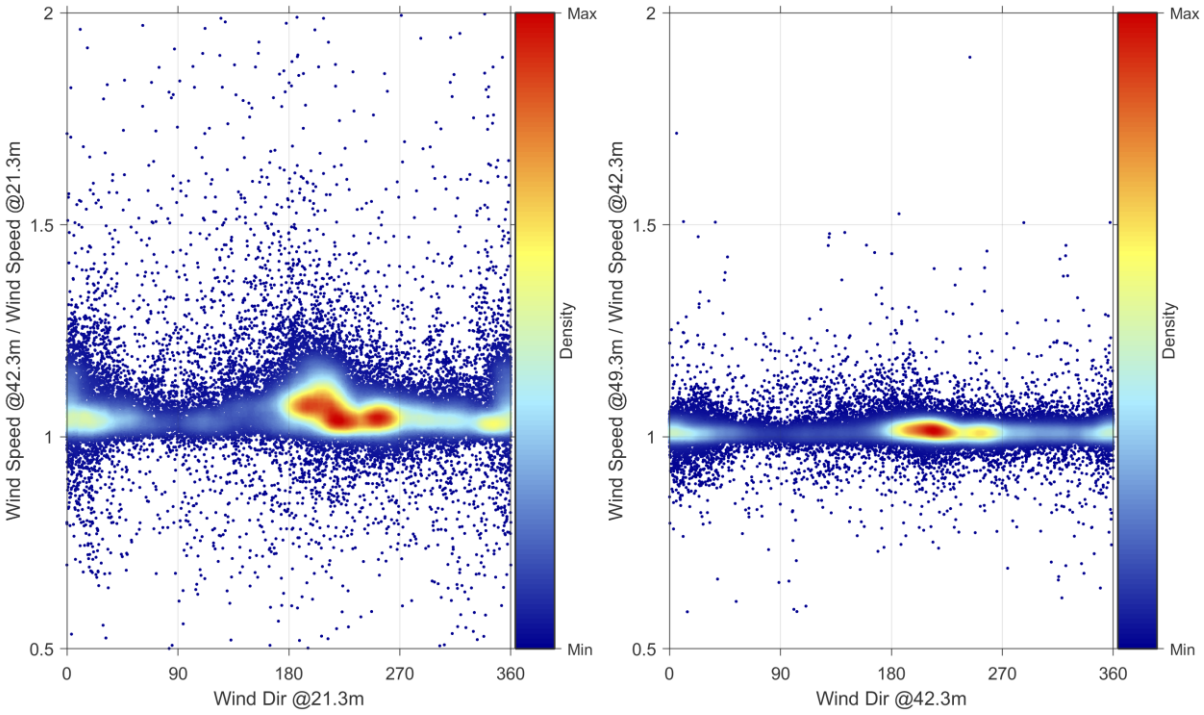



Figure B.6: Directional speed ratios, Arklow LiDAR.

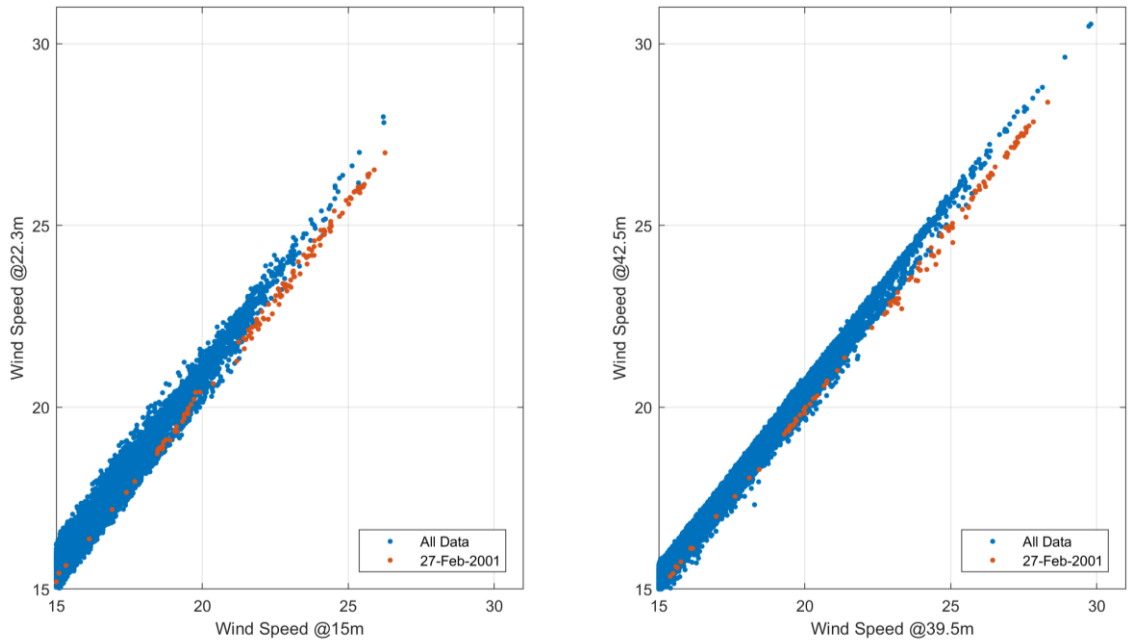



Figure B.7. February 27th 2001, Arklow Met Mast (Original).

### B.4.2.3 Wind Speed Validation: Original Dataset

Omnidirectional validation plots and statistics comparing the Vortex model data with the Arklow Met Mast (Original) measurements are shown in Figure B.8. Here, and in all subsequent comparisons, unless otherwise stated, one hour mean wind speeds are used for measured data.

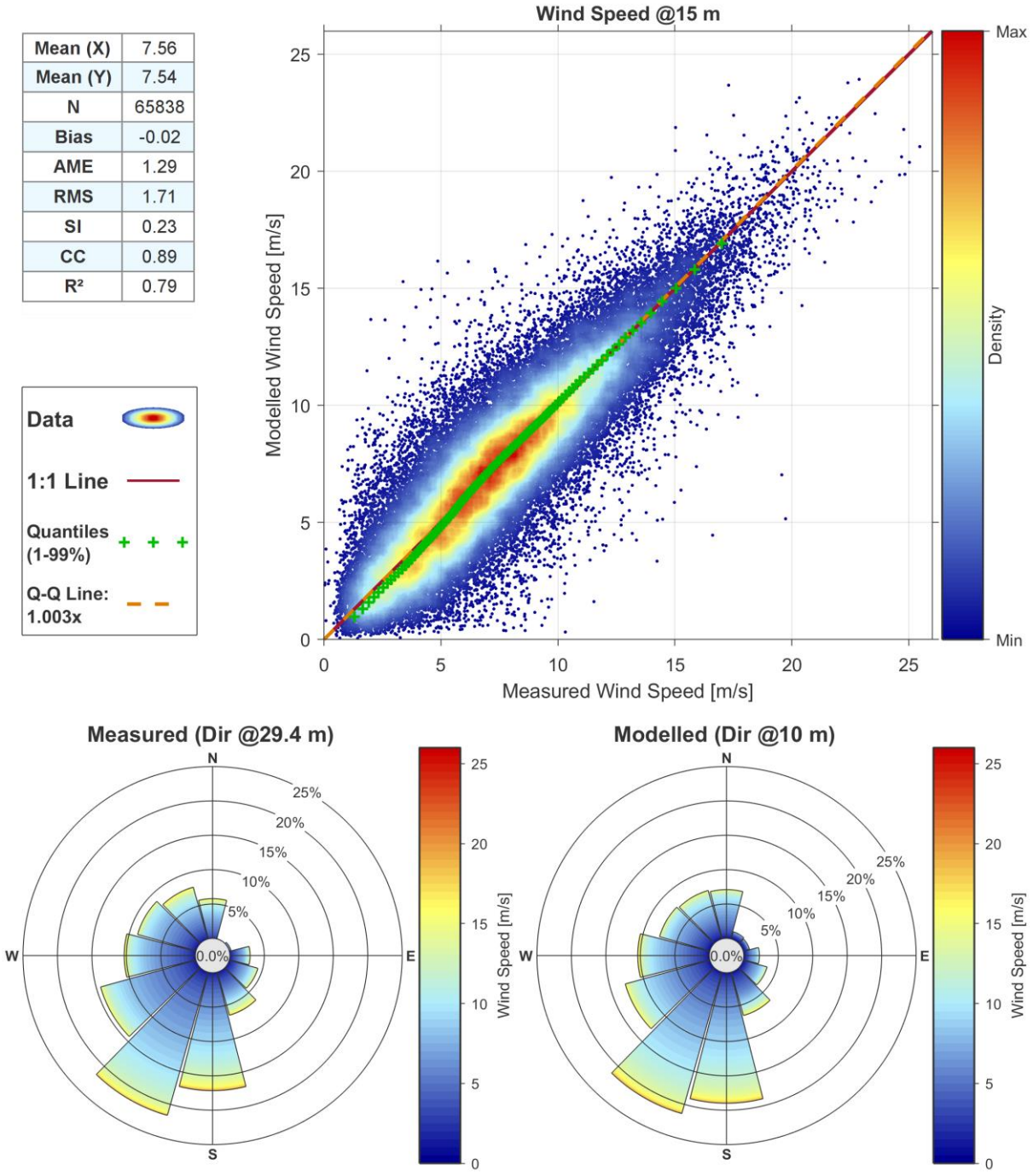



Figure B.8. Model validation, Arklow Met Mast (Original), wind speeds at 15 mAMSL.

Data split by directional sector are shown in Figure B.9. In reviewing this Figure, it is also worth noting that directions between 7 and 67 °N have been removed due to shading effects of the mast. However, as stated in Section B.4.2.2, *combined* wind directions from *both* vanes were used in this quality control step, whilst this Figure classifies data by the *closest* wind vane to 15m. As such, some values do appear in the sector from 15 to 45° which might otherwise be expected to be empty.

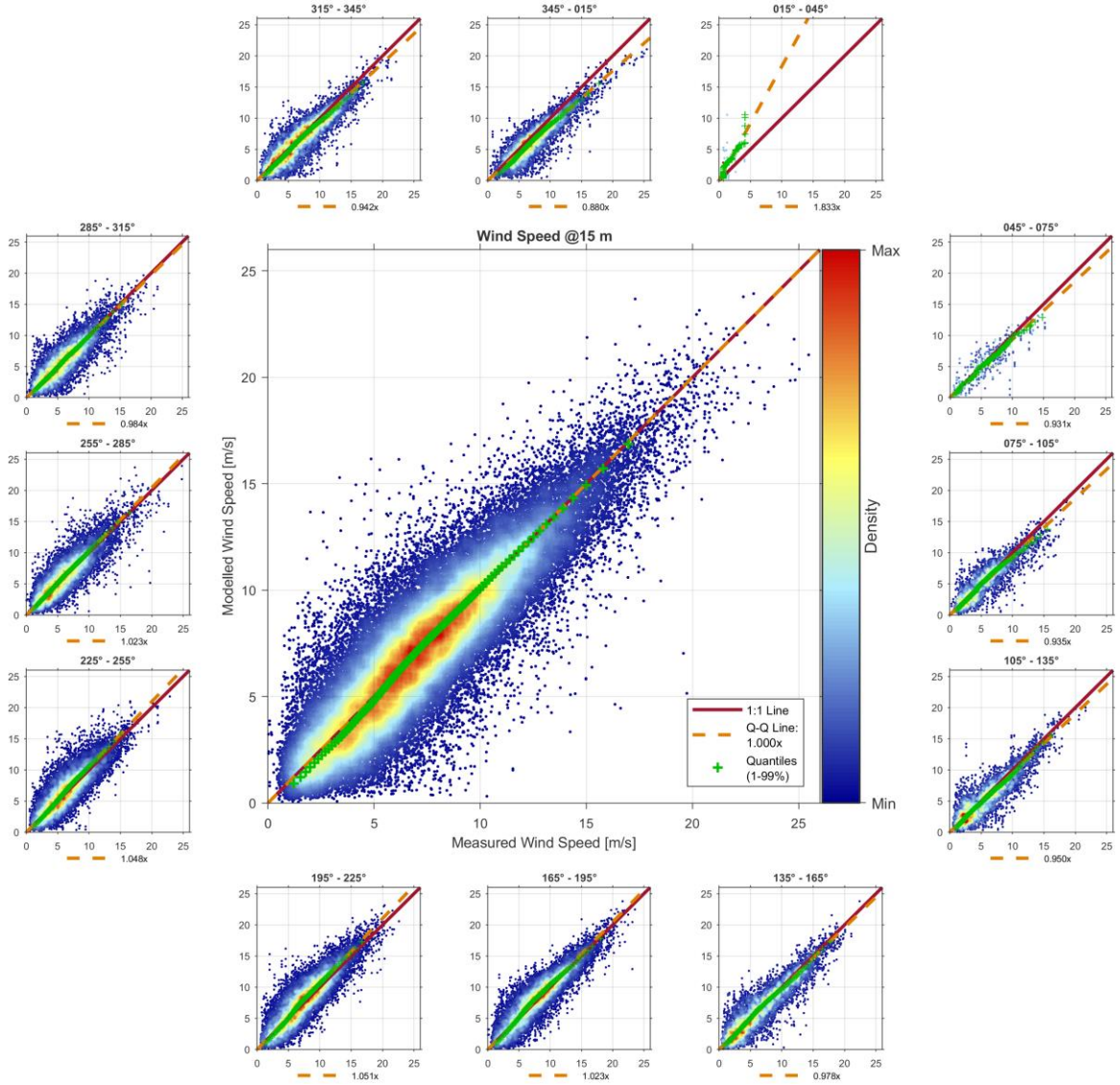



Figure B.9. Model validation, directional sectors, Arklow Met Mast (Original), wind speeds at 15 mAMSL.

Across both Figure B.8 and Figure B.9, model performance appears good, with the exception of the 345 to 15 °N sector, where there is significant underprediction, in particular at the highest wind speed levels. As was the case when reviewing the measurements themselves in Section B.4.2.2, there is no conclusive evidence as to whether this is due to mast effects or some natural phenomenon that is not fully captured in the model. It is worth noting that the differences seen at higher wind speeds from these northerly directions reach up to 5 m/s, much larger than the discrepancies of approximately 0.5 m/s seen when comparing met mast levels in Figure B.3. However, this does not eliminate mast effects as a cause, at least in part: it may simply be that measurements at all levels are impacted, but by different amounts at different elevations. Again, in the absence of firm evidence, we do not discard any additional data here, but note that these differences from northern sectors may warrant more investigation if they are also apparent at other locations used for validation.

Validation plots at 22.3, 29.6, 39.5 and 42.5 mAMSL are provided in Figure B.10 through Figure B.13. Directional behaviour at these levels is similar to that seen at the 15 mAMSL level seen in Figure B.9, with very

good performance for all sectors from directions unaffected by the met mast itself, *except* for the sector from 345 to 15 °N, where the model underpredicts.

| | |
|---|---|
| Mean (X) | 7.93 |
| Mean (Y) | 7.93 |
| N | 88156 |
| Bias | -0.00 |
| AME | 1.32 |
| RMS | 1.75 |
| SI | 0.22 |
| CC | 0.89 |
| $R^2$ | 0.80 |

Data
1:1 Line
Quantiles (1-99%)
Q-Q Line: 1.002x

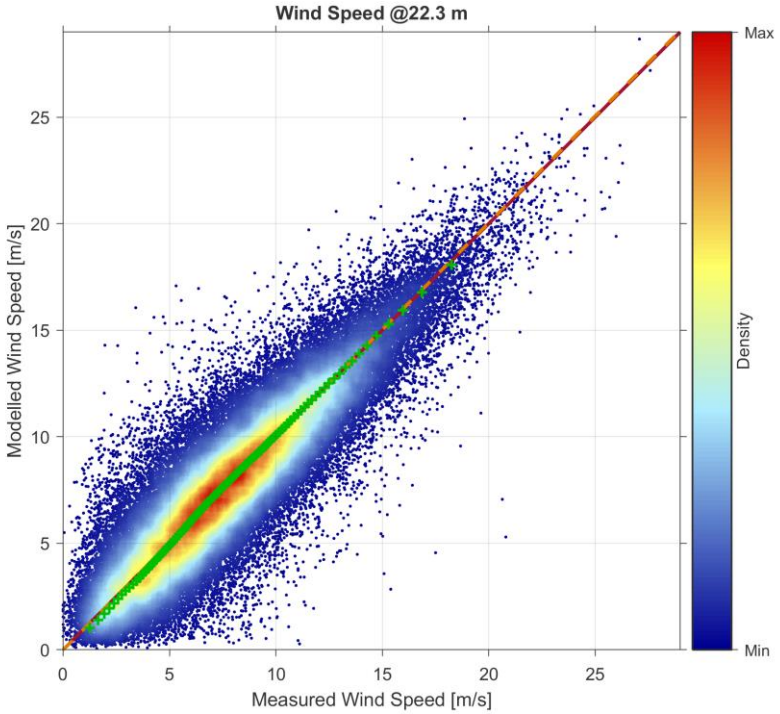



Figure B.10. Arklow Met Mast (Original), wind speeds at 22.3 mAMSL.

| | |
|---|---|
| Mean (X) | 8.09 |
| Mean (Y) | 8.15 |
| N | 121674 |
| Bias | 0.06 |
| AME | 1.35 |
| RMS | 1.80 |
| SI | 0.22 |
| CC | 0.89 |
| $R^2$ | 0.80 |

Data
1:1 Line
Quantiles (1-99%)
Q-Q Line: 1.008x

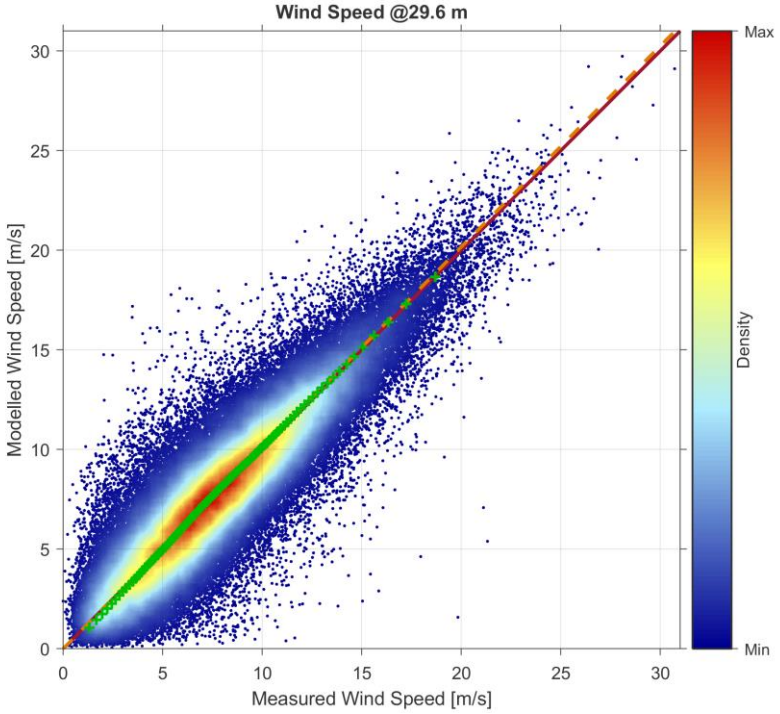



Figure B.11. Arklow Met Mast (Original), wind speeds at 29.6 mAMSL.

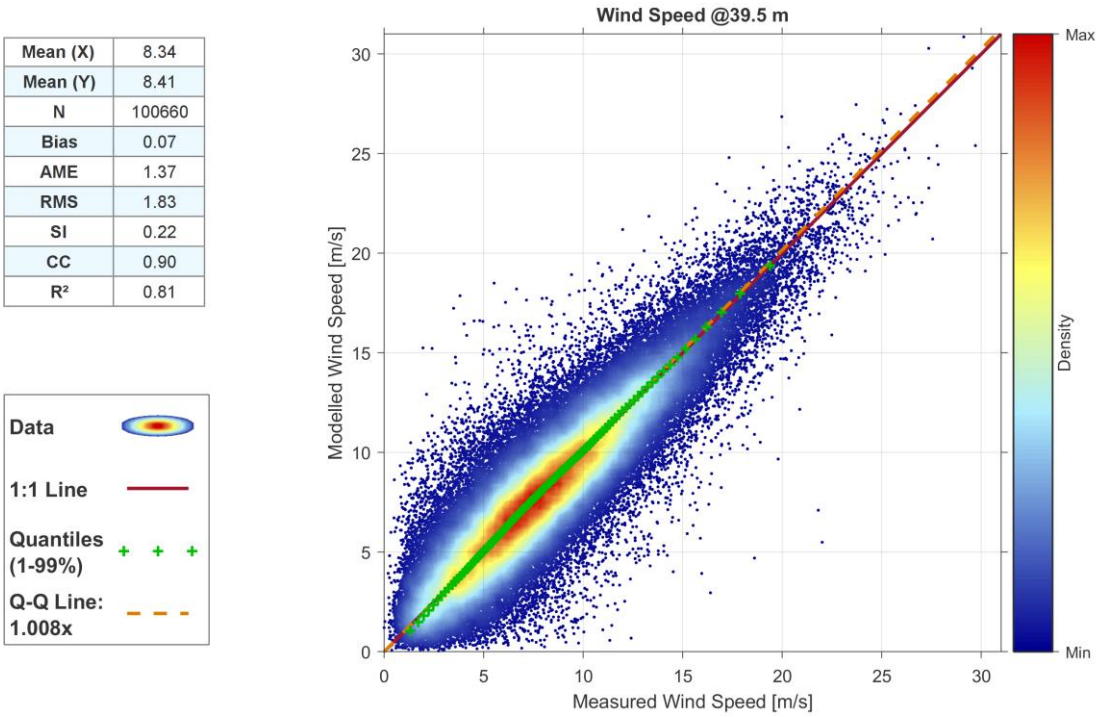



Figure B.12. Arklow Met Mast (Original), wind speeds at 39.5 mAMSL.

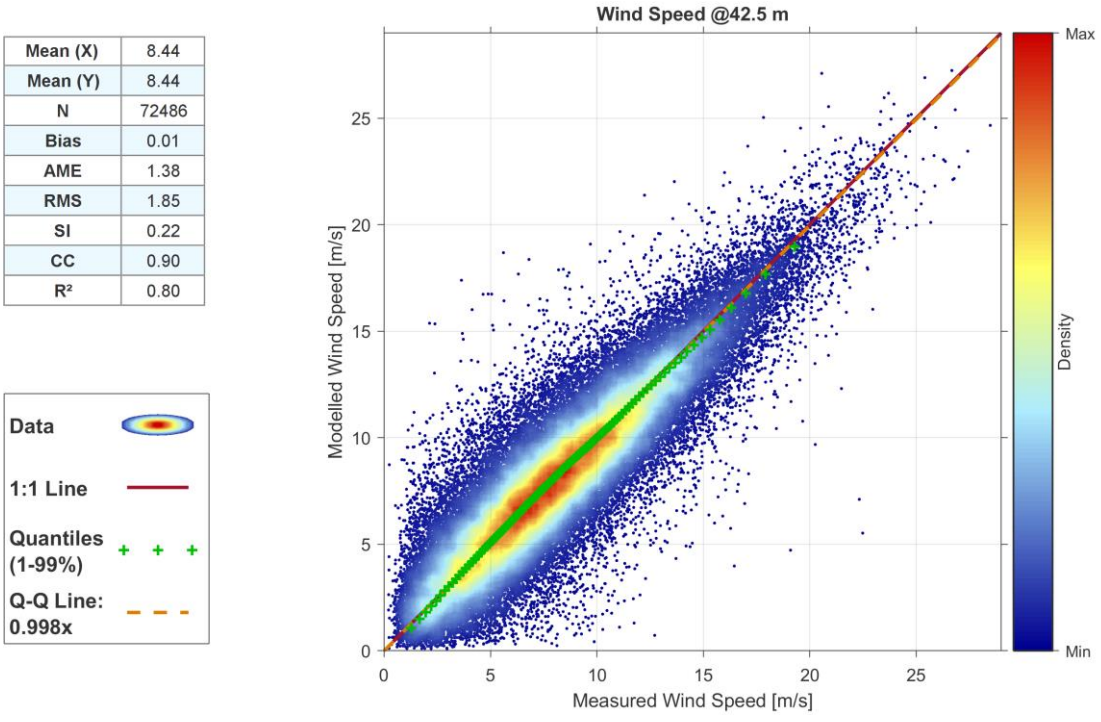



Figure B.13. Arklow Met Mast (Original), wind speeds at 42.5mAMSL.

As such, directional sector plots for these levels are omitted for conciseness, though can be provided upon request. It is perhaps worth noting that the performance for this sector gradually improves with elevation, as shown in Figure B.14, though again the reasons are unclear. For example, it may be caused by mast effects reducing as the mast narrows with elevation. But equally, since the model has levels representative of 10 mAMSL and 50 mAMSL, it may reflect better model performance at 50 mAMSL, with boundary effects not fully represented by the model for this sector leading to increased underprediction closer to the surface.

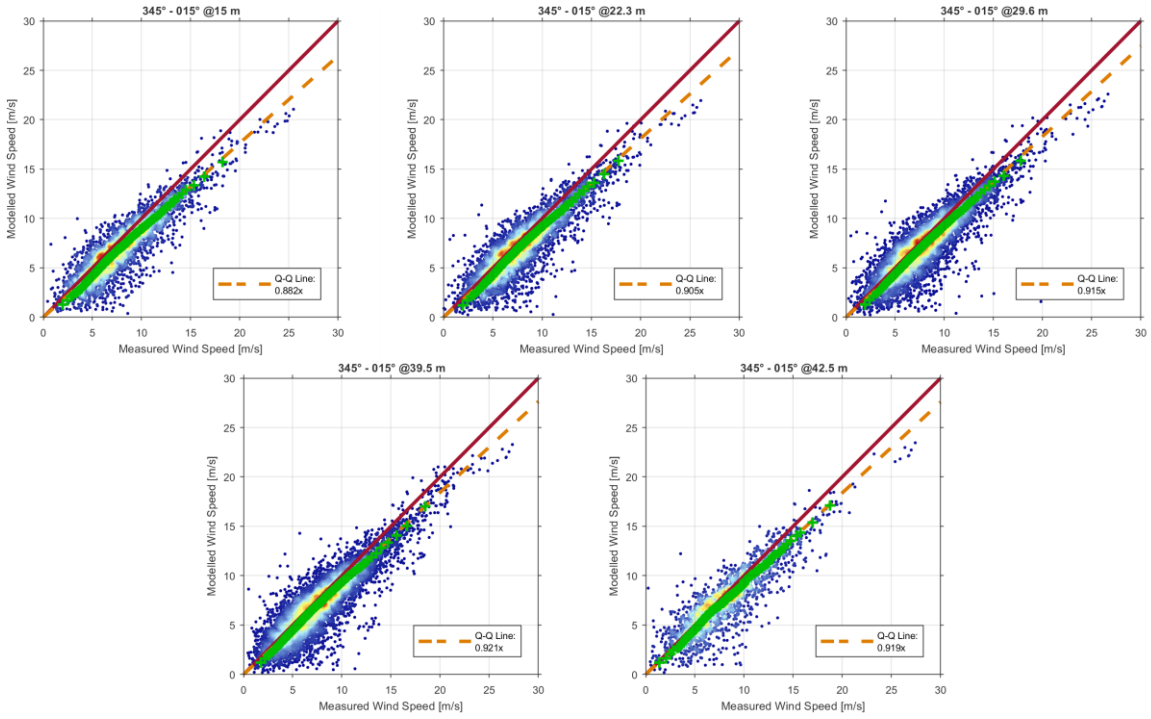



Figure B.14. Arklow Met Mast (Original), 345 to 15 °N wind speeds.

### B.4.2.4 Wind Speed Validation: Synthesised Dataset

An omni-directional validation of wind speeds at 42.5 mAMSL from the *synthesised* Arklow met mast dataset is shown in Figure B.15, with values split by directional sector shown in Figure B.16. Unsurprisingly, given the origin of the measured dataset, there is very little difference in model performance when compared to the original met mast dataset.

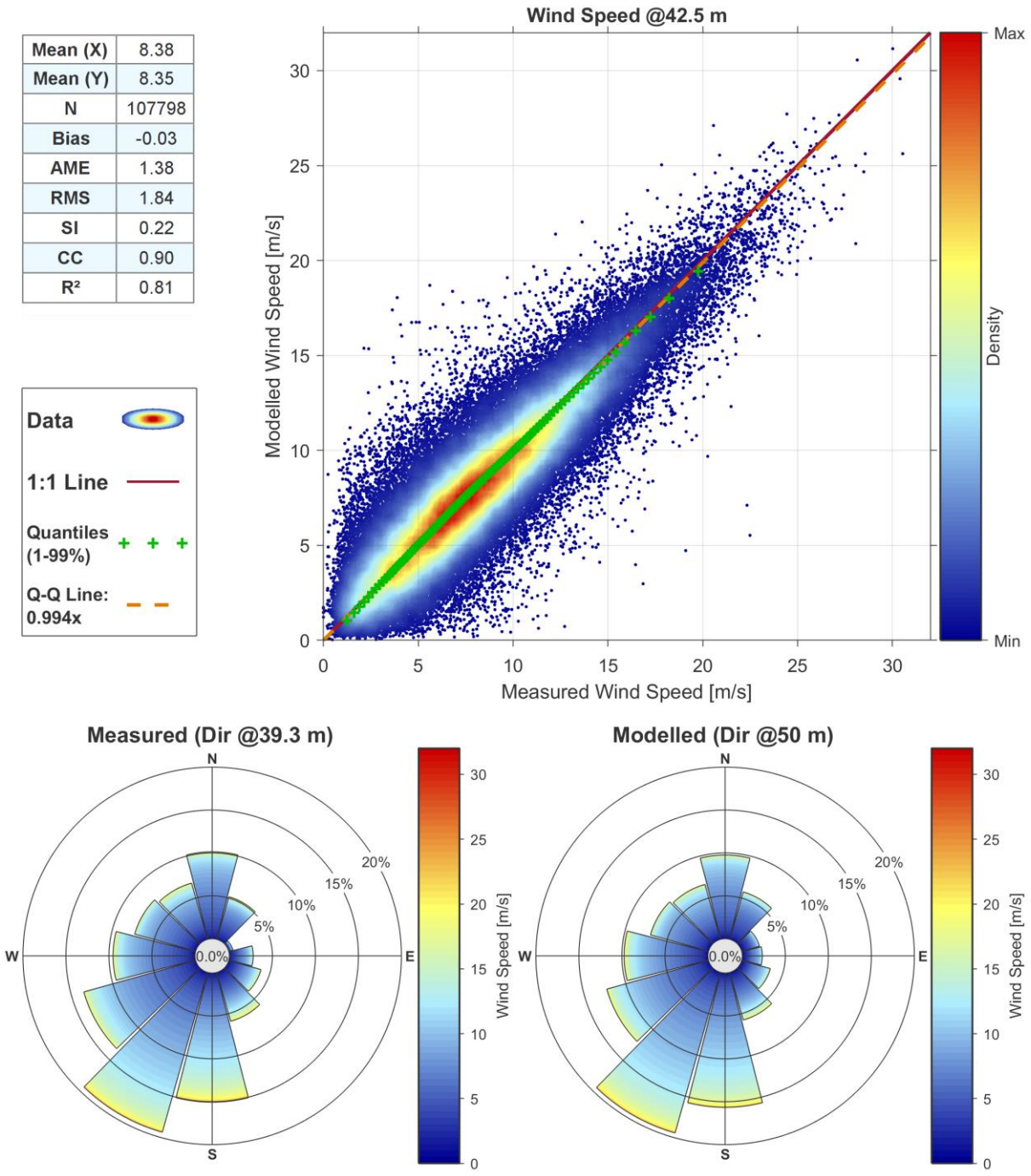



Figure B.15. Model validation, Arklow Met Mast (Synthesised), wind speeds at 42.5 mAMSL.

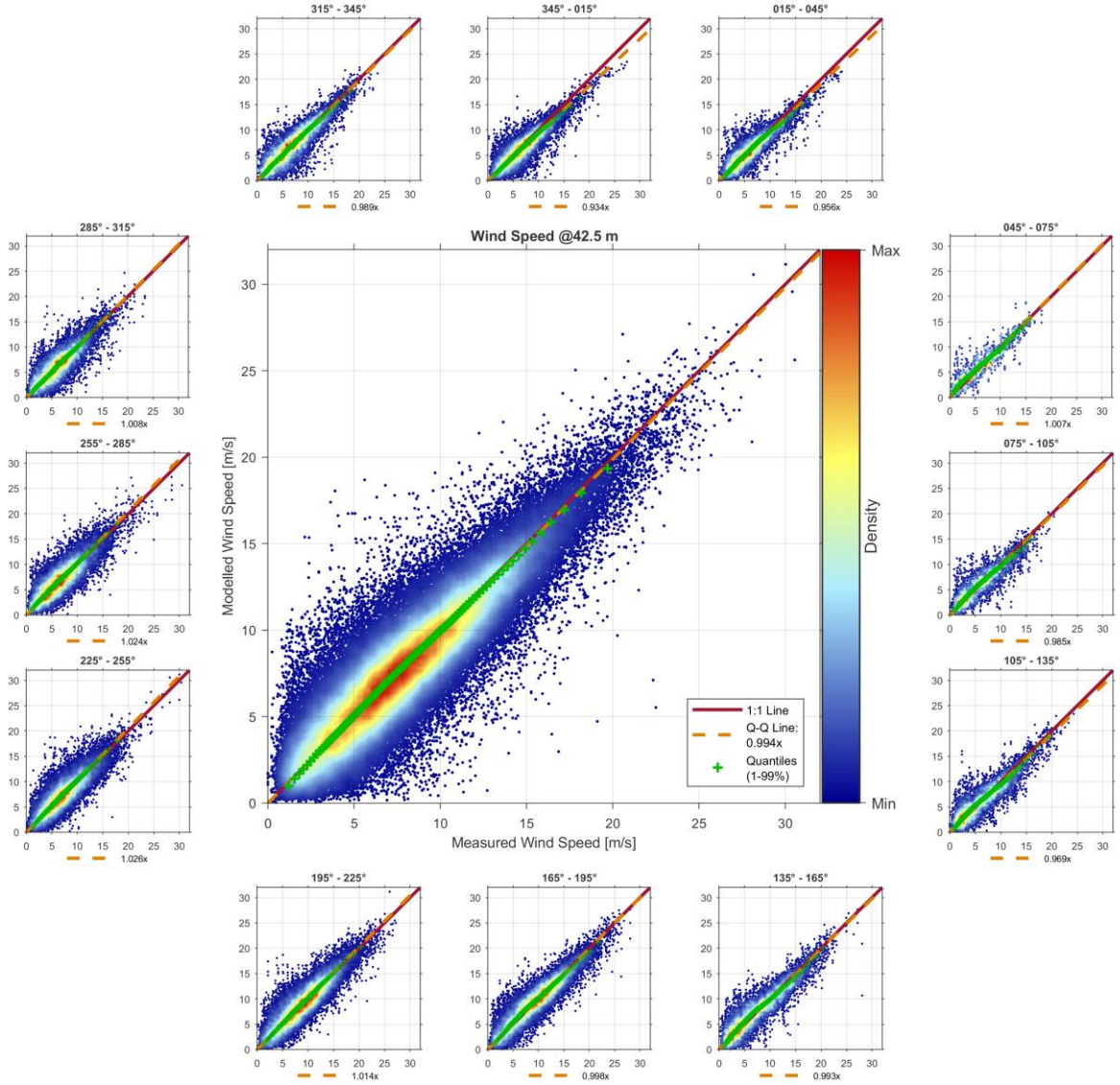



Figure B.16. Model validation, directional sectors, Arklow Met Mast (Synthesised), wind speeds at 42.5 mAMSL.

### B.4.2.5 Wind Direction Validation

Directional validations for the original met mast dataset are shown in Figure B.17 and Figure B.18. Please note that:

a) Measurements are compared to model data at the closest model level, and in particular, unlike with the wind speeds of previous comparisons, no interpolation or assumed profile is used to adjust model values to measured elevations.
b) Where necessary, plotted measured directions are adjusted by adding or subtracting 360 degrees such that differences between modelled and measured directions are always in the range [-180°, 180°].

In both cases, the model is shown to perform well.

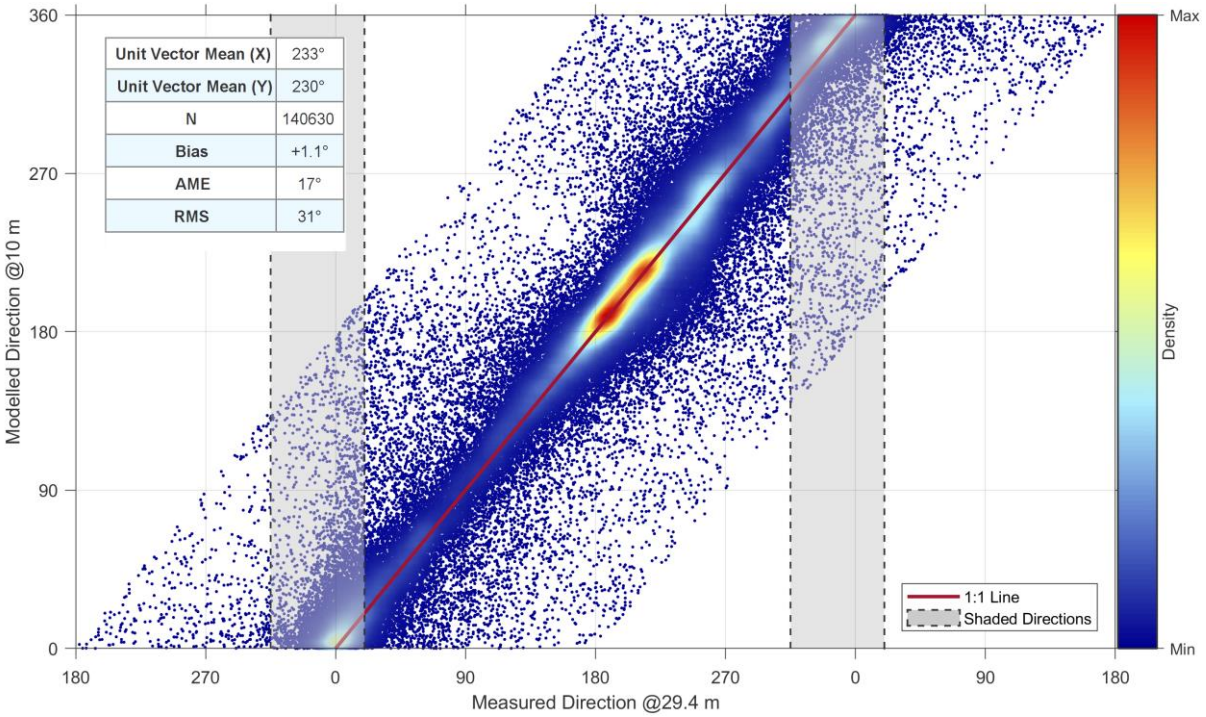



Figure B.17. Model validation, Arklow Met Mast (Original), wind directions at 29.4 mAMSL.

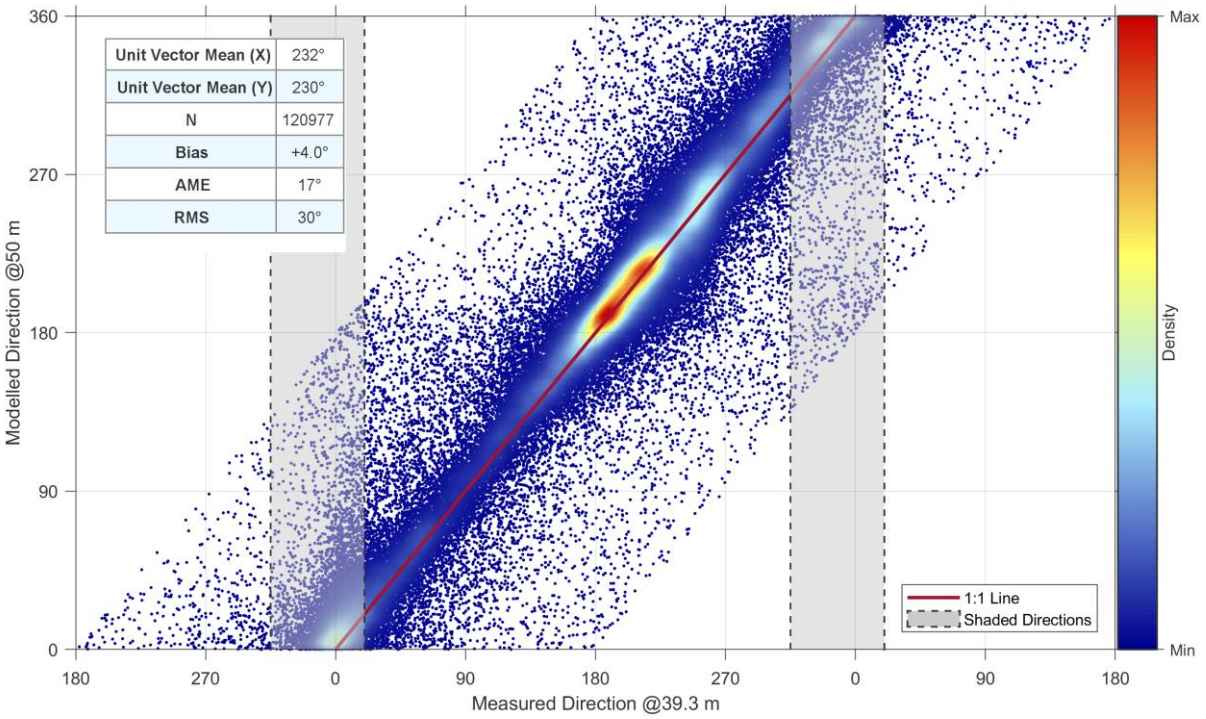



Figure B.18. Model validation, Arklow Met Mast (Original), wind directions at 39.3 mAMSL.

### B.4.3 Arklow LiDAR

#### B.4.3.1 Overview

The Arklow Met Mast (see Section B.4.2) was replaced by a LiDAR, which provides measurements from November 2019 to the present. At the time of writing, this gives twelve months of measurements, though as modelled data are only available through to 29th August 2020, just under 10 months of values can be compared in this Section. Full details of the LiDAR and accompanying data can be found in the SSE met mast and LiDAR Wind Analysis Report [21], but by way of summary:

- Wind speeds and directions are available at elevations of 21.3, 42.3, 49.3, 74.3, 99.3, 129.3, 159.3, 184.3, 219.3 and 299.3 mAMSL.
- Data begins on 7th November 2019 at all levels, except that at 74.3 m, which begins on 5th September 2020.
- Additional wind speeds and directions are available from a met station attached to the LiDAR, at an elevation of approximately 12 mAMSL. The reliability of these data is unclear – indeed, wind speeds regularly exceed those of the LiDAR at much higher levels – and as such they are not included in the comparisons which follow.

#### B.4.3.2 Quality Control

As described in Section 4.2 of the SSE Wind Analysis Report [21] for the Arklow Met Mast and LiDAR, a number of steps were taken in order to review the data, correct issues related to directional alignment, and flag faulty values as necessary. The data file supplied to MetOceanWorks specifies that values *are* included for the following flags:

> <Unflagged data>, Synthesized, potentialSpeedIssue

but omitted for data flagged by:

> Invalid, MaxVertSpeed, MinPts, PotentialDirectionIssue

As described for the Arklow Met Mast in Section B.4.2.2, time series and scatter plots of the data were reviewed, but no additional data were removed prior to carrying out model validation.

#### B.4.3.3 Model Validation

Validation plots for measured wind speeds at 21.3 m and 49.3 m are shown in Figure B.19 and Figure B.20, whilst validations split by direction are shown in Figure B.21 and Figure B.22. Behaviour is very similar to that seen above for the met mast, although comparisons in the 345 to 15 °N sector are a little improved. Any conclusions which may be drawn from this must be somewhat limited by the lack of higher wind speeds corresponding to this directional sector for the period in which modelled and measured data overlay.

Whilst only Figures for two measured elevations – being those closest to the two lowest model levels – are included here for conciseness, similar Figures for all LiDAR elevations can be supplied upon request.

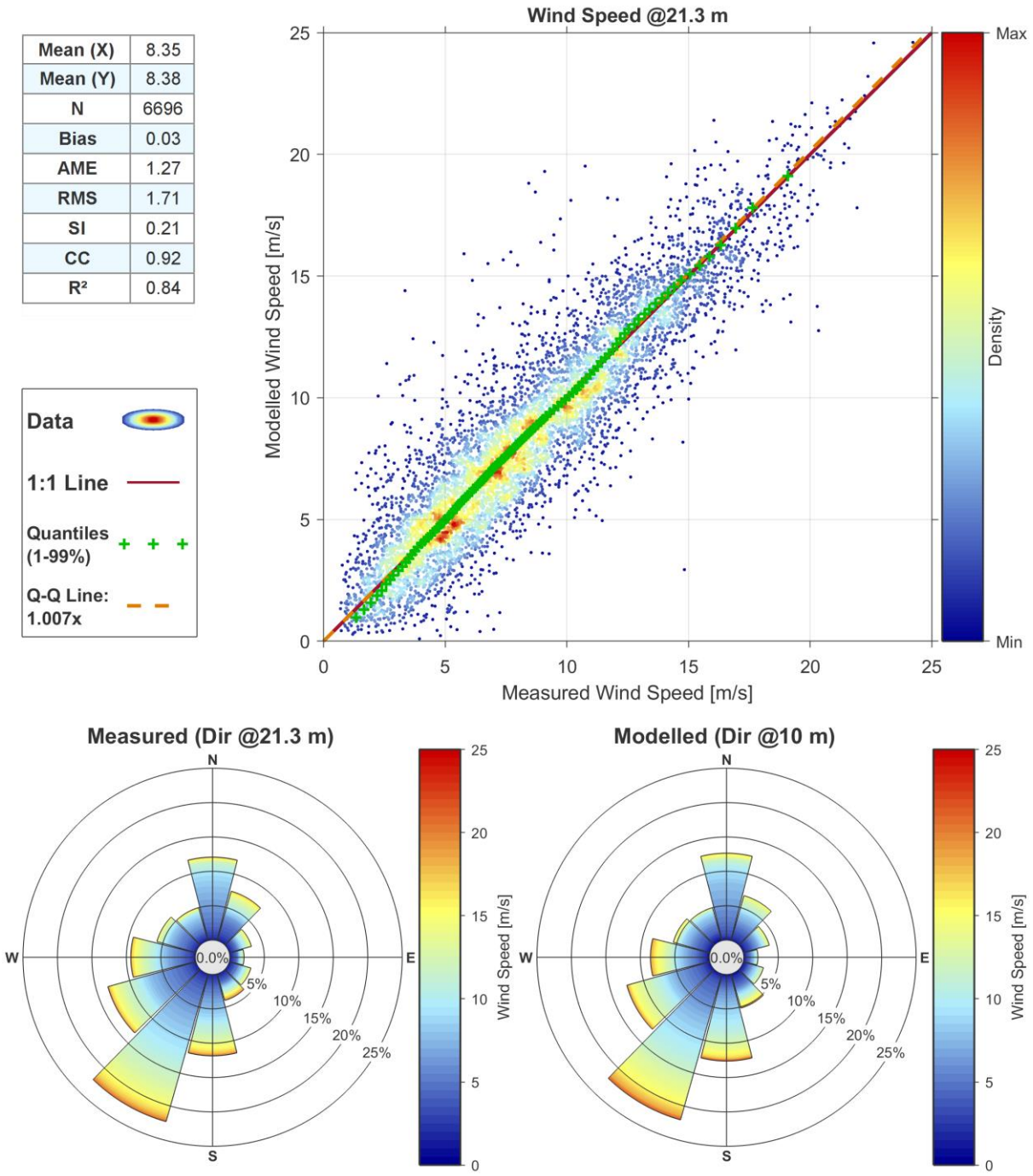



Figure B.19. Model validation, Arklow LiDAR, wind speeds at 21.3 mAMSL.

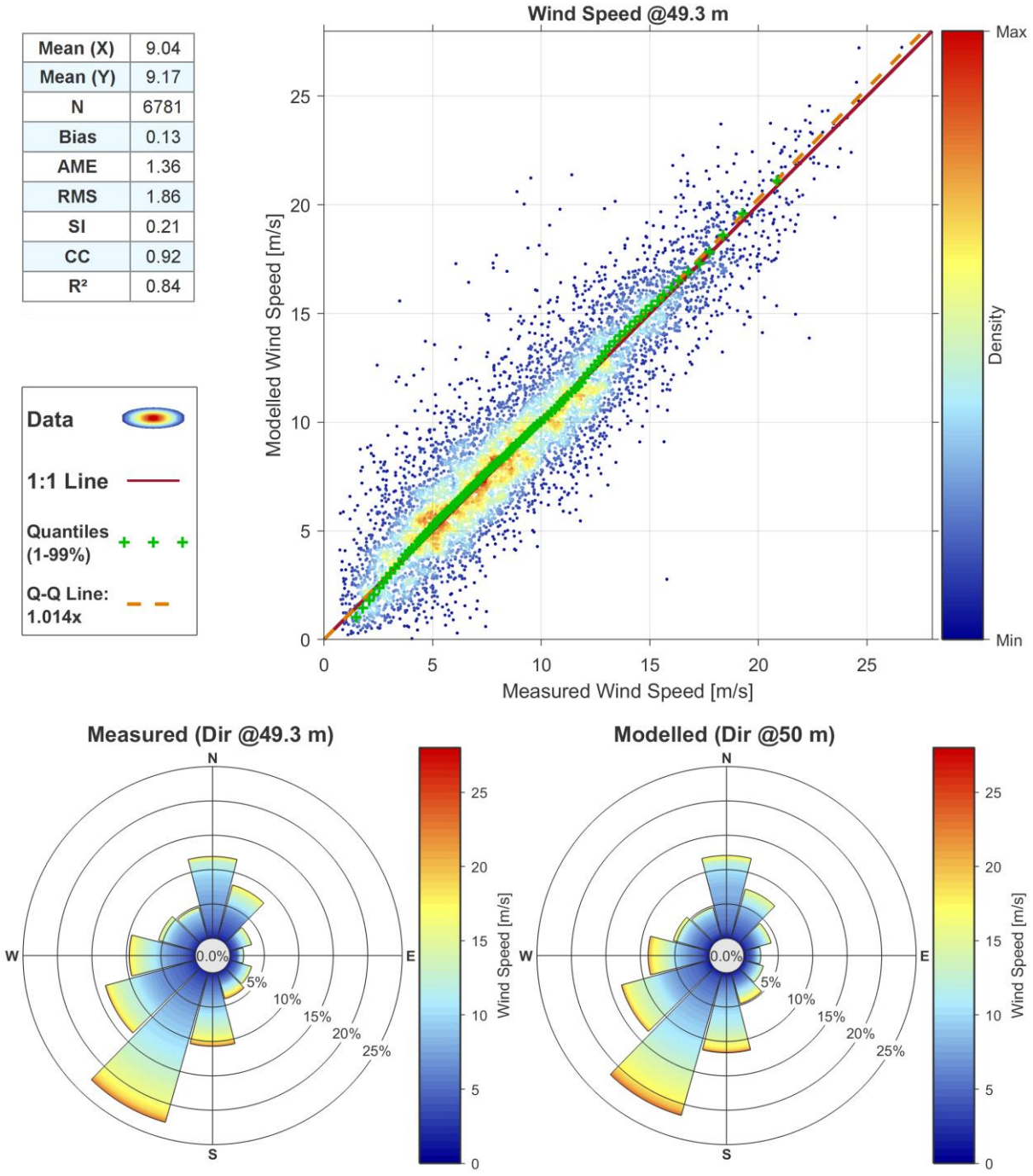



Figure B.20. Model validation, Arklow LiDAR, wind speeds at 49.3 mAMSL.

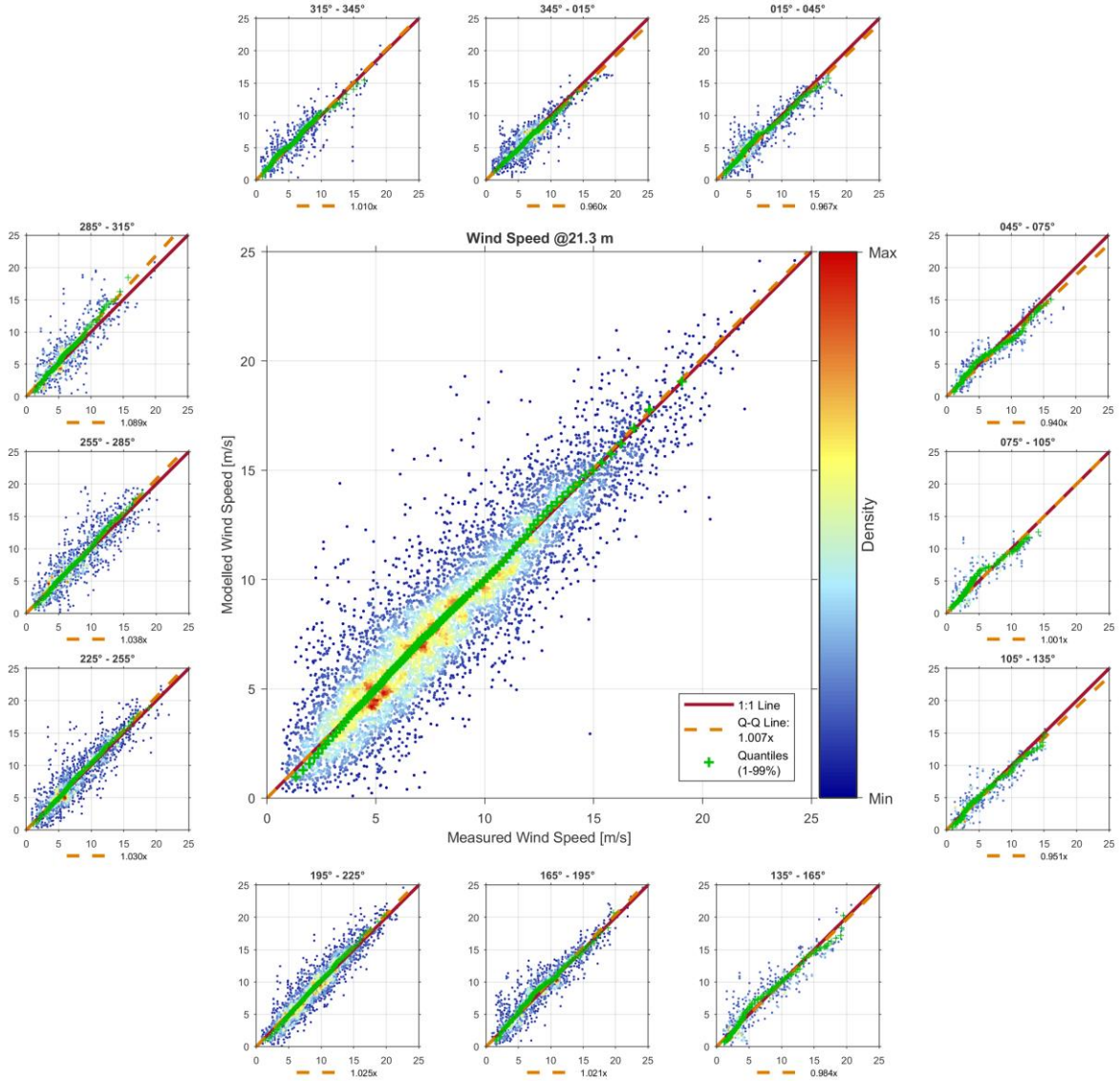



Figure B.21. Model validation, directional sectors, Arklow LiDAR, wind speeds at 21.3 mAMSL.

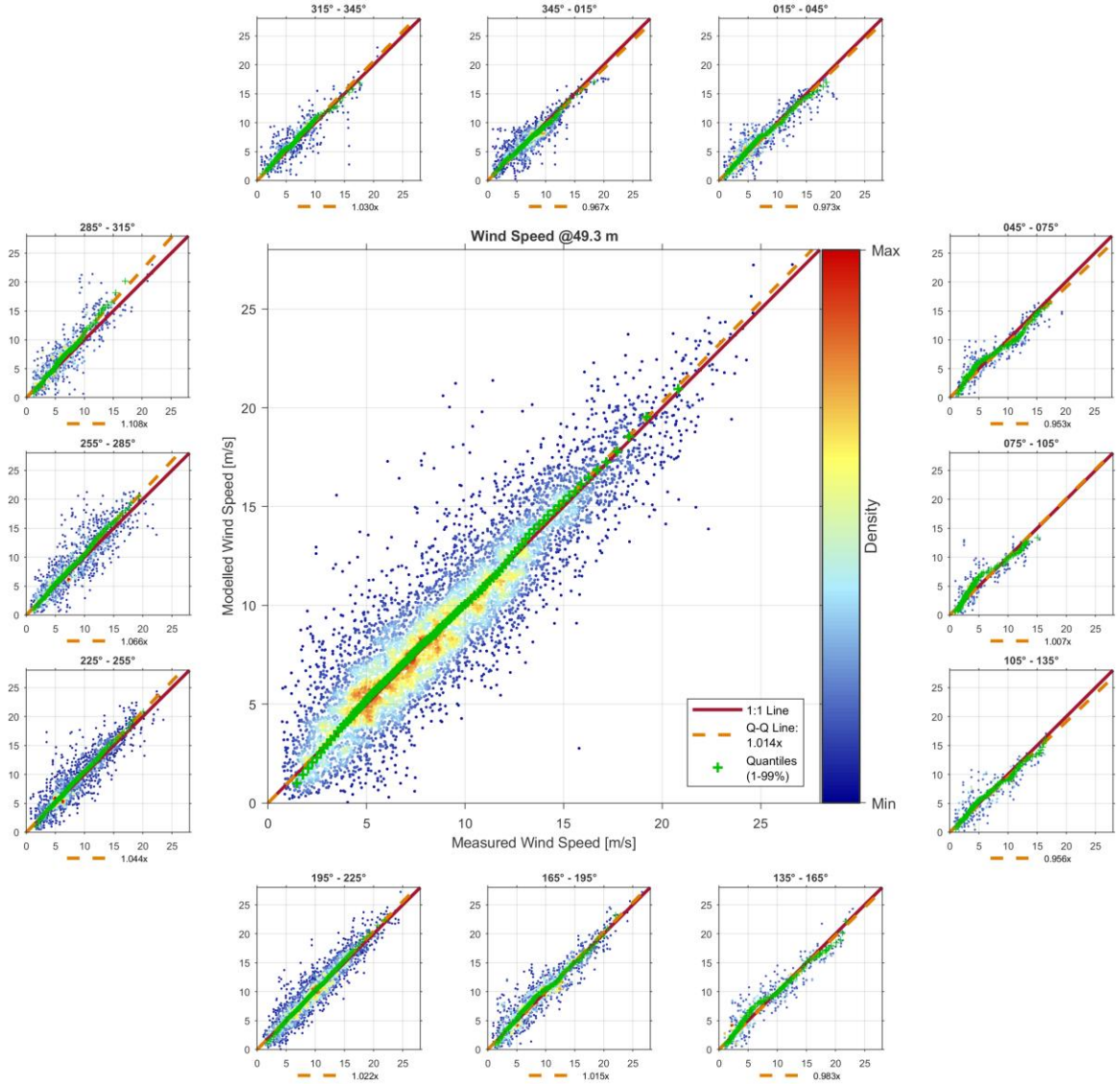



Figure B.22. Model validation, directional sectors, Arklow LiDAR, wind speeds at 49.3 mAMSL.

### B.4.4 M2 and M5 Buoys

#### B.4.4.1 Overview

The Irish Marine Data Buoy Observation Network[5] is managed by the Irish Marine Institute in collaboration with Met Éireann and the UK Met Office. The five available met buoys are shown in Figure B.23.

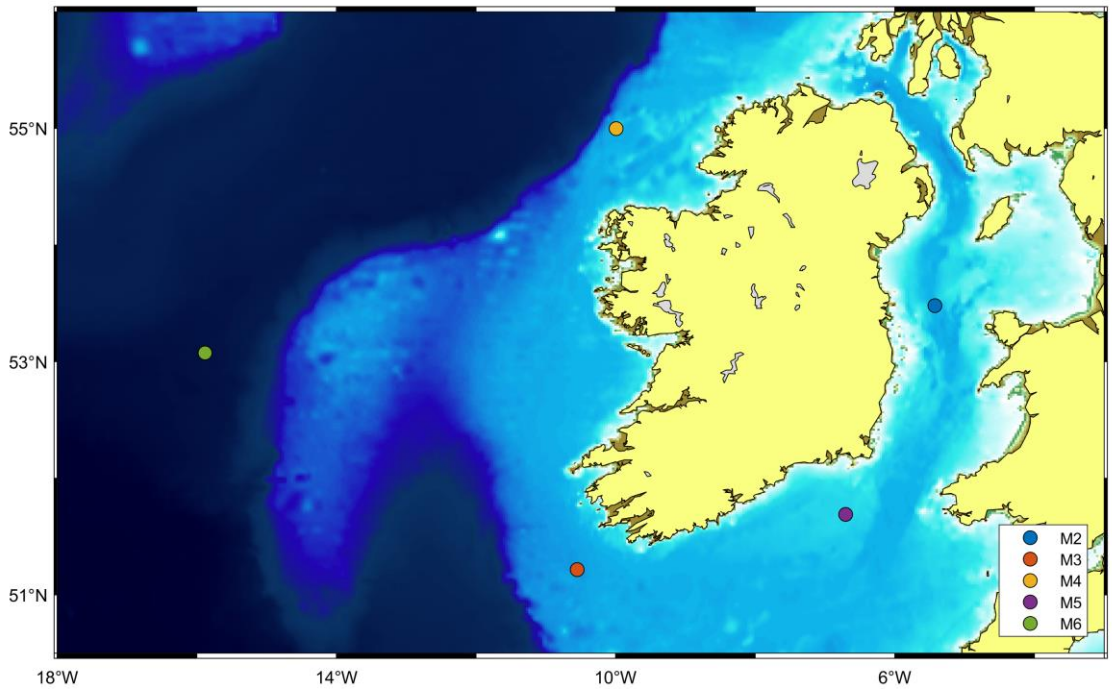



Figure B.23. Met buoy locations.

For this project, the M2 and M5 buoys are used for model validation, providing wind speed and direction at an elevation of approximately 3.5 mASL for the following periods:

- M2: 03-May-2001 to 27-Apr-2020 (the date when the data were downloaded).
- M5: 18-Oct-2004 to 27-Apr-2020 (the date when the data were downloaded).

#### B.4.4.2 Quality Control

As with all measurement datasets considered in this Appendix, time series of wind speed and direction were reviewed. In the case of the M2 and M5 datasets, a number of short periods of data were removed, primarily due to either repeated values or spikes in wind speed at or close to zero.

In reviewing the time series, it is also clear in both cases that buoys were updated part way through their measurement periods, with the resolution of wind speed values increasing. See Figure B.24 for example time periods before and after this update at M5.

[5] Please see http://www.marine.ie/Home/site-area/data-services/real-time-observations/irish-marine-data-buoy-observation-network for more details.

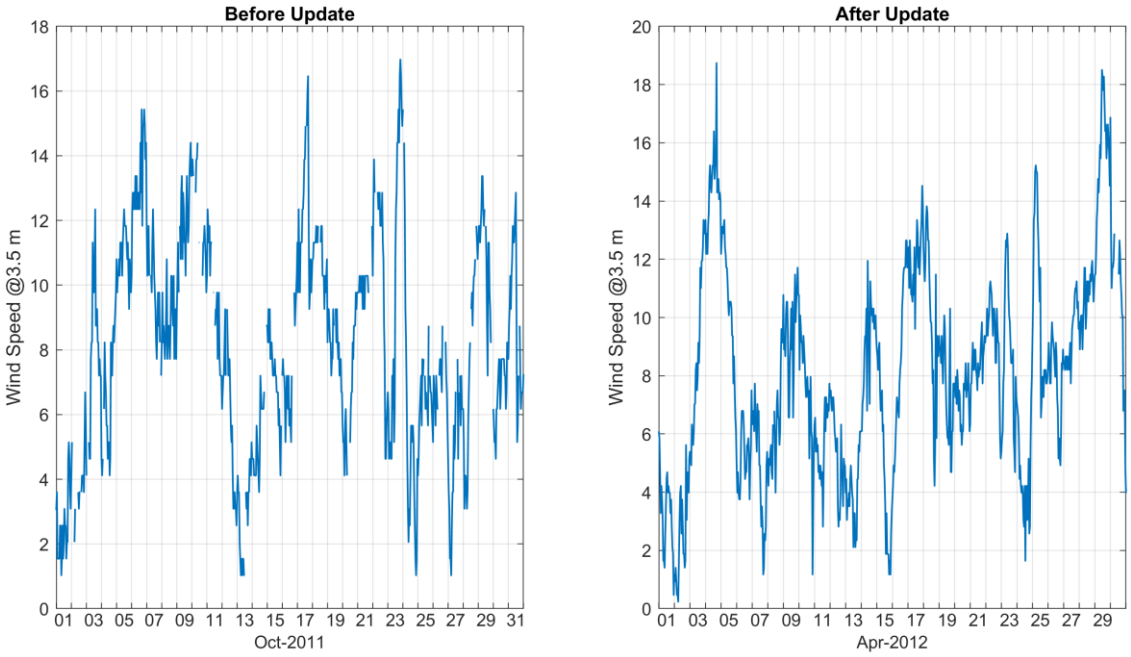



Figure B.24. Example periods before and after instrumentation update, M5.

We have not yet been able to establish exact dates of these changes from, for example, instrument documentation, but from the time series themselves have selected the following[6]:

- M2: 26-Oct-2010
- M5: 21-Feb-2012

When comparing to Vortex modelled data, there is also a marked change in relationships either side of these dates. For example, a number of key validation statistics, calculated for rolling 90-day periods are shown for M2 in Figure B.25 and M5 in Figure B.26. In both cases, prior to the update, there are much larger difference between mean wind speed values, and a notable trend in the "Q-Q Fit Multiplier". This is the slope of the straight line passing through (0, 0) which is the best fit to quantiles of modelled and measured data. After the update, the model appears to perform much better, and behaviour of statistics remain similar.

Though the differences seen may be due to change in *model* performance, similar behaviour is not seen when compared at the Arklow met mast. Further, the stark change in behaviour, particularly at M2 which are coincident with instrument update, suggests that it is the accuracy of the measurements which should be in question. As a result, for the validation and calibration steps which follow, only data *after* the estimated dates noted above are used with older data ignored.

[6] Indeed, the differences are even more apparent when considering the wave data from these instruments, and as discussed in Section C.3.3.2 are at least in part explained by a change in the met buoy itself.

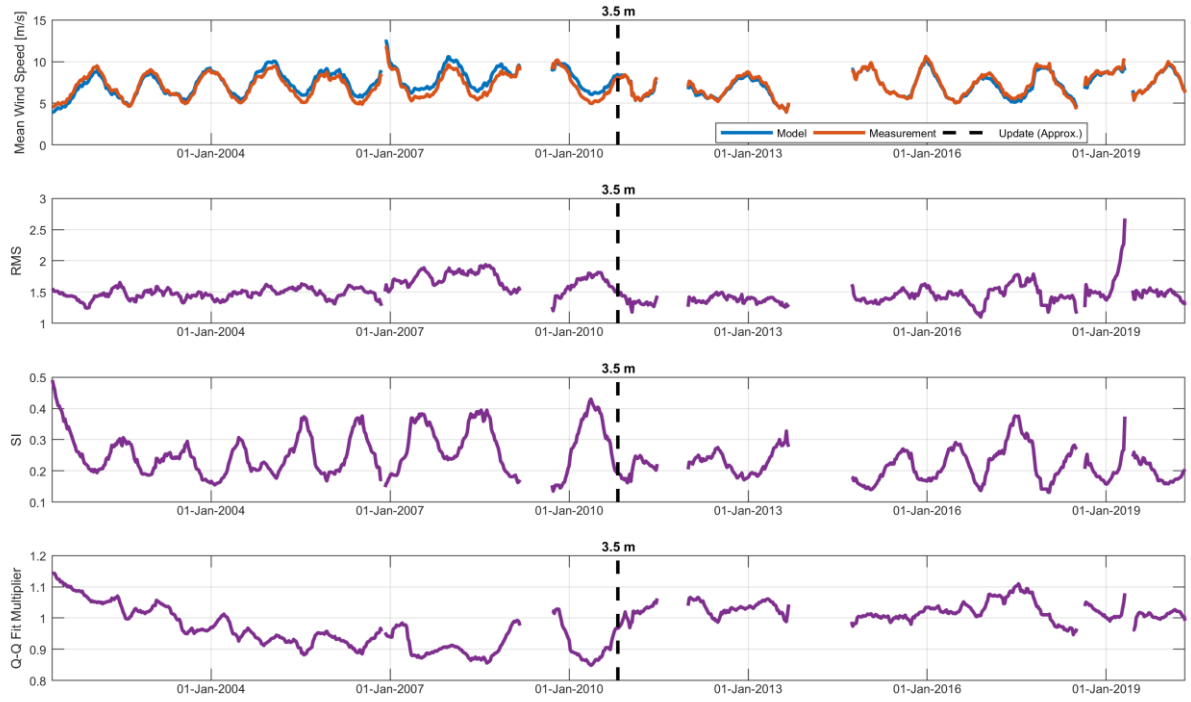



Figure B.25. Validation statistics, rolling 90-day period centred on date plotted, M2.

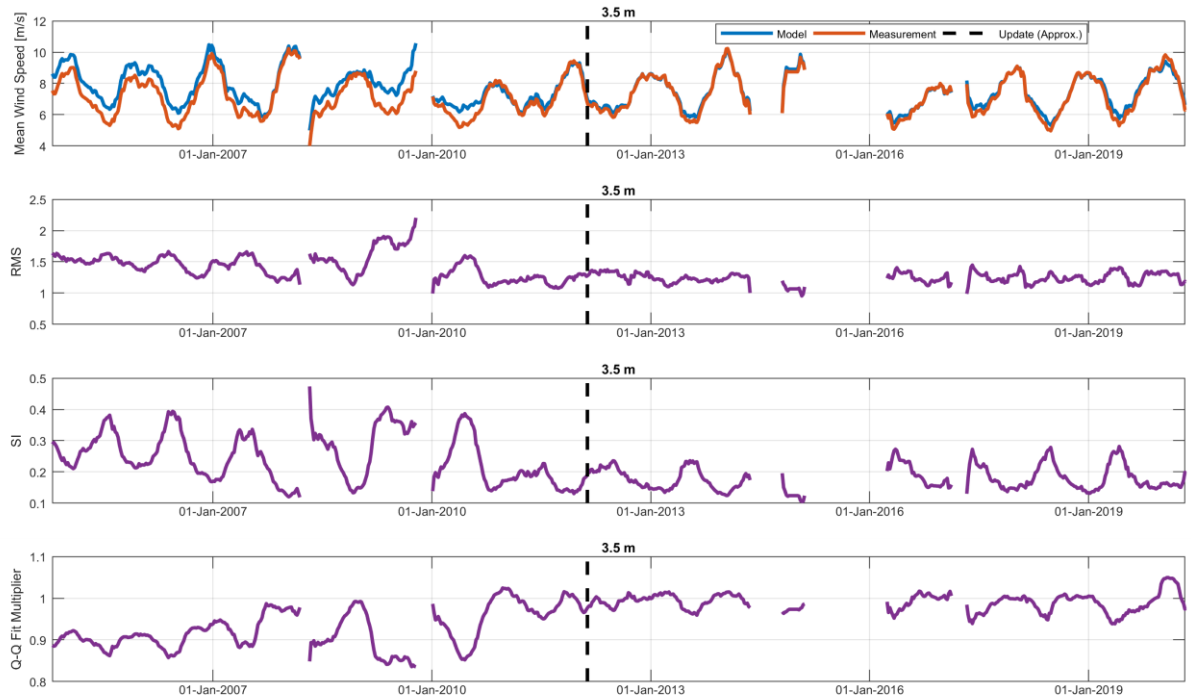



Figure B.26. Validation statistics, rolling 90-day period centred on date plotted, M5.

### B.4.4.3 Model Validation

Validation plots for measured wind speeds are shown for M2 in Figure B.27 and M5 in Figure B.28, with values split by directional sector in Figure B.29 (M2) and Figure B.30 (M5). Please note that these measurements are 10-minute averages reported every hour. In both cases, the model performs well throughout, though predictions from northern sectors appear lower than others, similar though less severe than behaviour at the Arklow Met Mast.

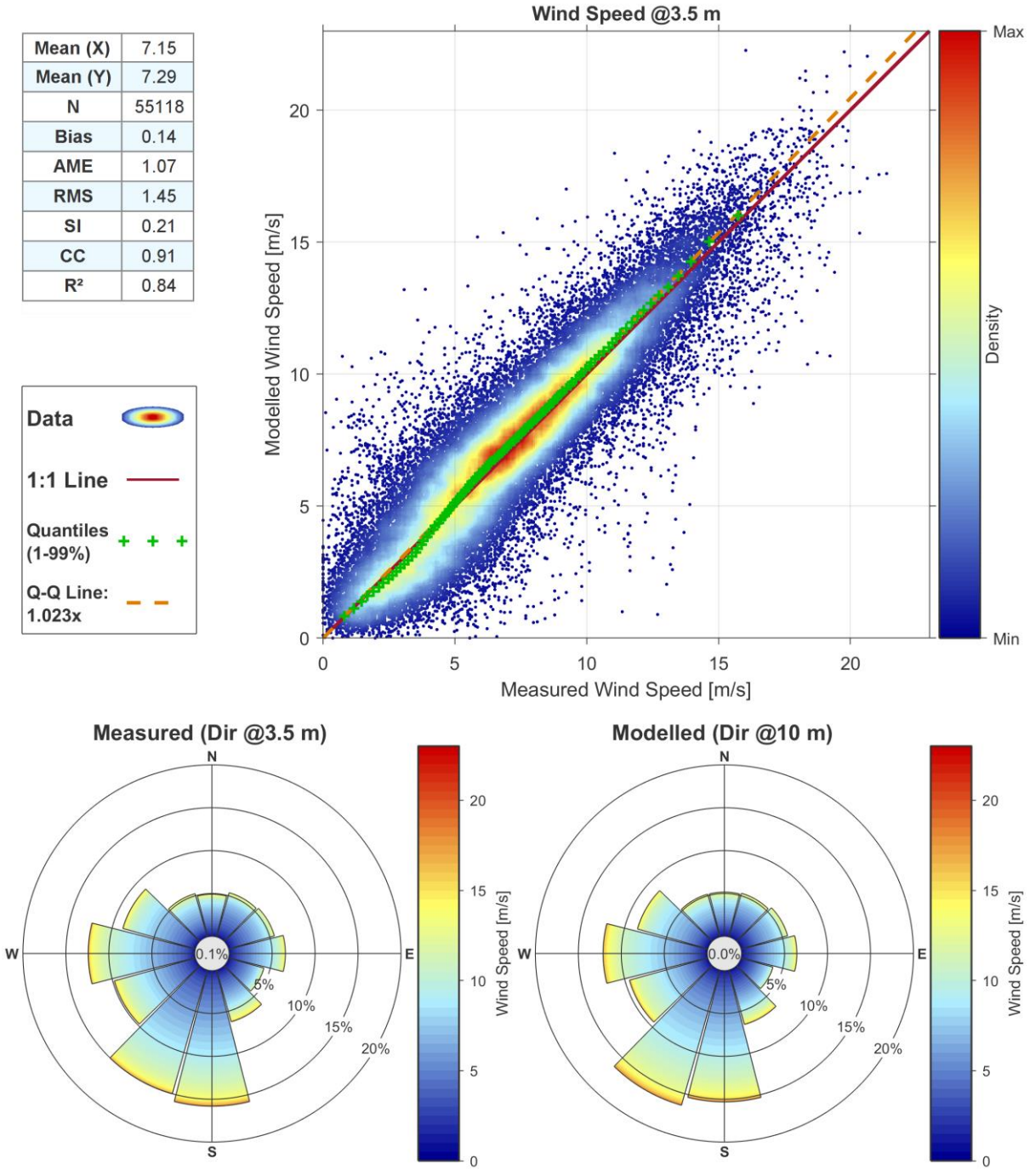



Figure B.27. Model validation, M2 met buoy, wind speeds at 3.5 mASL.

There is some underprediction at the lowest wind speeds, particularly at M5 (Figure B.28), though above mean wind speeds, the model and measurements are better matched. This behaviour is not limited to the met buoys, and can also be seen, though to a much lesser extent, at the Arklow met mast (for example, see Figure B.8).

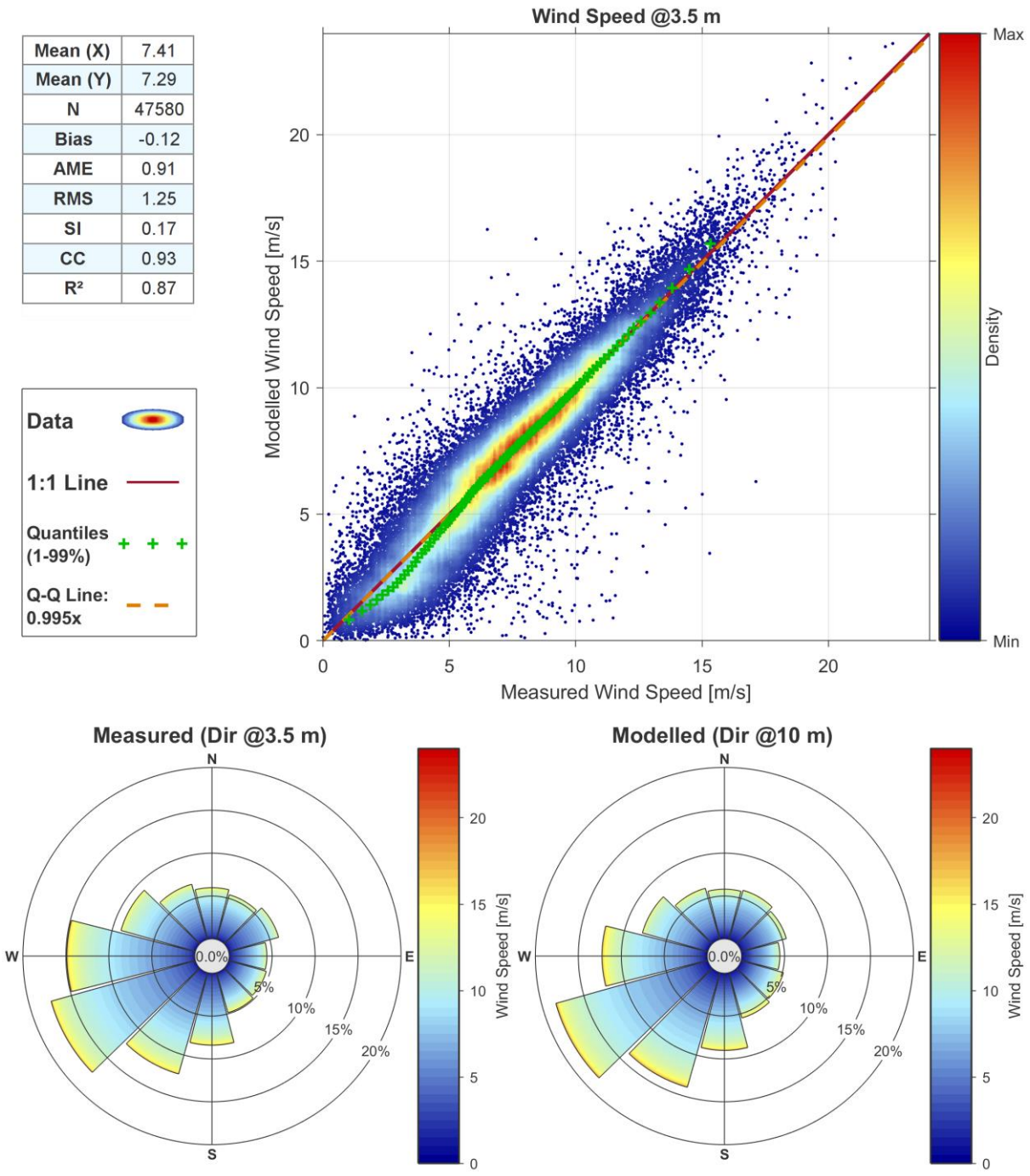



Figure B.28. Model validation, M5 met buoy, wind speeds at 3.5 mASL.

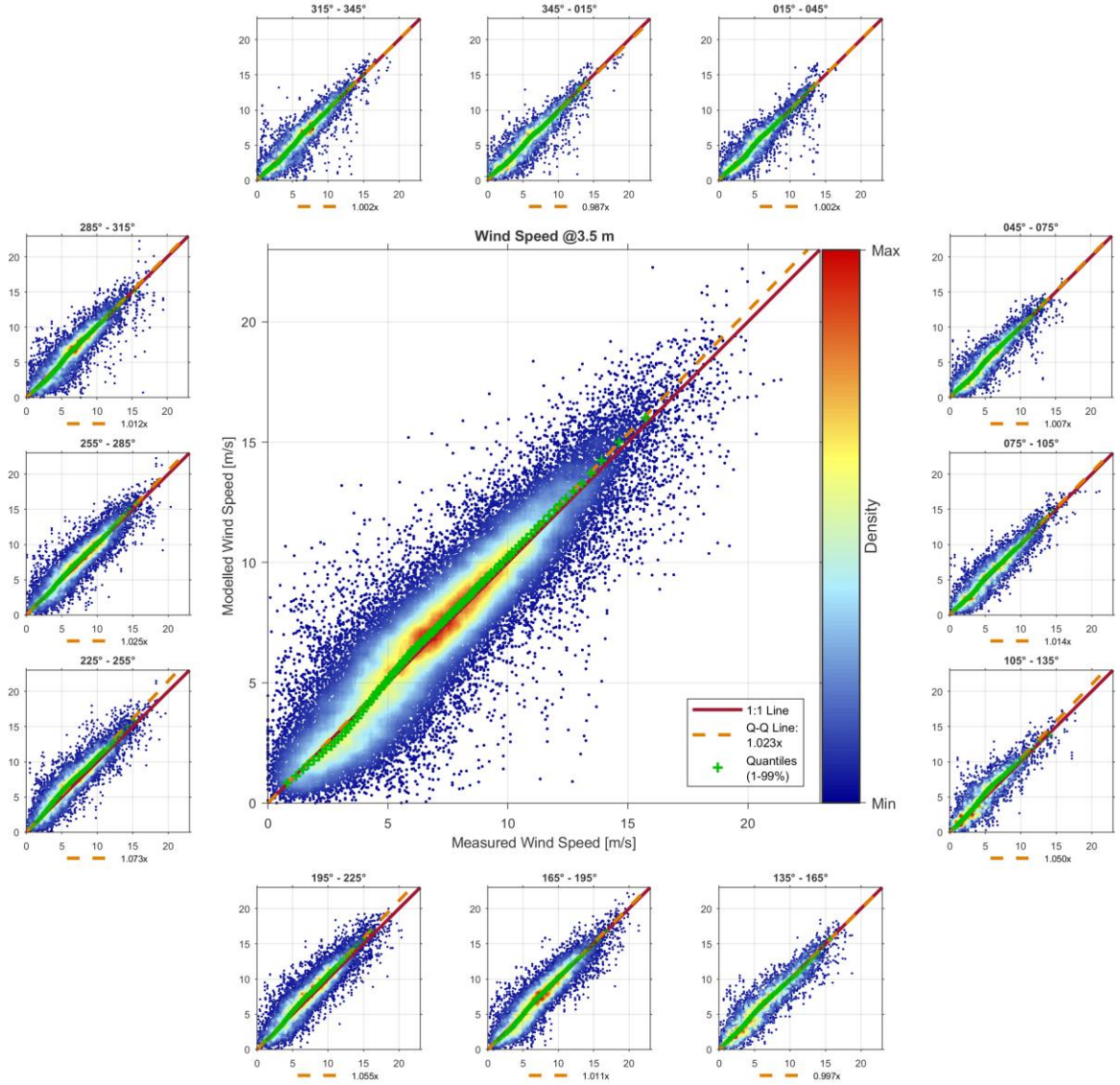



Figure B.29. Model validation, directional sectors, M2 met buoy, wind speeds at 3.5 mASL.

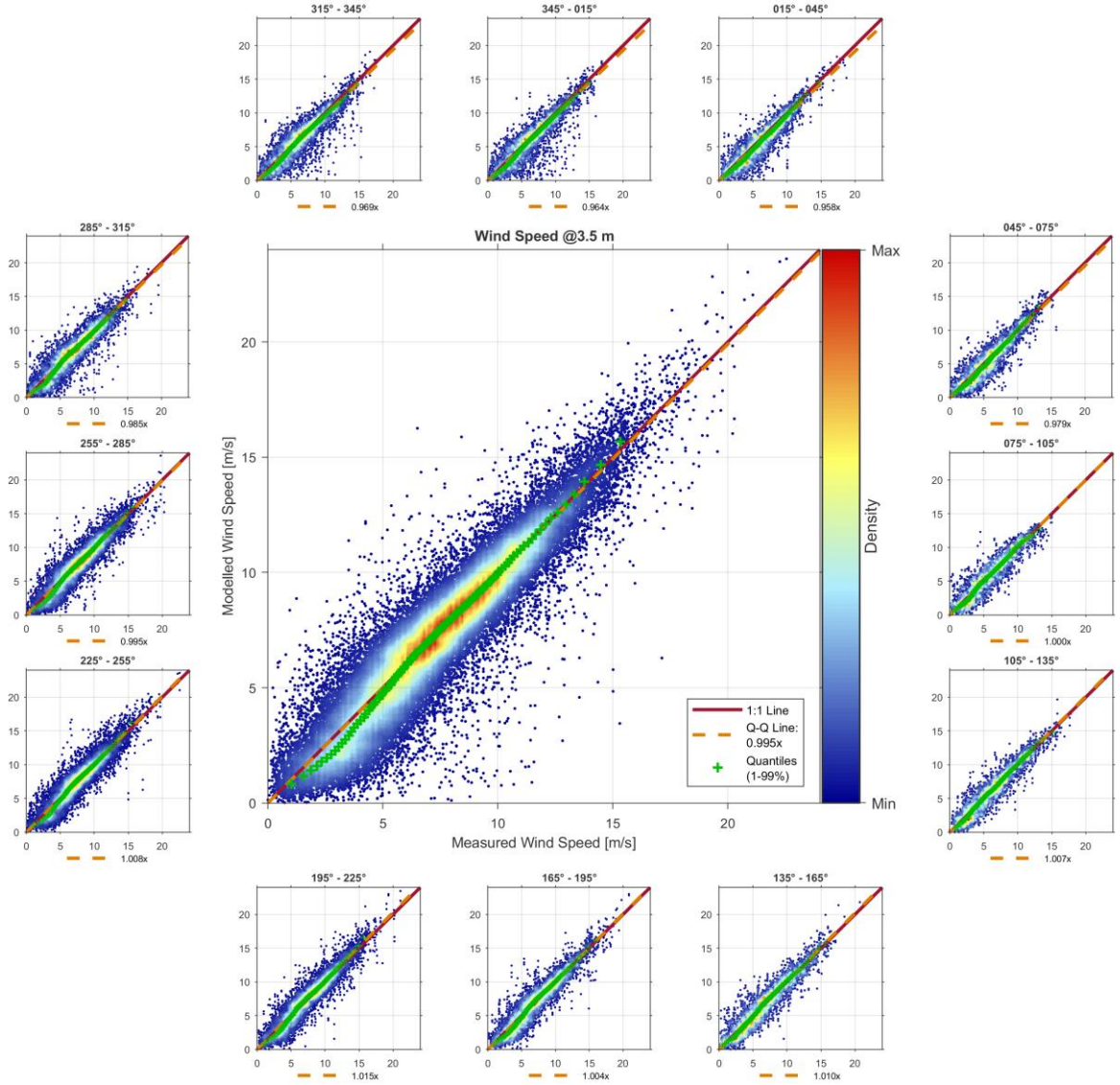



Figure B.30. Model validation, directional sectors, M5 met buoy, wind speeds at 3.5 mASL.

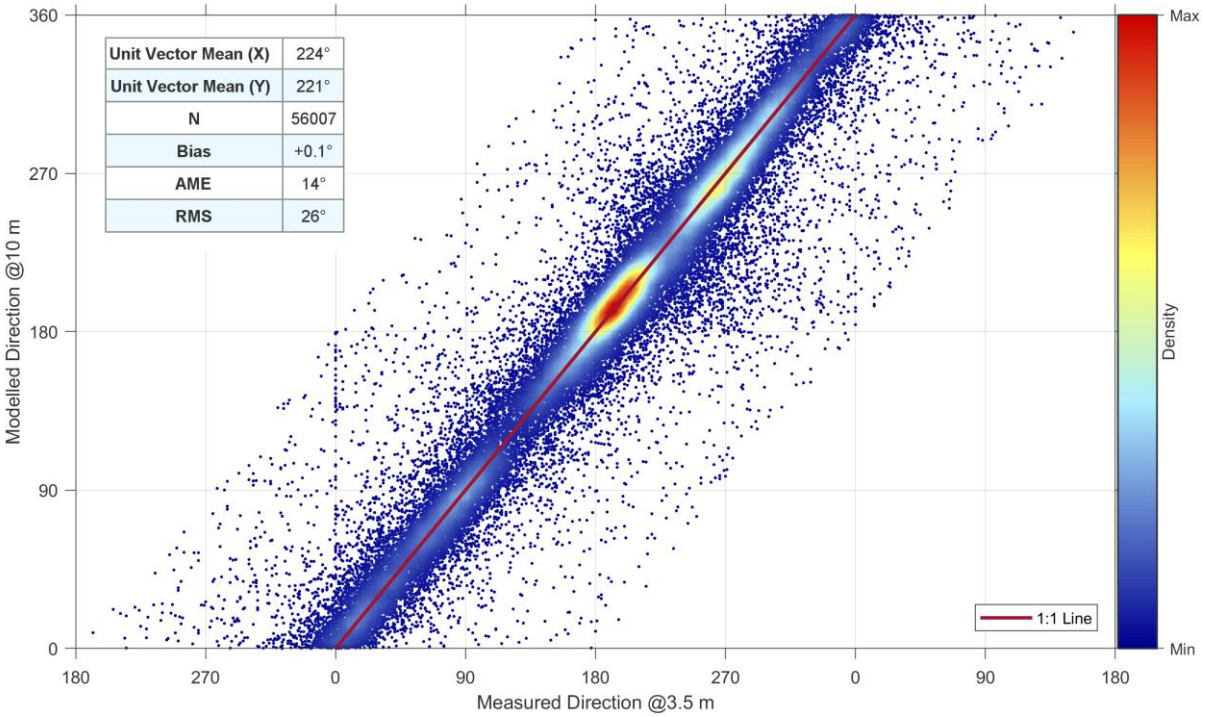



Figure B.31. Model validation, M2, wind directions at 3.5 mASL.

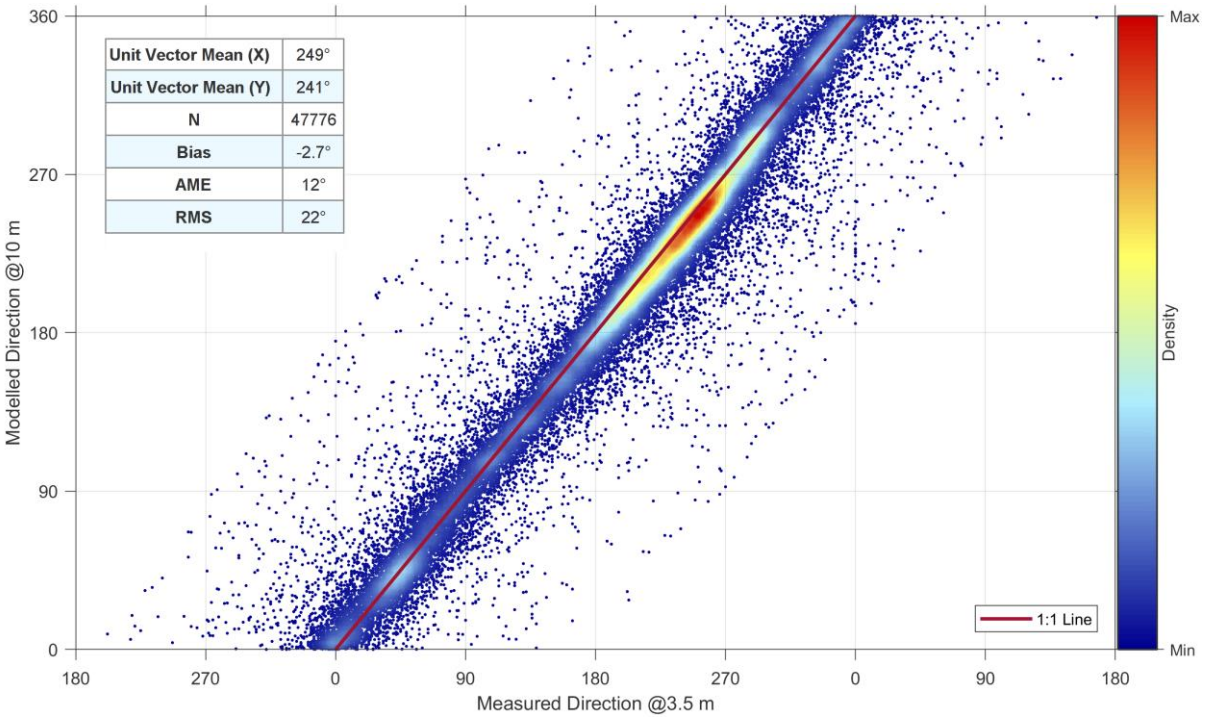



Figure B.32. Model validation, M5, wind directions at 3.5 mASL.

### B.4.5 Splaugh and Coningbeg

#### B.4.5.1 Overview

The Commissioners of Irish Lights maintain a number of buoys and lighthouses collecting weather and sea state data[7], as shown in Figure B.33. For this project, data from the buoys at Splaugh and Coningbeg were acquired for the period 01-Apr-2016 to 01-Jan-2018.

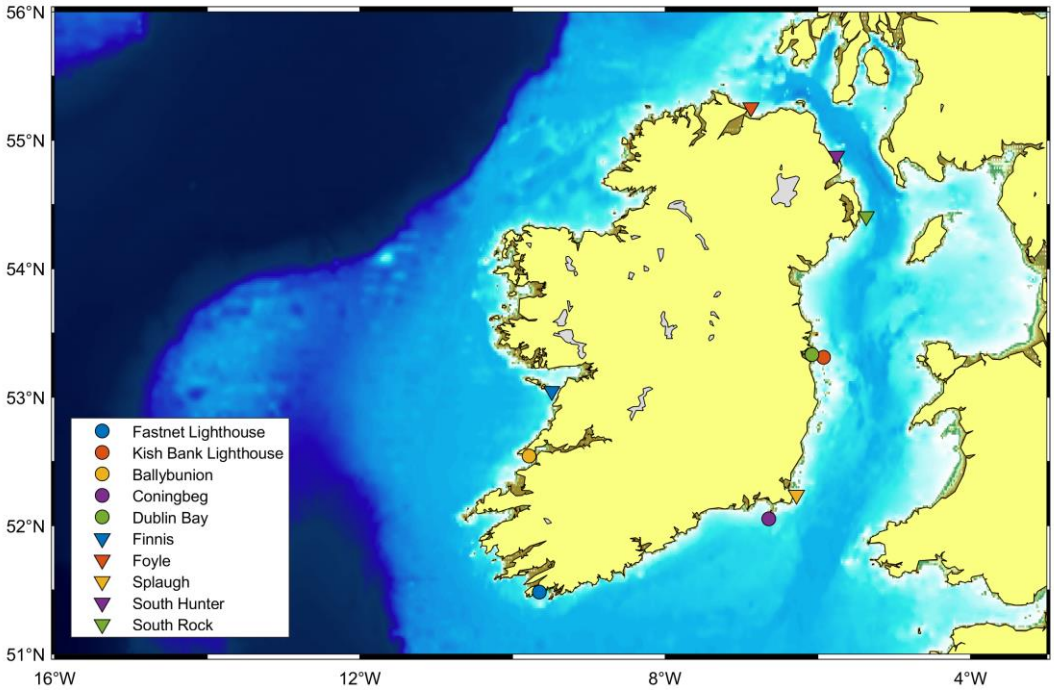



Figure B.33. Irish Lights measured data locations.

#### B.4.5.2 Quality Control

As with all measurement datasets considered in this Appendix, time series of wind speeds and directions were reviewed. At Splaugh, four isolated spikes were removed from wind speeds, but no wind directions removed. At Coningbeg, no wind speeds were removed, however the behaviour of wind directions is more complex. Values before 8th April 2016 repeatedly stick at 0, 180 and 359 °N, and as such all data from this period is considered invalid. Whilst the directional data seen thereafter initially appear reasonable, from early October 2016, there is a significant increase in larger semi-diurnal directional variations. See for example, the contrasts shown in Figure B.34. Indeed, if the periods before and after 1st October 2016 are compared to the modelled data, the differences are clear, as shown in Figure B.35. These lead us to only including directional data from between 8th April and 1st October 2016 in the validation plots which follow.

[7] See https://www.irishlights.ie/technology-data-services/metocean-charts.aspx for more details.

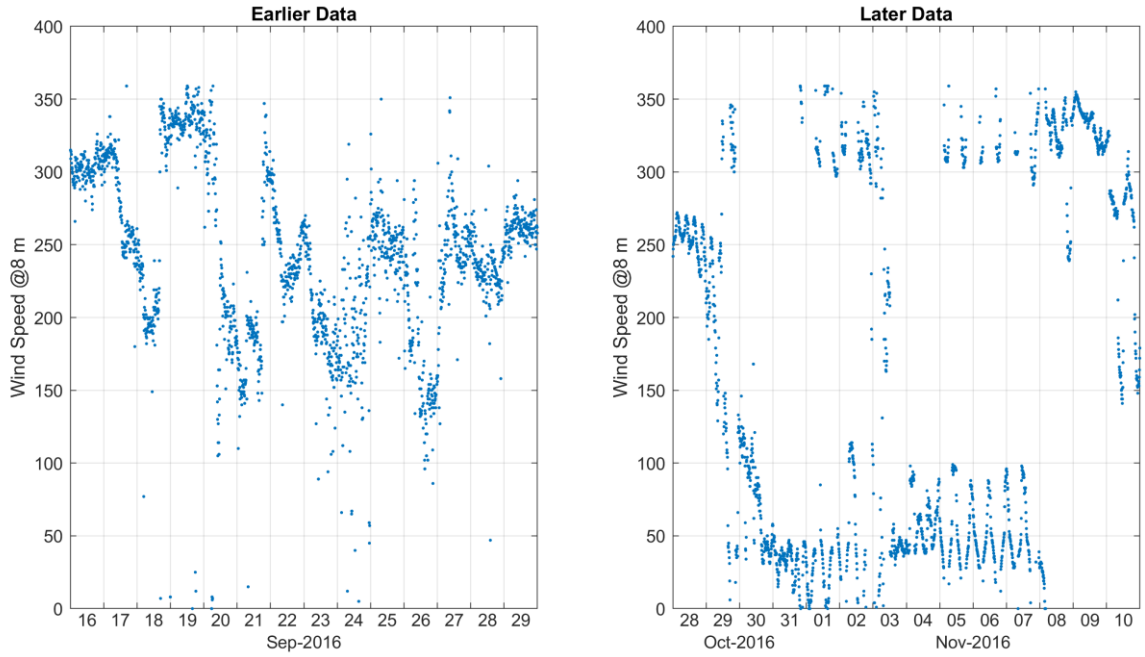



Figure B.34. Coningbeg wind directions, example periods.

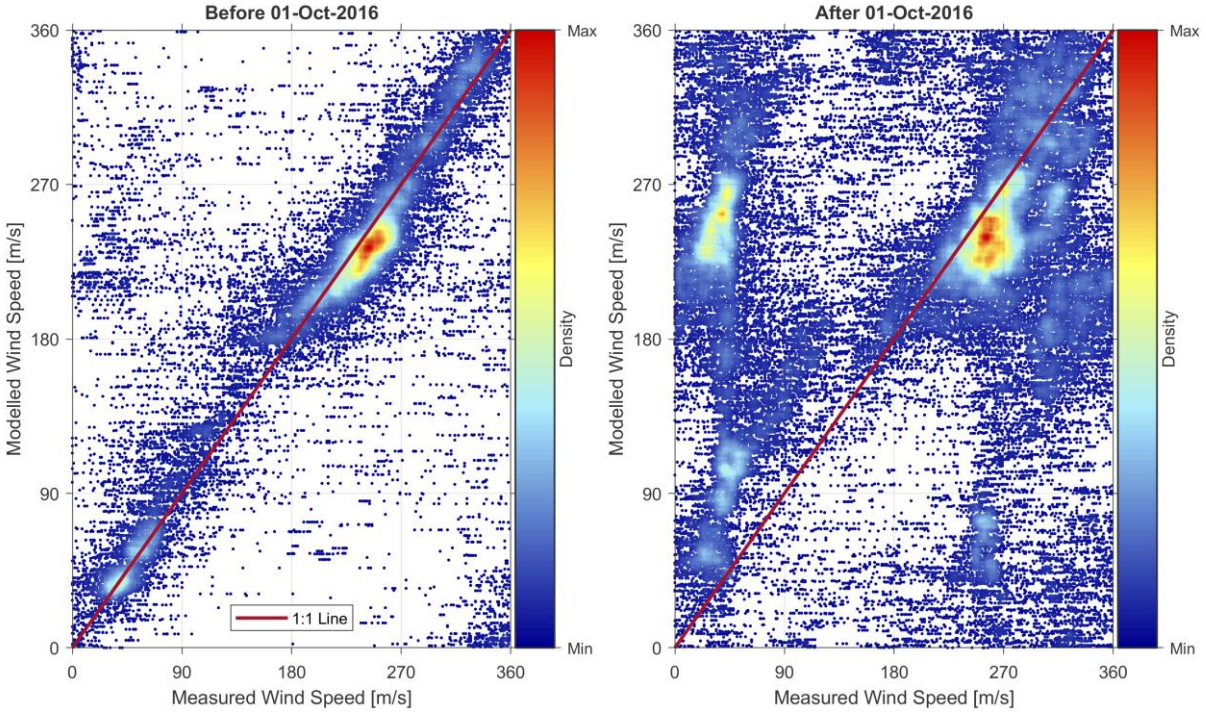



Figure B.35. Coningbeg wind direction comparisons.

### B.4.5.3 Model Validation

Validation plots for measured wind speeds are shown for Coningbeg in Figure B.36 and Splaugh in Figure B.37, with values split by directional sector in Figure B.38 (Coningbeg) and Figure B.39 (Splaugh). Note that directional groupings are based on *measured* directions, which differ somewhat from *modelled* directions for these met buoys, as seen in Figure B.35 for Coningbeg and Figure B.40 for Splaugh.

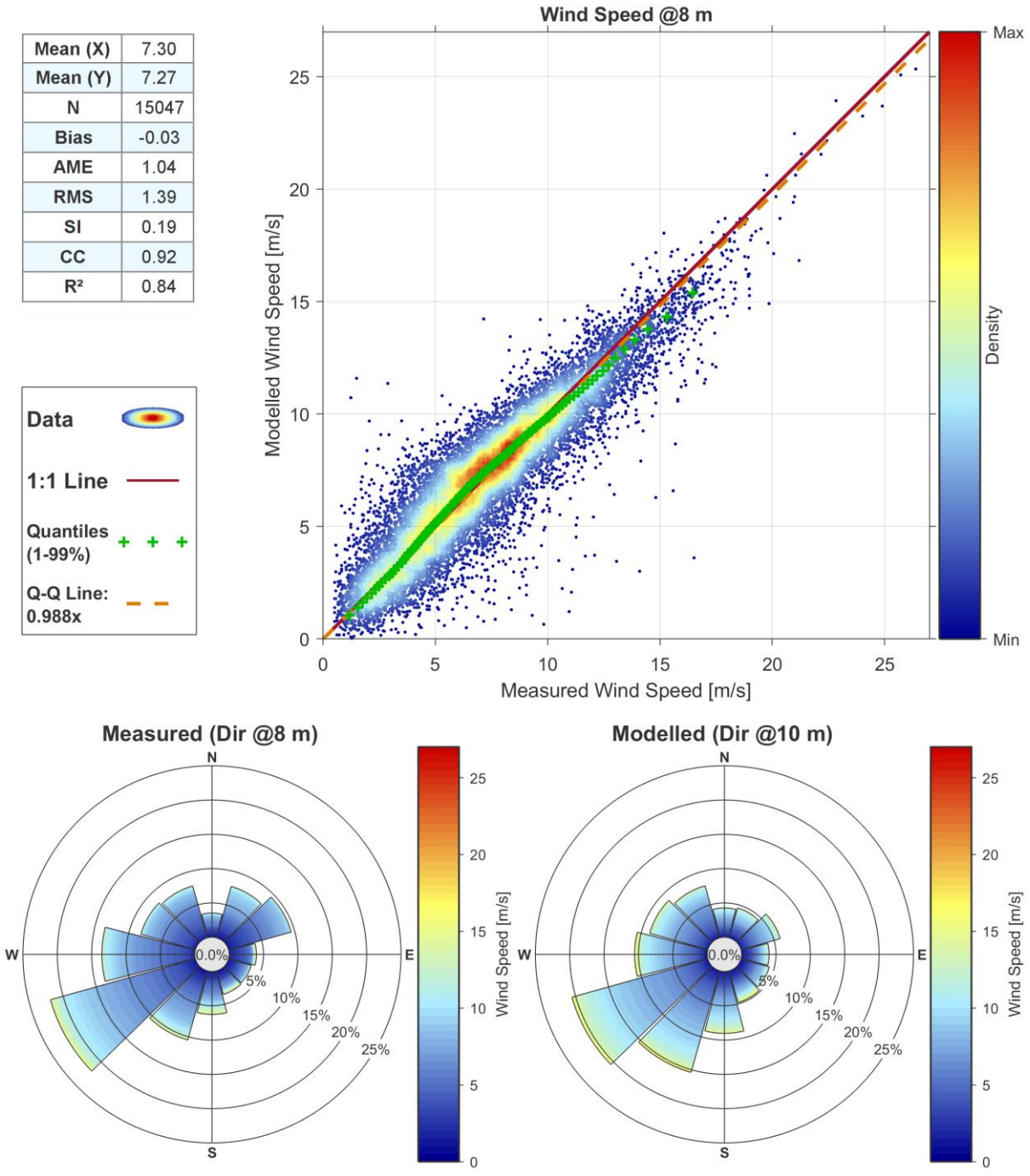



Figure B.36. Model validation, Coningbeg met buoy, wind speeds at 8 mASL.

The comparison of modelled and measured wind speeds at Coningbeg shows very similar behaviour to that at other locations, both in terms of fit statistics and the behaviour of the compared quantiles, with a steeper slope at lower values than higher. At Splaugh, there is more scatter overall, but the same change in slope of the plotted quantiles, close to the mean value.

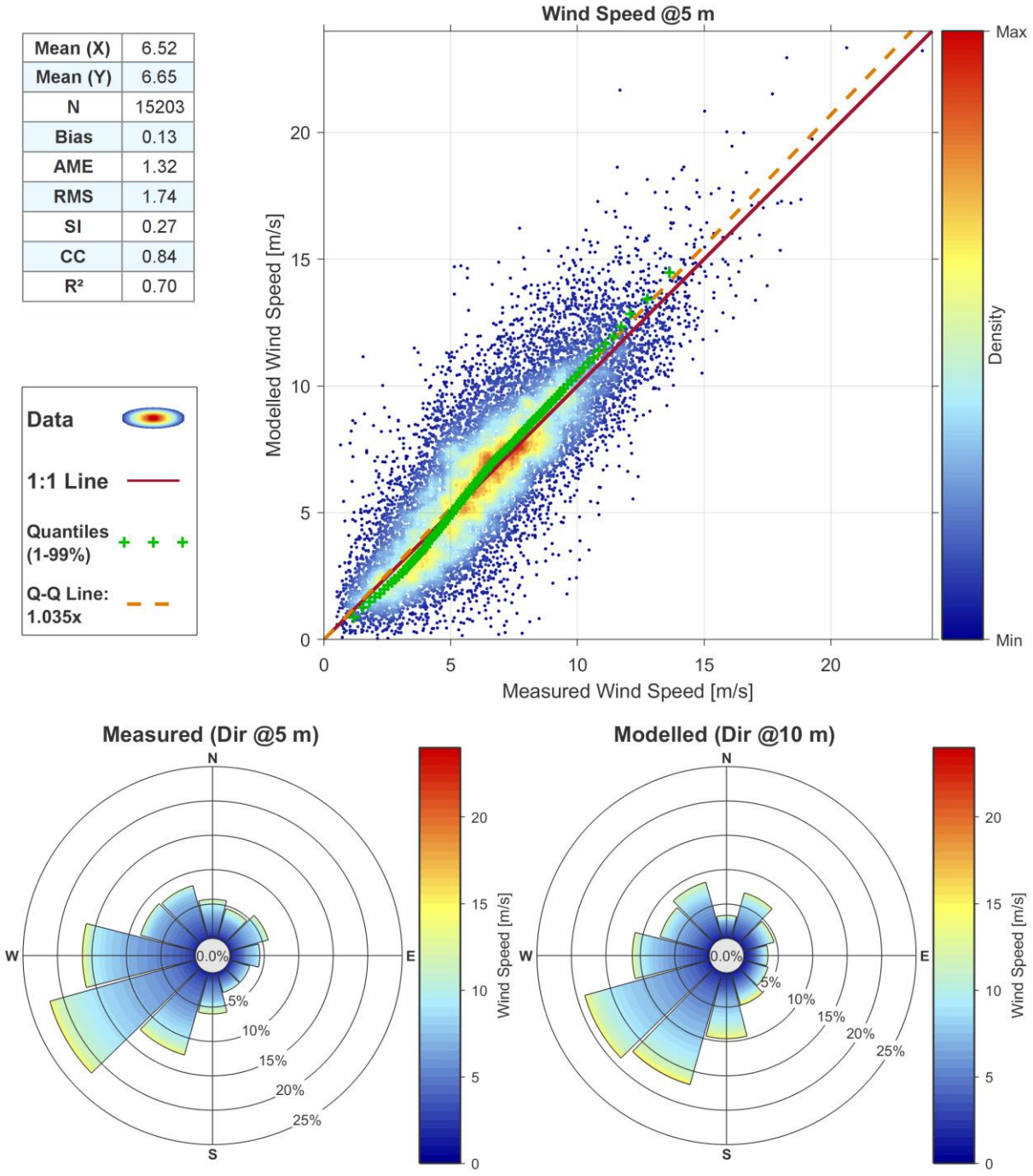



Figure B.37. Model validation, Splaugh met buoy, wind speeds at 5 mASL.

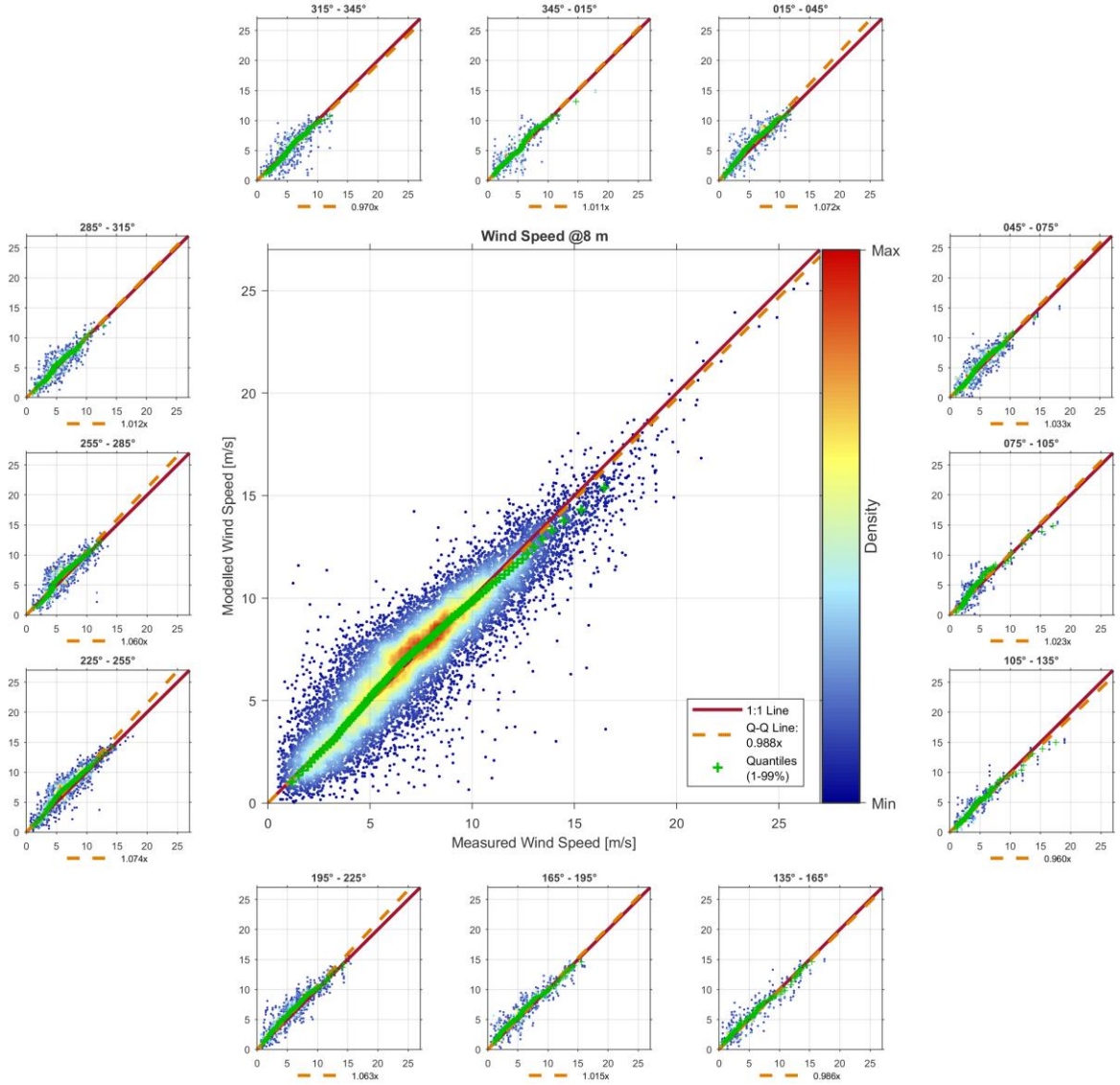



Figure B.38. Model validation, directional sectors, Coningbeg met buoy, wind speeds at 8 mASL.

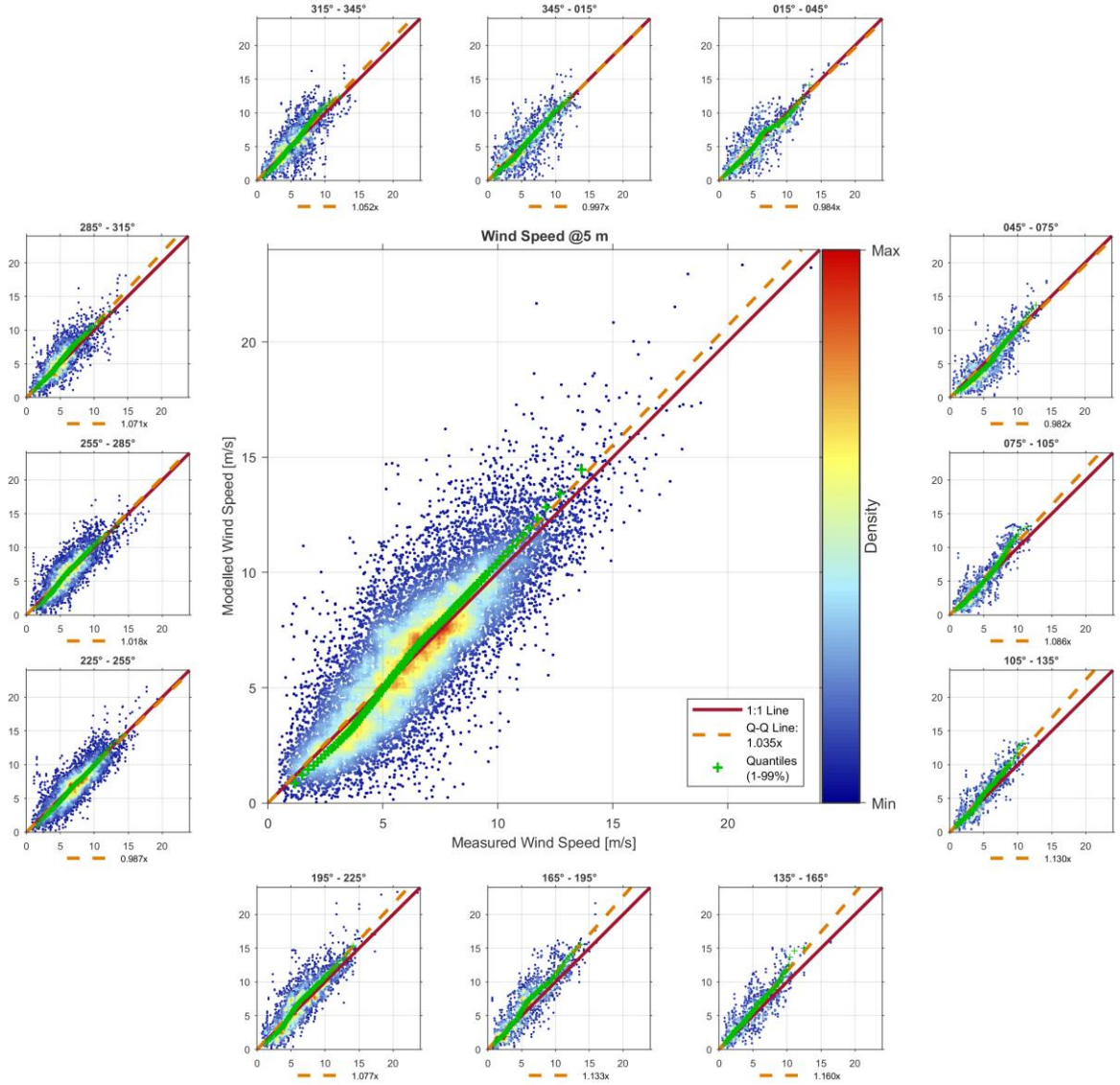



Figure B.39. Model validation, directional sectors, Splaugh met buoy, wind speeds at 5 mASL.

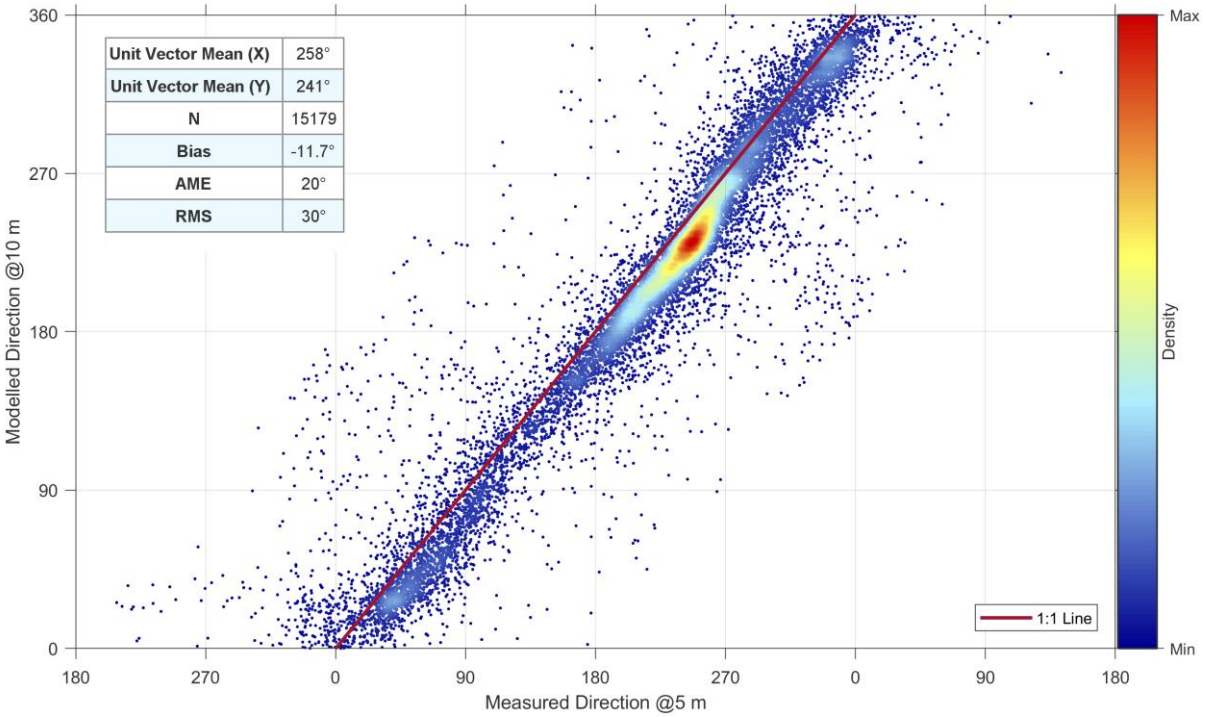



Figure B.40. Model validation, Splaugh, wind directions at 5 mASL.

## B.5 Vortex 10m Calibration

### B.5.1 Overview

Throughout Section B.4, a number of validation plots were considered comparing the Vortex model wind speeds against measurements. In almost all cases, the model performs well, with only very minor underprediction at the lowest wind speeds (below perhaps 5 m/s) and a notable "kink" in the quantile-quantile line (between approximately 5 and 10 m/s). At the highest wind speeds, again performance is good, though with the suggestion of a minor underprediction for some of the largest storms at the Arklow met mast. Given the limitations of the met mast structure itself, it is unclear as to whether such behaviour is at least in part due to the measurements themselves. However, for the sake of caution, we assume that a minor uplift to the model at these levels is of benefit, and is described in this section.

### B.5.2 Methodology

The calibration is applied only to the 10 mAMSL model level needed to drive metocean models and is as follows:

**STEP 1: Determine the measured datasets to use**

Since we are calibrating wind data with a view to driving wave models covering the Irish Sea, rather than solely using datasets from Arklow Bank for the calibration, we instead consider all measured wind datasets described in Section B.4. Ultimately, five of these have been used: Arklow met mast (Original); Arklow met mast (Synthesised); Arklow LiDAR; M2 met buoy; and M5 met buoy. Due to the greater uncertainty surrounding the quality of the Irish Lights datasets at Splaugh and Coningbeg, they have been omitted from the calibration process.

**STEP 2: Calculate a set of wind speeds at 10 m AMSL for each dataset**

In order to calculate a set of 10 m AMSL wind speeds based *only* on measurements, for each dataset we:

a) Take wind speeds from the closest measured level, being: 15 m for Arklow met mast (Original); 42.5 m for Arklow met mast (Synthesised); 21.3 m for the Arklow LiDAR; and 3.5 m for both the M2 and M5 met buoys.
b) Use the Frøya wind profile to adjust data to the 10 m level.

The Frøya profile, based on wind speeds on the Norwegian coast, is often used to describe offshore wind conditions, and is given in DNVGL-RP-C205 [22] as:

$$U(T,z) = U_0 \cdot \left\{1 + C \cdot \ln\frac{z}{H}\right\} \cdot \left\{1 - 0.41 \cdot I_U(z) \cdot \ln\frac{T}{T_0}\right\}$$

Where:

*U(T,z)* is the wind speed with averaging period *T* at elevation z

$U_0$ is the *one-hour* mean wind speed

$T_0$ is one hour.

*H* is 10 metres.

$C = 5.73 \cdot 10^{-2}\sqrt{1 + 0.148U_0}$

$$I_U = 0.06 \cdot (1 + 0.043U_0) \cdot \left(\frac{z}{H}\right)^{-0.22}$$

In our case, we do *not* consider a change in averaging period, thus the equation reduces to:

$$U_{1hr}(z) = U_0 \cdot \left\{1 + C \cdot \ln\frac{z}{H}\right\}$$

This has the benefit of describing the entire wind speed profile in the vertical using only the value at a single level – in the above equation, this is the hourly wind speed at ten metres elevation, however any elevation can easily be utilized. The commonly used power law and logarithmic profiles are described by two parameters, and as such require either wind speeds at (at least) two levels to fit to, or alternate assumptions, for example a pre-determined power law exponent[8].

The parameterization of the Frøya profile means it can be used for all the measured datasets, even those with only a single measurement level. The trade-off for a single-parameter formulism is a reduction in the flexibility that would be given by a second parameter. However, at higher wind speeds – generally considered the priority when calibrating *for the purpose of driving wave models* – this flexibility is less important than at lower wind speeds.

By way of example, let us consider extrapolation downwards from the measurements at the Arklow met mast to 10m. One possibility is to carry out the following for each timestamp:

a) Fit a power law profile to the measurements, for example by using a least-squares fit to all valid wind speeds at the timestamp being considered.
b) Use the fitted profile to estimate the wind speed at 10m.

The power law exponent, α, of resultant fitted profiles is plotted against wind speeds at one of the measured levels in Figure B.41. To the left of the Figure, at lower wind speeds, a very large range of scatter is seen in the α values. However, as wind speeds increase to the right, this range narrows significantly. Such narrowing is in line with our expectations, based on similar analyses at numerous measured datasets across European waters, as well as what can be found in the associated literature (see for example Emeis [23] for analysis on this topic at the FINO1 mast in the German Bight).

Since the Frøya profile is based on the *logarithmic* profile, rather than the power law profile, we cannot compare directly on this Figure. However, if we consider ratios between wind speeds at different elevations, rather than the power law α, we *can* create such a comparison. Thus, Figure B.42 shows as a scatter plot the same fitted profiles, but rather than α itself, the ratio each α would give between wind speeds at the measurement level shown (22.3 m) and at the 10m level. Overlaid are a number of statistics derived from these ratios (mean, median and percentiles), as well as the ratio that the Frøya profile specifies between these levels. Here we see that, as wind speeds increase and the scatter narrows, mean and median ratios are very close to that given directly by the Frøya profile. Similar results are seen for the Arklow LiDAR in Figure B.43. Note that in both Figures, the y-axes do not go below 1. Such values would correspond to inverted profiles, with higher wind speeds at lower elevations. Since these only occur in both sets of measurements at lower wind speeds, and our interest here is heavily weighted towards higher wind speeds, they are not of any particular significance in this analysis and can safely be ignored.

[8] In fact, the Frøya profile is itself a logarithmic profile, but with an additional wind speed dependent relationship incorporated which replaces the need for a second parameter.

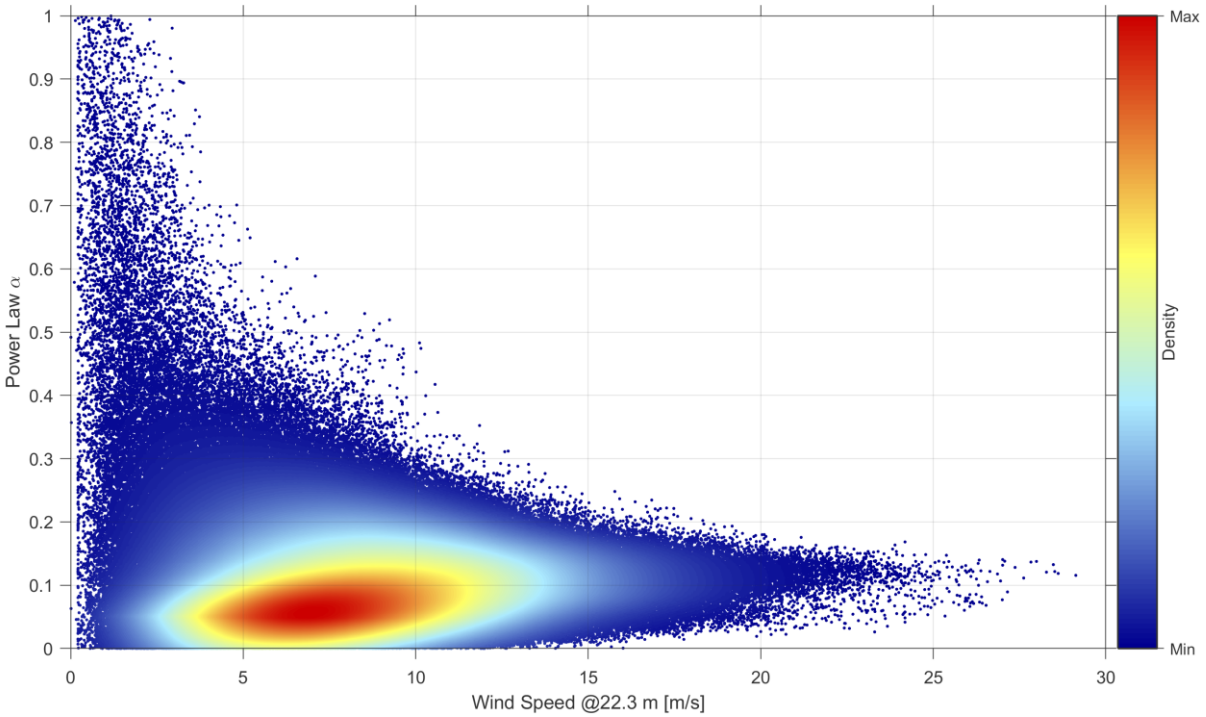



Figure B.41: Arklow met mast, fitted Power Law α.

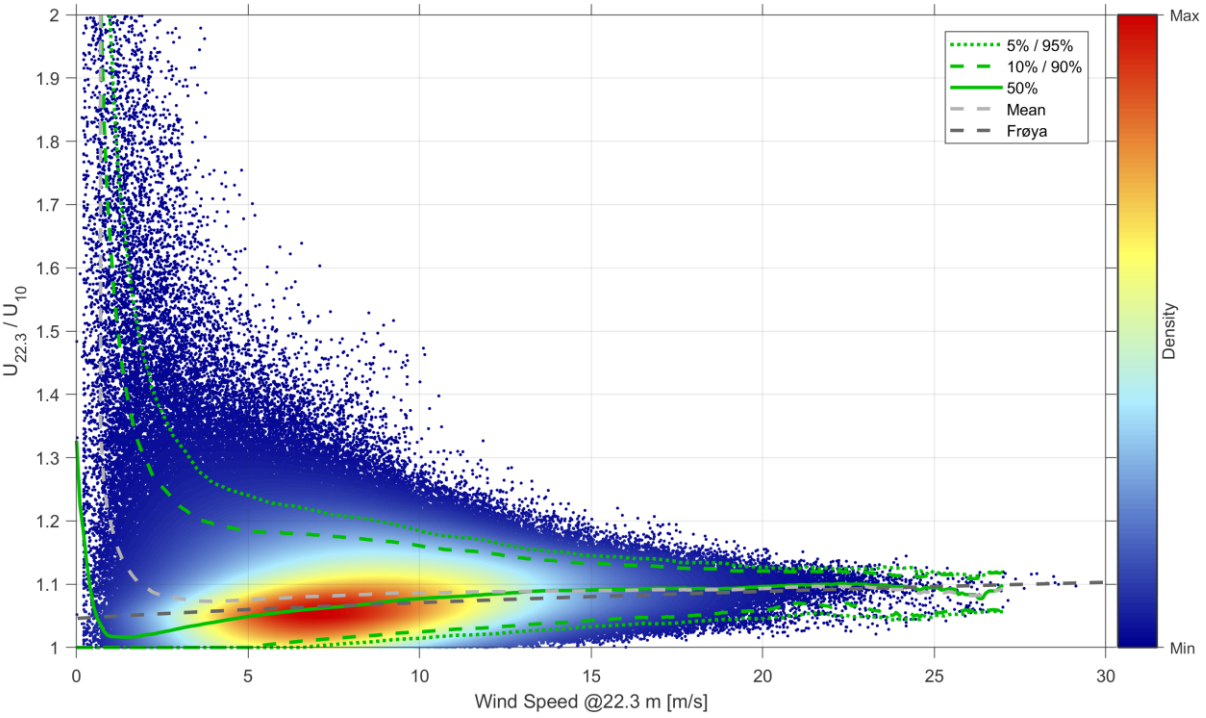



Figure B.42. Arklow met mast, wind speed ratios 22.3 to 10 mAMSL.

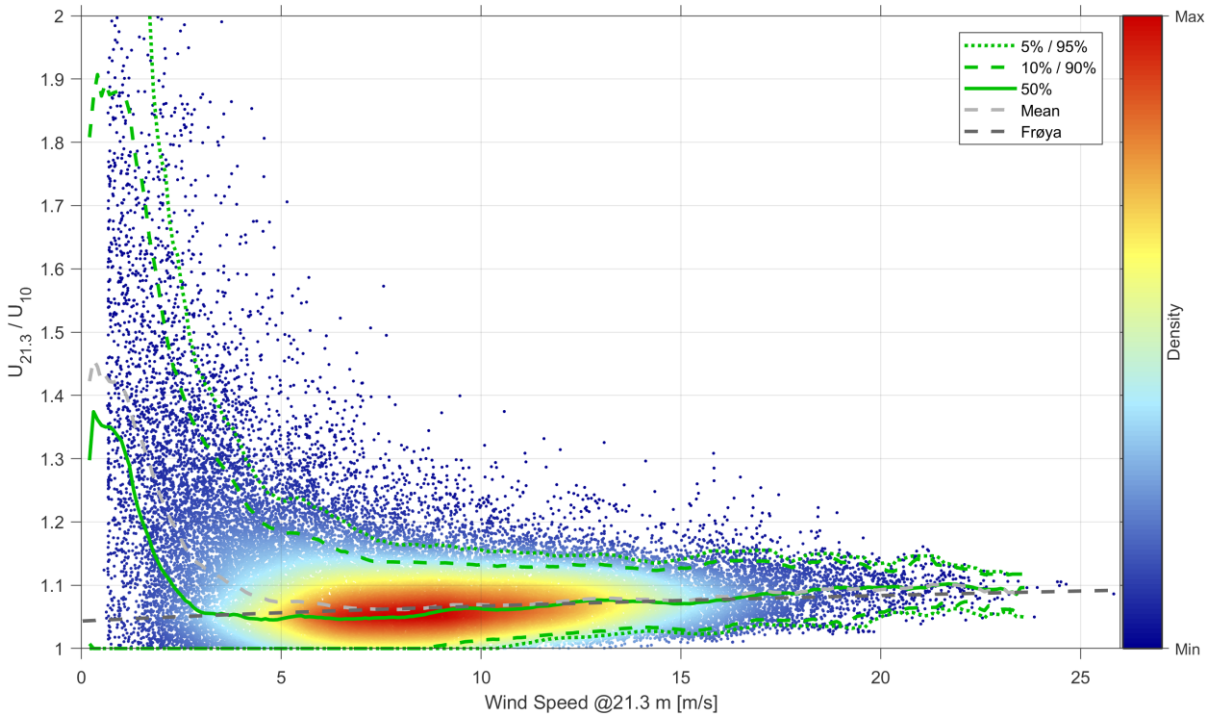



Figure B.43. Arklow LiDAR, wind speed ratios 21.3 to 10 mAMSL.

As a result of this behaviour, the Frøya profile is generally considered suitable for maritime wind profiles at higher wind speeds. For example, DNVGL-RP-C205 [22] specifies it can be used 'for extreme mean wind speeds corresponding to specified return periods in excess of approximately 50 years' whilst ISO 19901-1 [24] is less restrictive in stating it is suitable for use 'in storm conditions'.

In deeming it appropriate for the process of calibrating winds *to drive the wave model* – to be clear, additional review would be recommended for its use in other analyses - it is worth noting that we are ultimately trying to find a calibration curve (see STEP 3) which corrects higher wind speeds, but has little to no effect on low to medium wind speeds. The failure of the Frøya profile to fully capture the larger spread of profile shapes at lower wind speeds is largely negated by the use of a calibration curve which ensures very little change to wind speeds at these levels. Its suitability at higher wind speeds, and the need for only a single measurement level, allows us to include the Arklow met mast (Synthesised), M2 and M5 buoys as part of the calibration process. Although an alternate method *could* be used for those datasets where more measured levels are available, we believe that use of a consistent method throughout is slightly preferential. In any case, the similarity of the Frøya profile to, e.g. fitted power law profiles, combined with the relatively short distance of extrapolation (from 15m and 21.3m to 10m at the Arklow met mast and LiDAR respectively) leads us to expect that such alternate methods would not lead to a significant change in the final calibration curves.

**STEP 3: Fit a third order polynomial to quantiles of modelled and measured data at 10m**

Measurements are then compared to modelled data from the closest node to the measurement location. A number of different forms were considered to form a calibration, based both on quantiles of the data and wind speeds at coincident time stamps. Of these, a third order polynomial fitted to the quantiles gives both sufficient flexibility within the range of the data, and transparency for extrapolated behaviour. Results for all datasets are shown in Figure B.44.

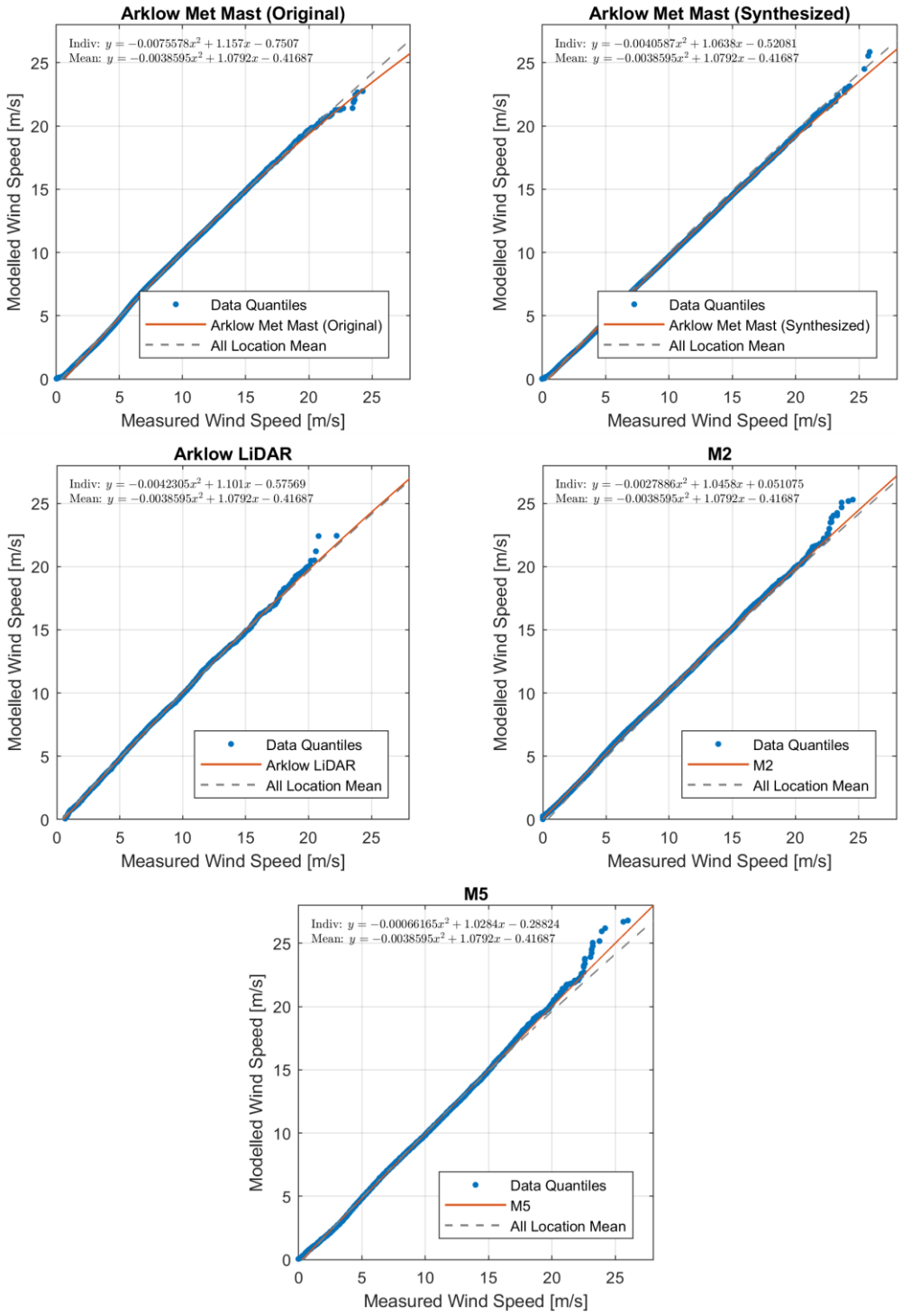



Figure B.44. Fitted polynomials for each dataset.

**STEP 4: Determine final calibration**

The final calibration is taken to be the mean of all individual calibrations, as shown in Figure B.45, and overlaid on the individual plots of Figure B.44. In this case, the mean curve is ultimately very close to that which would be given by the LiDAR alone.

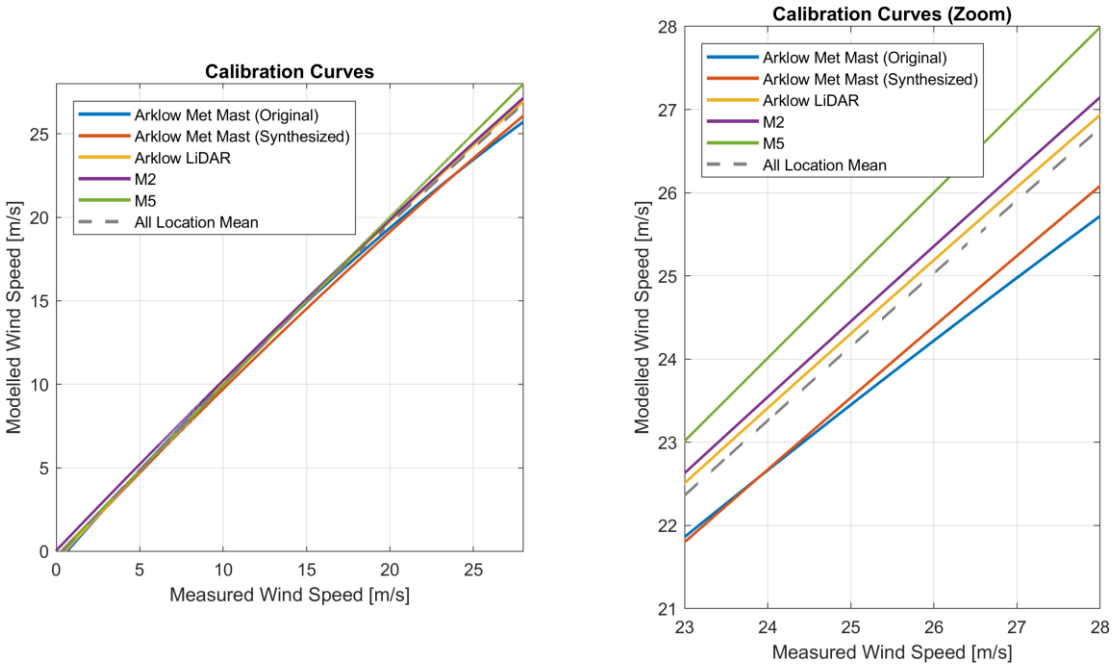



Figure B.45. Fitted polynomials for all datasets.

## B.5.3 Results

The results of applying this calibration to modelled data at 10 mAMSL is compared to measurements at 10 mAMSL (again derived using the Frøya profile) in Figure B.46 through Figure B.50. It can be seen that there is very little change to wind speeds below approximately 20 m/s throughout. According to this calibration, wind speeds of 30 m/s would increase to 31.8 m/s.

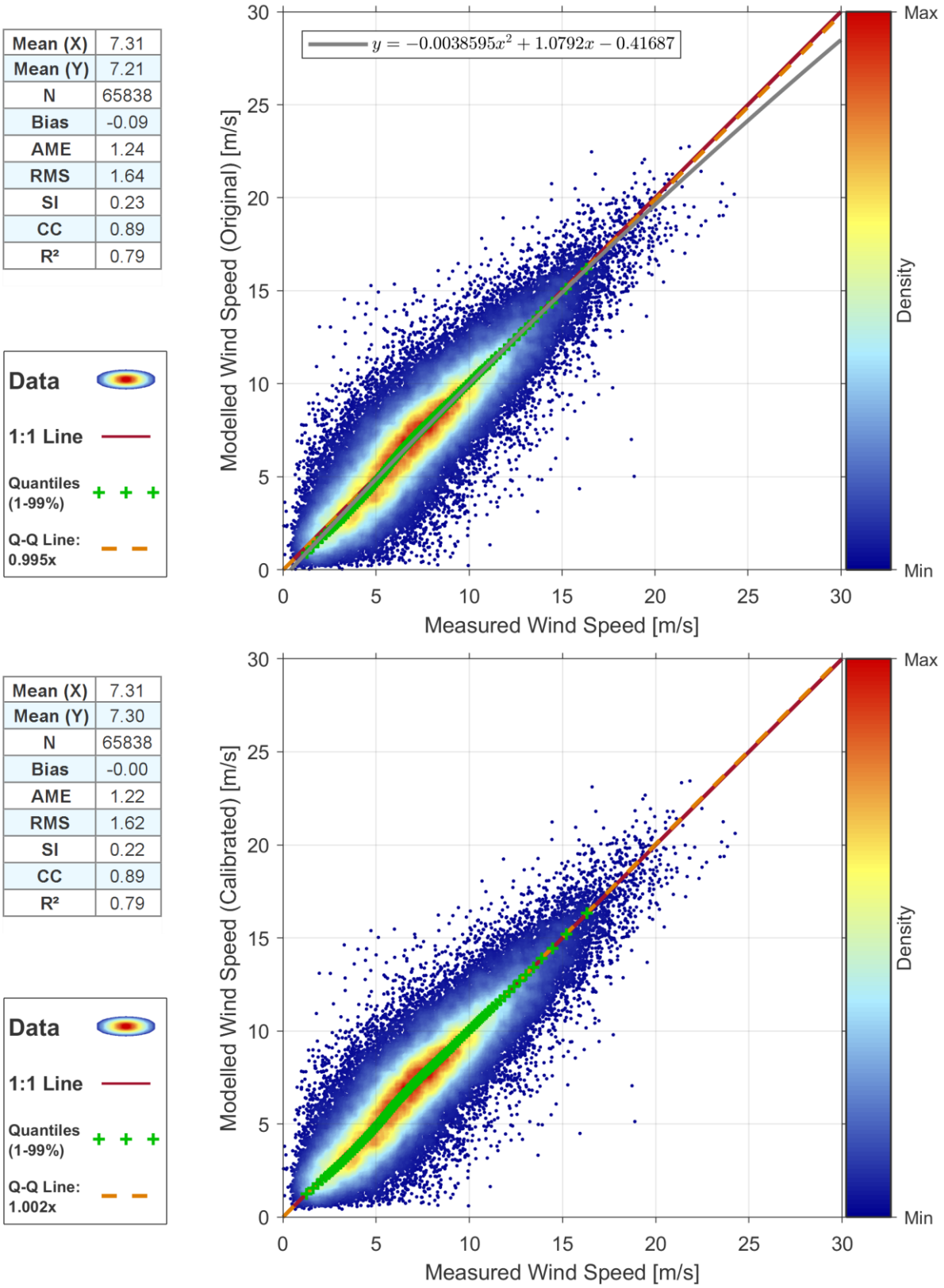
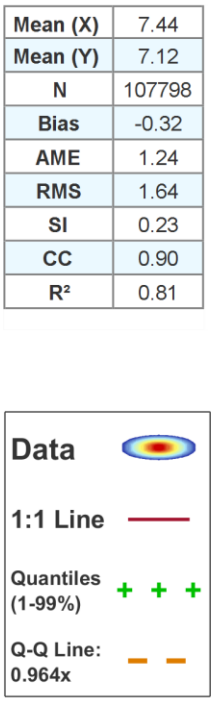
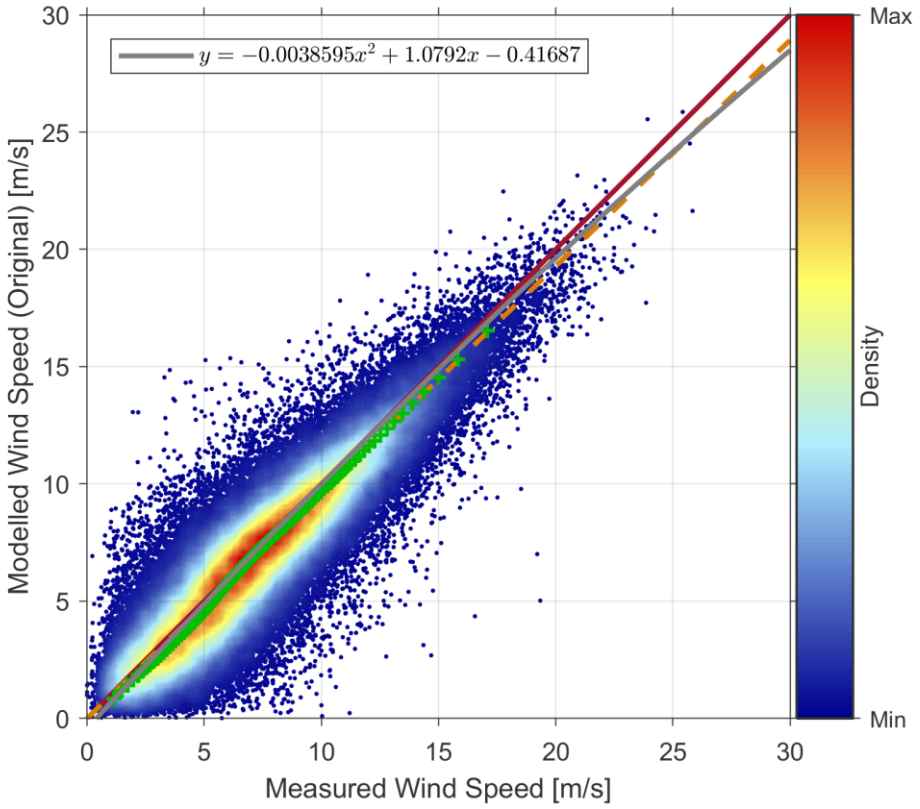


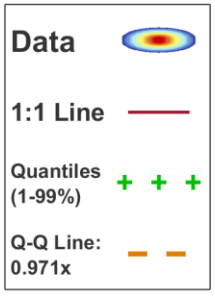

Figure B.46. Arklow met mast (Original) from 15m AMSL.

| | |
|---|---|
| Mean (X) | 7.44 |
| Mean (Y) | 7.12 |
| N | 107798 |
| Bias | -0.32 |
| AME | 1.24 |
| RMS | 1.64 |
| SI | 0.23 |
| CC | 0.90 |
| $R^2$ | 0.81 |




| | |
|---|---|
| Mean (X) | 7.44 |
| Mean (Y) | 7.21 |
| N | 107798 |
| Bias | -0.23 |
| AME | 1.21 |
| RMS | 1.60 |
| SI | 0.22 |
| CC | 0.90 |
| $R^2$ | 0.81 |



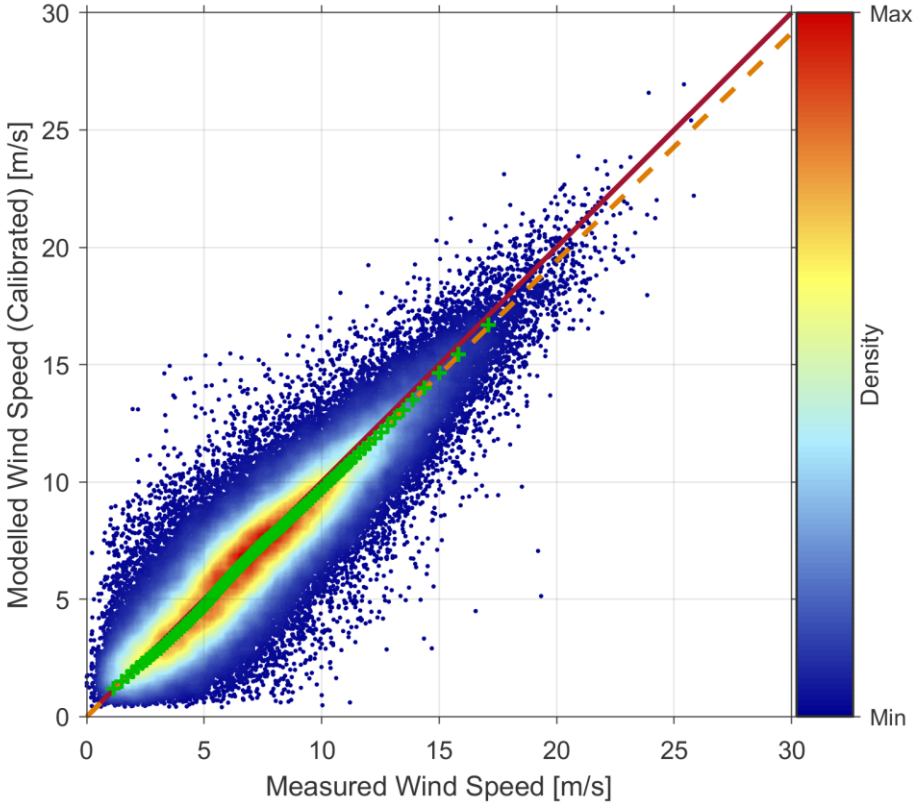




Figure B.47. Arklow met mast (Synthesised) from 42.5 m.

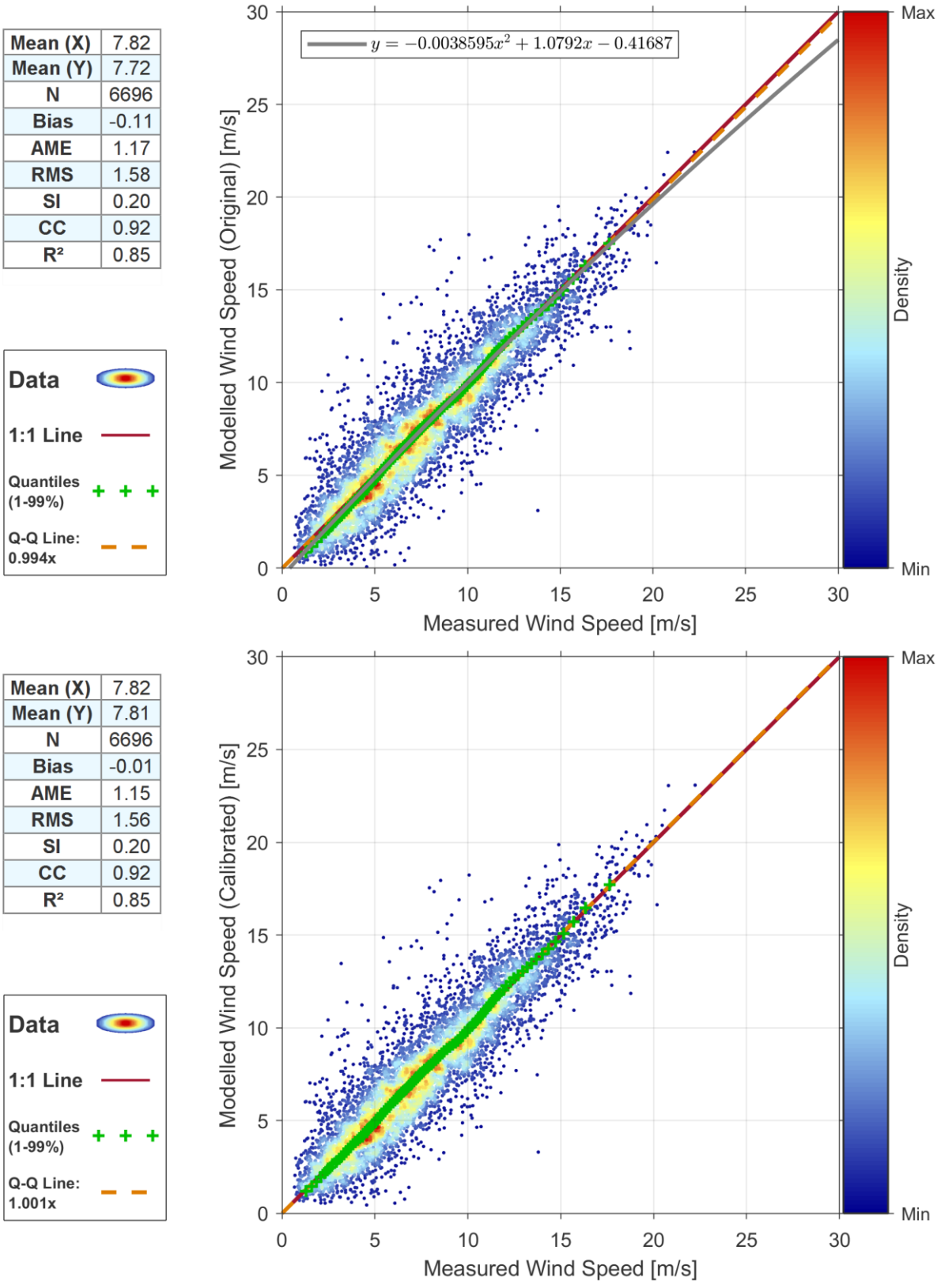



Figure B.48. Arklow LiDAR from 21.3 m.

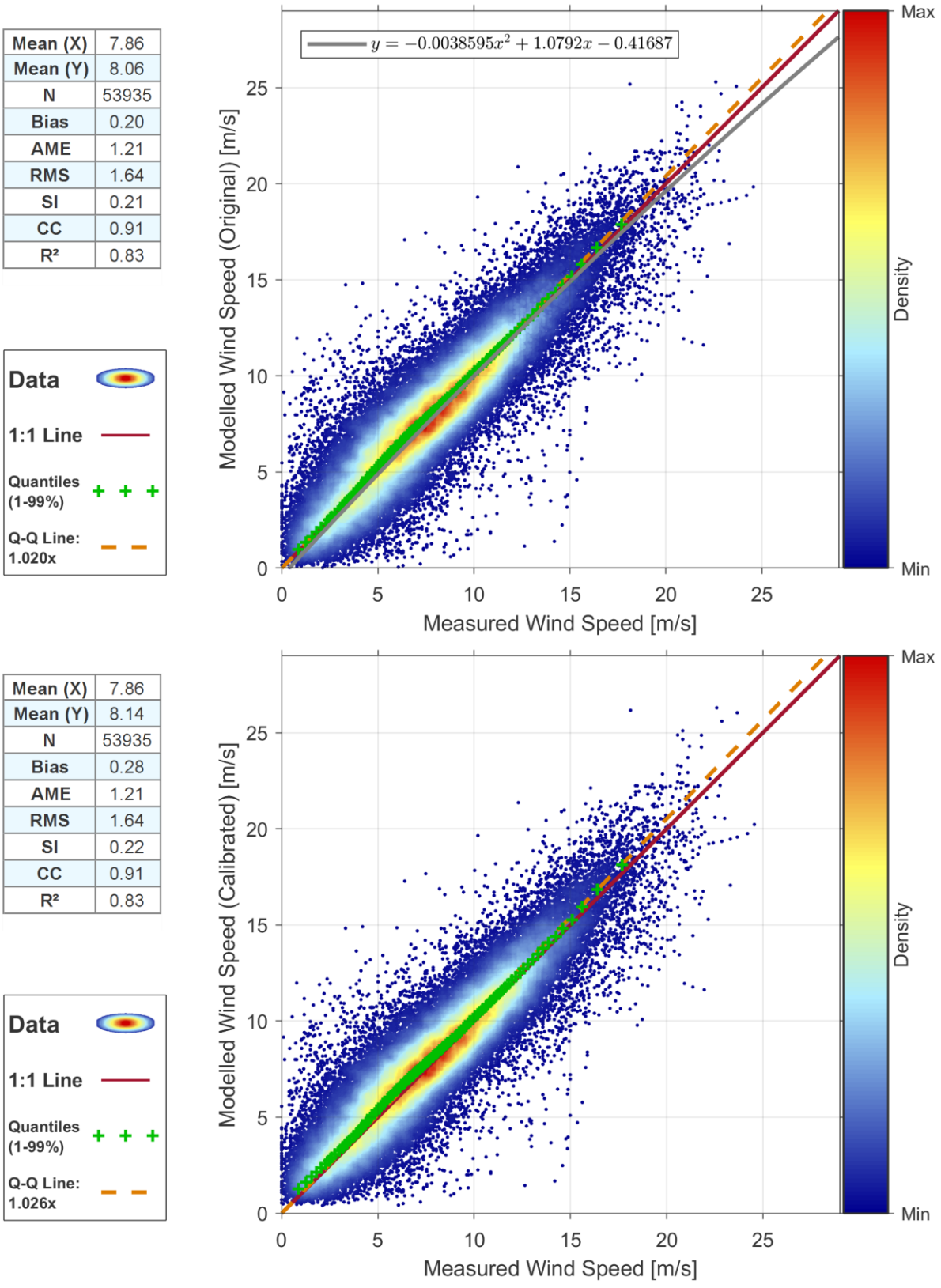
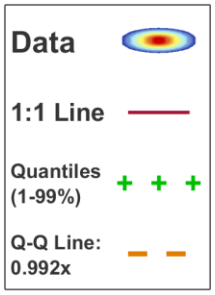
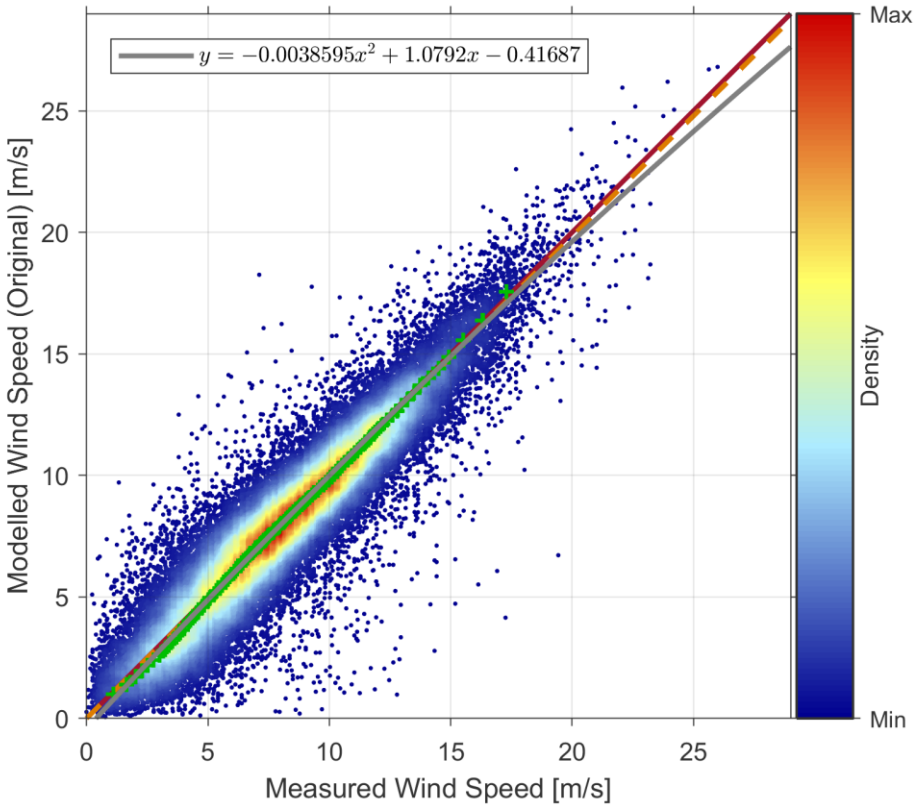


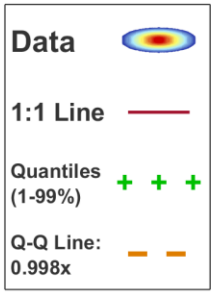

Figure B.49. M2 met buoy.

| | |
|---|---|
| Mean (X) | 8.17 |
| Mean (Y) | 8.06 |
| N | 47580 |
| Bias | -0.11 |
| AME | 1.00 |
| RMS | 1.37 |
| SI | 0.17 |
| CC | 0.93 |
| R² | 0.87 |




| | |
|---|---|
| Mean (X) | 8.17 |
| Mean (Y) | 8.14 |
| N | 47580 |
| Bias | -0.03 |
| AME | 0.99 |
| RMS | 1.36 |
| SI | 0.17 |
| CC | 0.93 |
| R² | 0.87 |



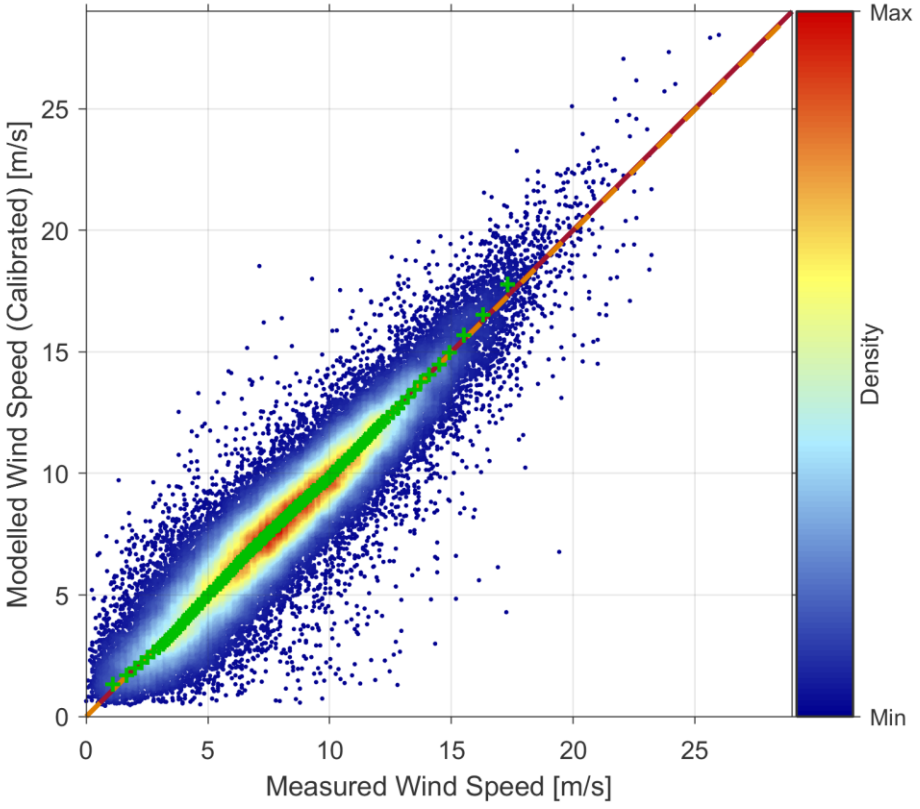




Figure B.50. M5 met buoy.

## B.6 ERA5 10m Calibration

As noted in Section 4.2, although the higher resolution nested wave models are driven by Vortex wind data, given their larger domains ERA5 data are used for the hydrodynamic and largest-scale wave models. Hence, we briefly describe here the steps taken to calibrate this dataset to against measurements.

ERA5 wind data are biased low for higher wind speeds near the surface, particularly at the 10m level, and require some adjustment prior to use. Our analyses of data from across Europe show that two factors influence this:

1. A region wide underprediction, seen across all offshore locations.
2. Coastal effects, whereby grid cells consisting of even a small fraction of land (as is the case at ABWF) can have a significant effect in lowering wind speeds at 10m.

This bias low is demonstrated in Figure B.51 which presents a scatter plot with overlaid Quantile-Quantiles of raw ERA5 10 m wind speeds and measurements at Arklow Met Mast. Detailed analyses of over a dozen met masts in European waters (and a similar number of coastal buoys, piers and platforms) has led us to a suitable set of adjustments to compensate for this bias.

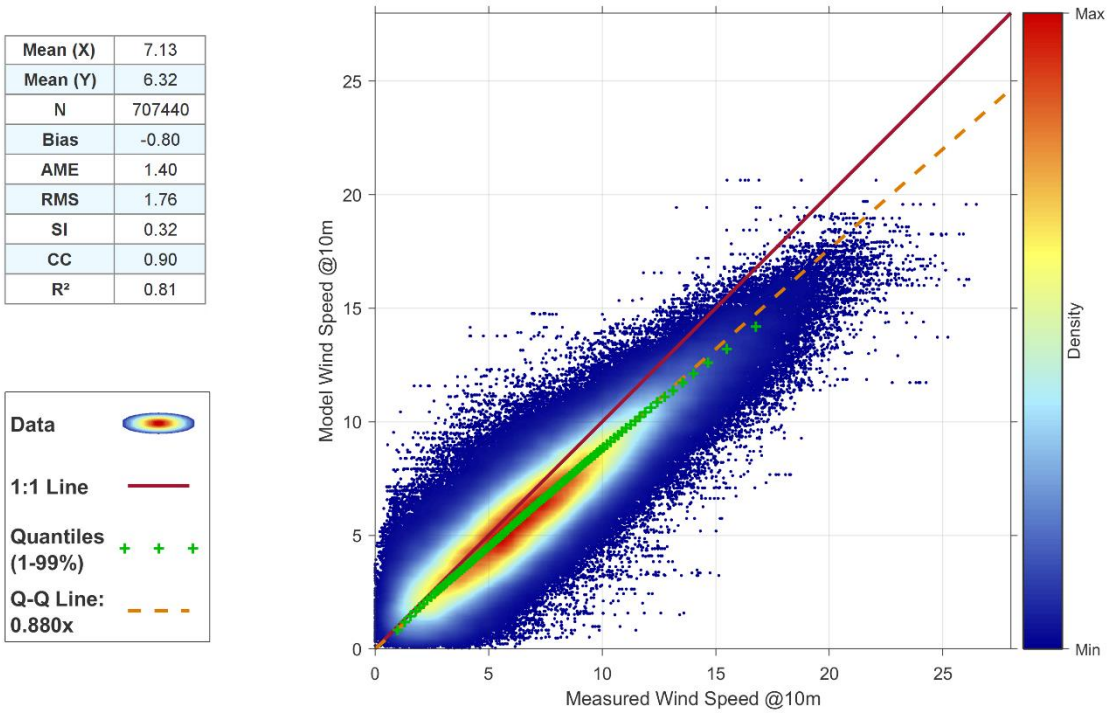



Figure B.51: Validation scatter with overlaid QQ plot of raw ERA5 10 m wind speeds at Arklow Met Mast.

Firstly, a region wide adjustment, based on behaviour seen consistently across all offshore locations is applied to data from all offshore ERA5 grid points. In general, ERA5 performs well offshore for "normal" wind conditions but under estimates higher wind speeds. Thus, the calibration balances three key priorities:

- Any effect on data during normal conditions is minimal.
- A smooth transition is included between normal wind speeds and higher wind speeds.
- Adjusted values better reflect measurements for higher wind speeds

For coastal locations, the regional adjustment alone generally provides good results at the 100m level. However, at the 10m level there is still significant bias. Thus, an additional second step is included which:

- Uses the ERA5 land-sea mask to determine whether land is expected to have an influence on each grid cell.
- Determines appropriate adjustments based on modelled values at 100m and wind profile relationships from nearby offshore grid points. Different directional behaviours are also taken into account.

The results of including both the regional and coastal adjustments at Arklow Met Mast are shown in Figure B.52. Making use of these two adjustments leads to significant improvements when compared to the measurements. It is also worth noting that with limited fetch to the west, winds from the east are more likely to affect any models driven by these data, and as such these alone are shown in Figure B.53.

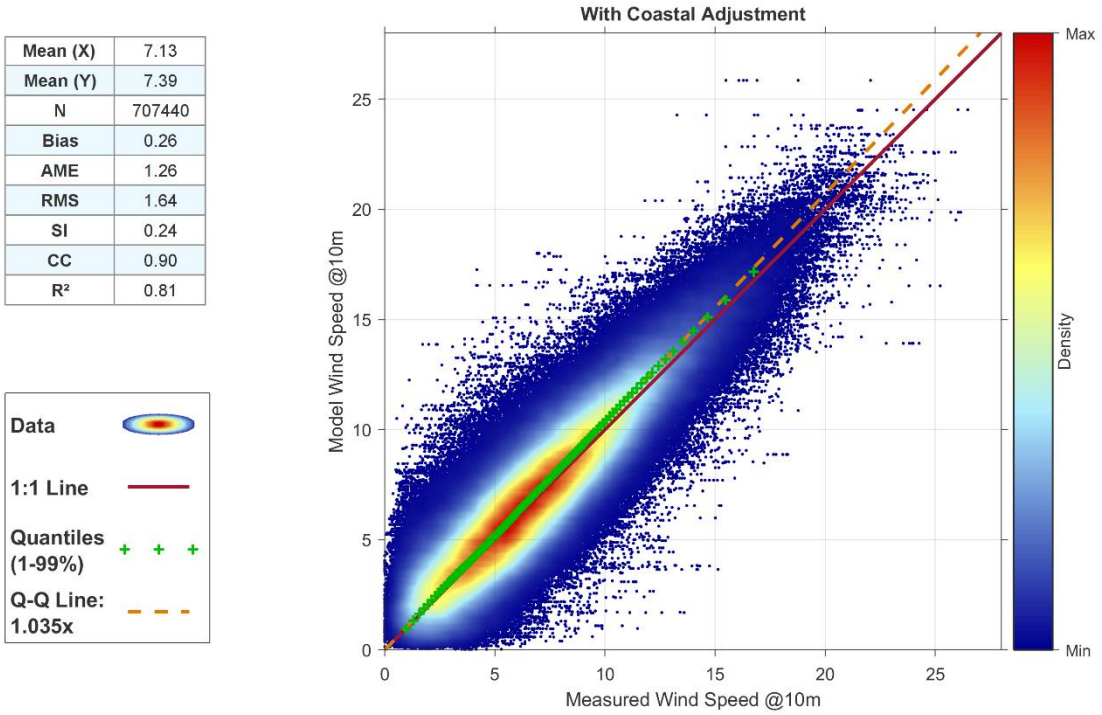



Figure B.52: Validation scatter with overlaid QQ plot of MetOceanWorks' adjusted ERA5 10 m wind speeds at Arklow Met Mast.

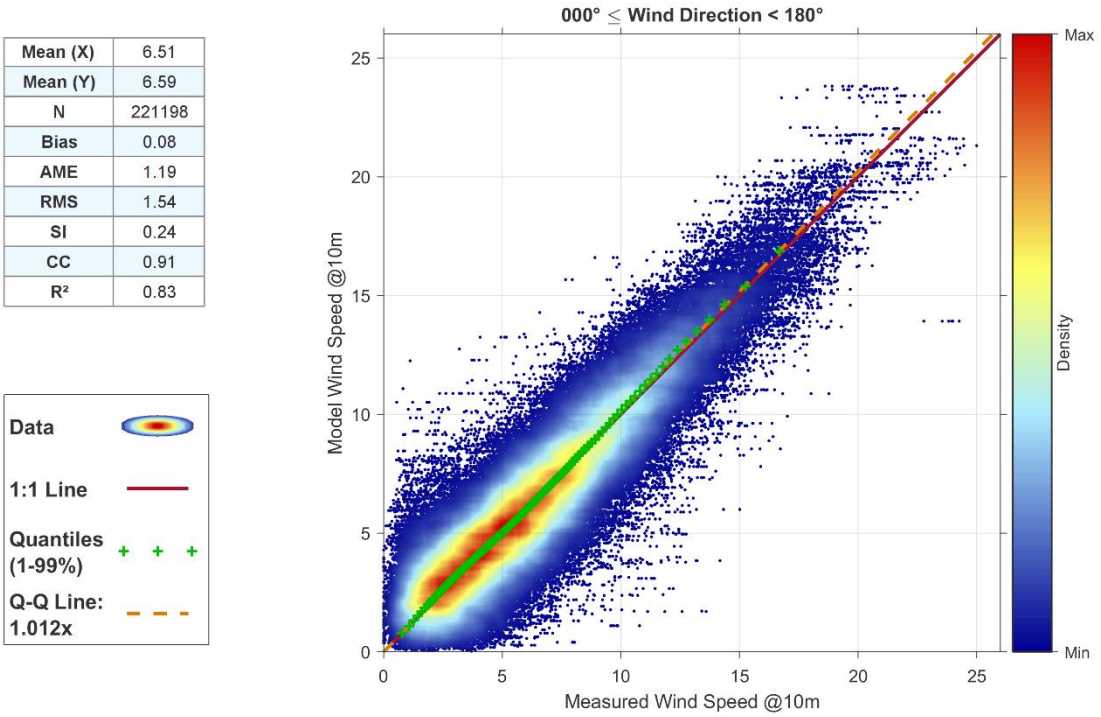



Figure B.53: Validation scatter with overlaid QQ plot of MetOceanWorks' adjusted ERA5 10 m wind speeds for directions between 0 and 180 degrees.

# Appendix C. Wave Model Validation

## C.1 Introduction

In Section 6, the modelled and measured wave datasets used in this project were introduced, and a number of validation details included, showing the suitability of the modelled data for deriving design statistics. In this Appendix, more detail is provided with regard to this wave model validation as follows:

- In Section C.2, a brief overview of the model is included (please see Sections 6.2 through 6.6 for fuller details).
- In Section C.3, the measured datasets used for model validation are reviewed, and details of any quality control (QC) steps applied are outlined.
- Prior to various comparisons which form the remainder of the Appendix, Section C.4 considers some technical details with regard to the calculation of the parameters being compared. Particular focus is given to differences in methodologies between datasets, and any necessary steps to compensate for them.
- Section C.5 presents validation plots of the key sea-state parameters significant wave height (Hm0), mean wave period (Tm01), mean zero-crossing wave period (Tm02), peak wave period (Tp) and mean wave direction (Mdir).
- In Section C.6, validations are split by mean wave direction. Two sets of directional sectors are used, one being a standard set of eight 45° sectors, the other being specifically determined for the Arklow Bank based on fetch in each direction.
- Section C.7 takes a more detailed look at wave spectra, with both directional and omni-directional behaviour compared.
- Section C.8 reviews a number of periods around significant wave height peaks, with time series and temporal evolution of wave spectra considered.
- Finally, Section C.9 compares the collection of significant wave height peaks predicted by the wave model with those found in the measurements.

## C.2 Modelled Data

Wave data were produced using a large-scale Irish Sea SWAN model with higher resolution nested models, culminating in a final model local to Arklow Bank (see Section 6.2). The large-scale model used a spatial resolution of 5.5 km whilst the highest resolution nested model had a horizontal resolution of approximately 110 m. The wave model extents and resolutions are shown in Figure 6.2 below.

At each measurement location, model data for validation is taken from the model nest with the highest available resolution.

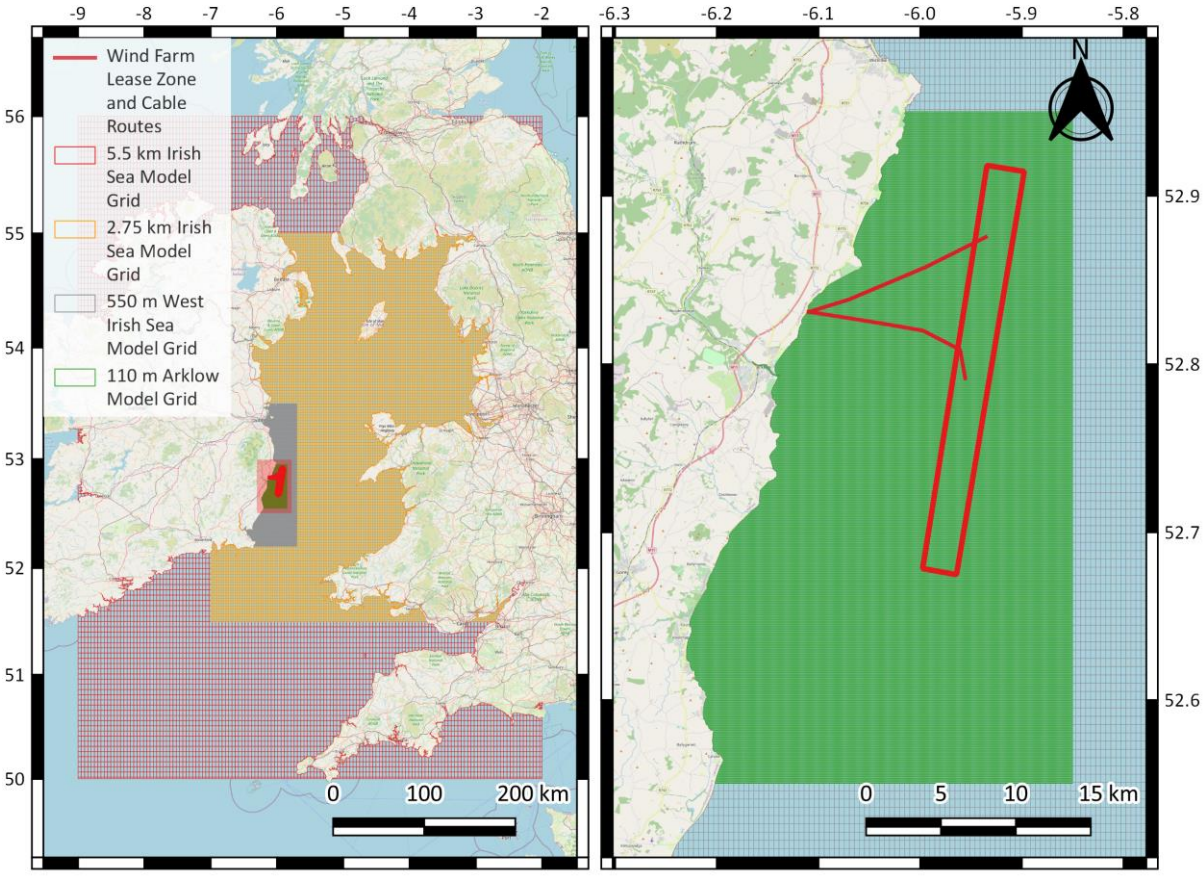



Figure C.1: Wave model domains.

## C.3 Measured Data

### C.3.1 Overview

The modelled data described in the previous Section were compared to the measured datasets shown in Table C.1. The locations of these datasets are shown in Figure C.2, and valid data return summarized in Figure C.3.

Table C.1: Measured datasets.

| Dataset | Deployment | Location | Time Period | Water Depth [m MSL] |
|---|---|---|---|---|
| **AWAC A** | 1 | 52.9096 °N, 5.9157 °W | 6-Nov-2019 to 18-May-2020 | 27.4 |
| | 2 | 52.9079 °N, 5.9172 °W | 1-Aug-2020 to 16-Oct-2020* | |
| | 3 | 52.9085 °N, 5.9172 °W | 5-Nov-2020 to 7-Mar-2021 | |
| **AWAC B1** | 2 | 52.8504 °N, 5.9461 °W | 2-Aug-2020 to 15-Oct-2020 | 30.2 |
| | 3 | 52.8487 °N, 5.9471 °W | 7-Nov-2020 to 7-Mar-2021 | |
| **AWAC C** | 1 | 52.8218 °N, 6.0206 °W | 24-Nov-2019 to 19-May-2020 | 26.3 |
| **AWAC D1** | 2 | 52.8595 °N, 6.9173 °W | 1-Aug-2020 to 16-Oct-2020 | 30.5 |
| | 3 | 52.8583 °N, 6.9169 °W | 7-Nov-2020 to 7-Mar-2021 | |
| **AWAC E** | 1 | 52.6910 °N, 5.9930 °W | 24-Nov-2019 to 19-May-2020 | 39.6 |
| | 2 | 52.6907 °N, 5.9943 °W | 2-Aug-2020 to 15-Oct-2020 | |
| | 3 | 52.6902 °N, 5.9946 °W | 22-Nov-2020 to 8-Mar-2021 | |
| **M2** | - | 53.4836 °N, 5.4302 °W | 3-May-2001 to 27-Apr-2020 | 89.4 |
| **M5** | - | 51.6904 °N, 6.7043 °W | 18-Oct-2004 to 27-Apr-2020 | 72.3 |
| **Splaugh** | - | 52.2394 °N, 6.2788 °W | 1-Apr-2016 to 9-Jun-2017† | 14.4 |

* No valid data was recorded was at AWAC A during Deployment 2 after 5th August 2020.

† The Splaugh dataset continues through until 1st January 2018, however as discussed in Section C.3.4, data quality deteriorates significantly towards the end of 9th June 2017, and as such only values before this time are used for model validation.

Through the subsections which follow, each of these datasets is introduced in more detail, and any quality control (QC) deemed necessary outlined. For convenience, datasets are grouped by source, with the project AWACs described in Section C.3.2, M2 and M5 from the Irish Marine Institute outlined in Section C.3.3, and the Splaugh dataset from the Commissioners of Irish Lights at considered in Section C.3.4.

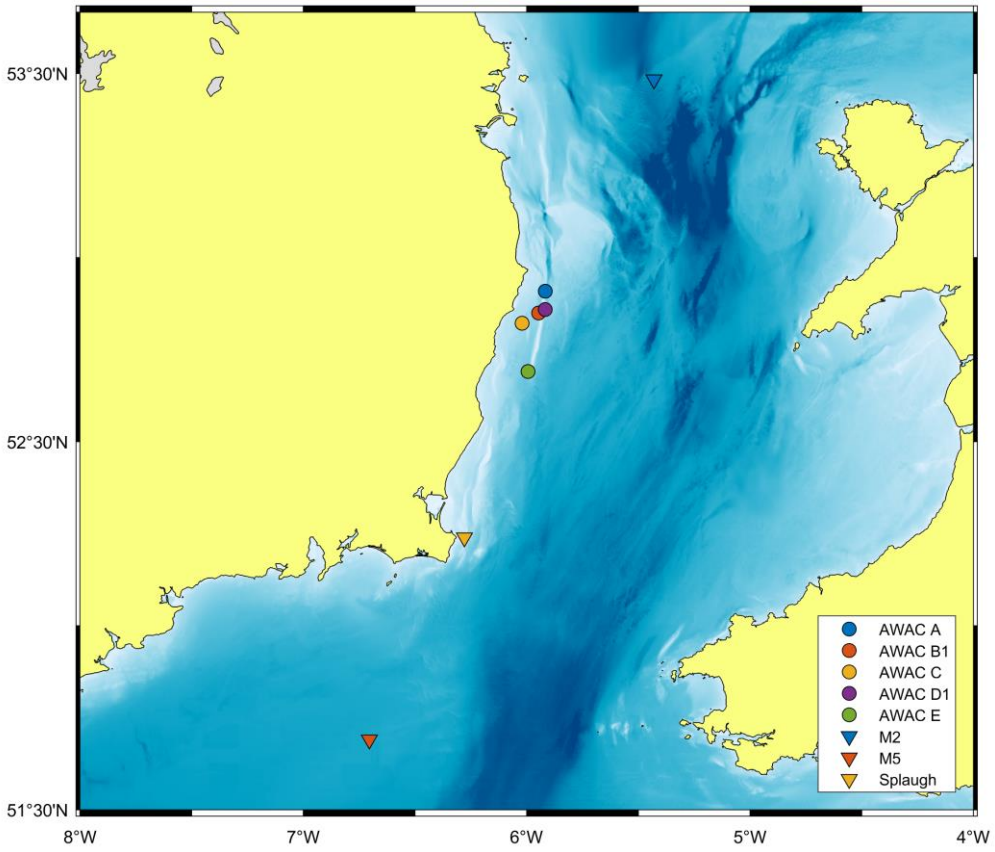



Figure C.2. Measured datasets.

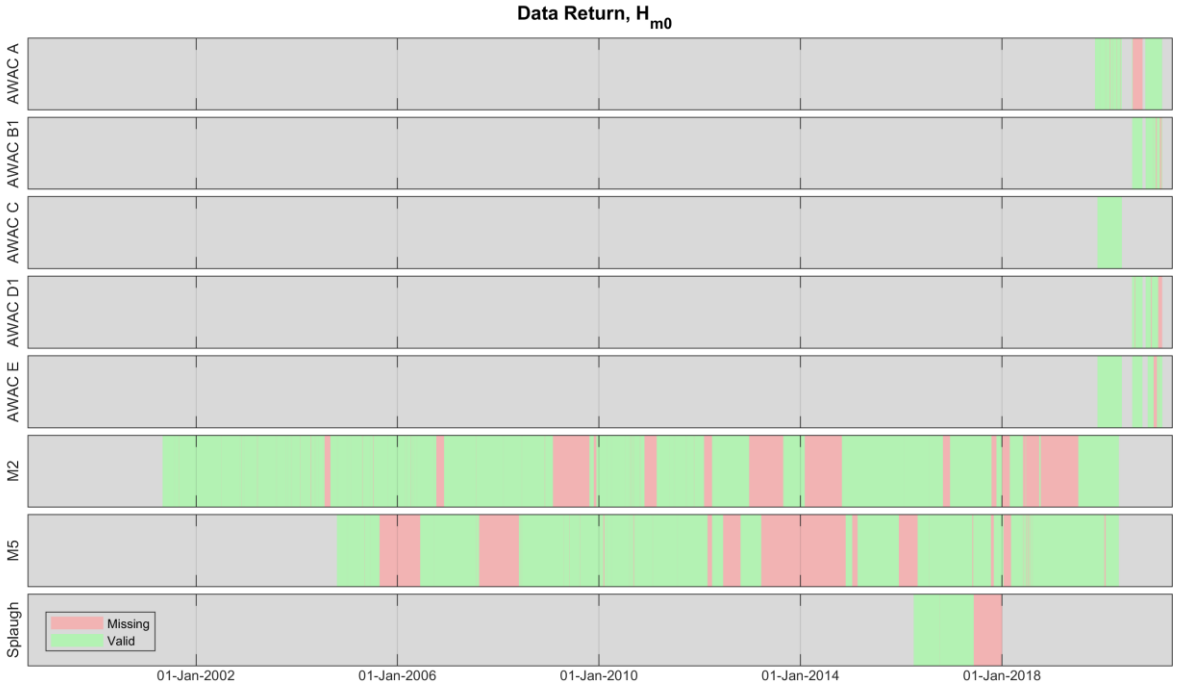



Figure C.3. Data return of measured datasets.

## C.3.2 AWACs A, B1, C, D1 and E

### C.3.2.1 Overview

A dedicated metocean campaign was conducted by Fugro on behalf of SPL for this project, with instruments measuring across three deployment periods as follows:

- **Deployment 1, November 2019 to May 2020:** Five seabed frames, configured with various instrumentation including Acoustic Wave and Current Profilers (AWACs), were deployed at locations denoted 'A', 'B', 'C', 'D' and 'E' (see Figure C.4). Unfortunately, at the interim six-month service visit, the frames deployed at location 'B' and 'D' were not recoverable and thus no data is available for these locations.
- **Deployment 2, August 2020 to October 2020:** Measurements were taken at A and E, alongside two additional locations, denoted 'B1' and 'D1', as shown in Figure C.4. Note that only four days of data are available at location A during this Deployment, due to disturbance of the seabed frame on 5th August 2020.
- **Deployment 3, November 2020 to March 2021:** Measurements were again taken at A, B1, D1 and E.

Valid data return for the project AWACs are shown in Figure C.5.

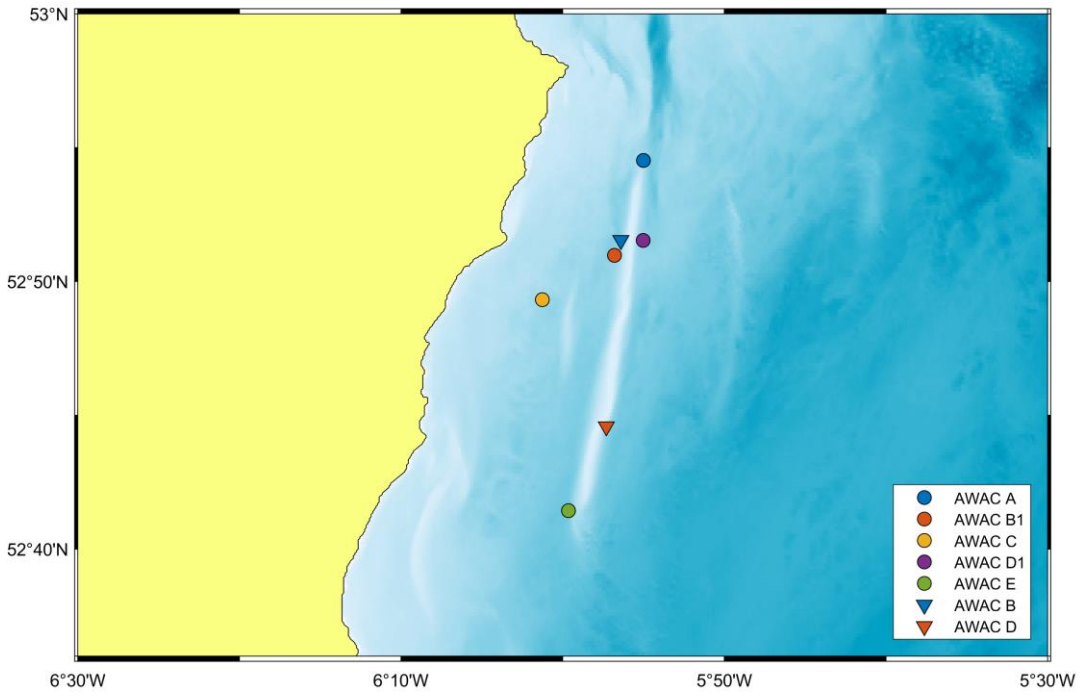



Figure C.4: Project AWAC locations.




Figure C.5: Data returns from project AWACs.

### C.3.2.2 Measurement Considerations

***Spectral Frequency Range***

The AWACs use two different methods to determine omni-directional and directional spectra as follows:

- Omni-directional spectra are calculated by an Acoustic Surface Tracking (AST) method, which provides a direct measure of the surface waves.
- Directional spectra are determined by combining the AST and wave orbital velocities measurements made close to the surface.

Please see the AWAC documentation [25] for full details.

All three AWACs are configured to sample the AST at a frequency of 2 Hz, and orbital velocities at 1 Hz, resulting in a frequency range of 0.02 Hz to 0.99 Hz for the omni-directional spectra, and 0.02 to 0.49 Hz for the directional spectra. However, both are subject to additional limitations. For the AST, this has a relatively minor effect: the AWAC documentation specifies a shortest measurable wave of 1.0 second in water depths of 24 m, and of 1.2 seconds in water depths of 36 m. For the directional spectra, limitations are much more severe, with the aforementioned shortest measurable wave significantly impacted by the intensity of background currents. For example, for an arbitrary but typical period of Deployment 1 at AWAC A, Figure C.6 shows the highest measured frequency (blue line, left hand scale)[9] plotted alongside current velocities along

[9] Note that the spikes here reflect unexpected behavior for a limited number (approx. 120) directional spectra at AWAC A only, where a cut-off is not applied, but instead low energy, equally spread in all directions is included. A more detailed review of these spectra shows that, due to the low energy in high bins, the lack of cut-off has no notable effect on Mdir, and as such we do *not* mark these points as invalid.

the line of mean wave direction (red line, right hand scale). All higher frequencies are marked as "missing" (i.e. given a value of -999) in the AWAC directional spectra data files.

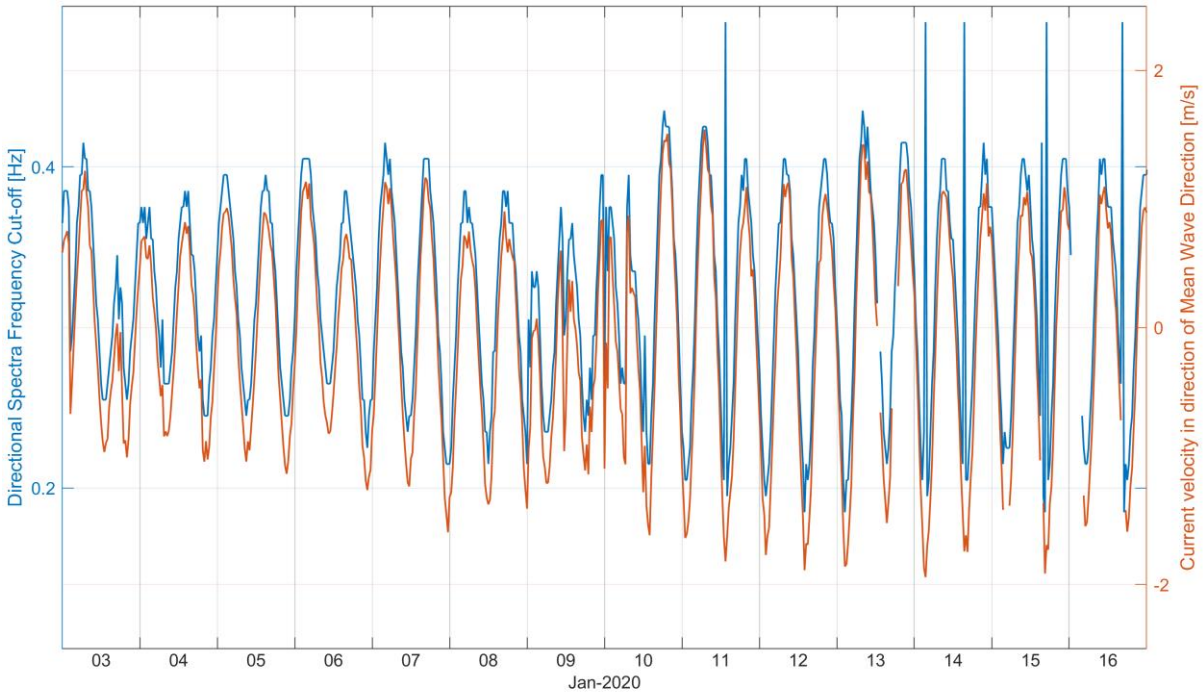



Figure C.6. AWAC directional spectra frequency limitations.

For example, during Deployment 1, at AWAC A, where this behaviour is most severe, this highest measured frequency ranges from 0.175 to 0.485 Hz across the measurement period (0.215 to 0.395 Hz at AWAC C, 0.195 to 0.335 Hz at AWAC E).

It should be noted that omni-directional spectral files provided by Fugro only span the range 0.02 to 0.49 Hz. For Deployment 1, we were able to obtain full spectra (up to 0.99 Hz) through Nortek, the instrument manufacturers. However, review of behaviour at these additional frequencies (see Section C.4.2) suggests that they add little of value, and may even be detrimental for comparisons of model and measured behaviour for parameters such as Tm01 and Tm02. As such, these fuller spectra have not been obtained for Deployments 2 and 3.

As a result of all these factors, in all that follows for the AWACs:

- Parameters derived from omni-directional spectra, i.e. Hm0, Tm01, Tm02 and Tp, take into account waves with periods between approximately 1 second and 50 seconds.
- Omni-directional spectra themselves span periods between 2 and 50 seconds (1 and 50 seconds for Deployment 1, if required).
- Directional spectra, and parameters derived from the directional spectra, i.e. mean wave direction (Mdir) use ranges which *vary* between approximately 2 to 50 seconds and 5 to 50 seconds.

Of particular note: whilst Hm0, Tm01, Tm02 and Tp should provide a good representation of wave conditions throughout, for cases where high frequency wind-sea dominates, Mdir may not always be fully representative of the real mean wave direction.



***Directional Behaviour During Deployments 2 and 3***

The Final Data Report which accompanies the measurements [1] notes that:

> *… the frames moved considerably during Deployments 2 and 3. In this instance, the data were subjected to a further realignment.*

This realignment, applied to locations B1, D1 and E, is determined based on the major axes of current velocities, and then:

> *In these cases, the peak and mean coming directions had the same directional offset applied as the current data […] for completeness. However, the wave spectra data files have not been altered.*

For the present report, these corrections have been applied to directional spectra where presented.

Additional issues are also seen in the full directional spectra provided by Fugro for Deployments 2 and 3 for AWACs B1, D1 and E. In particular:

a) For Deployment 3 of AWAC D1, directional spectra are marked invalid (i.e. -999) at all but the lowest frequency.
b) The time varying upper frequency limit (as shown in Figure C.6) is unexpectedly absent from the remaining directional spectra for these instruments and deployments. It *is* seen in directional parameters provided elsewhere, and thus can be determined for each timestep, but is *not* seen in directional spectra which provide values for all frequencies throughout.

Where presented in validation plots, we treat the first of these (i.e. Deployment 3, AWAC D1) as being invalid, but do not make any adjustment for the latter.

The uncertainty in these directions may have an impact on the various validation plots for AWACs B1, D1 and E as follows:

- Mean wave directions (Mdir) may be erroneous for Deployments 2 and 3 should the corrections applied not prove sufficient.
- In validations which split the data by measured mean direction, any such errors may lead to some sea-states being misclassified.
- Directional spectra, where presented, may not only suffer from the same problems as seen for Mdir, but may also include results for higher frequencies than can accurately be measured.

For convenience, an additional Mdir validation plot for Deployment 1 only of AWAC E is included in Section C.5.

***Sampling Regime and Spectral Averaging***

All three AWACs are configured to record in bursts of 512 seconds (8 minutes and 32 seconds) every 30 minutes. From each such burst, omni-directional and directional spectra are formed, and from these summary sea-state parameters such as Hm0, Tm02 and Tp are derived.

Each *individual* burst would generally be considered somewhat short in duration. For example, the AWAC documentation itself [25] includes the following:

> *Waves are random and therefore measuring waves requires sampling over a period of time that will best "capture" or represent the complete sea state statistically. The objective is to measure the wave event over a long enough time so that the random event can be properly characterized. Sampling theory*

*suggests, as a rough rule of thumb that the measurement duration is long enough to capture a minimum of 100 cycles of an event (wave). When we measure ocean waves we have to consider what the longest expected wave period is going to be; 100 cycles of this longest wave will be the minimum wave burst duration. As an example, if waves are to be measured in the Mediterranean Sea, we would expect the waves to be 10 seconds or shorter. Therefore 10 seconds x 100 cycles is 1000 seconds. Sampling rate and number of samples defines the sampling length. A corresponding configuration could be either 1024 samples at 1 Hz or 2048 samples at 2 Hz.*

In order to compensate, rather than using the spectra and sea-state parameters from *individual* bursts in the model validations included in this document, we instead carry out the following steps:

1. Create a new set of omni-directional spectra which consist of *three-burst* moving averaged spectra. For example, the new spectrum for time *t* is the mean of the three original spectra determined for time *t, t* minus 30 minutes, and *t* plus 30 minutes.
2. Recalculate sea-state parameters from these averaged spectra.
3. Use the recalculated parameters for all model validations.

Given the uncertainties noted above with regard to directional spectra, including their absence for Deployment 3 of AWAC D1, mean wave directions are *not* calculated using this approach. Instead, they are taken to be the unit vector three-burst moving average of the Mdir *parameter*. All directional spectra presented in validation plots are three-burst averages.

As a result, the parameters used in model validations are, in general, based on a total of 25 minutes and 36 seconds of data within a 68 minute and 32 second time period. As might be expected, the result of such averaging is to smooth the derived parameters somewhat, for example as shown in Figure C.7. As discussed in Section F.4 of Appendix F, it is not possible to ascribe a specific "sea-state duration" to this averaged time-series, given the gaps present, however it is perhaps reasonable to consider it to be approximately representative of a 1-hour sea state.

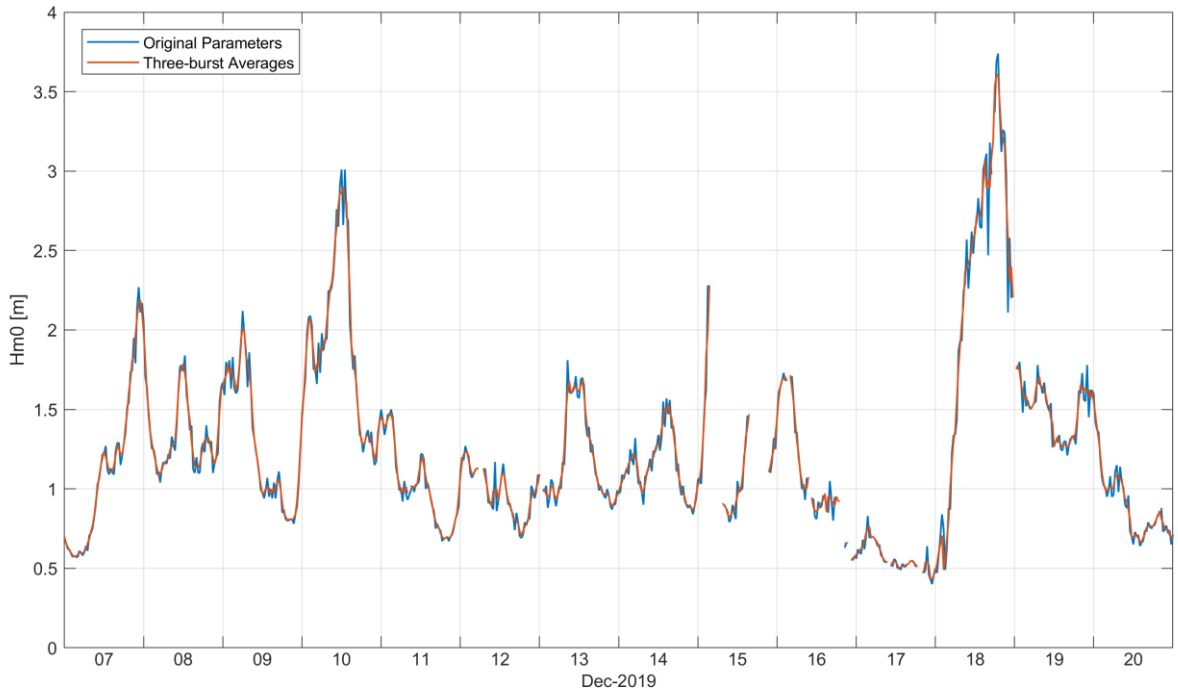


Figure C.7. AWAC averaging, example period.

### C.3.2.3 Data Review and Quality Control

Sea-state parameters calculated for each *individual* burst have been supplied by Fugro for each of the three AWACs. These parameters appear to have been subjected to detailed QC by Fugro and after review of timeseries, no additional data were removed. However, as noted above, these parameters for individual bursts are not used in the model validation plots, but instead parameters re-derived from three-burst moving averages. In order to maintain the same level of quality control in these re-derived parameters, the following method is used:

1) Any spectra for individual bursts are marked as invalid if *any* of the corresponding Hm0, Tm02 or Tp parameters are marked invalid.
2) Moving mean spectra are calculated as described in Section C.3.2.2 above, using only valid spectra. That is the new spectrum for time *t* is the mean of only *valid* spectra from time *t*, *t* minus 30 minutes and *t* plus 30 minutes. If *none* of these spectra are valid then no valid spectrum is created for time *t*.
3) Parameters are calculated for the model spectra only at timestamps with valid mean spectra.

Note that this does mean that for some timestamps – those where only one of the three spectra averaged is valid – no averaging is carried out, and only one individual burst is used. However, it is hoped that this provides a reasonable balance between making the most of the data available, and adjusting for the relatively short burst duration.

A similar process is used for directional parameters, with Mdir only derived using valid values from individual bursts, and directional spectra only used where all of Mdir, Hm0, Tm02 and Tp are valid.

### C.3.3 M2 and M5 Buoys

#### C.3.3.1 Overview

The Irish Marine Data Buoy Observation Network[10] is managed by the Irish Marine Institute in collaboration with Met Éireann and the UK Met Office. The five available met buoys are shown in Figure B.23.

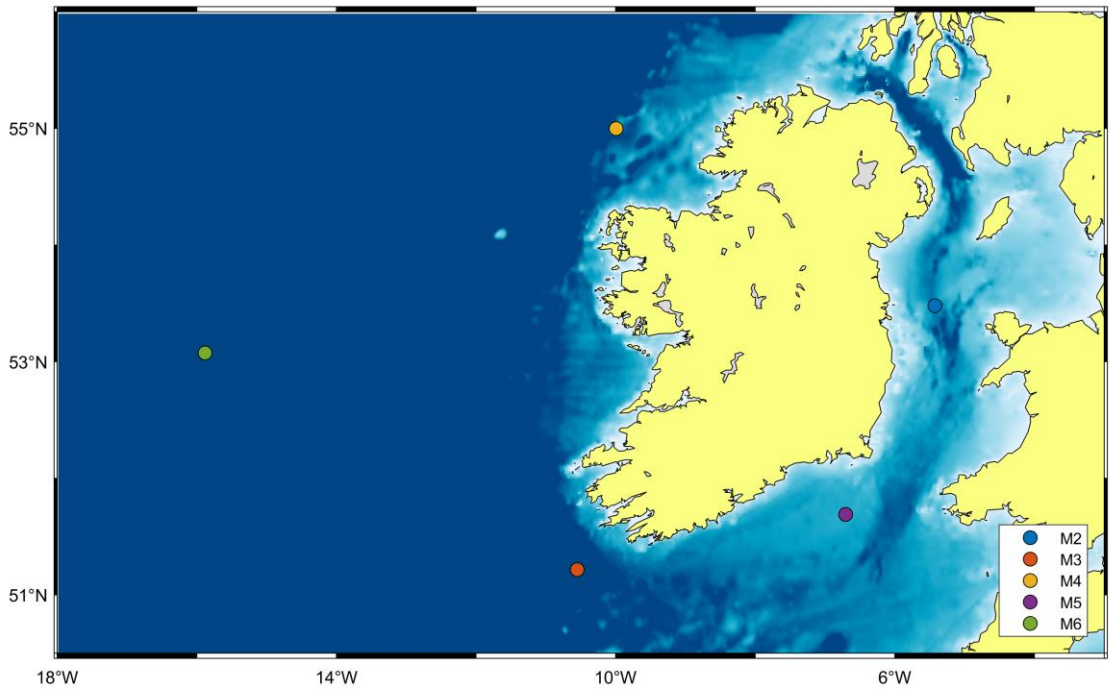



Figure C.8. Met buoy locations.

For this project, the buoys M2 and M5 are used for validation of modelled wave heights. These buoys provide wave parameters for the following periods:

- M2: 03-May-2001 to 27-Apr-2020 (the date when the data were downloaded).
- M5: 18-Oct-2004 to 27-Apr-2020 (the date when the data were downloaded).

#### C.3.3.2 Data Review and Quality Control

As with all measured datasets considered in this Appendix, time series of sea-state parameters were reviewed before use in any calibrations. It is unclear as to the level of quality control already applied to the data prior to download, however for a small number of timestamps Hm0 is marked as invalid where other parameters (e.g. Mdir) are not, suggesting that at least some QC has been applied. Indeed, given that:

a) Our review has led to only the removal of a small number of data points, primarily suspicious Tm02 and Mdir values where Hm0 has already been marked invalid.
b) Overall, as seen for example in Figure C.3, there are a much larger number of data points already marked as invalid.

it does appear that a sufficient level of QC has already been applied to the data.

[10] Please see http://www.marine.ie/Home/site-area/data-services/real-time-observations/irish-marine-data-buoy-observation-network for more details.



In reviewing the time series, it is also clear that both M2 and M5 buoys have been updated part way through their measurement periods. For example, at M2:

- Before 23rd October 2009, Tm02 is only recorded to the nearest second and Mdir is not available.
- From 23rd October to 24th November 2009, the resolution of Tm02 is significantly higher, and Mdir is now included.
- There is then a gap in the data to 10th December 2009, before the original behaviour returns up to 26th October 2010.
- Thereafter, Tm02 is of higher resolution and Mdir present through to the end of the recording period.

At M5, behaviour is similar but simpler: 1 second resolution Tm02 and no Mdir up to midday on 21th February 2012, higher resolution Tm02 and Mdir included thereafter.

We have not yet been able to establish in full the reasons for this behaviour, however one source (dated 2014) [26] states that for M2 there has been a "*Fugro [Oceanor Wavescan] buoy at this location since 26 Oct 2009"* and for M5 a *"Fugro [Oceanor Wavescan] buoy at this location since 21 Feb 2012".* This would fully explain the changes at M5, though does not quite provide a full picture for M2, with a slight difference in dates, and also no explanation for the changes later in 2009 and in 2010.

These changes significantly affect the behaviour of Tm02 and Mdir, but not Hm0. Though the resolution of values does improve a little when the instrumentation appears to be first updated (for example, from 0.1 to approx. 0.08 m at M2 in October 2010) it then changes repeatedly in later deployments (e.g. M2 has resolution of approx. 0.16 m from March 2012, then 0.04 m from October 2014, then back to 0.16 m from January 2016, etc.). After comparing, for example, Hm0 validations from before and after the apparent instrumentation change, we see no reason to treat any one period of recording as more trustworthy than another, and as a result carry out validations at M2 and M5 on *all* valid Hm0 across the measurement period.

## C.3.4 Splaugh

### C.3.4.1 Overview

The Commissioners of Irish Lights maintain a number of buoys and lighthouses collecting weather and sea state data[11], as shown in Figure B.33.

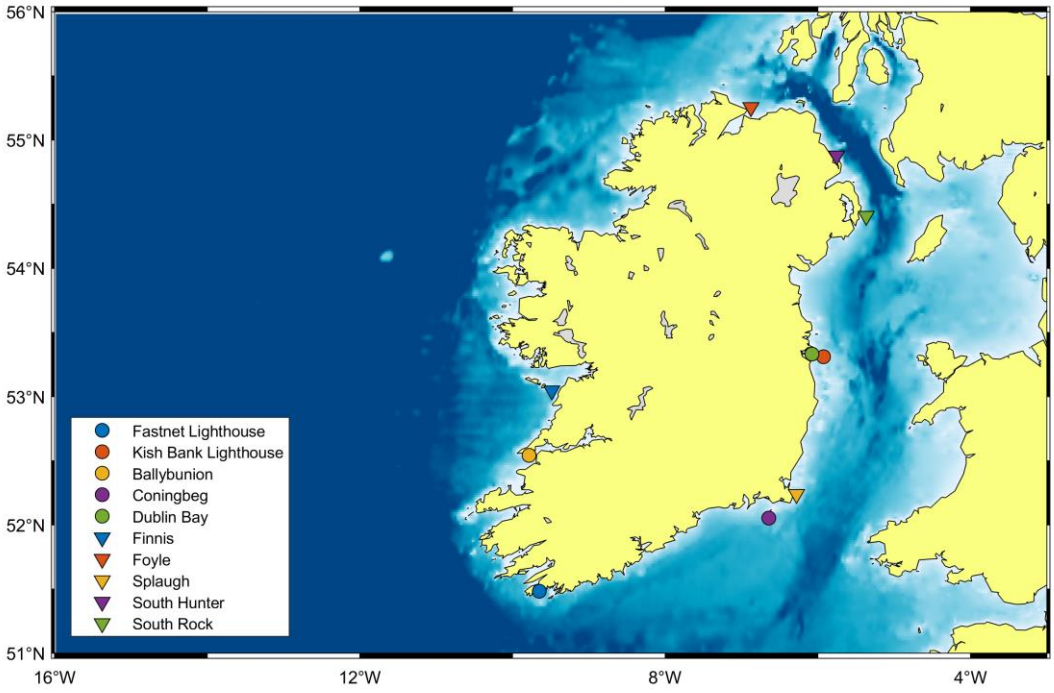



Figure C.9. Irish Lights measured data locations.

For this project, data from the buoys at two locations, Splaugh and Coningbeg, were acquired for the period 01-Apr-2016 to 01-Jan-2018. Unfortunately, data from Coningbeg are extremely poor quality – see for example Figure C.10 – with at most the first week of Hm0 appearing reasonable. As such, only the Splaugh dataset has been considered for validation of the wave model.

[11] See https://www.irishlights.ie/technology-data-services/metocean-charts.aspx for more details.

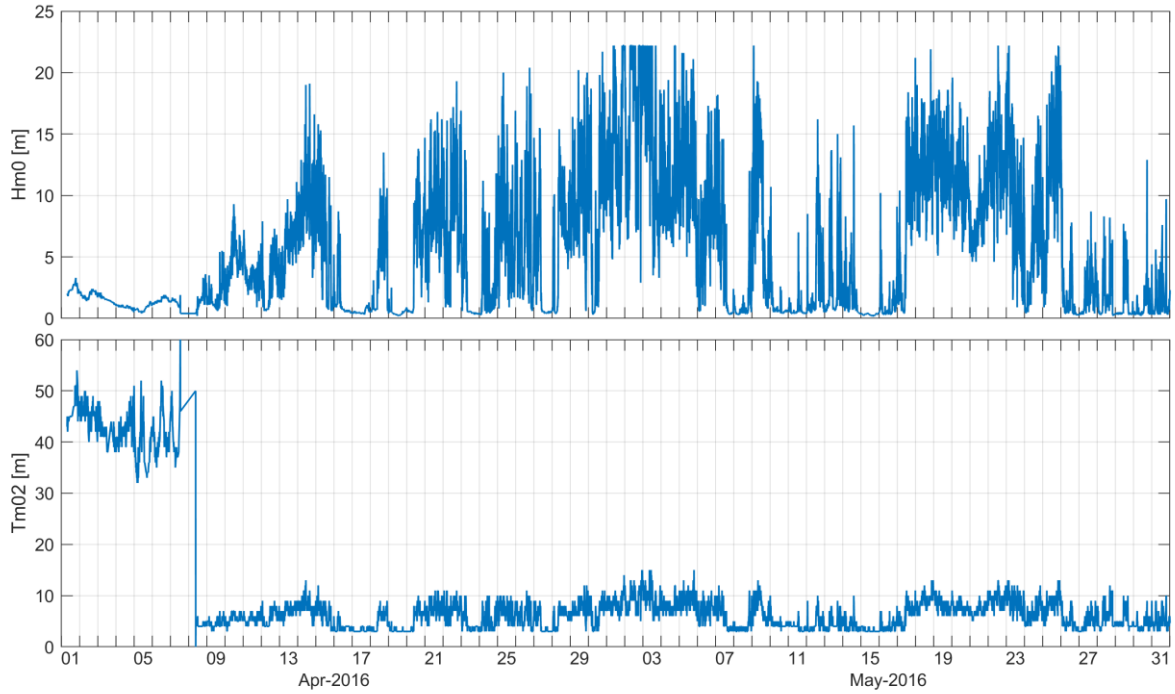



Figure C.10. Coningbeg data, start of measurement period.

### C.3.4.2 Data Review and Quality Control

The documentation that accompanied these data states:

> *The MetOcean Data is not subjected to full quality control or quality assurance procedures and may not meet the criteria and standards of the International Hydrographic Organisation (IHO) or the International Association of Marine Aids to Navigation and Lighthouse Authorities (IALA) AtoN performance and response requirements. The MetOcean Data should be used only for information purposes and never relied upon in isolation. It does not purport to be comprehensive and as preliminary data is to be used with appropriate caution*

At Splaugh, Tm02 values are only reported to the nearest second, and add little of value with regard to model validation. Hm0 data, at a resolution of 0.1m, appear to be of reasonable quality from the start data (1st April 2016) through to the 9th June 2017. From this point however, through to the end of the dataset on 1st January 2018, there is significant deterioration, as shown for example in Figure C.11.

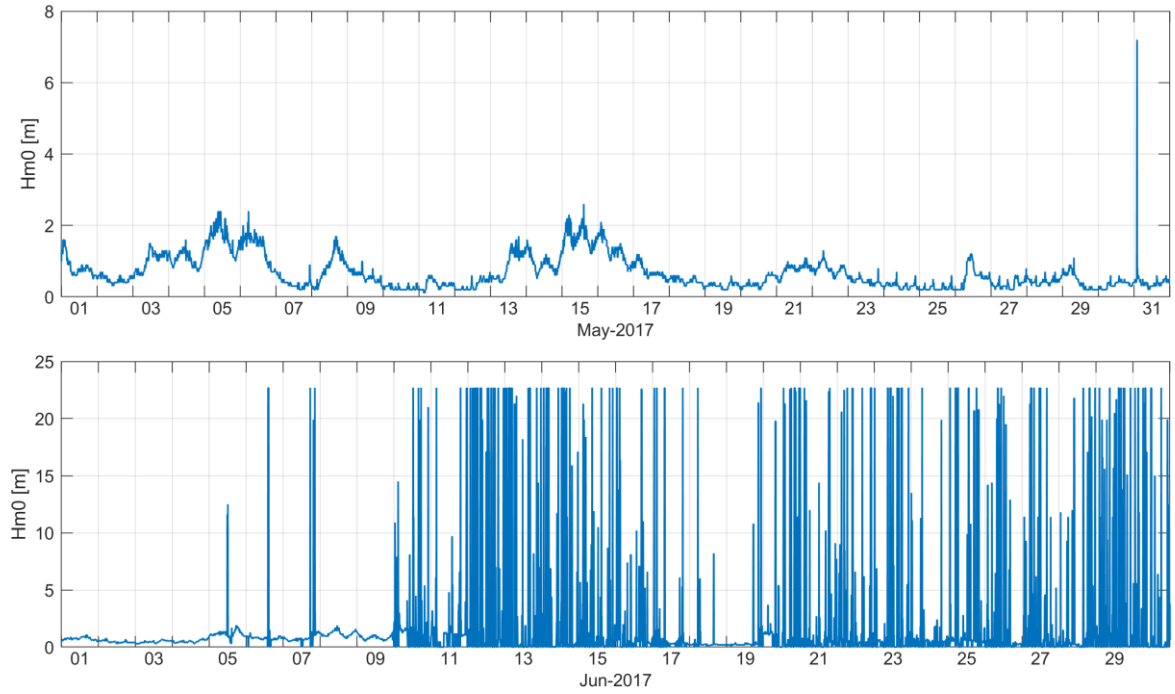



Figure C.11. Splaugh Hm0, May and June 2017.

Although there may be some small sections in the later period where valid data can be found, since these are so sporadic, their selection highly subjective, and significant doubts surround the instrumentation, only data from the earlier period are used hereafter. In this earlier period, only a small number of isolated spikes or unexpected zeroes have been removed. Some doubt does remain, even in this earlier data. There are tidal fluctuations in the Hm0 measurements which may be spurious or may indeed be real due wave/current interactions. However, these interactions are only included in the highest resolution nest around the Arklow Bank and Splaugh lies outside this model domain. Therefore, even if these fluctuations are real, we would not expect the model to represent them.

Given the apparent lower quality of the Splaugh dataset, and the tidal behaviour seen in the measurements not being captured by the model, validation plots for Splaugh are included for general reference only and have not been used for detailed model validation.

## C.4 Parameter Derivation

### C.4.1 Introduction

Before proceeding to validation plots of sea-state parameters, there is some benefit in a brief discussion on their derivation, since apparently small differences in methodology can have a notable effect on validation results. For example, Figure C.12 shows two validation plots for zero crossing period (Tm02) where significant wave height (Hm0) is greater than 0.5 m, with alternate sources of Tm02 as follows:

- **Top validation**: Measured Tm02 are those calculated directly by the AWAC, modelled Tm02 are those reported directly by the SWAN model.
- **Bottom validation**: Both modelled and measured Tm02 are recalculated from omni-directional spectra using frequencies only up to 0.5 Hz.

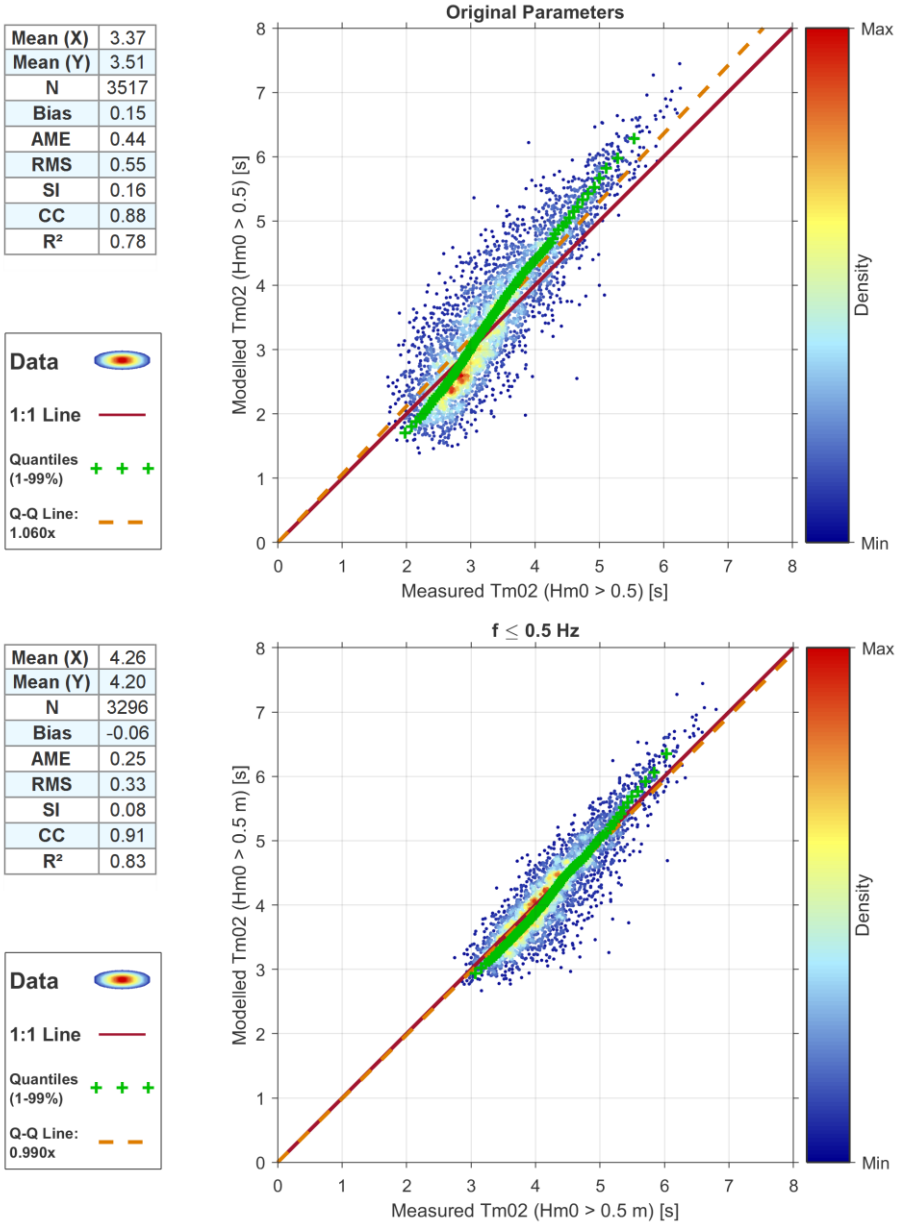



Figure C.12. AWAC A, Tm02 validations, different calculation methods.

Note that in both cases, measured data is taken from a *single* burst of the AWAC such that any differences must be explained by the parameter calculation method, rather than the spectral averaging that is used in the final validation plots of later sections.

Though both plots might be said to "compare modelled and measured Tm02", they paint notably different pictures with regard to model performance. In order to determine what is most appropriate, a more detailed look at the calculations used is necessary here, and perhaps also for other parameters being compared. As such:

- Section C.4.2 discusses derivation of parameters which come from spectral moments, i.e. significant wave height (Hm0), mean wave period (Tm01) and mean zero-crossing period (Tm02).
- Section C.4.3 discusses the calculation of peak wave period (Tp).
- Section C.4.4 discusses the calculation of mean wave direction (Mdir).

## C.4.2 Omni-directional Parameters from Spectral Moments (Hm0, Tm01, Tm02)

Although differences in derivation of spectra themselves (e.g. spectral resolution) can affect the calculation of Hm0, Tm01 and Tm02, for this project both modelled and measured spectra are of high enough resolution for this to have little impact. Of far more importance is the presence, and treatment of, energy in the high frequency tail of spectra.

### C.4.2.1 Example Spectrum

To consider this, we first begin with the simple spectrum shown in Figure C.13. This is in fact a JONSWAP spectrum with Hm0 of 2.5m, Tp of 7s and γ of 1.5, though the same reasoning holds for any shape with high frequency content.

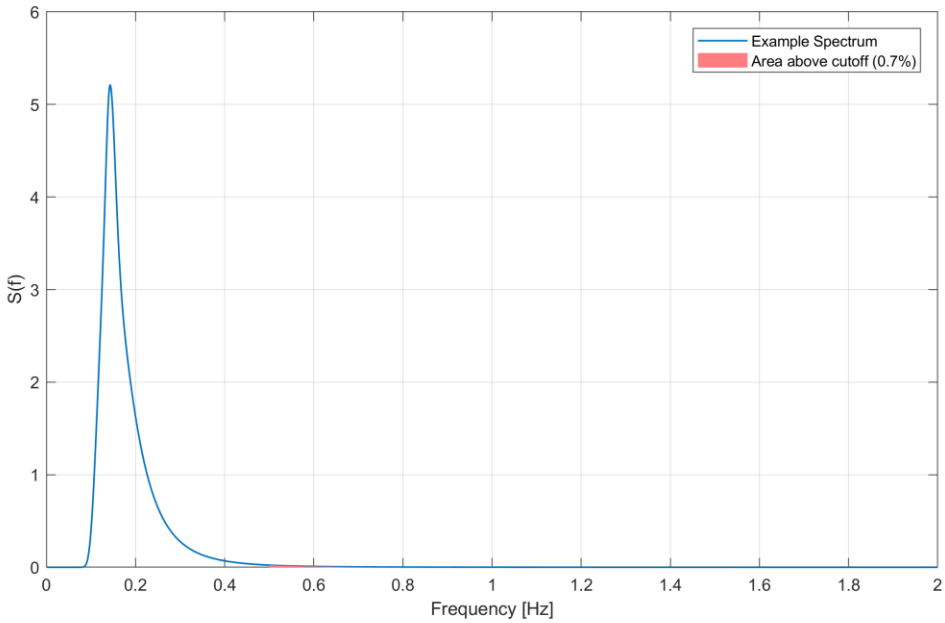



Figure C.13. Example wave spectrum.

The zeroth moment of the spectrum, $m_0$, is given by:

$$m_0 = \int_0^\infty S(f)\mathrm{d}f$$

i.e. it is the area under the blue curve shown above. If we *only* use frequencies up to, say, 0.5 Hz, a small amount of this area would *not* be included – that shown in red above. This is only 0.7% of the total area, so its inclusion or exclusion in the overall integral has a limited effect in calculating $m_0$. Significant wave height, Hm0, is given by:

$$H_{m0} = 4\sqrt{m_0}$$

Thus, the inclusion or exclusion of energy above 0.5 Hz similarly has little effect on Hm0. In the case of our example spectrum, Hm0 is 2.50 m with the tail and 2.49 m without.

The first moment of the spectrum, $m_1$, is given by:

$$m_1 = \int_0^\infty fS(f)\mathrm{d}f$$

i.e. the area under the blue curve in Figure C.14. For this parameter, the area above the cut-off is a slightly higher proportion, at 2.7% of the total area. Mean wave period, Tm01, given by:

$$T_{m01} = m_0/m_1$$

is therefore affected a little more than Hm0 by the inclusion or exclusion of these frequencies. For our example spectrum, Tm01 is 5.54 s with the tail, and 5.65 s without.

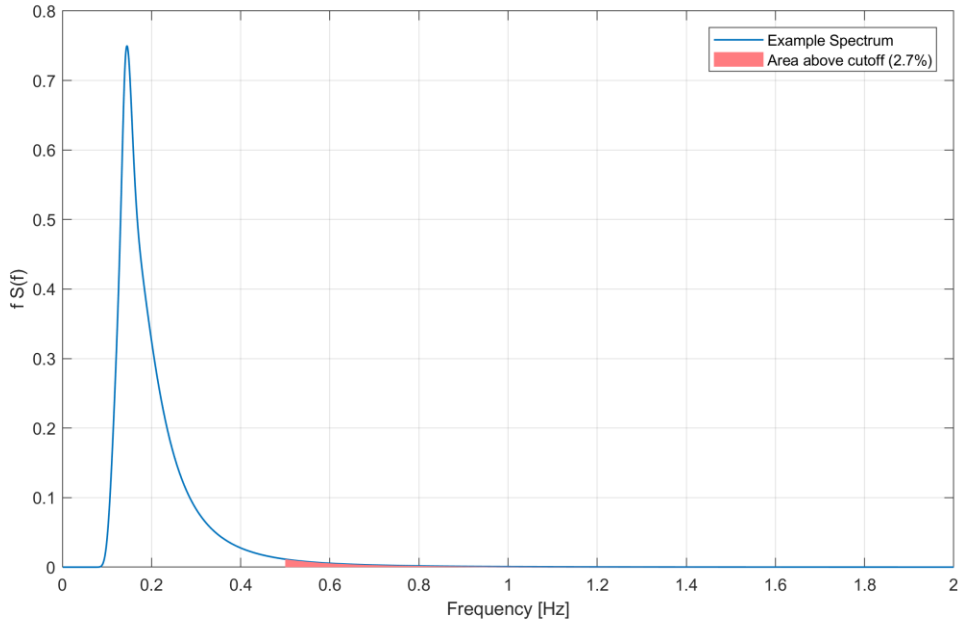



Figure C.14. Area for first moment.

By the time we reach the second moment, $m_2$, given by:

$$m_2 = \int_0^\infty f^2 S(f) \mathrm{d}f$$

We start to see a more severe impact, as shown in Figure C.15. Now the area above the cut-off is some 9.1% of the total value of $m_2$.

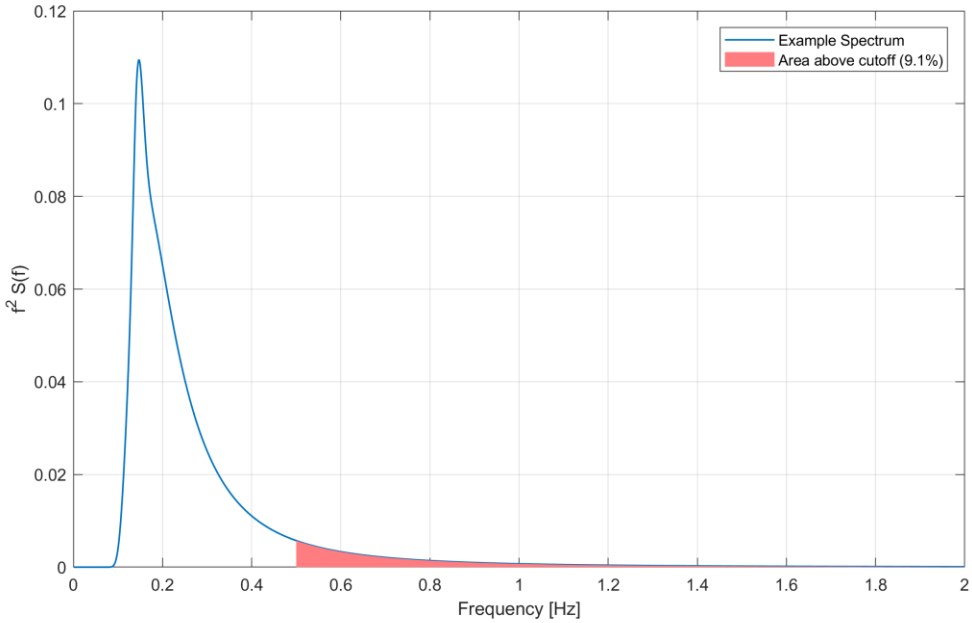



Figure C.15. Area for second moment.

In calculating the mean-zero crossing period, Tm02:

$$T_{m02} = \sqrt{m_0/m_2}$$

such a change starts to become noticeable. In this example, *without* the cut-off region, $m_2$ will be only 90.9% of its value *with* the cut-off region included. We saw above though that $m_0$ remains relatively unchanged, *without* the cut-off being 99.3% of the value with it being included. As a result of the large change in $m_2$ and the small change in $m_0$, we would end up with a Tm02 of 5.13 seconds with the frequencies in the cut-off region, and 5.36 seconds without them.

### C.4.2.2 AWAC Measurements

In the example above, the impact of including/excluding frequencies above 0.5 Hz becomes more significant as higher order moments are used in the calculation. At worst though, for Tm02, the difference remains less than 5%. The example itself is somewhat friendly in this regard: the proportion of energy above this 0.5 Hz threshold is small, and being a JONSWAP spectrum, energy for frequency, *f*, in the upper tail decreases proportionally to $f^{-5}$. In the case of the AWAC measurements, this is regularly not the case. For example, the left side of Figure C.16 shows a timestamp for AWAC A where modelled and measured spectra are particularly well matched[12]. Very minor discrepancies can be seen in the upper and lower tails, but on the whole, the model and measured omni-directional spectra are very similar.

[12] The spectrum used is taken from Deployment 1, where spectra including frequencies up to 0.99 Hz have been provided by Nortek, the instrument manufacturer.

However, the right-hand side, showing the spectral energy multiplied by frequency squared – used to calculate Tm02 – shows a much wider gap in the higher tail, leading to significant differences between modelled and measured Tm02 (6.12 and 5.33 s respectively).

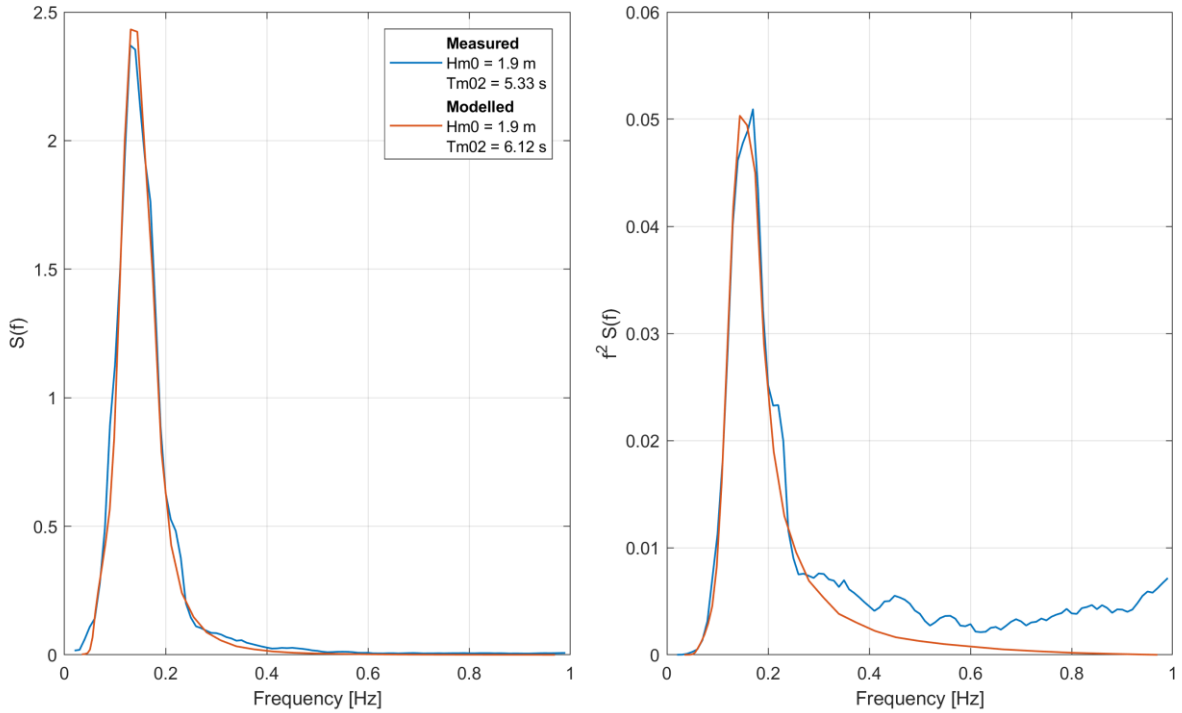



Figure C.16. Example spectra, AWAC A, 27 November 2019.

Of particular note is that on the left-hand side, the two lines are almost indistinguishable above 0.6 Hz, but on the right, this range accounts for at least half of the difference between them. Such behaviour is seen because even though there is very little energy in this upper tail of the measured spectrum, it reduces at a rate much slower than would be expected from, for example the theoretical $f^{-5}$ tail of the JONSWAP spectrum noted above. This is a common occurrence across the AWAC measurements.

### C.4.2.3 AWAC Validation Plots

The cause of this upper tail behaviour in the AWAC measurements is unclear. Measured spectral data is only available for the AWACs, and as such we cannot corroborate with other measurements. What is clear is that the upper tail of the model does not generally behave in the same way, with energy in the upper tail falling at a higher rate – much closer to, for example, the $f^{-5}$ tail of a JONSWAP spectrum.

If validation plots are carried out using the entire frequency range of modelled and measured AWAC data up to 1 Hz:

- For Hm0, the differences in the upper tail have little effect (compare for example differences in area in the left-hand side of Figure C.16).
- For Tm02, validation plots are somewhat dominated by these differences in the upper tail. Seemingly well matched spectra (as in Figure C.16) give very different Tm02 values. Indeed, such plots perhaps cease to be a particularly useful validation measure for spectra *as a whole* and begin to be a very sensitive validation measure for the upper tail.



Though there certainly may be some circumstances where such a sensitive validation measure for the upper tail is of use, we believe that a more useful choice for *the majority of the energy in the spectra* is Tm02 calculated only up to a lower threshold. Review of mean spectra (see Section C.7) suggests that an upper limit of 0.5 Hz strikes a reasonable balance between using the majority of spectral energy whilst reducing the impact of the behaviour seen above.

As seen in Section C.4.2.1, the impact on Tm01 is somewhere between that for Hm0 and Tm02. For this report, we have used an approach consistent with Tm02 – i.e. only frequencies up to 0.5 Hz - since all data required for such a calculation is readily available in the files supplied by Fugro, whilst additional information would be necessary to extend the calculation to 1 Hz[13]. Thus, by way of summary, for AWAC validation plots:

- **Modelled Data:** Hm0 is calculated from modelled spectra using all frequencies. Tm01 and Tm02 are calculated using only model frequencies up to 0.5 Hz.
- **AWAC Data:** Hm0 is calculated from measured spectra using all frequencies. Tm01 are Tm02 are calculated using only measured frequencies up to 0.5 Hz.

Note that in calculating spectral *parameters* to output from the model, SWAN automatically adds a theoretical high frequency tail above the highest modelled frequency (in this project: 0.9695 Hz). A similar procedure is used by the AWAC in calculating parameters from the *directional* spectra, but not from the *omni-directional* spectra. To be clear, in the AWAC validations, both modelled and measured parameters are recalculated from spectra and such a theoretical tail is ***not*** added.

*Please note that we are happy to provide validation plots using alternate thresholds or theoretical tail extrapolation upon request.*

### C.4.2.4 M2, M5 and Splaugh Validation Plots

Only validation plots for Hm0 are included for M2, M5 and Splaugh. In each case it is not clear at this stage as to whether any high frequency cut-off is applied, or whether a theoretical tail is or is not included. Spectra are also not available for recalculation. However, as discussed above, whilst this information would be very important to validations of Tm02, the impact on Hm0 is expected to be minimal. As such, validation plots for these datasets compare the measured Hm0 parameter values reported with the SWAN *parameter* values. As noted above, these are calculate using a theoretical high frequency tail above 0.9695 Hz.

## C.4.3 Peak Period (Tp)

Peak period validations are included for the AWACs only. Measured periods are taken directly from spectra provided by the Acoustic Surface Tracking (AST), i.e. are measured at a fixed point. This might initially seem an odd point to highlight, but some caution is required with the SWAN model output Tp. SWAN documentation [27] describes two parameters:

> ***RTP Relative peak period (in s) of E(σ) (equal to absolute peak period in the absence of currents).***
>
> *Note that this peak period is related to the absolute maximum bin of the discrete wave spectrum and hence, might not be the 'real' peak period.*

[13] Note that the definition of Hm0 as 4 times the square root of the area under the spectrum (denoted m0) allows a three-burst average to be calculated in the absence of full spectral information. Instead, m0 can be calculated from each Hm0, its three-burst average determined, and a corresponding three-burst Hm0 calculated. This provides analogous values to averaging the full spectra (up to 0.99 Hz) themselves.



***TPS Relative peak period (in s) of E(σ).***

*This value is obtained as the maximum of a parabolic fitting through the highest bin and two bins on either side the highest one of the discrete wave spectrum. This 'non-discrete' or 'smoothed' value is a better estimate of the 'real' peak period compared to the quantity RTP.*

Here, *σ*, is used to denote frequency in a frame of reference which is *moving* with the currents. This differs to frequency as measured from a fixed point, for example as measured by the AST. If there are *no* currents, the two will be the same – thus the note against the RTP parameter that it is "equal to absolute peak period in the absence of currents". However, in our case there certainly are currents, and thus the SWAN parameters – calculated in this moving frame of reference - do not match those of the AST. Unfortunately, SWAN does not directly output a peak period based on frequency as measured from a fixed point. Fortunately, it *does* output directional spectra in this format, and these have been used throughout this project. An appropriate Tp for validation has also been calculated from these directional spectra using the same method as described above for the TPS parameter, i.e. using a parabolic fit through the highest bin and two bins on either side in each omni-directional spectrum for a fixed frame of reference.

### C.4.4 Mean Wave Direction (Mdir)

Mean wave direction validations are provided for the AWACs only. As described in Section C.3.2.2, measurement limitations mean that the highest frequency included in the AWAC directional spectra varies significantly with current speeds. To ensure a fair comparison, Mdir from the SWAN model is recalculated from directional spectra at each timestep using the same high frequency cut-off as for the measured data at the closest timestamp. The following is used for this calculation:

$$\theta_{mean} = \arctan\left(\frac{\int \sin\theta \cdot S(f,\theta)\mathrm{d}f\mathrm{d}\theta}{\int \cos\theta \cdot S(f,\theta)\mathrm{d}f\mathrm{d}\theta}\right)$$

where $S(f,\theta)$ is the directional wave spectrum, and both integrals are carried out only across the measured frequency range for each timestep.

## C.5 Wave Parameter Validation

### C.5.1 Introduction

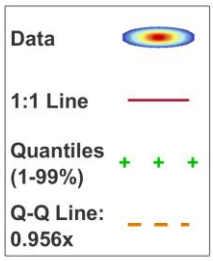
In this Section, validation plots are included as follows:

- Section C.5.2 provides validation plots for AWAC A for the parameters significant wave height (Hm0), mean wave direction (Mdir), mean wave period (Tm01), mean zero-crossing wave period (Tm02), and peak wave period (Tp).
- Sections C.5.3 through C.5.6 provide analogous plots for AWACs B1, C, D1 and E.
- Section C.5.7 provides validation plots for M2, M5 and Splaugh for significant wave height (Hm0) only.

As noted in Section C.4, all Tm01 and Tm02 plots only make use of spectral energy up to 0.5 Hz. A more detailed investigation into the behaviour of Tp at AWAC E for higher wave periods can be found in Appendix D.

## C.5.2 AWAC A

| | |
|---|---|
| Mean (X) | 1.12 |
| Mean (Y) | 1.05 |
| N | 7061 |
| Bias | -0.07 |
| AME | 0.15 |
| RMS | 0.21 |
| SI | 0.17 |
| CC | 0.95 |
| $R^2$ | 0.90 |



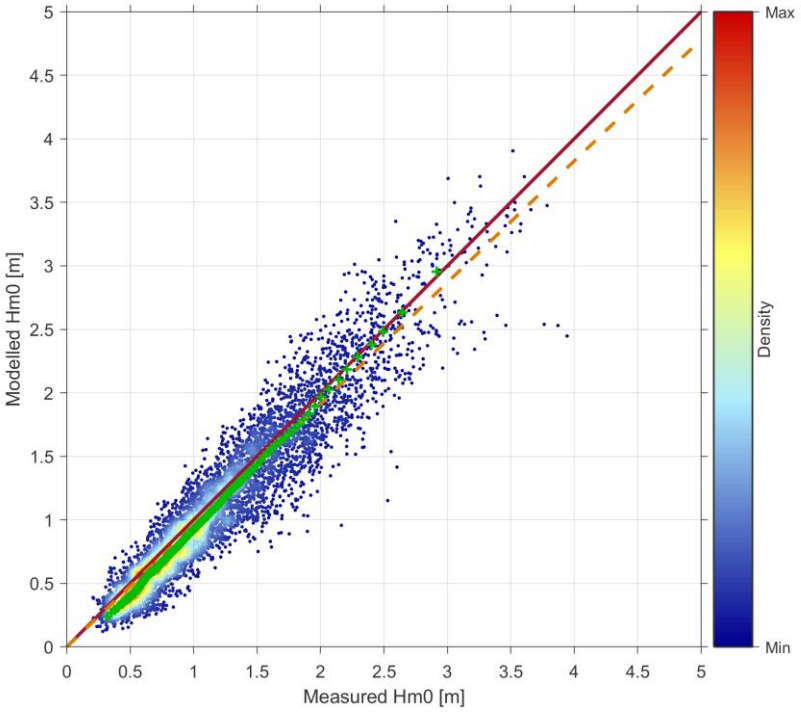




Figure C.17. AWAC A, Hm0 validation, all data.

| | |
|---|---|
| Unit Vector Mean (X) | 144° |
| Unit Vector Mean (Y) | 143° |
| N | 6919 |
| Bias | -2.3° |
| AME | 25° |
| RMS | 41° |

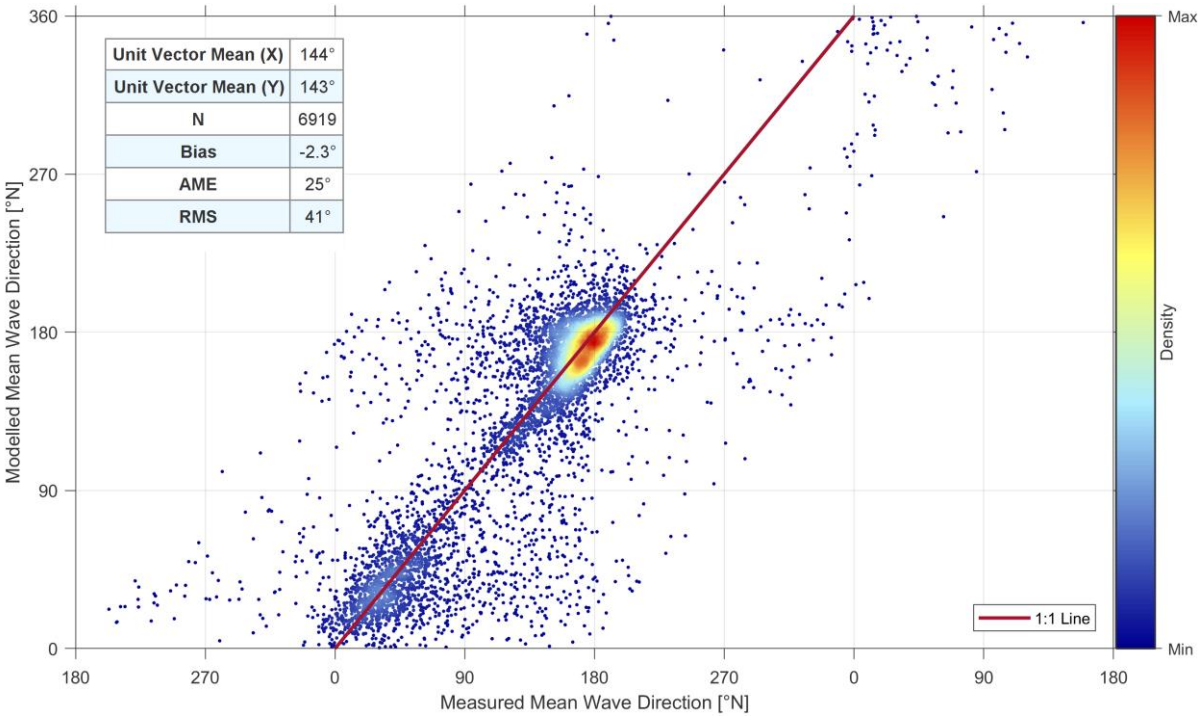
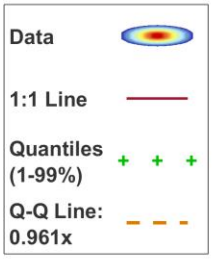



Figure C.18. AWAC A, Mdir validation, all data.

| | |
|---|---|
| Mean (X) | 4.51 |
| Mean (Y) | 4.31 |
| N | 7060 |
| Bias | -0.20 |
| AME | 0.33 |
| RMS | 0.46 |
| SI | 0.09 |
| CC | 0.89 |
| $R^2$ | 0.80 |



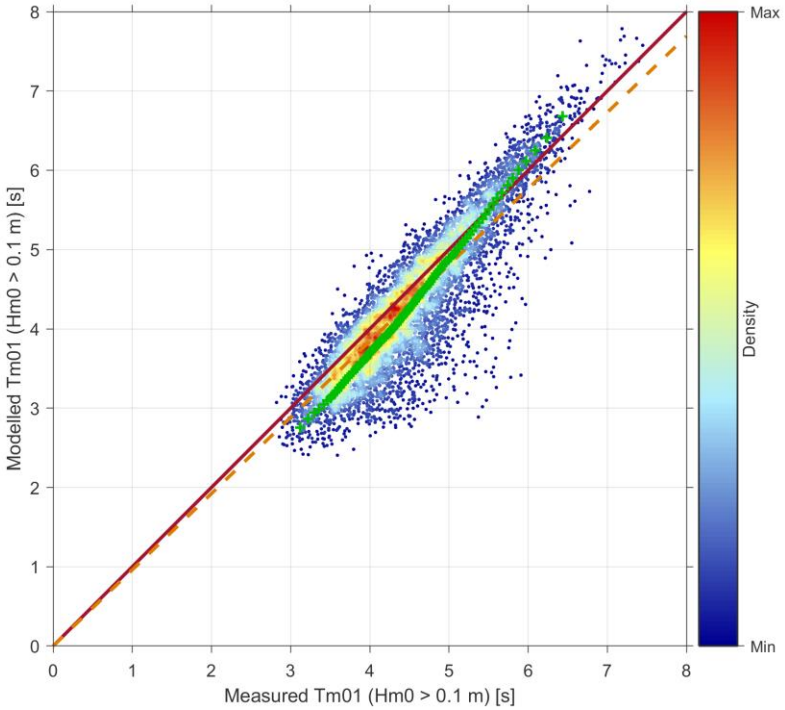
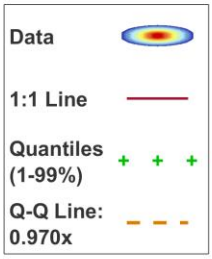




Figure C.19. AWAC A, Tm01 validation, timestamps with Hm0 > 0.1 m, all data.

| | |
|---|---|
| Mean (X) | 4.58 |
| Mean (Y) | 4.42 |
| N | 6333 |
| Bias | -0.16 |
| AME | 0.30 |
| RMS | 0.41 |
| SI | 0.08 |
| CC | 0.90 |
| $R^2$ | 0.81 |



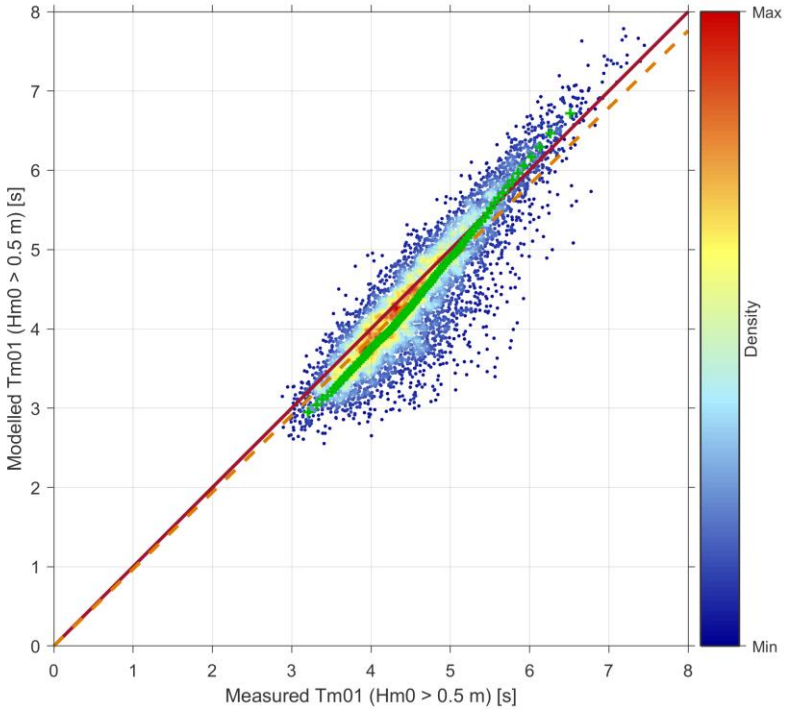




Figure C.20. AWAC A, Tm01 validation, timestamps with Hm0 > 0.5 m, all data.

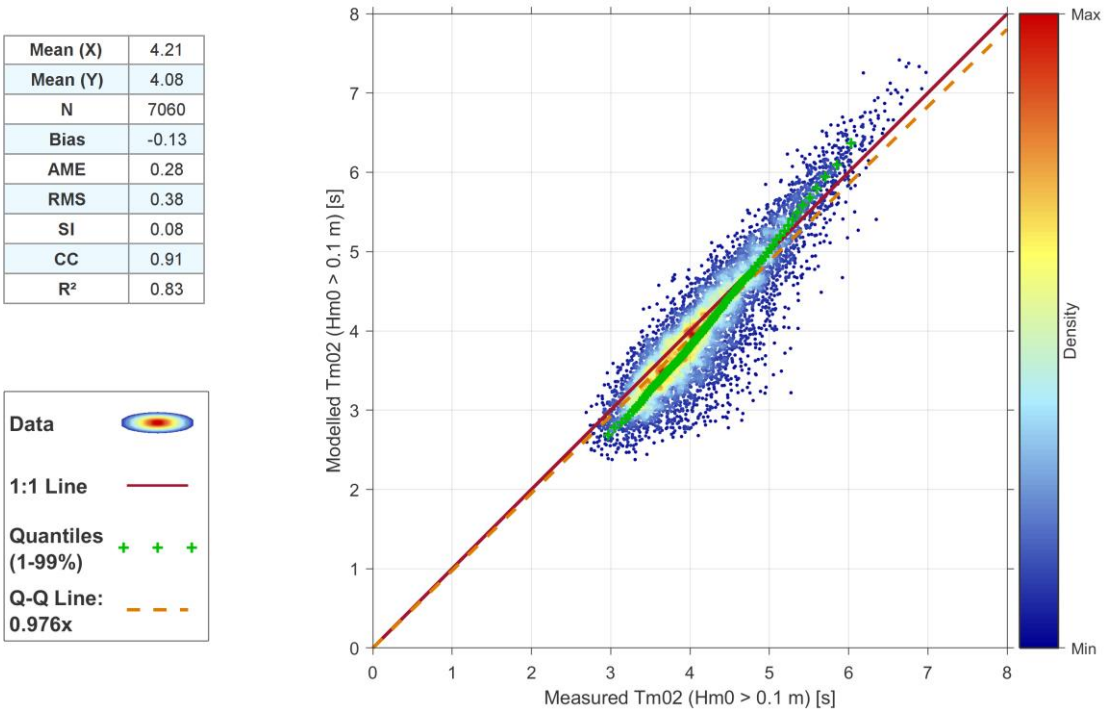



Figure C.21. AWAC A, Tm02 validation, timestamps with Hm0 > 0.1 m, all data.

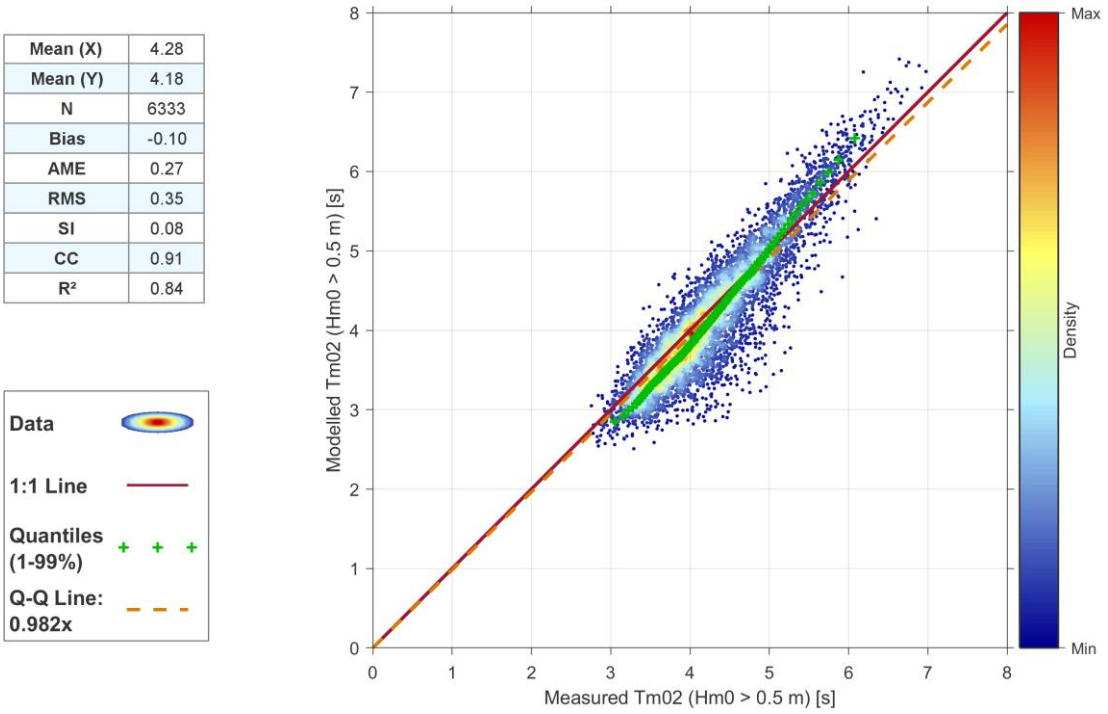



Figure C.22. AWAC A, Tm02 validation, timestamps with Hm0 > 0.5 m, all data.

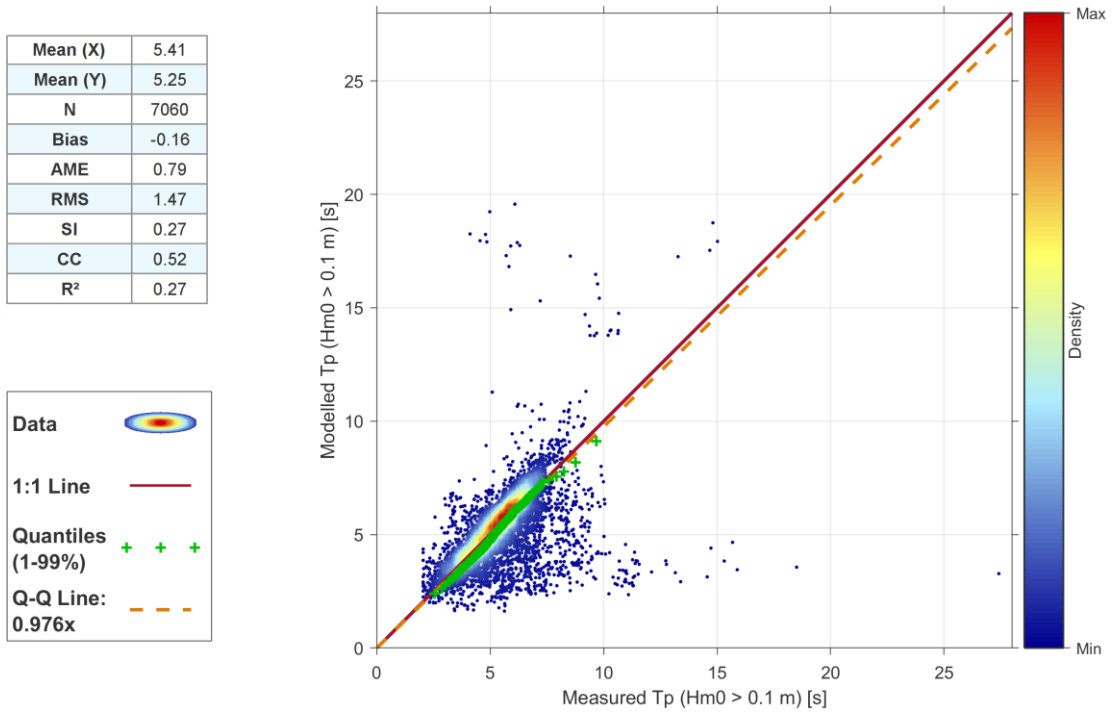



Figure C.23. AWAC A, Tp validation, timestamps with Hm0 > 0.1 m, all data.

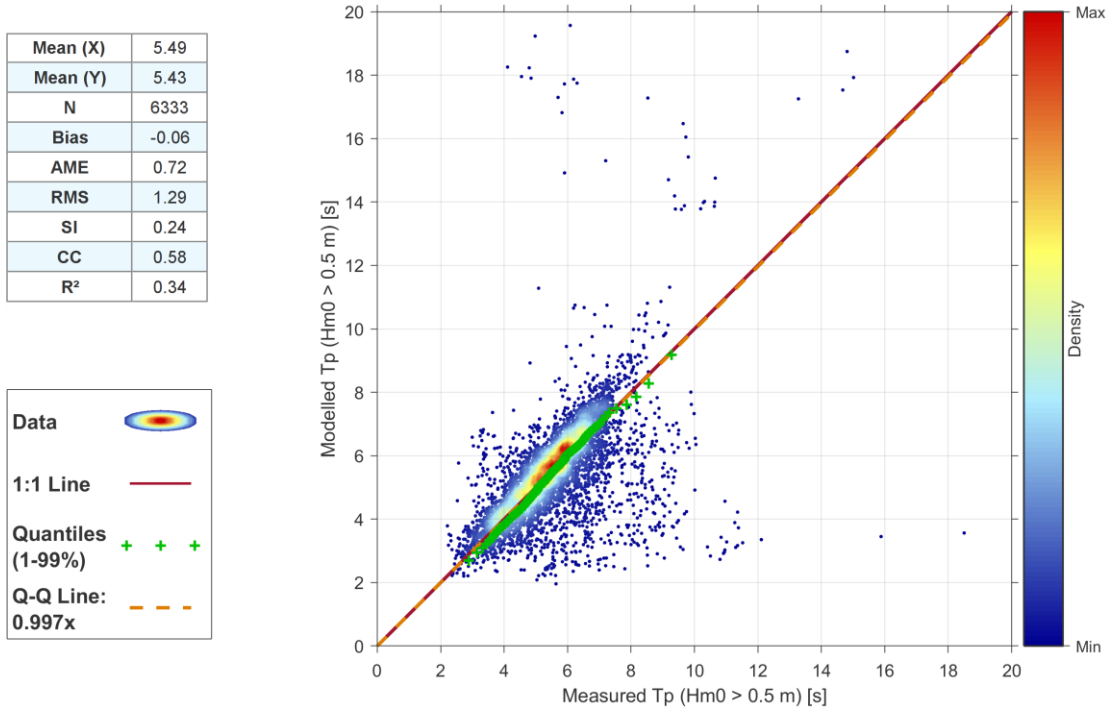



Figure C.24. AWAC A, Tp validation, timestamps with Hm0 > 0.5 m, all data.

### C.5.3 AWAC B1

| | |
|---|---|
| Mean (X) | 0.92 |
| Mean (Y) | 0.91 |
| N | 4020 |
| Bias | -0.01 |
| AME | 0.14 |
| RMS | 0.20 |
| SI | 0.22 |
| CC | 0.92 |
| $R^2$ | 0.86 |

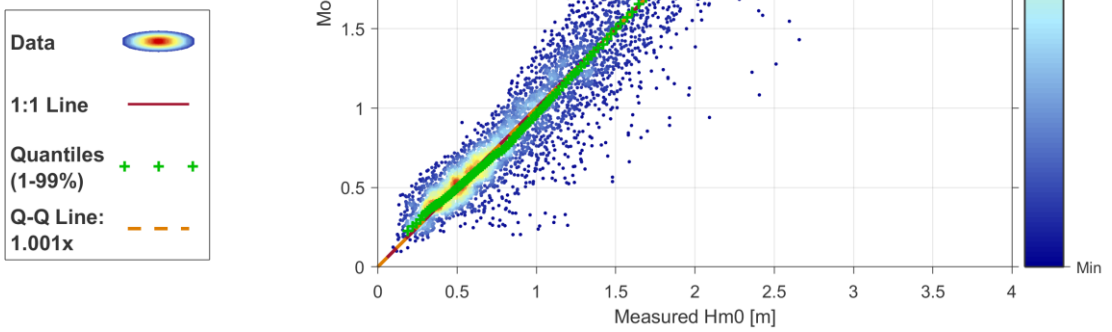



Figure C.25. AWAC B1, Hm0 validation, all data.

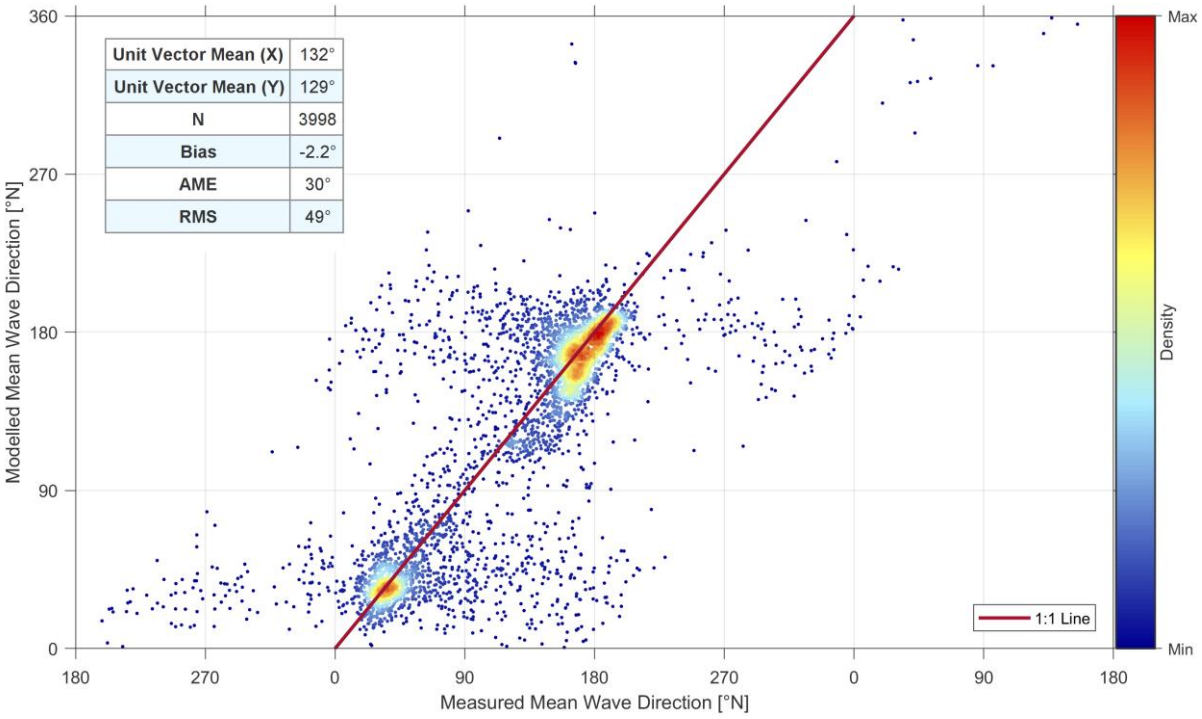



Figure C.26. AWAC B1, Mdir validation, all data.

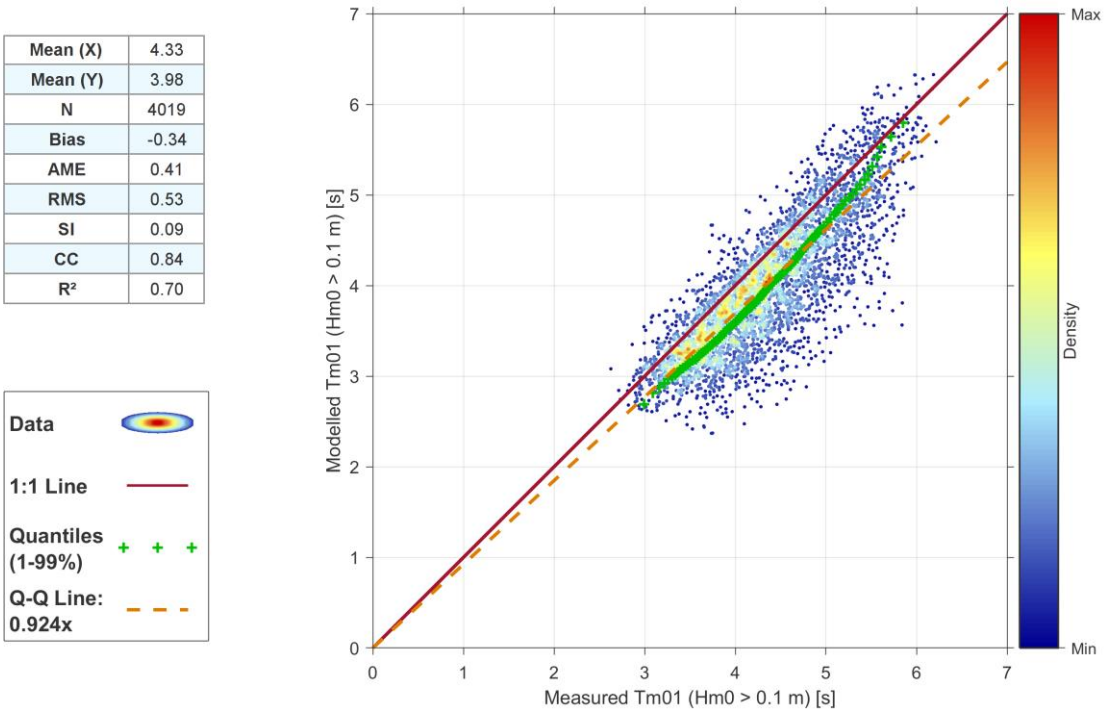



Figure C.27. AWAC B1, Tm01 validation, timestamps with Hm0 > 0.1 m, all data.

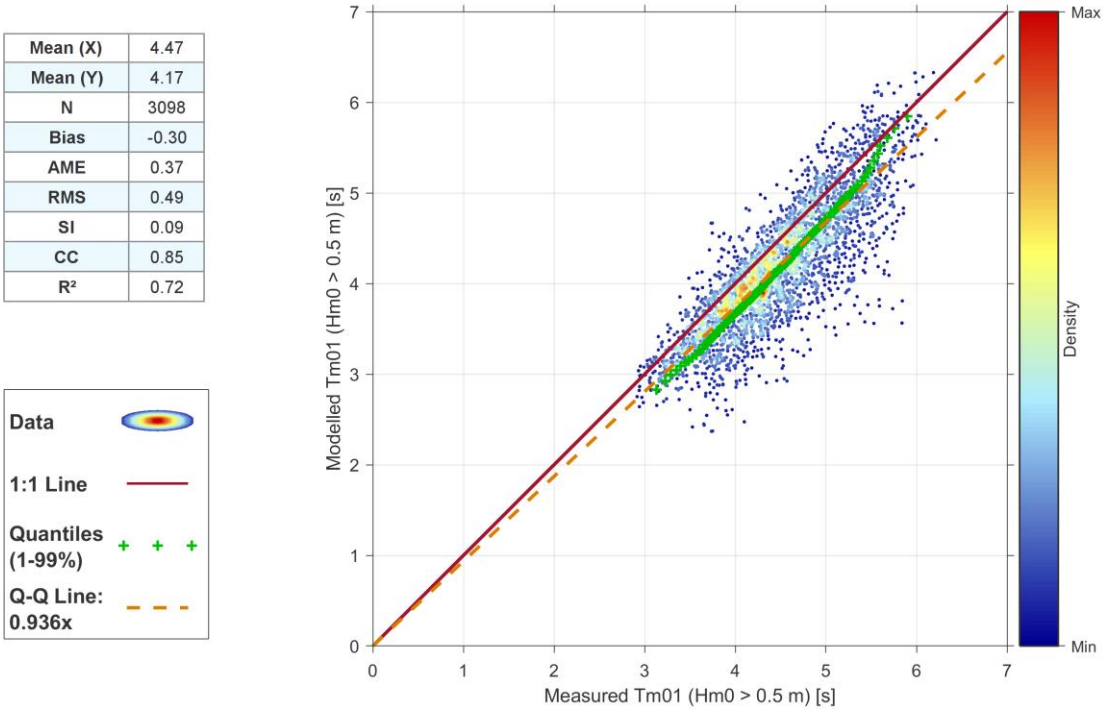



Figure C.28. AWAC B1, Tm01 validation, timestamps with Hm0 > 0.5 m, all data.

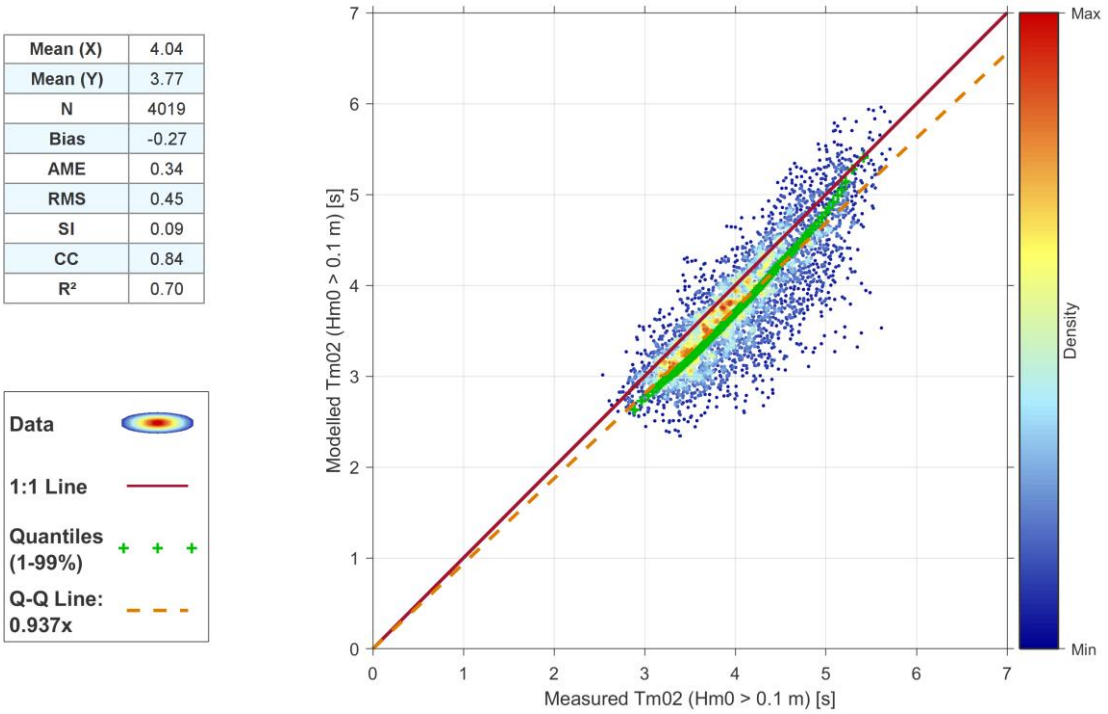



Figure C.29. AWAC B1, Tm02 validation, timestamps with Hm0 > 0.1 m, all data.

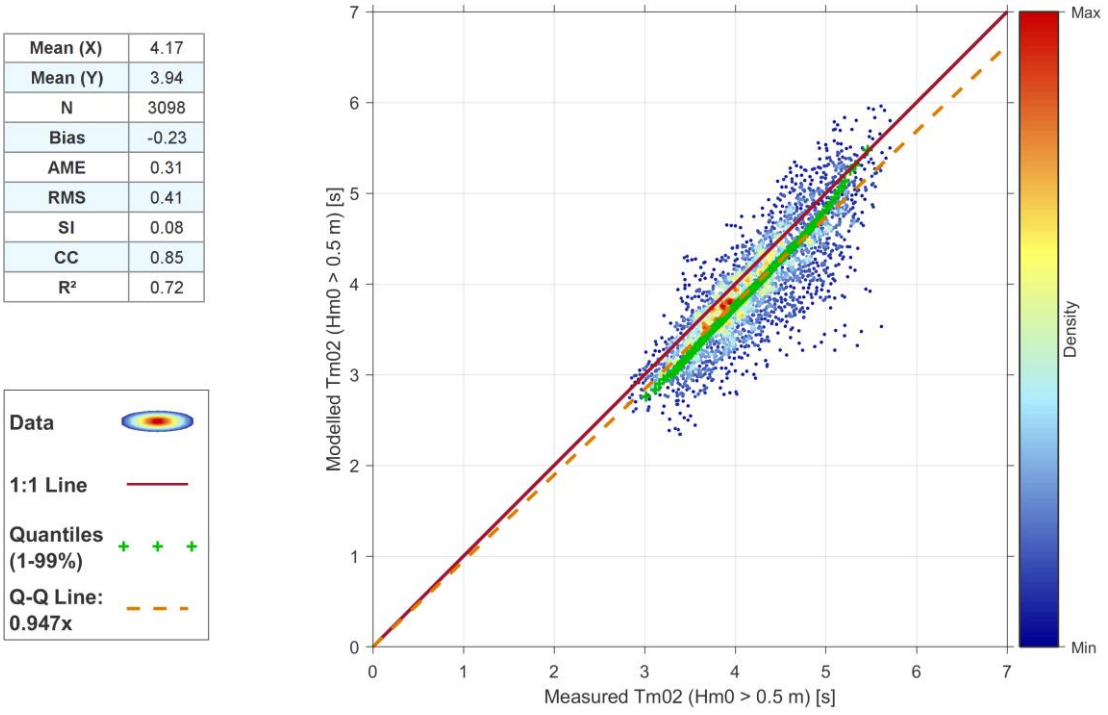



Figure C.30. AWAC B1, Tm02 validation, timestamps with Hm0 > 0.5 m, all data.

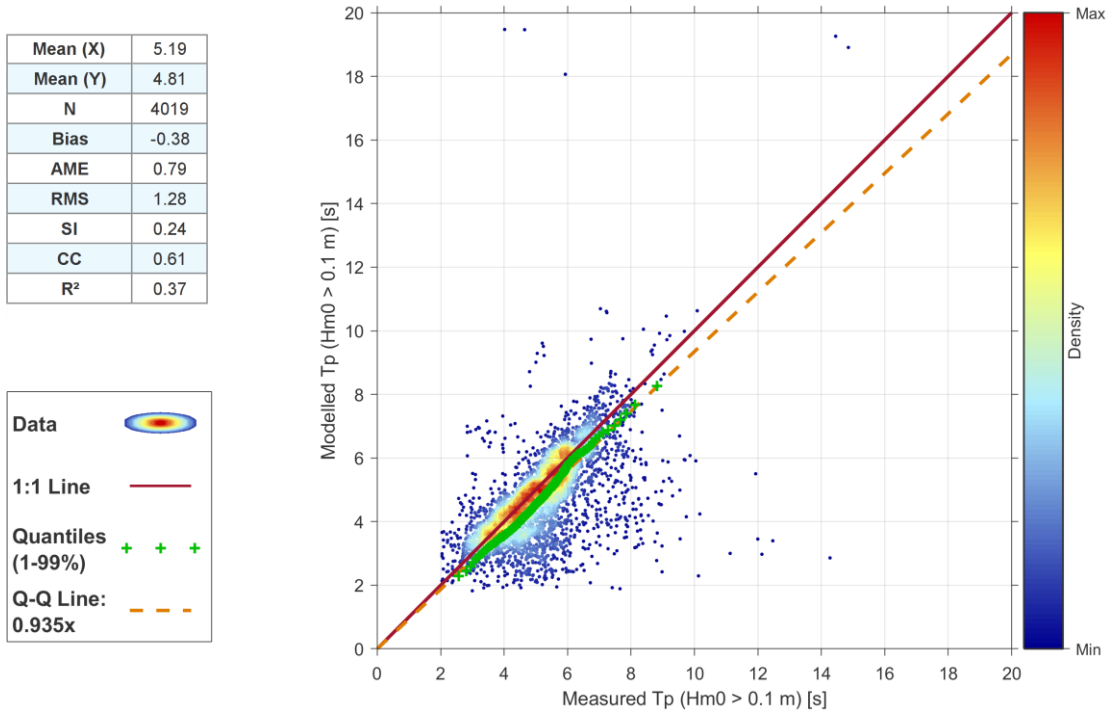



Figure C.31. AWAC B1, Tp validation, timestamps with Hm0 > 0.1 m, all data.

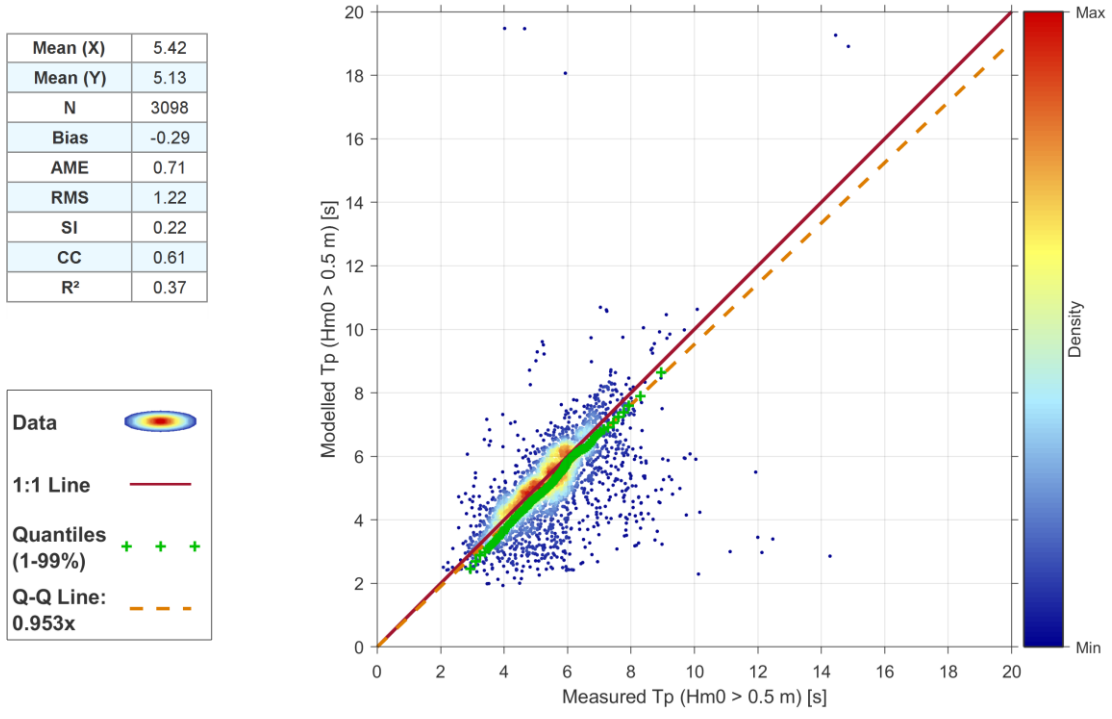



Figure C.32. AWAC B1, Tp validation, timestamps with Hm0 > 0.5 m, all data.

### C.5.4 AWAC C

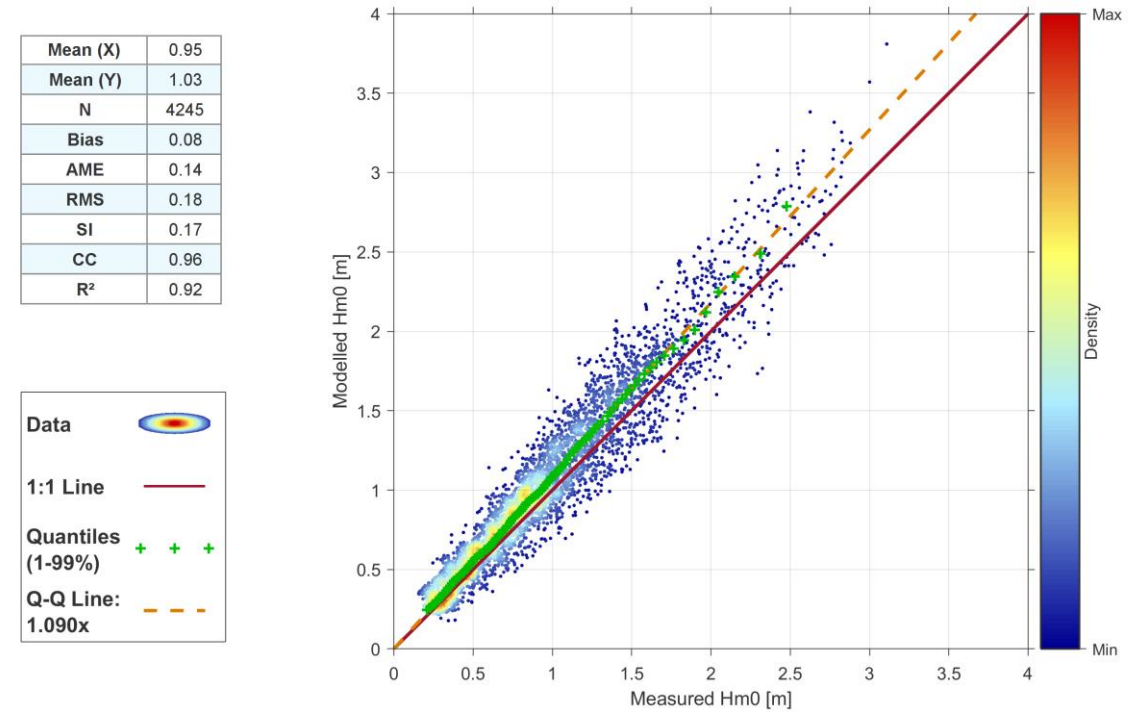



Figure C.33. AWAC C, Hm0 validation, all data.

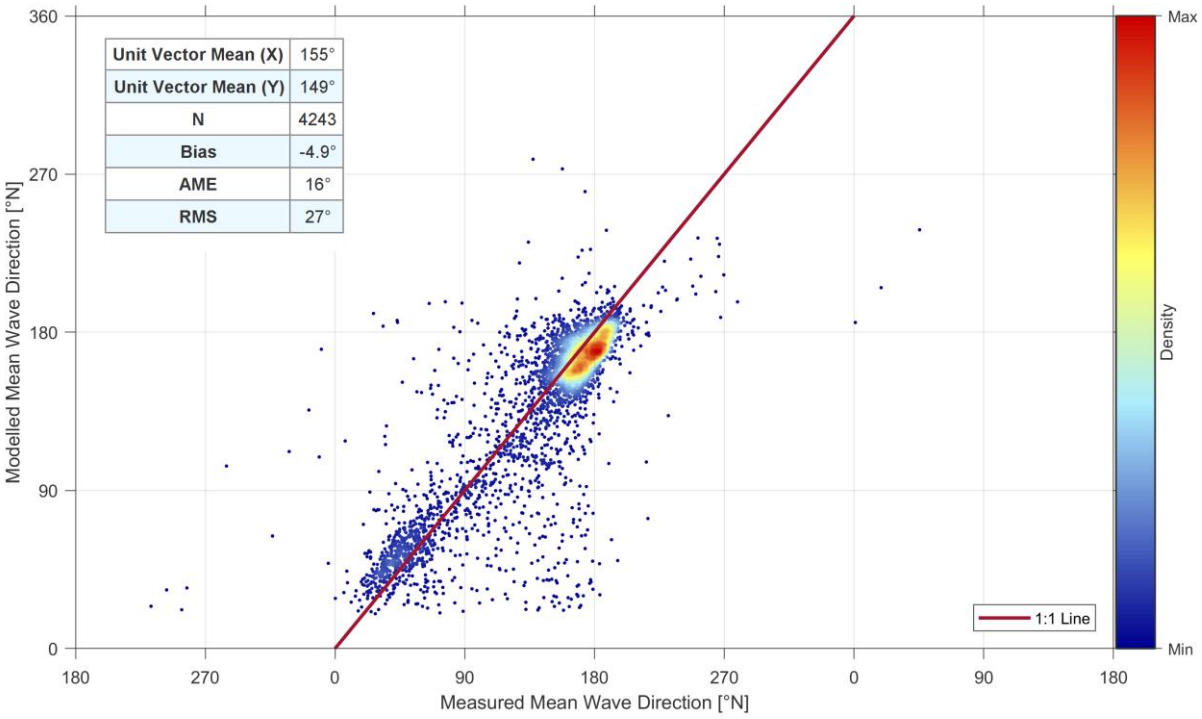



Figure C.34. AWAC C, Mdir validation, all data.

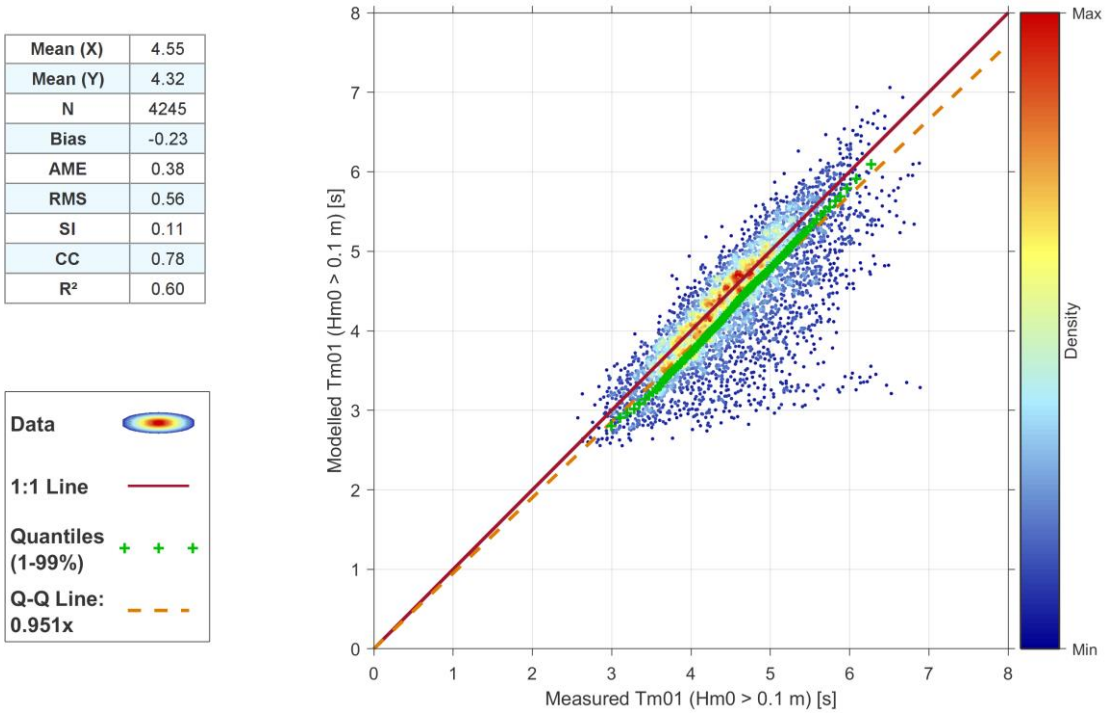



Figure C.35. AWAC C, Tm01 validation, timestamps with Hm0 > 0.1 m, all data.

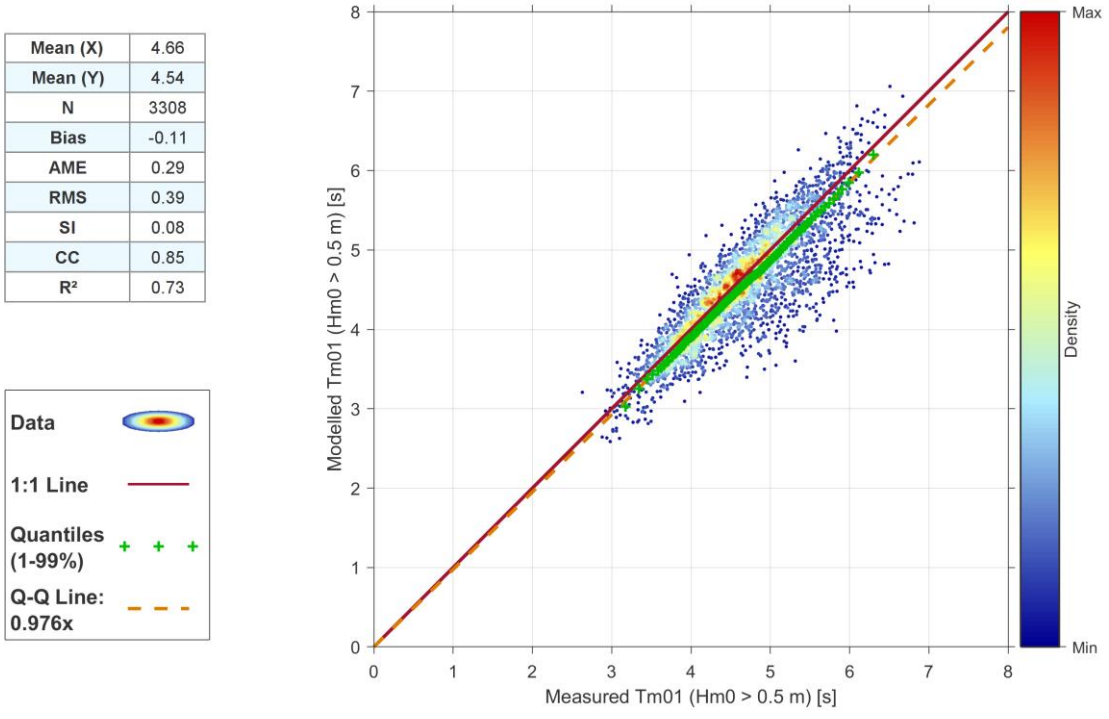



Figure C.36. AWAC C, Tm01 validation, timestamps with Hm0 > 0.5 m, all data.

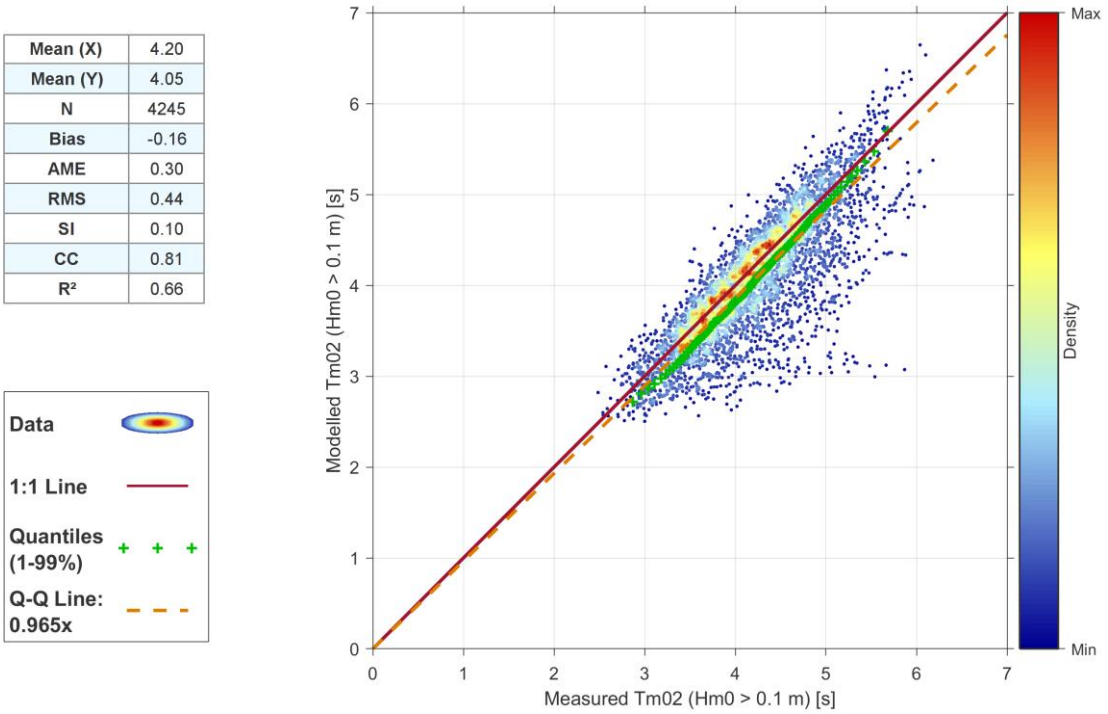



Figure C.37. AWAC C, Tm02 validation, timestamps with Hm0 > 0.1 m, all data.

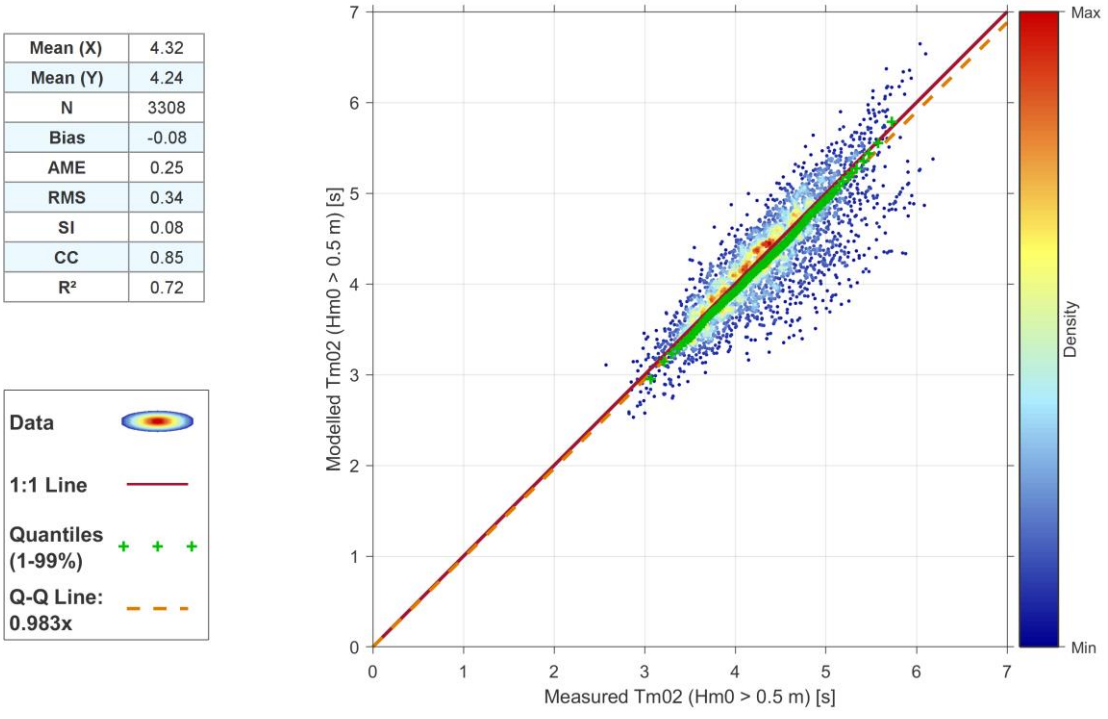



Figure C.38. AWAC C, Tm02 validation, timestamps with Hm0 > 0.5 m, all data.

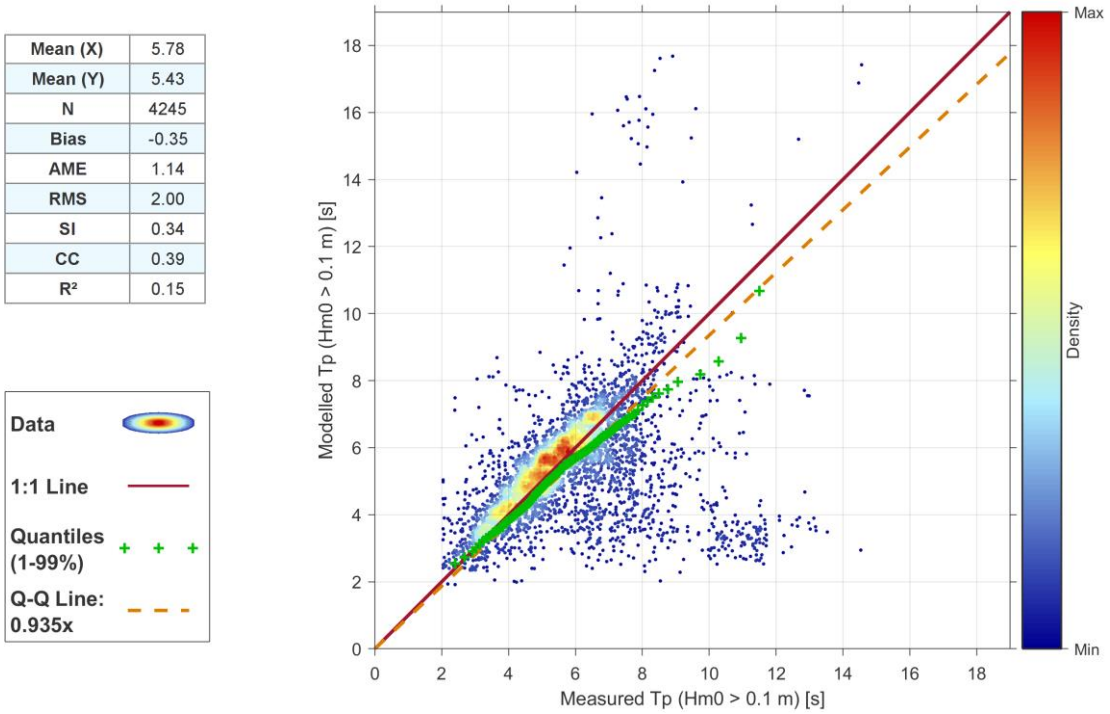



Figure C.39. AWAC C, Tp validation, timestamps with Hm0 > 0.1 m, all data.

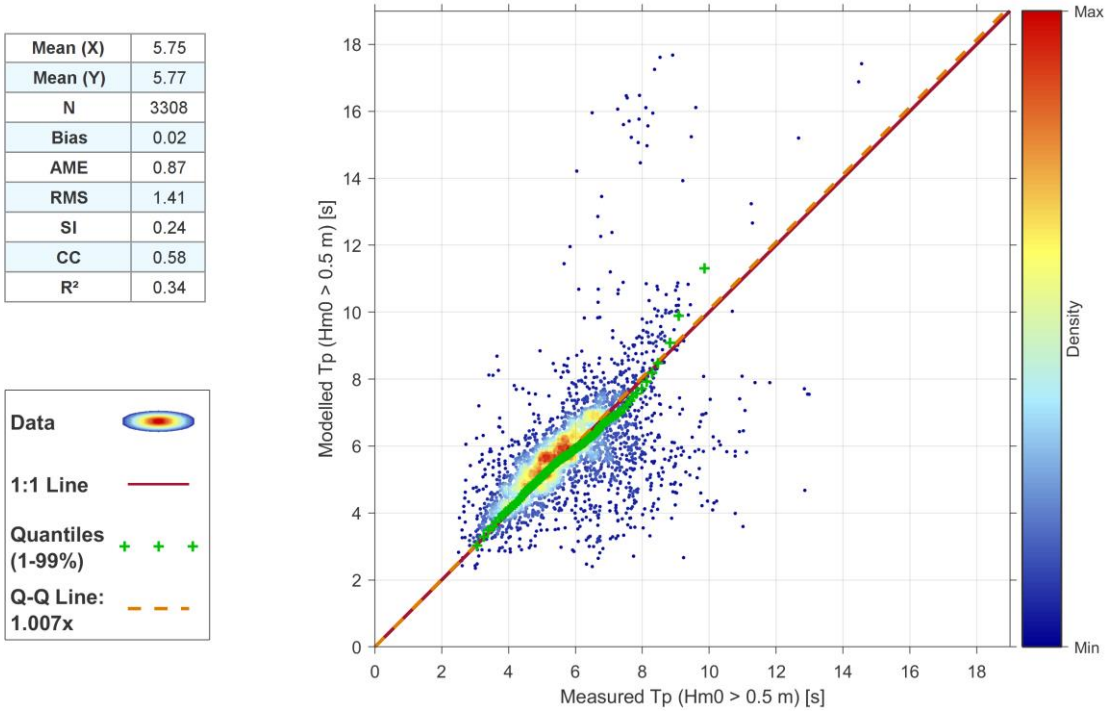



Figure C.40. AWAC C, Tp validation, timestamps with Hm0 > 0.5 m, all data.

### C.5.5 AWAC D1

| | |
|---|---|
| Mean (X) | 0.96 |
| Mean (Y) | 0.95 |
| N | 3803 |
| Bias | -0.02 |
| AME | 0.12 |
| RMS | 0.17 |
| SI | 0.18 |
| CC | 0.95 |
| $R^2$ | 0.91 |

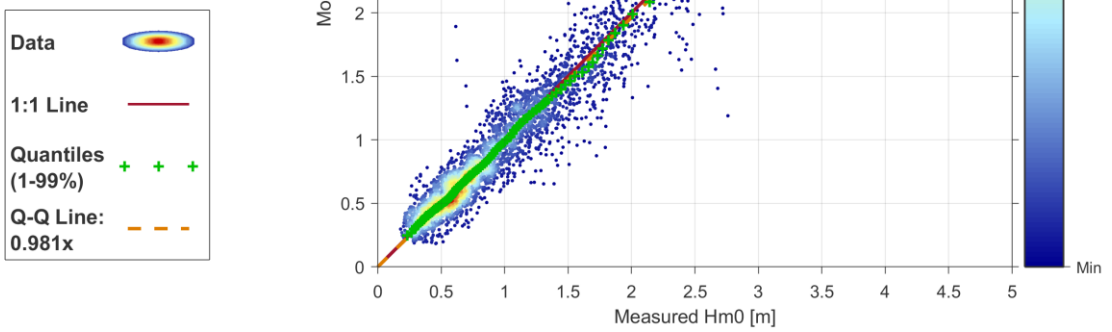



Figure C.41. AWAC D1, Hm0 validation, all data.

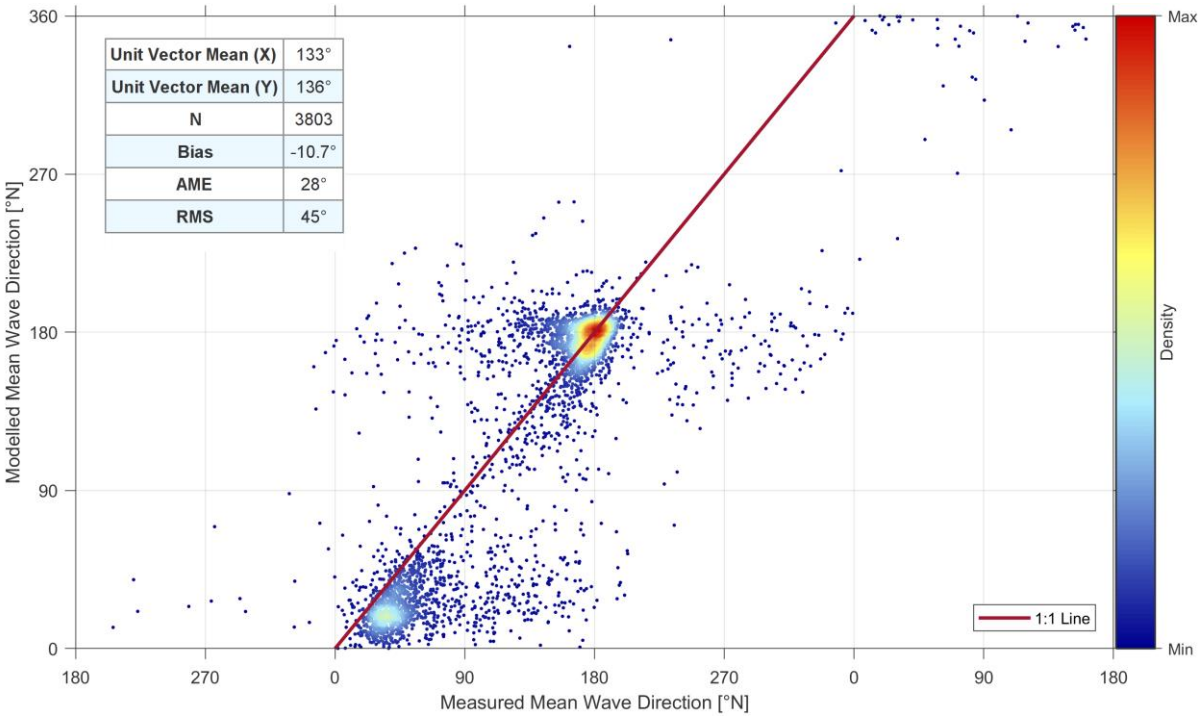



Figure C.42. AWAC D1, Mdir validation, all data.

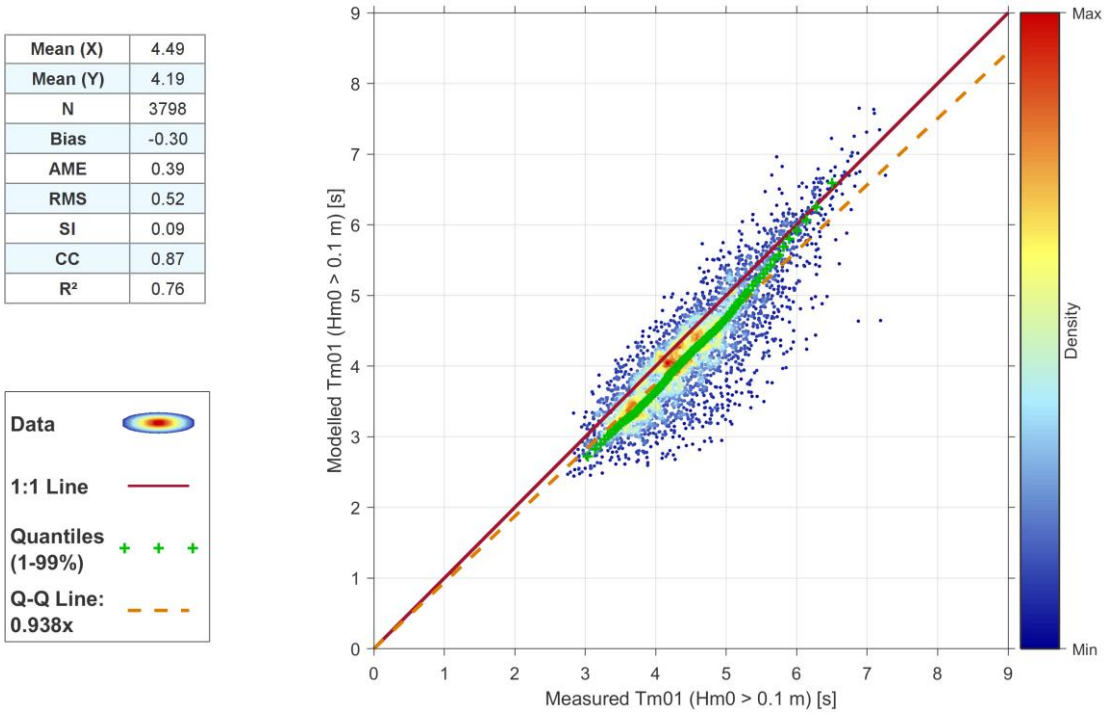



Figure C.43. AWAC D1, Tm01 validation, timestamps with Hm0 > 0.1 m, all data.

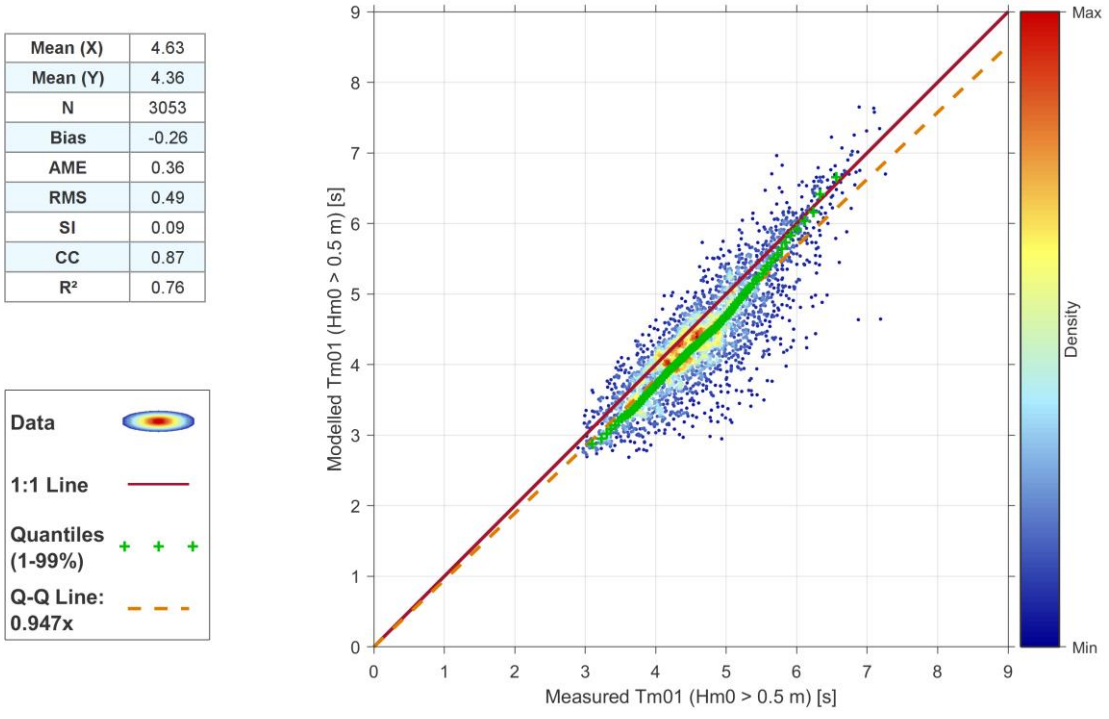



Figure C.44. AWAC D1, Tm01 validation, timestamps with Hm0 > 0.5 m, all data.

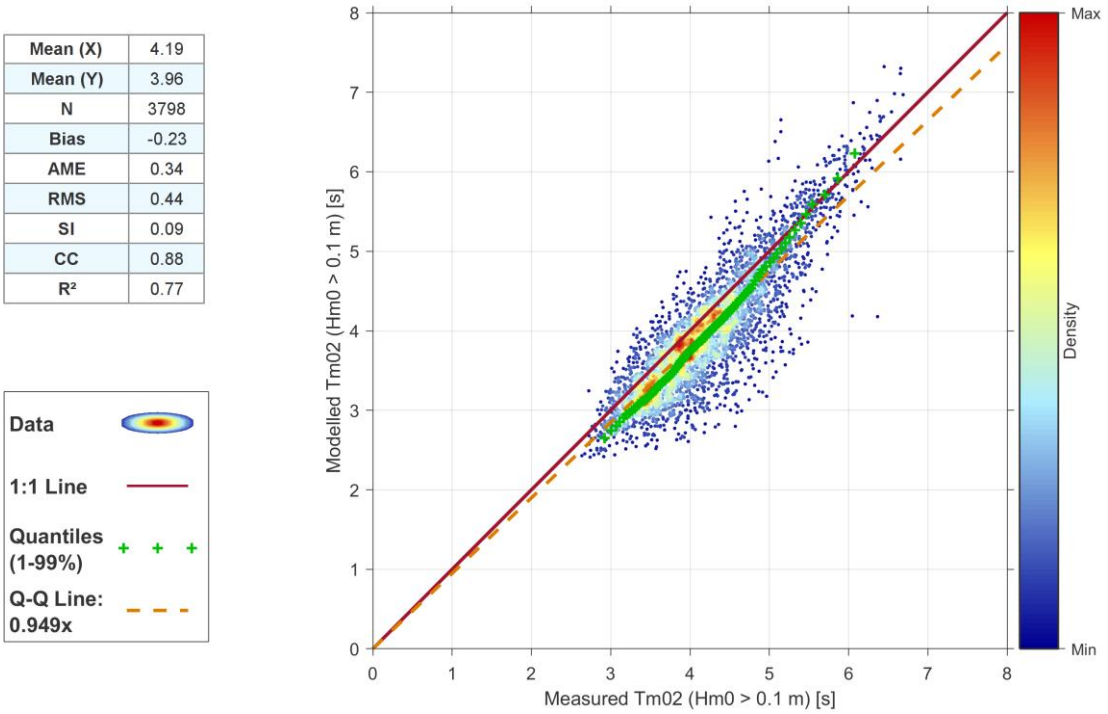



Figure C.45. AWAC D1, Tm02 validation, timestamps with Hm0 > 0.1 m, all data.

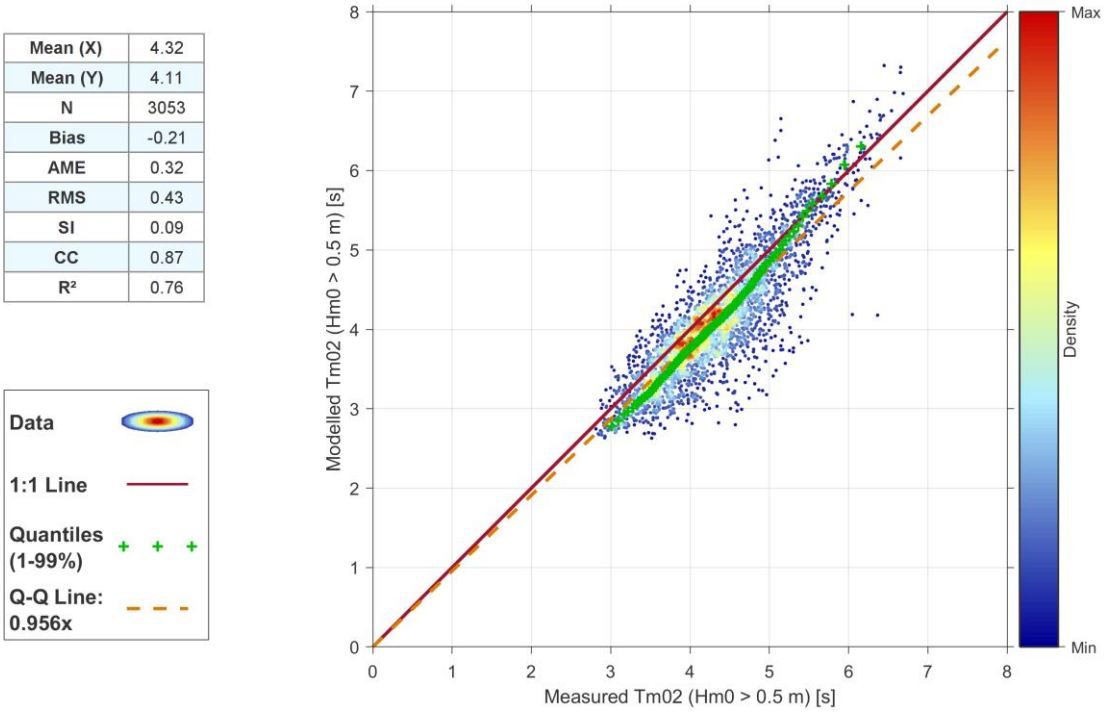



Figure C.46. AWAC D1, Tm02 validation, timestamps with Hm0 > 0.5 m, all data.

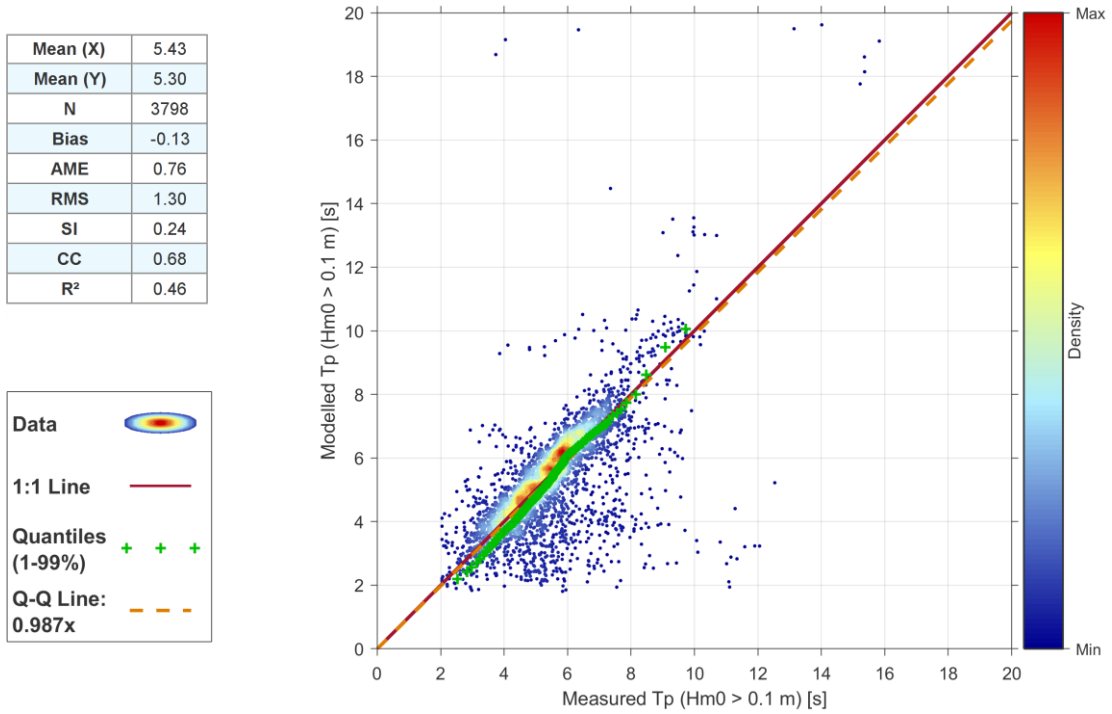



Figure C.47. AWAC D1, Tp validation, timestamps with Hm0 > 0.1 m, all data.

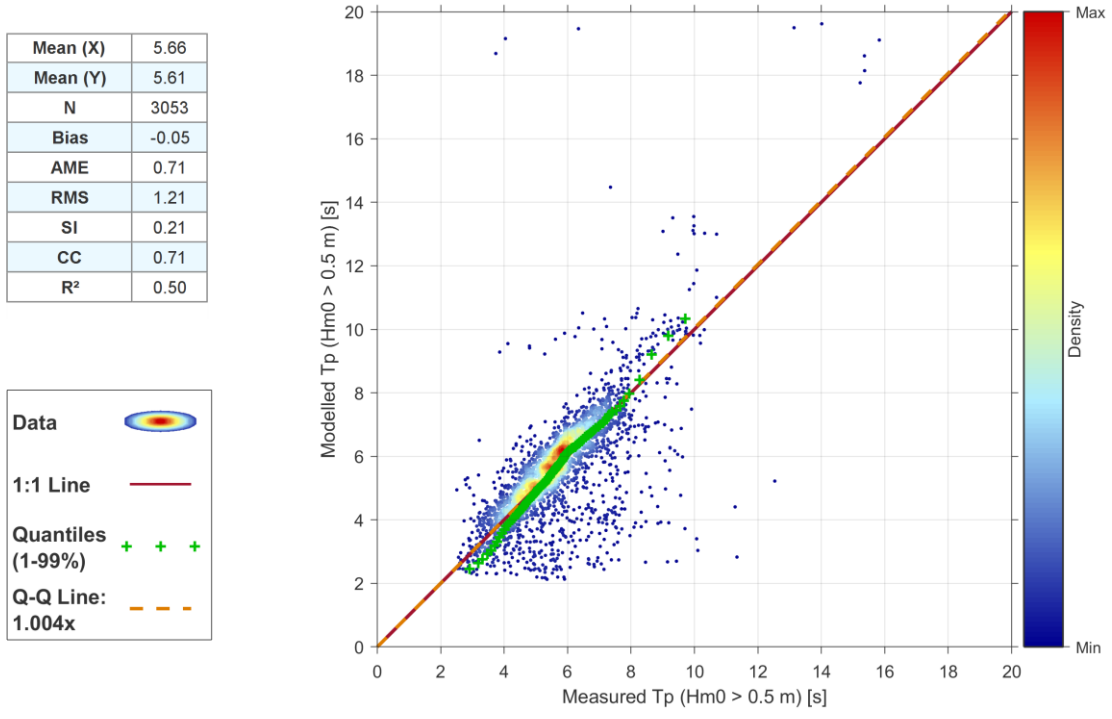



Figure C.48. AWAC D1, Tp validation, timestamps with Hm0 > 0.5 m, all data.

### C.5.6 AWAC E

| | |
|---|---|
| Mean (X) | 1.06 |
| Mean (Y) | 1.09 |
| N | 7723 |
| Bias | 0.03 |
| AME | 0.17 |
| RMS | 0.22 |
| SI | 0.21 |
| CC | 0.94 |
| $R^2$ | 0.89 |

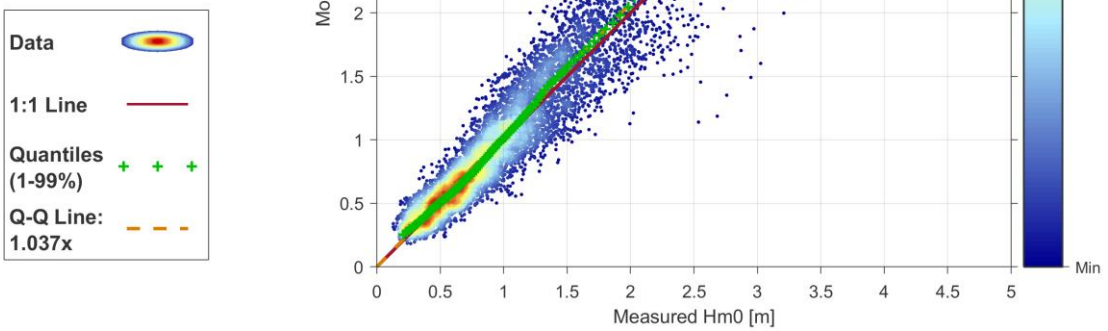



Figure C.49. AWAC E, Hm0 validation, all data.

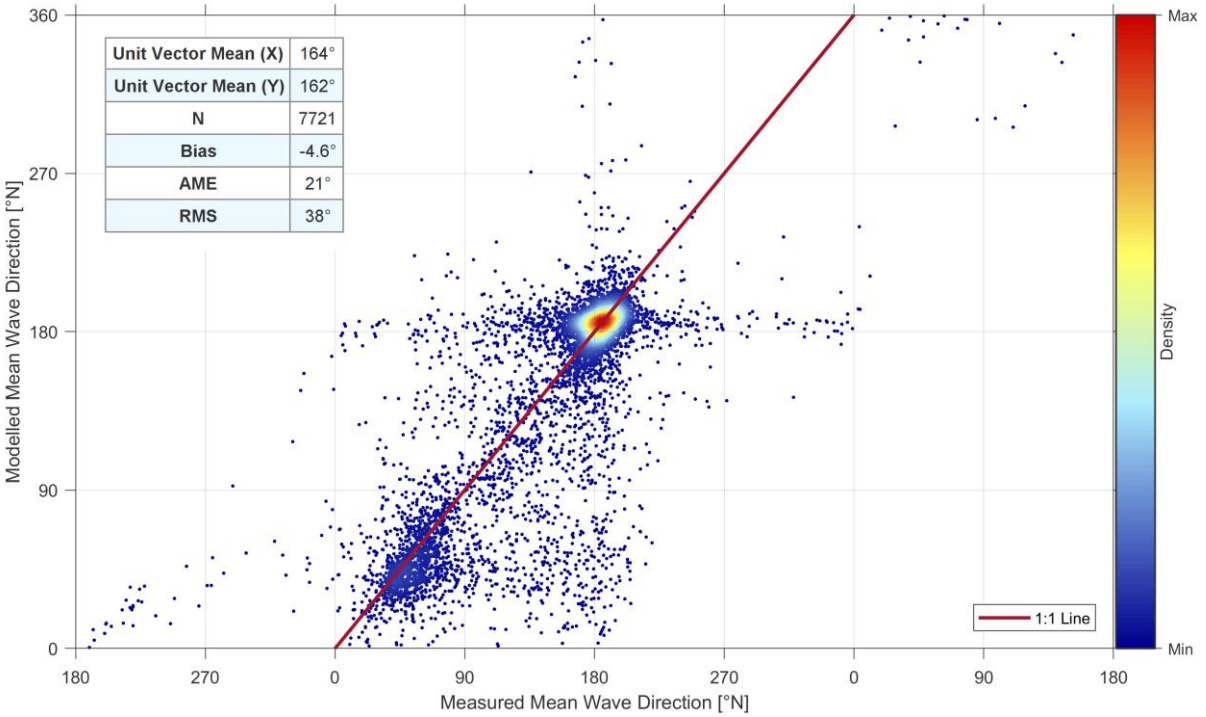



Figure C.50. AWAC E, Mdir validation, all data.

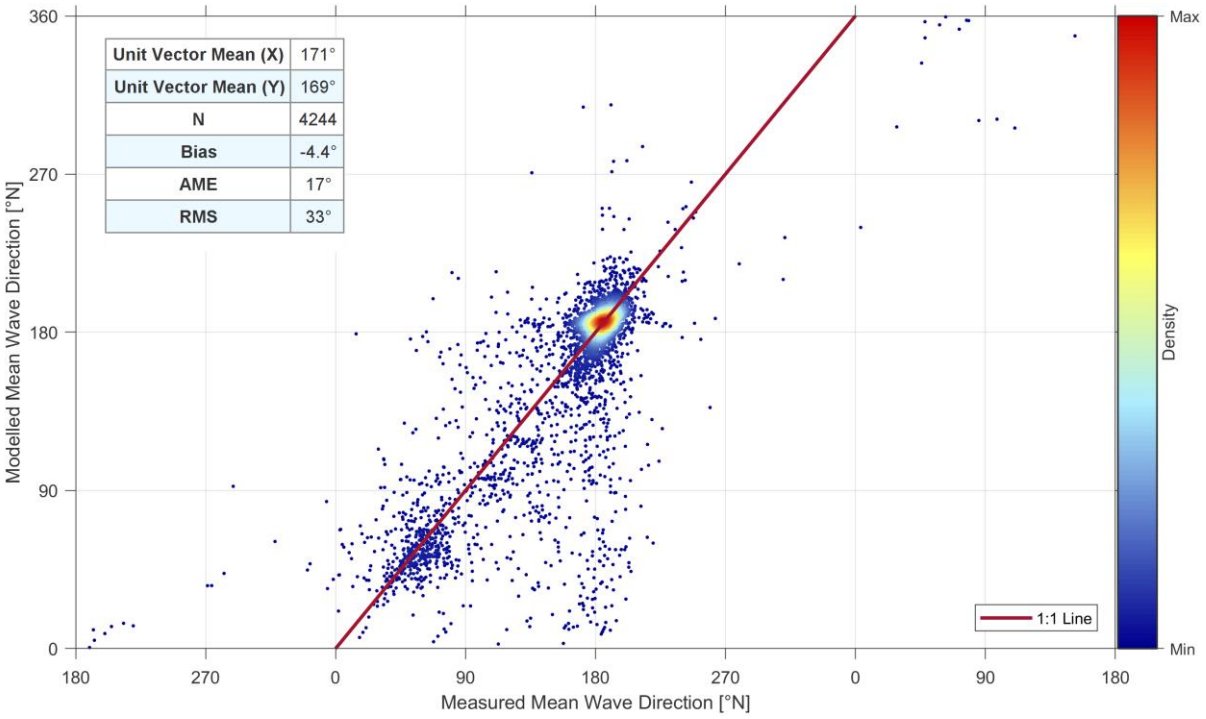
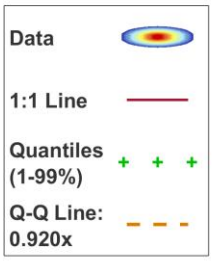



Figure C.51. AWAC E, Mdir validation, Deployment 1 only.

| | |
|---|---|
| Mean (X) | 4.73 |
| Mean (Y) | 4.35 |
| N | 7723 |
| Bias | -0.38 |
| AME | 0.49 |
| RMS | 0.73 |
| SI | 0.13 |
| CC | 0.82 |
| $R^2$ | 0.66 |



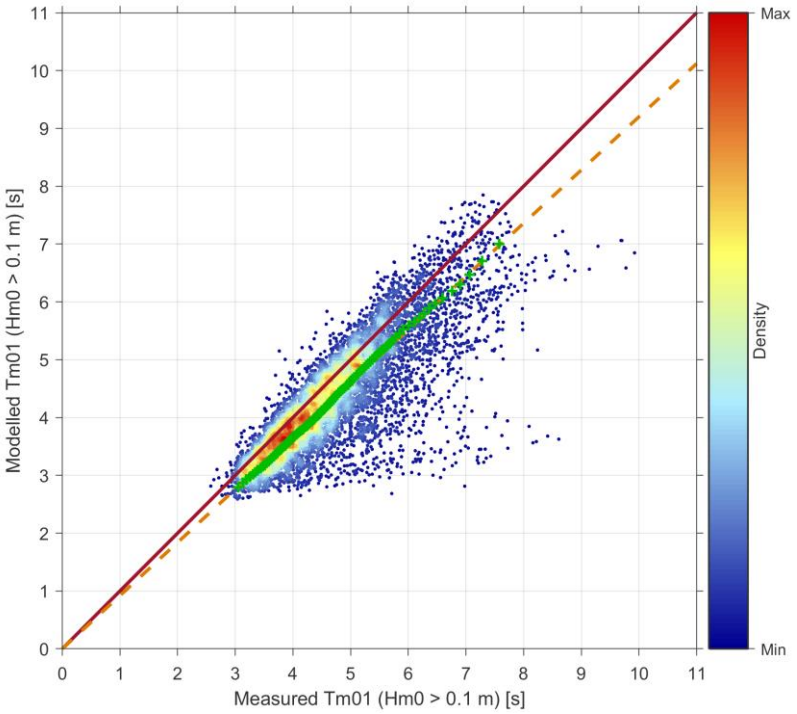
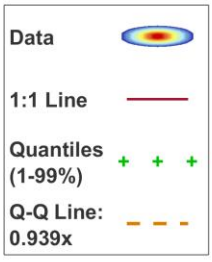




Figure C.52. AWAC E, Tm01 validation, timestamps with Hm0 > 0.1 m, all data.

| | |
|---|---|
| Mean (X) | 4.83 |
| Mean (Y) | 4.54 |
| N | 6318 |
| Bias | -0.29 |
| AME | 0.41 |
| RMS | 0.58 |
| SI | 0.11 |
| CC | 0.87 |
| $R^2$ | 0.76 |



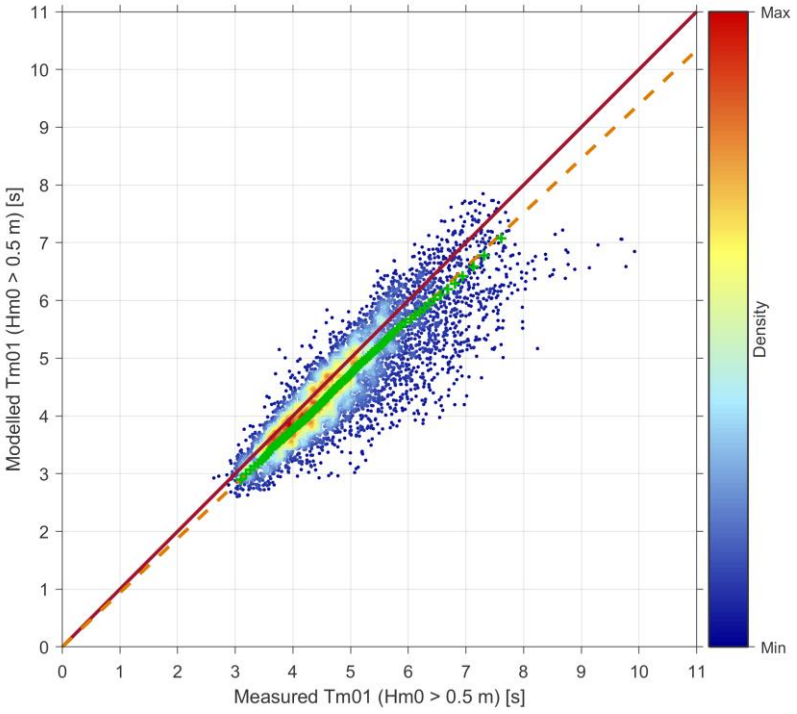




Figure C.53. AWAC E, Tm01 validation, timestamps with Hm0 > 0.5 m, all data.

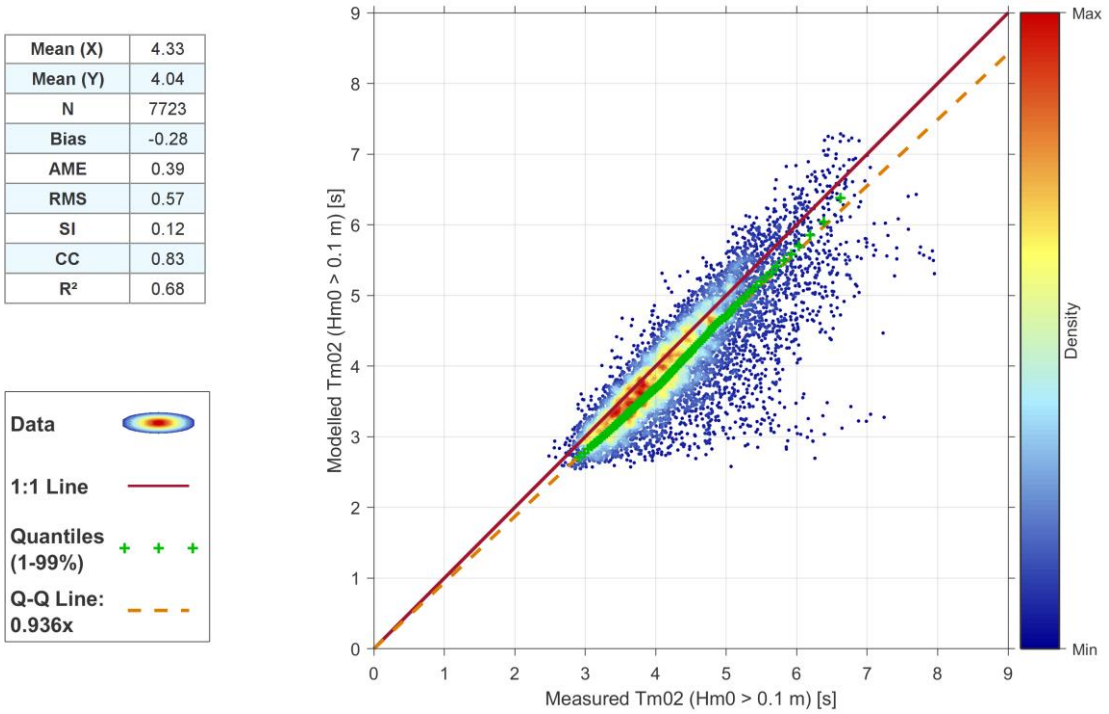



Figure C.54. AWAC E, Tm02 validation, timestamps with Hm0 > 0.1 m, all data.

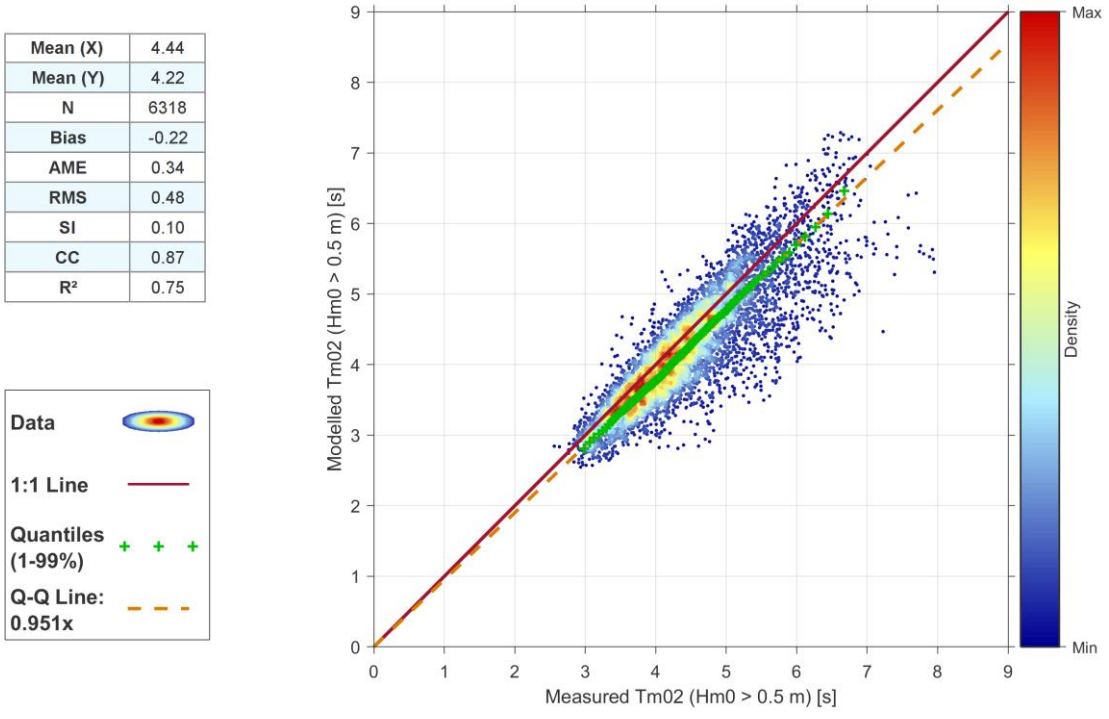



Figure C.55. AWAC E, Tm02 validation, timestamps with Hm0 > 0.5 m, all data.

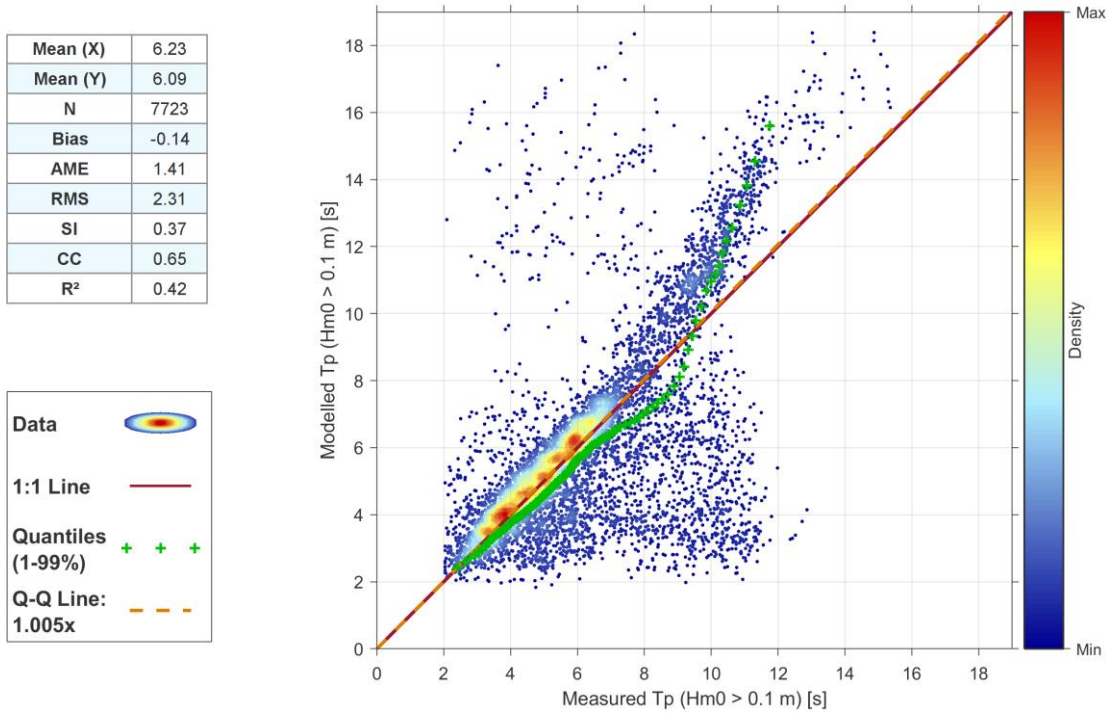



Figure C.56. AWAC E, Tp validation, timestamps with Hm0 > 0.1 m, all data.

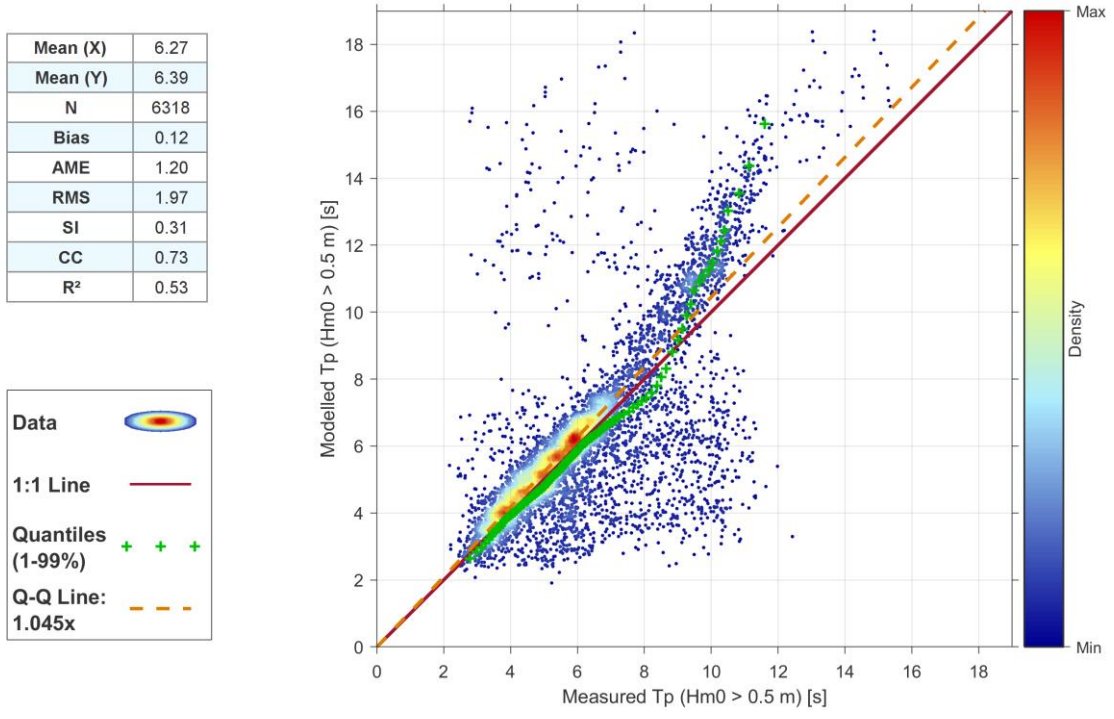



Figure C.57. AWAC E, Tp validation, timestamps with Hm0 > 0.5 m, all data.

### C.5.7 M2, M5 and Splaugh

| | |
|---|---|
| Mean (X) | 1.20 |
| Mean (Y) | 1.22 |
| N | 119977 |
| Bias | 0.02 |
| AME | 0.19 |
| RMS | 0.26 |
| SI | 0.22 |
| CC | 0.94 |
| $R^2$ | 0.88 |

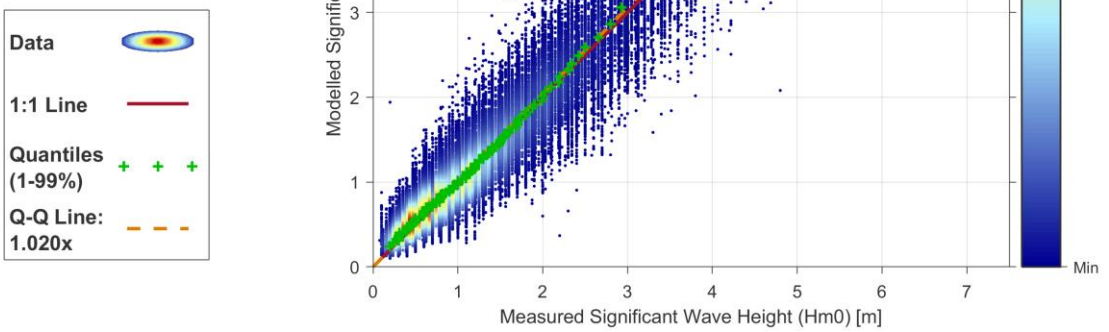



Figure C.58. M2, Hm0 validation.

| | |
|---|---|
| Mean (X) | 1.86 |
| Mean (Y) | 1.89 |
| N | 93559 |
| Bias | 0.03 |
| AME | 0.19 |
| RMS | 0.26 |
| SI | 0.14 |
| CC | 0.97 |
| $R^2$ | 0.94 |

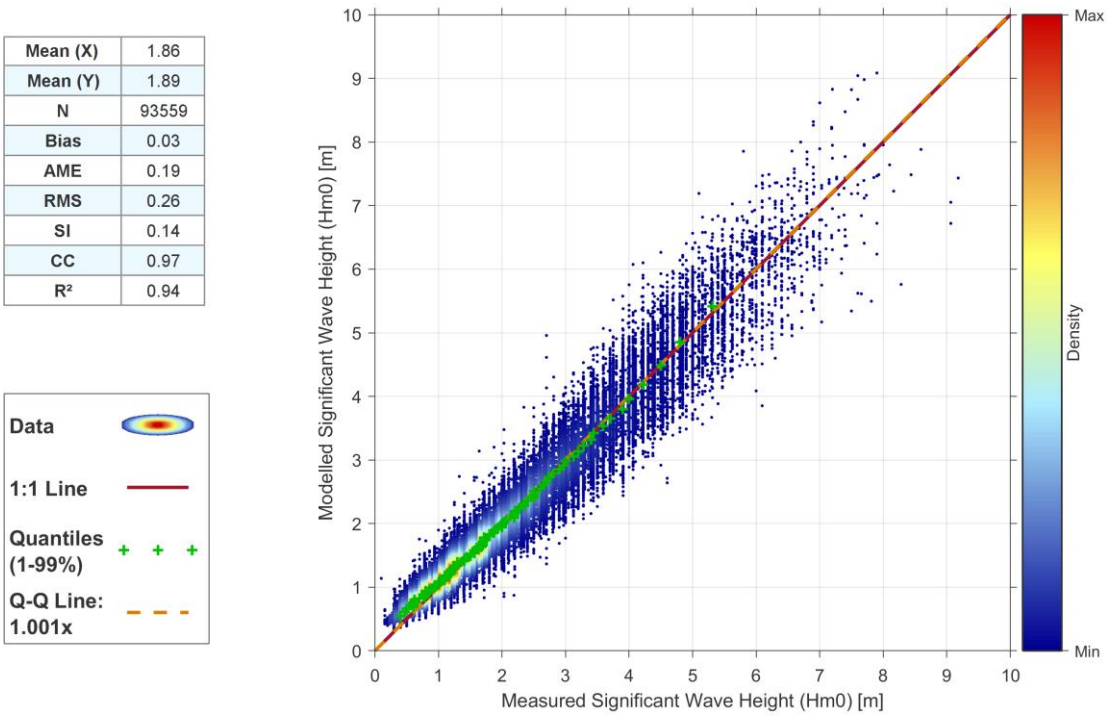
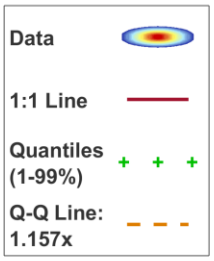



Figure C.59. M5, Hm0 validation.

| | |
|---|---|
| Mean (X) | 0.77 |
| Mean (Y) | 0.98 |
| N | 53251 |
| Bias | 0.21 |
| AME | 0.28 |
| RMS | 0.35 |
| SI | 0.65 |
| CC | 0.87 |
| $R^2$ | 0.75 |



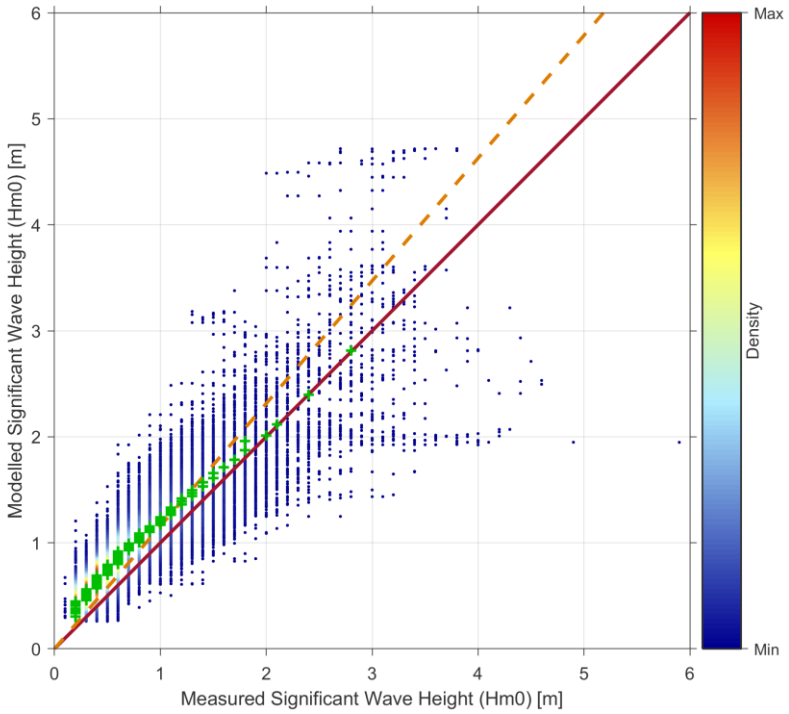




Figure C.60. Splaugh, Hm0 validation.

## C.6 Directional Sector Validation

### C.6.1 Introduction

In this Section, the behaviour of the wave model when compared to measurements from the project AWACs are compared by directional sector. Two sets of sectors are used:

- In Section C.6.2, standard 45° sectors are used. The first sector *starts* at 0°, rather than being centred there, to more closely align with the Irish coast to the west.
- In Section C.6.3, four custom sectors are instead used, to broadly coincide with wave directions coming from:
  - The Irish coast.
  - Longer fetch to the north, between the Irish coast and Anglesey.
  - The Welsh and English coast.
  - Very long fetch to the south, between the English and Irish coastlines.

  More precise details can be found in Section C.6.3.1.

### C.6.2 45° Sectors

#### C.6.2.1 Sector Specification

For the first set of validations, standard 45° sectors were used. The first sector *starts* at 0° which, as shown in Figure C.61, provides a better alignment with various features of the coastline – in particular the Irish coast – than would be the case were the first sector to be *centred* at 0°.

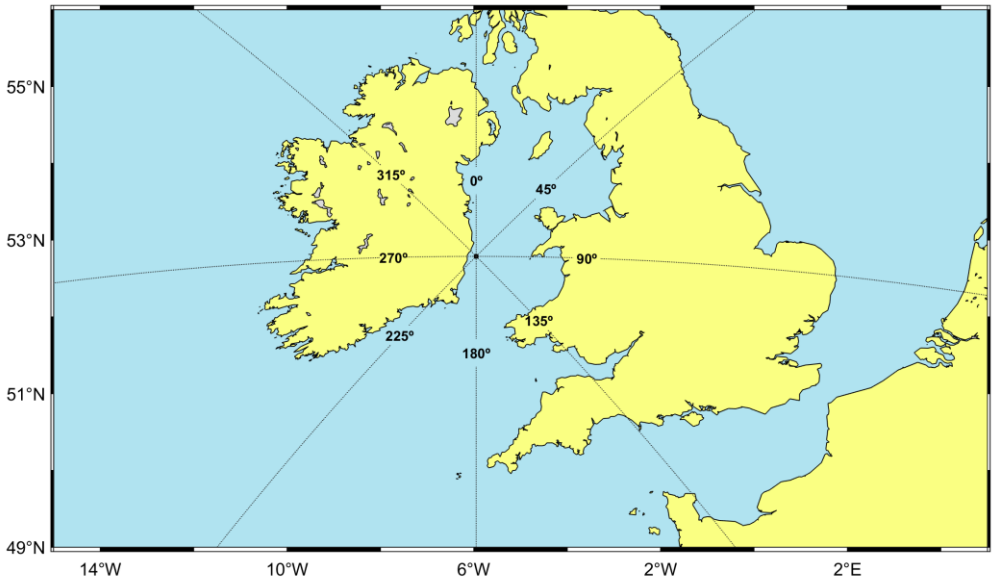



Figure C.61. 45° Directional Sectors.

### C.6.2.2 Overview

Validation plots for AWAC A are included in Section C.6.2.3 as follows:

- **Significant Wave Height (Hm0):** Plots for each sector are show in Figure C.62.
- **Mean Wave Period (Tm01):** Plots for all timestamps *except* those with the very smallest Hm0 (less than or equal to 0.1 m) are shown in Figure C.63, whilst Figure C.64 includes only timestamps with Hm0 greater than the higher threshold of 0.5 m. Note that, as discussed in Section C.4.2, Tm01 for both modelled and measured data are calculated using frequencies up go 0.5 Hz only.
- **Mean Zero Crossing Period (Tm02):** Analogous plots can be found for Tm02 in Figure C.65 (Hm0 > 0.1 cm) and Figure C.66 (Hm0 > 0.5m). Again, as discussed in Section C.4.2 Tm02 for both modelled and measured data are calculated using frequencies up go 0.5 Hz only.
- **Peak Wave Period (Tp):** Analogous plots for Tp can be found in Figure C.67 and Figure C.68.

Thereafter, corresponding plots are included for all other AWACs in Sections C.6.2.4 through C.6.2.7.

Please note that throughout, parameters are classified to a directional sector according to *measured* mean wave direction (Mdir). For example, a measured Hm0 which corresponds to a measured Mdir of 20° would be assigned to the 000° to 045° bin. It would then be plotted against the temporally closest modelled Hm0 (at most 16 minutes away) on the appropriate set of axes. Of particular note: the *modelled* Mdir is not used in forming these figures. As discussed in Section C.3.2.2, there are some limitations in the measured values of Mdir, whereby:

a) The highest frequency available varies significantly with current velocities.
b) Directions in Deployments 2 and 3 for AWACs B1, D1 and E have been subject to significant manual correction.

### C.6.2.3 AWAC A

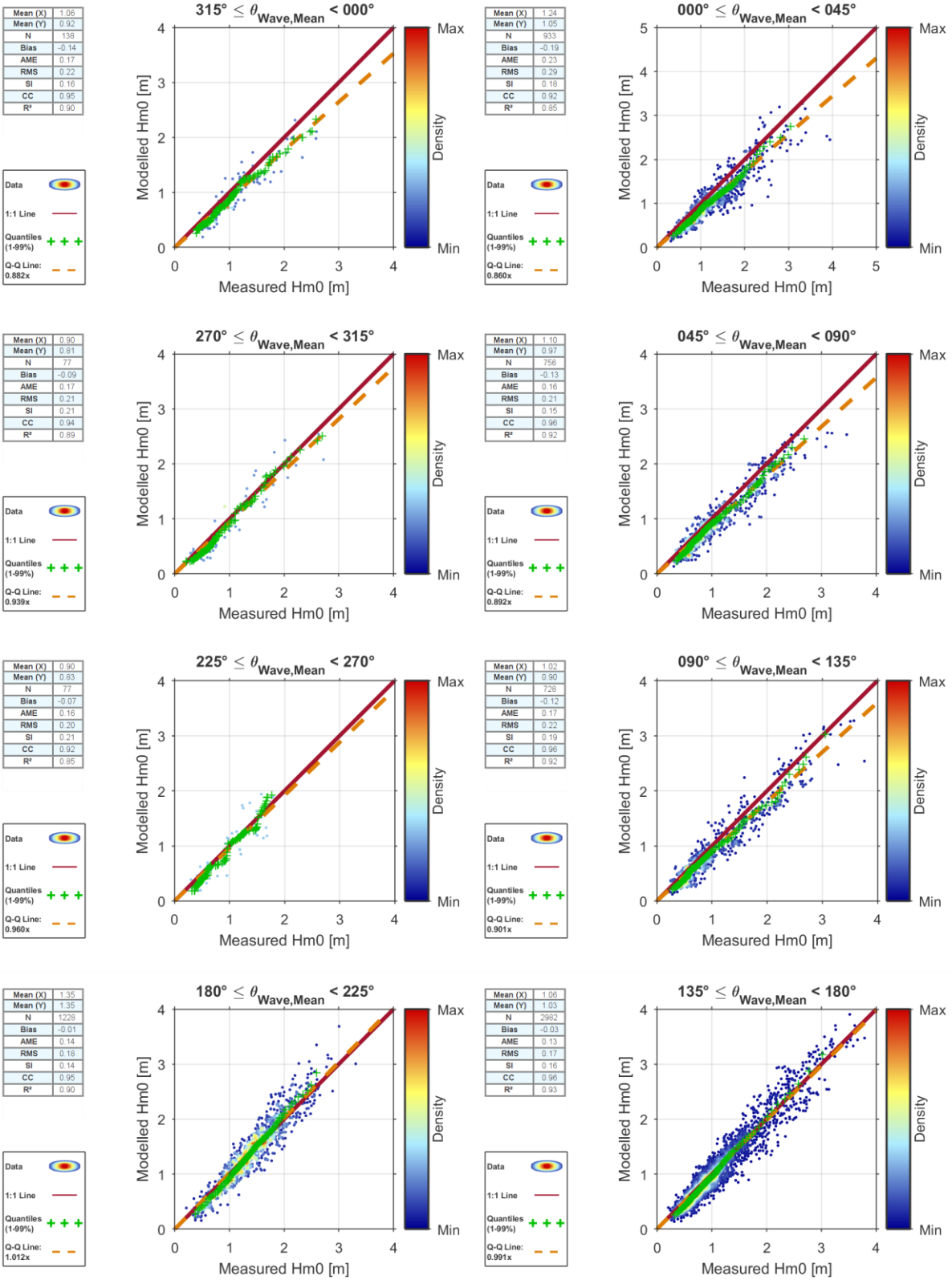



Figure C.62. AWAC A, Hm0 validation, 45° Directional Sectors.

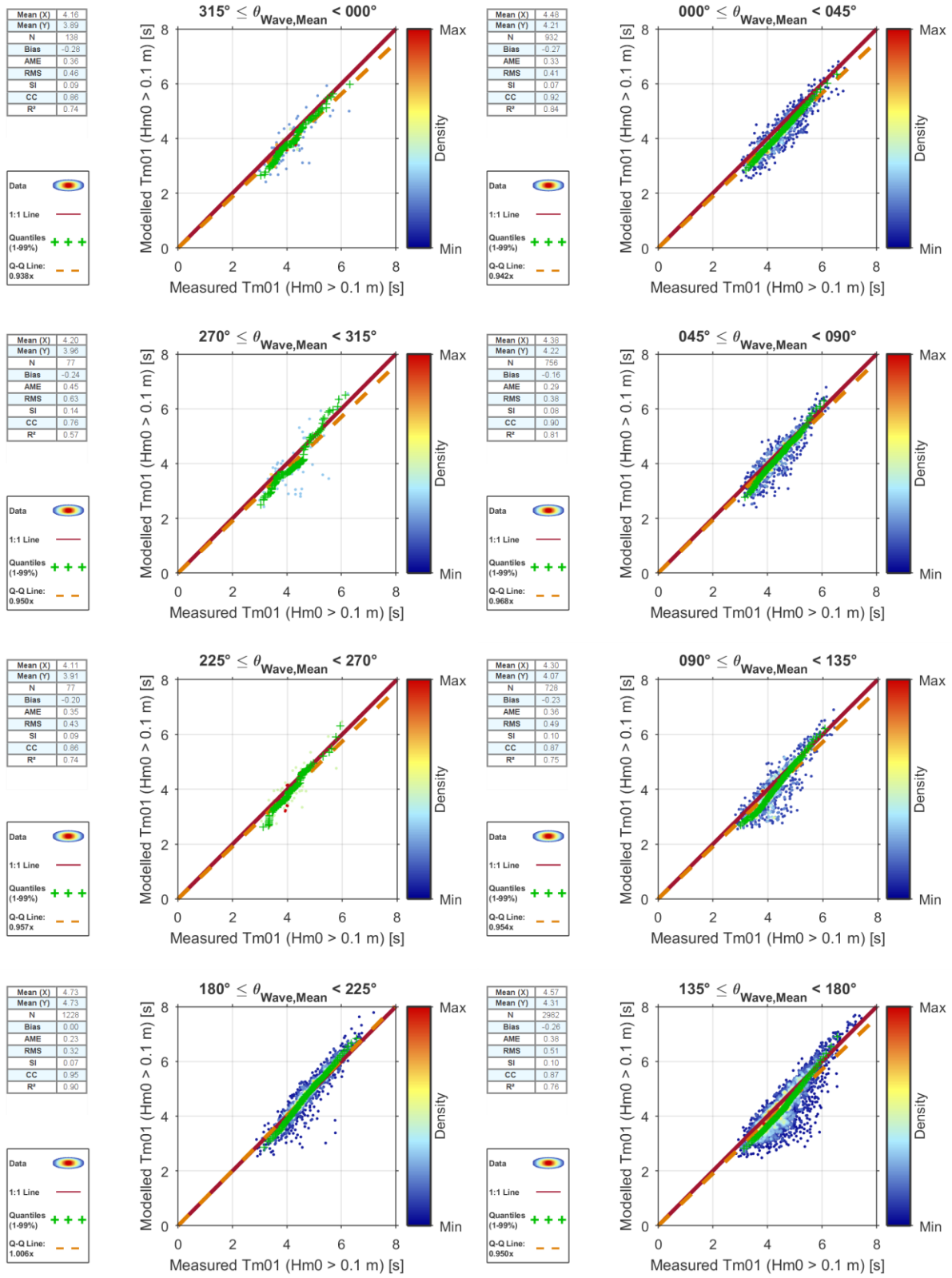



Figure C.63. AWAC A, Tm01 validation, timestamps with Hm0 > 0.1 m, 45° Directional Sectors.

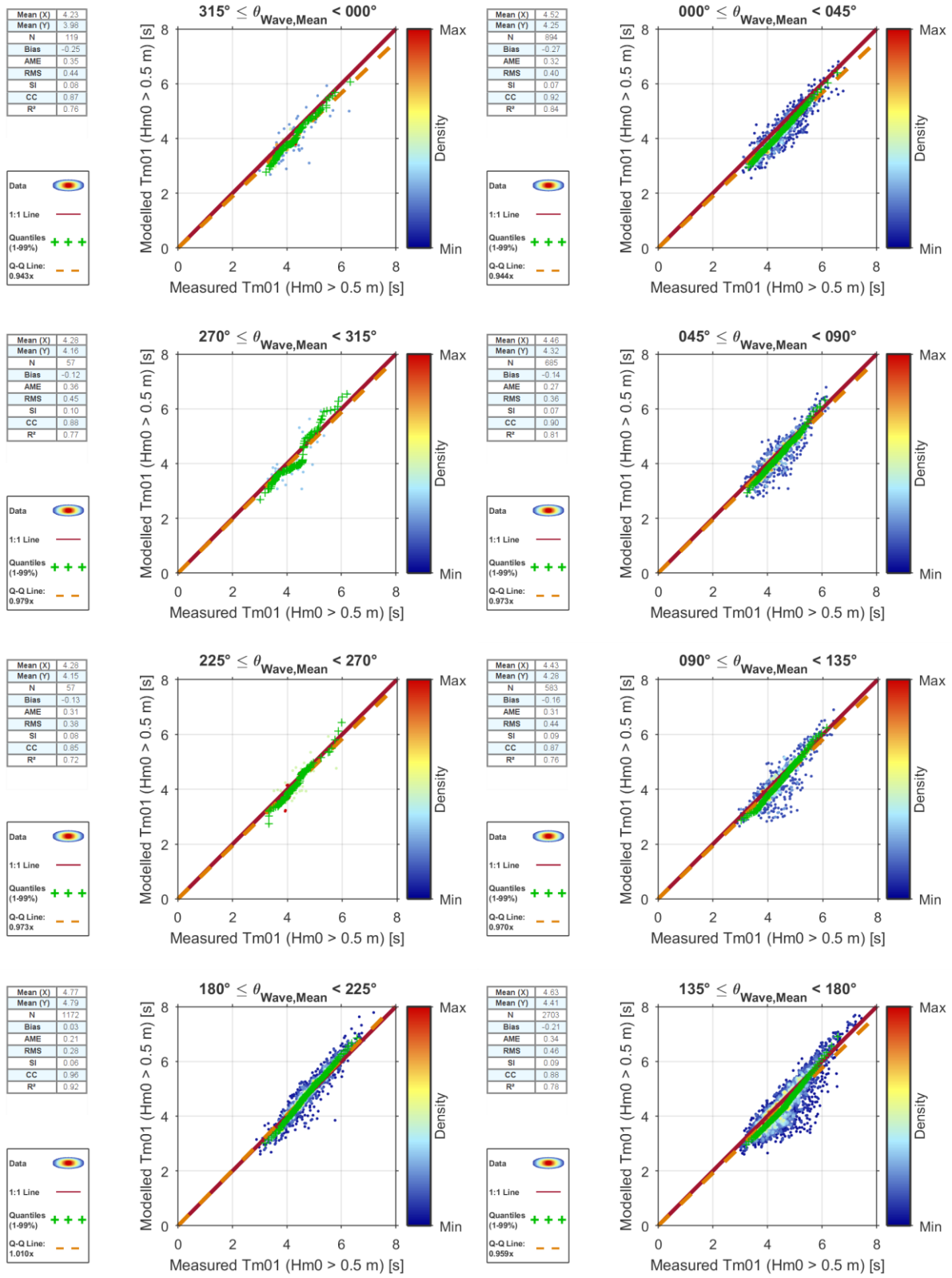



Figure C.64. AWAC A, Tm01 validation, timestamps where Hm0 > 0.5 m, 45° Directional Sectors.

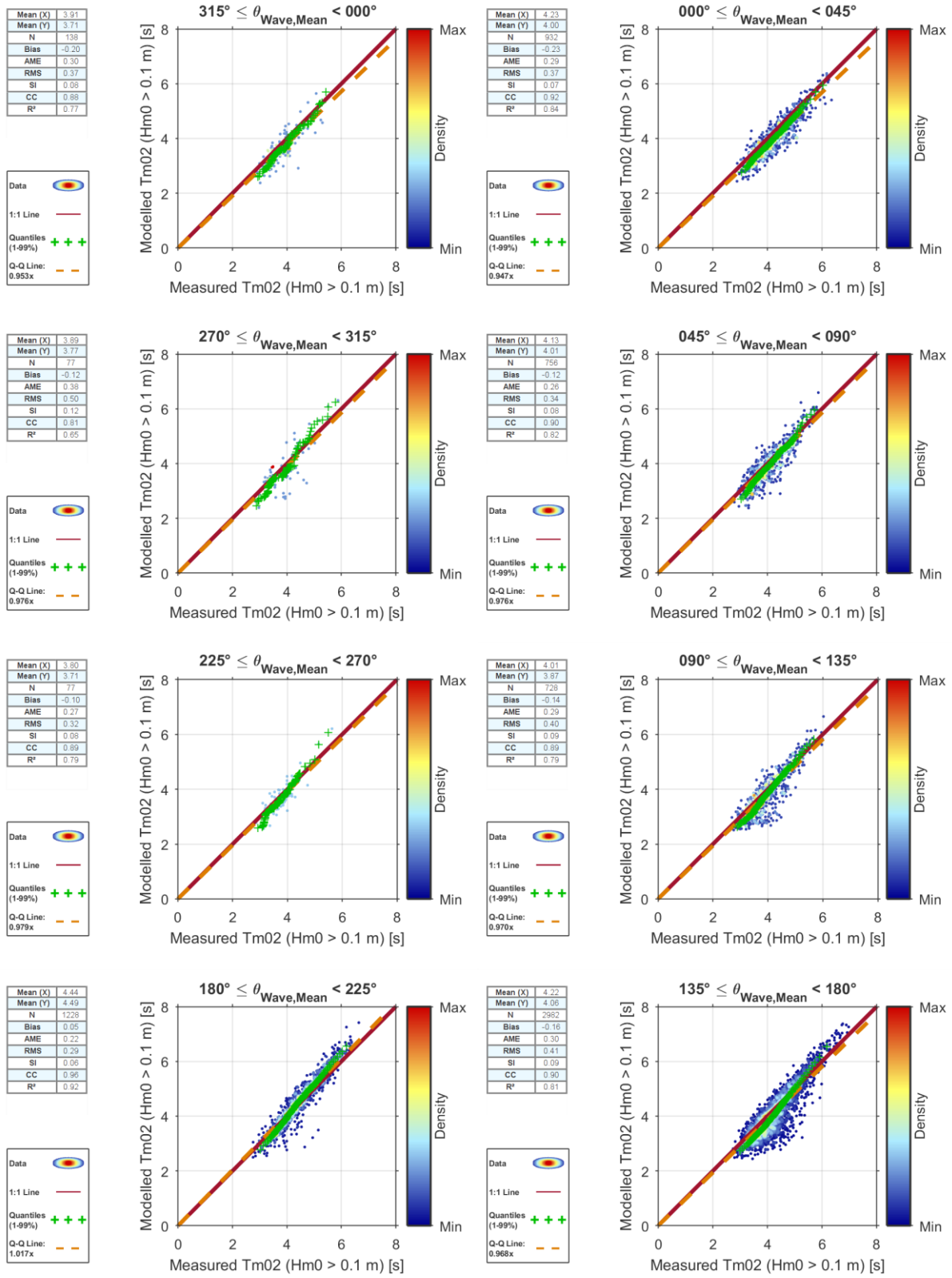



Figure C.65. AWAC A, Tm02 validation, timestamps with Hm0 > 0.1 m, 45° Directional Sectors.

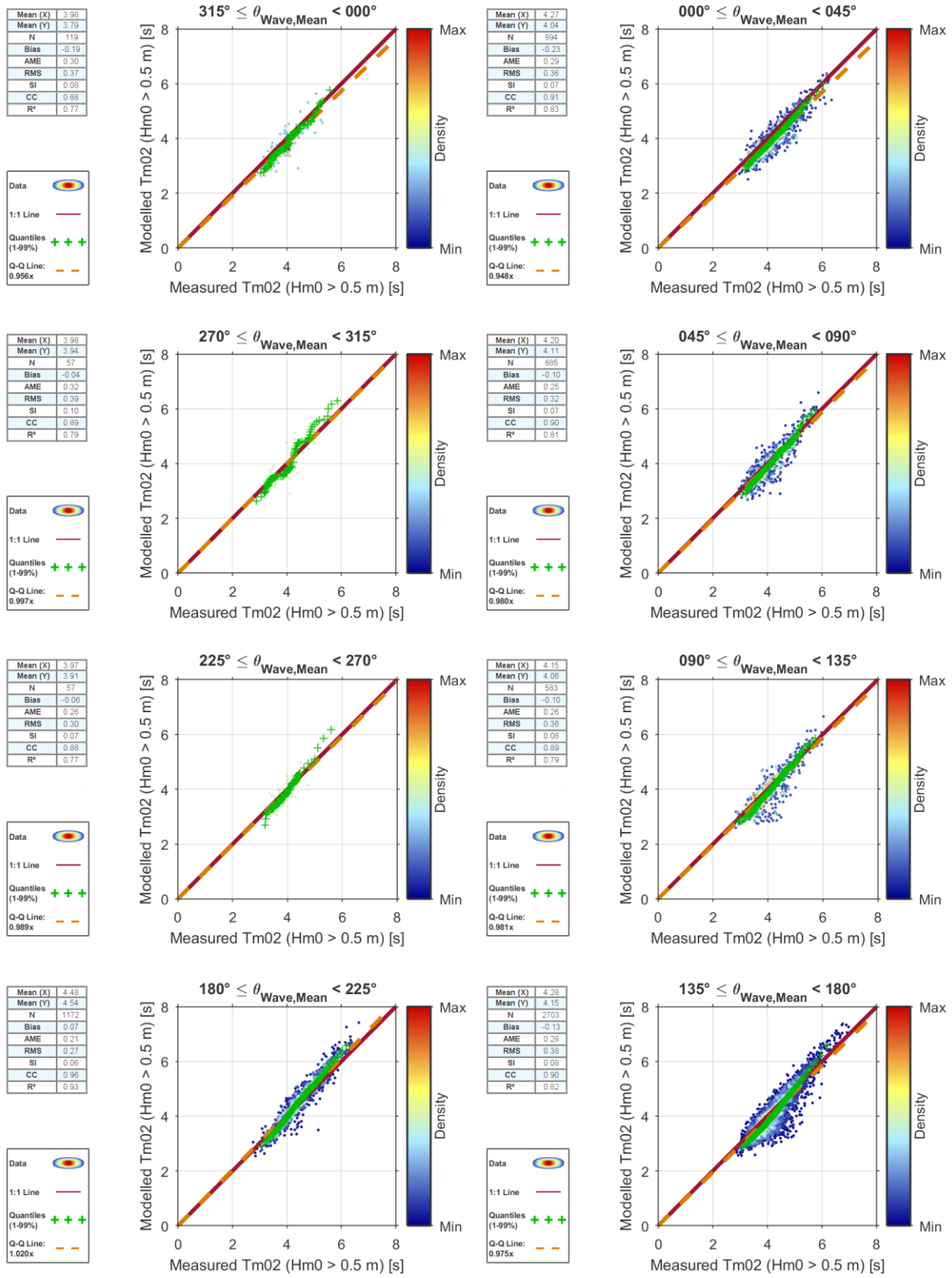



Figure C.66. AWAC A, Tm02 validation, timestamps with Hm0 > 0.5 m, 45° Directional Sectors.

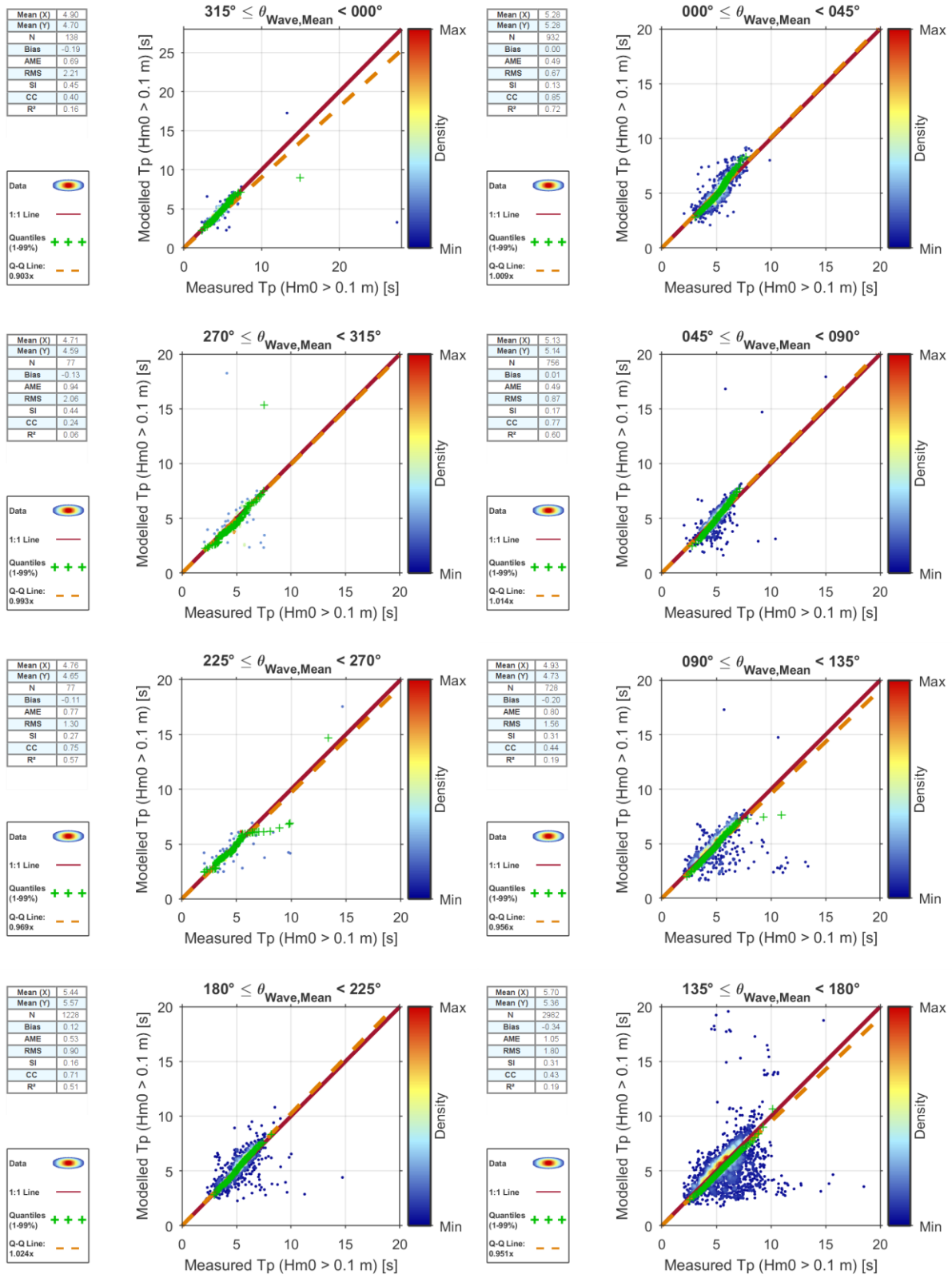



Figure C.67. AWAC A, Tp validation, timestamps with Hm0 > 0.1 m, 45° Directional Sectors.

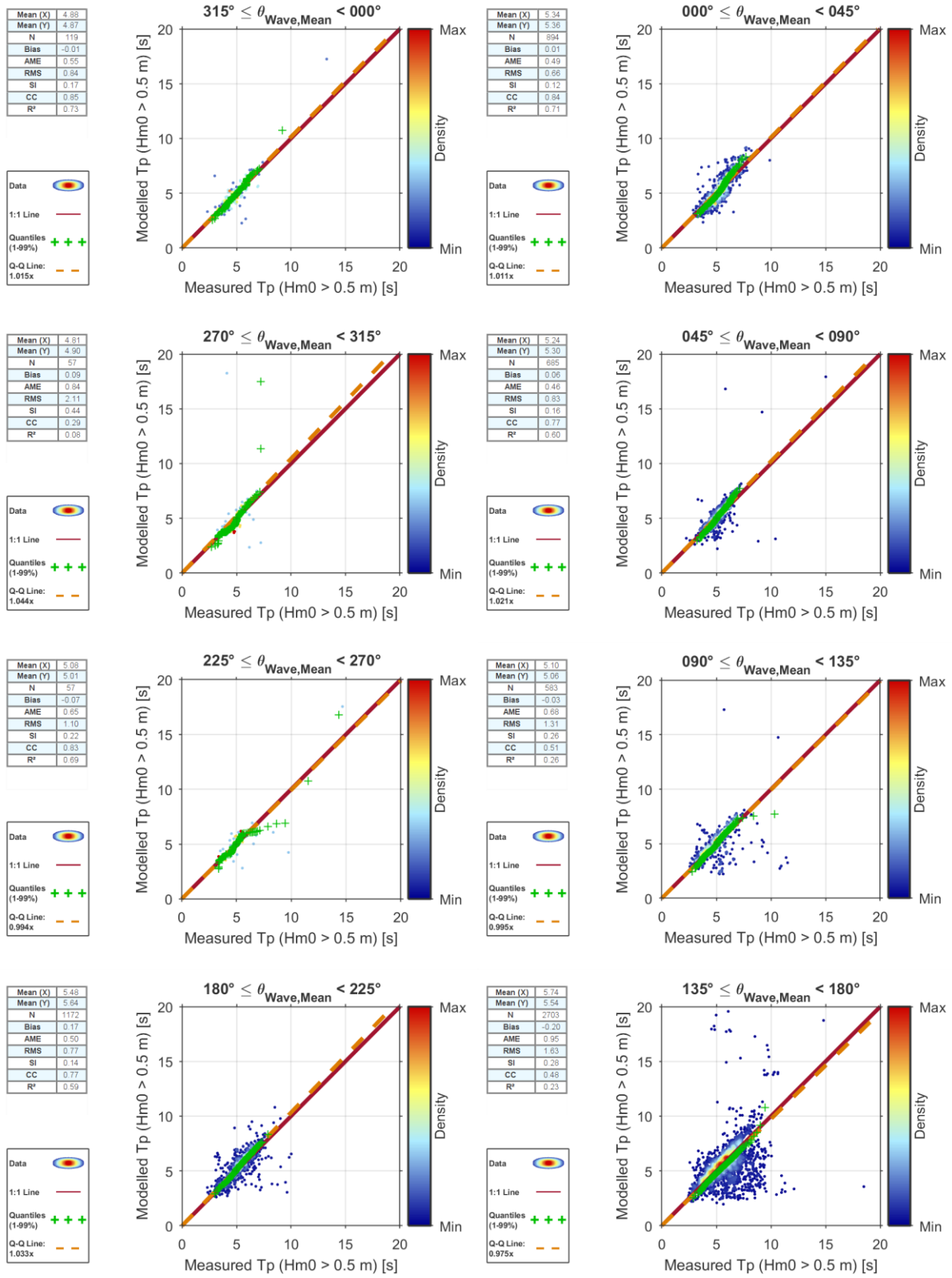



Figure C.68. AWAC A, Tp validation, timestamps with Hm0 > 0.5 m, 45° Directional Sectors.

## C.6.2.4 AWAC B1

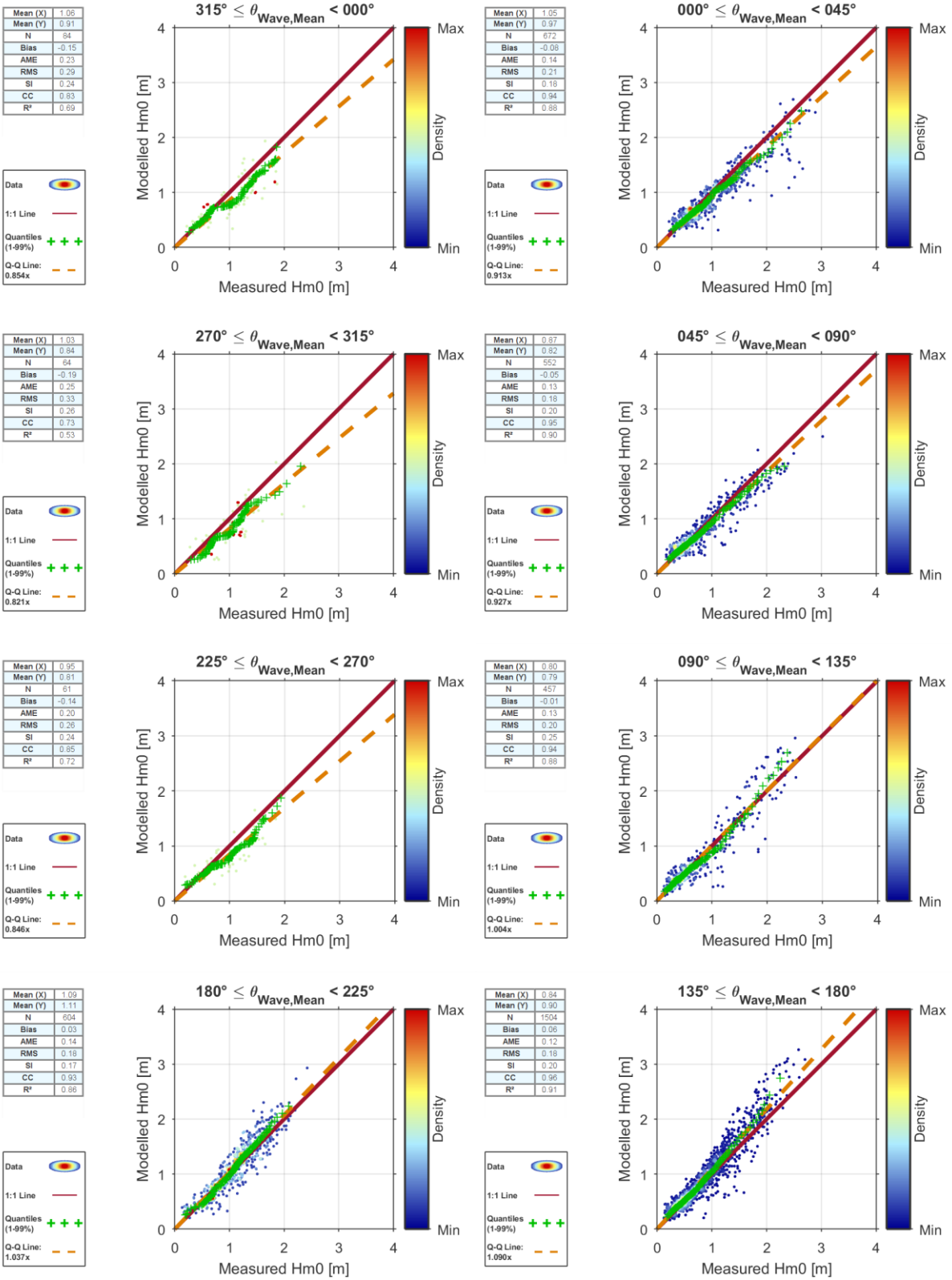



Figure C.69. AWAC B1, Hm0 validation, 45° Directional Sectors.

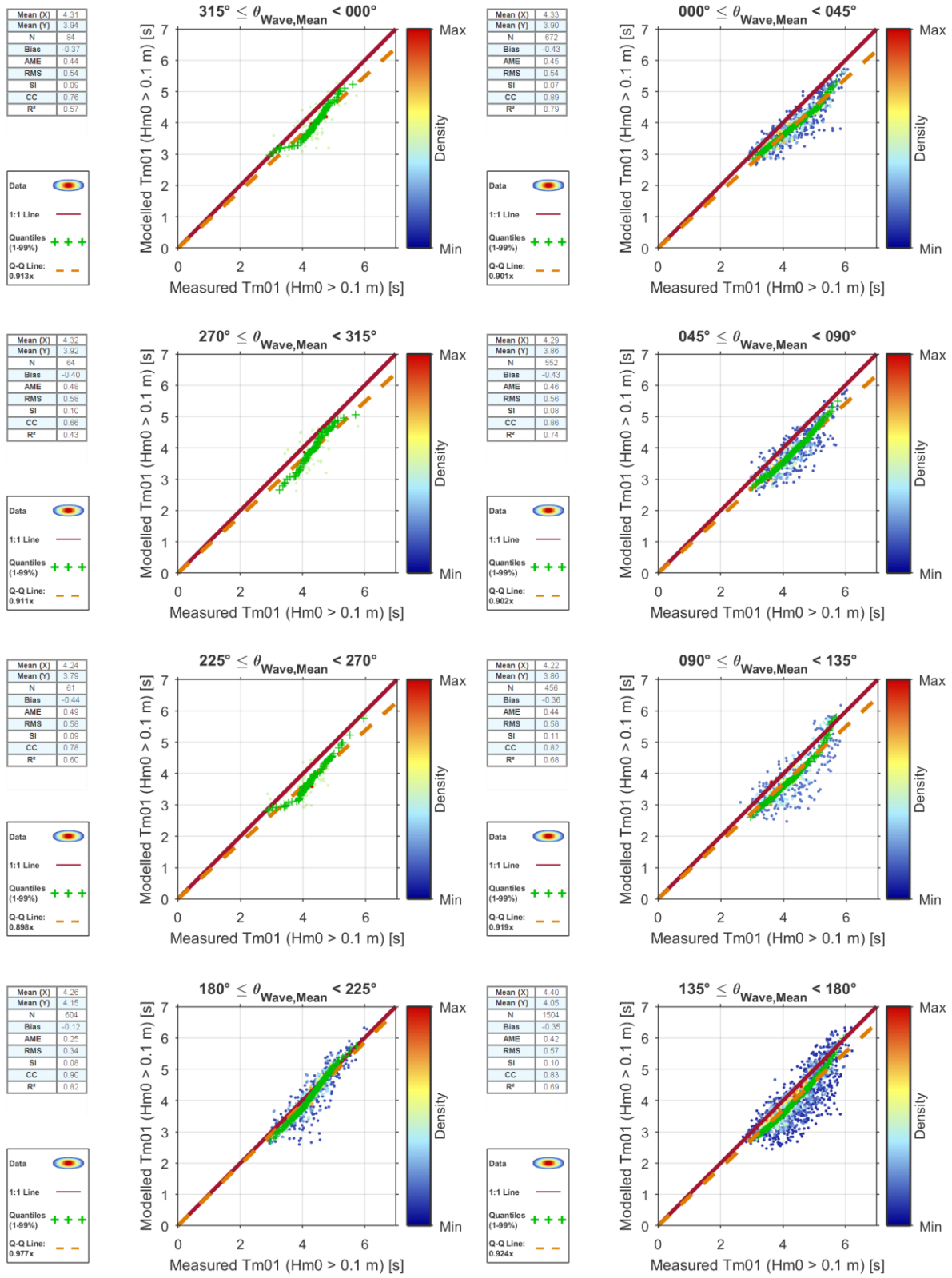



Figure C.70. AWAC B1, Tm01 validation, timestamps with Hm0 > 0.1 m, 45° Directional Sectors.

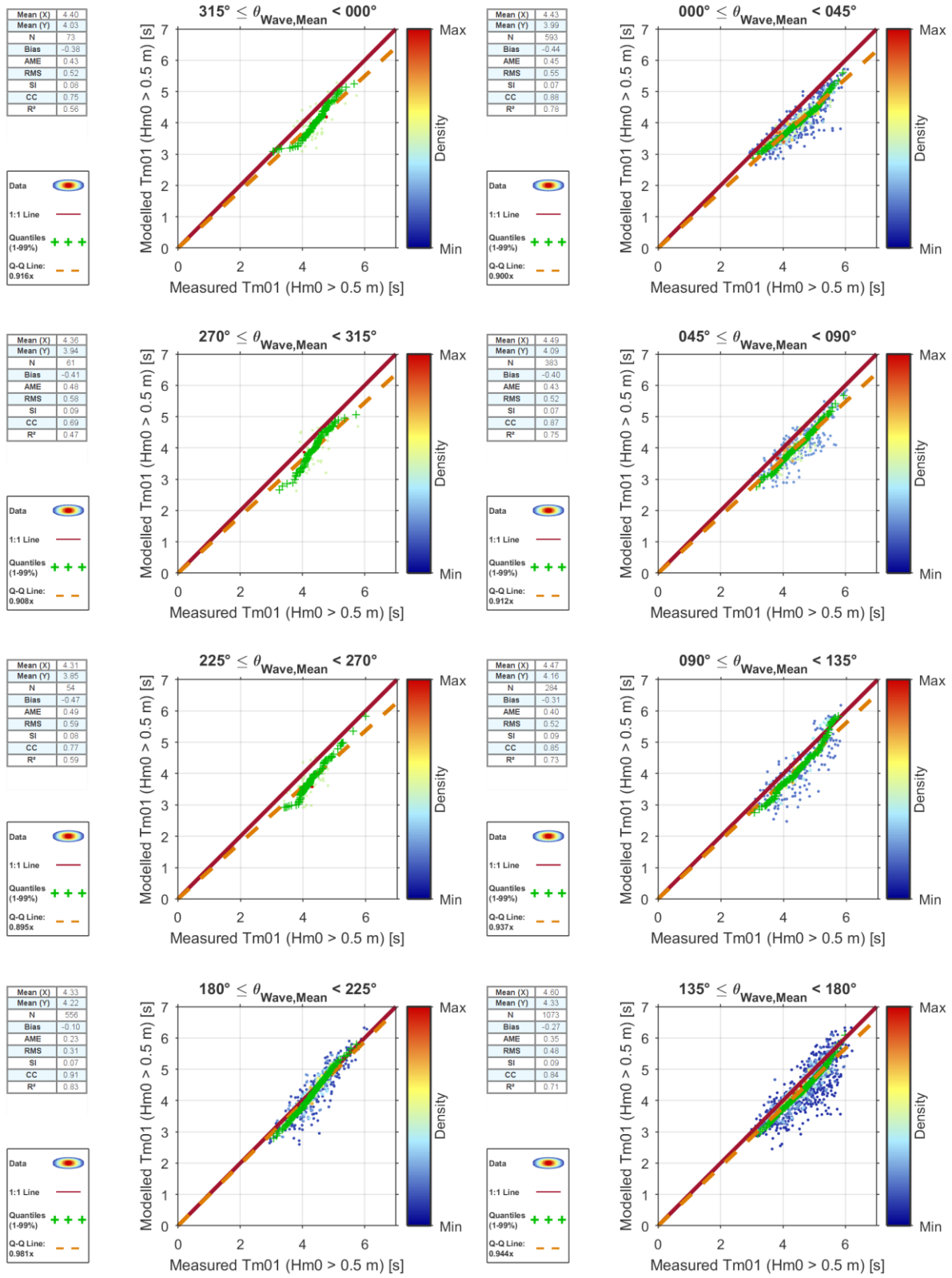



Figure C.71. AWAC B1, Tm01 validation, timestamps where Hm0 > 0.5 m, 45° Directional Sectors.

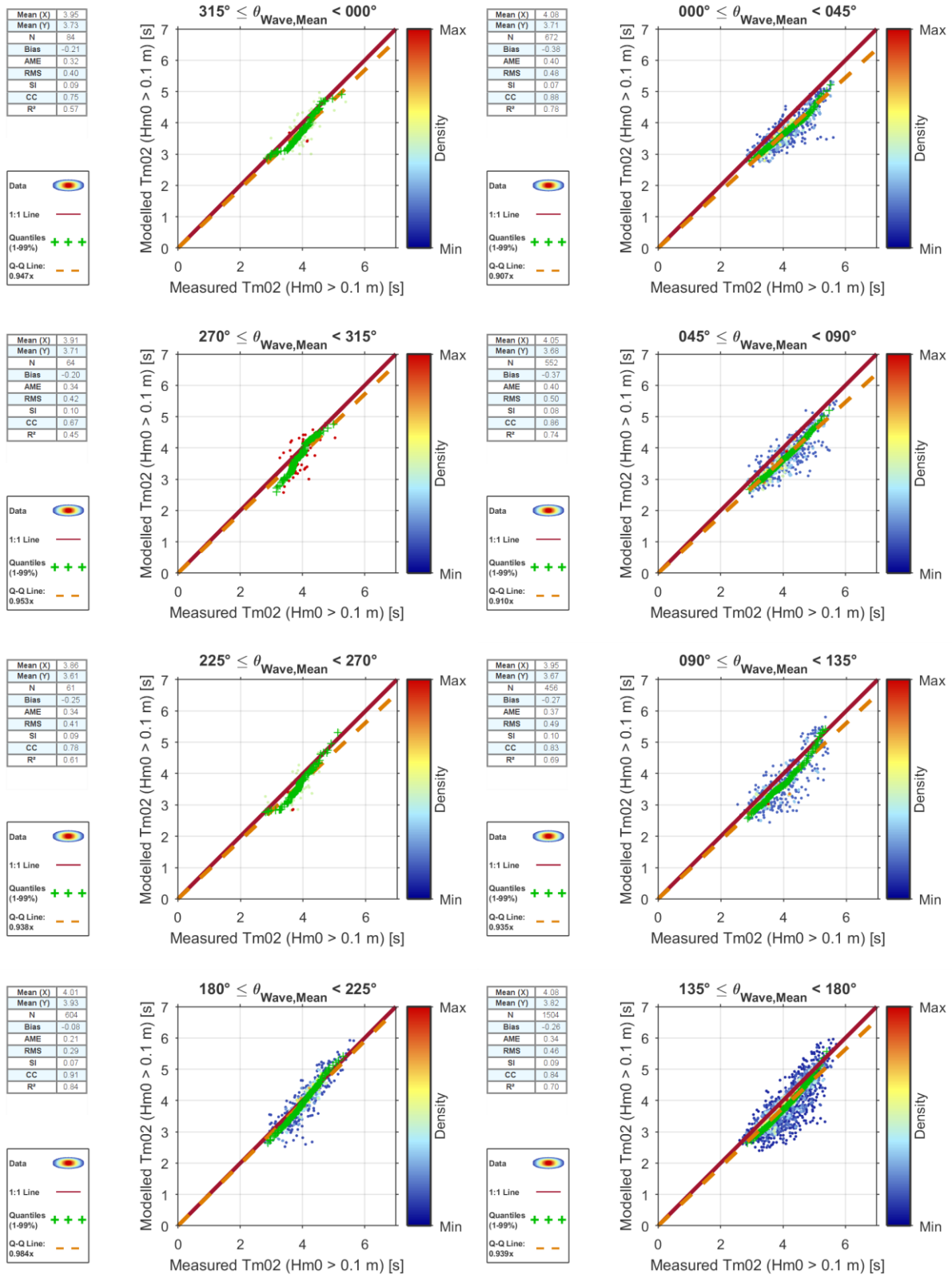



Figure C.72. AWAC B1, Tm02 validation, timestamps with Hm0 > 0.1 m, 45° Directional Sectors.

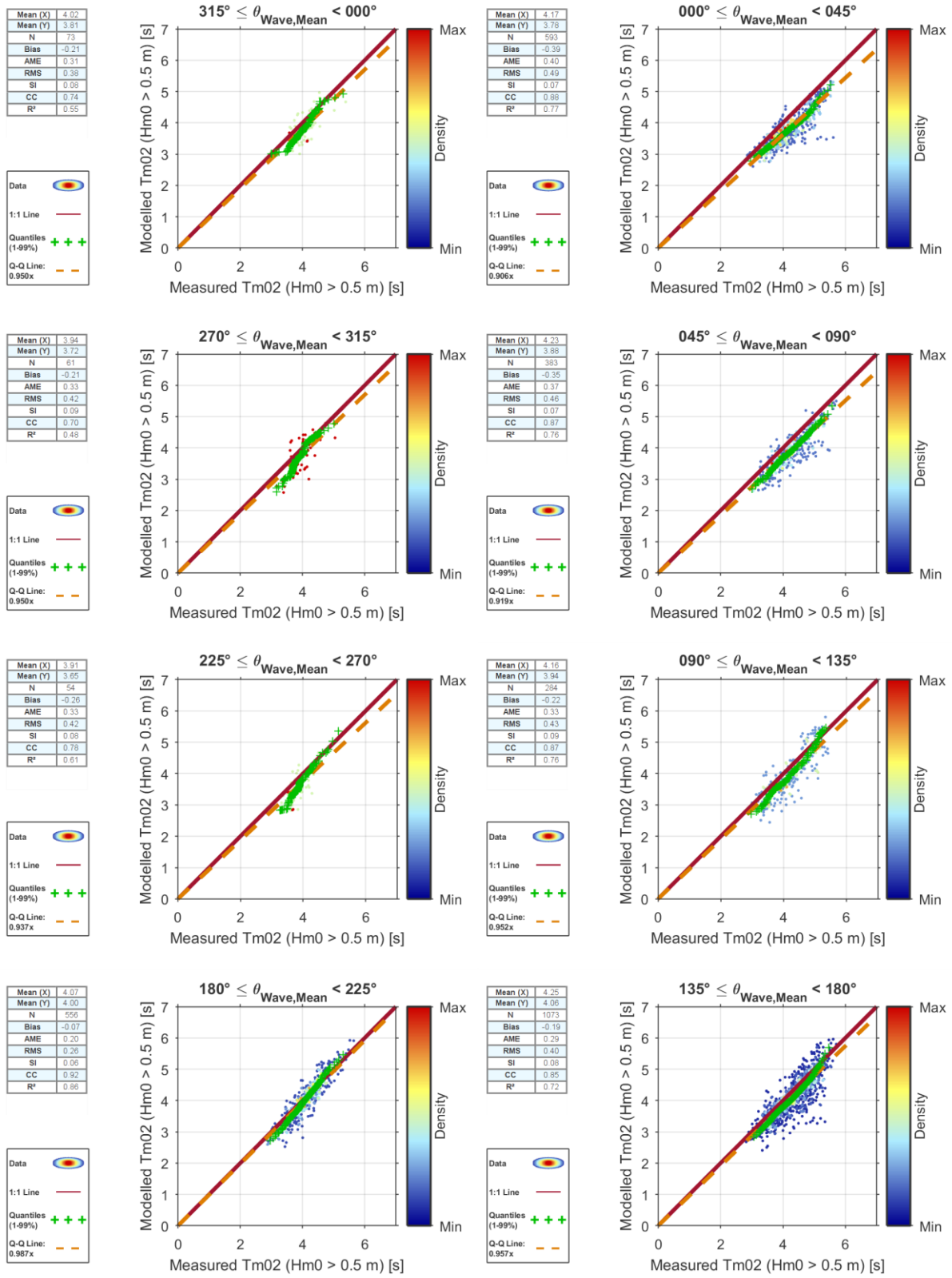



Figure C.73. AWAC B1, Tm02 validation, timestamps with Hm0 > 0.5 m, 45° Directional Sectors.

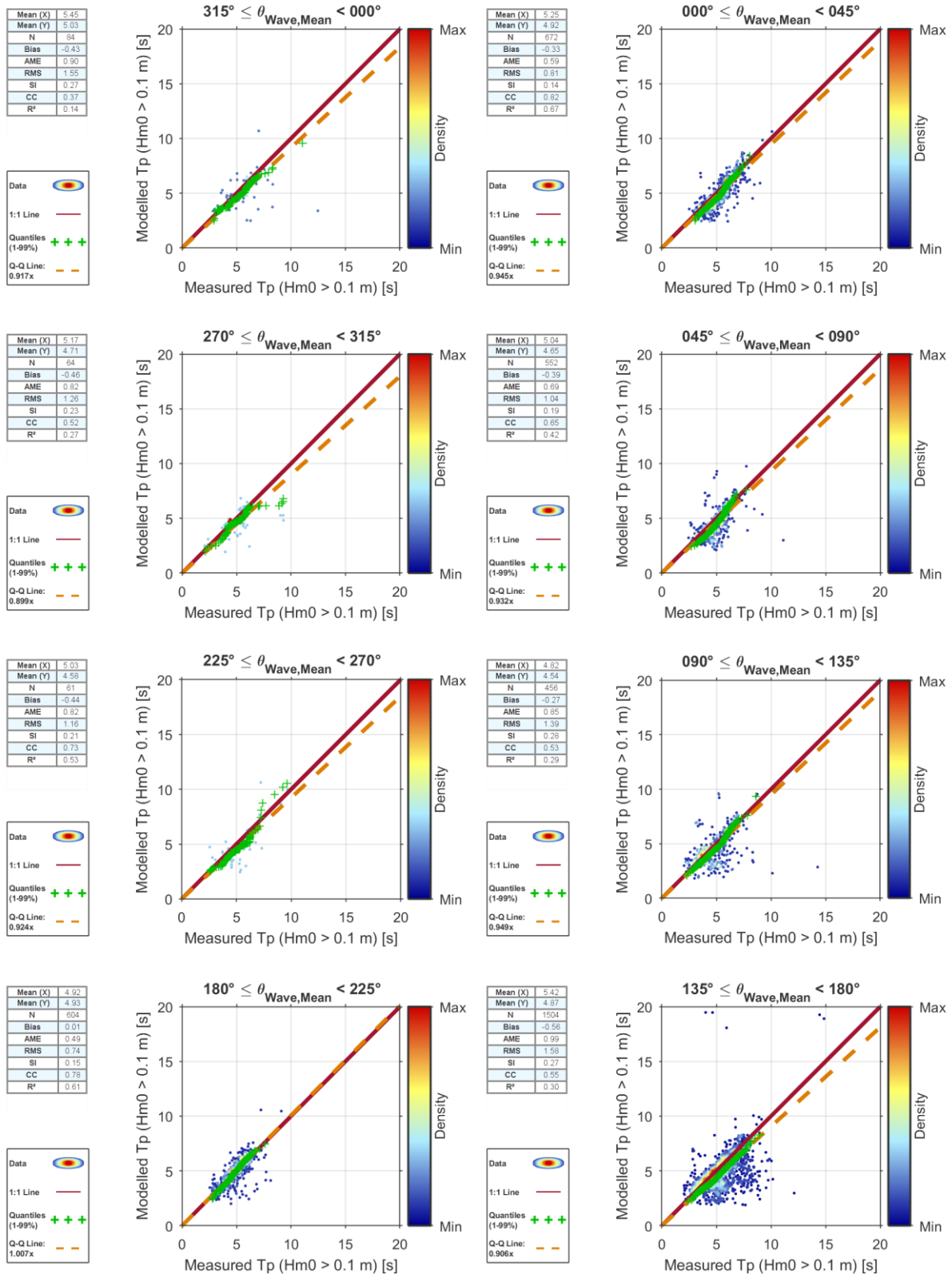



Figure C.74. AWAC B1, Tp validation, timestamps with Hm0 > 0.1 m, 45° Directional Sectors.

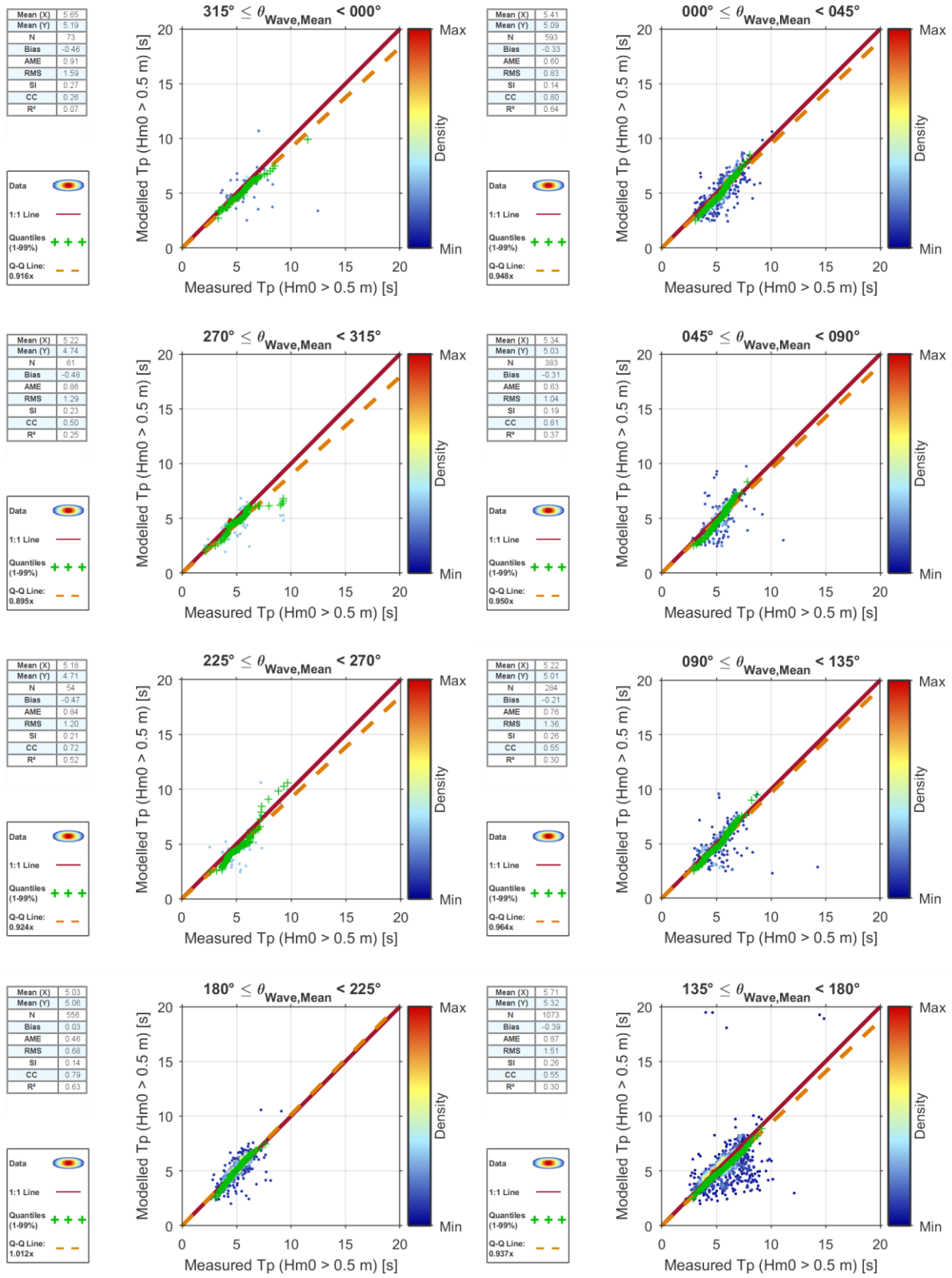



Figure C.75. AWAC B1, Tp validation, timestamps with Hm0 > 0.5 m, 45° Directional Sectors.

### C.6.2.5 AWAC C

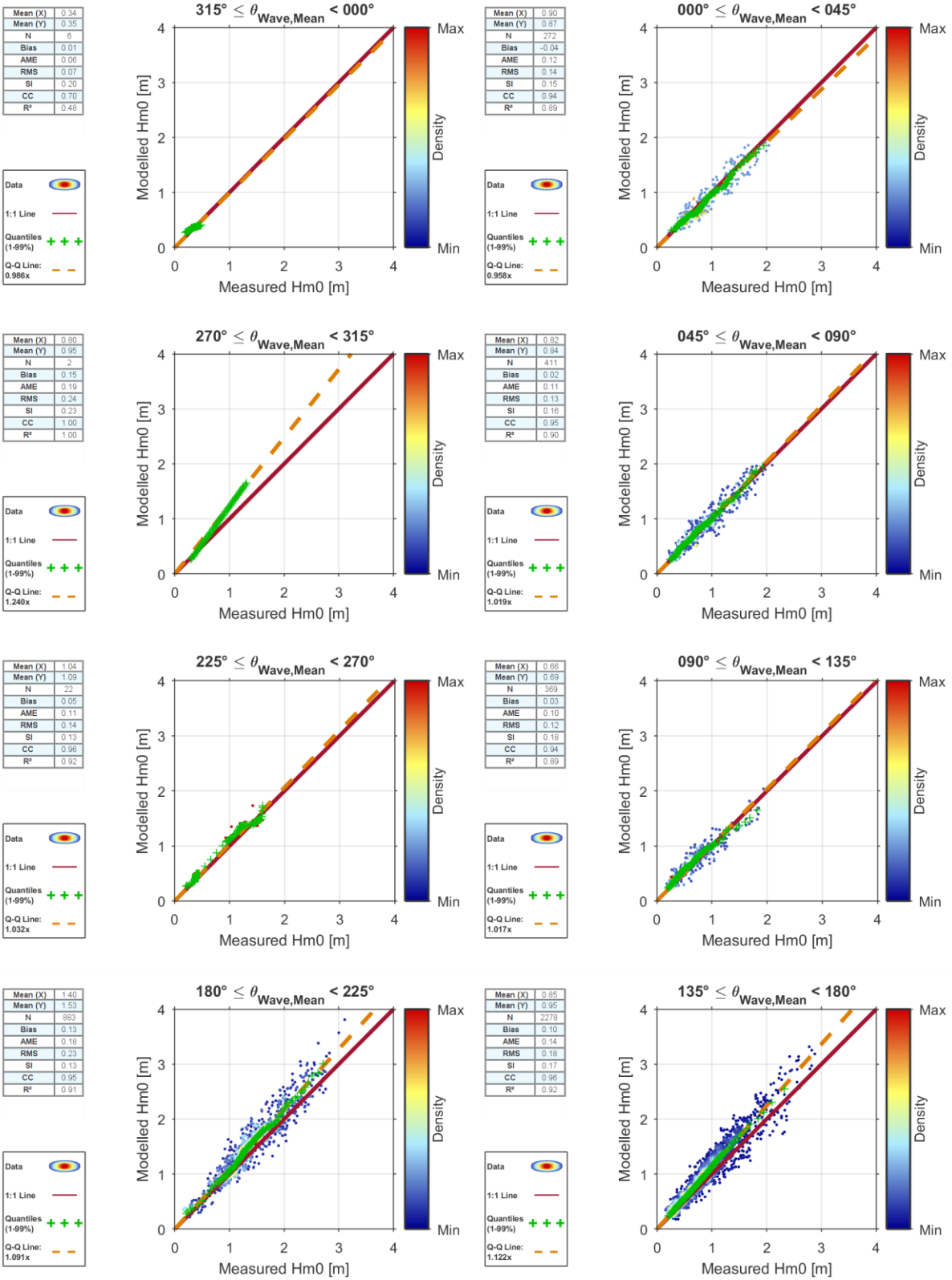



Figure C.76. AWAC C, Hm0 validation, 45° Directional Sectors.

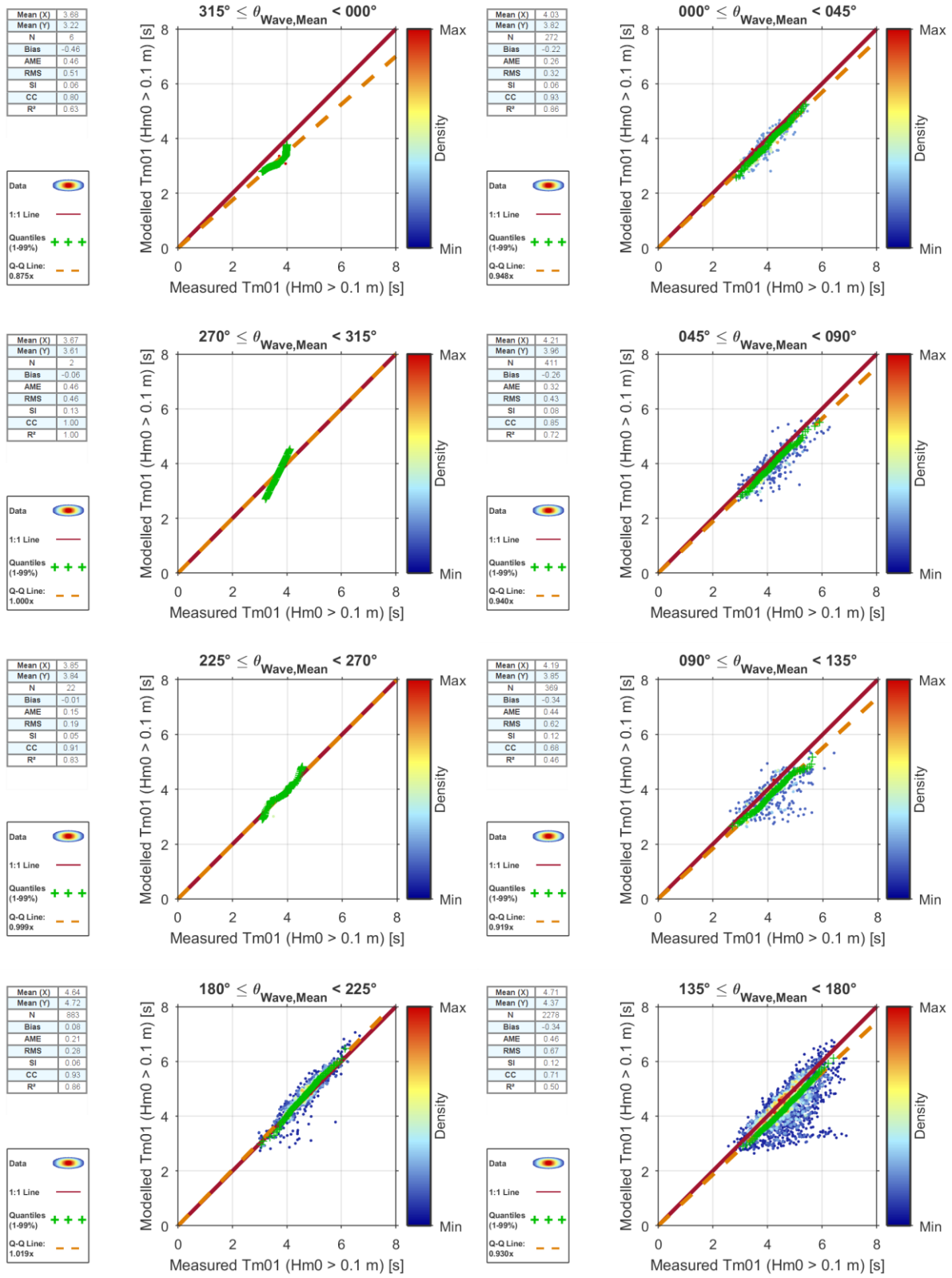



Figure C.77. AWAC C, Tm01 validation, timestamps with Hm0 > 0.1 m, 45° Directional Sectors.

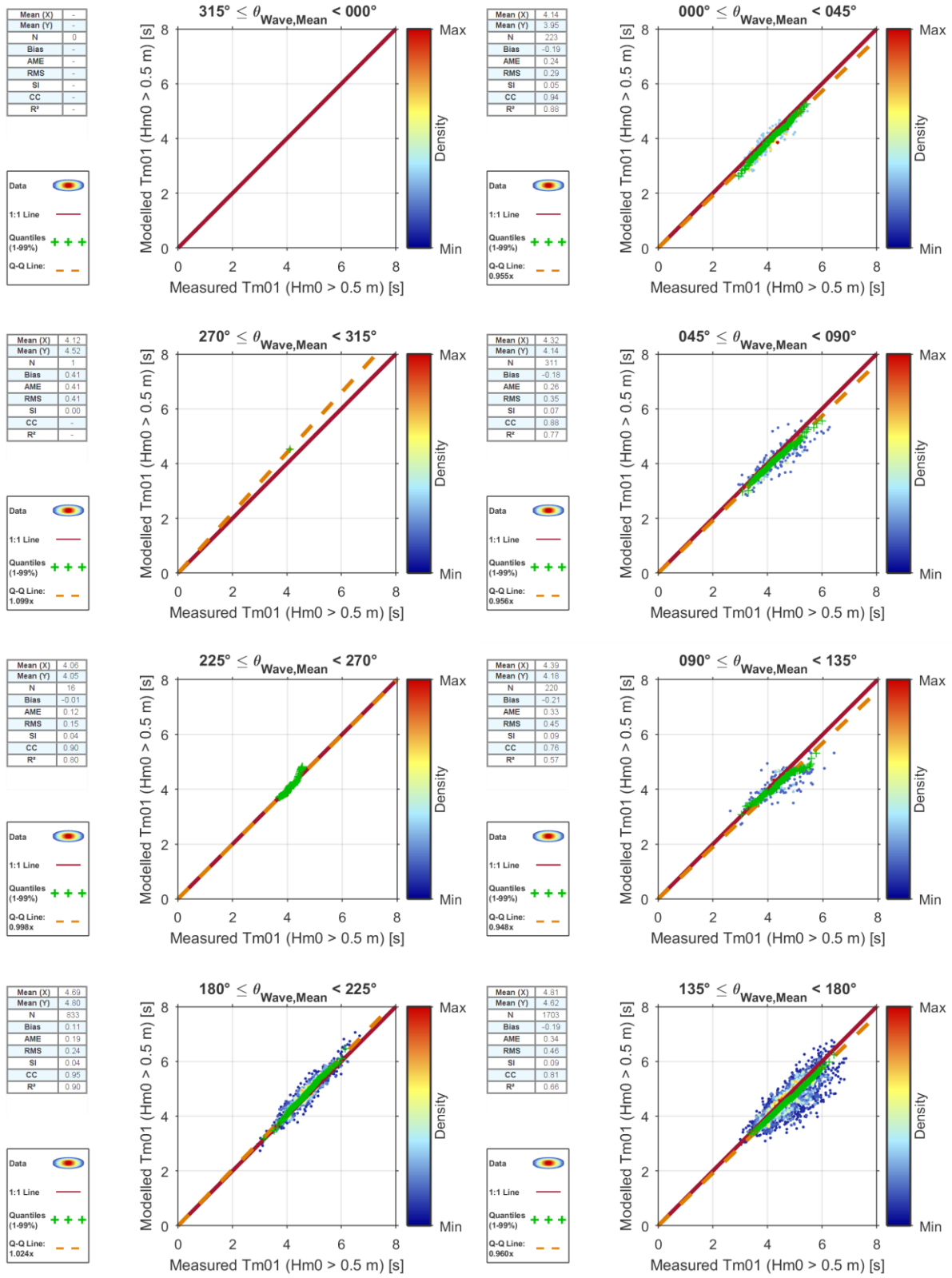



Figure C.78. AWAC C, Tm01 validation, timestamps with Hm0 > 0.5 m, 45° Directional Sectors.

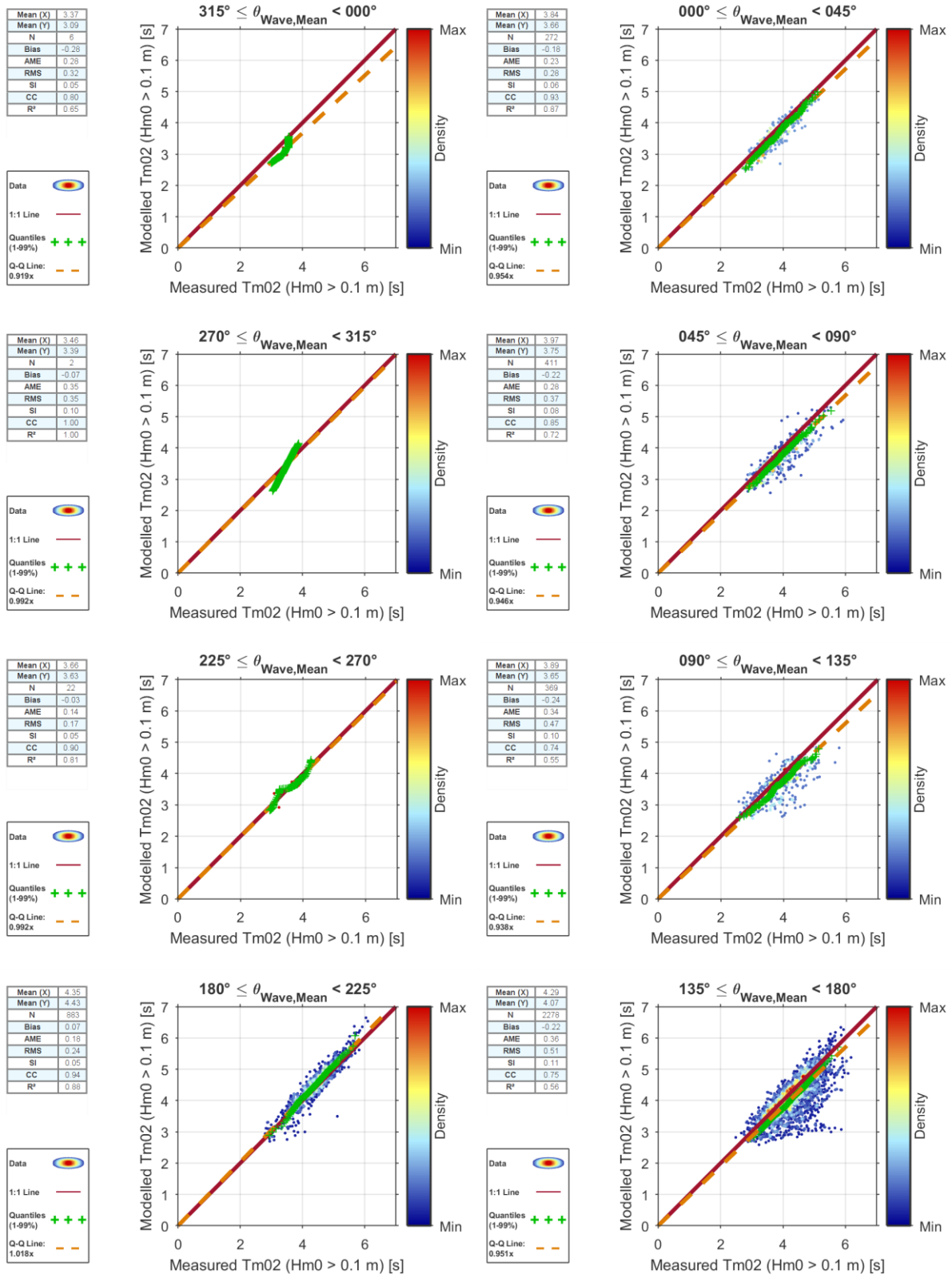



Figure C.79. AWAC C, Tm02 validation, timestamps with Hm0 > 0.1 m, 45° Directional Sectors.

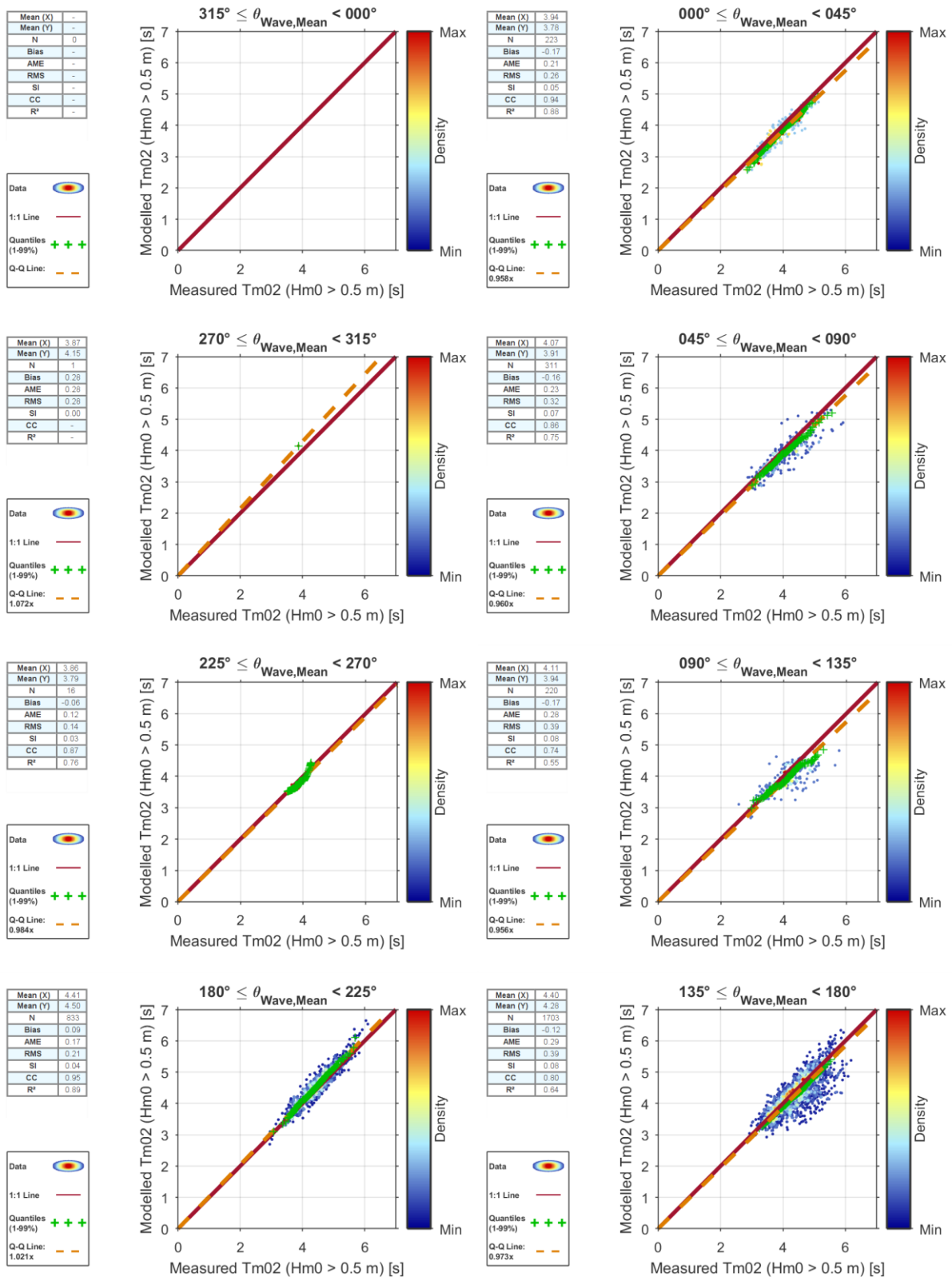



Figure C.80. AWAC C, Tm02 validation, timestamps with Hm0 > 0.5 m, 45° Directional Sectors.

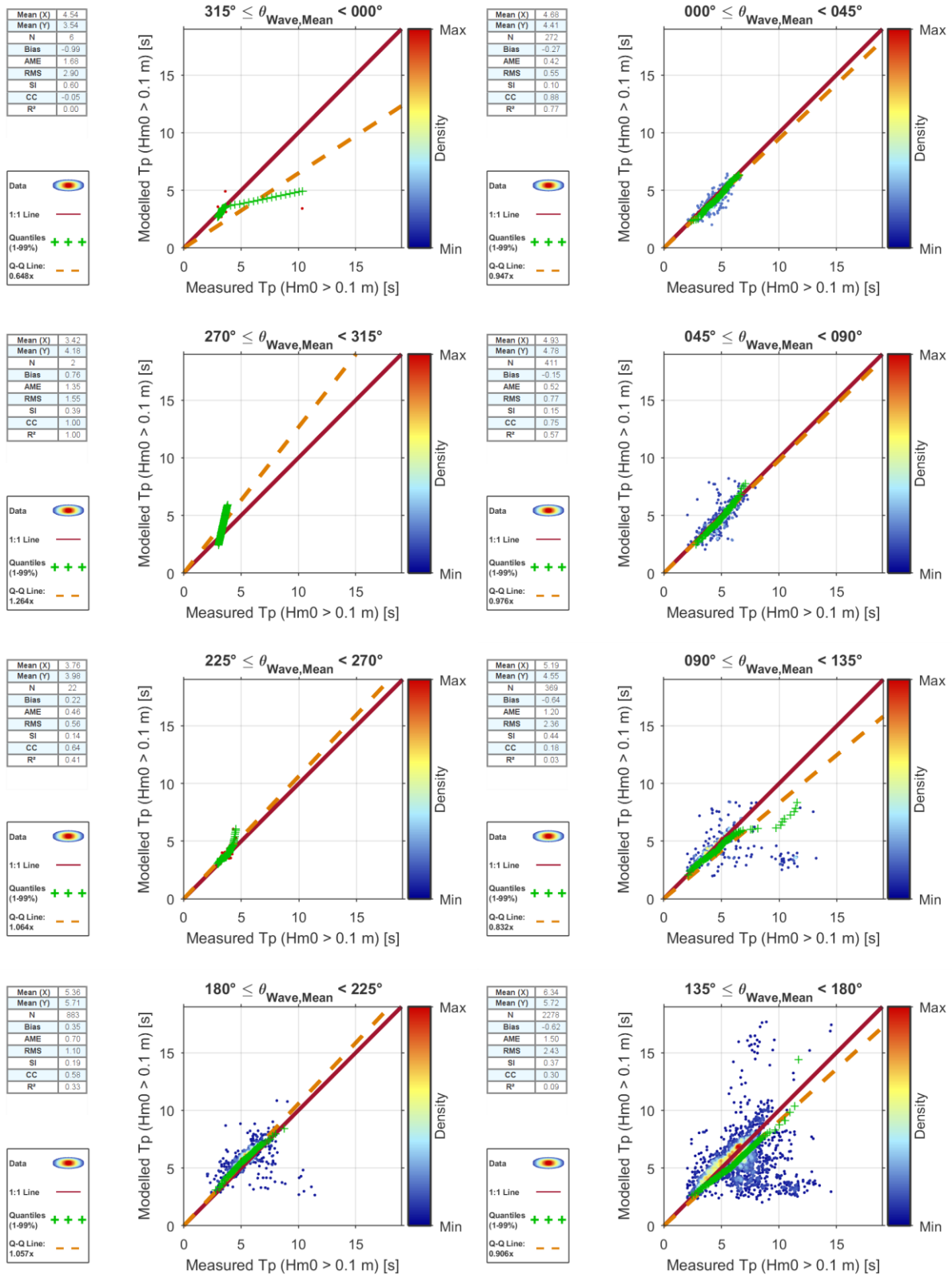



Figure C.81. AWAC C, Tp validation, timestamps with Hm0 > 0.1 m, 45° Directional Sectors.

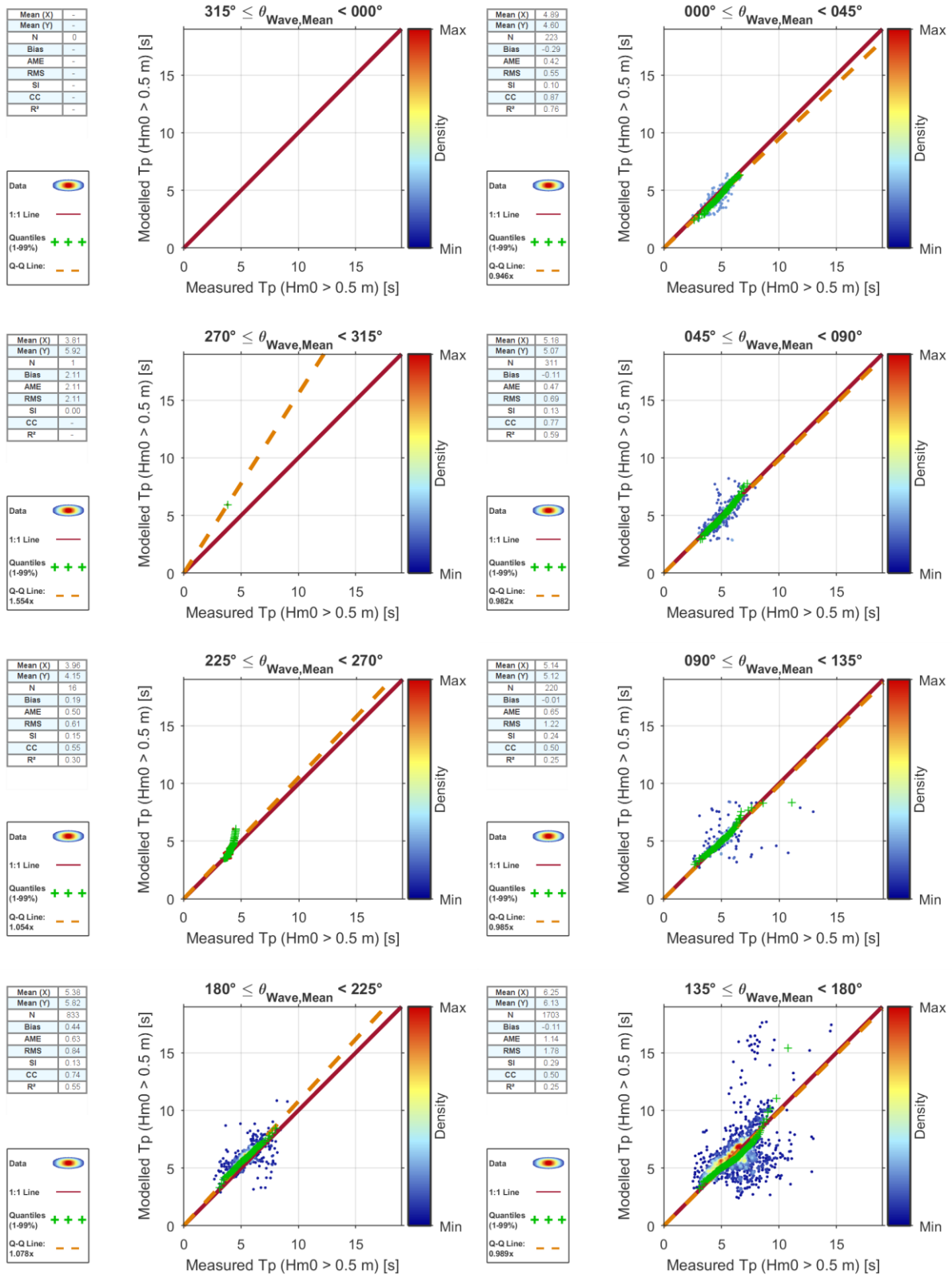



Figure C.82. AWAC C, Tp validation, timestamps with Hm0 > 0.5 m, 45° Directional Sectors.

## C.6.2.6 AWAC D1

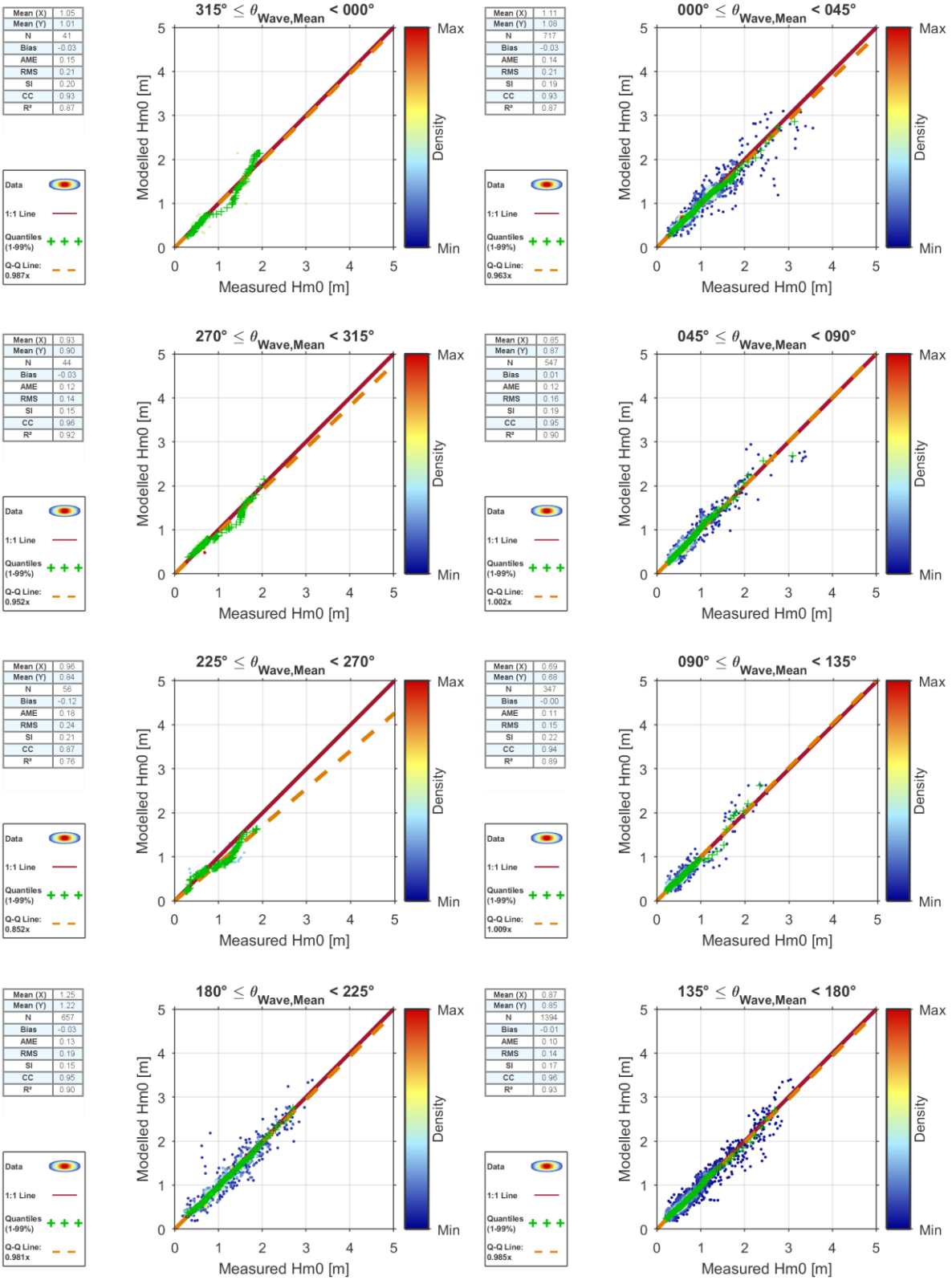



Figure C.83. AWAC D1, Hm0 validation, 45° Directional Sectors.

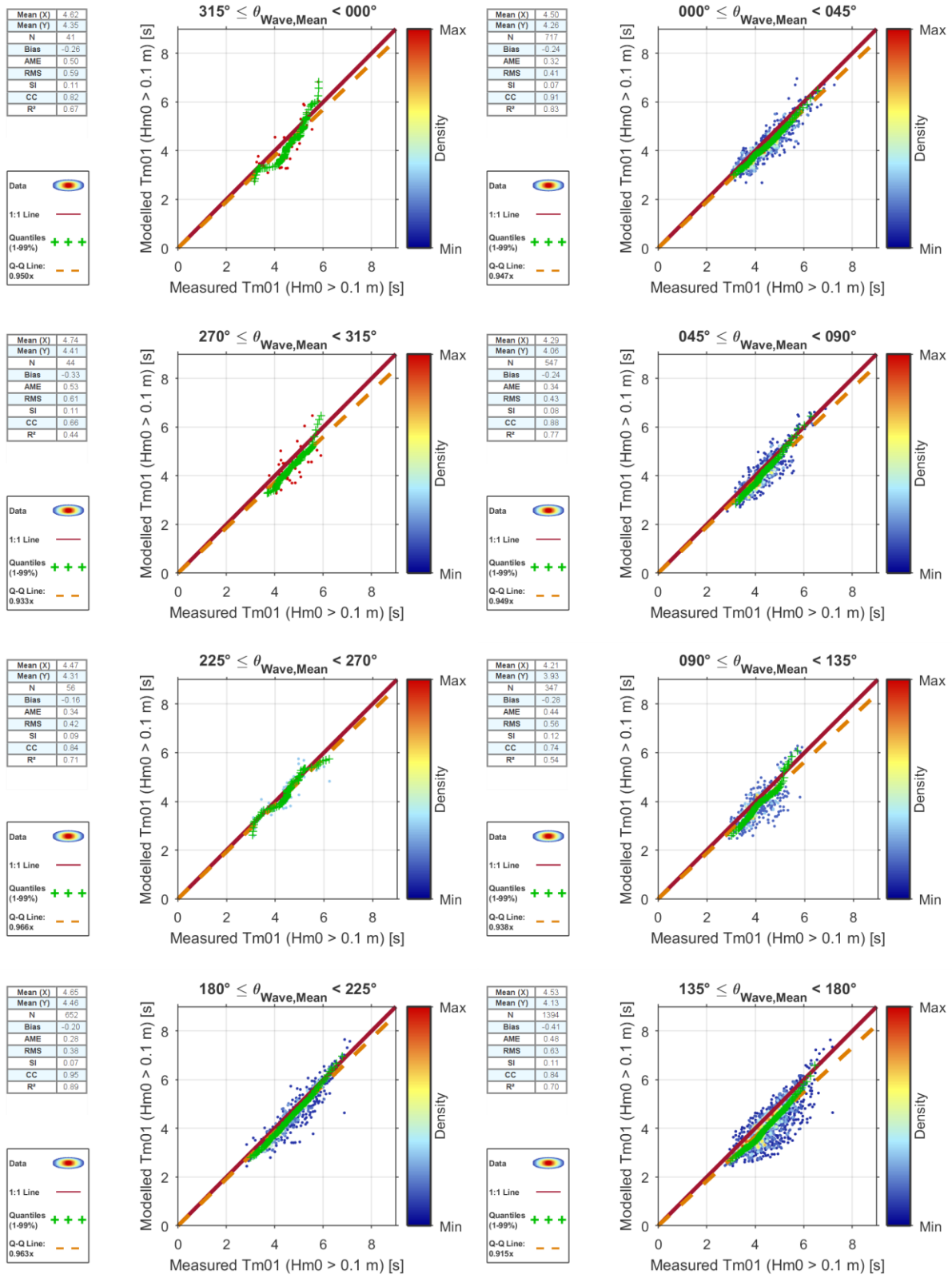



Figure C.84. AWAC D1, Tm01 validation, timestamps with Hm0 > 0.1 m, 45° Directional Sectors.

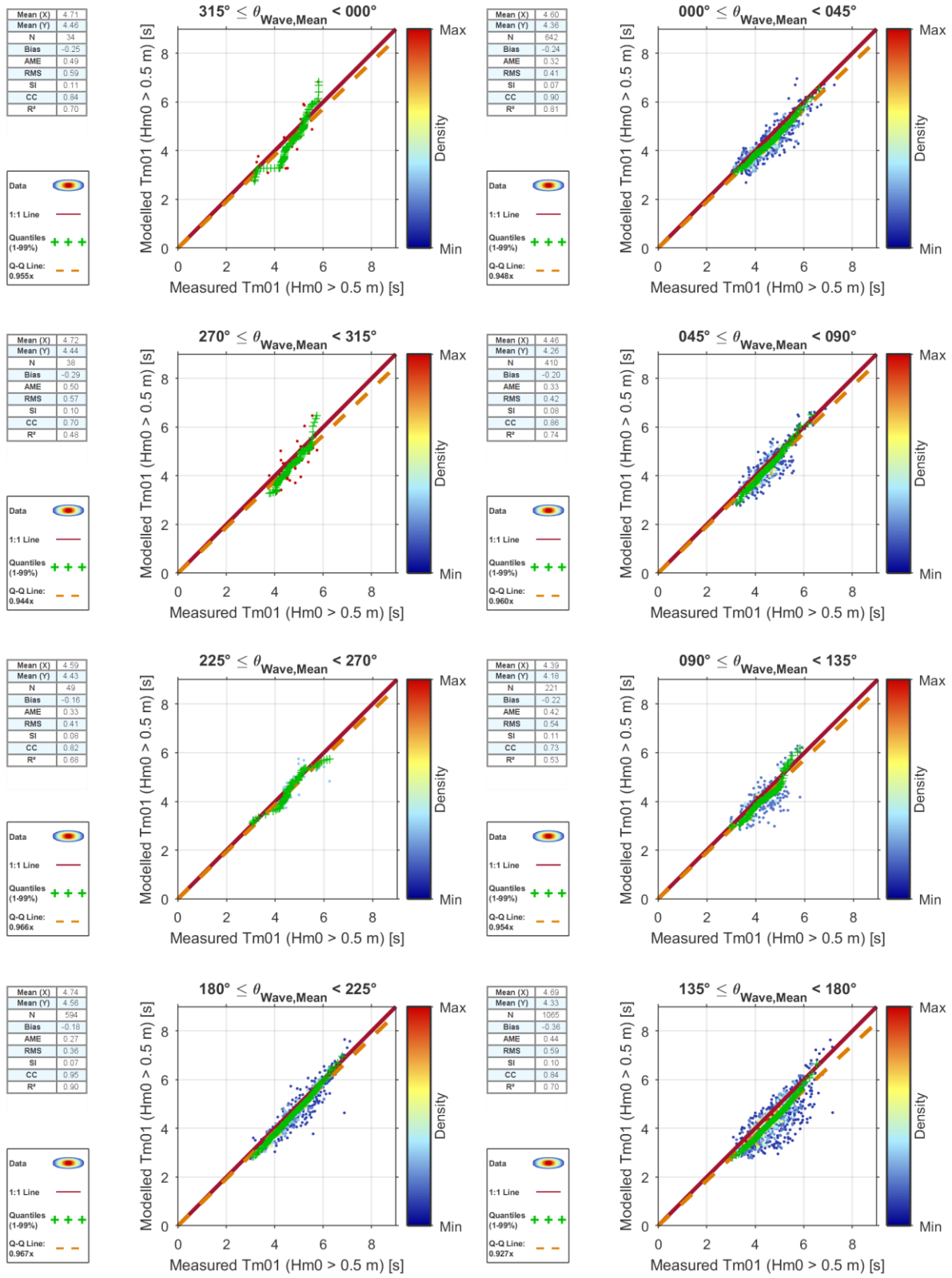



Figure C.85. AWAC D1, Tm01 validation, timestamps with Hm0 > 0.5 m, 45° Directional Sectors.

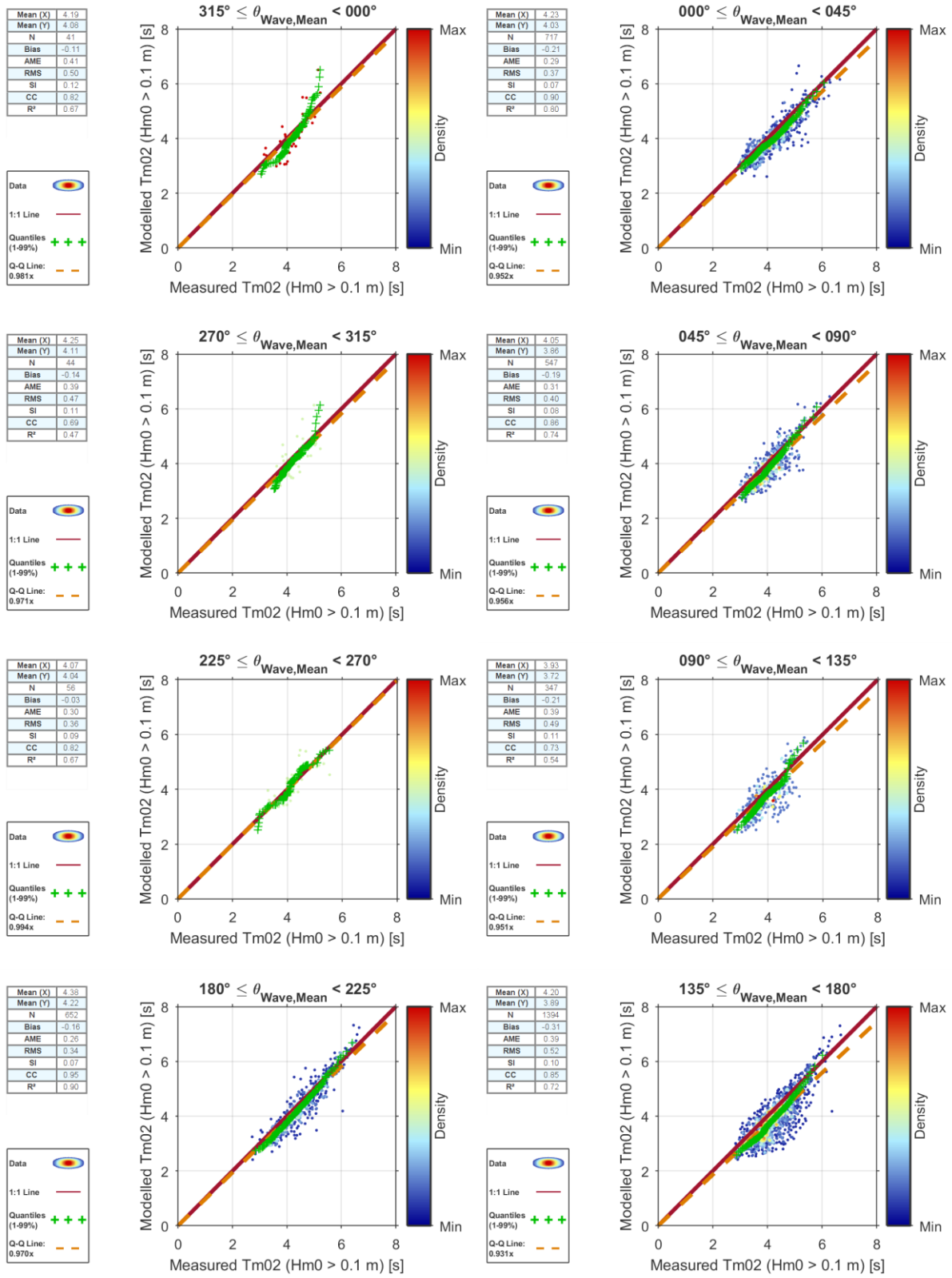



Figure C.86. AWAC D1, Tm02 validation, timestamps with Hm0 > 0.1 m, 45° Directional Sectors.

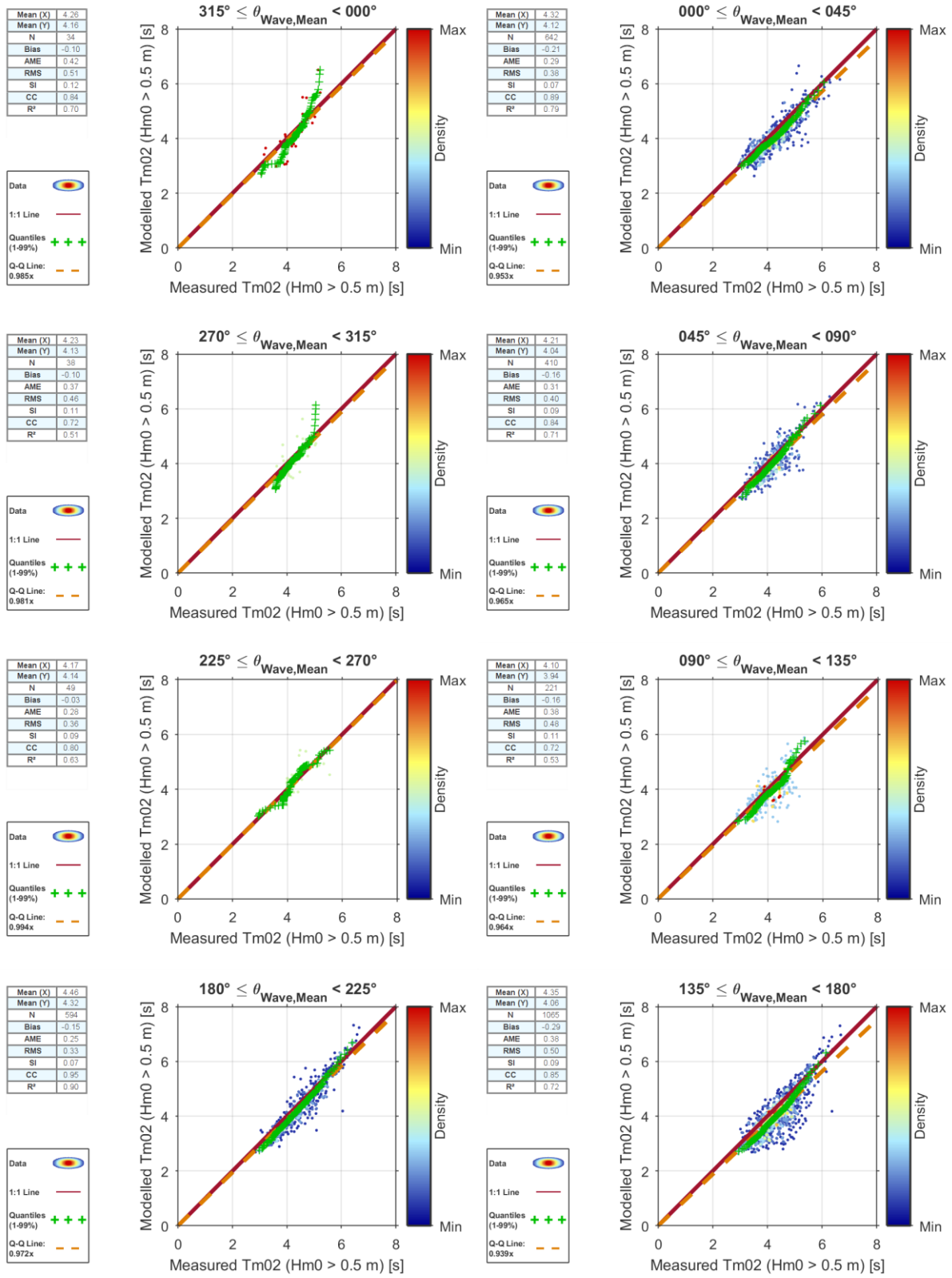



Figure C.87. AWAC D1, Tm02 validation, timestamps with Hm0 > 0.5 m, 45° Directional Sectors.

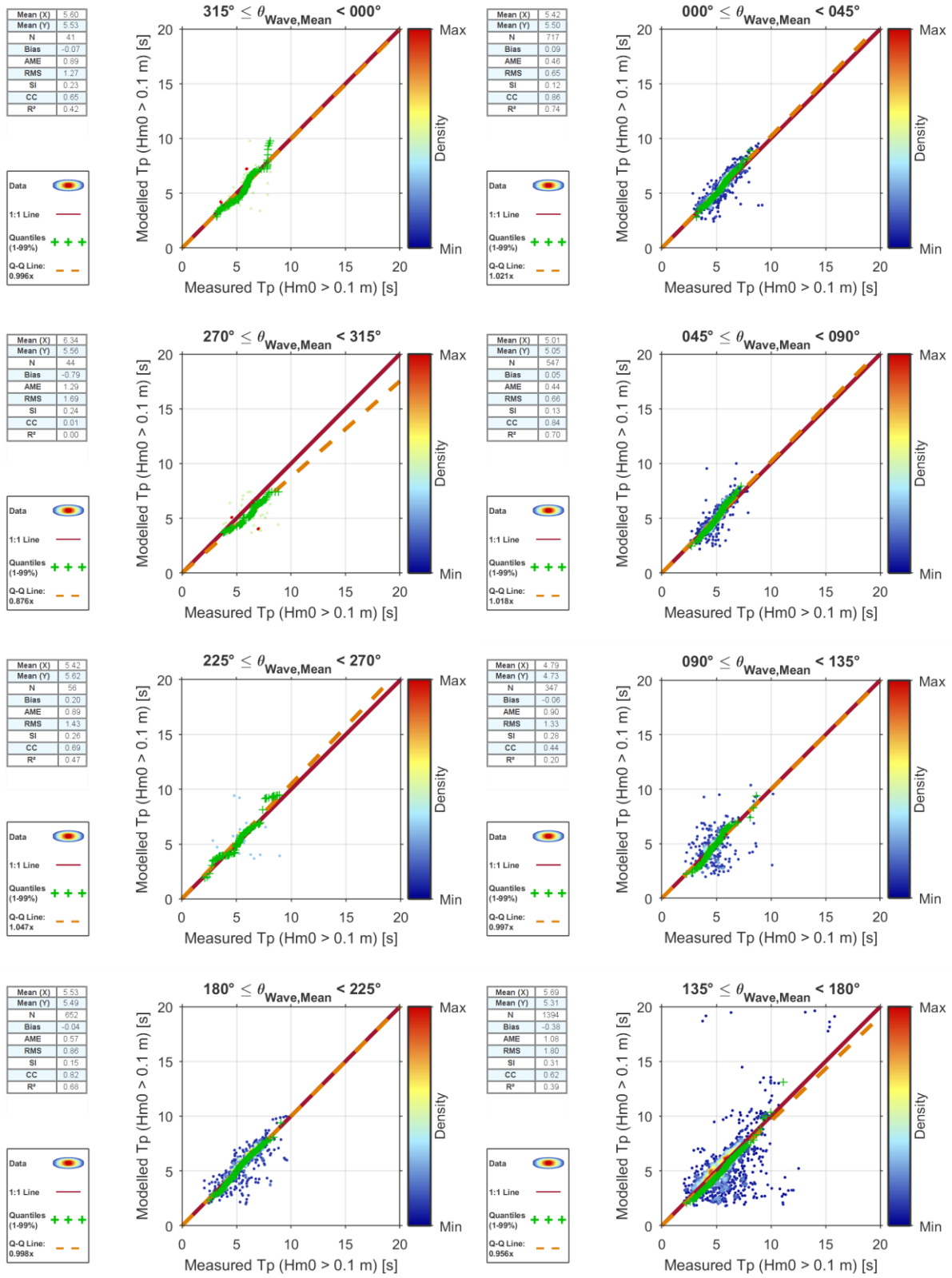



Figure C.88. AWAC D1, Tp validation, timestamps with Hm0 > 0.1 m, 45° Directional Sectors.

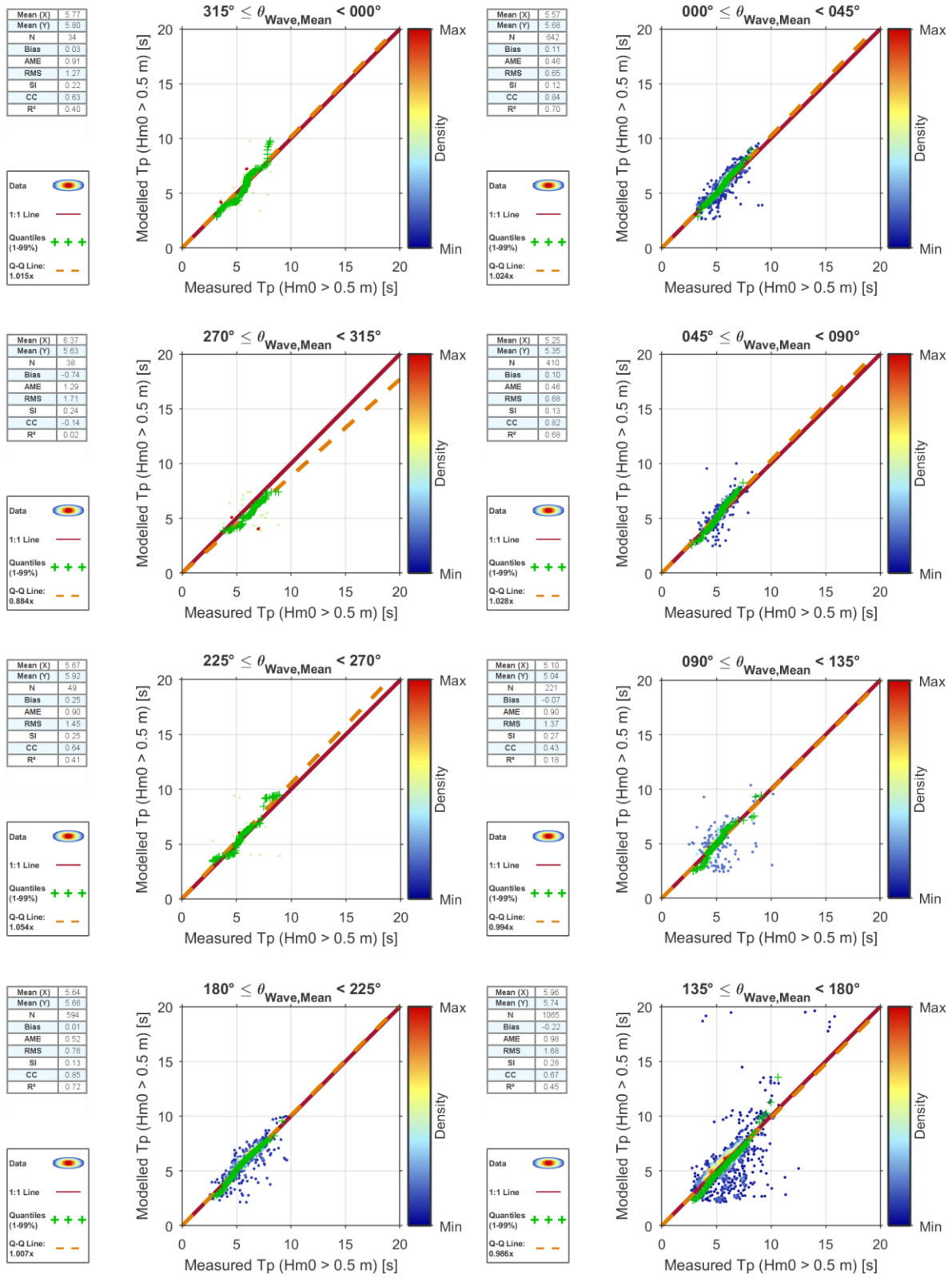



Figure C.89. AWAC D1, Tp validation, timestamps with Hm0 > 0.5 m, 45° Directional Sectors.

## C.6.2.7 AWAC E

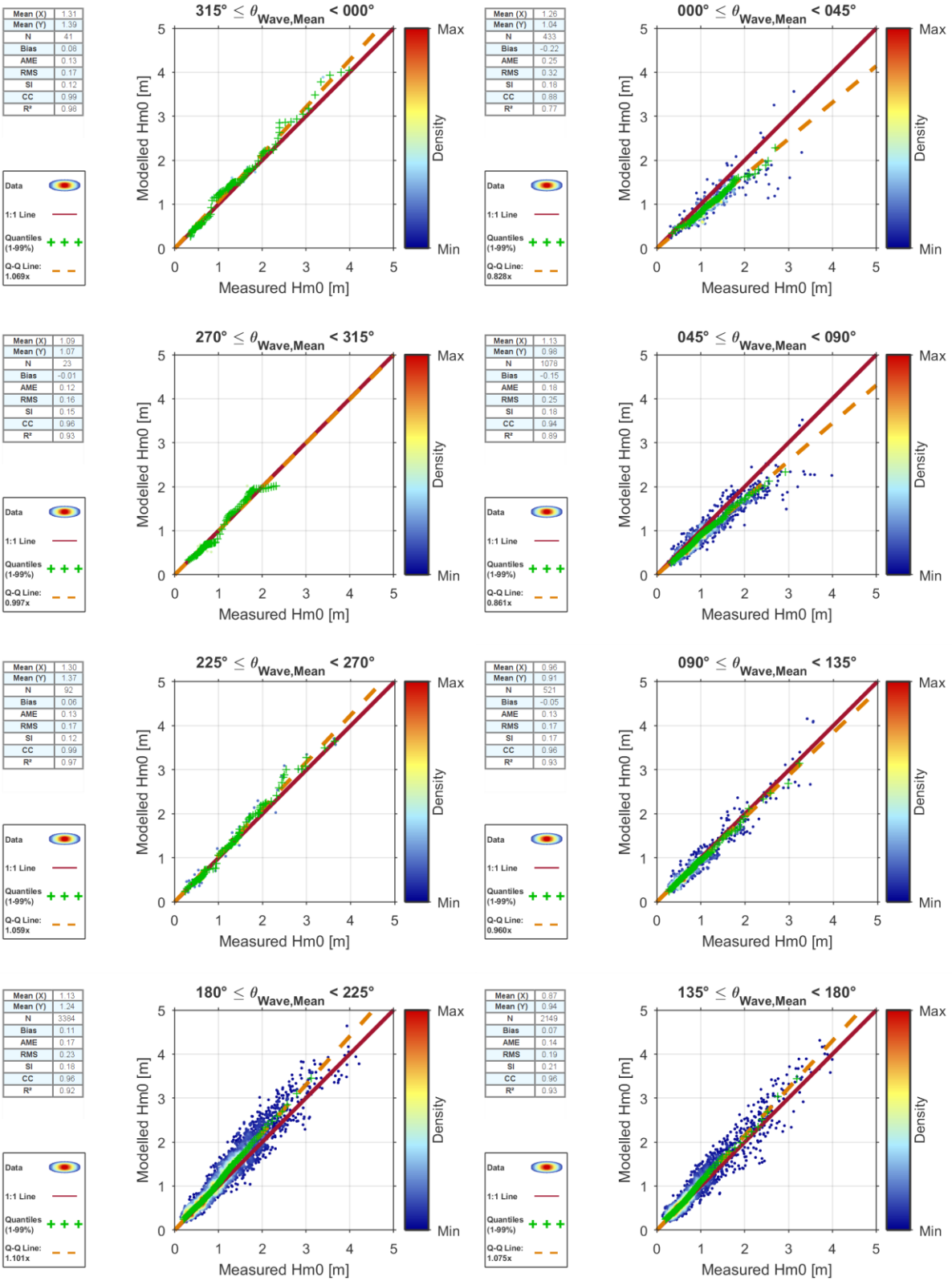



Figure C.90. AWAC E, Hm0 validation, 45° Directional Sectors.

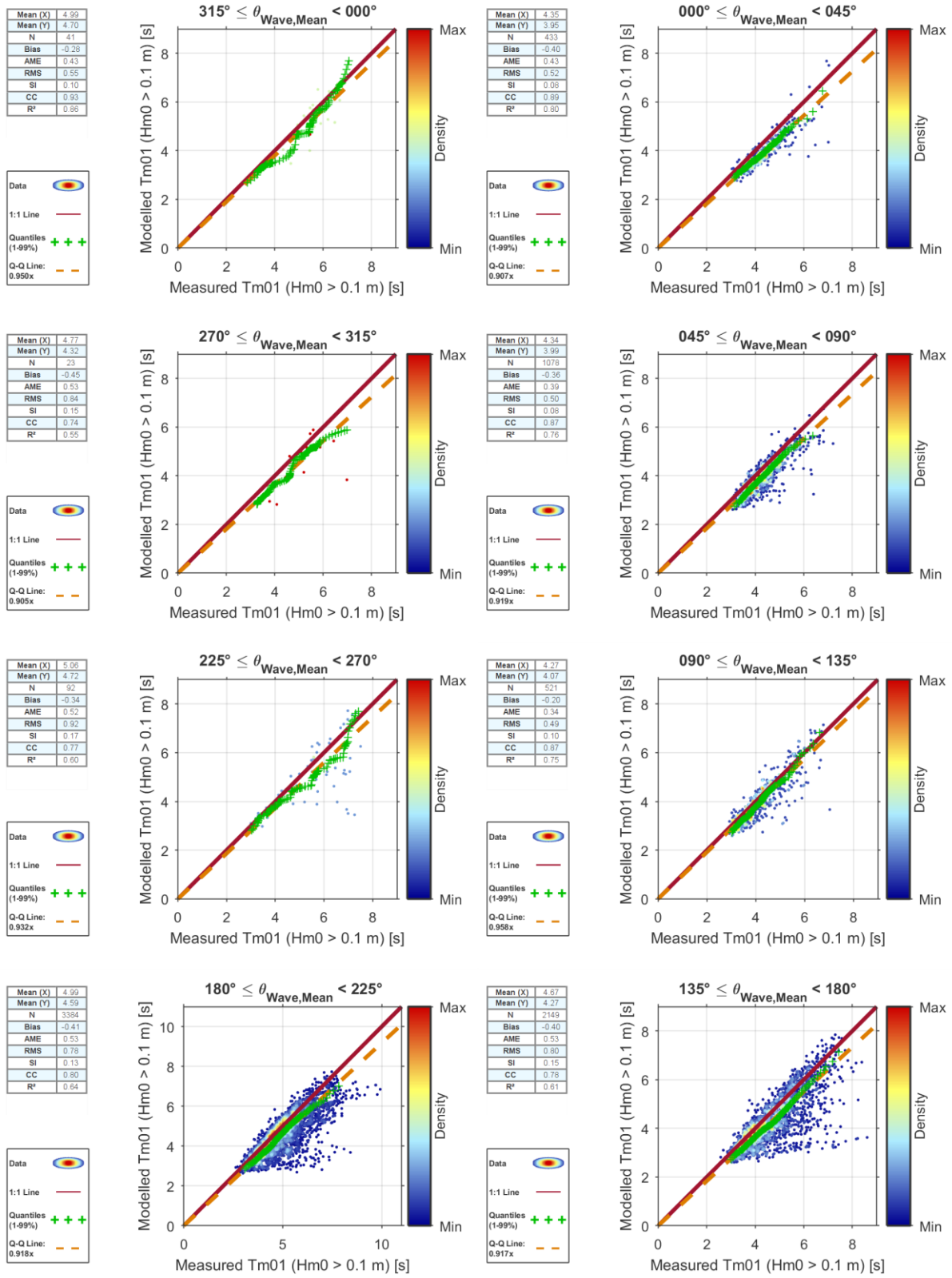



Figure C.91. AWAC E, Tm01 validation, timestamps with Hm0 > 0.1 m, 45° Directional Sectors.

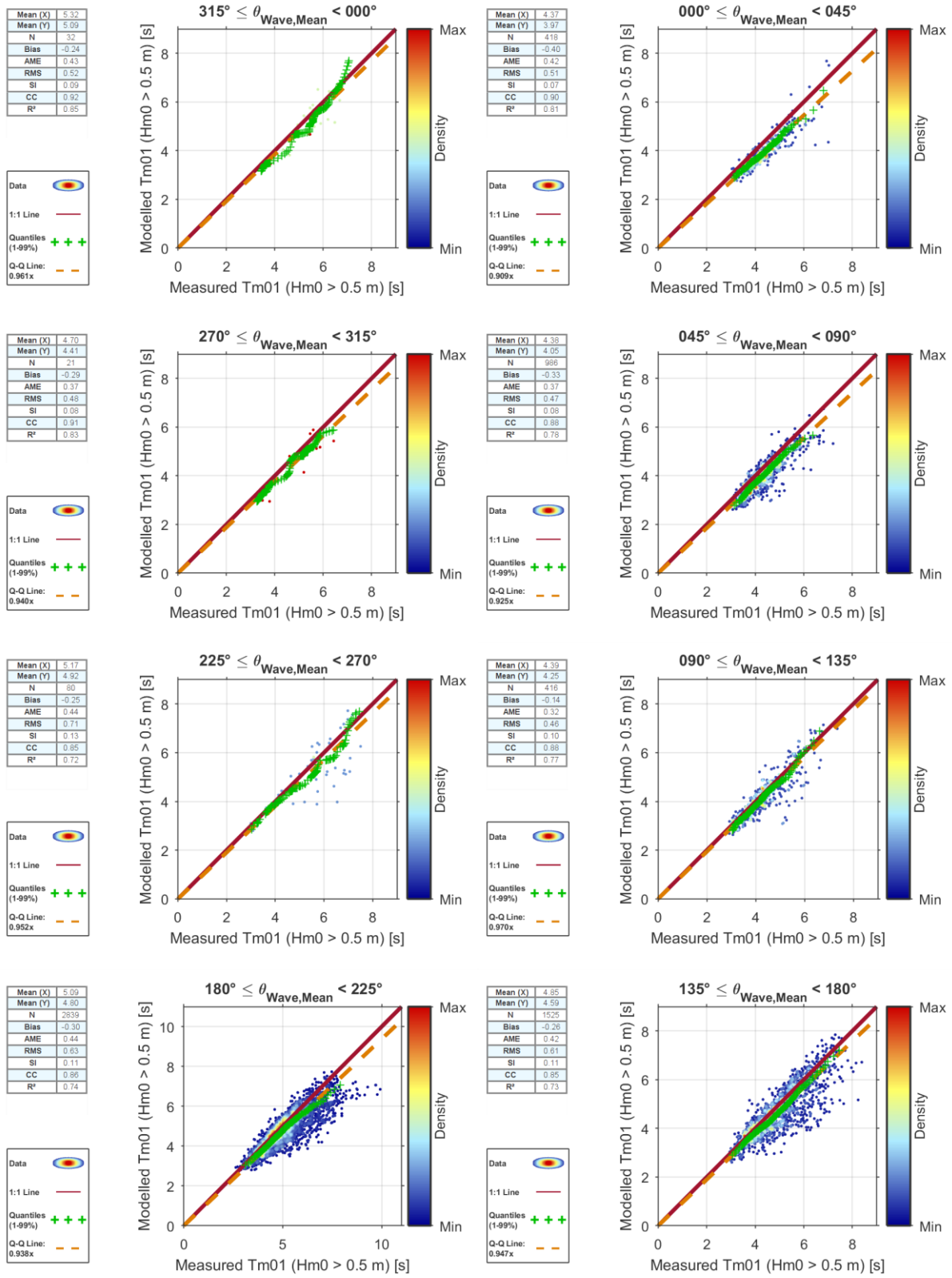



Figure C.92. AWAC E, Tm01 validation, timestamps with Hm0 > 0.5 m, 45° Directional Sectors.

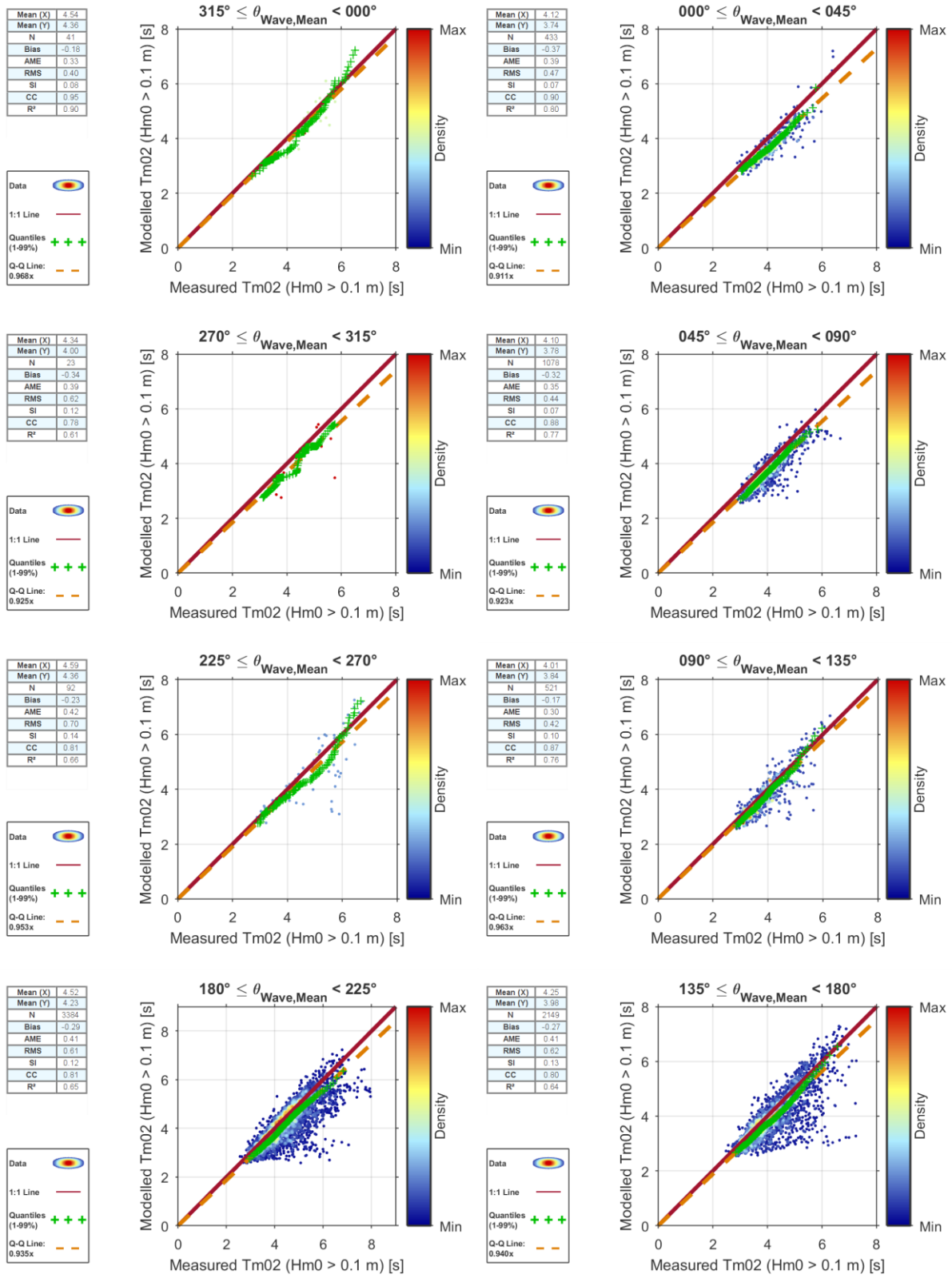



Figure C.93. AWAC E, Tm02 validation, timestamps with Hm0 > 0.1 m, 45° Directional Sectors.

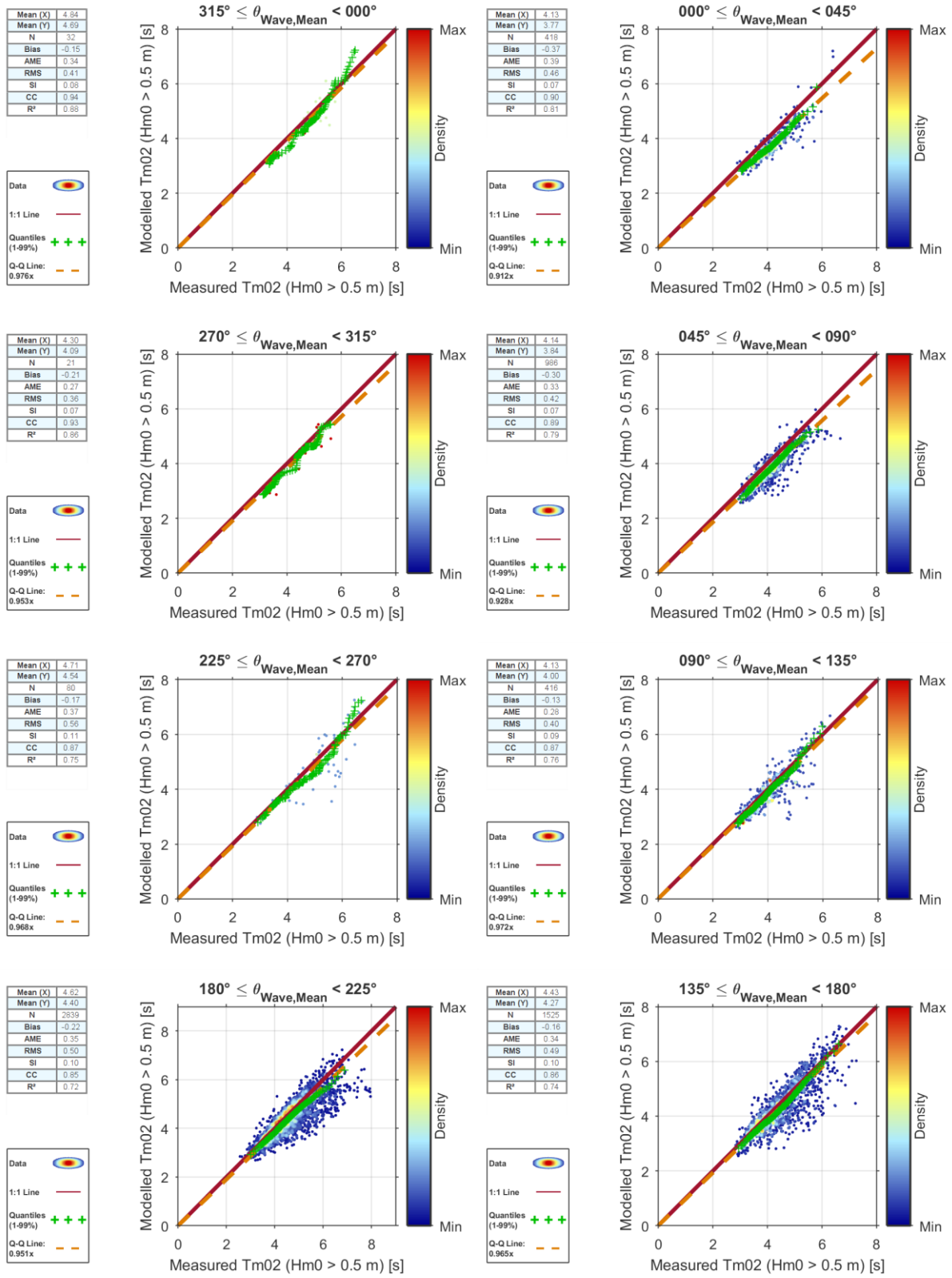



Figure C.94. AWAC E, Tm02 validation, timestamps with Hm0 > 0.5 m, 45° Directional Sectors.

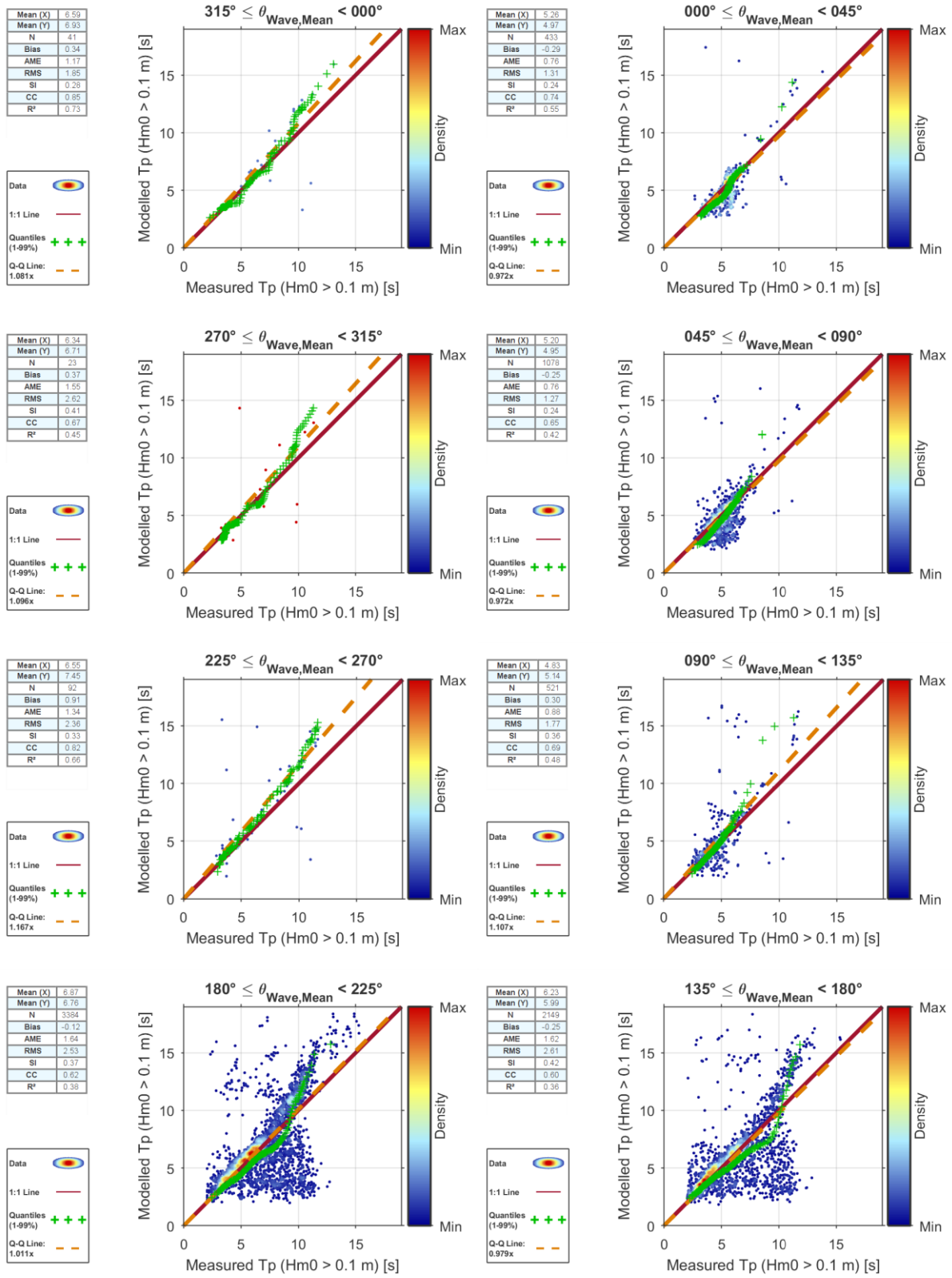



Figure C.95. AWAC E, Tp validation, timestamps with Hm0 > 0.5 m, 45° Directional Sectors.

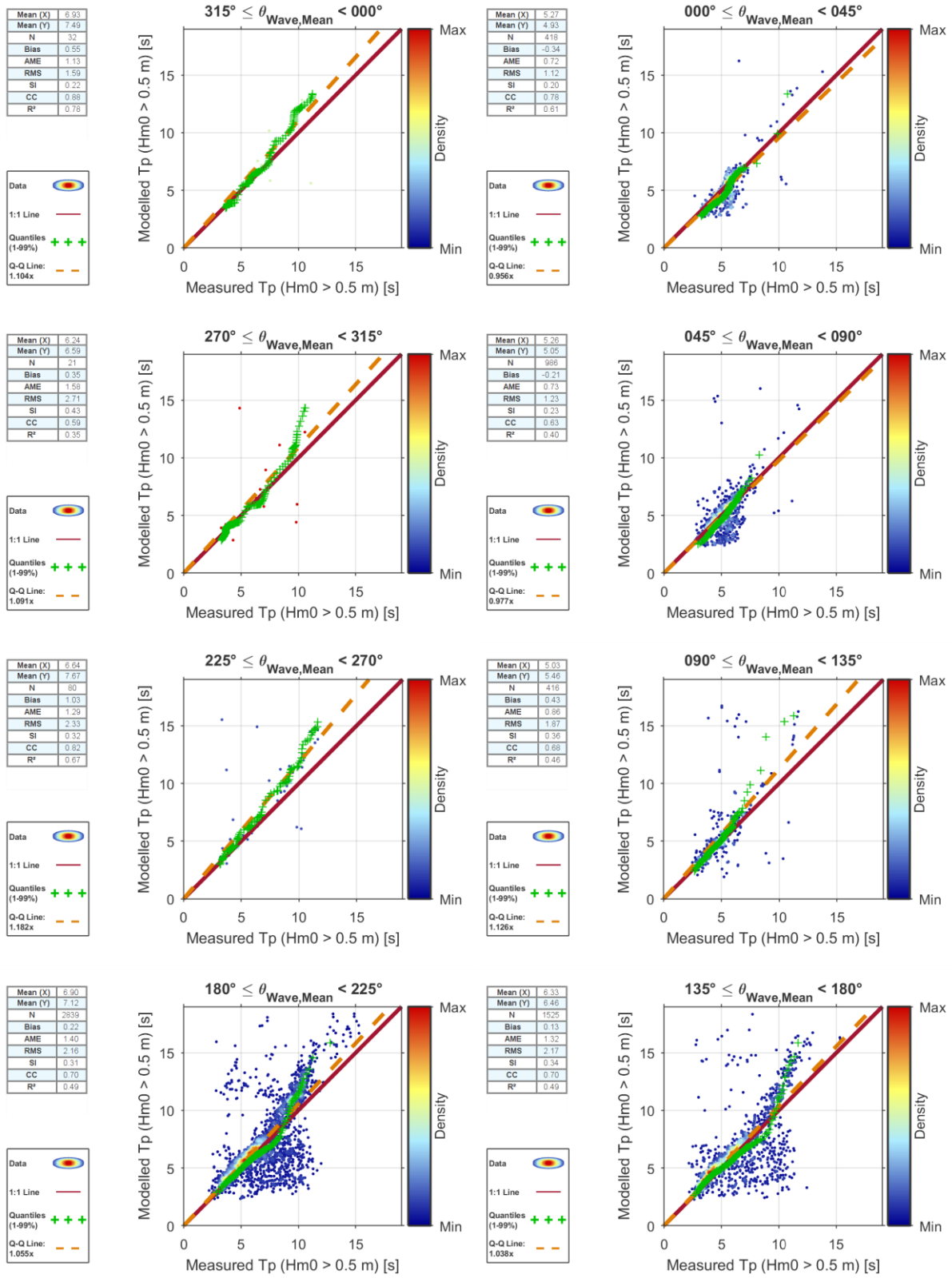



Figure C.96. AWAC E, Tp validation, timestamps with Hm0 > 0.5 m, 45° Directional Sectors.

## C.6.3 Custom Sectors

### C.6.3.1 Sector Specification

Though the standard 45° sectors of the previous section provide valuable additional insight into model performance, the sector choice is somewhat arbitrary. In this Section, the same steps are repeated, but for a smaller number of custom sectors. Sector boundaries are shown in Figure C.97, and are selected based on both a review of the map itself, and a more detailed analysis of the distance from the centre of the Arklow Bank to land in each direction, as shown in Figure C.98.

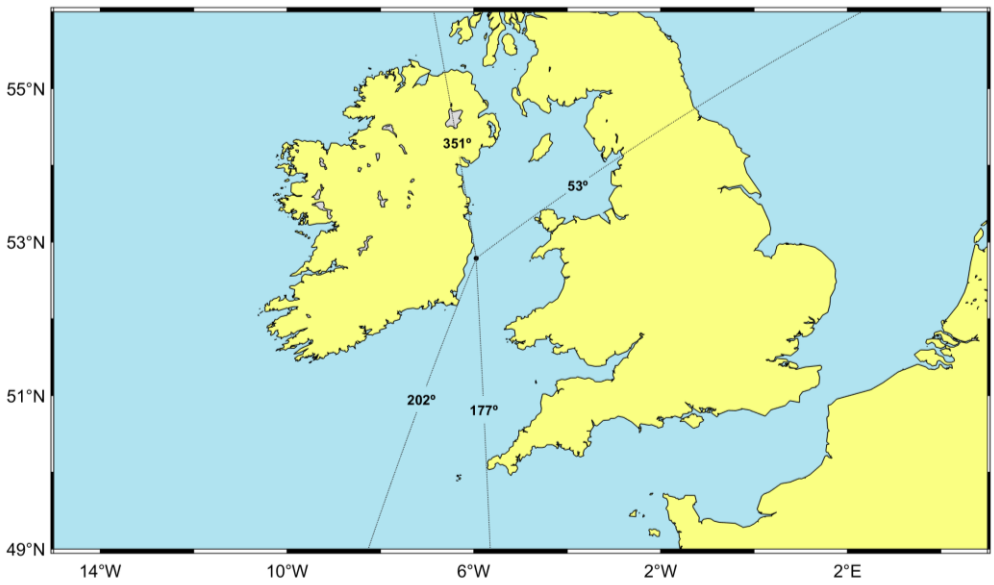



Figure C.97. Custom Directional Sectors.

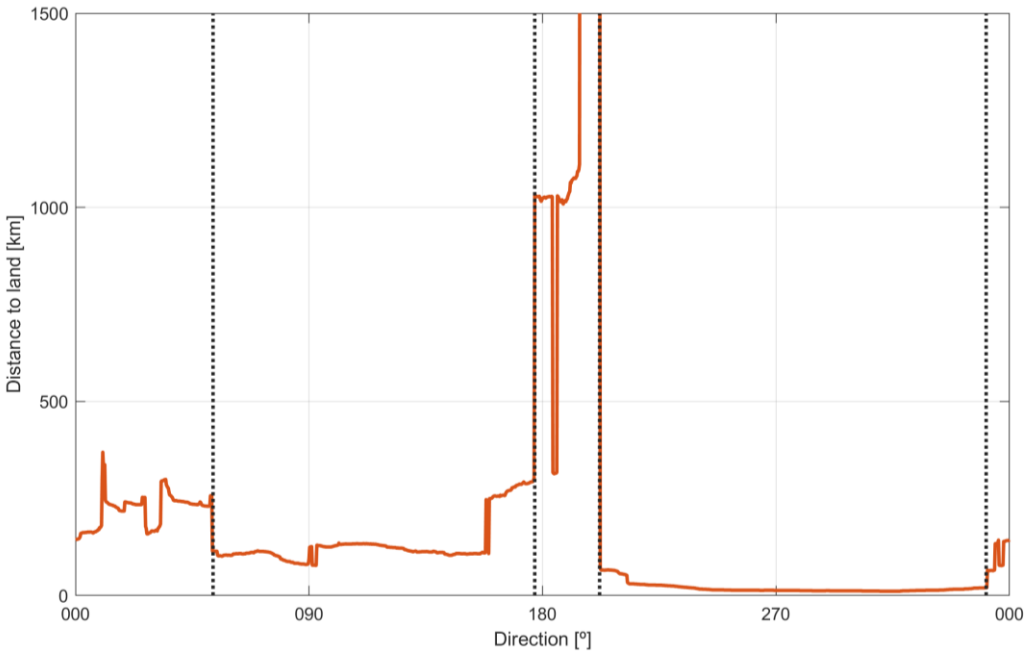



Figure C.98. Fetch from the middle of the Arklow Bank.

### C.6.3.2 Overview

Validation plots are included below for the project AWACs using these custom sectors in Sections C.6.3.3 through C.6.3.7. The same methodology previously described for standard 45° sectors is used throughout, with only the sectors themselves differing. The reader is referred to Section C.6.2.2 for details of the parameters show, including high frequency limits in their derivation, and the method used to allocate data points to sectors.

### C.6.3.3 AWAC A

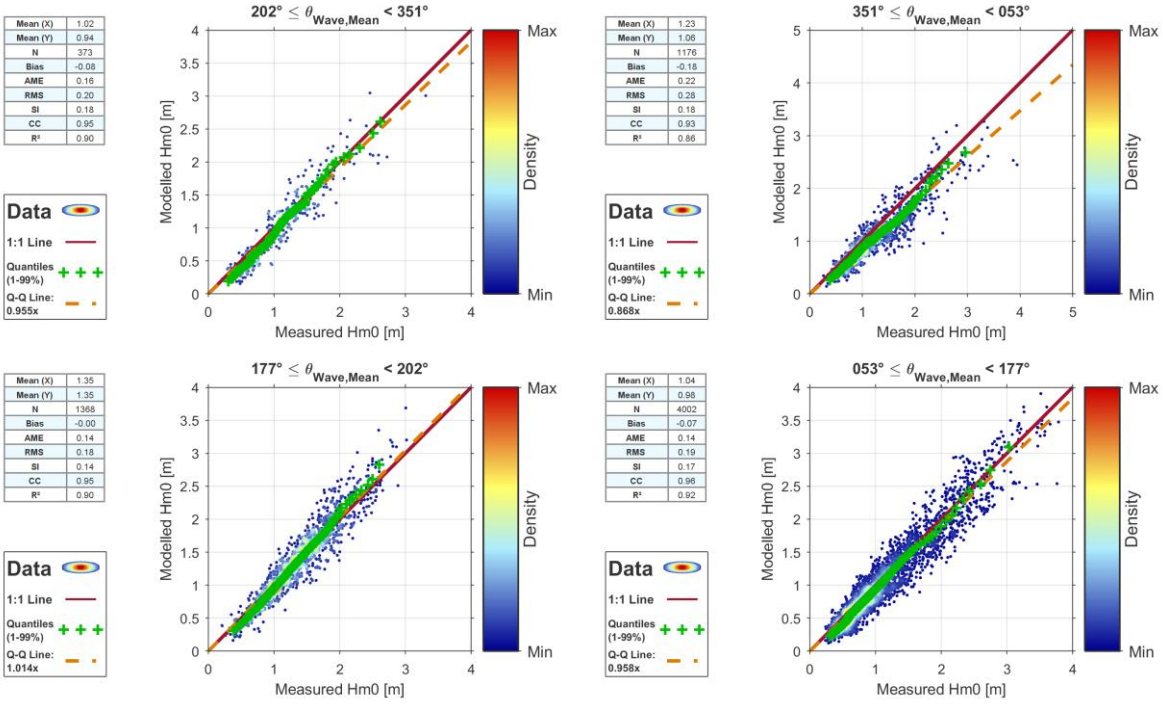



Figure C.99. AWAC A, Hm0 validation, Custom Directional Sectors.

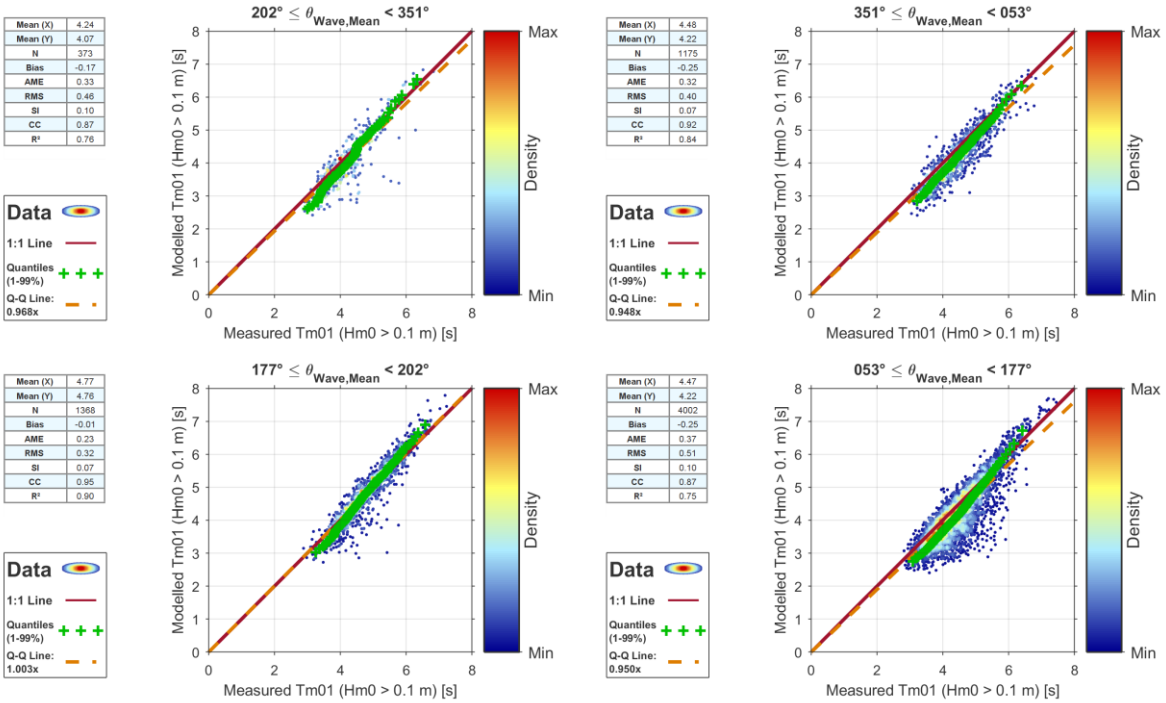



Figure C.100. AWAC A, Tm01 validation, timestamps with Hm0 > 0.1 m, Custom Directional Sectors.

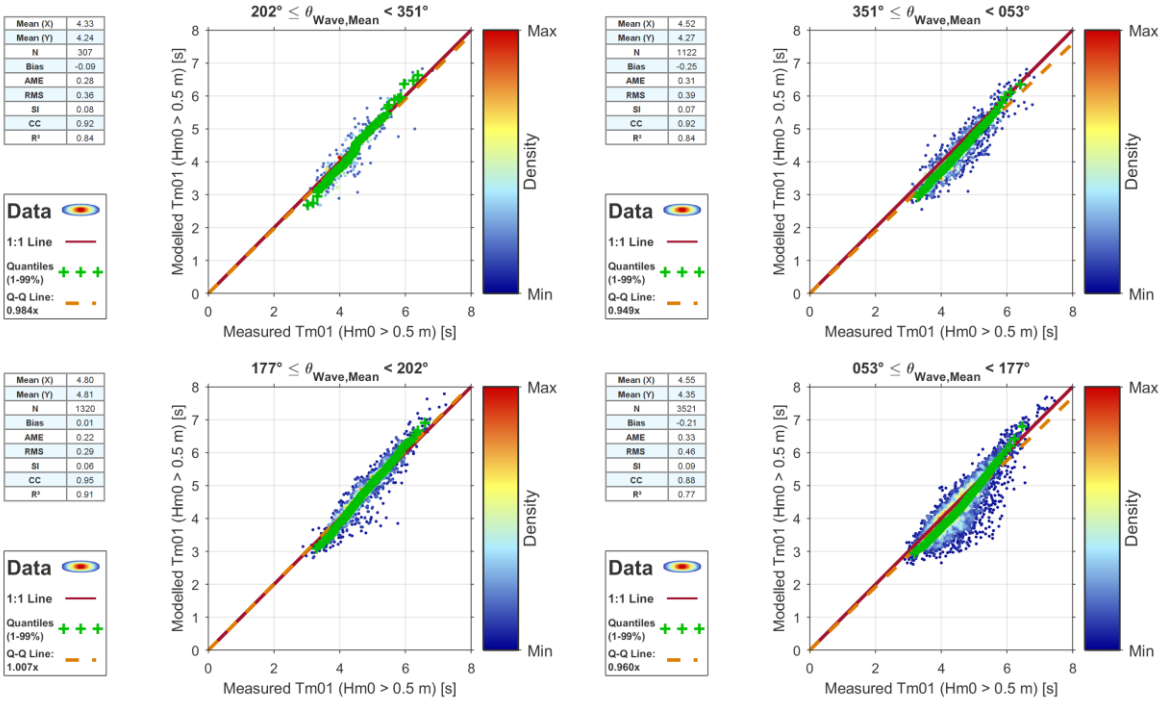



Figure C.101. AWAC A, Tm01 validation, timestamps where Hm0 > 0.5 m, Custom Directional Sectors.

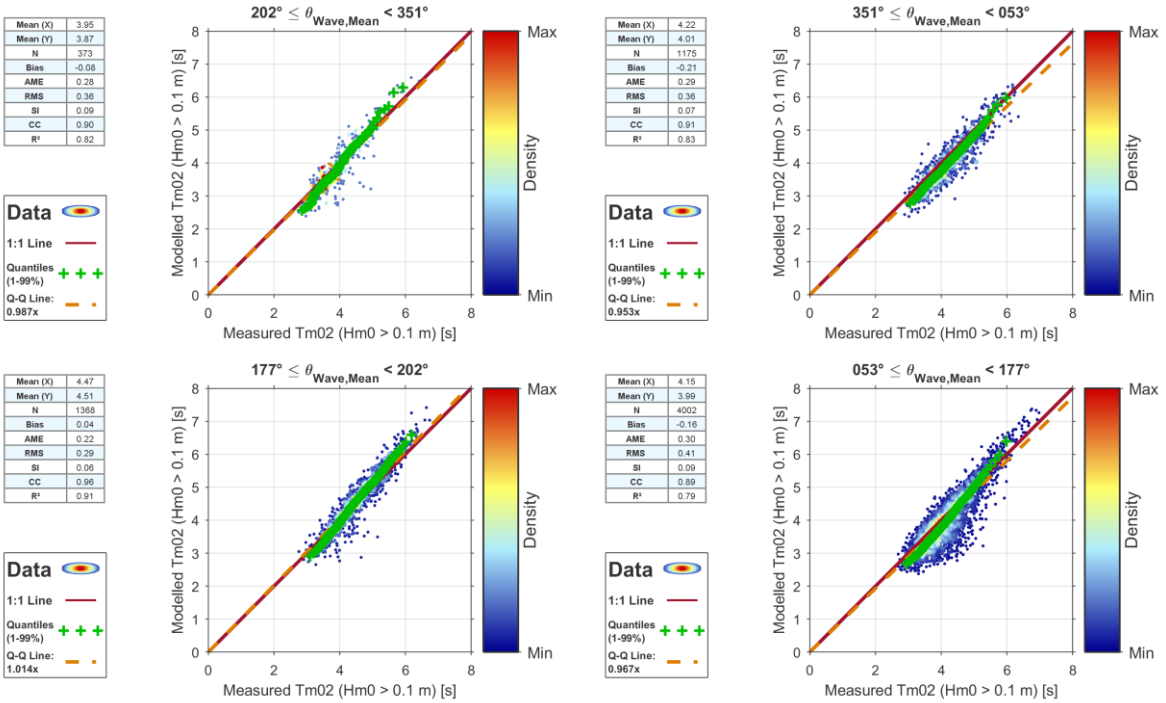



Figure C.102. AWAC A, Tm02 validation, timestamps with Hm0 > 0.1 m, Custom Directional Sectors

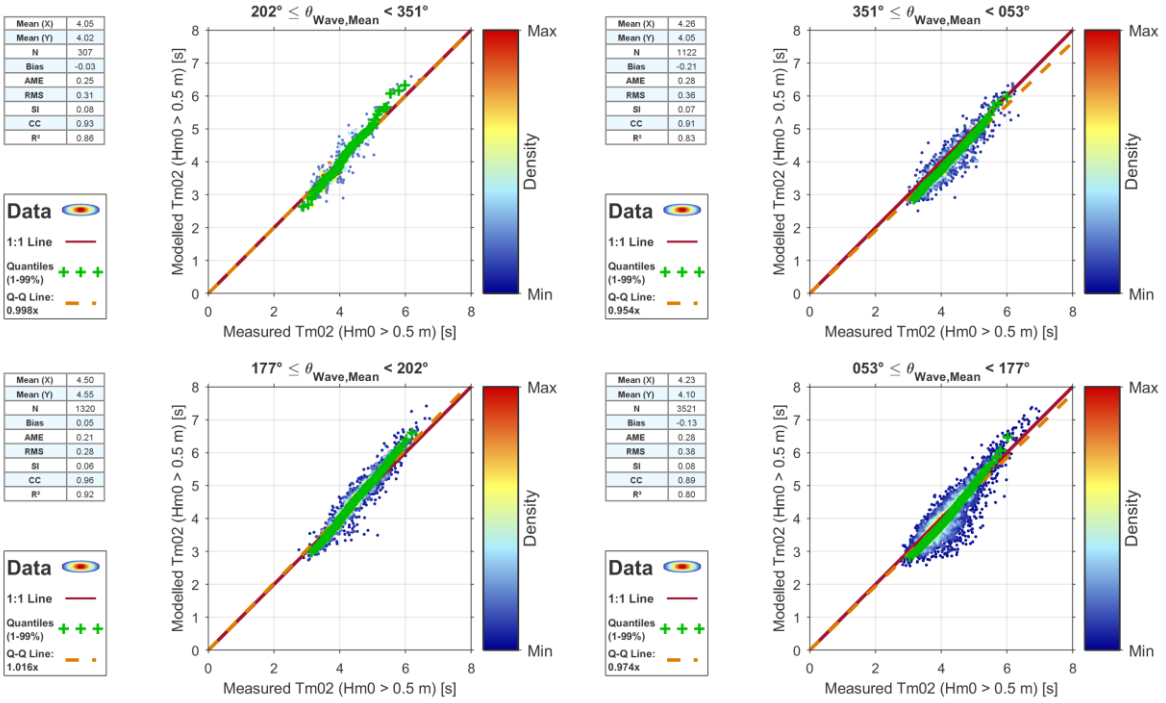



Figure C.103. AWAC A, Tm02 validation, timestamps with Hm0 > 0.5 m, Custom Directional Sectors.

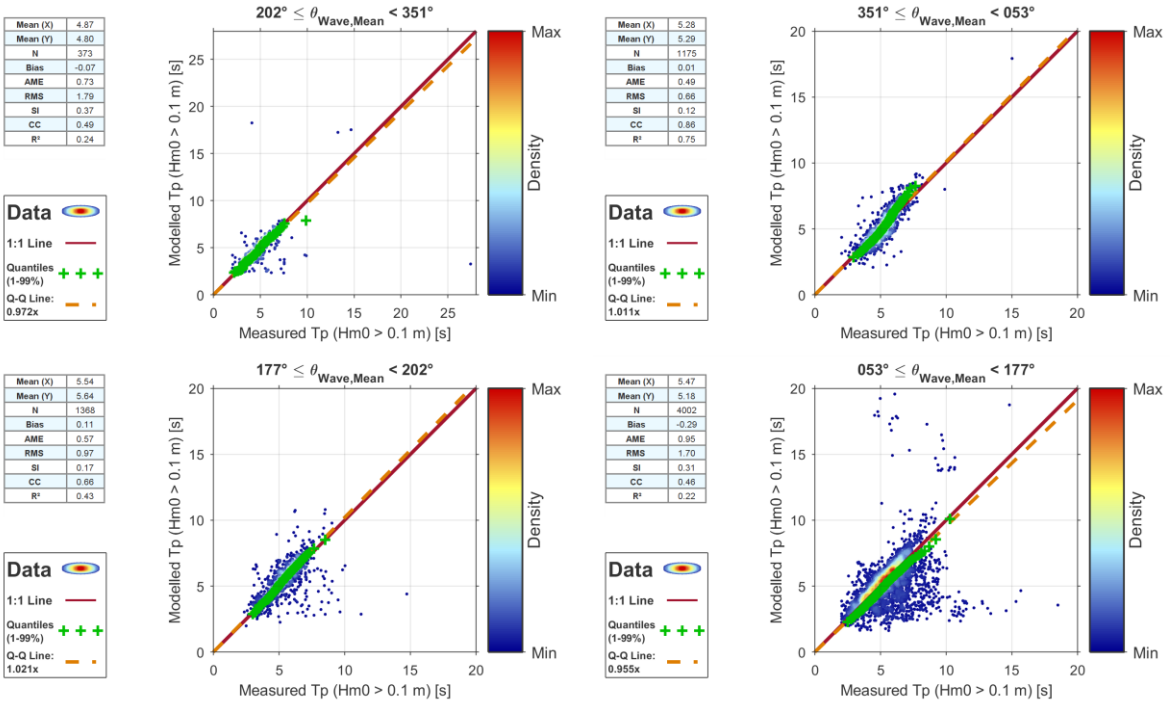



Figure C.104. AWAC A, Tp validation, timestamps with Hm0 > 0.1 m, Custom Directional Sectors.

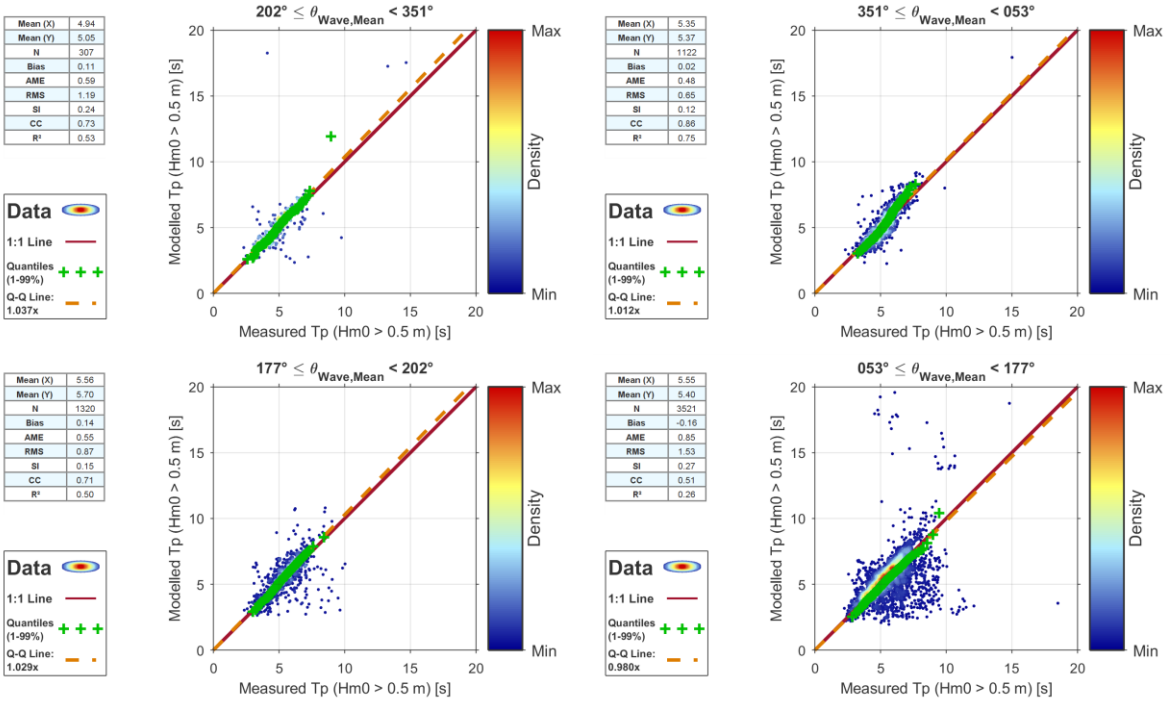



Figure C.105. AWAC A, Tp validation, timestamps with Hm0 > 0.5 m, Custom Directional Sectors.

### C.6.3.4 AWAC B1

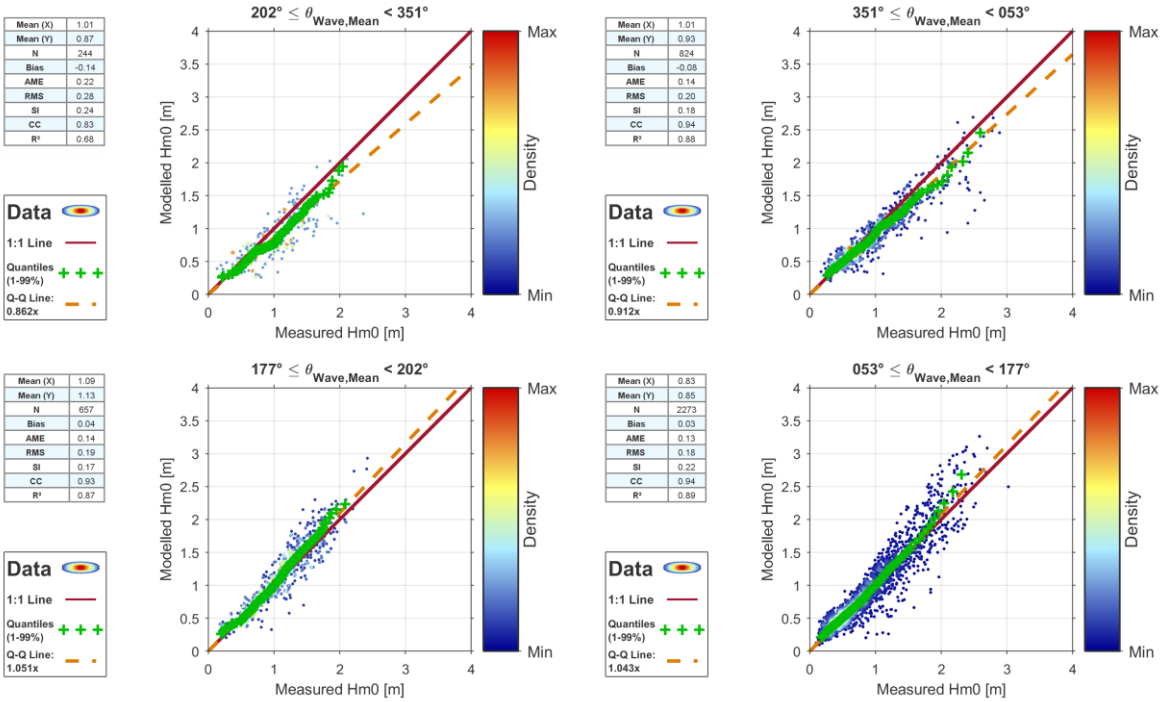



Figure C.106. AWAC B1, Hm0 validation, Custom Directional Sectors.

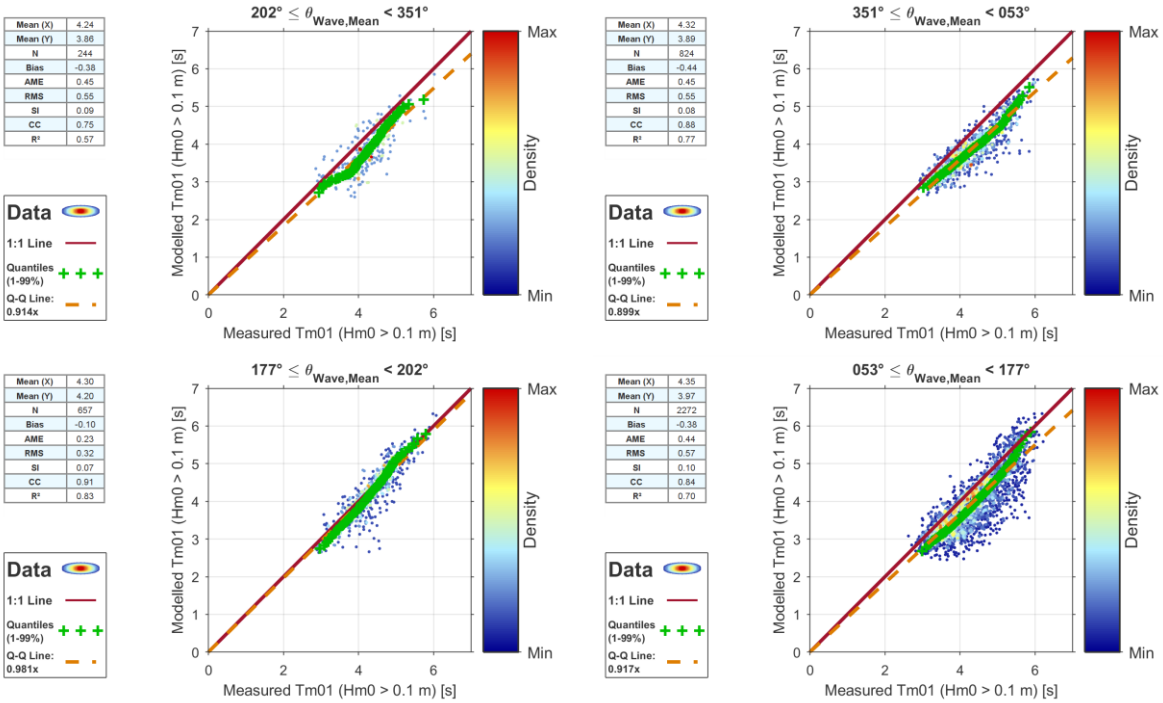



Figure C.107. AWAC B1, Tm01 validation, timestamps with Hm0 > 0.1 m, Custom Directional Sectors.

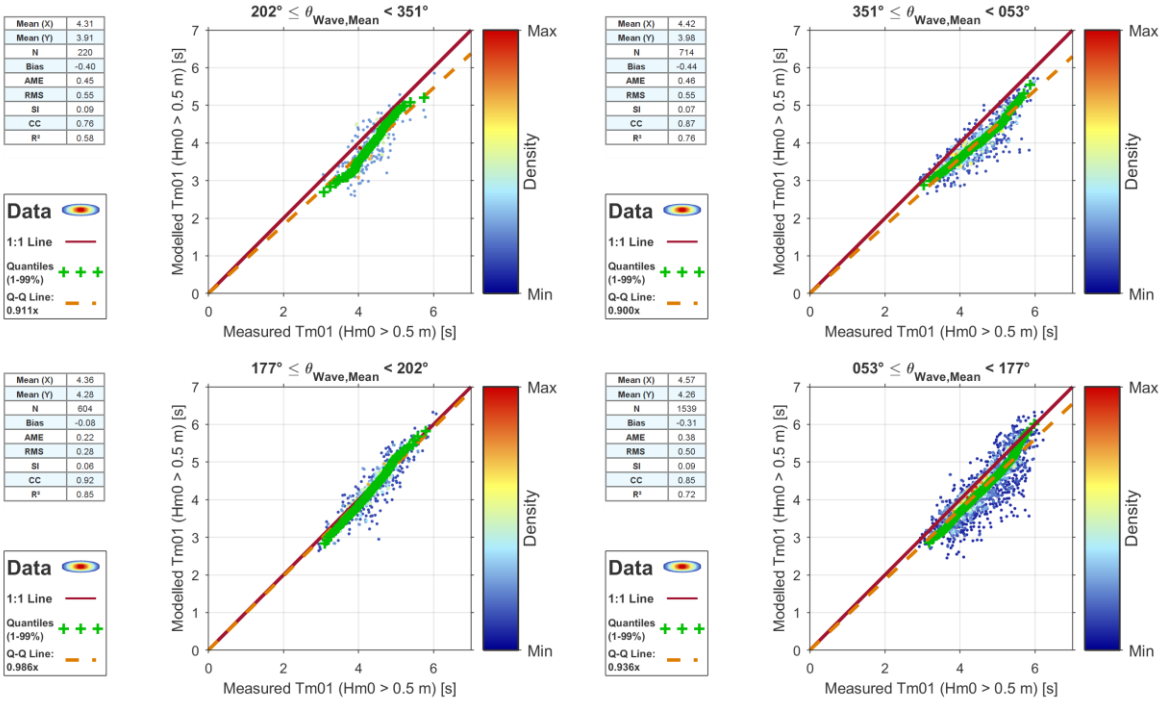



Figure C.108. AWAC B1, Tm01 validation, timestamps where Hm0 > 0.5 m, Custom Directional Sectors.

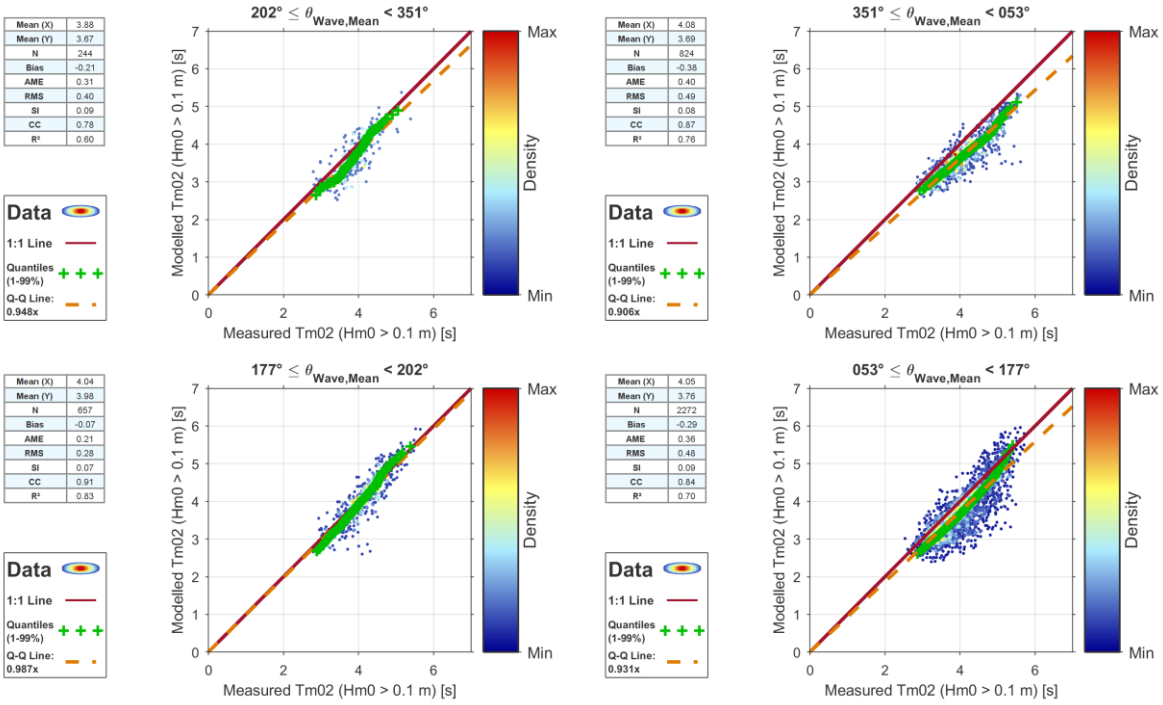



Figure C.109. AWAC B1, Tm02 validation, timestamps with Hm0 > 0.1 m, Custom Directional Sectors

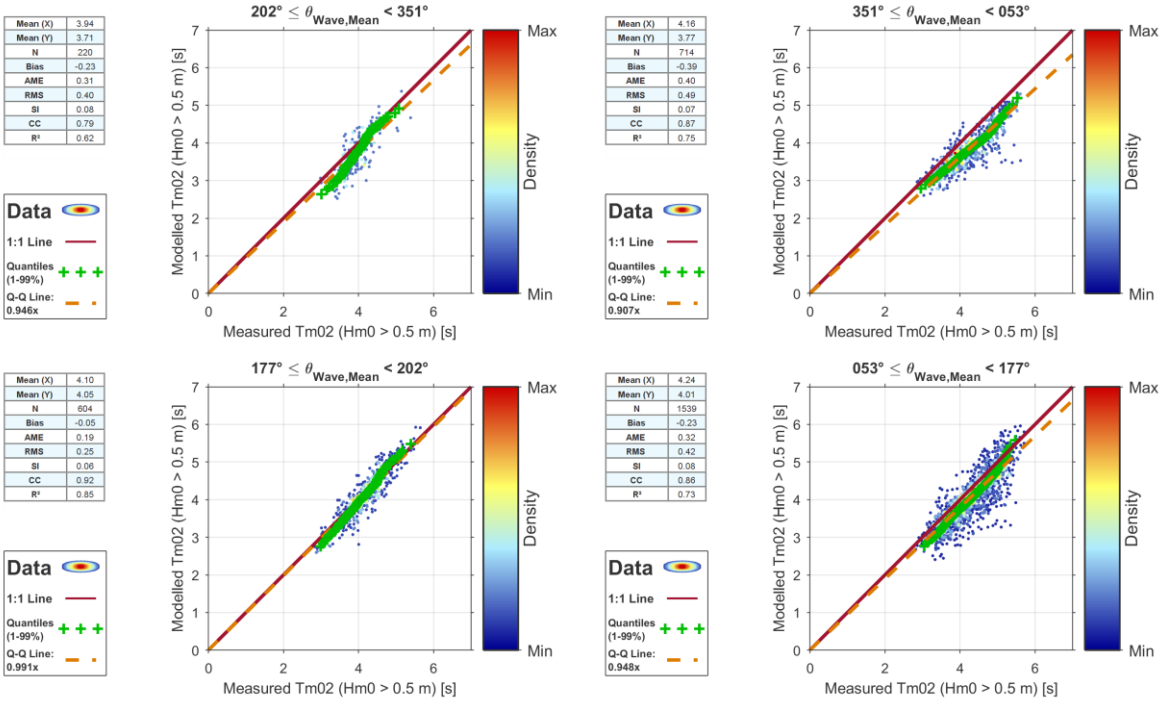



Figure C.110. AWAC B1, Tm02 validation, timestamps with Hm0 > 0.5 m, Custom Directional Sectors.

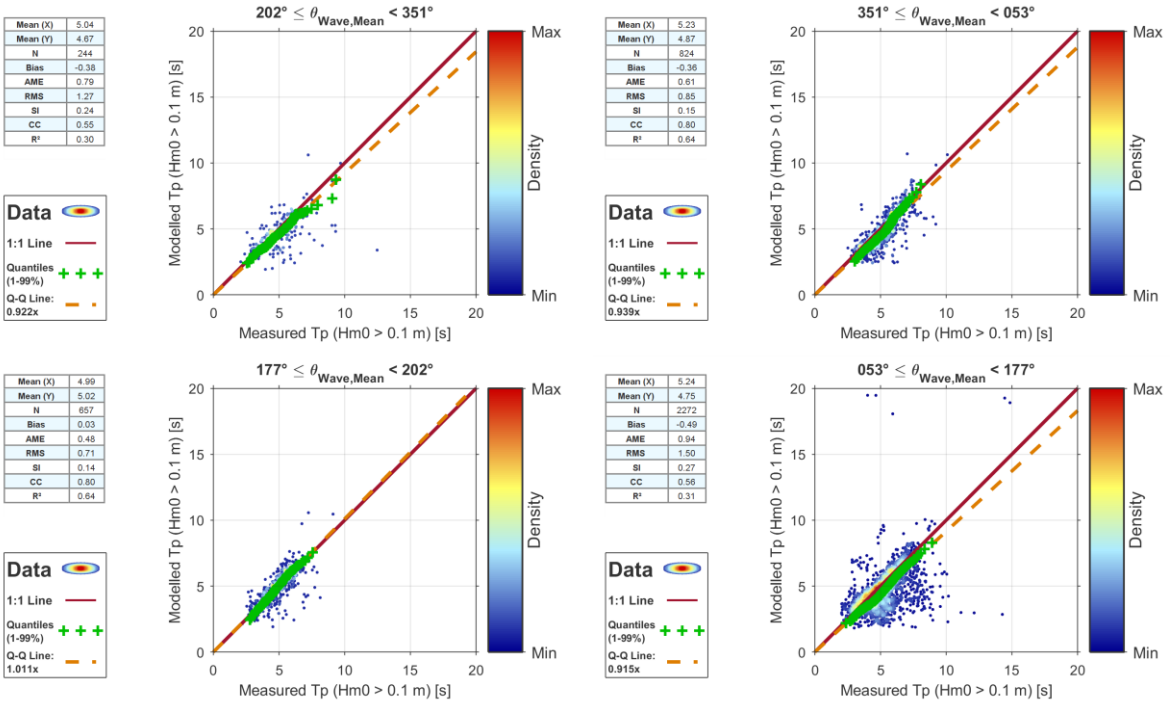



Figure C.111. AWAC B1, Tp validation, timestamps with Hm0 > 0.1 m, Custom Directional Sectors.

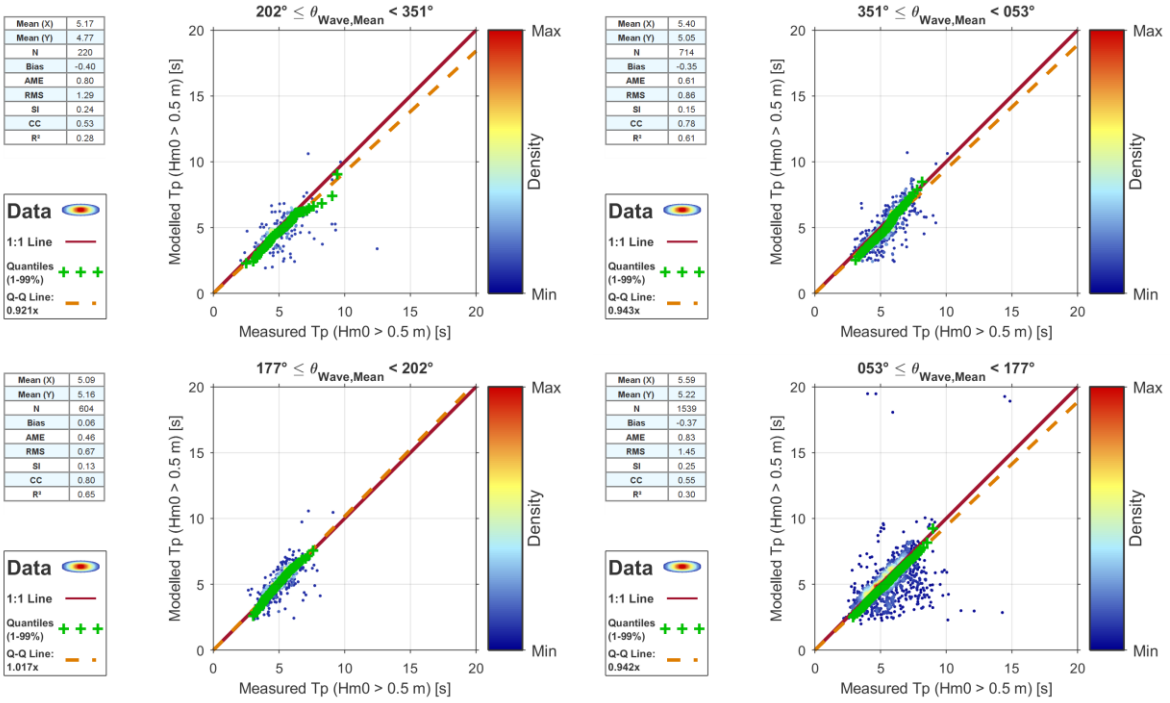



Figure C.112. AWAC B1, Tp validation, timestamps with Hm0 > 0.5 m, Custom Directional Sectors.

### C.6.3.5 AWAC C

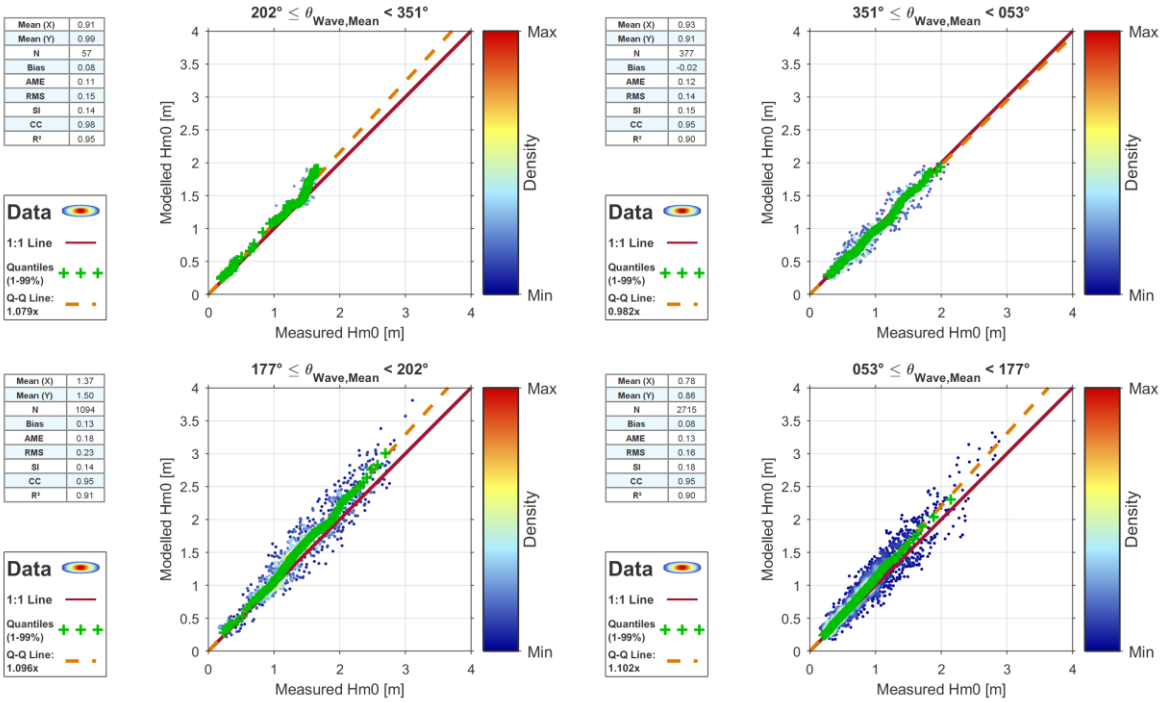



Figure C.113. AWAC C, Hm0 validation, Custom Directional Sectors.

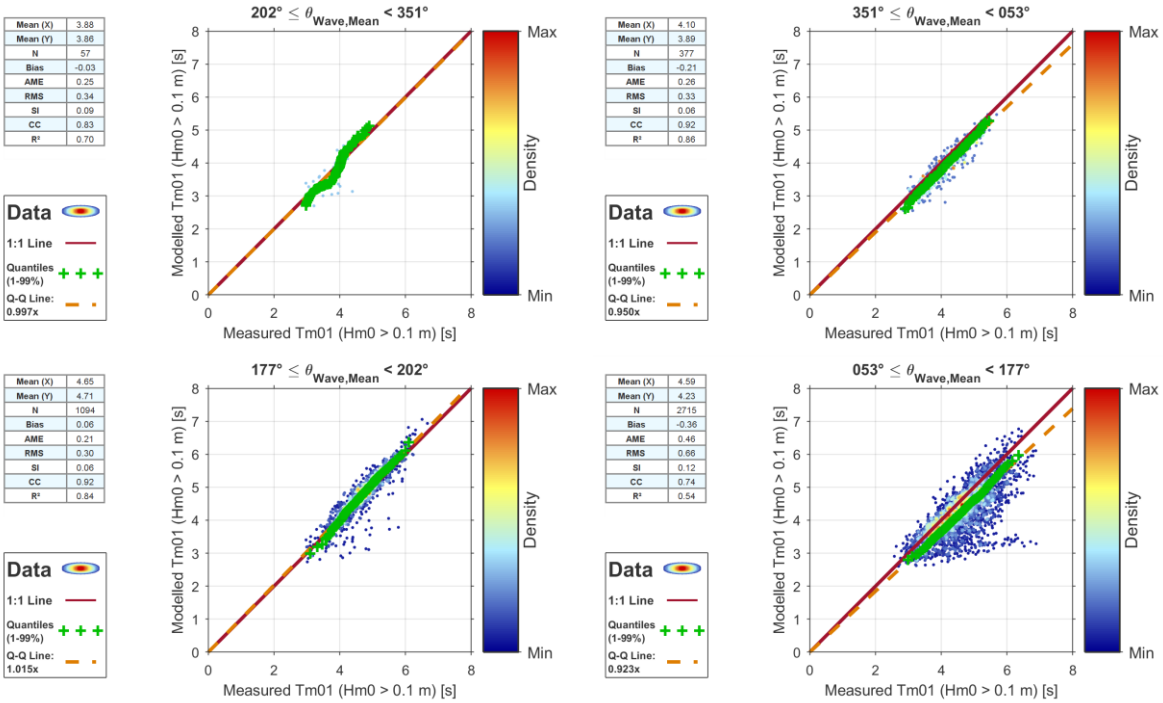



Figure C.114. AWAC C, Tm01 validation, timestamps with Hm0 > 0.1 m, Custom Directional Sectors.

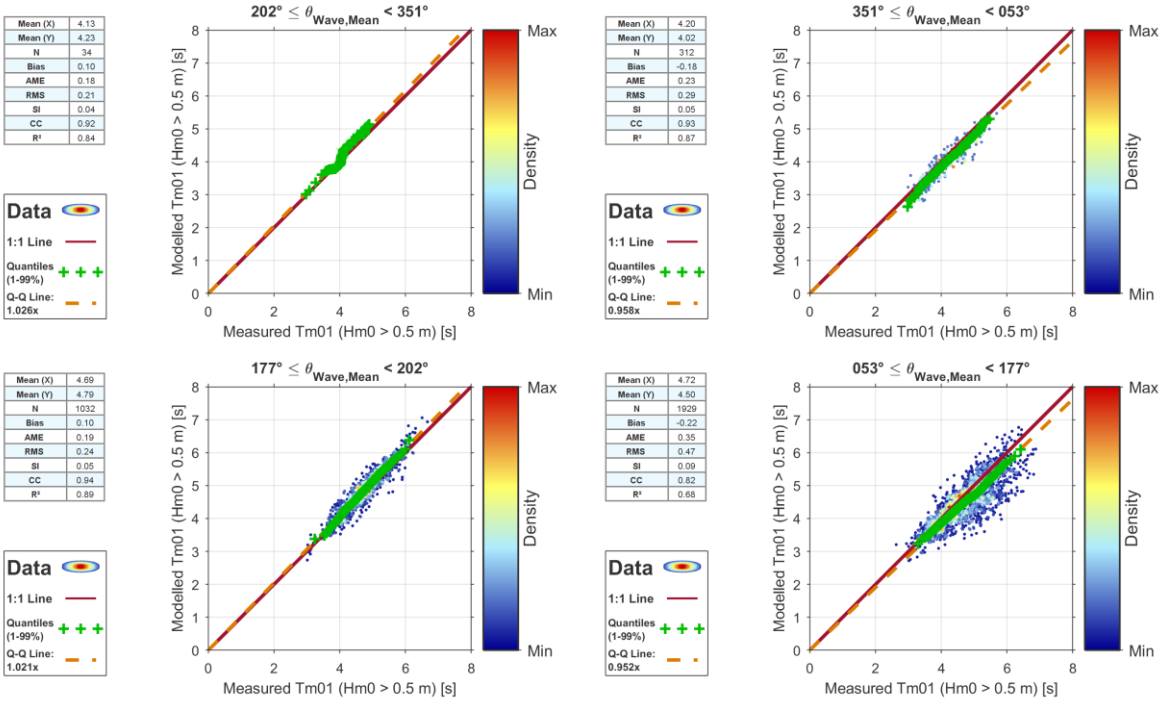



Figure C.115. AWAC C, Tm01 validation, timestamps with Hm0 > 0.5 m, Custom Directional Sectors.

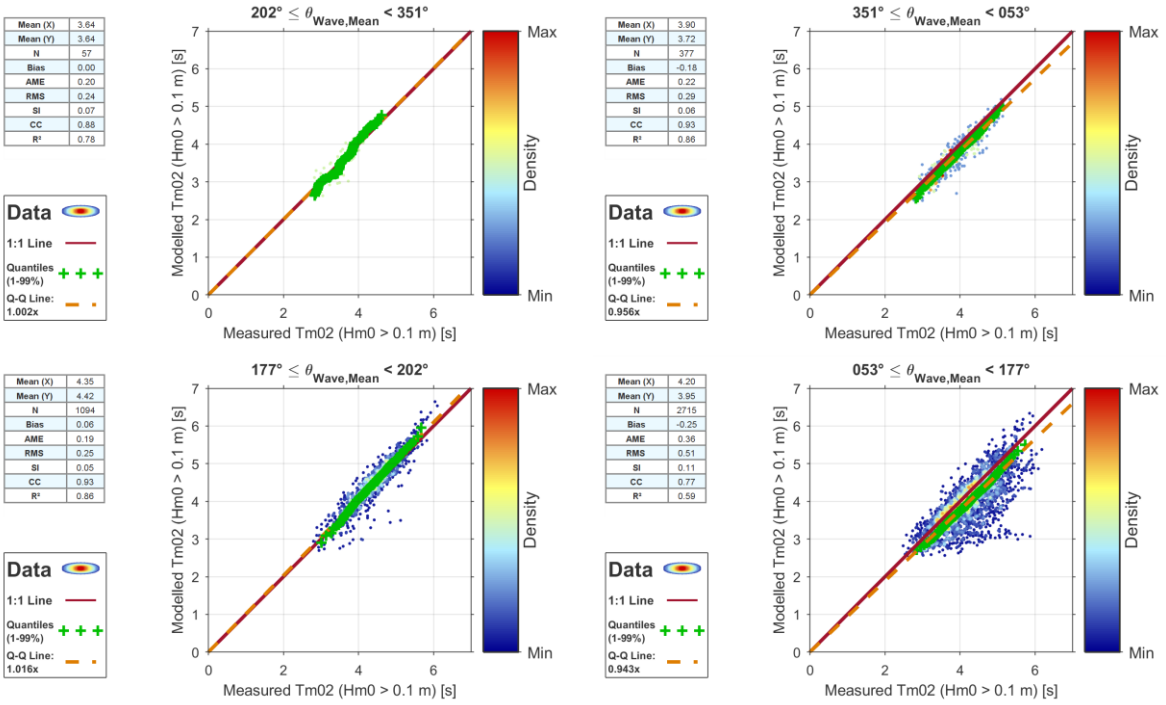



Figure C.116. AWAC C, Tm02 validation, timestamps with Hm0 > 0.1 m, Custom Directional Sectors.

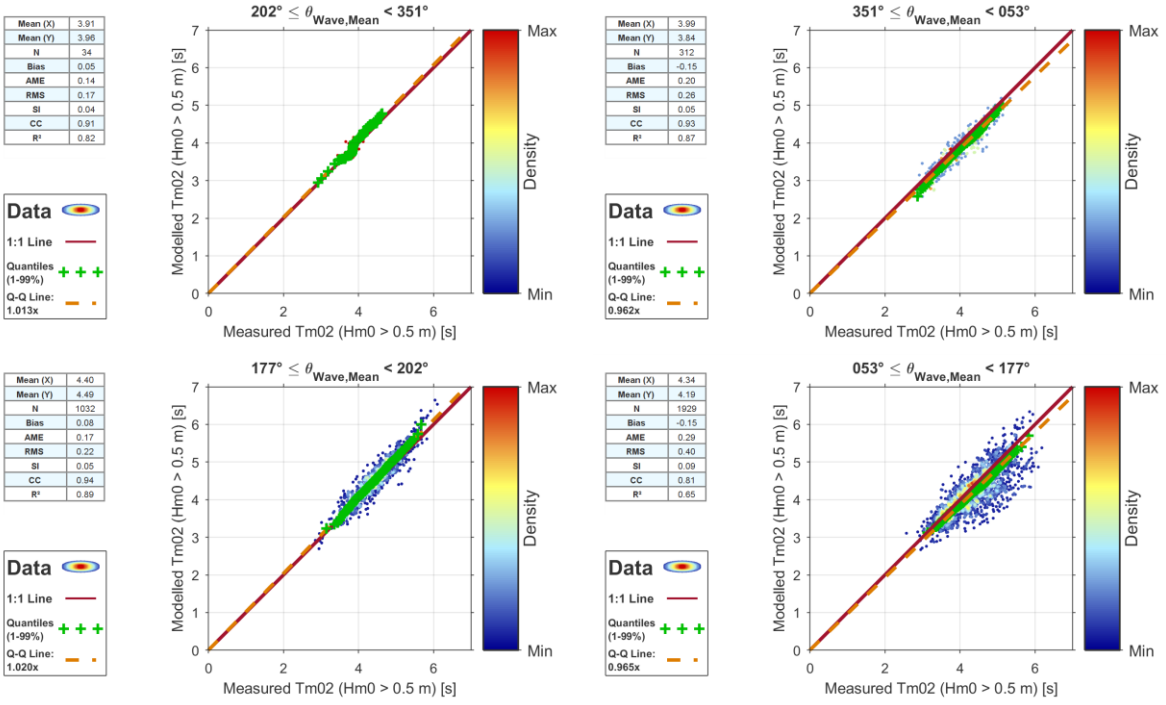



Figure C.117. AWAC C, Tm02 validation, timestamps with Hm0 > 0.5 m, Custom Directional Sectors.

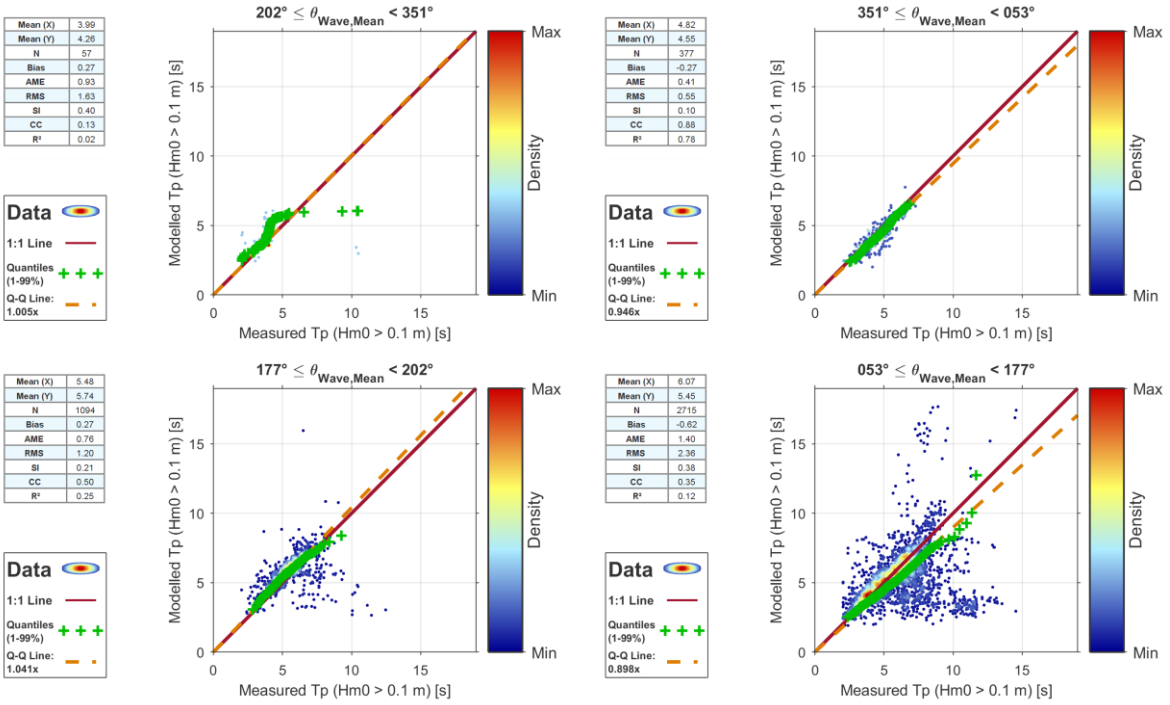



Figure C.118. AWAC C, Tp validation, timestamps with Hm0 > 0.1 m, Custom Directional Sectors.

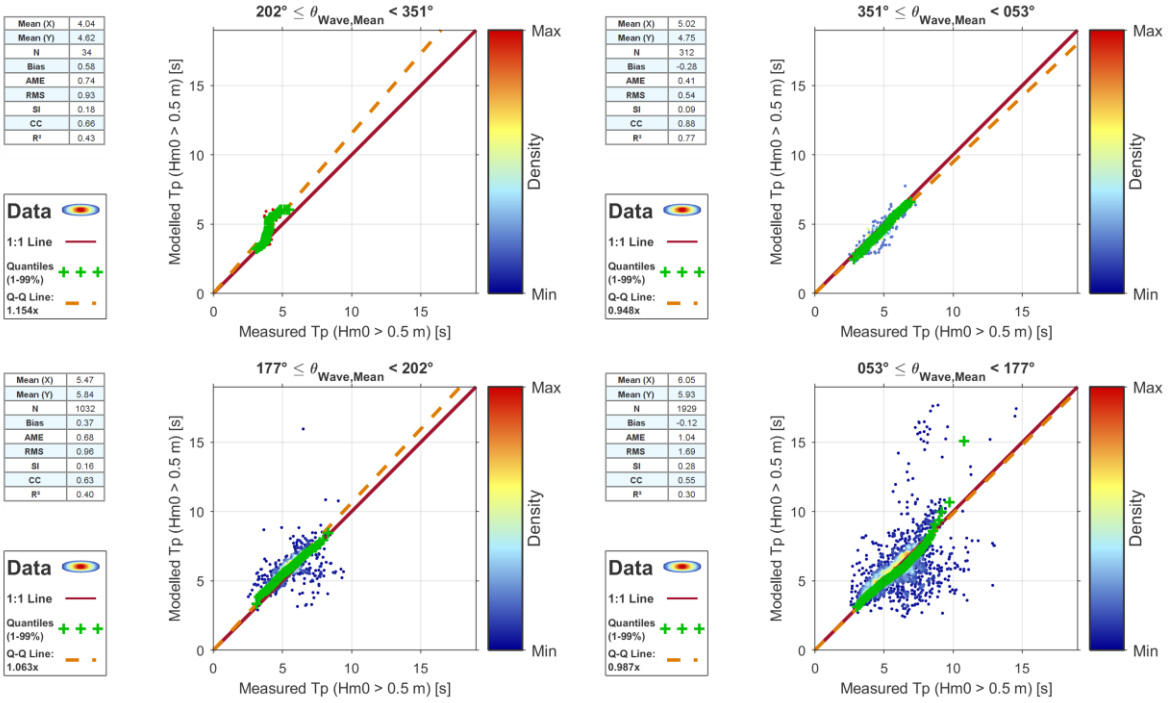



Figure C.119. AWAC C, Tp validation, timestamps with Hm0 > 0.5 m, Custom Directional Sectors.

## C.6.3.6 AWAC D1

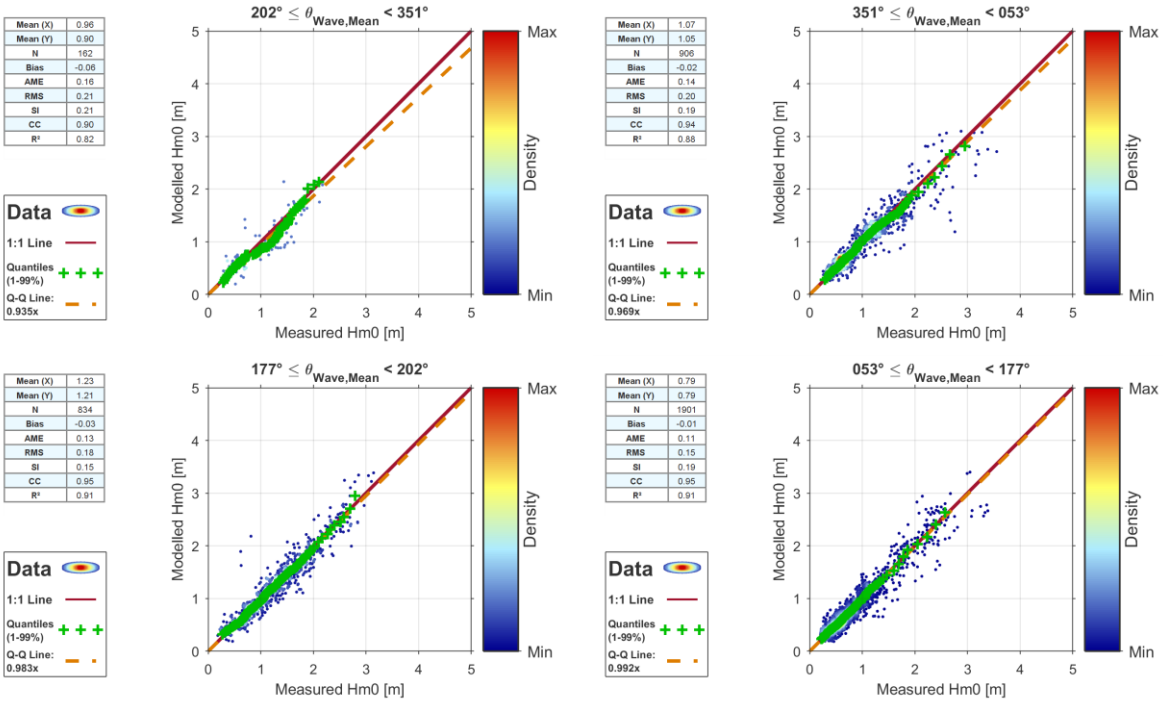



Figure C.120. AWAC D1, Hm0 validation, Custom Directional Sectors.

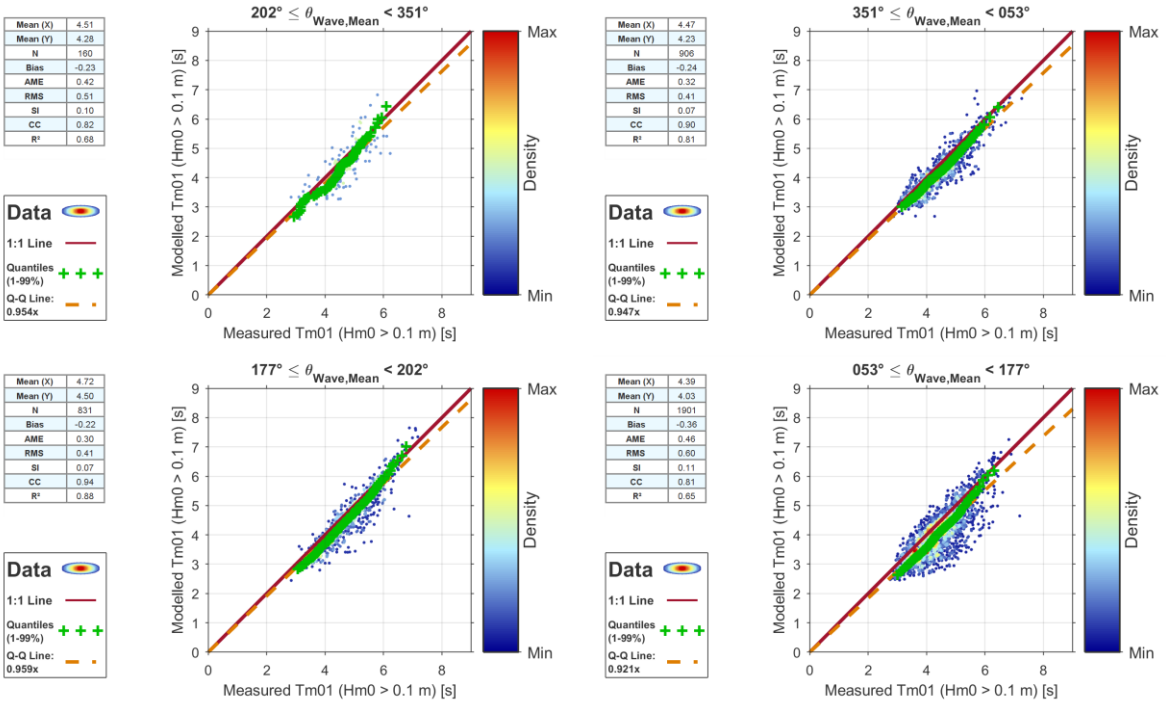



Figure C.121. AWAC D1, Tm01 validation, timestamps with Hm0 > 0.1 m, Custom Directional Sectors.

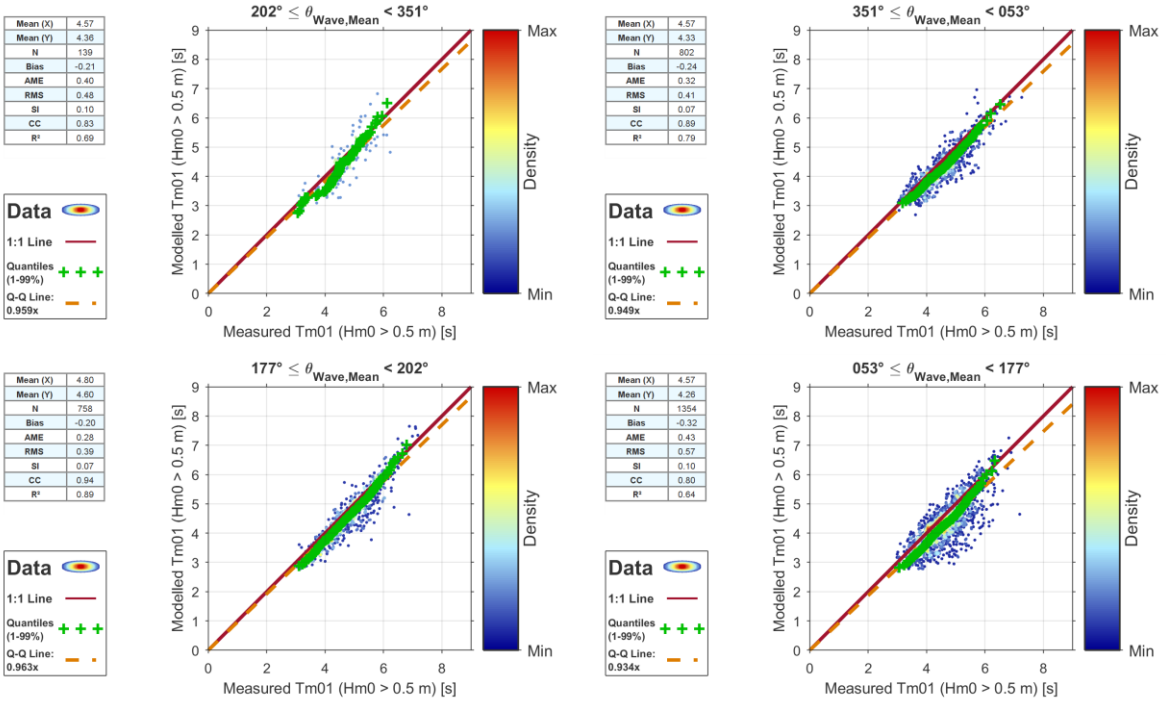



Figure C.122. AWAC D1, Tm01 validation, timestamps with Hm0 > 0.5 m, Custom Directional Sectors.

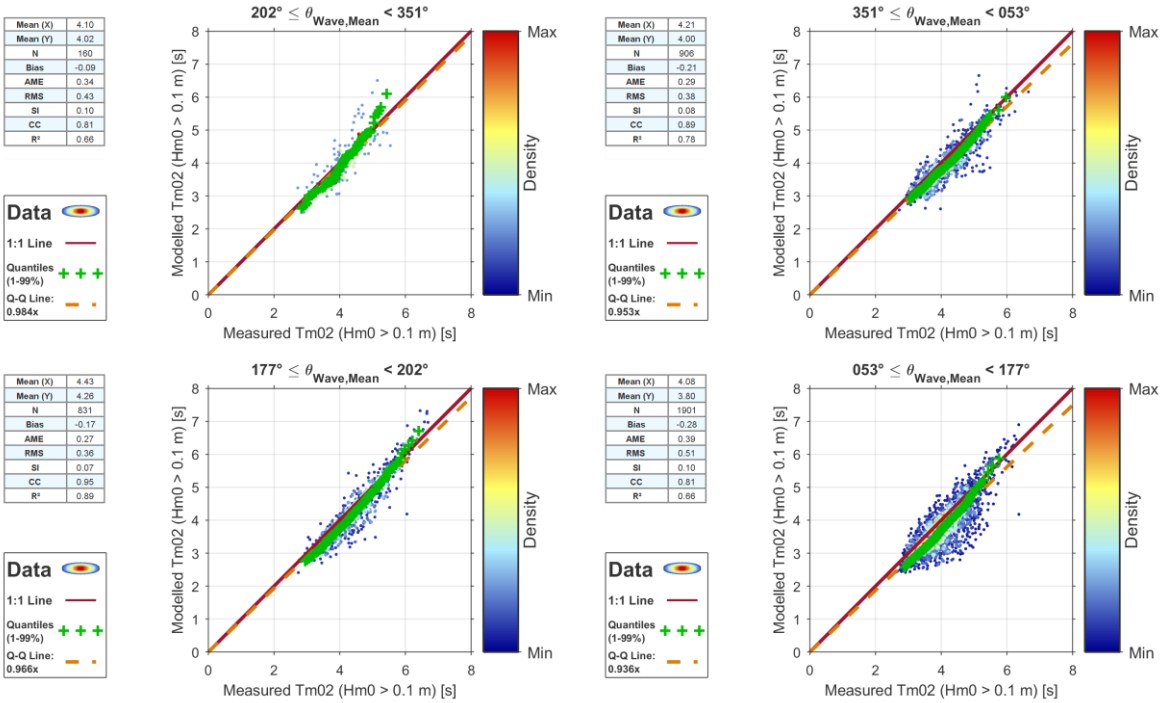



Figure C.123. AWAC D1, Tm02 validation, timestamps with Hm0 > 0.1 m, Custom Directional Sectors.

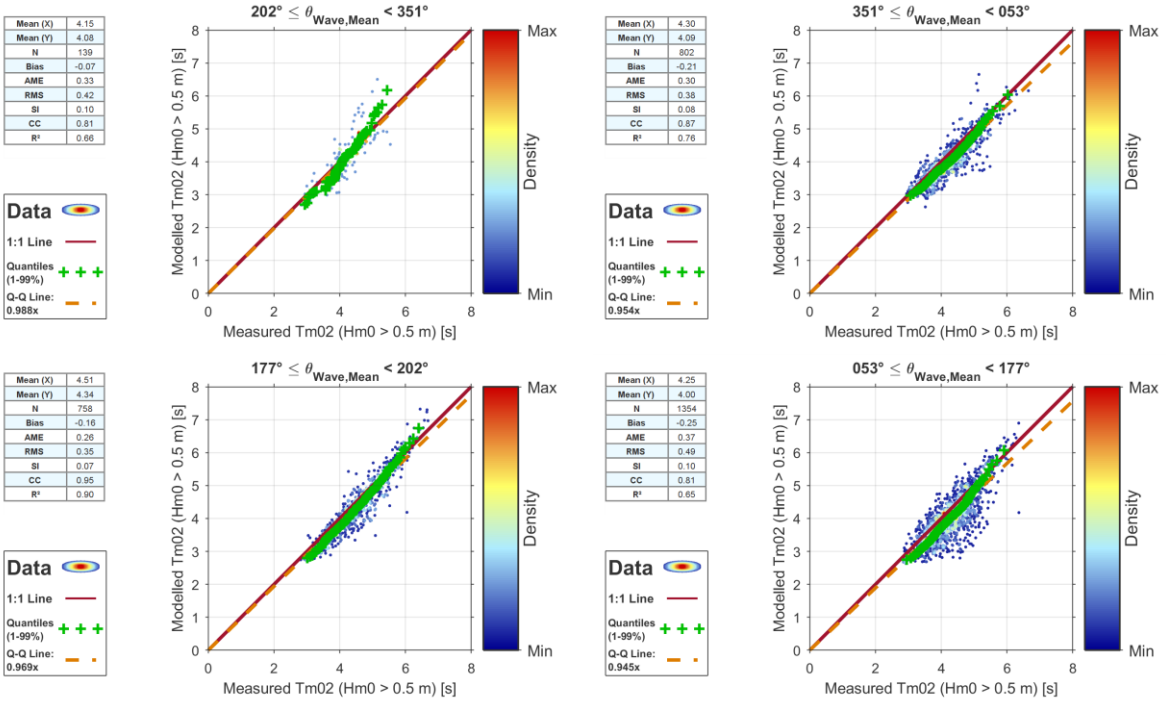



Figure C.124. AWAC D1, Tm02 validation, timestamps with Hm0 > 0.5 m, Custom Directional Sectors.

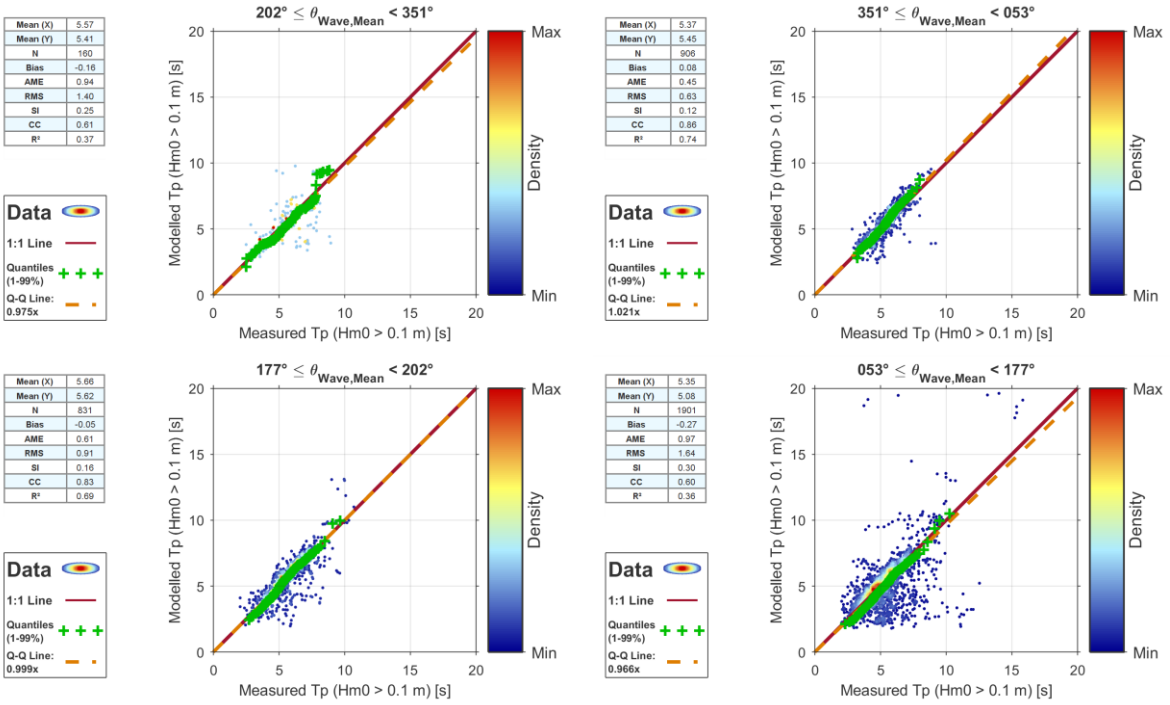



Figure C.125. AWAC D1, Tp validation, timestamps with Hm0 > 0.1 m, Custom Directional Sectors.

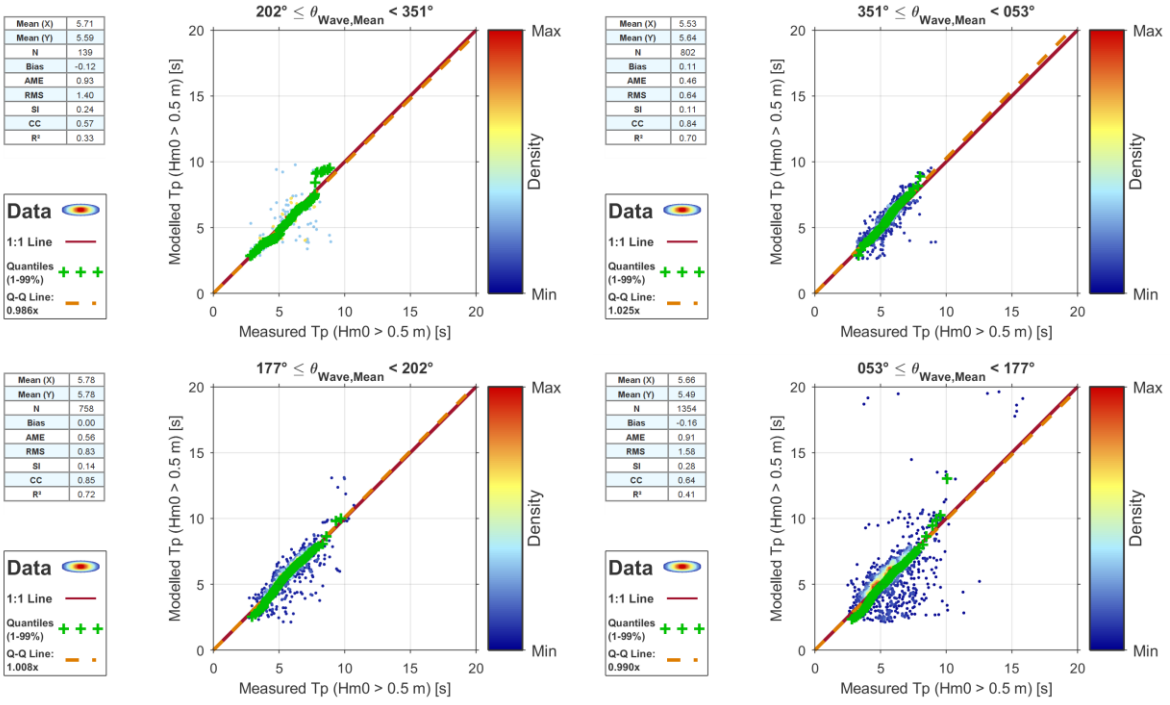



Figure C.126. AWAC D1, Tp validation, timestamps with Hm0 > 0.5 m, Custom Directional Sectors.

## C.6.3.7 AWAC E

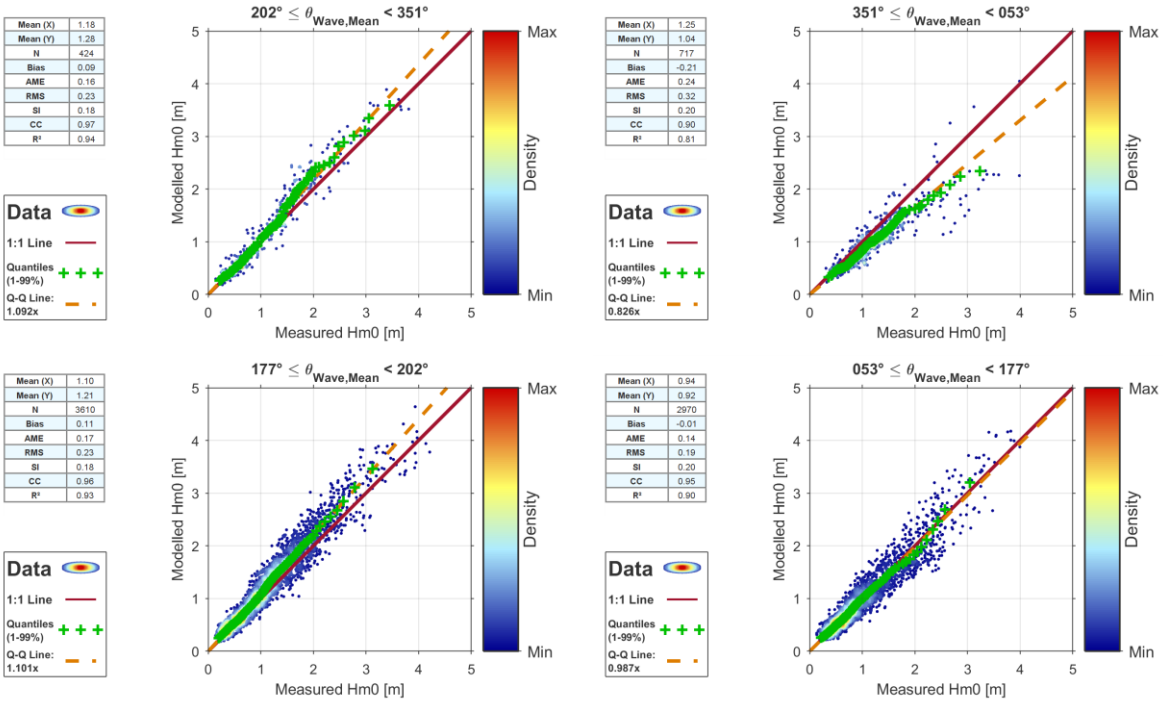



Figure C.127. AWAC E, Hm0 validation, Custom Directional Sectors.

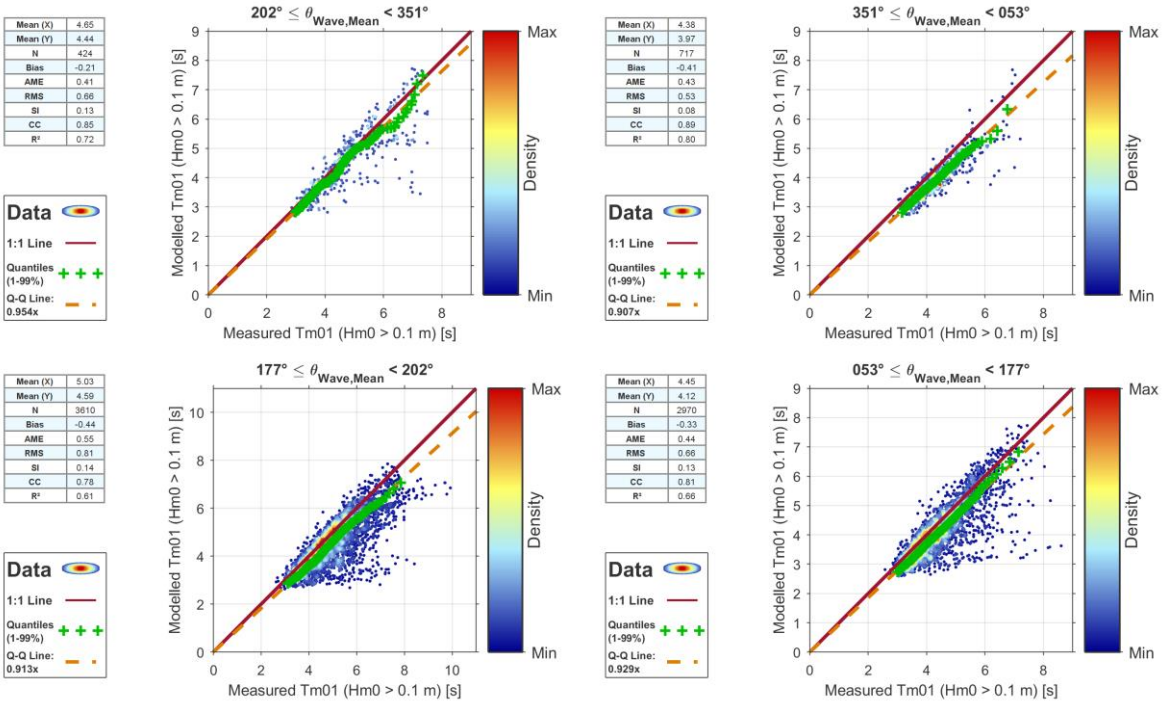



Figure C.128. AWAC E, Tm01 validation, timestamps with Hm0 > 0.1 m, Custom Directional Sectors.

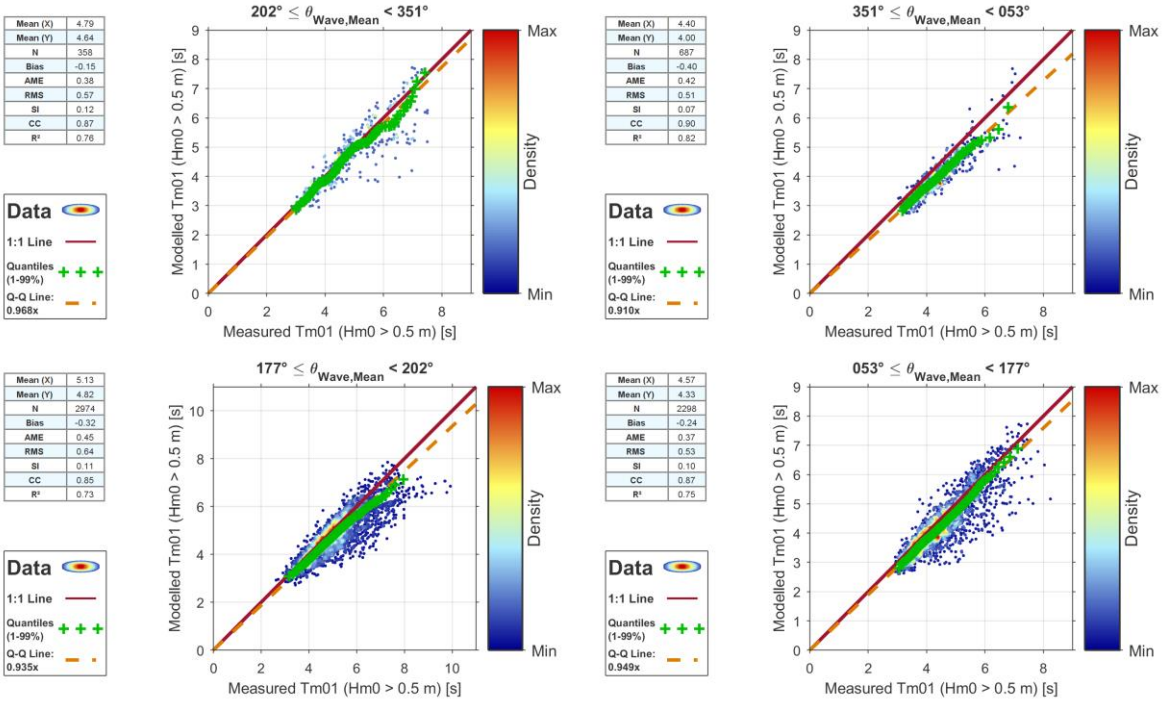



Figure C.129. AWAC E, Tm01 validation, timestamps with Hm0 > 0.5 m, Custom Directional Sectors.

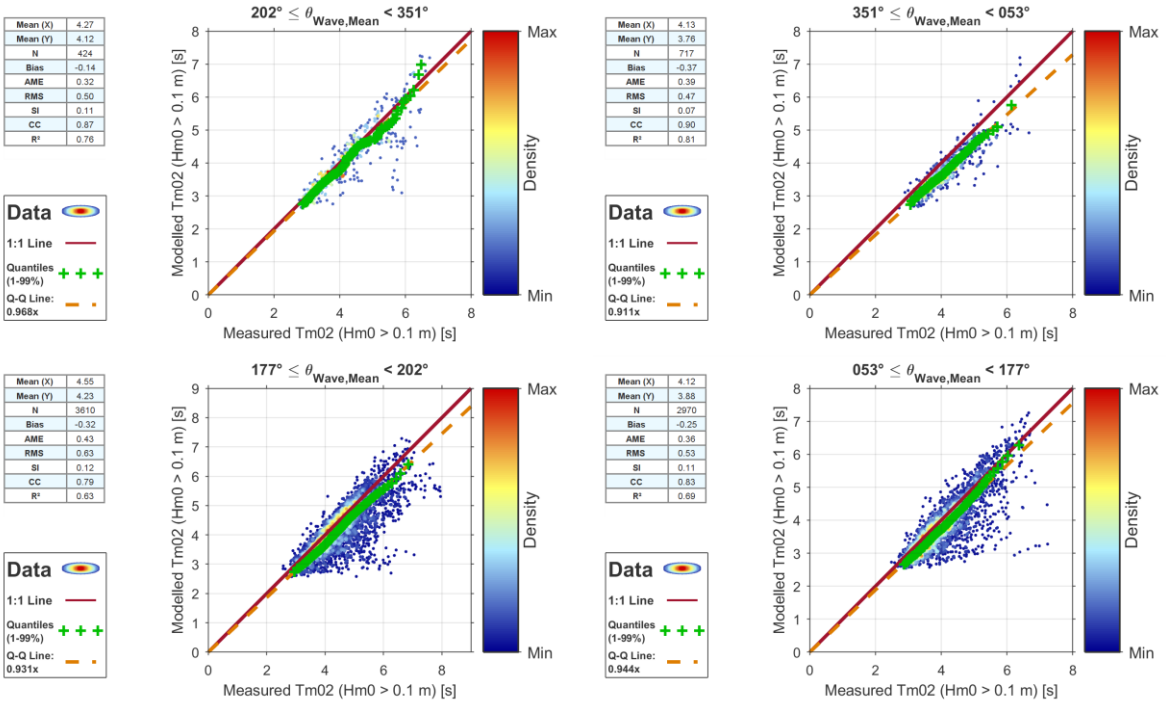



Figure C.130. AWAC E, Tm02 validation, timestamps with Hm0 > 0.1 m, Custom Directional Sectors.

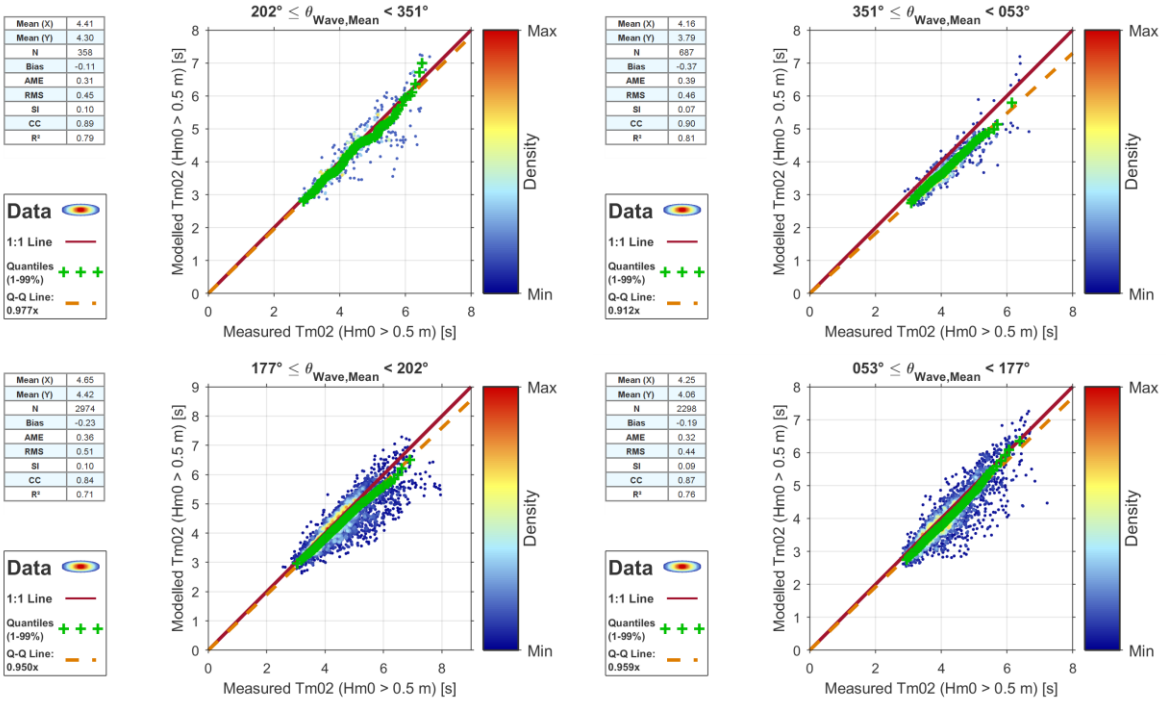



Figure C.131. AWAC E, Tm02 validation, timestamps with Hm0 > 0.5 m, Custom Directional Sectors.

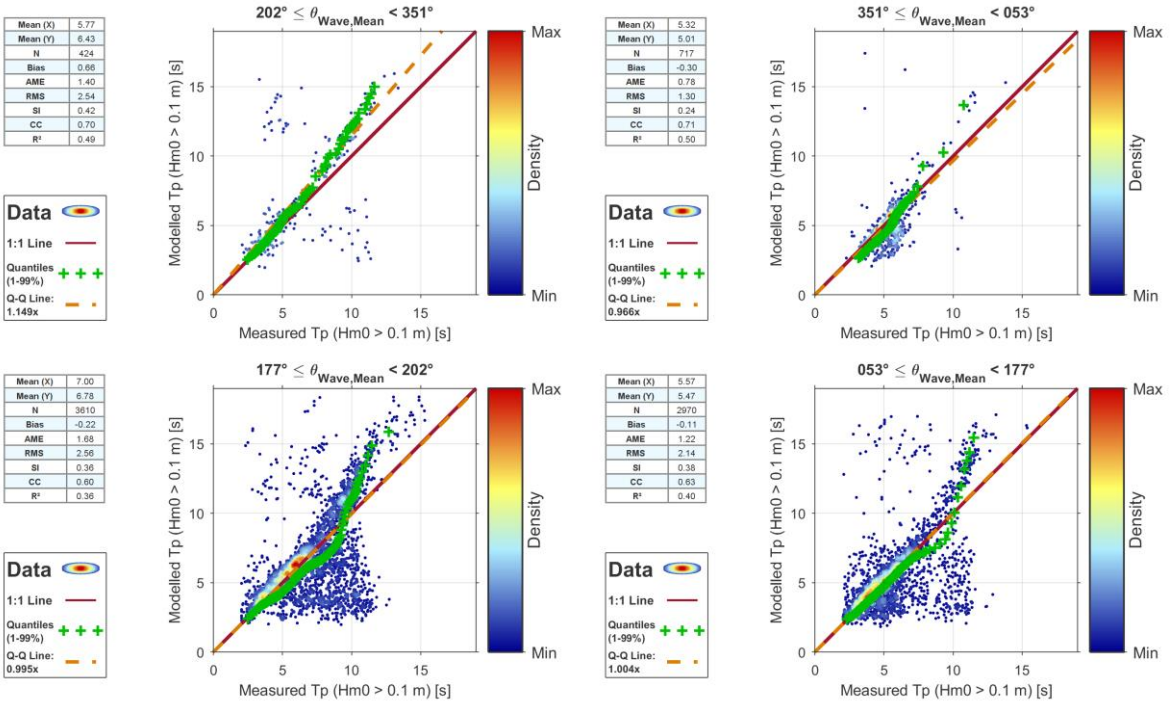



Figure C.132. AWAC E, Tp validation, timestamps with Hm0 > 0.1 m, Custom Directional Sectors.

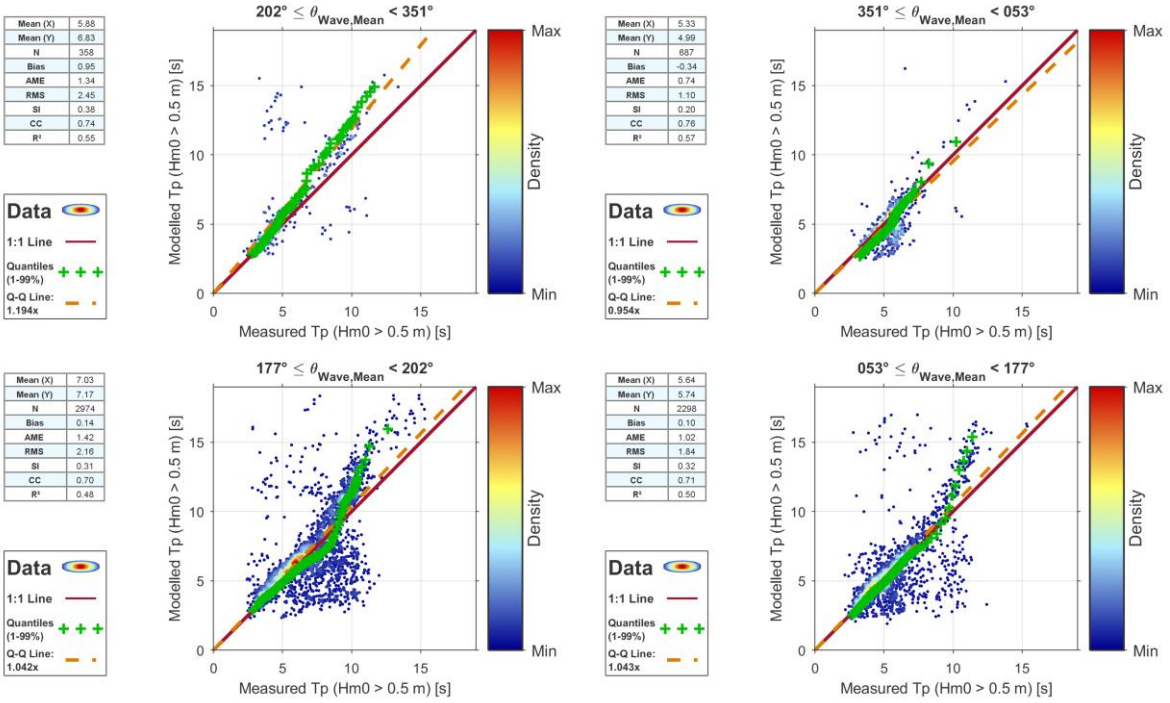



Figure C.133. AWAC E, Tp validation, timestamps with Hm0 > 0.5 m, Custom Directional Sectors.



## C.7 Spectral Validation

### C.7.1 Introduction

In this Section, comparisons of measured and modelled spectra are provided. Given the need in the project deliverables for JONSWAP spectral characterisation for total-sea state, wind-sea, and swell components, we consider not just the modelled spectral directly output from the wave model, but instead *three* different versions as follows:

1. **Raw modelled spectra:** Wave spectra directly output by the wave model with no treatment applied. For conciseness, these are labelled **Modelled** in the Figures which follow.
2. **2 peak spectra:** For each output time step, the raw modelled spectrum is partitioned into one swell and one wind-sea component. To each partition, a JONSWAP spectrum is fitted, resulting in five parameters per partition: significant wave height, peak wave period, peak enhancement factor, mean wave direction and a directional spreading parameter. A second version of the modelled spectra, labelled **2 JONSWAP** in the Figures which follow, reconstructed from only these ten parameters (five for swell, five for wind-sea) is subsequently used throughout the validation.
3. **1 peak spectra:** For each output time step, a JONSWAP spectrum is fitted to the full raw spectrum, resulting in five parameters for the entire spectrum: significant wave height, peak wave period, peak enhancement factor, mean wave direction and a directional spreading parameter. A third version of the modelled spectra, labelled **1 JONSWAP** in the Figures which follow, reconstructed from only these five parameters, is subsequently used throughout the validation.

More details on the construction of the 1 and 2 JONSWAP spectra can be found in Appendix E.

This Section proceeds as follows:

- In Section C.7.2, spectra for AWAC A are considered.
    - **Section C.7.2.1 Omni-Directional:** Figure C.134 shows the mean of modelled spectra (red line) and measured spectra (blue line) across *all* time-steps for which both datasets are available. Overlaid are also means of the 2 JONSWAP spectra (green) and 1 JONSWAP (dashed purple). In the top right corner, the number of modelled spectra which have been averaged are shown (red text) along with the number of measured spectra averaged (blue text). Note that modelled data are hourly, and measurements generally half-hourly, thus the number of spectra averaged differ. Thereafter, in Figure C.135, spectra are grouped by measured Hm0 and Tp, and a single comparison of mean spectra for each grouping is included.
    - **Section C.7.2.2 45° Sectors:** In Figure C.136, spectra are split into the 45° sectors of Section C.6.2 and mean spectra compared for each sector are compared. This splitting is based on *measured* mean wave directions: measured spectra are assigned to a bin directly, along with modelled spectra that are closest temporally, i.e. *model* wave direction is not used. Thereafter, in Figure C.137 through Figure C.144, for each sector in turn, spectra are grouped by Hm0 and Tp, and a single comparison of mean spectra for each grouping in that directional sector is included.
    - **Section C.7.2.3 Custom Sectors**: This process is then repeated for the custom directional sectors of Section C.6.3.
- In Sections C.7.3 through C.7.6 the entire process is repeated for AWACs B1, C, D1 and E.

## C.7.2 AWAC A

### C.7.2.1 Omni-Directional

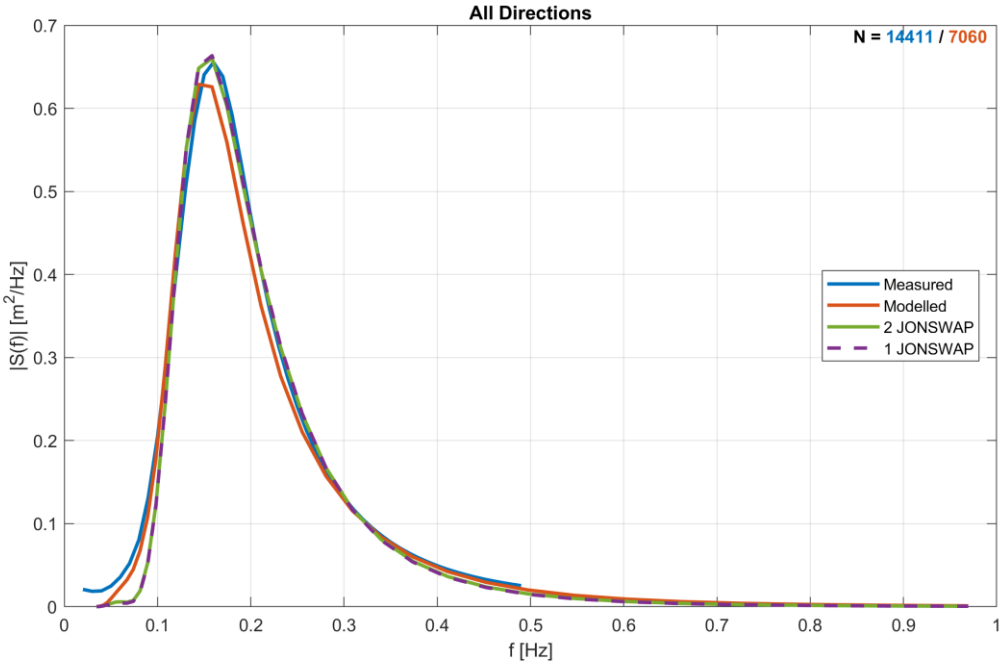



Figure C.134. AWAC A, omni-directional spectral validation, all data.

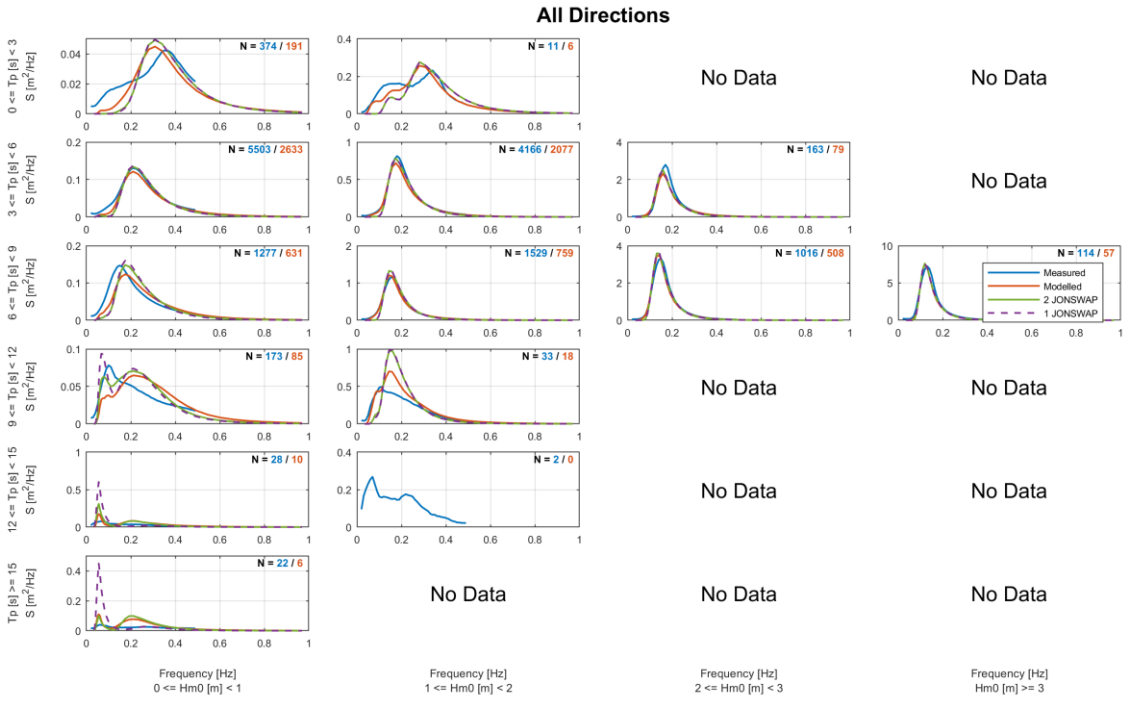



Figure C.135. AWAC A, omni-directional spectral validation, by Hm0 and Tp, all directions.

### C.7.2.2 45° Sectors

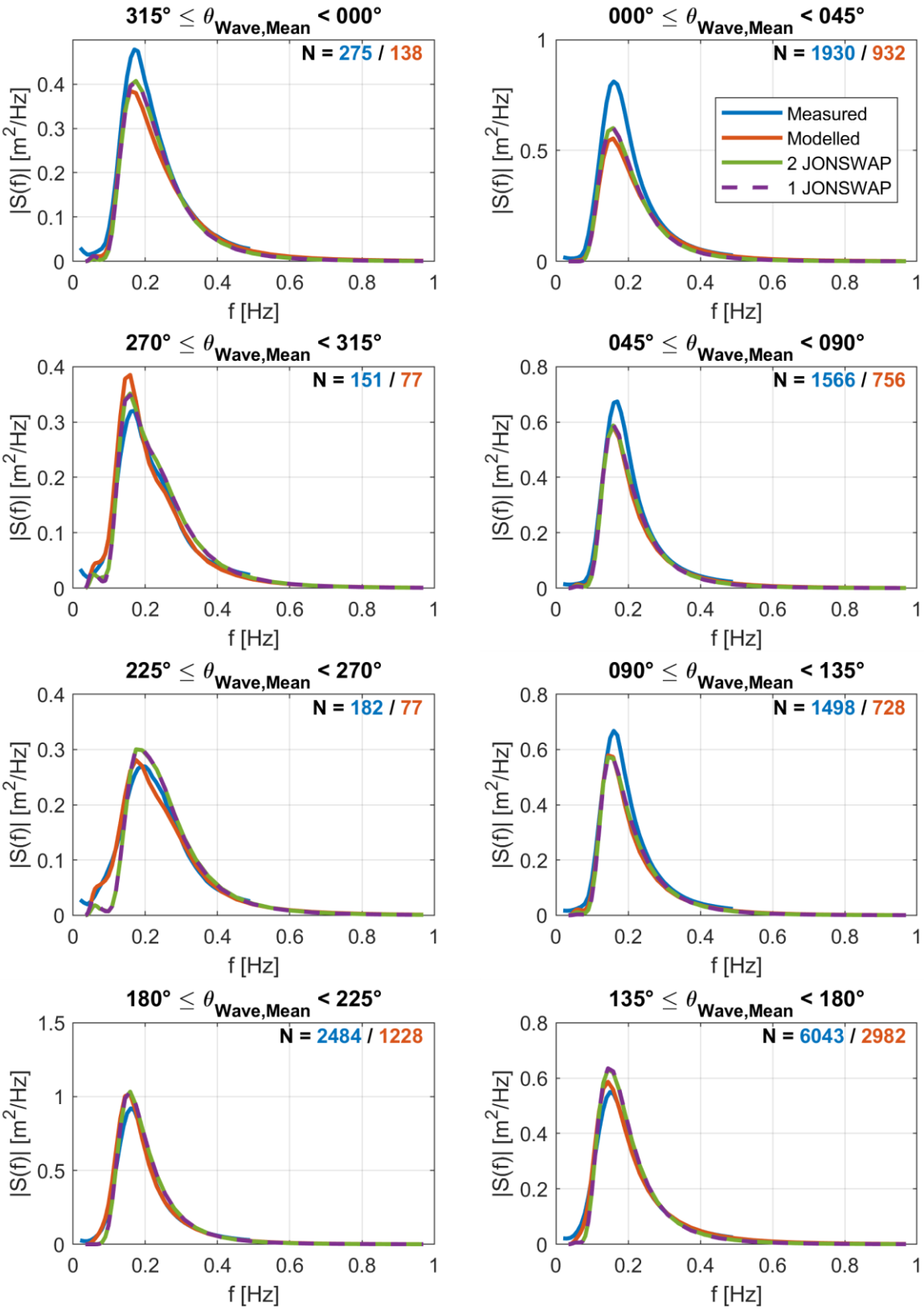



Figure C.136. AWAC A, omni-directional spectral validation, 45° sectors.

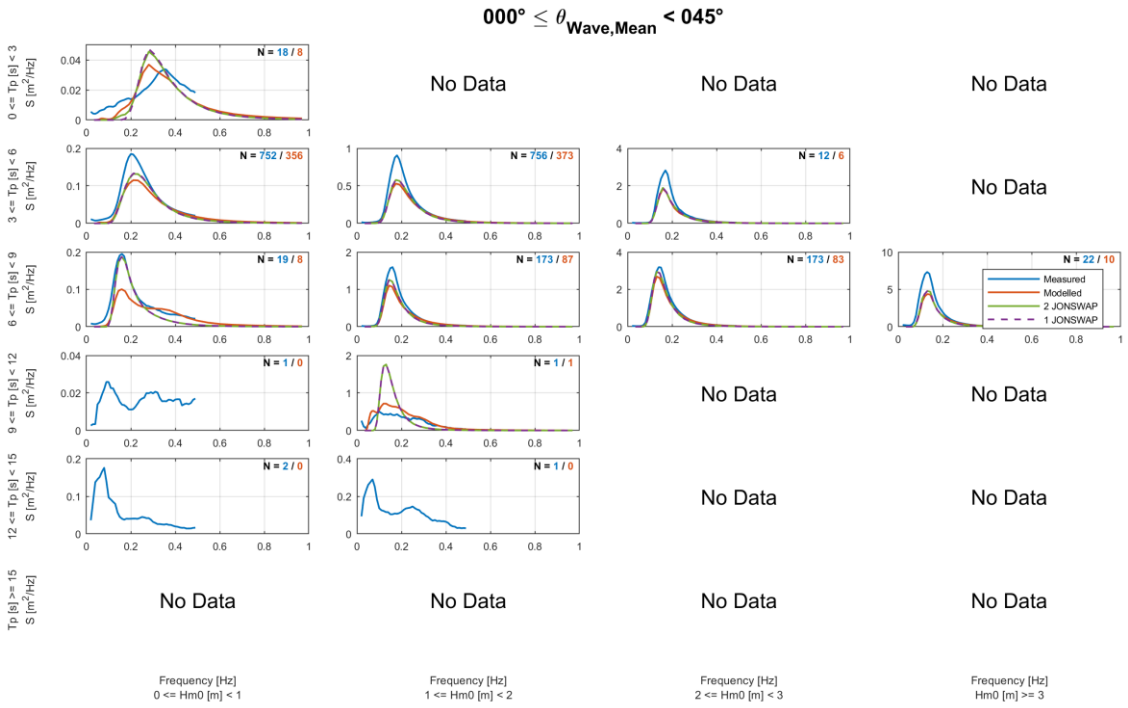



Figure C.137. AWAC A, omni-directional spectral validation, by Hm0 and Tp, 0-45° sector.

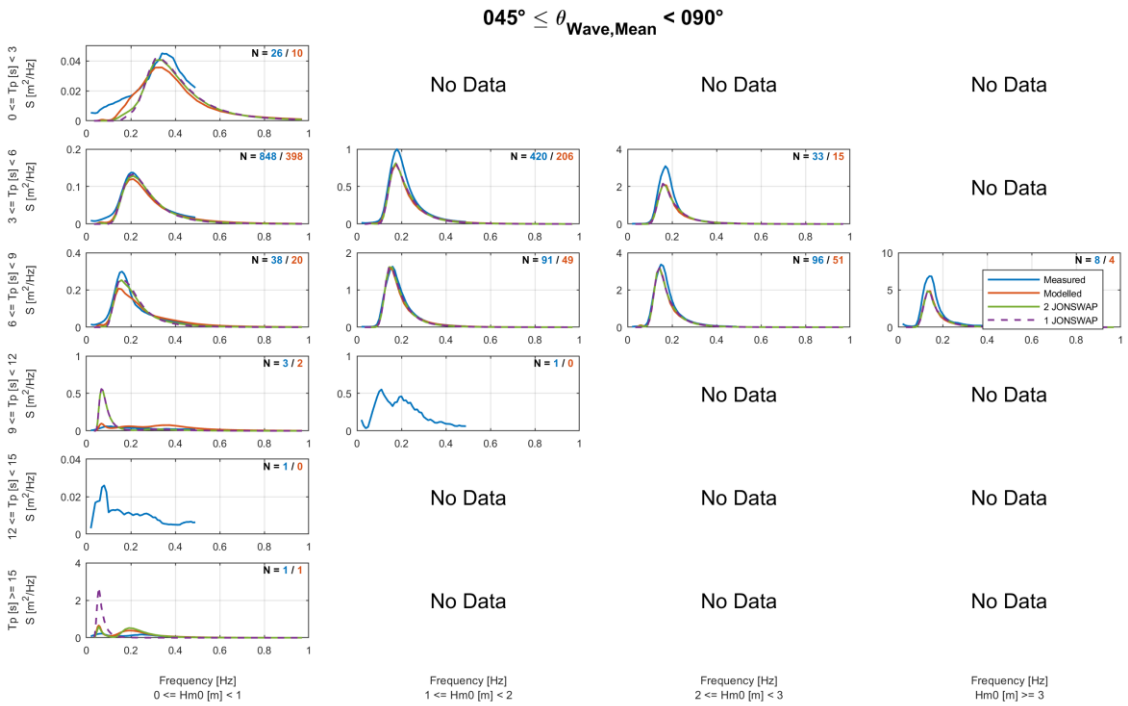



Figure C.138. AWAC A, omni-directional spectral validation, by Hm0 and Tp, 45-90° sector.

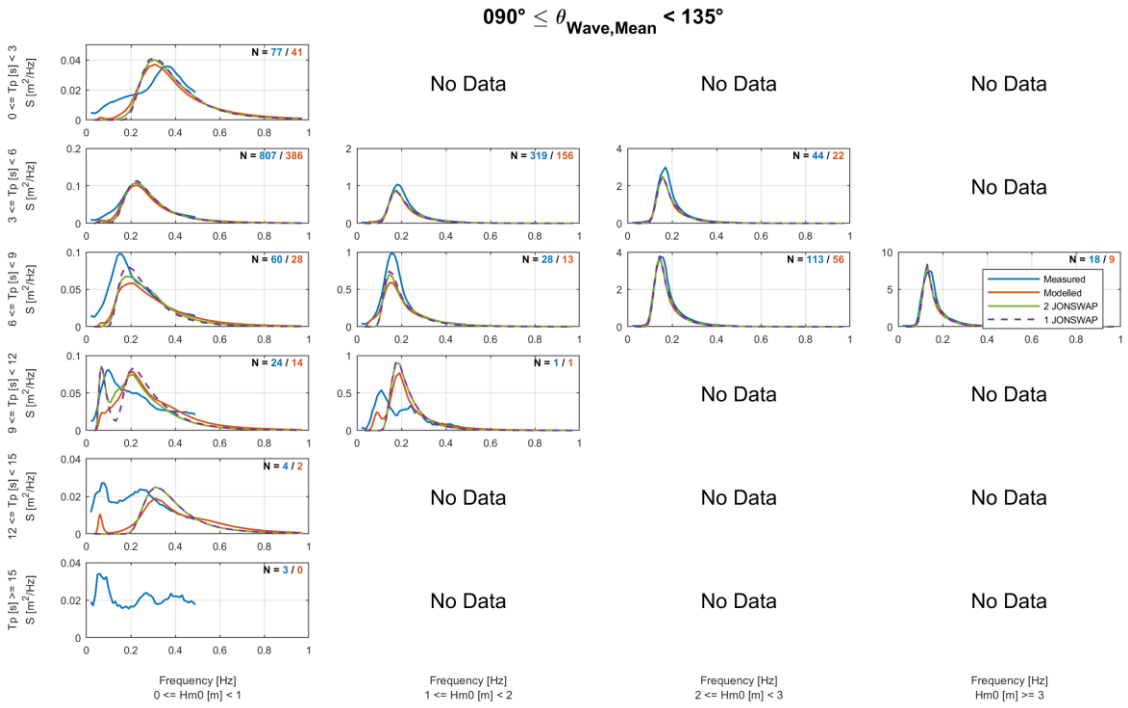



Figure C.139. AWAC A, omni-directional spectral validation, by Hm0 and Tp, 90-135° sector.

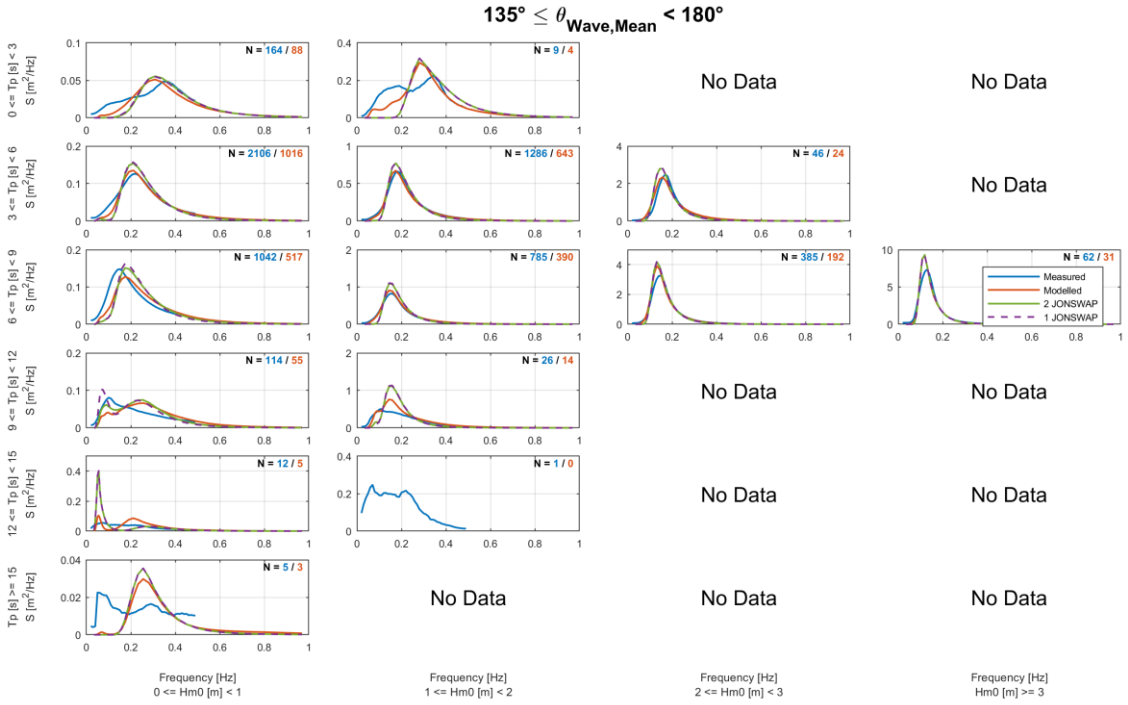



Figure C.140. AWAC A, omni-directional spectral validation, by Hm0 and Tp, 135-180° sector.

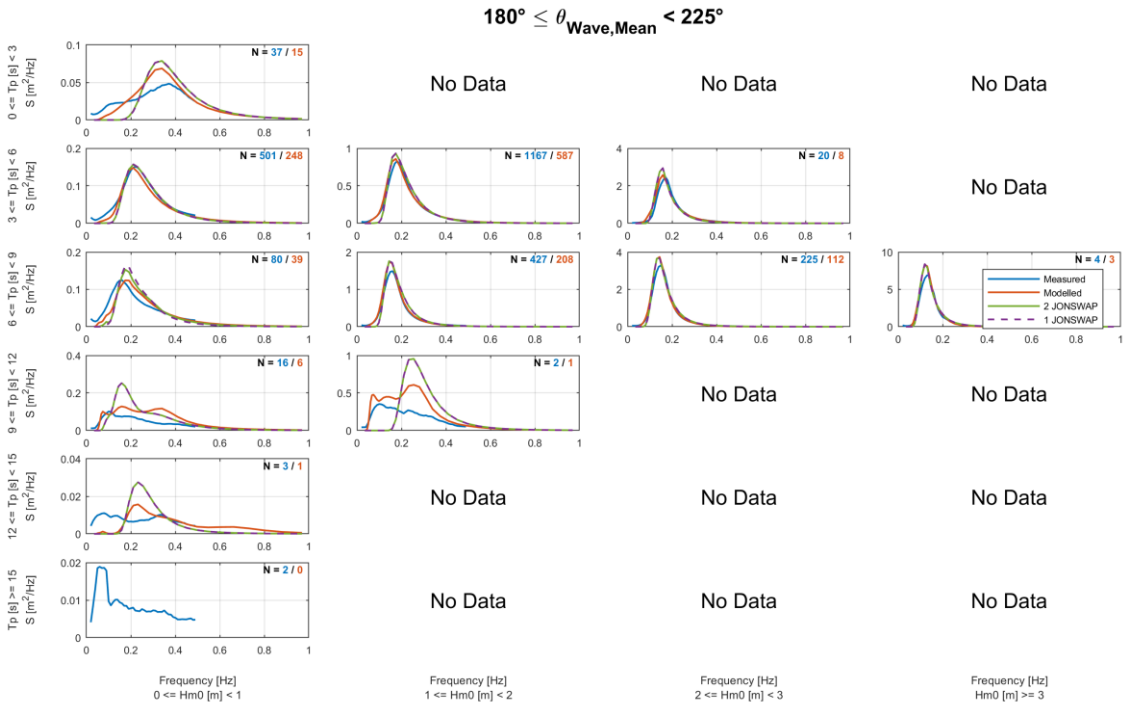



Figure C.141. AWAC A, omni-directional spectral validation, by Hm0 and Tp, 180-225° sector.

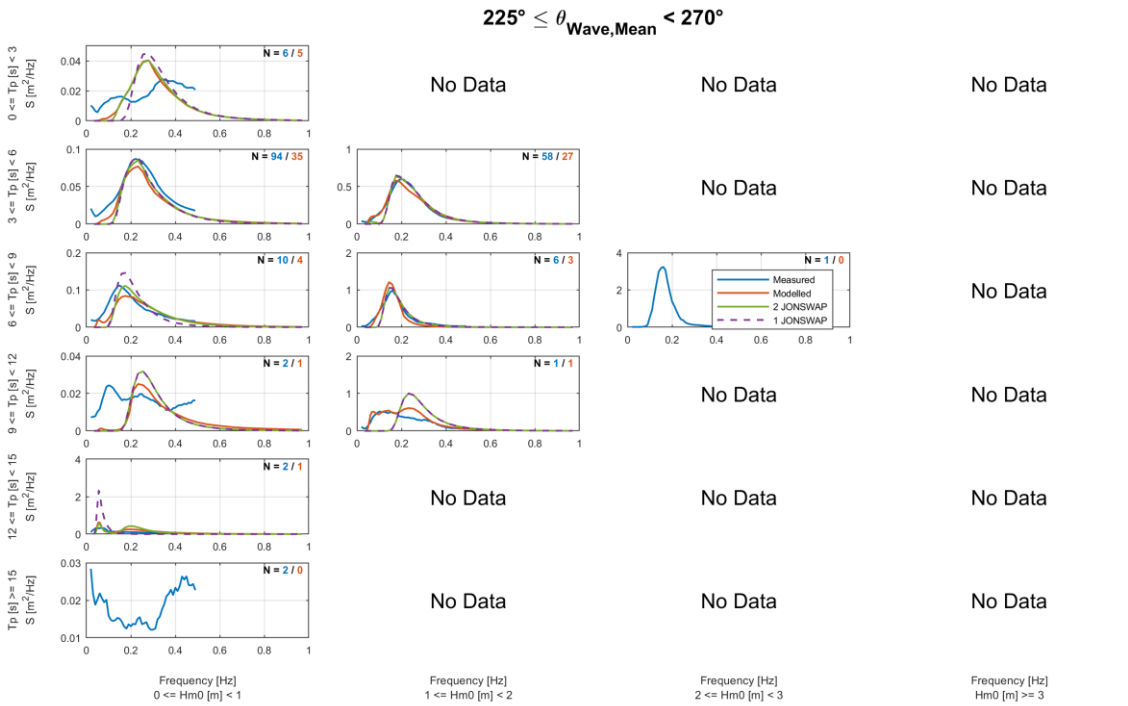



Figure C.142. AWAC A, omni-directional spectral validation, by Hm0 and Tp, 225-270° sector.

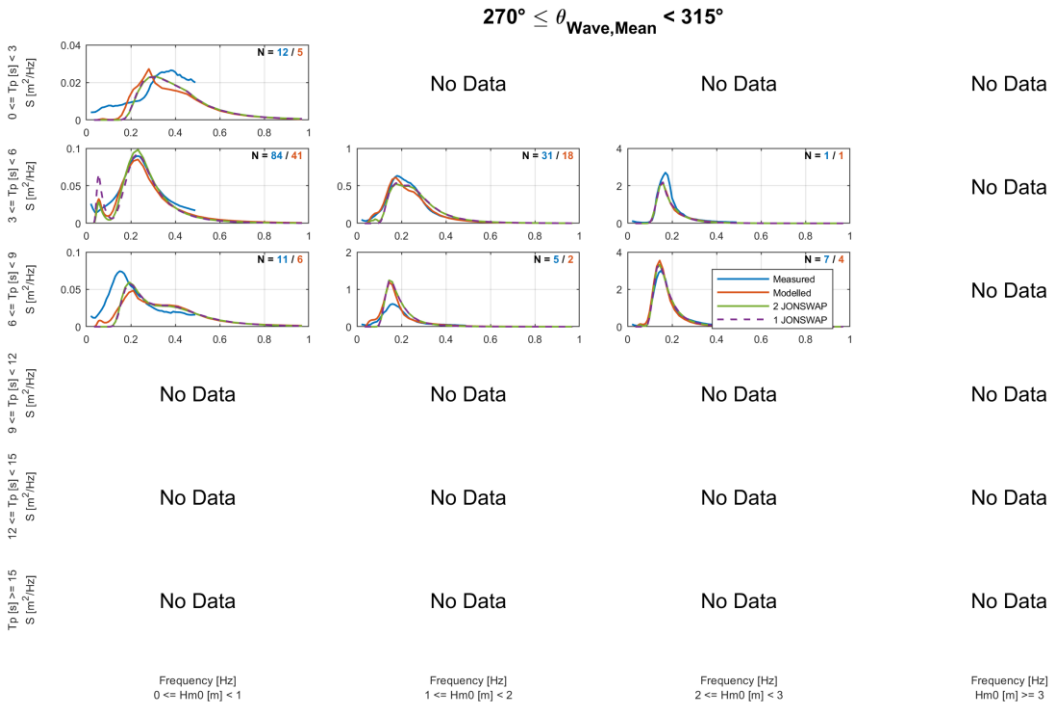



Figure C.143. AWAC A, omni-directional spectral validation, by Hm0 and Tp, 270-315° sector.

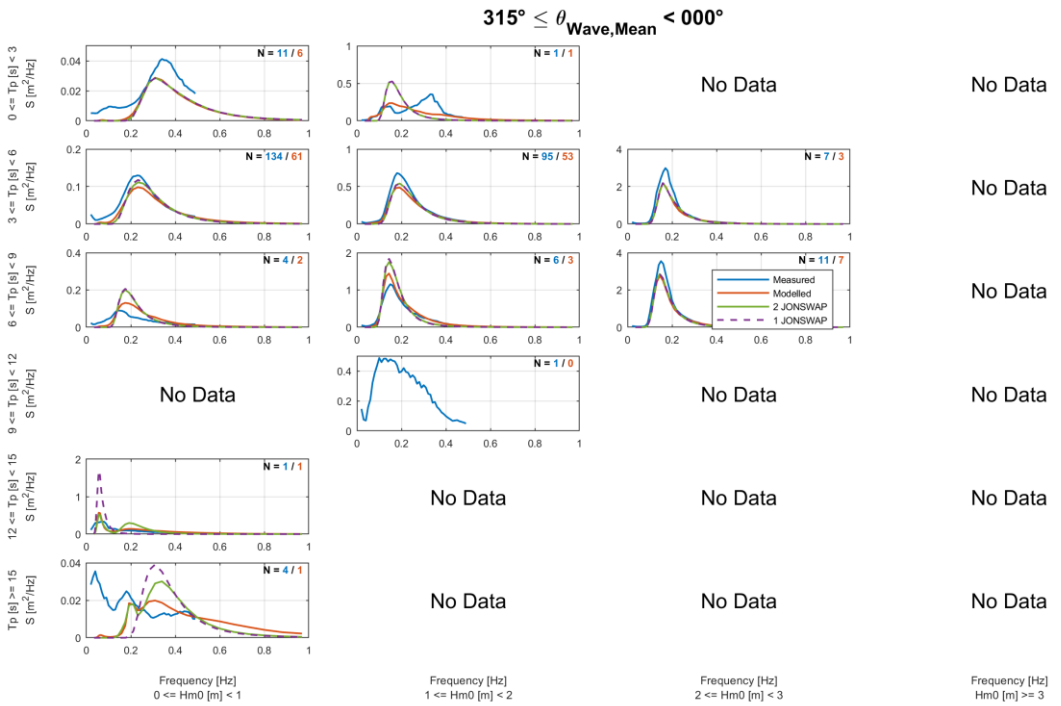



Figure C.144. AWAC A, omni-directional spectral validation, by Hm0 and Tp, 315-0° sector.

### C.7.2.3 Custom Sectors

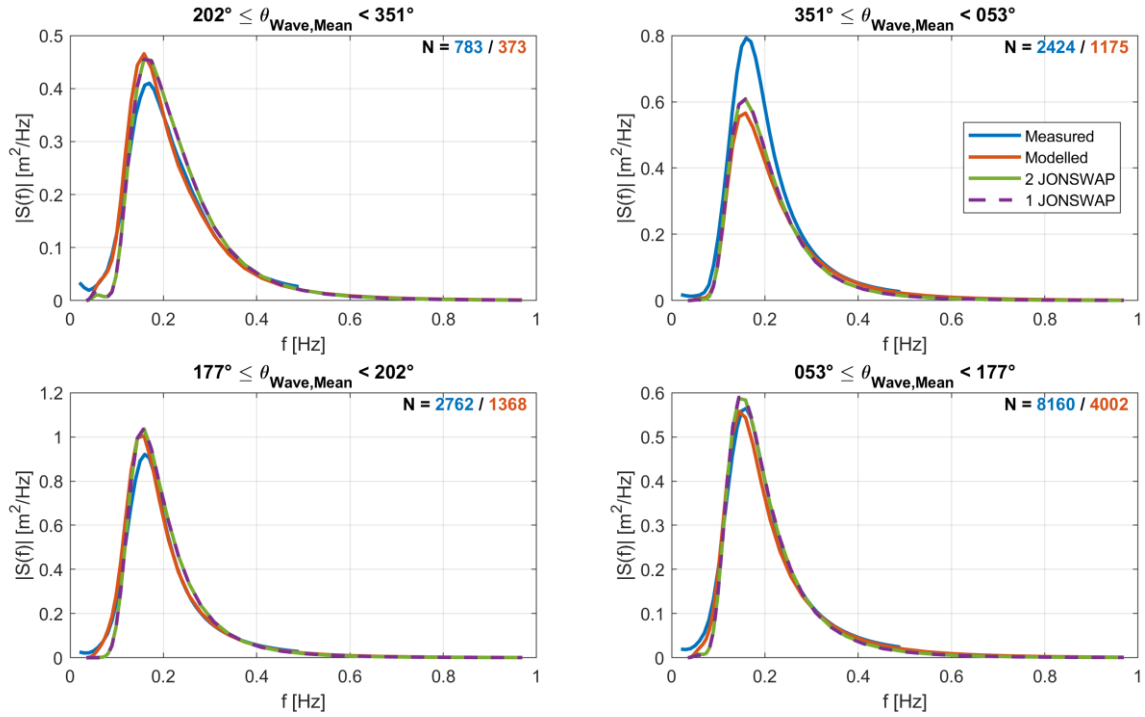



Figure C.145. AWAC A, omni-directional spectral validation, custom sectors.

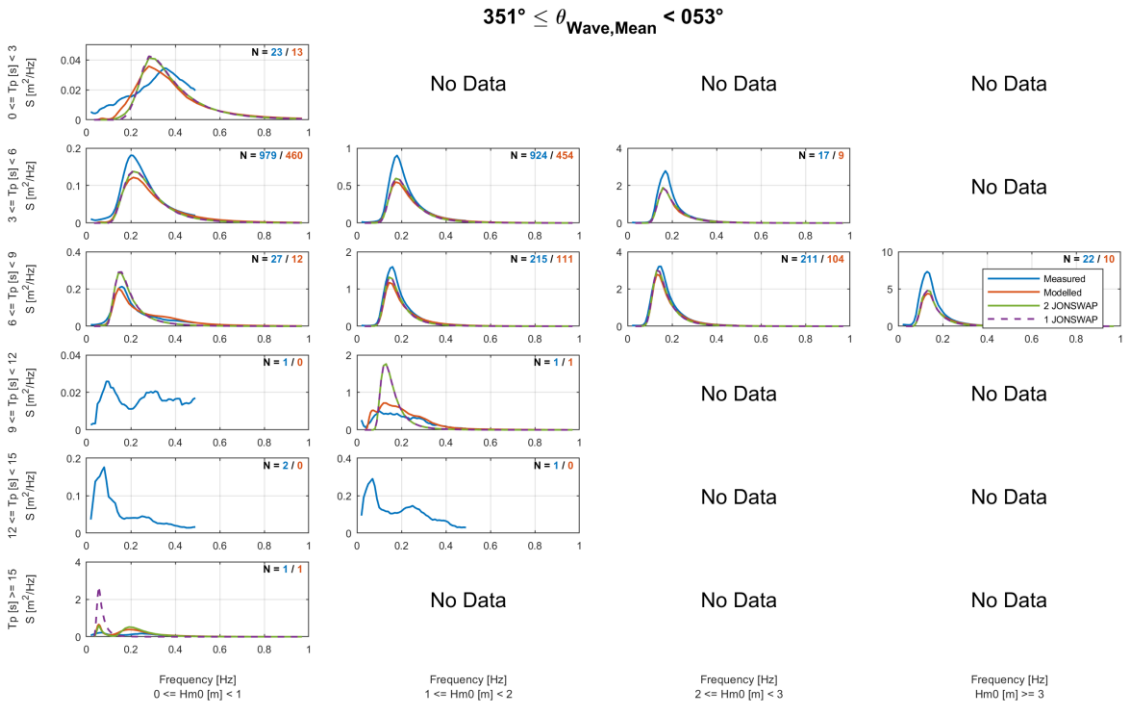



Figure C.146. AWAC A, omni-directional spectral validation, by Hm0 and Tp, 351-053° sector.

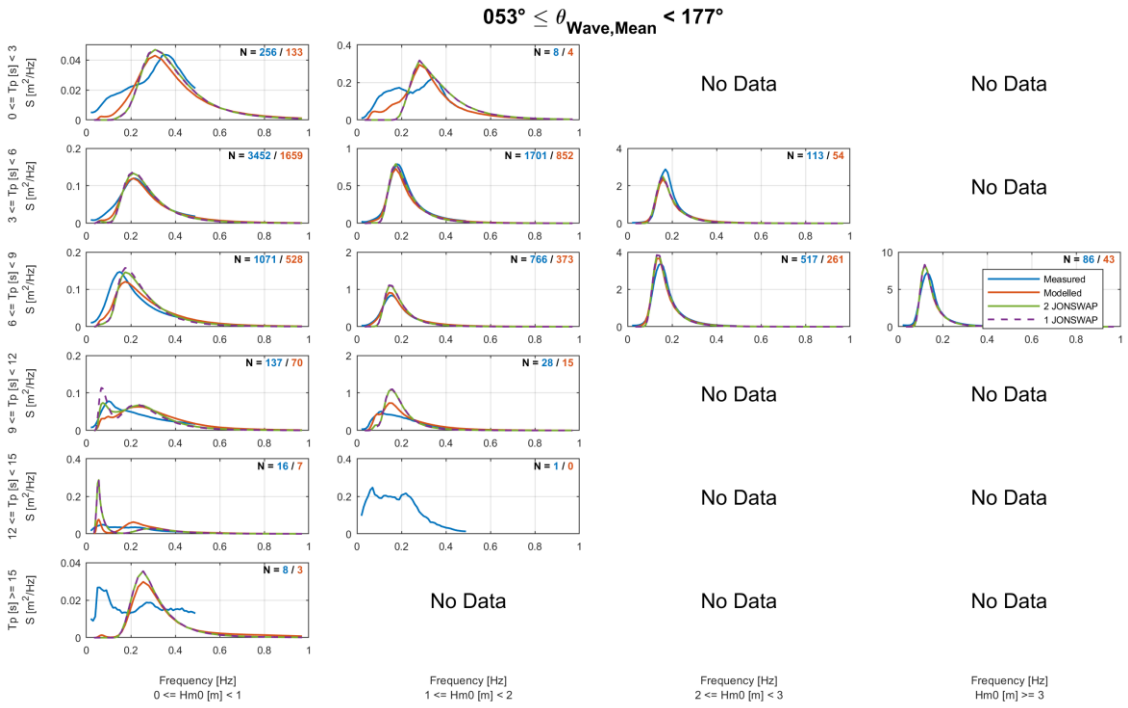



Figure C.147. AWAC A, omni-directional spectral validation, by Hm0 and Tp, 053-177° sector.

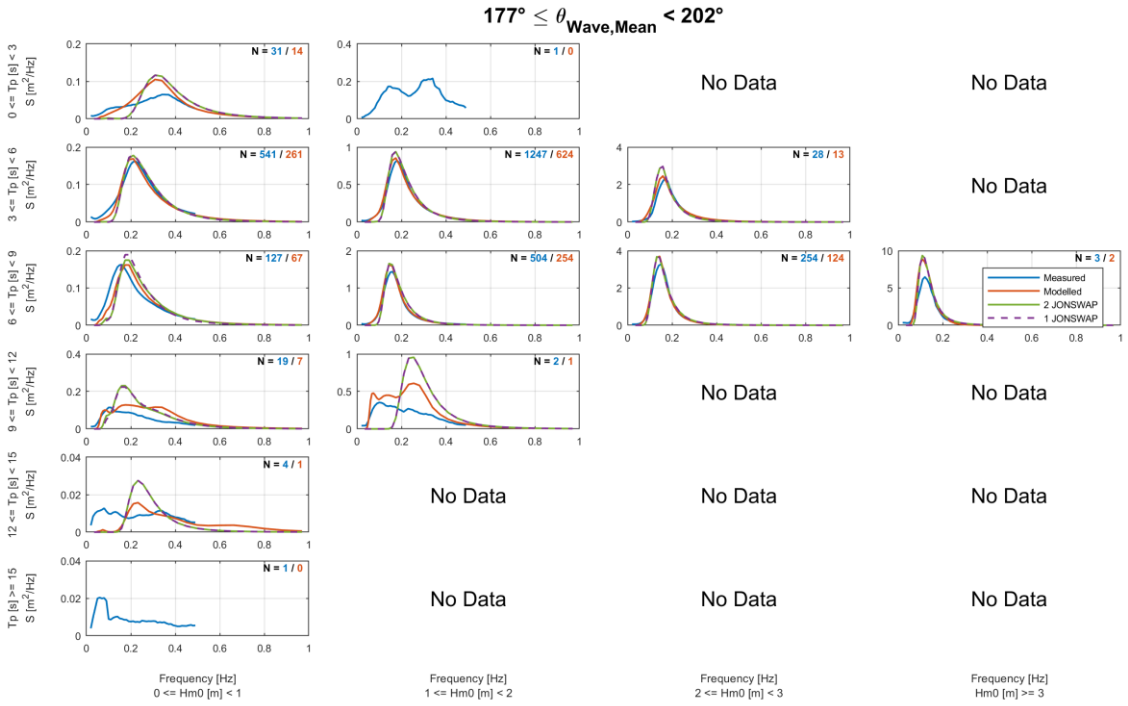



Figure C.148. AWAC A, omni-directional spectral validation, by Hm0 and Tp, 177-202° sector.

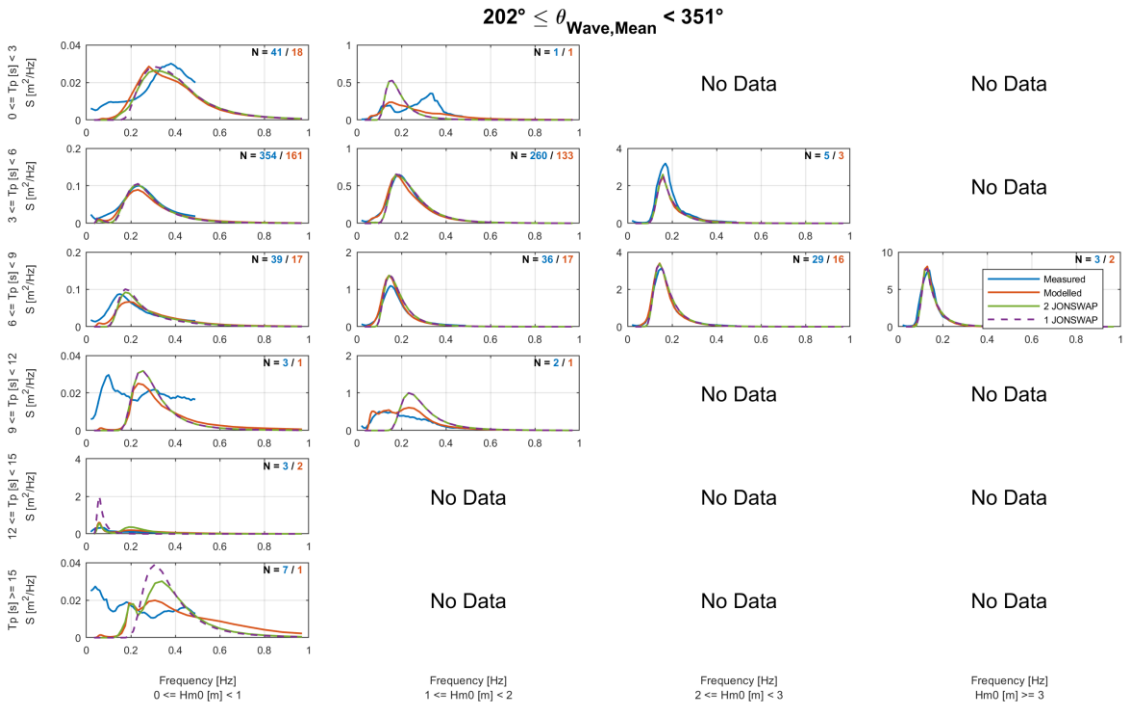



Figure C.149. AWAC A, omni-directional spectral validation, by Hm0 and Tp, 202-351° sector.

## C.7.3 AWAC B1

### C.7.3.1 Omni-Directional

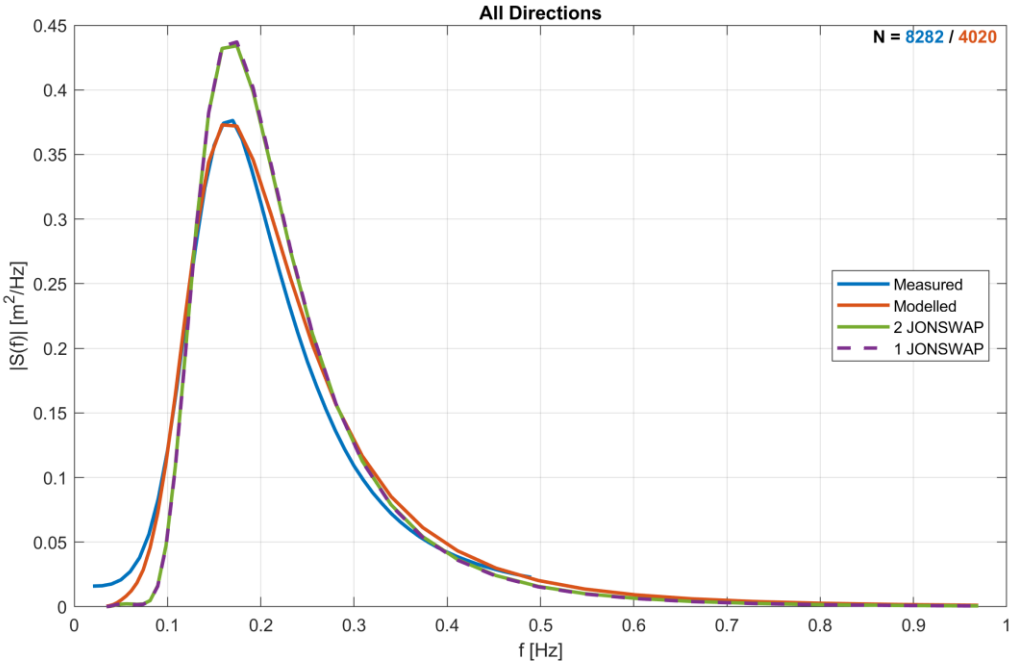



Figure C.150. AWAC B1, omni-directional spectral validation, all data.

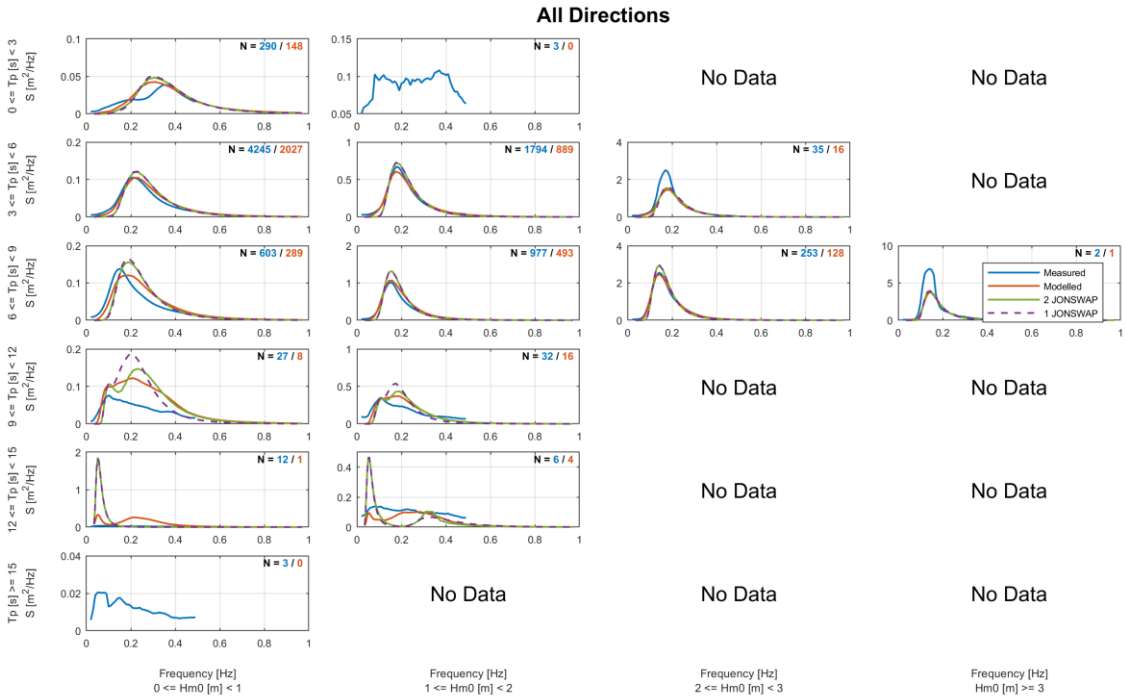



Figure C.151. AWAC B1, omni-directional spectral validation, by Hm0 and Tp, all directions.

### C.7.3.2 45° Sectors

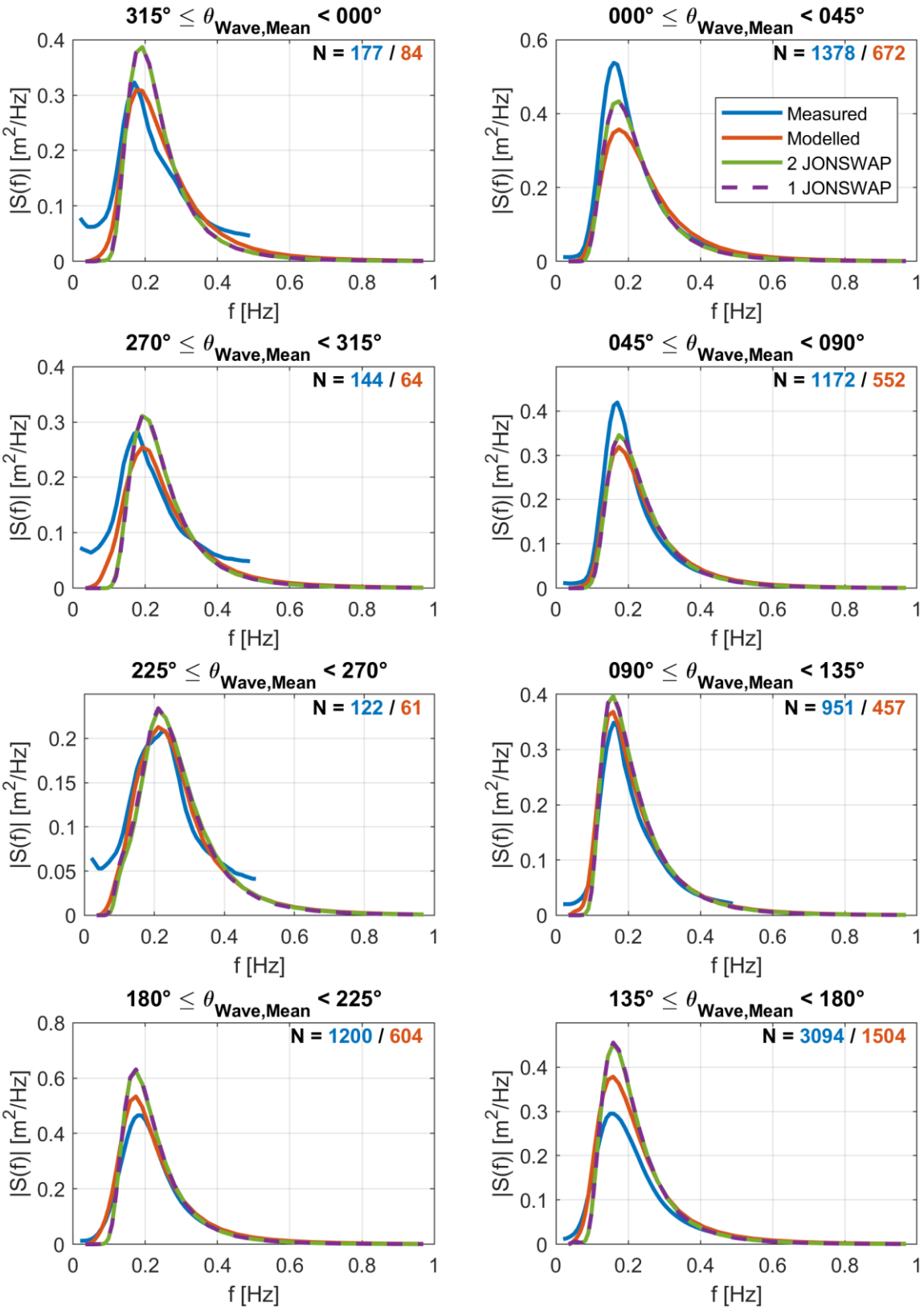



Figure C.152. AWAC B1, omni-directional spectral validation, 45° sectors.

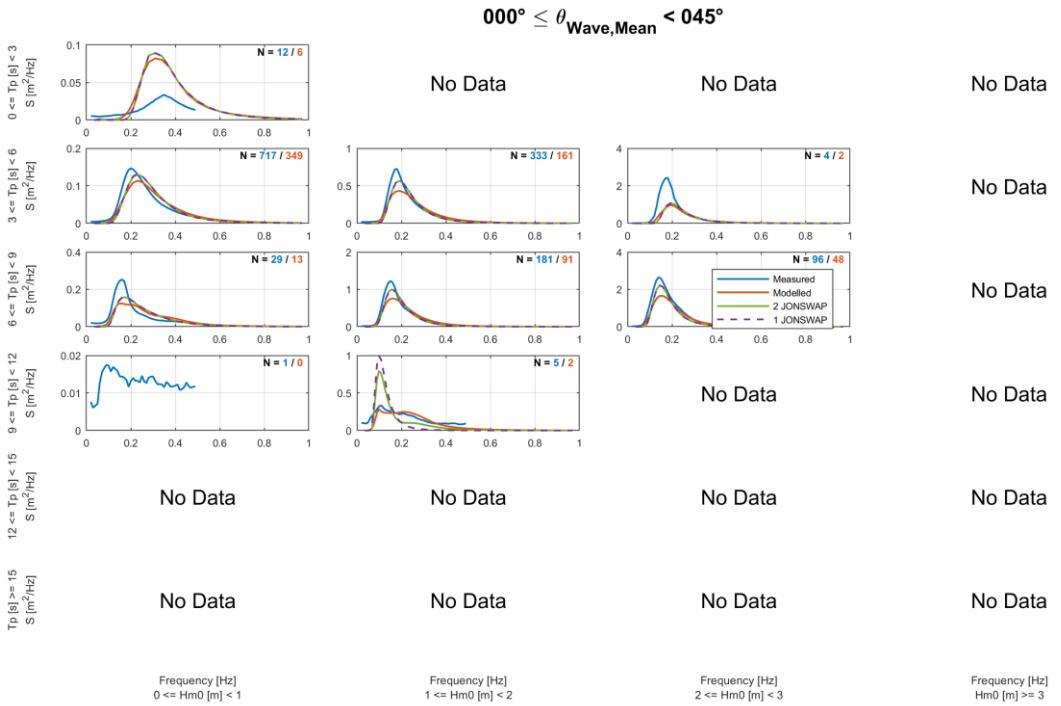



Figure C.153. AWAC B1, omni-directional spectral validation, by Hm0 and Tp, 0-45° sector.

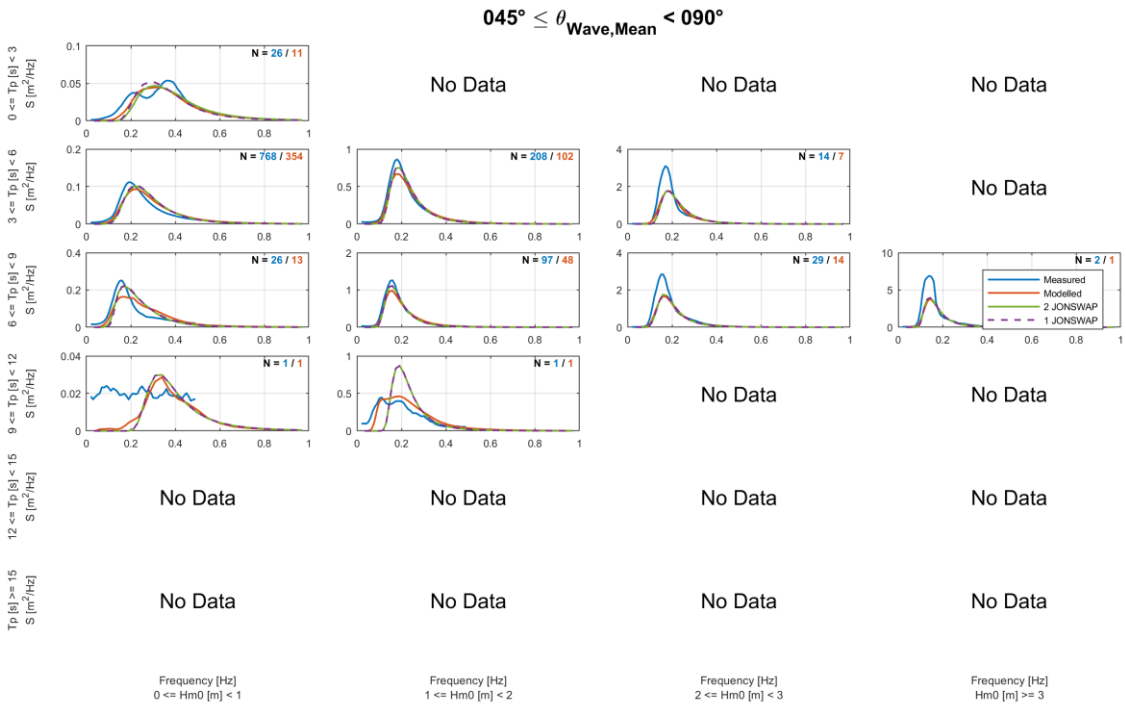



Figure C.154. AWAC B1, omni-directional spectral validation, by Hm0 and Tp, 45-90° sector.

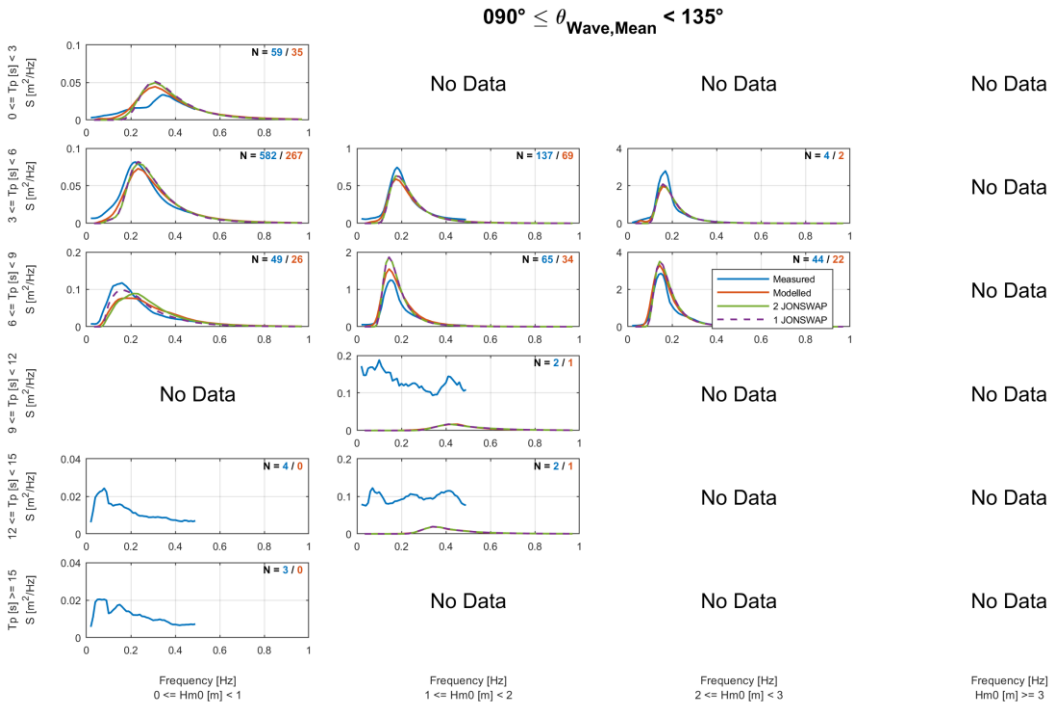



Figure C.155. AWAC B1, omni-directional spectral validation, by Hm0 and Tp, 90-135° sector.

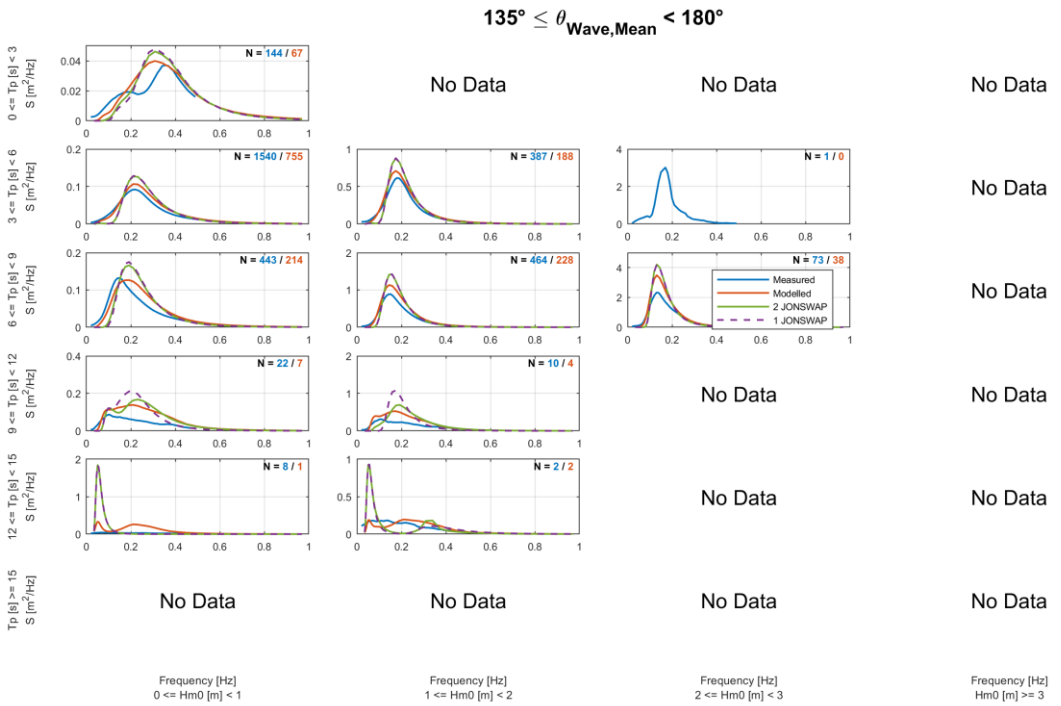



Figure C.156. AWAC B1, omni-directional spectral validation, by Hm0 and Tp, 135-180° sector.

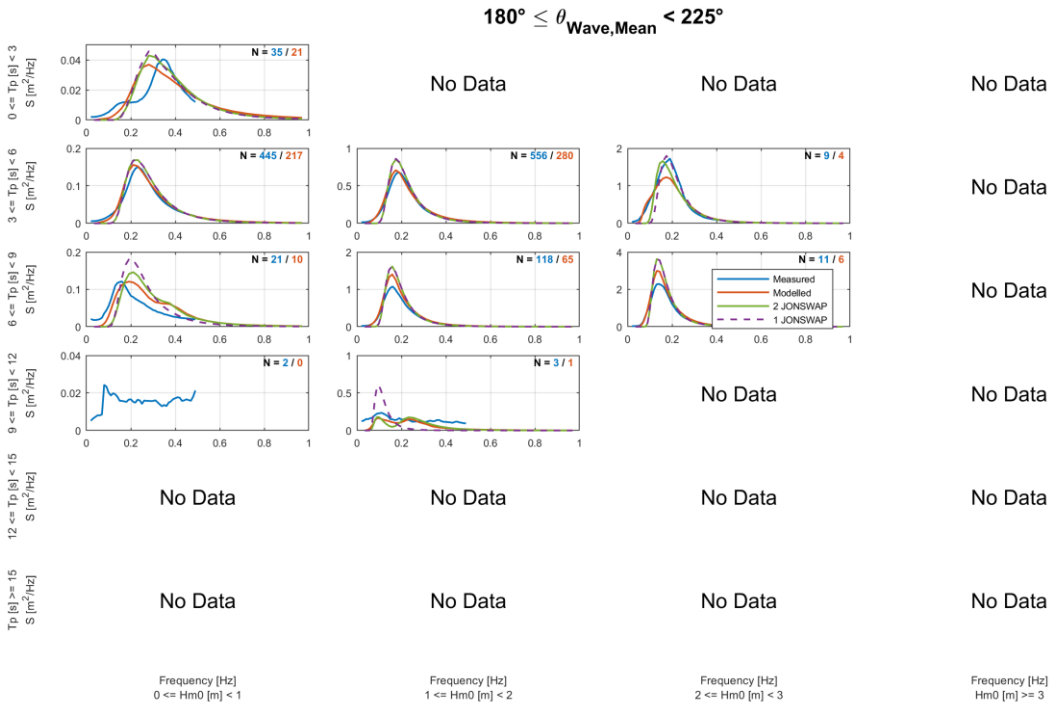



Figure C.157. AWAC B1, omni-directional spectral validation, by Hm0 and Tp, 180-225° sector.

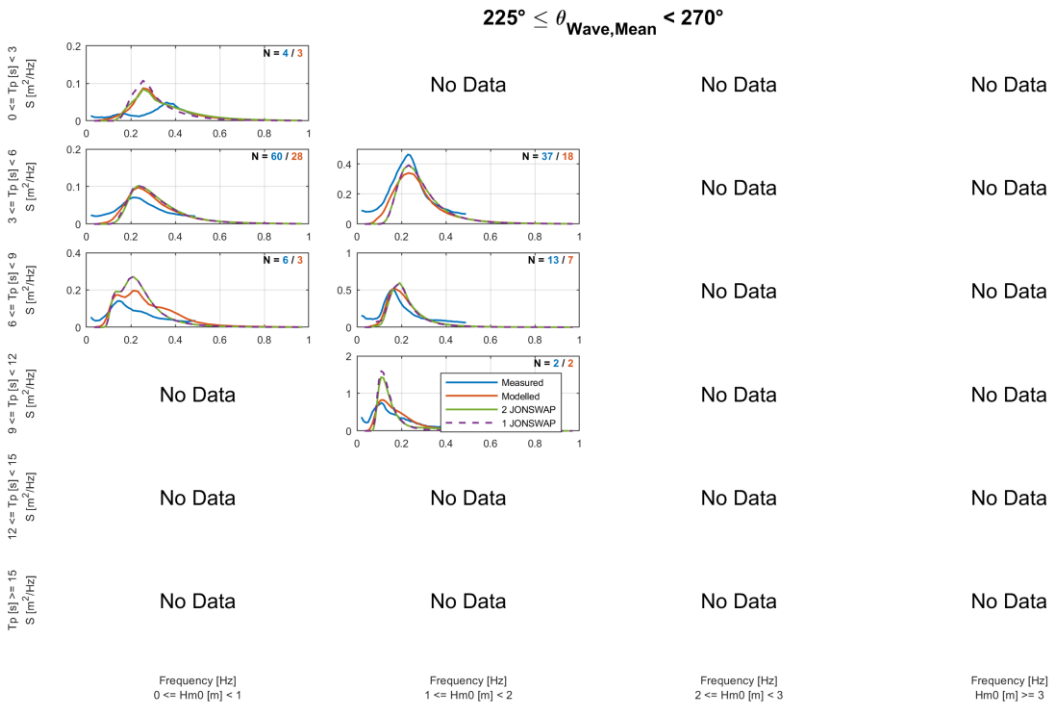



Figure C.158. AWAC B1, omni-directional spectral validation, by Hm0 and Tp, 225-270° sector.

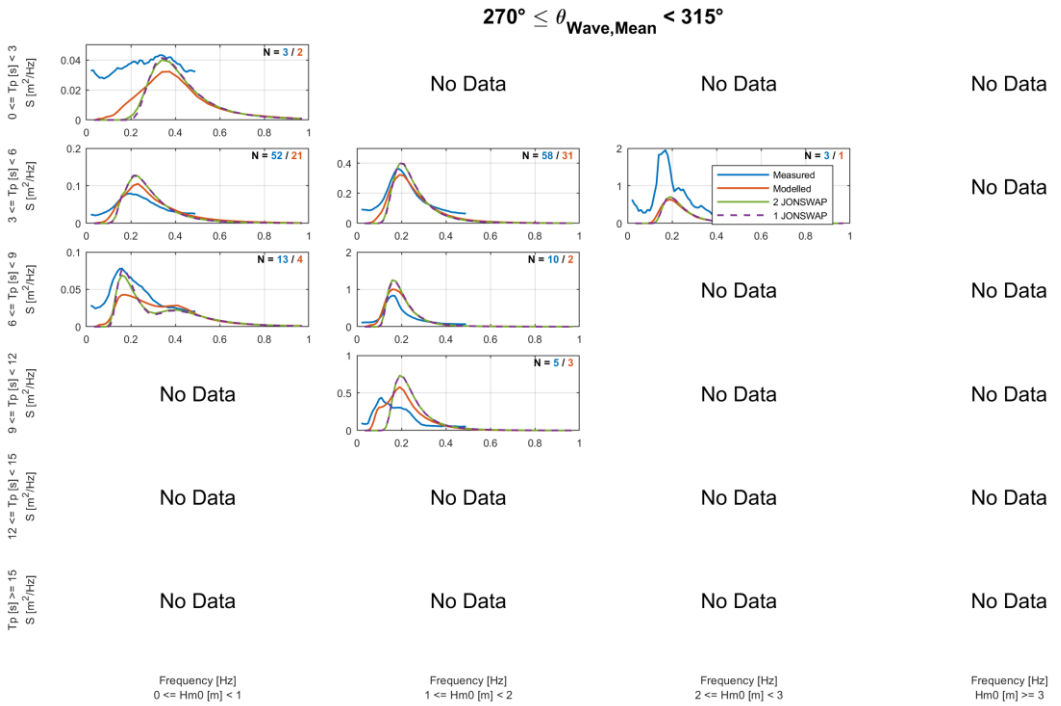



Figure C.159. AWAC B1, omni-directional spectral validation, by Hm0 and Tp, 270-315° sector.

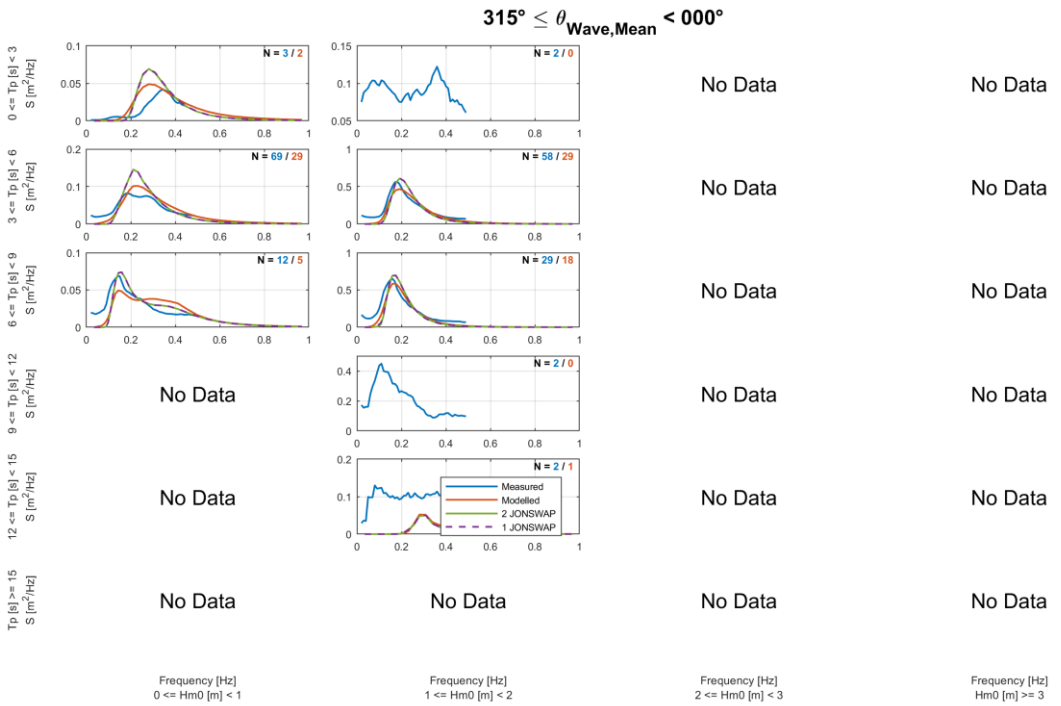



Figure C.160. AWAC B1, omni-directional spectral validation, by Hm0 and Tp, 315-0° sector.

### C.7.3.3 Custom Sectors

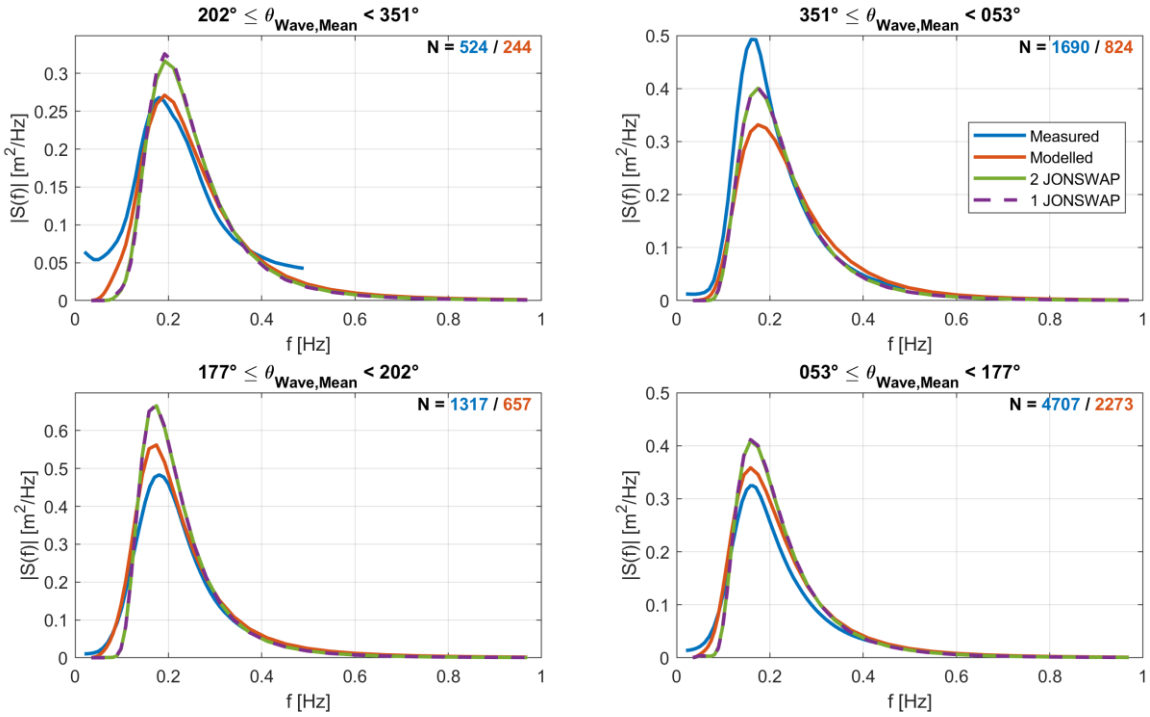



Figure C.161. AWAC B1, omni-directional spectral validation, custom sectors.

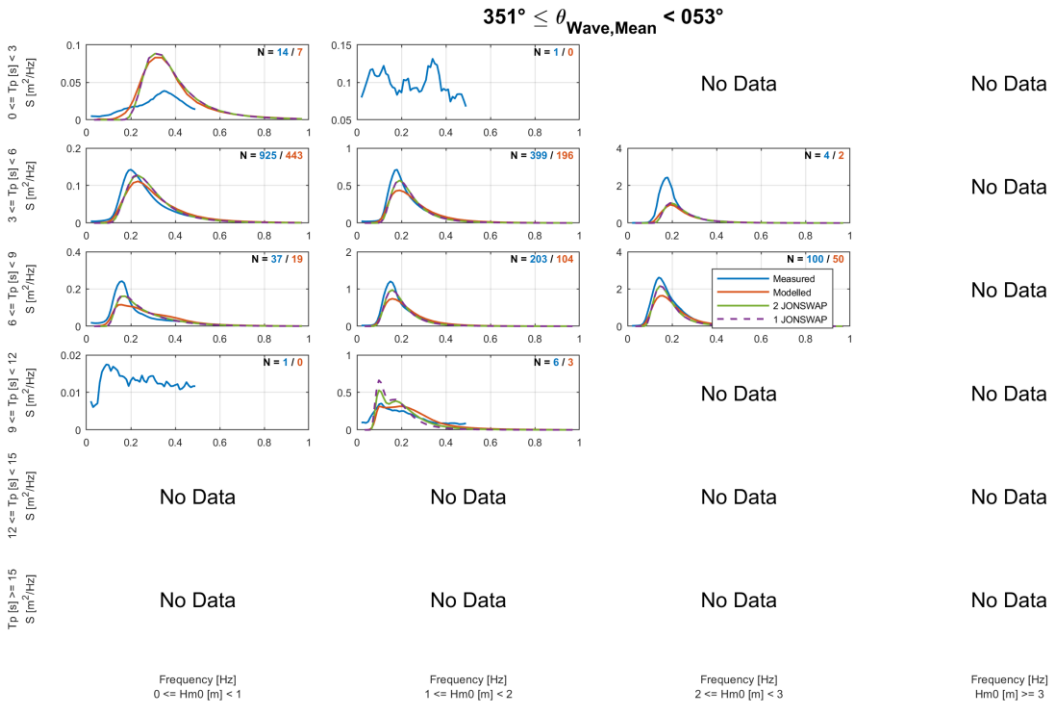



Figure C.162. AWAC B1, omni-directional spectral validation, by Hm0 and Tp, 351-053° sector.

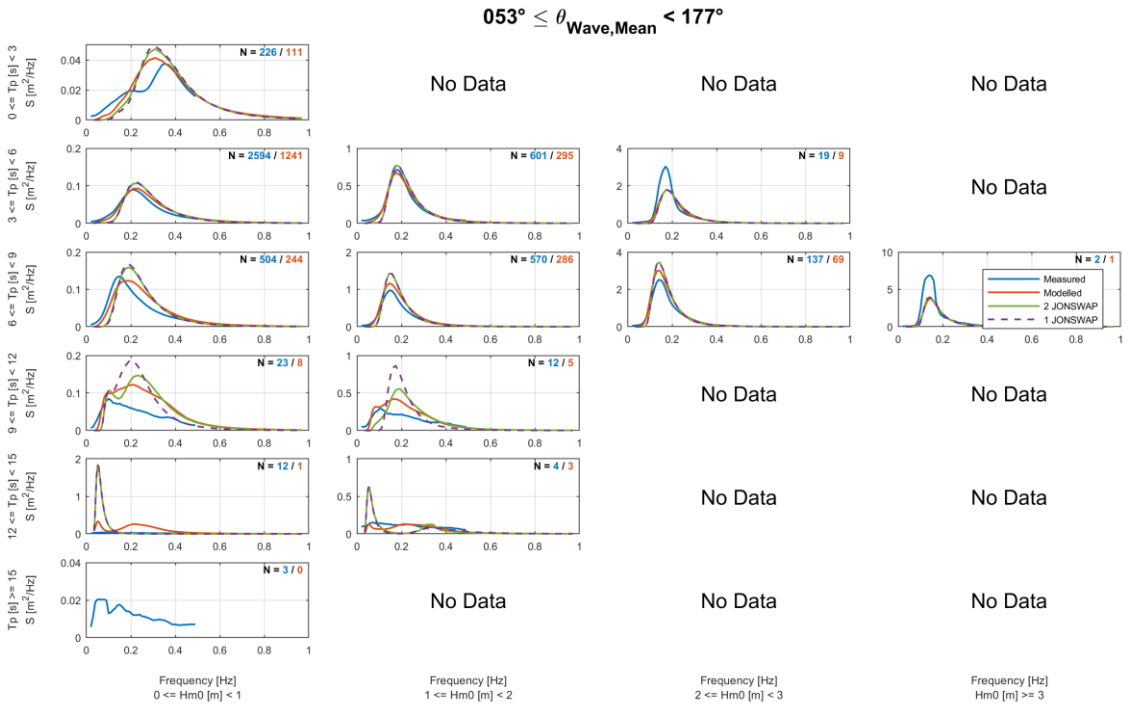



Figure C.163. AWAC B1, omni-directional spectral validation, by Hm0 and Tp, 053-177° sector.

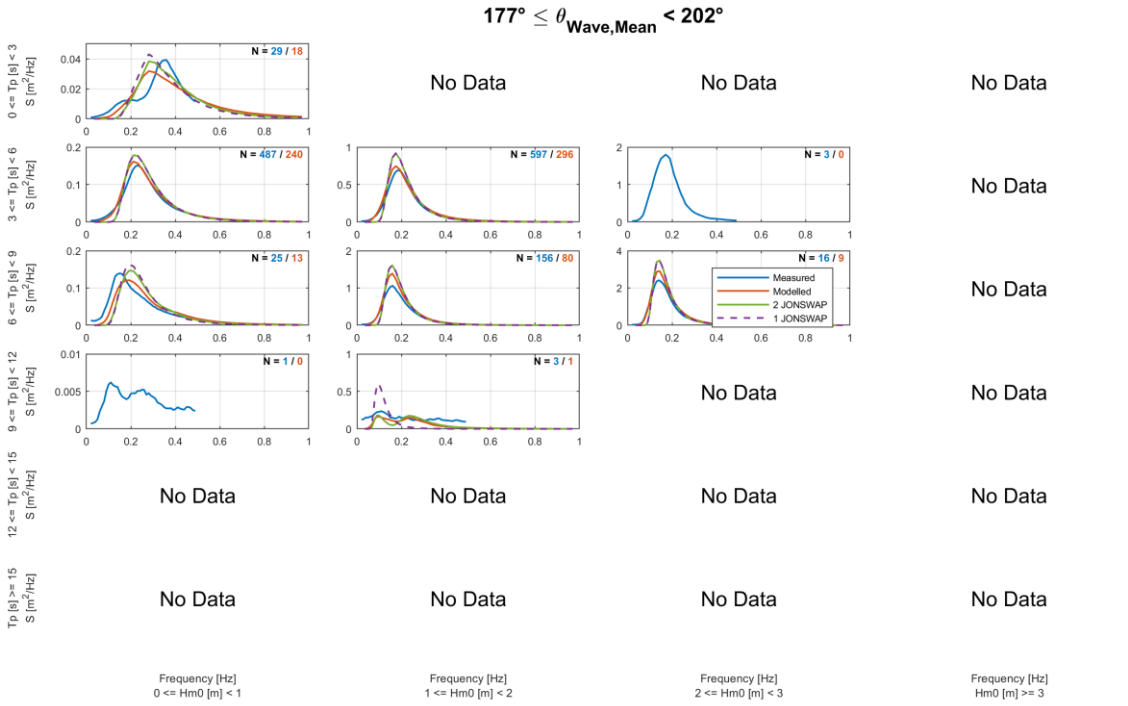



Figure C.164. AWAC B1, omni-directional spectral validation, by Hm0 and Tp, 177-202° sector.

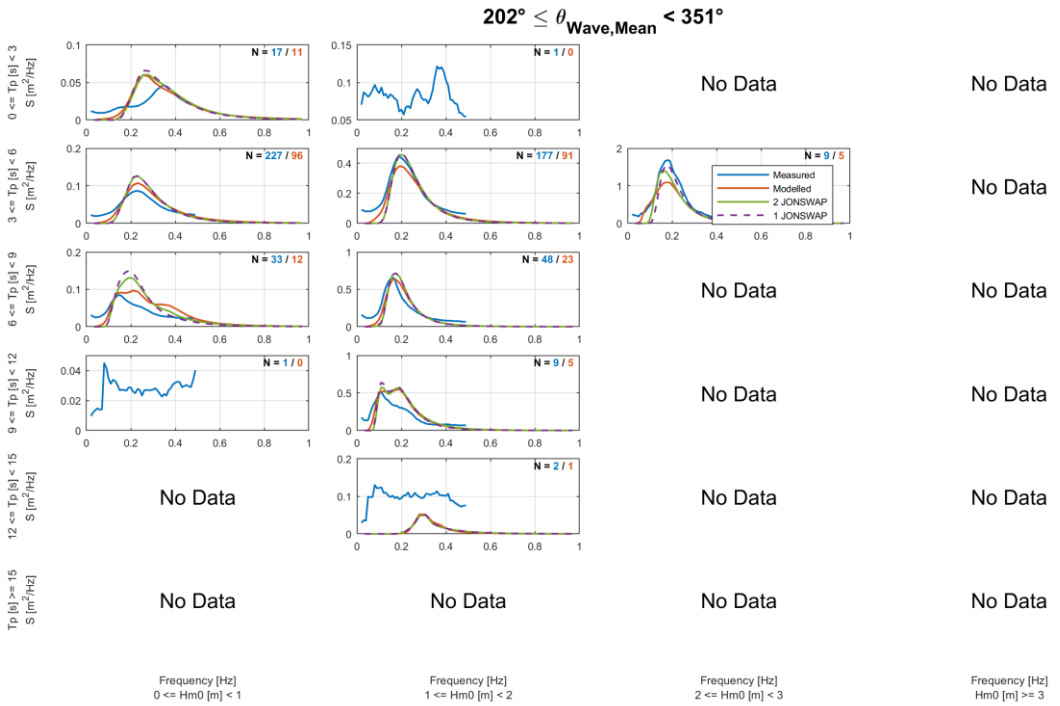



Figure C.165. AWAC B1, omni-directional spectral validation, by Hm0 and Tp, 202-351° sector.

## C.7.4 AWAC C

### C.7.4.1 Omni-Directional

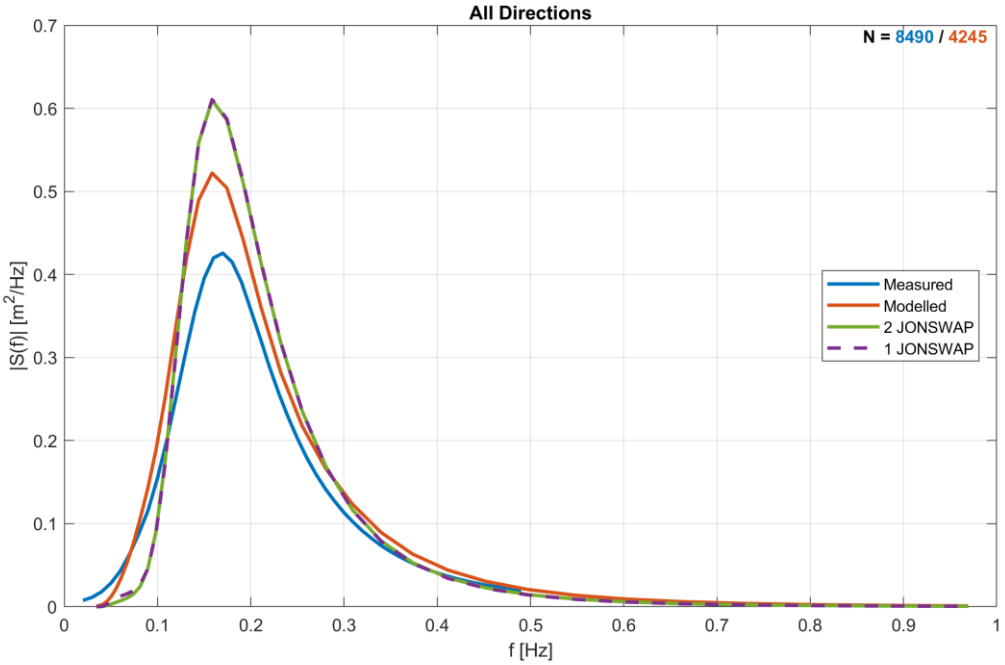



Figure C.166. AWAC C, omni-directional spectral validation, all data.

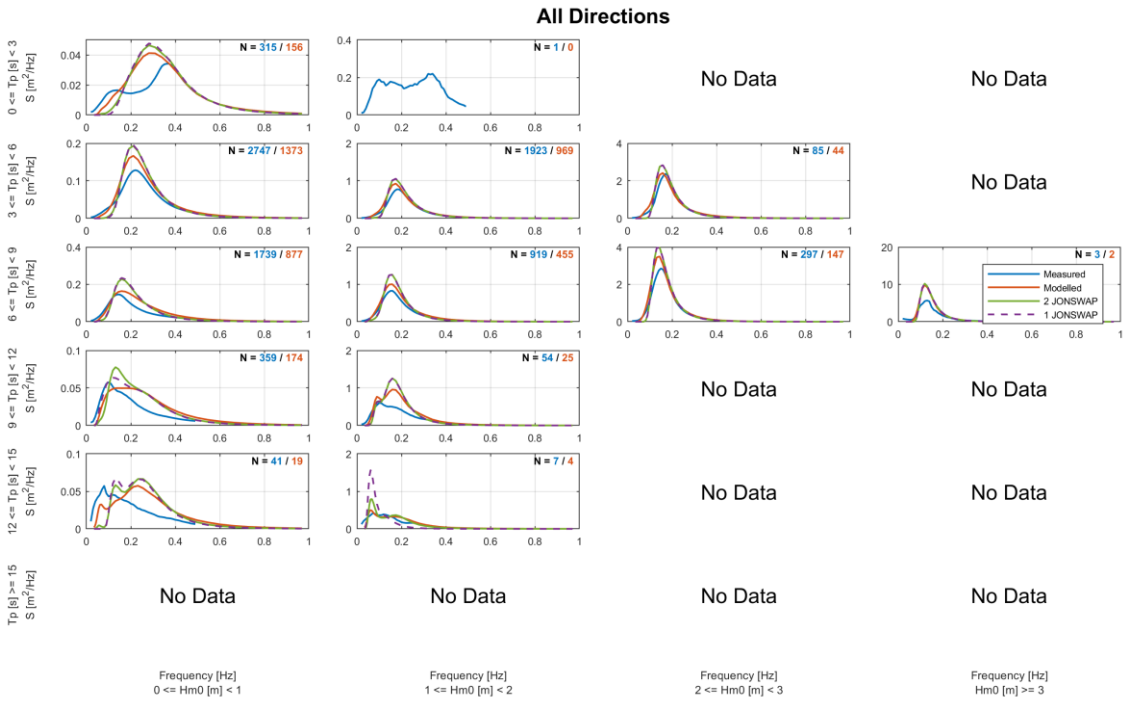



Figure C.167. AWAC C, omni-directional spectral validation, by Hm0 and Tp, all directions.

### C.7.4.2 45° Sectors

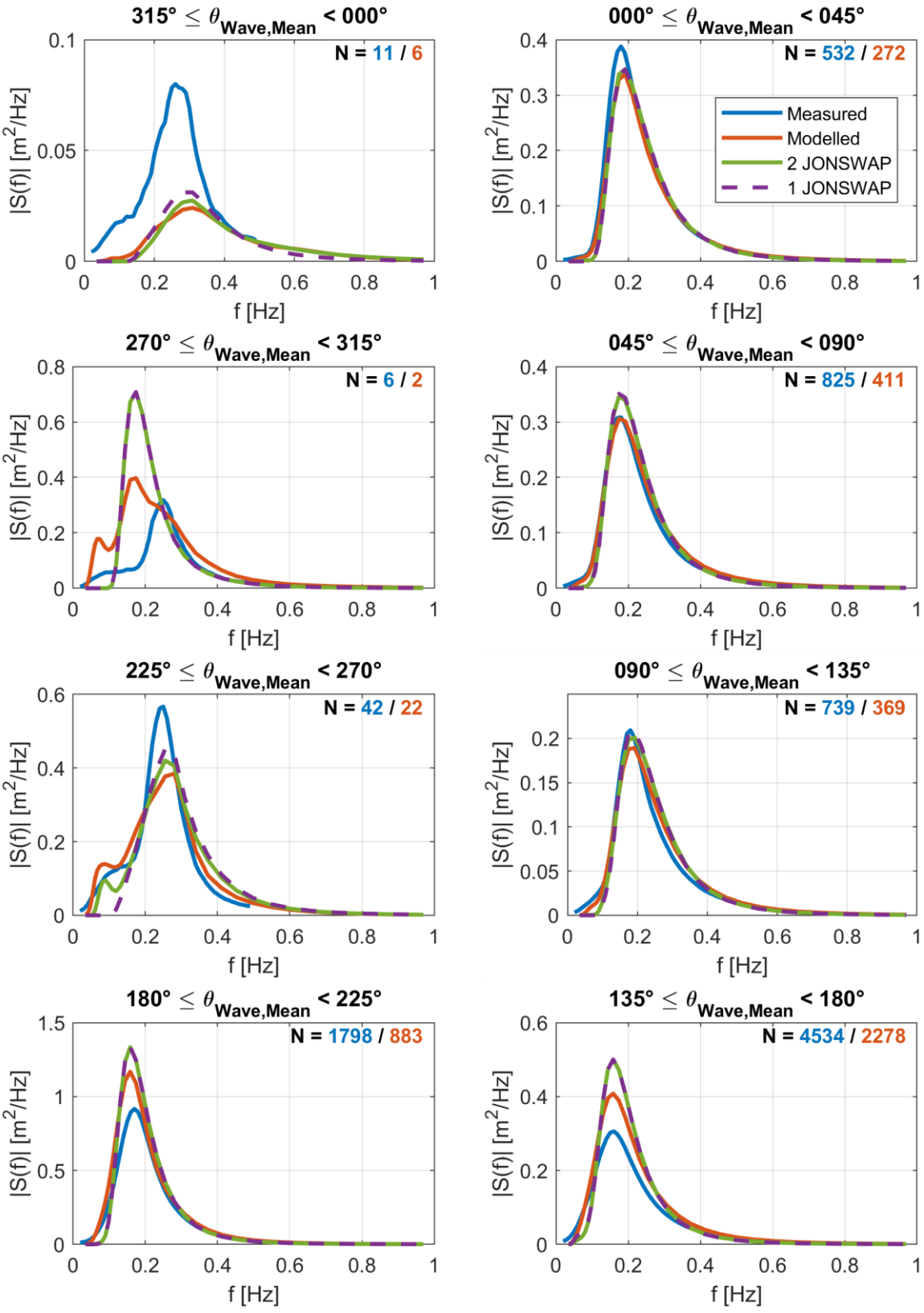



Figure C.168. AWAC C, omni-directional spectral validation, 45° sectors.




Figure C.169. AWAC C, omni-directional spectral validation, by Hm0 and Tp, 0-45° sector.

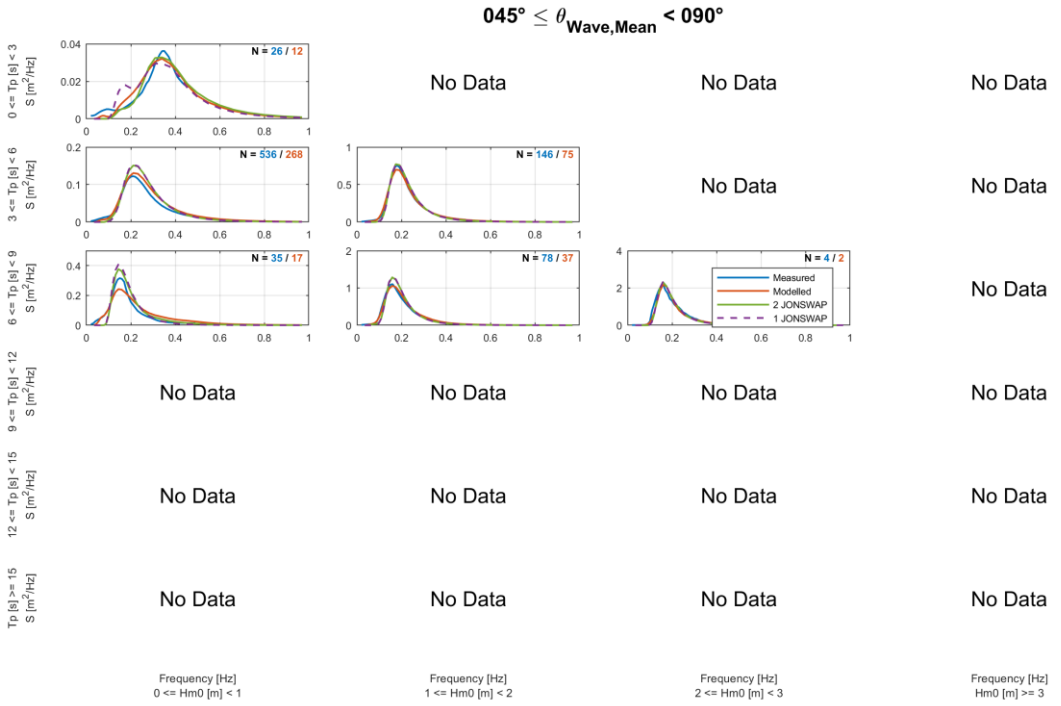



Figure C.170. AWAC C, omni-directional spectral validation, by Hm0 and Tp, 45-90° sector.

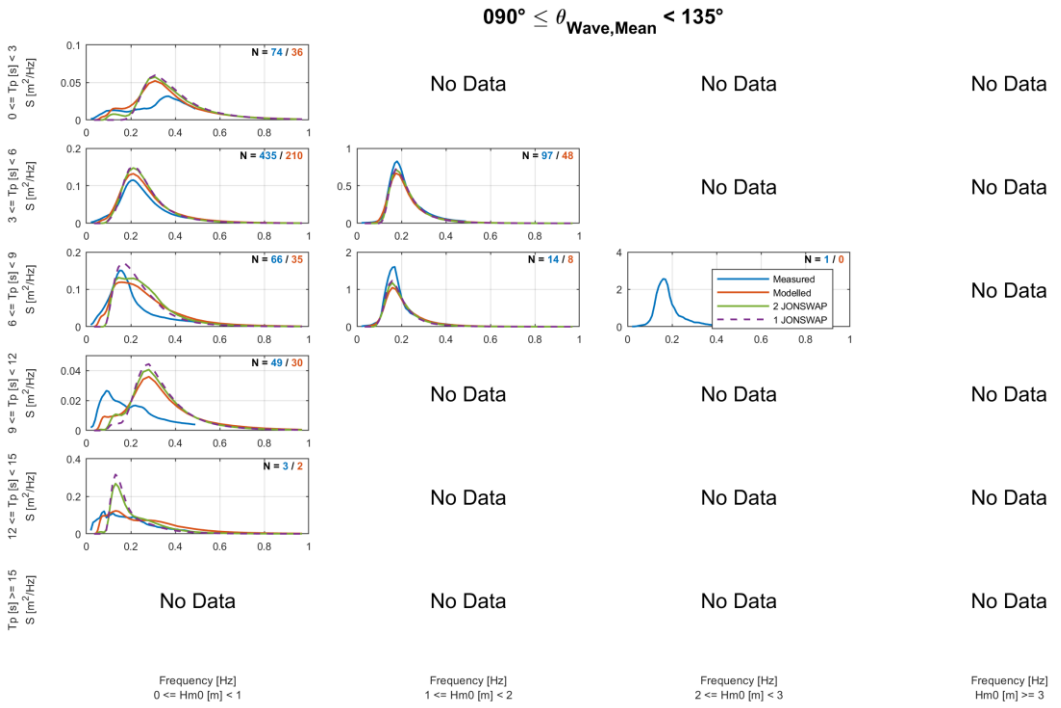



Figure C.171. AWAC C, omni-directional spectral validation, by Hm0 and Tp, 90-135° sector.

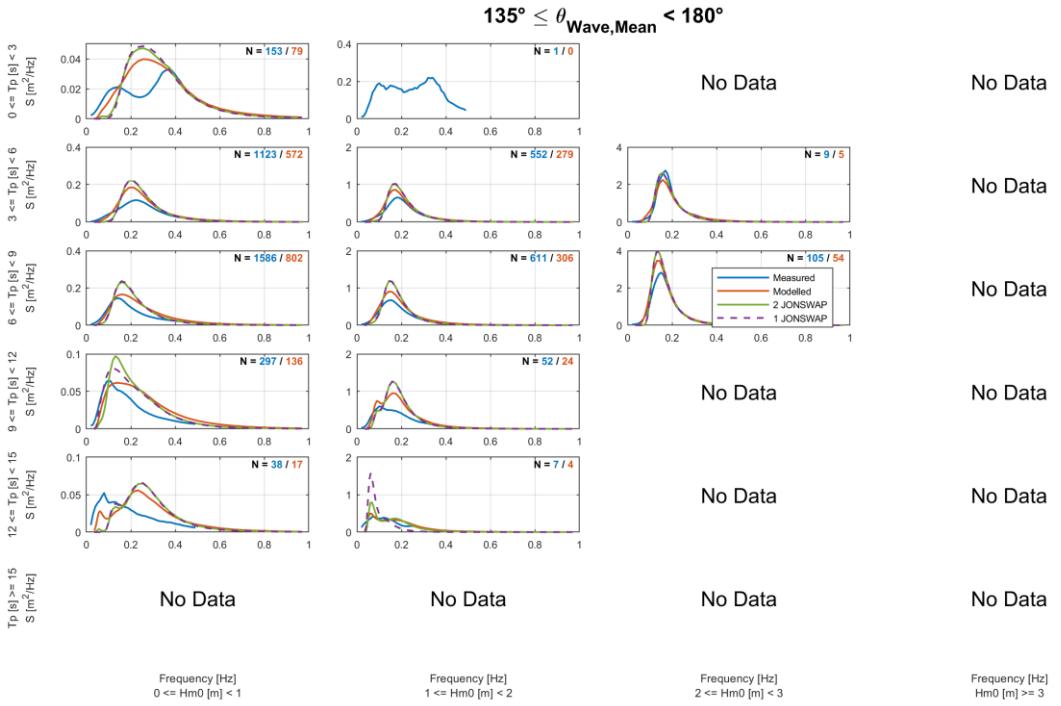



Figure C.172. AWAC C, omni-directional spectral validation, by Hm0 and Tp, 135-180° sector.

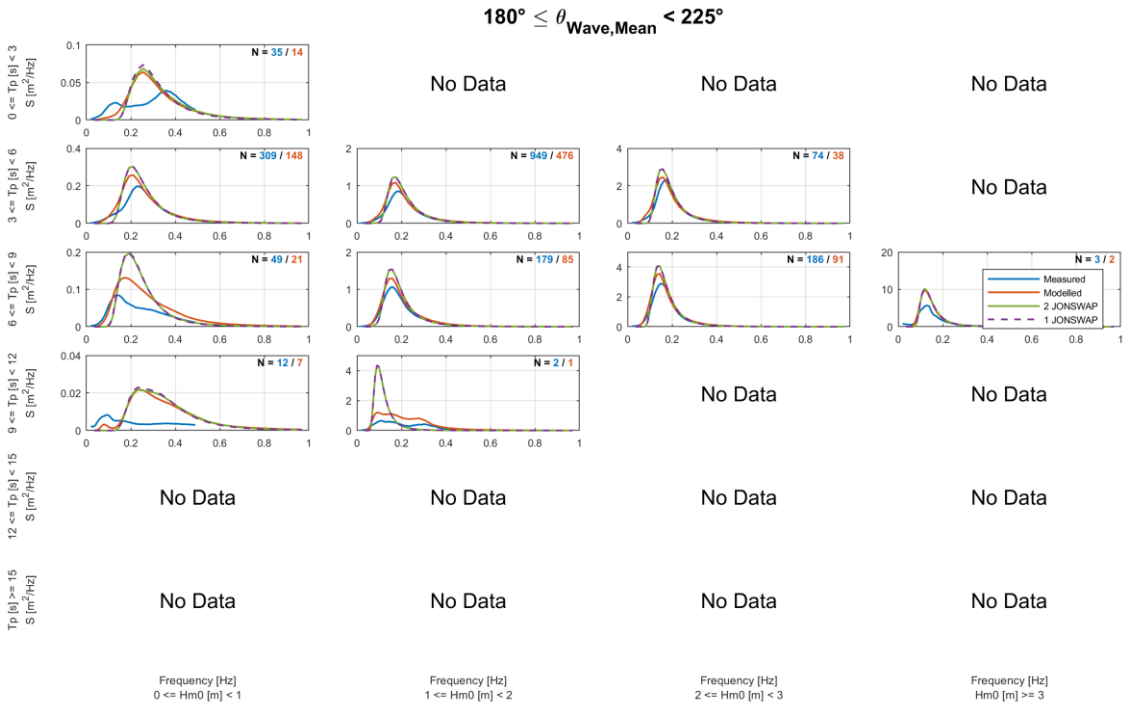



Figure C.173. AWAC C, omni-directional spectral validation, by Hm0 and Tp, 180-225° sector.




Figure C.174. AWAC C, omni-directional spectral validation, by Hm0 and Tp, 225-270° sector.

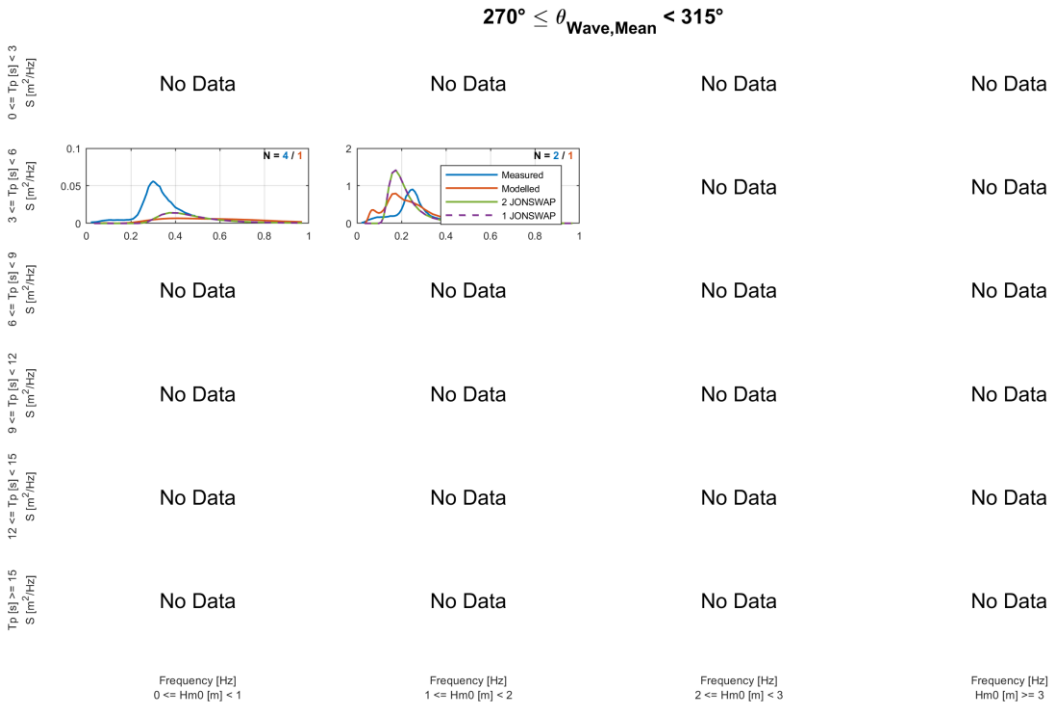



Figure C.175. AWAC C, omni-directional spectral validation, by Hm0 and Tp, 270-315° sector.

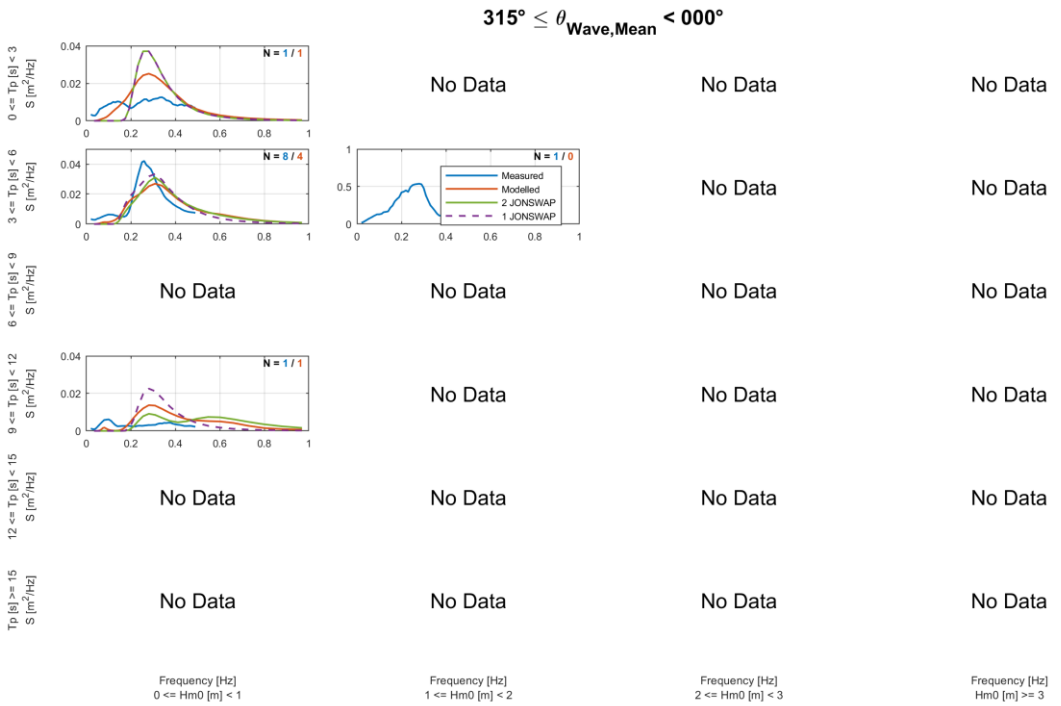



Figure C.176. AWAC C, omni-directional spectral validation, by Hm0 and Tp, 315-0° sector.

### C.7.4.3 Custom Sectors

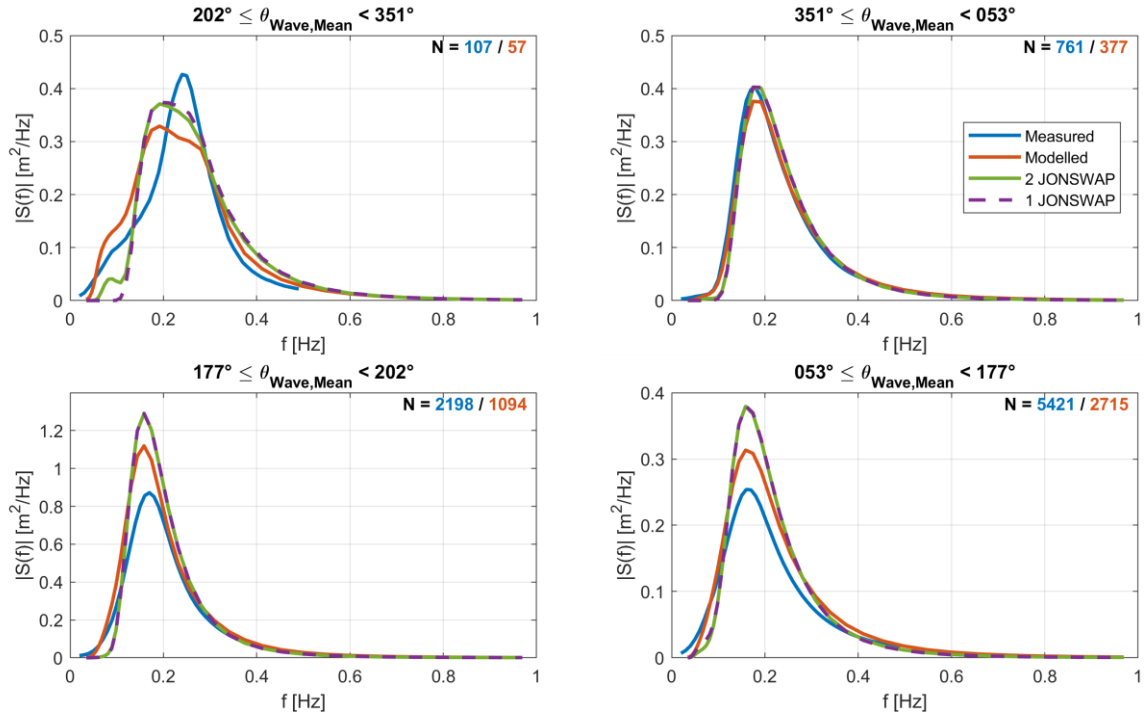



Figure C.177. AWAC C, omni-directional spectral validation, custom sectors.

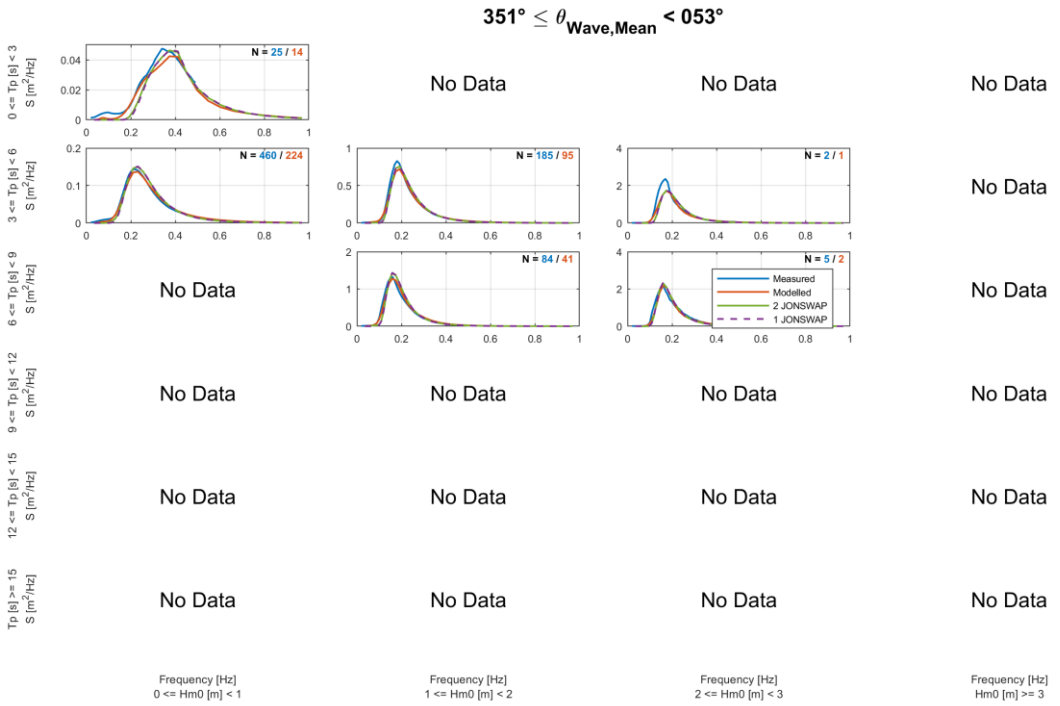



Figure C.178. AWAC C, omni-directional spectral validation, by Hm0 and Tp, 351-053° sector.

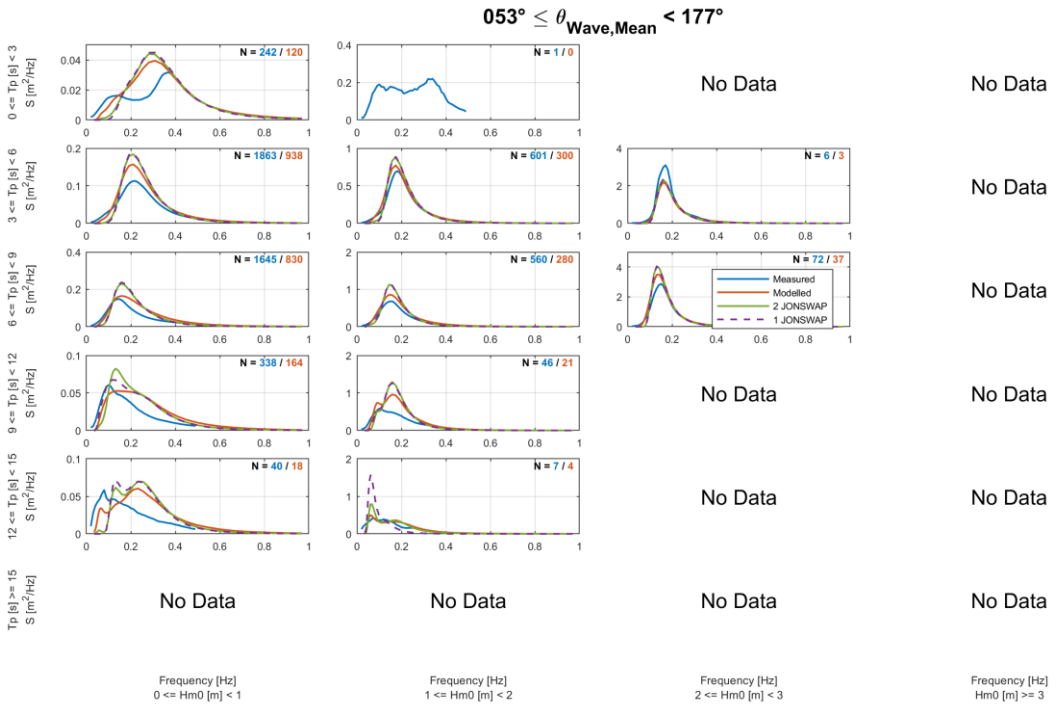



Figure C.179. AWAC C, omni-directional spectral validation, by Hm0 and Tp, 053-177° sector.

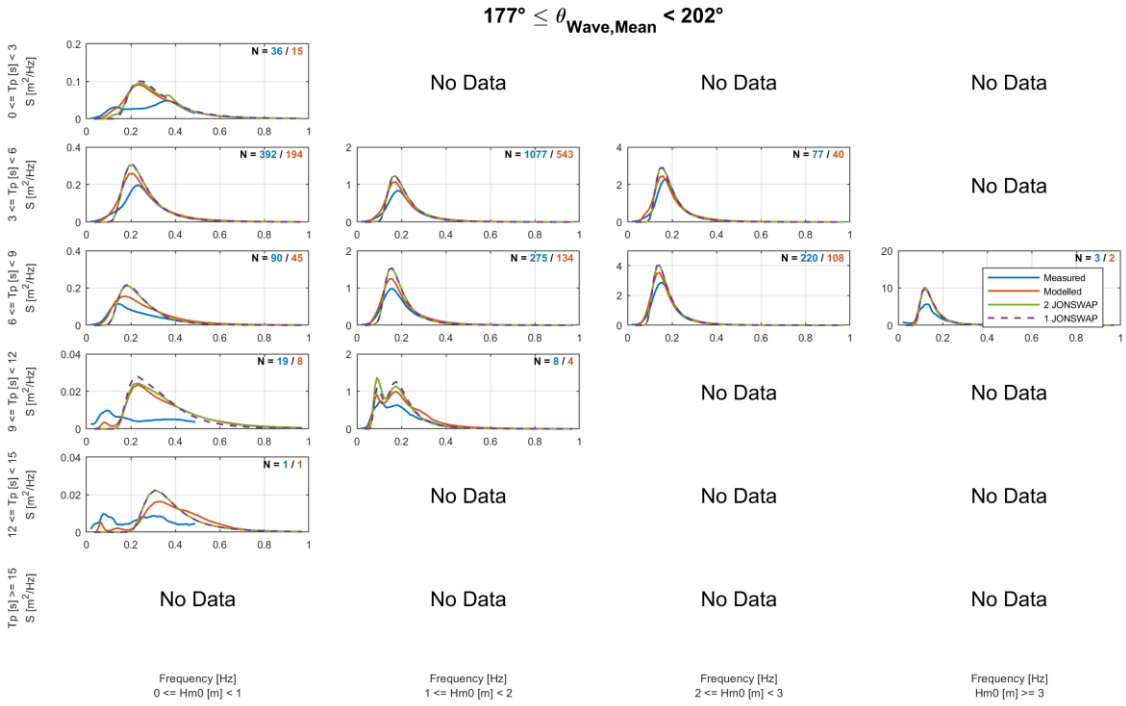



Figure C.180. AWAC C, omni-directional spectral validation, by Hm0 and Tp, 177-202° sector.

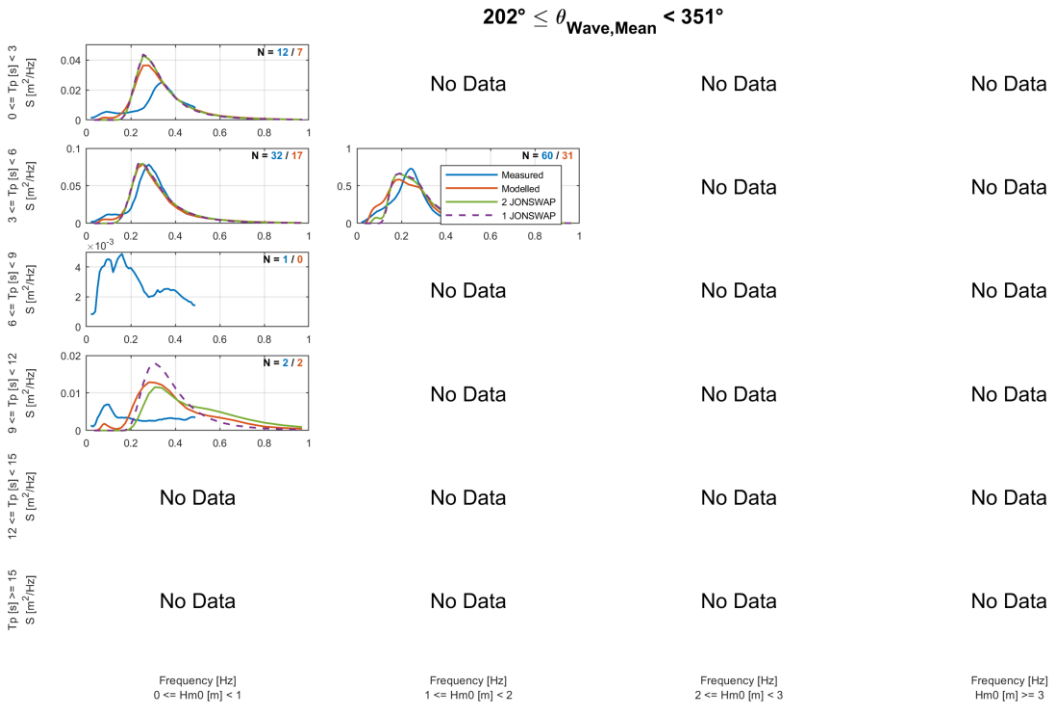



Figure C.181. AWAC C, omni-directional spectral validation, by Hm0 and Tp, 202-351° sector.

## C.7.5 AWAC D1

### C.7.5.1 Omni-Directional

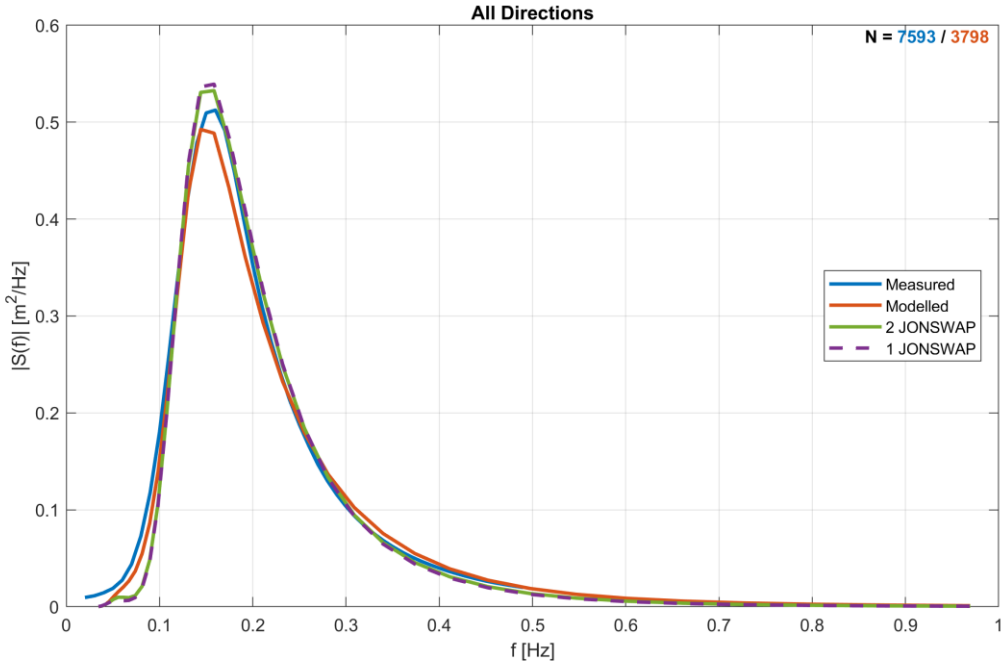



Figure C.182. AWAC D1, omni-directional spectral validation, all data.

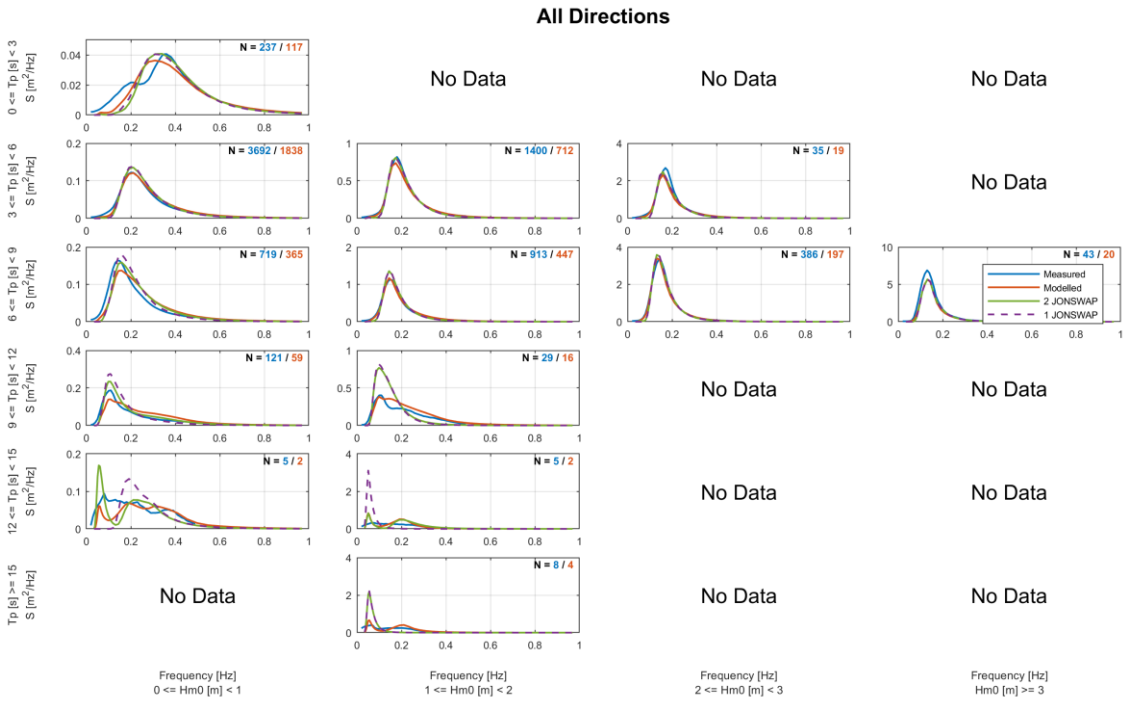



Figure C.183. AWAC D1, omni-directional spectral validation, by Hm0 and Tp, all directions.

### C.7.5.2 45° Sectors

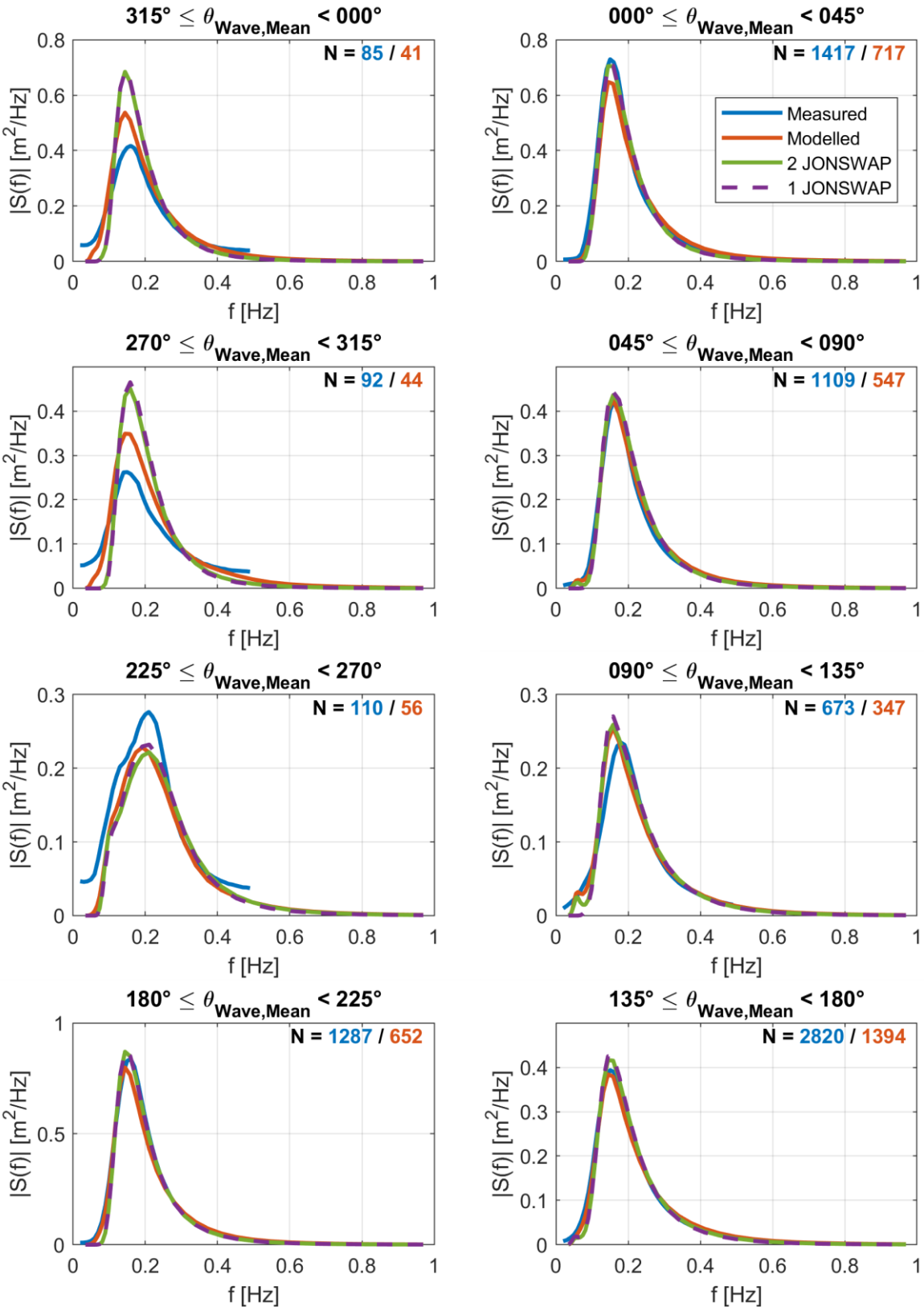



Figure C.184. AWAC D1, omni-directional spectral validation, 45° sectors.

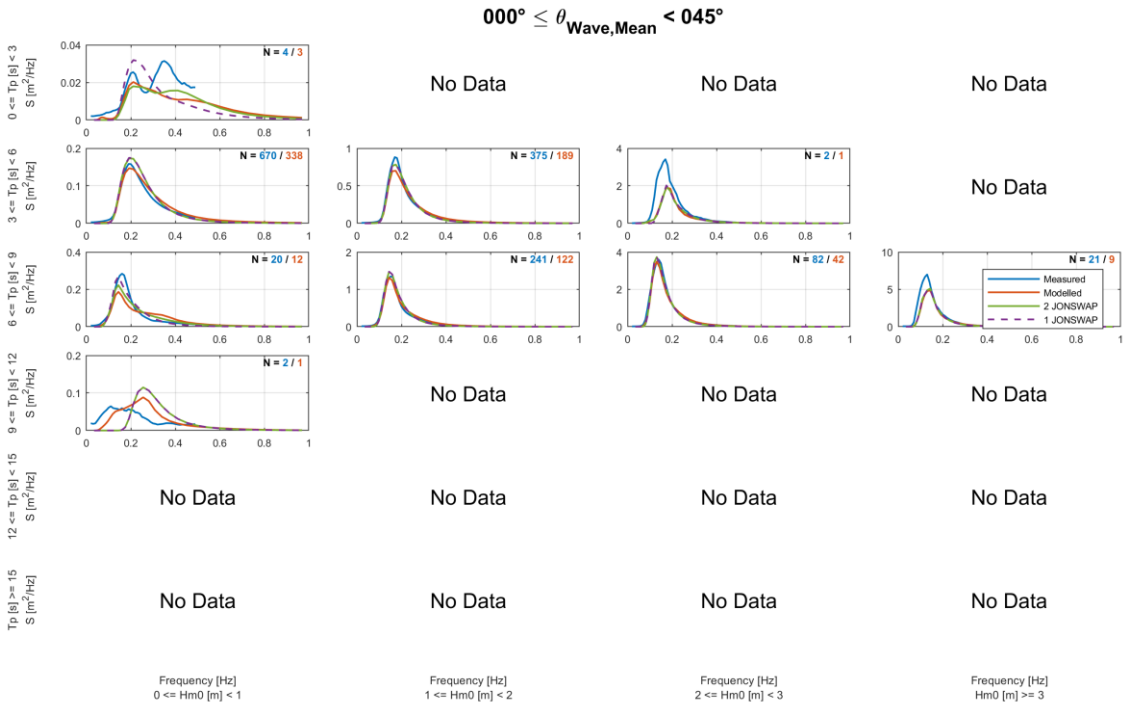



Figure C.185. AWAC D1, omni-directional spectral validation, by Hm0 and Tp, 0-45° sector.

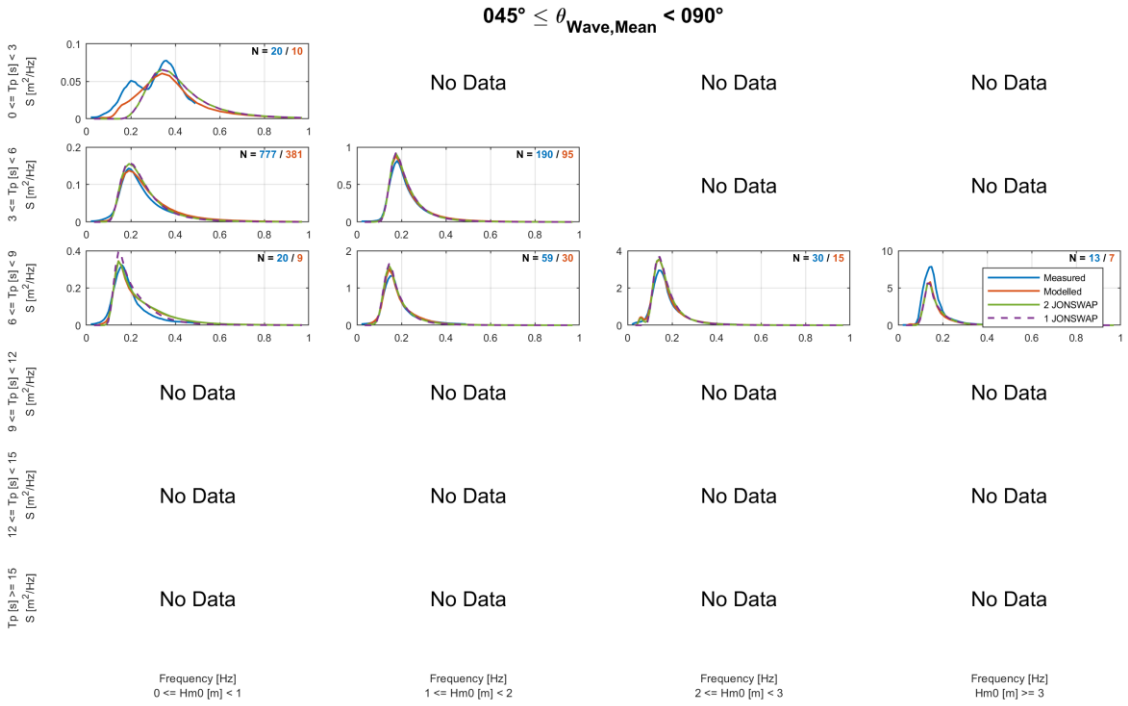



Figure C.186. AWAC D1, omni-directional spectral validation, by Hm0 and Tp, 45-90° sector.

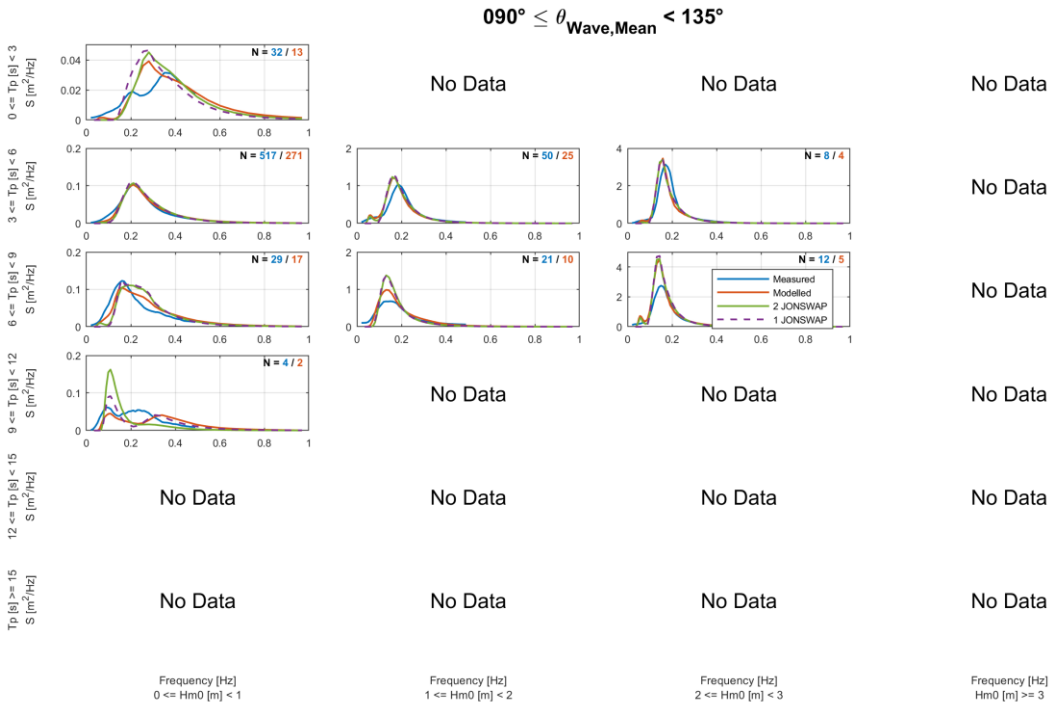



Figure C.187. AWAC D1, omni-directional spectral validation, by Hm0 and Tp, 90-135° sector.

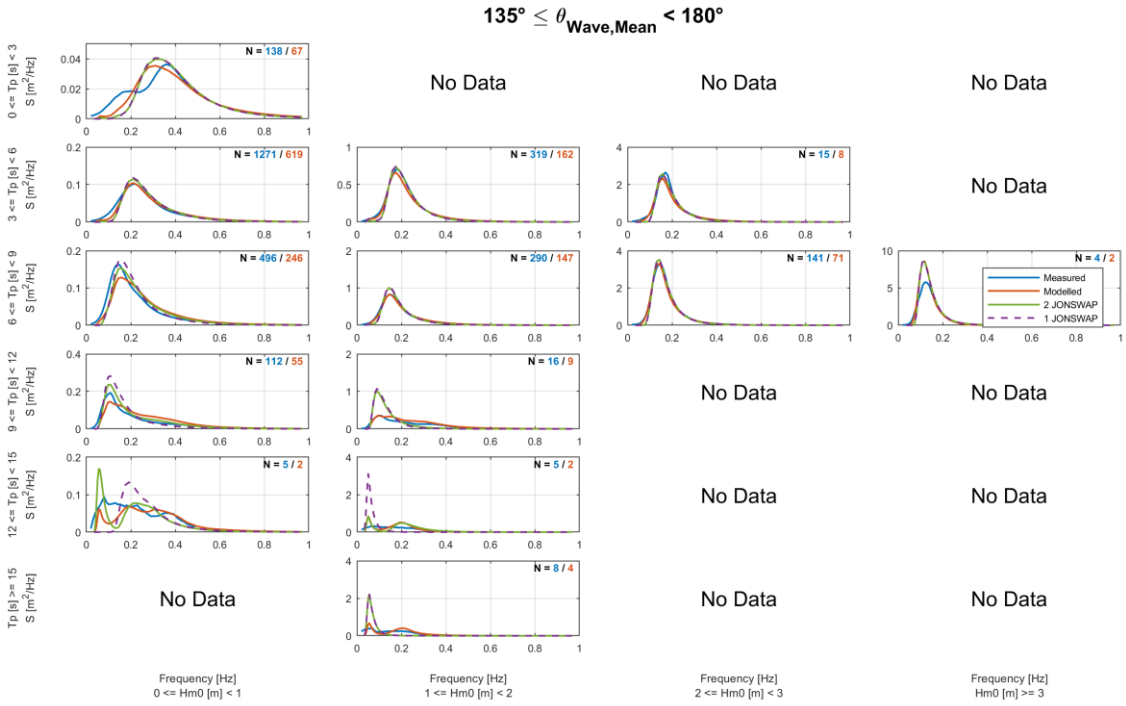



Figure C.188. AWAC D1, omni-directional spectral validation, by Hm0 and Tp, 135-180° sector.

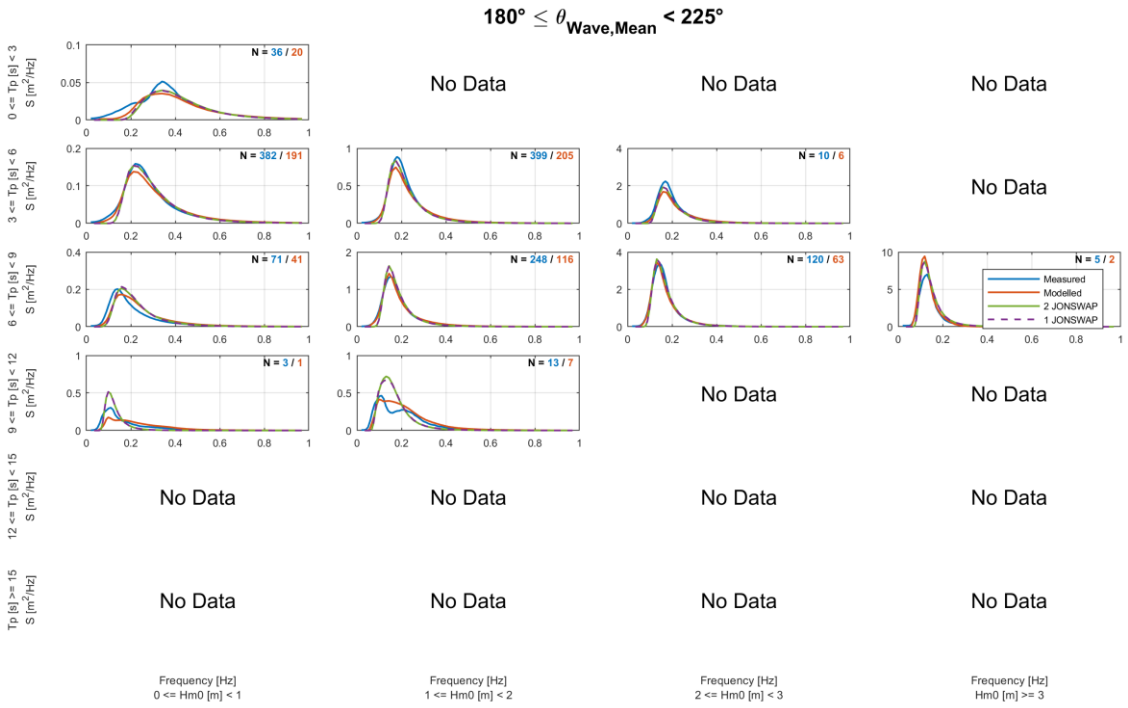



Figure C.189. AWAC D1, omni-directional spectral validation, by Hm0 and Tp, 180-225° sector.

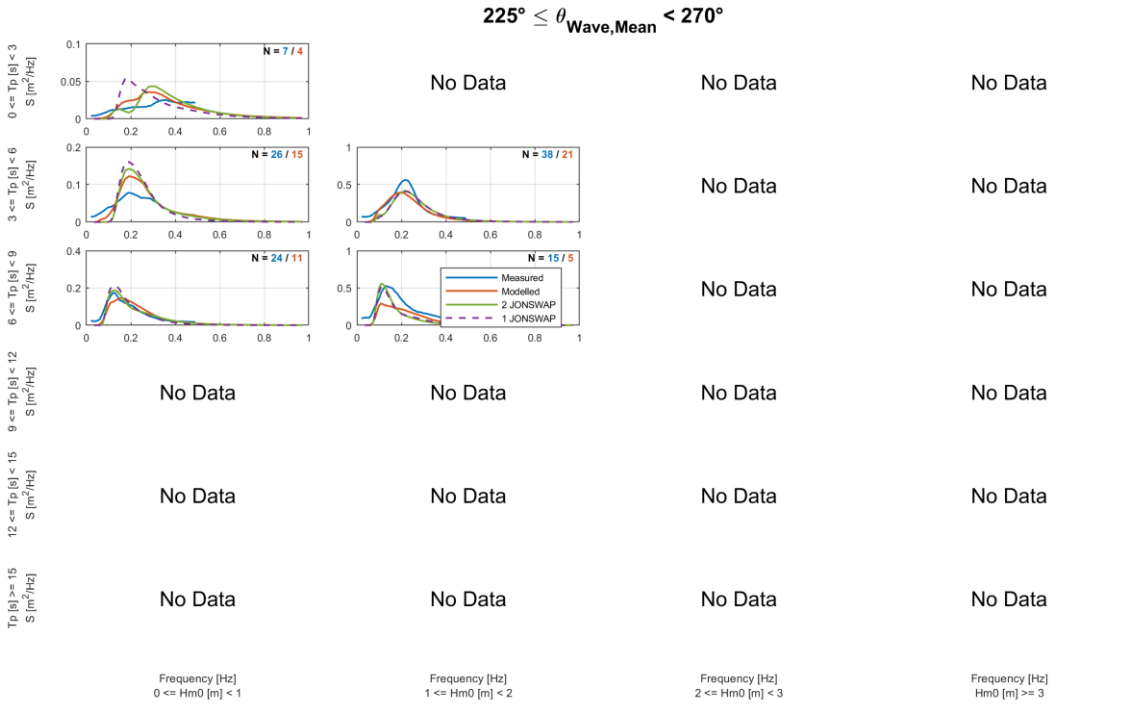



Figure C.190. AWAC D1, omni-directional spectral validation, by Hm0 and Tp, 225-270° sector.

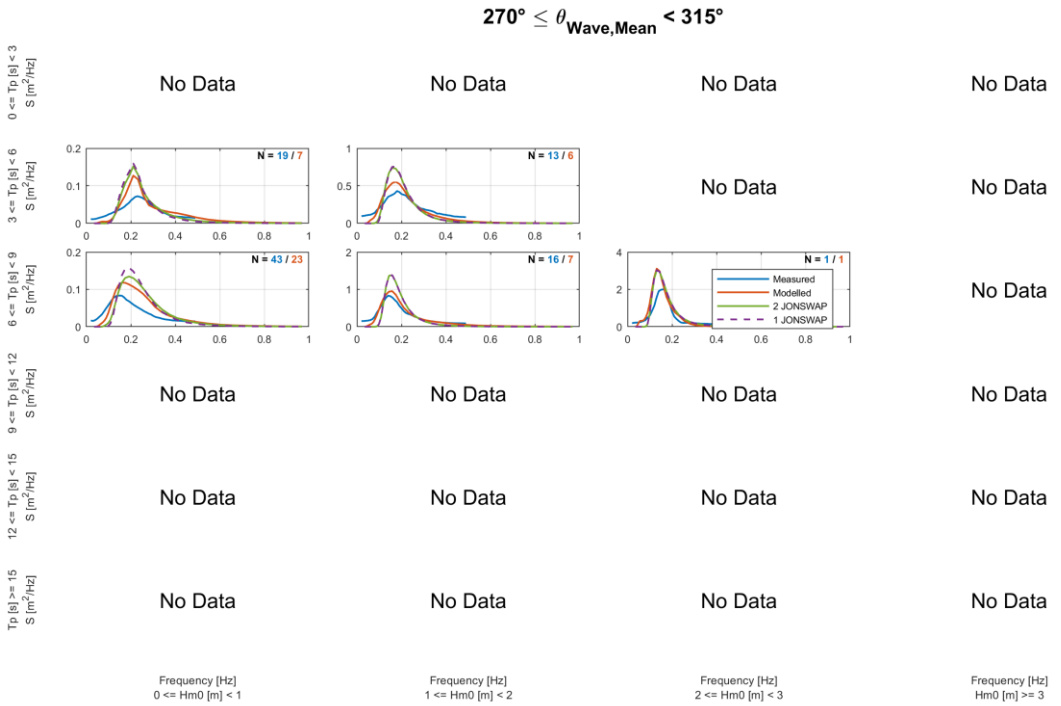



Figure C.191. AWAC D1, omni-directional spectral validation, by Hm0 and Tp, 270-315° sector.

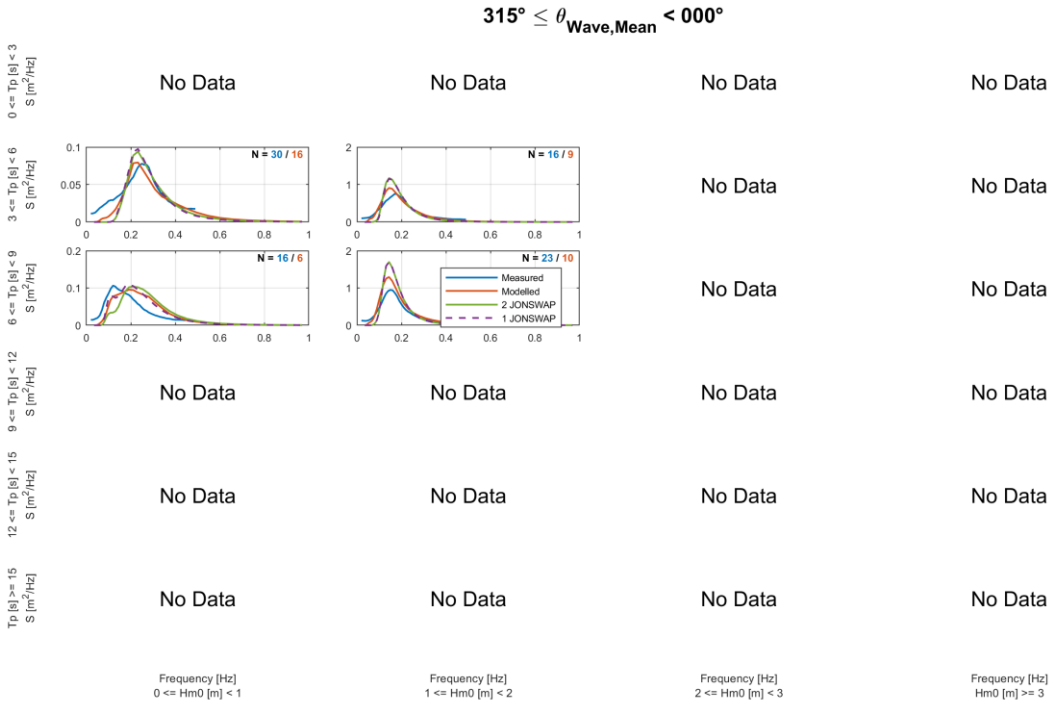



Figure C.192. AWAC D1, omni-directional spectral validation, by Hm0 and Tp, 315-0° sector.

### C.7.5.3 Custom Sectors

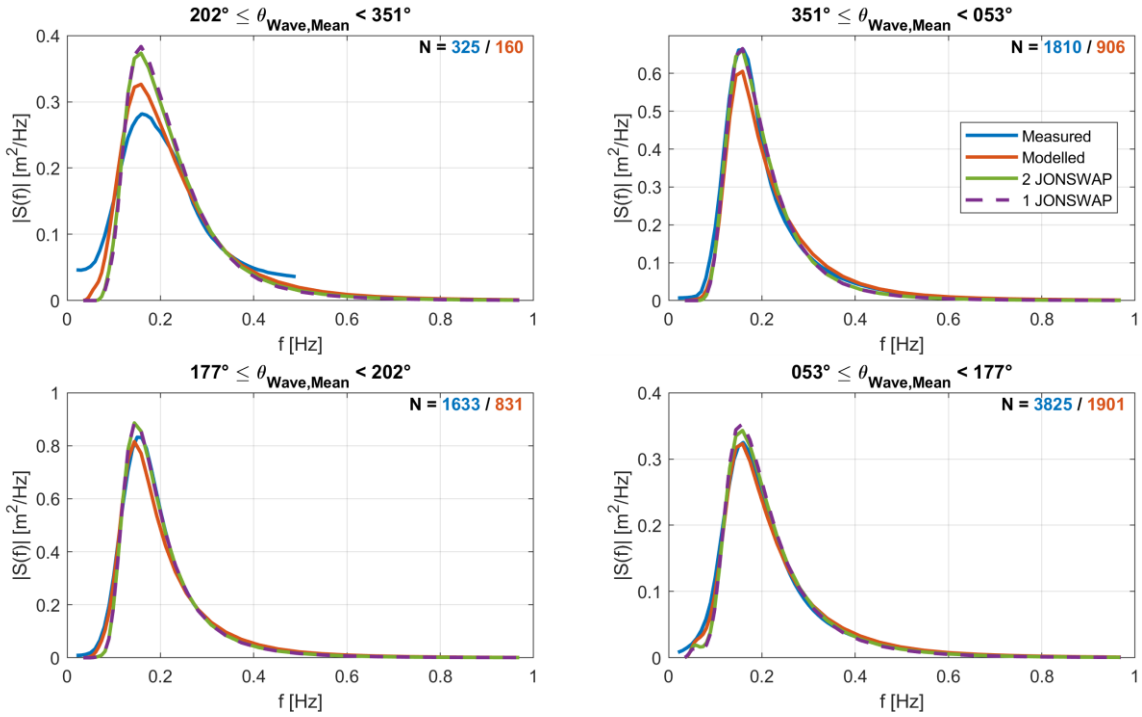



Figure C.193. AWAC D1, omni-directional spectral validation, custom sectors.

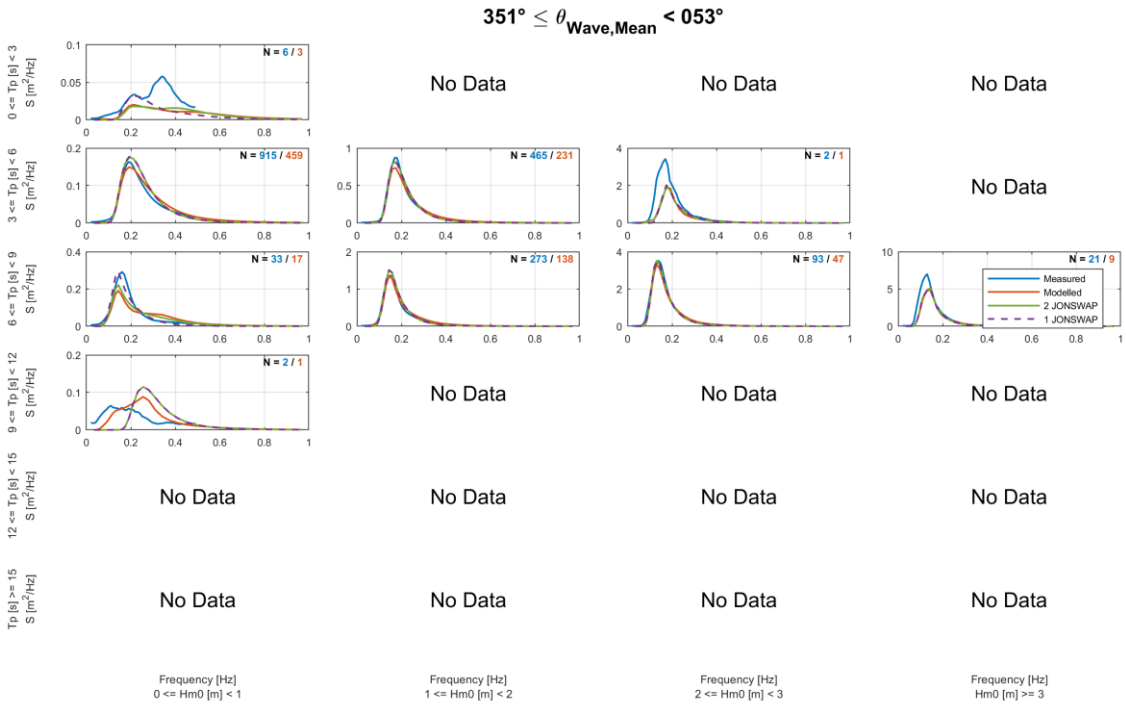



Figure C.194. AWAC D1, omni-directional spectral validation, by Hm0 and Tp, 351-053° sector.

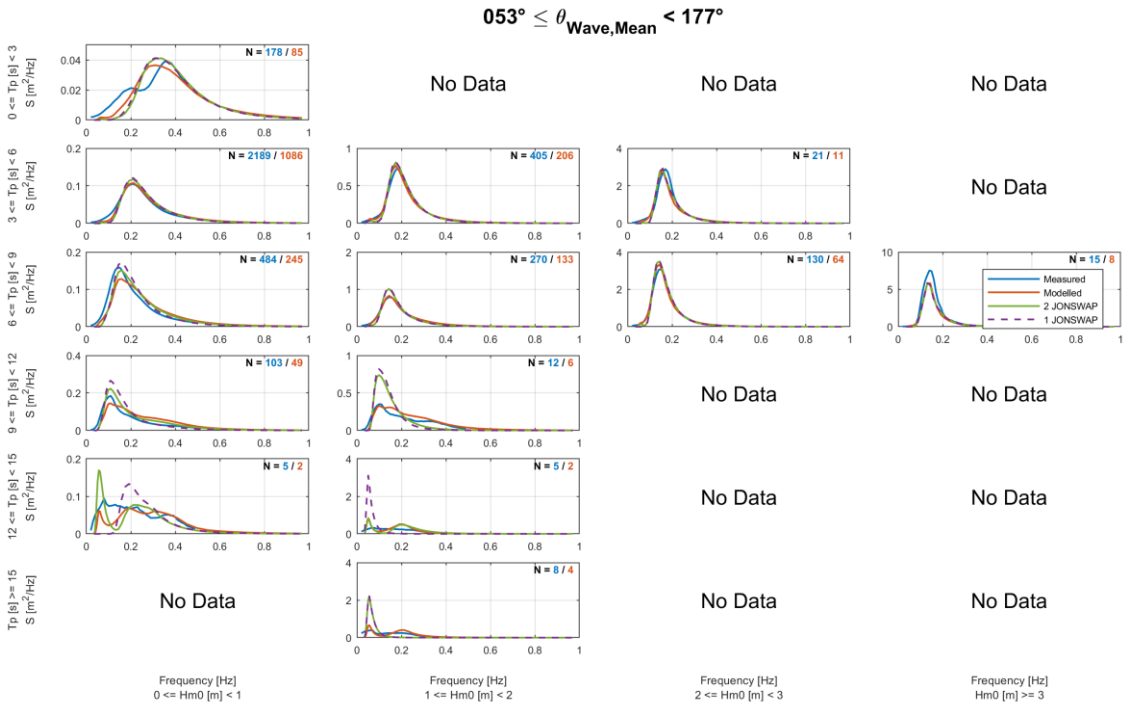



Figure C.195. AWAC D1, omni-directional spectral validation, by Hm0 and Tp, 053-177° sector.

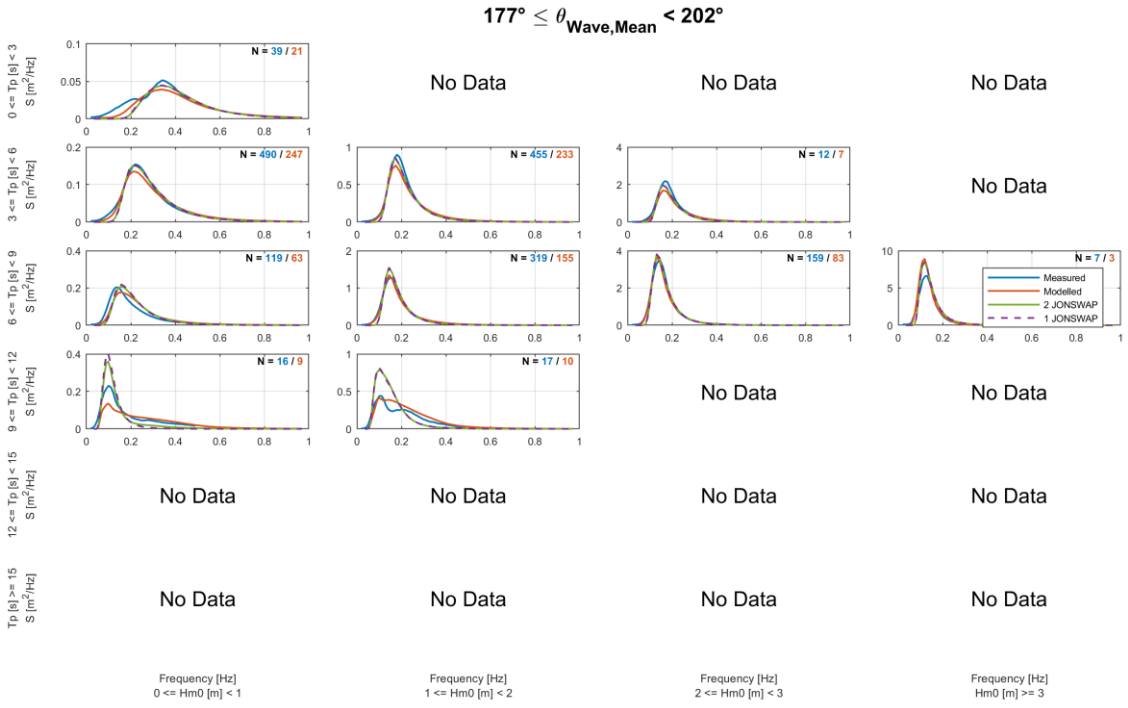



Figure C.196. AWAC D1, omni-directional spectral validation, by Hm0 and Tp, 177-202° sector.

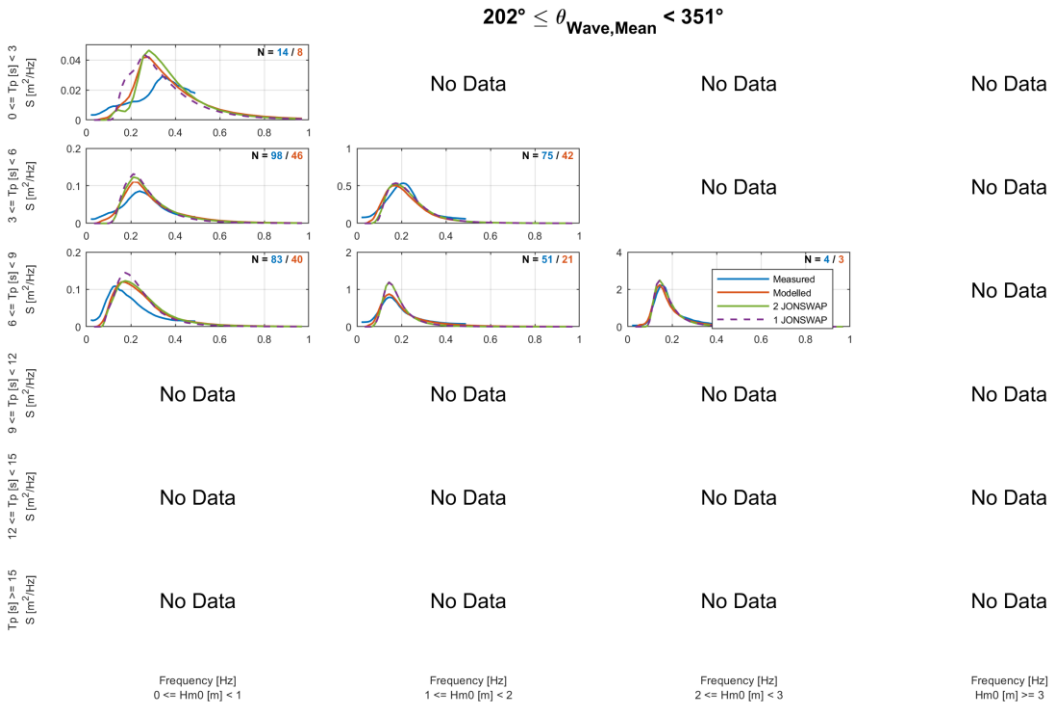



Figure C.197. AWAC D1, omni-directional spectral validation, by Hm0 and Tp, 202-351° sector.

## C.7.6 AWAC E

### C.7.6.1 Omni-Directional

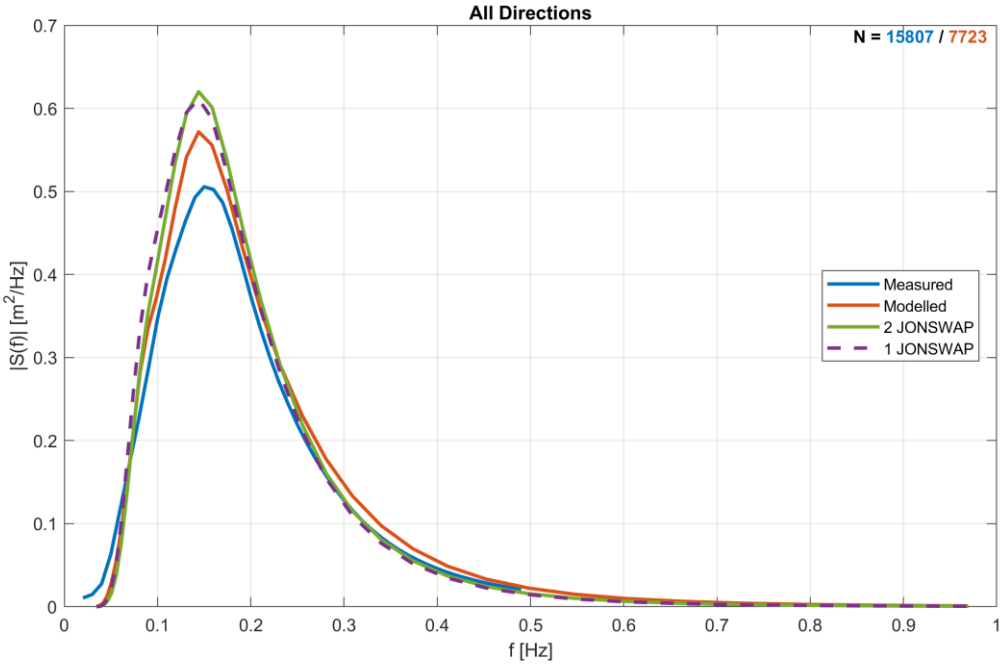



Figure C.198. AWAC E, omni-directional spectral validation, all data.

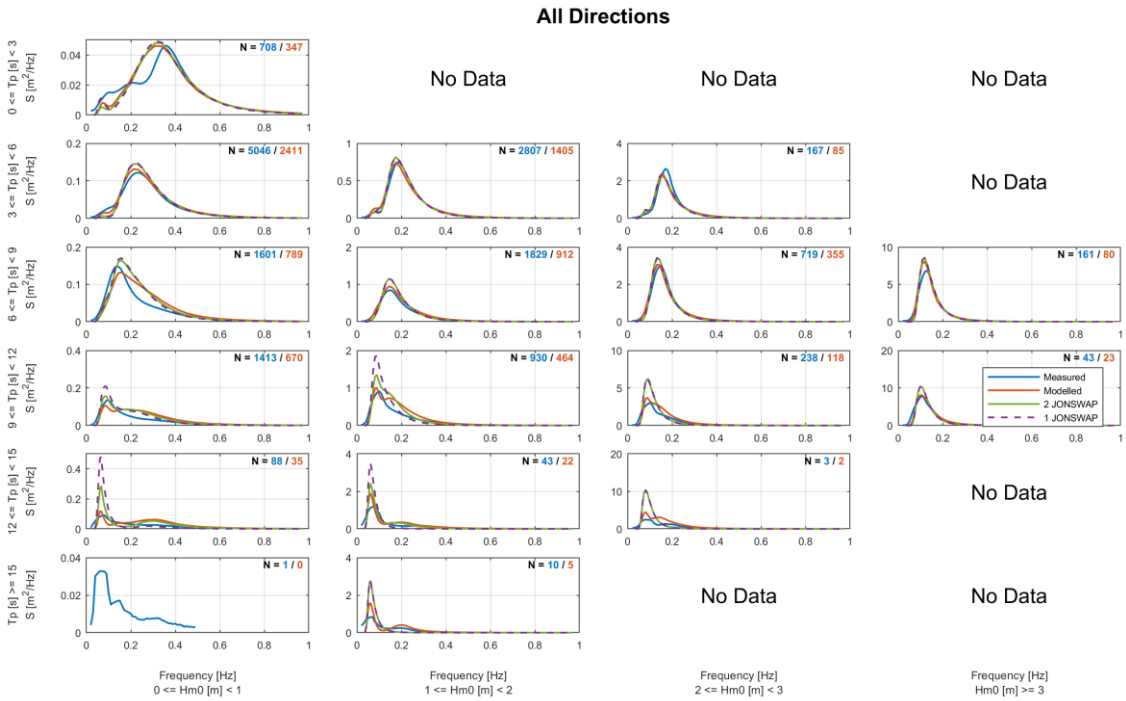



Figure C.199. AWAC E, omni-directional spectral validation, by Hm0 and Tp, all directions.

### C.7.6.2 45° Sectors

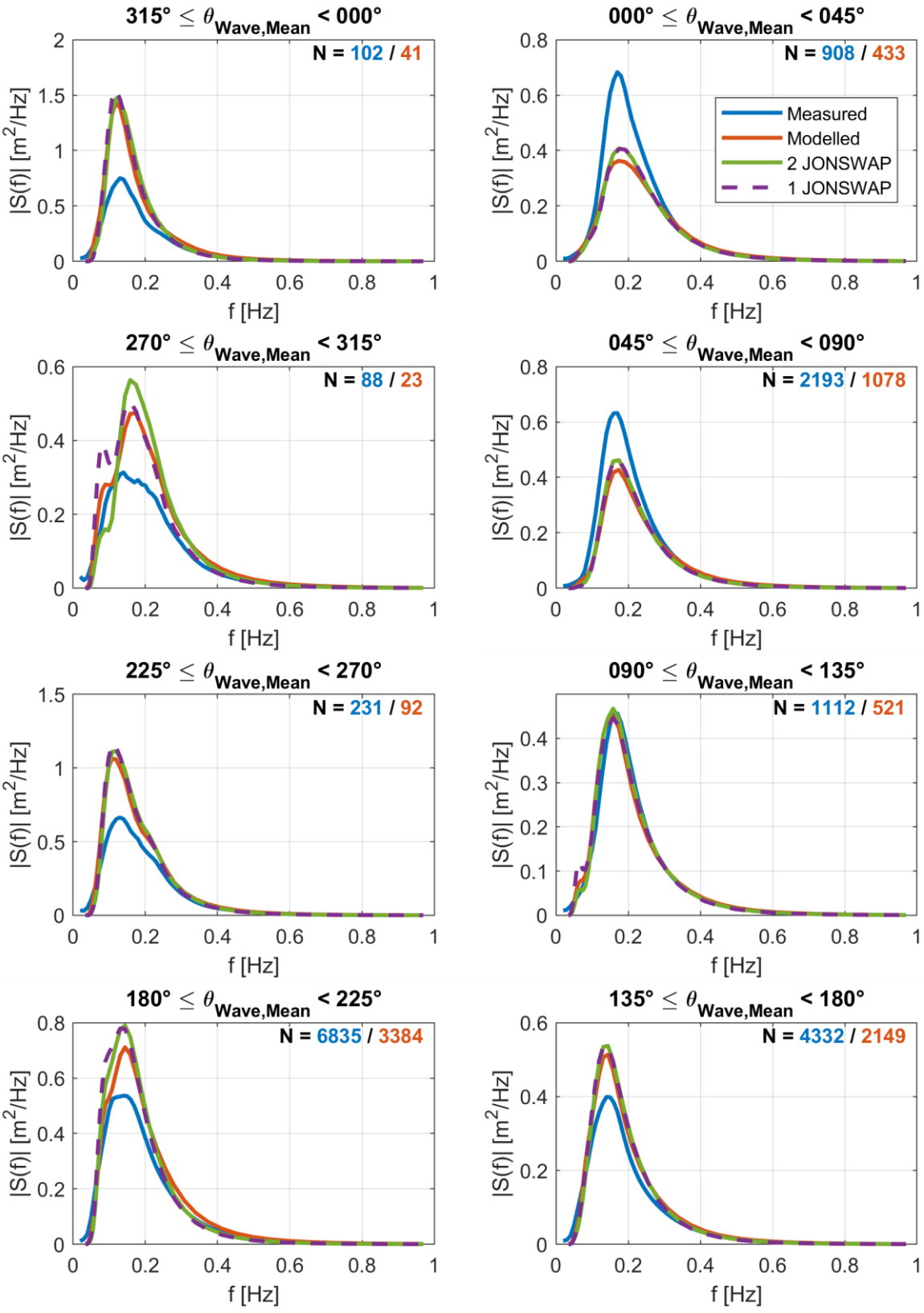



Figure C.200. AWAC E, omni-directional spectral validation, 45° sectors.

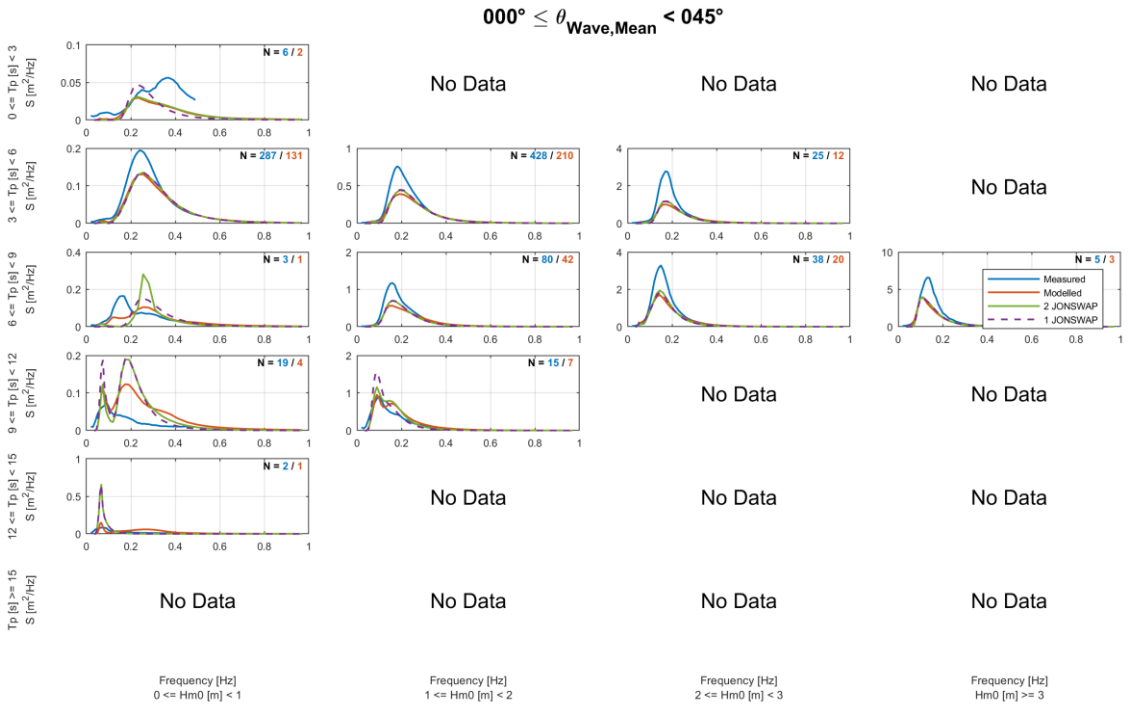



Figure C.201. AWAC E, omni-directional spectral validation, by Hm0 and Tp, 0-45° sector.

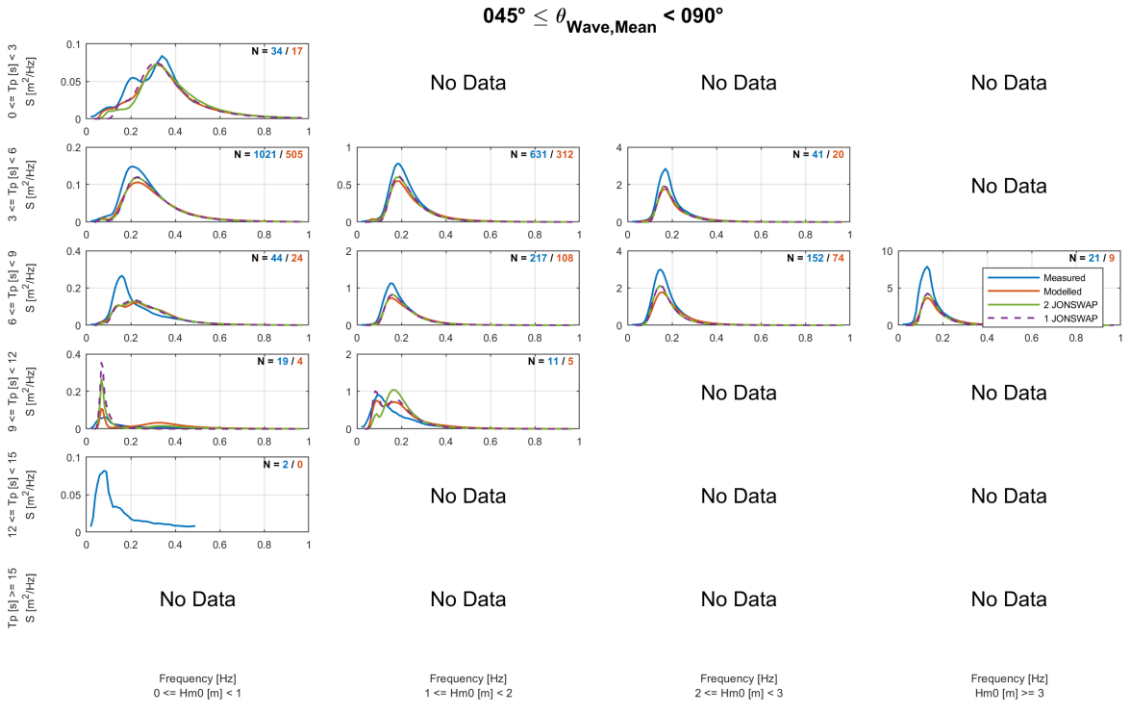



Figure C.202. AWAC E, omni-directional spectral validation, by Hm0 and Tp, 45-90° sector.

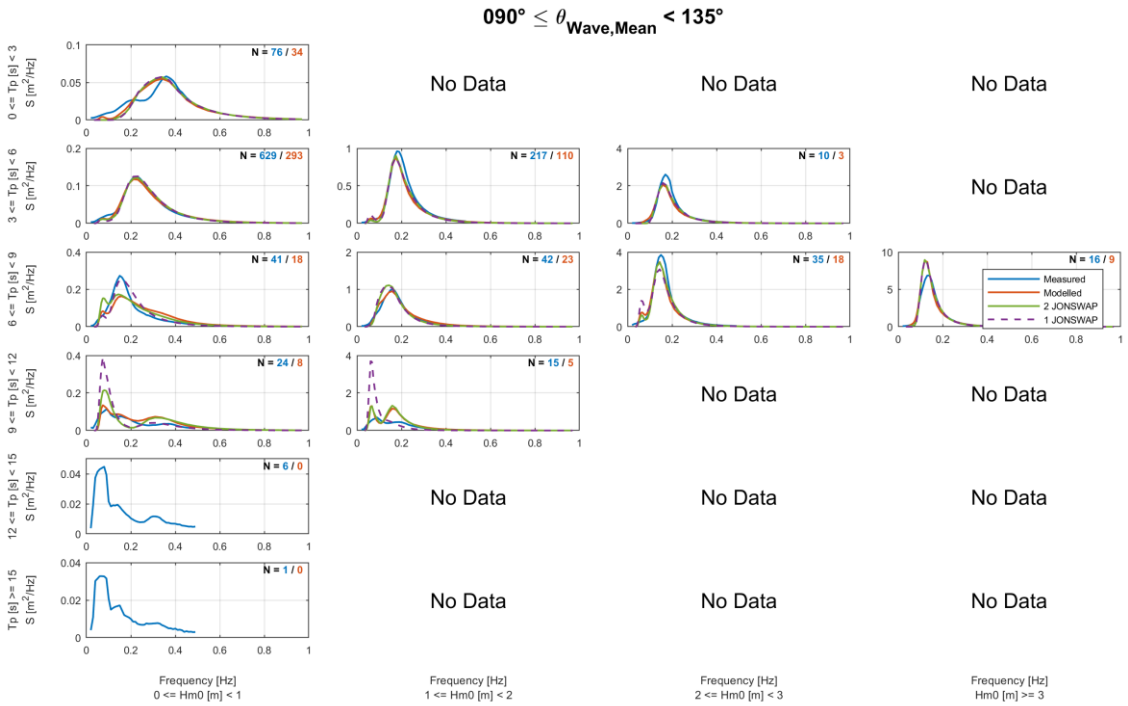



Figure C.203. AWAC E, omni-directional spectral validation, by Hm0 and Tp, 90-135° sector.

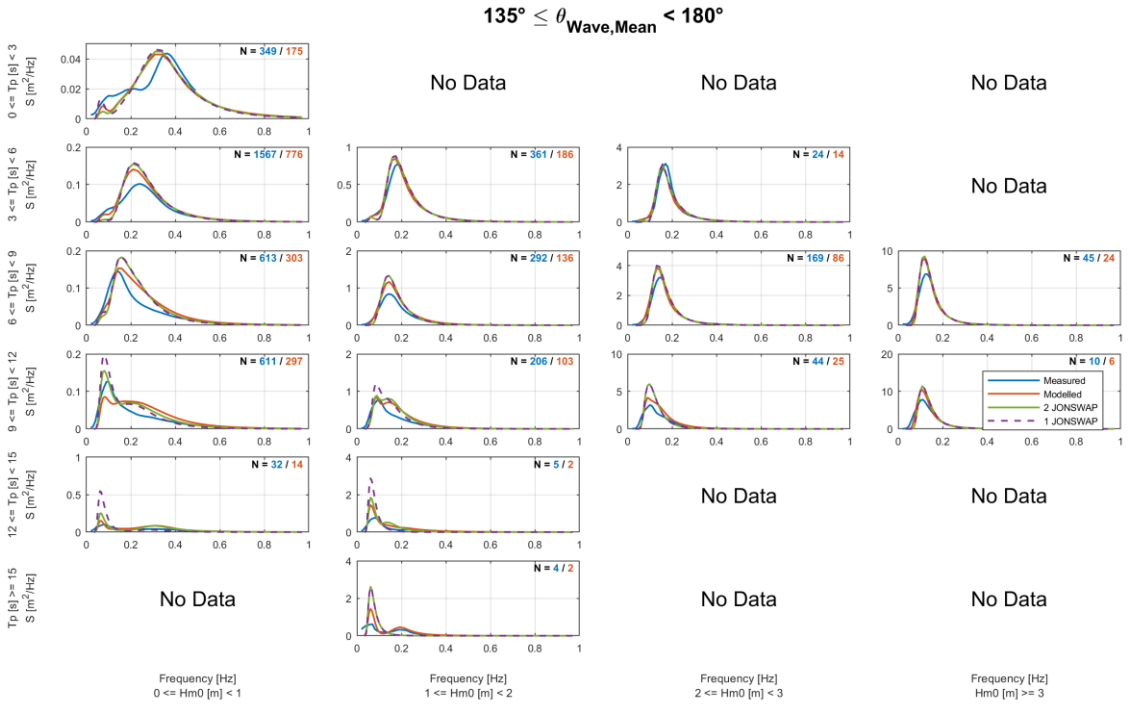



Figure C.204. AWAC E, omni-directional spectral validation, by Hm0 and Tp, 135-180° sector.

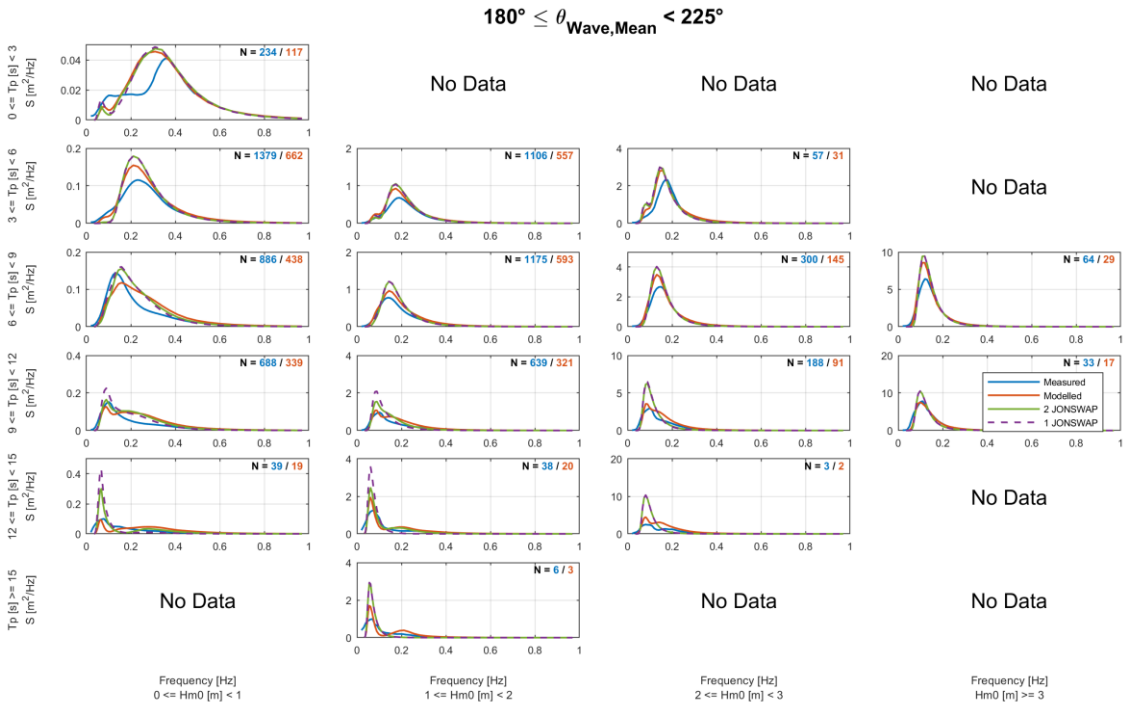



Figure C.205. AWAC E, omni-directional spectral validation, by Hm0 and Tp, 180-225° sector.

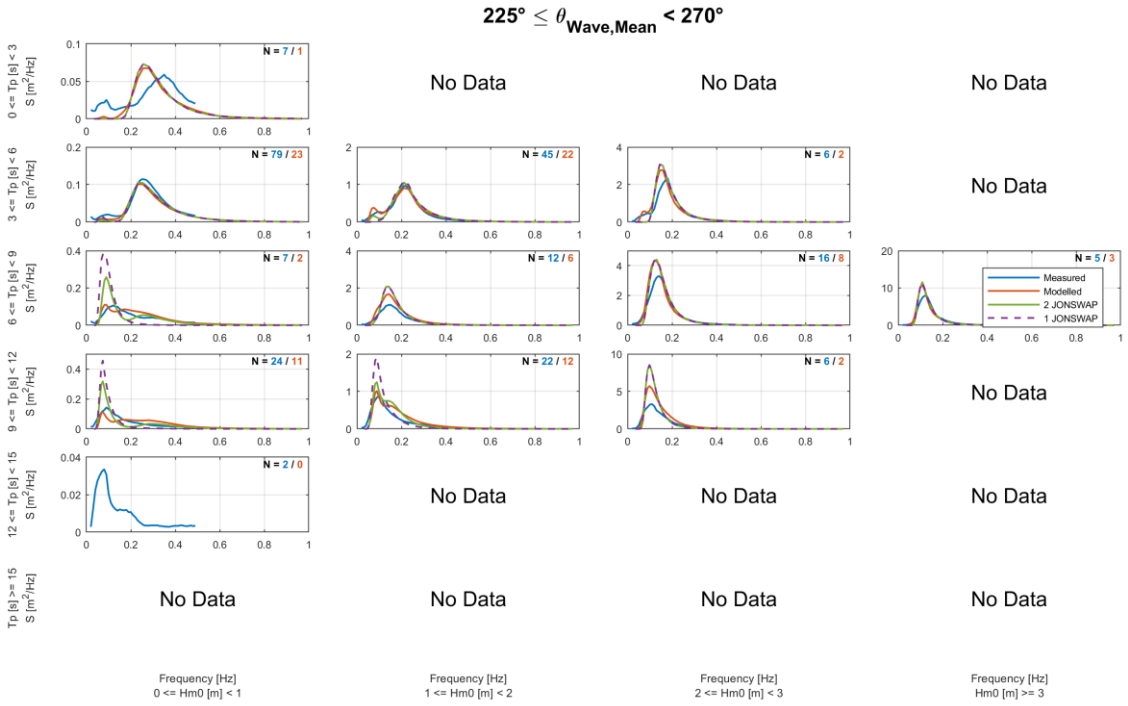



Figure C.206. AWAC E, omni-directional spectral validation, by Hm0 and Tp, 225-270° sector.

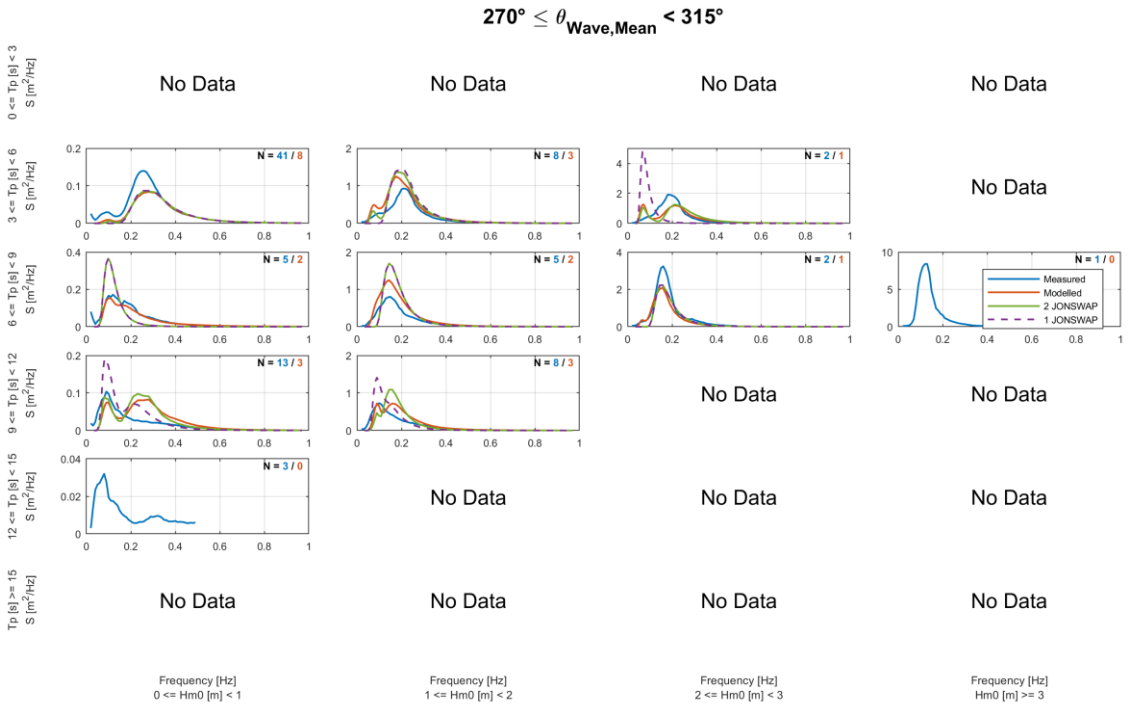



Figure C.207. AWAC E, omni-directional spectral validation, by Hm0 and Tp, 270-315° sector.

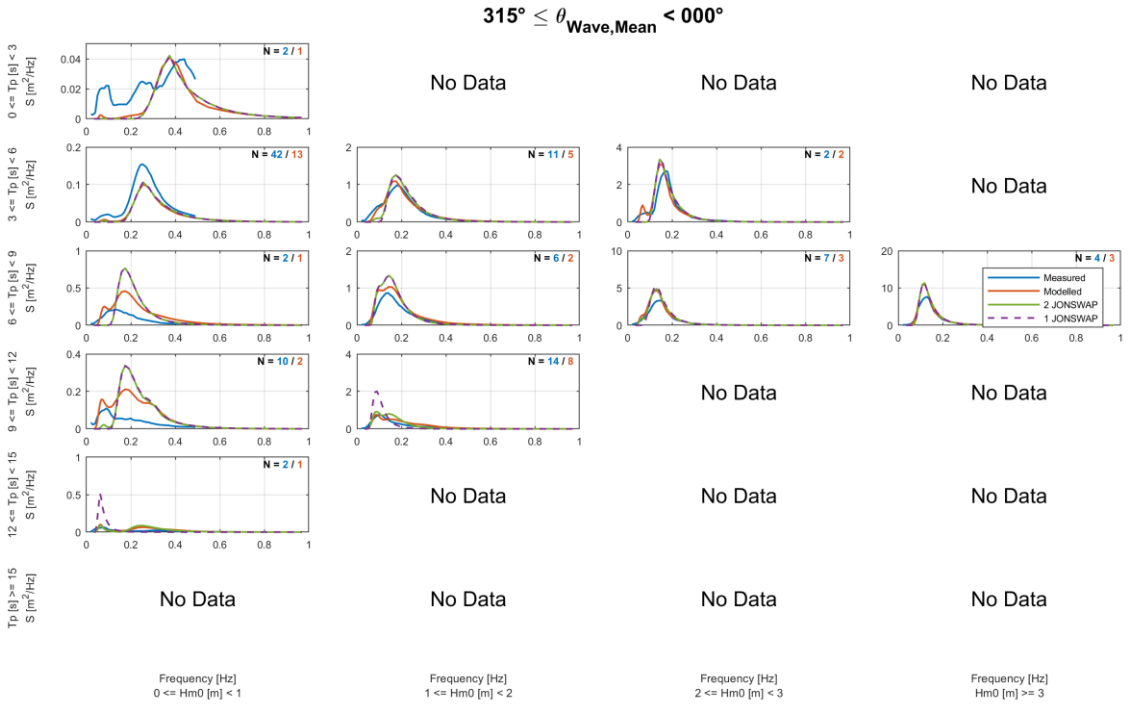



Figure C.208. AWAC E, omni-directional spectral validation, by Hm0 and Tp, 315-0° sector.

### C.7.6.3 Custom Sectors

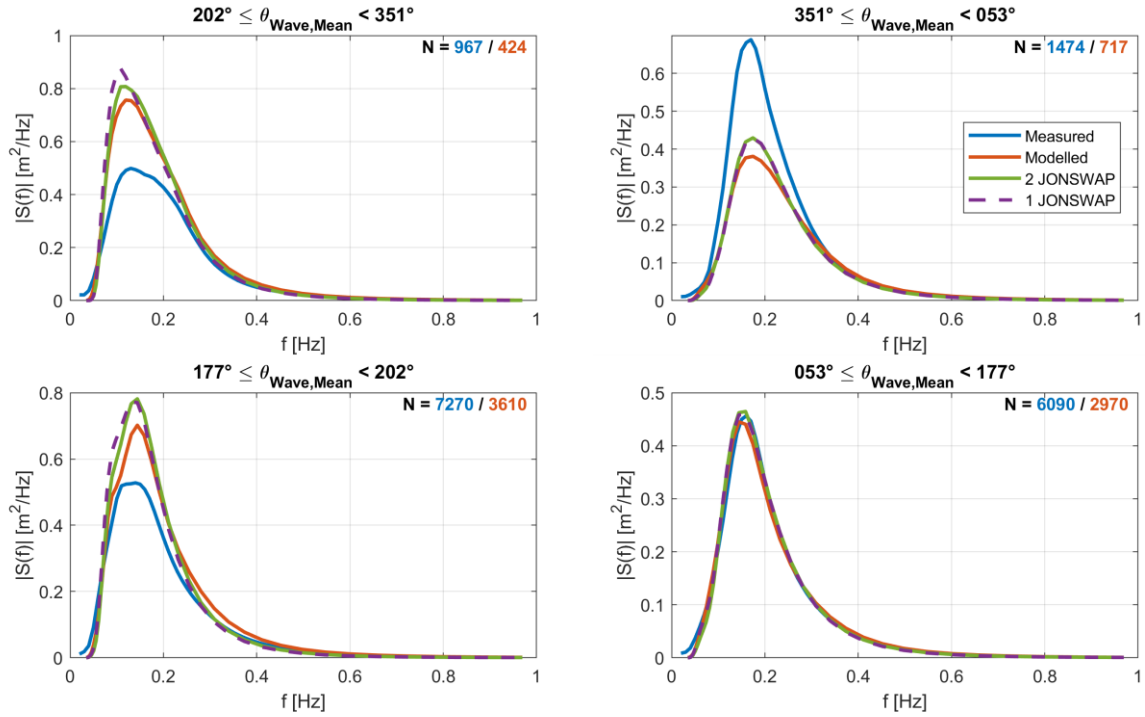



Figure C.209. AWAC E, omni-directional spectral validation, custom sectors.

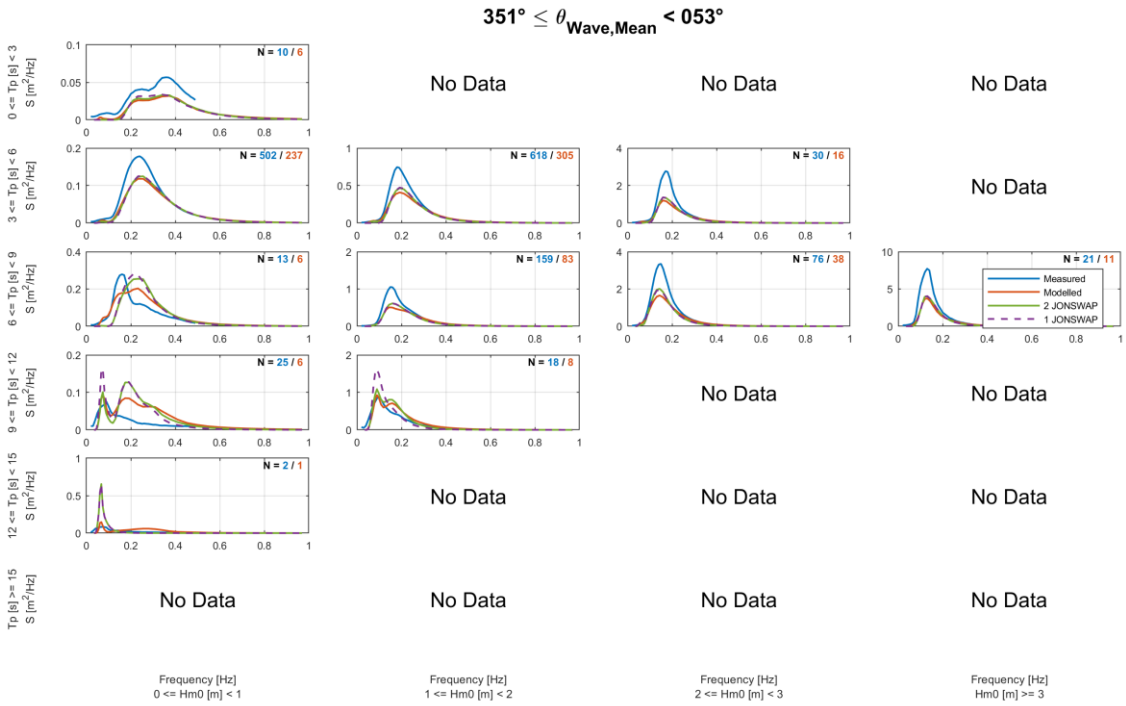



Figure C.210. AWAC E, omni-directional spectral validation, by Hm0 and Tp, 351-053° sector.

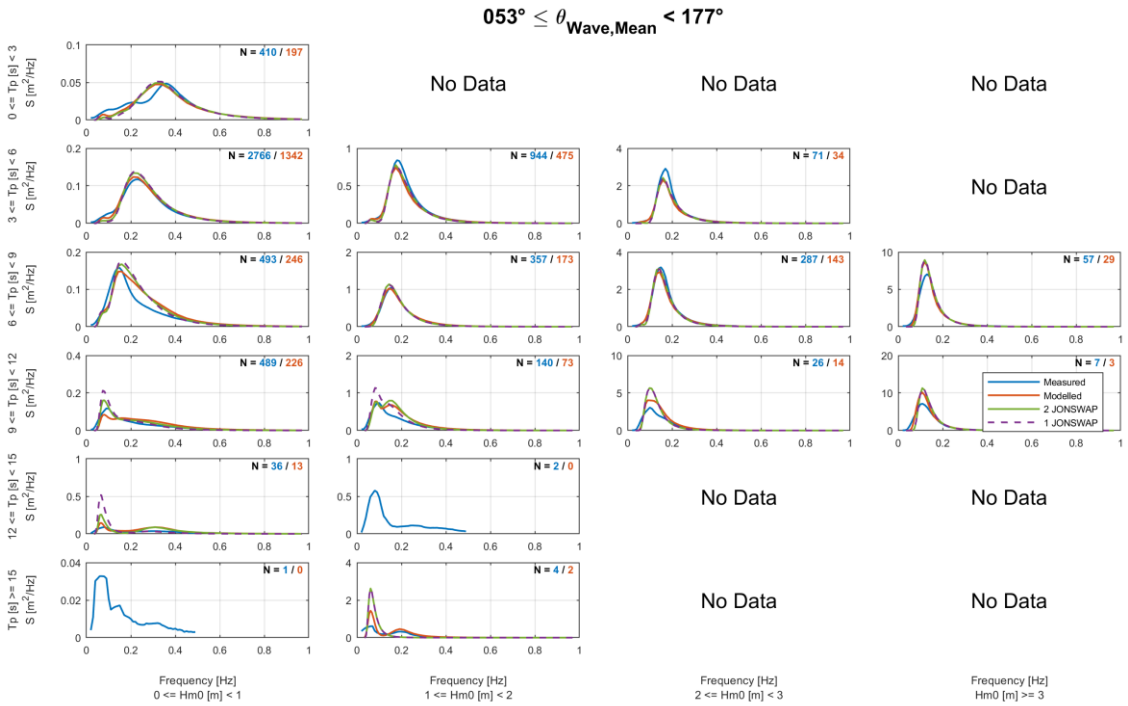



Figure C.211. AWAC E, omni-directional spectral validation, by Hm0 and Tp, 053-177° sector.

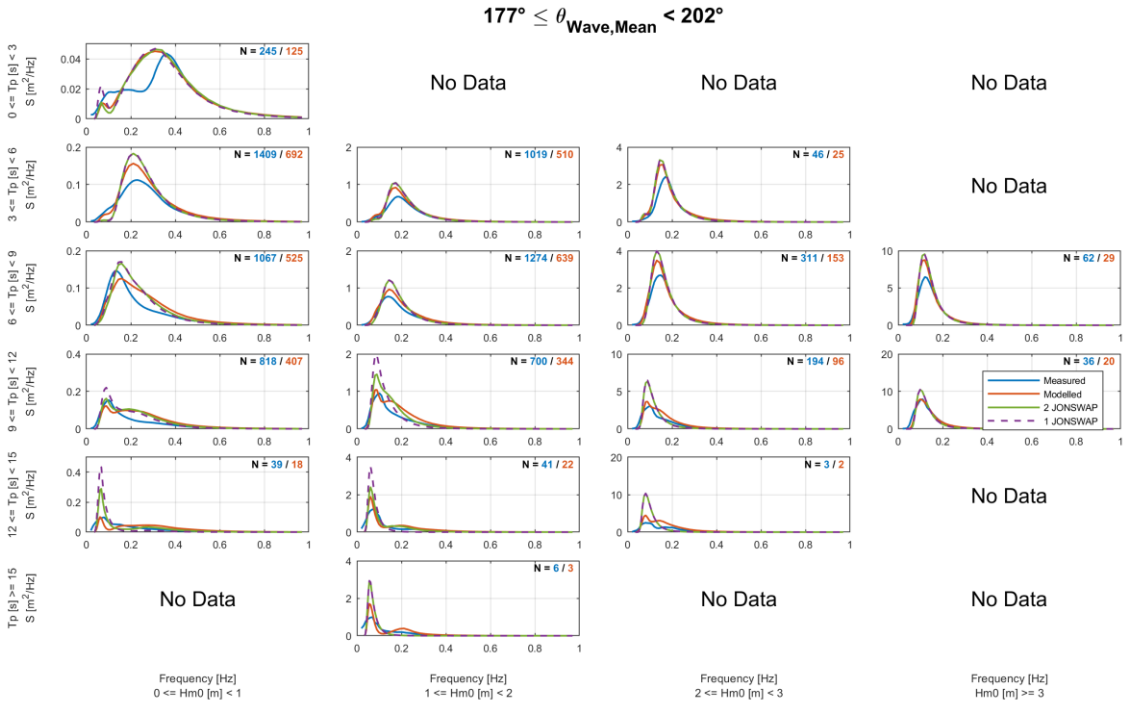



Figure C.212. AWAC E, omni-directional spectral validation, by Hm0 and Tp, 177-202° sector.

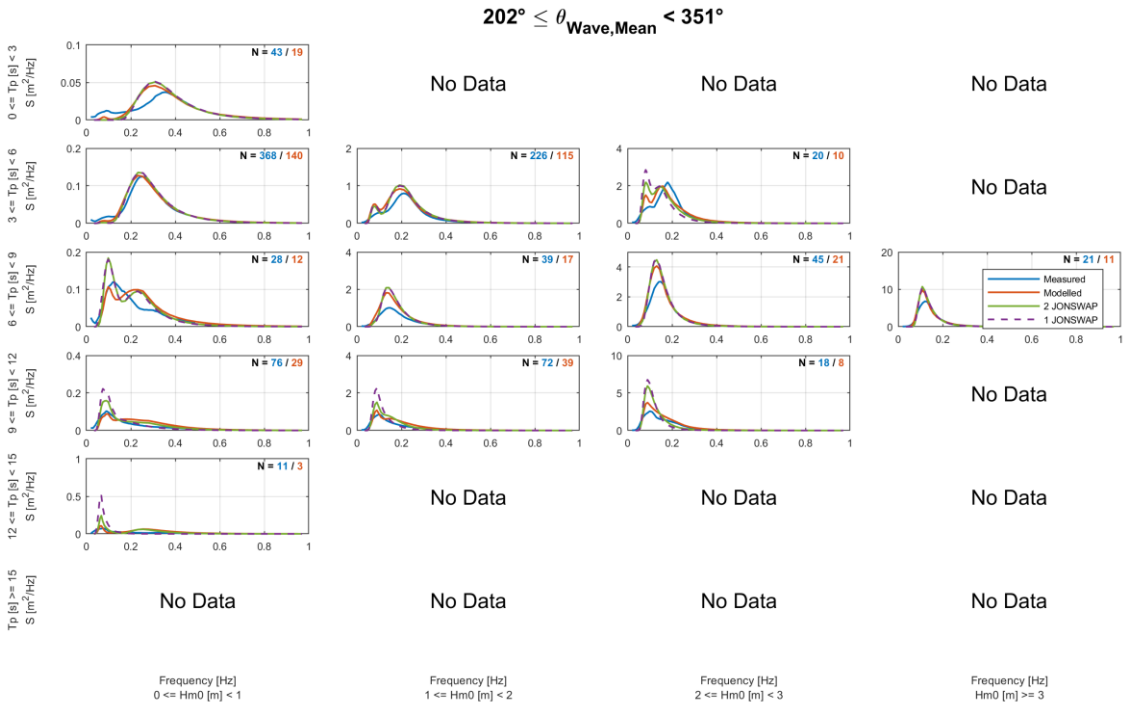



Figure C.213. AWAC E, omni-directional spectral validation, by Hm0 and Tp, 202-351° sector.

## C.8 Selected Events

### C.8.1 Introduction

In this Section, plots are included to explore the temporal evolution of modelled and measured parameters and spectra around:

- Time stamps corresponding to the highest measured values of Hm0.
- Time stamps corresponding to the largest wind speeds from the north, south, east and west quadrants.

For AWAC A, such plots are included in Section C.8.2, with those for AWACs B1, C, D1 and E in Sections C.8.3 through C.8.6. In each case, the five events with the highest Hm0 are shown, and one event for each of the four wind direction quadrants. Each figure contains the following:

- Time-series of **significant wave height** (Hm0, second row), **peak wave period** (Tp, third row) and **mean wave direction** (Mdir, fourth row). Throughout, measurements are shown in blue, model data in red.
- Time-series of **wind speed** and **wind direction** (fifth and sixth rows respectively). Again, measurements are shown in blue, model data in red. Please note that measurements are taken from the lowest level of the Arklow LiDAR (see Section B.4.3) at 21.3 mAMSL, whilst model data comes from the Vortex modelled data (see Section B.2) at 10 mAMSL for the LiDAR location. Since the wind speeds are provided for indicative purposes only in reviewing the *wave* model, no adjustments have been made to account for the differences in elevations.
- **Omni-directional spectra** at three-hour intervals from nine hours before the peak Hm0 to three hours after the peak Hm0 (top row). Note that if data are not available exactly at the required time, the closest spectrum is plotted. For clarity, the timestamp of each spectrum is shown in the top right of each omni-directional spectrum plot. Again, measurements are shown in blue, model data in red. 1 JONSWAP and 2 JONSWAP representations of the model data (see Section C.7 for full descriptions) are overlaid in dashed purple and green respectively.
- **Directional spectra** at three-hour intervals from nine hours before the peak Hm0 to three hours after the peak Hm0 (row five: measured data; row six: modelled data; row seven: 2 JONSWAP representation; row eight: 1 JONSWAP representation). As with omni-directional spectra, if data is not available exactly at the required time, the closest spectrum is shown. For clarity, the timestamp of each spectrum is shown directly above where it is drawn.
- **Time-series of omnidirectional spectra** (bottom two rows, measured and raw modelled only).

### C.8.2 AWAC A

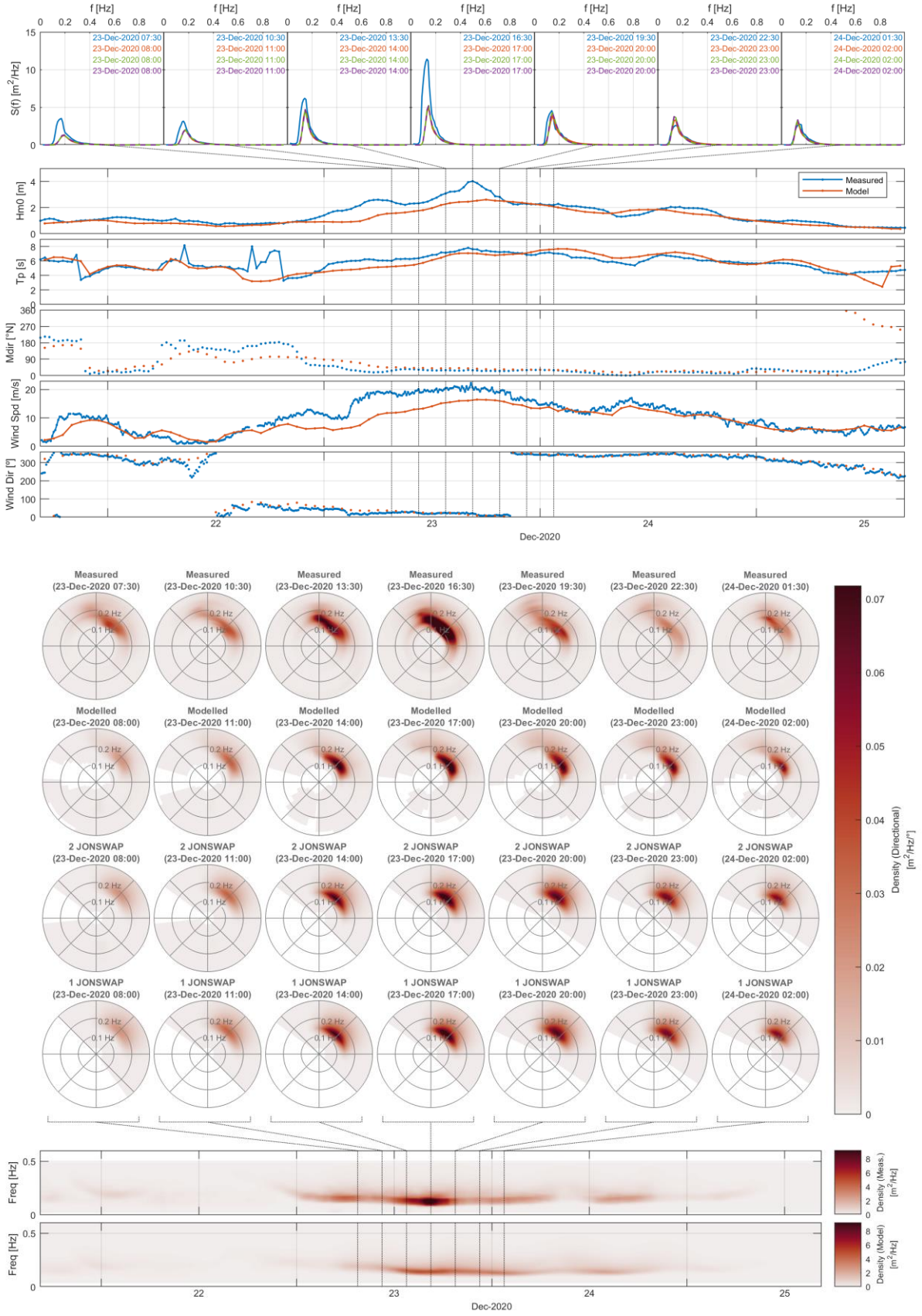



Figure C.214. AWAC A, largest Hm0 peak.

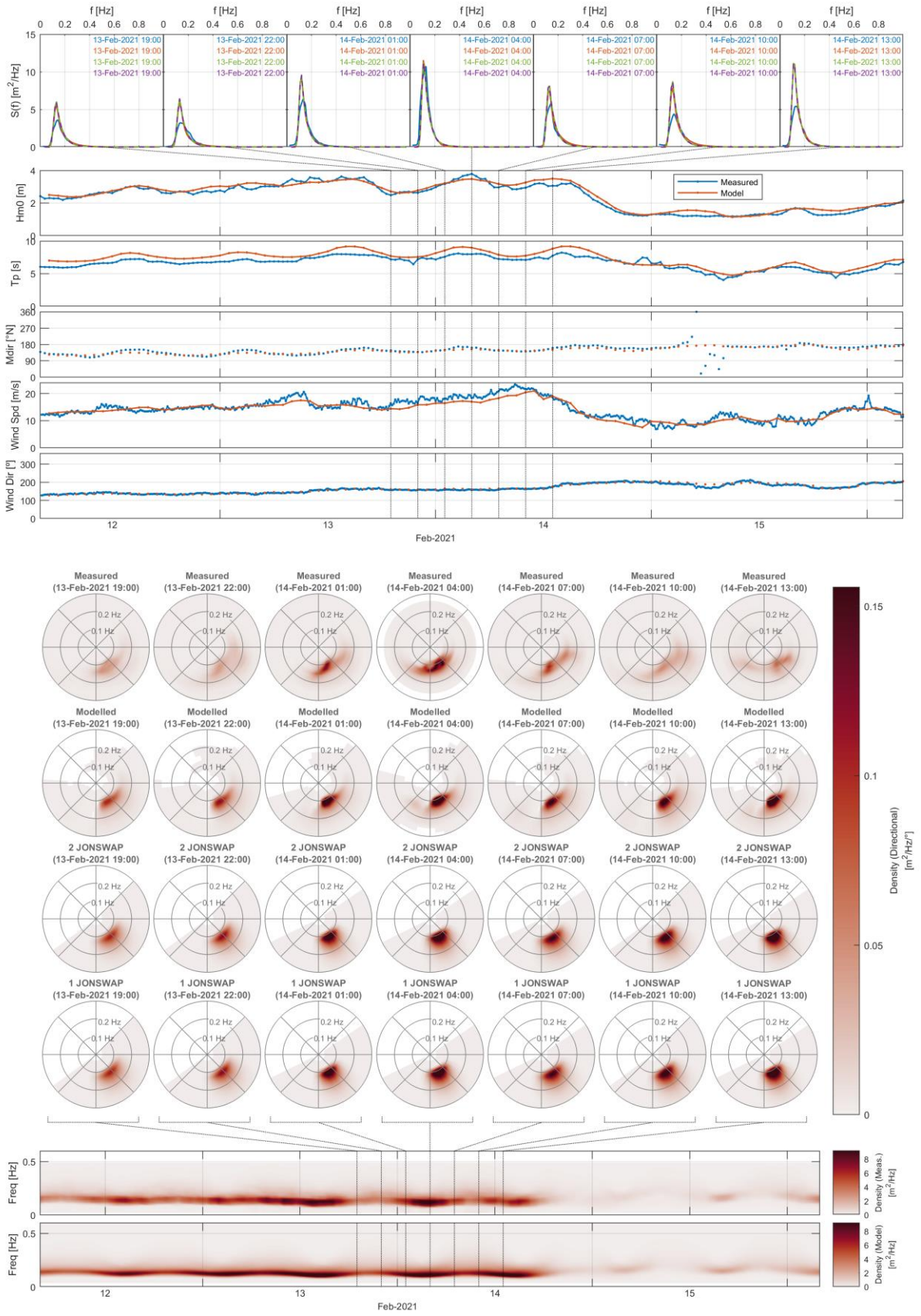



Figure C.215. AWAC A, second largest Hm0 peak.

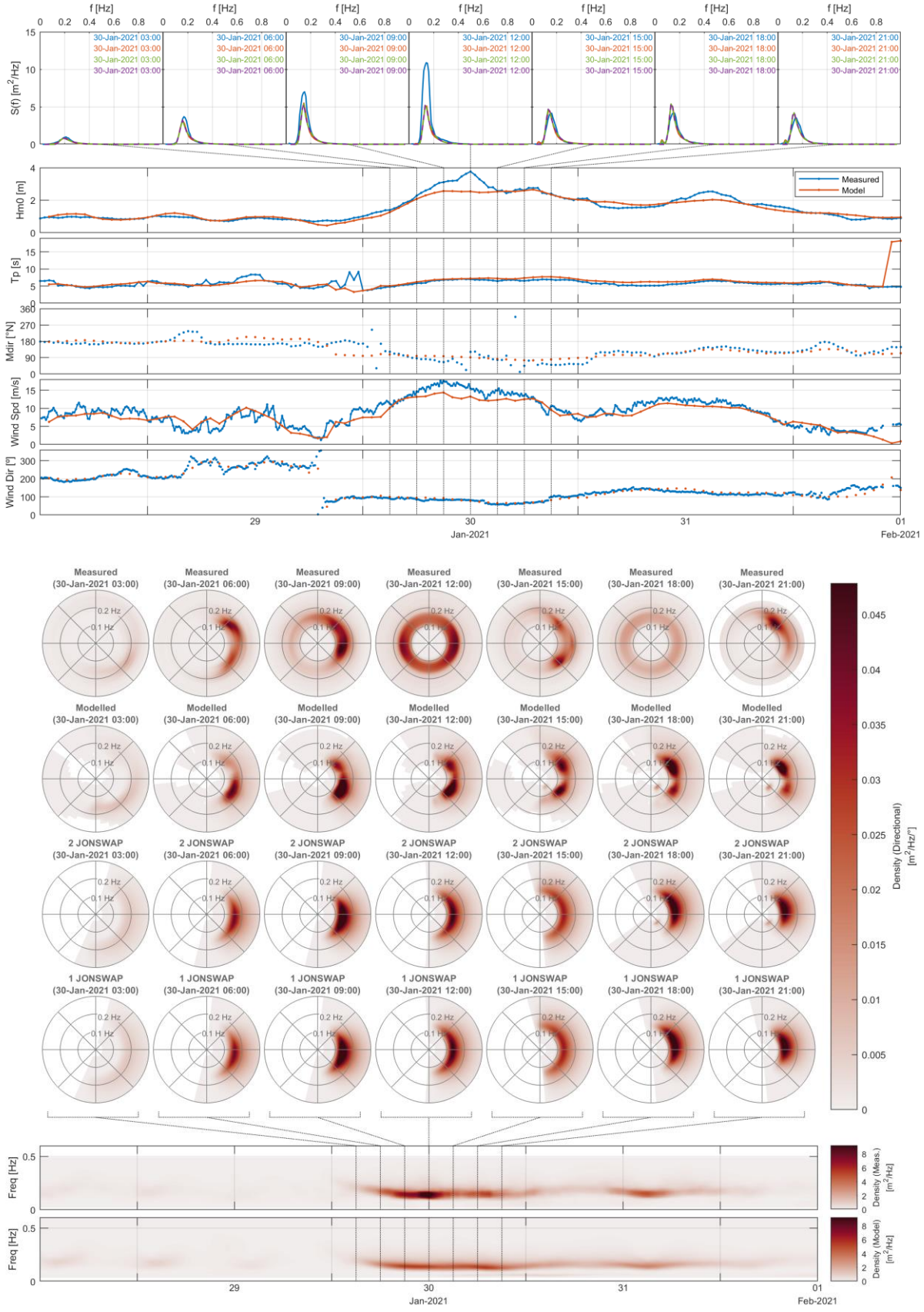



Figure C.216. AWAC A, third largest Hm0 peak.

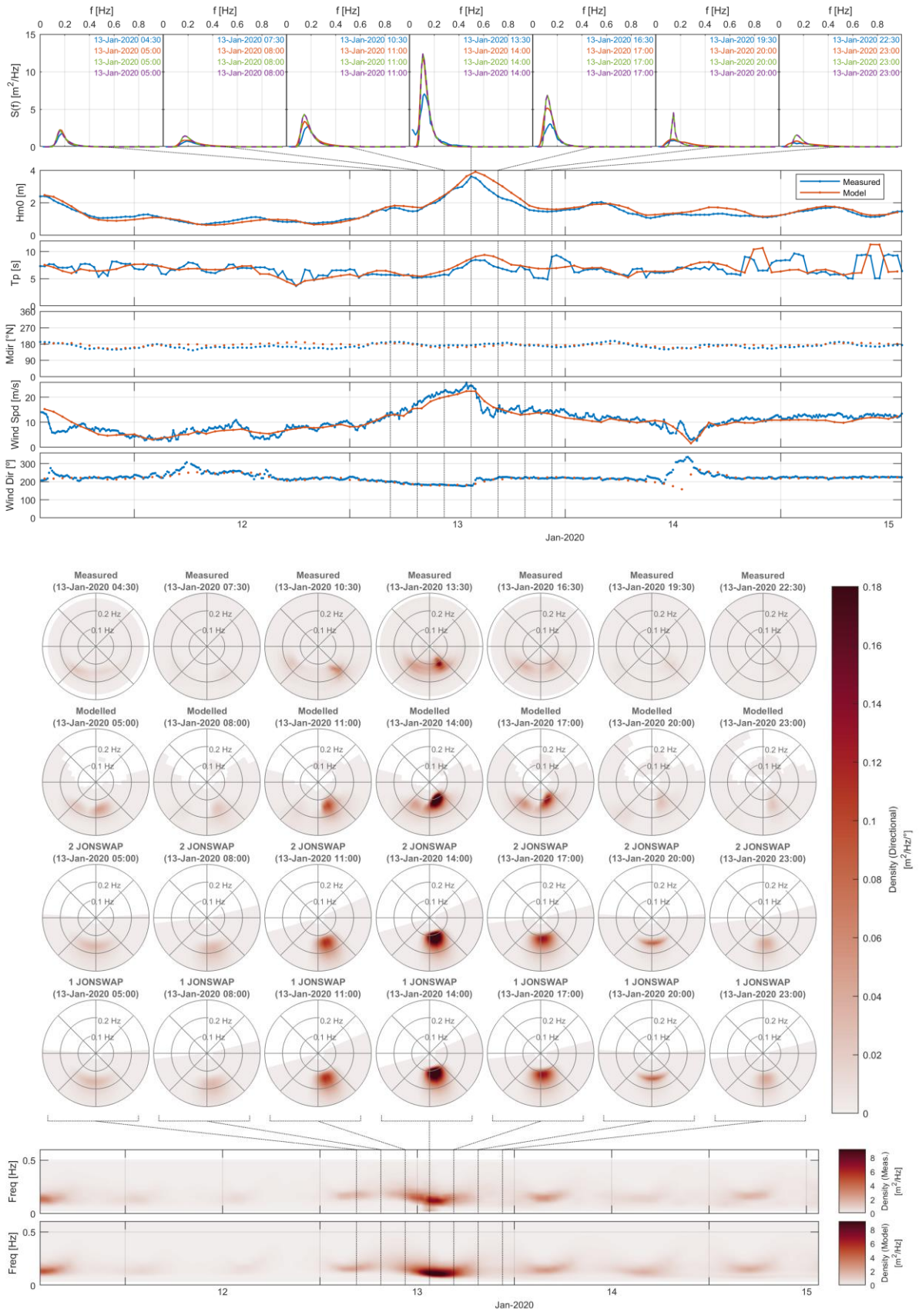



Figure C.217. AWAC A, fourth largest Hm0 peak.

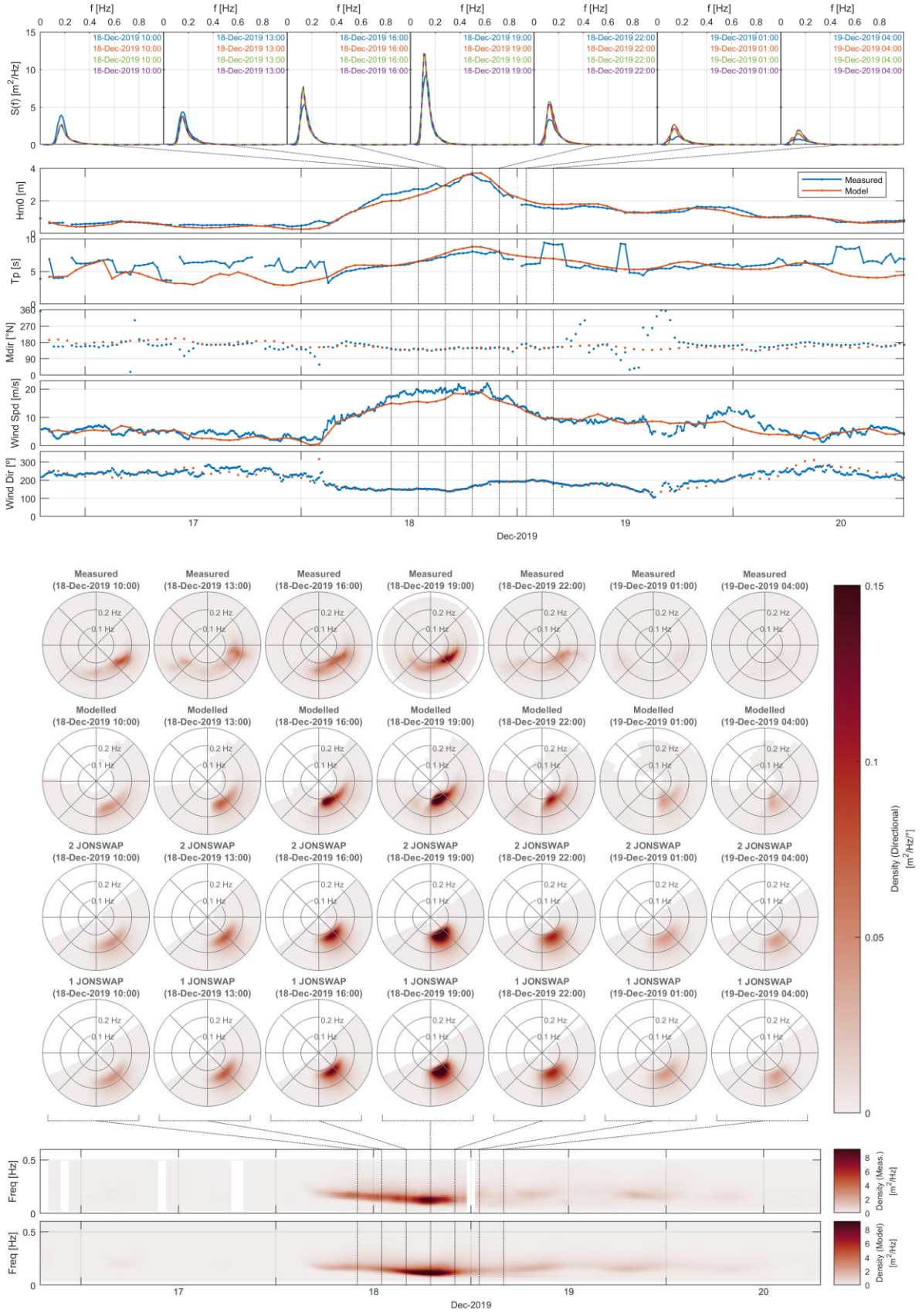



Figure C.218. AWAC A, fifth largest Hm0 peak.

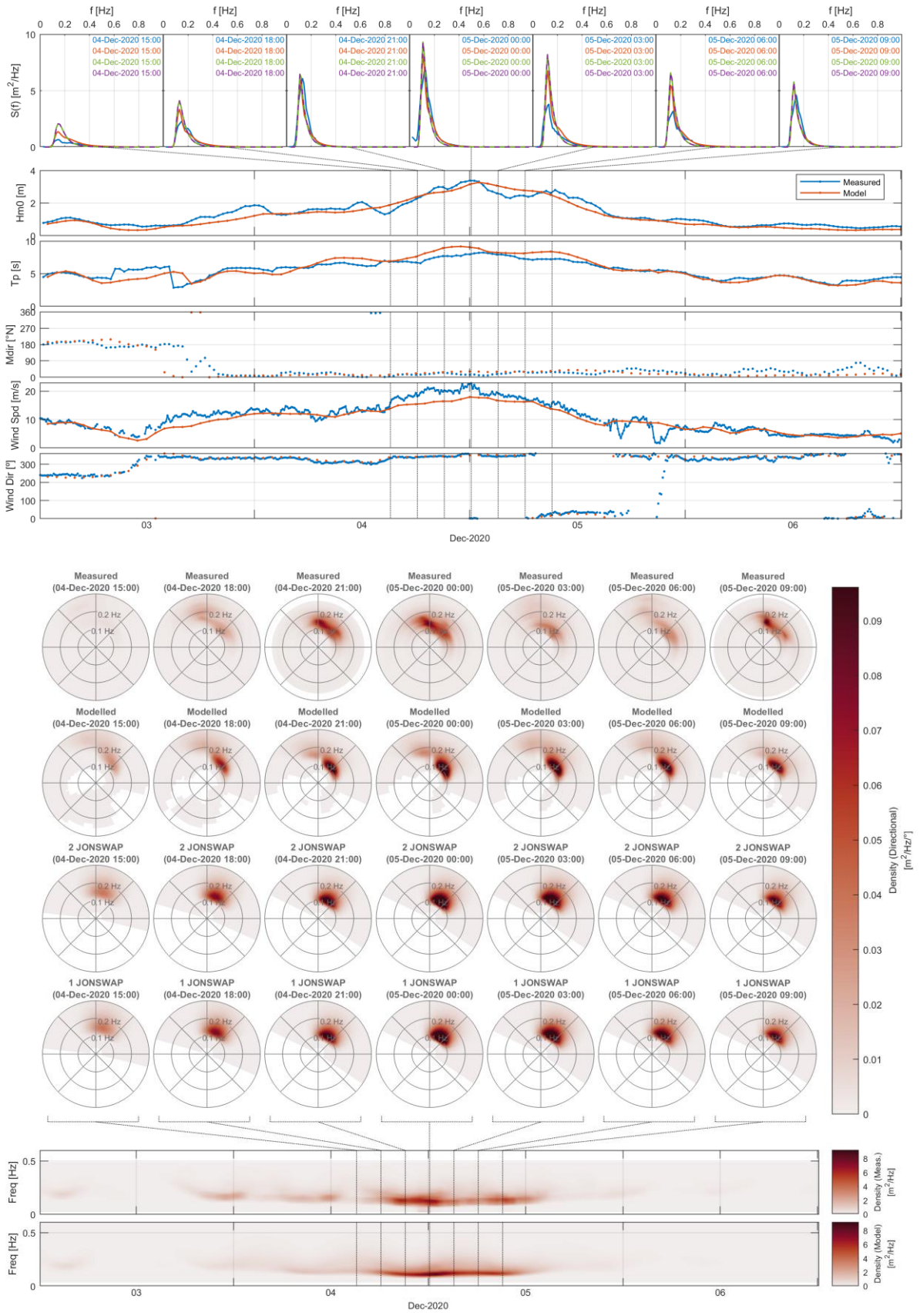



Figure C.219. AWAC A, largest measured wind speed from the north.

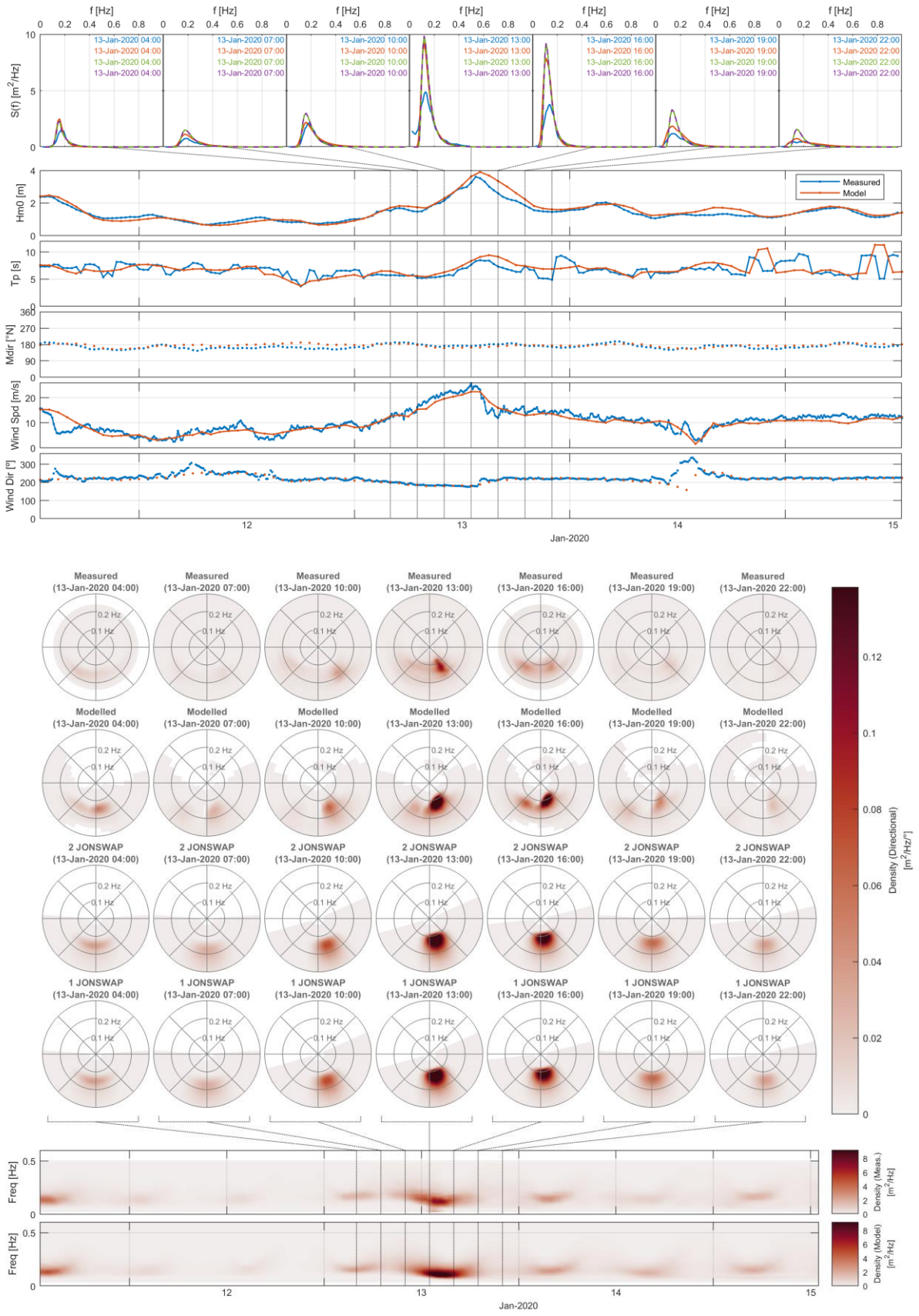



Figure C.220. AWAC A, largest measured wind speed from the south.

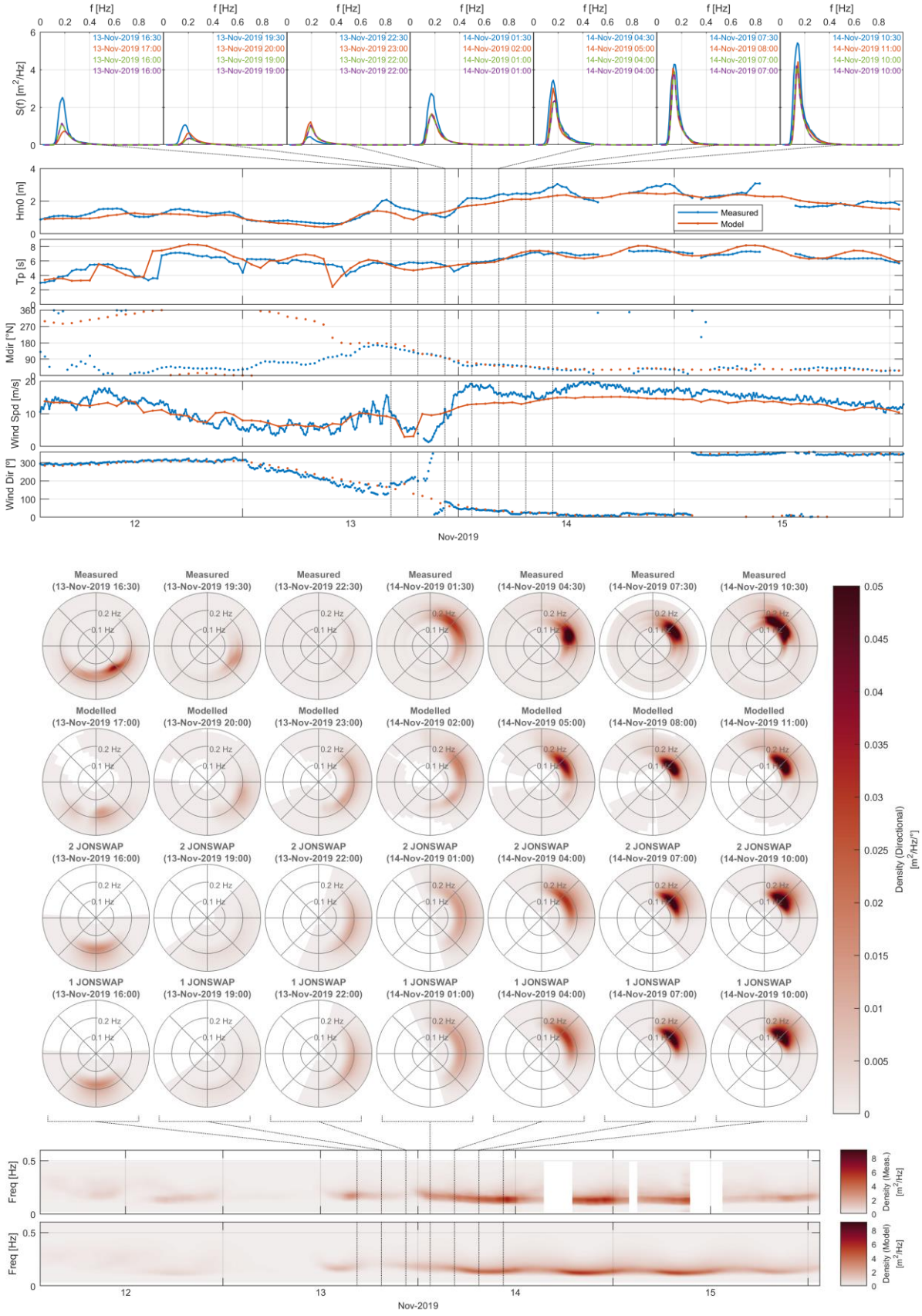



Figure C.221. AWAC A, largest measured wind speed from the east.

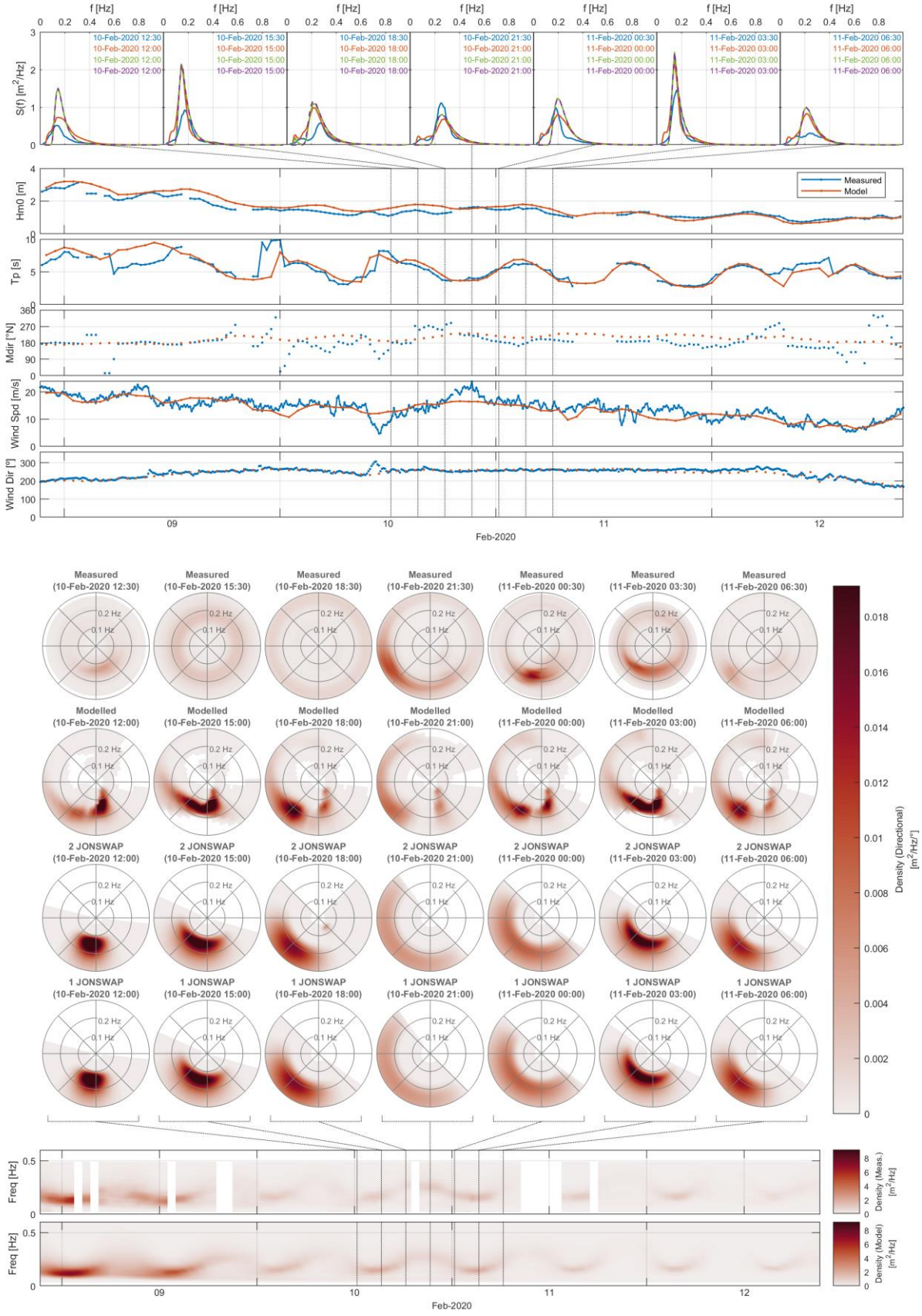



Figure C.222. AWAC A, largest measured wind speed from the west.

### C.8.3 AWAC B1

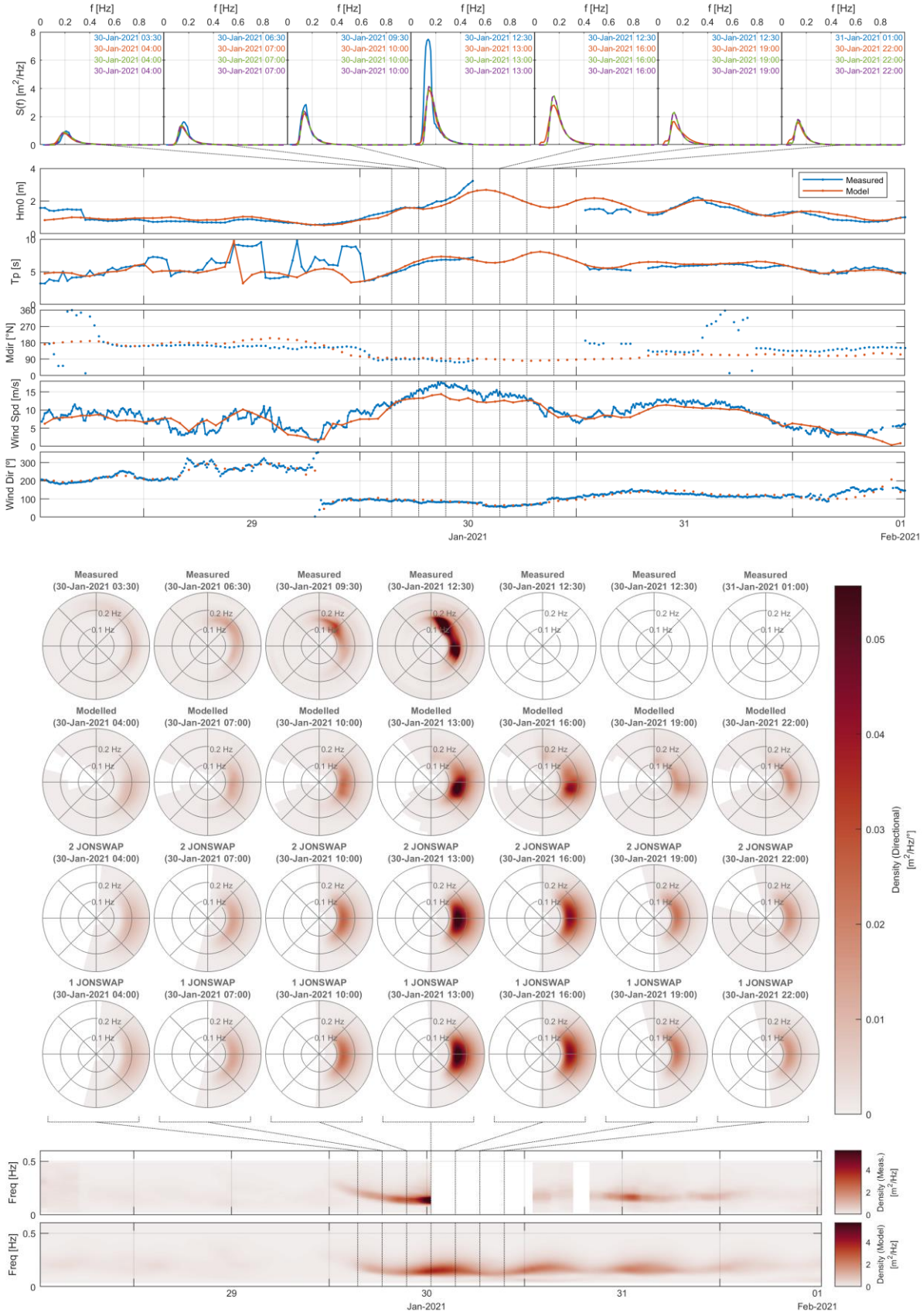



Figure C.223. AWAC B1, largest Hm0 peak.

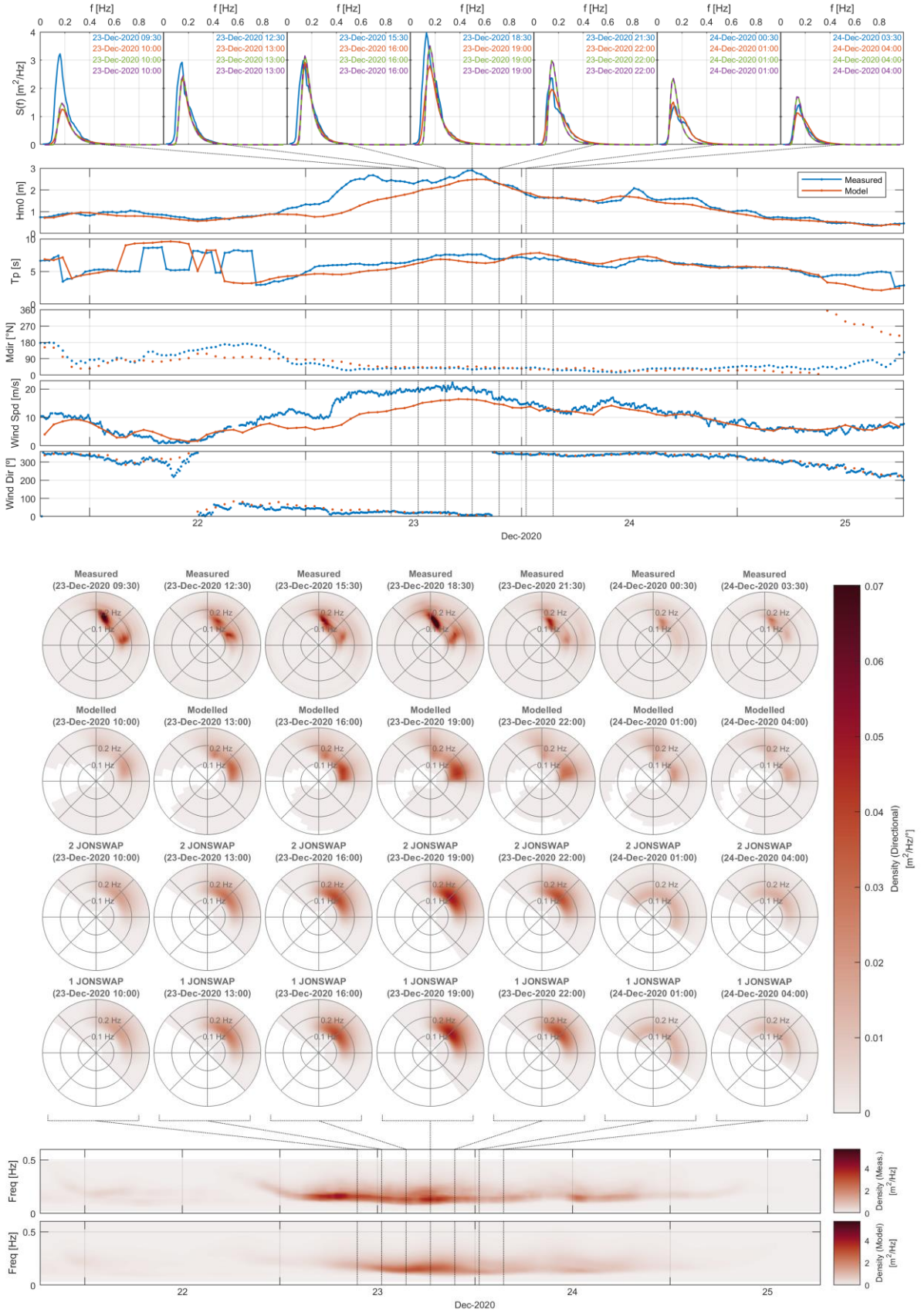



Figure C.224. AWAC B1, second largest Hm0 peak.

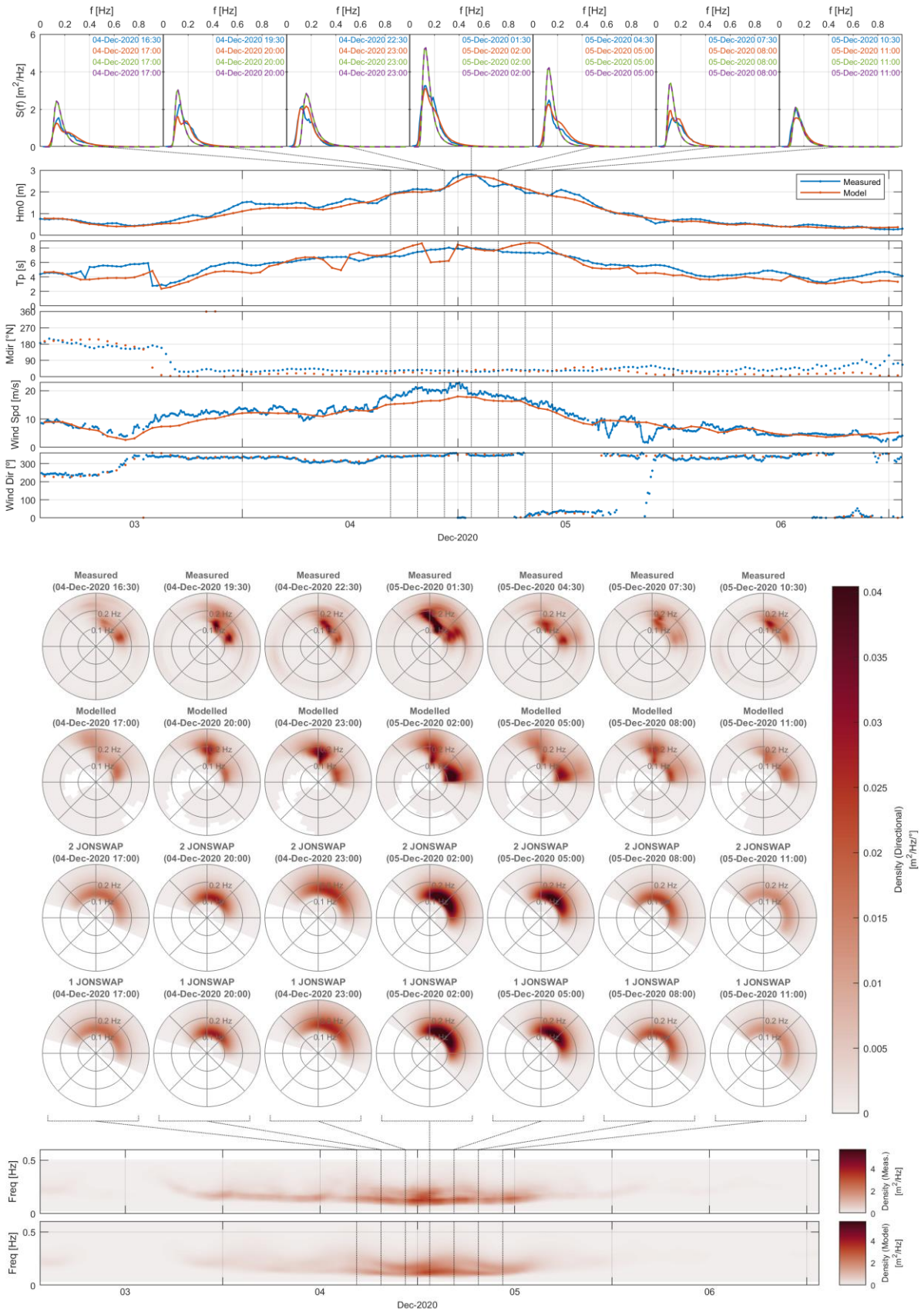



Figure C.225. AWAC B1, third largest Hm0 peak.

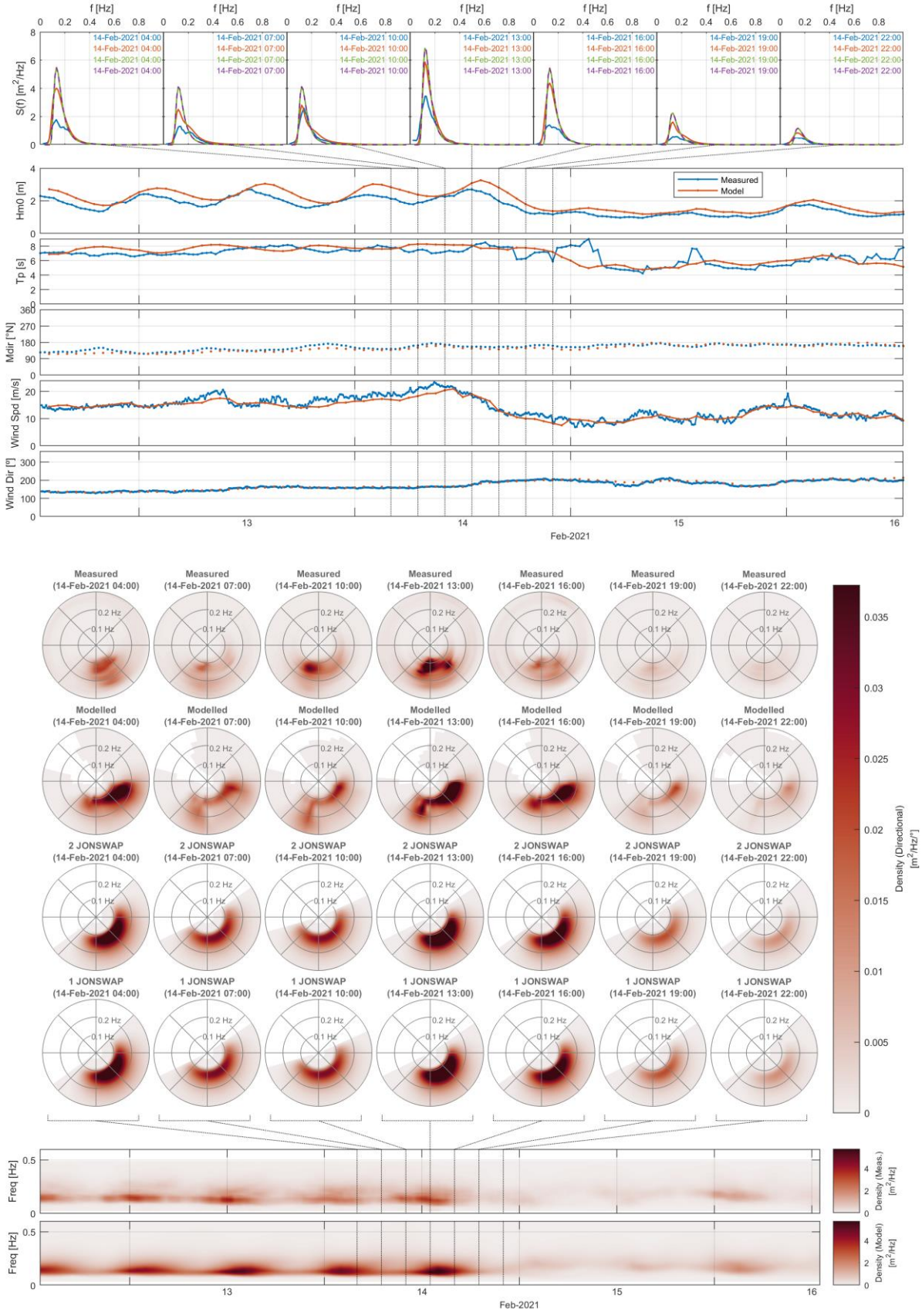



Figure C.226. AWAC B1, fourth largest Hm0 peak.

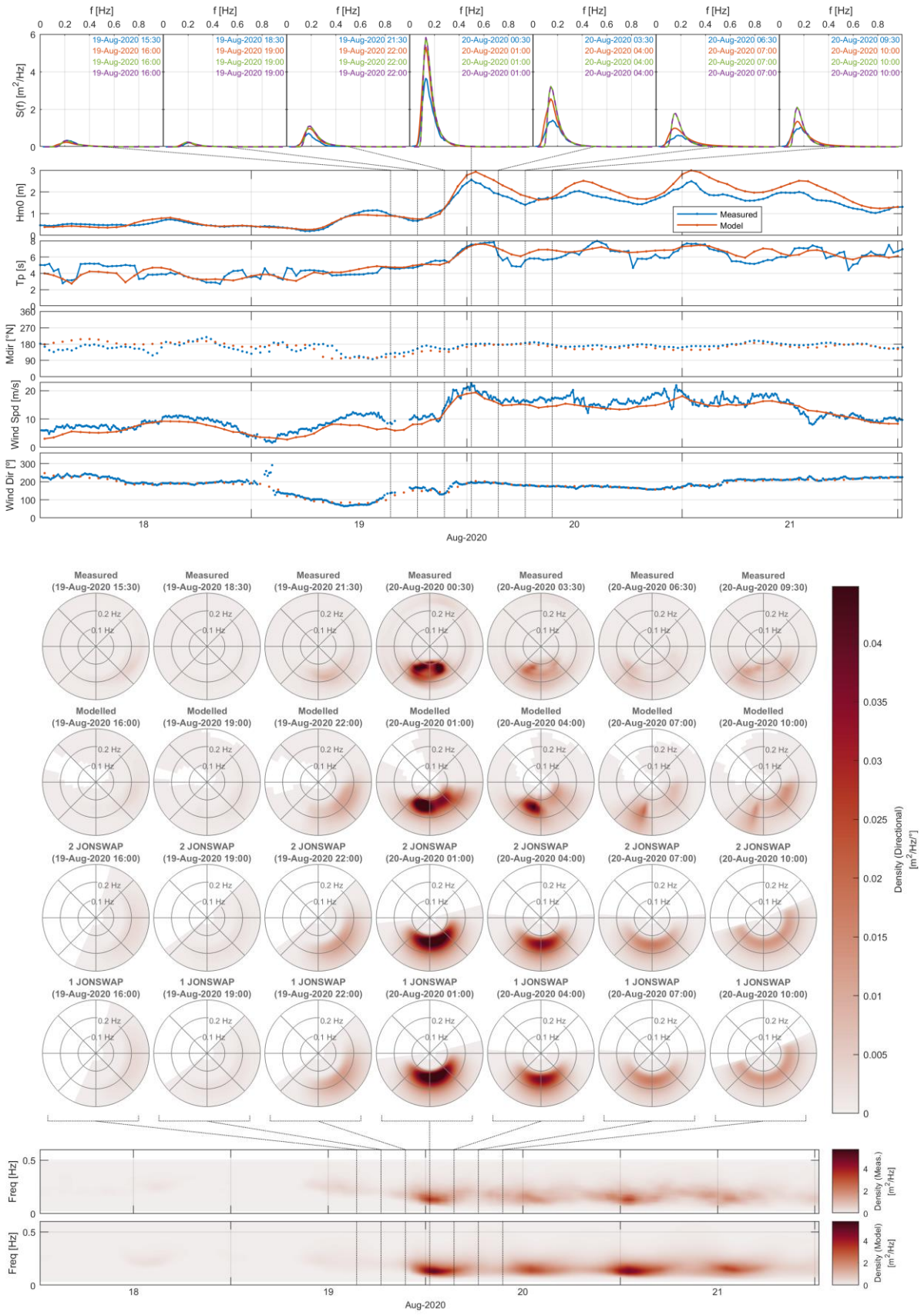



Figure C.227. AWAC B1, fifth largest Hm0 peak.

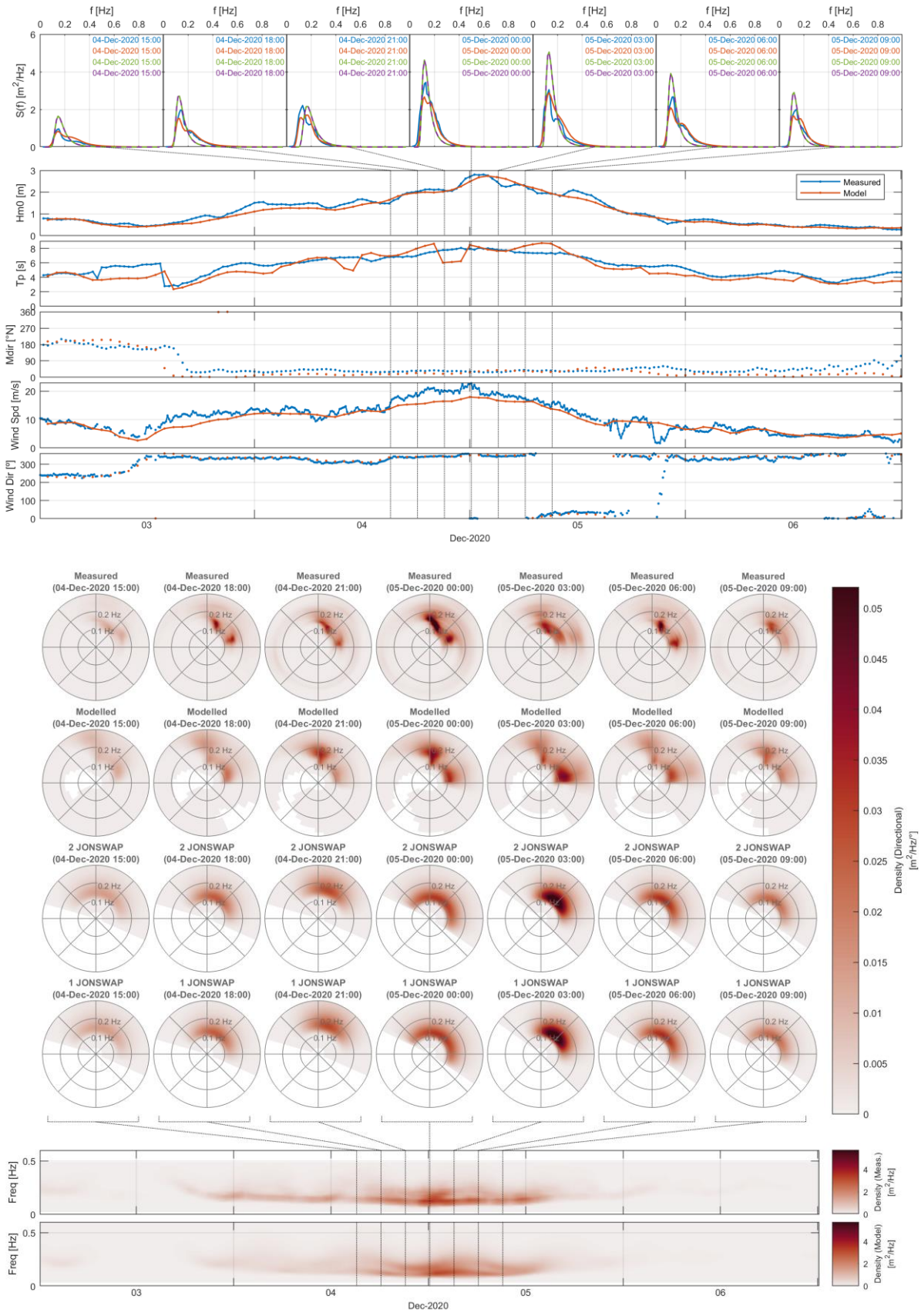



Figure C.228. AWAC B1, largest measured wind speed from the north.

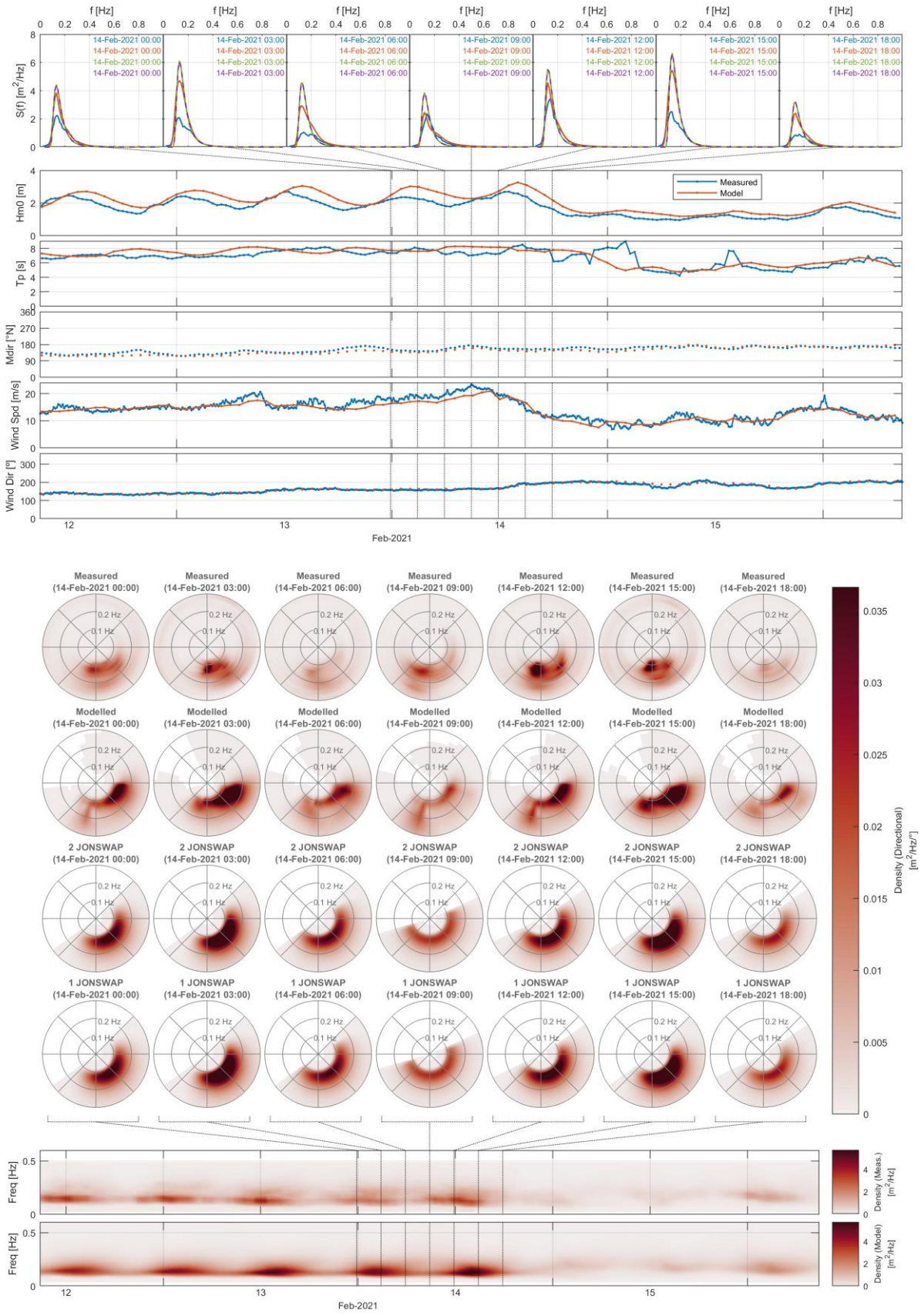



Figure C.229. AWAC B1, largest measured wind speed from the south.

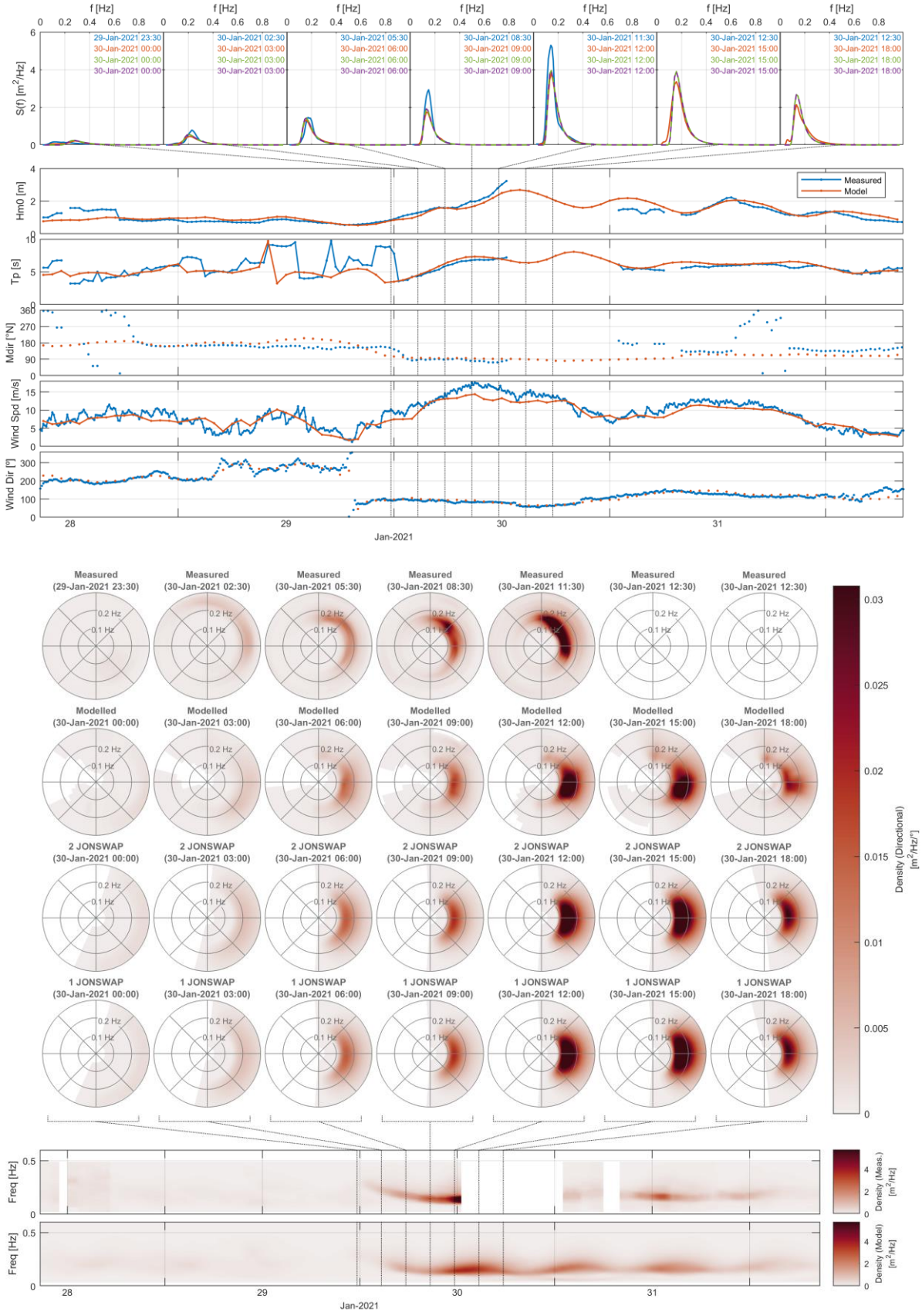



Figure C.230. AWAC B1, largest measured wind speed from the east.

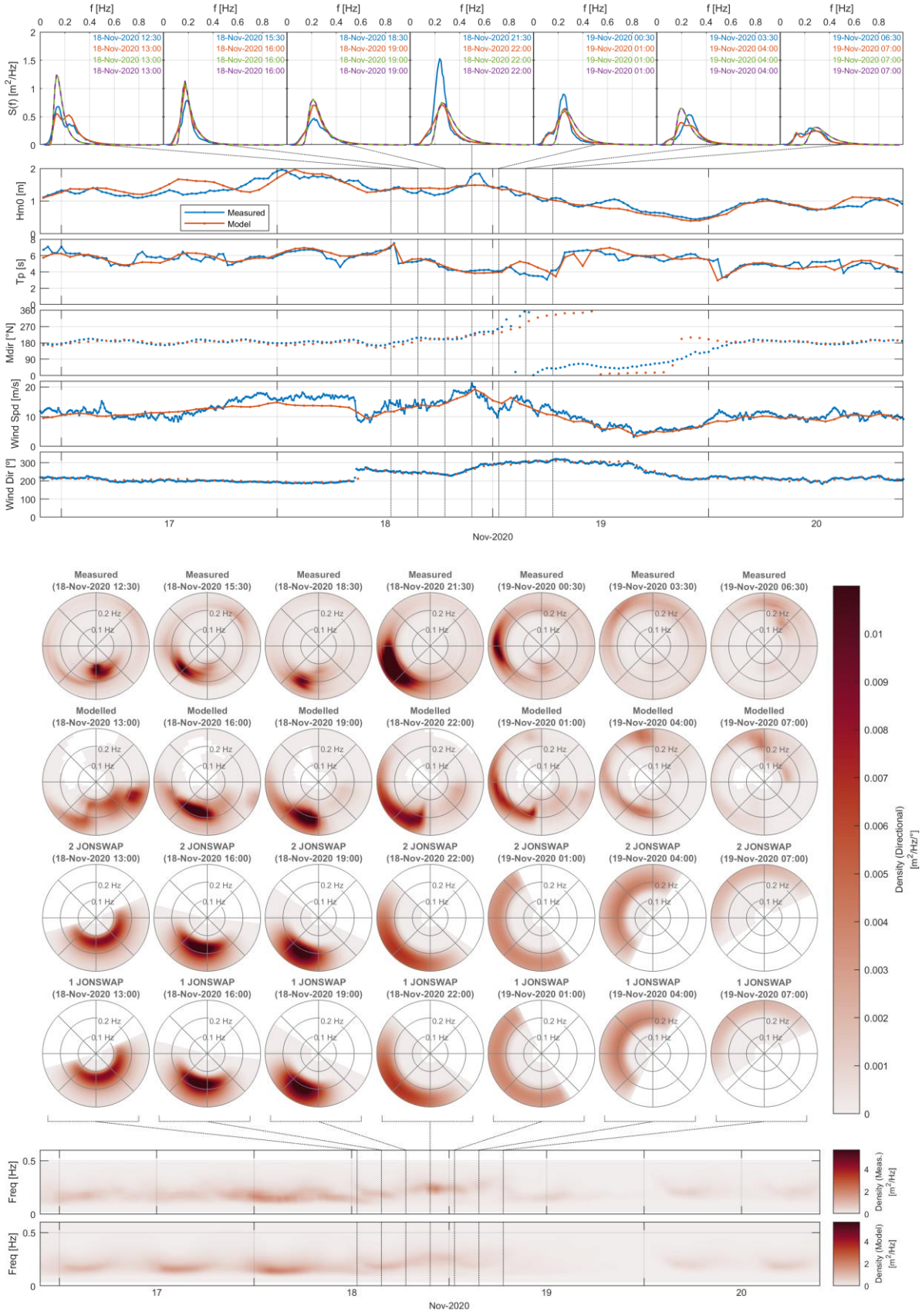



Figure C.231. AWAC B1, largest measured wind speed from the west.

### C.8.4 AWAC C

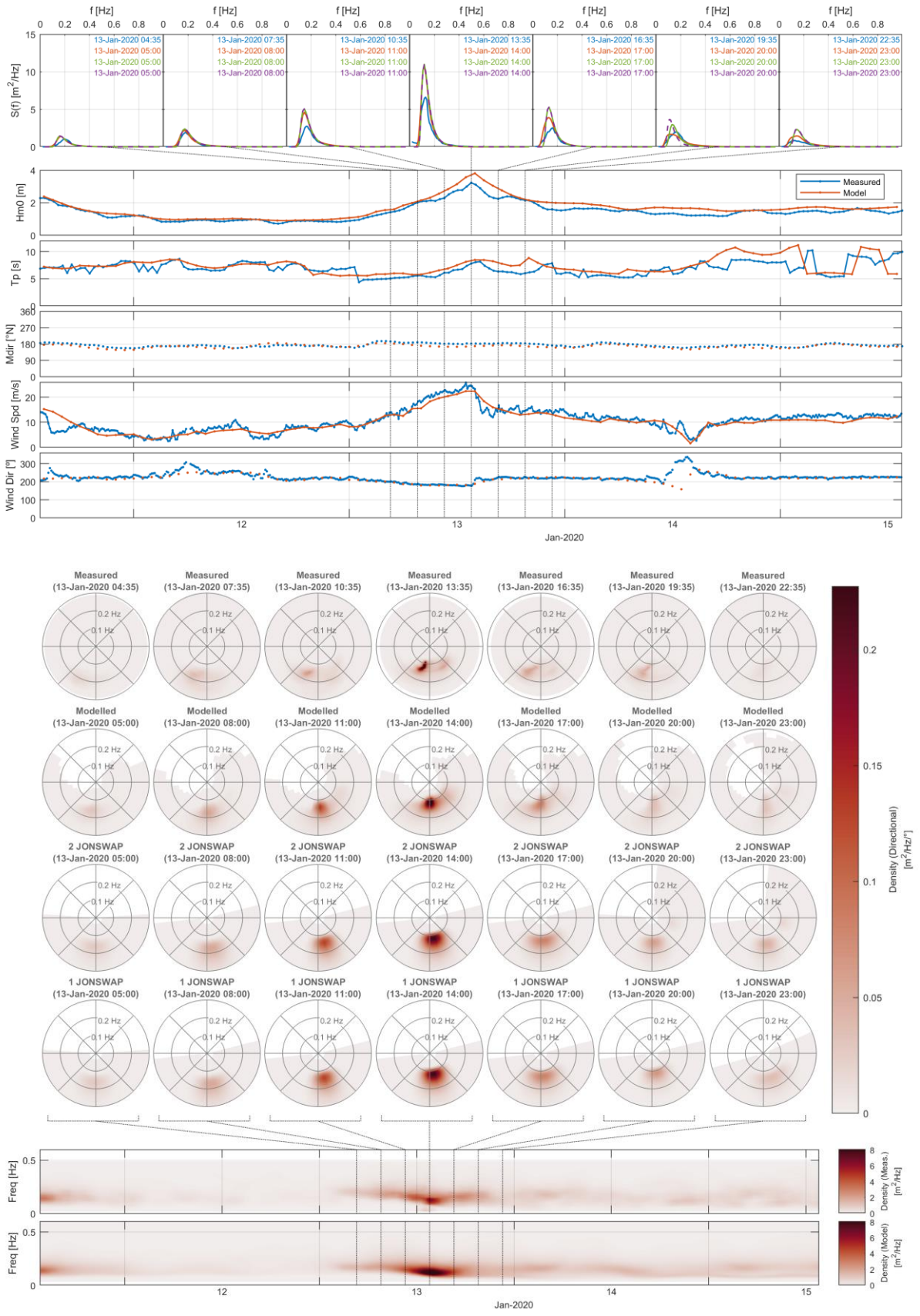



Figure C.232. AWAC C, largest Hm0 peak.

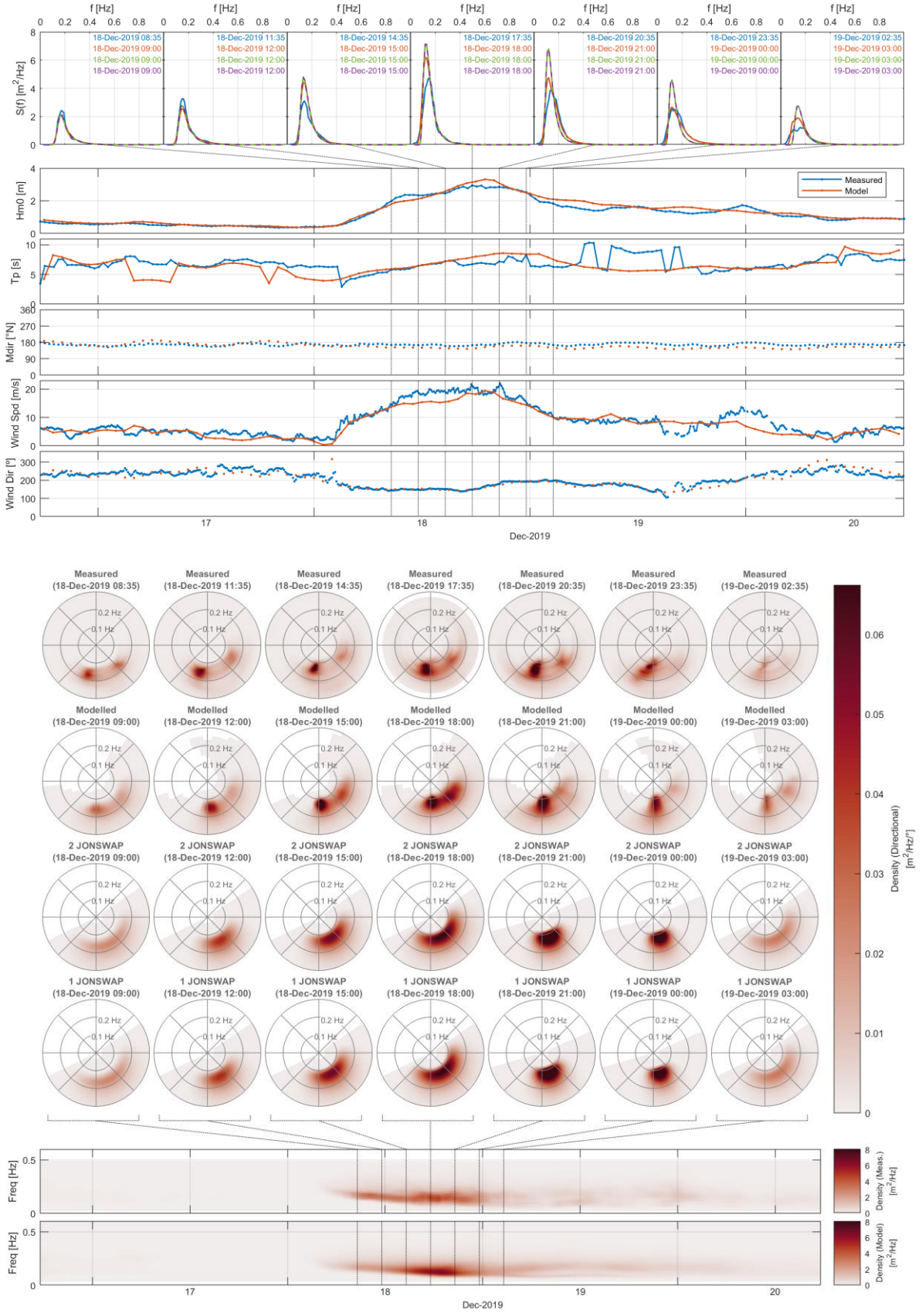



Figure C.233. AWAC C, second largest Hm0 peak.

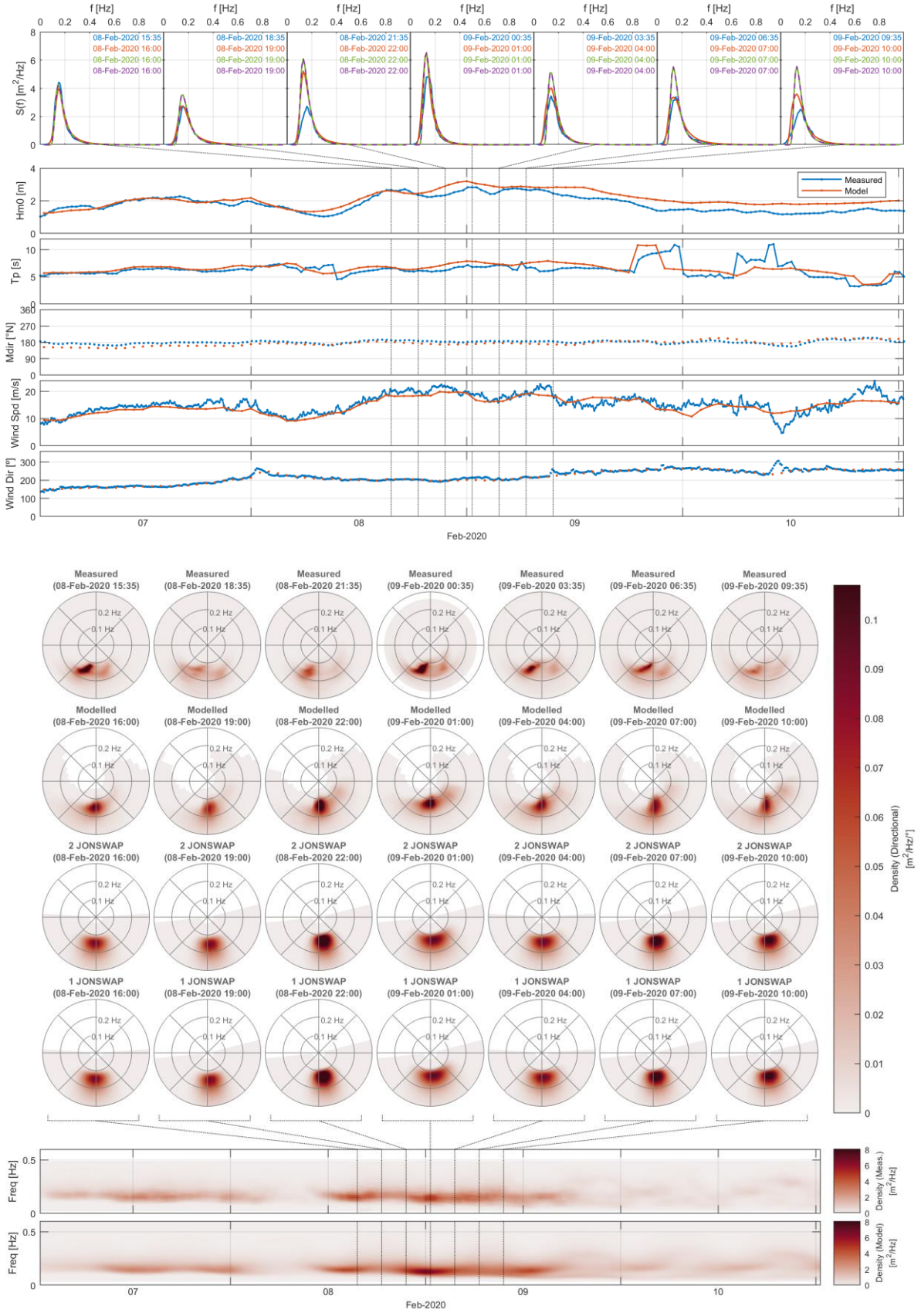



Figure C.234. AWAC C, third largest Hm0 peak.

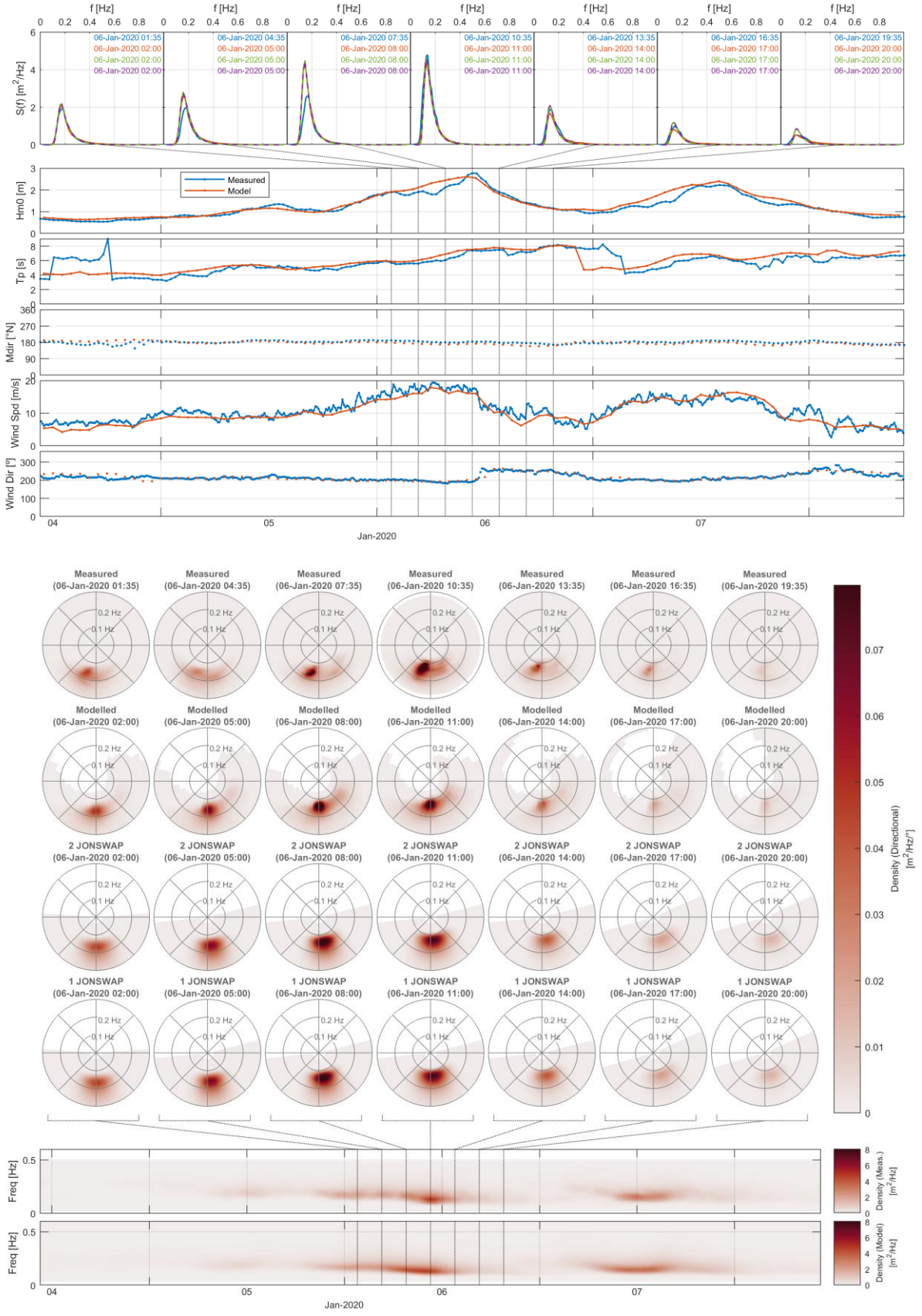



Figure C.235. AWAC C, fourth largest Hm0 peak.

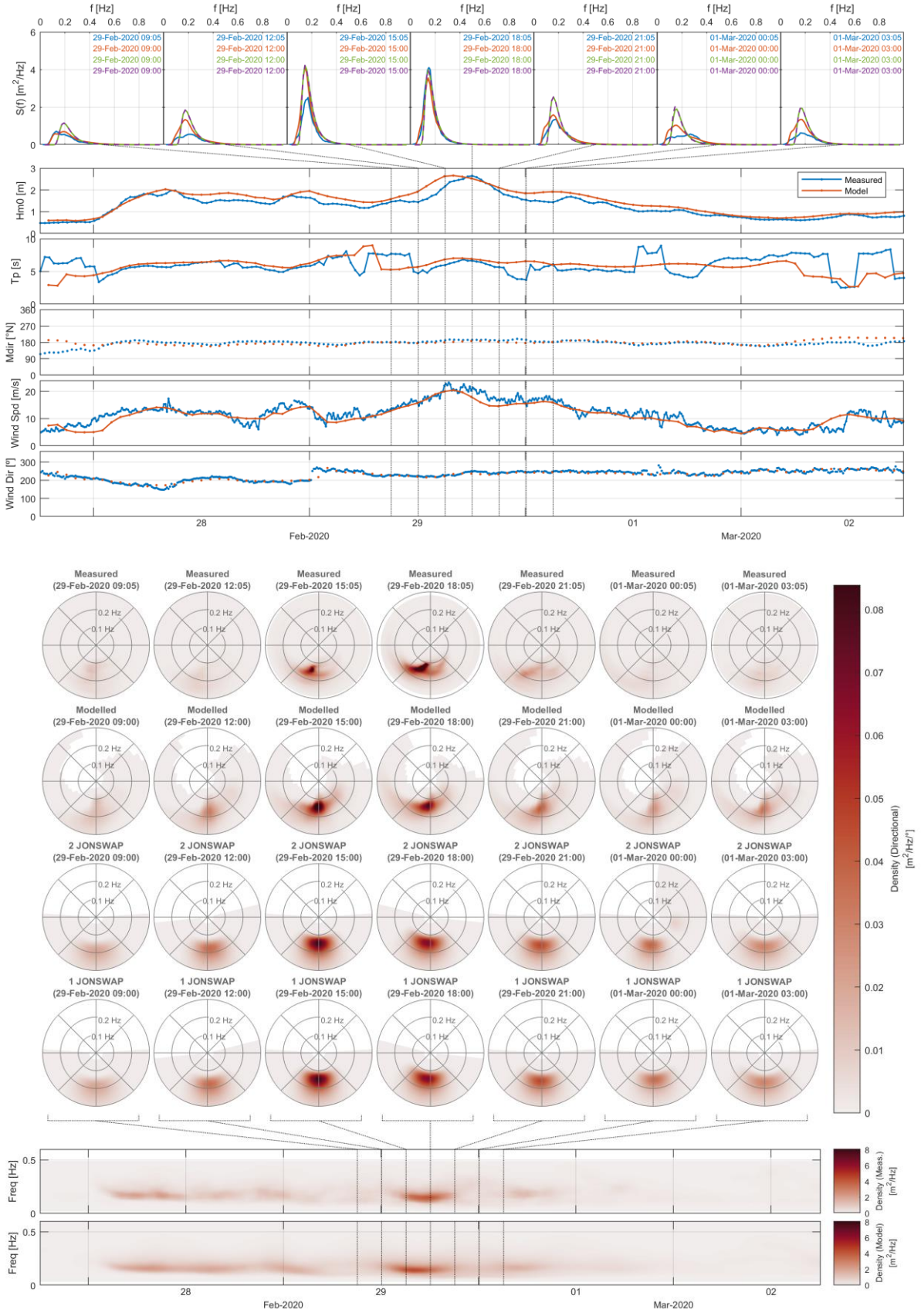



Figure C.236. AWAC C, fifth largest Hm0 peak.

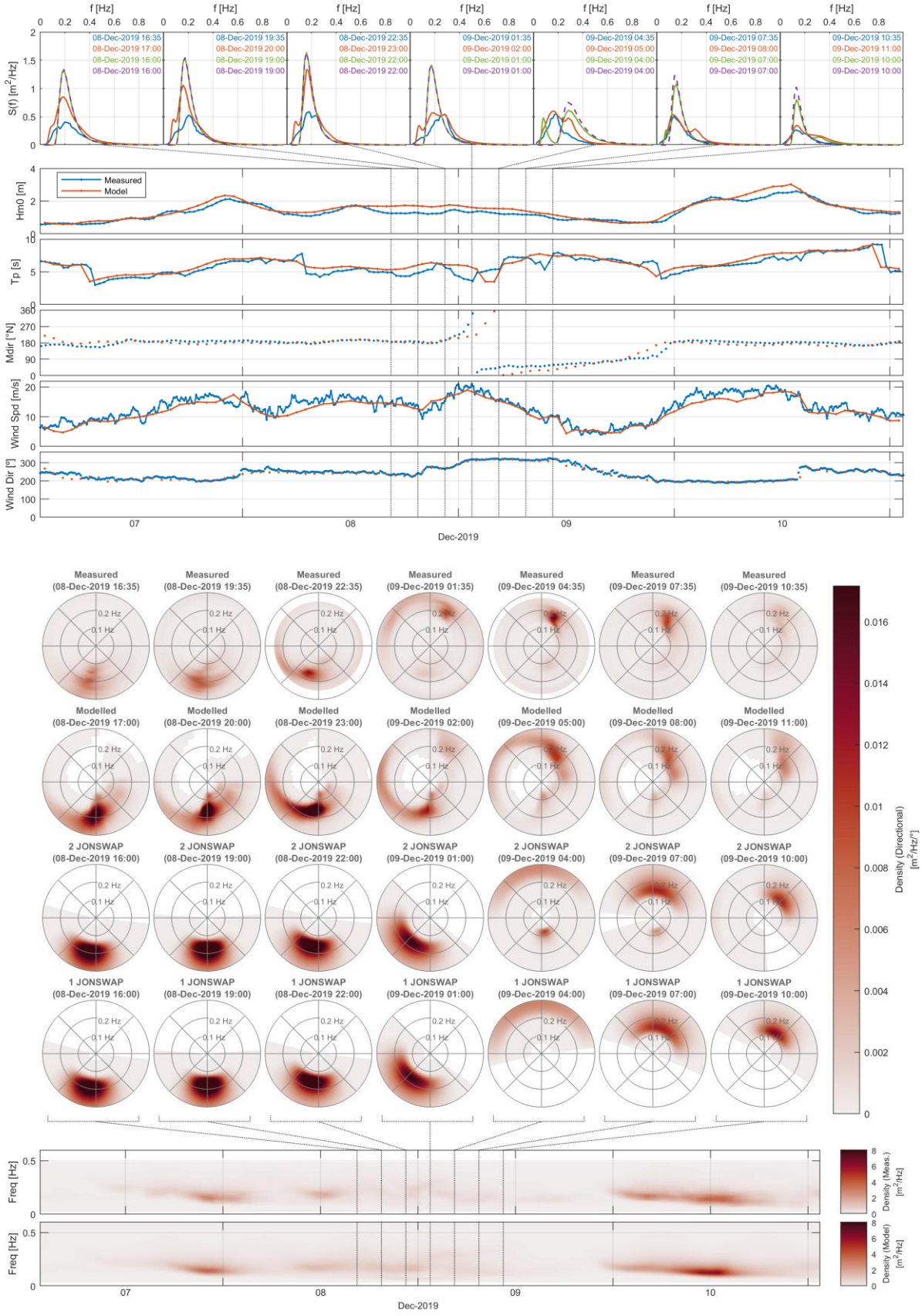



Figure C.237. AWAC C, largest measured wind speed from the north.

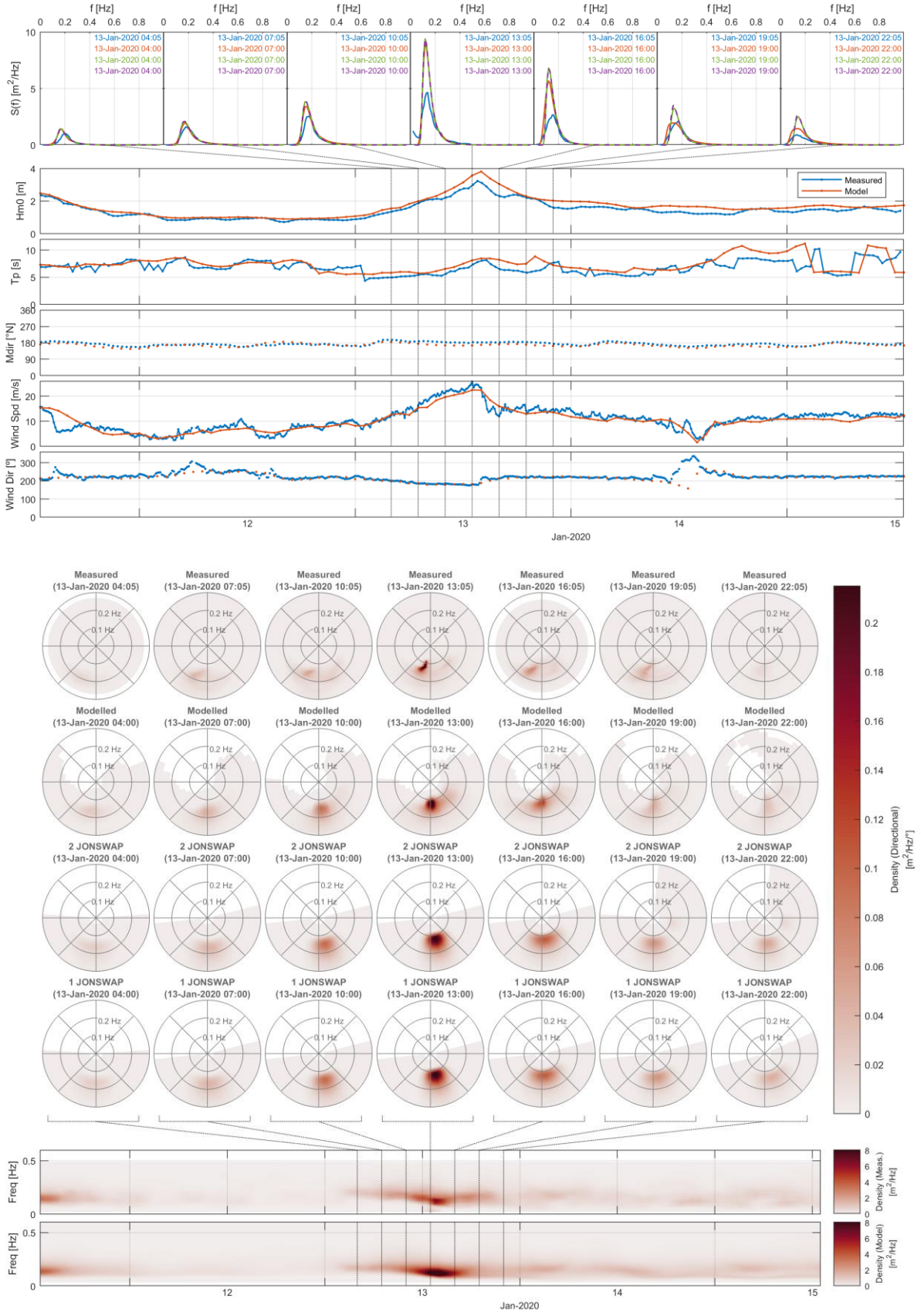



Figure C.238. AWAC C, largest measured wind speed from the south.

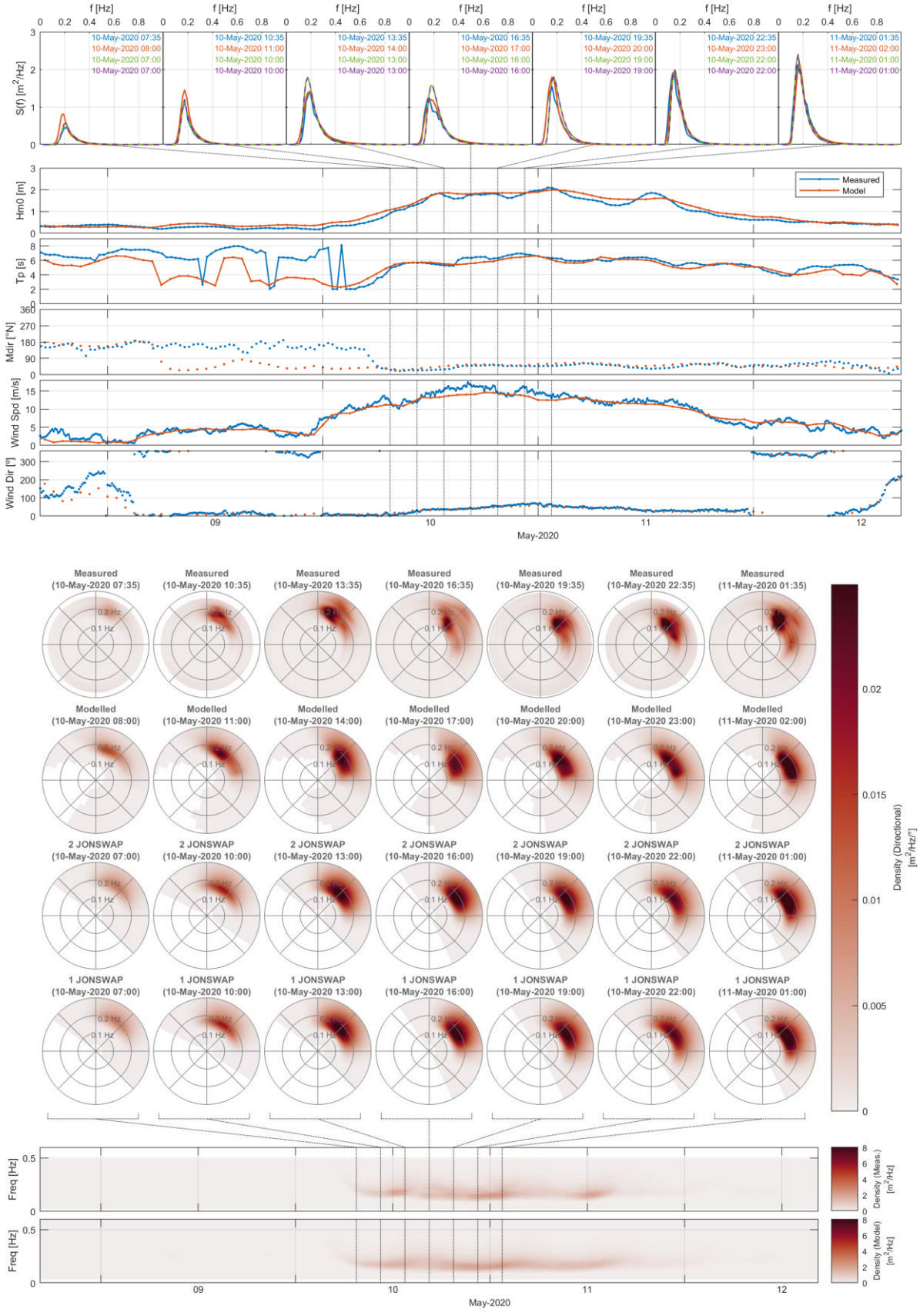



Figure C.239. AWAC C, largest measured wind speed from the east.

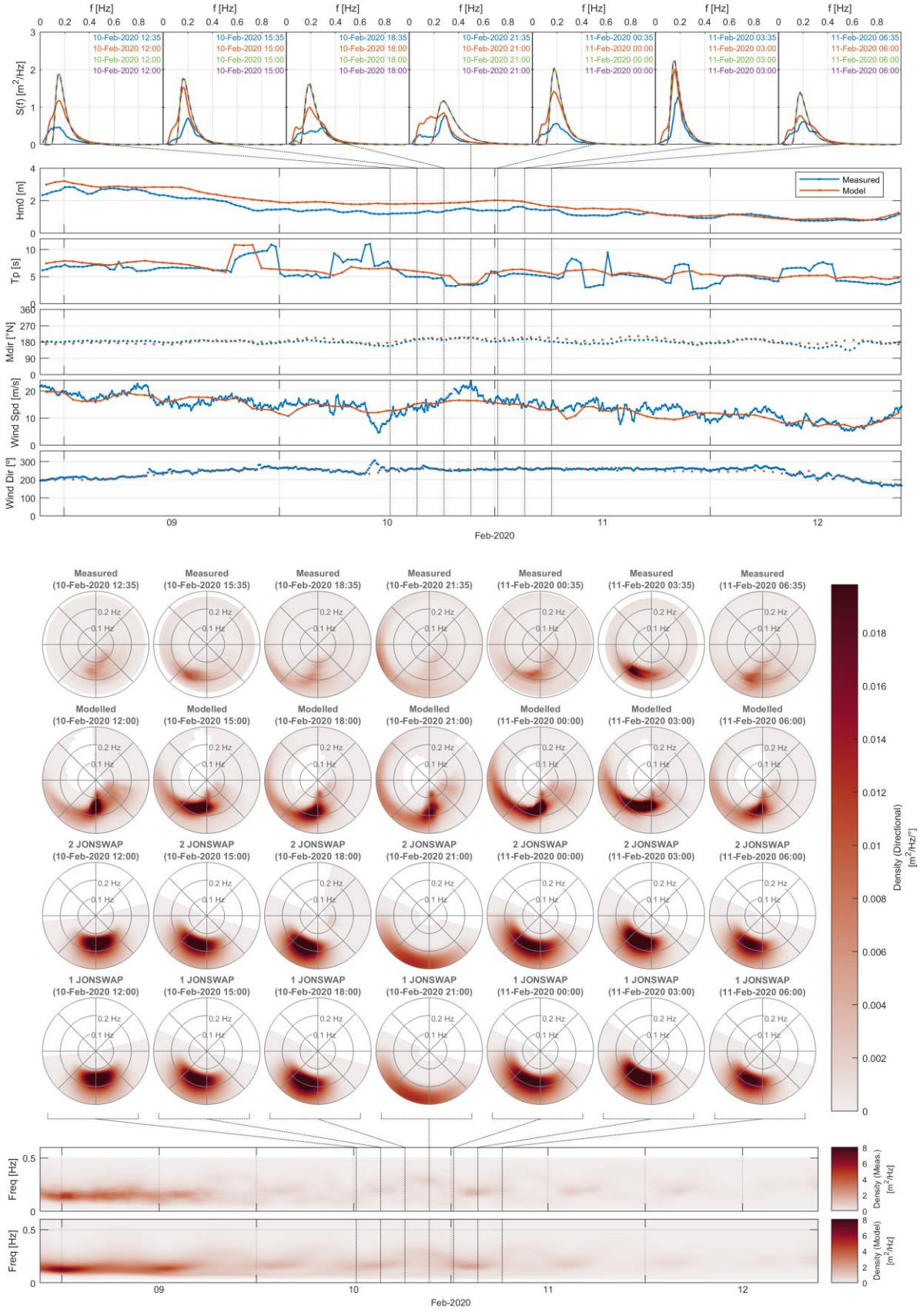



Figure C.240. AWAC C, largest measured wind speed from the west.

### C.8.5 AWAC D1

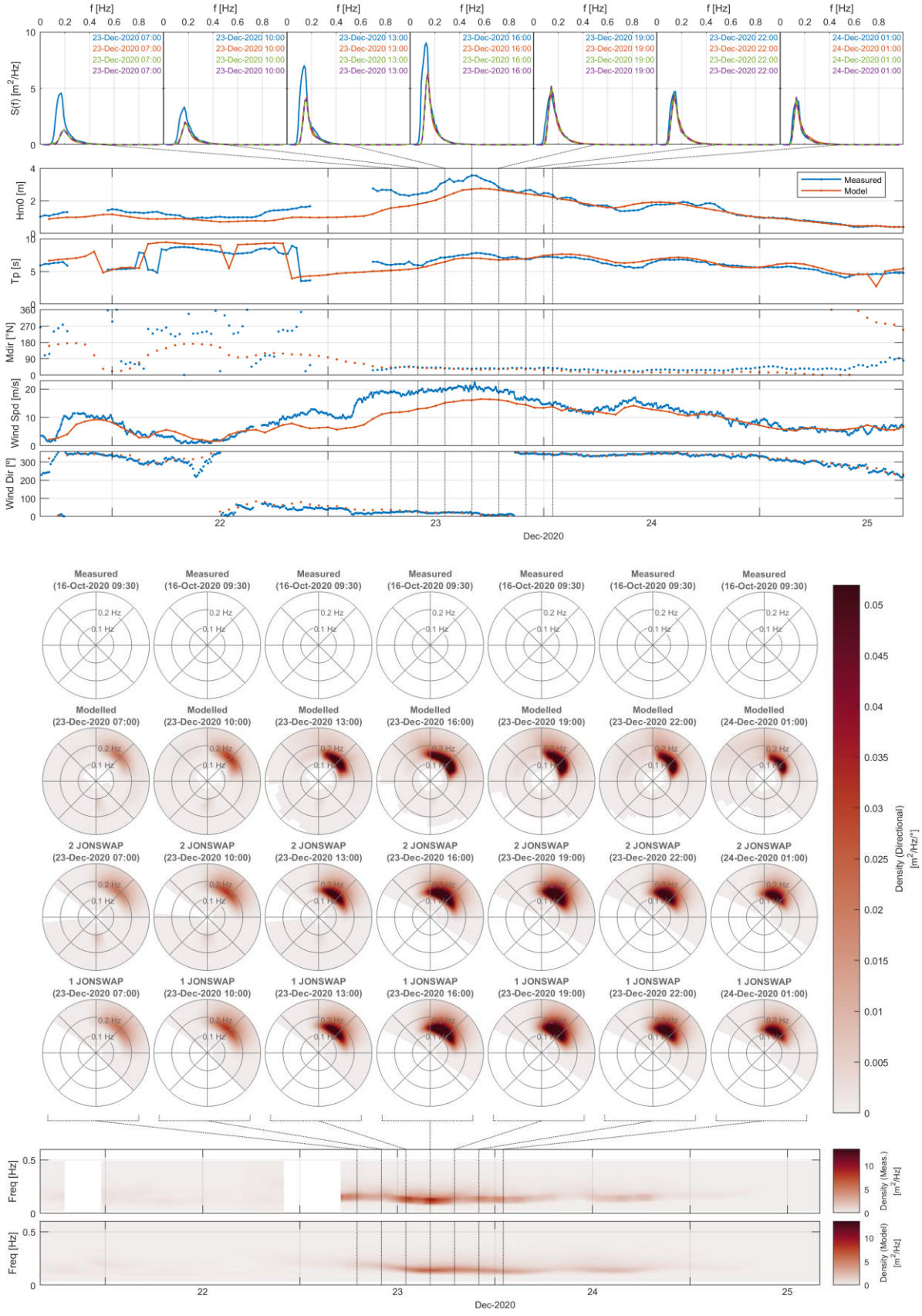



Figure C.241. AWAC D1, largest Hm0 peak.

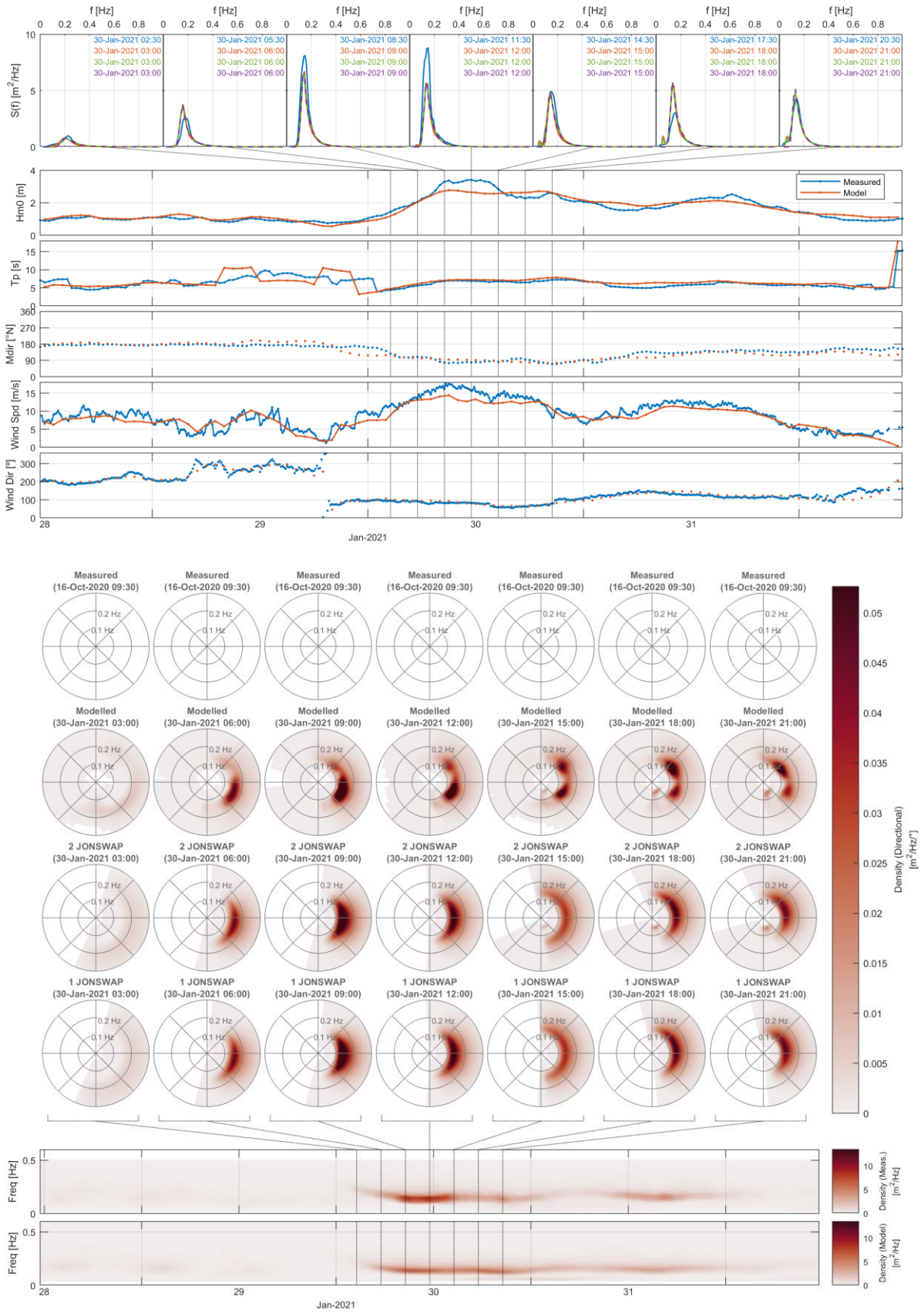



Figure C.242. AWAC D1, second largest Hm0 peak.

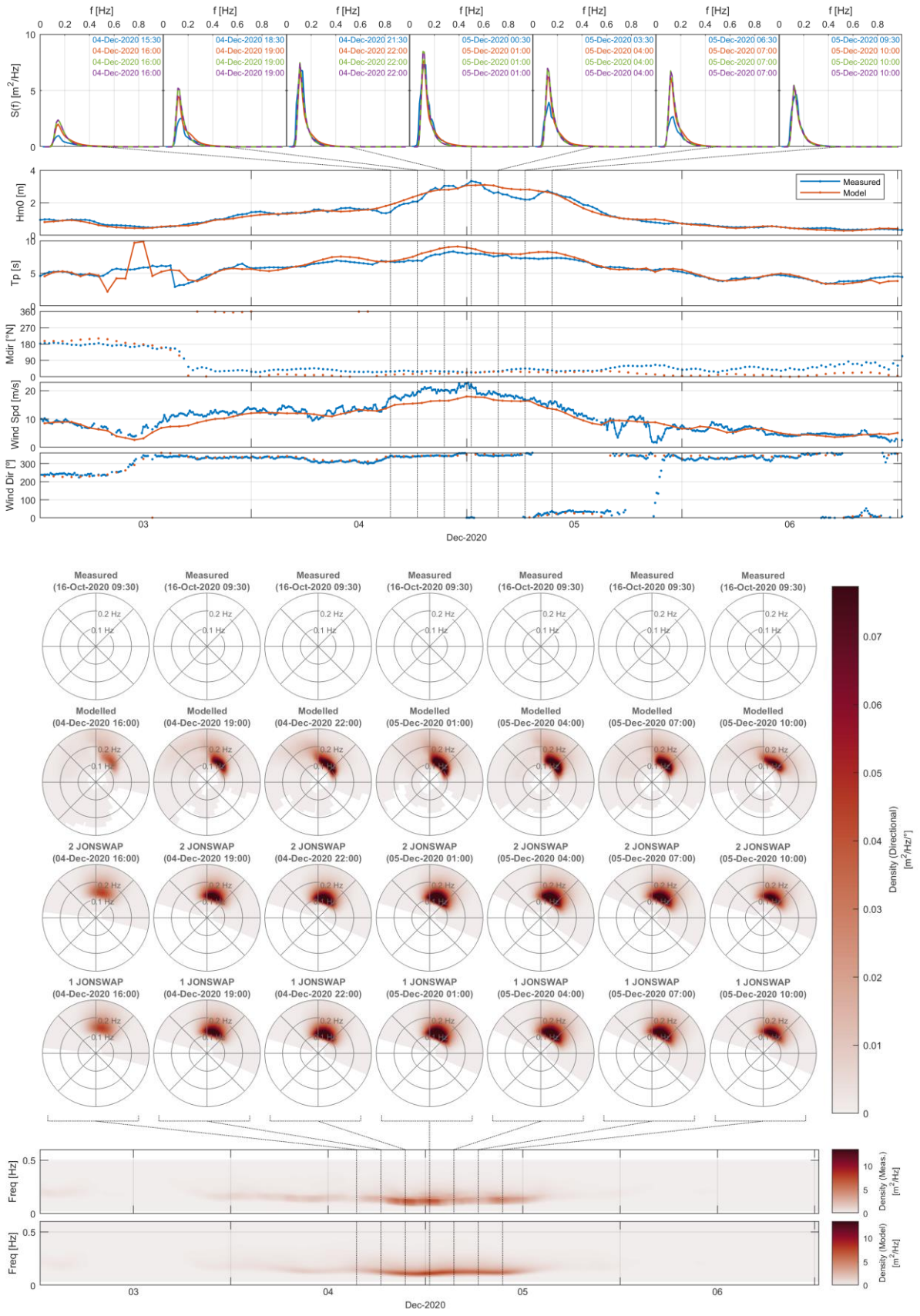



Figure C.243. AWAC D1, third largest Hm0 peak.

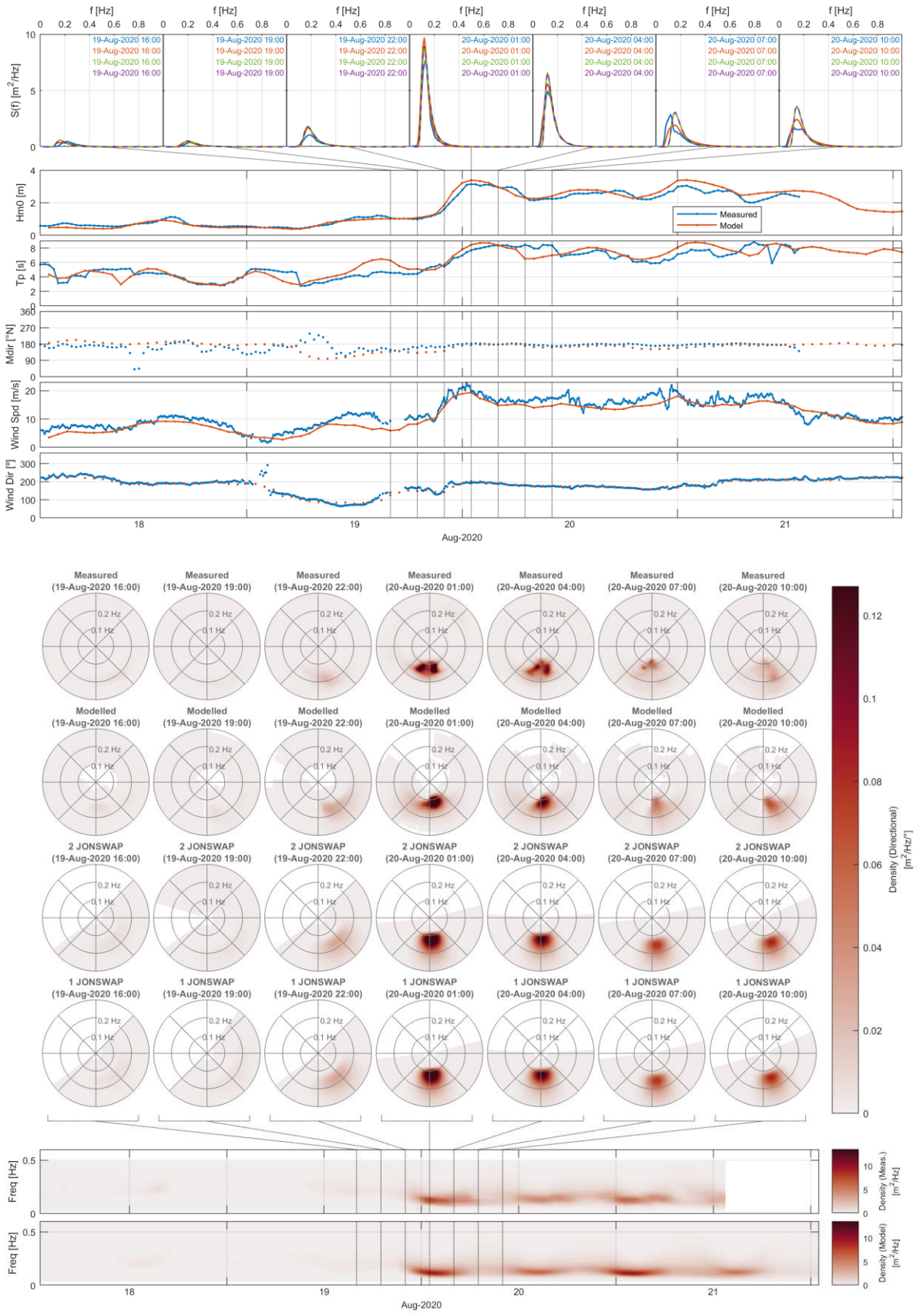



Figure C.244. AWAC D1, fourth largest Hm0 peak.

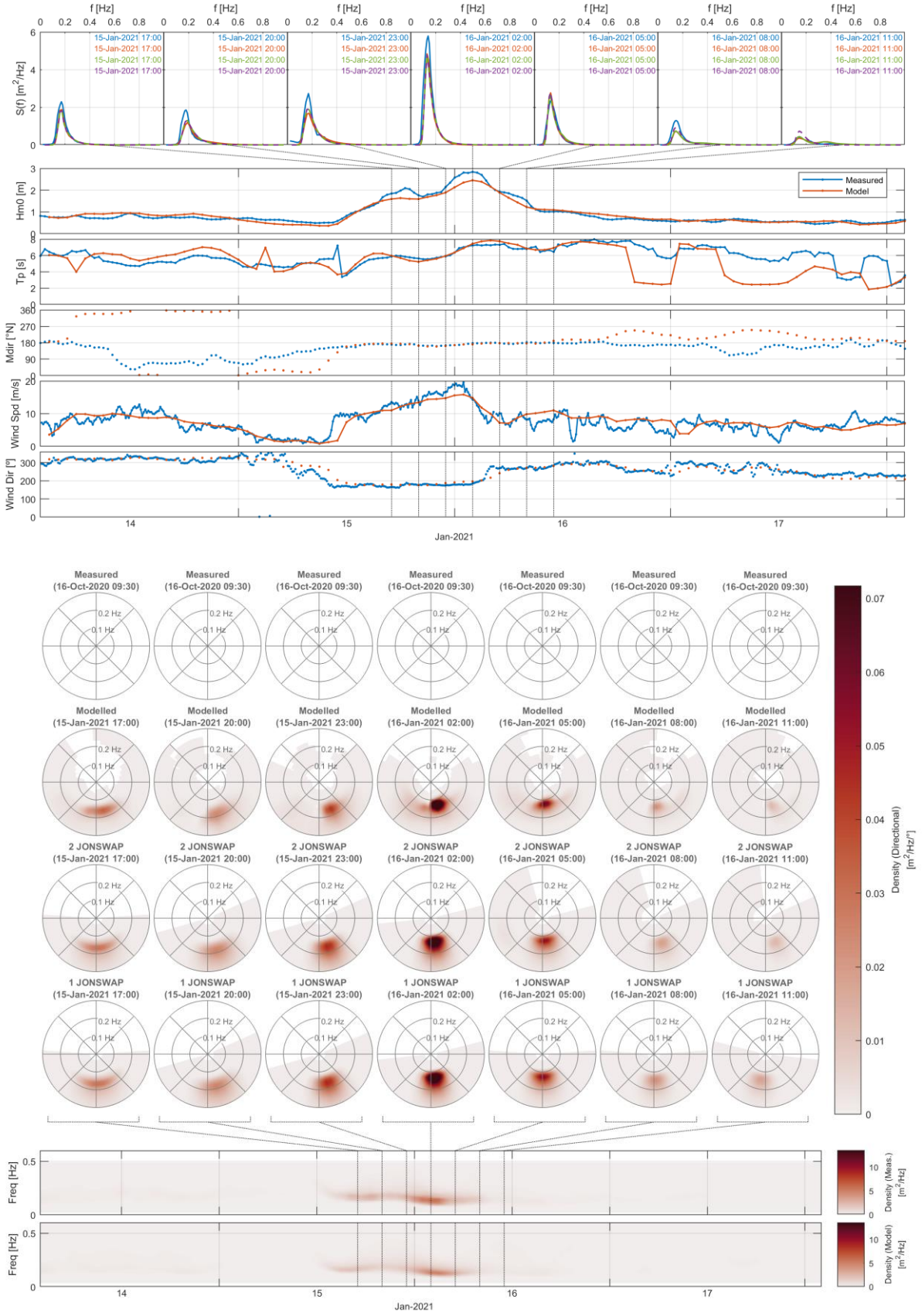



Figure C.245. AWAC D1, fifth largest Hm0 peak.

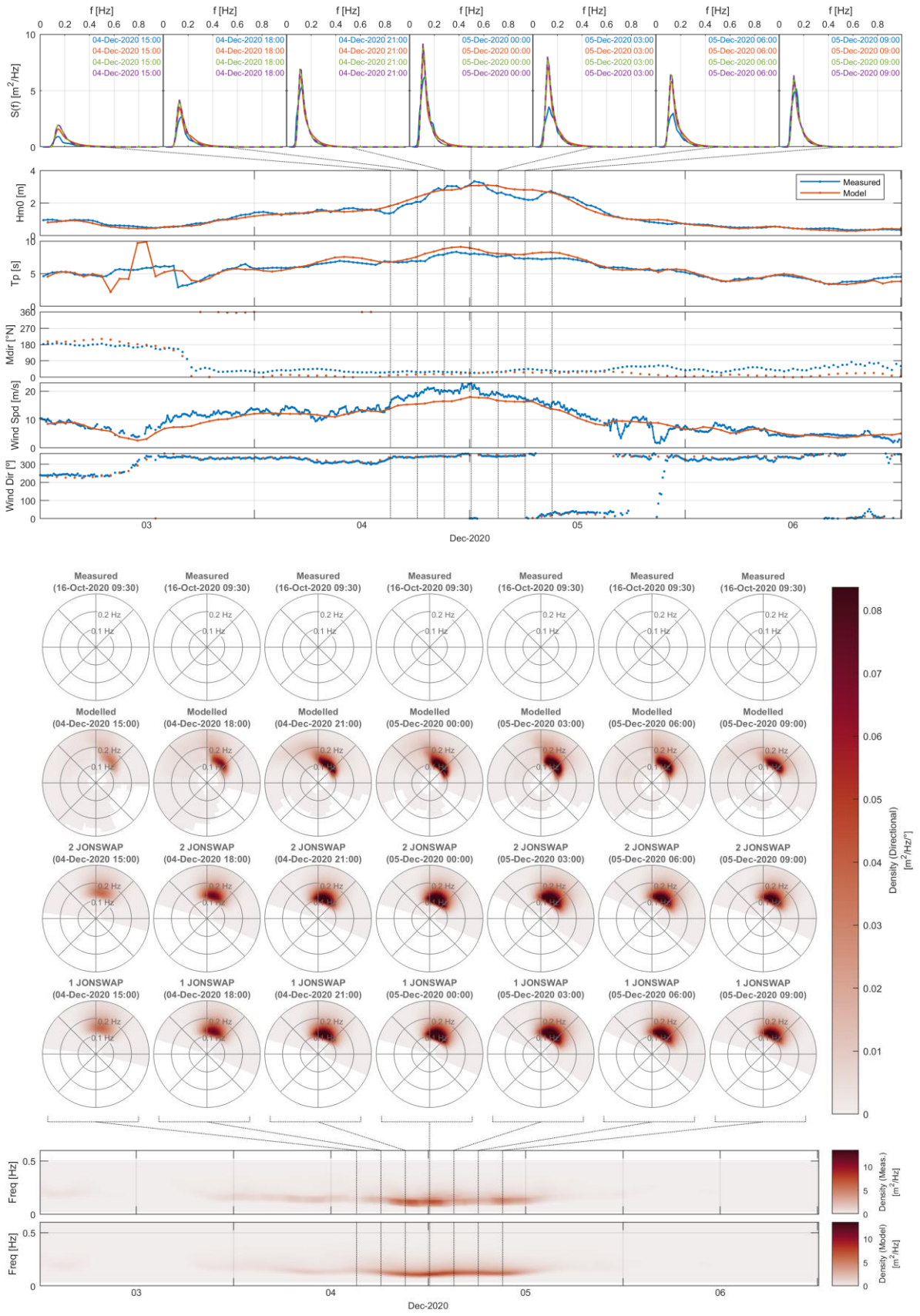



Figure C.246. AWAC D1, largest measured wind speed from the north.

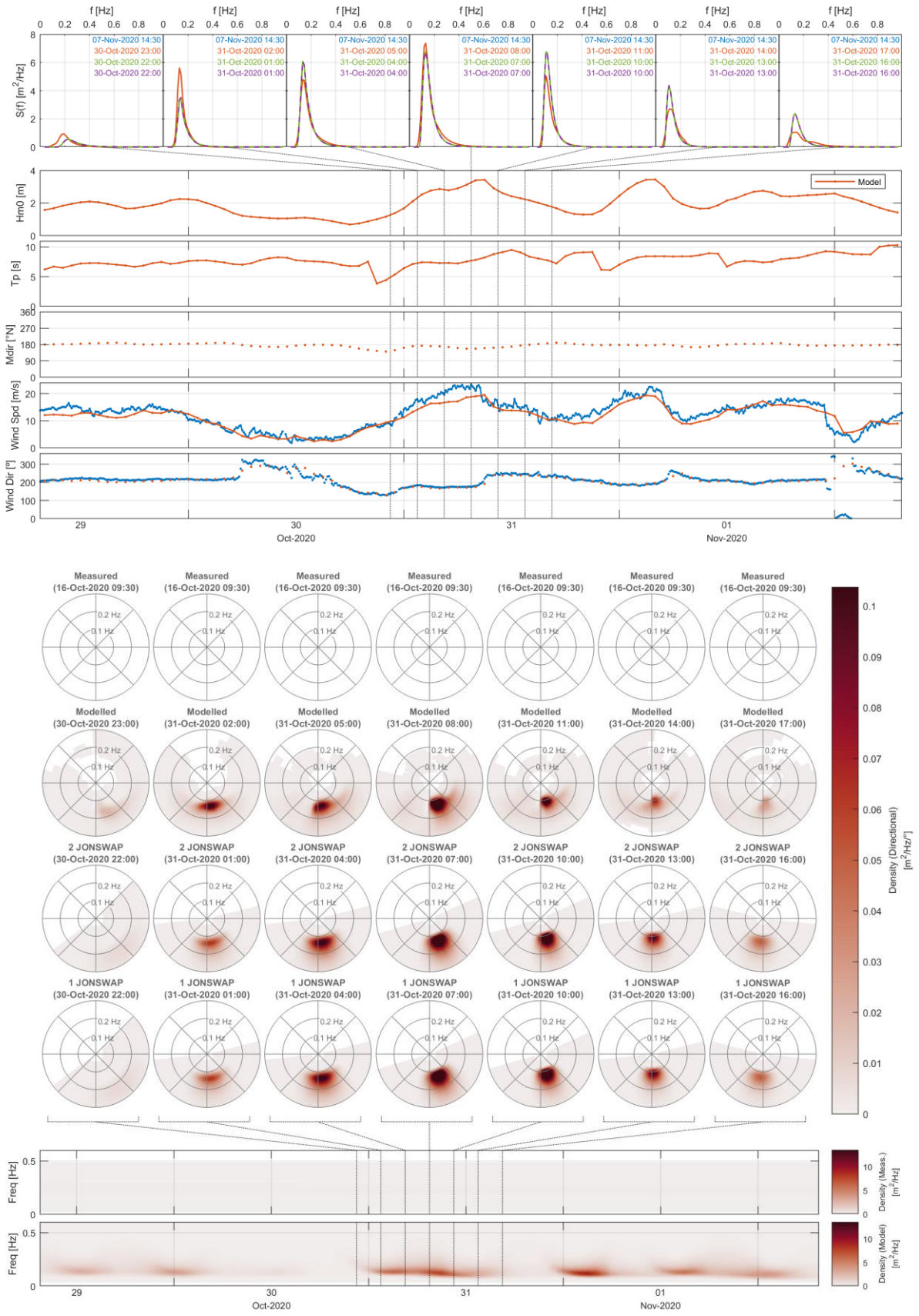



Figure C.247. AWAC D1, largest measured wind speed from the south.

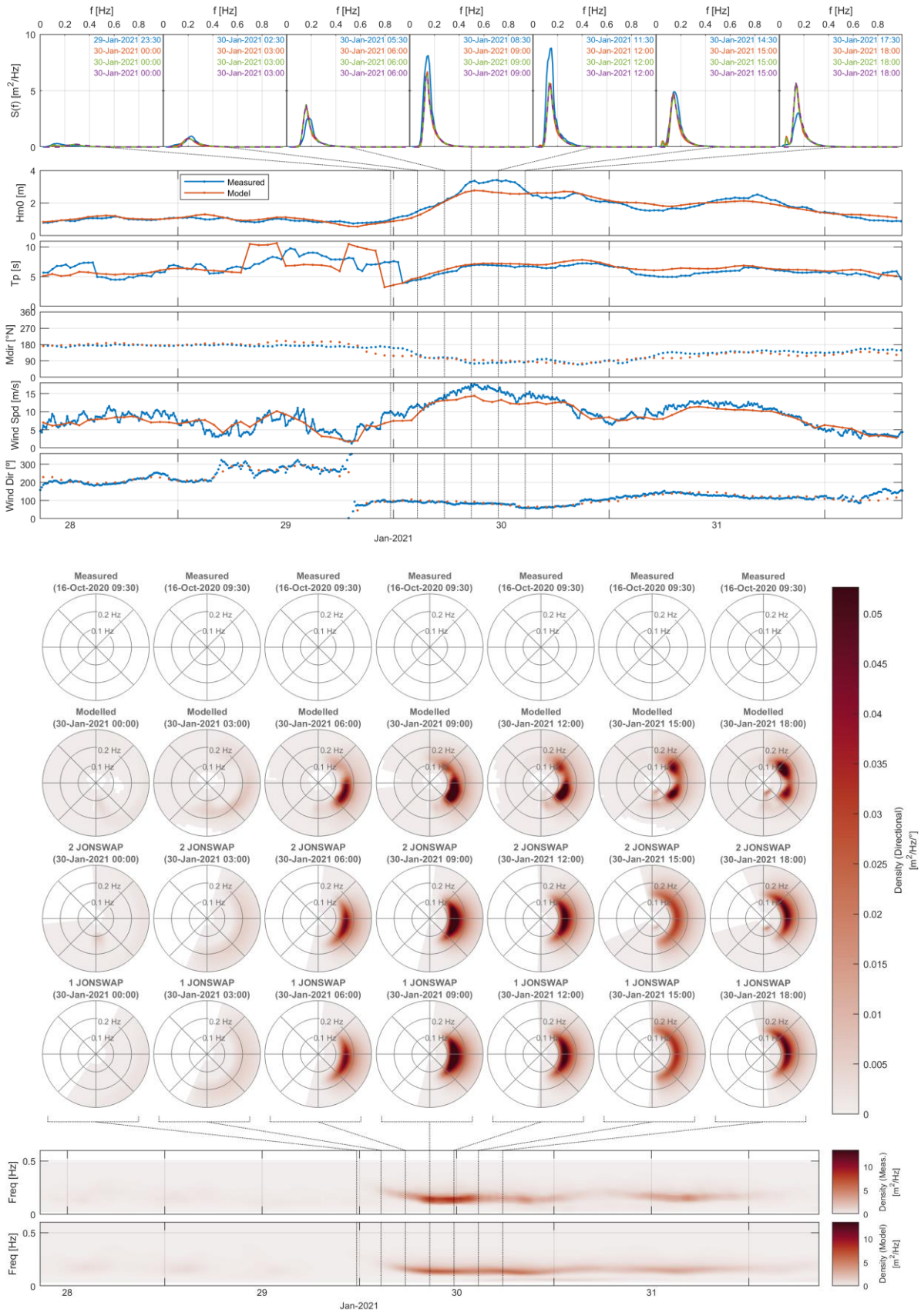



Figure C.248. AWAC D1, largest measured wind speed from the east.

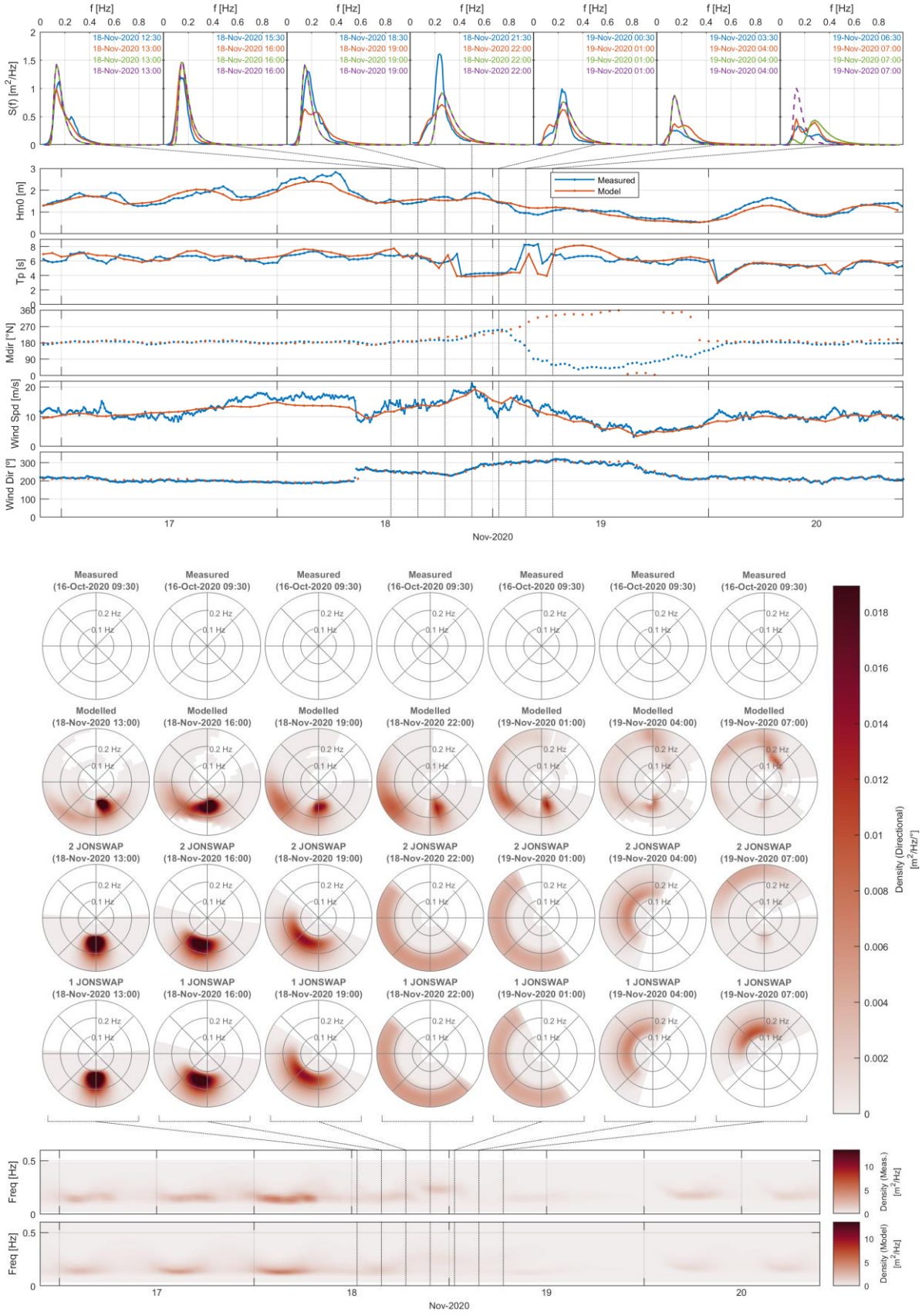



Figure C.249. AWAC D1, largest measured wind speed from the west.

### C.8.6 AWAC E

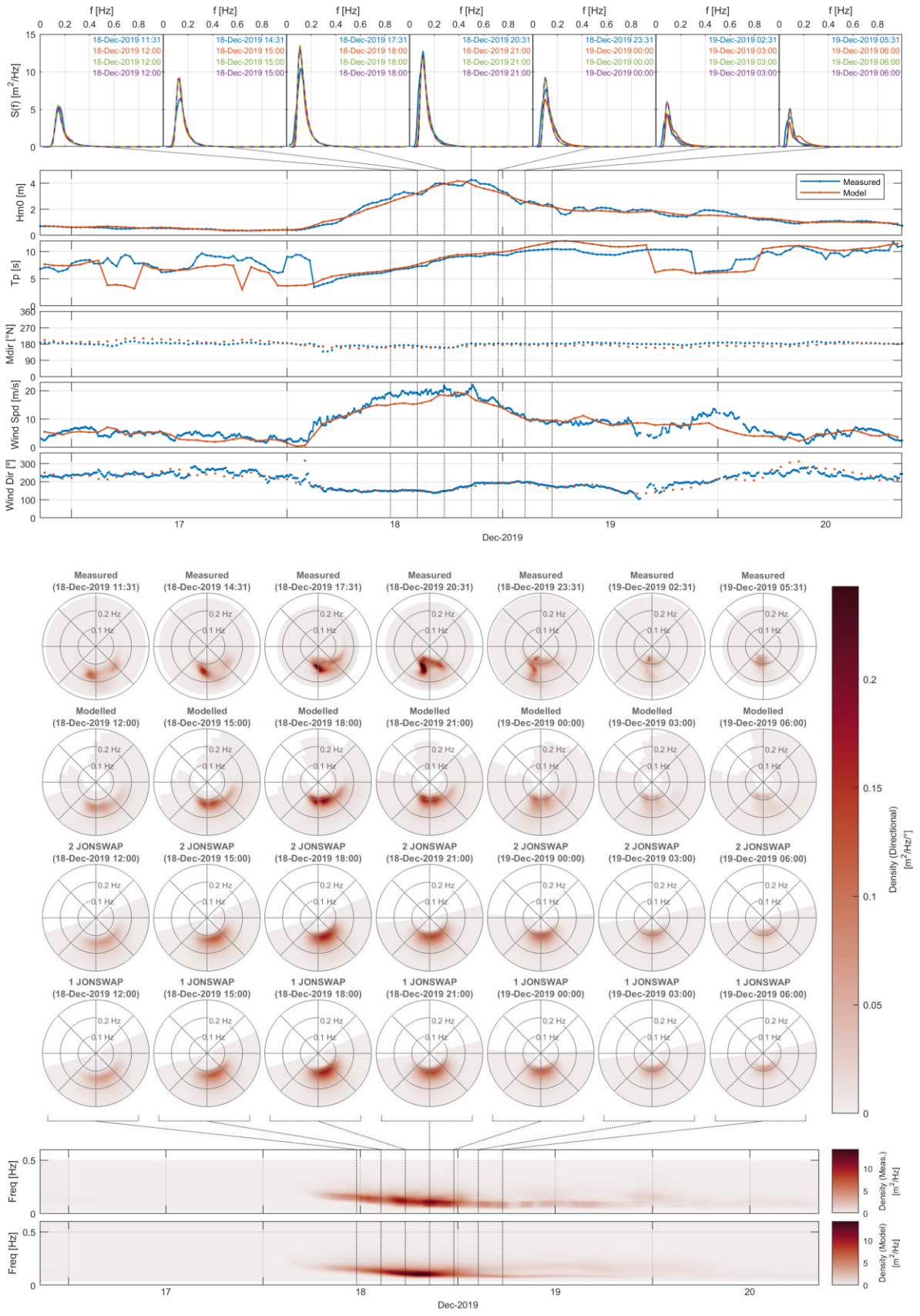



Figure C.250. AWAC E, largest Hm0 peak.

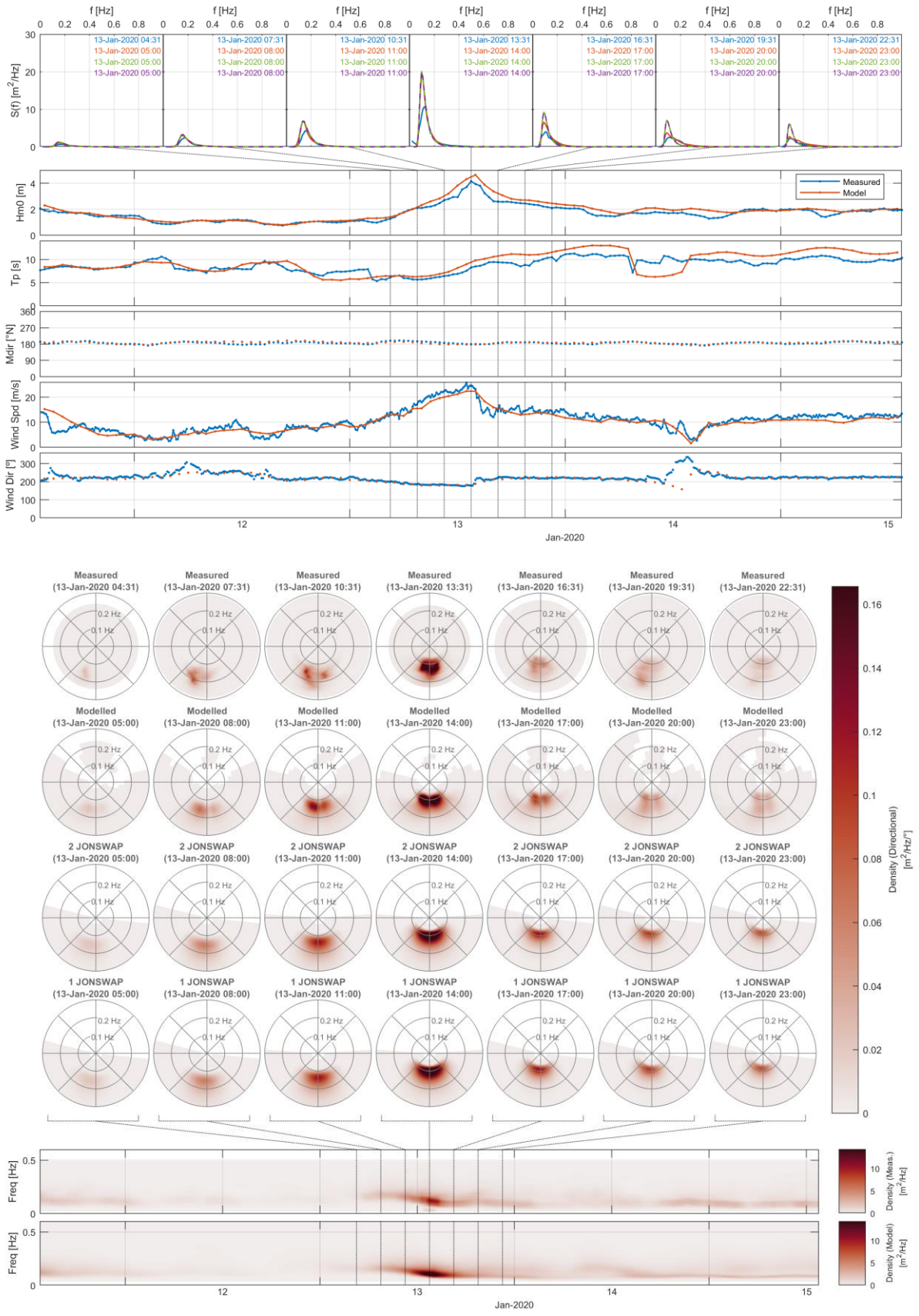



Figure C.251. AWAC E, second largest Hm0 peak.

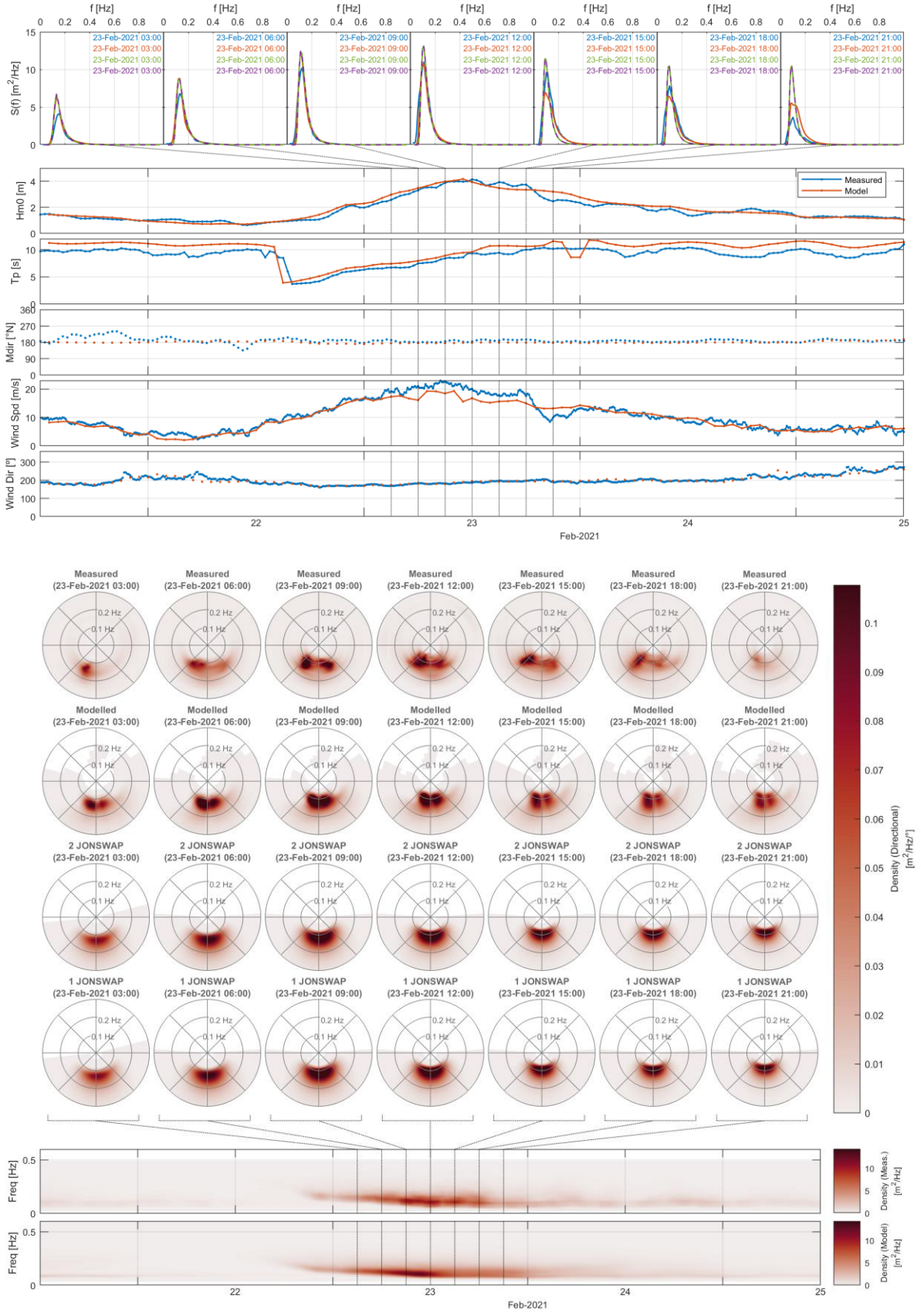



Figure C.252. AWAC E, third largest Hm0 peak.

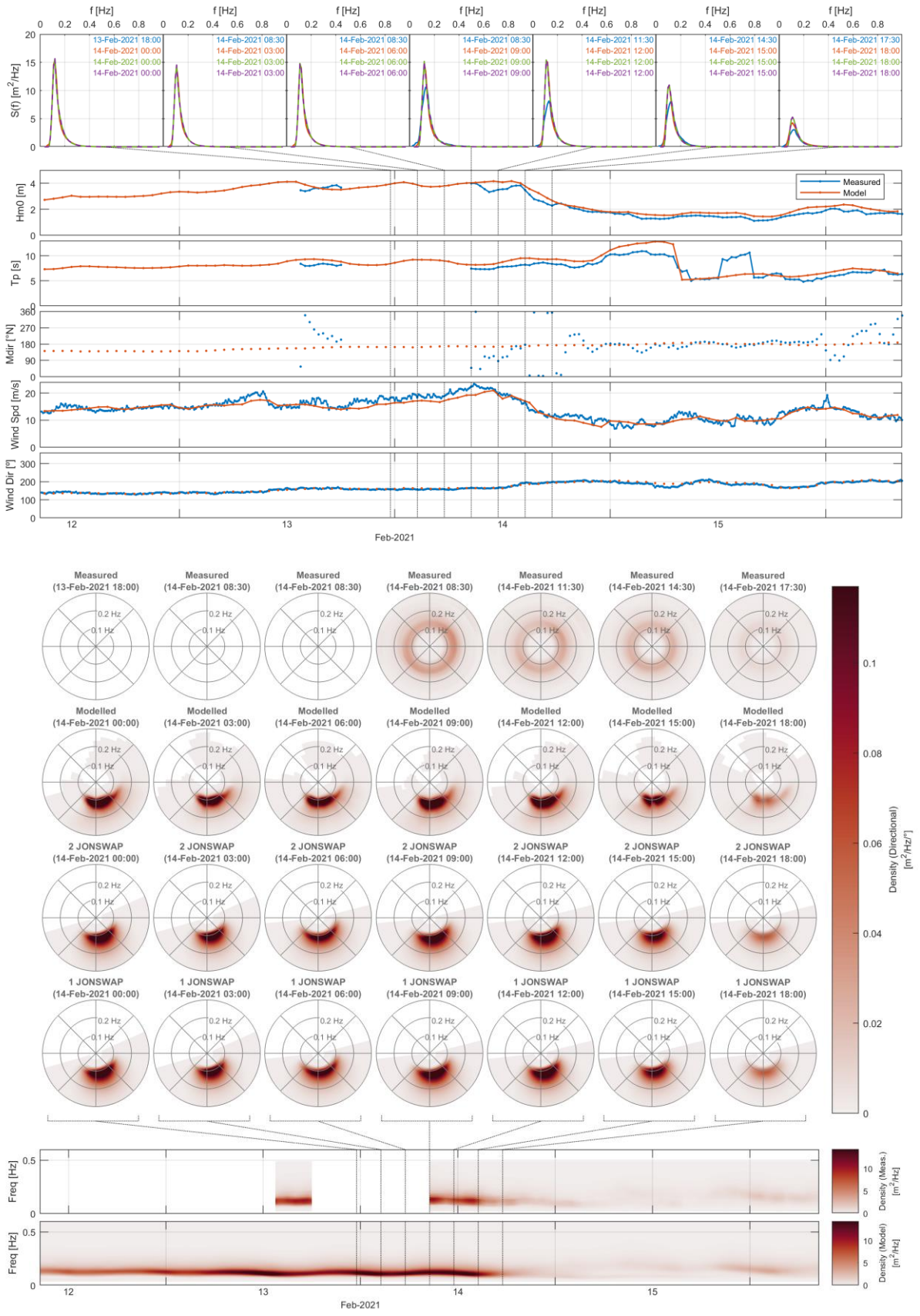



Figure C.253. AWAC E, fourth largest Hm0 peak.

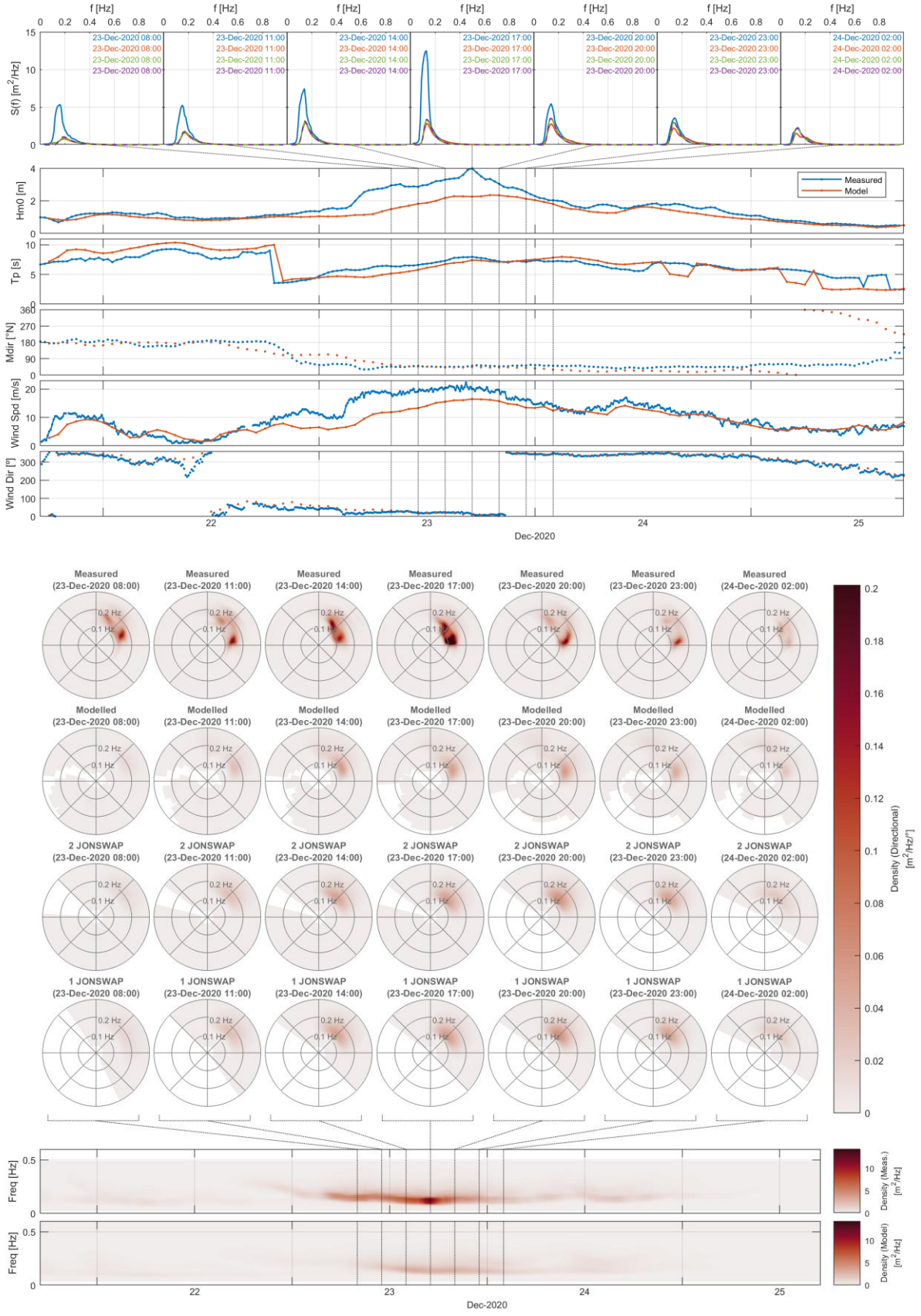



Figure C.254. AWAC E, fifth largest Hm0 peak.

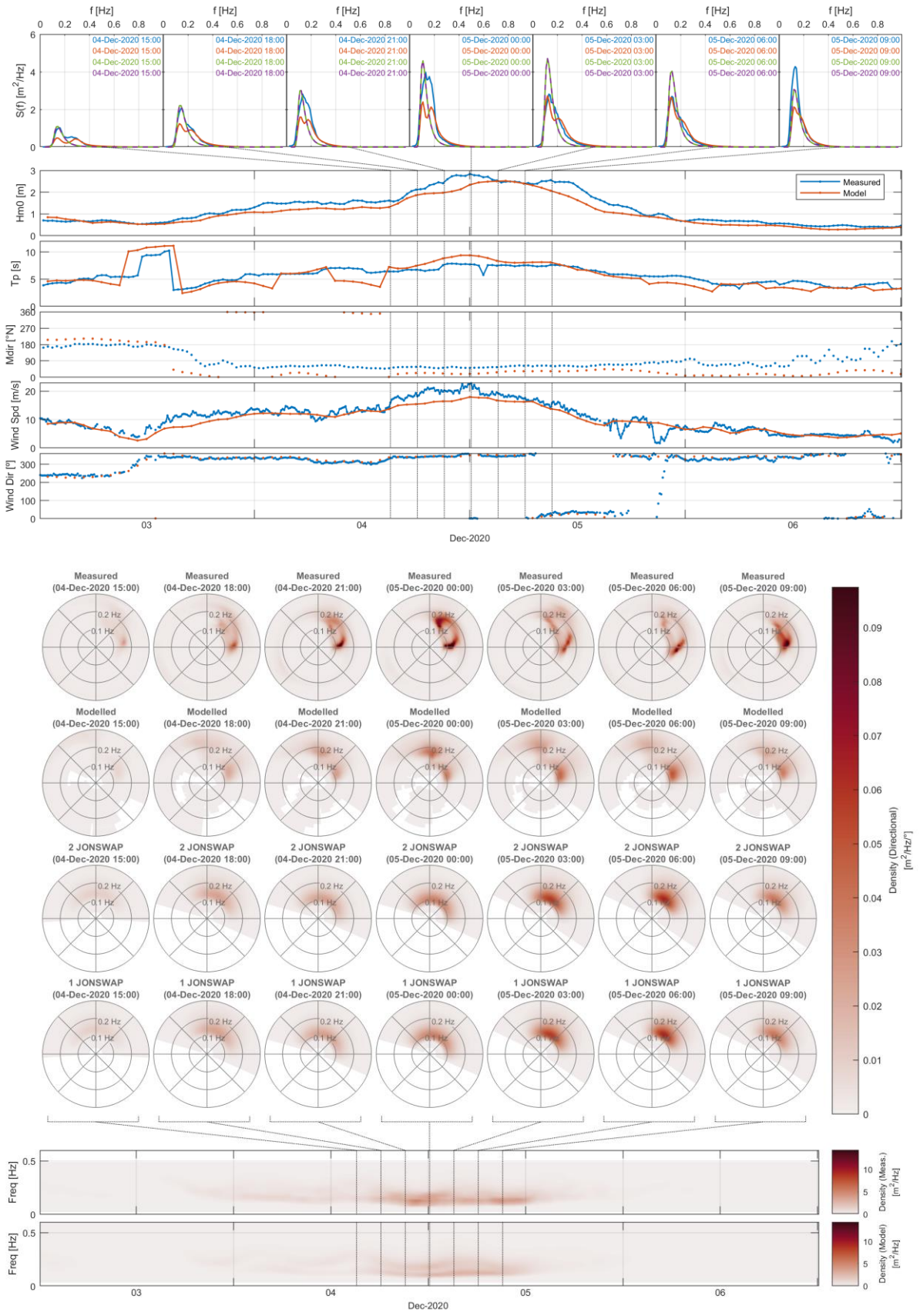



Figure C.255. AWAC E, largest measured wind speed from the north.

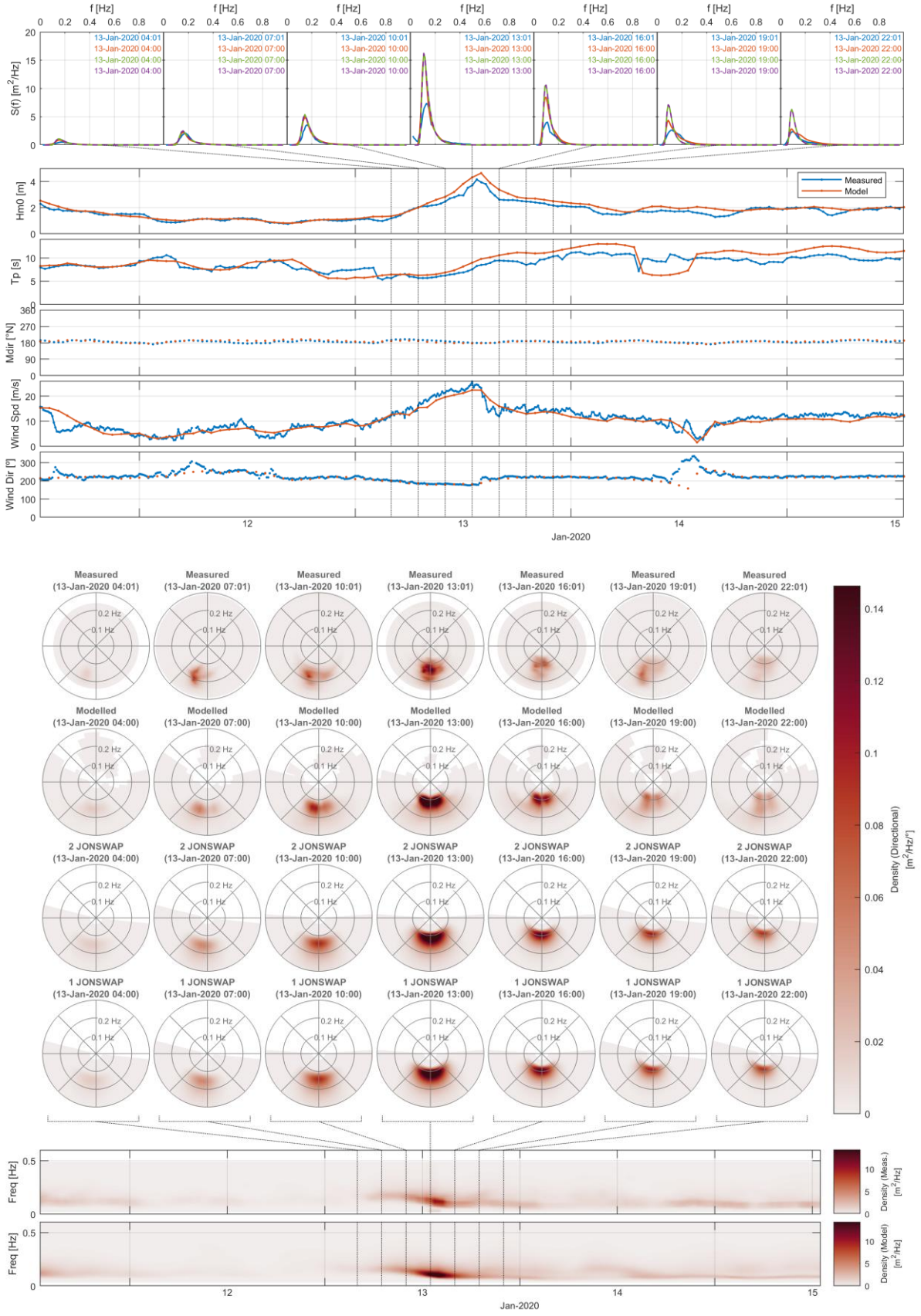



Figure C.256. AWAC E, largest measured wind speed from the south.

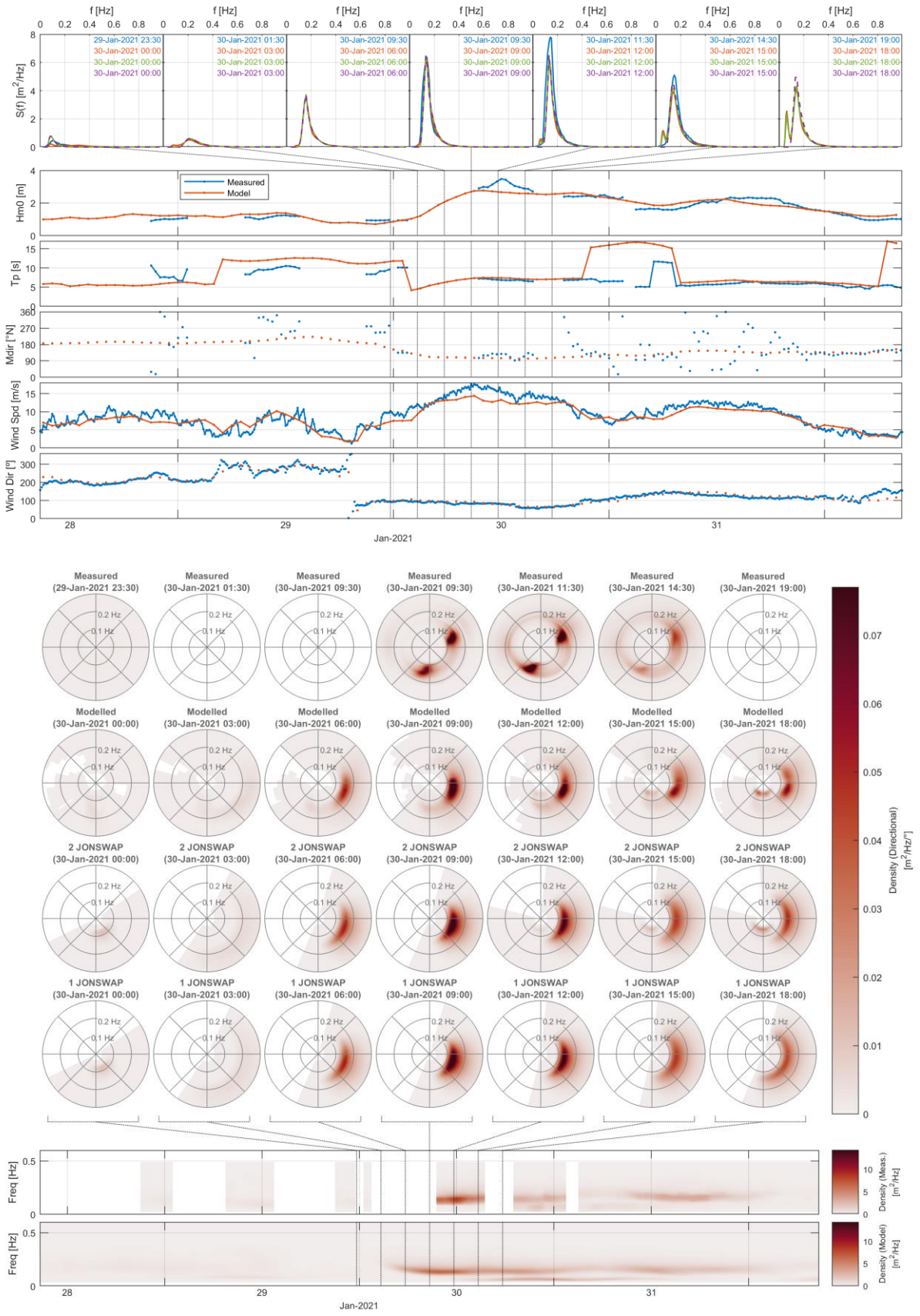



Figure C.257. AWAC E, largest measured wind speed from the east.

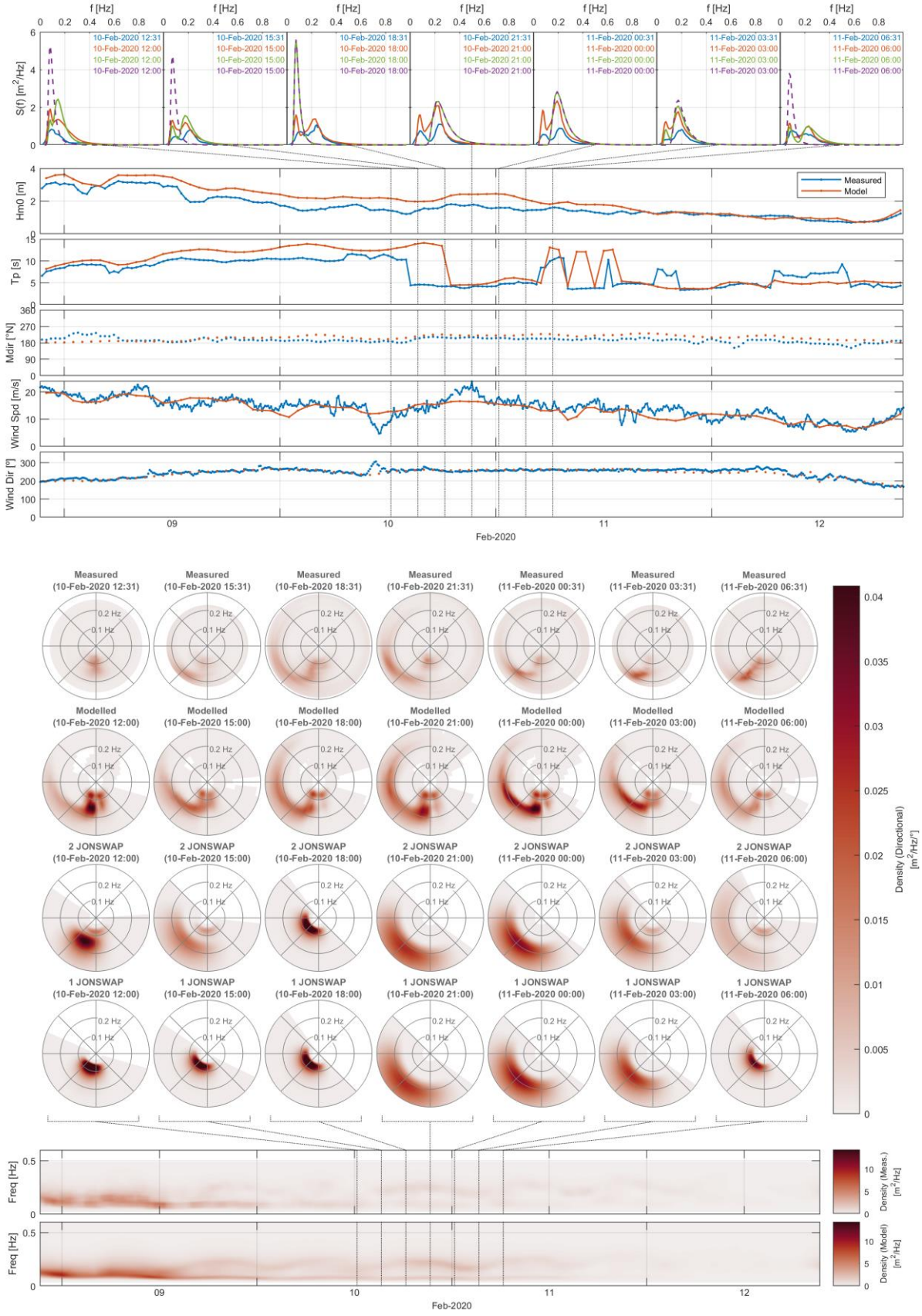



Figure C.258. AWAC E, largest measured wind speed from the west.

## C.9 Event Peak Comparison

In this Section, peak Hm0 values from model and measured data at the AWAC locations are compared. The following methodology is used:

**STEP 1: Find peaks in the measured data**

A peaks-over-threshold method is used as follows:

a) Split data into points above and below threshold of 1.5 m.
b) Discard all points below, creating a new time-series of only values above the threshold.
c) Place the first point in "Cluster 1". If the second point is temporally within 48 hours of the first, it too is in Cluster 1. Otherwise, Cluster 1 is complete and this becomes the first point in Cluster 2.
d) Proceed to the third point. If it is within 24 hours of the second point, it is in the same cluster. Otherwise, it is the start of a new cluster.
e) Continue through the entire time-series until all data above the threshold are assigned to a cluster.
f) Take the maximum of each cluster.

It should be noted that a low threshold of 1.5 m will return a number of peaks which would by no means be considered "extreme" in the context of an extreme value analysis. However, given that only approximately 6 months of data are available for each location, such a low value is necessary to provide sufficient peaks for any meaningful comparison.

**STEP 2: Find peaks in the modelled data**

The same process is used to determine peaks in the modelled data. To ensure only data from the period corresponding to measurements is used, only model data with a timestamp within 24 hours of a valid measured Hm0 is used.

**STEP 3: Match peaks**

Modelled and measured peaks are paired together if they fall within 24 hours of each other. For all measured peaks which do *not* correspond to a model peak, the largest model value is found within +/- 24 hours. Similarly, for all modelled peaks which do not correspond to a measured peak, the largest measured value within +/- 24 hours is found.

**STEP 4: Plot results**

In Figure C.259 through Figure C.263, peaks are compared for each AWAC as follows:

- In the top left, matched peaks are plotted against each other. Points which represent modelled and measured peaks within 24 hours of each other are shown as purple plusses. Measured peaks with no corresponding model peak are plotted against the maximum model value within +/- 24 hours as blue circles, whilst modelled peaks with no corresponding measured peak are similarly plotted against the maximum measured peak in +/- 24 hours as red circles.
- In the top right, modelled and measured peaks are ordered independently by decreasing Hm0, and the value for each ordered peak plotted. Note that there is no matching here, for example, the third highest modelled and measured peak may occur at entirely different times.
- In the bottom left, measured Hm0 peaks are sorted in descending order and their value plotted as in red, with "Peak 1" being the highest, "Peak 2" the second highest, etc. For each peak, the

corresponding modelled values are plotted in blue, as a plus if the value is a modelled peak, and a circle if it is not.

- In the bottom right, the same process is repeated, but for *modelled* peaks.
- At the very bottom of each plot, "Peak Ratio" values are specified. The Peak Ratio is defined here to be the mean value of the highest *n* modelled peaks divided by the mean value of the highest *n* measured peaks. In each figure, two values are given for differing values of *n*. The first uses as *n* the smaller of the number of measured peaks and the number of modelled peaks, the second *n = 10*. As noted for STEP 1 above, given the relatively short measurement period, a low threshold is used to find sufficient peaks to analyse, and many of these would not be considered particularly "extreme". Use of only the highest 10 in calculating a Peak Ratio improves on this somewhat, though of course, this still relates to approximately 20 peaks per year.

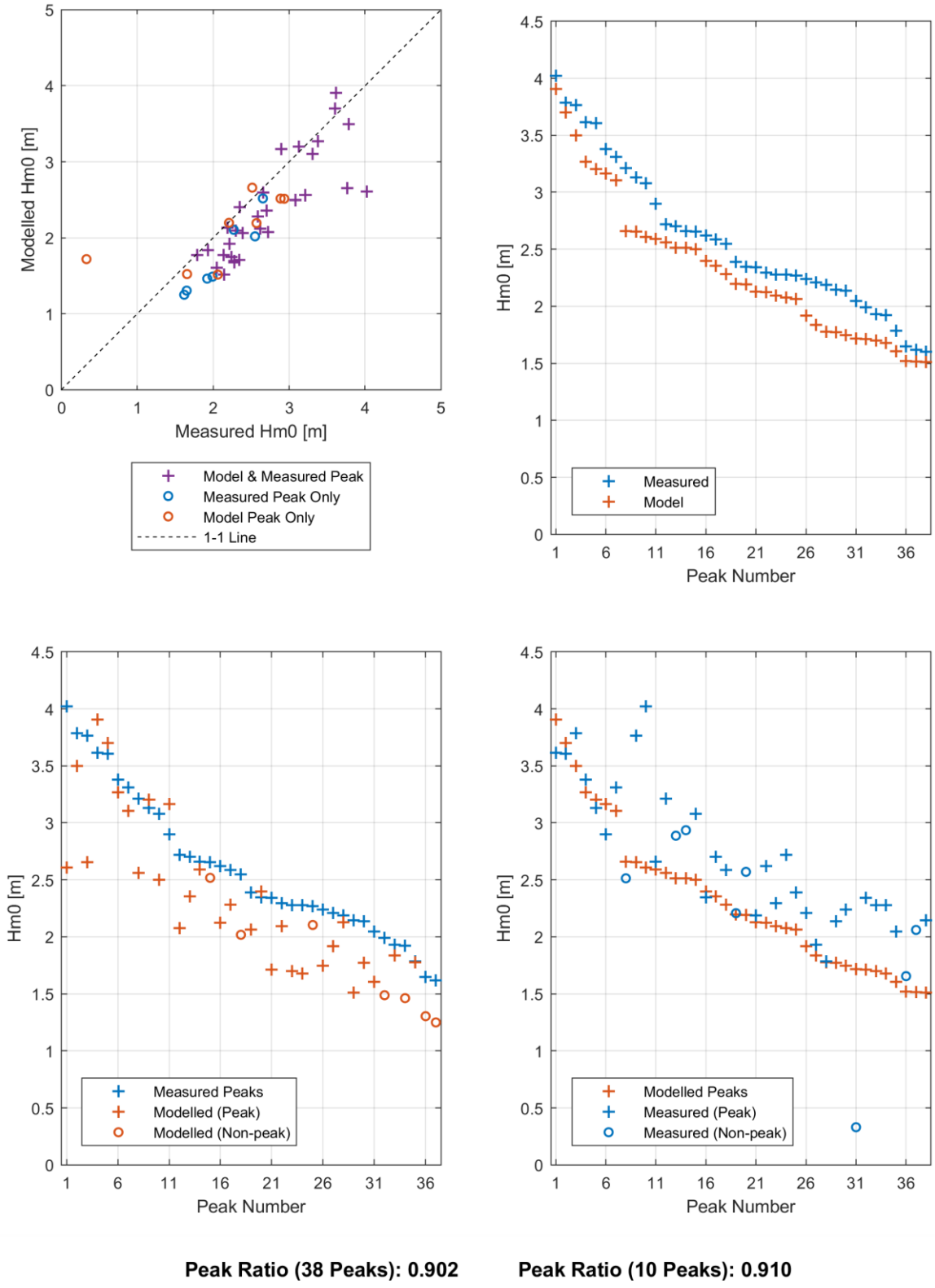



Figure C.259. AWAC A, peak comparison.

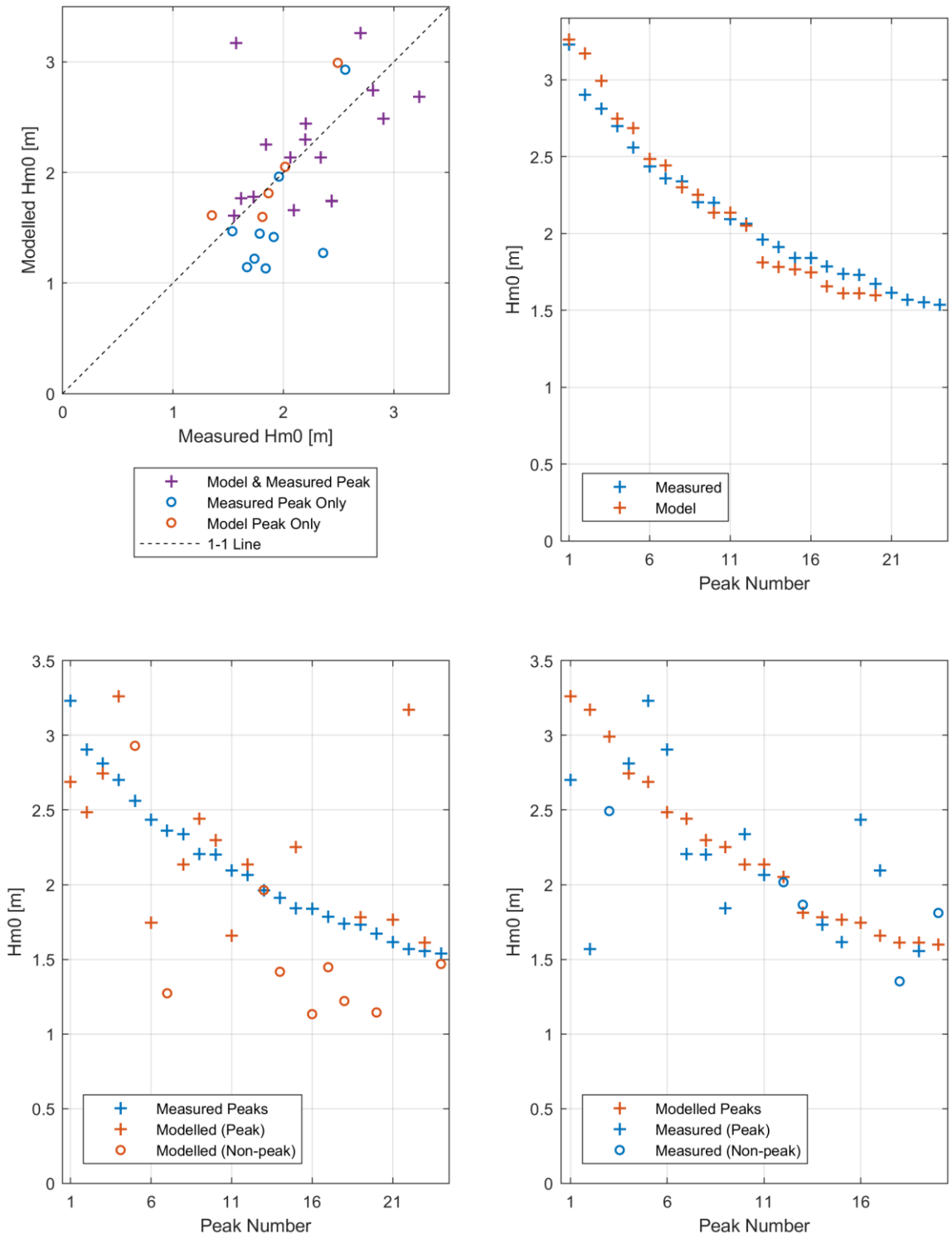



Figure C.260. AWAC B1, peak comparison.

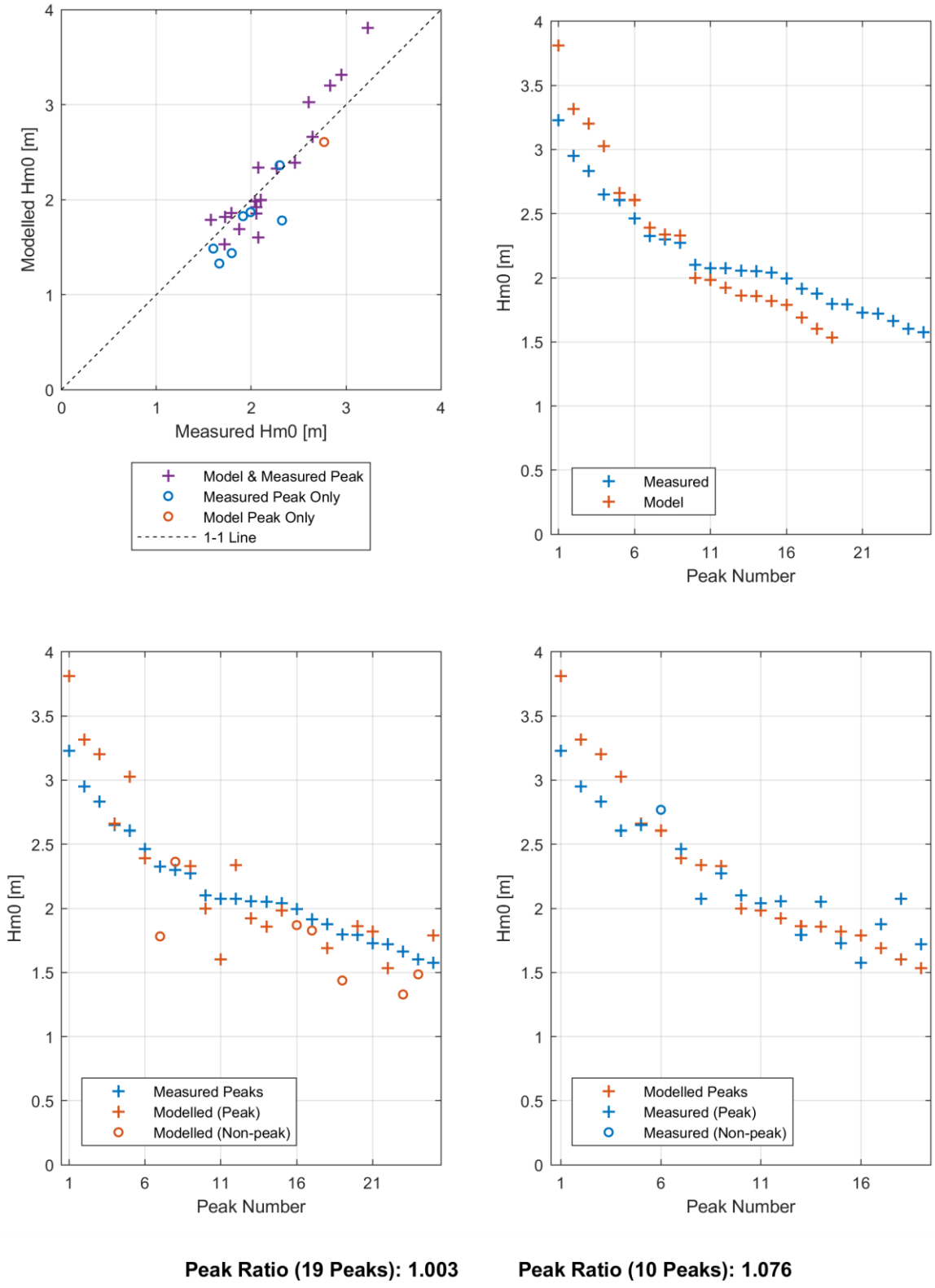



Figure C.261. AWAC C, peak comparison.

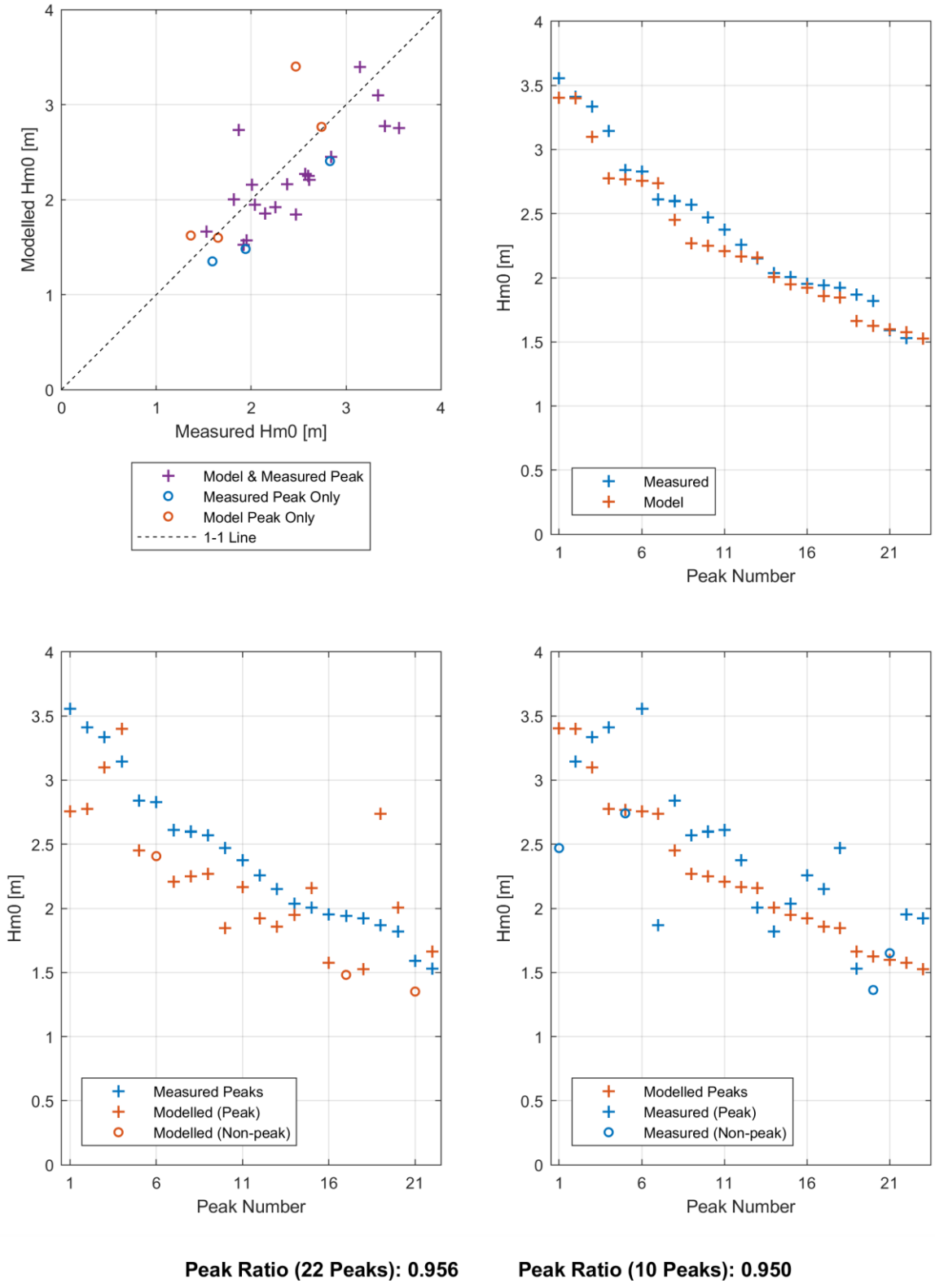



Figure C.262. AWAC D1, peak comparison.

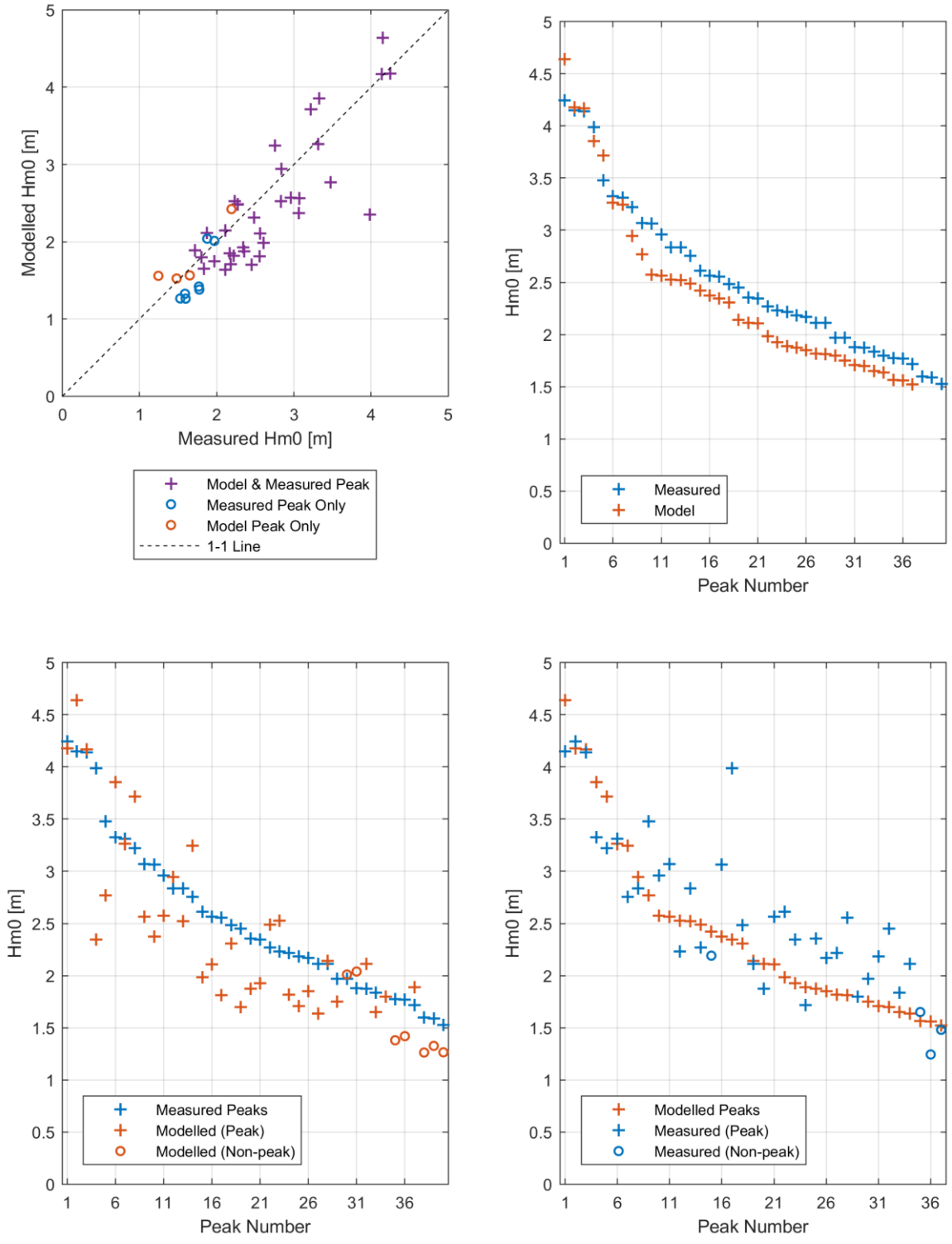



Figure C.263. AWAC E, peak comparison.

# Appendix D. Peak Periods at AWAC E

## D.1 Introduction

Validation plots of wave parameters are included in Section 6.7 of this report. Almost all show good model performance throughout, however there are some more notable deviations in the validation plot for peak wave period (Tp) at AWAC E, which is duplicated Figure D.1 below for convenience, with three regions of interest highlighted.

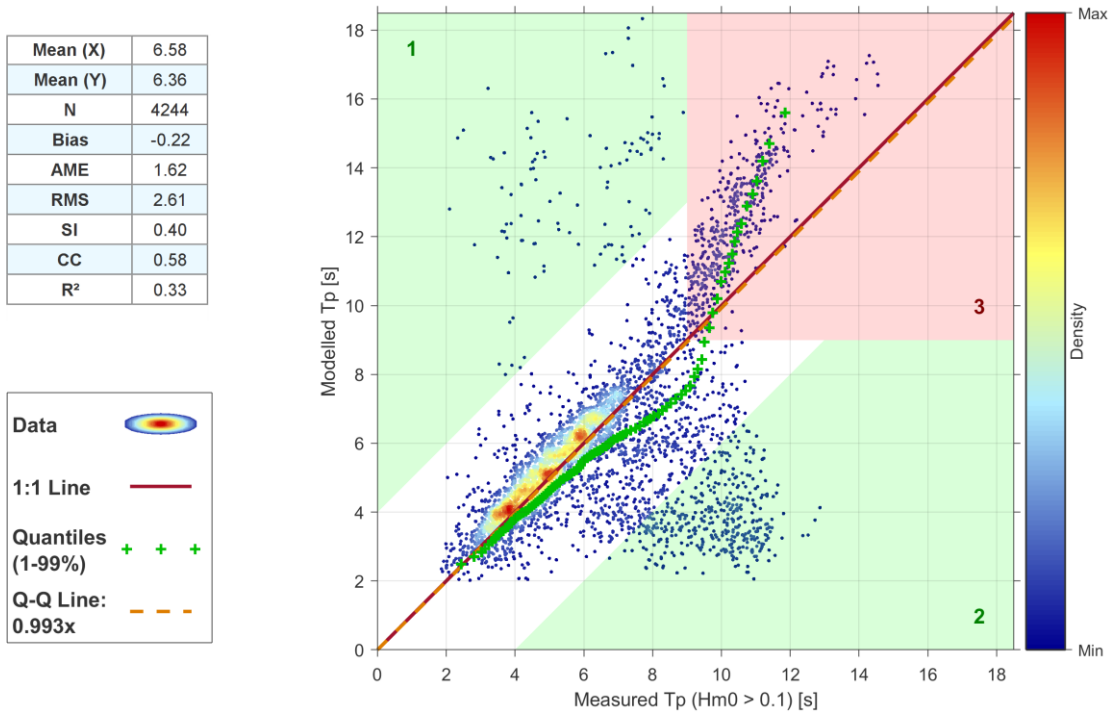



Figure D.1. AWAC E, Tp validation, timestamps with Hm0 > 0.1 m, all data.

Some of the scatter seen in this validation – largely in regions 1 and 2 highlighted above – is generally expected for a validation of Tp. Points in these areas generally correspond to bi-modal sea-states where two systems, well separated in frequency, have a similar level of energy. One of the two systems has a slightly higher peak in the model, whilst the other system has the higher peak in the measurements. In such a case, the spectra may not differ two greatly but show very different Tp values. By way of example, omni-directional spectra from regions 1 and 2 with the highest Hm0 values are compared in Figure D.2.

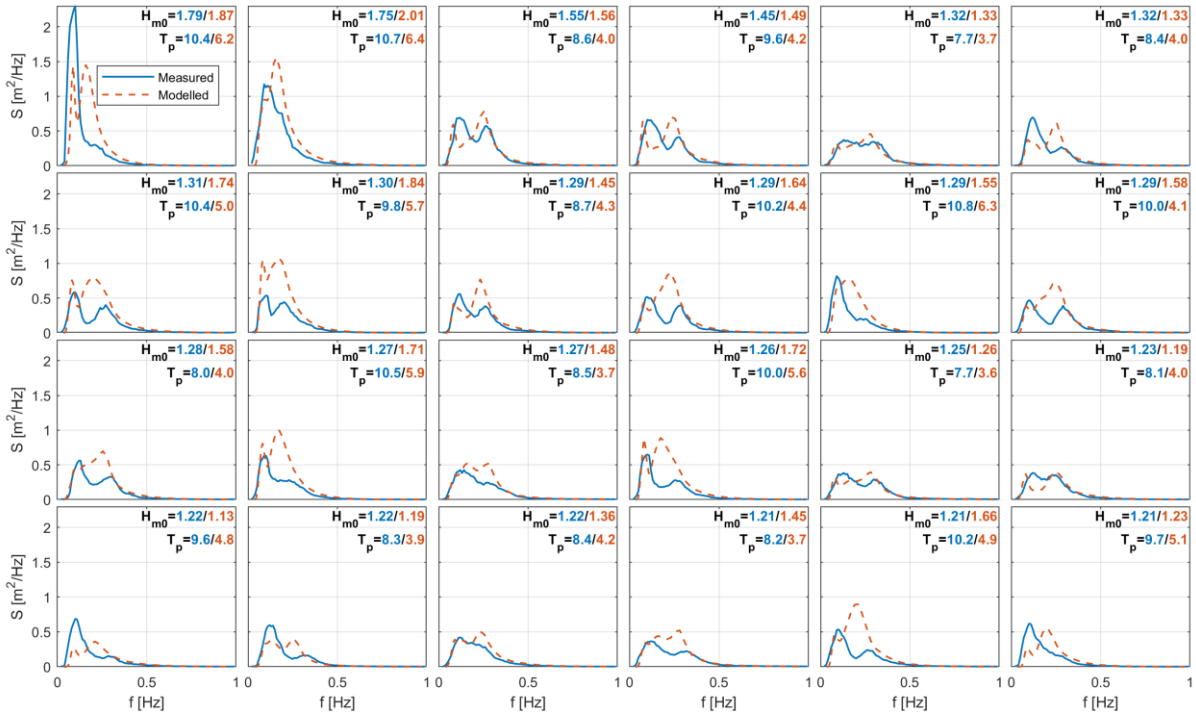



Figure D.2. AWAC E, example bi-modal sea-states.

The differences seen in the top right (region 3) of the validation plot, where modelled and measured Tp are above approximately 9 seconds, *are* unexpected in this context. As such, they warrant a more detailed investigation and are the subject of the remainder of this Appendix.

## D.2 Peak Periods from Other Instruments

Before proceeding to investigate fully the behaviour at AWAC E, it is worth briefly noting that such behaviour is not seen at either AWAC A (Figure D.3) and AWAC C (Figure D.4). However, the absence of any longer period Tp values at either location means that they simply provide no additional information in this regard, rather than any definitive support for the model.

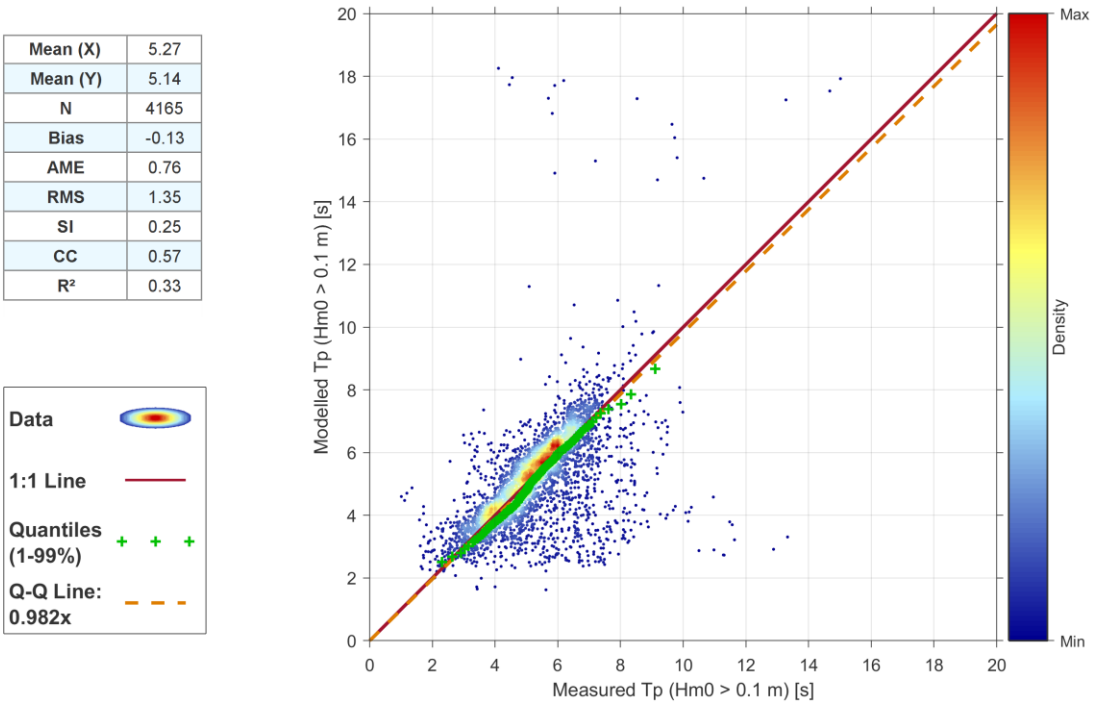



Figure D.3. AWAC A, Tp validation, timestamps with Hm0 > 0.1 m.

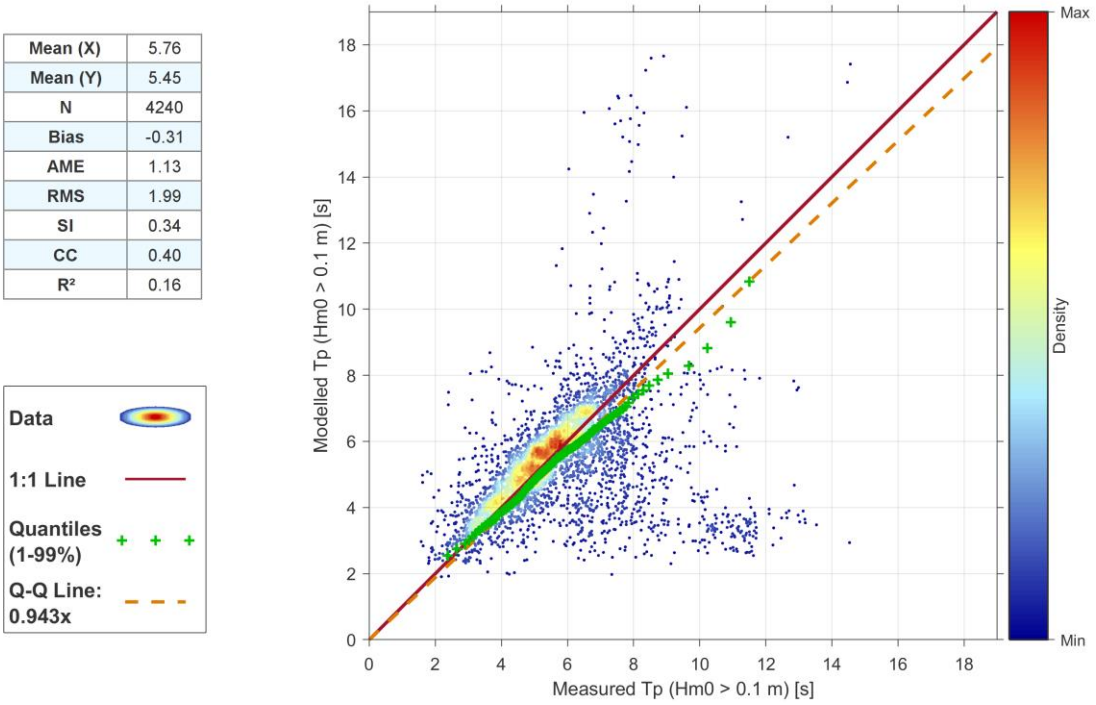



Figure D.4. AWAC C, Tp validation, timestamps with Hm0 > 0.1 m.

Further south, at the M5 buoy, there *are* longer period Tp values, as illustrated in Figure D.5, but the differences seen at AWAC E are not present.

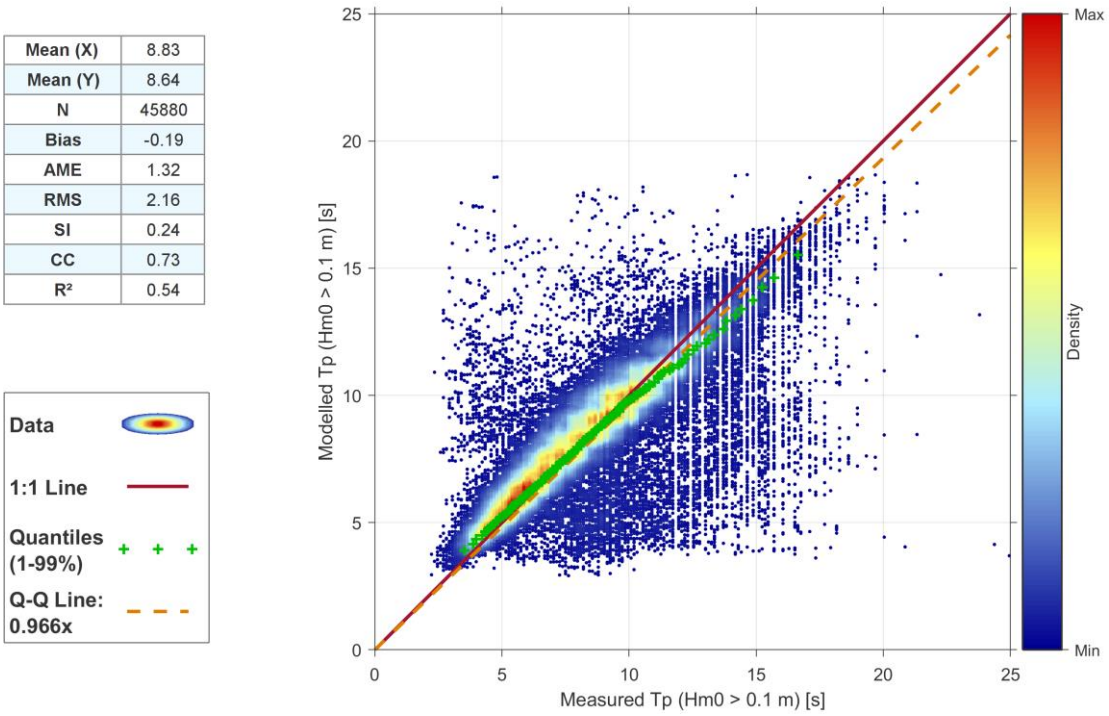



Figure D.5. M5, Tp validation, timestamps with Hm0 > 0.1 m.

Thus, in the sections which follow, we limit our analysis to measurements from AWAC E only. It is also worth noting that the unexpected behaviour is *not* seen for Tm01 and Tm02 at AWAC E (see Section C.5.6 of Appendix C) and as such we focus only on Tp.

## D.3 Instrument Setup

Before looking in detail at *model* behaviour, it is worth a brief review of the *measurement* setup across the AWACs. As outlined in Section C.3.2 of Appendix C, omni-directional spectra and the resultant Tp are recorded by the Acoustic Surface Tracking (AST) method. This records at 2Hz for 512 seconds every 30 minutes, before calculating an omni-directional spectrum from 0.02 Hz to 0.99 Hz in increments of 0.01 Hz.

According to the AWAC documentation [25], 512 seconds is somewhat short in terms of sample duration for these longer period waves, with said documentation stating:

> *Sampling theory suggests, as a rough rule of thumb that the measurement duration is long enough to capture a minimum of 100 cycles of an event (wave). When we measure ocean waves we have to consider what the longest expected wave period is going to be; 100 cycles of this longest wave will be the minimum wave burst duration. As an example, if waves are to be measured in the Mediterranean*



*sea, we would expect the waves to be 10 seconds or shorter. Therefore 10 seconds x 100 cycles is 1000 seconds. Sampling rate and number of samples defines the sampling length. A corresponding configuration could be either 1024 samples at 1 Hz or 2048 samples at 2 Hz.*

Fugro have provided the following comment with regard to the instrument setup (as forwarded to MetOceanWorks by SSE on 15th March 2021):

*It is a complex thing to cover simply, but in essence these are the key points:*

1. *512 seconds allows interleaving of waves and currents with no current records lost (the half hourly wave measurement is performed in between current measurements so that no interpolation is needed. A 1024 second burst would run over a current burst and so that current "measurement" would actually be interpolated). The wave heights are also measured at 2 Hz using the acoustic beam.*
2. *When processing the wave data having a long burst length is important when looking for long period waves. As we are looking for waves with periods <25 seconds a burst of 512 seconds allows us to capture >20 such waves at the longest periods. This is more than enough to define the wave data we are after.*
3. *In order to understand the impact of reducing the burst length (and data frequency) Fugro took other data, from an area exposed to long period waves direct from the Atlantic, and compared them going from 60 minute burst down to 5 minute burst. It is clear that the wave data is not compromised until the burst is around 5 minutes, and even then it is simply noisy rather than very wrong.*

For our waves of interest – between approximately 9 and 15 seconds – the sampling duration of 512 seconds would give between 34 and 57 waves. Though short of the 100 stated in the AWAC documentation, these are comfortably more than the >20 stated by Fugro. As such, we will proceed under the assumption that the measurements are indeed trustworthy.

It is worth briefly noting here also that the omni-directional spectrum at a resolution of 0.01 Hz gives relatively low resolution at these longer periods when compared to shorter periods. Frequencies of 0.05, 0.06, …, 0.11 Hz relate to periods of 20.0, 16.7, 14.2, 12.5, 11.1, 10.0 and 9.1 seconds. Although interpolation and smoothing techniques are used to determine Tp they will originate from spectra where there is less precision in terms of *period* than would be the case for higher frequencies.

## D.4 Spatial Variability

We now proceed to investigate the *model*, beginning with a brief check to see if the behaviour seen is due to any high level of spatial sensitivity in the model. To this end, the measured Tp values from AWAC E were compared to the 9 locations shown in Figure D.6.

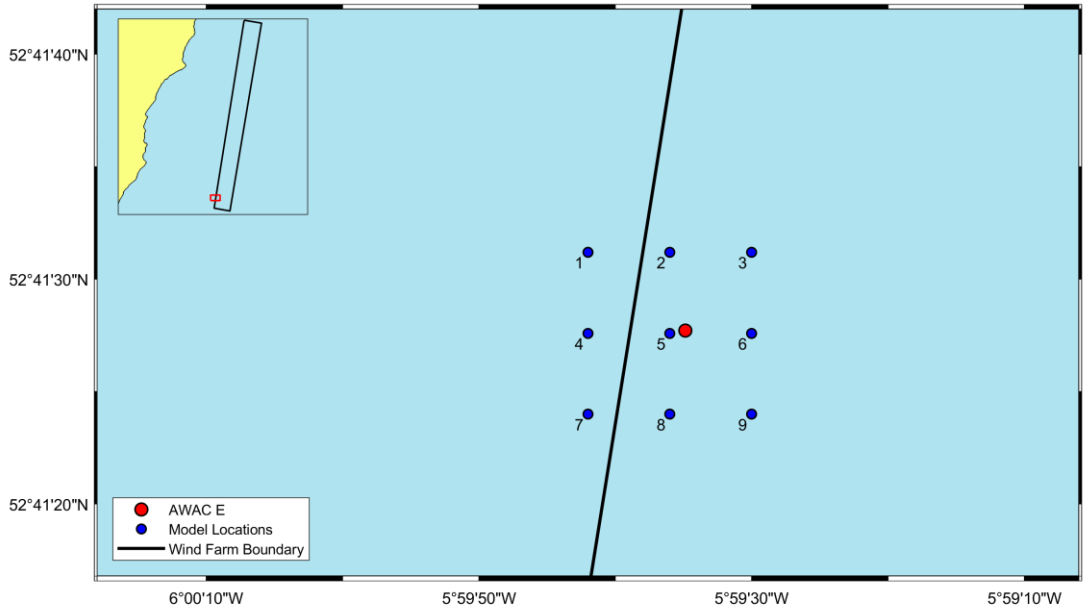



Figure D.6. AWAC E, Micro-siting locations.

These locations span a region of up to approximately 175 m from AWAC E, but as shown in Figure D.7, there is no notable change in the unexpected Tp behaviour. As such, localized spatial variability does not appear to be the cause.

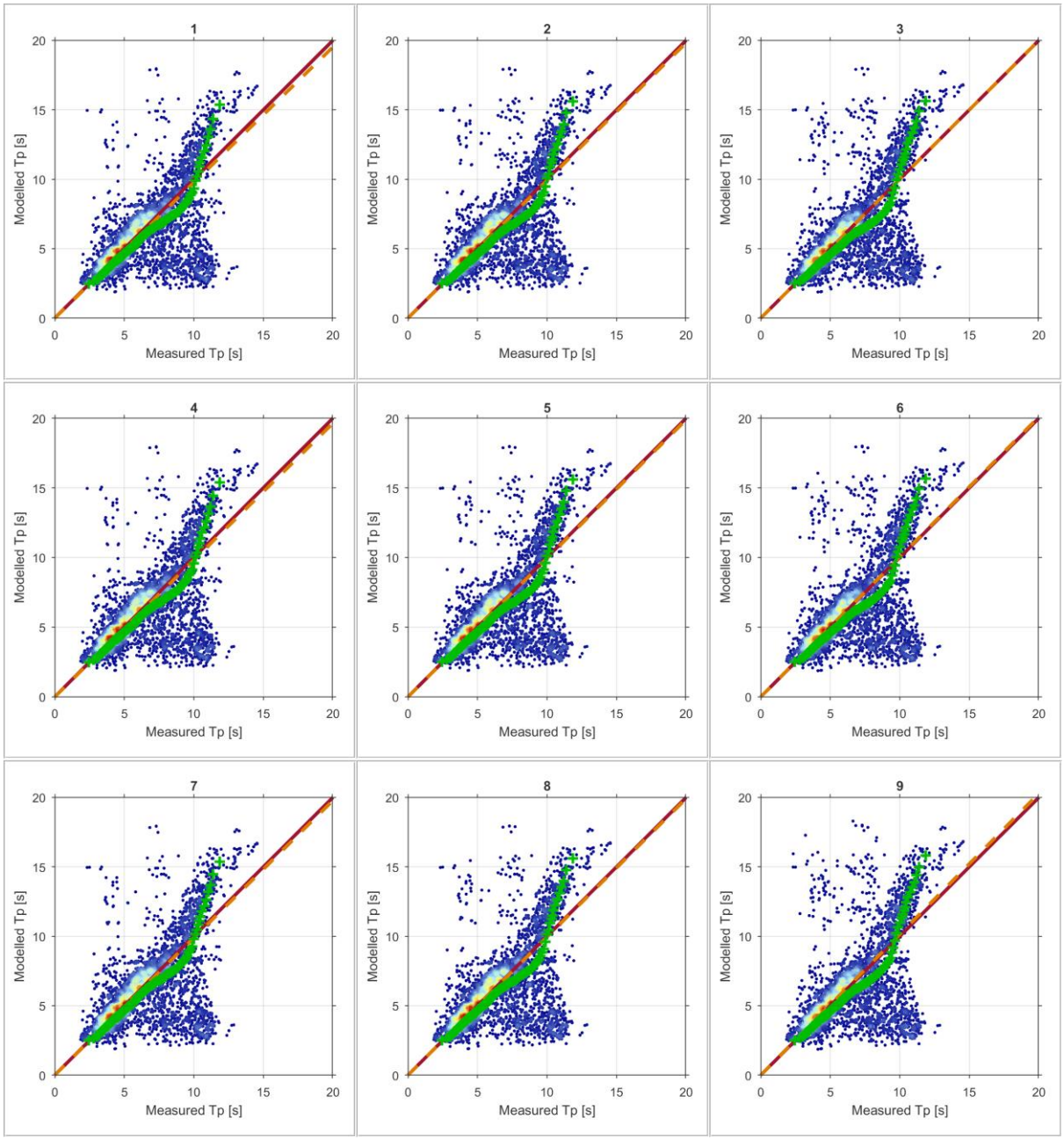



Figure D.7. AWAC E, Tp validations, measurements vs. model at nearby locations.

## D.5 Wave Parameters

To provide an overview of modelled and measured wave parameters at AWAC E, time-series of significant wave height (Hm0), peak wave period (Tp) and mean wave direction (Mdir) are shown in Figure D.7 through Figure D.13. Time periods where both modelled and measured Tp are greater than 9 seconds are highlighted red. Also overlaid with dashed vertical lines are those timesteps at which individual spectra are reviewed in Section D.6 of this Appendix.

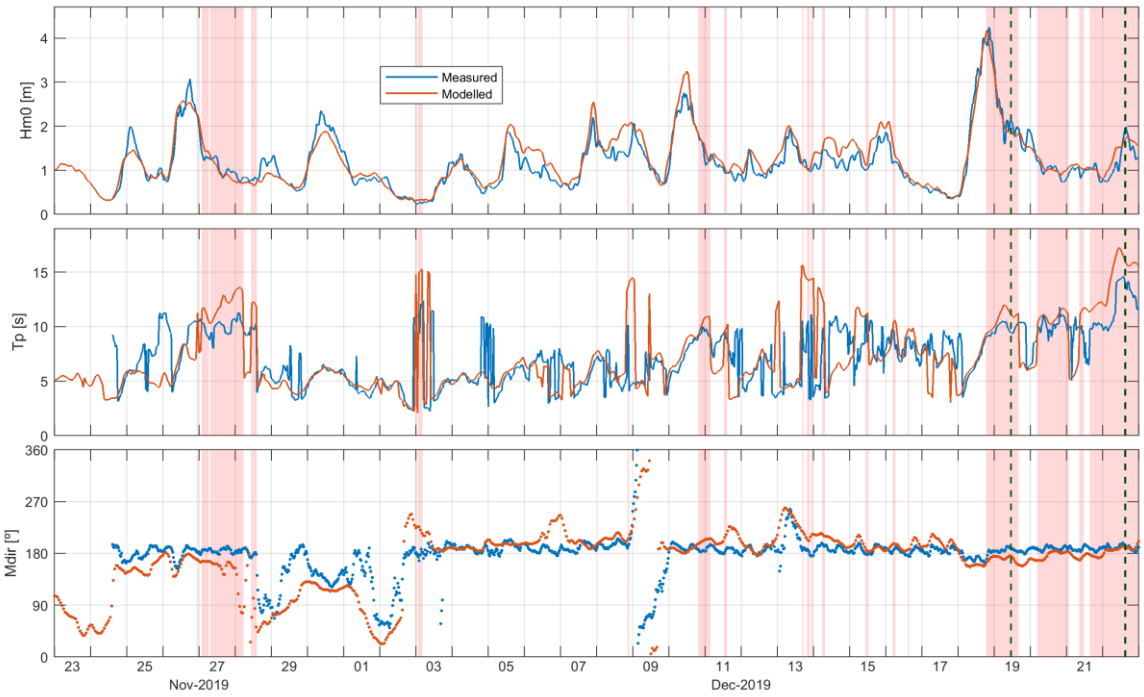



Figure D.8. AWAC E, parameter time-series (1).




Figure D.9. AWAC E, parameter time-series (2).




Figure D.10. AWAC E, parameter time-series (3).




Figure D.11. AWAC E, parameter time-series (4).

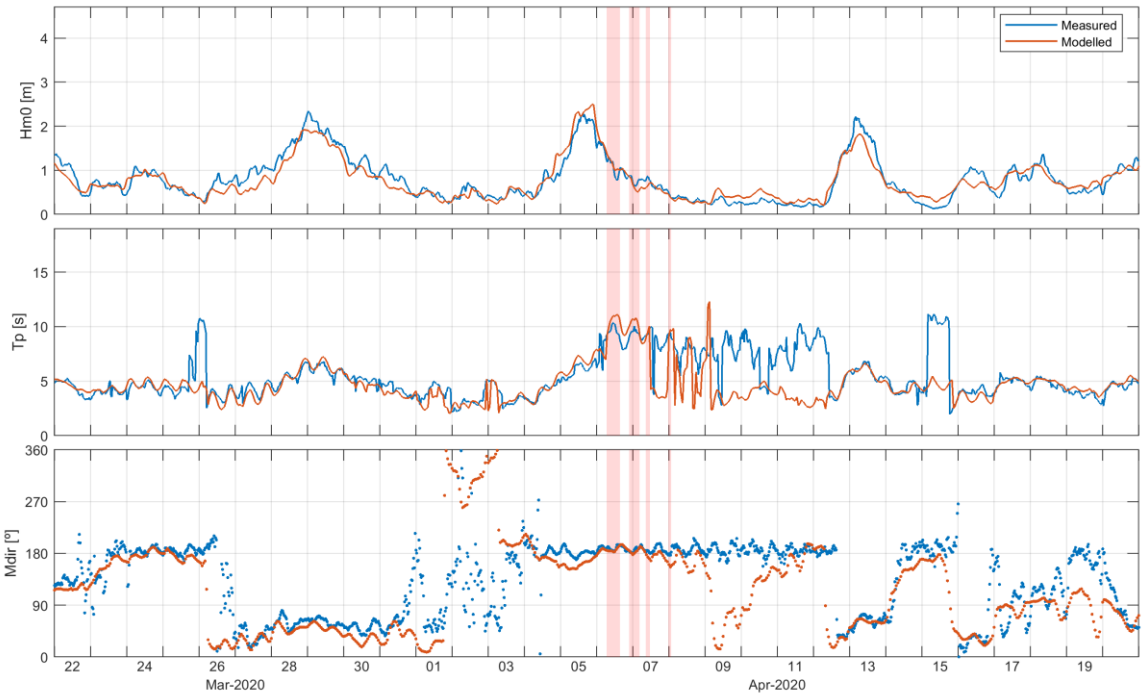



Figure D.12. AWAC E, parameter time-series (5).

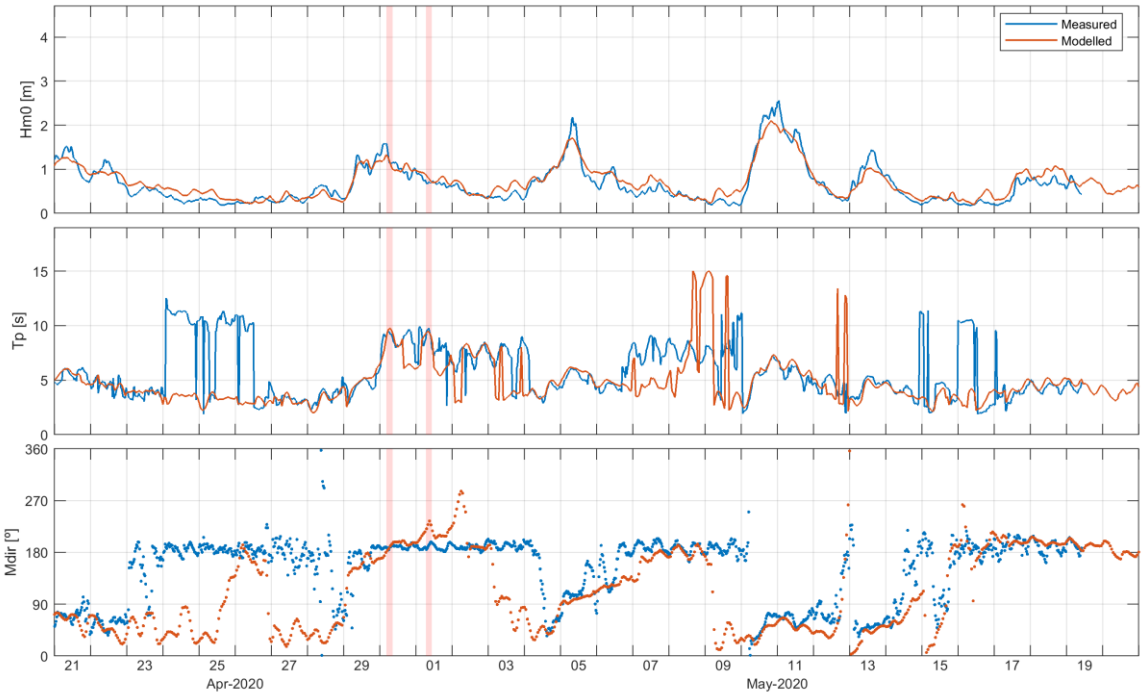



Figure D.13. AWAC E, parameter time-series (6).



Two features are immediately apparent from these time-series:

- The differences in larger Tp values are far more common between November and February than from March to May.
- These differences occur only when mean wave direction is from the south – as expected, given that the much longer fetch in this direction.

It is not clear though that much can be inferred beyond these points. For some periods where Tp differences are seen, there are also variations in Hm0, (e.g. February 9th through 17th Figure D.10) but this is by no means a systematic difference (e.g. throughout Figure D.8 and Figure D.9). Similarly, some periods show differences in Mdir, but again this is generally not the case as a whole.

## D.6 Wave Spectra

Given the lack of any explanation in the wave parameters, we turn our attention to wave spectra. Initially, we focus on a subset selected as follows:

a) Find all sea-states where modelled and measured Tp are greater than 9 seconds and differ by more than 1.5 seconds. This gives 335 comparison timesteps from the 4244 seen in the validation plot of Figure D.1.
b) Reduce by taking only those where measured Hm0 is greater than 1.5 metres. This leaves 101 comparison time-stamps.
c) From these, remove any time-stamps with a *higher* Hm0 within 4-hours. This leaves a more manageable set of 20 spectra to review individually.

The timestamps of the 20 spectra selected are shown with dashed vertical lines in Figure D.7 through Figure D.13. Note that we do not intend to ignore the other spectra completely, but will return to them with any useful information found from this subset.

Omni-directional and directional plots of the spectra, in temporal order, are shown for these 20 spectra in Figure D.14 through Figure D.18.

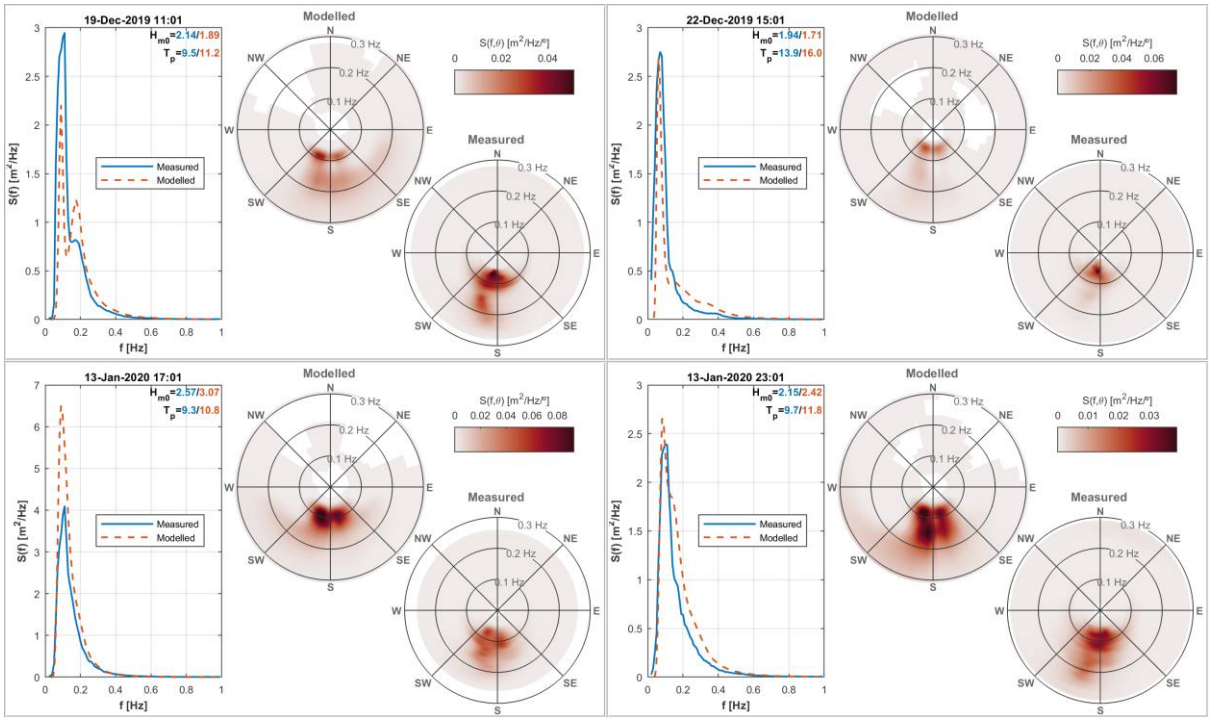



Figure D.14. AWAC E, example spectra (1).

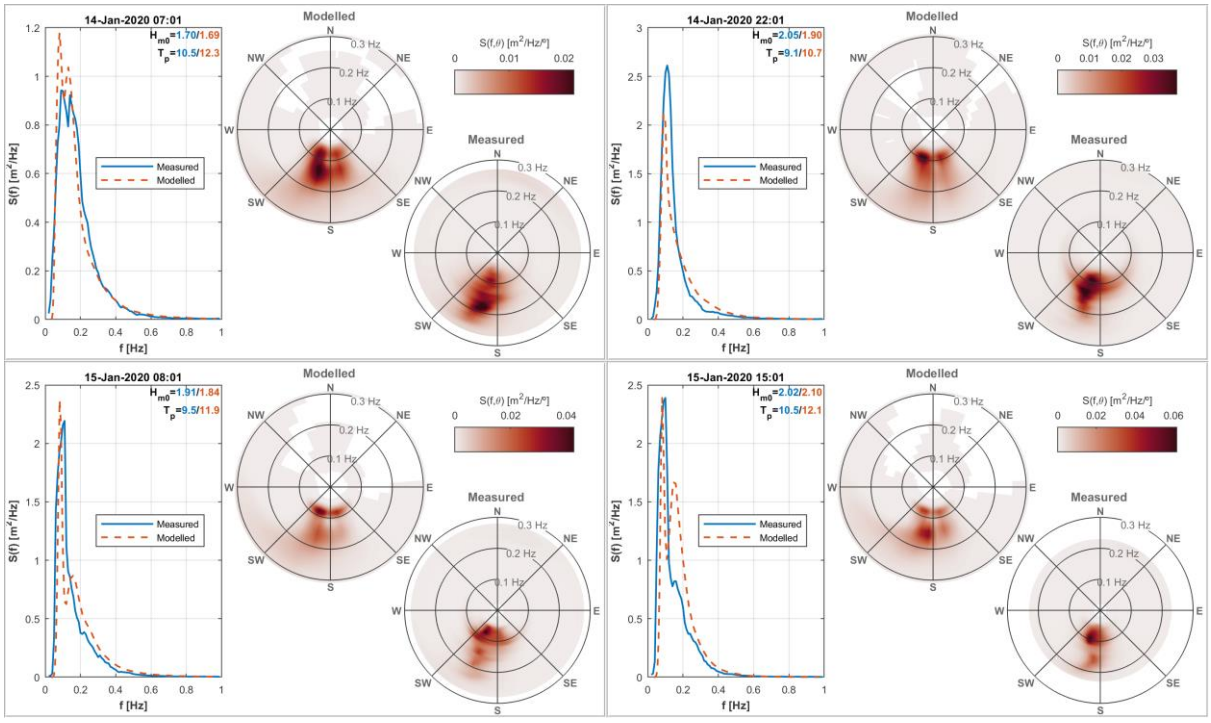



Figure D.15. AWAC E, example spectra (2).

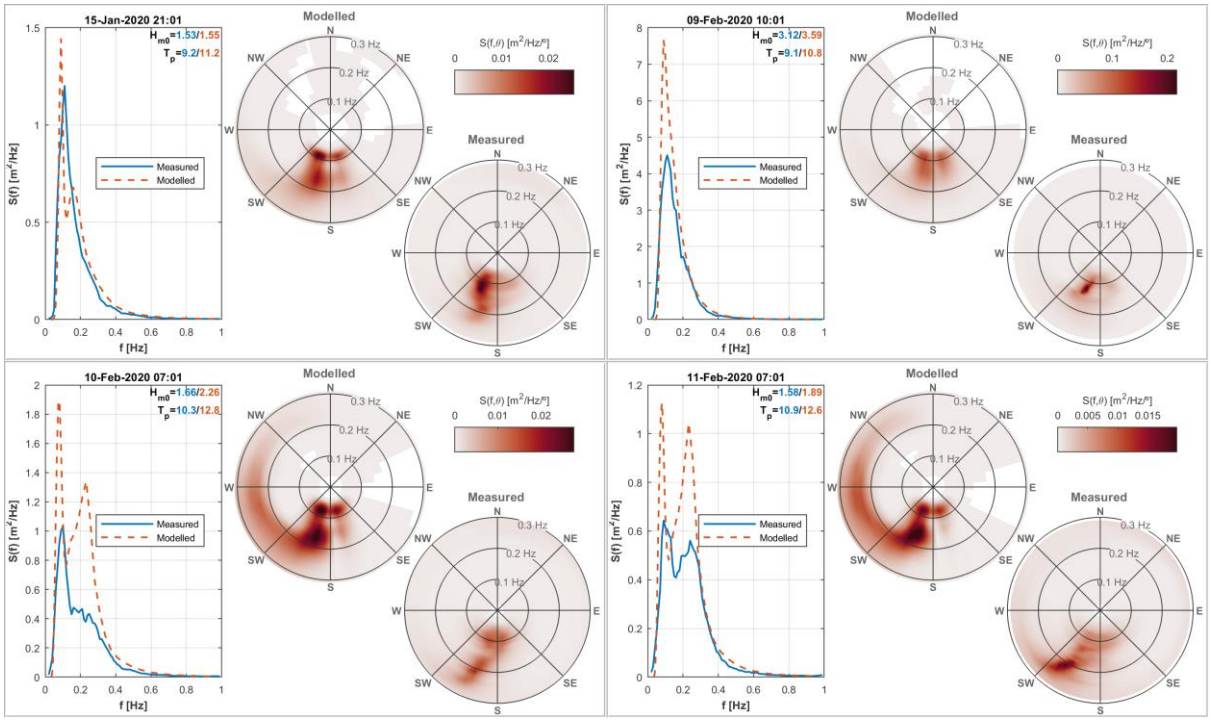



Figure D.16. AWAC E, example spectra (3).

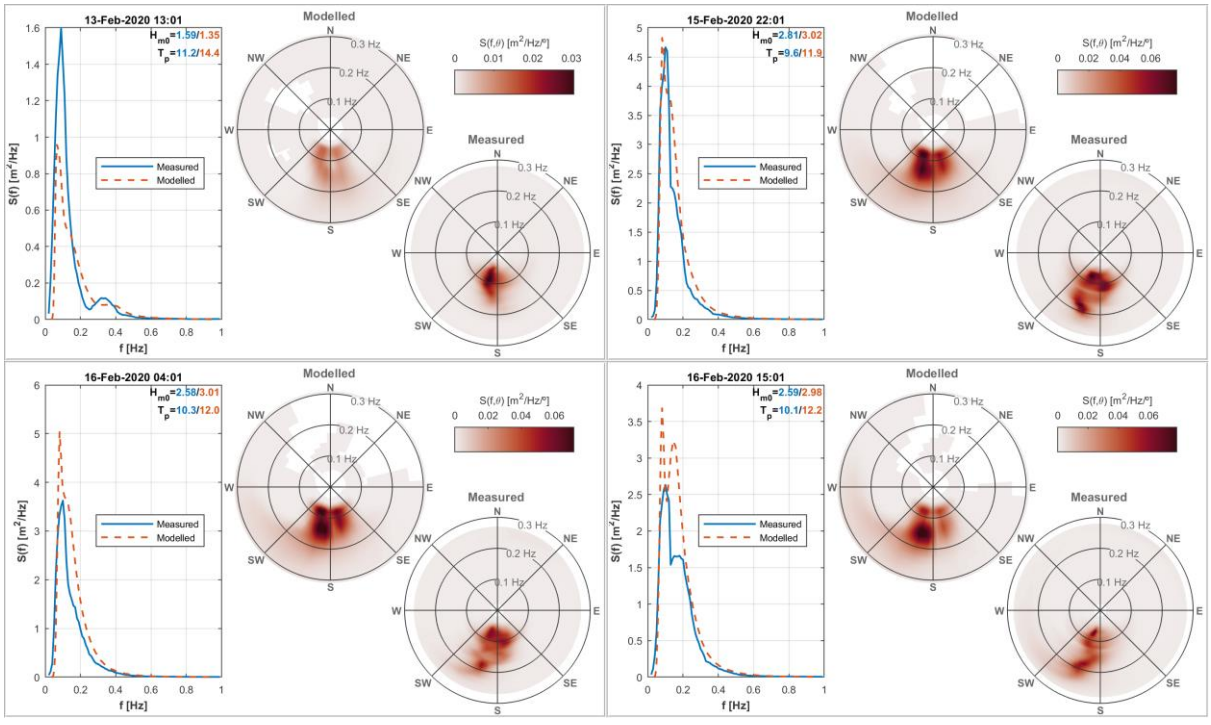



Figure D.17. AWAC E, example spectra (4).

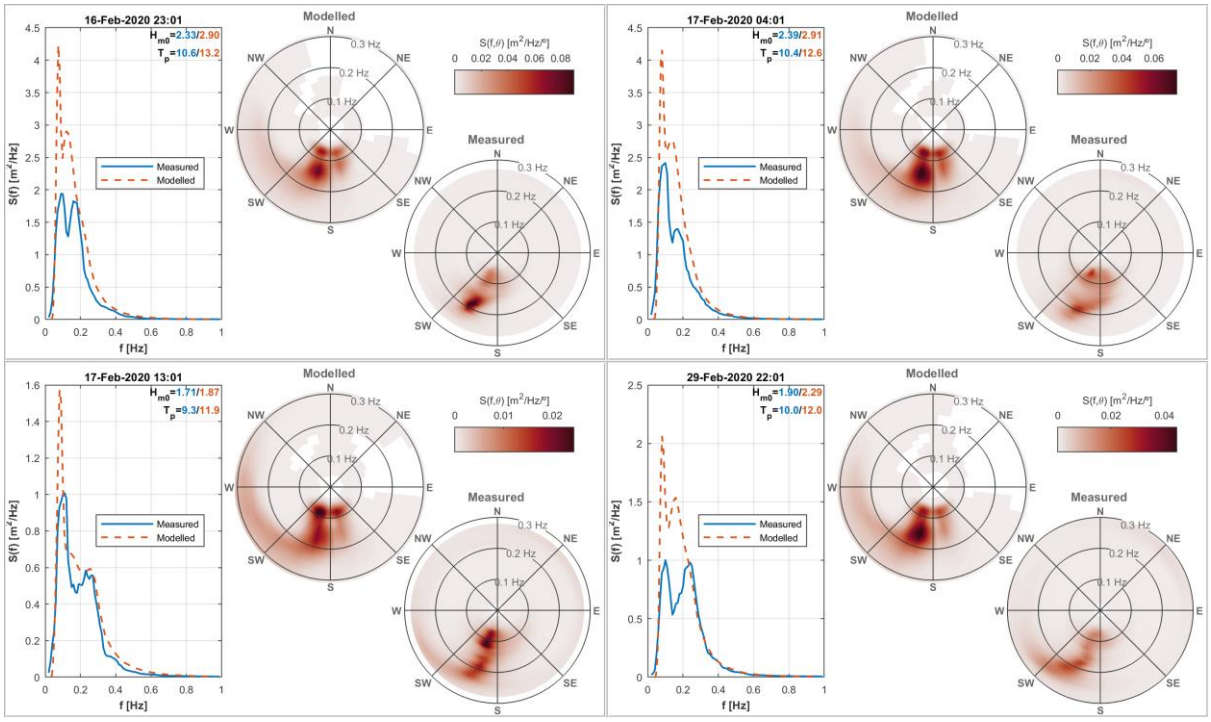



Figure D.18. AWAC E, example spectra (5).

Some differences are to be expected when comparing individual spectra, for example relating to minor differences in timing between model and measurements. However, when comparing peaks of omni-directional spectra here far more similarity is seen between model and measurements than might be expected from the differences in Tp. Taken as a collective, the *mean* spectra, shown in Figure D.19, only highlight this further. In particular:

- For all model spectra and almost all frequencies, the model overpredicts spectra energy slightly, with the overprediction larger for systems with more energy. This is as expected from, for example, the validation plot of Hm0 shown in Figure 6.29.
- Differences between modelled and measured peak periods from the *mean* spectra where Tp > 9 seconds are *not* because of large differences in the location of spectral energy as a whole, but because of a relatively minor difference in the location of the peak itself. In particular, the model peak is slightly asymmetric towards lower frequencies, the measured peak slightly asymmetric towards higher peaks. Similar behaviour is seen at a number of peaks in Figure D.14 through Figure D.18.

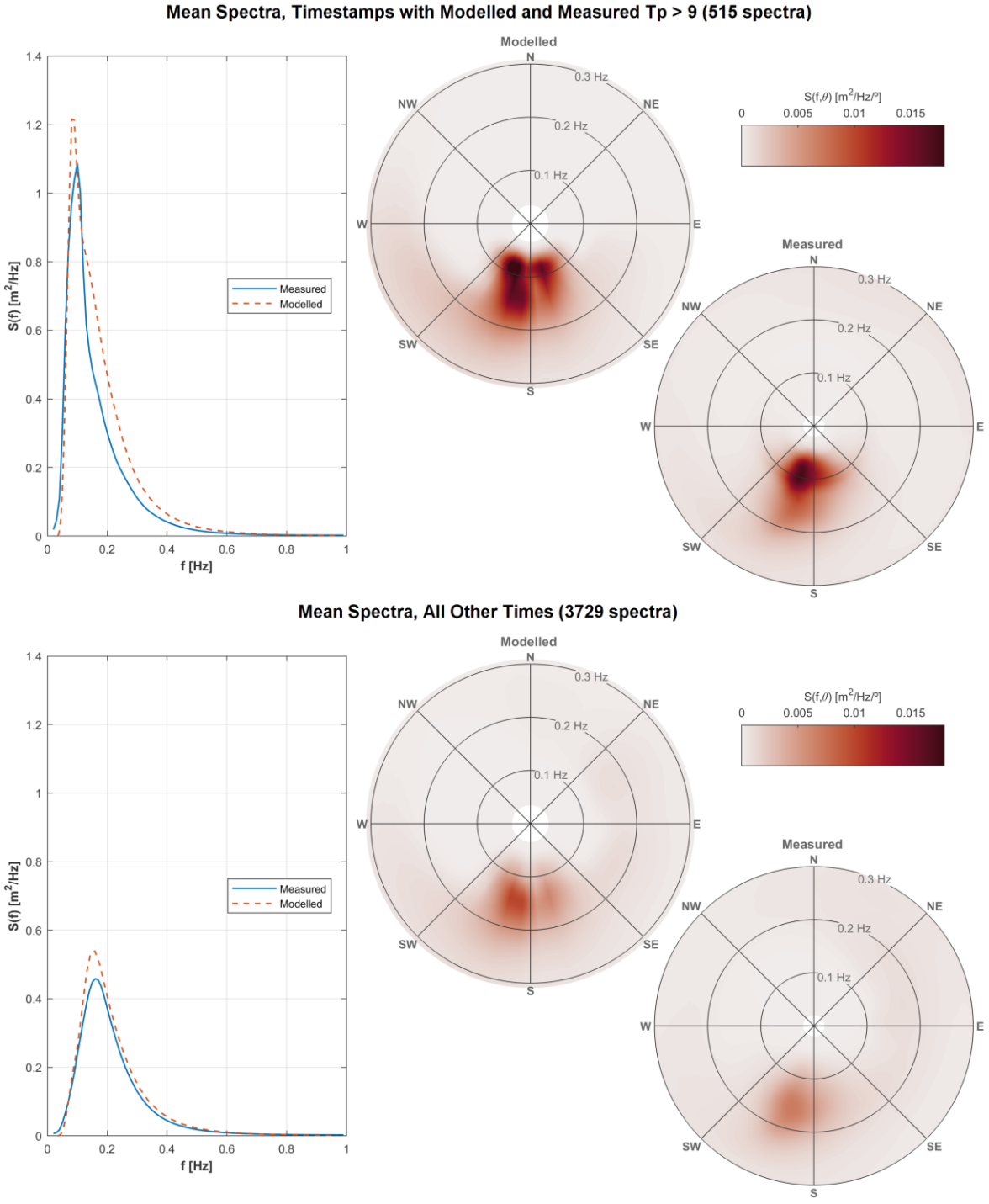



Figure D.19. Mean Spectra, split by Tp behaviour.

## D.7 Peak Symmetry

To investigate this difference in peak symmetry further, we consider an alternate parameter, hereafter denoted $T_{80\%,mid}$ which is calculated as follows:

1. Find the peak of the omni-directional spectrum.
2. Find the frequency *below* the peak at which the spectral energy is 80% of the peak value.
3. Find the frequency *above* the peak at which the spectral energy is 80% of the peak value.
4. Take $T_{80\%,mid}$ as the mid-point between the frequencies found in 2 and 3.

Thus, rather than the period of the exact peak of the spectrum (Tp), $T_{80\%,mid}$ represents the *middle* of the highest 20% of this peak. Note that this is in no way proposed as an *alternative* to Tp, just a parameter through which we can explore the asymmetry of the highest part of the spectrum.

$T_{80\%,mid}$ is plotted against Tp for the measured dataset in Figure D.20, where there is a clear increase in the difference, and thus asymmetry of the peak at higher periods. The same is not apparent for modelled data, as shown in Figure D.21.

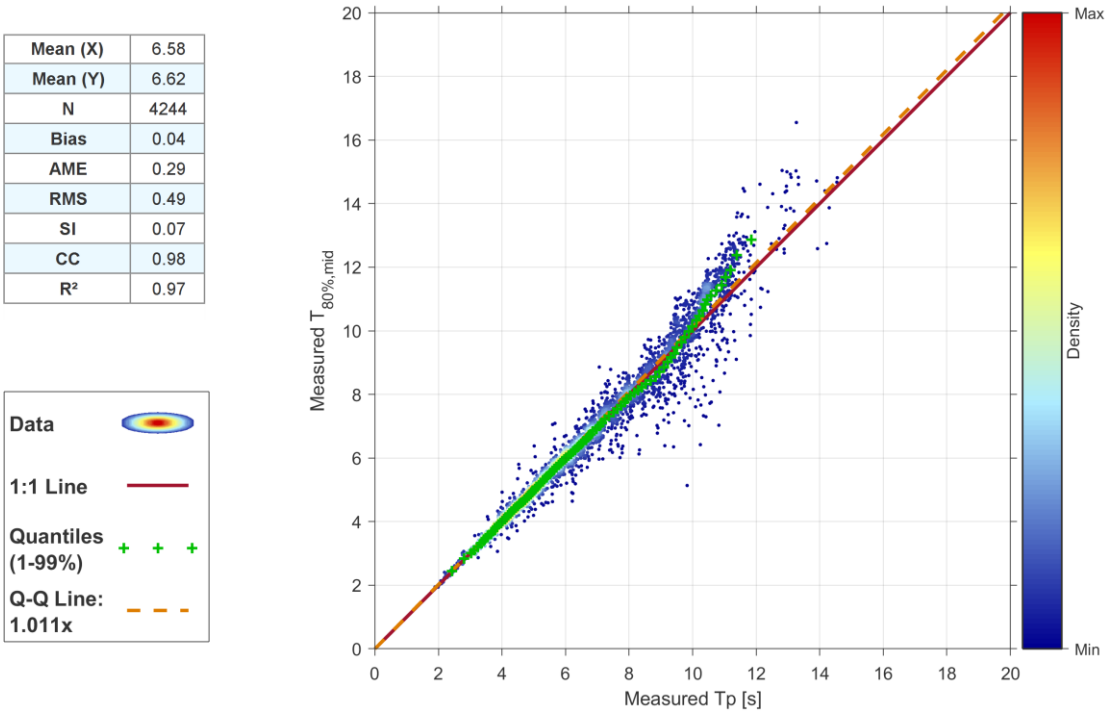



Figure D.20. Measured $T_{80\%,mid}$ versus Tp, AWAC E.

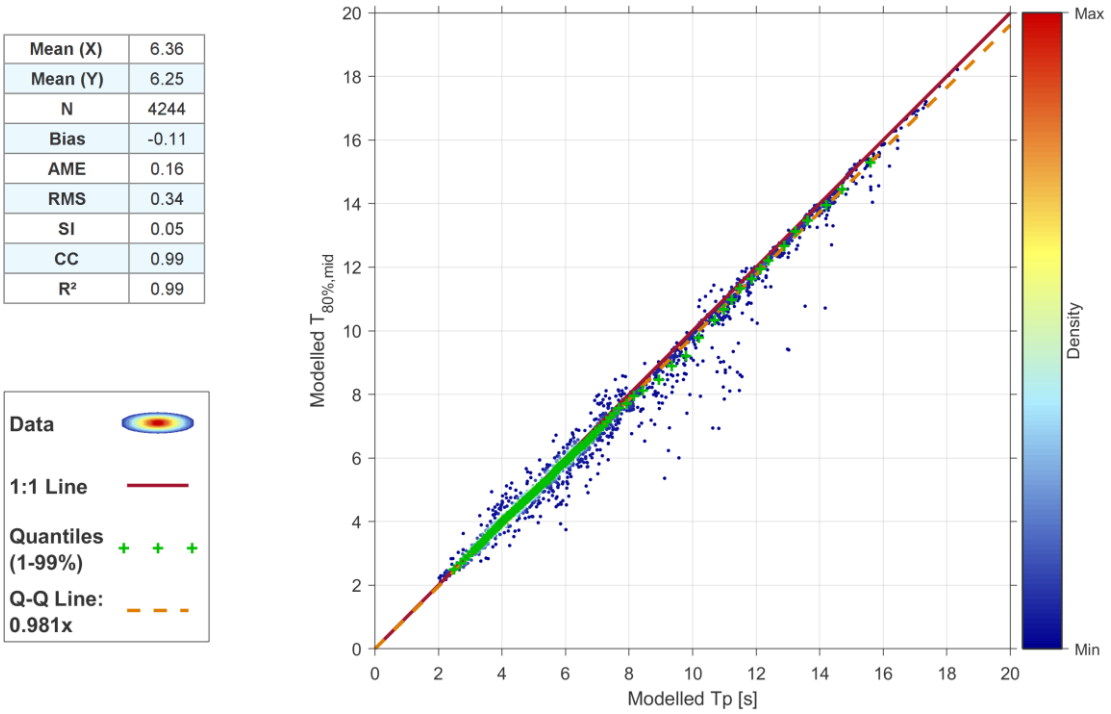



Figure D.21. Modelled $T_{80\%,mid}$ versus Tp, AWAC E.

When comparing this $T_{80\%,mid}$ parameter between model and measurements, as seen in Figure D.22, there is notable improvement over the comparison of Tp (see Figure D.1). Whilst still not a perfect match, this does certainly suggest that a large part of the differences for Tp itself are caused by the different symmetry at the spectral peak.

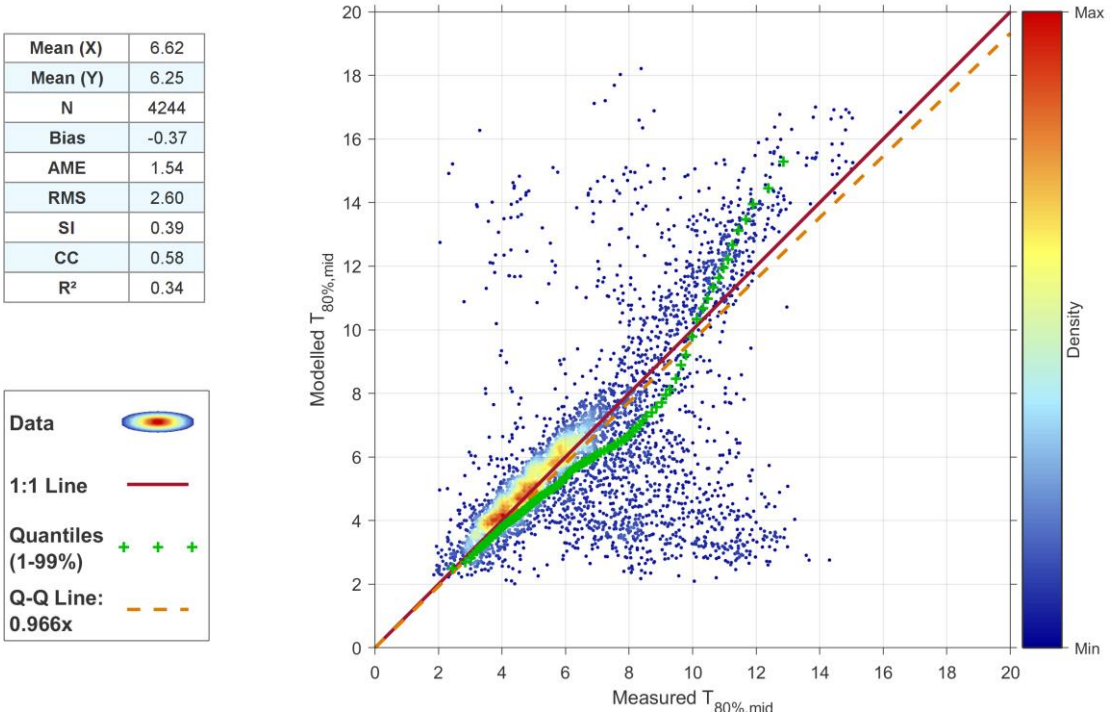



Figure D.22. Measured and Modelled$T_{80\%,mid}$, AWAC E.

## D.8 Spectral Energy by Frequency Band

Through the previous Sections, we have seen that, although the values of Tp itself differ notably between model and measurements for Tp > 9 seconds, the overall distribution of spectral energy compares far better. To review this aspect further, Figure D.23 shows validation plots of modelled and measured Hm0 by frequency range. For each range of frequencies:

- The zeroth moment, denoted $m_{0,b}$, for the frequency range from $f_{low}$ to $f_{high}$ is calculated as:

$$m_{0,b} = \int_{f_{low}}^{f_{high}} S(f)\, df$$

- The significant wave height for the band is calculated as $4\sqrt{m_{0,b}}$

Throughout these plots, model performance is largely in line with that of Hm0 as a whole. In particular, there is no large movement of energy between periods as might be suggested by the differences in Tp.

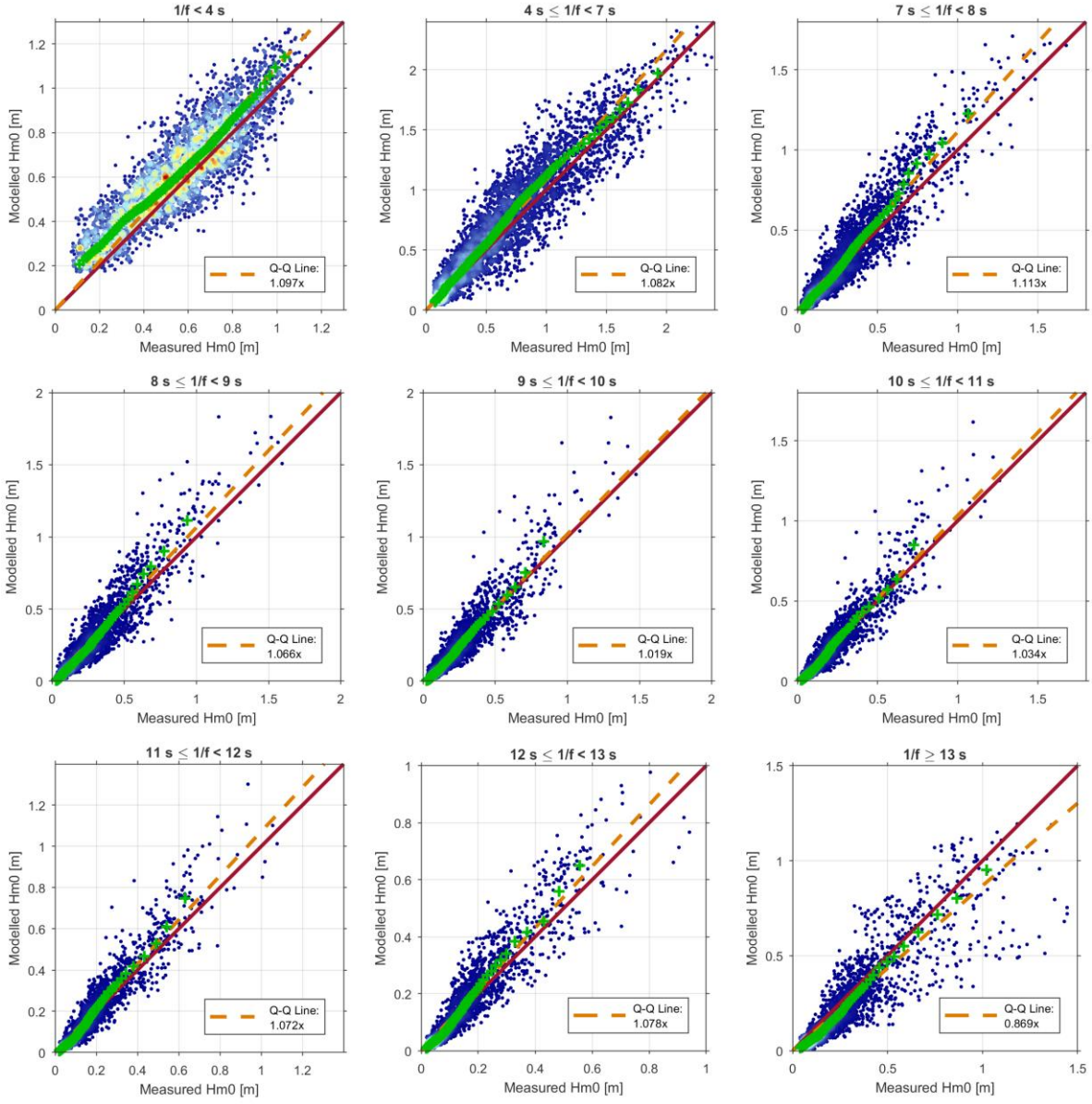



Figure D.23. Validation of Hm0 by frequency band.

## D.9 Summary

A more detailed review of model and measurements at AWAC E has not found any specific reason for the differences seen in Tp at higher wave periods. As such, we can neither attribute them conclusively to measurement error or features not fully captured by the model. It *does* appear, however, that these are *not* symptoms of large differences between modelled and measured spectra, but instead largely caused by minor differences in the symmetry of spectral peaks. In particular, spectral energy within a number of frequency ranges has been reviewed and shows model performance in line with that seen for Hm0 when taken as a whole.

As a whole the model appears to perform suitably well at AWAC E, particularly given the challenging location. Whilst we do not believe any adjustments are necessary to wave periods at this location, should others deem them necessary for future analyses, we would strongly advise that they are carried out based on spectral review rather than the validation plot of Tp alone. For example, changes to Tp, when combined with the theoretical JONSWAP spectrum, may lead to the movement of significant portions of spectral energy between frequency ranges – a result which Figure D.23 suggests is not warranted.

# Appendix E. JONSWAP Fitting

## E.1 Introduction

In Sections C.7 and C.8 of Appendix C, measured wave spectra were compared to not only modelled spectra, but also spectral representations given by 1 and 2 JONSWAP spectra. In general terms, these representations are constructed as follows:

**2 JONSWAP**

a) Separate each modelled spectrum into at most one wind-sea and one swell component.
b) For each component, fit a JONSWAP spectral shape to the omni-directional spectrum, and use a cos2n directional distribution to represent the directional behaviour.

**1 JONSWAP**

a) Fit a JONSWAP spectral shape to the omni-directional spectrum as a whole, and use a cos2n directional distribution.

This Appendix provides more details on these steps, with the method used to partition spectra described in Section E.2, and the fitting of spectral shapes described in Section E.3.

## E.2 Partitioning

In Sections C.7 and C.8 of Appendix C, measured wave spectra were compared not only to modelled spectra, but also spectral representations given by 1 and 2 JONSWAP spectra. In order to determine the 2 JONSWAP representation, modelled spectra were first separated into wind-sea and swell partitions, before fitting a JONSWAP spectral shape

For separating wind-sea and swell components, a multi-stage approach has been used as follows:

1. Partition the spectrum into separate systems using a watershed method.
2. Determine which systems are considered wind-sea and which swell.
3. Merge systems as appropriate, e.g. if peaks are close, or we seek a final description with a limited number of systems, e.g. a single wind-sea and a single swell.

This is carried out using XWaves, a third-party ocean surface wave field analysis toolbox for MATLAB. Please see https://www.waveforcetechnologies.com/xwaves for more details.

By way of example of the process, we will consider the spectrum shown[14] in Figure E.1. Overlaid (green line) is the wind direction. Here we can see what appears to be wind-sea from an easterly direction, with a more concentrated swell from the north, and perhaps a second swell from NNW.

[14] Please note that this is just a useful spectrum to describe the methodology, taken from a location in the southern North Sea, rather than being specific to this project.

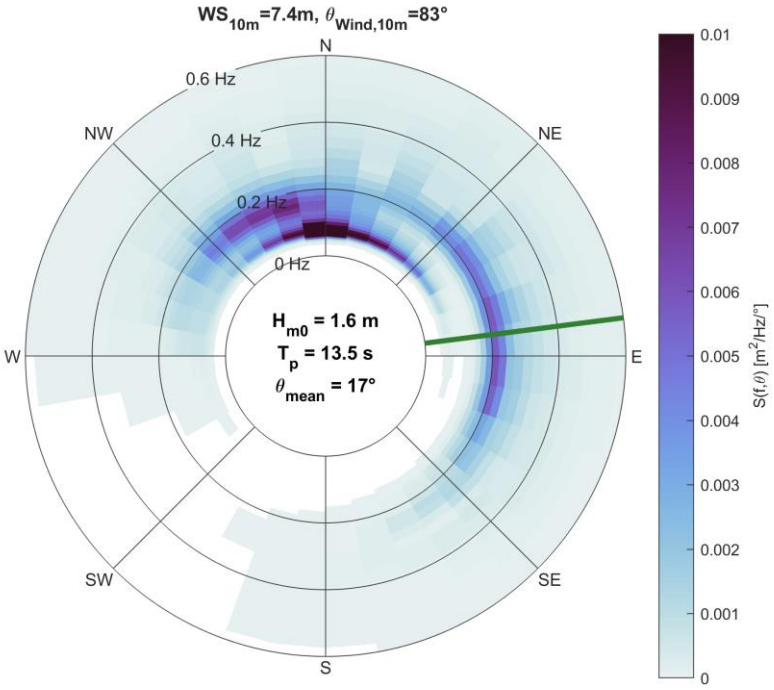



Figure E.1. Example directional spectrum for watershed method.

### E.2.1 Wave System Identification

As noted above, the first stage in the partitioning algorithm is to split the spectrum into different systems. For performance reasons, this calculation is carried out using watershed algorithms commonly used in image processing applications. These are certainly beyond the scope of this document, however to conceptually understand the process, we consider a slightly simpler approach (as described in Hansen & Phillips, 2001 [28]).

Firstly, we take the spectrum as a three-dimensional surface, whose elevation corresponds to spectral energy. For our example spectrum, this is shown in Figure E.2.

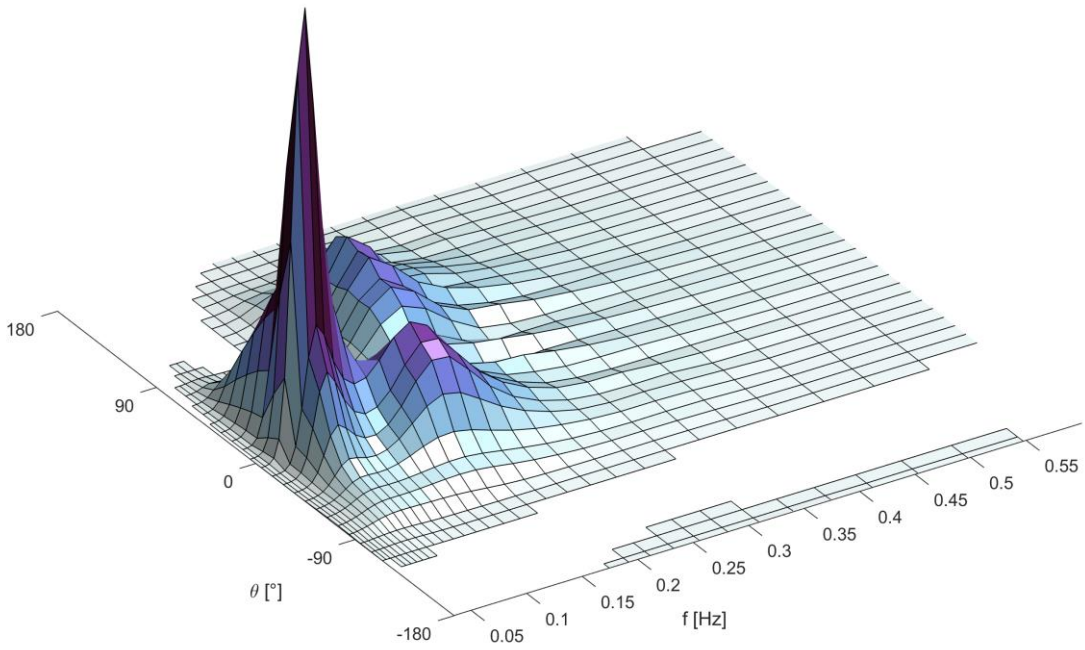



Figure E.2. Directional spectrum, with S(f,θ) used to give elevations.

Then we *invert* elevations, as shown in Figure E.3.

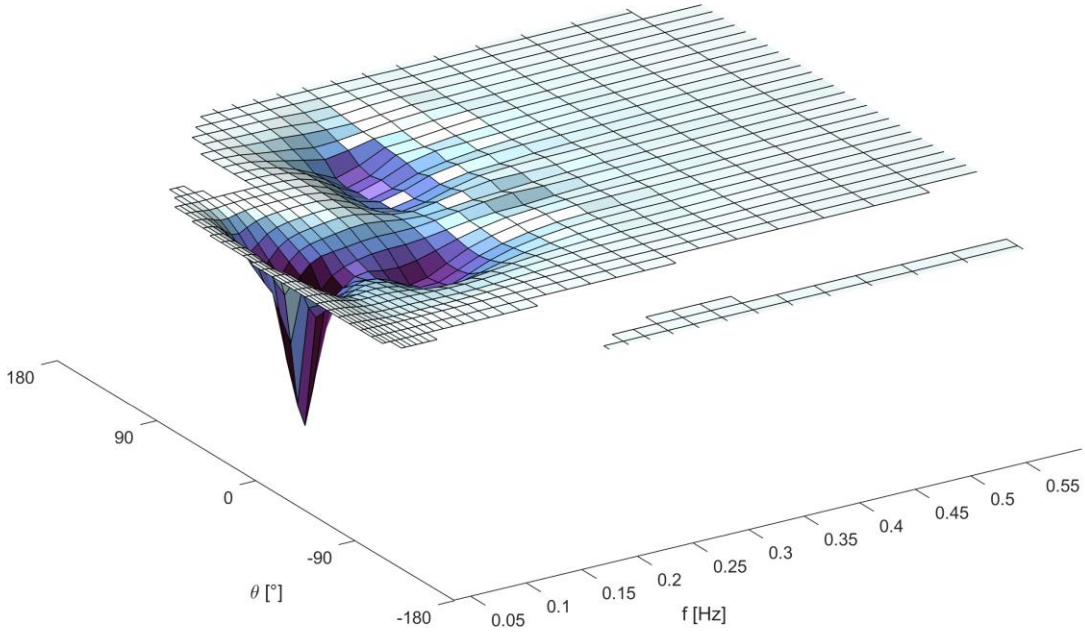



Figure E.3. Directional spectrum, with minus S(f,θ) used to give elevations.

Now imagine a drop of water falling on this surface. Under the assumption that the drop flows downhill in the direction of the steepest slope, if the drop falls at, say f = 0.35 Hz, θ = 95° (green dot in Figure E.4) it will follow such a downhill path (magenta line in Figure E.4) until it reaches the bottom of a trough (red dot in Figure E.4).

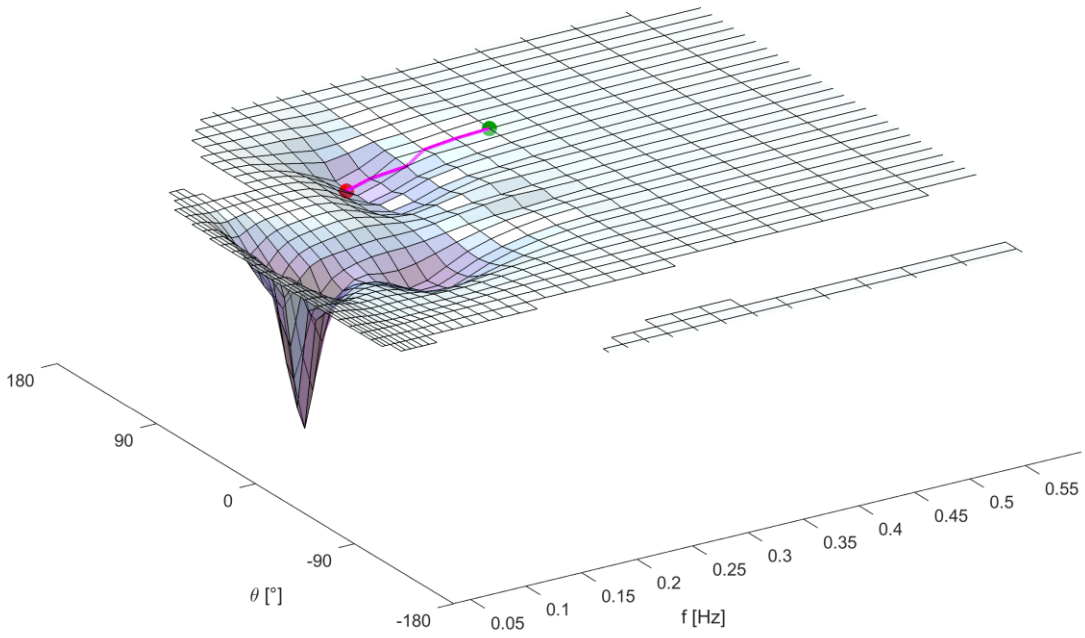



Figure E.4. Downward path for example frequency/direction bin.

If we repeat this for all frequency and direction bins with non-zero values of S(f,θ), there will be some collection of start points for which the rain drop ends up in the deepest minimum. Let us term this collection of points “Partition 1”. Similarly, there will be another collection for which it ends up at a second minimum, say, “Partition 2”, etc. If some additional caution is taken with regard to flat sections, or indeed local minima which are little different to their surroundings, ultimately all values with non-zero energy will be assigned to a relatively small number of discrete sets of partitions.

Whilst the actual steps used differ – more analogous with flooding the surface with a rising water level from below, and assigning boundaries when two basins join – the resultant partitions are very similar. In our example, such a method leads to the boundaries shown in Figure E.5, and ultimately three partitions.

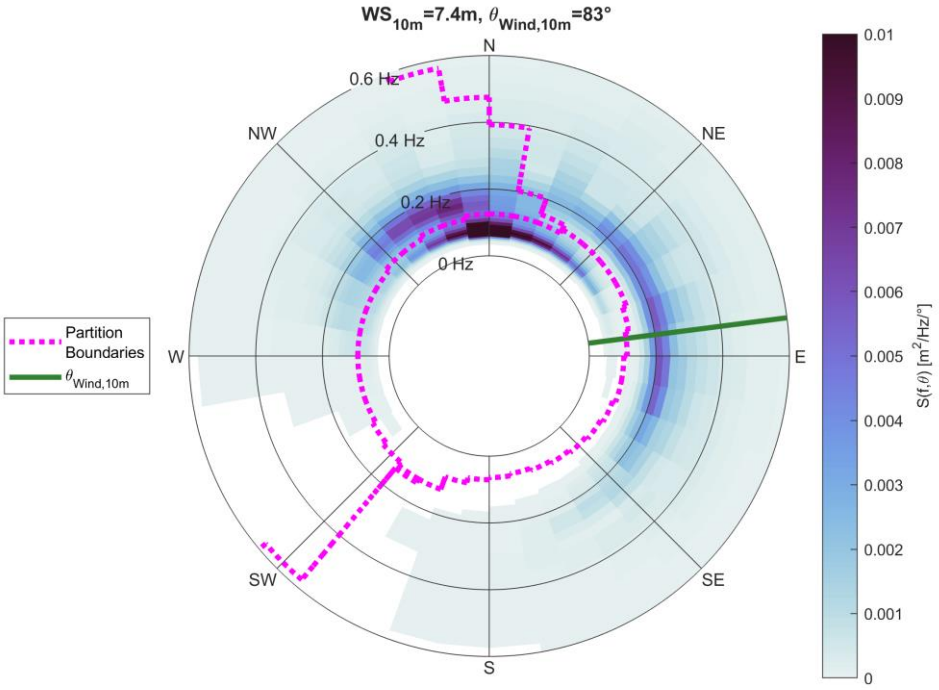



Figure E.5. Example directional spectrum, with watershed boundaries.

### E.2.2 Wave System Classification

After splitting the spectrum into various partitions, they are subsequently categorised as wind-sea or swell based on a variant of the wave-age criterion. This is carried out for each identified partition independently as follows:

**STEP 1: Split into wind-sea and swell**

Each spectral bin of the partition is classified as swell if the following condition is met:

$$\frac{WS_{10m}}{c} \cdot \cos\left(\frac{\theta_{Wave} - \theta_{Wind,10m}}{2}\right) < WA_{SL}$$

Where:

- $WS_{10m}$ is the wind speed at 10 m.
- $\theta_{Wind,10m}$ is the wind direction at 10 m.
- $\theta_{Wave}$ is the direction of the spectral bin.
- c is the wave phase velocity of the spectral bin.
- $WA_{SL}$ is a user defined wave-age swell limit.

If the condition is not met, the spectral bin is considered wind-sea.

It is worth noting that this step is very similar to the standard wave-age criterion, which would generally assign each spectral bin to wind-sea or swell directly using a condition of the form:

$$\frac{WS_{10m}}{c} \cdot \cos\left(\theta_{Wave} - \theta_{Wind,10m}\right) < WA_{SL}$$



One key difference here is the halving of the angle between wind and wave directions, which ultimately means a widening of the directions which are considered wind-sea. This can significantly improve performance with turning winds, or where coastal effects play a significant role. A second key difference is that here the criterion only forms *part* of the overall process. In particular, misclassification of an individual frequency bin at this stage will not necessarily mean that it is misclassified in the final results, as would be the case if the wave-age criterion alone is used.

**STEP 2: Classify partition based on fraction of energy that is wind-sea**

An entire partition is considered wind-sea if:

$$F_{wind-sea} = \frac{E_{wind-sea}}{E_{total}} \geq WF$$

For some "wind-force limit", *WF*, where $E_{\text{wind-sea}}$ is the sum of the partition spectral energy considered wind-sea, and $E_{\text{total}}$ the total partition energy.

The results of applying this method to our example spectrum are shown in Figure E.6. Here, each of the three partitions identified by the watershed method are shown. Overlaid are the wind direction (green line) and the boundary determined by STEP 1 of this process with a typical $WA_{SL}$ value of 0.59 (brown dashed line).

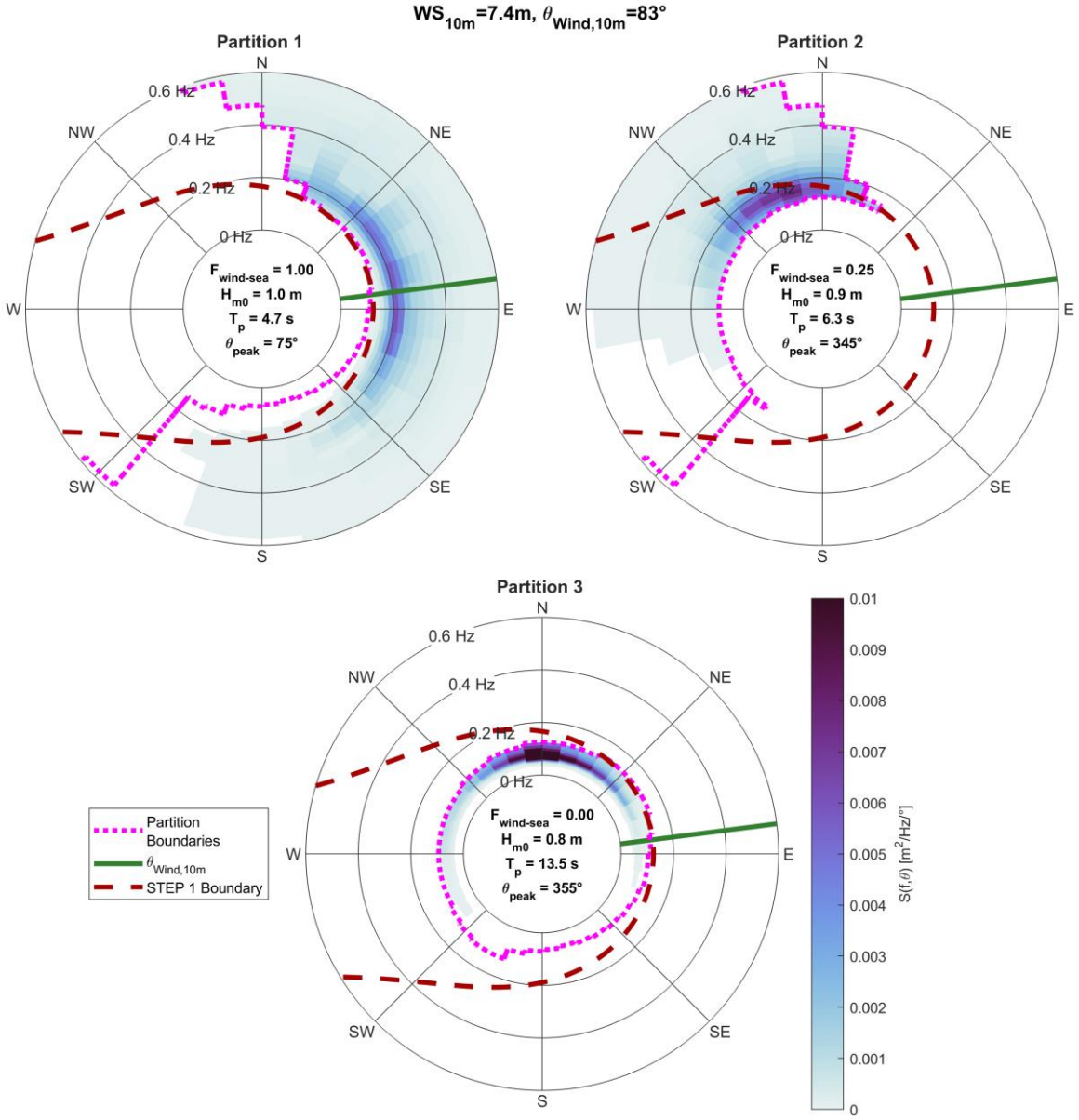



Figure E.6. Example directional spectrum, system classification.

Here we see that for the partition denoted “Partition 1”, almost all of the energy is to the right of this boundary, i.e. on the same side of the boundary as the wind. Indeed, the fraction of the partition energy that is determined to be wind-sea by STEP 1 (denoted $F_{wind\text{-}sea}$) is 1.00. Thus, for any reasonable choice of wind-force-limit, this entire partition would be considered wind-sea. Similarly, Partition 3, with $F_{wind\text{-}sea} = 0.00$, would be considered swell. Classification of Partition 2, $F_{wind\text{-}sea} = 0.25$, is certainly more dependent on the threshold, *WF*. In most cases a value of 0.5 is reasonable – if more than half the energy is wind-sea then the partition itself is deemed to be wind-sea, otherwise it is swell – and in such a case, Partition 2 would also be classified as swell.

### E.2.3 Combining Systems

It is certainly possible that the previous steps can lead to more partitions than are ultimately required. The first case to consider is that where the watershed algorithm splits the data into too many parts. For example, local minima caused by noisiness in measured data may lead to such over-partitioning. This can be addressed through a variety of steps, including:

- Combining systems deemed to be wind-sea such that there is only one such partition.
- Combining swells whose peaks are close to each other in direction and/or frequency when compared to the spreads of each system.
- Combining swells where the lowest value between them is close in value to the smaller peak.

The second case to consider is that where the required description includes less partitions than are actually present in the spectrum. For example, we may wish to describe all spectra using *one* swell partition and *one* wind-sea partition, but the spectrum we are using as an example consists of three systems. The simplest approach is perhaps to simply combine all components considered swell. However, if our ultimate aim is an accurate representation of the spectrum through two systems described by a small number of parameters (for example, two JONSWAP spectra) this may not be optimal. So instead, the partitions are sorted in order of energy, and those swells whose ranking is below the number of systems required are merged with their nearest neighbours in frequency-direction space. Whilst this may ultimately lead to systems which were previously considered swell being merged with those considered wind-sea, as a whole it leads to less merging of dissimilar systems.

In our example, the partition with least energy, that labelled Partition 3, is merged with its nearest neighbour (Partition 2) yielding a final split as shown in Figure E.7.

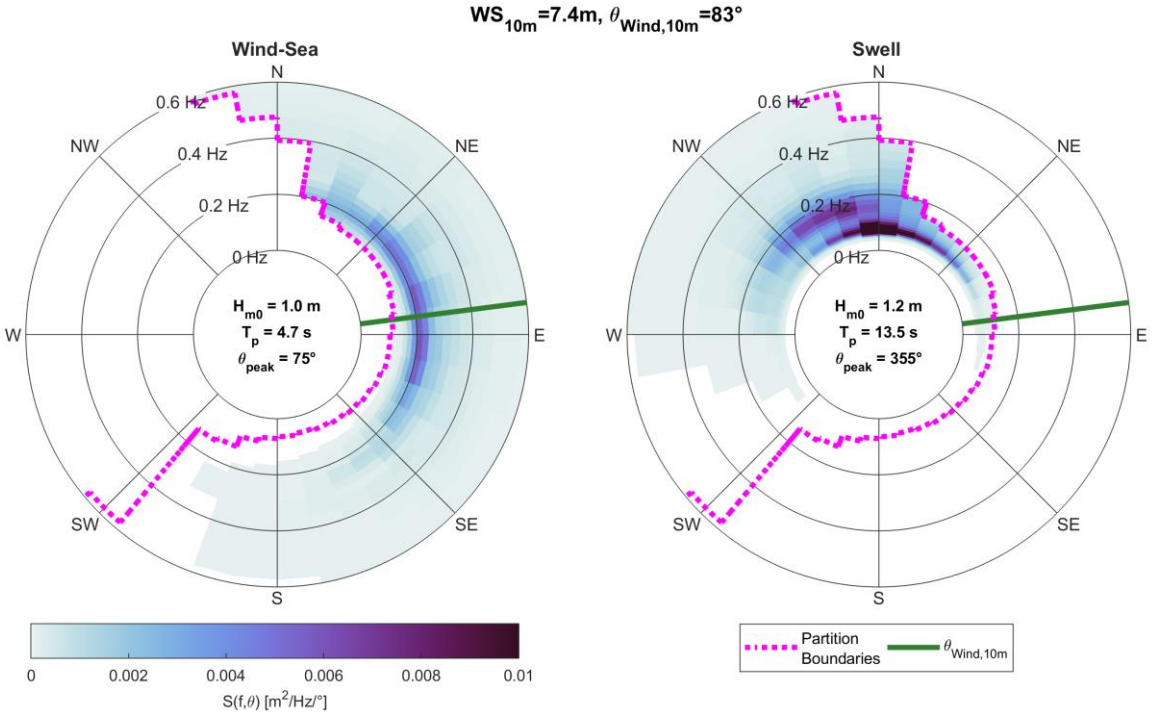



Figure E.7. Example directional spectrum, final partitions.

### E.2.4 Additional Considerations

When compared to the wave-age criterion method, the watershed method does have advantages, most notably:

a) In using spectral energy, in addition to wind speed and direction, it is able to ensure that systems as a whole are kept together, rather than regularly split in two.
b) It is not limited to a single swell partition, and as such can be used to give a much more detailed view of wave systems at a particular location, even if merging is ultimately required to give a more concise final description.

However, it is also important to remember that it is by no means a "perfect" solution. Often systems will merge, leaving no dip in energy at which to divide them. This may be particularly problematic when both wind-sea and swell come from exactly the same direction. Similarly, small dips in noisy spectra may lead to over-partitioning, although this can be to some extent addressed with a variety of smoothing algorithms. Finally, it is worth noting that the line between what should be considered "wind-sea" and "swell" can be somewhat subjective – a problem for any partitioning method.

## E.3 Fitting of Spectral Shapes

We now move our attention to the fitting of parametric spectral shapes to the directional spectra. For each timestamp independently:

- For the **1 JONSWAP** dataset, a single parametric spectrum is fitted to the directional spectrum in its entirety.
- For the **2 JONSWAP** dataset, a parametric spectrum is fitted to any wind-sea and swell partitions identified. These are then added together to form the full spectrum.

Each parametric spectrum consists of two parts:

a) A JONSWAP spectral shape to represent the omni-directional spectrum.
b) A cos2n directional distribution, specified through a single central direction and directional spread value for each spectrum.

All fitting is carried out in the XWaves software mentioned in Section E.2. For reference, more details on the spectral shapes used are included in the sections below.

### E.3.1 JONSWAP Spectral Shape

The JONSWAP spectrum (see for example Annex B of IEC 61400-3 [29]) specifies that the omni-directional spectral density, $S_{JS}$, of the surface elevation is given, for frequency $f$ in Hertz, by:

$$S_{JS}(f) = C(\gamma) \cdot S_{PM}(f) \cdot \gamma^{\alpha}$$

Where:

- $S_{PM}(f)$ is the Pierson-Moskowitz spectrum, which for significant wave height, $H_{m0}$, and peak frequency, $f_p = 1/T_p$, is defined as:

$$S_{PM}(f) = 0.3125 \cdot {H_{m0}}^2 \cdot {f_p}^4 \cdot f^{-5} \cdot \exp\left(-1.25\left(\frac{f_p}{f}\right)^4\right)$$



- The exponent, $\alpha$, is given by:

$$\alpha = \exp\left(-\frac{(f-f_p)^2}{2\sigma^2 {f_p}^2}\right)$$

With $\sigma = 0.07$ for $f \leq f_p$ and $\sigma = 0.09$ for $f > f_p$

- $C(\gamma)$ is a normalizing factor, with various empirical forms included in the guidelines. For example, IEC 61400-3 states:

$$C(\gamma) = 1 - 0.287 \cdot \ln(\gamma)$$

whist DNVGL-RP-C205 [22] gives:

$$C(\gamma) = \frac{0.2}{0.065\gamma^{0.803} + 0.135}$$

and ISO 19901-1 [24] gives:

$$C(\gamma) = \frac{0.0624}{0.3125 \cdot (0.230 + 0.0336\gamma - 0.185 \cdot (1.9 + \gamma)^{-1})}$$

Note that in practise, there is little difference between these three forms for 1 ≤ γ < 5.5, nor between the DNV and ISO options for at least 1 ≤ γ < 10. For this work, we have used the DNV equation, largely because its inclusion in an earlier (2005) issue of ISO 19901-1 for 1 ≤ γ < 10 gives at least some corroboration between guidelines.

### E.3.2 Cos2n Directional Distribution

After the JONSWAP parameters have been determined for the *omni*-directional spectrum, a central wave direction, $\theta_c$, and directional spreading parameter, *n*, are determined through a least-squares fit, such that the full parametric directional spectrum, $S_P(f,\theta)$, is represented by:

$$S_P(f,\theta) = S_{JS}(f)D(\theta)$$

With:

$$D(\theta) = \begin{cases} D_{2n}\cos^{2n}(\theta - \theta_c) & \text{if} \quad |\theta - \theta_c| \leq 90° \\ 0 & \text{otherwise} \end{cases}$$

And $D_{2n}$ is a normalization function given by:

$$D_{2n} = \frac{\sqrt{\pi}}{180}\frac{\Gamma(n+1)}{\Gamma(n+1/2)}$$

Where $\Gamma$ is the Gamma function.

Though not of concern in the current work, a little caution is generally necessary in interpreting the spread parameter *n* here, since some sources (e.g. XWaves and thus this report) describe the distribution through an equation of the form $\cos^{2n}$ whilst others (e.g. DNVGL-RP-C205 [22]) use an equation of the form $\cos^{n}$. Whilst these are just two ways to describe the same distribution, the value of the parameter *n* is not directly interchangeable between the two without being doubled/halved as necessary.

# Appendix F. Wind and Wave Averaging Periods

## F.1 Overview

In this Appendix, the "effective averaging interval" of the wind and wave modelled data is considered through comparison to available measurements. By way of overview of the overall procedure used, we begin with a simple example of modelled and measured wind speeds for an arbitrary period, as shown in Figure F.1. Here the measurements (ten-minute averages every ten-minutes) show a great deal more variation than the model values (instantaneous hourly values representative of a grid location) which are considerably smoother.

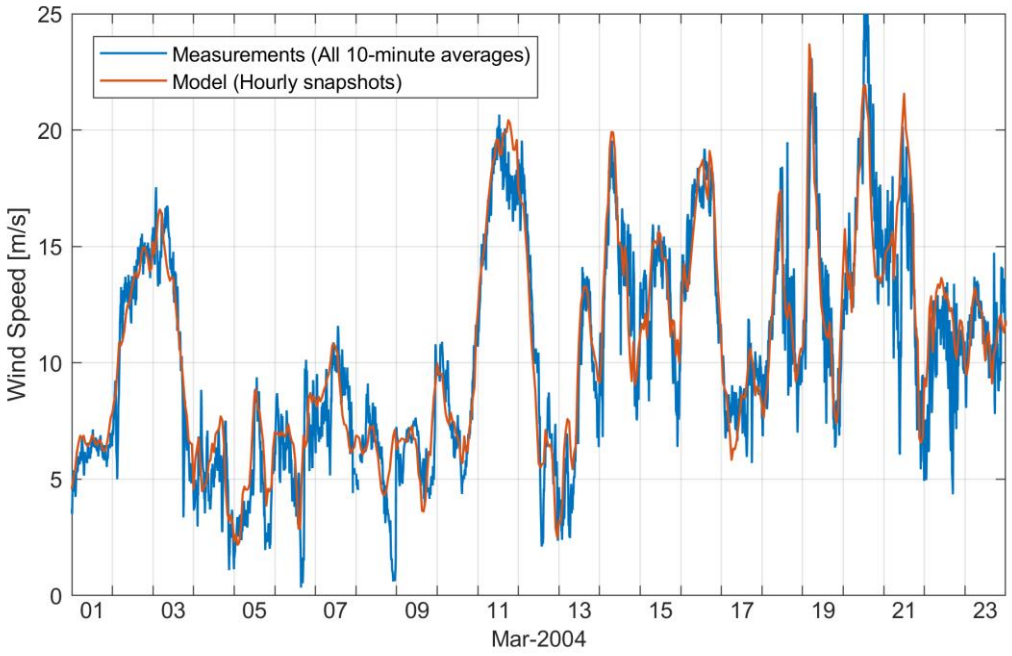



Figure F.1. Example time series, modelled and measured

To a large extent, plotting *all* measured data (i.e. a value every 10 minutes as opposed to hourly for the model) exaggerates this effect. However, if we use only *hourly* measured values, i.e. every sixth ten-minute average, we still see very similar behaviour, as shown in Figure F.2.

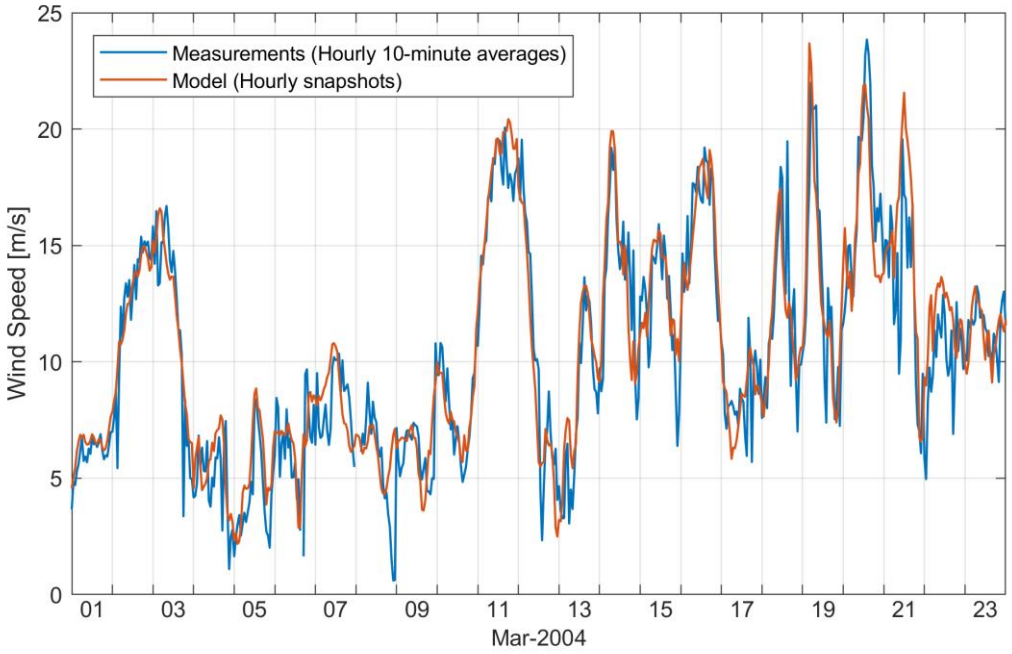



Figure F.2. Example time series, modelled and hourly measured

If, rather than taking hourly ten-minute averages, we take hourly *one-hour* averages, or *three-hour* averages, or even *six-hour* averages from the measured data, we get smoother lines, for example as shown in Figure F.3

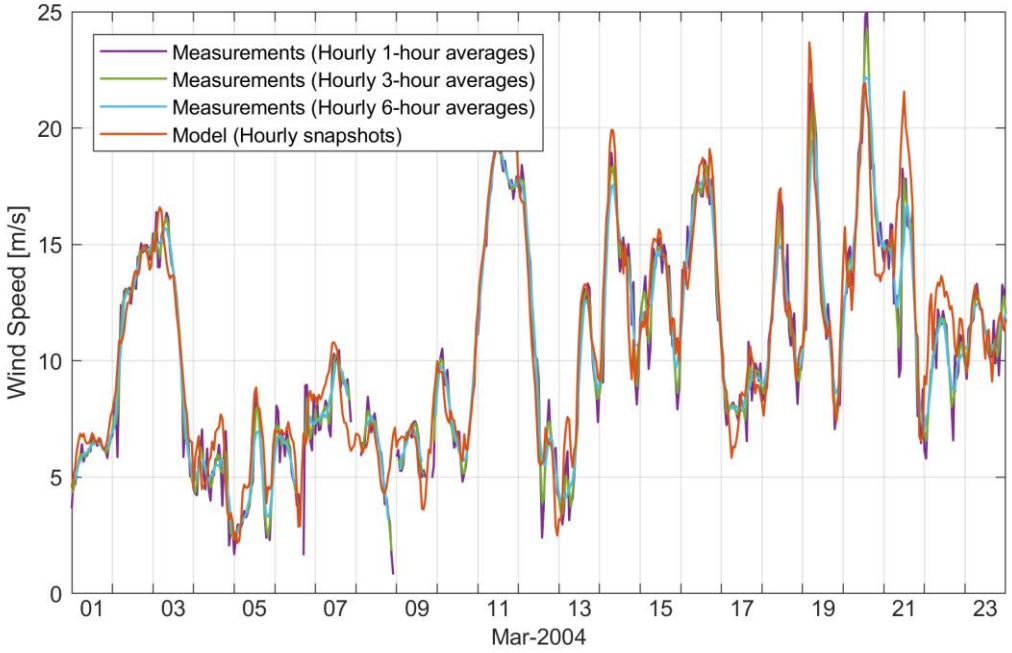



Figure F.3. Example time series, modelled and measured

Whilst it is impossible to draw firm conclusions from the above, it does appear that the one-hour average is still less smooth than the model data line, the six-hour average is smoother, and the three-hour average is quite similar.

Though the modelled data represent instantaneous wind speeds, some form of spatial averaging and/or smoothing has been included in their creation – if not in the model itself, then at least in the inputs driving the model. This has a very similar effect to *temporal averaging* of the measurements. Since our aim is to treat the model as representative of measurements at a single location, we must determine what level of such temporal averaging corresponds to the spatial averaging seen in the model, determining an effective averaging period for the model.

## F.2 Diagnostic Plots

In order to assess this effective averaging period, we review a series of diagnostic plots comparing the model to measured data. An example, for wind speeds at the 15 m level of the Arklow met mast, is shown in Figure F.4.

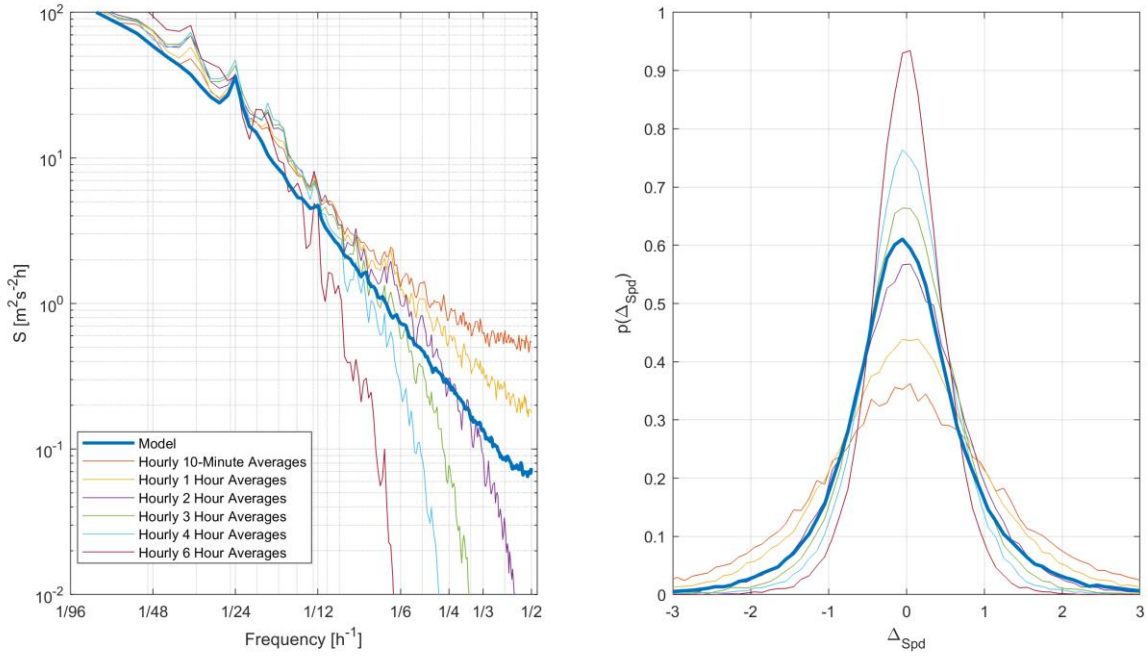



Figure F.4. Effective averaging period diagnostic, Arklow Met Mast (Original), wind speeds at 15 mAMSL.

To the left-hand side, a **spectral** plot of measured and modelled data is shown. For the model data, and a selection of hourly datasets of different averaging periods derived from the original measurements, the spectral density is found and all results overlaid. Those shown are calculated from overlapping 16-day windows, starting at 00:00 each day, though a variety of alternative windows were also reviewed, leading to very similar behaviour.

To the right hand-side, the **distribution of differences** between consecutive hourly values of each time-series is shown. For an hourly timeseries of wind speed, *U*, the difference between consecutive values, $\Delta_{Spd}$, is given by:

$$\Delta_{Spd}(t) = U(t) - U(t - 1\text{hour})$$

The probability (P) of all differences for each time-series is overlaid. In general, it would be expected in all cases, that the distributions would be centred around a difference of zero, but that smoother time-series would have a narrower distribution, i.e. smaller changes would be more common.

## F.3 Wind Hindcast

A number of additional such diagnostic plots are shown for the Arklow met mast and LiDAR in Figure F.5 through Figure F.9. Note that the plots for the LiDAR cover a shorter measurement period than those for the met mast, and thus would be expected to appear somewhat "noisier" in general. Throughout these, and indeed plots reviewed at other elevations and locations, the model behaviour is somewhere between that of the 2- and 3-hour measured averages. Where an averaging period is required for estimating extreme values of wind speeds, we would recommend taking the more conservative choice of attributing a 3-hour averaging period to the modelled data.

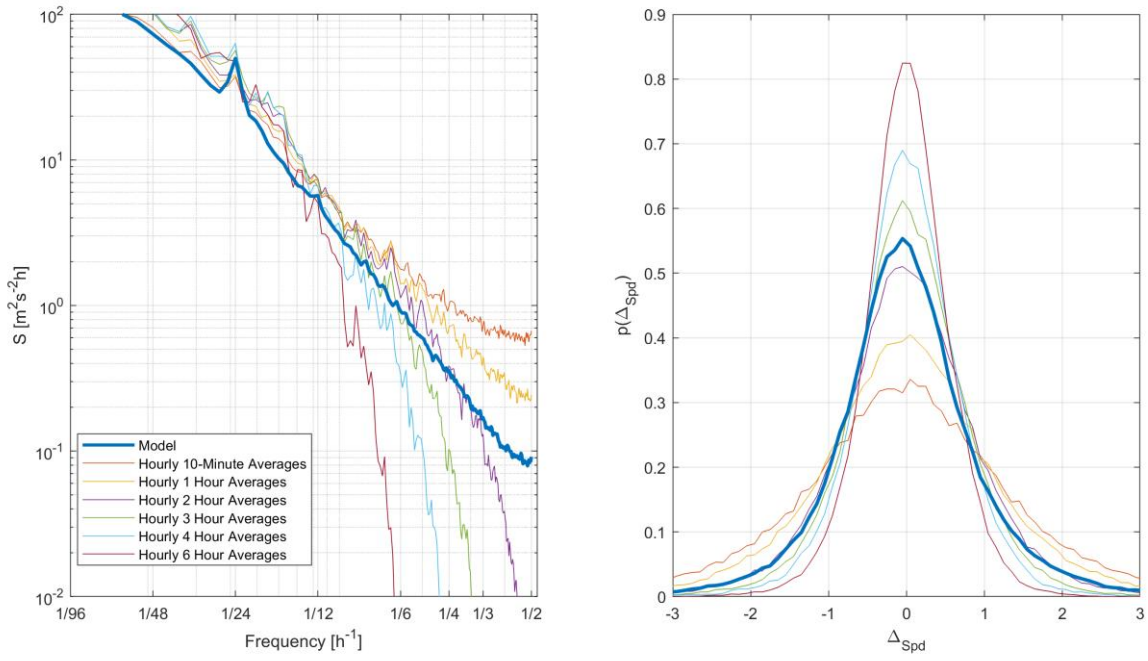



Figure F.5. Effective averaging period diagnostic, Arklow Met Mast (Original), wind speeds at 42.5 mAMSL.

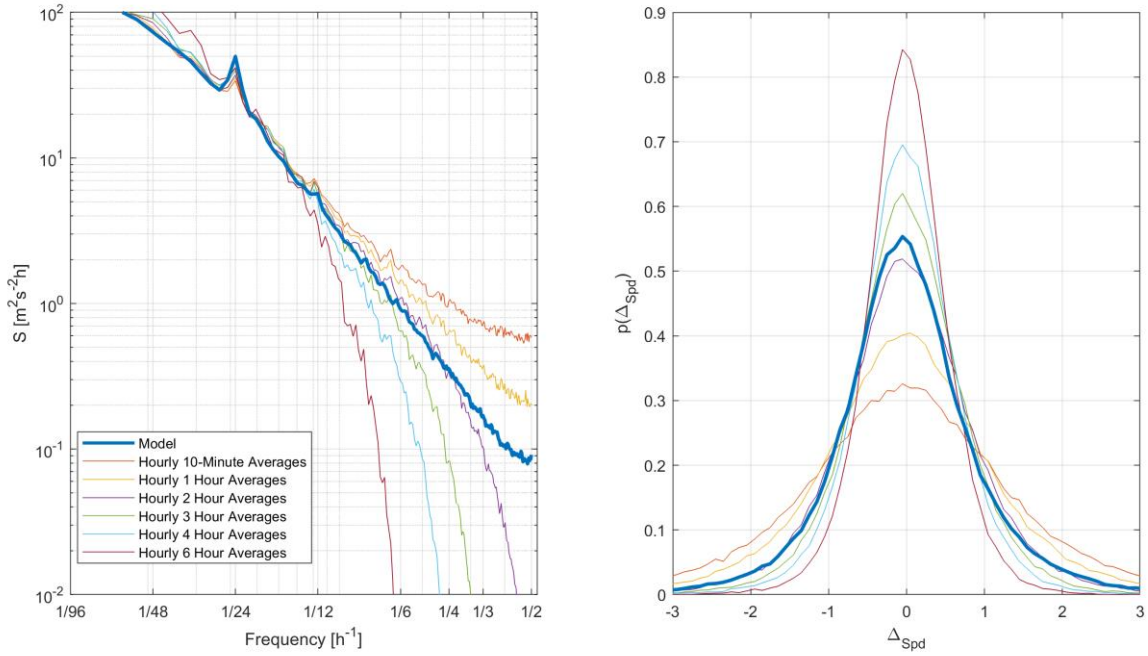



Figure F.6. Effective averaging period diagnostic, Arklow Met Mast (Synthesised), wind speeds at 42.5 mAMSL.

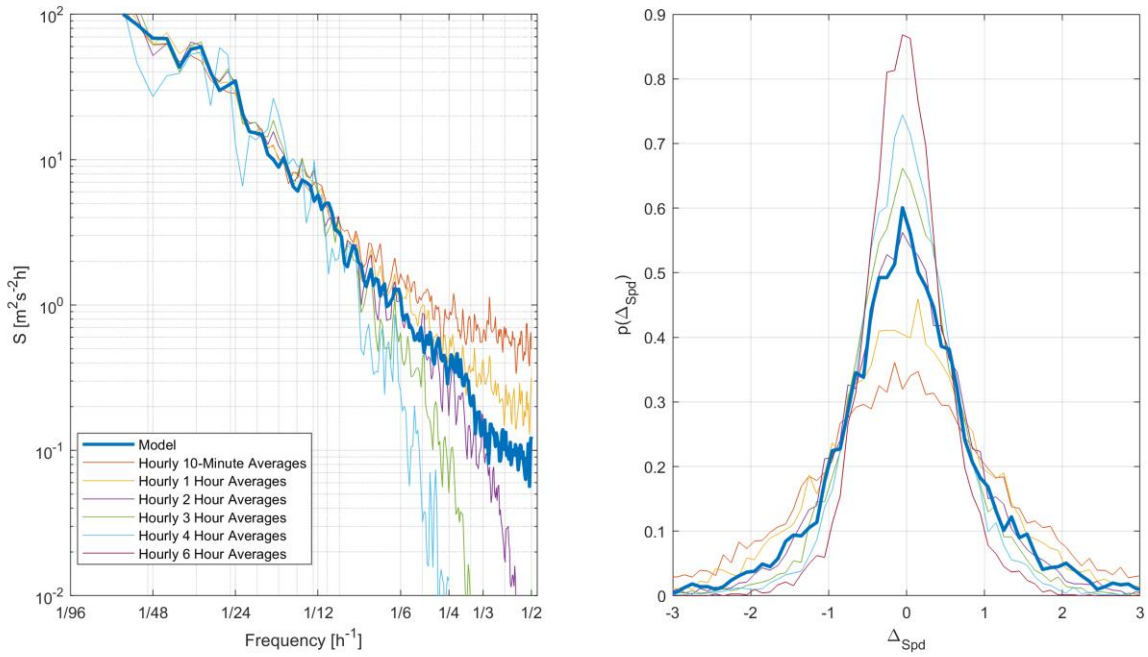



Figure F.7. Effective averaging period diagnostic, Arklow LiDAR, wind speeds at 21.3 mAMSL.

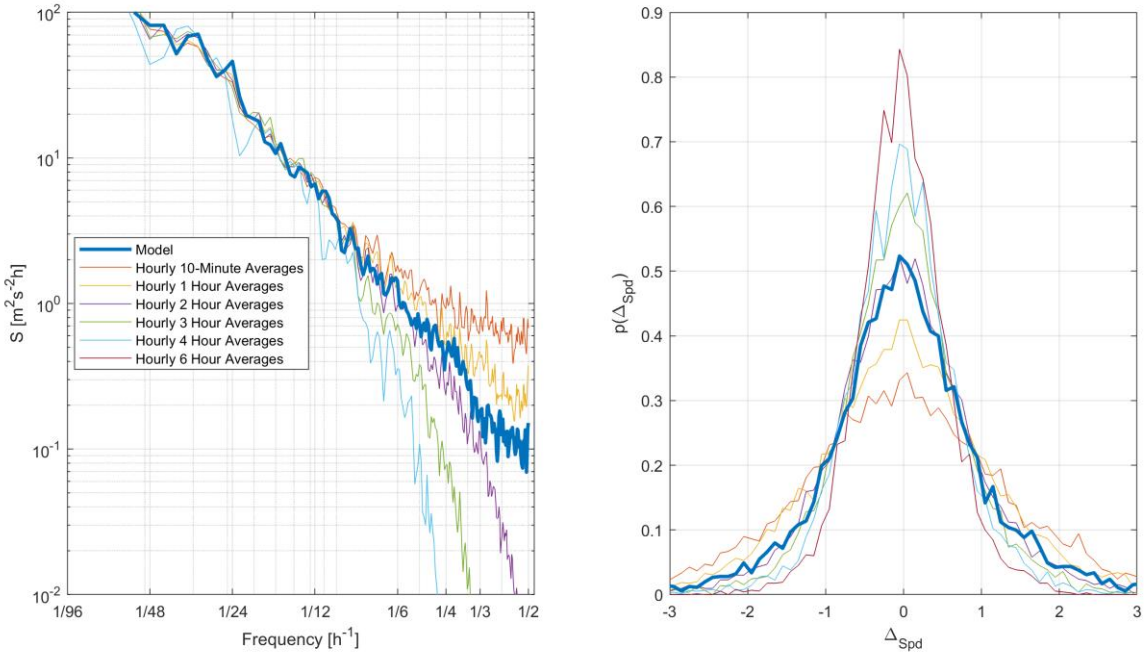



Figure F.8. Effective averaging period diagnostic, Arklow LiDAR, wind speeds at 49.3 mAMSL.

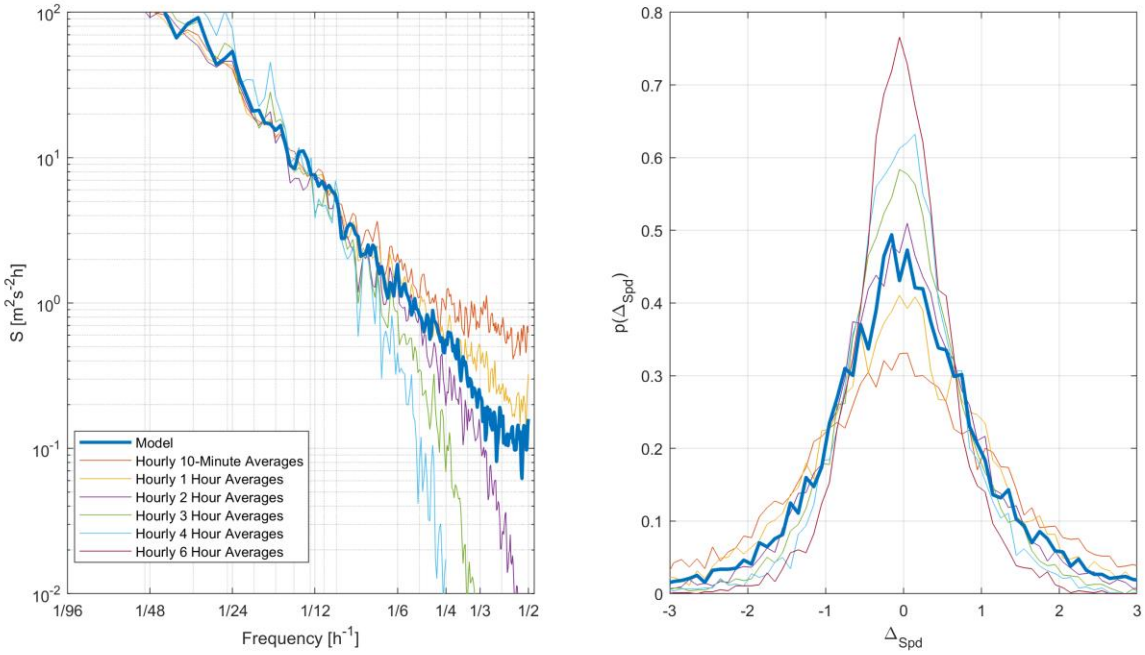



Figure F.9. Effective averaging period diagnostic, Arklow LiDAR, wind speeds at 129.3 mAMSL.

## F.4 Wave Hindcast

In order to assess the averaging period to associate with the wave model, a similar approach is followed. Unfortunately, there is a little more uncertainty in this case, since measurements from the AWACs are only taken for 512 seconds (8 minutes, 32 seconds) every 30 minutes. This means we cannot use contiguous periods of measurements to create Hm0 time series for, say, 1-hour, 2-hour, 3-hour sea-states in the same way as *was* possible for wind speeds. Instead, we can only calculate averages for consecutive bursts, and make some approximate assumptions as to the period length over which they are representative.

Comparisons against such burst averages are shown for AWACs A, C and E in Figure F.10 through Figure F.12. In all cases, burst averages are calculated by taking the mean of *spectra* rather than Hm0 directly, or equivalently as second power means of Hm0 with:

$$H_{m0,nBurst} = \sqrt{\frac{1}{n}\sum_{i=1}^{n} {H_{m0,i}}^2}$$

Note that measurements for AWAC A have a number of periods of missing data, which, though relatively short in duration, lead to the spectral plot being calculate from relatively few 16-day contiguous periods, making it far noisier than corresponding plots for AWACs C and E.

Any decision here is certainly less clear-cut than was the case for the wind hindcast. In taking all six diagnostics as a collective whole, we would recommend the model be considered closest to the behaviour of Hm0 from a 7-Burst mean. Further, we would expect this to be representative of an approximately 3-hour sea-state, being taken across a period of 3 hours, 8 minutes and 32 seconds. Though this only corresponds to approximately one-hour of measurement time in total (7 x 512 seconds being 59 minutes 44 seconds) this should be sufficient to average out much of the shorter-term variation related to 512-second burst periods, making the average more representative of the 3-hours as a whole.

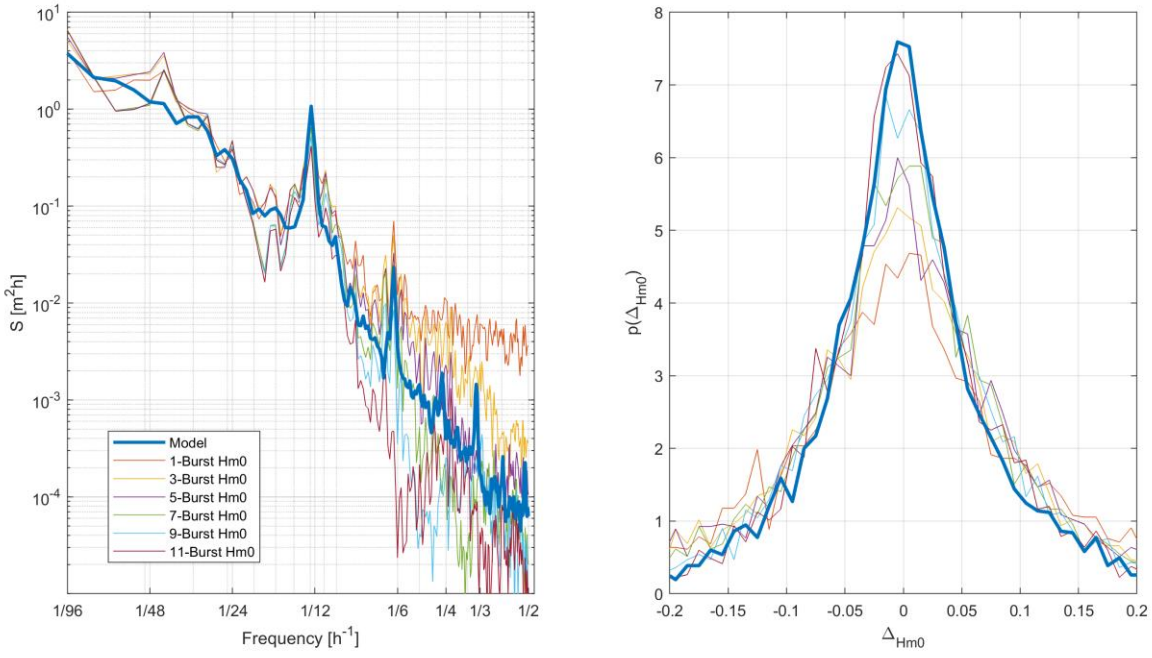



Figure F.10. Effective averaging period diagnostic, Hm0, AWAC A.

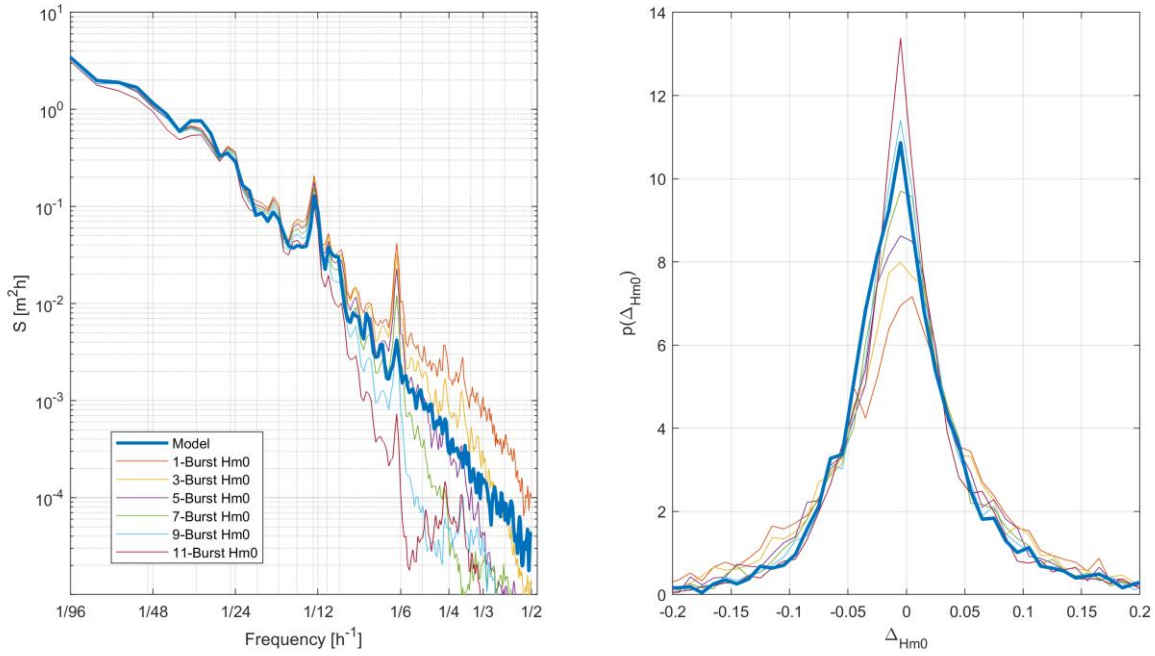



Figure F.11. Effective averaging period diagnostic, Hm0, AWAC C.

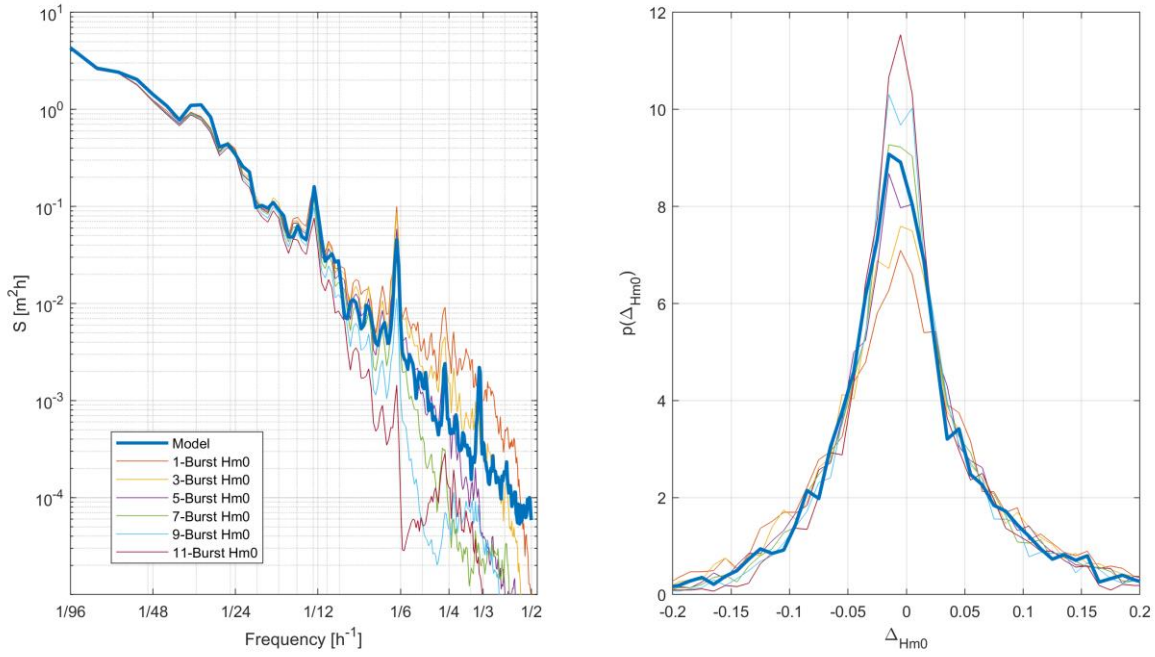



Figure F.12. Effective averaging period diagnostic, Hm0, AWAC E.

# Appendix G. Extreme Value Maps Methodology

## G.1 Introduction

This Appendix outlines the methods used to calculate the extreme value wave maps shown in Section 7.2.2. Whilst the principles follow those that we would normally use to determine extreme values for design criteria at a single location – briefly outlined in Section G.2 below - the need to process over 18,000 grid points means that it is not feasible for all fits to be assessed by an analyst. Instead, the assessment is automated, using the process described in Section G.3.

Whilst this approach allows analyses to be carried out across the entire region of interest, less scrutiny is applied to each location than is necessary for detailed design criteria. As such, the maps should be used for general guidance only. Furthermore, parameters have been optimised based on locations within the lease area, and as such a little more caution should be appointed to values further from this region. Of particular interest in this study are the variations in the difference between the highest and second highest Hm0 peak across the wind farm region, and their effect on extremal fitting, as highlighted in Section G.3.6.

As well as maps for significant wave height (Hm0), maps are also generated for maximum wave and crest heights (Hmax and Cmax respectively). Additional steps are required as part of this calculation, and are discussed in Section G.4.

Finally, Section G.5 describes the methods used to determine maps of Hm0, Hmax and Cmax, for only sea states where water levels are below mean sea level (MSL).

## G.2 General Approach, Single Location

Here we briefly outline those steps which we would generally carry out in determining extreme values of Hm0 for each *individual* location considered in a set of design criteria.

**Step 1: Data Preparation and Review**

Carry out of a detailed review of the model data, including calibrations against measurements.

**Step 2: Method Selection**

Decide whether to extrapolate from Peaks over Threshold (PoT), block maxima, or all data. Preference is given to PoT should there be sufficient data. Investigate any potential concerns with an all-year, omni-directional approach, e.g. larger waves arriving from very different directions, with potentially different extreme distributions or different driving mechanisms.

***Note:*** *For this study, a PoT approach has been used throughout, thus only relevant steps are included hereafter.*

**Step 3: Find peaks over threshold**

a) Split data into points above and below a user specified *Threshold*.
b) Discard all points below, creating a new time-series of only values above the *Threshold*.
c) Place the first point in "Cluster 1". If the second point is temporally within a user specified *Reset Duration* of the first, it too is in Cluster 1. Otherwise, Cluster 1 is complete and this becomes the first point in Cluster 2.

d) Proceed to the third point. If it is within *Reset Duration* of the second, it is in the same cluster. Otherwise, it is the start of a new cluster.
e) Continue through the entire time-series until all data above the *Threshold* are assigned to a cluster.
f) Take the maximum of each cluster.

Review time series of original data and selected cluster peaks. In particular, check high data peaks close to one another since their inclusion/exclusion may significantly affect extreme values. Adjust clustering parameters as necessary, and if highly subjective decisions affect inclusion/exclusion of high peaks, continue separate analysis on each option to review implications.

**Step 4: Fit Distributions to Highest Peaks**

Carry out independent fits to highest 50, 60, 70, …, 100 ,125, 150, …, 250 cluster peaks. For each, include the following fits:

- 3-Parameter Weibull (Maximum Likelihood (MLM), Method of Moments (MoM), Maximum Product of Spacings (MPS), L-Moments (Lmom)).
- Generalized Pareto (MLM, MoM, MPS, Lmom)
- Exponential (MLM, MoM, Lmom)

**Step 5: Review Fits**

Review each fit, including the following:

- If the fitted distribution is a bad fit to the data, discard.
- If the extreme values are not stable to changes in the number of peaks, discard (e.g. if results for a 60 peak fit are considerably different to for a 50 and 70 peak fits).

**Step 6: Decide on Extreme Values**

Of the remaining fits, a representative fit is selected. This is generally a fit whose 100-year extreme value is slightly conservative and is within the 50th – 70th percentile of estimates of all remaining fits. However, some subjectivity is included to take into account the level of conservatism considered appropriate.

## G.3 Automated Fit Assessment

The steps outlined in the previous section allow for subjective input from an analyst throughout - in determining storm thresholds; in deciding which fits are and are not representative of extremal behaviour; in determining the appropriate percentile for the final prediction. For design criteria at a small selection of locations, these decisions can be made by the analyst manually reviewing a number of diagnostics. For the generation of maps, more automated steps are necessary, and are described in the subsections which follow.

### G.3.1 Storm Peaks

Based on previous experience of extreme value analysis of wave heights in European waters, and corroborated by review of time-series data at a selection of sites across the region, for each grid point, the storm threshold was set to be 45% of the maximum significant wave height at the location. A minimum reset duration of three days was required between storms.

### G.3.2 Distribution Fitting

Fits were carried out to the highest 50 storm peaks, then 60 peaks, increasing in steps of 10 peaks to a maximum of 250. For each collection, the following fits were used:

- Exponential distribution (maximum likelihood, method of moments, L-moments)
- 3-Parameter Weibull distribution (maximum likelihood, method of moments, L-moments, maximum product of spacings)
- Generalized pareto distribution (maximum likelihood, method of moments, L-moments, maximum product of spacings)

### G.3.3 Fit Assessment

To outline the process used to assess each collection of fits, let us first consider fits to the highest 100 peaks at a single grid point, shown in Figure G.1.

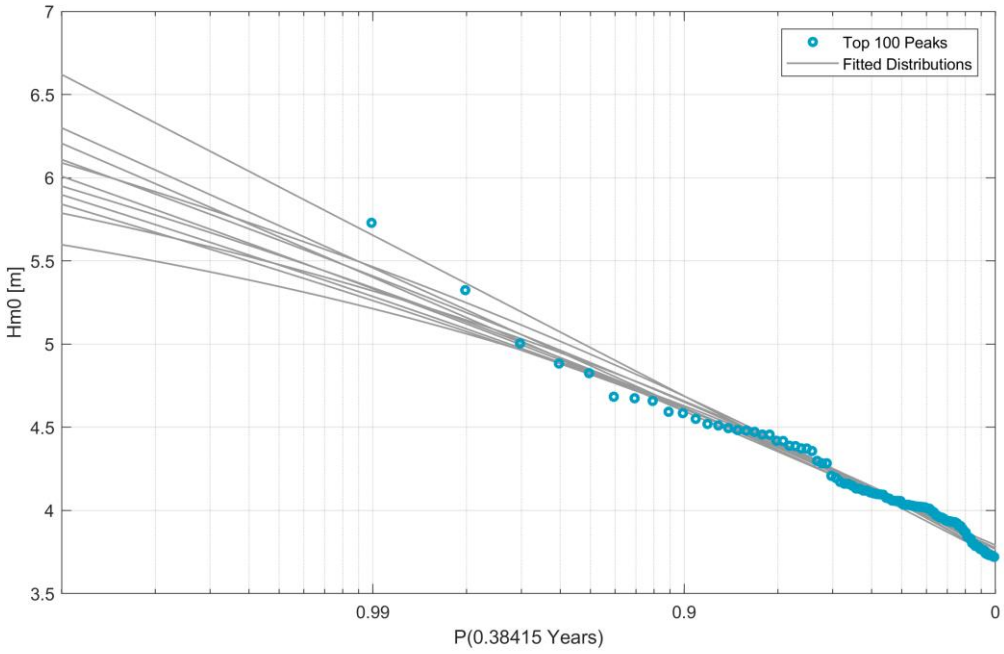



Figure G.1: Example fits, 100 peaks.

Firstly, bounds are placed around each data point independently to allow for a certain percentage of error in the value predicted by the fit. For this example, we use the range from a 3% underprediction to a 5% overprediction, though more detail on the values used in creating the final maps can be found in Section G.3.5. The resulting ranges are shown in Figure G.2. Here, and for all ranges considered, slightly more margin is allowed towards overprediction for the sake of conservatism.

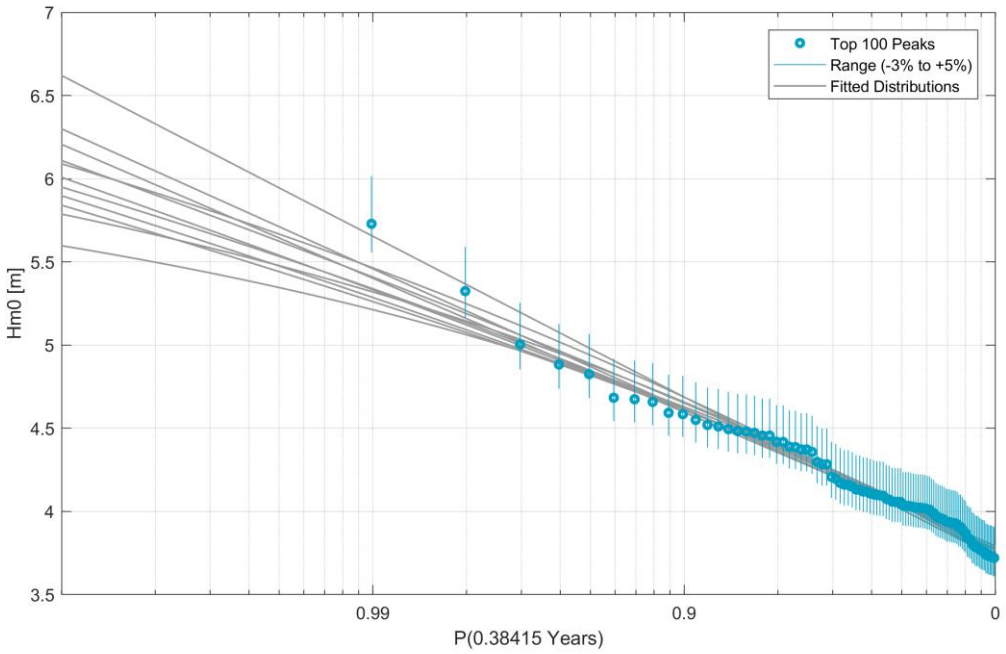



Figure G.2: Example fits, with over/underprediction ranges, 100 peaks.

Next, for each fit, we determine if it passes through this range for *all* data points, all data points *except* one, all data points *except* two, etc. In our example, we will consider a fit "reasonable" if it misses at most one range, under which criterion all reasonable fits are highlighted in green in Figure G.3.

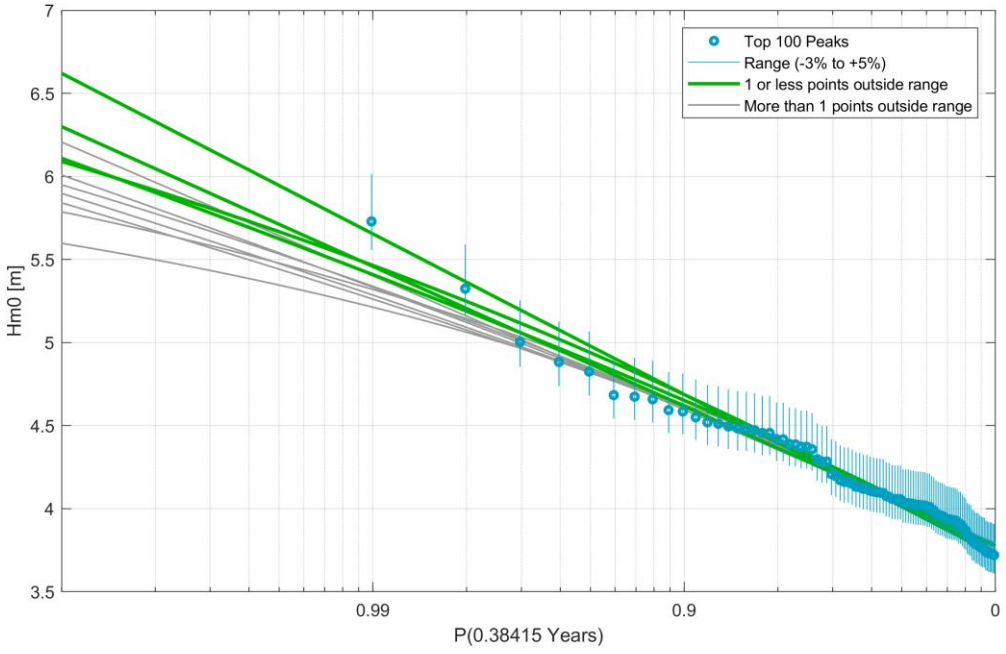



Figure G.3: Example fits, with automated assessment, 100 peaks.

This process is subsequently repeated across *all* collections of peaks, i.e. 50 peaks, 60 peaks, …, 240 peaks, 250 peaks. The result is a larger collection of selected fits, as shown for our example location in Figure G.4.

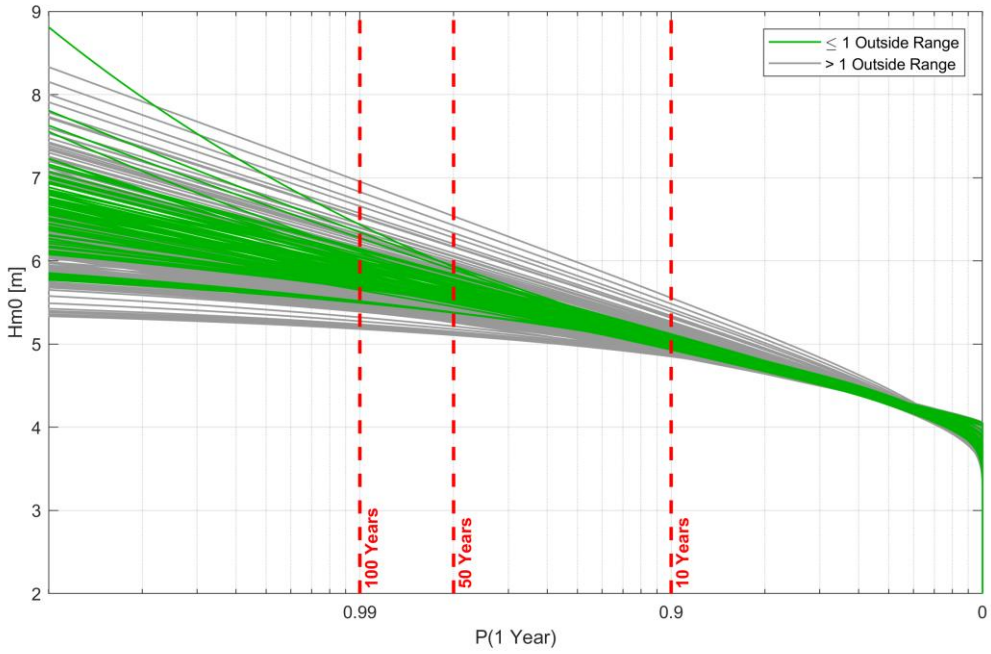



Figure G.4: Example fits, with automated assessment, all peak collections.

### G.3.4 Extreme Value Selection

The collection of selected fits leads to a range of potential extreme values, as shown for this example in Figure G.5. From this range, the final extreme value shown in the maps is taken to be the 70$^{th}$ percentile of extreme values for all selected fits, determined by comparisons between automated and more detailed manual analyses. Note that if less than 20 fits (of over 230 considered) are considered reasonable for a given location, no extreme value is given: the map will have missing data at these locations.

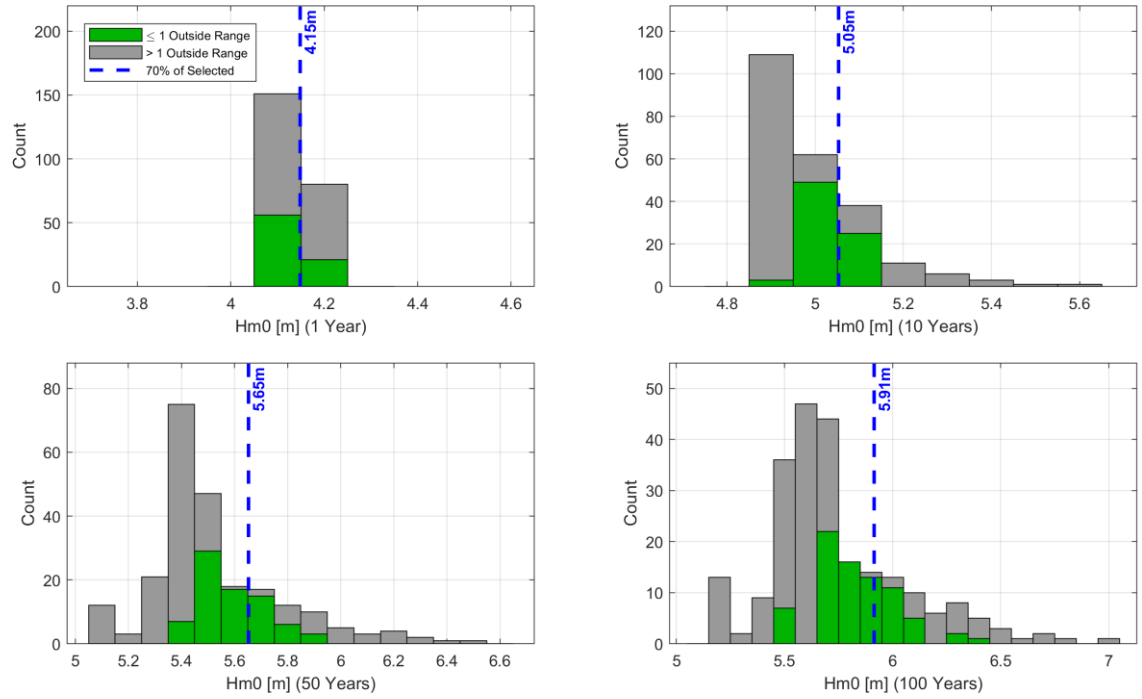



Figure G.5: Example extreme values, with automated assessment.

### G.3.5 Parameter Settings

Through the previous examples, fits have been considered representative if based on:

- A prediction range between -3% and +5% for each data value.
- Falling outside this range for *at most* one data value.

For significant wave height (Hm0), this leads to the 100-year Hm0 map shown on the left of Figure G.6. Note that whilst results are returned for the vast majority of the area shown, in some small regions, less than 20 representative fits are found and thus no value shown. Various alternate options are also considered comprising each combination of:

- Prediction ranges: -3% to 5%; -5% to 7.5%; -7.5% to 10%.
- 0, 1, 2 or 3 data points falling outside the prediction range.

Fits are reviewed at a selection of locations under each option, with maps as a whole also compared. The final set of parameters after this review were:

- A prediction range between -7.5% to 10% for each data value.
- Falling outside this range for *at most* one data value.

The central and right-hand map of Figure G.6 show this in fact leads to only small changes to the map when compared to the narrower prediction range, whilst covering the full region. This final selection is generally a little more conservative overall, with the exception of a small band close to the crest of the bank where the 100-year extreme values are just a few centimetres lower.

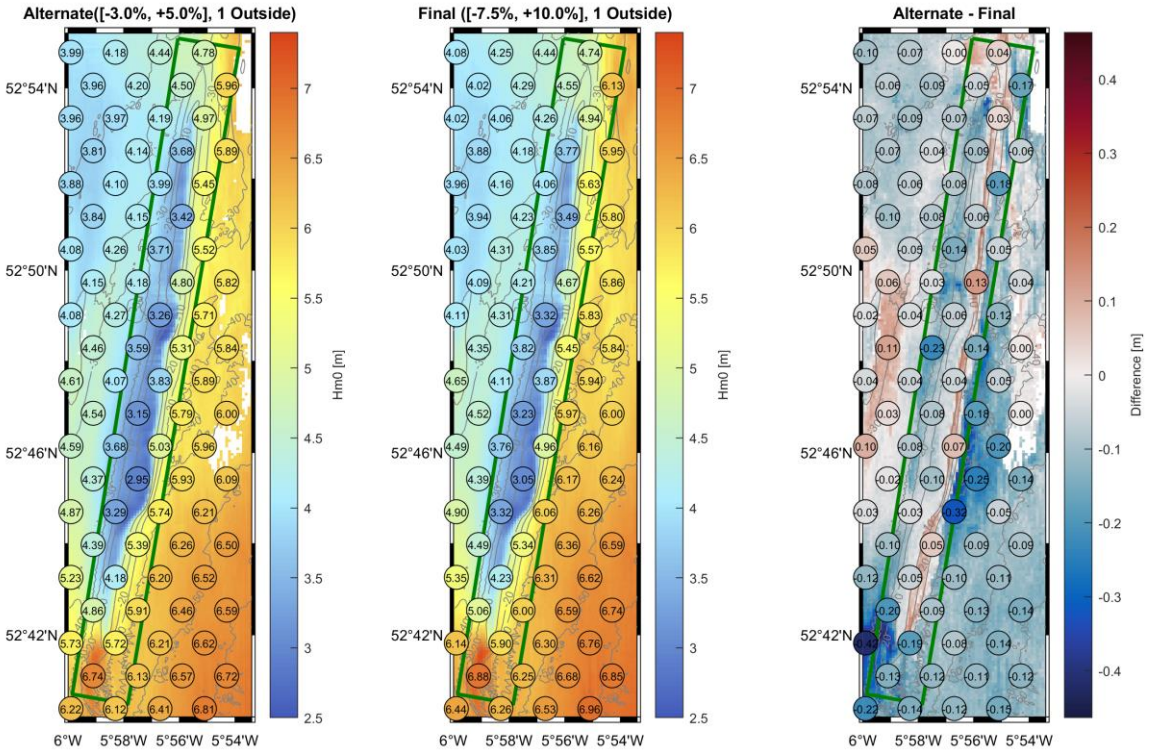



Figure G.6: Alternate parameter selection.

### G.3.6 Largest Storm Peak

Although the same set of parameters is used across the entire region, it is worth noting that this does not necessarily mean that the overall fit characteristics are the same throughout. In particular, significant location dependent differences are seen in the relationship between the very highest storm peak and all other peaks. For example, Figure G.7 shows fits to the highest 100 peaks for five locations across the map. At Location A, the highest peak falls in line with the trend seen across all other peaks. At Location C, this is also the case – perhaps only a few centimetres higher than might be estimated by eye from lower peaks. At Location B the highest peak is a little higher still when compared to others, and yet more so at E. At Location D, in the centre of the region with the very highest Hm0 in the maps, this highest peak (Storm Ophelia, October 2017) is far in excess of what might be predicted from all other peaks.

Two comments are perhaps worth making with regard to how this behaviour relates to the maps:

a) Where the highest peak is considerably higher than all others, the decision as to the appropriate balance between this peak and all other data is somewhat subjective. In the case of the maps, where such subjectivity is applied by tuning map-wide parameters, decisions for individual locations may be sub-optimal.

b) As can be seen for the example locations in Figure G.7, a range of fits are applied to the Hm0 peaks. Many have a tendency to curve down with the body of the data, giving a significant underprediction for the highest peak. Exponential fits are, by definition, straight lines on these plots, and so do not – and cannot – curve down with the body of the data. These, in effect, *force* the fit to be closer to the highest point.
Including both such options in the automated process gives some balance between the body of the data and the highest peak. However, for the locations where this highest peak falls in line with the

rest of the data, e.g. Location A, it is clear that the exponential fits are less appropriate, and if included will provide bias towards higher extreme values. It is certainly possible to omit these fits for a portion of the wind-farm area, though this would add a little complexity in ensuring no artificial discontinuities result. For the present, exponential fits *are* included for all locations.

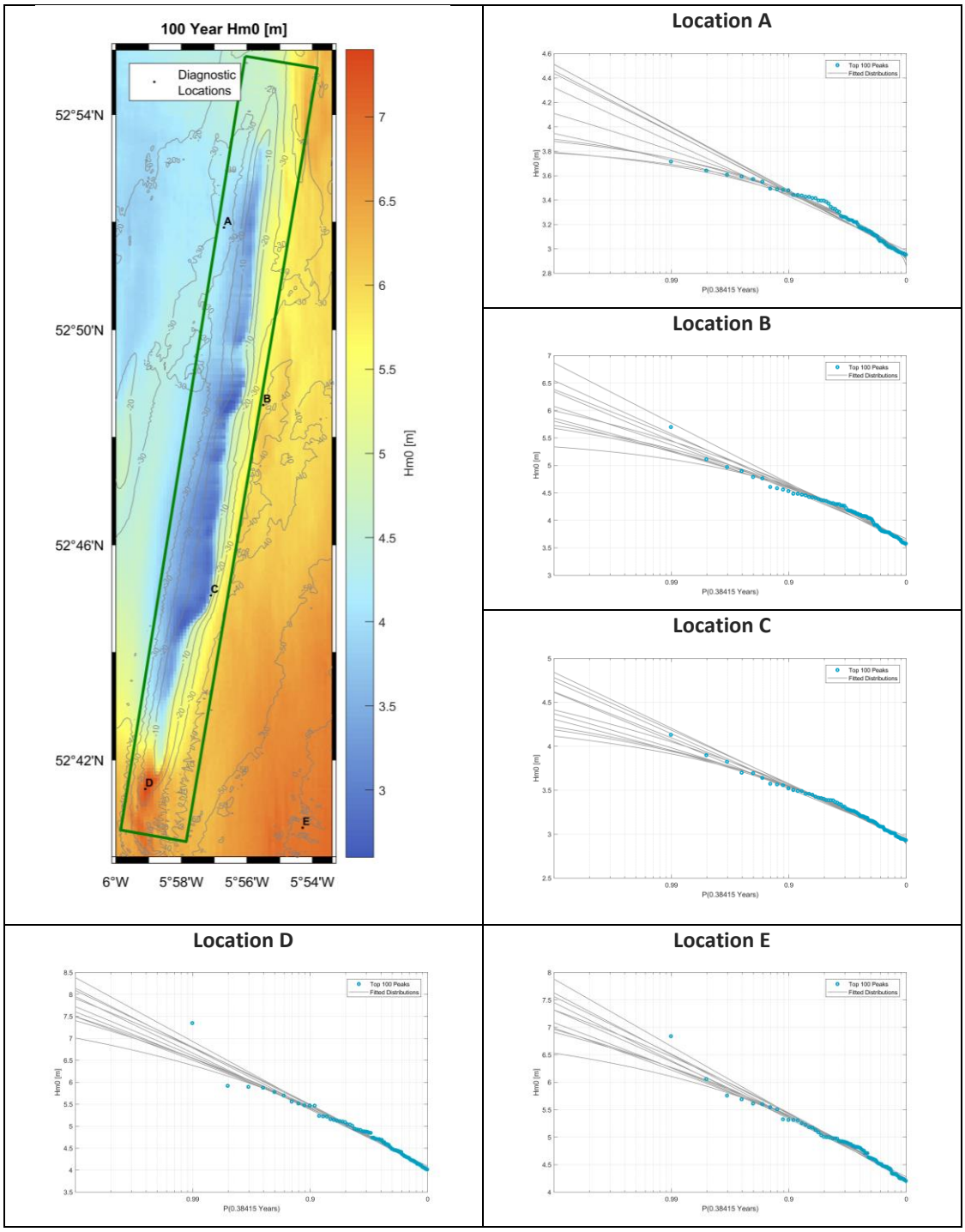



Figure G.7: Diagnostic locations, fits to highest 100 peaks.

For reference, a simple diagnostic for this type of variation – the difference between the highest and second highest Hm0 storm peaks – is shown in Figure G.8.

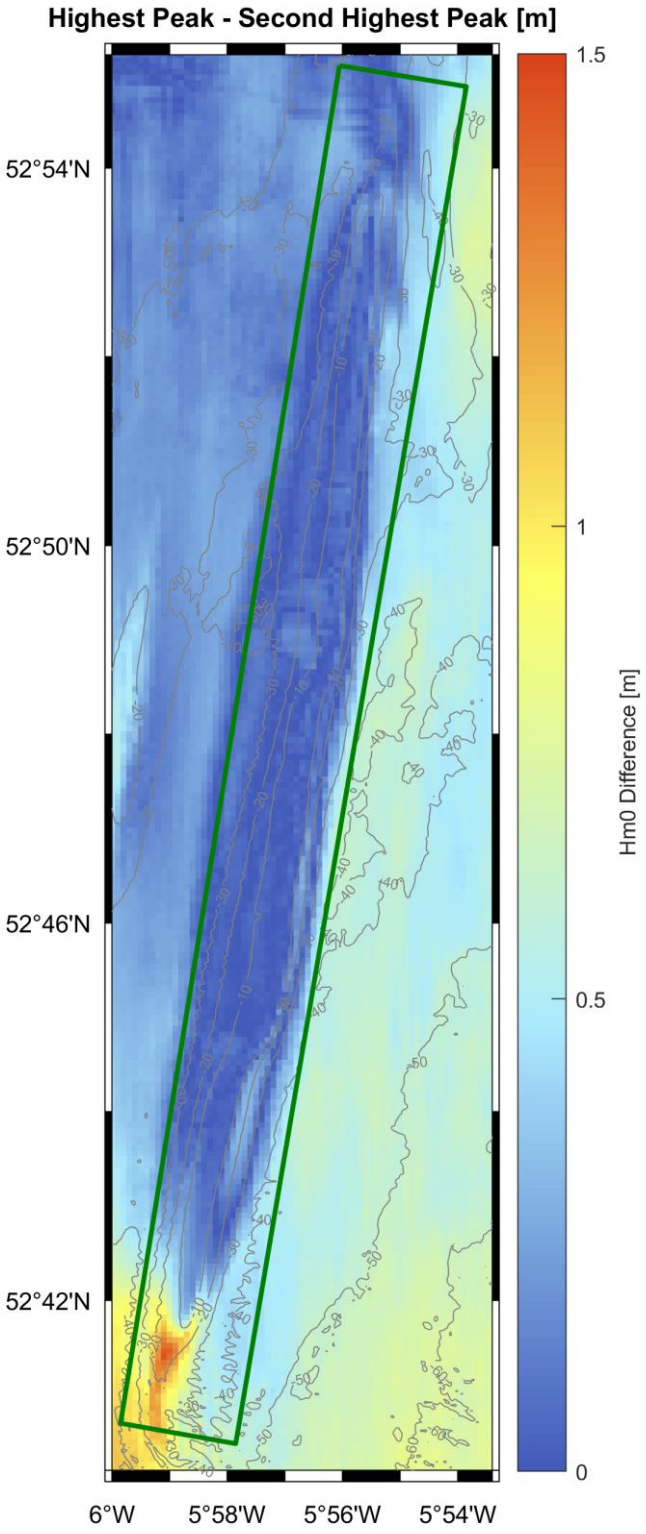



Figure G.8: Difference between highest and second highest Hm0 peaks.



## G.4 Hmax and Cmax

### G.4.1 Methodology, Single Location

In line with ISO guidelines, all maximum wave height (Hmax) and maximum crest height extreme values are calculated using the method of Tromans and Vanderschuren [30]. Again, we begin by considering those steps which we would take for determining design criteria for a *single* location, which proceed as follows:

**Step 1: Data Preparation and Review**

Carry out of a detailed review of the model data, including calibrations against measurements.

**Step 2: Method Selection**

Preference is to use the storm-based approach of Tromans and Vanderschuren (TVM). For shorter datasets, all data (or higher sea-state) convolutions of Hm0 and short-term wave height/crest distributions are also considered.

Also, we need to select appropriate short-term wave height and crest height distributions. In deep water, we use Forristall deep water distribution for wave height and Forristall 3D distribution for crest height [31]. In shallow water, a number of alternatives are considered.

***Note:*** *For this study a TVM approach is used throughout, thus only relevant steps are included hereafter.*

**Step 3: Identify Storms**

Split data into storms above a specified threshold. Merge storms that are temporally within a configurable reset duration.

Review time series of original data and storms. In particular, review larger storm peaks which may or may not have been merged into the same storm. Adjust parameters as necessary, and if highly subjective decisions affect merging of high peaks, continue separate analysis on each option to review implications.

**Step 4: Calculate Hmp and Cmp for each storm**

For each storm combine Hm0 with Tm01 or Tm02 values with the short-term distribution selected to determine the most probable extreme wave height (Hmp) or crest (Cmp) for the storm.

**Step 5: Fit Distributions to Hmp/Cmp**

Carry out independent fits to highest 50, 60, 70, …, 190, 200 Hmp/Cmp values. For each, include the following fits:

- 3-Parameter Weibull (Maximum Likelihood (MLM), Method of Moments (MoM), Maximum Product of Spacings (MPS), L-Moments (Lmom)).
- Generalized Pareto (MLM, MoM, MPS, Lmom)
- Exponential (MLM, MoM, Lmom)

**Step 6: Convolution**

For each fitted distribution, carry out a final convolution between the fitted distribution and that of individual heights/crests in a single storm given Hmp/Cmp. The individual heights/crests in a storm are those given by Tromans and Vanderschuren, with N taken to be the mean number of waves per storm.



**Step 7: Review Fits**

Review each fit, including the following:

- If the fitted distribution is a bad fit to the data, discard.
- If the extreme values are not stable to changes in the number of peaks, discard (e.g. if results for a 60-peak fit are considerably different to for a 50- and 70-point fit).
- Consider if physical implications of extreme behaviour are realistic, e.g. unbounded fits in shallow water, fits that rapidly reach an upper bound (i.e. similar 100- and 10,000-year extremes) in deep water with long fetch. If not, discard.

**Step 8: Determine Extreme Values**

The previous step normally gives a large selection of options. If all cover a similar range of extreme values, then choose a representative fit, generally slightly conservative in the 50$^{th}$ – 70$^{th}$ percentile of estimates. If they do not (e.g. the three different distributions may suggest three different ranges) decision can be far more subjective, often needing more investigation, discussion with client, precedence in the region, etc. before a final decision.

### G.4.2 Automated Fitting

Though more complex than the steps used for Hm0 outlined previously, very similar adjustments are needed to again automate the process when fitting at all locations across the model domain. In particular:

- In STEP 3, as was the case with derivations of Hm0, a value of 0.45 times the maximum Hmp value is used as a storm threshold.
- In STEP 7 all fits are assessed using the same steps described in Section G.3.2.
- In STEP 8 extreme values are again taken as the 70$^{th}$ percentile of all predictions considered appropriate.

Unfortunately, though not restrictive for a single dataset, the computational time for the convolution of STEP 6 becomes somewhat time-consuming when applied to upwards of 50 applicable fits at each of the 18,176 data points. As such, the decision of STEP 8 is actually taken earlier – a single distribution is selected after STEP 5 whose 50- and 100- year extreme values are closest to the 70$^{th}$ percentile of all selected distributions. The convolution is then carried out only once per location, rather than on all selected fits. This reduces run-time from a number of days per map to a few hours. We do not expect a significant impact, except perhaps at the 1-year level, where more variation may be seen.

### G.4.3 Short term wave height distributions

The Forristall wave height distribution is used to provide the short-term distribution of wave heights conditional on sea state parameters. This has a Cumulative Distribution Function (CDF) given by:

$$F_H(x) = 1 - \exp\left(-\left(\frac{x}{\alpha_H H_{m_0}}\right)^{\beta_H}\right)$$

Where with $\alpha_H = 0.681$ and $\beta_H = 2.126$. Other options are also included across guidelines, which by way of summary:



- **IEC61400-3-1:** Rayleigh distribution for deep water. Goda model, Battjes and Groenendijk (under certain conditions) and Forristall distributions for shallow waters, with references also given for shallow water distributions by Naess and Glukhovskiy[15].
- **DNVGL-RP-C205:** Rayleigh distribution (with spectral bandwidth dependence) or Forristall distribution. No distinction is made for water depth.
- **DNVGL-ST-0437:** Rayleigh distribution (with spectral bandwidth dependence) for deep water. Battjes and Groenendijk (under certain conditions), with references also given for shallow water distributions by Glukowski, Bitner and Naess (all caveated with *"may be used […] as long as they provide an adequate representation of the true distribution of the wave heights"*).
- **ISO 19901-1:** Forristall distribution. No distinction is made by water depth.

A little more detail on a number of these distributions is included below for reference:

**Forristall Distribution**

The Forristall wave height distribution described above is included in the recommendations of DNVGL-RP-C205, IEC61400-3-1 and ISO19901-1. Although the distribution was originally fitted to storms in the Gulf of Mexico, all three of these guidelines note that it has been shown to be applicable elsewhere. For example, ISO19901-1 states that *"though the above coefficients were developed using hurricane data, Krogstad's distribution based on North Sea storms is virtually the same".* There is no dependence on water depth in the distribution, aside from any arising in Hm0 itself, though IEC61400-3-1 does begin its description by stating that the *"Forristall distributions for wave heights and crest heights have been often used even for shallow waters"*.

**Rayleigh Distribution**

A Rayleigh distribution is also mentioned across various guidelines, not least being part of the derivation of the oft-used rule of thumb that Hmax = 1.86 Hm0. ISO19901-1 states that it is the *"classical description of the distribution of crest to trough heights in narrow-banded seas"* but that *"in practice, most seas are not narrow-banded and using the Rayleigh distribution would tend to over-predict the height of waves*". DNVGL sources (e.g., DNVGL-RP-C205 or DNVGL-ST-0437) address this by introducing a dependence on spectral bandwidth. However, DNVGL-ST-0437 also states that *"In shallow waters, the wave heights will be limited by the water depth. Unless data indicate otherwise, the maximum wave height may be taken as 78% of the water depth. The Rayleigh distributions of the wave heights become distorted in the upper tail to approach this limit asymptotically. The use of the unmodified Rayleigh distribution for representation of the distribution of wave heights in shallow waters may therefore be on the conservative side*". IEC61400-3-1 simply mentions that "*in shallow waters the […] distribution of individual wave heights will deviate from a Rayleigh distribution*", before proceeding to a small number of examples where the Rayleigh distribution is generally, though not always, more conservative than other options.

**Battjes and Groenendijk Distribution**

This distribution is described in both DNVGL-ST-0437 and IEC61400-3-1, and takes into account both water depth *and* seabed slope. However, in both cases a number of conditions are placed on its usage. For example, in DNVGL-ST-0437:

[15] Note that anglicizations from the original Russian differ between references.



*The Battjes and Groenendijk distribution has the drawback that it has an unphysical "knee" at the transition height. Its upper-tail behaviour may also be of concern. The Battjes and Groenendijk distribution should therefore be used with caution and only when supported by data.*

Similarly, IEC61400-3-1:

*It is recommended that the following conditions are fulfilled if the Battjes and Groenendijk model is to be used:*

*a) the direction of wave propagation is within 30° of the direction of steepest seabed slope,*

*b) considering values of seabed slope averaged over distances of 1 and 3 deepwater wavelengths in the upwave direction from the turbine position, the greater of the two values should be positive and not greater than 0,05 rad,*

*c) considering the seabed slope over a distance of 10 deepwater wavelengths in the upwave direction from the turbine position and the average seabed slope within each one-wavelength segment, each of the ten values of seabed slope should not differ by more than 0,02 rad from the slope calculated in b) and no value of slope should differ by more than 0,005 rad from the slopes of adjacent segments,*

*d) the current velocity should be less than 1.5 m/s.*

**Other Distributions**

- The Goda model, one of the three options described in detail in IEC61400-3-1 (alongside Forristall and Battjes and Groenendijk distributions), includes dependencies on water depth and sea-floor angle with respect to direction of wave propagation into its calculations. It is certainly the most detailed of those described in IEC61400-3-1, but although it originates from a 1975 paper, we have not seen it used elsewhere. That said, it is a relatively recent addition to this IEC document: the 2009 version of IEC61400-3 only describes the Battjes and Groenendijk distribution and neither the Goda nor Forristall distributions are included. As such, it is clear that a more recent study has been used to determine its inclusion.
- The Glukowski/Glukhovskiy/Gluhovski distribution is mentioned in both IEC61400-3-1 and DNVGL-ST-0437, though with the former citing a paper in Russian from 1966, and the latter making no citation. Fortunately, alternate sources, e.g. Wu et al. [32], include sufficient detail for implementation, though since the formulism is dependent on a mean wave height rather than significant wave height, alternate sources do differ in some of the details.
- A review of a number of the above distributions (though not that by Goda) can be found in Wu et al. [32]. Also included therein are some of the results of the Limits on Waves in Shallow Water (LoWiSh) Joint Industry Project, and in particular a "Forristall Shallow Water" distribution, which was developed and reported as part of the aforementioned project, but remains unpublished. Both the original Forristall distribution and shallow water versions appear to perform well for the limited shallow water datasets included in the study.

The various descriptions above show that a variety of options are indeed available to specify the short-term distribution, and moreover, that the choice of the "best" is not clear without, for example, measured wave height information. For the present version of the maps, the Forristall distribution introduced at the start of this section – hereafter the Forristall *deep water* distribution to avoid ambiguity – is used.

By way of preliminary investigation into the impact of different distributions, it has been compared to use of both the Gluhovski and Forristall shallow water distributions, with maps for the 100-Year maximum wave height shown in Figure G.9 through Figure G.11 A few features are clearly noticeable:

- In comparing Forristall deep and shallow water distributions (Figure G.9), results are very similar outside of the 20m water depth contour. This is to be expected – as depth increases, the shallow water distribution becomes very similar to the deep-water distribution. Within the 20m depth contour, the deep-water distribution is more conservative, with increasing conservatism towards the shallowest waters.
- In comparing the Forristall deep water and Gluhovski distributions (Figure G.10), the former is more conservative in shallow waters, but less conservative in deeper waters. Again, this is largely to be expected: the Gluhovski distribution attempts to more closely capture shallow water effects. But in deeper waters, it approaches a *Rayleigh* distribution for narrow banded seas, with regard to which, as mentioned already above, ISO 19901-1 notes "*in practice, most seas are not narrow-banded and using the Rayleigh distribution would tend to over-predict the height of waves"*.
- In comparing the two shallow water distributions (Figure G.11), the Gluhovski distribution is most conservative throughout, though there is a reasonable match between perhaps the 10 and 30 metre depth contours.

Thus, these maps show that use of the Forristall deep water distribution is certainly a reasonable *start* point, although more detailed investigation may be useful to reduce some of the conservatism it produces for water depths below 20m. Such an investigation must also be carried out in conjunction with similar analyses for wave crests to ensure that any reduction in wave *heights* as a result of a shallow water distribution remain consistent with *crest* heights.

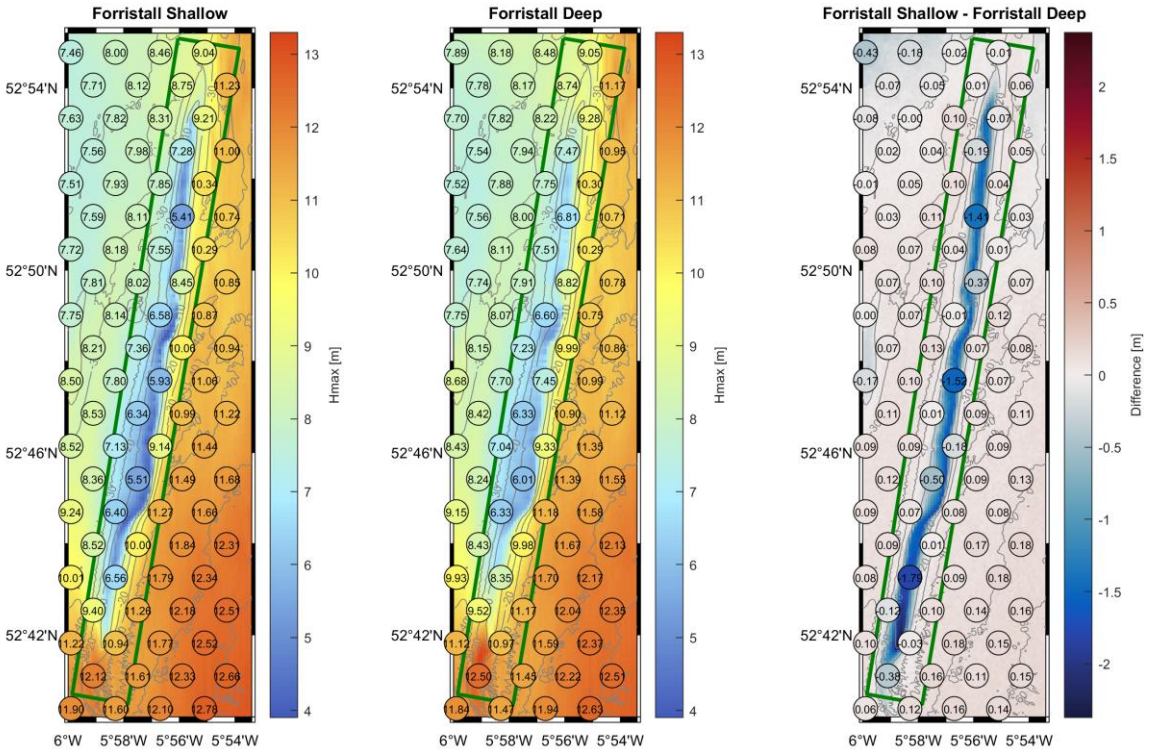



Figure G.9: 100-Year Hmax, using Forristall shallow- and deep-water distributions.

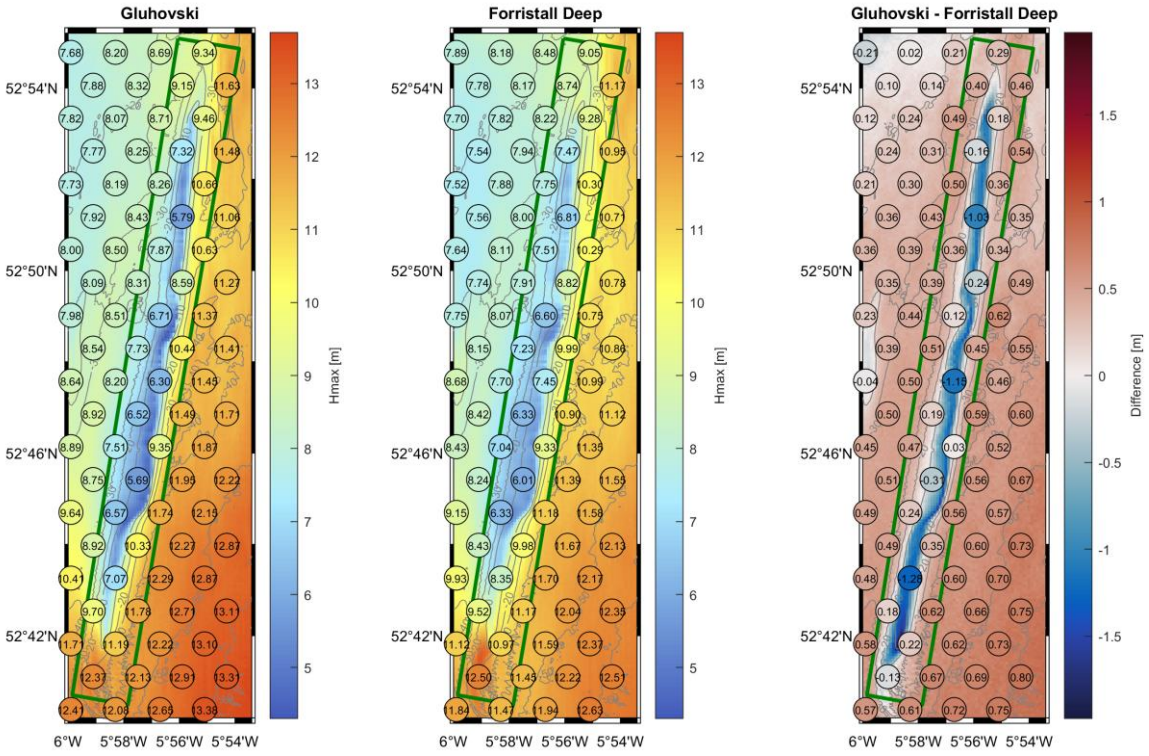



Figure G.10: 100-Year Hmax, using Gluhovski and Forristall deep-water distributions.

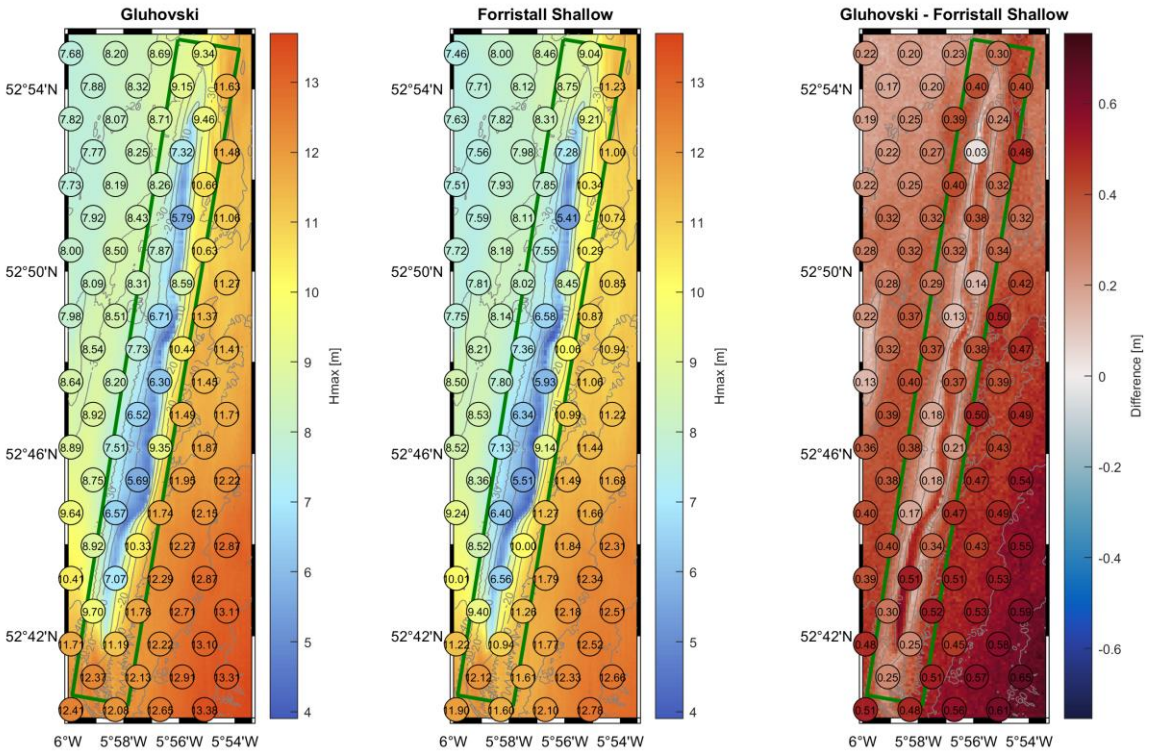



Figure G.11: 100-Year Hmax, using Gluhovski and Forristall shallow-water distributions.

### G.4.4 Short term crest height distribution

Similar considerations are needed for the short-term wave crest distribution, where two options – the Forristall 2D and 3D distributions – are commonly suggested. DNVGL-RP-C205 recommends the Forristall 2D distribution for long-crested seas, and the 3D distribution for short-crested seas. Both distributions are also given in IEC61400-3-1, though the only note to differentiate between the two is to state that they are based on 2D and 3D irregular wave train simulations respectively. No particular guidance is given with regard to their usage. ISO19901-1 only specifies the 3D equation and introduces it with:

*Recent research suggests that crest elevations for seas with typical directional spreading of wave energy are satisfactorily predicted by second order, random, directional wave theory.*

One further point is worth consideration: DNVGL-RP-C205 states that:

*It should be noted that the Forristall distribution is based on second order simulations. Higher order terms may result in slightly higher crest heights. Hence extremes predicted by this distribution are likely to be slightly on the low side. To account for higher order non-linearities, it is recommended to increase the maximum crest height with a factor of 1.05.*

The final sentence – specifically recommending a factor of 1.05 – is a new addition in the 2019 revision of this recommended practice and was not present in the 2017 edition.

In creating the present version of the extreme crest height maps, the Forristall 3D distribution has been used, and no increase, such as that noted above, has been applied. However, we are happy to investigate differences between these results and those provided by the 2D distribution, if required.

## G.5 Below MSL extreme values

As seen in Figure G.12, larger Hm0 values tend to correspond to water levels *above* MSL. As such the extreme behaviour of Hm0, Hmax and Cmax have also been evaluated for sea-states where water levels are *below* MSL, to determine how much lower these values may be.

### G.5.1 Hm0

In the case of Hm0, the methodology is straight forward: all sea-states with water-levels of 0mMSL and above are discounted, and the same peaks over threshold method and parameters are used to determine storm peak values. As shown in Figure G.12, for an example location to the south of the bank (Location D in Figure G.7), the values of such peaks are generally significantly lower than those taken from all the data.

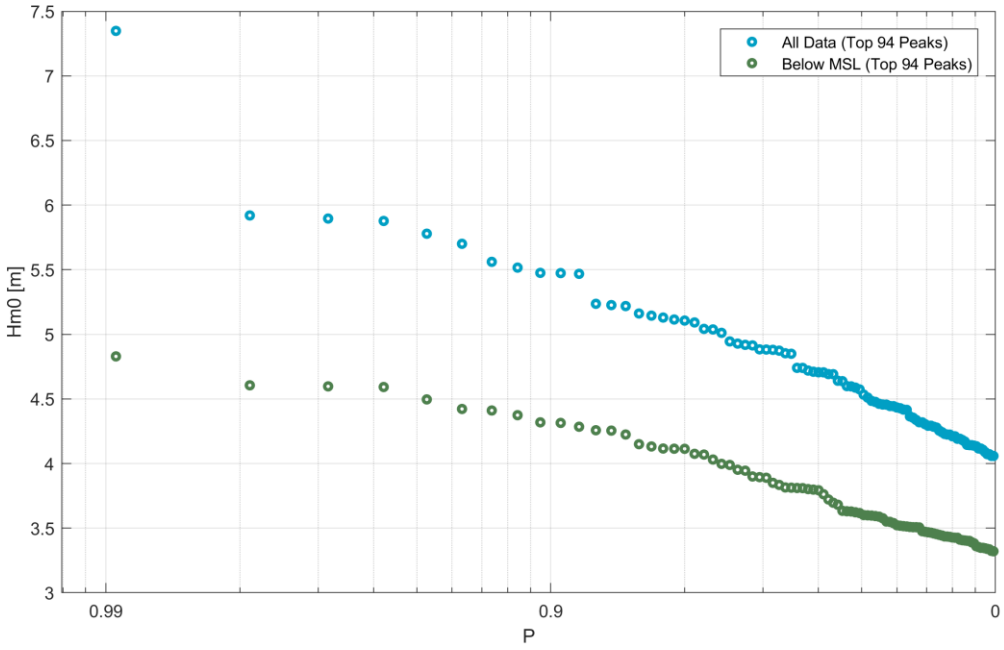



Figure G.12: Hm0, all sea-states, and those below MSL, example location.

After peaks have been found using this modified method, the analysis proceeds in an analogous manner to that using all water levels. However, one further minor change is necessary. Figure G.13 shows time periods around the four largest storms at the same location (note that for convenience, the background of each plot is coloured according to water level – red above MSL and green below MSL).

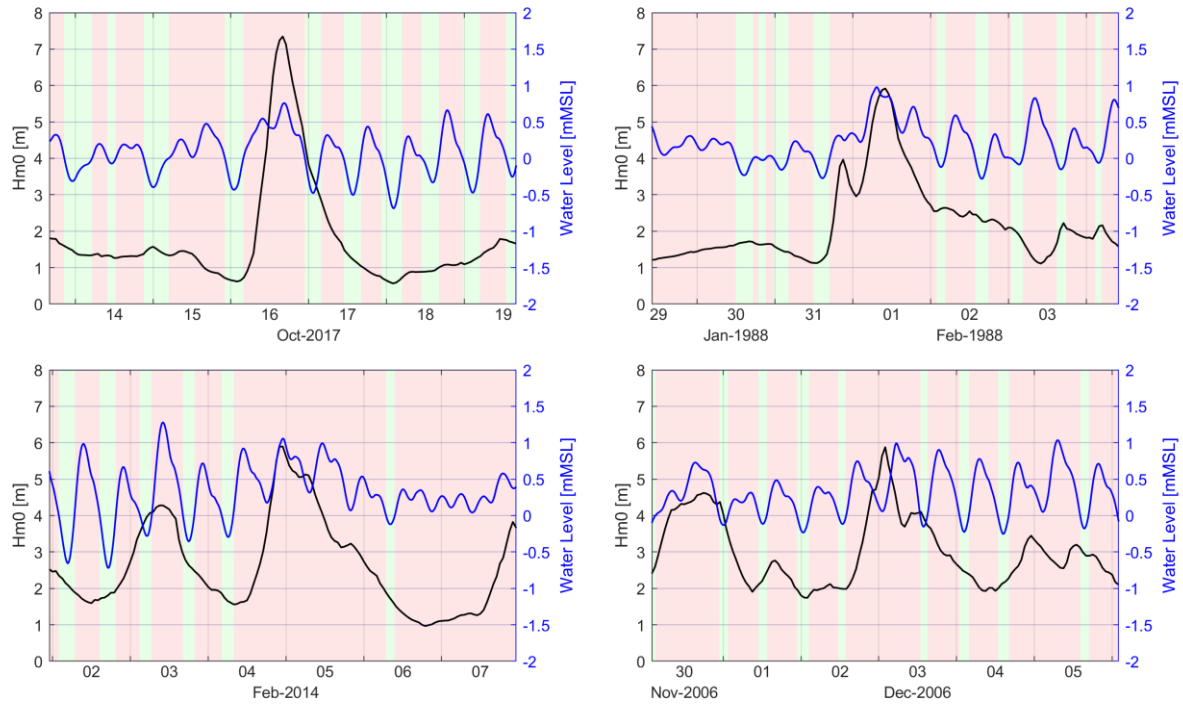



Figure G.13: Hm0 and water levels, four largest storms, example location.

At this location, for all four of these highest storms, water levels are above MSL for almost the entire central storm period. Whilst there are still high Hm0 values for water levels below MSL, it is of particular note that not all of the storms providing "extreme" values for all-data fits will provide values that might similarly be considered "extreme" for the below-MSL case. When taken as a whole over the entire model duration, this behaviour leads to a smaller collection of extreme peaks for water levels below MSL, and as a result, a slight modification in the automated process is included: whereas the all-data fits included collections up to 250 storm peaks, the below-MSL fits only use a maximum of 130 peaks.

### G.5.2 Hmax and Cmax

Recall (Section G.4) that as part of calculating Hmax and Cmax for *all* water levels we:

*b) For each storm, combine a short-term wave/crest height distribution with sea state parameters such as Hm0, Tm01 and Tm02 and water depth through the storm period to estimate the distribution of maximum wave/crest heights for the storm.*

In this case, the same step is carried out, *but ignoring sea-states where water level is* below MSL. Thereafter, the same process is repeated throughout.

# Appendix H. Measured Current Profiles

## H.1 Introduction

In this Appendix, the vertical profiles of measured currents are reviewed. The datasets used are those introduced in Section 5.1, and summarized in Table H.1 and Figure H.1 below.

Table H.1: Measured datasets used for review of current profiles.

| Dataset | Location | Time Period | Water Depth [mMSL] |
|---|---|---|---|
| **AWAC A** | 52.9096 °N, 5.9157 °W | 6-Nov-2019 to 18-May-2020 | 29.0 |
| **AWAC C** | 52.8218 °N, 6.0206 °W | 24-Nov-2019 to 19-May-2020 | 26.5 |
| **AWAC E** | 52.6910 °N, 5.9930 °W | 24-Nov-2019 to 19-May-2020 | 39.0 |

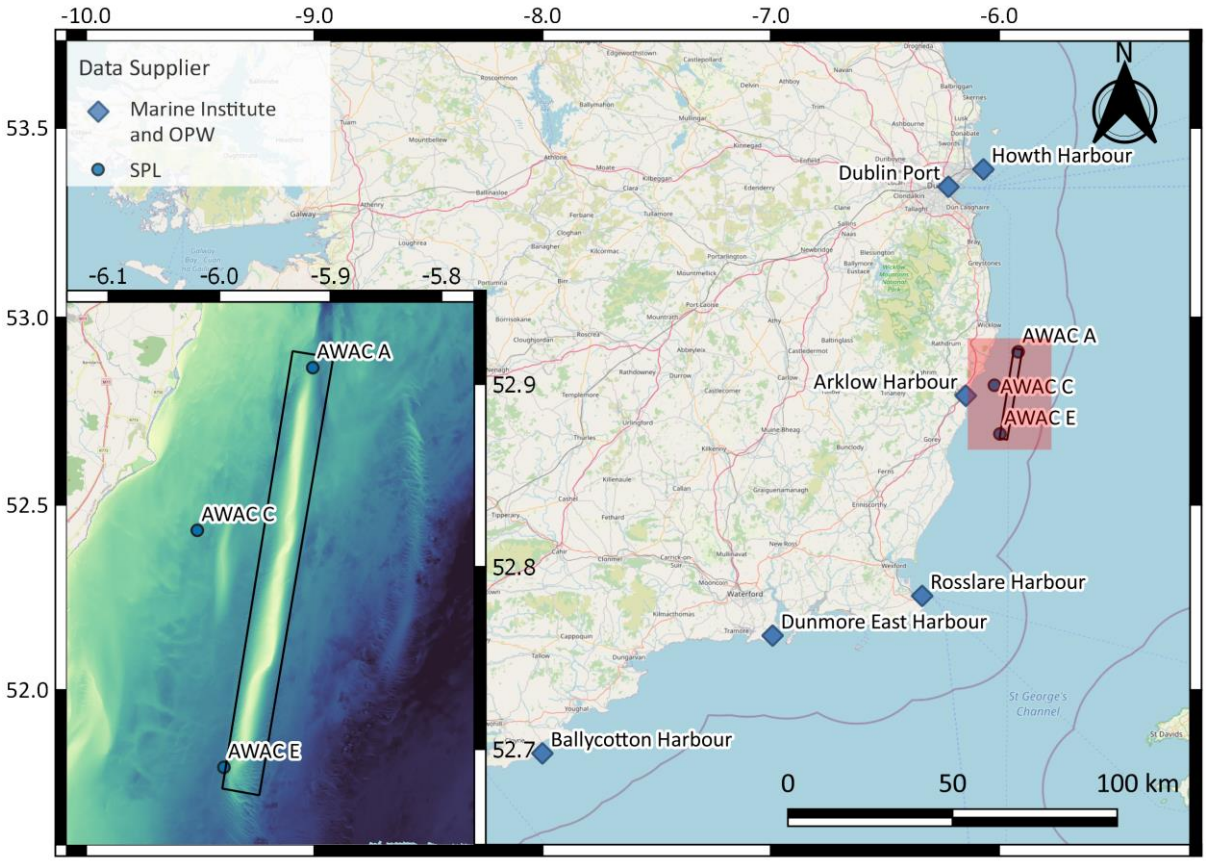



Figure H.1: Measured datasets used for review of current profiles.

## H.2 Data Overview

Current speed and directions for various heights above bed are shown for the three AWACs in Figure H.2 through to Figure H.4. Note that the highest bin shown in each figure is close to the mean water depth, and thus may be out of the water (or very close to the surface) for large parts of the flow.

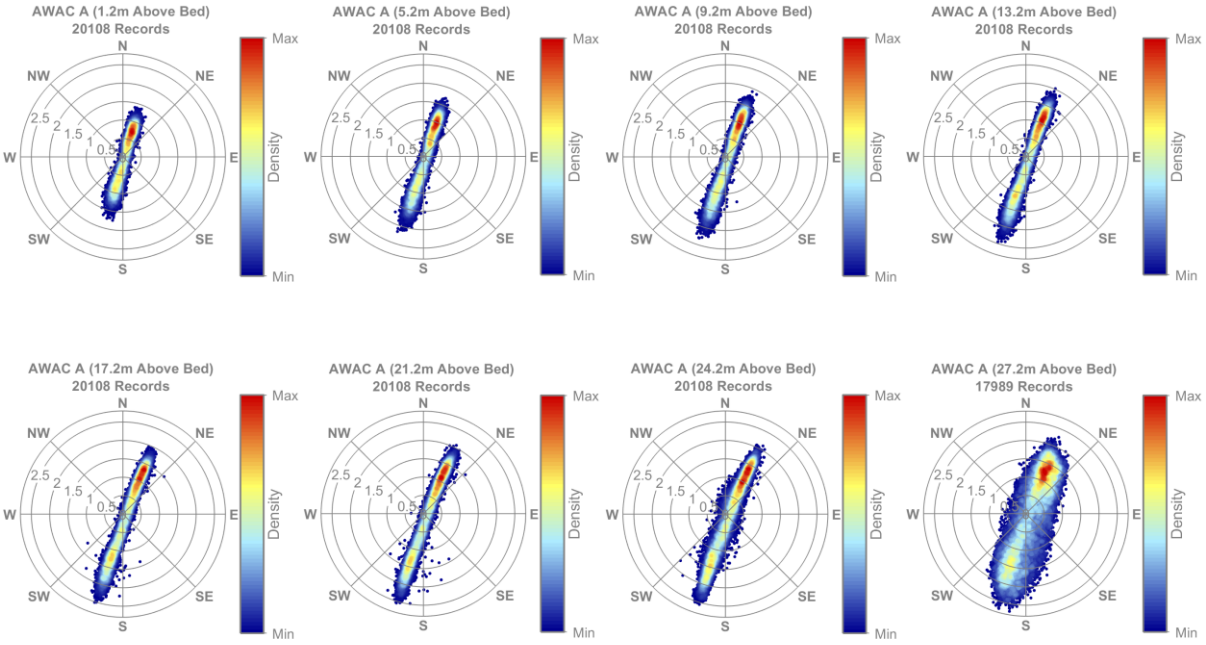



Figure H.2. Current speed and direction, AWAC A.

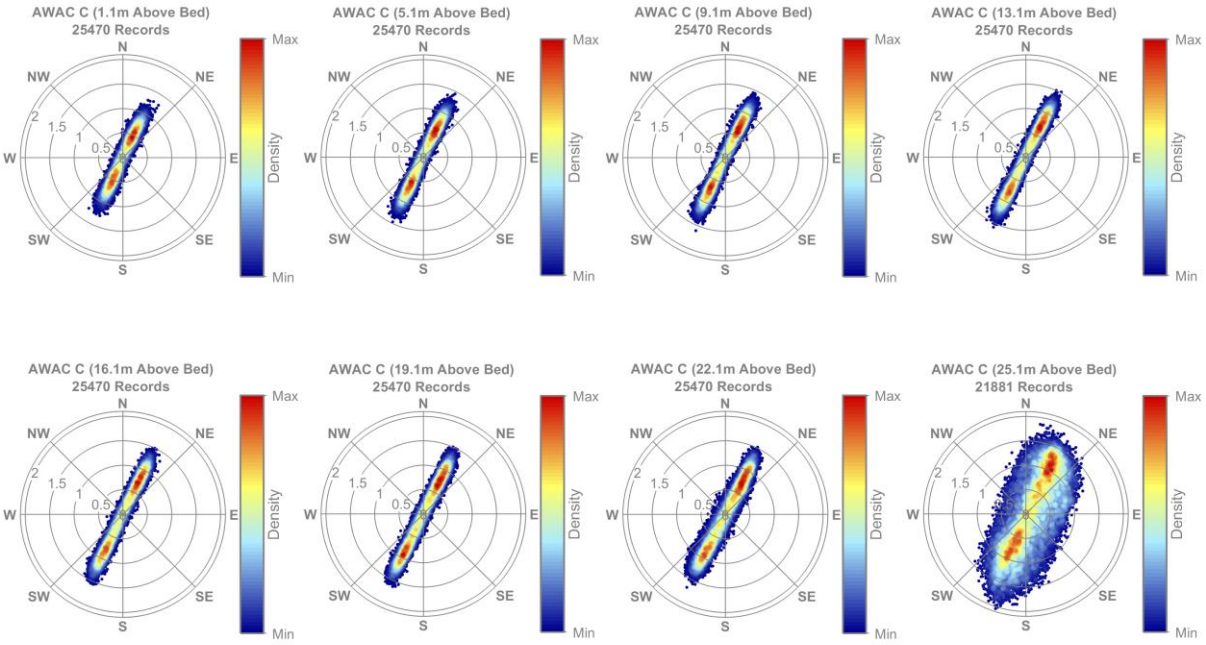



Figure H.3. Current speed and direction, AWAC C.

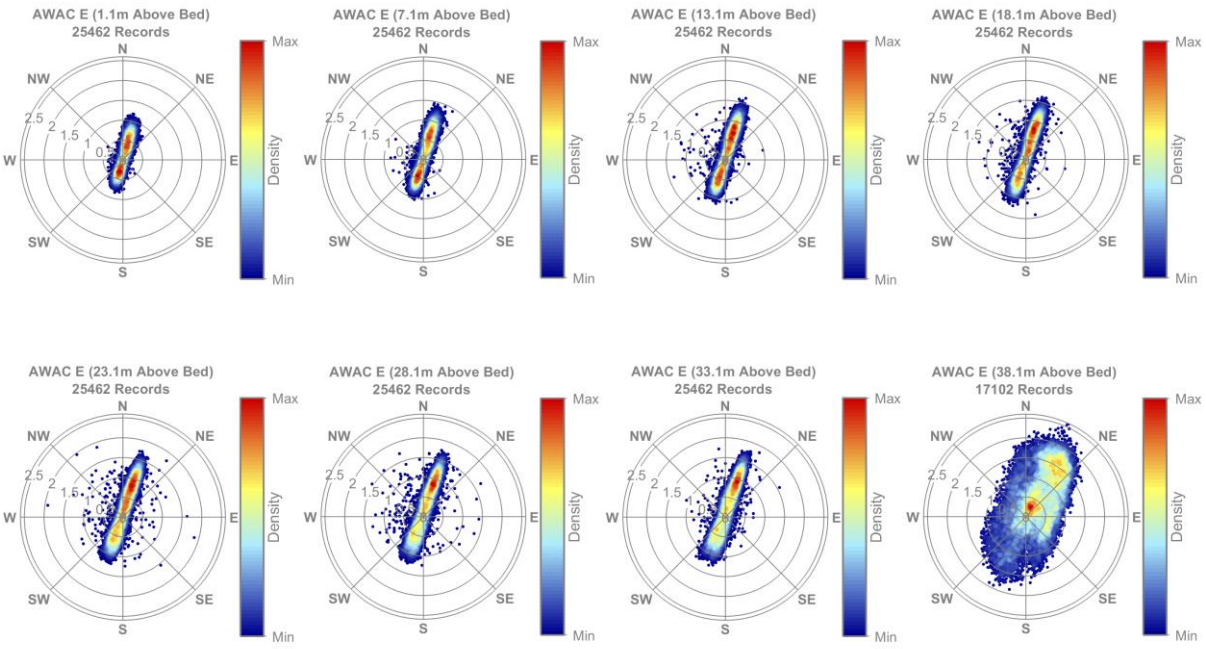



Figure H.4. Current speed and direction, AWAC E.

Current speed peaks for the same levels at each location are shown in Figure H.5 through Figure H.7. Overlaid in each case are the boundaries used to divide between ebb and flood flows throughout this Appendix, being:

- AWAC A: 109°/289°
- AWAC C: 116°/296°
- AWAC E: 108°/288°

These are determined by:

a) Finding the principal axis of flow at each level up to 80% of the mean water depth.
b) Taking the mean of these directions.
c) Splitting along directions perpendicular to this mean principal direction.

It is worth noting that, as shown in Figure H.8, there is some variation in this direction of flow by depth, particularly at AWAC A. In addition, some of these Figures show a small directional offset between ebb and flood flows. It is not expected that these small deviations will impact the analyses which follow in this Appendix, where direction is only used to split data into ebb and flood profiles, however they are highlighted here should they be of interest elsewhere.

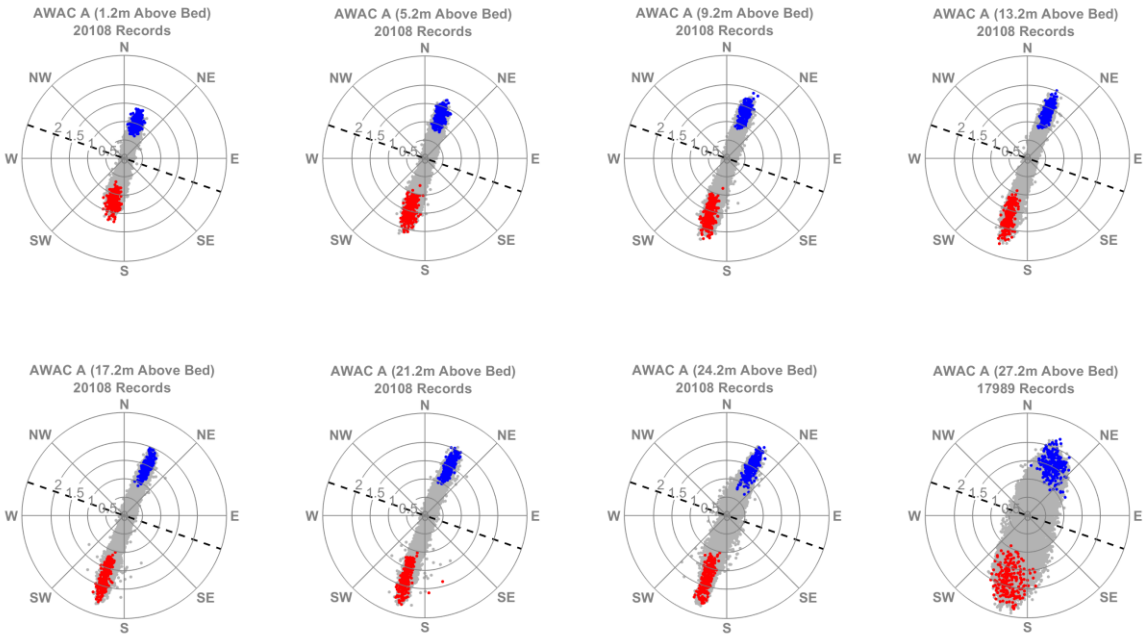



Figure H.5. Current speed and direction, AWAC A, current speed peaks highlighted (flood: blue; ebb: red).

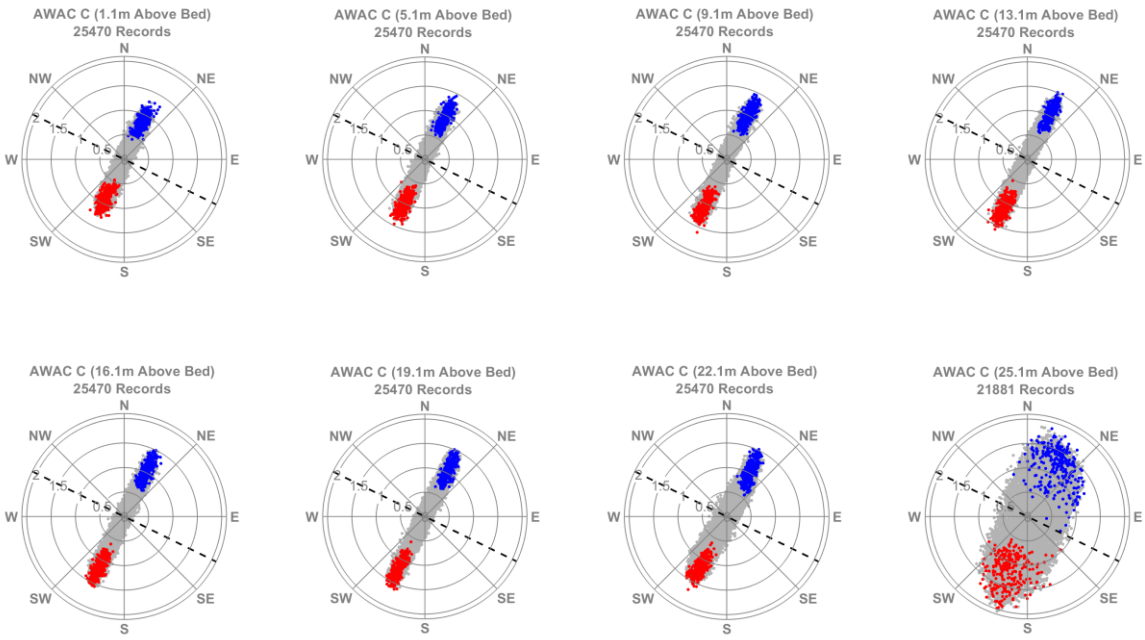



Figure H.6. Current speed and direction, AWAC C, current speed peaks highlighted (flood: blue; ebb: red).

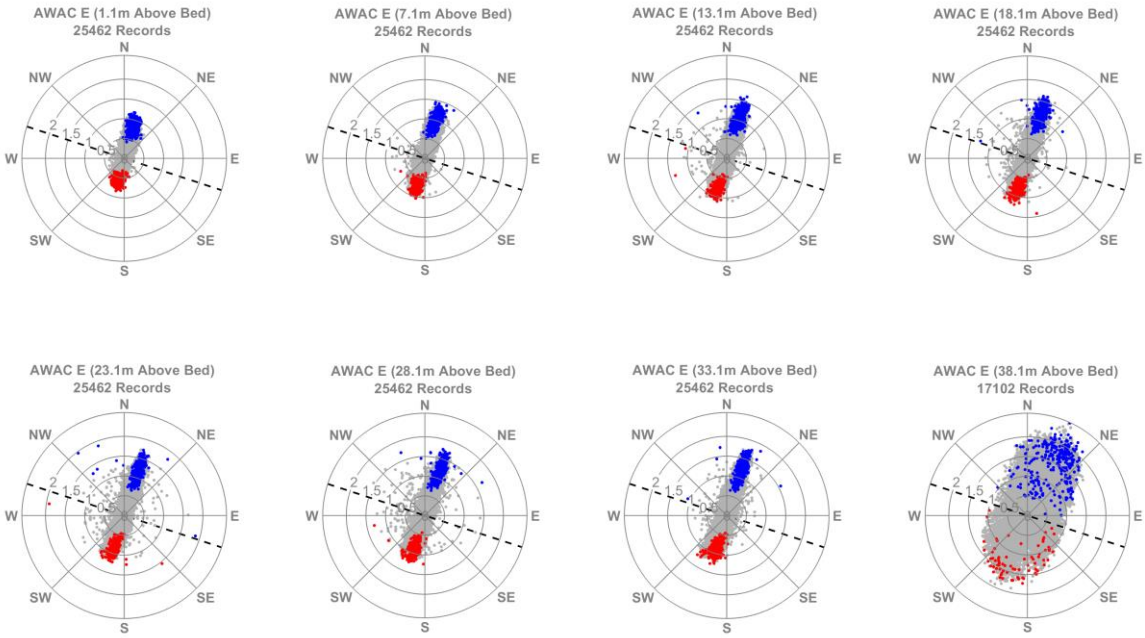



Figure H.7. Current speed and direction, AWAC E, current speed peaks highlighted (flood: blue; ebb: red).

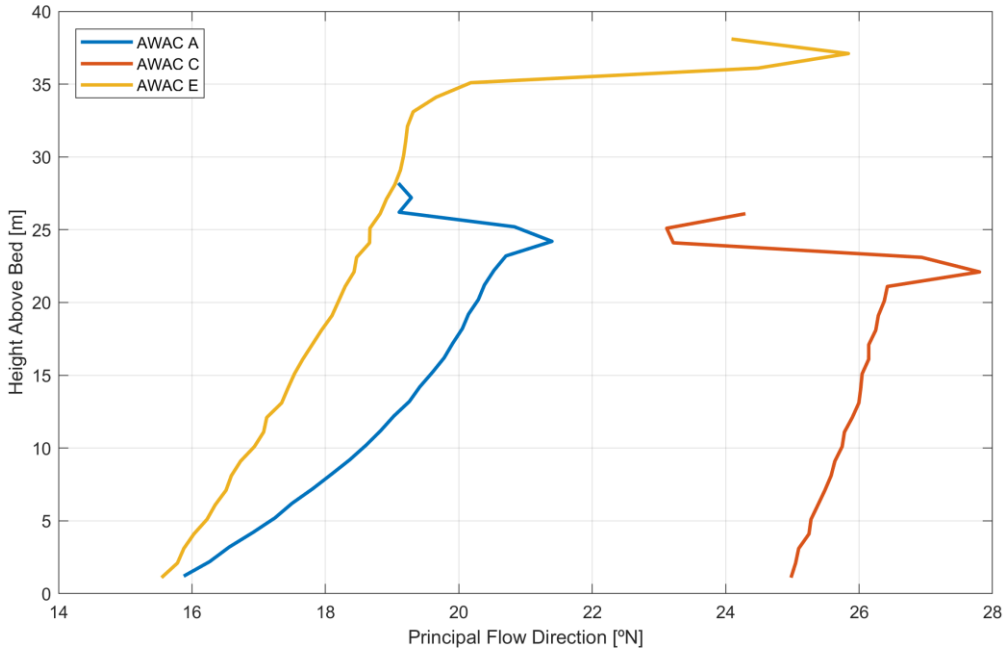



Figure H.8. Principal direction of flow by height above bed, AWACs A, C and E.

## H.3 Percentiles by Height Level

Percentiles of current speeds for both flood/northward and ebb/southward flow at each instrument height level, are shown in Figure H.9 through to Figure H.11. Note that throughout, the higher levels should be treated with some caution, being very close to the surface, or even out of the water much of the time. Profiles are split according to the following:

- If all current directions below 80% of the mean water depth are from the 180° sector allocated to flood, the profile as a whole is denoted “flood”.
- If all current directions below 80% of the mean water depth are from the 180° sector allocated to ebb, the profile as a whole is denoted “ebb”.
- If neither of the above are true, the profile is denoted “mixed”.

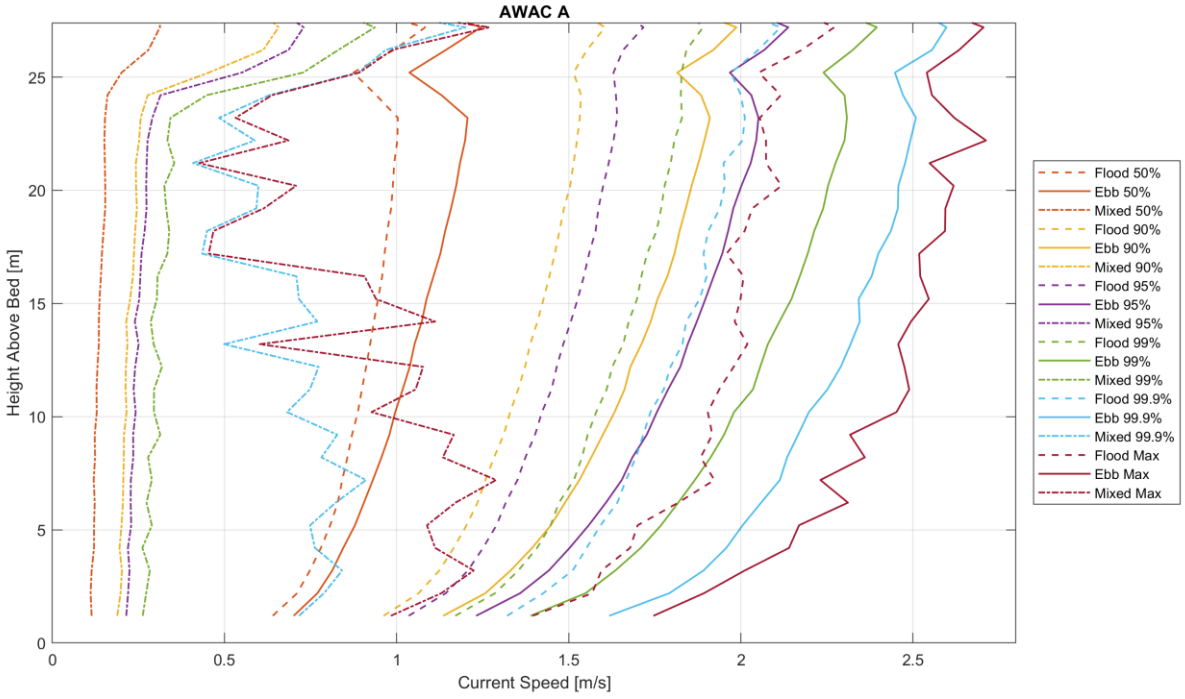



Figure H.9: Percentiles by height, AWAC A.

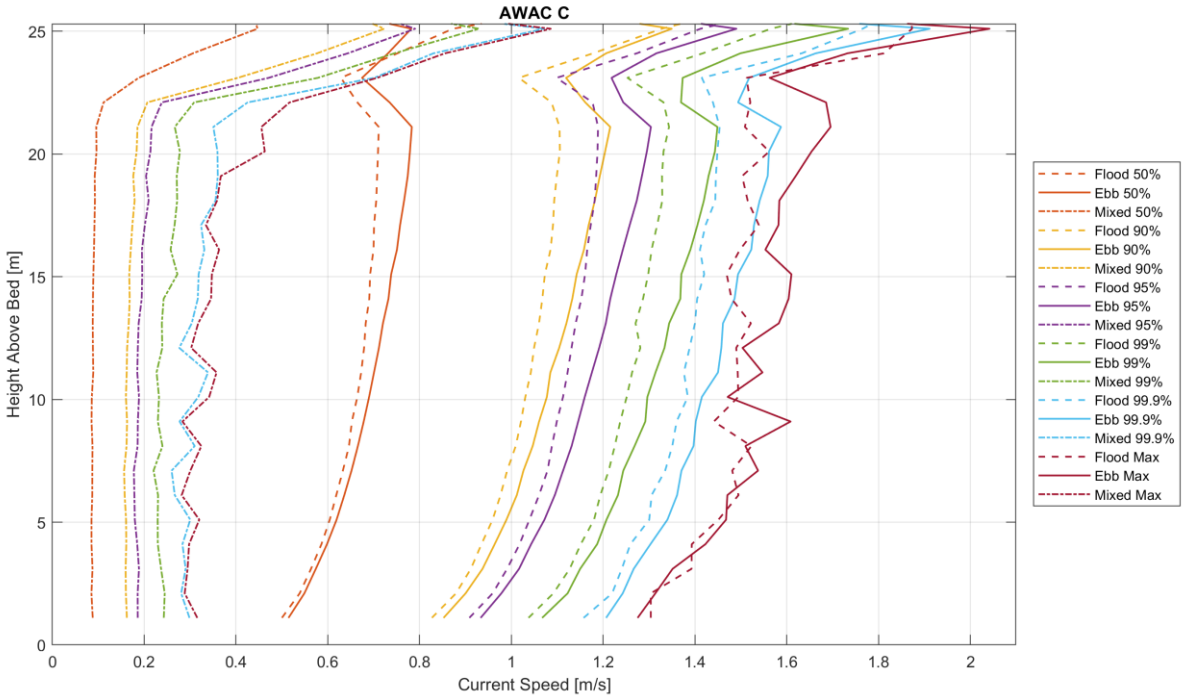



Figure H.10: Percentiles by height, AWAC C.

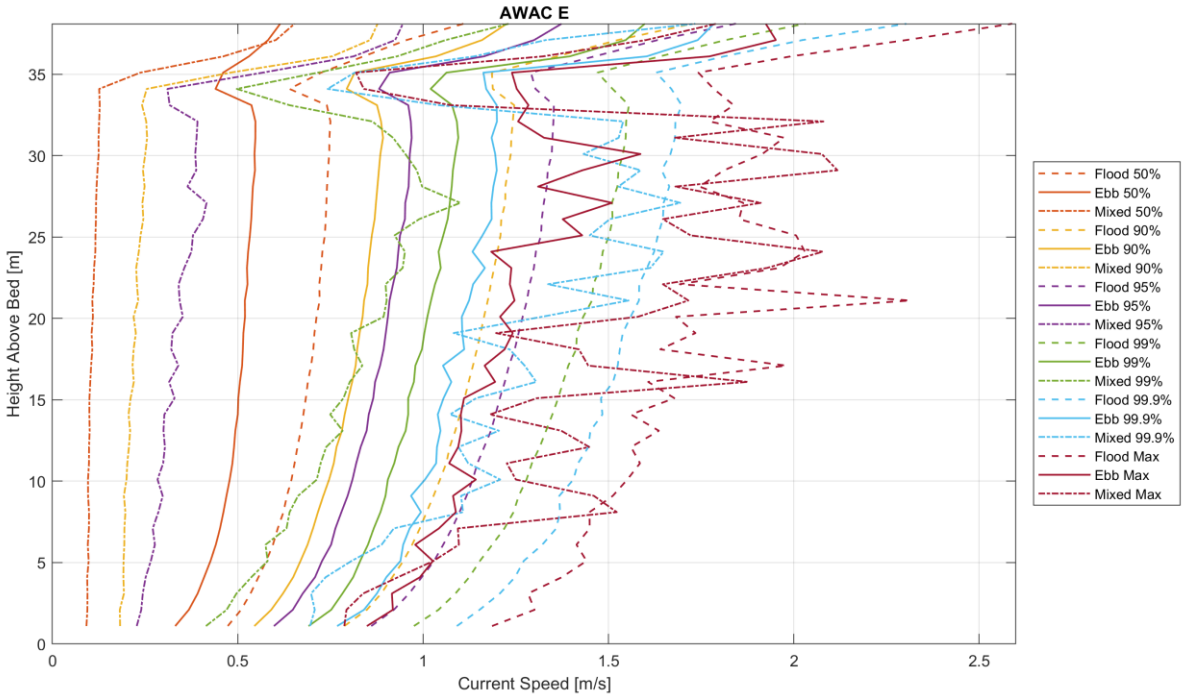



Figure H.11: Percentiles by height, AWAC E.

Differences between the strength of ebb and flood flows are clearly heavily dependent on location. Similarly, profile shapes – discussed in more detail in the next section - vary across the three AWACs.

Note that a little caution is necessary when interpreting some of the *mixed* current percentiles here. These would normally be expected to occur at lower current speeds when the tide is turning, although may in some cases reflect the presence of wind driven currents in the upper water column that are strong relative to tidal currents. However, at AWAC E in particular, significantly larger speeds are seen than might be expected.

An initial review of the measurements for some of these profiles suggests that they may reflect instrumentation errors, rather than real features. For example, Figure H.12 shows those mixed profiles with the highest current speeds at a selection of levels at AWAC E. Throughout, the level for which the profile reflects a maximum is highlighted in red. Each of these profiles shows significant variability in either speed or direction with depth, which may either lead to unexpectedly large current speeds in individual levels, or misclassification of entire profiles as mixed.

In all that follows in this Appendix, we concentrate solely on ebb and flood profiles. However, there may be some benefit in revisiting these measurements in a little more detail to determine whether these mixed profiles really do represent features of interest, or can safely be attributed to measurement errors.

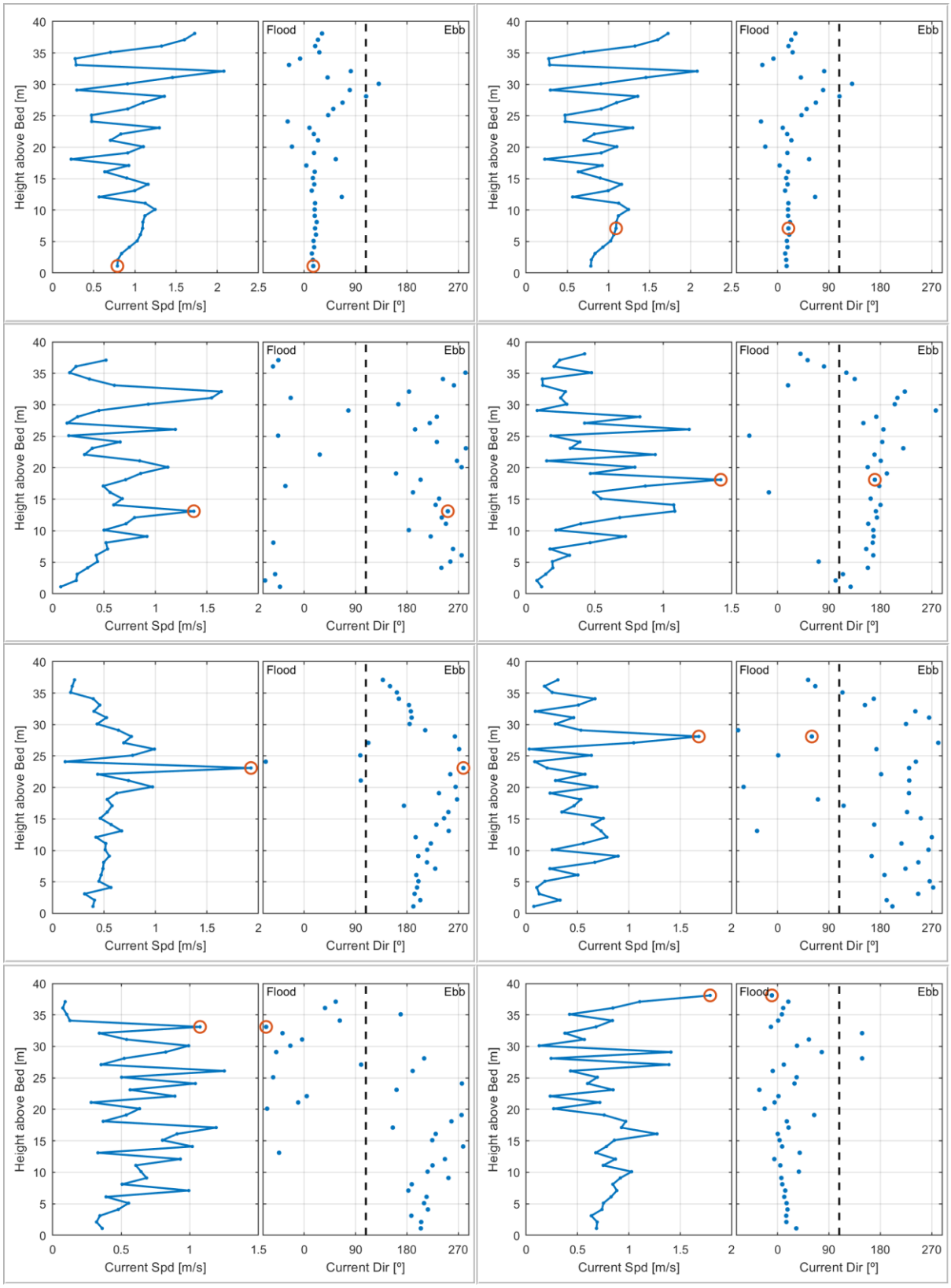



Figure H.12: Profiles contributing to maximum mixed profile current speeds.

## H.4 Individual Profile Shapes

We now move our attention to *individual* profiles (i.e. the profile at each recorded time step), and attempt to fit a power law to each in turn, that being:

$$v_c(z)=v_c(0)\left(\frac{d+z}{d}\right)^{\alpha}$$

Where:

$v_c(z)$ is the current speed at elevation z.

z is the distance from still water level, positive *upwards*. E.g.$v_c(0)$ is current speed at still water level.

d is the water depth to still water level (taken positive)

α is an exponent, typically taken as 1/7, but fitted at each time step below.

The resultant exponent values are shown in Figure H.13 to Figure H.15. Across all locations, larger variations in the exponent, α, are seen at lower current speeds which narrow as speeds increase. When considering locations individually:

- **AWAC A:** Mean and median current speeds transition from an α of approximately 1/8 at lower speeds to an α of 1/6 at higher speeds. For Ebb currents, this transition occurs between 0.5 and 0.9 m/s whilst for Flood it is between 1.0 and 1.4 m/s.
- **AWAC C:** Profiles exhibit less shear than at either AWAC A or AWAC E, particularly Flood currents. Mean and median α are generally below 1/8 throughout, and perhaps a value as low as 1/10 being more appropriate for the largest current speeds.
- **AWAC E:** Behaviour is not too dissimilar to that at AWAC A, with mean and median α again transitioning from 1/9 at lower current speeds to 1/6 at the highest speeds. However, this transition takes place over a larger range of speeds, with a value of close to 1/7 for much of the range. At lower current speeds, there are a significantly larger population of profiles with α values below 1/10 than was the case at AWAC A.

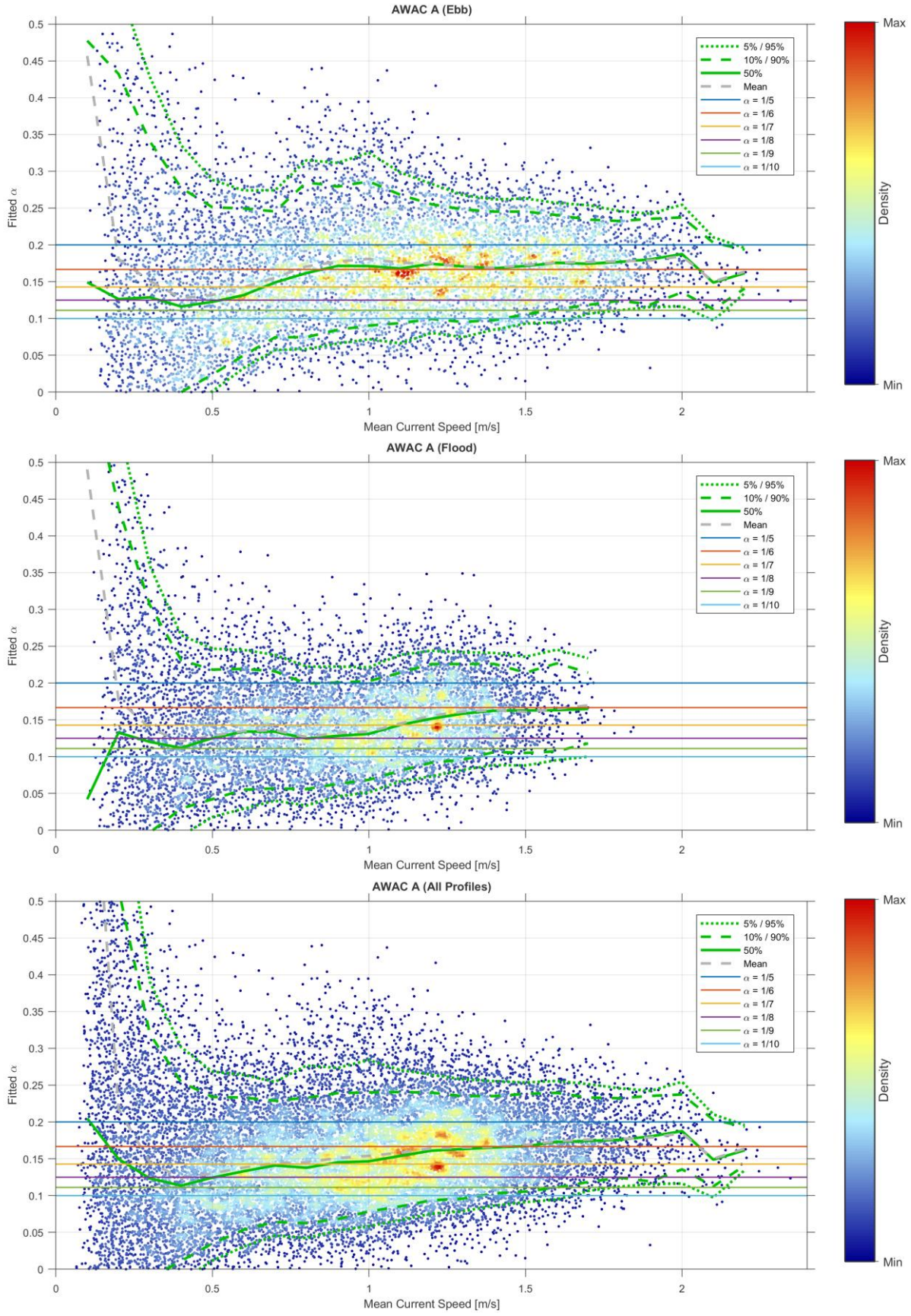



Figure H.13: Individual profile fits, AWAC A.

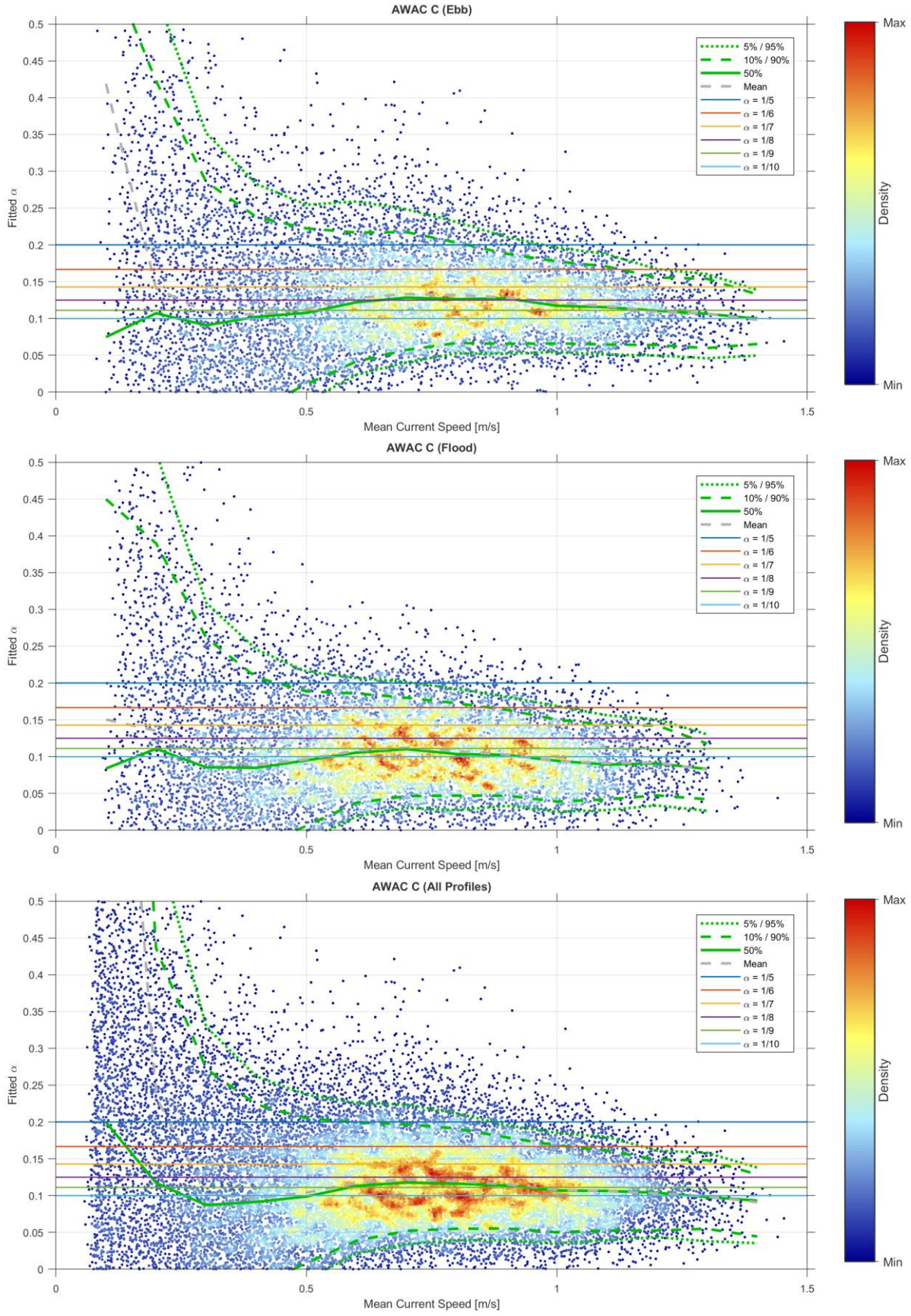



Figure H.14: Individual profile fits, AWAC C.

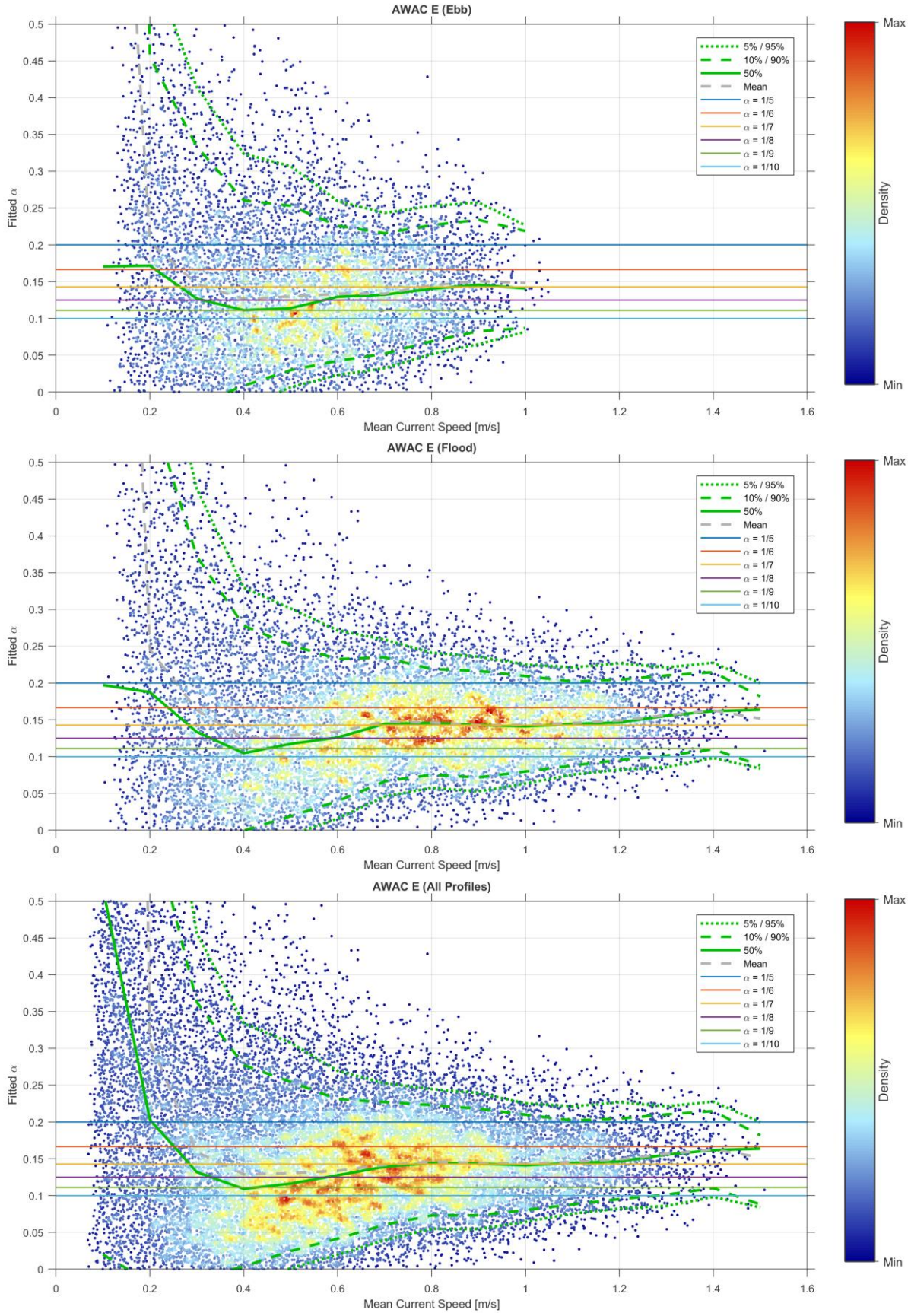



Figure H.15: Individual profile fits, AWAC E.

## H.5 Normalised Profiles

An alternate view of the profile shapes can be obtained by reviewing *all profiles* together, though with suitable normalization factors. To do so, we begin with all profiles, as shown for AWAC A in Figure H.16.

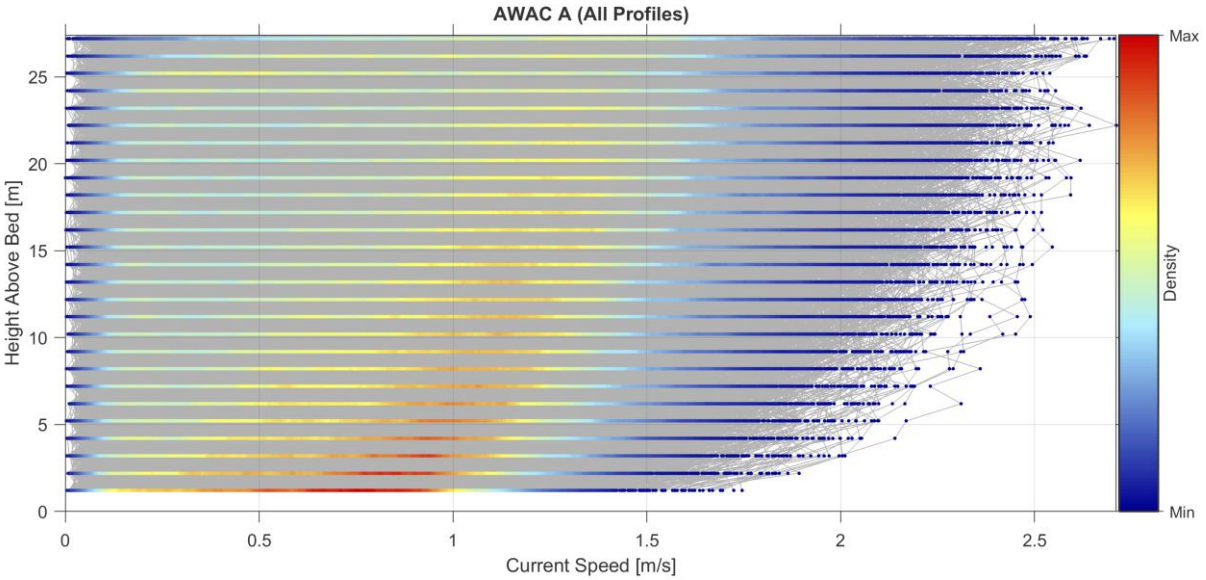



Figure H.16: All profiles, AWAC A.

The different magnitude of each profile makes it difficult to infer any information about profile shape here. But if we return to the equation we are fitting, i.e.

$$v_c(z)=v_c(0)\left(\frac{d+z}{d}\right)^{\alpha} \quad (1)$$

we see that the *shape* of the profile is determined by the term $\left(\frac{d+z}{d}\right)^{\alpha}$ whilst its *magnitude* is determined by the term $v_c(0)$. Thus, a suitable normalization might be do divide through by this magnitude factor and thus compare the two sides of the following:

$$\frac{v_c(z)}{v_c(0)}=\left(\frac{d+z}{d}\right)^{\alpha}$$

Unfortunately, the left-hand side here is heavily dependent on the single 'surface' value, $v_c(0)$, which we may not have, or might well consider the least reliable amongst our recorded values. Instead, we note that Equation (1) directly gives a *depth averaged* mean value of:

$$v_{c,mean}=v_c(0)\left(\frac{1}{\alpha+1}\right)$$

Thus, we can alternatively write our profile of interest as:

$$v_c(z)=v_{c,mean}(\alpha+1)\left(\frac{d+z}{d}\right)^{\alpha}$$

And instead review the relationship:

$$\frac{v_c(z)}{v_{c,mean}}=(\alpha+1)\left(\frac{d+z}{d}\right)^{\alpha}$$

If we subsequently plot the left-hand side – hereafter termed "Normalised Current Speed" – against height above bed, we get the far more meaningful plot of Figure H.17.

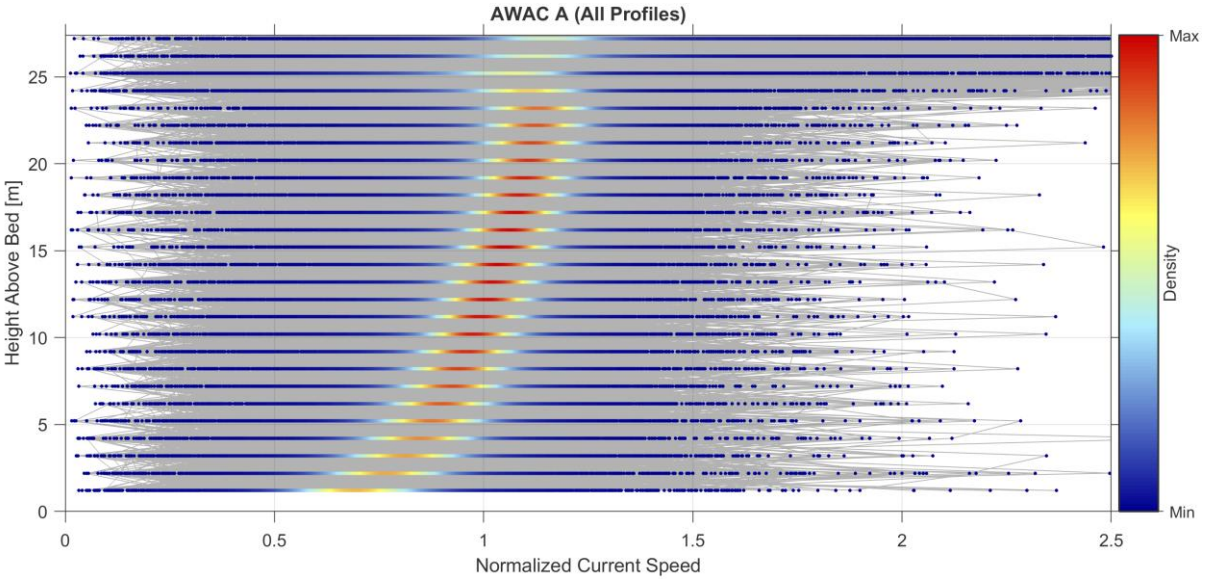



Figure H.17: All profiles, normalised current speeds, AWAC A.

One additional step is also useful. Given the varying water levels throughout the measurement period, if we also define a "Normalised Height Above Bed" as (d+z)/d then comparing our "Normalised Height Above Bed" and our "Normalised Current Speed" gives the results of Figure H.18. Note that at this stage, we have also removed the grey lines joining individual profiles as they add little of use to these Figures hereafter.

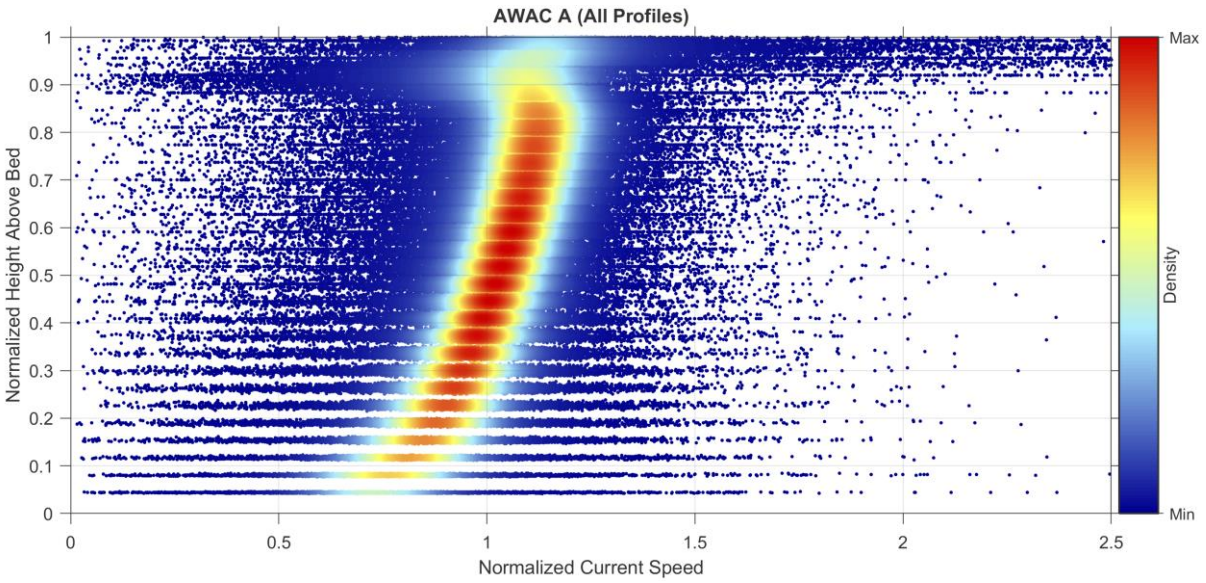



Figure H.18: All profiles, normalised current speeds and heights, AWAC A.

Finally, overlaying:

$$(\alpha+1)\left(\frac{d+z}{d}\right)^{\alpha}$$

for various values of α, for example as shown in Figure H.19, we can obtain some indication of how suitable such values are when compared to the data.

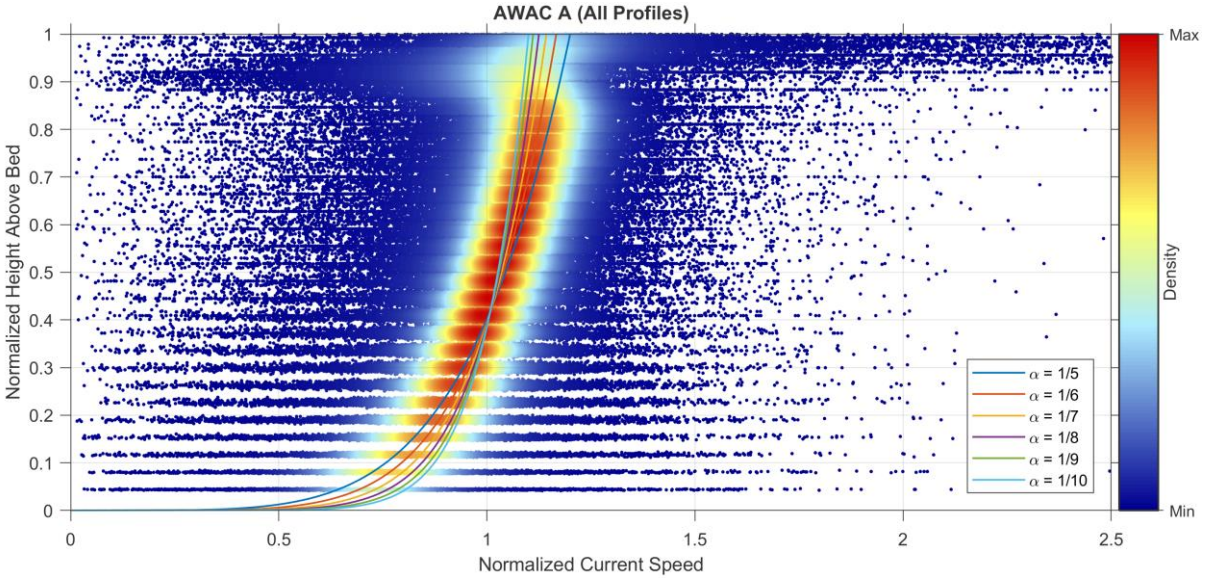



Figure H.19: All profiles, normalised current speeds and heights, overlaid α, AWAC A.

These comparisons are shown, for ebb, flood, and all profiles in Figure H.20 (AWAC A), Figure H.21 (AWAC C) and Figure H.22 (AWAC E). Thereafter, in Figure H.23 through Figure H.25, the same information is shown, but *only* for the 500 profiles in each category with the highest mean current speeds.

Any selections of the most appropriate α values made from these plots are largely in line with those seen in Section H.4, whereby:

- Values of between 1/6 and 1/8 appear most appropriate across AWAC A and AWAC E for both the "all data" Figures and those with the highest 500 mean current speeds. There are certainly variations in behaviour: between the two locations; between both flood and ebb currents; and between "all data" and "highest current speed" Figures. If selecting a single profile shape to use throughout, a value of α=1/7 strikes a reasonable balance between these differences.
- At AWAC C, a steeper profile is necessary, with a value of α=1/9 being more appropriate.
- It is again noticeable that at AWAC E, more variation is seen in the profile shapes when taken as a whole, compared to AWAC A, in particular with regard to the Ebb currents.

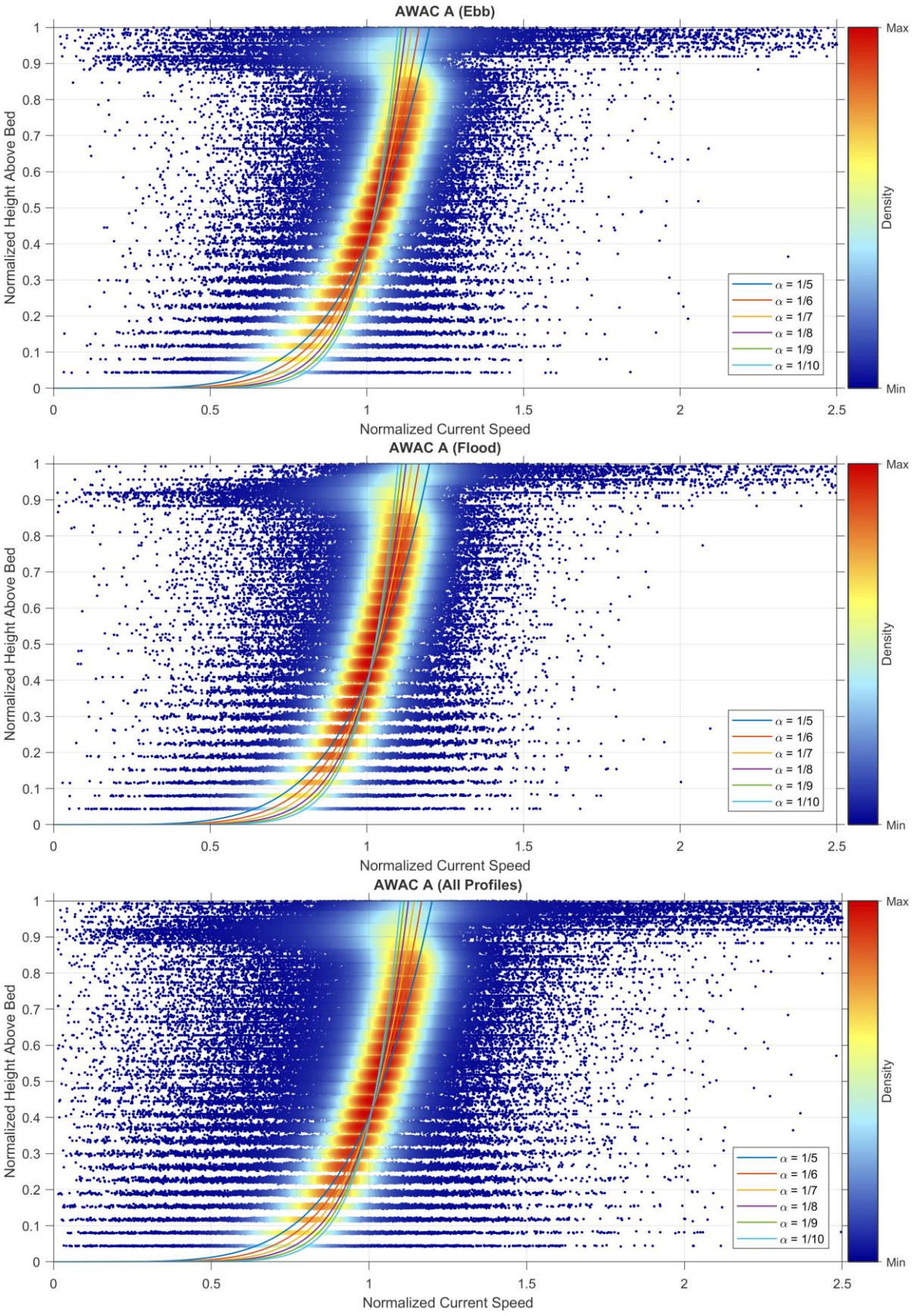



Figure H.20: Normalised profiles, AWAC A.

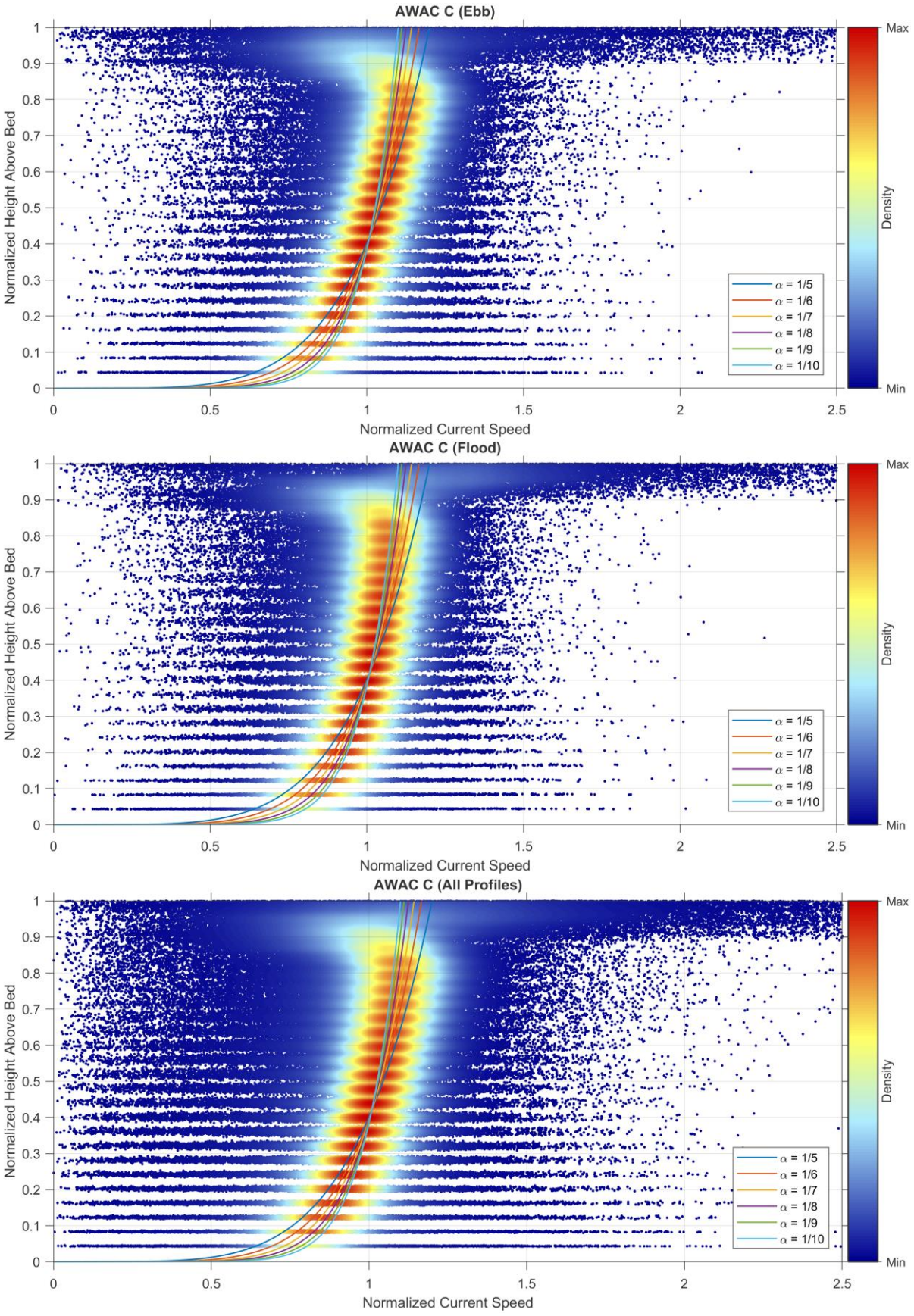



Figure H.21: Normalised profiles, AWAC C.

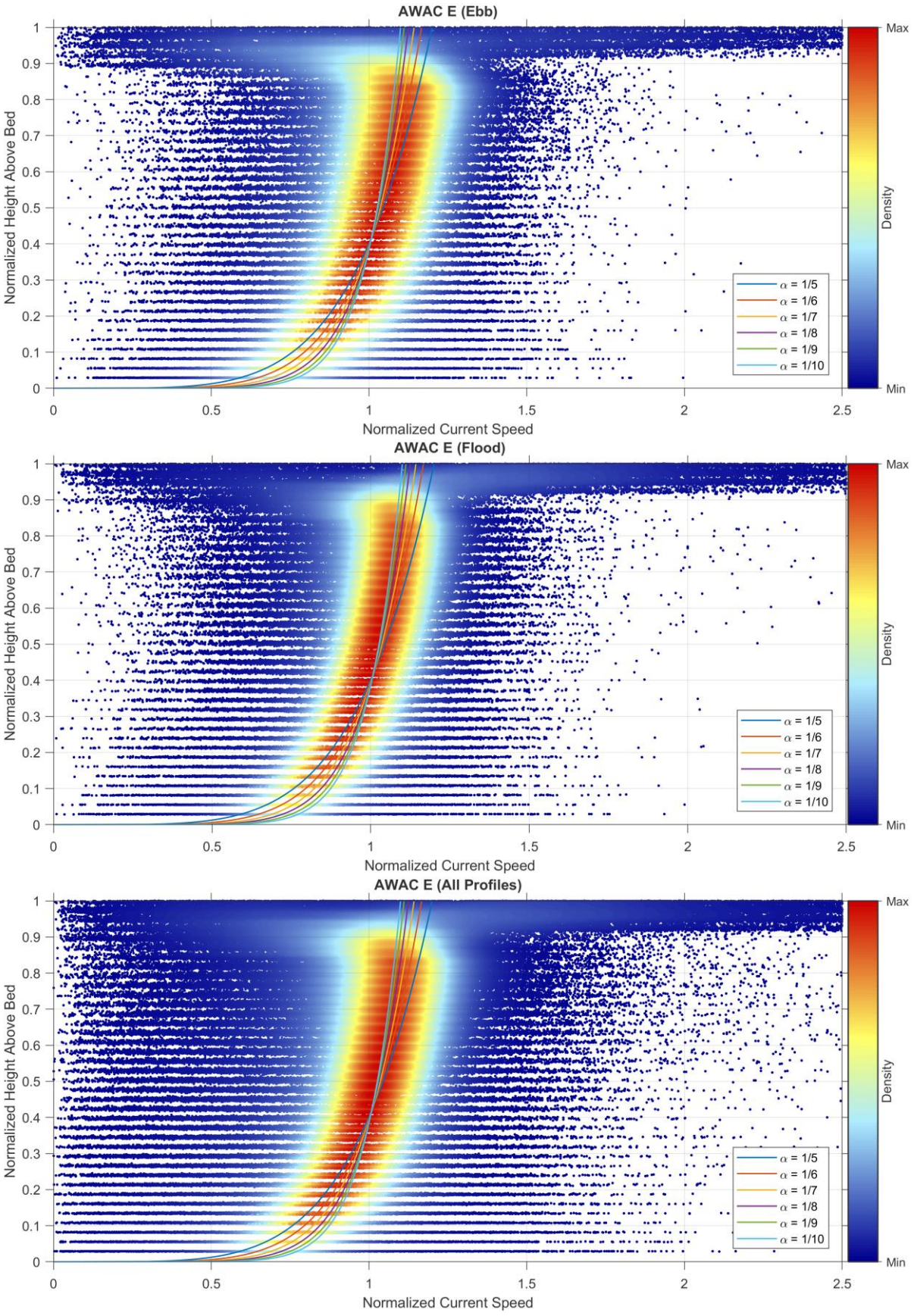



Figure H.22: Normalised profiles, AWAC E.

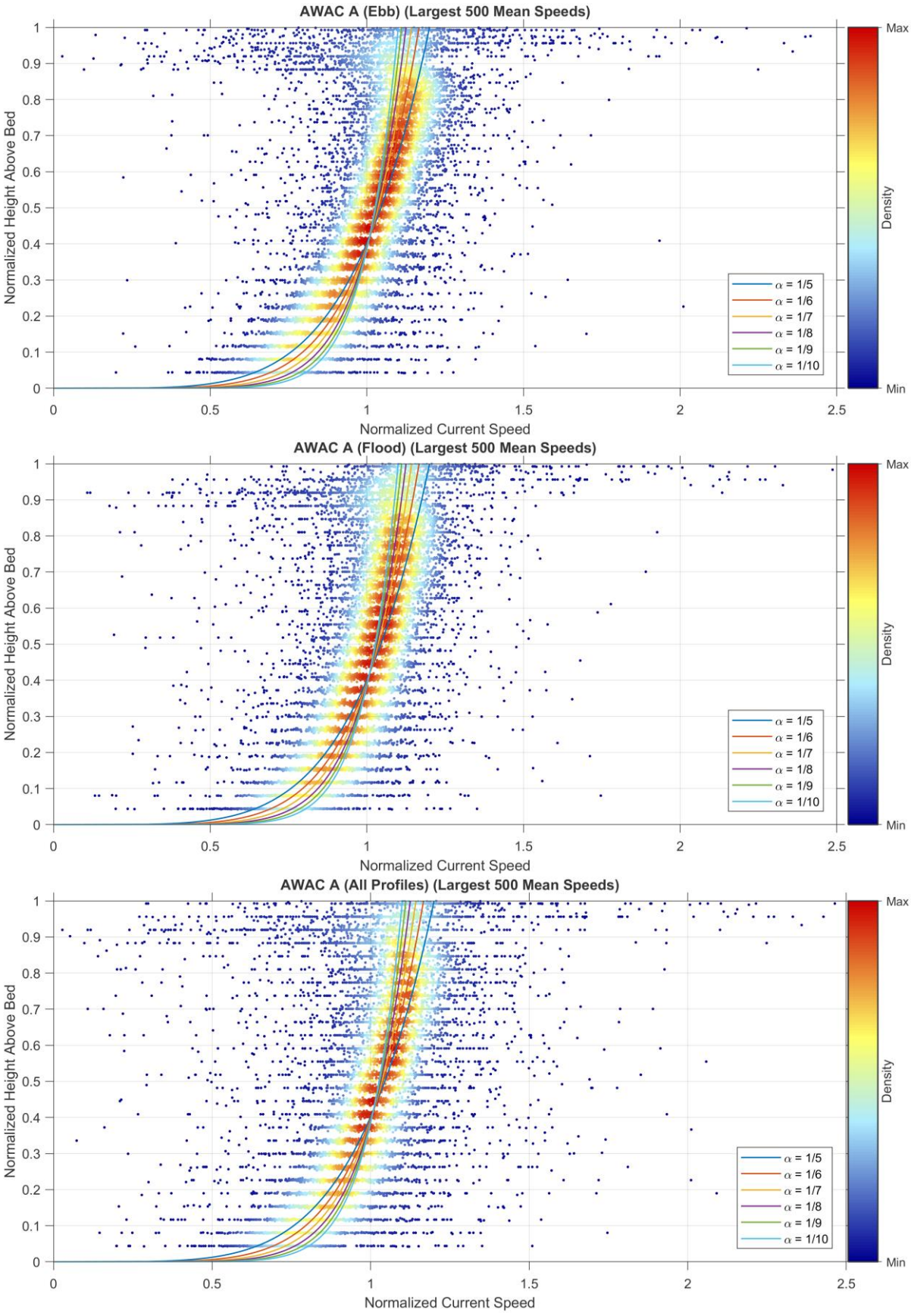



Figure H.23: Normalised profiles, highest 500 mean speeds, AWAC A.

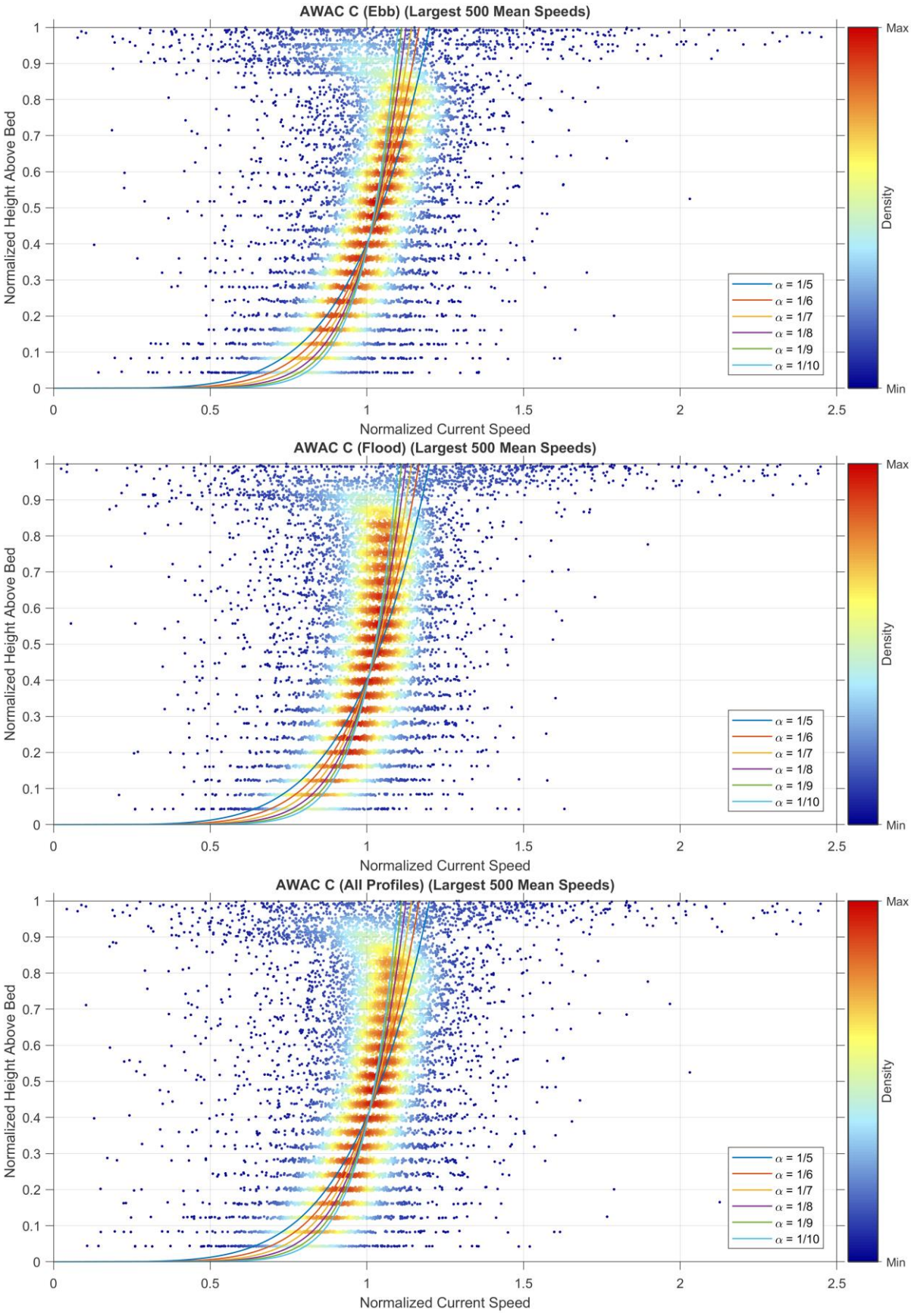



Figure H.24: Normalised profiles, highest 500 mean speeds, AWAC C.

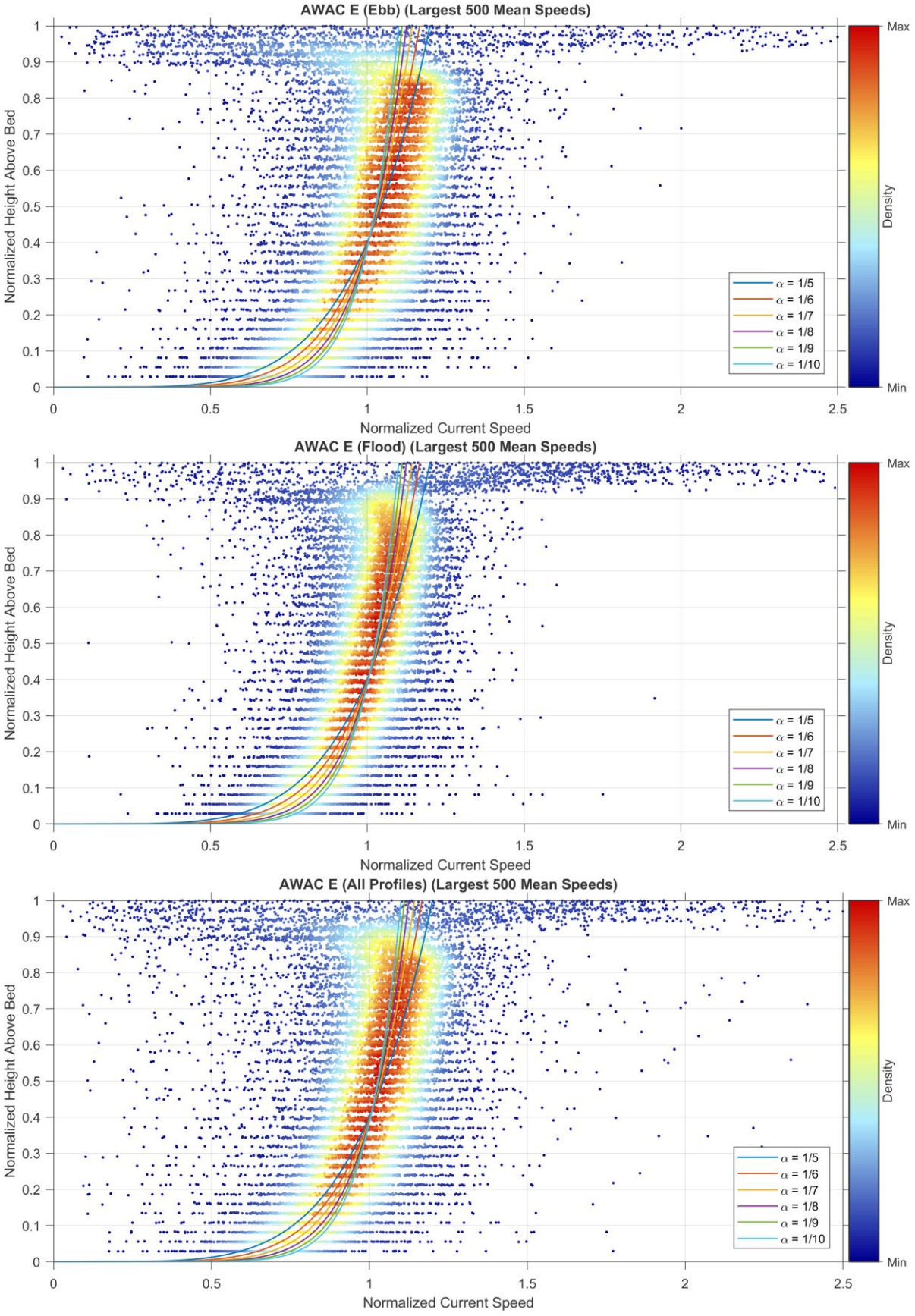



Figure H.25: Normalised profiles, highest 500 mean speeds, AWAC E.

## H.6 Selected Profile Shapes: Highest Current Speeds

In order to confirm the suitability of these values for the exponent, α, at higher current speeds, in this Section we compare those profiles with the highest mean current speeds to the theoretical profiles specified. In Figure H.26 and Figure H.27, the forty profiles at AWAC A with the highest mean current speed are shown. For each profile, the following is included:

- Measured data (blue line)
- Individually fitted profile (red line)
- The recommended theoretical profile for AWAC A, with α = 1/7 (purple line)
- An alternate theoretical profile, with α = 1/6, for comparison (green line)

Thereafter, in Figure H.28 and Figure H.29, profiles are presented for AWAC C, with the recommended profile of α = 1/9 and alternate profile of α = 1/10 used for purple and green lines respectively. Finally, Figure H.30 and Figure H.31 show profiles for AWAC E, again reverting back to recommended profile of α = 1/7 and alternate profile of α = 1/6.

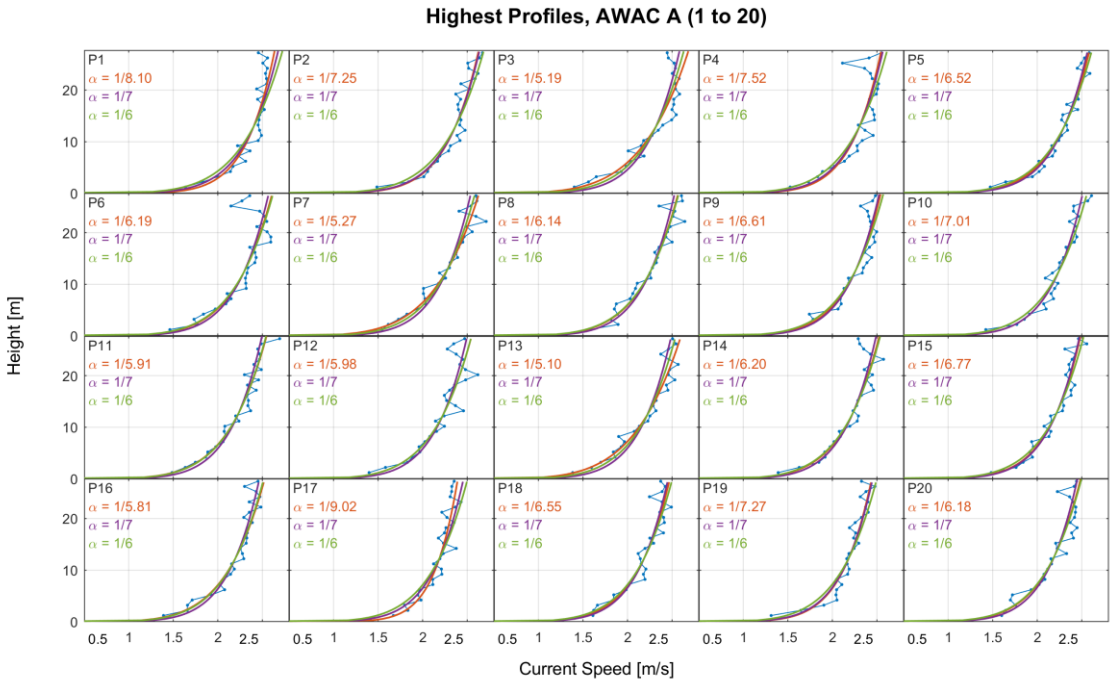



Figure H.26: Highest Profiles, AWAC A (1 to 20).

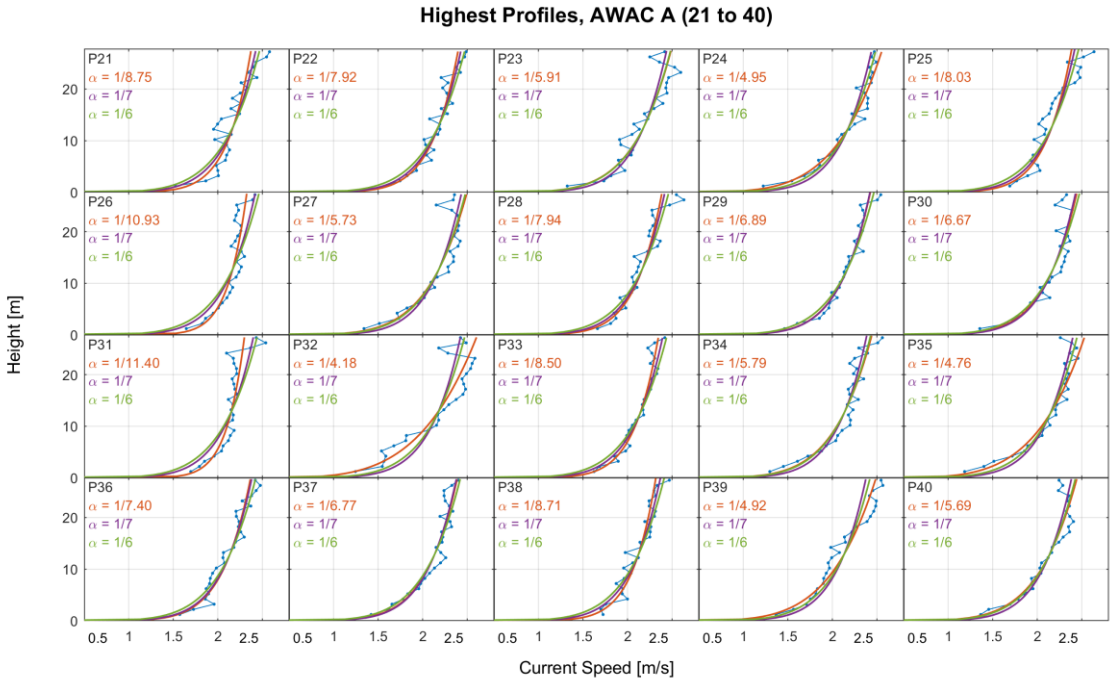



Figure H.27: Highest Profiles, AWAC A (21 to 40).

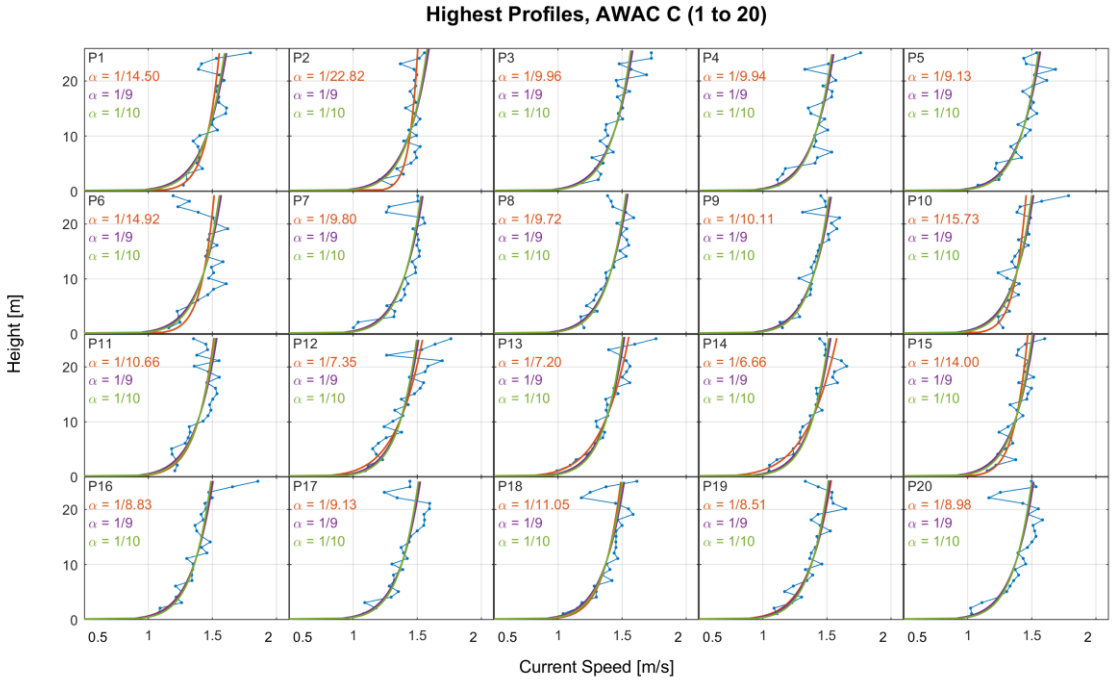



Figure H.28: Highest Profiles, AWAC C (1 to 20).

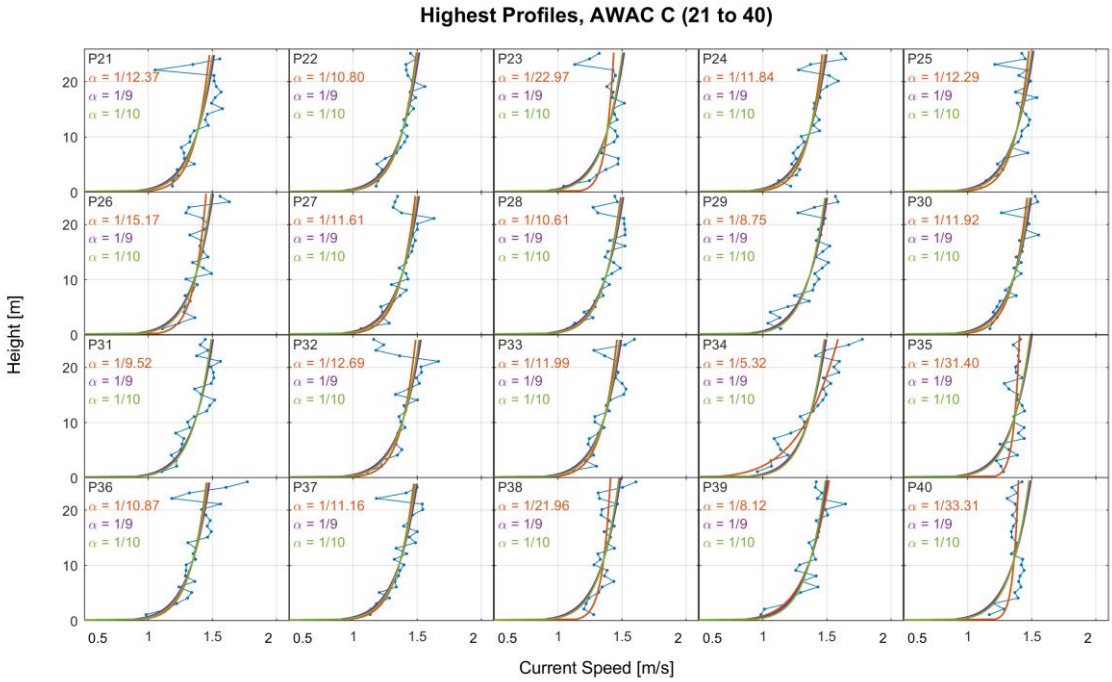



Figure H.29: Highest Profiles, AWAC C (21 to 40).

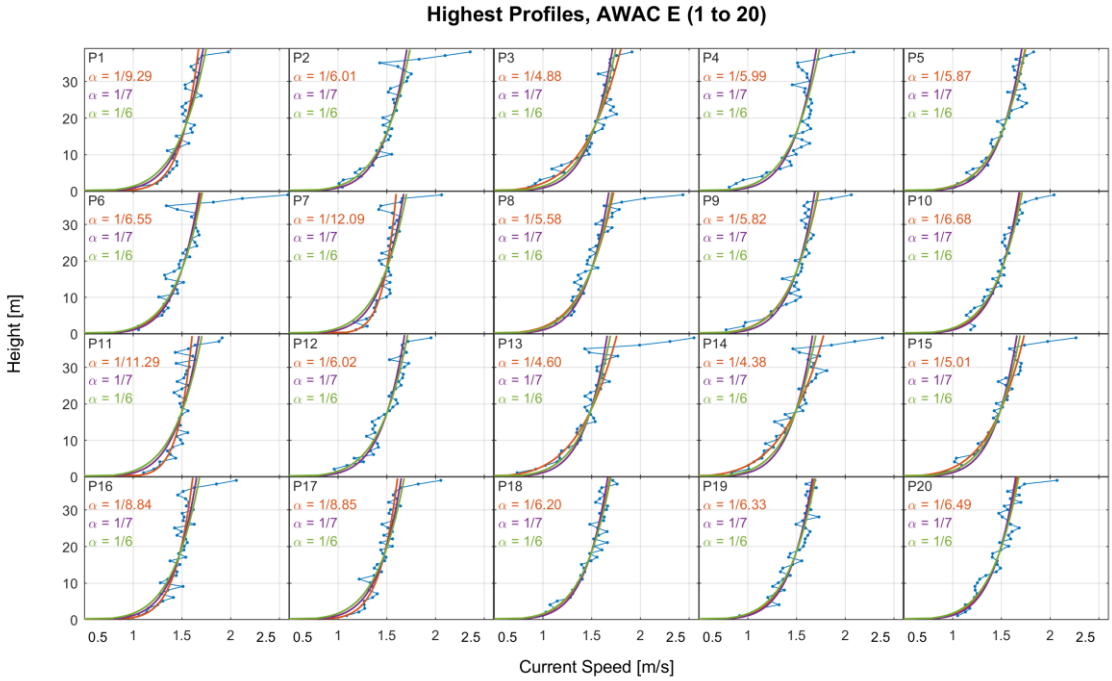



Figure H.30: Highest Profiles, AWAC E (1 to 20).

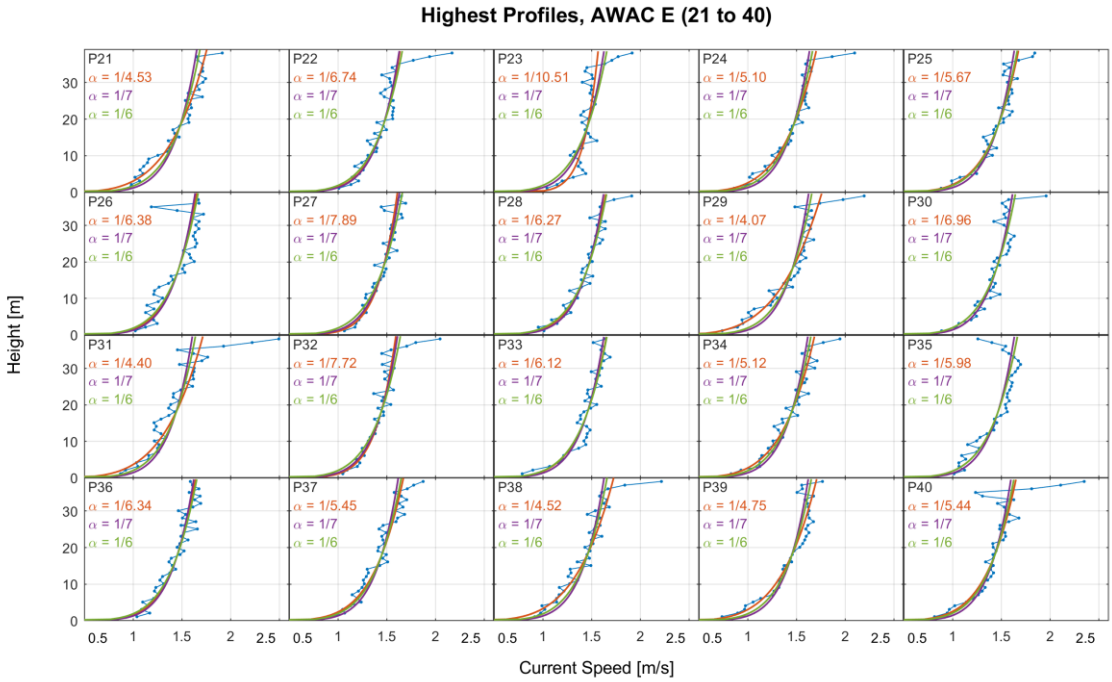



Figure H.31: Highest Profiles, AWAC E (21 to 40).

# Appendix I. Effects of Bedform Evolution

## I.1 Introduction

In this Appendix, the sensitivity of modelled wave heights and current speeds to changes in bathymetry is reviewed. For this purpose, the hydrodynamic hindcast model described in Section 5 and wave hindcast model described in Section 5 were rerun for the two-year period from 2016 to 2017 using:

- Bathymetry supplied by SPL, collected in 2000.
- Bathymetry supplied by SPL, collected in 2016.

These, combined with outputs from the main model runs - using bathymetry from a 2019 survey (see Section 3.1) – provide three sets of model results to compare for this two-year period. The years 2016 and 2017 were chosen for this comparison in order to provide a long enough dataset to yield stable statistics whilst also including Storm Ophelia in October 2017 which generated the largest regional waves for the full 38-year hindcast duration.

The results of running the models with three different bathymetries are presented as follows:

- In Section I.2, spatial maps showing the mean, 50$^{th}$ and 99.9$^{th}$ percentiles, and maximum values for current speed and significant wave height (Hm0) for each bathymetry are included.
- In Section I.3, spatial maps showing *differences* between the results for the three bathymetries are shown.
- In Section I.4, all data from the most severe individual locations within a series of regions 3km in diameter across the lease zone are compared.

These describe the sensitivity of the hindcast to geomorphological change and contextualise the envelope of uncertainty associated with current and wave parameters arising out of bedform migration.

## I.2 Parameter Maps

Maps of Hm0 and current speed statistics for the two years 2016 and 2017 are included for each of the three bathymetries as follows:

- For Hm0: Figure 7.1 shows mean values; Figure I.2 and Figure I.3 show 50$^{th}$ and 99.9$^{th}$ percentiles respectively; Figure I.4 shows maxima.
- For current speeds: Figure I.5 shows mean values; Figure I.6 and Figure I.7 show 50$^{th}$ and 99.9$^{th}$ percentiles respectively; Figure I.8 shows maxima.

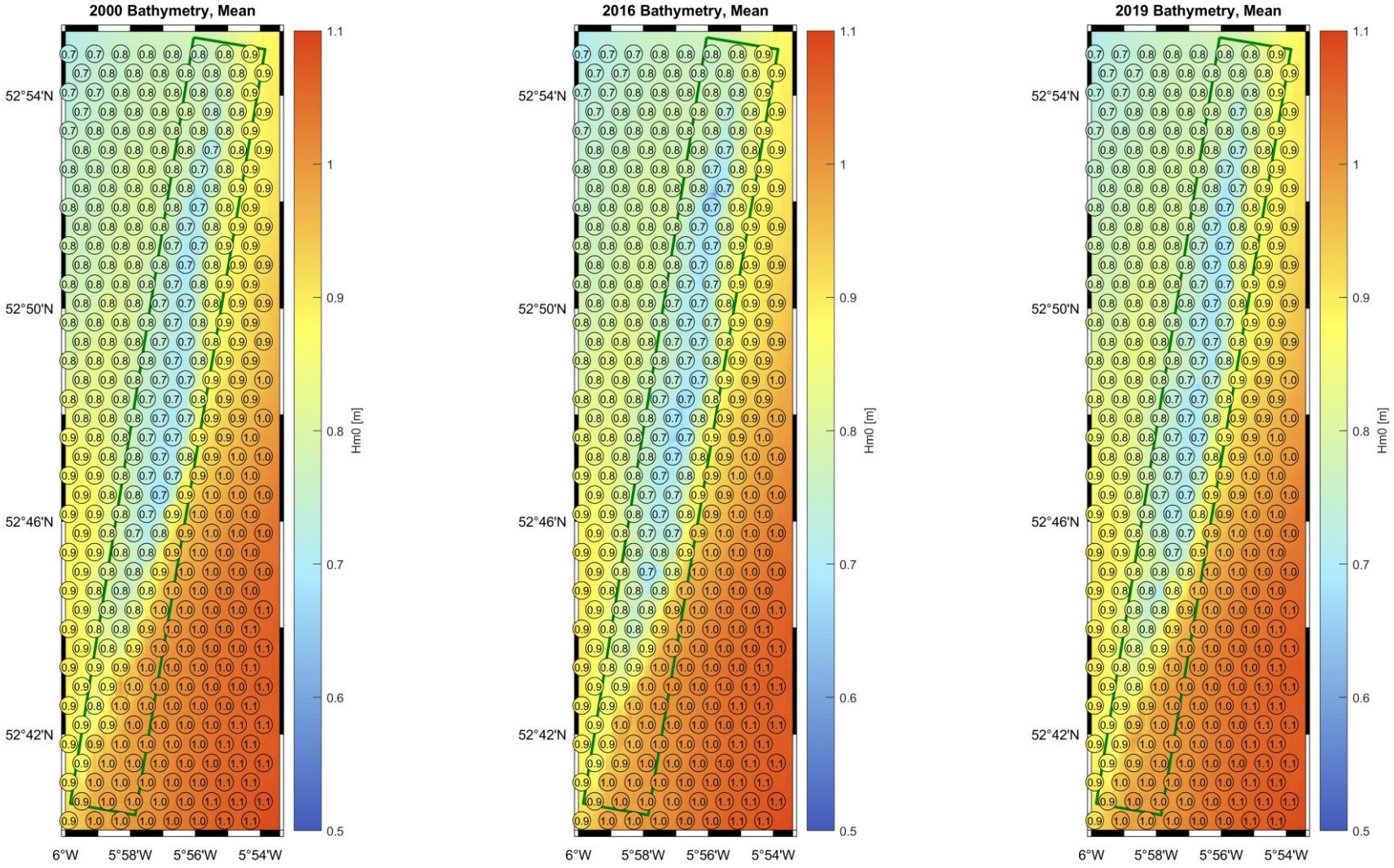



Figure I.1: Mean Hm0, 2000 bathymetry (left), 2016 bathymetry (centre) and 2019 bathymetry (right).

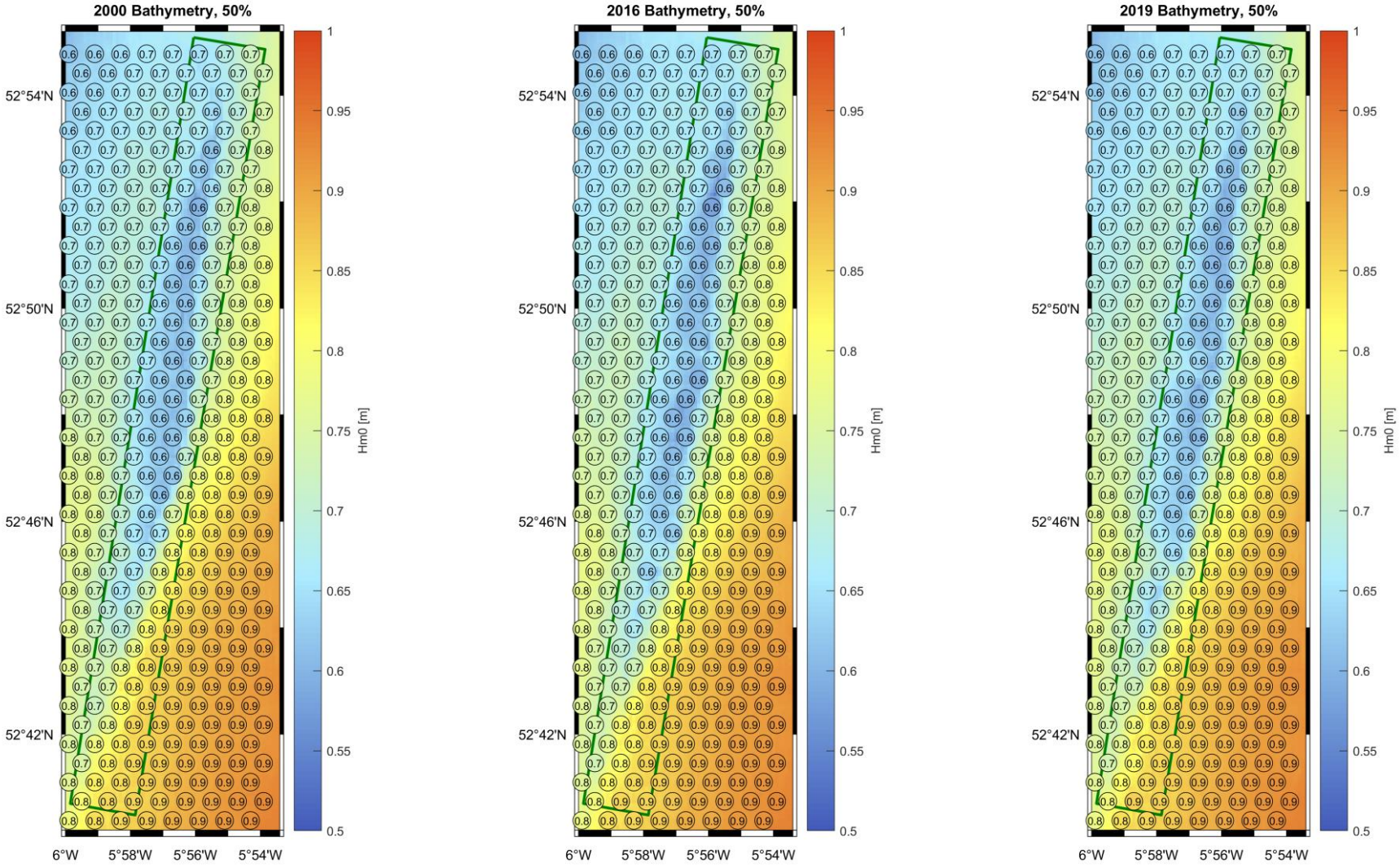



Figure I.2: 50th percentile of Hm0, 2000 bathymetry (left), 2016 bathymetry (centre) and 2019 bathymetry (right).

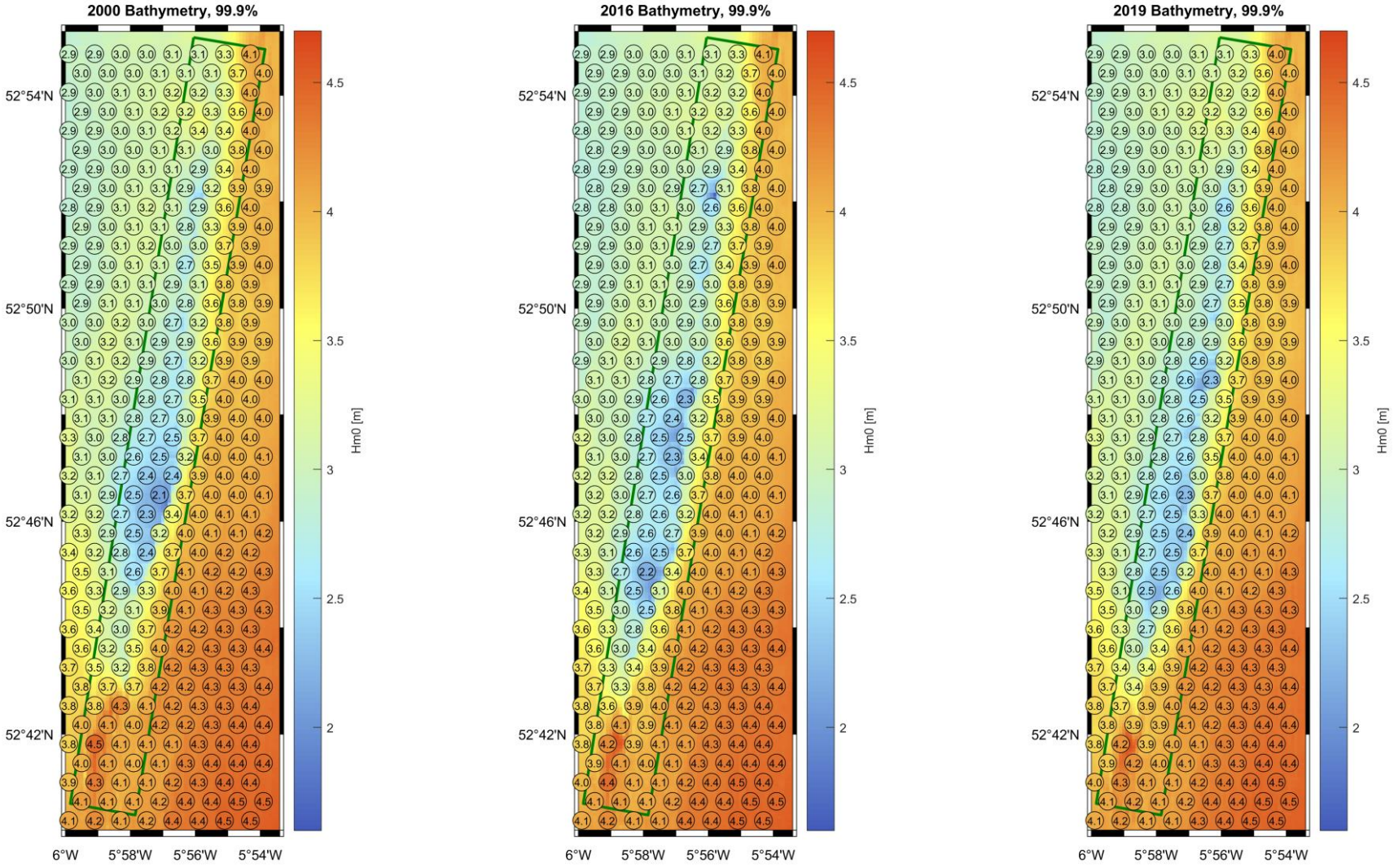



Figure I.3: 99.9th percentile Hm0, 2000 bathymetry (left), 2016 bathymetry (centre) and 2019 bathymetry (right).

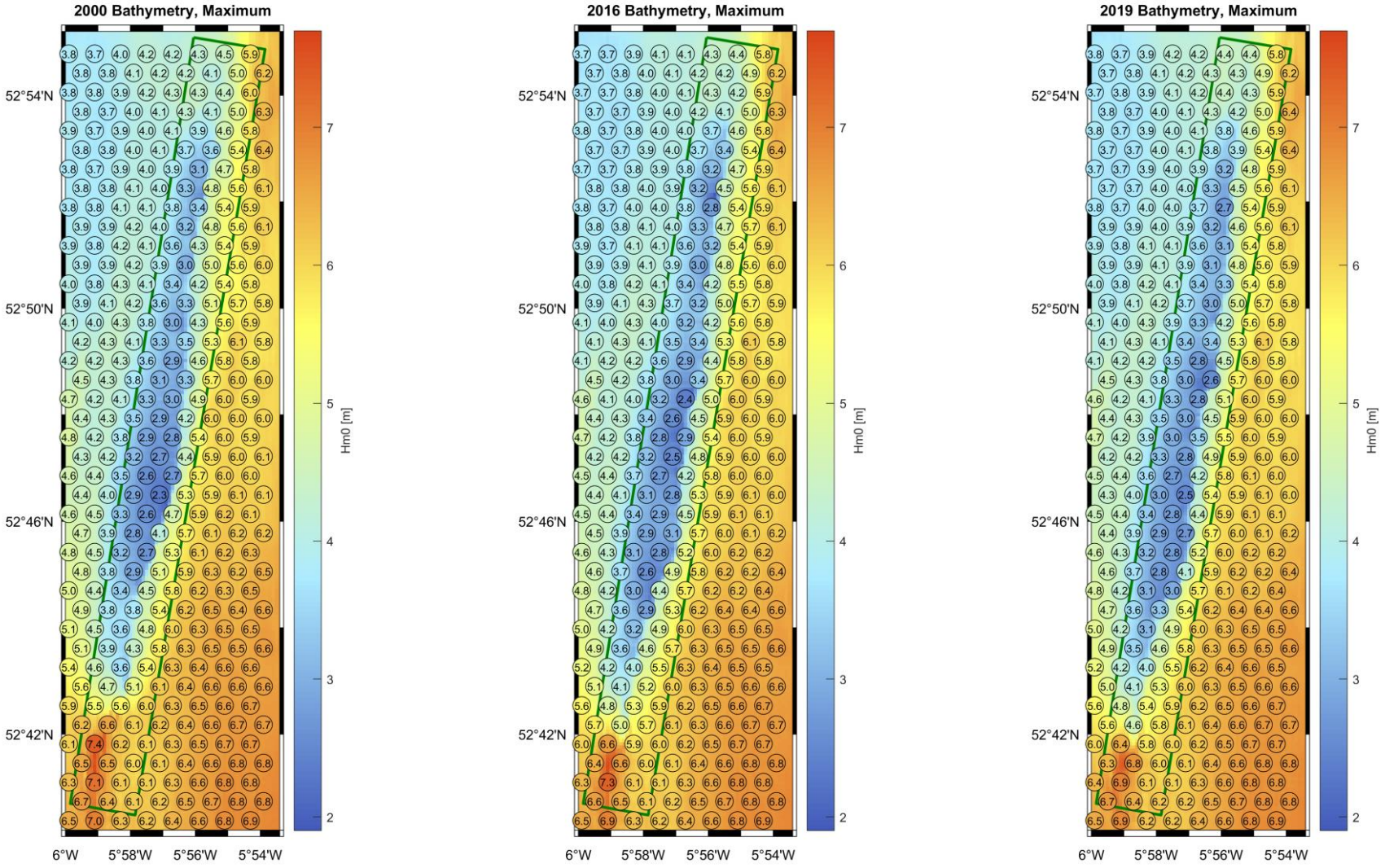



Figure I.4: Maximum Hm0, 2000 bathymetry (left), 2016 bathymetry (centre) and 2019 bathymetry (right).

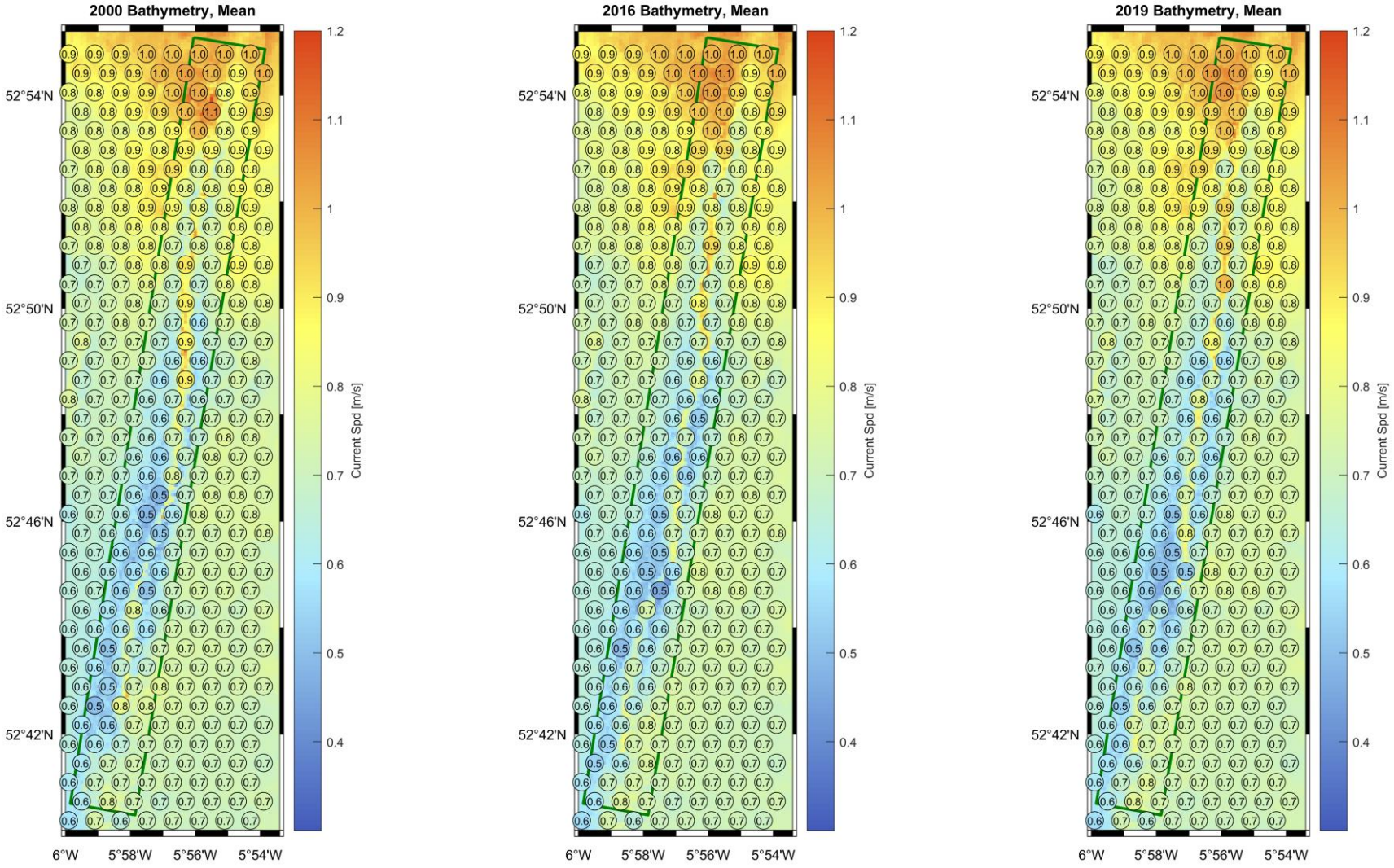



Figure I.5: Mean current speed, 2000 bathymetry (left), 2016 bathymetry (centre) and 2019 bathymetry (right).

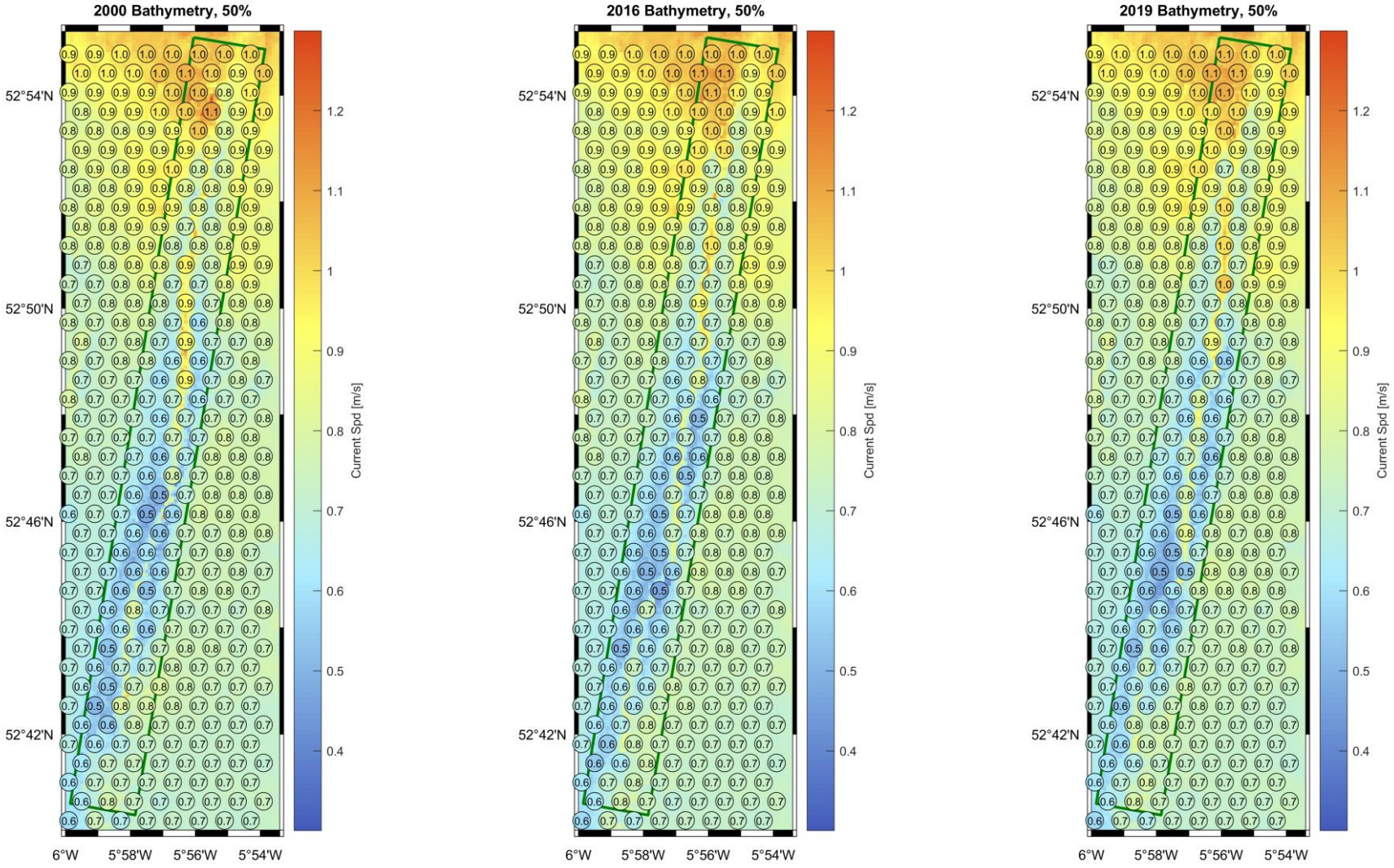



Figure I.6: 50th percentile of current speed, 2000 bathymetry (left), 2016 bathymetry (centre) and 2019 bathymetry (right).

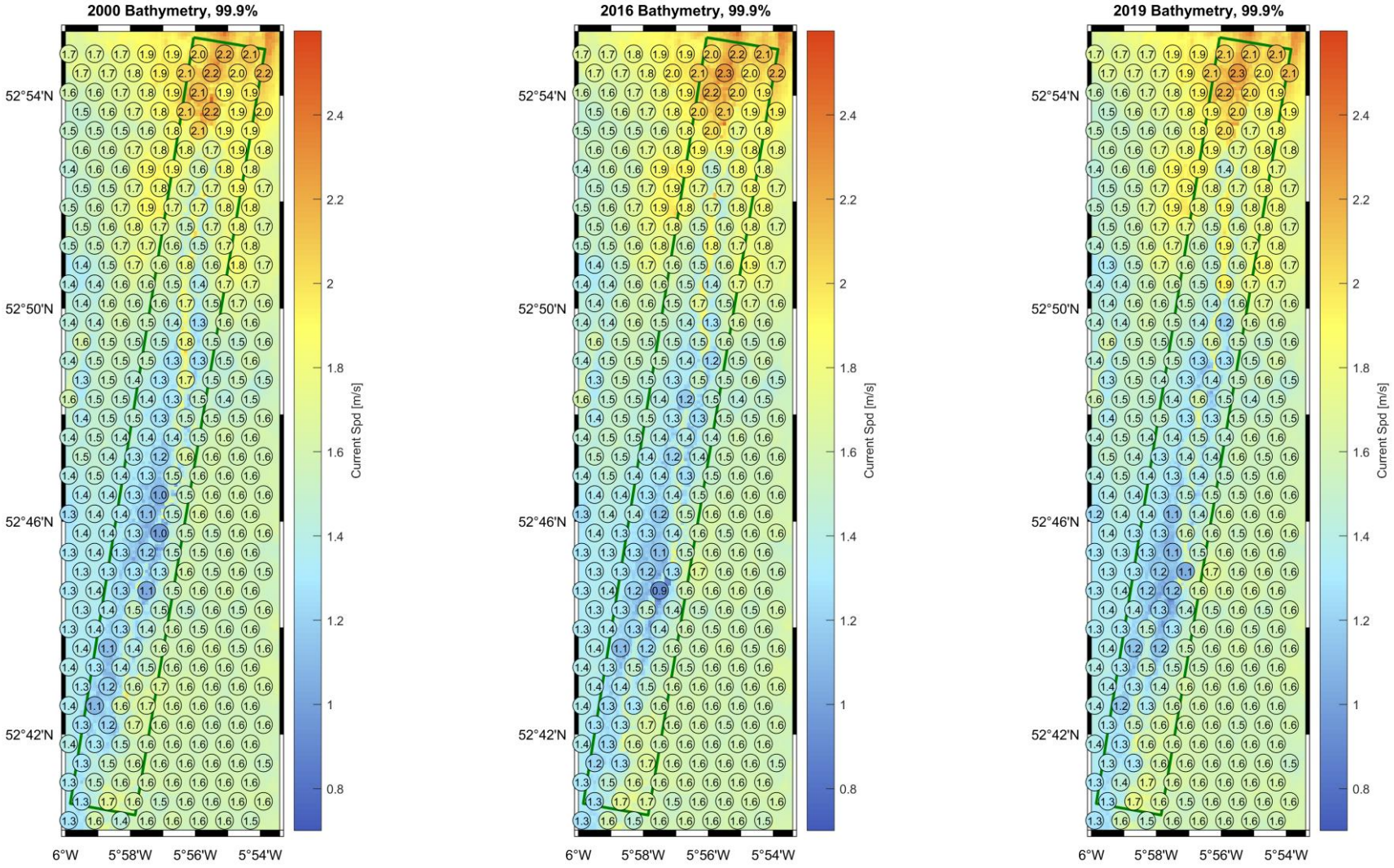



Figure I.7: 99.9th percentile of current speed, 2000 bathymetry (left), 2016 bathymetry (centre) and 2019 bathymetry (right).

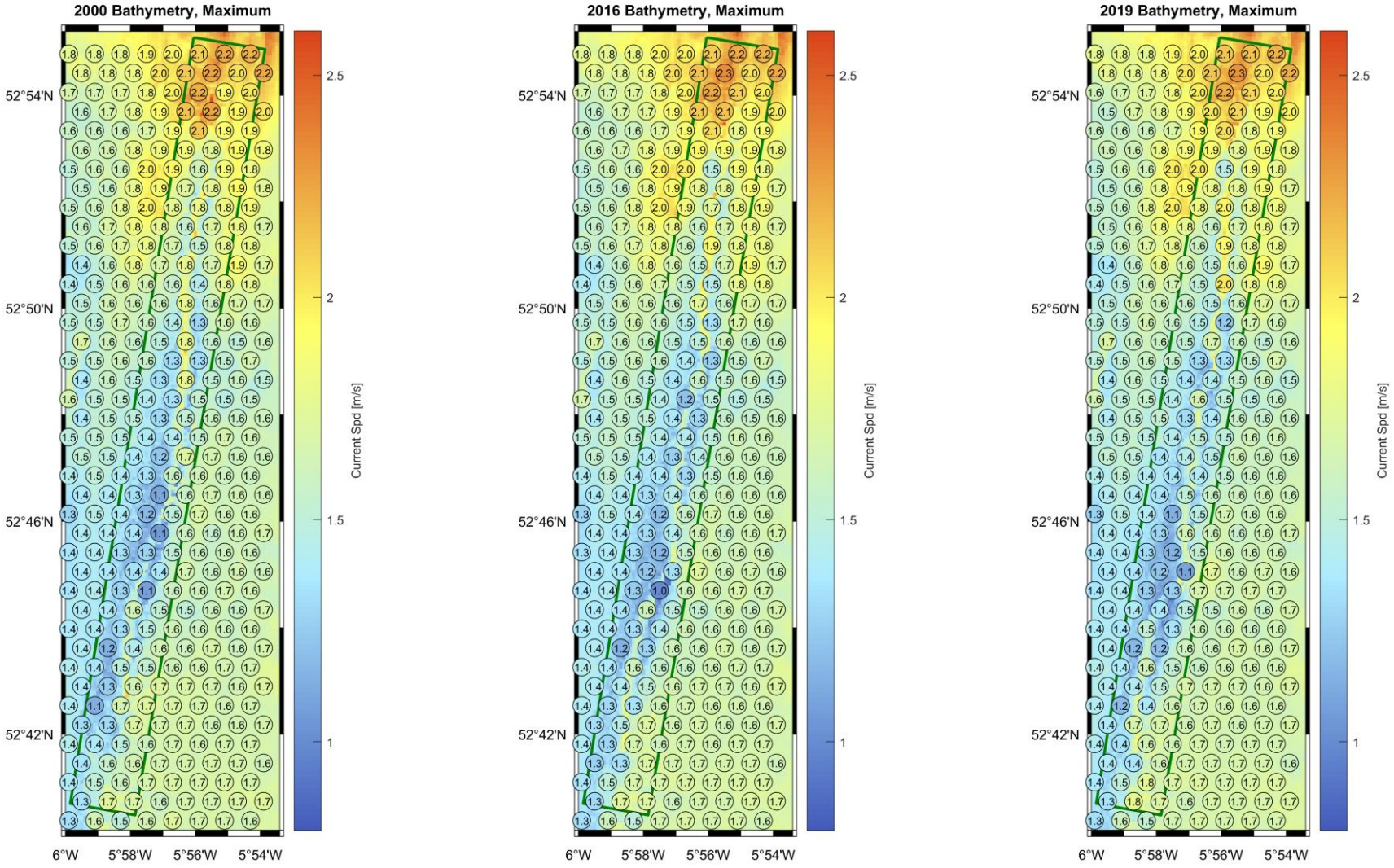



Figure I.8: Maximum current speed, 2000 bathymetry (left), 2016 bathymetry (centre) and 2019 bathymetry (right).



## I.3 Difference Maps

In this Section, maps of *differences* between Hm0 and current speed statistics for each of the three bathymetries are shown as follows:

- For Hm0: Figure I.9 shows differences between mean values; Figure I.10 shows differences between 50$^{th}$ percentiles; Figure I.11 shows differences between 99.9$^{th}$ percentiles; Figure I.12 shows differences between maxima.
- For current speeds: Figure I.13 shows differences between mean values; Figure I.14 shows differences between 50$^{th}$ percentiles; Figure I.15 shows differences between 99.9$^{th}$ percentiles; Figure I.16 shows differences between maxima.

As in the case throughout this Appendix, only results for the two-year period 2016 to 2017 are used for all three bathymetries.

Please note that for conciseness, these Figures use the notation “2000 – 2016” (e.g., the leftmost panel of Figure I.9) to denote that the values shown have been calculated by taking the specified statistic from the model run using bathymetry from 2000 and subtracting the same statistic from the model run using bathymetry from 2016. The notation “2000 – 2019” and “2016 – 2019” should be interpreted analogously.

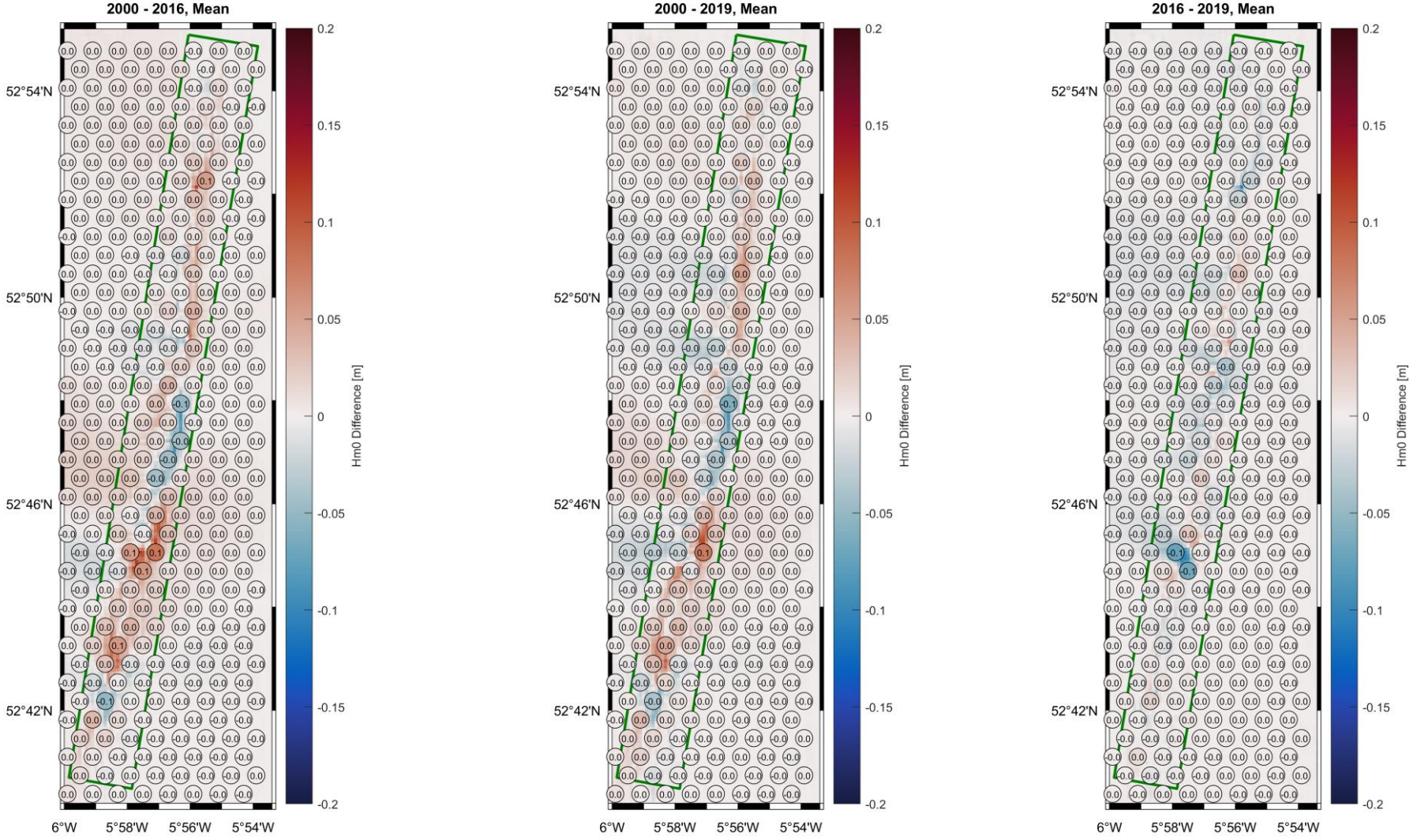



Figure I.9: Differences, mean Hm0.

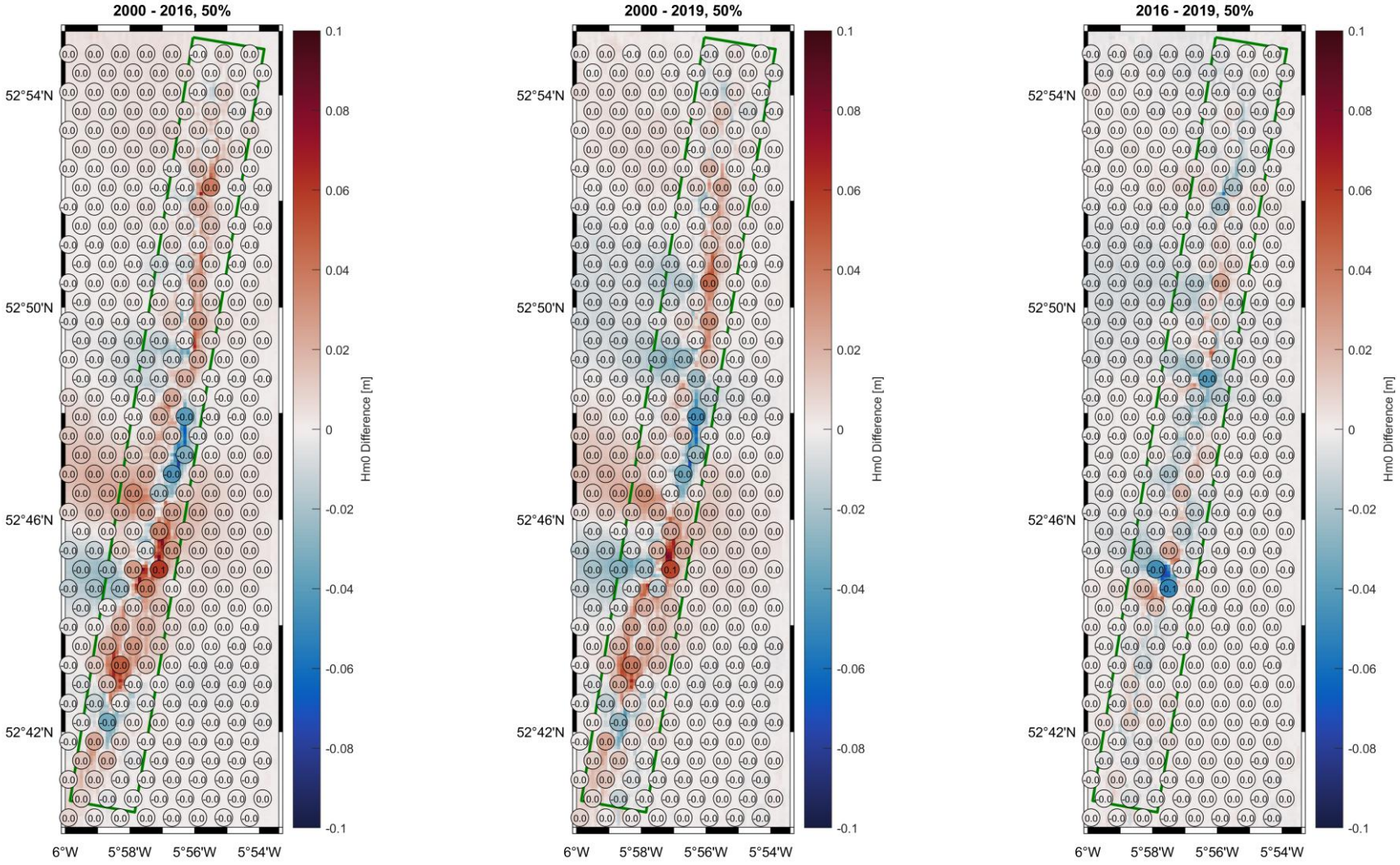



Figure I.10: Differences, 50th percentile of Hm0.

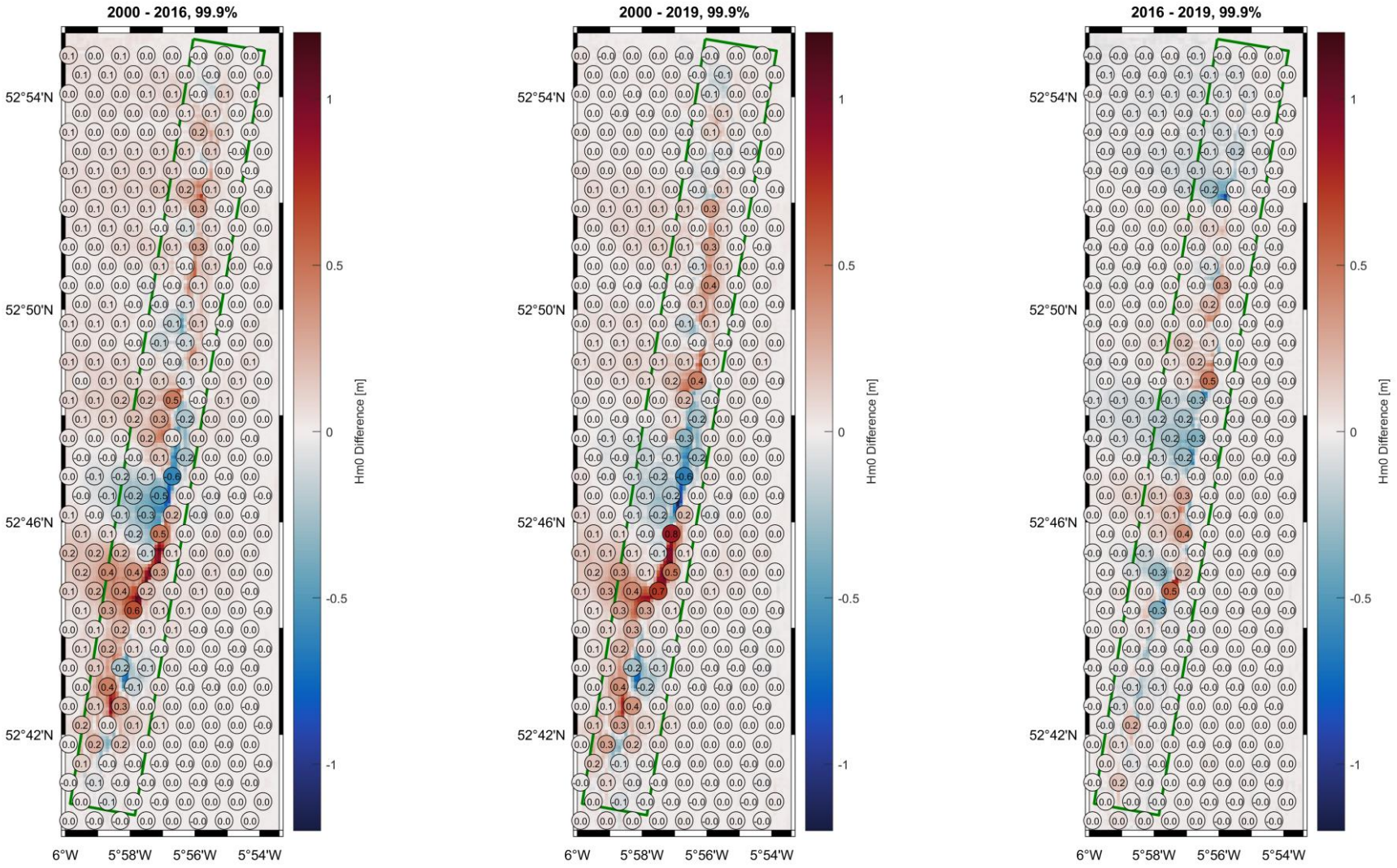



Figure I.11: Differences, 99.9$^{th}$ percentile Hm0.

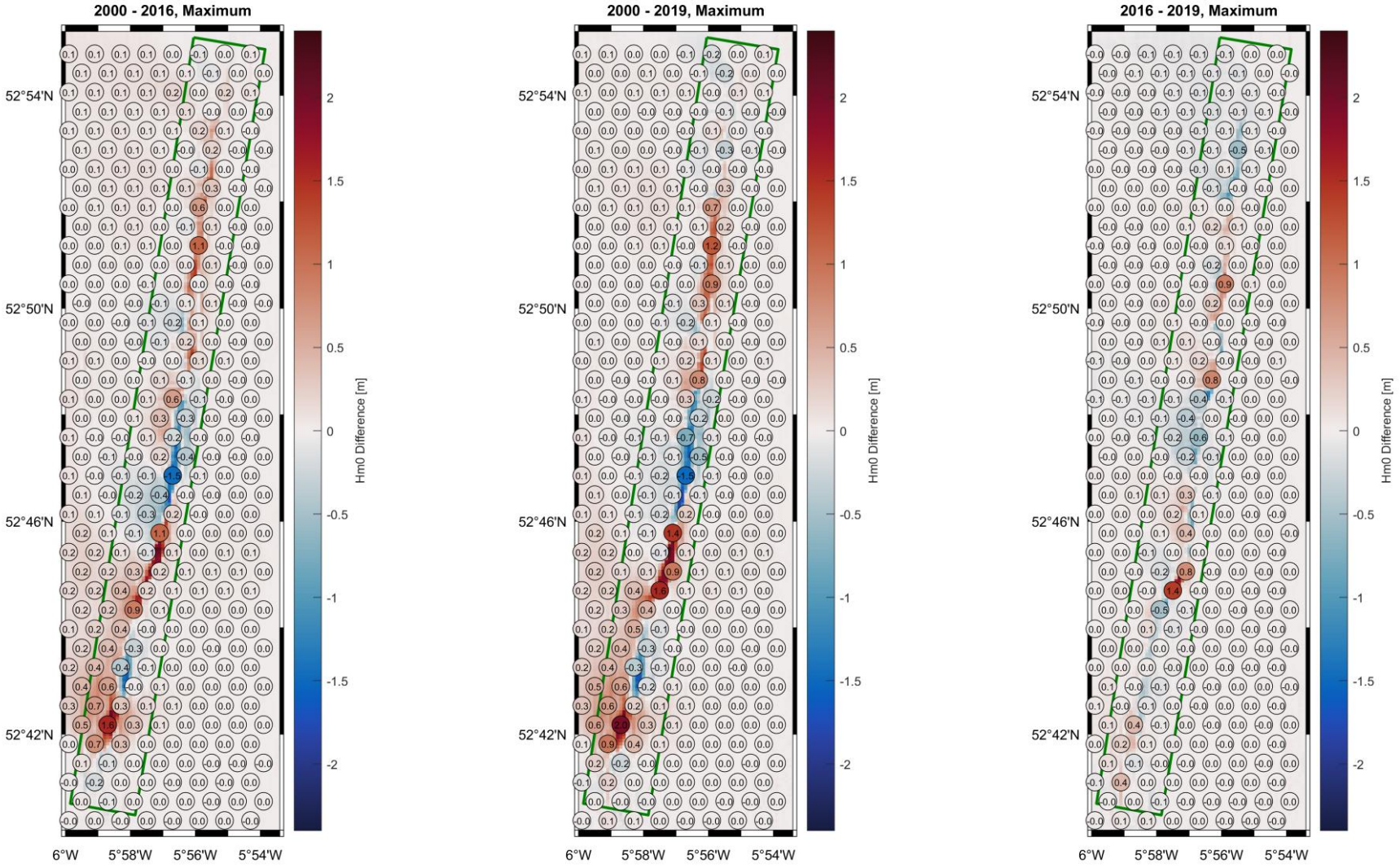



Figure I.12: Differences, maximum Hm0.

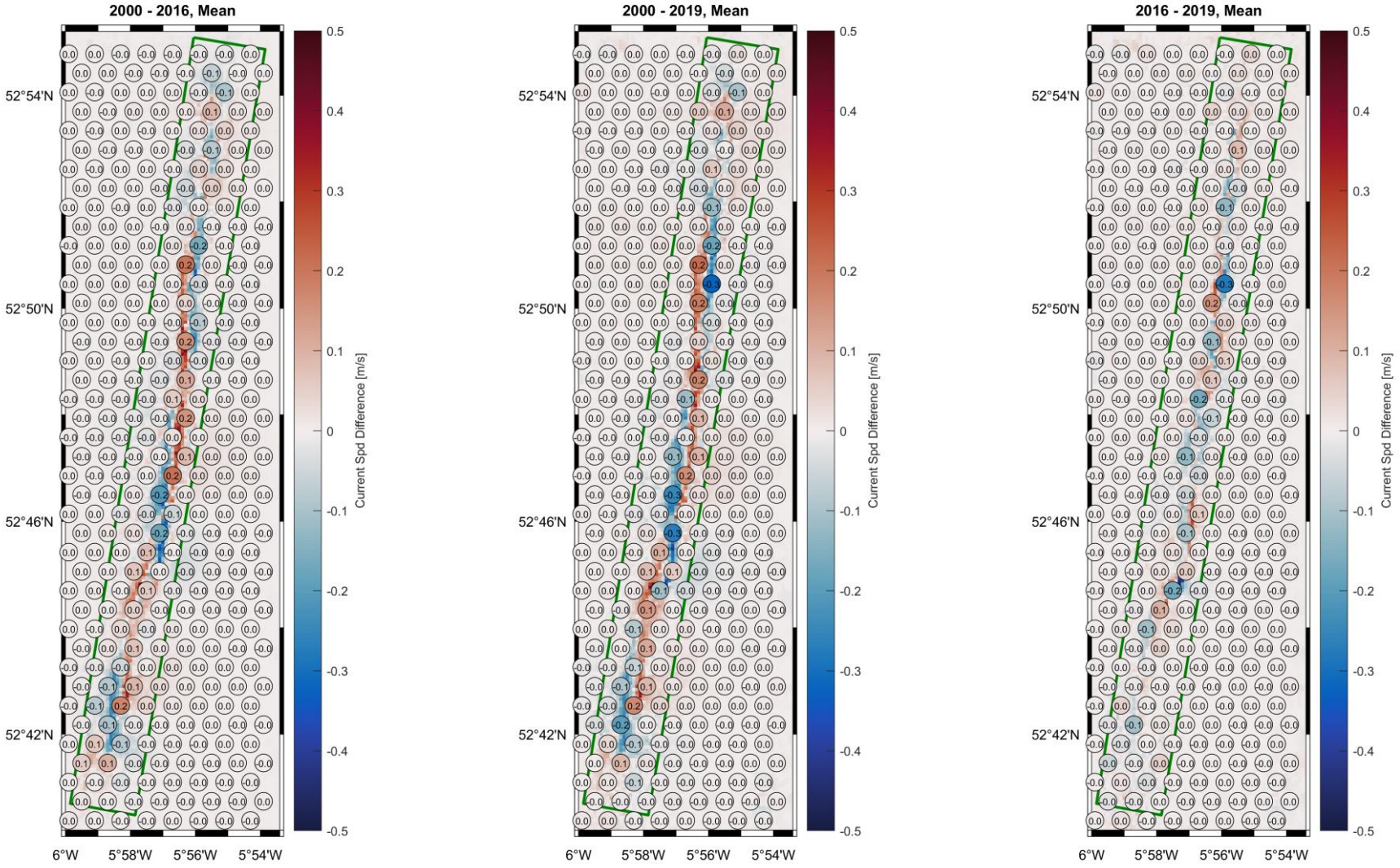



Figure I.13: Differences, mean current speed.

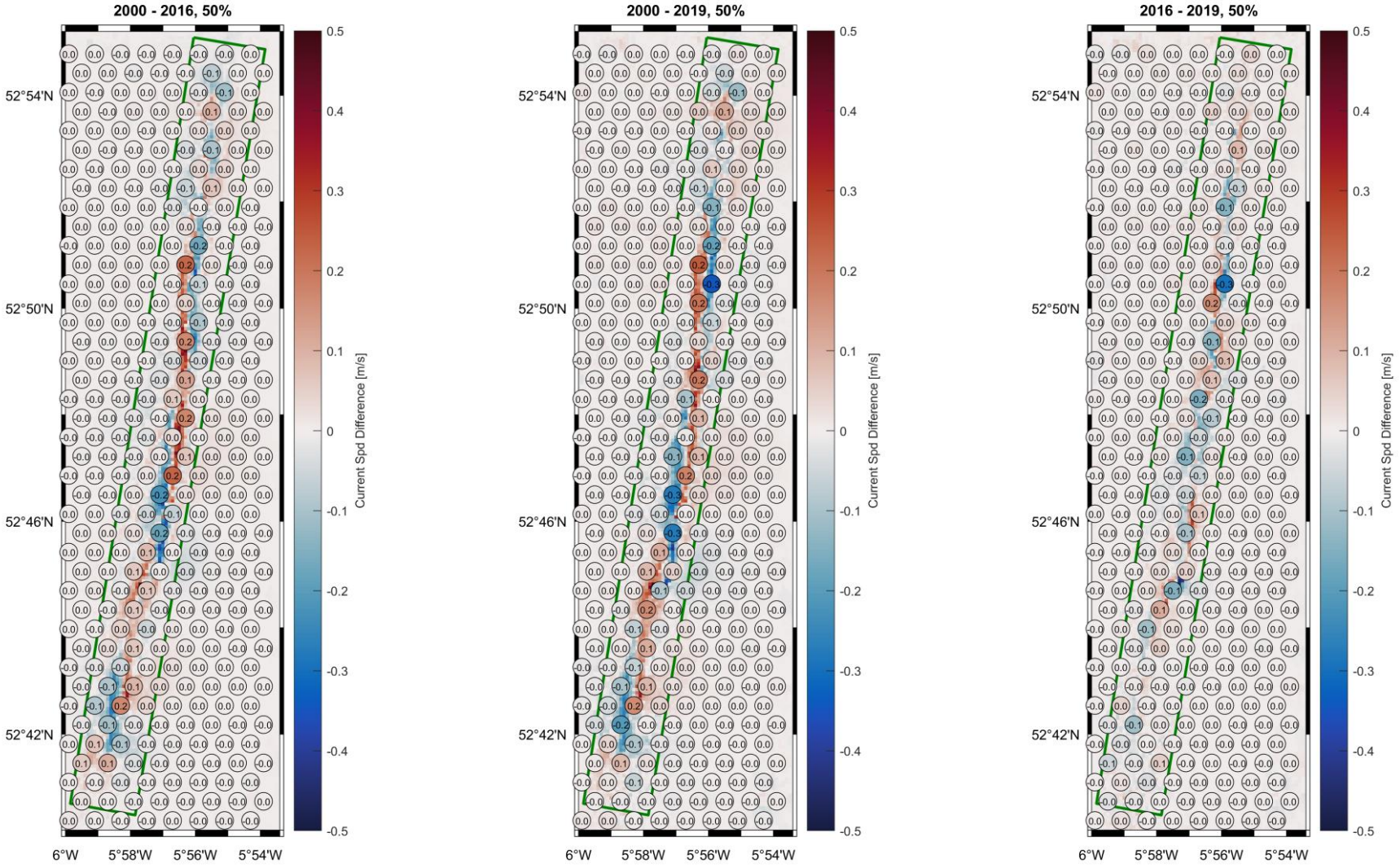



Figure I.14: Differences, 50th percentile of current speed.

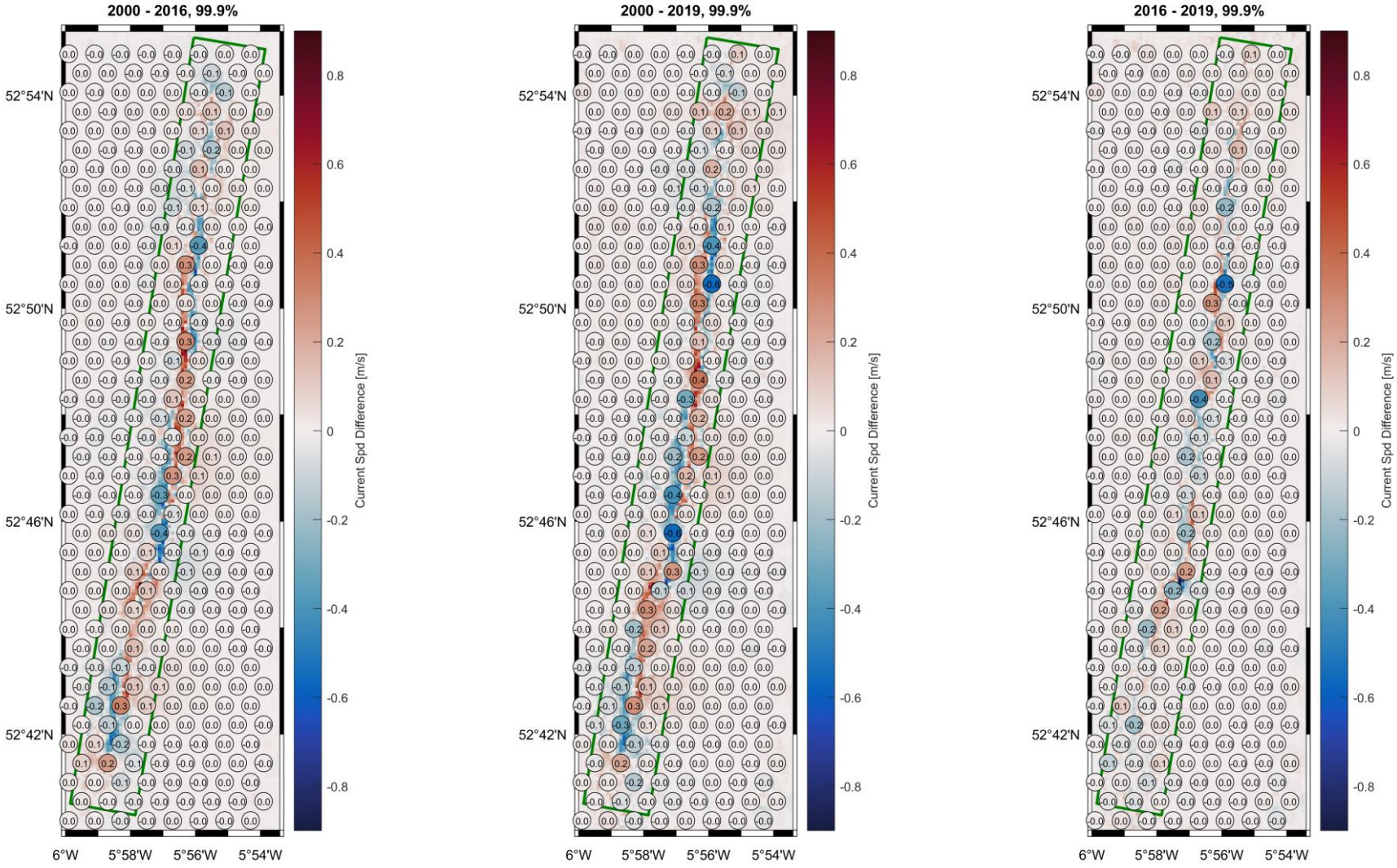



Figure I.15: Differences, 99.9th percentile of current speed.

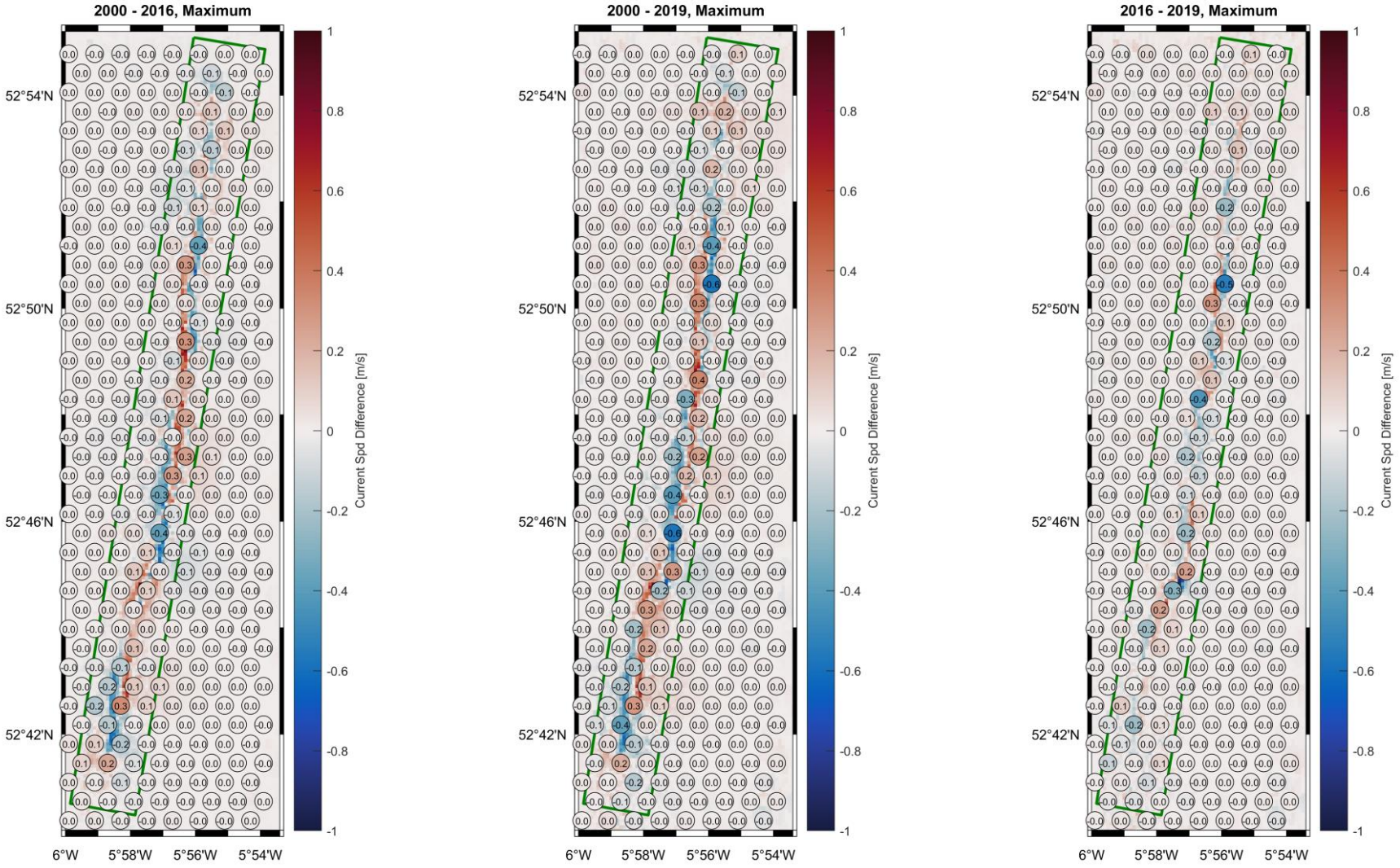



Figure I.16: Differences, maximum current speed.

## I.4 Selected Location Comparisons

In this Section more detailed comparisons are included for a number of selected locations across the lease area. For Hm0, these locations are determined as follows:

a) Nine regions of 3km diameter are defined across the lease zone. These are labelled R1, R2, … R9 in Figure I.17, and are overlaid on a spatial map of maximum Hm0.
b) For each bathymetry and each of the nine circular regions independently, we find the model location with the highest maximum Hm0 that is:
    - Within the circular region *and*
    - Within the lease zone boundary.

    These locations are marked by smaller circles in Figure I.17, with said maximum Hm0 also shown.
c) All Hm0 values from the selected location in R1 for the 2000 bathymetry model, are then compared to those from the selected location in R1 for the 2016 bathymetry model as a scatter plot with overlaid quantile-quantile plot (see Figure I.19). As throughout this Appendix, only data from the two-year period from 2016 to 2017 are used.
d) This is repeated for the selected locations in R1 for the 2000 and 2019 bathymetries (see Figure I.20) and the 2016 and 2019 bathymetries (Figure I.21). It is then repeated for R2, R3, … R9 and all combinations of bathymetry.

The same process is then followed for current speeds, with selected locations shown in Figure I.18, whilst comparison plots for the selected locations in R1 can be found in Figure I.22 through Figure I.24.

For conciseness, comparison plots are included in this Appendix for only R1 (Section I.4.1), R6 (Section I.4.2) and R9 (Section I.4.3). However, we are happy to supply analogous Figures for the other circular regions upon request.

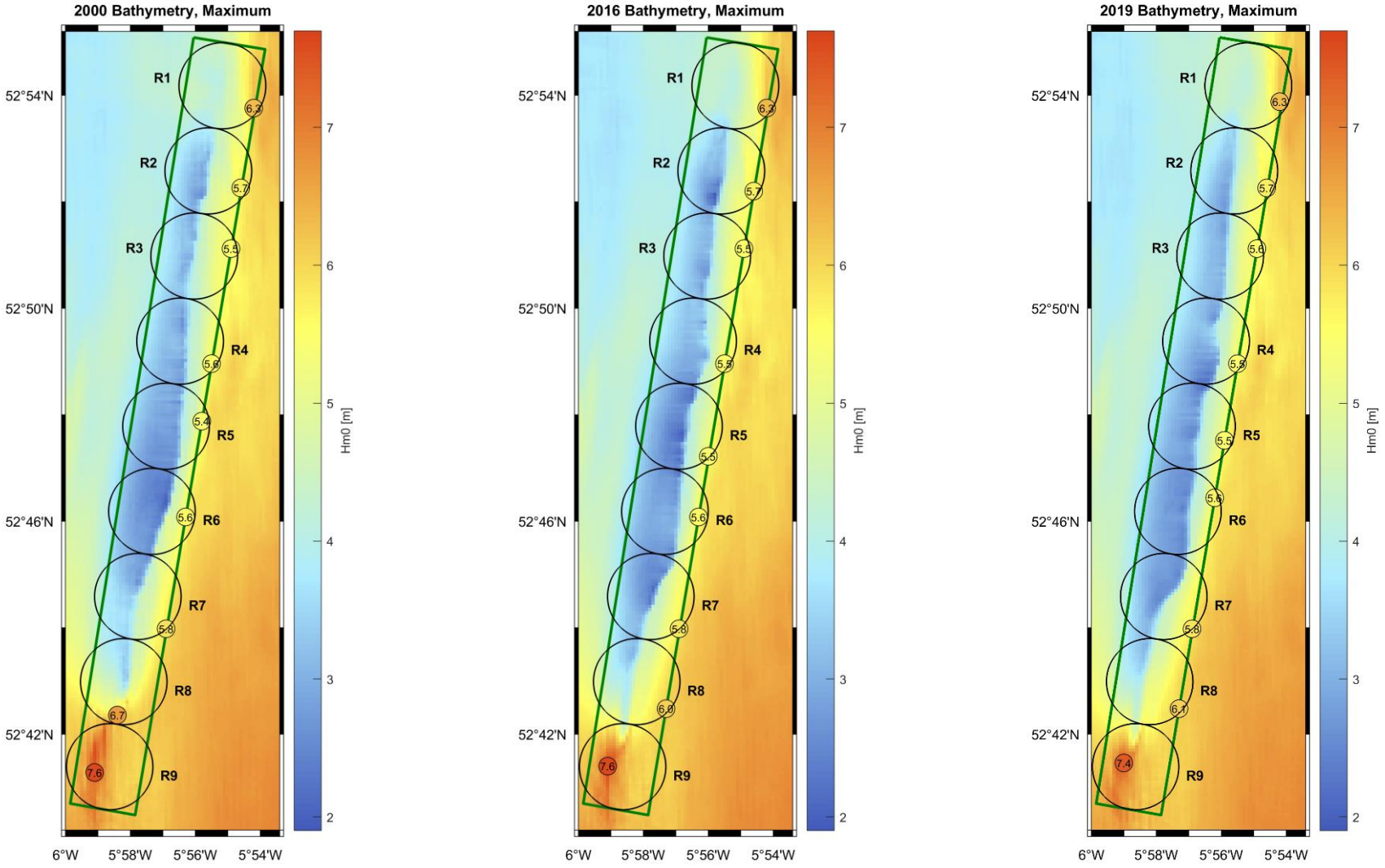



Figure I.17: Locations within each region with maximum Hm0.

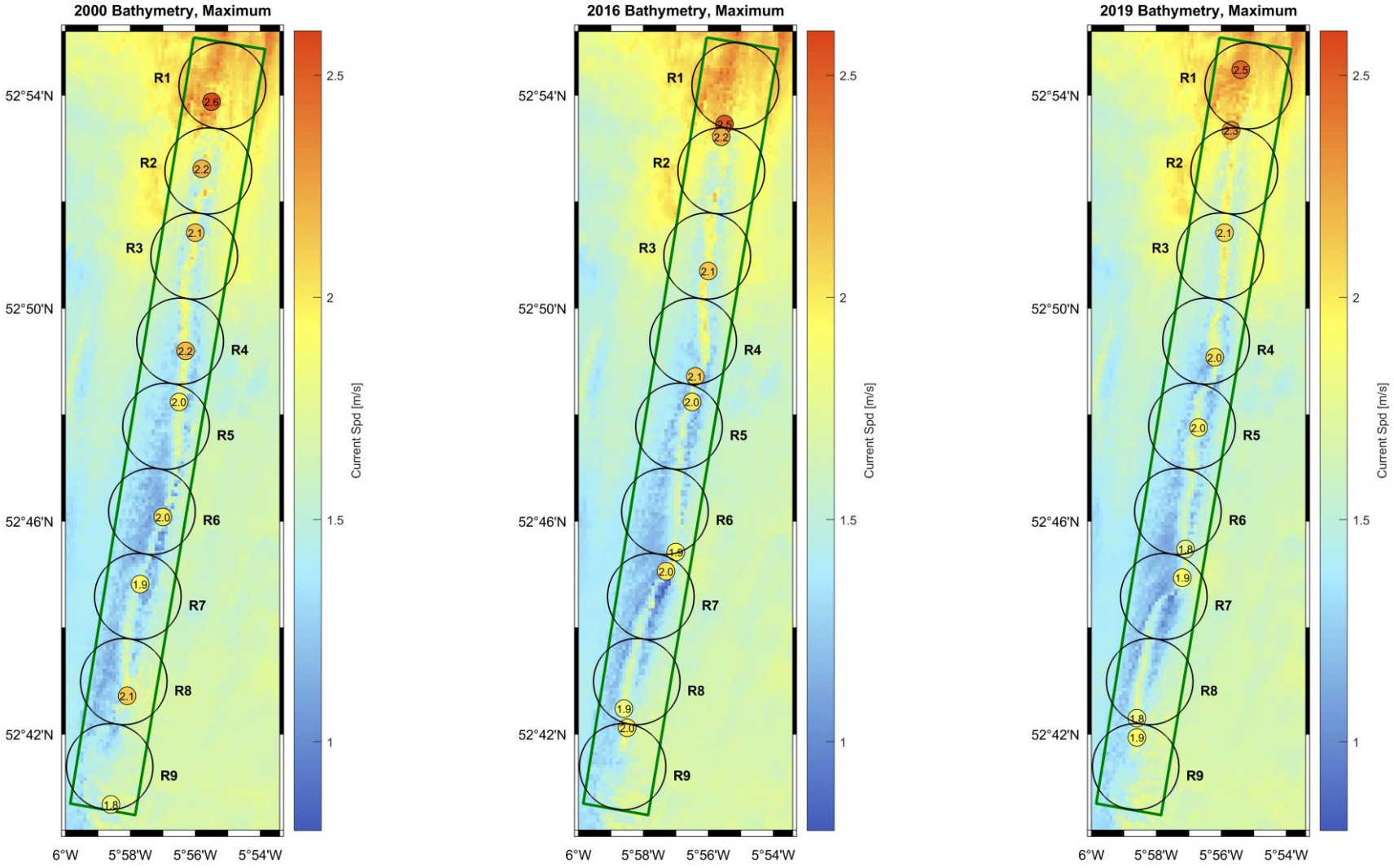



Figure I.18: Location with each region with maximum current speed.

### I.4.1 Comparison Plots, R1

| | |
|---|---|
| Mean (X) | 0.87 |
| Mean (Y) | 0.87 |
| N | 17544 |
| Bias | 0.01 |
| AME | 0.01 |
| RMS | 0.01 |
| SI | 0.01 |
| CC | 1.00 |
| R² | 1.00 |

Data
1:1 Line
Quantiles (1-99%)
Q-Q Line: 1.005x

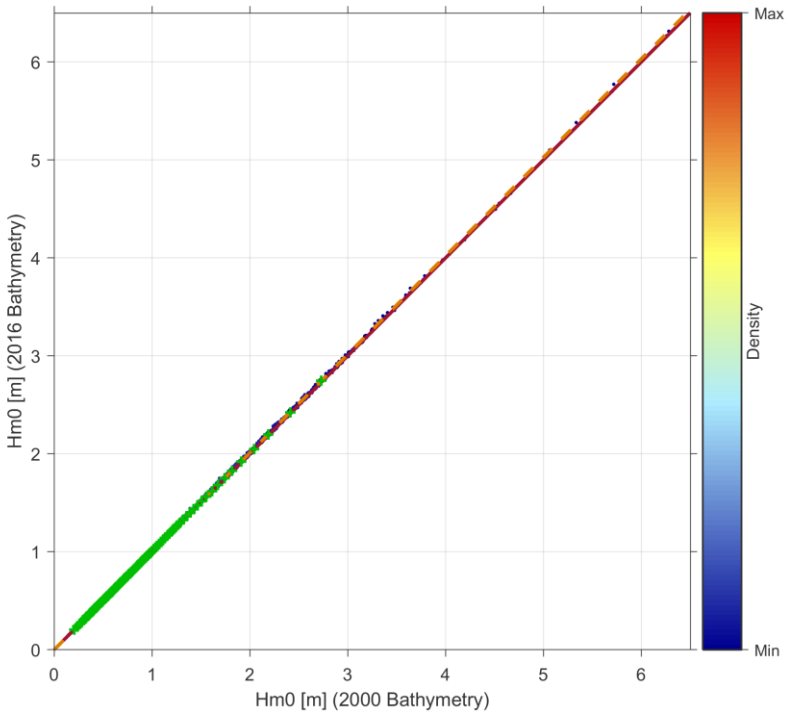



Figure I.19: Hm0, 2016 bathymetry vs 2000 bathymetry, selected locations, R1.

| | |
|---|---|
| Mean (X) | 0.87 |
| Mean (Y) | 0.87 |
| N | 17544 |
| Bias | 0.00 |
| AME | 0.01 |
| RMS | 0.01 |
| SI | 0.01 |
| CC | 1.00 |
| R² | 1.00 |

Data
1:1 Line
Quantiles (1-99%)
Q-Q Line: 1.003x

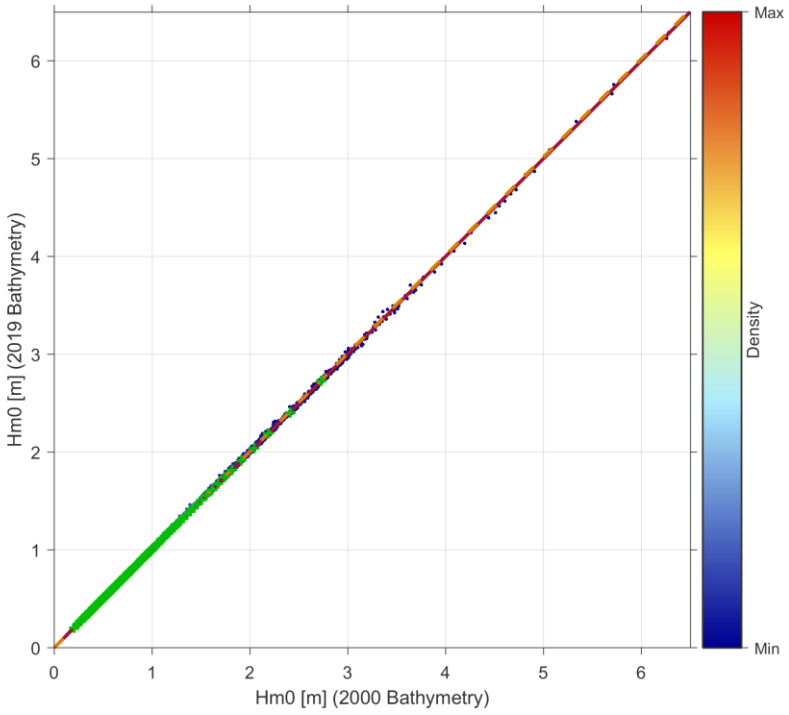



Figure I.20: Hm0, 2019 bathymetry vs 2000 bathymetry, selected locations, R1.

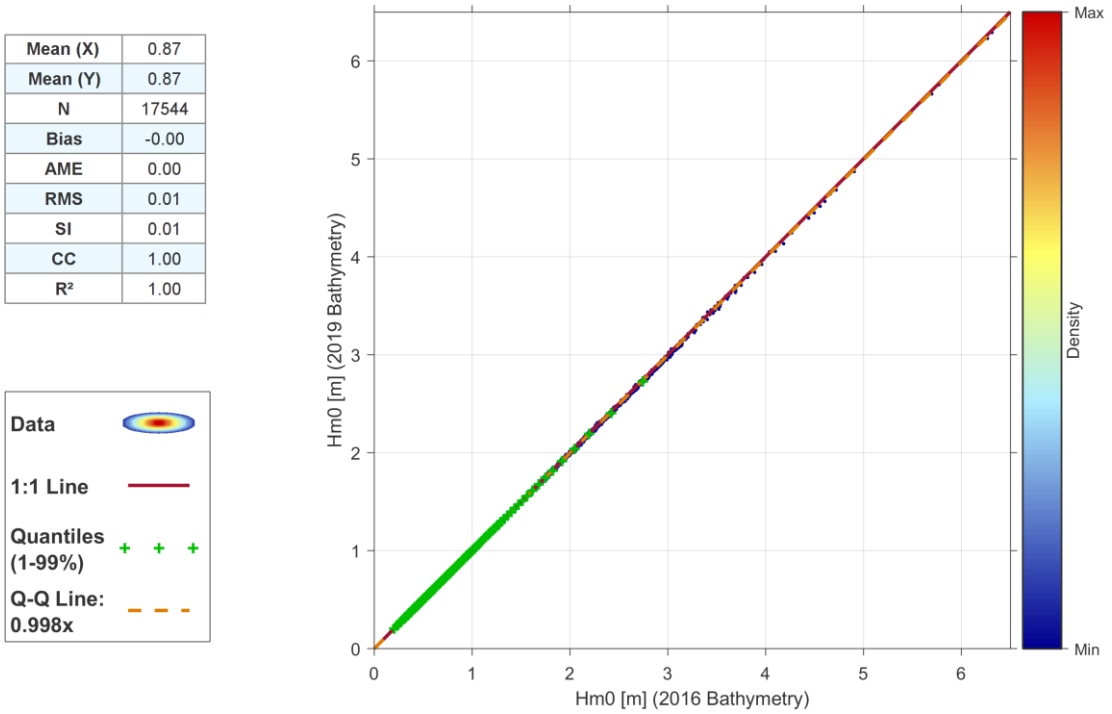



Figure I.21: Hm0, 2019 bathymetry vs 2016 bathymetry, selected locations, R1.

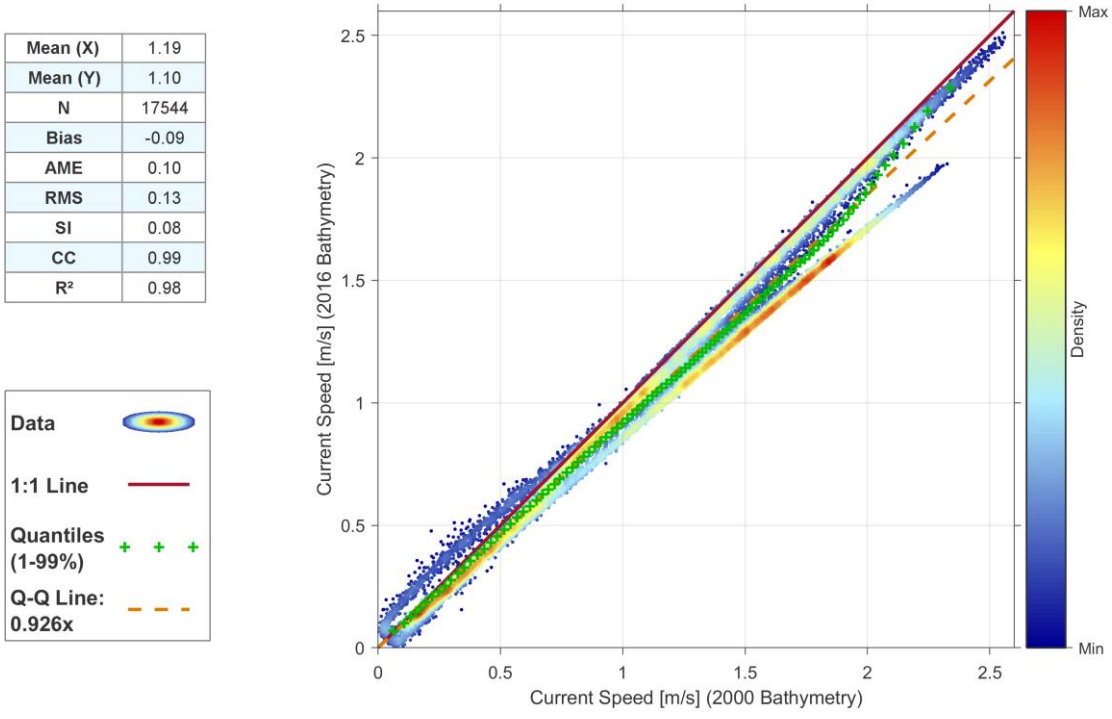



Figure I.22: Current speed, 2016 bathymetry vs 2000 bathymetry, selected locations, R1.

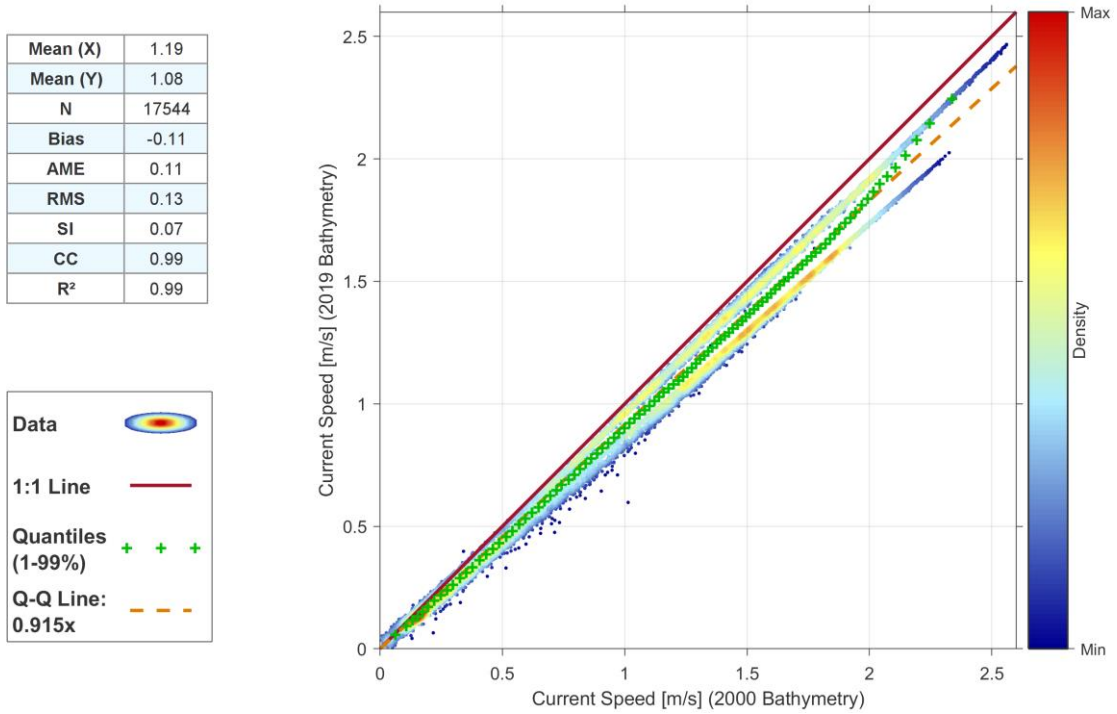



Figure I.23: Current speed, 2019 bathymetry vs 2000 bathymetry, selected locations, R1.

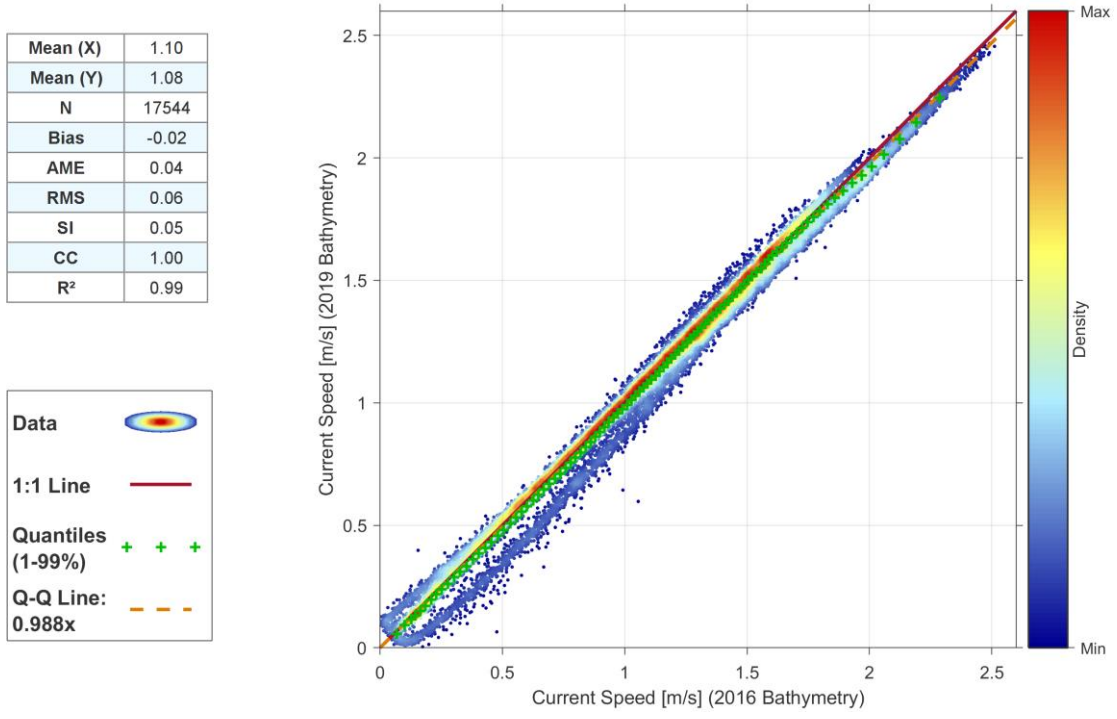



Figure I.24: Current speed, 2019 bathymetry vs 2016 bathymetry, selected locations, R1.

### I.4.2 Comparison Plots, R6

| | |
|---|---|
| Mean (X) | 0.93 |
| Mean (Y) | 0.91 |
| N | 17544 |
| Bias | -0.02 |
| AME | 0.02 |
| RMS | 0.02 |
| SI | 0.02 |
| CC | 1.00 |
| R² | 1.00 |

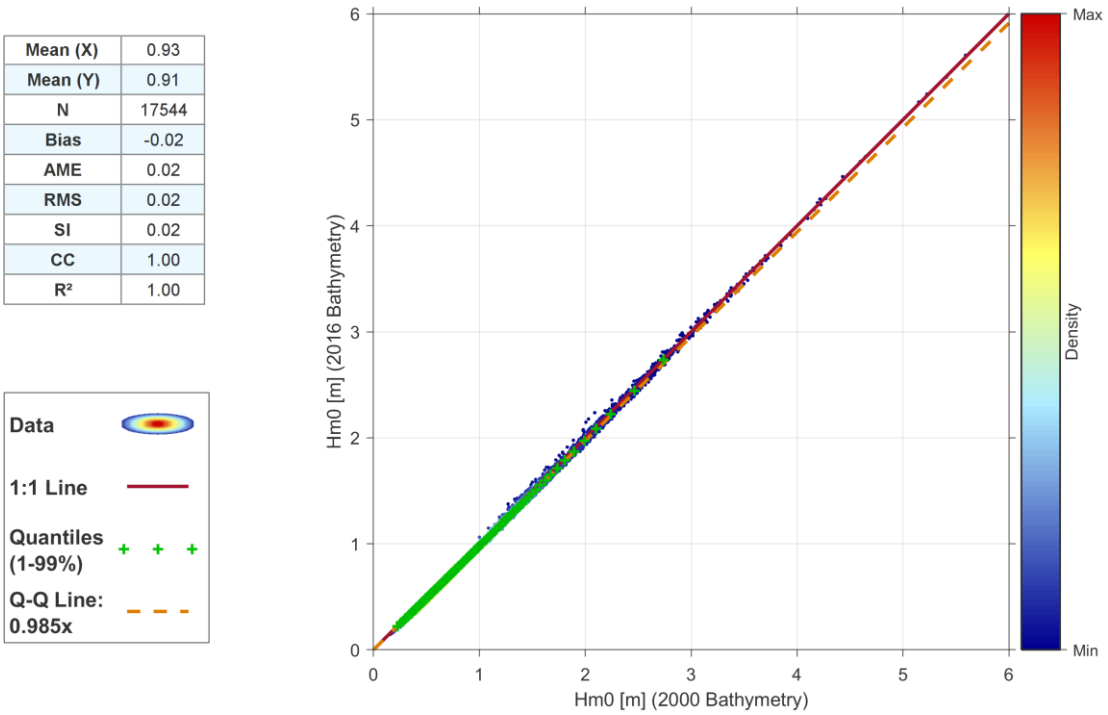



Figure I.25: Hm0, 2016 bathymetry vs 2000 bathymetry, selected locations, R6.

| | |
|---|---|
| Mean (X) | 0.93 |
| Mean (Y) | 0.91 |
| N | 17544 |
| Bias | -0.02 |
| AME | 0.02 |
| RMS | 0.03 |
| SI | 0.02 |
| CC | 1.00 |
| R² | 1.00 |

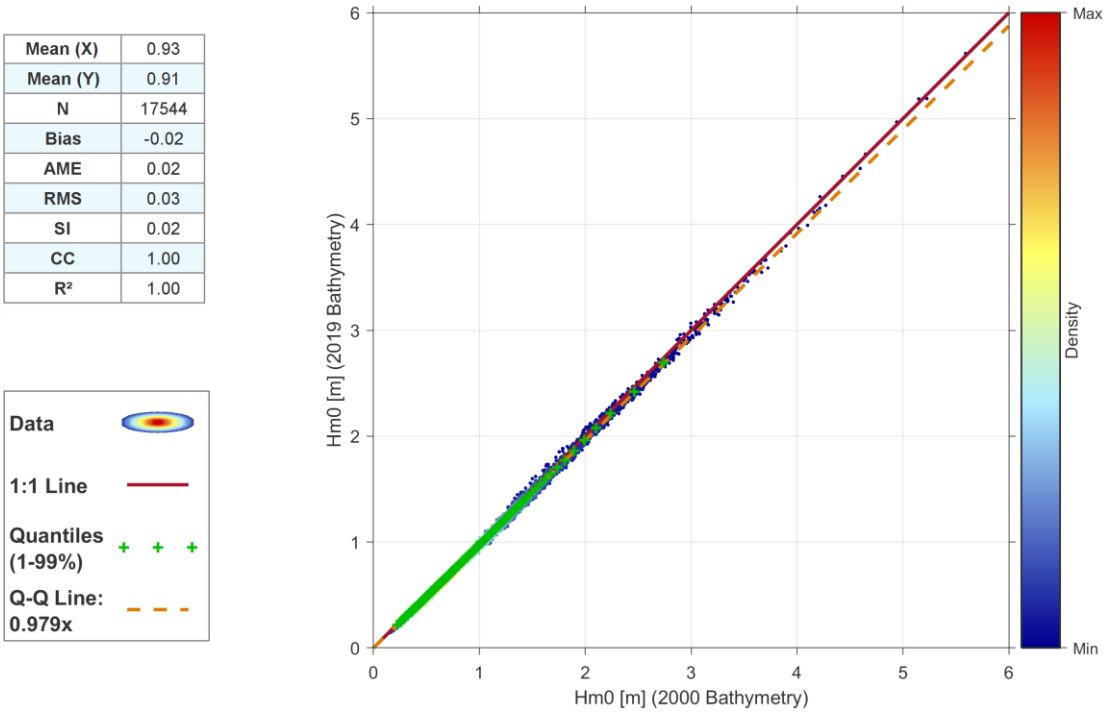



Figure I.26: Hm0, 2019 bathymetry vs 2000 bathymetry, selected locations, R6.

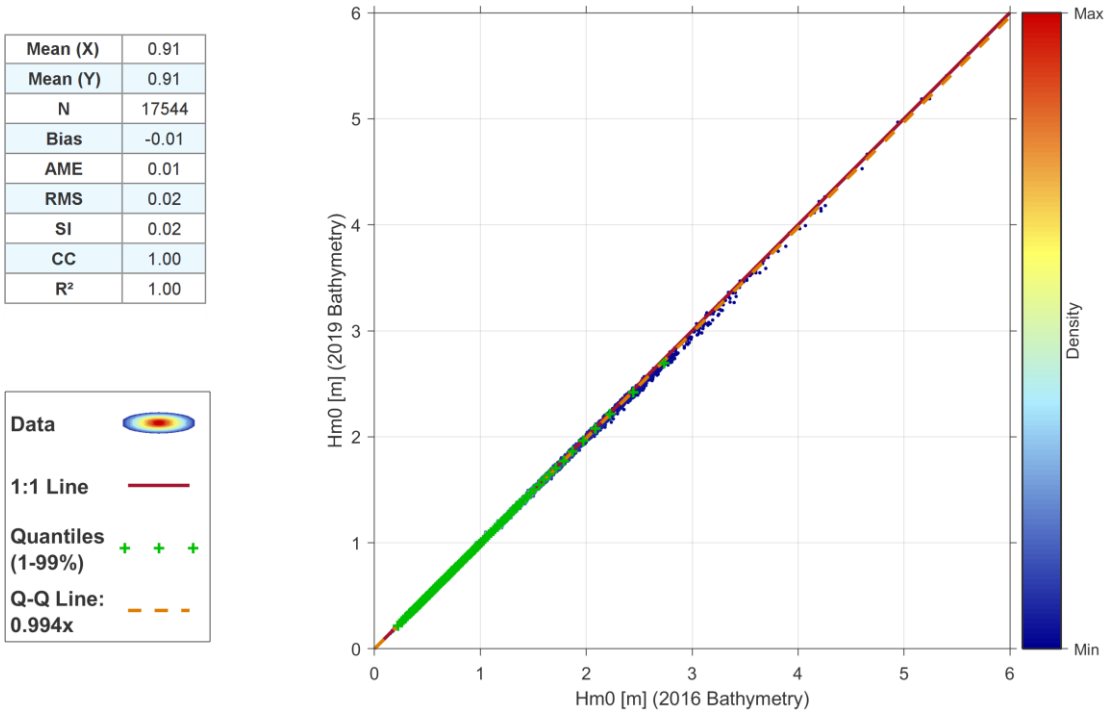



Figure I.27: Hm0, 2019 bathymetry vs 2016 bathymetry, selected locations, R6.

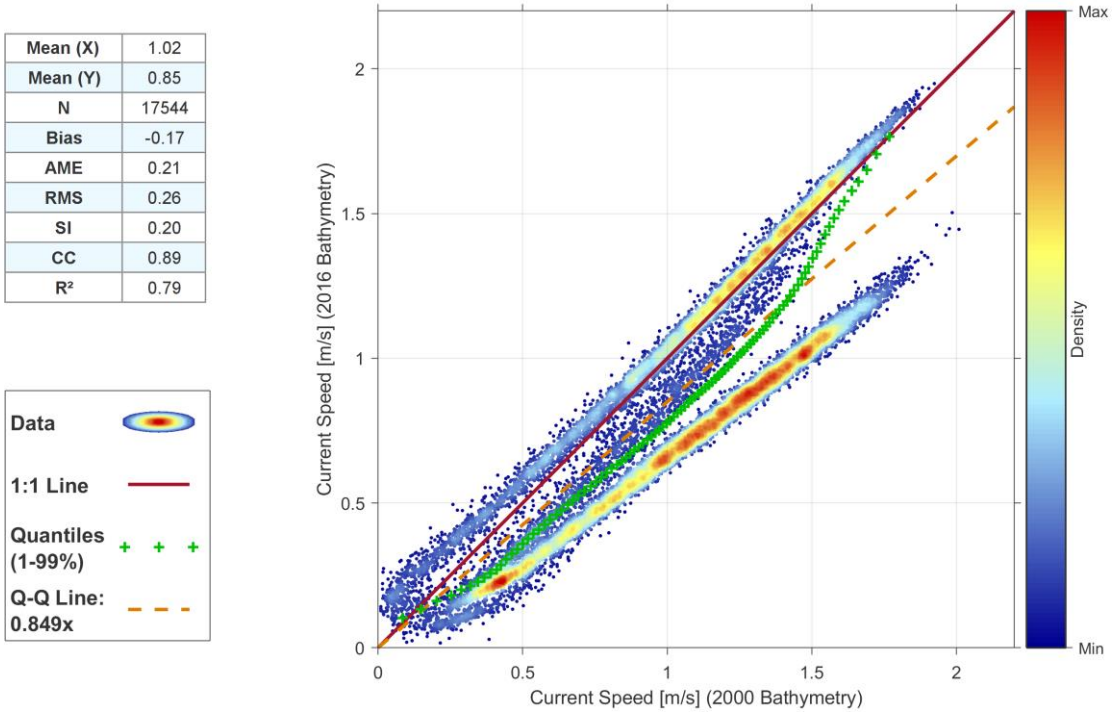



Figure I.28: Current speed, 2016 bathymetry vs 2000 bathymetry, selected locations, R6.

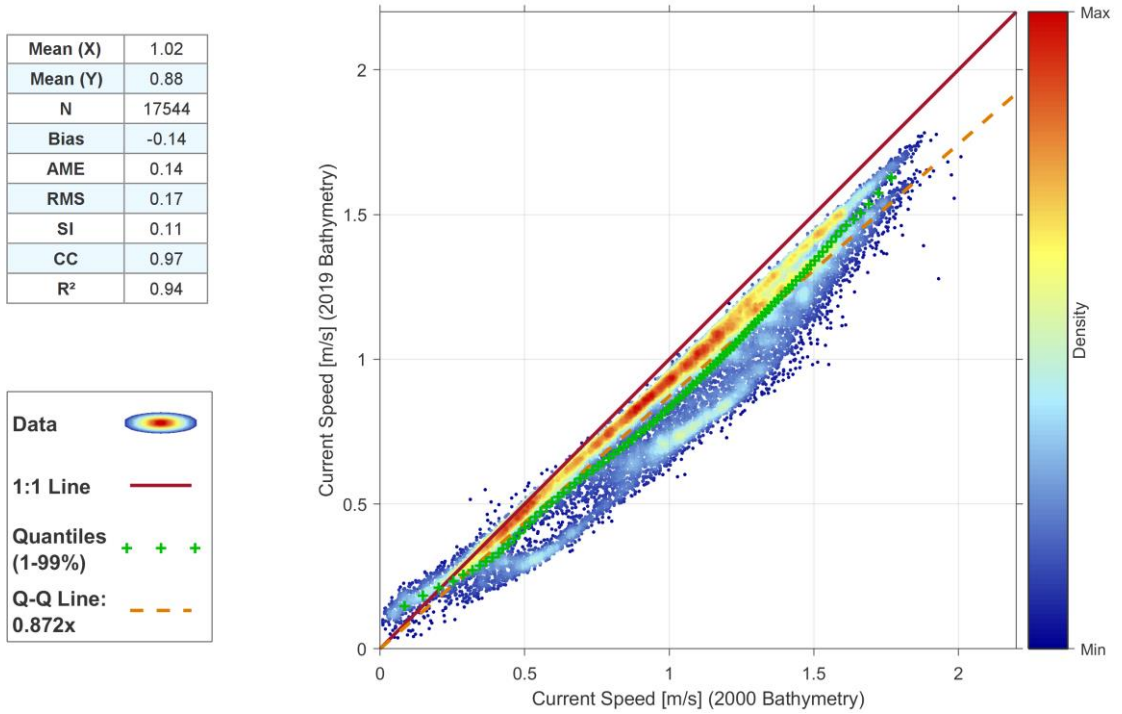



Figure I.29: Current speed, 2019 bathymetry vs 2000 bathymetry, selected locations, R6.

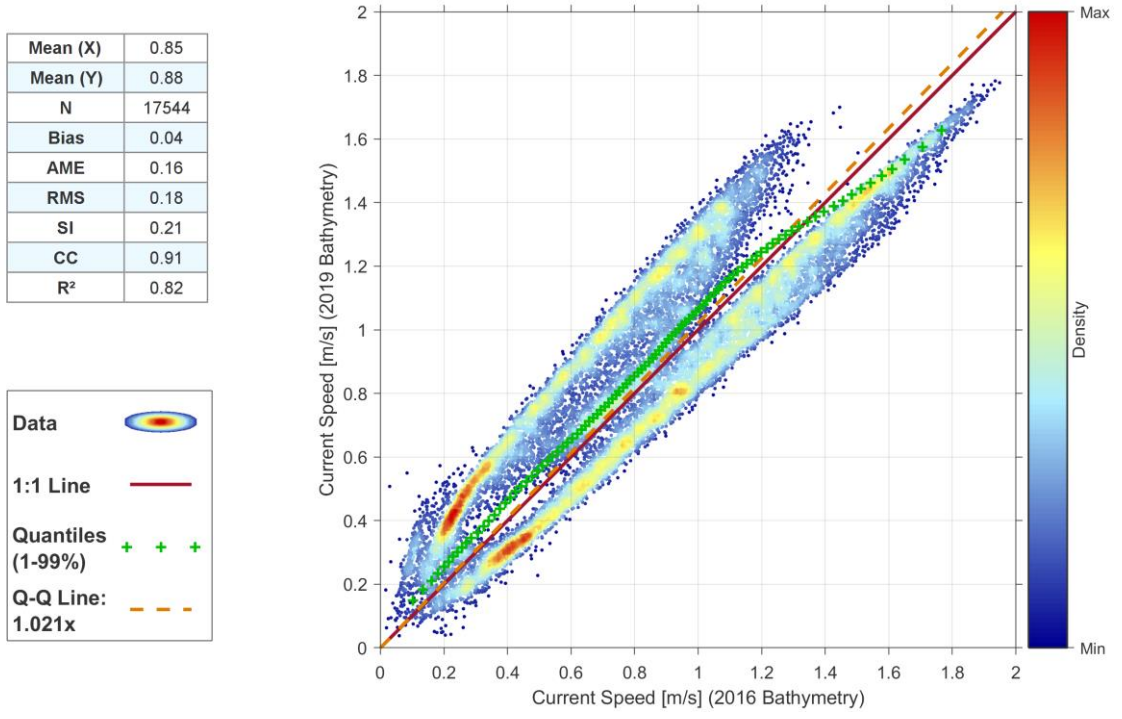



Figure I.30: Current speed, 2019 bathymetry vs 2016 bathymetry, selected locations, R6.

### I.4.3 Comparison Plots, R9

| | |
|---|---|
| Mean (X) | 0.96 |
| Mean (Y) | 0.94 |
| N | 17544 |
| Bias | -0.02 |
| AME | 0.02 |
| RMS | 0.04 |
| SI | 0.03 |
| CC | 1.00 |
| R² | 1.00 |

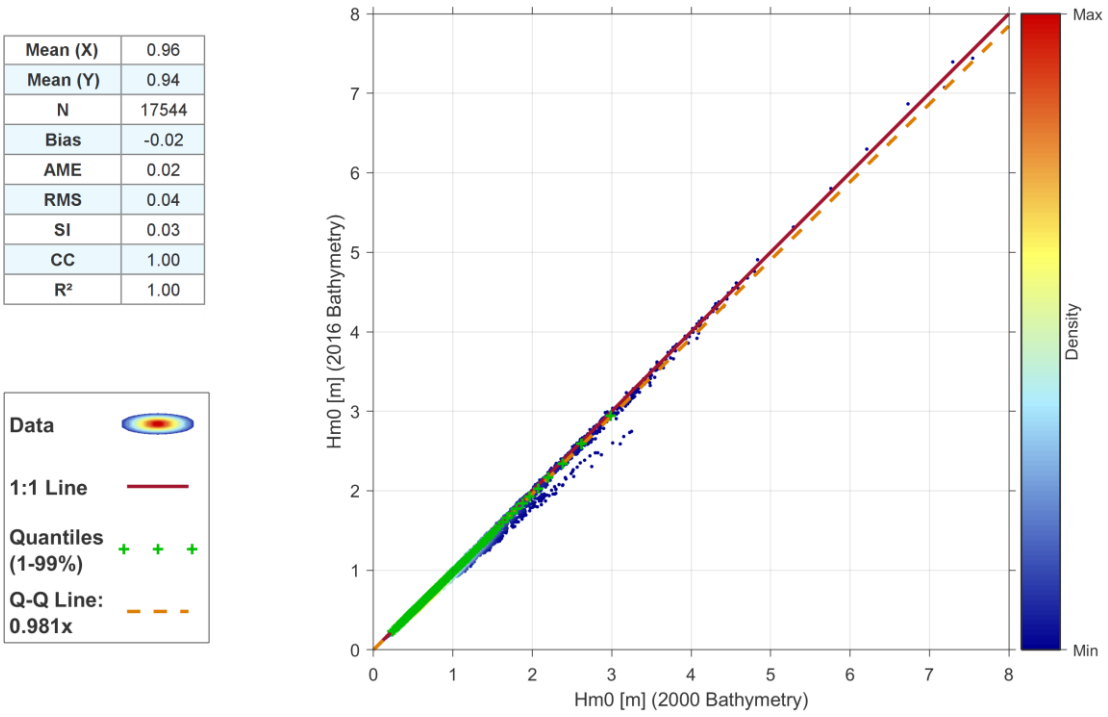



Figure I.31: Hm0, 2016 bathymetry vs 2000 bathymetry, selected locations, R9.

| | |
|---|---|
| Mean (X) | 0.96 |
| Mean (Y) | 0.94 |
| N | 17544 |
| Bias | -0.02 |
| AME | 0.02 |
| RMS | 0.04 |
| SI | 0.03 |
| CC | 1.00 |
| R² | 1.00 |

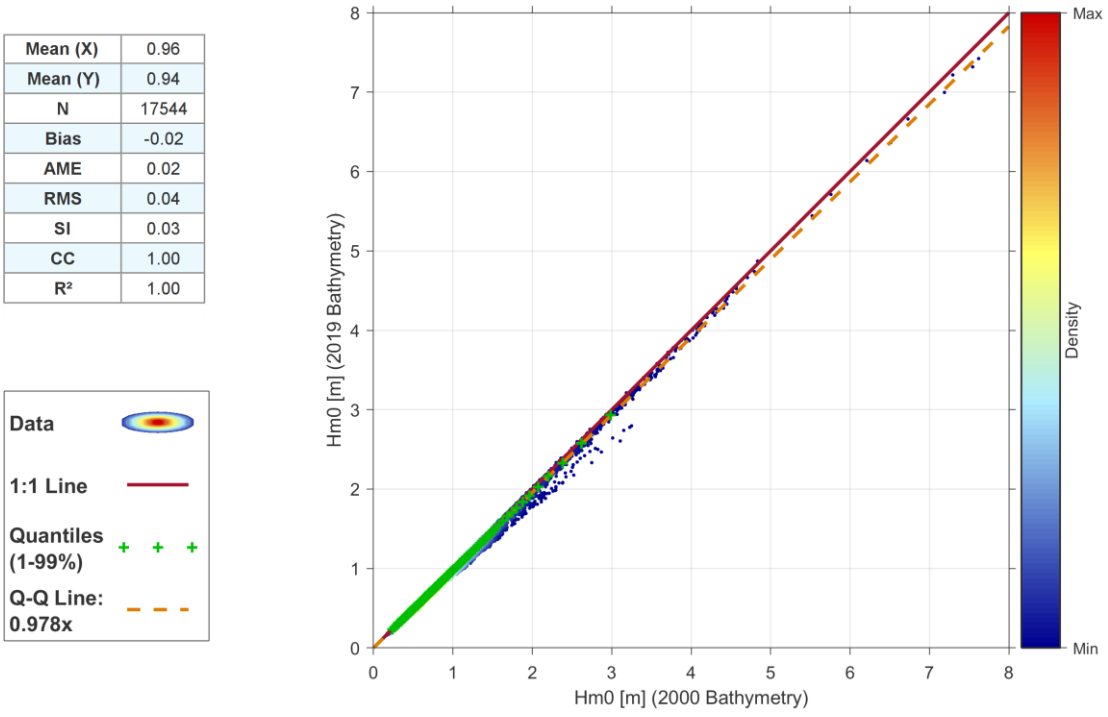



Figure I.32: Hm0, 2019 bathymetry vs 2000 bathymetry, selected locations, R9.

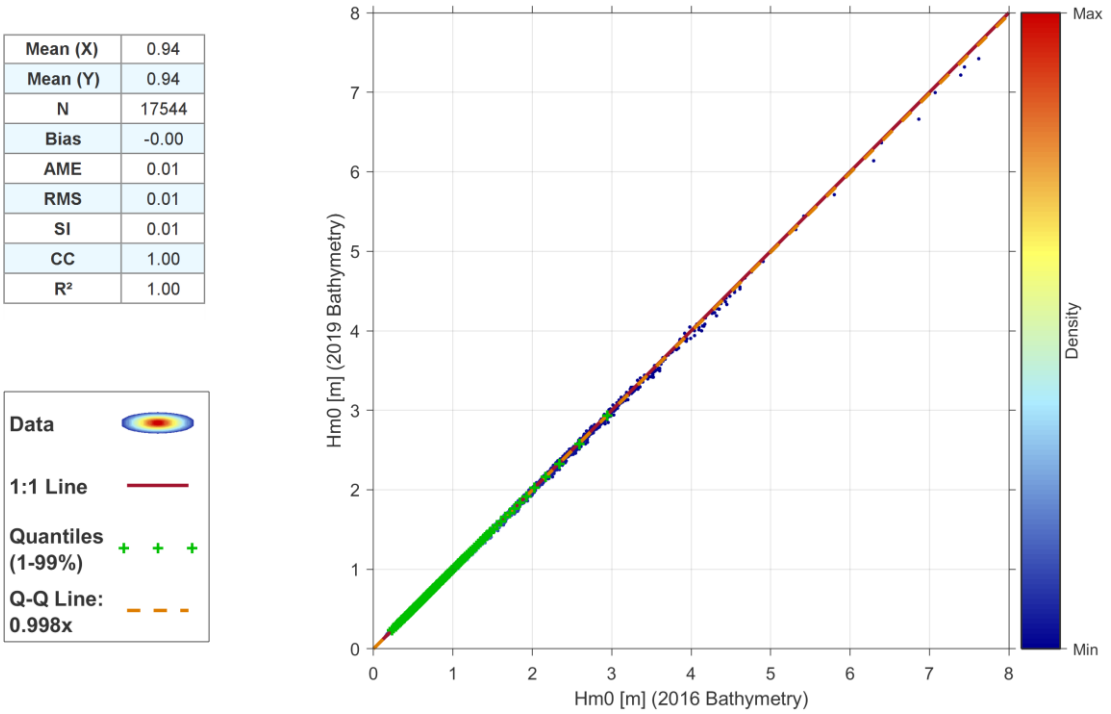



Figure I.33: Hm0, 2019 bathymetry vs 2016 bathymetry, selected locations, R9.

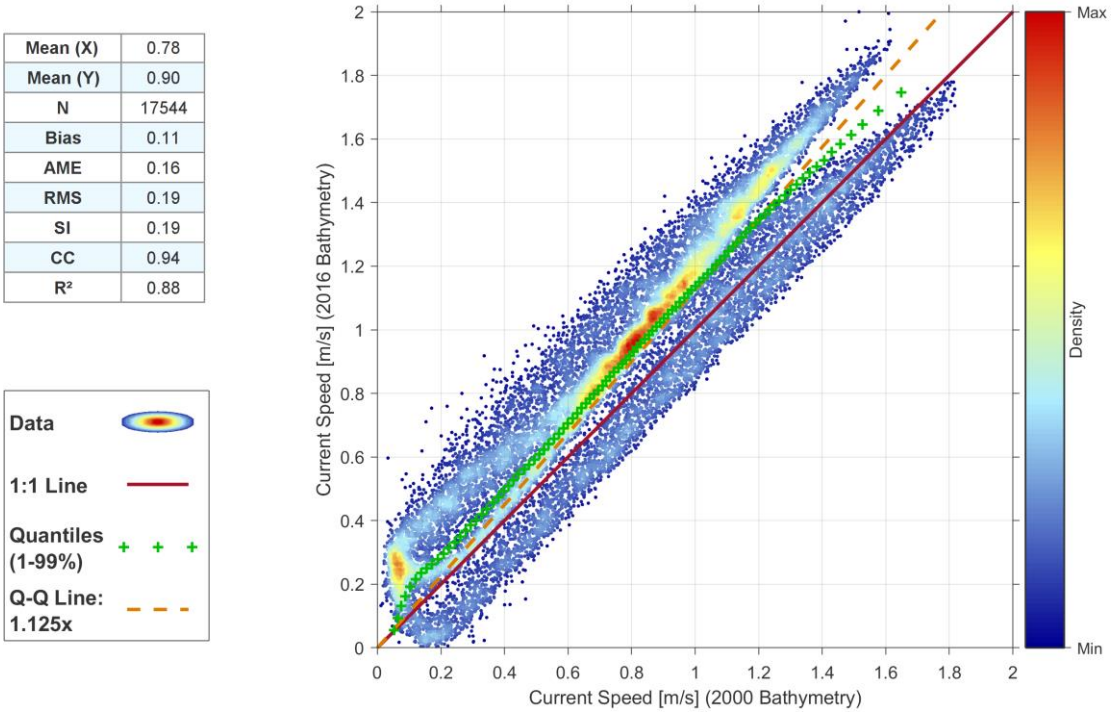



Figure I.34: Current speed, 2016 bathymetry vs 2000 bathymetry, selected locations, R9.

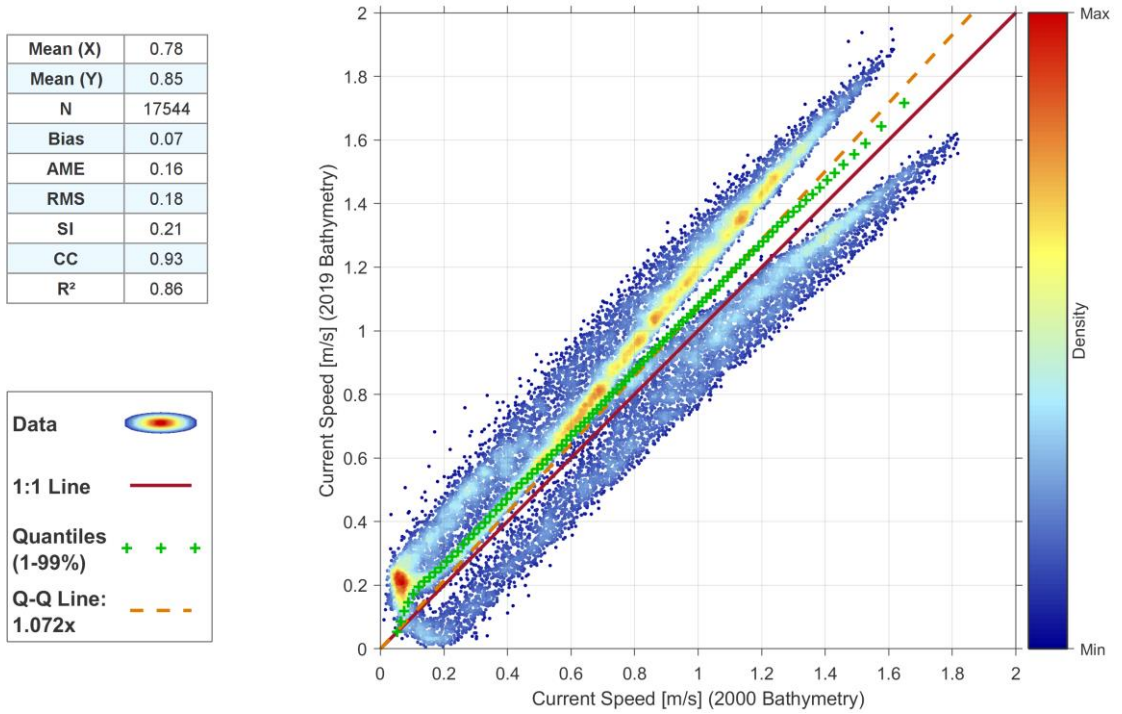



Figure I.35: Current speed, 2019 bathymetry vs 2000 bathymetry, selected locations, R9.

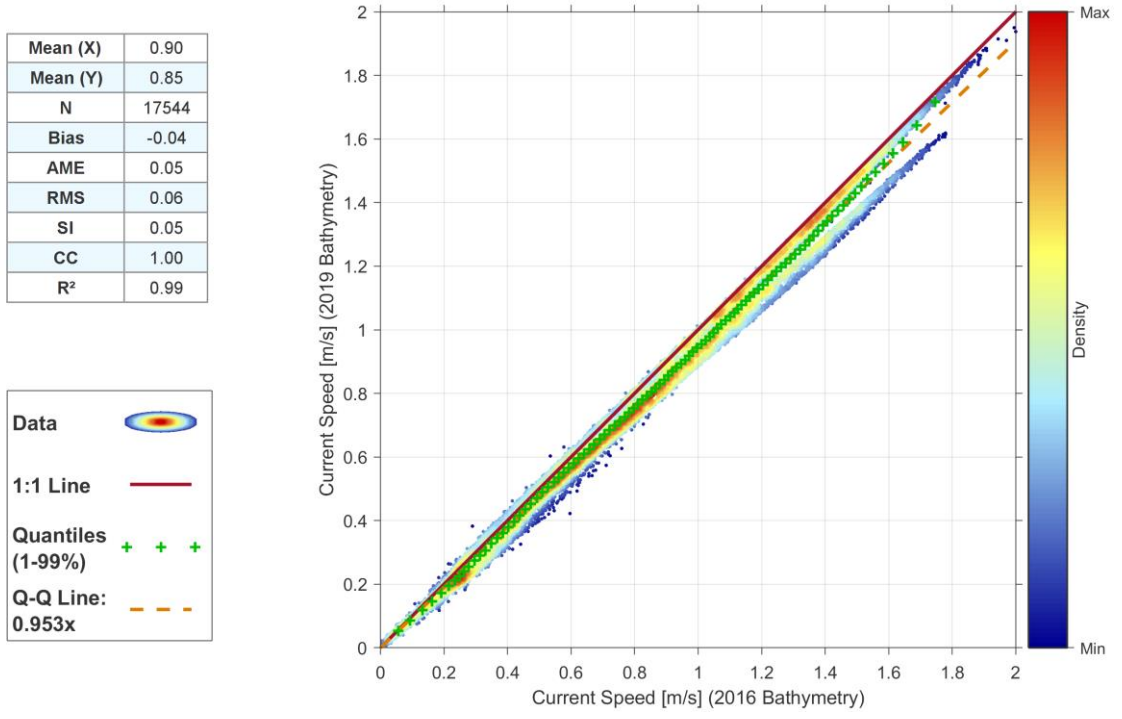



Figure I.36: Current speed, 2019 bathymetry vs 2016 bathymetry, selected locations, R9.